ANL-7310

# Argonne National Laboratory

## REACTOR PHYSICS DIVISION

## ANNUAL REPORT

July 1, 1966 to June 30, 1967

The facilities of Argonne National Laboratory are owned by the United States Government. Under the terms of a contract (W-31-109-Eng-38) between the U. S. Atomic Energy Commission, Argonne Universities Association and The University of Chicago, the University employs the staff and operates the Laboratory in accordance with policies and programs formulated, approved and reviewed by the Association.

MEMBERS OF ARGONNE UNIVERSITIES ASSOCIATION

The University of Arizona
Carnegie-Mellon University
Case Western Reserve University
The University of Chicago
University of Cincinnati
Illinois Institute of Technology
University of Illinois
Indiana University
Iowa State University
The University of Iowa
Kansas State University
The University of Kansas
Loyola University
Marquette University
Michigan State University
The University of Michigan
University of Minnesota
University of Missouri
Northwestern University
University of Notre Dame
The Ohio State University
Ohio University
The Pennsylvania State University
Purdue University
Saint Louis University
Southern Illinois University
The University of Texas at Austin
Washington University
Wayne State University
The University of Wisconsin

**NOTICE**

This report was prepared as an account of work sponsored by the United States Government. Neither the United States nor the United States Atomic Energy Commission, nor any of their employees, nor any of their contractors, subcontractors, or their employees, makes any warranty, express or implied, or assumes any legal liability or responsibility for the accuracy, completeness or usefulness of any information, apparatus, product or process disclosed, or represents that its use would not infringe privately-owned rights.

Printed in the United States of America
Available from
National Technical Information Service
U.S. Department of Commerce
5285 Port Royal Road
Springfield, Virginia 22151
Price: Printed Copy $6.00; Microfiche $0.95

ANL-7310
Reactor Technology (TID-4500)
AEC Research and
Development Report

Argonne National Laboratory
9700 South Cass Avenue
Argonne, Illinois 60439

# REACTOR PHYSICS DIVISION ANNUAL REPORT

## July 1, 1966 to June 30, 1967

Robert Avery, Division Director
Harry H. Hummel, Associate Division Director
W. C. Redman, Associate Division Director
William J. Sturm, Assistant Division Director
Lyman J. Templin, Assistant Division Director

January 1968

# Foreword

This is the fourth successive issue of the Reactor Physics Division Annual Report and, in format, it simulates the preceding report, ANL-7210. As in previous reports, it emphasizes the work performed by members of the Division, rather than the integrated programmatic accomplishments. Nevertheless, when reasonable and possible, papers related to a given subject are grouped together, as for example, the papers concerned with the Argonne Advanced Research Reactor.

In order to assist those who may wish to pursue a given subject more extensively, a list of pertinent references is included in each article. A catalog of open-literature and report publications and of abstracts prepared by staff of the Reactor Physics Division during the reporting period are appended in Section VIII to further aid those who may be interested in having additional information concerning work done in this Division.

# Table of Contents

## SECTION I

## FISSION PROPERTIES AND CROSS SECTION DATA


I-1. Neutron Scattering ..... 3
A. B. SMITH

I-2. Intermediate Structure in Elastic Neutron Scattering ..... 3
S. A. Cox

I-3. Neutron Polarization Measurements ..... 4
S. A. Cox

I-4. Elastic and Inelastic Neutron Scattering from Light and Medium Nuclei ..... 6
A. B. SMITH

I-5. Neutron Scattering from Deformed Even-Even Nuclei ..... 8
G. SHERWOOD[1] and A. B. SMITH

I-6. Fast Neutron Scattering From Tantalum, Rhenium, and Platinum ..... 8
A. B. SMITH, P. T. GUENTHER, R. HAYES and J. F. WHALEN

I-7. Fast Neutron Cross Sections ..... 10
J. F. WHALEN

I-8. The $(n,n'\gamma)$ Process in Germanium ..... 11
D. LISTER and D. STUPEGIA[2]

I-9. Correlation of Mass, Energy, and Angle in Thermal and 6-MeV Neutron Fission of U-235 ..... 13
J. W. MEADOWS

I-10. The $Li^7(p,n)Be^7$ Reaction ..... 17
D. LISTER and E. F. BENNETT

I-11. Theory of Resonance Reactions ..... 18
P. A. MOLDAUER

I-12. Theory of T-Violating Reactions ..... 18
P. A. MOLDAUER

I-13. Cross Section for $Ne^{21}(n_{th},\alpha)O^{18}$ ..... 19
E. F. BENNETT and W. C. REDMAN

I-14. Spontaneous Fission Half-Life of Am-241 ..... 20
R. GOLD, R. J. ARMANI and J. ROBERTS[3]

I-15. Compilation of ENDF/B Cross Sections for Magnesium, Titanium, Vanadium, Molybdenum and Gadolinium ..... 22
E. M. PENNINGTON


## SECTION II

## THERMAL REACTOR PHYSICS


II-1. High Conversion (Hi-C) Uniform Lattice Calculations ..... 33
E. M. PENNINGTON

II-2. Concluding Pre-Irradiation Critical Experiments of the Experimental Boiling Water Reactor (EBWR) Plutonium Recycle Experiment ..... 35
P. H. KIER


[1] Student, Northwestern University, Evanston, Illinois.
[2] Chemical Engineering Division, Argonne National Laboratory.
[3] Northwestern University, Evanston, Illinois.

II-3. Power Operation of the Experimental Boiling Water Reactor (EBWR) During the Plutonium Recycle Experiment ..... 38
P. H. KIER

II-4. Measurement of Capture-to-Fission Ratio of Pu-239 and Pu-241 in the Plutonium Loading of the Experimental Boiling Water Reactor (EBWR) ..... 39
H. P. ISKENDERIAN

II-5. Physics of Plutonium-Fueled Thermal Research and Test Reactors ..... 42
C. N. KELLER

II-6. Argonne Advanced Research Reactor Critical Experiments—Mockup Experiments and Critical Experiments with Stainless Steel Core ..... 45
K. E. PLUMLEE, J. W. DAUGHTRY, T. W. JOHNSON, W. R. ROBINSON, R. A. SCHULTZ and G. S. STANFORD

II-7. Argonne Advanced Research Reactor Critical Experiments—Absolute Peak Thermal Flux in the Internal Thermal Column ..... 52
G. S. STANFORD and W. R. ROBINSON

II-8. Argonne Advanced Research Reactor Critical Experiments—Activation and Power Distribution Measurements ..... 57
W. R. ROBINSON and G. S. STANFORD

II-9. Argonne Advanced Research Reactor Critical Experiments—Neutron Temperature in the Internal Thermal Column and Reactivity Worths of Samples and Voids ..... 63
K. E. PLUMLEE, W. R. ROBINSON and T. W. JOHNSON

II-10. Argonne Advanced Research Reactor Critical Experiments—Reactivity Worths Obtained by Traversing Small Samples in the Critical Facility ..... 69
J. W. DAUGHTRY

II-11. Argonne Advanced Research Reactor Critical Experiments—Measurements of Control and Safety Enhancement Devices ..... 71
K. E. PLUMLEE, T. W. JOHNSON, F. H. MARTENS and W. R. ROBINSON

II-12. Argonne Advanced Research Reactor Critical Experiments—Beam Tube Yield and Reactivity Worth Measurements ..... 74
T. W. JOHNSON and K. E. PLUMLEE

II-13. Argonne Advanced Research Reactor Critical Experiments—Neutron Flux Distribution Measurements with Mocked-Up Pressure Vessel, Beam Tube, and Shroud ..... 77
K. E. PLUMLEE, J. W. ARMSTRONG and R. A. SCHULTZ

II-14. Argonne Advanced Research Reactor Critical Experiments—Determination of Gamma-Ray Heating by Thermoluminescent Dosimetry ..... 82
G. S. STANFORD and T. W. JOHNSON

II-15. Argonne Advanced Research Reactor Critical Experiments—Rossi-Alpha and Pulsed Neutron Measurements ..... 84
J. W. DAUGHTRY

II-16. Argonne Advanced Research Reactor Critical Experiments—Improved Neutron Cross Section for Formation of 60-Day Half-Life Sb-124 ..... 88
K. E. PLUMLEE

II-17. Argonne Advanced Research Reactor Calculations—Preface ..... 92
D. H. SHAFTMAN

II-18. Argonne Advanced Research Reactor Calculations—Analysis of Critical Experiments with the Intermediate-Spectrum Core ..... 94
R. P. SAVIO[4] and D. H. SHAFTMAN

II-19. Argonne Advanced Research Reactor Calculations—General Reactor Physics Design Analysis ..... 99
D. H. SHAFTMAN and R. P. SAVIO[4]

II-20. Argonne Advanced Research Reactor Calculations—Spatial and Energy Distributions of Thermal Neutron Flux in the Internal Thermal Column ..... 107
R. P. SAVIO,[4] D. H. SHAFTMAN and L. K. VOLODKA

[4] Reactor Operations Division, Argonne National Laboratory.

II-21. Argonne Advanced Research Reactor Calculations—General Shield-Design Analysis. 113
A. E. McArthy, D. H. Shaftman and I. Charak[5]
II-22. Argonne Advanced Research Reactor Calculations—Analyses of Accidents Associated with Major Reactivity Insertions. 119
D. H. Shaftman and J. H. Tessier[5]
II-23. Argonne Advanced Research Reactor Calculations—Analysis of Biological Doses from Maximum Credible Accident. 124
D. H. Shaftman and H. Moses[6]

## SECTION III
## FAST REACTOR PHYSICS

III-1. Analysis of Small-Sample Doppler-Effect Measurements. 139
R. A. Lewis and C. E. Till
III-2. Fissile Doppler Effect Measurement and the Effects of Thermal Expansion. 143
C. E. Till
III-3. U-235 Doppler Effect Measurement Data and Techniques. 151
C. E. Till, R. A. Lewis and E. F. Groh
III-4. Doppler Effect Measurements in $CH_2$-Softened Spectra; ZPR-9 Assemblies 13–17. 159
R. Pond and C. E. Till
III-5. Comparison and Analysis of Theoretical Doppler Coefficient Results for Fast Reactors. 163
R. N. Hwang and K. Ott[7]
III-6. Measured Physics Parameters in a Large Uranium Carbide Fast Core, Assembly 5 of ZPR-6. 167
R. A. Karam, L. R. Dates, E. Groh, W. Y. Kato, R. A. Lewis, G. Main, J. E. Marshall, G. K. Rusch and C. Till
III-7. Note on Worth Ratios in Zoned Versus Full Size Critical Assemblies. 189
D. A. Meneley
III-8. ZPR-9 Assemblies 11 and 12—Two Small Zoned Versions of the 2600-Liter Assembly 5 ZPR-6. 190
R. A. Lewis, L. G. LeSage and R. A. Karam
III-9. The Effect of Sodium Voiding on the Spectrum of ZPR-6 Assembly 5. 196
E. F. Bennett
III-10. Experimental Neutron Spectrum Comparison of a Zoned and a Homogeneous Fast Critical Assembly. 198
E. F. Bennett
III-11. A Review of Data Pertaining to Spectral Equilibration and Spectral Matching in Zoned Cores. 199
L. G. LeSage, R. A. Karam, R. A. Lewis, E. F. Bennett and G. W. Main
III-12. A Simple Flux-Synthesis Method for the Calculation of the Sodium-Void Effect in Reflected Single-Zone Fast Breeder Reactors. 205
A. Travelli
III-13. Two-Dimensional Study of Voiding of Sodium from a Fast Reactor Core with Zoned Enrichment. 209
V. Z. Jankus and H. H. Hummel
III-14. Calculational Studies of Sodium-Void Reactivity Variations Due to Heterogeneities in Fast Control Assemblies. 212
D. Meneghetti
III-15. Heterogeneity Effects on the Reactivity of ZPR-6 Assembly No. 3. 216
D. Meneghetti

[5] Reactor Engineering Division, Argonne National Laboratory.
[6] Radiological Physics Division, Argonne National Laboratory.
[7] Purdue University, Lafayette, Indiana.

III-16. Pulsed Neutron Measurements on ZPR-6, Assembly No. 5 ..... 217
F. H. HELM
III-17. Nuclear Analysis Methods Development for EBR-II ..... 223
D. KUCERA, J. T. MADELL and P. J. PERSIANI
III-18. Multigroup Cross Section Sets for Neutronic Calculations of EBR-II ..... 223
J. T. MADELL
III-19. Investigation of the Temperature Coefficient of EBR-II, Run 25 ..... 228
J. T. MADELL
III-20. Some Effects of Iron, Molybdenum, and Nickel Reflectors Placed Between the Core and Blanket of EBR-II ..... 230
J. T. MADELL
III-21. Development of the Critical Experiment Program for the Fast Fuels Test Facility .. 232
P. J. PERSIANI, J. K. LONG, A. J. ULRICH and D. A. KUCERA
III-22. Theoretical Study of the ZPR-3 Critical Experiments in Support of the Fast Fuels Test Reactor Concept ..... 238
A. J. ULRICH, P. J. PERSIANI and J. C. BEITEL
III-23. The Critical Experiments and Preliminary Analysis of Multifueled, Nonuniform Core Loadings ..... 241
P. J. PERSIANI, A. L. HESS[8] and D. KUCERA
III-24. Physics Studies of Molten-Salt-Fueled Fast Reactor Systems ..... 242
D. K. BUTLER[9] and D. MENEGHETTI
III-25. Preliminary Study of the Use of U-235 in a Fast Reactor Era ..... 242
K. A. HUB[10] and V. Z. JANKUS

## SECTION IV
## FAST REACTOR SAFETY

IV-1. Initial (7-Pin) EBR-II Cluster Fast Reactor Safety Integral Loop Experiments in the Transient Reactor Test (TREAT) Facility ..... 251
L. E. ROBINSON, C. E. DICKERMAN and F. L. WILLIS
IV-2. Analyses and Significance of Initial EBR-II Mark I Cluster Fast Reactor Safety Integral Loop Experiments in the Transient Reactor Test Facility (TREAT) ..... 255
C. E. DICKERMAN, R. PURVIANCE and A. B. COHEN
IV-3. Fast Reactor Safety Integral Loop Experiment on an Argon-Bonded EBR-II Pin .. 258
C. E. DICKERMAN, F. L. WILLIS, R. SMITH and A. B. COHEN
IV-4. Properties of 6 a/o Burnup Oxide Fast Reactor Fuel Pins Prior to Transient Reactor Test (TREAT) Facility Exposure ..... 260
R. STEWART, C. E. DICKERMAN, W. DOE[11] and N. STALICA[12]
IV-5. Results from Transient Reactor Test (TREAT) Facility Fast Reactor Oxide Fuel Pin ..... 276
C. E. DICKERMAN and R. STEWART
IV-6. Hybrid Computer Program for Transient Temperature Calculations of Transient Reactor Test (TREAT) Facility Fast Reactor Safety Experiments ..... 280
L. T. BRYANT,[13] L. W. AMIOT,[13] C. E. DICKERMAN and W. P. STEPHANY[14]
IV-7. Design of the Glovebox Facility for the Transient Reactor Test (TREAT) Facility Loop and Capsule Operations with Plutinium-Bearing Samples ..... 281
C. E. DICKERMAN, L. E. ROBINSON and R. IVINS[15]

[8] Idaho Division, Argonne National Laboratory.
[9] Liquid Metal Fast Breeder Reactor Program Office, Argonne National Laboratory.
[10] Reactor Engineering Division, Argonne National Laboratory.
[11] Remote Control Division, Argonne National Laboratory.
[12] Chemical Engineering Division, Argonne National Laboratory.
[13] Applied Mathematics Division, Argonne National Laboratory.
[14] Student, University of Michigan, Ann Arbor, Michigan.
[15] Liquid Metal Fast Breeder Reactor Program Office, Argonne National Laboratory.

IV-8. Remotely Operated Sodium Extruder Facility for Inert Atmosphere Glove Box... 282
C. AUGUST and L. E. ROBINSON

IV-9. Extended Capability for the Fast Neutron Hodoscope Used at the Transient Reactor Reactor Test (TREAT) Facility... 284
A. DEVOLPI, R. PECINA,[16] C. H. FREESE,[16] E. ROLNICKI,[16] D. TRABIS[16] and G. LARSEN[17]

IV-10. Instrumentation and Control of the Mark II Integral Sodium Transient Reactor Test Facility (TREAT)... 289
L. E. ROBINSON, R. PURVIANCE and K. SCHMIDT

IV-11. Development of a Family of Annular Linear Induction Pumps for Use in Fast Reactor Safety Integral Loop Experiments... 291
R. CARLSON[18] and L. ROBINSON

IV-12. Conversion of the Transient Reactor Test (TREAT) Facility for Testing Fast Fuel Subassemblies... 295
H. P. ISKENDERIAN

IV-13. Fast Reactor Accident Analysis Through Computer Program Development... 299
J. C. CARTER, G. J. FISCHER, T. HEAMES, D. R. MACFARLANE, N. A. MCNEAL, C. K. SANATHANAN, W. T. SHA and C. K. YOUNGDAHL[18]

IV-14. Transient Vaporization of Sodium in Reactor Coolant Channels... 300
D. R. MACFARLANE

IV-15. Theoretical Studies of the Response of Fast Reactors During Sodium Boiling Accidents... 310
D. R. MACFARLANE, N. A. MCNEAL, D. A. MENELEY and C. K. SANATHANAN

IV-16. Heat Transfer Computation for Ceramic Fuels Undergoing Reactor Transients... 317
C. K. SANATHANAN and N. A. MCNEAL

IV-17. Convective Heat or Mass Transfer with Phase Changes... 320
J. KAELLIS,[18] D. MILLER and D. T. WASAN[19]

IV-18. Heat Fraction in Coolant and Fuel During Transient Heating... 322
R. O. BRITTAN and H. GREENSPAN[20]

IV-19. Fuel Element Deformation Program for the Fast Reactor Safety Analysis System... 324
C. K. YOUNGDAHL[18]

IV-20. Reactor Stability Considerations In Safety Analysis... 328
J. H. TESSIER,[18] D. W. SPARKS[18] and J. C. CARTER

IV-21. Properties of Alkali Metals... 334
D. MILLER, A. B. COHEN and C. E. DICKERMAN

IV-22. Physical Properties of Solids and Liquids Under Extreme Conditions... 335
D. MILLER

IV-23. Physical Properties of Uranium Monocarbide at the Melting Temperature and in the Liquid State... 339
H. K. RICHARDS

IV-24. Comparison of Methods for Determining Containment Leakage Rates... 343
R. O. BRITTAN

IV-25. A Proposed Core Test Facility for Safety Analysis... 351
J. C. CARTER

IV-26. Calculation of the Energy Yield in the Kiwi Transient Nuclear Test, Kiwi-TNT... 363
V. Z. JANKUS

IV-27. Qualitative Consideration of a Nuclear Excursion Initiated by a Shock Wave... 370
V. Z. JANKUS

[16] Electronics Division, Argonne National Laboratory.
[17] Idaho Division, Argonne National Laboratory.
[18] Reactor Engineering Division, Argonne National Laboratory.
[19] Illinois Institute of Technology, Chicago, Illinois.
[20] Applied Mathematics Division, Argonne National Laboratory.

## SECTION V

## EXPERIMENTAL PHYSICS TECHNIQUES AND FACILITIES

V-1. Preparation of Pu-239 and Pu-241 Isotopes for Capture-to-Fission Measurements in the Experimental Boiling Water Reactor ..... 379
R. J. ARMANI

V-2. Accurate Fission Rate Measurements by Fission Track Counting ..... 380
R. J. ARMANI, R. GOLD and J. H. ROBERTS[21]

V-3. Experience with a New Manganese Bath System ..... 383
A. DEVOLPI and K. PORGES

V-4. Transport of Decaying Activity Through Laminar and Turbulent Flow Systems ..... 386
K. PORGES

V-5. Note on the Design Logic of Transient Detection Systems ..... 389
K. PORGES

V-6. Time Resolution in NaI Scintillator-Junction Detector Fast Coincidence Systems ..... 393
K. PORGES and R. GOLD

V-7. Versatile Gated Discriminator with Adjustable Paralysis Useful in Fast-Slow Coincidence Experiments ..... 396
A. DEVOLPI, J. J. ENGLISH,[22] A. J. METZ,[22] K. PORGES and S. J. RUDNICK[22]

V-8. A Monitor for Airborne Plutonium Contamination ..... 399
W. G. KNAPP

V-9. Further Development of the DDP-24 Computer System ..... 402
C. E. COHN

V-10. Experiments in the Computer Control of Critical Assemblies ..... 408
C. E. COHN

V-11. Study of a Linearized Sampled-Data Control Algorithm for Zero-Power Reactors ..... 410
T. J. MARCINIAK[23]

V-12. Fast-Reactor Noise Analysis by Polarity Cross Correlation ..... 415
C. E. COHN

V-13. The Integrating Sampler ..... 420
C. E. COHN

V-14. Progress in On-Line Computer Utilization ..... 423
J. F. WHALEN

V-15. A Multiplexing System for an On-Line Computer ..... 424
J. F. WHALEN and J. W. MEADOWS

V-16. Remote Station for On-Line Computer Control ..... 425
J. F. WHALEN and J. J. EICHHOLZ[24]

V-17. Design of the Fast Neutron Generator Facility Building ..... 426
J. W. MEADOWS

V-18. A High Intensity Gas Target ..... 427
J. W. MEADOWS

V-19. Electrostatic Analyzer for Accelerator Energy Control ..... 428
S. A. COX

V-20. Neutron Precession Solenoid ..... 429
S. A. COX

V-21. Rotary Time-of-Flight Collimators ..... 429
A. B. SMITH

V-22. Pulsed and Bunched Ion Source ..... 430
A. B. SMITH

---

[21] Northwestern University, Evanston, Illinois.
[22] Electronics Division, Argonne National Laboratory.
[23] Student, University of Notre Dame, Notre Dame, Indiana.
[24] Electronics Division, Argonne National Laboratory.

## SECTION VI

## REACTOR COMPUTATION METHODS AND THEORY

VI-1. The Argonne Reactor Computation (ARC) System ..... 433
B. J. TOPPEL
VI-2. Further Development of the MC² Code ..... 436
B. J. TOPPEL, H. H. HUMMEL, R. N. HWANG and A. L. RAGO[25]
VI-3. Generation of Multigroup Cross Sections Using a Coupled MC²-THERMØS Code ..... 437
D. A. SARGIS, B. J. TOPPEL and A. L. RAGO[25]
VI-4. Fortran Codes for Processing Neutron Cross Section Data ..... 442
E. M. PENNINGTON, J. C. GAJNIAK and W. BOHL[26]
VI-5. ADRIFT, A Code to Compute Bilinearly-Weighted Absorption Cross Sections ..... 444
P. H. KIER
VI-6. RABBLE and RABZPR: Two Codes to Compute Resonance Absorption in Multi-Composition Reactor Cells ..... 445
P. H. KIER
VI-7. The Present Status of the Unresolved Parameters for U-235, Pu-239 and U-238 ..... 450
R. N. HWANG and A. TRAVELLI
VI-8. The Crystalline Effects on the Doppler-Broadened Cross Section and Resonance Integrals of Urnaium in a $UO_2$ Lattice ..... 462
C. R. ADKINS,[27] P. J. PERSIANI and R. N. HWANG
VI-9. Comparative Physics Analysis of Fast Reactor as a Function of Refinement in Multigroup Cross Section Preparation ..... 463
B. J. TOPPEL and H. H. HUMMEL
VI-10. Effects of Cross Section Errors on Neutron Spectra ..... 466
C. N. KELBER
VI-11. Calculations of Detailed Neutron Fluxes Across Interfaces Between Resonance-Scattering Media ..... 467
D. MENEGHETTI, A. L. RAGO[28] and K. E. PHILLIPS
VI-12. Space-Time Kinetics—The QX1 Code ..... 471
D. A. MENELEY, K. OTT[29] and E. S. WIENER
VI-13. Space Dependent Effects on Fast-Thermal System Parameters ..... 476
C. N. KELBER and J. T. MADELL
VI-14. Two-Group Space-Dependent Kinetics In Reflected Reactors ..... 480
R. A. KARAM
VI-15. PROGRAM MOVER: Point Kinetics Algorithm ..... 492
L. K. VOLODKA
VI-16. Fast Reactor Fuel Cycle Studies—Formulation and Solution Methods ..... 493
D. A. MENELEY, G. K. LEAF[28] and P. M. WALKER[28]
VI-17. Intercomparison of Various Multigroup Transport Approximations of the Dispersion Law of Neutron Waves ..... 501
A. TRAVELLI
VI-18. Orthogonal Polynomial Solutions and Error Estimates for Eigenvalues to the Integral Transport Equation ..... 504
D. A. SARGIS
VI-19. A Directed-Search Subroutine for Finding Minima ..... 507
G. S. STANFORD

---

[25] Applied Mathematics Division, Argonne National Laboratory.
[26] Student, University of Wisconsin, Madison, Wisconsin.
[27] Carnegie Institute of Technology, Pittsburgh, Pennsylvania.
[28] Applied Mathematics Division, Argonne National Laboratory.
[29] Purdue University, Lafayette, Indiana.

## SECTION VII

## MISCELLANEOUS

VII-1. Nuclear Pumped Carbon Dioxide Gas Laser—Model I Experiments ..... 515
J. A. DeShong, Jr.
VII-2. Analysis of Plasma Ion Frequency in Low Pressure Alkali Metal Vapor Thermionic Conversion Cells ..... 517
H. K. Richards
VII-3. Experimental Investigation of Electrical Conduction Through Noble Gases at High Temperatures ..... 519
H. K. Richards
VII-4. Radiocarbon Production Rate Near Sea Level ..... 521
R. Gold
VII-5. Energy Spectrum of Fast Cosmic Ray Neutrons Near Sea Level ..... 522
R. Gold

## SECTION VIII

## PUBLICATIONS AND REPORTS, REACTOR PHYSICS DIVISION (July 1, 1966 to June 30, 1967)

Open Literature ..... 523
Reports ..... 525
Abstracts ..... 526

# Section I

# Fission Properties and Cross Section Data

In close support of the reactor program, experimental and theoretical studies of neutron interactions with those nuclei found in the structural and fuel components of reactor systems continue to be carried out. This work is performed prinicpally to provide information necessary for optimal reactor physics design. The major portion of this effort is devoted to studies of fast neutron induced processes, especially those which are important in fast reactors. The studies are directed toward neutron elastic and inelastic scattering, neutron induced reactions including capture, and to the characteristics of the fission processes.

# I-1. Neutron Scattering

A. B. Smith

## Introduction

It is the objective of the neutron scattering studies to: a) meet specific and current needs of the reactor development program for neutron scattering data, b) obtain information relevant to the future needs of the reactor program, c) provide support information necessary for measurements in direct response to reactor needs, and d) establish the experimental foundation necessary for the extrapolation and interpolation of measured quantities to unmeasurable data requisite to the reactor program.

# I-2. Intermediate Structure in Elastic Neutron Scattering

S. A. Cox

During the last several years, a large body of experimental information bearing on intermediate structure has been accumulated. The widths associated with this structure lie between the very broad single particle levels (~1 MeV) and the fine structure associated with the many resonances of the compound nucleus (~1 keV). In light and intermediate weight nuclei ($A < 100$) the observed fluctuations have widths of ~100 keV. The question no longer is: does intermediate structure exist?, but rather what is the source of the intermediate structure? Several possible explanations for intermediate structure have been proposed. The most prominent are the Doorway State theory of H. Feshbach, A. Kerman and R. Lemmer,[1] the vibrational state theory of A. Lande and G. Brown,[2] and theories based on the statistical model.[3]

Results of elastic neutron scattering measurements were reported previously[4] and discussed in terms of the several models. The conclusion was that the results, which covered the mass range $50 < A < 140$, were qualitatively consistent with the doorway state theory. Of the several suggested explanations offered in Ref. 4, the only one which could be ruled out is the one based on a chance distribution in level density. Since the previous report, the data have been analyzed in more detail in order to check another of the predictions of the doorway state theory which states that the fluctuation amplitude shall be largest near the peaks in the strength function and near positions of shell closure. The analysis proceeded as follows: The cross section was fitted by least squares to a quadratic series to generate an "average" cross section from which deviations could be calculated. The rms deviations of the cross section from the "average" cross section were then calculated for the full energy range of the data. The same procedure was also applied to the Legendre polynomial expansion coefficients, $B_L$, which occur in the expression for the differential cross sections; that is,

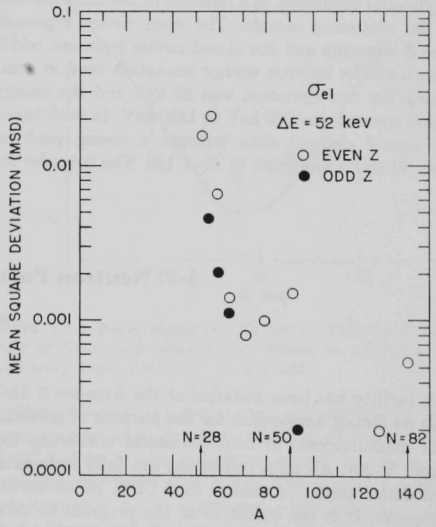


Fig. I-2-1. Mean Square Deviation of $\sigma_{el}$ from $\bar{\sigma}_{el}$. *ANL Neg. No. 112-9097.*

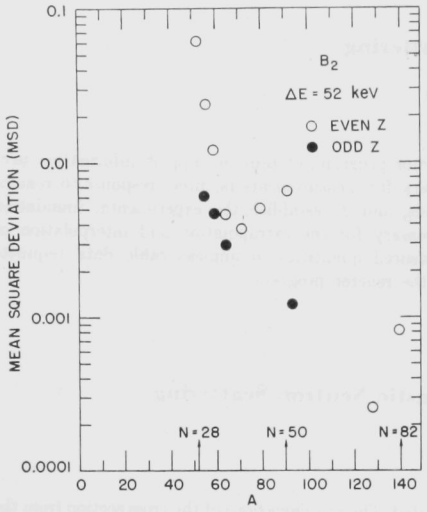


FIG. I-2-2. Mean Square Deviation of Second Order Legendre Polynomial Coefficient ($B_2$) from $\bar{B}_2$. *ANL Neg. No. 112-9096.*

$$\sigma_{el}(\theta) = \sum B_L P_L (\cos \theta).$$

Figures I-2-1 and I-2-2 give the rms deviation of the elastic scattering cross section and the second Legendre polynomial coefficient as a function of the mass number of the scattering sample. The open circles represent even-Z elements and the closed circles represent odd-Z elements. The neutron energy resolution used in computing the rms deviation was 52 keV and the energy region covered was 700 keV to 1250 keV. In both cases, the even-Z element data indicate a strong peak at $A \approx 50$ and a minimum at $A \approx 150$. The behavior for the odd-Z elements is somewhat different. The points at A = 55, 59, and 64 follow the same trend as do the even-Z elements but at a slightly reduced amplitude for the rms deviation as compared with the even-Z elements. Although the reason for this is not certain, it is known that niobium has more inelastic channels available at the incident neutron energies used here (~700 keV to ~1250 keV) than do the other elements and that the introduction of more channels in an observed reaction decreases the amplitude of the cross section fluctuation. Peaks in the *s*-wave neutron strength function occur at $A \approx 50$ and 150 and in the *p*-wave strength function at $A \approx 90$. The mass numbers corresponding to the neutron magic numbers 28, 50, and 82 are indicated in the figures. It is evident that the even-Z element data are in agreement with the prediction of the doorway state theory and that the amplitude of cross section fluctuation is largest near strength function peaks and near neutron magic numbers. A number of these nuclei are those closely associated with the structural materials of reactor systems, iron, nickel, and chromium, for example. Understanding the intermediate structure phenomena permits the physically meaningful use of the respective nulcear cross sections in a region where the more familiar compound nucleus structure is far too detailed for precise measurement and application.

### REFERENCES

1. H. Feshbach, A. K. Kerman and R. H. Lemmer, *Intermediate Structure and Doorway States in Nuclear Reactions*, Ann. Phys. **41**, 230 (1967).
2. A. Lande and G. E. Brown, *Vibrations, Strength Functions, and Intermediate Structure*, Nucl. Phys. **75**, 344 (1966).
3. P. A. Moldauer, *Statistical Theory of Intermediate Resonances*, Phys. Rev. Letters **18**, 249 (February 13, 1967).
4. S. A. Cox, *Elastic Neutron Scattering from Elements of Intermediate Weight*, Reactor Physics Division Annual Report, July 1, 1965 to June 30, 1966, ANL-7210, pp. 3–5.

## I-3. Neutron Polarization Measurements

S. A. Cox

A facility has been installed at the Argonne 3 MeV Van de Graaff accelerator for the purpose of polarization measurements in neutron elastic scattering (see Paper V-20). All data collections are fully automated and under executive control of a CDC 160-A on-line computer. It is the objective of the program to carry out a comprehensive survey of elements selected from most of the periodic table. Both polarization and elastic neutron scattering cross sections will be obtained over the incident neutron energy range ~400 to ~1500 keV. Such a compilation should permit a critical comparison between experimental and theoretical models; for example, the optical model permitting the extrapolation and interpolation of measured values to nuclei of critical importance to reactor design.

The experimental arrangement is given in Fig. I-3-1. Partially polarized neutrons, emitted at 51 deg from the Li($p$,$n$) reaction enter a tapered collimator placed along the axis of a powreful solenoid magnet. After emerging from the collimator and solenoid some of the neutrons are scattered by a 1 in. diam × 1 in. high scattering sample. The scattered neutrons are detected simultaneously by 4 neutron detectors spaced at 40 deg intervals. γ-ray rejection circuitry is used to eliminate γ-rays.[1] The four detectors may be placed in each of two angular orientations: 20, 60, 100, 140 deg and 35, 75, 115, and 155 deg, respectively. In this way scattered neutron angular distributions are determined at alternate 15 and 20 deg intervals from 20 to 155 deg. Samples are selected by computer control from eight possible choices. Massive shielding is required to reduce the neutron background at the detectors to an acceptable level. Further, since the neutron detectors are liquid scintillator photomultiplier tube combinations, they must be protected from the external magnetic field of the solenoid.

The solenoid is about 20 in. long and 15 in. i.d. The maximum current of 200 A corresponds to a total power of 20 kW and a central field of ~7 kG. At full operating power, the solenoid is capable of precessing the spin of 2.1 MeV neutrons 180 deg or the spin of 8.4 MeV neutrons 90 deg.

Some polarization results for silicon are given in Fig. I-3-2. The neutron energy resolution is ~20 keV and the neutron energy range covered is from ~400 to ~1100 keV. The product $P_1(51\text{ deg}) \cdot P_2(87.5\text{ deg})$ is

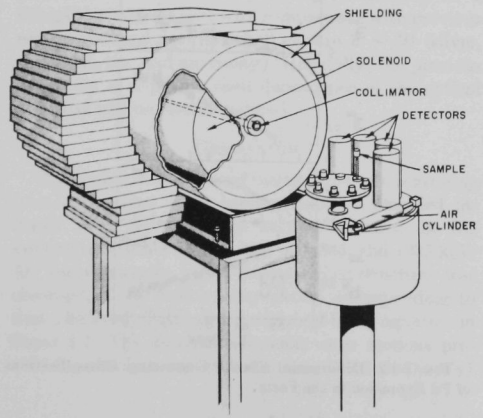


FIG. I-3-1. Experimental Facility for Polarization Measurements in Elastic Neutron Scattering. *ANL Neg. No. 112-8411 Rev. 1.*

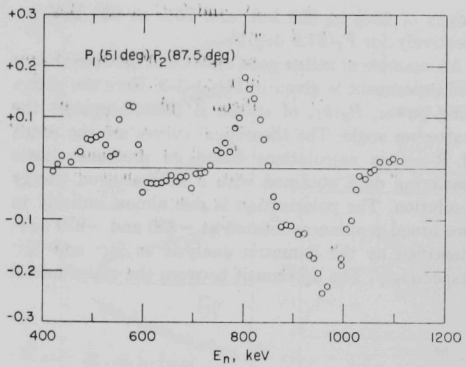


FIG. I-3-2. The Products $P_1(51)$ $P_2$ (87.5 deg) of Neutrons Emitted at 51 deg from the $Li^7(p,n)Be^7$ Reaction and Subsequently Scattered at 87.5 deg from Silicon. *ANL Neg. No. 112-8714.*

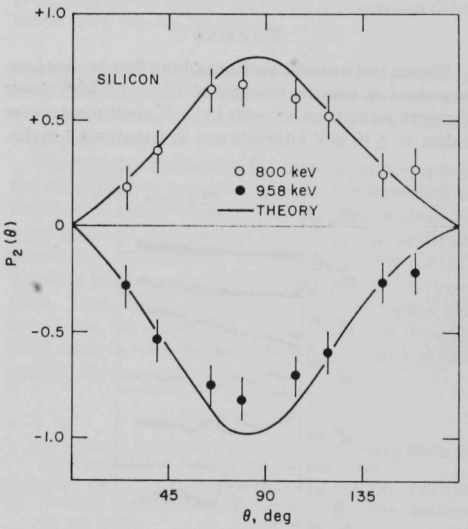


FIG. I-3-3. Experimental and Theoretical Polarizing Power $P_2(\theta)$ of Neutrons Scattered from Silicon as a Function of Scattering Angle. *ANL Neg. No. 112-9022.*

plotted, where $P_1(51\text{ deg})$ is the polarization of neutrons emitted at 51 deg from the Li($p$,$n$) reaction and $P_2(87.5\text{ deg})$ is the polarizing power of silicon for scattering neutrons at 87.5 deg. The largest values of polarization occur at ~800 and ~960 keV. According to A. Elwyn and R. Lane,[2] the values of $P_1(51\text{ deg})$ are 0.28 at 800 keV and 0.32 at 960 keV. This yields

values of 65% at 800 keV and 75% at 960 keV respectively for $P_2$(87.5 deg).

An example of rather good agreement between theory and experiment is given in Fig. I-3-3. Here the polarizing power, $P_2(\theta)$, of silicon is plotted against the scattering angle. The theoretical curves are the result of R-matrix calculations based on previous elastic scattering data obtained with 5 keV neutron energy resolution. The polarization is due almost entirely to two broad resonances located at ~820 and ~970 keV, identified by the R-matrix analysis as $\frac{3}{2}^-$ and $\frac{1}{2}^-$ respectively. The agreement between the experimental results and the R-matrix calculations lends support to the previous measurements of the polarization of neutrons emitted at 51 deg from the Li$(p,n)$ reaction.

### References

1. S. A. Cox. *Multiple Angle Detector Apparatus for Neutron Elastic Scattering and Polarization Measurements*, Reactor Physics Division Annual Report, July 1, 1965 to June 30, 1966, ANL-7210, pp. 340-342.
2. A. J. Elwyn and R. O. Lane, *Polarization of Neutrons in Scattering from Light Nuclei and in the $Li^7(p,n)Be^7$ Reaction*, Nucl. Phys. **31**, 78 (1962).

## I-4. Elastic and Inelastic Neutron Scattering from Light and Medium Nuclei

A. B. Smith

### Fluorine

Elastic and inelastic scattering from fluorine has been examined at neutron energies of 0.3 to 1.5 MeV using incident resolutions of ~20 keV. Measurements were taken at $\lesssim$10 keV intervals and at 8 scattering angles.

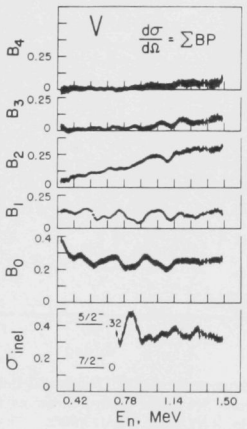


Fig. I-4-1. Elastic and Inelastic Neutron Scattering Cross Sections of V. The Elastic Differential Cross Section is Expressed in the Form

$$\frac{d\sigma}{d\pi} = \sum_{i=0}^{4} B_i P_i .$$

The Resolution is Averaged to ~50 keV and Intermediate Structure is Evident. *ANL Neg. No. 112-8851.*

The primary motivation was the confirmation of the reported intermediate structure in the scattering process.[1] Such structure was observed. However, there appears little correlation between processes in differing exit channels. More data are being taken in an attempt to obtain better definition $\gtrsim$1.2 MeV and total cross section measurements with resolutions of $\lesssim$1 keV are in

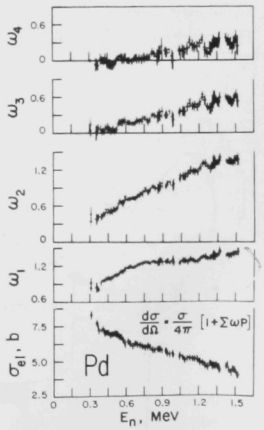


Fig. I-4-2. Differential Elastic Scattering Cross Sections of Pd Expressed in the Form.

$$\frac{d\sigma}{d\Omega} = \frac{\sigma}{4\pi}\left[1 + \sum_i \omega_i P_i\right].$$

*ANL Neg. No. 112-9095.*

progress. Detailed interpretations are underway, based upon: 1) autocorrelation analysis of the data,[2] 2) $S$-matrix statistical model of P. Moldauer,[3] and 3) detailed multi-level fits to the high resolution total cross section information.[4] Initial results, while not precluding intermediate structure, in the sense of H. Feshbach and A. Kerman, are consistent with a statistical distribution of individual resonances.

### Vanadium

The experimental studies of elastic neutron scattering from vanadium have been completed and a number of inelastic results obtained. Representative measured elastic and inelastic scattering cross sections are shown in Fig. I-4-1. From a phenomenological point of view, an intermediate resonance structure is apparent. Its physical interpretation is far less clear. Attempts to analyze the results in terms of correlation functions related to distributions of compound nucleus level widths and spacings and in terms of the particle-hole model have both proved disappointing.[1,5] A third approach employing an "intermediate optical model" is showing some initial promise.

### Palladium

The study of fast neutron scattering from palladium is nearing completion. The measurements extend to incident neutron energies of about 1.5 MeV and over the laboratory scattering angles 25–155 deg. The elastic scattering cross sections derived from this work are shown in Fig. I-4-2. Careful inelastic angular distribution measurements will complete the work. The interpretation of the measurements is proceeding in a straightforward manner with comparisons with previous results obtained near the shell closure $Z \sim 50$ (silver, cadmium, tin, and antimony). Hopefully, the previous indication of a proton shell dependence of the optical potential will be further verified.

### Germanium

The studies of elastic and inelastic neutron scattering from germanium have been completed. Detailed inelastic cross sections have been determined for the excitation of states at 560, 590, 690, 835, and 1035 keV. At lower energies some intermediate structure was observed in the elastic cross section corresponding to that observed in the total cross sections reported in Paper I-7. The measured inelastic cross sections provide the absolute normalization points for the $(n,n'\gamma)$ measurements described in Paper I-8. The experimental results, summarized in Fig. I-4-3, compare well with calculations based upon the optical model and Hauser-Feshbach theory.

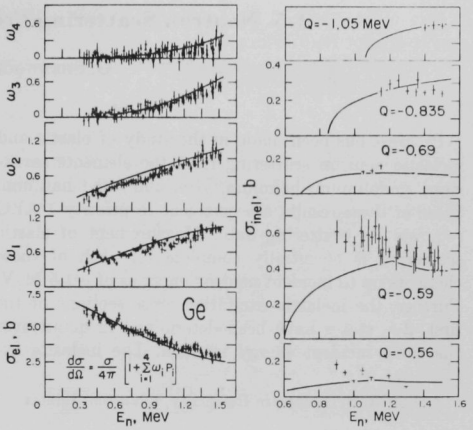


Fig. I-4-3. Elastic and Inelastic Scattering Cross Sections of Ge. Solid Curves Indicate the Results of Theoretical Calculations. *ANL Neg. No. 112-9103.*

The primary motivation for these measurements is the acquisition of gamma-ray emission information in response to direct requests from the reactor development program. With present technology, the optimum gamma-ray measurement techniques employ Ge(Li) detectors which must operate in a fast neutron environment. Thus, before gamma-ray emission results can be reliable, the inelastic scattering within the detector itself must be well known. The above results should provide the necessary information.

### References

1. H. Feshbach, *Intermediate Structure and Doorway States in Nuclear Reactions*, Ann. of Phys. **41**, 230 (1967).
2. I. Hall, *Finite Energy Range and Modulation Effects In The Analysis Cross-Section Fluctuation Data*, Phys. Letters, **10**, 199 (1964).
3. P. A. Moldauer, *Statistical Theory of Nuclear Reactions*, Bull. Am. Phys. Soc. II, **12**, 27 (1967).
4. M. Preston, *Physics of the Nucleus*, (Addison-Wesley Company, Reading, Massachusetts, 1962).
5. G. Pappalardo et al., *Statistical Fluctuation of Compound Nucleus Level Density and Nuclear Cross Sections*, Nucl. Phys. *47*, 129 (1963).

## I-5. Neutron Scattering From Deformed Even-Even Nuclei

G. Sherwood* and A. B. Smith

Progress has been made in the study of elastic and inelastic neutron scattering from the elements samarium, gadolinium, holmium, ytterbium, and hafnium. Some of these results are pertinent to priority 1 AEC requests for scattering data. Measurement of elastic scattering is essentially complete for each of these elements up to incident neutron energies of ~1.5 MeV. Further, the inelastic excitation cross sections of the first, 2+, states have been determined in detail over the same incident energy interval. The inelastic excitation of higher energy states is complex and the experimental study of the processes continues. The preliminary experimental results are in qualitative agreement with spherical optical model calculations. It is hoped that the use of the recently operational 2-PLUS coupled-channel optical model code will lead to a quantitative agreement with experiment and make reasonable the extrapolation of the results to the active rare-earth fission products. Scattering from these cannot be determined with present experimental techniques and one must rely on such extrapolation to assay their scattering properties.

* Student, Northwestern University, Evanston, Illinois

## I-6. Fast Neutron Scattering From Tantalum, Rhenium, and Platinum[1]

A. B. Smith, P. T. Guenther, R. Hayes and J. F. Whalen

The scattering of neutrons with energies of $\lesssim$1.5 MeV from the elements tantalum, rhenium and platinum was experimentally studied. Elastic and inelastic neutron scattering angular distributions were determined at incident neutron energy intervals of $\lesssim$20 keV throughout the range 0.3 to 1.5 MeV. Time-of-flight measurements were made concurrently at eight or more scattering angles between 25 and 155 deg with sufficient scattered neutron energy resolution to separate the elastic scattered component from most inelastic scattered neutron groups. Differential inelastic scattering cross sections corresponding to excitation of states in tantalum at 144 ± 10 (doublet), 313 ± 15, 506 ± 20, 620 ± 20, 720 ± 20, and 930 ± 25 keV; in rhenium at 132 ± 10, 219 ± 15, 313 ± 15, 387 ± 18, 518 ± 20, 637 ± 20, 767 ± 25, 865 ± 25, 963 ± 25, 1060 ± 25, and 1135 ± 25 keV; and in platinum at 130 ± 20, 214 ± 20, 348 ± 15, 420 ± 15, 620 ± 20, 719 ± 15, 838 ± 25, and 935 ± 20 keV were observed. Typical results pertaining to elastic and to inelastic neutron scattering from tantalum are shown in Figs. I-6-1 and I-6-2, respectively. The elastic and inelastic neutron scattering results were not always consistent with reported total cross section values.[2] For this reason, the total cross sections of tantalum and rhenium were carefully redetermined with the results indicated in Fig. I-6-3. These present total cross section values did not agree with previously reported measurements, but

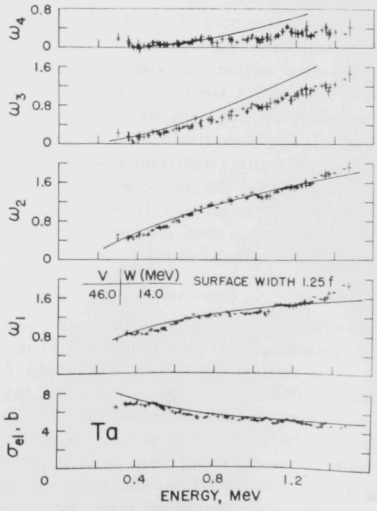


Fig. I-6-1. Differential Elastic Scattering Cross Sections of Ta Expressed in the Form of a Legendre Expansion. The Solid Curves are the Result of Optical Model Calculations. The Distributions are Inclusive of Inelastic Scattering Exciting the 6 keV State in Ta. Real ($V$) and Imaginary ($W$) Potential Values are Indicated. *ANL Neg. No. 112-8256.*

did substantiate the elastic and inelastic neutron scattering results.

The present experiments extended the knowledge of elastic and inelastic neutron scattering and total cross sections of tantalum, rhenium, and platinum at incident neutron energies of $\lesssim$1.5 MeV. The measured results were reasonably described by calculations based upon a local, energy independent optical potential and the theory of average compound-nucleus cross sections.[4] The calculations demonstrated the applicability of a well chosen spherical, surface absorption, optical potential for the interpolation and extrapolation of measured scattering cross sections over a region of large and rapidly changing deformation. Comparison with experiment indicated a proportionality between the strength of the surface absorption and the degree of deformation. Resonance width fluctuation effects were examined and found to be small. Uncertainties in calculated inelastic scattering cross sections, particularly at excitations >500 keV, tended to be more the result of inadequate knowledge of excited nuclear structure than of deficiencies in the potential employed.

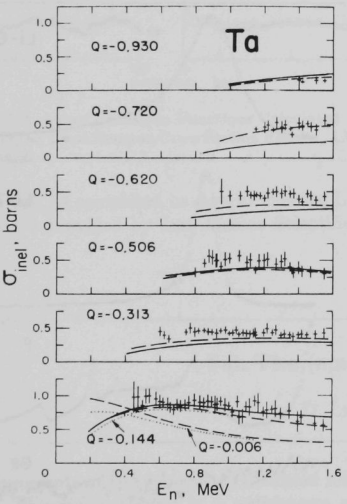


FIG. I-6-2. Inelastic Excitation Cross Sections of Ta. Experimental Points Pertaining to the Respective $Q$ Values (in MeV) are Shown by Crosses Which are Indicative of Estimated Error in Cross Section and Incident Neutron Energy Resolution. Solid Lines are the Results of Calculations Based upon the Structure Reported in the Literature. The Dashed Lines were Obtained Using a Structure "MODEL". Dotted Curves were Obtained by Applying Fluctuation Corrections to the MODEL Calculations. The Lower Portion of the Figure Indicates the Calculated (not Experimental) Excitation of the First State at 0.006 MeV. *ANL Neg. No. 112-8231 Rev. 1.*

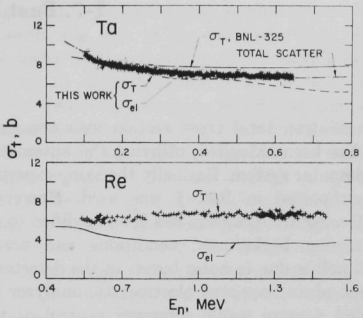


FIG. I-6-3. Total Neutron Cross Sections of Ta and Re. The Data Points Represent the Measured Values. $\sigma_{el}$ Curves were Obtained from the Present Work and the Total Scattering Curve Taken from Langsdorf et al.[3] *ANL Neg. No. 112-7886.*

The derivation of structure information for the measurements was restricted by experimental resolutions and sensitivities and by the isotopic complexity of the natural elements employed in the work. Despite these restrictions the experiments indicated that there were omissions and/or inappropriate spin and parity assignments in the reported low energy excited structure of both tantalum and rhenium. Revisions of the excited structure of tantalum consistent with the unified model and experimental observation were proposed. Modifications of and additions to the reported structure of rhenium were indicated by the experimental results inclusive of a specific state attributed to the predicted single particle configuration in Re-185. The experimental results are of extensive value in reactor development programs since both tantalum and rhenium are structural materials with excellent high temperature properties. The results obtained for rhenium fully satisfied a reactor development request for basic cross section information.

## REFERENCES

1. A. B. Smith, P. T. Guenther, R. Hayes and J. F. Whalen, *Fast Neutron Scattering from Ta, Re, and Pt,* Phys. Rev. (to be published).
2. BNL-325, *Neutron Cross Sections,* 2nd Supplement, Second Ed. 1967.
3. A. Langsdorf, Jr., R. O. Lane and J. E. Monahan, *Neutron Scattering Angular Distribution,* ANL-5567 Rev. (1961).
4. P. Moldauer, *Optical Model of Low Energy Neutron Interactions With Spherical Nuclei,* Nucl. Phys. **47,** 65 (1963). See also, *Average Compound-Nucleus Cross Sections,* Rev. Mod. Phys. **36,** 1079 (1964).

## I-7. Fast Neutron Cross Sections

J. F. WHALEN

The neutron total cross section measurement program has been extended, utilizing the automated on-line computer system. Basically the same experimental set-up reported in Ref. 1 was used. However, the executive control program has been modified to correct for varying background conditions and occasional "wild" points due to noise bursts in the detectors. The addition of an improved electrostatic analyzer system provided a more stable computer control of the accelerator and therefore increased precision in the cross section measurements.

The following elements have been studied during the past year with the respective total cross section results shown in Fig. I-7-1: zinc, vanadium, sodium, carbon, tantalum, Li-6, Li-7, fluorine, germanium and yttrium. The total cross section of fluorine was determined by using a Teflon sample ($CF_2$), then subtracting the carbon cross section and dividing by two to account for the extra fluorine. The values of the carbon cross section used in this correction were determined with the same system. The lithium measurements were made with samples originally prepared for scattering studies of a different orientation. This resulted in small transmissions which reduced the precision of this system appreciably while passing over the large resonance at ~260 keV. This fact, plus the presence of some slight fine structure possibly due to contaminants, necessitated the procurement of additional samples. The new Li-7 samples have been completed and are scheduled for measurement. New Li-6

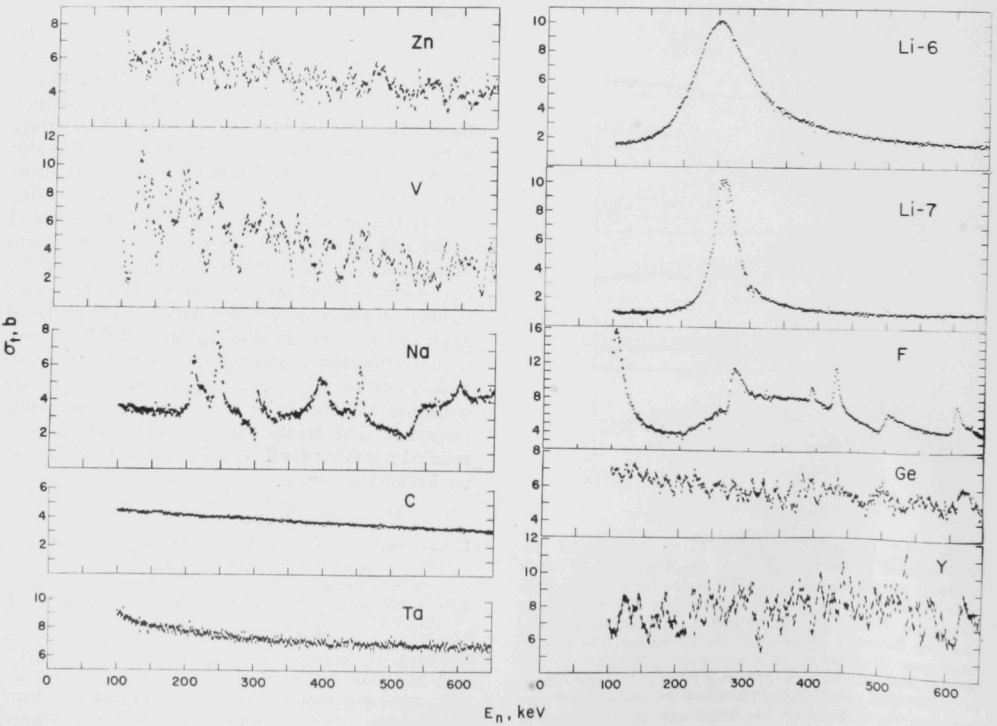


FIG. I-7-1. Representative Results of Total Neutron Cross Section Measurements Using the Automated Accelerator Facility. *ANL Neg. No. 112-9272.*

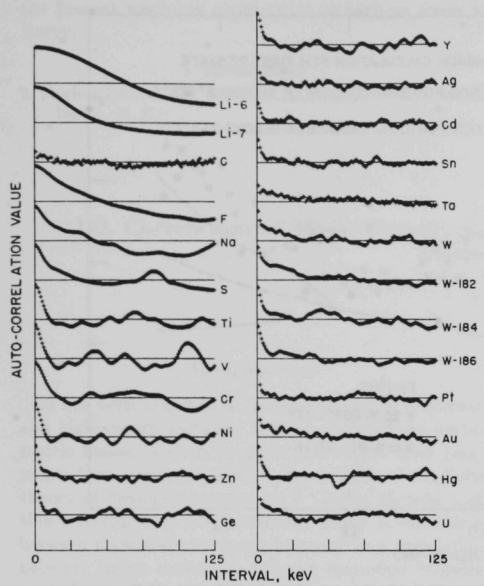


FIG. I-7-2. Auto-Correlation Functions Calculated From a Number of the Total Neutron Cross Section Results. *ANL Neg. No. 112-8843.*

samples will be completed in several months. Lithium samples are provided by Los Alamos Scientific Laboratory.

The above total neutron cross section measurements are a continuing part of the program. They provide data requested by the applied nuclear energy programs, information in support of the other portions of the Argonne measurement program, and finally they are of importance in the science of physics itself. The data are sufficiently detailed and precise to make possible a meaningful correlation analysis leading to the determination of the average widths of the pertinent nuclear resonance structure.[2] Auto-correlation results of this type are shown in Fig. I-7-2. The initial drop of these correlation functions from the zero energy interval is related to the average widths of the contributing resonance structure. In no case was a width observed which differed significantly from that expected from the usual compound nucleus processes and, particularly, no clear indication of a distinct intermediate structure was observed. Rather generally, the small "wiggles" observed in many of these cross sections were of much less magnitude than previously reported and not clearly related to nuclear shell structure, deformation, or strength function.[3]

REFERENCES

1. J. F. Whalen, R. Roge, and A. B. Smith, *A Digital Computer System for the Executive Control of a Fast Neutron Laboratory*, Nucl. Instr. Methods, **39**, No. 2 (1966).
2. A. Agodi and G. Pappalardo, *Statistical Fluctuation of Compound Nucleus Level Density and Nuclear Cross Sections*, Nucl. Phys. **47**, 129 (1963).
3. K. Seth, *Neutron Total Cross Sections and Intermediate Resonances*, Phys. Letters **16**, 306 (1965).

## I-8. The $(n,n'\gamma)$ Process in Germanium

D. LISTER and D. STUPEGIA*

Measurements of the gamma rays emitted following neutron inelastic scattering is a well-known method by means of which $(n,n')$ cross sections of many materials may be inferred, even down to the reaction threshold. Interest in this method has increased as a result of the development of the lithium-drifted germanium detector. The detector functions as a gamma-ray spectrometer of high resolution and good efficiency. A background originating from neutron-induced reactions within the detector is always present in the pulse-height spectrum. Detailed information regarding such processes is necessary if precise inelastic cross sections are to be determined. For incident neutron energies of less than 1.5 MeV, the important backgrounds arise from $(n,n'\gamma)$ and $(n,\gamma)$ reactions in germanium. Of the two, the former comprise the dominant contribution, giving rise to sharp full-energy peaks and accompanying Compton distributions in the pulse height spectrum. The latter produce a rather smooth distribution of lower intensity. In the present study self-detection gamma-ray spectra obtained from bombarding a lithium-drifted germanium detector with mono-

* Chemical Engineering Division, Argonne National Laboratory.

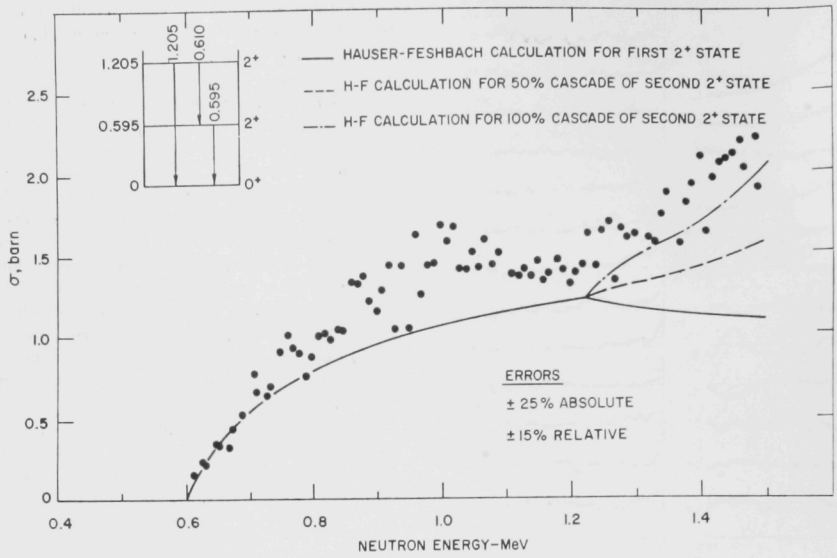


FIG. I-8-1. Excitation Function for the Production of Gamma Rays of Approximately 0.60 MeV Energy Following Inelastic Neutron Scattering from $Ge^{74}$. The Measured and Theoretically Calculated Results Are Referred to Istopically Pure $Ge^{74}$. *ANL Neg. No. 112-9159.*

energetic neutrons were analyzed to provide absolute gamma-ray production cross sections. The results were then compared with the statistical compound nucleus theory of Hauser and Feshbach.

The experimental procedure consisted of allowing neutrons emitted in the forward direction from the $Li^7(p,n)Be^7$ source reaction to impinge on a cooled lithium-drifted germanium detector of 6 $cm^3$ active volume in a sequence of energies between 0.55 MeV and 1.49 MeV. Measurements were made at ~10 keV intervals with resolutions of ~14 keV throughout the range. The source reaction was monitored using both proton beam current integration and a "long counter". The neutron flux at the detector position in a heavy-metal collimator was measured with respect to the total *n-p* cross section by replacing the germanium detector with a hydrogen-filled proportional counter. The collimator served the purpose of defining the active volume of the proportional counter, thus maintaining the geometry. Background, taken with a blocked collimator, was subtracted from the open aperature data. Calibrated gamma-ray sources were used to calibrate the full-energy peak efficiencies of the germanium detector. Because of the difference in the source-detector geometry in the calibration (sources separated from detector) and during neutron bombardment (sources throughout the entire volume of germanium) numerical computations were performed to estimate the detector sensitivity under the experimental conditions. Cross sections for excitation of individual excited states in germanium isotopes were deduced from the measured intensities of the full-energy peaks assuming natural isotopic abundances and published electromagnetic decay branching ratios.[1] Corrections for neutron beam attenuation and the presence at higher energies of a second group of neutrons of lower energy from the $Li^7(p,n^1)Be^{7*}$ reaction were included.

Cross sections for excitation of the following states were obtained: the 1.038-MeV state in $Ge^{70}$, the 0.693- and 0.835-MeV states in $Ge^{72}$, the 0.594- and 1.202-MeV states in $Ge^{74}$, and the 0.567-MeV state in $Ge^{76}$. Figure I-8-1 illustrates the results for the 0.567-MeV state in $Ge^{74}$. The smooth curve in this figure indicates the result of a Hauser-Feshbach calculation for this level, with transmission coefficients obtained from optical model calculations employing parameters adjusted to fit the neutron elastic scattering measurements of A. Smith.[2] A similar study has been reported by J. Barry[3] in which the cross sections were normalized to neutron inelastic cross section results of A. Smith.[2] The results of this work agree with those of Barry on a relative scale, but the absolute cross sections found in

the present work are about twice as high as those of Barry.


### References

1. Nuclear Data Sheets, National Academy of Sciences, Washington, D. C.
2. A. B. Smith, Argonne National Laboratory (private communication).
3. J. F. Barry, *Gamma Rays from Neutron Inelastic Scattering in Germanium*, International Conference on Nuclear Data-Microscopic Cross Sections and Other Data Basic for Reactors, IAEA, Paris, 1966, Paper CN-23/59.


## I-9. Correlation of Mass, Energy, and Angle in Thermal and 6-MeV Neutron Fission of U-235

J. W. Meadows

### Introduction

It has been observed in fission induced by moderate and high energy particles[1] that fragments from asymmetric fission tend to be more anisotropic than fragments from symmetric fission. An analysis of the Bohr theory of fission anisotropy by J. Griffin[2] showed that this behavior does not necessarily imply a correlation between mass and anisotropy but may be a correlation between fission events at different excitation energies caused by fission following neutron emission. For a particular $(n,xnf)$ reaction, the anisotropy decreases with excitation energy while the symmetric fission yield increases. At moderate and high energies selection of a symmetric fission event is equivalent to the selection of one with a larger excitation energy. However, if a correlation of mass and anisotropy exists for fission at well defined excitation energies, such as below the $(n,n'f)$ threshold, it may be evidence that the saddle point for symmetric fission is different from that for asymmetric fission and support the two-mode fission hypothesis.

There are few data available on the correlation of mass and angle for neutron induced fission in this energy range. Measurements which have been made on U-235 at 4 MeV[3] and U-238 at 3 MeV[4] suggest that there is a correlation of mass and angle and that symmetric fission is less anisotropic than symmetric fission. However a measurement of the angular distribution in the U-234$(d,pf)$ reaction, where the excitation energy was defined by the kinetic energy of the proton, showed no correlation of mass and angle.[5]

The results of an earlier experiment to determine the mass-energy distribution for 6-MeV neutron fission of U-235 indicated no correlation of mass and angle.[6] However, that experiment was not designed to determine angular dependence except in a very rudimentary fashion. This paper reports the preliminary results of an attempt to obtain more precise information of any correlation of mass and angle in the 6-MeV neutron induced fission of U-235.

### The Experimental Method

The experimental arrangement is shown in Fig. I-9-1. Neutrons were produced by the D$(d,n)$He$^3$ reaction using a 3-MeV Van de Graaff generator. The uranium target covered an area 1-cm in diameter and had a thickness of 120 $\mu$g/cm$^2$. It was made by evaporating metallic U-235 onto a 130 $\mu$g/cm$^2$ nickel foil. The common detector, immediately behind the fission source, had an active area of 4 cm$^2$. The other three detectors had active areas of 3 cm$^2$. All the detectors were of the surface-barrier type and had resistivities

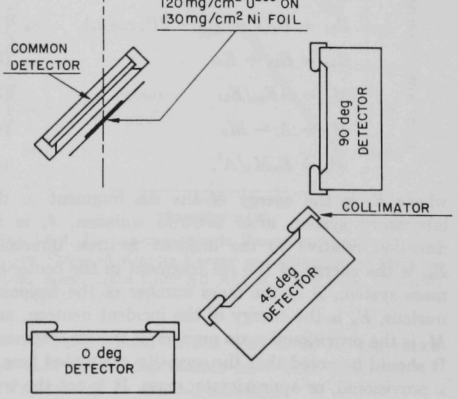


Fig. I-9-1. Schematic Diagram of the Experimental Arrangement. *ANL Neg. No. 112-8730.*

in the vicinity of 500 Ω-cm. The collimators were 1/16 in. thick and were adjusted to shield the edges of the detectors from fission fragments. The edges of the collimators were rounded to minimize scattering. The detector biases were initially set at 60 V. Since the leakage currents of the detectors increased continuously because of radiation damage, the bias supplies were adjusted at frequent intervals in order to keep the detector biases at 58–60 V. Amplifier gains and zero levels were adjusted so that 64 channels covered the energy interval from ~40 to ~120 MeV. The energy calibration was obtained from the pulse height spectra for thermal neutron fission of U-235 using the method of H. Schmitt, et al.[7]

When a pair of fission fragements was detected simultaneously in the common detector and one of the other detectors the event was recorded in one of three 64 x 64 arrays with the rows representing the pulse height of one fragment and the columns the pulse height of the other. Data were collected in four hour periods for 6 days. Once each day the fission chamber was surrounded with 6 in. of paraffin wax and a set of thermal fission spectra was recorded. These provided the thermal data and the energy calibration.

## Analysis

The original pulse-height versus pulse-height array, $N(x_1, x_2)$, was transformed into a provisional mass versus total kinetic energy array, $N(M_2, E_{KT})$. The pulse-heights are related to the fragment kinetic energies by a mass dependent-calibration equation[7] which was determined separately for each detector. In turn, the kinetic energies of the fragments are related to the total kinetic energy and the provisional fragment masses by

$$E_{ki} = E_i(1 + P_i^2 - 2P_i \cos\theta_i) \tag{1}$$

$$E_{kt} = E_{k1} + E_{k2} \tag{2}$$

$$M_2 = AE_{ki}/E_{kt} \tag{3}$$

$$M_1 = A - M_2 \tag{4}$$

$$P_i = E_n M_i / A^2, \tag{5}$$

where $E_i$ is the energy of the $i$th fragment in the laboratory system after neutron emission, $\theta_i$ is its direction relative to the incident neutron direction, $E_{ki}$ is the energy of the $i$th fragment in the center-of-mass system, $A$ is the mass number of the fissioning nucleus, $E_n$ is the energy of the incident neutron, and $M_i$ is the provisional mass number of the $i$th fragment. It should be noted that the quantity calculated here is a provisional, or approximate, mass. It is not the true fragment mass either before or after neutron emission. The energy deposited in the detectors, $E_i$, was the fragment kinetic energy after neutron emission. If recoil effects are neglected, it is related to the fragment energy before neutron emission by

$$E_i^* = E_i + (\nu_i E_i^*/M_i^*), \tag{6}$$

where $\nu_i$ is the number of neutrons emitted by the $i$th fragment and $M_i^*$ is its true mass before neutron emission.

If $E_i^*$ is used in Eq. (1), we obtain $M_i^*$, the fragment mass before neutron emission. Determination of this quantity requires either a different experimental method or an accurate knowledge of the dependence of $\nu$ on mass. In this experiment the average value of $\nu_i E_i^*/M_i^*$ is ~1 MeV. Thus $E_i \approx E_i^*$ and the provisional mass values are nearly equal to those before neutron emission.

To perform the transformation the $(M_2, E_{KT})$ array was divided into cells 1.2 mass units by 1.5 MeV. The corners of each of these cells were transformed onto the $(x_1, x_2)$ array and the cells in this array, which were entirely or partly covered by the $(M_2, E_{KT})$ cell, were identified. Then the number of events recorded in these cells were entered into the $(M_2, E_{KT})$ cell according to the fraction of coverage.

## Results

In the ideal case the absence of any mass-angle correlation should result in

$$\frac{Y(M_2, \theta_i)}{Y(M_2, 90 \text{ deg})} = 1.0, \tag{7}$$

where $Y$ is the fission yield. However small experimental effects can introduce large errors in the above ratio. This is particularly true in comparing the 45 deg results with the 0 and 90 deg results. At 45 deg the energy lost by the average fission fragment in the source, support foil, and detector window is ~3-MeV if it enters the common detector and ~6-MeV if it enters the 45 deg detector. The maximum spread of this energy loss due to the angular resolution of the detector is ~ ± 2%. At 0 and 90 deg the average fission fragment loses ~40% more energy and the maximum spread due to the angular resolution is ~ ± 30%. The detector calibration compensates for the average energy loss but the distribution of the loss results in slightly broader peaks for the 0 and 90 deg results. Furthermore, this effect may influence the location of the fission peaks in the calibration measurements. An error of only 0.1 channel in the location of one peak can shift $\langle M \rangle$ by ~0.1 mass unit and $\sigma^2(M)$ by ~0.3. This is illustrated in Table I-9-I by the results for thermal fission. Ideally the results at all angles should be the same. The 0 and 90 deg results, where the experimental conditions were similar, show very good agreement. The 45 deg data show small but significant differences.

While these effects are small, they can cause serious

errors in the yield ratio in the regions where $dY/dM$ is large. This is illustrated in Figs. I-9-2 and I-9-3 which show the ratios of the thermal fission yields at 0 and 45 deg to the yield at 90 deg. The 0 to 90 deg ratios are near 1.0 for all mass values. The 45 to 90 deg ratios show that the 45 deg masses have been shifted away from symmetry by a small amount.

Figures I-9-3 and I-9-4 show similar ratios for 6-MeV fission. The 0 to 90 deg ratio follows the thermal results very closely. The 45 to 90 deg ratios show a divergence

TABLE I-9-I. The Average Values of Mass and Energy and the Variances of their Distributions for Thermal and 6 MeV Neutron Fission of U-235

| $E_n$ | Thermal | | | 6 MeV | | |
|---|---|---|---|---|---|---|
| Angle | 0 | 45 | 90 | 0 | 45 | 90 |
| $\langle M_L \rangle$ | 97.3 | 97.0 | 97.4 | 98.0 | 97.7 | 97.9 |
| $\sigma^2(M_L)$ | 34.8 | 34.5 | 34.8 | 45.9 | 46.5 | 45.8 |
| $\langle M_H \rangle$ | 139.1 | 139.4 | 139.1 | 138.6 | 138.8 | 138.2 |
| $\sigma^2(M_H)$ | 34.6 | 34.4 | 34.9 | 47.1 | 47.5 | 46.3 |
| $\langle E_{KL} \rangle$ | 100.2 | 100.1 | 100.2 | 99.0 | 98.8 | 99.1 |
| $\langle E_{KL} \rangle$ | 70.3 | 69.9 | 70.3 | 70.2 | 69.7 | 70.4 |
| $\langle E_{KT} \rangle$ | 170.5 | 170.0 | 170.5 | 169.2 | 168.5 | 169.5 |
| $\sigma^2(E_{KT})$ | 112.6 | 114.9 | 111.7 | 114.9 | 118.0 | 113.7 |
| Peak/Valley | 294 | 333 | 304 | 21.9 | 22.4 | 22.1 |

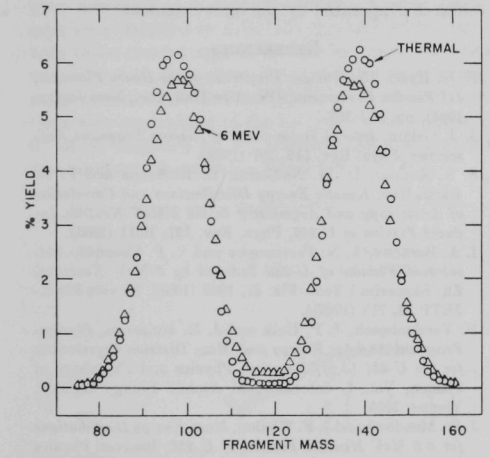


FIG. I-9-2. Mass Yield Distribution for Thermal and 6-MeV Neutron Fission of $U^{235}$ from the 0 deg Detectors. *ANL Neg. No. 112-8733.*

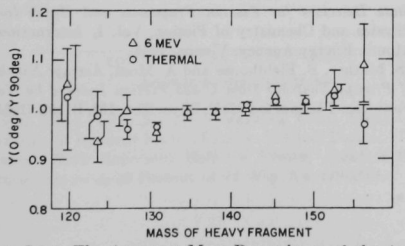


FIG. I-9-3. The Apparent Mass Dependence of the Anisotropy $[Y(M_2, 0 \text{ deg})/Y(M_2, 90 \text{ deg})]$. *ANL Neg. No. 112-8731.*

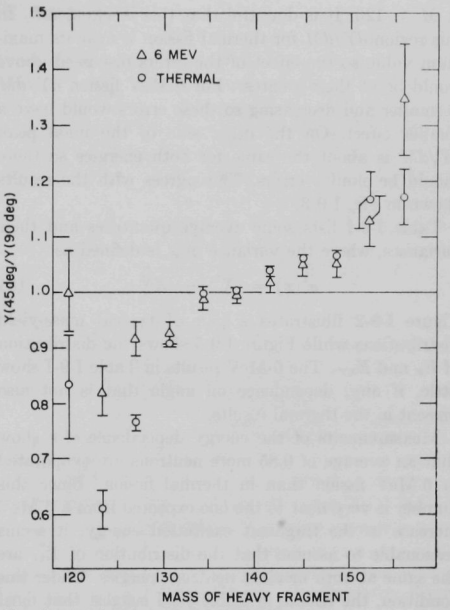


FIG. I-9-4. The Apparent Mass Dependence of the Anisotropy $[Y(M_2, 45 \text{ deg})/Y(M_2, 90 \text{ deg})]$. *ANL Neg. No. 112-8732.*

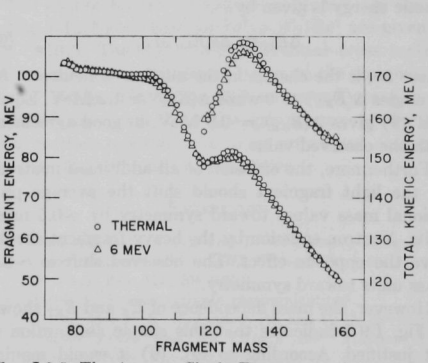


FIG. I-9-5. The Average Single Fragment and Total Post Neutron Emission Kinetic Energy as a Function of the Provisional Mass. Data from All Angles Have Been Summed. *ANL Neg. No. 112-8734.*

at $M \approx 125$. It is doubtful that this is significant. In this region $dY/dM$ for thermal fission is near its maximum value so the effect of the errors discussed above would be at their greatest. For 6-MeV fission $dY/dM$ is smaller and decreasing so these errors would have a smaller effect. On the other side of the mass peak $dY/dM$ is about the same for both energies so there should be similar errors. This agrees with the results shown in Fig. I-9-3.

Table I-9-I lists some average quantities and their variances, where the variance of $x$ is defined as

$$\sigma^2(x) = \langle X^2 \rangle - \langle X \rangle^2 \tag{8}$$

Figure I-9-2 illustrates a pair of typical mass-yield distributions while Figure I-9-5 shows the distribution of $E_K$ and $E_{KT}$. The 6-MeV results in Table I-9-I show little, if any, dependence on angle that is not also present in the thermal results.

Measurements of the energy dependence of $\bar{\nu}$ show that an average of 0.85 more neutrons are evaporated in 6-MeV fission than in thermal fission.[8] Since this number is very near to the one expected from a 6 MeV increase in the fragment excitation energy, it seems reasonable to assume that the distribution of $E^*_{ki}$ are the same at both incident neutron energies. Under this condition, the results in Table I-9-I suggest that most of these additional neutrons come from the light fragment. It may be shown that the change in the observed kinetic energy is given by

$$\Delta E_{ki} \approx \Delta \nu_i E_{ki}/M_i\,, \tag{9}$$

where $\Delta \nu_i$ is the change in the number of neutrons. At all angles $\Delta\langle E_{KH} \rangle \approx 0$ while $\Delta\langle E_{KL} \rangle \approx 1.2$ MeV. Equation (9) gives $\Delta\langle E_{KL} \rangle = 0.9$ MeV, in good agreement with the observed value.

Furthermore, the emission of all additional neutrons by the light fragment should shift the average provisional mass values toward symmetry by $\sim$0.5 mass units. Neutron emission by the heavy fragment should have the opposite effect. The observed shift is $\sim$0.6 mass units toward symmetry.

However, the mass dependence of $E_K$ and $E_{KT}$ shown in Fig. I-9-5 indicates that this simple assumption is not justified. According to Eq. (9) it would require $E_{KT}(th) - E_{KT}(E_n)$ to be positive and nearly constant for all mass values. Instead it varies from $\sim +2.5$ MeV near $M_H = 130$ to $\sim -1.0$ MeV above $M_H = 150$.

Since the data in Fig. I-9-5 are presented in terms of provisional masses the $\Delta E_K$ and $\Delta E_{KT}$ values will not be the true energy differences. However, the magnitude of the correction should be $\lesssim$1 mass unit and should not greatly affect the qualitative results. Thus inspection of the $E_K$ values suggests that most of the additional neutrons come from the heavy side of the light peak.

## Conclusions

The mass versus total kinetic energy correlations for thermal and 6-MeV neutron induced fission of U-235 are very similar except for the greatly increased yield at 6 MeV. The yield ratios, $Y(M_2, \theta)/Y(M_2, 90$ deg), do not show any correlation of fragment mass and angle. They do show an apparent correlation, but comparison of the thermal and 6-MeV data show that this is caused by experimental effects. The differences in $\langle E_{Ki} \rangle$ and $\langle E_{KT} \rangle$ show that at 6 MeV $\sim$1 additional neutron is evaporated by the light fragment.

## References


1. E. K. Hyde, *The Nuclear Properties of the Heavy Elements, III Fission Phenomena*, (Prentice-Hall, Inc., New Jersey, 1964), pp. 362–380.
2. J. J. Griffin, *Energy Dependence of Fission Fragment Anisotropy*, Phys. Rev. **116**, 107 (1959).
3. S. S. Kupoor, D. M. Nadkarni, R. Ramanna and P. N. Rama Rav, *Kinetic Energy Distributions and Correlation of Anisotropy and Asymmetry in the 4-MeV Neutron Induced Fission of U-235*, Phys. Rev. **137**, B511 (1965).
4. I. A. Baranov, A. N. Protopopov and V. P. Eismunt, *Anisotropic Fission of U-238 Induced by 3-MeV Neutrons*, Zh. Eksperim i Teor. Fiz. **41**, 1003 (1961), [Soviet Phys.-JETP **14**, 713 (1962)].
5. R. Vandenbosch, J. P. Unik and J. R. Huizenga, *Fission-Fragment Angular Energy and Mass Division Correlations for the U-234 (d,pf) Reaction*, Physics and Chemistry of Fission, Vol. I, International Atomic Energy Agency, Vienna, 1965.
6. J. W. Meadows and J. F. Whalen, *Mass-Energy Distributions for 6.0 MeV Neutron Fission of U-235*, Reactor Physics Division Annual Report, July 1, 1964 to June 30, 1965, ANL-7110, pp. 21-23.
7. H. W. Schmitt, W. M. Gibson, J. H. Neiler, F. J. Walter and T. D. Thomas, *Absolute Energy Calibration of Solid State Detectors for Fission Fragments and Heavy Ions*, Physics and Chemistry of Fission, Vol. I, International Atomic Energy Agency, Vienna, 1965.
8. D. S. Mather, P. Fieldhouse and A. Moat, *Average Number of Prompt Neutrons from U-235 Fission Induced by Neutrons from Thermal to 8 MeV*, Phys. Rev. **133**, B140B (1964).

# I-10. The $Li^7(p,n)Be^7$ Reaction

D. Lister and E. F. Bennett

The $Li^7(p,n)Be^7$ reaction is a widely used laboratory source of monoenergetic fast neutrons. Detailed knowledge of the cross sections for this reaction as well as those of competing reactions are pertinent to its precise use in the determination of neutron cross sections.

Angular distributions for the $Li^7(p,n)Be^7$ reaction were measured at a large number of incident proton energies between 1.9 and 2.7 MeV. Neutrons were detected in a hydrogen-filled proportional counter by means of the proton-recoil method. Reduction of the data is currently in progress.

The production cross sections for the 0.48-MeV gamma rays from the $Li^7(p,p'\gamma)Li^7$ process and the 0.43-MeV gamma rays from the $Li^7(p,n'\gamma)Be^7$ process were measured in a second experiment. The gamma rays were detected in a Ge(Li) detector concurrently with those gamma rays of interest in Paper I-8. Data were obtained throughout the incident proton energy range between 2.31 and 3.18 MeV. Absolute cross sections were normalized to the $Li^7(p,n)$ cross sections at 0° of F. Gabbard et al,[1] utilizing the neutron flux measurements described in Paper I-8.

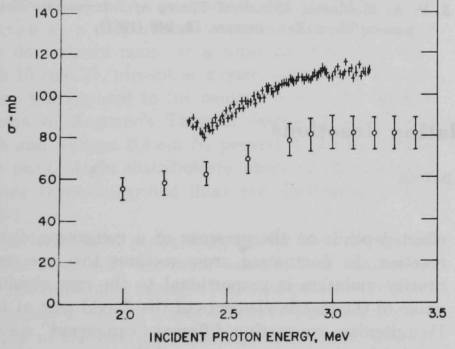


FIG. I-10-1. $Li^7(p,p'\gamma)Li^7$ Integrated Cross Section as a Function of Incident Proton Energy. Vertical Bars on Data of Present Work Represent Relative Errors; Absolute Uncertainties are $\sim \pm$ 30 Percent. *ANL Neg. No. 112-9092.*

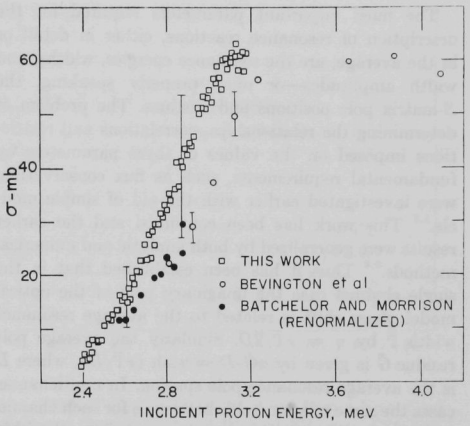


FIG. I-10-2. $Li^7(p,n'\gamma)Be^7$ Integrated Cross Section as a Function of Incident Proton Energy. Representative Errors are Indicated. *ANL Neg. No. 112-9393.*

The results for the $Li^7(p,p'\gamma)Li^7$ process are shown in Fig. I-10-1 and those for $Li^7(p,n'\gamma)Be^7$ are given in Fig. I-10-2. The integrated differential cross section results of other investigators based on the emission of second group protons[2] as well as second group neutrons[3,4,5] are lower than the gamma-ray production cross sections reported here to an extent just compatible with the combined uncertainties.

## References

1. F. Gabbard, R. H. Davis and T. W. Bonner, *Study of the Neutron Reactions $Li^6(n,\alpha)H^3$, $F^{19}(n,\gamma)F^{20}$, and $I^{127}(n,\gamma)I^{128}$*, Phys. Rev. **114**, 201 (1959).
2. G. Bardolle, France (private communication).
3. S. G. Buccino, C. E. Hollandsworth and P. R. Bevington, *Neutron Yields from the $Li^7(p,n')Be^{7*}$ Reaction Near Threshold*, Nucl. Phys. **53**, 375 (1964).
4. P. R. Bevington, W. W. Rolland and H. W. Lewis, *Relative Yields of Neutron Groups from the $Li^7(p,n)Be^{7*}$ Reactions*, Phys. Rev. **121**, 871 (1961).
5. R. Batchelor and G. C. Morrison, *The Angular Distribution of $Li^7(p,n)Be^{7*}$ Neutrons for Proton Energies Between 2.5 and 2.9 MeV*, Proc. Roy. Soc. (London) **A68**, 1081 (1955).

## I-11. Theory of Resonance Reactions

P. A. MOLDAUER

The most important parameters required for the description of resonance reactions, either in detail or in the average, are the resonance energies, widths, and width amplitudes—or more properly speaking, the $S$-matrix pole positions and residues. The problem of determining the relationships, correlations and restrictions imposed on the values of these parameters by fundamental requirements, such as flux conservation, were investigated earlier with the aid of simple models.[1,2] This work has been continued and the earlier results were generalized by both analytic and numerical methods.[3,4] Thus it has been established that in the single channel case the imaginary part of the optical model phase shift is related to the average resonance width $\bar{\Gamma}$ by $\eta = \pi\bar{\Gamma}/2D$. Similarly the average pole residue $\bar{G}$ is given by $\pi\bar{G}/D = \sinh(\pi\bar{\Gamma}/D)$, where $D$ is the average resonance pole spacing. In multichannel cases the same relation holds between $\eta$ for each channel and the corresponding average partial channel width, while the channel residues become larger than in the single channel case.

These considerations have a very strong influence on the properties of resonance reactions and modify appreciably the interpretation and calculation of cross sections of this type. This is particularly true when strongly absorbed channels are open (transmission coefficients $T \to 1$, $\eta \to \infty$). One aspect of these strong absorption phenomena which has been studied, is the distribution of widths and residues about their mean values and the properties of the attendant cross section fluctuations.[5] It was found that in strong absorption cases the distributions of both widths and residues are very much broader than had generally been assumed, and that as a result the cross sections up to rather high energies should exhibit "intermediate" resonance features which are attributable to the resonance poles with anomalously large widths, rather than to "Ericson fluctuations" arising from poles with average widths. Computer programs were developed for calculating these effects and computations are being made.

### REFERENCES

1. P. A. Moldauer, *Flux Conservation in Resonance Reactions*, Proc. International Conference on Nuclear Physics, Gatlinburg, Tennessee, September 12–17, 1966, CONF. 660906 (to be published).
2. P. A. Moldauer, *Unitary Models of Nuclear Resonance Reactions*, Phys. Rev. **157**, 907 (1967).
3. P. A. Moldauer, *Statistical Theory of Nuclear Reactions*, Invited paper BA2 presented at the Annual Meeting of the American Physical Society, New York, January 30, 1967; Bull. Am. Phys. Soc. II, **12**, 27 (1967) (to be published).
4. P. A. Moldauer, *Strong Absorption and Direct Effects in Compound Reactions*, submitted to the Conference on Nuclear Structure, Tokyo, September 1967.
5. P. A. Moldauer, *Statistical Theory of Intermediate Resonances*, Phys. Rev. Letters, **18**, 249 (1967).

## I-12. Theory of T-Violating Reactions

P. A. MOLDAUER

Recent discoveries of the violation of time reversal invariance in the decay of $K$ mesons have raised the question of possible effects of such $T$ violation on nuclear reaction cross section, in particular on the reciprocity relations. The connection between $T$ violation and reciprocity violation has been calculated for the cases of direct reactions, isolated resonances, average and fluctuating cross sections.[1] It was found that in direct reactions the reciprocity violation is proportional to the matrix elements of the $T$-odd part of the Hamiltonian connecting different residual states, divided by the energy separation of these residual states. In isolated resonances and in average cross sections the effect depends on the presence of a competing direct reaction. In fluctuating cross sections the rms reciprocity violation is proportional to the rms absolute value of the matrix elements of the $T$-odd part of the Hamiltonian, connecting different "compound" states, divided by the geometric mean of the average spacing and the average width of these compound states. Strong absorption effects tend to enhance the reciprocity violation.

### REFERENCES

1. P. A. Moldauer, *Effects of T-Violation in Nuclear Reactions*, Phys. Rev. **165**, 1136 (1968).

# I-13. Cross Section for $Ne^{21}(n_{th},\alpha)O^{18}$

E. F. Bennett and W. C. Redman

A. Abramov and M. Yutkin[1] have measured the $Ne^{21}(n,\alpha)O^{18}$ cross section for thermal neutrons and suggested that this reaction would be useful for fast neutron spectroscopy. For this reason, in addition to an interest in the contribution of this reaction in experiments on neutron excitation of a helium-neon laser, the cross section has been remeasured.

Abramov and Yutkin detected pulses in a neon-filled ionization chamber which they attributed to the $Ne^{21}(n,\alpha)O^{18}$ reaction. Their calculations showed that the nuclear masses were such that this was the only exothermal reaction with emission of charged particles for neon. The observed reaction energy of 0.696 ± 0.019 MeV confirmed the calculated value of $Q$ = 0.704 MeV. By comparison with $He^3(n,p)H^3$, they obtained a cross section for the $Ne^{21}(n,\alpha)O^{18}$ reaction of 96 ± 33 b for thermal neutrons.

This reported cross section is inconsistent with a thermal neutron absorption cross section of 32 ± 9 mb for neon, measured[2] by the pile oscillator technique. From the measured 96 ± 33 b for the $Ne^{21}(n,\alpha)$ reaction and the 0.257% isotopic abundance, a contribution of 247 ± 85 mb to the thermal neutron absorption cross section for neon would be expected. This is a factor of 8 higher than that observed.

The cross section for the $Ne^{21}(n,\alpha)O^{18}$ reaction has been determined by a comparison with the $N^{14}(n,p)C^{14}$ reaction in a proportional counter.[3] The counter gas was dominantly neon, at a total pressure of 2 atm, with 15 cm $CH_4$ present as a quenching agent. The detector was exposed to the neutron flux in the thermal column of Argonne's Thermal Source Reactor, both with and without 0.4 cm $N_2$ present in the filling gas. The pulse-height distributions observed for identical fluence (time-integrated flux) are illustrated in Fig. I-13-1.

The location of peaks observed for both fillings occurs at essentially the same value of total ionization. The one containing nitrogen provided pulses equivalent to protons of energy about 615 keV. This is the more intense of the two distributions. The second, without nitrogen, produces a line about 0.27 as intense as the first. If the source of this line is the $Ne^{21}(n,\alpha)$ reaction, an upper limit of 1.5 b is calculated, based on the value of 1.81 ± 0.05 b for the $N^{14}(n,p)C^{14}$ reaction with thermal neutrons, the number of nitrogen and neon atoms present in the two fillings, and the isotopic abundance of Ne-21. This corresponds to a contribution of ≤ 4 mb to the total thermal neutron absorption cross section of 32 ± 9 mb for neon.

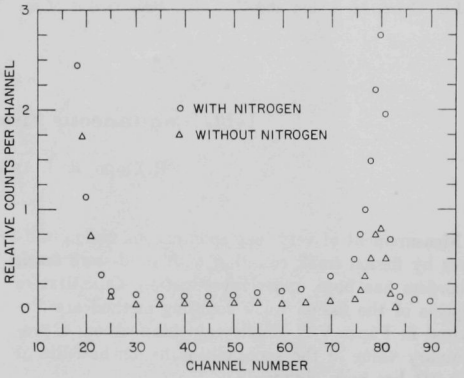


FIG. I-13-1. Pulse Height Distributions from a Neon-filled Proportional Counter With and Without Nitrogen. *ANL Neg. No. 112-8496.*

The calculated[4] $Q$ values are 699 keV for the $Ne^{21}(n,\alpha)$ reaction and 626 keV for the $N^{14}(n,p)$ reaction. Since the difference is about three times the resolution of the counter, observation of the peaks at the same ionization is surprising. The average energy loss per ion pair formed, W, would not be expected to be sufficiently different for alpha particles and protons to account for this. It is possible that the neon gas used here, and earlier, contained nitrogen as a contaminant. Only 0.1% $N_2$ present in the neon is required to account for the total reaction rate observed. This does not affect the upper limit of 1.5 b for the $Ne^{21}(n,\alpha)O^{18}$ reaction with thermal neutrons established by these measurements. This upper limit is less than 2% of the previously reported value.

The thermal neutron cross section of approximately 5300 b for the $He^3(n,p)H^3$ reaction makes insignificant any contribution from the $Ne^{21}(n,\alpha)$ reaction in a neutron pumped $He^3$-Ne gas laser. Furthermore, the small cross section for the $Ne^{21}(n,\alpha)$ reaction makes its use for fast neutron spectroscopy unattractive, compared with $He^3(n,p)$, even though it would lead to a four-fold improvement in the neutron energy at which recoil nuclei begin to interfere with the pulses from the reaction products.

REFERENCES

1. A. I. Abramov and M. G. Yutkin, *The $He^{21}(n,\alpha)O^{18}$ Reaction on Slow Neutrons*, J. Exptl. Theoret. Phys. (USSR) **41**, 1023 (1961). [Transl. in Soviet Phys.—JETP **14**, 728 (1962)].
2. J-C. Carré, M. Robin and R. Vidal, *Measurement of the Absorption Cross Section of Natural Neon for Thermal Neutrons*, Compt. rend. **252**, 3973 (1961).
3. E. F. Bennett, *Fast Neutron Spectroscopy by Proton-Recoil Proportional Counting*, Nucl. Sci. Eng. **27**, 16 (1967).
4. J. H. E. Mattauch, W. Thiele and A. H. Wapstra, *1964 Atomic Mass Table*, Nucl. Phys. **67**, 1 (1965).


## I-14. Spontaneous Fission Half-Life of Am-241

R. GOLD, R. J. ARMANI and J. ROBERTS*

Measurement of very long spontaneous fission half-lives by fission track counting with solid-state track recorders has been under investigation. Quantitative aspects of the fission track counting method are discussed in Paper V-2. Employing this method, a preliminary value of the spontaneous fission half-life of Am-241 has been obtained.[1]

In this application of fission track counting, pre-etched mica is used to record the spontaneous fission tracks. The present measurements demonstrate that mica can tolerate extremely high integral alpha particle flux and still retain sensitivity to fission fragments. The pre-etching discriminates against virtually all fossil fission fragment tracks due to the natural uranium content of the mica. The tracks observed in a pre-etched mica sample (under suitable microscope magnification) that has been exposed to a source of fission fragments are displayed in the photograph of Fig. I-14-1. The large diamond-shaped track in the center of Fig. I-14-1 is a pre-etched track. The smaller tracks in this field of view are due to the subsequent exposure of the mica sample to fission fragments, which is followed by further suitable etching.

The experimental results of four separate measurements with two different electrodeposited Am-241 sources are summarized in Table I-14-1. The weighted average obtained from these four measurements yields a preliminary value of $T_f = (1.29 \pm 0.03) \times 10^{14}$ $y$ for the Am-241 spontaneous fission half-life. The experimental error quoted above is due to counting statistics only and does not include possible systematic errors.

TABLE I-14-I. SUMMARY OF TRACK MEASUREMENTS FOR Am-241

| Source No. | Alpha Activity (alphas/min) $\times 10^9$ | Exposure Time, min | Exposure Condition | Observed Tracts | $T_f$, $y \times 10^{14}$ |
|---|---|---|---|---|---|
| 1 | 6.906 | 8,419 | Bare | 179 | $1.33 \pm 0.10$ |
| 1 | 6.890 | 51,506 | Bare | 1136 | $1.28 \pm 0.04$ |
| 2 | 5.805 | 159,758 | Cd-Covered | 2909 | $1.31 \pm 0.02$ |
| 2 | 5.562 | 51,597 | Cd-Covered | 943 | $1.25 \pm 0.04$ |


REFERENCES

1. R. Gold, R. J. Armani, J. H. Roberts and A. Behkami, *Accurate Determination of Very Long Spontaneous Fission Half-Lives ($\gtrsim 10^{14}y$) by Fission Track Counting*, Bull. Am. Phys. Soc. **11**, 825 (1966).


* Northwestern University, Evanston, Illinois.

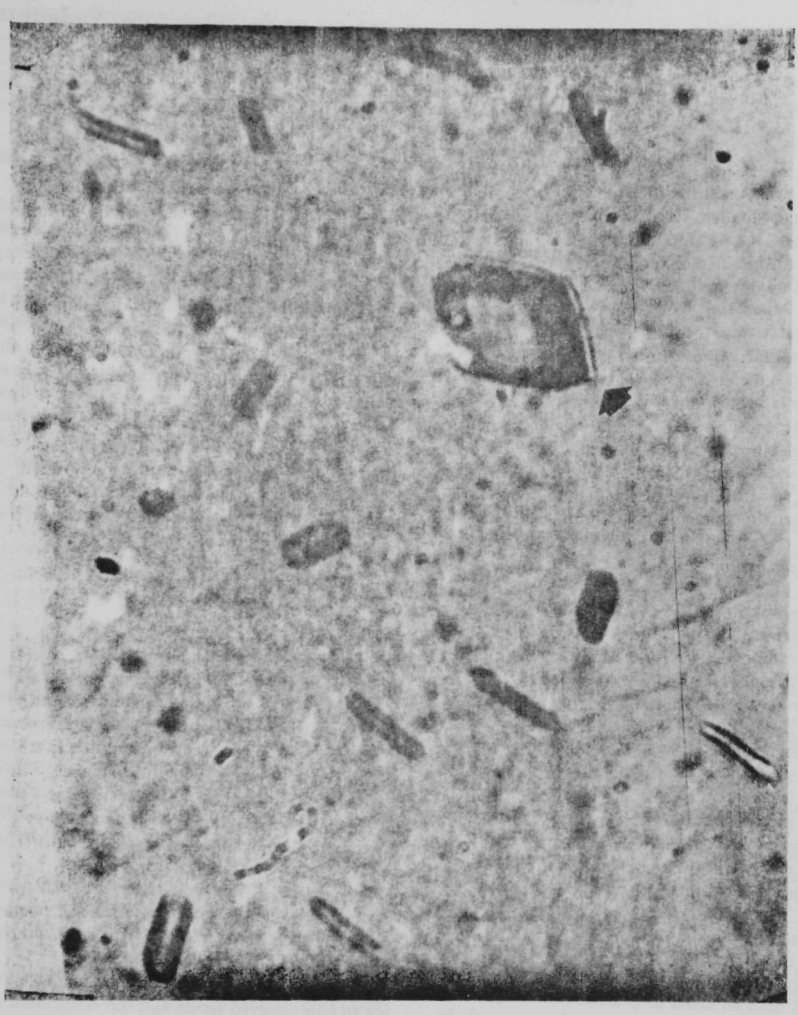

FIG. I-14-1. A Photograph of Pre-etched Mica Under Suitable Microscope Magnification. The Large Pre-etched Track (Arrow) in the Center Demonstrates The Discrimination That Can Be Attained Between Natural and Induced Fission Fragment Tracks by Employing the Pre-etching Technique. *ANL Neg. No. 112-8419.*

# I-15. Compilation of ENDF/B Cross Sections for Magnesium, Titanium, Vanadium, Molybdenum and Gadolinium

E. M. Pennington

The Cross Section Evaluation Working Group (CSEWG) was organized in the spring of 1966 to produce a coordinated system among laboratories for the evaluation, storage, and processing of neutron cross section data. Meetings of the group, which consists of representatives of approximately 15 government and industrial laboratories, have been held at Brookhaven National Laboratory in June and November of 1966 and May of 1967. At the June 1966 meeting, members of the group agreed to compile cross section data for the materials of interest in nuclear reactor applications and to supply Fortran codes to process the data. The Argonne contribution to the project was to consist of the MC[2] code,[1] which calculates multigroup cross sections from basic nuclear data, and the compilation of cross sections for magnesium, titanium, vanadium, molybdenum, and gadolinium. The compilation of the data for these five materials is reported here.

The cross sections and other nuclear data compiled by the CSEWG members form the ENDF/B system. Here the letters ENDF stand for Evaluated Nuclear Data File, while the letter B is used to distinguish the system from the previously existing ENDF/A.[2] The ENDF/B system contains complete evaluations for each material in the sense that all data required to perform reactor calculations involving that material are included. The ENDF/A system, on the other hand, may contain partial evaluations, such as a certain type of cross section over a limited energy range, for example. Descriptions of the types of data included in ENDF/B and the punched card formats involved are given in Ref. 3.

In order to complete the compilation of the ENDF/B data within a reasonable time interval, it was decided that members of the CSEWG should use already existing compiled data as much as possible. In many cases, including those of the five materials assigned to Argonne, the existing compilations did not cover all types of data required or were sufficiently old that better experiments had later been performed, which could be used to improve the evaluations. The chief source of data for the evaluations of magnesium and titanium was the compilation by N. Tralli et al.[4] of United Nuclear Corporation. The titanium data of Tralli et al. was later slightly modified at AWRE[5] and is included in ENDF/A. The main data sources for molybdenum and gadolinium were the Karlsruhe evaluations by J. J. Schmidt[6] and J. J. Schmidt and I. Siep,[7] respectively. In the case of vanadium, the present compilation is almost entirely new. The evaluations were done under a time limit, with the target date being the November 1966 meeting of the CSEWG. The original versions of the data for all five materials were completed by that time. Later some modifications were made in the titanium and vanadium data, as suggested by the review committee of the CSEWG, in order to take account of later experimental data. It is hoped that the compiled data for the five Argonne materials are reasonably good, although the short time limit necessitated somewhat of a compromise between performing the best possible evaluations and getting the data compiled in a reasonable time. Use of the data in reactor calculations should point out any serious shortcomings.

The following five sections describe the compilations for each of the materials.

## Magnesium

### Outline of Data Included

Smooth total, elastic, inelastic, $(n,2n)$, $(n,\gamma)$, $(n,p)$, and $(n,\alpha)$ cross sections are given, along with values of $\bar{\mu}_L$, $\xi$, and $\gamma$ calculated from the Legendre coefficients mentioned below. Here $\bar{\mu}_L$ is the average cosine of the angle of elastic scattering in the laboratory system, $\xi$ is the average logarithmic energy decrement in an elastic collision, and $\gamma$ is the average of the square of the logarithmic energy decrement divided by twice the average logarithmic energy decrement. The energy range is 0.001 eV to 18 MeV.

Legendre coefficients in the center of mass system are presented for elastic scattering at 33 energies, along with the transformation matrix from the center of mass to the laboratory system.

Secondary energy distributions for inelastic scattering to four resolved levels and the continuum are given along with tabulated nuclear temperatures. Nuclear temperatures for the $(n,2n)$ reaction are also included.

Parameters for the free gas thermal scattering law are given.

### Sources of Magnesium Data

#### *Total Cross Section*

The total cross section over most of the energy range is based on Table 13 of UNC-5002,[4] which gives data at 400 energies from 0.0383 eV to 18 MeV. An exten-

sion was made downward to 0.001 eV by summing the scattering and capture cross sections described below. From about 2.3 MeV to about 8.5 MeV, new values of $\sigma_{nT}$ based on the more recent measurements presented on the figures on pages 12-0-3 and 12-0-4 of Ref. 8 were used.

*Elastic Scattering Cross Section*

The elastic scattering cross section over most of the energy range was taken from Table 13 of UNC-5002, with a constant value of 3.41 b being used below 1.5 eV. Since new total cross sections were used from 2.3 to 8.5 MeV, new elastic cross sections were determined in this range by subtracting other cross sections from the total.

*Inelastic Scattering Cross Section*

The inelastic cross section is based on Table 13 of UNC-5002, with the $(n,n')$ and $(n,np)$ cross sections being added to give the inelastic cross section at high energies.

*$(n,\gamma)$ Cross Section*

The $(n,\gamma)$ cross section is from Table 13 of UNC-5002, extended down to 0.001 eV on a 1/v basis with a cross section of 0.073 b at 0.0253 eV.

*$(n,2n)$, $(n,p)$, and $(n,\alpha)$ Cross Sections*

Values of $\sigma_{n,2n}$, $\sigma_{np}$, and $\sigma_{n\alpha}$ are all from Table 13 of UNC-5002.

*$\bar{\mu}_L$, $\xi$ and $\gamma$*

A code was written using modified versions of some of the CHAD[9] subroutines in order to calculate $\bar{\mu}_L$, $\xi$ and $\gamma$ from Legendre coefficients. The CHAD code already had provision for calculation of $\bar{\mu}_L$ and $\xi$. The calculation of $\gamma$ is done in a manner similar to that of $\xi$, presented in Section VII of Ref. 9. Since there is a tendency for large terms to almost cancel one another in the calculation of $\gamma$, and to a lesser extent in the calculation of $\xi$, especially for heavy elements, the computations were done using double precision arithmetic on the CDC-3600, which involves approximately 25 decimal digits.

*Elastic Scattering Legendre Coefficients*

Legendre coefficients in the center of mass system were obtained from Table 14 of UNC-5002, with enough energies being chosen so that linear-log interpolation could reasonably be used between successive energies. Truncation of the series after too few terms at high energies in Table 14 leads to negative $d\sigma/d\Omega$ values over part of the angular range. Thus the coefficients at 9.89 MeV were slightly modified, and the coefficients at 14 and 18 MeV were derived from Abacus-2[10,11] optical model calculations. The well parameters used in Abacus-2 were those of F. Bjorklund and S. Fernbach,[12] since the Legendre coefficients at high energies in Table 14 are based on their optical model calculations. The angular distributions from the Abacus-2 problems were fit by least-squares techniques using the SAD code.[13] The maximum number of Legendre coefficients used in the magnesium angular distributions is 10. Thus a transformation matrix from the center of mass to the laboratory system involving terms through $l = 10$ was calculated using the CHAD code.

*Secondary Energy Distributions*

Probabilities of exciting each of the four resolved levels considered in inelastic scattering are tabulated from threshold up to 6.0 MeV, based on Table 15 of UNC-5002. A nuclear temperature for continuum inelastic scattering is given for higher energies. This was determined as follows. At several energies nuclear temperatures were found for the Maxwellian distribution which would yield the same average energy loss as the tabulated values of $\sigma_{nn'}(E,E')$ in Table 16 of UNC-5002, which correspond to distributions that are decidedly non-Maxwellian. A smooth curve of temperature versus energy was drawn, guided by these calculated temperatures. This led to nuclear temperatures of the same order of magnitudes as those given by the Yiftah-Okrent-Moldauer prescription[14] over part of the range but which decreased drastically at high energies.

Nuclear temperatures for the $(n,2n)$ reaction are given at threshold and at 18 MeV, determined as follows. In Ref. 5, one neutron was assumed to have an energy $E' = 0.3(E - E_{thr})$, and the other an energy $E' = 0.4(E - E_{thr})$, where $E_{thr}$ is the threshold energy. Since the peak of a Maxwellian distribution occurs at $E' = \theta(E)$, the value of $\theta(E)$ at 18 MeV was taken as $0.35(E - E_{thr})$ MeV. At $E = E_{thr}$, an arbitrary value of 0.1 MeV was used rather than zero, since a zero value might cause difficulty in processing programs.

*Thermal Neutron Scattering Law*

A free gas thermal scattering law was assumed. The cutoff above which the static model is used was taken to be 1.5 eV, and a value of 3.41 b was used for the free atom scattering cross section.

COMMENTS ON MAGNESIUM CROSS SECTIONS

The radiative capture cross section is quite uncertain, except at thermal and near thermal energies. Even at thermal energy, the value of 0.073 b used at 0.0253 eV is somewhat higher than the value of 0.063 $\pm$ 0.005 b

recommended in Ref. 8. Since the capture cross section is rather small, the errors are probably tolerable.

The inelastic scattering cross section is uncertain at high energies, although it should be reasonably good over most of the energy range.

The procedure used in UNC-5002 to obtain the $(n,2n)$ cross section yields only a very rough estimate, but the high threshold of this reaction makes it of little importance for reactor calculations.

## Titanium

### OUTLINE OF DATA INCLUDED

Smooth total, elastic, inelastic, $(n,2n)$, $(n,\gamma)$, $(n,p)$, and $(n,\alpha)$ cross sections are presented along with values of $\bar{\mu}_L$, $\xi$, and $\gamma$ calculated from the elastic scattering Legendre coefficients. The energy range covered is 0.001 eV to 18 MeV.

Elastic scattering Legendre coefficients are given in the center of mass system for 23 energies, along with the transformation matrix.

Inelastic scattering secondary energy distributions for four resolved levels and the continuum are pre sented. Nuclear temperatures are tabulated for inelastic scattering and the $(n,2n)$ reaction.

Free gas thermal scattering law parameters are included.

### SOURCES OF TITANIUM DATA

#### *Total Cross Section*

The total cross section below 100 eV was obtained by adding the scattering and capture cross sections. From 100 eV to 2.5 keV, the UNC-5002[4] total cross section was used. From 2.5 keV to almost 220 keV, values of $\sigma_{nT}$ were read from the graphs on pp. 22-0-2, 22-0-3, and 22-0-4 of Ref. 15. The UNC-5002 values were used above 220 keV, except in the region from 2.4 to 15 MeV, where values were read from the figures on page 22-0-5 of Ref. 15.

#### *Elastic Scattering Cross Section*

Below 100 eV, the elastic scattering cross section from UNC-5002 was used, except that a constant value of 4.13 b was assumed below 1.5 eV. At all higher energies, $\sigma_{nn}$ was obtained by subtracting all other cross sections from the total cross section.

#### *$(n,\gamma)$ Cross Section*

A 1/v capture cross section with a value of 6.1 b at 0.0253 eV, as recommended in Ref. 15, was assumed up to 100 eV. From 100 eV to 22.5 keV, the capture cross section was calculated using the heavy-type resonance parameters in Ref. 15 in the single-level Breit-Wigner formula without Doppler broadening. An assumed $\Gamma_\gamma$ of 0.75 eV was used, along with the 1/v contribution necessary to give $\sigma_{n\gamma} = 6.1$ b at 0.0253 eV. The 4.18 keV resonance in Ti-48 was omitted in these calculations, as its parameters do not agree with the total cross section curve. It is felt that this resonance may belong to another titanium isotope. From 22.5 keV to almost 1 MeV, the capture cross section was read from the smooth curve on the figure on p. 22-0-7 of Ref. 15. At higher energies, UNC-5002 values were used.

In the region of calculations from resonance parameters, the capture cross section is in general quite different from that in UNC-5002. This is because the UNC-5002 values are based on old resonance parameters, which have been greatly revised.

#### *Inelastic Scattering, $(n,2n)$, $(n,p)$, and $(n,\alpha)$ Cross Sections*

The values of $\sigma_{nn'}$, $\sigma_{n,2n}$, $\sigma_{np}$ and $\sigma_{n\alpha}$ are all from Table 1 of UNC-5002.

#### *$\bar{\mu}_L$, $\xi$, and $\gamma$*

Values of $\bar{\mu}_L$, $\xi$ and $\gamma$ were calculated from the elastic scattering Legendre coefficients, using the modified versions of the CHAD code[9] subroutines, as outlined above in the documentation of magnesium cross sections.

#### *Elastic Scattering Legendre Coefficients*

Legendre coefficients in the center of mass system were obtained from Table 2 of UNC-5002. The same energies were used as in Ref. 5, except above 10 MeV. Since the coefficients of Table 2 yield negative $d\sigma/d\Omega$ values over part of the angular range at high energies, new coefficients were calculated at 14 and 18 MeV. These were derived from Abacus-2[10,11] calculations, using the well parameters of Bjorklund and Fernbach.[12] The angular distributions from the Abacus-2 problems were fit by least-squares techniques, using the SAD code.[13] A transformation matrix from the center of mass to the laboratory system was calculated using CHAD.[9] This matrix involves elements through $l = 12$, since 12 is the largest number of expansion coefficients used in the titanium angular distributions.

#### *Secondary Energy Distributions*

Probabilities of exciting each of the four resolved levels considered in inelastic scattering, based on Table 3 of UNC-5002, are tabulated from threshold to 4.44 MeV. A nuclear temperature for continuum inelastic scattering, determined as described above for magnesium, is tabulated for higher energies. The nuclear temperatures so determined do not differ nearly as much from those given by the prescription of Ref. 14 as was the case for magnesium.

Nuclear temperatures for the $(n,2n)$ reaction were determined as for magnesium.

*Thermal Neutron Scattering Law*

A thermal scattering law according to the free gas model was assumed. The cutoff energy above which the static model is used was taken as 1.5 eV, and a value of 4.13 b was used for the free atom scattering cross section.

COMMENTS ON TITANIUM CROSS SECTIONS

The capture cross section is uncertain in the energy range in which it was calculated from resonance parameters, as there is no experimental data in that range and a value of $\Gamma_\gamma$ had to be assumed. The $(n,\alpha)$ and $(n,2n)$ cross sections are also questionable. The $(n,\alpha)$ cross section is too small to matter much in reactor calculations, while the high threshold of the $(n,2n)$ reaction makes it of little importance for reactors. Values of $\sigma_{n,2n}$ calculated by S. Pearlstein's method[16] might have been better.

## Vanadium

OUTLINE OF DATA INCLUDED

Smooth total, elastic, inelastic, $(n,2n)$, $(n,\gamma)$, $(n,p)$, and $(n,\alpha)$ cross sections are given, as well as values of $\bar{\mu}_L$, $\xi$, and $\gamma$ derived from the Legendre coefficients. The energy range is 0.001 eV to 15 MeV.

Elastic scattering Legendre coefficients in the center of mass system are given for 42 energies, along with the transformation matrix.

Secondary energy distributions for four resolved levels and the continuum in the case of inelastic scattering are included, along with tabulated nuclear temperatures. Nuclear temperatures are also given for the $(n,2n)$ reaction.

Parameters for the free gas thermal scattering law are given.

SOURCES OF VANADIUM DATA

*Total Cross Section*

The total cross section below 100 eV is the sum of the scattering and capture cross sections. From 100 eV to about 2 keV, $\sigma_{nT}$ was read from the graph in Ref. 17. From 2 keV to 220 keV, values were read from the graphs on pp. 23-0-3 and 23-0-4 of Ref. 15. Values from Ref. 17 were then used up to about 0.4 MeV, followed by values from pp. 23-0-5 and 23-0-6 of Ref. 15 at higher energies, except for the range from 1.3 to 2.0 MeV in which data from Ref. 17 were used.

*Elastic Scattering Cross Section*

An elastic scattering cross section of 5 b was used at tabulated energies below 100 eV. At all higher energies, $\sigma_{nn}$ was obtained by subtracting the other cross sections from the total cross section.

*$(n,\gamma)$ Cross Section*

The capture cross section was taken as 1/v up to 1.5 eV, based on the recommended value[15] of 5.06 b at 0.0253 eV. From 1.5 eV up to 22.5 keV, the capture cross section was calculated from parameters for the first two resonances in V-50 and the first six resonances in V-51 as given in Ref. 15, along with the 1/v contribution required to give agreement with the experimental cross section at 0.0253 eV. The single-level Breit-Wigner formula without Doppler broadening was used. Values of 0.60 and 0.75 eV were assumed for $\Gamma_\gamma$ for the V-50 and V-51 resonances, respectively. These values were suggested by S. Kapchigashev[18] to give agreement with his broad resolution measurements of capture cross section shown on p. 23-0-3 of Ref. 15. From 22.5 keV to 2 MeV, the capture cross section was read from the smooth curve for V-51 on p. 23-51-5 of Ref. 15. A $1/E$ dependence for $\sigma_{n\gamma}$ was assumed at higher energies.

*Inelastic Scattering Cross Section*

Inelastic scattering cross sections were calculated up to 2.4 MeV for scattering to four resolved levels in V-51 using the Abacus-2[10,11] and Nearrex[19] optical model codes. The optical model parameters used were those of Eq. (8) of Ref. 20. The parameter $Q$ in the Nearrex calculations was taken to be 1.0. Energies of the four resolved levels considered in V-51 are 0.320, 0.930, 1.609, and 1.813 MeV. The spins and parities of the ground state and the first four excited states were taken as 7/2-, 5/2-, 3/2-, 11/2-, and 9/2-, respectively.[21] Since V-50 has an abundance of only 0.24%, it was not considered in the inelastic scattering calculations. From 2.4 to 5.0 MeV, the inelastic scattering cross section was arbitrarily extrapolated using the assumption that compound elastic scattering vanished at 5 MeV. At higher energies, the other reaction cross sections were subtracted from the total optical model reaction cross section to yield $\sigma_{nn'}$.

Recent experimental data,[15,22] for inelastic scattering to the first four resolved levels, for an incident energy of 2.35 MeV only, is in rather good agreement with the calculations as is shown in Table I-15-I below. Calculations using $Q = 0.0$ rather than 1.0 in the Nearrex code did not agree quite as well with these experimental data.

*$(n,2n)$ Cross Section*

The $(n,2n)$ cross section was calculated for V-51 according to the method of Pearlstein[16] and was then

TABLE I-15-I. VANADIUM INELASTIC SCATTERING AT 2.35 MeV

| Level, MeV | $\sigma$ Experimental, mb | $\sigma$ Calculated, mb |
|---|---|---|
| 0.320 | 360 ± 30 | 369 |
| 0.930 | 160 ± 8 | 153 |
| 1.609 | 207 ± 10 | 207 |
| 1.813 | 145 ± 15 | 186 |

increased by about 20% throughout the entire energy range in order to pass through a single experimental point.[23] In this calculation, no distinction was made between the laboratory and center of mass systems. This is in contrast to the calculations reported below for molybdenum and gadolinium in which the distinction between the systems was treated correctly.

*(n,p) Cross Section*

A smooth curve was drawn through the experimental $V^{51}(n,p)Ti^{51}$ points given in Ref. 24. Since the experimental points were measured only at energies well above threshold, the curve was extrapolated downward to an assumed effective threshold of 3 MeV. This value was estimated by inspecting $\sigma_{np}$ cross sections for other isotopes with $Z$ values near that of vanadium and observing how far effective thresholds are above actual thresholds. The smooth curve on p. 23-51-6 of Ref. 15 is almost in agreement with the $\sigma_{np}$ values used here in the range above 13 MeV covered by the curve.

*(n,α) Cross Section*

The $(n,\alpha)$ cross section was read from the smooth curve on p. 23-51-8 of Ref. 15, and extended downwards to an effective threshold of 7 MeV, estimated as for the $(n,p)$ reaction.

*$\bar{\mu}_L$, $\xi$, and $\gamma$*

Values of $\bar{\mu}_L$, $\xi$, and $\gamma$ were calculated from the elastic scattering Legendre coefficients, as outlined above for magnesium.

*Elastic Scattering Legendre Coefficients*

Below 1.8 MeV, the Legendre coefficients are based on the experimental results of A. Langsdorf et al.,[25] who plot coefficients in the laboratory system as a function of energy. Values were read from these curves, renormalized as in ENDF/B, and transformed to the center of mass system using the transformation matrix routine from CHAD.[9] Since these experimental results include inelastically scattered neutrons, corrections were made above the inelastic scattering threshold, assuming isotropic scattering in the center of mass system. The elastic scattering angular distributions of the Abacus-2 problems were fit at 1.8 MeV and above, using the least-squares fitting routine of SAD.[13] From 2.6 through 4.0 MeV, the coefficients were adjusted using an estimated compound elastic scattering cross section, assumed isotropic in the center of mass system. At 5 MeV and above, it was assumed that compound elastic scattering is negligible. Since 12 Legendre coefficients are used at high energies, a transformation matrix from the center of mass to laboratory systems including terms through $l = 12$ was calculated.

*Secondary Energy Distributions*

The probabilities of exciting each of the four resolved inelastic levels of the Abacus 2-Nearrex calculations are tabulated from threshold to 2.4 MeV. Nuclear temperatures, calculated from the prescription of Ref. 14, are given at 2.4 and 15 MeV as the variation is linear on a log-log scale.

*Thermal Neutron Scattering Law*

A free gas thermal scattering law was assumed. The cutoff above which the static model is used was taken to be 1.5 eV, and a free atom scattering cross section of 5.0 b was used.

COMMENTS ON VANADIUM CROSS SECTIONS

The recent measurements of $\sigma_{n\gamma}$ by Kapchigashev[18] have helped to reduce the uncertainty in the capture cross section in the resonance region. Experimental data[15,22] on inelastic scattering are available only at 2.35 MeV, but the good agreement between these results and the optical model calculations does give some confirmation of the validity of the calculations. There is uncertainty in the $(n,p)$ and $(n,\alpha)$ cross sections at low energies since the data had to be extrapolated downward from higher energies, with the extrapolation covering a rather large energy range in the case of the $(n,p)$ cross section. No elastic angular distribution measurements exist above 1.8 MeV. However, optical model calculations of elastic angular distributions are generally rather reliable above a few MeV.

## MOLYBDENUM

OUTLINE OF DATA INCLUDED

Smooth total, elastic, inelastic, $(n,2n)$, $(n,3n)$ and $(n,\gamma)$ cross sections are included, along with values of $\bar{\mu}_L$, $\xi$, and $\gamma$ calculated from the Legendre coefficients. The energy range extends from 0.001 eV to 15 MeV.

Resolved resonance parameters for 32 resonances are given, with the resonance calculations extending from 4 eV to 1 keV.

Legendre coefficients for elastic scattering are given

in the center of mass system for 39 energies, along with the transformation matrix.

Secondary energy distributions are given for inelastic scattering to four resolved levels and the continuum, along with tabulated nuclear temperatures. Nuclear temperatures for the $(n,2n)$ and $(n,3n)$ reactions are also included.

Thermal scattering law parameters according to the free gas model are given.

## SOURCES OF MOLYBDENUM DATA

### *Total Cross Section*

The total cross section below 4 eV is the sum of the scattering and capture cross sections. From 4 eV to 1 keV, the total cross section is the sum of that calculated from resonance parameters and a smooth cross section which is entirely capture. Above 1 keV and up to 10 MeV, the KFK-120 data[6] were used. From 10 to 15 MeV, $\sigma_{nT}$ was read from the graph of Ref. 17.

### *Elastic Scattering Cross Section*

A constant value of $\sigma_{nn} = 5$ b, which is close to the tabulated values of Ref. 6, was used below 1.5 eV. At 4 eV and 1 keV, 5.008 and 5.780 b were used, respectively, since these numbers correspond to those calculated from resonance parameters. Between 4 eV and 1 keV, $\sigma_{nn}$ is calculated entirely from resonance parameters. From 1 to 200 keV, the values of Ref. 6 were used. Above 200 keV, $\sigma_{nn}$ was found by subtracting other cross sections from the total.

### *$(n,\gamma)$ Cross Section*

The capture cross section was taken from Ref. 6 over most of the energy range, with linear extrapolation on a log-log scale from $10^{-2}$ to $10^{-3}$ eV and from 10 to 15 MeV. Between 4 eV and 1 keV, $\sigma_{n\gamma}$ is calculated from resonance parameters, with a smooth contribution being added to yield about the same $\sigma_{n\gamma}$ as in Ref. 6 between resonances.

### *Inelastic Scattering Cross Section*

From 200 keV to 1.5 MeV, the inelastic scattering cross section was derived by summing values read off smooth curves drawn through experimental points for the excitation of four levels given in Ref. 26. A smooth curve was drawn from the value so determined at 1.5 MeV to meet the 2 MeV value of Ref. 6. The values from Ref. 6 were used from 2 to 10 MeV, except that $\sigma_{n,2n}$ and $\sigma_{n,3n}$ were subtracted from these values above their thresholds. Above 10 MeV, the total reaction cross section was assumed constant, and $\sigma_{n,2n}$, $\sigma_{n,3n}$, and $\sigma_{n\gamma}$ were subtracted from the reaction cross section to yield $\sigma_{nn'}$.

### *$(n,2n)$ and $(n,3n)$ Cross Sections*

Both the $(n,2n)$ and $(n,3n)$ cross sections were calculated by S. Pearlstein, using the methods of Ref. 16.

### *$\bar{\mu}_L$, $\xi$, and $\gamma$*

The values of $\bar{\mu}_L$, $\xi$, and $\gamma$ were computed from the elastic scattering Legendre coefficients, as described above for magnesium.

### *Resonance Parameters*

Parameters for a total of nineteen $l = 0$ resonances and thirteen $l = 1$ resonances in six of the molybdenum isotopes are included. These are based on experimental data for separated molybdenum isotopes.[27] There are more resonances than are present in the same energy range in Ref. 6, but the cross section contributions from most $l = 1$ resonances are small.

### *Elastic Scattering Legendre Coefficients*

Legendre coefficients in the center of mass system, obtained from H. Alter,[28] were used up to 6 MeV. Coefficients were computed at five energies above 6 MeV by performing Abacus-2[10,11] calculations, using the well parameters of P. Moldauer,[20] and fitting the shape-elastic angular distributions using the least-squares techniques of SAD.[13] A transformation matrix from the center of mass to the laboratory system was calculated using CHAD.[9] The matrix involves elements through $l = 16$, since there are 16 coefficients given for the high energy Legendre expansions.

### *Secondary Energy Distributions*

Probabilities of exciting the four resolved levels by inelastic scattering[26] are tabulated from threshold to 1.5 MeV. Actually the top two of the four levels are combinations of levels with nearly the same energies. Nuclear temperatures, calculated as in Ref. 14, are given at 1.5 and 15 MeV.

Nuclear temperatures for the $(n,2n)$ and $(n,3n)$ reactions are given. The $(n,2n)$ temperatures were determined as described for magnesium, while the $(n,3n)$ temperatures were found in a similar manner, assuming $E' = 0.2\ (E - E_{thr})$ rather than $0.35\ (E - E_{thr})$.

### *Thermal Neutron Scattering Law*

The free gas thermal neutron scattering law involves a cutoff of 1.5 eV above which the static model is used and a value of 5.0 b for the free atom scattering cross section.

## COMMENTS ON MOLYBDENUM CROSS SECTIONS

The recent revision[29] of the Karlsruhe evaluation of

molybdenum provides a good source of data with which to compare the present evaluation. This revision was not available when the ENDF/B compilation was made. As in the present evaluation, J. Schmidt[29] recommends the use of resolved resonance parameters only up to 1 keV on the grounds that resonances are being missed experimentally at higher energies. The recommended resonance parameters in Table Mo-R4 of Ref. 29 differ from those in ENDF/B mainly by having smaller values of $\Gamma_\gamma$. Schmidt's resonance parameters give a non-1/v contribution of 22.5[(29)] for the molybdenum capture resonance integral up to 1 keV. The ENDF/B parameters yield 24.5 b for the same quantity. As Schmidt points out, the discrepancies between various measured resonance integrals are so large that the measurements do not help much in evaluating the compiled resonance parameters.

Schmidt[29] has revised the smooth capture cross sections in the energy range above 1 keV. Essentially, he has used the results of Kapchigashev[30] up to 50 keV and those of Y. Staviskii and A. Shapar[31] above 50 keV. These data[30,31] are shown on pp. 42-0-6 and 42-0-16 of Ref. 32. A comparison of Schmidt's new evaluation and his old evaluation, which is used in ENDF/B, is shown on Fig. Mo-C6 of Ref. 29. The most significant difference is in the energy range below 10 or 15 keV, where Schmidt's new values are considerably lower than the old values.

It therefore appears from the preceding discussion that the capture cross section used in ENDF/B is probably somewhat high over most of the energy range above thermal.

Newer data on total cross section are available and they show considerably more structure in the energy range above 1 keV than do the values used in ENDF/B. Schmidt's reevaluation[29] shows more structure in the kilovolt energy range than does his original evaluation.[6] The data of Wynchank, et al. from Columbia, which were not available at the time of Schmidt's reevaluation, have the best resolution, and extend up to 66 keV. These data are plotted on pp. 42-0-6 through 42-0-9 of Ref. 32.

Neither $(n,p)$ nor $(n,\alpha)$ data were included in the ENDF/B molybdenum compilation. This was because data were available only for some of the isotopes, either at only one energy around 14 MeV or averaged over a fission spectrum. The $(n,\alpha)$ data are especially skimpy, and $\sigma_{n\alpha}$ is also quite small because of the large Coulomb barrier. Schmidt has included an $(n,p)$ cross section for molybdenum in his reevaluation.[29] This $(n,p)$ cross section was assumed equal to that of Zr-90.

## Gadolinium

### Outline of Data Included

Smooth total, elastic, inelastic, $(n,2n)$, $(n,3n)$ and $(n,\gamma)$ cross sections are included, as well as values of $\bar{\mu}_L$, $\xi$, and $\gamma$ computed from the Legendre coefficients. The energy range covered extends from 0.001 eV to 15 MeV.

Resolved resonance parameters for 24 resonances in Gd-155 and 5 resonances in Gd-157 are included.

Legendre coefficients for elastic scattering in the center of mass system are given for 32 energies, along with the transformation matrix.

Nuclear temperatures are given for inelastic scattering and for the $(n,2n)$ and $(n,3n)$ reactions. No resolved levels were considered for inelastic scattering.

Free gas thermal scattering law parameters are included.

### Sources of Gadolinium Data

#### *Total Cross Section*

The total cross section up to 50 eV is calculated from resonance parameters. From 50 eV to 10 keV, $\sigma_{nT}$ was read from the BNL-325 graphs.[17] Values from 10 keV to 10 MeV were obtained from KFK-352.[(7)] The total cross section was extended from 10 to 15 MeV using the sparse data of Ref. 17 as a guide.

#### *Elastic Scattering Cross Section*

Below 50 eV, the elastic scattering cross section is calculated from the resonance parameters. From 50 eV to 10 keV, $\sigma_{nT}$ was split into scattering and capture components using a computer program based on Eqs. (39), (40), (43), and (44) of KFK-352. Equations (39) and (40) are expressions for the average scattering and capture cross sections for $l = 0$ neutrons in the unresolved resonance region for Gd-155. The parameters used in these equations were determined by averaging the known resonance parameters. Since not enough resolved parameters are known to find average parameters for the other isotopes, Gd-155 was assumed typical of natural gadolinium. Equations (43) and (44) merely use Eqs. (39) and (40) to split the experimental $\sigma_{nT}$ into the scattering and capture components.

From 10 keV to 10 MeV, values of $\sigma_{nn}$ were obtained from KFK-352. The reaction cross section was subtracted from the total cross section to give the elastic scattering cross section from 10 to 15 MeV.

#### *$(n,\gamma)$ Cross Section*

The $(n,\gamma)$ cross section is calculated from resonance parameters below 50 eV. From 50 eV to 10 keV, $\sigma_{n\gamma}$ was determined as described above in the discussion of the elastic scattering cross section. Values from KFK-352 were used from 10 keV to 10 MeV, with the extension of 15 MeV being made on the basis of linear extrapolation on a log-log scale.

*Inelastic Scattering Cross Section*

The inelastic scattering cross section was obtained up to the threshold of the $(n,2n)$ reaction from KFK-352. From the $(n,2n)$ threshold to 10 MeV, $\sigma_{n,2n}$ was subtracted from the $\sigma_{nn'}$ of KFK-352 to give the inelastic cross section. From 10 to 15 MeV, the reaction cross section of KFK-352 was extrapolated on a basis of a value at 15 MeV equal to 1.01 times the sum of $\sigma_{n,2n}$, $\sigma_{n,3n}$, and $\sigma_{n\gamma}$. Then $\sigma_{nn'}$ in this range was obtained by subtracting the other reactions from the total reaction cross section.

*$(n,2n)$ and $(n,3n)$ Cross Sections*

The $(n,2n)$ and $(n,3n)$ cross sections were both calculated by S. Pearlstein, according to the methods of Ref. 16.

*$\bar{\mu}_L$, $\xi$, and $\gamma$*

The values of $\bar{\mu}_L$, $\xi$, and $\gamma$ were calculated from the Legendre coefficients, as described above for magnesium.

*Resonance Parameters*

Resonance parameters are included for 24 $s$-wave resonances in Gd-155 and 5 $s$-wave resonances in Gd-157. The parameters for the first three resonances in Gd-155 and the first two in Gd-157 are from Ref. 33. Parameters for the remaining resonances are from BNL-325.[17]

*Elastic Scattering Legendre Coefficients*

Legendre coefficients in the center of mass system, which were obtained from H. Alter,[28] were used in the energy range from 0.3 to 1.5 MeV. Below 0.3 MeV, coefficients were estimated from extrapolation of the Alter data, with isotropic scattering assumed below 5 keV. Above 1.5 MeV, coefficients were calculated at 7 energies by performing Abacus-2[10,11] calculations and fitting the resulting shape elastic angular distributions using SAD.[13] The parameters used in these optical model calculations were derived from approximations to Eq. (35) of Ref. 34, since the optical model parameters used in KFK-352 were also obtained in this manner. This equation is used to obtain local parameters which are approximately equivalent to non-local ones. As in KFK-352, the parameters of Table 4 of Ref. 34 without the spin-orbit term were used for the non-local parameters.

The transformation matrix from the center of mass to laboratory system, calculated using CHAD,[9] includes elements through $l = 19$ in agreement with the number of coefficients in the high energy Legendre expansions.

*Secondary Energy Distributions*

Nuclear temperatures for inelastic scattering, calculated from the prescription of Ref. 14, are given at 60 keV and 15 MeV. Only continuum inelastic scattering was considered, both in this evaluation and in KFK-352, since there are many low-lying levels in the various gadolinium isotopes above the $(n,n')$ threshold.

Nuclear temperatures are given for the $(n,2n)$ and $(n,3n)$ reactions. These were determined by the methods described under magnesium and molybdenum.

*Thermal Neutron Scattering Law*

The free gas thermal scattering law has a cutoff of 1.5 eV above which the static model is used and a value of 8.0 b for the free atom scattering cross section. This 8 b value is that which is calculated from resonance parameters near 1.5 eV.

COMMENTS ON GADOLINIUM CROSS SECTIONS

The cross section of gadolinium in the thermal energy range is the largest of any stable element. The resonance parameters of Ref. 33, which were used in this evaluation, give a very good fit to the gadolinium cross section at low energy.

There is not a great deal of experimental data available for gadolinium above one or two MeV. Thus optical model calculations were used to a large extent at higher energies. The $(n,2n)$ and $(n,3n)$ cross sections are based entirely on calculation. No $(n,p)$ and $(n,\alpha)$ cross sections are included in this compilation, but the Coulomb barrier is sufficiently high to make these cross sections quite small.

REFERENCES


1. B. J. Toppel, A. L. Rago and D. M. O'Shea, *MC²—A Code to Calculate Multigroup Cross Sections*, ANL-7318 (to be published).
2. H. Honeck, *ENDF Evaluated Nuclear Data File Description and Specifications*, BNL-8381 (June 1964).
3. H. Honeck, U. S. Atomic Energy Commission, (private communication).
4. N. Tralli, et al., *Fast Neutron Cross Sections for Titanium, Potassium, Magnesium, Nitrogen, Aluminum, Silicon, Sodium, Oxygen and Manganese*, UNC-5092 (January 1962).
5. S. Miller and K. Parker, *Neutron Cross Sections of Natural Titanium in the Energy Range 0.001 eV–18 MeV—Incorporation of United Nuclear Corporation Data in the UKAEA Nuclear Data Library*, AWRE O-77/64 (October 1964).
6. J. J. Schmidt, *Neutron Cross Sections for Fast Reactor Materials*, KFK-120. Part II: Tables. Part III: Graphs. (December 1962).
7. J. J. Schmidt and I. Siep, *26 Gruppen-Wirkungquerschnitte für Europium, Samarium, Gadolinium und Hafnium*, KFK-352 (August 1965).
8. J. R. Stehn, et al., *Neutron Cross Sections*, BNL-325, Second Edition, Supplement No. 2, Volume I, Z = 1 to 20 (May 1964).

9. R. F. Berland, *CHAD, Code to Handle Angular Data*, NAA-SR-11231 (December 1965).
10. E. H. Auerbach, et al., *Abacus-1: A Program for the Calculation of Nuclear Cross Sections Using the Cloudy Crystal Ball Model*, KAPL-3020 (June 1, 1964).
11. E. H. Auerbach, *Abacus-2 (Revised Version), Program Operation and Input Description*, BNL-6562 (November 1962).
12. F. Bjorklund and S. Fernbach, *Optical Model Analyses of Scattering of 4-, 7-, and 14-MeV Neutrons by Complex Nuclei*, Phys. Rev. **109**, 1295–1298 (1958).
13. E. M. Pennington, J. C. Gajniak and R. A. Mewaldt, *Programs for Analysis of Scattering Angular Distributions*, ANL-7306 (to be published).
14. S. Yiftah, D. Okrent and P. A. Moldauer, *Fast Reactor Cross Sections* (Pergamon Press, New York, 1960), p. 49.
15. M. D. Goldberg, et al., *Neutron Cross Sections*, BNL-325, Second Edition, Supplement No. 2, Volume IIA, Z = 21 to 40 (February 1966).
16. S. Pearlstein, *Analysis of (n,2n) Cross Sections for Medium and Heavy Mass Nuclei*, Nucl. Sci. Eng. **23**, 238–250 (November 1965).
17. D. J. Hughes and R. B. Schwartz, *Neutron Cross Sections*, BNL-325, Second Edition (July 1, 1958).
18. S. P. Kapchigashev, *Cross Sections of V, Zr, $Zr^{90}$, $Zr^{91}$ and $Zr^{94}$ for Radiative Capture of Neutrons with Energies 1–50,000 eV*, Soviet J. At. Energy **19**, 1212 (1965), Translated from At. Energ. (USSR), Vol. 19, No. 3, 294–296 (September 1965).
19. P. A. Moldauer et al., *Nearrex, A Computer Code for Nuclear Reaction Calculations*, ANL-6978 (1964).
20. P. A. Moldauer, *Optical Model of Low Energy Neutron Interactions with Spherical Nuclei*, Nucl. Phys. **47**, 65–92 (1963).
21. J. E. Schwager, *Capture Gamma Determination of Vanadium Levels*, UCRL-6003 (January 1960).
22. A. T. G. Ferguson, *Inelastic Neutron Scattering*, p. 63–69 of *Nuclear Structure Study with Neutrons*. Proc. International Conference on the Study of Nuclear Structure with Neutrons, Antwerp, July 19–23, 1965. (North Holland Publishing Co., 1966). Figure 6a.
23. V. J. Ashby, et al., *Absolute Measurements of (n,2n) Cross Sections at 14.1 MeV*, Phys. Rev. **111**, 616–621 (1958).
24. M. Bormann, et al., *Investigation of the Energy Dependence of Nuclear Reactions of Neutrons in the Energy Range between 12 and 19 MeV*, Z. Physik. **174**, 1–17 (1963).
25. A. Langsdorf, et al., *Angular Distributions of Scattered Neutrons*, Phys. Rev. **107** (No. 4), 1077–1087 (1957). Also ANL-5800, 2nd Edition, *Reactor Physics Constants*, p. 62.
26. A. B. Smith and R. Hayes, *Fast Neutron Scattering from Elemental Mo, Sn, Sb and Te*, Nuclear Physics, **A93**(3), 609–630 (1967).
27. M. I. Pevzner, et al., *Investigation of Nuclear Levels by Neutron Spectroscopy. 1. Neutron Cross Sections of Molybdenum Isotopes in the 7–15,000 eV Energy Range*, Soviet Physics JETP **17**, No. 4, 803–808 (October 1963).
28. H. Alter, Atomics International, (private communication). See also R. W. Campbell, et al., *Compilation, Evaluation and Reduction of Neutron Differential Scattering Data*, NAA-SR-11980, Volume IV (April 1967).
29. J. J. Schmidt, *Neutron Cross Sections for Fast Reactor Materials*, KFK-120. Part I: Evaluation, (February 1966).
30. S. P. Kapchigashev and Y. P. Popov, *Capture Cross Sections for Neutrons with Energies up to 50 keV of Certain Structural Materials*, Soviet Journal of Atomic Energy **15**, 808 (1964).
31. Y. Y. Staviskii and A. V. Shapar, *Neitronnaya Fizika*, (Moscow Gosatomizdat, 1961) p. 310; Consultants Bureau Translation, 1963, p. 227 (Mo).
32. M. D. Goldberg, et al., *Neutron Cross Sections*, BNL-325, Second Edition, Supplement No. 2, Volume IIB, Z = 41 to 60 (May 1966).
33. H. B. Möller, et al., *Low Energy Neutron Resonances in Erbium and Gadolinium*, Nucl. Sci. Eng. **8**, 183–192 (1960).
34. F. Perey and B. Buck, *A Non-Local Potential Model for the Scattering of Neutrons by Nuclei*, Nucl. Phys. **32**, 353–380 (1962).

# Section II

# Thermal Reactor Physics

Thermal reactor physics is distinguished from fast reactor physics by the relatively larger amount of attention that is given to the analysis of heterogeneity effects in the former. There is also an arbitrary distinction based on the neutron spectrum, but this is less realistic than the former distinction. The influence of heterogeneity effects is particularly evident in the first paper, which discusses the high conversion ratio lattice experiments. Three intervening papers refer to the plutonium recycle program which was carried out in EBWR and which was concluded at the end of the fiscal year being reported. The next paper treats the physics of plutonium fueled thermal research and test reactors. The remaining eighteen papers relate to work on the Argonne Advanced Research Reactor (AARR).

# II-1. High Conversion (Hi-C) Uniform Lattice Calculations

E. M. Pennington

The analysis of the High Conversion (Hi-C) uniform lattice experiments has been completed and a report has been written giving all of the calculational methods and results.[1] The experimental methods and results have been given in Ref. 2, and a recent paper[3] has covered the highlights of both the experimental and analytical results. Previous Reactor Physics Division Annual Reports[4,5,6] have outlined much of the analytical work. More recent work has included calculations of gold and indium cadmium ratios and considerations of the effects of cross section changes on reactivity. These two topics are treated below.

## Gold and Indium Cadmium Ratios

Both gold and indium cadmium ratios were measured in almost all of the Hi-C lattices. Calculated values were obtained using the B512/RP foil activation program.[7]

The B512/RP program calculates both the neutron absorption in a bare foil of thickness $t$ and the absorption in the same foil between two identical covers (usually cadmium) of thickness $l_0$ in slab geometry. The cadmium cutoff energy, $E_{cut}$, is also computed. Flux depression in the foil and covers, resulting from neutron absorption, is considered in the program. The flux is assumed to impinge isotropically on the outer surface of the bare foil or on the outer surface of the covers. The flux has the energy dependence of a Maxwellian plus a $1/E$ tail. More specifically, the energy dependence is

$$\phi(X) = \frac{2r}{\sqrt{\pi}} Xe^{-X} + \frac{X_0^{\frac{1}{2}}}{X} \Delta(X), \qquad (1)$$

where $r$ is a constant, $X = E/E_m$, $X_0 = E_{2200}/E_m$ and $\Delta(X)$ is zero for $X < \mu$ and unity for $X \geq \mu$. Here $E$ is the neutron energy, $E_m$ is the energy at the peak of the Maxwellian distribution, and $E_{2200}$ is the energy corresponding to a velocity of 2200 m/sec. In most of the calculations, the parameter $\mu$ was taken to be 5. Scattering by the foil and covers is neglected, so that their cross sections represent absorption only. The energy dependence of the cross sections is a sum of single level Breit-Wigner resonances without Doppler broadening along with a $1/V$ component.

For cadmium and indium, the cross sections were considered to be given completely by the resonances at 0.178 and 1.457 eV, respectively. In the case of gold, a $1/V$ component yielding a cross section of 5.05 barns at 0.0253 eV was added to the cross section produced by the 4.906 eV resonance. The resonance parameters used were taken from Refs. 8 and 9.

Values of the parameters $r$ and $E_m$ involved in Eq. (1) were determined as described in Ref. 1. The foil thicknesses used in the experiments were 1.1, 1.2 and 20 mils for gold, indium and cadmium, respectively. Results of the calculations are presented in Table II-1-I, along with experimental values from Table XXV of Ref. 2. Under the heading "Lattice," the first item is the pitch in cm, the second item is □ for a square array or △ for a triangular array, and the third item is S for stainless steel clad or A for aluminum clad. The compositions and dimensions of the lattice constituents are presented in detail in Ref. 2. Briefly, the lattices consist of 3.04 w/o enriched $UO_2$ pellets of 0.935 cm diameter in either aluminum or stainless steel clad surrounded by light water moderator.

The calculated gold cadmium ratios are generally somewhat lower than the experimental ratios, with the discrepancy becoming greater as the lattice pitch is decreased. Calculated values of the cadmium ratio minus one (CR-1) are about 10% too low for the looser lattices and 45% too low for the tightest lattice. Agreement between theory and experiment is a little better in the case of indium, although the trend of calculated values for tightly packed lattices continues to be too low. The value of CR-1 in the tightest lattice is only about 20% too low. The effect of flux depression in the gold or indium foils is quite important, even for the thin foils used here, since the cross sections of the dominant resonances are very large. This effect is seen by comparing the calculated cadmium ratios of the 1.24□A lattice for the actual value of $t$ = 20 mils and for $t$ = 0.

The calculations described here have a number of deficiencies. The treatment of the energy dependence of the flux as a Maxwellian plus a $1/E$ tail is not very accurate. There is some departure from Maxwellian behavior, especially for the tighter lattices. The high absorption causes the tail to depart from a $1/E$ form. Also the cutoff of $\mu$ = 5 is not strongly justified. An idea of the effect of changing $\mu$ is obtained by comparing the cadmium ratios for $\mu$ = 3, 5 and 10 for the 1.24□A lattice. The method described in Ref. 1 for determining the parameters $r$ and $E_m$ is also approximate.

TABLE II-1-I. GOLD AND INDIUM CADMIUM RATIOS FOR Hi-C UNIFORM LATTICES

| Lattice | Region | $E_m$, eV | $r$ | Gold | | | Indium | | |
|---|---|---|---|---|---|---|---|---|---|
| | | | | $E_{cut}$ eV | CR Calculated | CR Experimental | $E_{cut}$ eV | CR Calculated | CR Experimental |
| 1.349□A | Fuel | 0.0370 | 2.537 | 0.5863 | 1.572 | 1.62 ± 0.02 | 0.7619 | 1.619 | 1.61 ± 0.03 |
| 1.349□S | Fuel | 0.0377 | 2.305 | 0.5864 | 1.525 | 1.58 ± 0.02 | 0.7620 | 1.574 | 1.58 ± 0.03 |
| 1.24 □A | Fuel | 0.0402 | 1.693 | 0.5866 | 1.401 | 1.455 ± 0.008 | 0.7620 | 1.453 | 1.482 ± 0.015 |
| 1.24 □A | Fuel[a] | 0.0402 | 1.334 | 0.5870 | 1.373 | 1.455 ± 0.008 | 0.7623 | 1.430 | 1.482 ± 0.015 |
| 1.24 □A | Fuel[b] | 0.0402 | 2.181 | 0.6085 | 1.454 | 1.455 ± 0.008 | 0.7764 | 1.493 | 1.482 ± 0.015 |
| 1.24 □A | Fuel[c] | 0.0402 | 1.693 | 0.7208 | 1.139 | — | 1.203 | 1.222 | — |
| 1.24 □A | $H_2O$ | 0.0346 | 2.085 | 0.5869 | 1.488 | 1.503 ± 0.015 | 0.7623 | 1.536 | 1.518 ± 0.020 |
| 1.24 □S | Fuel | 0.0408 | 1.534 | 0.5867 | 1.369 | 1.435 ± 0.008 | 0.7621 | 1.422 | 1.469 ± 0.008 |
| 1.24 □S | $H_2O$ | 0.0346 | 1.917 | 0.5870 | 1.455 | 1.442 ± 0.008 | 0.7624 | 1.503 | 1.483 ± 0.020 |
| 1.27 △A | Fuel | 0.0421 | 1.277 | 0.5868 | 1.316 | 1.361 ± 0.015 | 0.7621 | 1.369 | 1.398 ± 0.015 |
| 1.27 △S | Fuel | 0.0428 | 1.146 | 0.5869 | 1.289 | 1.346 ± 0.015 | 0.7621 | 1.343 | 1.373 ± 0.007 |
| 1.166△A | Fuel | 0.0489 | 0.618 | 0.5869 | 1.175 | 1.221 ± 0.008 | 0.7620 | 1.231 | 1.260 ± 0.008 |
| 1.166△S | Fuel | 0.0496 | 0.546 | 0.5870 | 1.160 | 1.201 ± 0.005 | 0.7621 | 1.216 | 1.234 ± 0.005 |
| 1.127△A | Fuel | 0.0517 | 0.399 | 0.5872 | 1.128 | 1.177 ± 0.010 | 0.7621 | 1.184 | 1.204 ± 0.020 |
| 1.127△S | Fuel | 0.0525 | 0.340 | 0.5873 | 1.115 | 1.152 ± 0.015 | 0.7622 | 1.171 | — |
| 1.069△S | Fuel | 0.0600 | 0.0793 | 0.5888 | 1.055 | 1.099 ± 0.008 | 0.7632 | 1.108 | 1.135 ± 0.008 |

[a] $\mu = 3$ rather than 5.
[b] $\mu = 10$ rather than 5.
[c] Foil thickness $t = 0$.

TABLE II-1-II. EFFECTS OF CROSS SECTION CHANGES ON REACTIVITY ($\Delta k_{eff}/k_{eff}$, %)

| Lattice | Cross Section[a] with +10% Change | | | | | | |
|---|---|---|---|---|---|---|---|
| | $\Sigma_{c1}$ | $\Sigma_{f1}$ | $\Sigma_{out1}$, $\Sigma_{12}$ | $\sigma_{c2}^{28}$ | $\sigma_{c3}^{28}$ | $\sigma_{c3}^{25}$ | $\sigma_{f3}^{25}$ |
| 1.349□A | −0.049 | +0.420 | +0.537 | −0.410 | −1.399 | −0.301 | +0.499 |
| 1.349□S | −0.052 | +0.424 | +0.303 | −0.424 | −1.422 | −0.301 | +0.586 |
| 1.24 □A | −0.057 | +0.529 | +0.331 | −0.561 | −1.676 | −0.382 | +0.669 |
| 1.24 □S | −0.062 | +0.524 | +0.086 | −0.583 | −1.718 | −0.386 | +0.780 |
| 1.27 △A | −0.067 | +0.604 | +0.162 | −0.693 | −1.852 | −0.449 | +0.807 |
| 1.27 △S | −0.065 | +0.600 | +0.080 | −0.714 | −1.901 | −0.446 | +0.944 |
| 1.166△A | −0.083 | +0.795 | −0.305 | −1.098 | −2.282 | −0.599 | +1.225 |
| 1.166△S | −0.082 | +0.773 | −0.559 | −1.149 | −2.385 | −0.594 | +1.423 |
| 1.127△A | −0.090 | +0.894 | −0.549 | −1.385 | −2.401 | −0.682 | +1.478 |
| 1.127△S | −0.091 | +0.862 | −0.802 | −1.462 | −2.544 | −0.674 | +1.708 |
| 1.069△S | −0.111 | +1.026 | −1.333 | −2.487 | −2.790 | −0.808 | +2.339 |

[a] Second subscript indicates energy group.

Other calculational deficiencies include the use of only one resonance in representing the cross sections, the neglect of Doppler broadening, and the neglect of scattering by the foils. In view of the approximate nature of the calculations, the discrepancies between theory and experiment are not surprising.

### EFFECTS OF CROSS SECTION CHANGES ON REACTIVITY

The criticality calculations for the Hi-C lattices were carried out in the framework of four-group diffusion theory, with the cross sections for three fast groups being obtained using GAM-I[10] and for those for the thermal group being derived from THERMØS.[11] It was found that the cross sections on the original GAM-I library tape[12] led to bucklings which were much higher than experimental values. Thus the cross sections for U-235 and U-238 were replaced by versions obtained from the Hanford Works, based on the data in Ref. 13. In order to investigate the reactivity effects of cross section changes in more detail, fundamental mode buckling calculations were performed in which certain cross sections were changed by 10% while the others were kept constant. The standard cross sections used are given in Tables IV and XII of

Ref. 1. Results of these calculations are presented in Table II-1-II in terms of $\Delta k_{eff}/k_{eff}$, where $k_{eff}$ is unity for the critical buckling determined by the standard cross sections. The effects of the indicated cross section changes on the diffusion coefficients were not treated. No changes were considered in the thermal group, since thermal group cross sections are relatively well known.

Table II-1-II shows that the calculated reactivities are quite sensitive to non-thermal cross section changes in general, with the sensitivity increasing as the lattice pitch is decreased, the lattices becoming more undermoderated. As might be expected, the sensitivity to the U-238 capture cross sections is quite pronounced. The major reason for the large reactivity differences obtained by substitution of the Hanford cross sections is the fact that the original GAM-I cross sections yield values of $\sigma_{c2}^{28}$ only about half as large as those based on Hanford cross sections. Inspection of Table II-1-II shows that such a difference represents a reactivity change of the order of 5% for the 1.166△A lattice. Although the reactivity is even more sensitive to $\sigma_{c3}^{28}$ than to $\sigma_{c2}^{28}$, the differences between Hanford and original GAM-I values of $\sigma_{c3}^{28}$ are small, and therefore do not contribute much to the large reactivity differences.

While it is necessary to use accurate calculational methods in the treatment of highly undermoderated lattices such as the Hi-C lattices, it is also very important that accurate basic cross section data be used as well.

References


1. E. M. Pennington, *Analysis of High Conversion Critical Experiments*, ANL-7270 (1967).
2. A. R. Boynton, Q. L. Baird, K. E. Plumlee, W. C. Redman, W. C. Robinson and G. S. Stanford, *High Conversion Critical Experiments*, ANL-7203 (1967).
3. K. E. Plumlee and E. M. Pennington, *Experiments and Calculations for Densely Loaded Slightly Enriched $UO_2$-Fuelled Cores*, Proc. International Conference on Physics Problems in Thermal Reactor Design, London, June 27–29, 1967.
4. E. M. Pennington, *Hi-C Uniform Lattice Calculations*, Reactor Physics Division Annual Report, July 1, 1963 to June 30, 1964, ANL-7010, pp. 44–46.
5. E. M. Pennington, *Hi-C Uniform Lattice Calculations*, Reactor Physics Division Annual Report, July 1, 1964 to June 30, 1965, ANL-7110, pp. 84–90.
6. E. M. Pennington, *High Conversion (Hi-C) Uniform Lattice Calculations*, Reactor Physics Division Annual Report, July 1, 1965 to June 30, 1966, ANL-7210, p. 28.
7. E. M. Pennington and W. L. Boettinger, *Foil Activation Programs, B 512/RP*, ANL-6822 (1964).
8. D. J. Hughes and R. B. Schwartz, *Neutron Cross Sections*, BNL-325, Second Edition (July 1, 1958).
9. D. J. Hughes, B. A. Magurno and M. K. Brussel, *Neutron Cross Sections*, BNL-325, Second Edition, Supplement No. 1 (January 1, 1960).
10. G. D. Joanou and J. S. Dudek, *GAM-I: A Consistent $P_1$ Multigroup Code for the Calculation of Fast Neutron Spectra and Multigroup Constants*, GA-1850 (June, 1961).
11. H. C. Honeck, *THERMØS, A Thermalization Transport Code for Reactor Lattice Calculations*, BNL-5826 (September 1961).
12. G. D. Joanou et al., *Nuclear Data for GAM-I Data Tape*, GA-2451, Vol. I, II, III (August 1961).
13. R. C. Liikala, *Updated RBU Basic Library*, HW-75716, Vol. 1, 2, 3 (May 20, 1963).


## II-2. Concluding Pre-Irradiation Critical Experiments of the Experimental Boiling Water Reactor (EBWR) Plutonium Recycle Experiment

P. H. Kier

To increase our understanding of the physics of mixed plutonium-uranium oxide-fueled, water-moderated reactors, pre-irradiation critical experiments were made as part of the EBWR Plutonium Recycle Program.[1] The results of these measurements of critical configurations, boric acid worths and uniform temperature coefficients for the partial (plutonium) loading and the initial full loading led to revisions in the calculational model.[2] Calculations made with the revised model predicted an operating power of about only 30 MW. As such a low initial power would unduly limit the exposure that could be reached during the time available for the program, it was decided to raise the reactivity of the full loading (and consequently the maximum attainable power) by replacing eight 6% enriched $UO_2$ assemblies with highly enriched spike assemblies used during the 100 MW operation of EBWR.[3] Results of the measurements of boric acid worth and of the uniform temperature for the revised loading are presented below.

### Boric Acid Worths for the Revised Full Loading

Operation of the reactor is subject to two restraints: (1) that the reactor can be shutdown by the insertion of all nine control rods when the reactor water is un-

TABLE II-2-I. Boric Acid Worth and Nine Rod Bank Worth for Revised Full Loading

| $H_3BO_3$, g/gal | | 9 Rod Bank Ht, in. | | $\Delta k$, % | $\Delta k/\Delta C$, % $\Delta k$/g-gal | $\Delta k/\Delta H$, % $\Delta k$/in. |
|---|---|---|---|---|---|---|
| Range | Change | Range | Change | | | |
| 8.22-7.41 | 0.81 ± 0.03 | 18.95-17.0 | 1.95 ± 0.05 | 0.90 ± 0.12 | −1.11 ± 0.18 | 0.42 ± 0.06 |
| 7.41-6.69 | 0.72 ± 0.03 | 17.0-15.5 | 1.50 ± 0.05 | 0.84 ± 0.11 | −1.17 ± 0.20 | 0.56 ± 0.09 |
| 6.69-6.15 | 0.54 ± 0.03 | 15.5-14.4 | 1.10 ± 0.05 | 0.714 ± 0.093 | −1.32 ± 0.24 | 0.65 ± 0.11 |
| 6.15-5.61 | 0.54 ± 0.03 | 14.4-13.4 | 1.00 ± 0.05 | 0.667 ± 0.087 | −1.24 ± 0.23 | 0.67 ± 0.12 |
| 5.61-5.14 | 0.47 ± 0.03 | 13.4-12.68 | 0.72 ± 0.05 | 0.575 ± 0.075 | −1.22 ± 0.25 | 0.80 ± 0.16 |
| 5.14-4.71 | 0.43 ± 0.03 | 12.68-12.0 | 0.68 ± 0.05 | 0.555 ± 0.072 | −1.29 ± 0.27 | 0.82 ± 0.17 |
| 4.71-4.33 | 0.38 ± 0.03 | 12.0-11.4 | 0.60 ± 0.05 | 0.476 ± 0.062 | −1.25 ± 0.27 | 0.79 ± 0.17 |
| 4.33-3.95 | 0.38 ± 0.03 | 11.4-10.9 | 0.50 ± 0.05 | 0.506 ± 0.066 | −1.33 ± 0.29 | 1.01 ± 0.23 |
| 3.95-3.60 | 0.35 ± 0.03 | 10.9-10.5 | 0.40 ± 0.05 | 0.475 ± 0.062 | −1.35 ± 0.30 | 1.18 ± 0.30 |

borated (nine-rod shutdown criterion) and (2) that the reactor can be shutdown by the insertion of eight control rods when the reactor water is borated (eight-rod shutdown criterion). Boric acid worth as a function of boric acid concentration was measured by use of the following procedure, which includes verification of the nine-rod shutdown criterion and determination of the minimum boric acid concentration for satisfaction of the eight-rod shutdown criterion.

With the reactor critical with all nine control rods banked at the same height, the differential worth of the center rod is determined from period measurements. Then boric acid is removed from the system and the center rod is inserted as necessary to maintain criticality. When a specified amount of boric acid has been removed, the differential worth of the center rod is again obtained as before. Then the critical height of the eight-rod bank with the center rod withdrawn and the critical nine-rod bank height are obtained. This procedure is repeated until further removal of boric acid would violate the eight-rod shutdown criterion. Extrapolation of the critical height of the eight-rod bank as a function of boric acid concentration to zero bank height yields the minimum boric acid concentration for eight-rod shutdown. If extrapolation of the critical height of the nine-rod bank as a function of boric acid concentration to zero boric acid concentration yields a positive intercept the nine-rod shutdown criterion is satisfied.

Boric acid worth, $\Delta k/\Delta C$, is obtained from the change in the critical height of the center rod, $\Delta h$, as a function of the change in boric acid concentration $\Delta C$. Assuming that differential rod worth ($\Delta k/\Delta h$) is linear over $\Delta h$, boric acid worth is obtained from

$$\Delta k/\Delta C = (\Delta k/\Delta h)_{ave}\Delta h(1/\Delta C), \qquad (1)$$

where $(\Delta k/\Delta h)_{ave}$ is the average of the differential rod worth obtained before and after a change in boric acid concentration. The procedure yields not only the distance the center rod must be moved to compensate for the reactivity introduced by the removal of boric acid but also the distance, $\Delta H$, the nine-rod bank must be inserted. Nine-rod bank worth, $\Delta k/\Delta H$, is obtained from an expression similar to that from which boric acid worth is obtained:

$$\Delta k/\Delta H = (\Delta k/\Delta h)_{ave}\Delta h(1/\Delta H). \qquad (2)$$

The measured boric acid worths and nine-rod bank worths are given in Table II-2-I. The boric acid worths tend to increase as concentration is reduced but because of the relatively large experimental error one can only report an average boric acid worth of $-0.0125 \pm 0.003$ $\Delta k$/g-gal between 3.6 and 8.2 g/gal. The experimental errors arise mainly from uncertainties in changes in boric acid concentration and in differential rod worth. Calculated values of $-1.1\%$ $\Delta k$ for a 1 g/gal addition of boric acid to the unpoisoned system and $-0.9\%$ $\Delta k$ for a 1 g/gal addition to the system having 9 g/gal were somewhat lower than measured values.

There is a definite increase in the nine-rod bank worth as the bank and the boric acid concentration are lowered, because the curvature of the flux increases as the bank is lowered. Since the effect of an incremental change on leakage and absorption increases with curvature of the flux, the nine-rod bank worth increases as the bank is lowered. Extrapolation of the nine-rod bank heights given in Table II-2-I to zero boric acid concentration yields a positive intercept; hence, the nine-rod shutdown criterion is satisfied.

The reactivity worth of the fuel replacement can be found from the change in the critical height of the nine rod bank at a fixed boric acid concentration. With a boric acid concentration of 6.68 g/gal, replacement of eight shim assemblies with spike assemblies required that the bank be lowered from 18.65 to 15.5 in. For this range of heights, the nine rod bank

TABLE II-2-II. $k_{eff}$ AS A FUNCTION OF TEMPERATURE AND $H_3BO_3$ CONCENTRATION AND THE UNIFORM TEMPERATURE COEFFICIENT FOR THE REVISED FULL LOADING

| Temp., F | $H_3BO_3$, g/gal | Critical Ht. of #4 Rod,[a] in. | $k$ With #4 Rod Withdrawn | $k$ for 6.25 g/gal | $\Delta k/\Delta T$, $\%\Delta k$/°F |
|---|---|---|---|---|---|
| 64.5 ± 1 | 5.71 ± 0.03 | 28.99 | 1.00131 ± 0.00016 | 0.99456 ± 0.00052 | 0.00435 ± 0.00083 |
| 152.5 ± 1 | 6.02 ± 0.02 | 29.91 | 1.00115 ± 0.00014 | 0.99843 ± 0.00039 | 0.00430 ± 0.00105 |
| 246 ± 1 | 6.16 ± 0.04 | 21.88 | 1.00357 ± 0.00025 | 1.00245 ± 0.00075 | 0.00236 ± 0.00148 |
| 321 ± 2 | 6.14 ± 0.04 | 15.53 | 1.00559 ± 0.00032 | 1.00422 ± 0.00082 | −0.00212 ± 0.00320 |
| 362 ± 2 | 6.35 ± 0.04 | 27.59 | 1.00210 ± 0.00021 | 1.00335 ± 0.00071 | |

[a] The center and the other three corner rods are withdrawn to their maximum allowable heights and the four-off-center, non-corner rods are fully inserted.

worth is (0.55 ± 0.12) $\%\Delta k$/in. By multiplying the bank worth by the distance the bank was moved, it is found that the fuel replacement increased the reactivity of the system by (0.0173 ± 0.0037) $\Delta k$. This measurement of the worth of the fuel replacement is in agreement with four-group 20-Grand[4] calculations that predicted a worth of 0.0195 $\Delta k$.

### UNIFORM TEMPERATURE COEFFICIENT OF REACTIVITY FOR THE REVISED FULL LOADING

The uniform temperature coefficient was measured between room temperature and 362°F when the system was poisoned with boric acid with concentrations between 5.71 and 6.35 g/gal. The experimental procedure was to obtain the multiplication constant, $k_{eff}$, of the system as a function of temperature and boric acid concentration for a configuration in which the center rod and the four corner rods are withdrawn, the other four rods being fully inserted. $k_{eff}$ is obtained from the differential reactivities that resulted when a corner rod (#4) was withdrawn in steps from its critical height (with four rods withdrawn and four inserted) to 36.5 in., its maximum allowable height with respect to the inverse rod worth effect.[2] Because a corner rod has appreciable strength for full loading, the #4 rod was withdrawn in steps of about 3 in. to obtain the asymptotic periods of about 60 sec. The #8 rod, at the opposite corner, was inserted as required to maintain criticality.

To obtain the temperature coefficient from these measurements, the values of $k_{eff}$ were normalized to a single boric acid concentration of 6.25 g/gal. Table II-2-II gives the resulting temperature coefficients for four temperature ranges. It is seen that the temperature coefficient is positive at low temperatures, becomes smaller as the temperature is increased, and apparently becomes negative near 300°F.

The PDQ-3[5] code was used to compute the temperature coefficient from $k_{eff}$ with four rods inserted at several temperatures. Spectrum dependent cross sections for each fuel material at each temperature were obtained from use of the GAM[6] and the Argonne-revised THERMØS[7] codes. Comparison between calculation and measurement is disappointing since the calculations predicted a temperature coefficient of approximately $-5 \times 10^{-5}$ $\Delta k$/°F for the temperature range of the calculation.

Part of the discrepancy between theory and experiment arises from the neglect of thermal expansion effects in the calculations. The reactor vessel is supported from above the core and is free to expand downward. On the other hand, the control rods are supported from below the core and are free to expand upward. Therefore axial thermal expansion causes the control rods to be withdrawn slightly from the core to add reactivity. If this effect were included in the calculations—and this is very difficult—they would yield a smaller negative temperature coefficient, which reduces the discrepancy.

Another possible source of error is in the interpretation of period measurements for differential reactivity. Reactivity was related to period through the inhour equation and the use of a $\beta_{eff}$ which was obtained from a perturbation calculation using eight groups of real and adjoint fluxes appropriate for an unrodded system. The temperature coefficients (and boric acid worths) were measured with partly rodded systems which have real and adjoint flux distributions appreciably different from those in an unrodded system. For the zoned loading in EBWR, where the delayed neutron fractions in the plutonium zone are quite different from those in the other zones, $\beta_{eff}$ is strongly dependent on the flux distribution. As the assumed flux distribution is inaccurate, $\beta_{eff}$, and therefore the experimental reactivities, may be in error.

### REFERENCES

1. B. J. Toppel, P. J. Vogelberger and E. A. Wimunc, *Safety Analysis Associated with the Plutonium Recycle Experiment in EBWR*, ANL-6841 (1966).
2. P. H. Kier, *Initial Critical Experiments of the EBWR Plutonium Recycle Program*, Reactor Physics Division Annual

Report, July 1, 1965 to June 30, 1966, ANL-7210, pp. 29–34.
3. R. Avery, K. Almenas, C. Carson, H. Iskenderian and C. Kelber, *EBWR Core 1A Physics Analysis*, ANL-6305 (1961).
4. M. L. Tobias and T. B. Fowler, *The Twenty Grand Program for the Numerical Solution of Few Group Neutron Diffusion Equations in Two Dimensions*, ORNL-3200 (February 1962).
5. W. Cadwell, *PDQ-3, A Program for the Solution of the Neutron Diffusion Equations in Two Dimensions on the IBM-704*, WAPD-TM-179 (1960).
6. G. D. Joanou and J. S. Dudek, *GAM-I, A Consistent $P_1$ Multigroup Code for the Calculation of Fast Neutron Spectra and Multigroup Constants*, GA-1850 (1961).
7. B. J. Toppel and I. Baksys, *The Argonne Revised THERMØS Code*, ANL-7023 (1965).

## II-3. Power Operation of the Experimental Boiling Water Reactor (EBWR) During the Plutonium Recycle Experiment

P. H. Kier

The primary objective of the EBWR Plutonium Recycle Program[1] is to irradiate mixed plutonium-uranium oxide fuel in an environment representative of a boiling-light water reactor. From the isotopic composition of the fuel as a function of exposure it is hoped that models for the calculation of burnup can be refined and that the performance of this type of fuel in boiling water reactors can be evaluated.

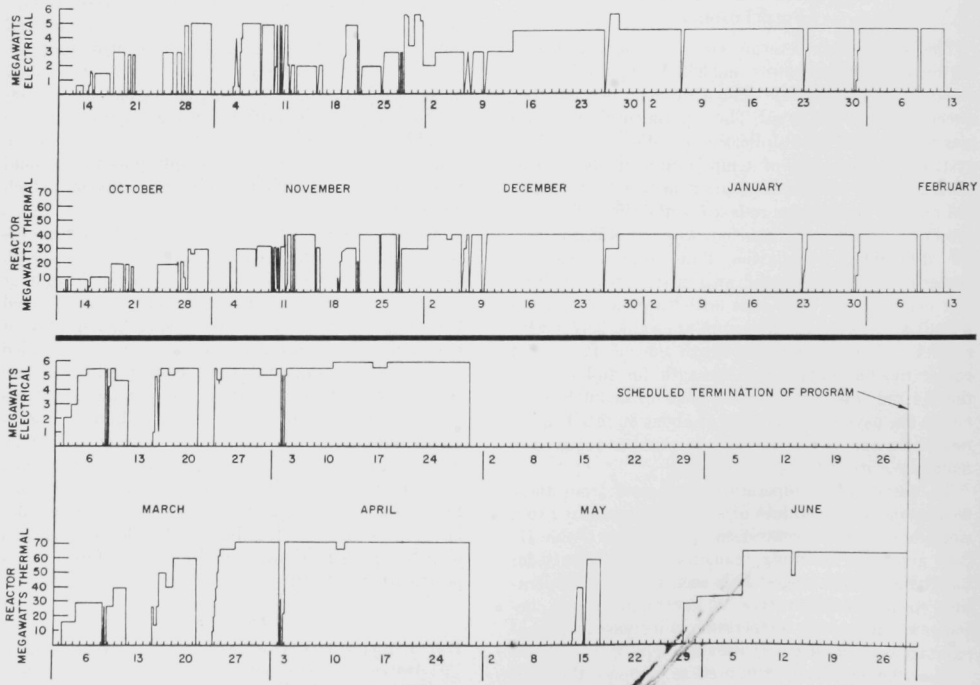


FIG. II-3-1. *EBWR* Power Trace During the Plutonium Recycle Program (1966–1967). *ANL Neg. No. 112-8639.*

Continuous operation of EBWR at 42 MW began in November 1966. During the preceding month, pile oscillator measurements of the reactor transfer function were made at several powers (5.2, 8.4, 15, 28 and 38.5 MW) to investigate the stability of the reactor. The power level above which instability might be expected can be obtained by either extrapolating the plot of the absolute gain versus power to a gain of 1.0 or extrapolating the plot of the phase margin versus power to a phase margin of 0 degrees. These extrapolations indicated that the reactor should be stable to powers higher than 120 MW.

The reactor was shutdown in February 1966, when the average exposure of the plutonium fuel was approximately 1300 MWd/tonne. During the shutdown, special fuel pins (those with compositions different from the ordinary fuel pins) and several ordinary pins were removed from the reactor for subsequent isotopic analysis at Battelle-Pacific Northwest Laboratory (BNWL). Because the duration of the program had been curtailed, the operating power during the next burnup was raised to 70 MW. Prior to operation at 70 MW, pile oscillator measurements were made at 27.5, 40.3, 49.5, 57 and 70 MW to recheck the stability of the reactor.

The reactor was shutdown again in early May 1967, when the average exposure of the plutonium fuel was approximately 2400 MWd/tonne. During this shutdown, special and ordinary fuel pins were removed for subsequent isotopic analysis at BNWL, plant repairs were made, and cadmium-covered and bare Pu-239, Pu-241 and gold foils were placed in several locations in the core to measure[2] the capture-to-fission ratio of Pu-239 and Pu-241 resulting from irradiation during the third burnup step.

The reactor regained power in early June 1967 and was operated at 60 MW during most of the month. When power operation was terminated on June 29, 1967, the average exposure of the plutonium fuel was approximately 3000 MWd/tonne. Figure II-3-1 is a histogram of the operating history of EBWR during the current experiment.

### References

1. B. J. Toppel, P. J. Vogelberger and E. A. Wimunc, *Safety Analysis Associated with the Plutonium Recycle Experiment in EBWR*, ANL-6841 (1966).
2. H. P. Iskenderian, *Measurements of Capture-to-Fission Ratios of Pu-239 and Pu-241 in the Plutonium Loading of the Experimental Boiling Water Reactor (EBWR)* Reactor Physics Division Annual Report, July 1, 1965 to June 30, 1966, ANL-7210, pp. 34-38.

## II-4. Measurement of Capture-to-Fission Ratio of Pu-239 and Pu-241 in the Plutonium Loading of the Experimental Boiling Water Reactor (EBWR)

H. P. Iskenderian

Samples containing Pu-239 and Pu-241 irradiated in the plutonium and U-235 enriched zones of the EBWR[1] have been removed from the core to be studied. During the irradiation phase of the experiment, these samples were enclosed in Zircaloy jackets (Fig. II-4-1) which were set flush on the surface of the fuel rods with the aid of mounting assemblies (Fig. II-4-2).

Calculations described in Ref. 2 were made for 40 MW power operation. Calculations subsequently made for 70 MW operation indicated no temperature rises sufficient either to melt the cadmium covers or overheat the fuel rod under some adverse conditions of flow rate and/or gap (Table II-4-I). Based on these calculations, samples were irradiated at operational levels up to 70 MW. There were 10 test samples which contained plutonium capsules with cadmium covers and 14 open type plutonium samples.

After the test samples were removed from the core, they were opened and examined. It was ascertained that there had been no fusion of cadmium cups and covers and that the cadmium pieces clearly retained their sharp edges. However, none of the gold foils contained in the cadmium covered samples were visible to the naked eye. Upon closer examination it was revealed that the gold foils had gone into a solid solution in the cadmium covers, forming an intermetallic compound which was of lower melting point than either gold or cadmium. This was verified by an examination of two of the cadmium covers which were ground and polished in a direction at right angles to the surface of the cover, and viewed under a microscope. A porous gold compound about 4 mil thick was seen (Fig. II-4-3) near the surface of the cadmium cover, instead of the 1 mil thick crystalline foil. A further study of the cadmium cover with the aid of an electron

probe microanalyzer indicated that the gold compound consisted of nearly 40% Au + 40% Cd + 20% O.

After removal of cadmium covers with the aid of $HNO_3$, all of the gold samples with and without cadmium covers were tested for activation. All of these data and values of cadmium ratios are listed in Tables II-4-II and II-4-III.

Prior to making radiochemical analysis the test capsules are being permitted to cool in order to reduce the activity of Cs-136. Mass spectrometric measurements will then follow, and the capture-to-fission ratio of plutonium will be obtained.

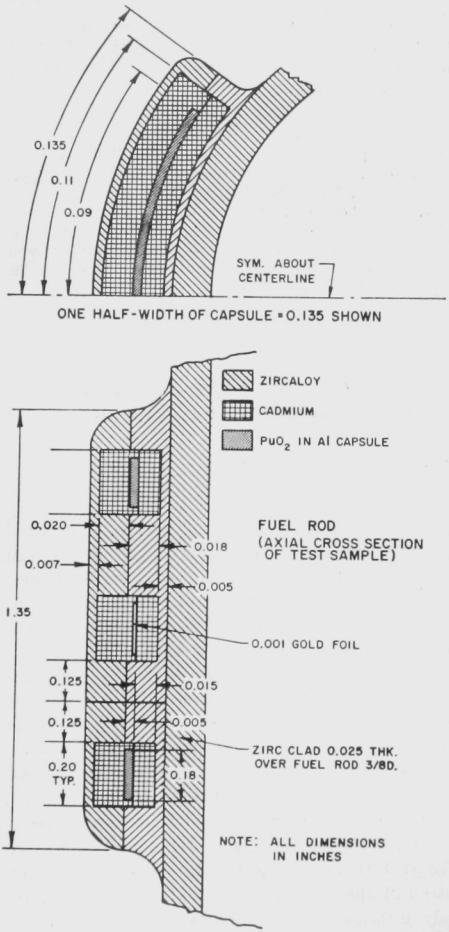


FIG. II-4-1. Test Specimen for Use in Making "$\alpha$" Measurements of Plutonium. *ANL Neg. No. 112-6825 Rev. 2.*

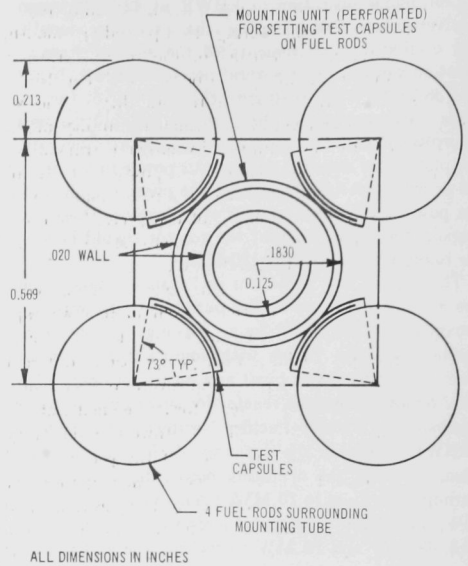


FIG. II-4-2. A Cross Section View of Mounting Assembly and Four Test Specimens With the Latter Set in Contact with the Four Surrounding Fuel Rods. *ANL Neg. No. 112-6823.*

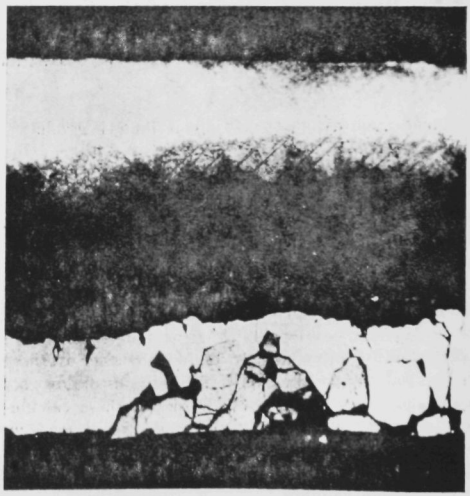

FIG. II-4-3. Microscopic View of Cadmium Cover Showing Formation of Intermetallic Porous Gold Cadmium Compound. *ANL Neg. No. 112-9046.*

TABLE II-4-I. Maximum Temperatures of Zircaloy Clad and Cadmium Covers of Test Unit for Different Flow Rates of Coolant, with and without Gaps in the Test Specimens

[*T(center line of fuel rod ≈900°F at 40 MW operation; ≈1176°F at 70 MW operation)*]

| | *T*(°F) | | | |
|---|---|---|---|---|
| | 40 MW Power Level | | 70 MW Power Level | |
| | Clad | Cadmium | Clad | Cadmium |
| I. *Full Flow Rate Around Fuel Rods and Test Specimens* | | | | |
| Zero gap between components of test specimen, including cladding | 541 | 510 | 572 | 532 |
| 0.00312 in. helium gap between outer Zircaloy wall and cadmium cover | 550 | 545 | 614 | 588 |
| 0.00624 in. helium gap between outer Zircaloy wall and cadmium cover | — | — | 633 | 609 |
| 0.00936 in. helium gap between outer Zircaloy wall and cadmium cover | — | — | 643 | 617 |
| II. *75% Flow Rate Around Test Specimen, Full Flow Over Remaining Area* | | | | |
| Zero gap between components of test specimen, including cladding | 542 | 512 | 584 | 534 |
| 0.00312 in. helium gap between outer Zircaloy wall and cadmium cover | 551 | 547 | 618 | 590 |
| 0.00624 in. helium gap between outer Zircaloy wall and cadmium cover | 556 | 558 | 636 | 610 |
| 0.00936 in. helium gap between outer Zircaloy wall and cadmium cover | 557 | 563 | 645 | 619 |
| III. *50% Flow Rate Around Half of Rod Covering Test Specimen, Full Flow Over Remaining Area* | | | | |
| Zero gap in specimen and rod | 545 | 515 | 584 | 540 |
| 0.00312 in. helium gap between outer Zircaloy wall and cadmium cover | 553.5 | 548.5 | 693 | 593 |
| 0.00624 in. helium gap between outer Zircaloy wall and cadmium cover | — | — | 640 | 614 |
| 0.00936 in. helium gap between outer Zircaloy wall and cadmium cover | — | — | 648 | 622 |
| IV. *25% Flow Rate Around Half of Rod Covering Test Specimen, Full Flow Over Remaining Area* | | | | |
| Zero gap in specimen and rod | 551 | 522 | 594 | 552 |
| 0.00312 in. helium gap between outer Zircaloy wall and cadmium cover | 560 | 553 | 628 | 600 |
| 0.00624 in. helium gap between outer Zircaloy wall and cadmium cover | — | — | 646 | 620 |
| 0.00936 in. helium gap between outer Zircaloy wall and cadmium cover | — | — | 654 | 629 |

TABLE II-4-II. Samples Irradiated in EBWR from 3/2/67 to 4/29/67

| Sample | Counts | Sample Weight, mg | Time of Counting | Bare | Cadmium Covered | Disinteg. per sec per mg | Corrected to This Time | CDR |
|---|---|---|---|---|---|---|---|---|
| B-1 | 67820/20 min | 9.20 | 6/21/67, 1155 | × | | 9600 | 6/21/67, 1155 | 1.215 |
| B-1[a] | 3849/100 min | 6.91 | 7/7/67, 2145 | × | | 9800 | 6/21/67, 1145 | 1.240 |
| B-2 | 64,733/20 min | 8.99 | 6/21/67, 1335 | × | | 9380 | 6/21/67, 1335 | 1.187 |
| B-3[a] | 2119/100 min | 4.45 | 7/7/67, 1715 | | × | 7900 | 6/21/67, 1200 | |
| B-4[a] | Sample lost due to failure for chemical separation. | | | | | | Average—1.21 | |

[a] Radiochemical separation performed.

TABLE II-4-III. SAMPLES IRRADIATED FROM 5/13/67 TO 6/29/67

| Sample from[a] | Disinteg. per sec. | Sample Weight, mg | Time of Counting | Bare | Cadmium Covered | Disinteg. per sec per mg | CD R |
|---|---|---|---|---|---|---|---|
| Pu 31 #1 | 6.53, $10^5$ | 7.46 | 8/11/67, 1515 | | × | 8.75, $10^4$ | 1.20 |
| #2 | 7.93, $10^5$ | 7.57 | 8/11/67, 1400 | × | | 1.05, $10^5$ | |
| #3 | Saved for microscopic study | | | | | | |
| #4 | 9.72, $10^5$ | 8.34 | 8/11/67, 1430 | × | × | 1.17, $10^5$ | |
| Pu 42 #1 | Lost in EBWR | | | | | | |
| #2 | 6.47, $10^5$ | 7.49 | 8/11/67, 1510 | | × | 8.64, $10^4$ | |
| #3 | 7.36, $10^5$ | 7.78 | 8/11/67, 1505 | | × | 9.46, $10^4$ | 1.29 |
| #4 | 9.11, $10^5$ | 7.45 | 8/11/67, 1435 | × | | 1.22, $10^5$ | |
| E144 #1 | 6.22, $10^5$ | 7.79 | 8/11/67, 1410 | × | | 7.98, $10^4$ | |
| #2 | 5.29, $10^5$ | 7.57 | 8/11/67, 1455 | | × | 6.99, $10^4$ | 1.14 |
| #3 | Saved for microscopic study | | | | × | | |
| #4 | 5.28, $10^5$ | 5.85 | 8/11/67, 1440 | × | | 9.04, $10^4$ | |
| E292 #1 | 5.70, $10^5$ | 7.69 | 8/11/67, 1450 | | × | 7.41, $10^4$ | 1.025 |
| #2 | 6.13, $10^5$ | 8.06 | 8/11/67, 1420 | × | | 7.60, $10^4$ | |
| #3 | 5.00, $10^5$ | 7.16 | 8/11/67, 1445 | | × | 6.98, $10^4$ | 1.185 |
| #4 | 6.59, $10^5$ | 7.97 | 8/11/67, 1425 | × | | 8.27, $10^4$ | |
| | Average of Cadmium Ratio Measurements in Plutonium Zone = 1.24 | | | | | | |
| | Average of Cadmium Ratio Measurements in Enriched Zone = 1.12 | | | | | | |

[a] Accuracy based on estimates of error ± <3%.


REFERENCES

1. Reactor Development Progress Report, ANL-7245 (July 1966) p. 1.
2. H. P. Iskenderian, *Measurement of Capture-to-Fission Ratios of Pu-239 and Pu-241 in the Plutonium Loading of the Experimental Boiling Water Reactor (EBWR)*, Reactor Physics Division Annual Report, July 1, 1965 to June 30, 1966, ANL-7210, pp. 34–38.


## II-5. Physics of Plutonium Fueled Thermal Research and Test Reactors[1]

C. N. KELBER

To date, no high flux test or research reactor has used a plutonium fuel except for the Materials Testing Reactor which had a plutonium fuel core in 1958.[2] No outstanding operational problems were encountered in the MTR which operated satisfactorily on plutonium fuel for a total of 262 MW days. At that time the MTR operated normally at a maximum power of 30 MW. The only operational problem ascribed to the plutonium fuel was the change in control rod drive speed necessitated by the lower value of the dollar of reactivity characteristic of Pu-239. As part of the test program with the plutonium core, flux maps were made and D. deBoisblanc and R. Marsden show that the peak thermal flux in the reflector with the plutonium core was about 37% higher than that observed with the U-235 loading normally used at that time.

Until 1958, most high-power thermal research and test reactor designs depended on a low value of absorption in the core together with a large moderating power to attain a high value of flux per unit power. That is, the designs were largely quasi-homogeneous. Thus the high thermal neutron cross section of plutonium was a disadvantage. The MTR, on the contrary, is the forerunner of a class of modern, very high flux research and test reactors which include the Argonne Advanced Research Reactor, (AARR), the High Flux Isotope Reactor, the High Flux Beam Reactor, and the Advanced Test Reactor. These designs emphasize external moderation and highly absorbing cores.

In reactors with highly absorbing cores and external moderation the experimenters use the flux in the external moderator where the flux is proportional to the

leakage of source neutrons from the core per fission. As was pointed out by C. Kelber, B. Spinrad and L. Templin,[3] and again by B. Spinrad,[4] plutonium fission yields more excess neutrons per fission than U-235. The excess neutrons per fission is just $\nu - (1 + \alpha)$, or more compactly, $\nu(\eta - 1)/\eta$. Typical values of this quantity for three possible fuels, U-233, U-235, and Pu-239, and three representative spectral conditions, thermal, intermediate, and fast, are given in Table II-5-I. Examination of this table shows that Pu-239 is the superior fuel in every energy range but the intermediate, where U-233 appears to have the edge; and even there plutonium is not at a great disadvantage. Most striking, however, is the marked advantage of Pu-239 in the intermediate energy range as compared with U-235, for it is in just this energy range that most of the fissions take place in current reactor designs.

This study is concerned with the flux increment to be expected in three more or less realistic examples when plutonium fuel is used instead of uranium fuel.

The first case is a fast, metal fueled core in spherical geometry, surrounded by an iron sheath and finally by a thick heavy water external reflector. The iron sheath represents a modest attempt to duplicate the effort that would have to be made in a realistic case to prevent an extreme power spike at the edge of the core. Since neutrons born in such a power spike contribute heavily to the flux in the reflector, it was felt that some realism should be introduced into this example in order that differences in the spike between the plutonium and uranium fueled cases should not unduly influence the results. This example is intended to illustrate the effects in a system which might be suitable for the irradiation of truly large amounts of isotope, say several thousand square centimeters of absorber, or a reactor designed for large numbers of beam tube experiments.

The second case is also a fast core, metal fueled, but this time in the form of a cylindrical annulus with a nickel outer reflector. An iron sheath is present between the inner radius of the core and a light water island or internal thermal column. Such a system might, for example, be used for isotope irradiation as is the case with the High Flux Isotope Reactor. Here an attempt is made to utilize all the excess neutrons by capture in samples placed in the internal thermal column.

The third case considered is most realistic since it is, in fact, a numerical duplication of a critical experiment done in connection with the design of AARR. This reactor is designed to provide room for isotope irradiations in an internal thermal column or island and also beam tube experiments located in an outer beryllium reflector. Excess neutrons in such a case may be absorbed either in the beryllium reflector or in the internal thermal column or may be divided between the two.

TABLE II-5-I. Available Neutrons per Fission $[\nu(\eta - 1)/\eta]$

| Energy Range | U-233 | U-235 | Pu-239 |
|---|---|---|---|
| Thermal | 1.41 | 1.26 | 1.43 |
| Intermediate | 1.39 | 0.96 | 1.28 |
| Fast | 1.50 | 1.41 | 1.90 |

TABLE II-5-II. Core Compositions (by Volume Fraction)

| Case | Material | | | | | |
|---|---|---|---|---|---|---|
| | Fuel | S.S. | Na | $H_2O$ | B | Al |
| 1 Spherical core | 0.3 | 0.2 | 0.5 | — | — | — |
| 2 Cylindrical annulus | 0.3 | 0.2 | 0.5 | — | — | — |
| 3 AARR mock-up | 0.0454 | 0.3952 | 0.0 | 0.5 | 0.0059 | 0.0341 |

TABLE II-5-III. Reactor Geometry and Dimension, cm

Case 1: Spherical Geometry
core: 0–14.18
sheath: 14.18–19.18 (iron)
reflector: 19.18–119.18 ($D_2O$)

Case 2: Cylindrical Geometry
ITC: 0–5 ($H_2O$)
sheath: 5–7 (iron)
core: 7–14.37
reflector: 14.37–24.37 (nickel)

Case 3: Cylindrical Geometry
ITC: 0–5.6 ($H_2O$)
sheath: 5.6–5.77 (stainless steel)
water gap: 5.77–5.88
core: 5.88–23.3
reflector: 23.3–54.4 (beryllium)

The core compositions for the cases considered are summarized in Table II-5-II, while the reactor geometry and dimensions used in the calculations are summarized in Table II-5-III. The only clearly realistic case is the third which is the AARR mock-up. The leakage characteristics of the fast cores, however, are such that we do not expect a sizable change in our fluxes should a core large enough to support a high total power be introduced.

## Computational Method

No particular significance was attached to the use of any special cross section set and no attempt was

made to check the cross section set against a wide range of critical experiments. It was, however, felt necessary to use an energy group breakdown sufficient to yield the detailed representation of the spectral changes between fast cores and thermal reflectors without complex averaging schemes. For this reason the Russian set or, as it is frequently referred to, the ABN set,[5] was used, self-shielding factors being introduced wherever necessary. Because the fast cores were expected to be small, a discrete ordinate method of calculation was used, the order of the calculation being either 4 or 8 depending on the degree of convergence required. When the fuel was U-235, the multiplication constant was adjusted to unity by changing the core radius in case 1 or the outer core radius in case 2. Case 3, the AARR mock-up, is a critical system and the radius was not adjusted. The predicted $k_{eff}$ was slightly greater than unity, but it was not felt that the difference was large enough to warrant further adjustments in the calculation.

Upon substituting plutonium for uranium, atom per atom in the fuel, the calculated $k_{eff}$ increased. Now $k$ can be restored to unity by:

(a) changing the core radius,
(b) increasing absorption in the core, or
(c) increasing absorption in the experimental regions.

The first method corresponds to lowering the core power in the case of operation at constant power density or increasing the power density in the case of operation at constant power. Neither case is representative for current high flux research reactor design where operation at maximum power density permitted by current technology and maximum power permitted by current budget is the rule. The second method of restoring criticality operates effectively by decreasing the $\eta$ of plutonium, thereby losing the advantage of the plutonium fuel. Obviously, of course, if one is operating on the principle that excess neutrons should be used outside the core, one does not want to absorb them inside the core. Method 3 corresponds to increasing absorption in experiments. The effect of a beam tube can be represented as the effect of a small amount of black absorber in a reflector or as simply as increased amount of leakage from the reflector. For case 1 criticality was restored by putting extra absorption into the reflector and calculating the total leakage from the reflector plus the increased absorption that occurs there; this divided by the leakage from the reflector for the U-235 fueled case gives the relative increase in effective beam tube flux or, more correctly, beam tube area that can be accommodated with plutonium fuel when it replaces U-235. In cases 2 and 3 emphasis was placed on computing the increase in absorption rate which can be accommodated in the internal thermal column, since this represents the possibility of increasing the amount of target material which can be placed in the island at a given effective flux level.

## Results

The first case, a spherical fast core surrounded by a heavy water reflector, could not be restored to criticality by putting increased absorber in the outer reflector since an infinite amount of absorber is equivalent to placing a black boundary at the reflector-core interface. A black boundary was put at the iron sheath-reflector interface and the leakage across this boundary was computed. When compared with the leakage plus absorptions in the outer reflector for the case just critical with U-235, it was found that the available neutrons increased by a factor of 1.75. Even so, the core was still somewhat super-critical and some of the excess neutrons had to be artificially removed by reducing the effective value of $\nu$ for Pu-239. Thus, a plutonium fueled fast core in a large thermal reflector, such as $D_2O$, can support a considerably larger number of beam experiments at the same flux level compared with what is possible using U-235.

In the second case, the annular cylindrical core with a nickel reflector, the excess neutrons tend to pile up in the island. Since the island is small compared with the remainder of the system, one can expect a large gain in effective capture rate in the island. This was measured by using a large amount of boron distributed in the island to mock-up capture in a target substance. The increase in capture rate necessary to restore the system to criticality corresponded to an increase in reaction rate in the target by a factor of 4.9.

In the third case, the AARR mock-up, the absorption occurs in both the internal thermal column and the beryllium outer reflector. For purposes of this calculation, only an increase in the absorption rate in the island was used to restore the system to criticality. To restore criticality the capture rate in the island had to be increased by a factor of 4 when plutonium was substituted for uranium. But this increase caused a change in the overall flux shape, and the absorption and leakage from the outer reflector decreased. Under these conditions it may be expected that by distributing experimental absorbers, that is to say target materials or beam tubes, in different ways other distributions of gain might be observed. These gains in capture rate might range from the order of 1.4 as observed in the MTR experiment to nearly 4 as calculated in the current instance.

Results are summarized in Table II-5-IV.

TABLE II-5-IV. GAIN IN ABSORPTIONS PER EXPERIMENT WHEN PLUTONIUM REPLACES URANIUM

| System | |
|---|---|
| Case 1: Fast Core | |
| $D_2O$ outer reflector | 1.75 |
| Case 2: Fast Annular Core | |
| $H_2O$ island | 4.9 |
| Case 3: "AARR" | 4[a] |

[a] In island only; absorptions in outer reflector are decreased.

## CONCLUSIONS

The increasing supply of plutonium and the increasing experience with plutonium fuel fabrication indicate that handling plutonium fuel is not an extraordinary problem. The supply of plutonium fuel compared with the needs for fuel by research and test reactors is so large that plutonium for research and test reactor purposes is not rare. The real problem is that associated with the hazards that occur should there be a large-scale release of fission products and fuel material from a plant. There is no denying that the bone dose from such biologically effective materials as plutonium-239 and -240 is a new and significant problem in reactor hazards. Nevertheless, in the case of plutonium substituted for uranium, atom for atom in AARR, the typical bone dose from the strontium isotopes after ninety days of full power operation is of the same order as the bone dose from the plutonium fuel. Thus, in this case the additional hazard in the use of plutonium is no more than a factor of 2 greater than that posed by uranium fuel. Of course, for fast cores with a higher inventory of plutonium the factor may be larger. Obviously, too, the Pu-240 content should be low since, gram for gram, Pu-240 is three-and-one-half times more biologically effective than Pu-239.

Balanced against this increase in hazards is the increase in the effective flux by a factor of 2 to 5. Hence for the same total number of captures the strontium inventory is reduced as well as the inventory of other long-lived products.

The conclusion is that a technologically sound and economical way to increase the neutron flux level per unit power in modern research and test reactors is to use plutonium fuel. In this connection, it should also be pointed out that historically the test and research reactors have been the proving grounds for advanced methods of fuel fabrication and design and for heat removal. Since progress in power reactor technology is so heavily dependent on progress in these fields, there is an added incentive over and above the needs of the research reatcor user to design research and test reactors with plutonium fuel.

## REFERENCES

1. C. N. Kelber, *Physics of Plutonium Fuelled Thermal Research and Test Reactors*, Proc. IAEA Symposium on the Use of Plutonium as a Reactor Fuel, March 15, 1967, Brussels, Belgium.
2. D. R. deBoisblanc and R. S. Marsden, *Operation of the MTR on a Plutonium Loading*, IDO-16508 (December 22, 1958).
3. C. N. Kelber, B. I. Spinrad and L. J. Templin, *Advanced High Flux Research Reactor Technology*, Trans. Am. Nucl. Soc. **5**, No. 2, 425 (1962).
4. B. I. Spinrad, *Limitations of Steady State, High Flux Reactors, Current and Future*, Proc. Symposium on Intense Neutron Sources, Santa Fe, New Mexico, September 19–23, 1966.
5. I. I. Bondarenko, (Ed.), *Group Constants for Nuclear Reactor* (Consultants Bureau, New York, 1964).

# II-6. Argonne Advanced Research Reactor Critical Experiments—Mockup Experiments And Critical Experiments With Stainless Steel Core

K. E. PLUMLEE, J. W. DAUGHTRY, T. W. JOHNSON, W. R. ROBINSON, R. A. SCHULTZ and G. S. STANFORD

Physics experiments performed in support of the design effort for the Argonne Advanced Research Reactor (AARR) included tests with mockups of internal thermal columns (ITC's); various control and safety elements; a graded or power-flattened fuel loading; modified beryllium reflector; beam tubes; aluminum shroud; and a section of pressure vessel. The critical experiment used a fairly detailed mockup of a densely loaded stainless steel clad core design for AARR (Fig. II-6-1).

The AARR design was changed recently to make use of the aluminum clad cores already being manufactured for the High Flux Isotope Reactor (HFIR) located at Oak Ridge National Laboratory. It is still

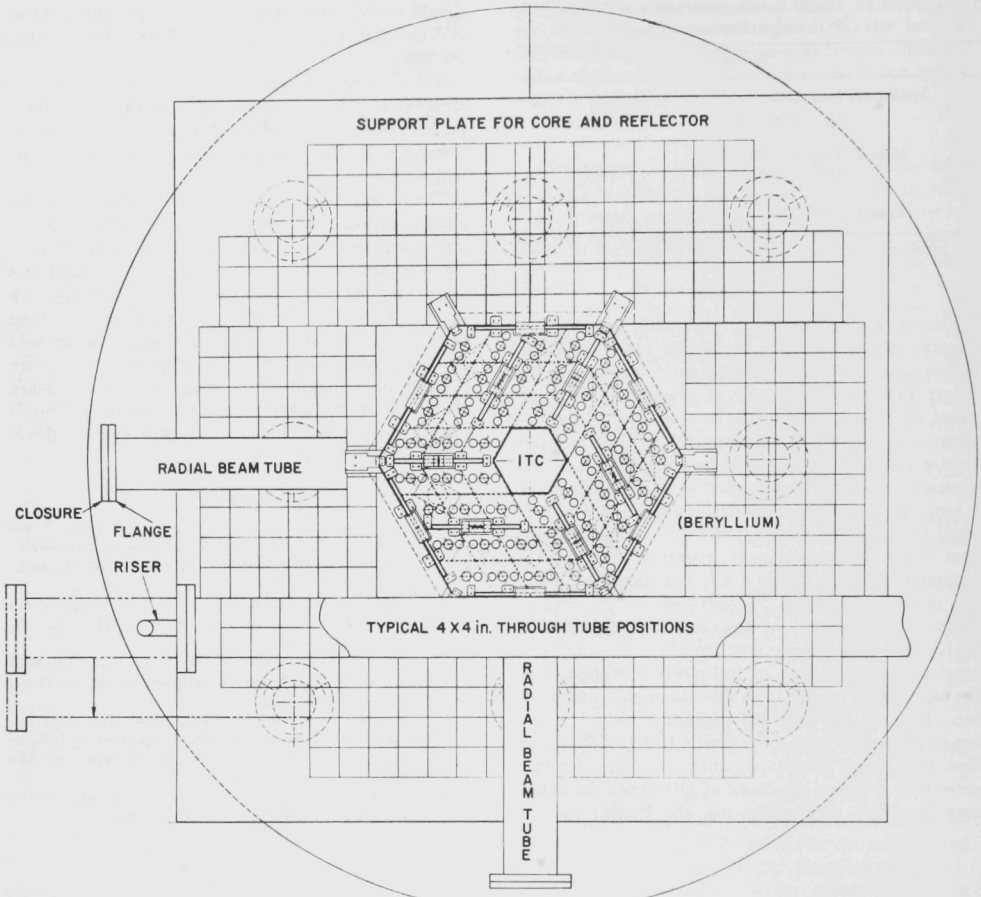


FIG. II-6-1. Plan View of Critical Facility. *ANL Neg. No. 112-9158.*

a possibility that the stainless steel core design will be considered for development as an advanced core to be used in future upgrading of AARR. Because of the rather short cycle time when using an HFIR type core, modifications of the core might be made during preparation and installation of replacement cores, without further interruption of reactor operation. The densely loaded stainless steel clad core is one of several alternatives which might be studied in selecting an advanced design. The critical experiment provided information which will be essential in evaluating advantages and disadvantages of the stainless steel clad core relative to other designs.

Three basic core assemblies (4a, 4b, and 5) were used while taking the data discussed in this report. Results obtained with Assemblies 1, 2a, 2b, and 3, as well as some information for 4a and 4b, have already been published.[1, 2, 3] The fuel loadings are given in Table II-6-I. The assemblies were reloaded to use more fuel as it became available. Thus Assembly 1 used 315 standard fuel strips and Assembly 4a used 1215 standard fuel strips (as described in Table II-6-II), and 1620 boron-stainless steel (B-SS) poison strips to compensate for the increased fuel loading. Assembly 4b was similar to 4a except that enlargement of the ITC necessitated removal of 42 fuel posi-

tions (7 from each of 6 adjacent fuel sub-assemblies) and replacement of some boron-stainless steel by plain stainless steel strips, for reactivity compensation. Assembly 5 was power-flattened by substituting thinner fuel foils for some of the standard thickness foils, thus reducing the peak power density. This graded fuel loading was a test of a physics reference design resulting from calculated flux and power distributions.[4] Compared with the uniformily loaded Assembly 4b, the graded loading involved reduced fuel composition around the ITC and also at the periphery of the fuel region. Stating nominal foil thicknesses as fractions of the standard 0.011 cm (0.0044 in.) thickness, the first eight fuel positions in each of the six sub-assemblies adjacent to the ITC were loaded with foils of the following thickness fractions, starting next to the ITC: 0.22, 0.28, 0.37, 0.47, 0.60, 0.75, 0.91 and 1.0. At the periphery only three foils were thinner than nominal, and starting with the outermost foil, the fuel positions were loaded as follows: 0.42, 0.57, 0.78 and 1.0. Typically there were 64 standard thickness foils along a row reaching between the regions having reduced foil thickness. The stainless steel envelopes containing the fuel foils were of compensating thickness so that the combined thickness of a foil and an envelope was the same (0.025 cm) for every foil thickness used.

There were several minor loading changes of short duration which were of concern only for a specific experiment. All of the loadings involved the same metal-to-water volume ratio, with changes being restricted to interchangeable parts of fuel positions.

The fuel region consisted of 45 rhombic subassemblies each of which contained 27 fuel plates except where the enlarged ITC limited the space available for the six surrounding subassemblies, restricting them to 20 plates each. Plate thickness was 0.10 cm, including up to 0.011 cm of highly enriched uranium metal. The remainder was composed of boron-stainless steel and stainless steel. Water content was determined mostly by the 0.10 cm spacing between fuel plates; however, there were local variations from the one-to-one metal-to-water ratio. Variations occurred near the ITC, near control blades, and near the top and bottom of the core.

The fuel region was approximately annular, en-

TABLE II-6-I. Basic Core Loadings

| Assembly No. | U-235 Loading[a], kg | Boron Loading, g | Measured Reactivity, % |
|---|---|---|---|
| 1 | 16.07 | 0 | 0.4[b] |
| 2a | 31.40 | 220 | 3.6[b] |
| 2b | 31.40 | 220 | 4.8 |
| 3 | 41.37 | 425 | 2.7 |
| 4a | 61.49 | 850 | 2.2[c] |
| 4b | 59.37 | 707 | 3.5[c] |
| 5 | 57.31 | 572 | 4.3[d] |

[a] Fuel loading estimates include final values for fuel enrichment and weight.

[b] Reflector for Assemblies 1 and 2a was 10% Plexiglas by volume. Plexiglas was in 1.12 cm thick horizontal layers separated by 10.2 cm thick beryllium layers.

[c] Measurements with Assembly 4 were with beryllium filled aluminum beam tubes installed in the reflector; a loss of reactivity of about 0.3% was caused by the aluminum beam tube walls and the necessarily incomplete beryllium filling.

[d] Measurements with Assembly 5 were with a tangential beam tube located 5.1 cm from the fuel zone, resulting in a loss of reactivity of about 0.2%.

TABLE II-6-II. AARR Fuel Foil Description

| Uranium Weight, g | Dimensions, in. | No. Available | Nominal Number in Fuel Assembly |
|---|---|---|---|
| | *Standard Fuel Foil* | | |
| 54.32 | 18.0 × 2.234 × 0.0044 | 1259 | 27[a] |
| | *Thin Fuel Foil* | | |
| 51.14 | 18.0 × 2.234 × 0.0041 | 9 | Replace |
| 47.54 | 18.0 × 2.234 × 0.0039 | 51 | heavier |
| 40.68 | 18.0 × 2.234 × 0.0033 | 35 | foils |
| 29.65 | 18.0 × 2.234 × 0.0025 | 36 | |
| 25.23 | 18.0 × 2.234 × 0.0020 | 15 | |
| 20.50 | 18.0 × 2.234 × 0.0016 | 36 | |
| 16.41 | 18.0 × 2.234 × 0.0012 | 9 | |
| 11.32 | 18.0 × 2.234 × 0.0009 | 15 | |
| 9.16 | 18.0 × 2.234 × 0.0007 | 9 | |
| 6.9[b] | 18.0 × 2.234 × 0.00055 | 15 | |

[a] Except adjoining large ITC.

[b] Estimated.

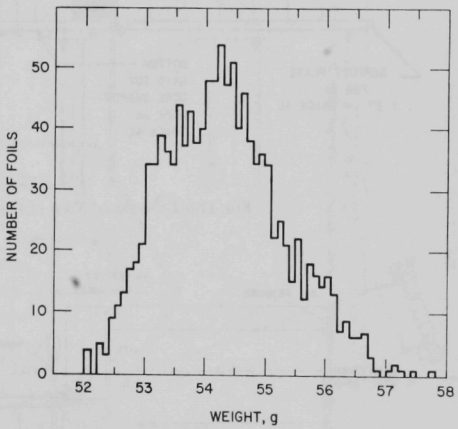


Fig. II-6-2. Foil Weight Distribution for 0.011 cm Nominal Thickness Foils. *ANL Neg. No. 112-9035.*

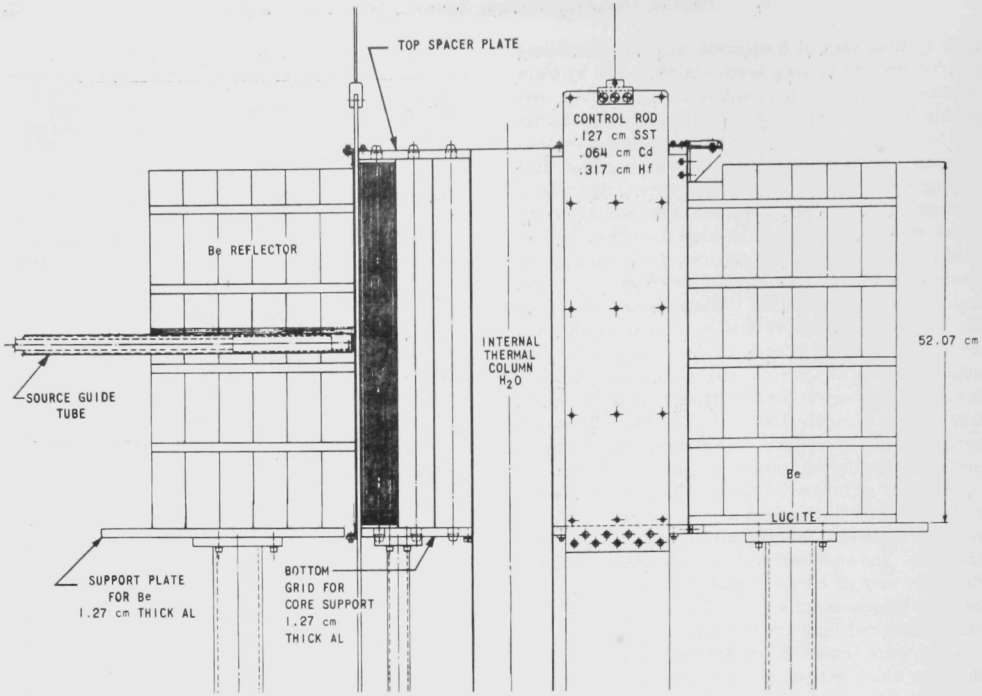


FIG. II-6-3. Sectional View of Critical Facility. *ANL Neg. No. 112-9031.*

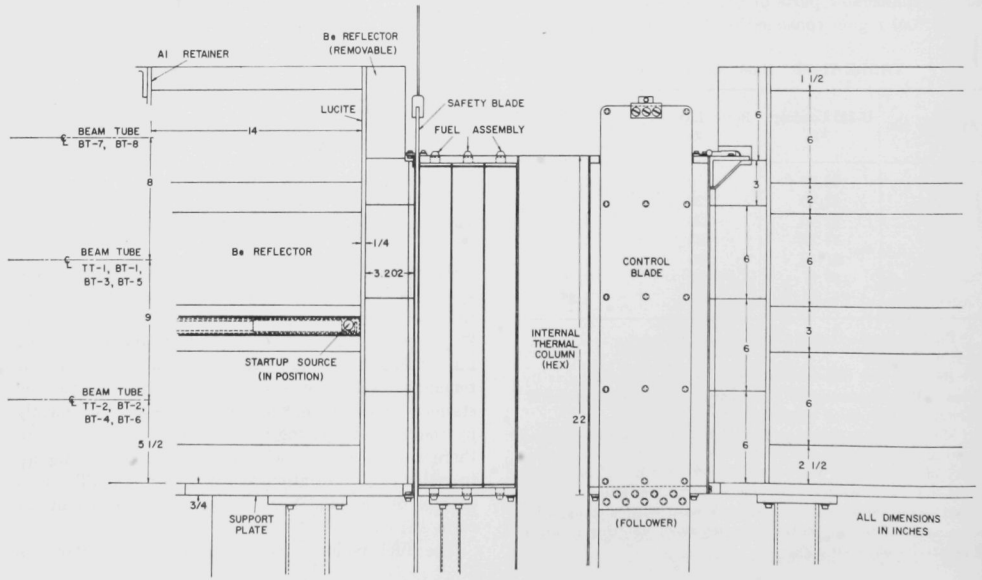


FIG. II-6-4. Elevation Drawing of Critical Facility with Detailed Reflector Mockup RP-44398-F. *ANL Neg. No. 112-9105.*

closing a hexagonal ITC of 4.8 or 7.3 liter volume. The six peripheral safety blades formed the outer boundary of the fuel zone. The fuel region volume was roughly 77 liters, including the ITC and six interior control blade channels (0.55 liter volume each). The six peripheral safety blade channels (0.76 liter volume each) are excluded from the total of 77 liters. The control and safety blades were equipped with aluminum followers, and the blades were generally 0.51 cm thick, with two thin (0.38 cm) blades and followers being installed in the interior set and two in the peripheral set during loadings 4 and 5, for use as safety blades. The thin blades were obtained to assure shutdown after it was found that the thick blades were rubbing in the 0.64 cm wide channels during temperature coefficient tests.

The following summary is given as an indication of the limitations encountered in fuel fabrication; these limitations have caused localized variations within the assemblies described in Table II-6-I. Thickness tolerances were ±0.00051 cm for the thicker foils, and ±0.0003 cm for the thinnest foils; the thinnest foils were prepared by Argonne National Laboratory, Metallurgy Division, rolling sandwiched foils. Among the

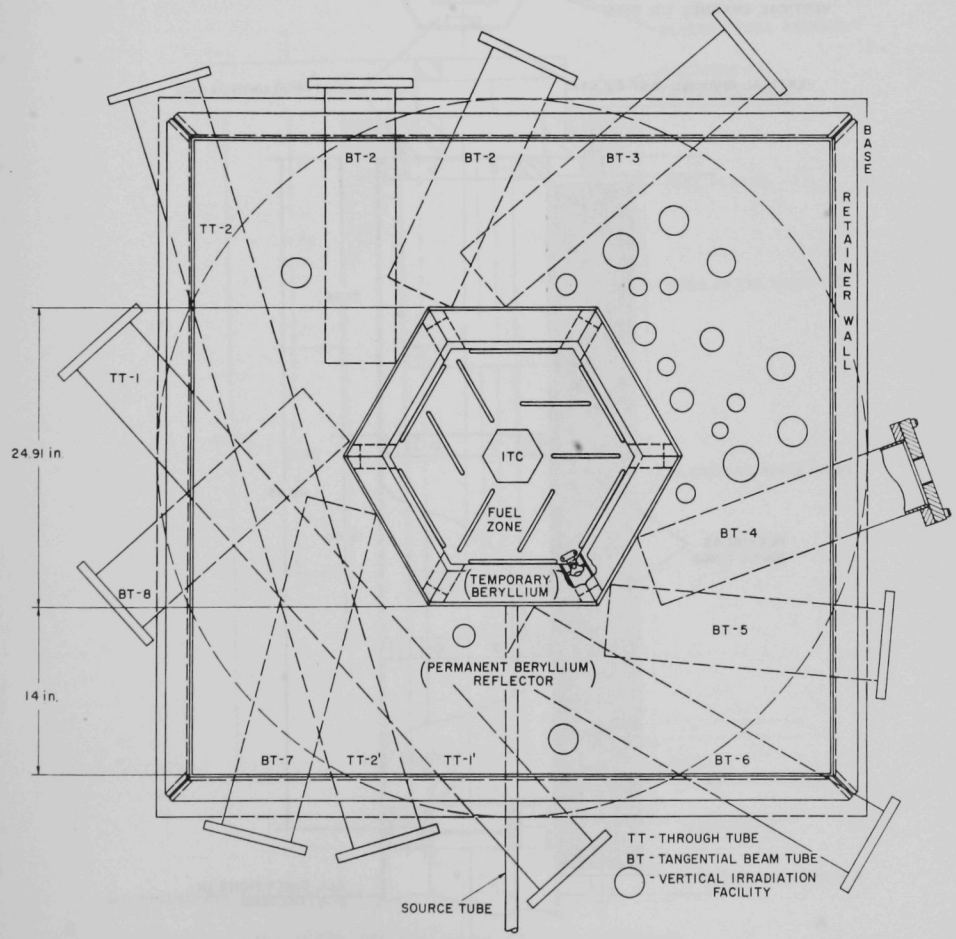


FIG. II-6-5. Plan View of Critical Facility With Detailed Reflector Mockup RP-1-44848-E. *ANL Neg. No. 112-9106.*

chemical purity requirements were limits on the increase in impurities during fabrication steps, including iron-150 ppm; carbon-300 ppm; and all others combined-400 ppm. Although some elements were given individual limits, no difficulty was encountered therewith, other than iron and carbon. The following elements occurred frequently with 100 ppm or greater concentrations: aluminum, copper, silicon, chromium,

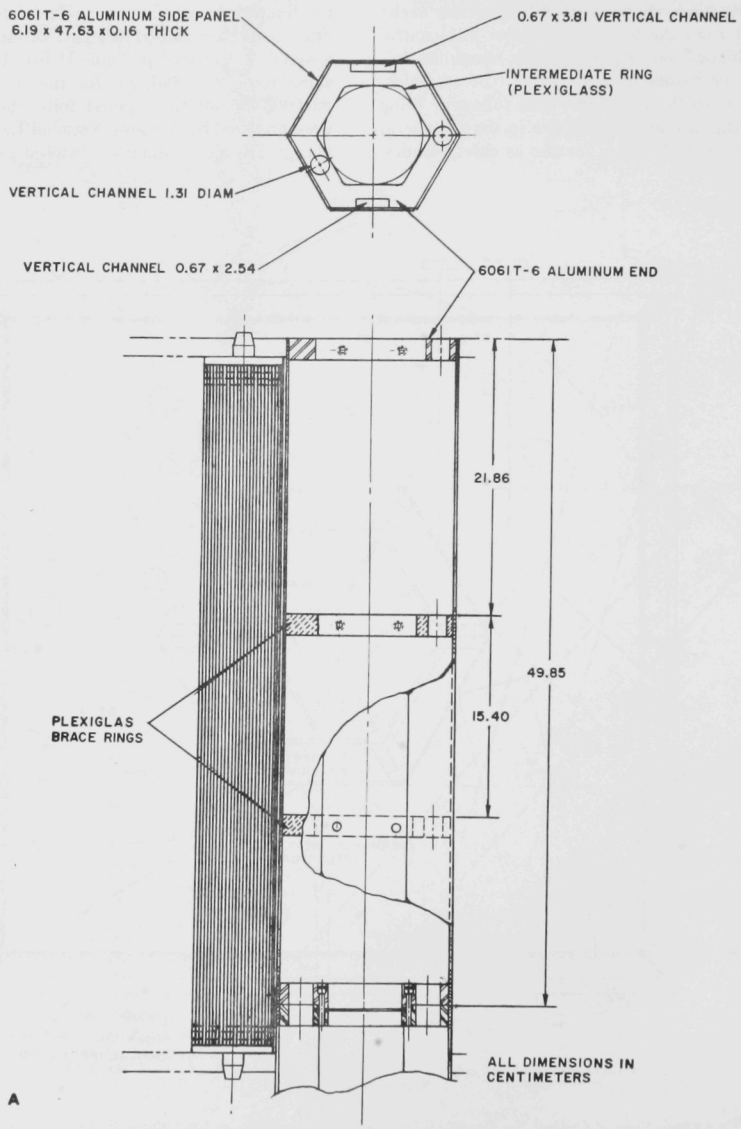


FIG. II-6-6a. ITC Arrangement. *ANL Neg. No. 112-8644.*

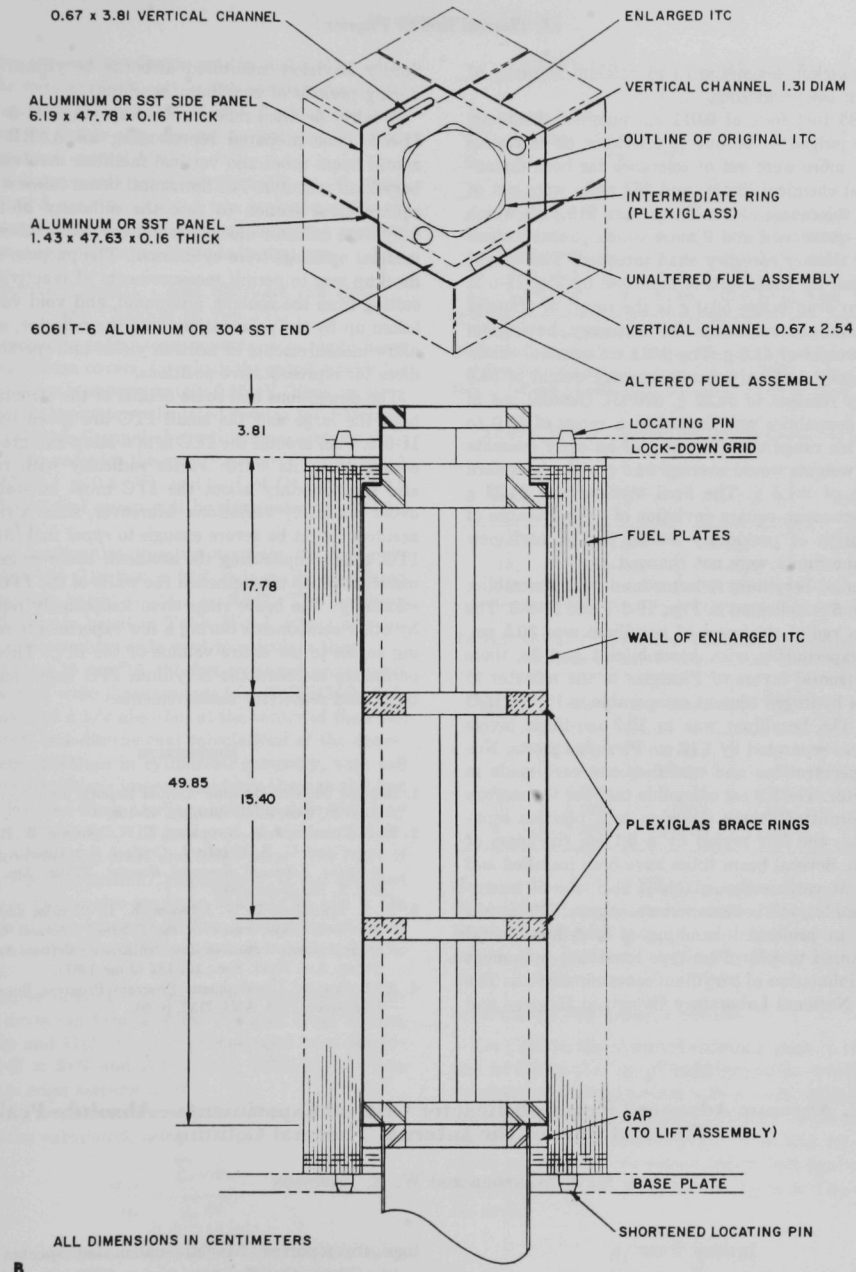


FIG. II-6-6b. ITC Arrangement. *ANL Neg. No. 112-8643.*

tungsten, nickel, magnesium and calcium in order of decreasing concentrations.

Of 1,485 fuel foils of 0.011 cm nominal thickness, 210 were judged to be out of tolerance on thickness alone; 87 more were out of tolerance for both dimensional and chemical limits; and 263 more were out of chemical tolerances alone. There were 916 foils which were not questioned and 9 more which passed inspection in a thinner category than intended. The weight distribution for those foils is indicated by Fig. II-6-2. The sharp drop below 53.0 g is the result of transfer into the adjacent thinner foil category having an average weight of 51.1 g. The 0.011 cm nominal thickness category declined from an average weight of 54.6 g in early receipts to 54.32 g, overall. General use in the fuel assemblies was limited to a range of 53.0 to 56.0 g. This range was the result of an early estimate that foil weights would average 54.5 g with a standard deviation of $\pm 1.5$ g. The final average was 54.32 g with a root-mean-square deviation of 1.0 g. Because of the retention of previously loaded fuel in each new loading the limits were not changed.

The radial beryllium reflector used with Assemblies 1 through 5 is indicated in Figs. II-6-1 and II-6-3. The minimum radial thickness of beryllium was 30.5 cm. During experiments with Assemblies 1 and 2a, there were horizontal layers of Plexiglas in the reflector to provide a hydrogen content comparable to 10 v/o $H_2O$ coolant. The beryllium was in 10.2 cm-thick layers which were separated by 1.12 cm Plexiglas sheets. Numerous penetrations and modifications were made in the reflector. The 2.9 cm o.d. guide tube for the startup source permitted source insertion to a position separated from the fuel region by a 5.1 cm thickness of beryllium. Several beam tubes have been installed and removed at various times; this is also true of instrument thimbles, foil holders and water gaps. (Personnel involved in prolonged handling of beryllium metal were required to wear filter type breathing equipment to avoid inhalation of beryllium contaminated air. The Argonne National Laboratory Industrial Hygiene and Safety Division monitored airborne beryllium levels during periods of beryllium handling).

A fairly detailed reflector mockup (Figs. II-6-4 and II-6-5) was prepared representing all AARR horizontal beam tubes and vertical facilities involving the beryllium reflector. The horizontal beam tubes were of square cross section to ease the difficulty of fitting beryllium reflector blocks around the beam tubes. The vertical openings were cylindrical. The purpose of the mockup was to permit measurements of reactivity resulting from the coolant, aluminum, and void volumes taken up by the penetrations into the reflector, and to allow measurements of neutron yields and spectral indices for representative positions.

The dimensions and some details of the structure of both the large and the small ITC are given by Fig. II-6-6. Fuel around the ITC is in a steep flux gradient, consequently its worth varies radically with radius, and the boundary about the ITC must be stable to avoid reactivity variations. Moreover, since a reactor accident might be severe enough to expel fuel into the ITC, thus complicating the accident, brace rings were installed which strengthened the walls of the ITC substantially. The brace rings were temporarily replaced by other components during a few experiments requiring access to the entire volume of the ITC. These experiments included the beryllium ITC liners and the large void reactivity measurements.

### References

1. Reactor Physics Division Annual Report, June 1, 1965 to June 30, 1966, ANL-7210, pp. 47–109.
2. K. E. Plumlee, J. W. Daughtry, T. W. Johnson, W. R. Robinson and G. S. Stanford, *Critical Experiments for the Argonne Advanced Research Reactor*, Trans. Am. Nucl. Soc. **9**, 182 (June 1966).
3. W. R. Robinson, T. W. Johnson, K. E. Plumlee and G. S. Stanford, *Experiments in the Internal Thermal Column of the Argonne Advanced Research Reactor Critical Facility*, Trans. Am. Nucl. Soc., **10**, 182 (June 1967).
4. ANL Reactor Development Program Progress Report for December, 1965, ANL-7132, p. 66.

## II-7. Argonne Advanced Research Reactor Critical Experiments—Absolute Peak Thermal Flux in the Internal Thermal Column

G. S. Stanford and W. R. Robinson

### Introduction

Measurements of the thermal flux at the center of the Internal Thermal Column (ITC), per watt of core power, for four of the AARR critical-assembly loadings are reported. Machine-calculated spectra were used to determine flux-averaged cross sections for the gold and uranium foils that were irradiated in the internal thermal columns; measured corrections for the

difference between the fission rate in fuel and in adjacent foil were applied; and in determining the actual operating power, consideration was given to the local reduction in fission rate caused by inserted and partially inserted control blades.

The measurements were for Cores 3, 4a, 4b (uniform), and 5 (graded). Core 1 was included in the effective-cross-section calculations, although an accurate power measurement was not made in that core.

### Effective Thermal Cross Sections for Gold and Uranium in the ITC

The cadmium-ratio measurements were made using 20-mil cadmium covers, for which the cutoff energy for a 1/v detector is approximately 0.55 eV. Thus, in using the 16-group computer-calculated spectra for determining the effective thermal absorption cross sections, it is necessary to consider the energy groups G16 (0 to 0.1 eV), G15 (0.1 to 0.4 eV), and part of G14 (0.4 to 1.0 eV). The partial group will be designated G14p (0.4 to 0.55 eV).

On the assumption (amply accurate for this purpose) that the G14 flux is $1/E$, it is easily calculated that the flux ratio $\phi_{14p}/\phi_{14}$ is 0.347. The resulting group fluxes are listed in Table II-7-I, which also indicates the computer code used to calculate them.

For groups 15 and 16, the flux-averaged group cross sections used were those provided by THERMØS calculations,[1] for a 1/v absorber at the center of the ITC. These were one-dimensional calculations of the space-dependent spectrum in cylindrical geometry, with cell boundary conditions imposed midway through the fuel region. For the three loadings calculated in this way (Cores 1, 3 and 4a), the two cross sections were virtually invariant at 0.434 and 0.935 barns (per barn of 2200 m/sec cross section), respectively. It was assumed that these values also apply to loadings 4b and 5. On the basis of an assumed 1/E flux in G14p, the effective 1/v cross section for that group was calculated to be 0.236 b.

The curve in BNL-325 was used to estimate the effect of deviation from 1/v for the gold cross section, for G14p and G15. The corrections used were respectively (47 ± 3)% and (18 ± 3)%. Table II-7-II lists the group cross sections used.

The effective thermal absorption cross sections, $\sigma_{eff}$, can now be calculated, using

$$\frac{\sigma_{eff}}{\sigma_0} = \frac{\sum_i \sigma_i \phi_i}{\sum_i \phi_i}, \qquad (1)$$

where $\sigma_i$ is the flux-averaged group cross section (relative to $\sigma_0$, the 2200 m/sec cross section) for the $i$th energy group, from Table II-7-II; and $\phi_i$ is the normalized group flux from Table II-7-I. The results are given in Table II-7-III. The uncertainties listed in Table II-7-II in the cross sections for G15 and G14p lead to an error of $\lesssim 1/3\%$ in $\sigma_{eff}$. It is arbitrarily assumed that the cross sections in Table II-7-III are good to ±2%.

TABLE II-7-I. Calculated ITC Fluxes

| Assembly No. | Loading[a] | ITC Radius, cm | Normalized Group Fluxes | | | | Code |
|---|---|---|---|---|---|---|---|
| | | | G14, $\times 10^{-2}$ | G14p, $\times 10^{-3}$ | G15 | G16 | |
| 1 | 315/000 | 5.9 | 2.437 | 8.46 | 0.2402 | 1.0000 | REX |
| 3 | 810/810 | 5.9 | 2.614 | 9.07 | 0.2501 | 1.0000 | REX |
| 4a | 1215/1620[b] | 5.9 | 2.704 | 9.39 | 0.2547 | 1.0000 | REX |
| 4b | 1173/1347 | 7.2 | 2.106 | 7.31 | 0.2143 | 1.0000 | MACH-1 |
| 5 | 1173/1089 | 7.2 | 2.038 | 7.07 | 0.2101 | 1.0000 | MACH-1 |

[a] The two numbers given are respectively the number of fuel plates and the number of boron-poisoned stainless steel strips.

[b] Calculations actually done for 1215/2000 loading, but effect of 380 extra boron-poisoned strips would be small.

TABLE II-7-II. Effective Group Cross Sections for ITC

| Group | Energy, eV | $\sigma_{1/v}/\sigma_0$ | $\sigma_{Au}/\sigma_0$ |
|---|---|---|---|
| 16 | 0–0.1 | 0.9347 | 0.9347 |
| 15 | 0.1–0.4 | 0.4343 | 0.512 ± 0.013 |
| 14p | 0.4–0.55 | 0.236 | 0.347 ± 0.007 |

TABLE II-7-III. Effective Thermal Absorption Cross Sections in the ITC of AARR Loadings

| Assembly No. | $\sigma_{1/v}/\sigma_0$ | $\sigma_{Au}/\sigma_0$ | $\sigma_{25}$ (fission), b | $\sigma_{Au}$, b |
|---|---|---|---|---|
| 1 | 0.8337 | 0.8494 | 481 | 83.9 |
| 3 | 0.8303 | 0.8466 | 479 | 83.6 |
| 4a | 0.8287 | 0.8452 | 478 | 83.5 |
| 4b | 0.8427 | 0.8572 | 486 | 84.7 |
| 5 | 0.8443 | 0.8584 | 487 | 84.8 |

#### Corrections for Cadmium Covers

Let $CdR$ be the observed cadmium ratio in the ITC, and let $CR$ be the "ideal" cadmium ratio—which would be observed if the cadmium were a perfect filter changing from black to transparent at 0.55 eV. Also let $A_b$ be the specific activation of a bare foil, and let $A_s$ and $A_e$ be respectively the sub-cadmium and epi-cadmium components of $A_b$. Then $CR \equiv A_b/A_e \equiv (A_s + A_e)/A_e$ and

$$A_s = \frac{CR - 1}{CR} A_b. \qquad (2)$$

It can be seen from Eq. (2) that the calculated value of the subcadmium activation $A_s$ is not sensitive to er-

rors in the measured cadmium ratio, provided $CdR \gg 1$. For the two values of the gold $CdR$ involved in these measurements—7.42 and 9.11—a 10% error in $CdR$ leads to errors of less than 1.8% and 1.4%, respectively, in $A_s$. In the case of the fission-product activity from U-235, where the cadmium ratios are 60 to 90, the corresponding errors are very much smaller.

It can also be shown that in calculating $A_s$ in these cases the effects of transmission of subcadmium neutrons by the cadmium can be neglected, along with the epicadmium absorption by the cadmium. Therefore, for these measurements, the cadmium can be considered to be a perfect filter with a sharp cutoff at 0.55 eV, and Eq. (2) is valid.

SELF-SHIELDING AND OUTER FLUX DEPRESSION

In 1-mil gold, there is, of course, a large amount of self-shielding at the 4.9 eV resonance. However, this does not pertain to the present determination of thermal flux, since it is the *sub*cadmium component of the bare-foil activation that is used for the flux determination.

In the thermal-energy region, the effects of both self-shielding and outer flux depression are covered by the well-known equation:[2]

$$G = \frac{A_s}{A_u} = \frac{\bar{\phi}}{\phi_u} = \frac{[\frac{1}{2} - E_3(\tau)]/\tau}{1 + [\frac{1}{2} - E_3(\tau)]g}, \qquad (3)$$

where $A_u$ and $\phi_u$ are the unperturbed thermal activation and flux, $\bar{\phi}$ is the thermal flux averaged over the volume of the foil, $\tau$ is the optical thickness $t\Sigma_a$ of the foil, and $E_3(\tau)$ is the third-order exponential integral. The factor $g$ is a function of the foil diameter, foil thickness and medium surrounding the foil. The gold and uranium foils used in these experiments were 0.28 cm in diam. For those foils, in a water medium, g is approximately 1.4.

Using an effective $\sigma_a$ of 84 b for gold, $\tau$ for a 1.1-mil foil is 0.0139, leading to $G = 0.946$.

In the case of the enriched (93.2%) uranium foils, the self-shielding and flux-depression factor $G$ is to be calculated using the total absorption cross section (693 b at 2200 m/sec), multiplied by the value of $\sigma_{1/v}/\sigma_0$ from Table II-7-III. The resulting values of $G$ are 0.824 and 0.694, respectively, for the 1-mil foils used in Core 3 and the 2-mil foils used in Core 4c.

FLUX DETERMINATIONS

The unperturbed subcadmium flux $\phi_s$ at the location of the foil is given by:

$$\phi_s = \frac{\rho A_s}{N\sigma_{eff}G}, \qquad (4)$$

where $A_s$ is the subcadmium saturated activation per gram of foil, $\rho$ is the density of the foil material, $G$ is the correction factor for self-shielding and flux depression, $N$ is the number of atoms per cm$^3$ of foil and $\sigma_{eff}$ is the spectrum-averaged subcadmium absorption cross section from Table II-7-III. The calculated fluxes for the seven runs that were made are listed in Table II-7-IV.

In Core 5 foils of both uranium (2 mil) and gold were used in the ITC, on three separate occasions. As can be seen from Table II-7-IV, there is good agreement between the gold and uranium results. The first measurement in Core 5 (run No. 53-1) was combined with an experiment which involved having several anomalously heavy fuel plates in the graded region

TABLE II-7-IV. CALCULATION OF ITC FLUX

| Core | Foil | $Cd\,R$ ± 10% | $Cd\,R - 1/Cd\,R$ ± 2% | Saturated Activations, sec$^{-1}$ g$^{-1}$ × 10$^8$ | | $\sigma_{eff}$ (from Table II-7-III), b | $\phi_s$, cm$^{-1}$ sec$^{-1}$ × 10$^8$ ±5% |
|---|---|---|---|---|---|---|---|
| | | | | $A_b$ ± 3%[a] | $A_s$ (Eq. 2) ±4% | | |
| 3 | Au | 7.42 | 0.887 | 2.41 | 2.14 | 83.6 | 8.85 |
| 4a | Au | 7.42 | 0.887 | 15.91 | 14.11 | 83.5 | 58.4 |
| 4b, Run 50-151 | Au | 9.11 | 0.890 | 7.28 | 6.48 | 84.7 | 26.4 |
| Run 50-156 | Au | 9.11 | 0.890 | 38.2 | 34.4 | 84.7 | 140.3 |
| 5, Run 53-1 | Au | 9.11 | 0.890 | 27.8 | 24.7 | 84.8 | 100.9 |
| | U-235 | 90 | 0.989[b] | 27.5[c] | 27.2[c] | 487 | 102.3 |
| 5, Run 54-5 | Au | 9.11 | 0.890 | 38.9 | 34.6 | 84.8 | 141.0 |
| | U-235 | 90 | 0.989[b] | 45.4[c] | 44.9[c] | 487 | 142.8 |
| 5, Run 54-6 | Au | 9.11 | 0.890 | 27.7 | 24.6 | 84.8 | 100.2 |
| | U-235 | 90 | 0.989[b] | 46.2[c] | 45.7[c] | 487 | 105.7 |

[a] $A_b$ is the saturated specific activation of the bare foil.
[b] ±0.2%.
[c] Fissions/g × 10$^{11}$.

near the ITC. As in the other cases, the calculation was performed for the core as it was when the run was made. In run No. 54–56, the measurement was repeated with the regular graded loading. The results are seen to agree within experimental precision.

## ABSOLUTE DETERMINATION OF CORE POWER

### *General Considerations*

The reactor power was determined by absolute counting of uranium foils or fuel samples (specifically, by absolute determination of Mo-99). The determination was performed by the Radiochemical Laboratory, Argonne National Laboratory. Using the known reactor running time, the fission rate during the run could then be determined for the sample or samples analyzed. Although there are some uncertainties and ambiguities in converting such a number to total core power, it is possible to get numbers which are meaningful within stated limits.

The principal uncertainty lies in the process of numerical integration over the core volume. The most clear-cut case occurs when all blades are withdrawn and criticality is controlled by water level, in which case the radial and vertical fission-product traverses taken under the same conditions can be used directly to determine the actual power at which the reactor was running. (However, relating such results to the fully-reflected operation of the power reactor becomes somewhat tenuous.) The measurements in Core 4b, and one in Core 5, were done in that manner. In Core 3, the measurement was made with full top reflector, and with criticality controlled by a cluster of three blades. In this case, it is necessary to consider, in doing the numerical integration, the power depression in the vicinity of the control blades. Since a certain amount of guessing is inherently involved, the uncertainty limits are consequently larger. The same sort of problem arises for the measurement made in Core 4a, where criticality was controlled by means of two partially inserted blades on opposite sides of the core.

Note that none of the above-mentioned operating conditions corresponds to the anticipated operating configuration in AARR, which is with peripheral blades banked somewhat below the top of the fuel, and internal blades banked at whatever position is required. Consequently, measurements were made in the graded loading (Core 5) with both water-level critical and banked-blade configurations. For the latter, the peripheral blades were banked with their tips 2.5 cm below the top of the fuel, and criticality was obtained with the internal-blade tips approximately 5 cm below the midplane of the core.

The ITC fluxes reported in this paper are per watt of core power, for the actual operating configuration of the critical assembly.

### *Numerical Integration*

The fission-rate determinations were made at locations near the midplane of the core and near the center of a 27-plate fuel assembly. The fission foil was retained in a 40-mil thick aluminum spear, which was inserted into the selected water channel. Experiments involving analysis of fuel-plate samples were done in Assembly 4b to investigate the relationship of these water-channel measurements to the actual fission rate in the fuel.

In doing a numerical integration to determine the total core power from such a single-point measurement, there are about five steps to be followed:

1. Since the fission rate is not constant across the width of a fuel plate, a factor consisting of the ratio of the average fission rate across the fuel plate to the fission rate at the center of the plate should be used. On the basis of the above-mentioned fuel-sampling experiments in Core 4b, plus wire-activation measurements,[3] the value $1.03 \pm 0.01$ has been used.

2. A multiplying factor is needed to convert the fission rate observed for a foil in an aluminum spear between the fuel plates to the fission rate in the fuel. From the experiments in Core 4b, this factor was found to be $1.16 \pm 0.02$. Such a measurement was not made in Core 3, but the factor would be expected to be somewhat smaller in that core, since the lighter fuel loading should lead to less shielding of the fission foil by the fuel. Consequently, for Core 3 the arbitrary factor $1.12 \pm 0.04$ has been used.

3. A factor for vertical averaging can be obtained by numerical integration of vertical fission-product traverses in the fuel region. For the blade criticals in Cores 3 and 4a, the factor is $0.77 \pm 0.04$. For Core 4b, water-level critical, the factor was $0.65 \pm 0.03$. (This factor is for the entire fuel region, including the part not covered by the water.) The factors for Core 5 were obtained similarly.

4. A factor for radial averaging can be obtained from the radial traverses. However, because of the very steep gradients at both the inner and outer boundaries of the fuel zone, and because of the generally nonhomogeneous nature of the core, the uncertainty in the result (as estimated by varying some of the input quantities) is of the order of $\pm 8\%$. The radial factors used for Cores 3, 4a and 4b were respectively 1.06, 1.18 and 1.11, each with an assigned error of $\pm 8\%$. For Core 5 the fact that that the loading was graded

made the result less sensitive to the values at the inner and outer boundaries of the core; the error assigned in that case was ±5%.

5. For the runs that were made with some of the control blades inserted, the reduction in fission rate near the inserted control blades must be taken into account. Data are not available to permit this factor to be much better than a rough estimate, but for the case of Core 3 some guidance can be had from Figs. II-12-17 and II-12-18 of Ref. 3. From those figures it can be seen that the flux is depressed by a factor of about two, over something like a quarter of the core volume. Averaged over the core, this amounts to, say, a reduction of (12 ± 4)%, leading to a multiplying factor of 0.88 ± 0.04. For Core 4a, two peripheral blades were approximately ⅘ inserted, inducing a perturbation estimated to be approximately ¾ as large as that for the case of Core 3. Thus the blade-perturbation factor used for Core 4a was 0.91 ± 0.05.

In the absence of detailed three-dimensional fission-rate surveys for the banked-blade configuration, the blade-perturbation factor for the two runs in Core 5 which were made with that configuration is even less certain. However, some relevant information can be gleaned from Fig. II-12-26 of Ref. 3, which shows vertical activation traverses made near a half-inserted control blade. The uranium foils for the power measurements were slightly below the level of the tips of the interior blades, and in the middle of an adjacent fuel assembly. Thus it can be inferred that the flux at

TABLE II-7-V. CALCULATION OF REACTOR POWER AND OF ITC THERMAL NEUTRON FLUX PER WATT

| Core No. | 3 | 4a | 4b | 4b | 5 | 5 | 5 |
|---|---|---|---|---|---|---|---|
| Run No. | | | 50-151 | 50-166 | 53-1[a] | 54-5 | 54-6 |
| Criticality controlled by | blades | blades | water level[b] | water level[b] | banked blades[c] | water level[d] | banked blades[c] |
| Reactor running time, sec | 675 | 960 | 985 | 1900 | 329 | 389 | 535 |
| Fissions/g at test point, × $10^{10}$ | 1.24 ± 6% | 7.04 ± 5% | 4.18 ± 5%[e] | 39.8 ± 5%[e] | 4.64 ± 5% | 8.29 ± 5% | 7.97 ± 5% |
| Correction Factors | | | | | | | |
| (1) Average across fuel plate | 1.03 ± 1% | 1.03 ± 1% | 1.03 ± 1% | 1.03 ± 1% | 1.03 ± 1% | 1.03 ± 1% | 1.03 ± 1% |
| (2) Rate in fuel/rate in channel | 1.12 ± 4% | 1.16 ± 2% | —[e] | —[e] | 1.16 ± 2% | 1.16 ± 2% | 1.16 ± 2% |
| (3) Vertical average | 0.77 ± 5% | 0.77 ± 5% | 0.65 ± 5% | 0.65 ± 5% | 0.76 ± 5% | 0.57 ± 5% | 0.76 ± 5% |
| (4) Radial average | 1.06 ± 8% | 1.18 ± 8% | 1.11 ± 8% | 1.11 ± 8% | 1.04 ± 5% | 1.03 ± 5% | 1.03 ± 5% |
| (5) Blade perturbation | 0.88 ± 5% | 0.91 ± 5% | —[f] | —[f] | 0.85 ± 12% | —[f] | 0.85 ± 12% |
| Composite factor: | 0.83 ± 11% | 0.99 ± 11% | 0.74 ± 9.5% | 0.74 ± 9.5% | 0.80 ± 14% | 0.70 ± 8% | 0.80 ± 14% |
| Reaction rate, averaged over core, fis/g/sec × $10^7$ | 1.52 ± 13% | 7.24 ± 12% | 3.15 ± 11% | 15.56 ± 11% | 11.31 ± 15% | 14.93 ± 9% | 11.84 ± 15% |
| Uranium present, kg | 44.4 | 66.0 | 63.7 | 63.7 | 61.6[a] | 61.5 | 61.5 |
| Core power, W | 21.8 ± 13% | 154 ± 12% | 64.8 ± 11% | 320 ± 11% | 224 ± 15% | 297 ± 9% | 235 ± 15% |
| Flux in ITC, $cm^{-2}$ $sec^{-1}$ × $10^8$ (from Table II-7-IV) | 8.85 ± 5% | 58.4 ± 5% | 26.4 ± 5% | 140.3 ± 5% | 101.6 ± 4%[g] | 141.9 ± 4%[g] | 103.0 ± 4%[g] |
| Flux/W of core power, $cm^{-2}$ $sec^{-1}$ $w^{-1}$ × $10^7$ | 4.2 ± 0.6 | 3.8 ± 0.5 | 4.1 ± 0.5 | 4.4 ± 0.5 | 4.53 ± 0.70 | 4.8 ± 0.5 | 4.39 ± 0.70 |

[a] For Run 53-1, there were four extra-thick fuel plates in the graded region near the ITC.
[b] 85% of fuel was flooded.
[c] Internal blades banked with tips ~5 cm below midplane of core; peripheral blades banked with tips ~2.5 cm below top of fuel.
[d] 77% of fuel was flooded.
[e] Analysis of sample punched from center of fuel plate.
[f] Runs were made with water-level control.
[g] Average of gold and uranium results.

the foil position was approximately 5% less than the asymptotic value.

Some approximate averaging over the volume of the core, on the basis of the above-mentioned figure, leads to an estimated blade-perturbation factor of 0.85 ± 0.10, including the 5% allowance for the foil position.

### Results and Discussion

The data are summarized in Table II-7-V, which gives the calculated power for each of the runs, and also the calculated flux per watt of core power.

It can be seen from Table II-7-V that, considering the (rather-broad) error limits, the peak flux in the ITC per watt of core power is roughly the same for all of the runs—which include two ITC sizes, several blade-reflector configurations and several fuel configurations. All of the values lie within 15% of the average value, which is $4.2 \times 10^7$ cm$^{-2}$ sec$^{-1}$ W$^{-1}$. The experimental precision is not sufficient to confirm the slight dependence on loading density that is indicated by theoretical calculations, which predict a 10% reduction in going from Core 1 to Core 4a.[3]

The measurements indicate that the peak flux at 100 MW would be approximately $4 \times 10^{15}$ n/cm$^2$-sec, and at 240 MW would have been within about 20% of $10^{16}$ n/cm$^2$-sec. Although most of the measurements were made with critical-assembly operating conditions different from the probable operating conditions of the design reactor, the error limits are broad enough that they are likely to encompass just about all possible blade-reflector configurations.

Appreciable reduction of the error limits would require a detailed program of three-dimensional fission-rate mapping in the fuel region.

### References

1. D. Shaftman and R. P. Savio, Argonne National Laboratory (private communication).
2. F. H. Helm, *Numerical Determination of Flux Perturbation by Foils*, Nucl. Sci. Eng. **16**, 235–238 (1963).
3. W. R. Robinson and G. S. Stanford, *Argonne Advanced Research Reactor Critical Experiments—Activation and Power Distribution Measurements*, Reactor Physics Division Annual Report, July 1, 1965 to June 30, 1966, ANL-7210, pp. 59–70.
4. D. H. Shaftman and R. P. Savio, *The Argonne Advanced Research Reactor (AARR)*, AEC-ENEA Seminar on Intense Neutron Sources (SINS), Santa Fe, New Mexico, September, 1966.

## II-8. Argonne Advanced Research Reactor Critical Experiments—Activation and Power Distribution Measurements

W. R. Robinson and G. S. Stanford

Foil activation traverses and power distribution measurements were made in the AARR critical experiment (Assembly 4b) to measure the effect of beryllium on the peak thermal-neutron flux in the internal thermal column (ITC) per unit reactor power; to locate and measure power peaks and flux perturbations throughout the core; and in Assembly 5 to determine the effect of grading the fuel in the vicinity of the inner and outer radial core boundaries on the peak fluxes in the ITC and in the beryllium. The AARR critical experiments utilized a stainless steel core. Experimental methods involved both disk-shaped foils and wires of uranium-aluminum alloy and have been reported in previous annual reports.[1, 2] The compositions of Assemblies 4b and 5 are given in Paper II-6.

### Results

#### Effect of Beryllium on the Peak Thermal Neutron Flux in the ITC

Beryllium is being considered for inserts in static-irradiation tubes in the ITC, when these tubes are not to be used during all or part of a core cycle. Introduction of a full length 2.5 x 2.5 cm beryllium column at the axis of the enlarged 7.2 cm area-equivalent radius stainless steel ITC increased the reactivity by 0.26%. A 5 x 5 cm column was worth 0.94%. Radial distributions in the presence of these axial columns were reported earlier;[2] they show flattened flux inside the beryllium regions, as would be expected because of the small slowing-down power and absorption cross section of beryllium. Inside the 5 x 5 cm column, the relative activity is approximately 10% lower than for the 100% water-filled ITC.

Recently, measurements were made with beryllium liners in the enlarged, aluminum-walled ITC. Radial distribution with U-235 fission detectors through these liners again show that as the amount of beryllium increases, the ratio of the peak-ITC to average-fuel-zone activity decreases. Figure II-8-1 shows the traverses and the thickness of the beryllium liners. Table II-8-I summarizes the water levels for criticality for various ITC loadings and indicates that as the amount

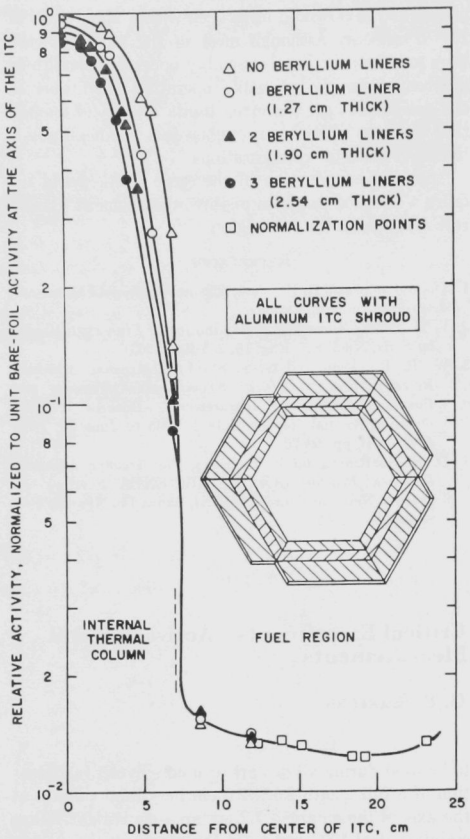


FIG. II-8-1. Radial Traverses of U-235-Fission Activity of Bare Foils through Beryllium Liners in the Large ITC. *ANL Neg. No. 112-8221.*

of beryllium increases in the ITC, the total reactivity of the system also increases.

COMPARISON OF STAINLESS STEEL AND ALUMINUM ITC

Comparison of the relative gain in reactivity from the 100% water-stainless steel ITC to the 100% water-aluminum ITC may be seen from the corresponding critical water levels in Table II-8-I. Radial U-235-fission distribution curves for the 100% water-filled ITC show the aluminum ITC peak value to be about 5% higher than that of the stainless steel ITC, with both curves normalized to common values in the fuel zone.

POWER DENSITY MEASUREMENTS IN THE GRADED FUEL REGION WITH URANIUM-ALUMINUM WIRES

Uranium-aluminum wires provide the fine spatial resolution needed to measure power peaks and flux perturbations. Detailed mappings near control blades have been presented earlier;[2] they show the flux peaking due to the water channels beside interior control blade followers. The measurements indicated that the azimuthal power peaking in the fuel near control-blade followers is little affected by the use of a stainless steel rather than aluminum followers. The power peaking was most pronounced within the first ½ cm of fuel at the control channel. The azimuthal maximum-to-average power ratio near the control blade follower was approximately 1.25.

The fuel in Assembly 5 was graded near the beryllium reflector and near the ITC. Assemblies 4b and 5 both contained the enlarged 7.2 cm area-equivalent radius aluminum ITC. Grading of fuel in the vicinity of the inner and outer radial core boundaries is required, in a practical reactor design, to reduce the peaks in power density which result from the steep gradients of thermal neutron flux near the edges of a heavily absorbing core with highly moderating reflectors.

These activations were made with all blades withdrawn, and criticality controlled by water level. The wire segments were located approximately 3 cm below the core midplane, at the positions shown in Figs. II-8-2 and II-8-3. Two irradiations were made, with normalizing points located in Region 1 (Fig. II-8-2).

The results are presented in Figs. II-8-4 through II-8-7, where the activation data are plotted as open

TABLE II-8-I. EFFECT OF BERYLLIUM IN THE INTERNAL THERMAL COLUMN

*Note: Both the beryllium columns and the liners were full length. The columns were centered at the axis of the ITC. The top of the active fuel zone nominally is at 132.4 cm. The level of the foils for the radial traverse was at 106.3 cm.*

| Condition of the ITC | Water Level at Criticality, cm | Relative Reactivity Change, % |
|---|---|---|
| 100% water[a] | 120.72 | 0.0 |
| 2.5-cm-square column of Be[a] | 120.36 | 0.26 |
| 5.1-cm-square column of Be[a] | 118.70 | 0.94 |
| 100% water[b] | 119.31 | — |
| 1.3-cm-thick Be liner[b] | 115.22 | — |
| 1.9-cm-thick Be liner[b] | 113.75 | — |
| 2.5-cm-thick Be liner[b] | 112.64 | — |

[a] Stainless steel shroud on the internal thermal column.
[b] Aluminum shroud on the internal thermal column.

points, normalized to unity at the innermost point of Region 3 (Figs. II-8-2 and II-8-6). In interpreting the graphs, it is necessary to refer to Figs. II-8-2 and II-8-3, where the symbols used in plotting are correlated with location in the core. For Regions 1, 3 and 4, the data permitted interpolation to determine the activation rate that would have been observed at the edges of some of the fuel plates. Those interpolations are plotted as open diamonds in Figs. II-8-4, II-8-6 and II-8-7.

To determine the relative power density, the smooth curves drawn through the activation data were used; the ordinate at the location of each fuel plate was multiplied by the weight of the fuel plate. The filled-in points in Figs. II-8-4 through II-8-7 result from that operation. Each such point indicates a fuel plate, although not all fuel-plate locations have been explicitly shown outside the graded zones. The normalization is consistent from curve to curve and figure to figure, permitting direct comparison of the relative power density at all locations investigated.

Figure II-8-4 (Region 1) shows the distribution in the graded region, eight plates deep, near the ITC. Figure II-8-5 (Region 2) shows the distribution in a graded assembly (graded region four plates deep) near the beryllium reflector. Also shown is a traverse taken earlier through a uniformly loaded subassembly. Figure II-8-6 (Region 3) shows the area around one of the three re-entrant corners at the ITC where ungraded fuel protrudes. Figure II-8-7 (Region 4) shows the distribution at the outer corner of the core where the graded fuel meets the reflector edge-on. The traverse points indicated by (◇) on Figs. II-8-2 and II-8-3 were obtained by taping the wire segments to the edge of the fuel subassembly so that the center of the wires was approximately 0.08 in. outside the plane of the edge of the fuel foils (Figs. II-8-8).

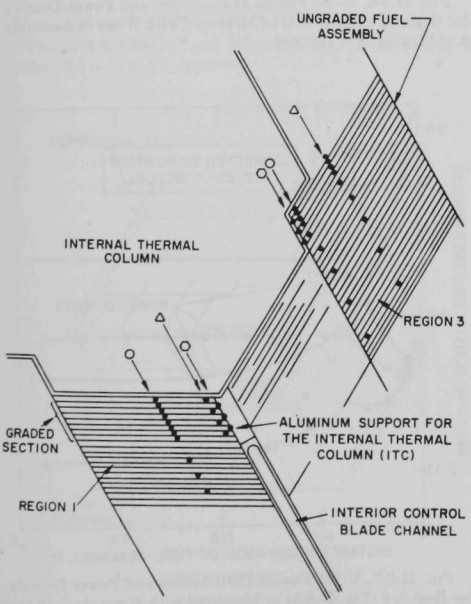


FIG. II-8-2. Wire Locations Near the ITC—(Assembly 5). *ANL Neg. No. 112-8994.*

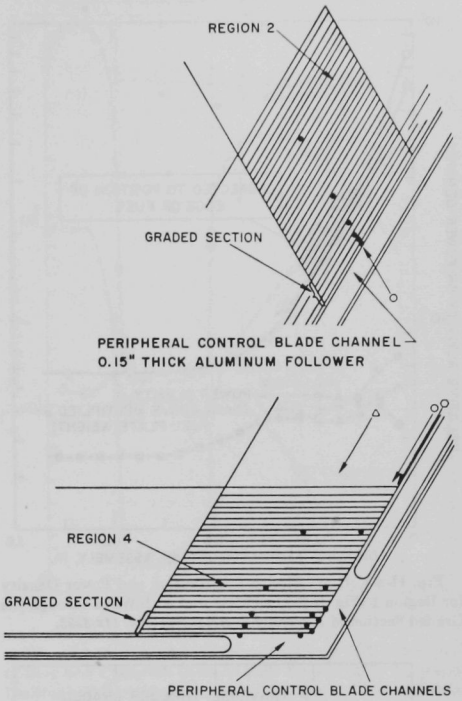


FIG. II-8-3. Peripheral Subassemblies, Showing Wire Locations—(Assembly 5). *ANL Neg. No. 112-9004 Rev. 1.*

RADIAL TRAVERSES OF U-235 FISSION ACTIVITY WITH DISK-SHAPED U-235—ALUMINUM DETECTOR FOILS

Bare and cadmium-covered radial traverses of U-235 fission activity through the graded fuel sections were obtained with disk-shaped U-235-aluminum detector foils. Lucite foil holders were used for the blacked-in

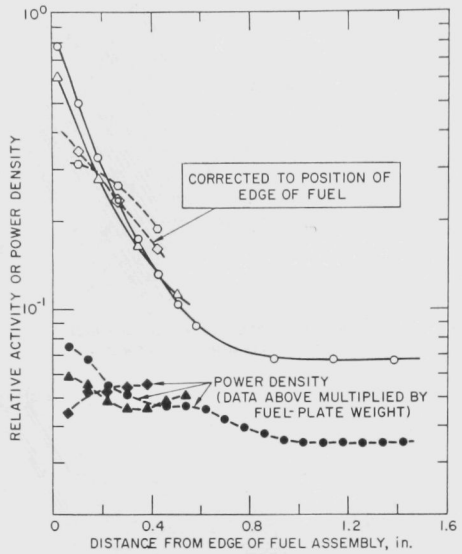


FIG. II-8-4. U-235 Fission Distribution and Power Density for Region 1 (Fig. II-8-2) as Measured with Wires through the Graded Section of Assembly 5. *ANL Neg. No. 112-8993.*

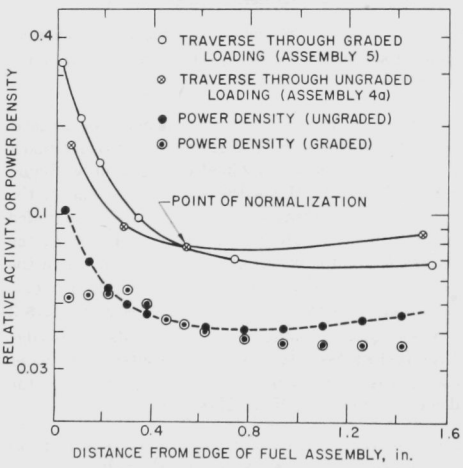


FIG. II-8-5. U-235 Fission Distribution and Power Density for Region 2 (Fig. II-8-3) as Measured with Wires through the Graded Section of Assembly 5, Compared with Data from Assembly 4a. *ANL Neg. No. 112-9003.*

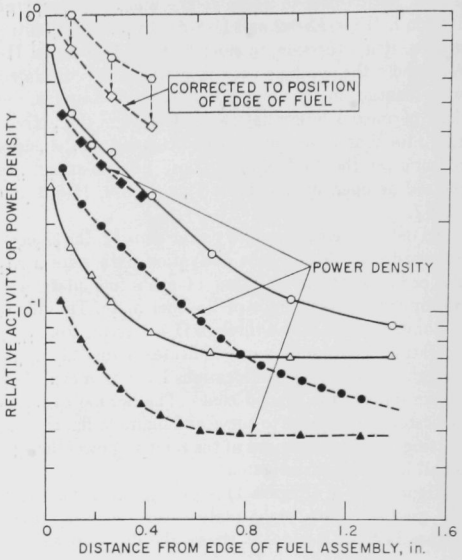


FIG. II-8-6. U-235 Fission Distribution and Power Density for Region 3 (Fig. II-8-2) as Measured with Wires in Assembly 5. *ANL Neg. No. 112-9002.*

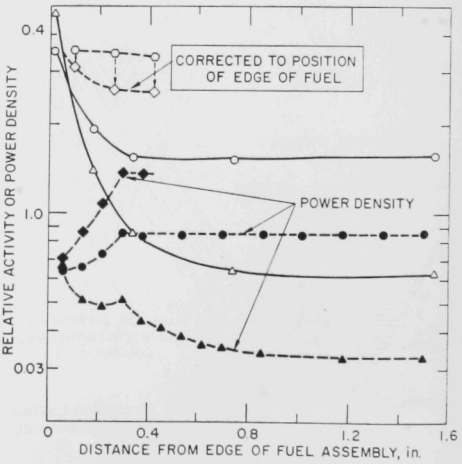


FIG. II-8-7. U-235 Fission Distribution and Power Density for Region 4 (Fig. II-8-3) as Measured with Wires through the Graded Section of Assembly 5. *ANL Neg. No. 112-9000.*

data points at 7.6 cm and 8.2 cm in Figs. II-8-9 and II-8-10 to maintain the metal-to-water ratio among the graded fuel foils. Previous measurements indicated that uranium-aluminum foils in Lucite and aluminum foil holders yield the same fission rates. To minimize control blade perturbation, criticality was adjusted by the water height with all control blades fully withdrawn.

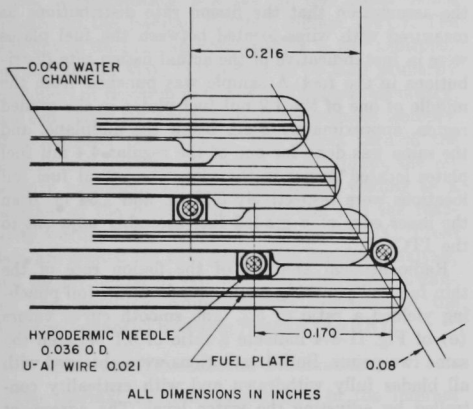


FIG. II-8-8. Channel and Wire Locations Near Fuel-Foil Edges. *ANL Neg. No. 112-8980.*

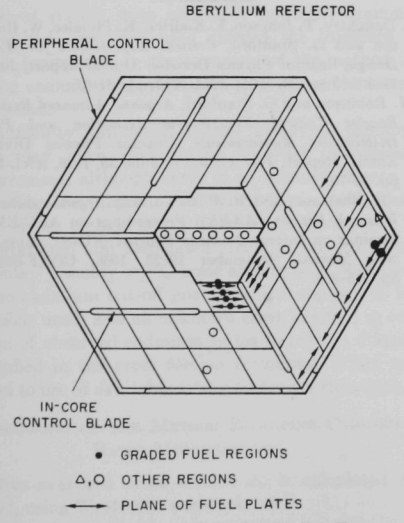


FIG. II-8-9. Locations of Foils for Radial Traverses of Activity, Graded Loading with an Oversized Aluminum ITC, Assembly 5. *ANL Neg. No. 112-8991.*

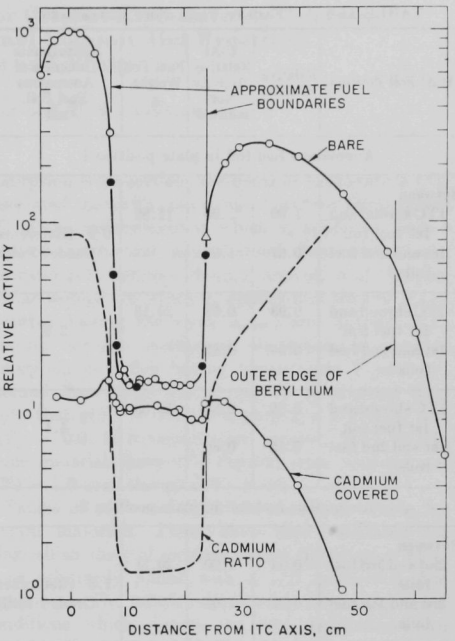


FIG. II-8-10. Radial Activation Traverses of U-235-Fission of Bare and Cadmium-Covered Foils for Assembly 5. Graded Loading and Oversized Aluminum ITC. For Foil Locations, see Fig. II-8-9. *ANL Neg. No. 112-8996.*

Results show that the bare traverse in the direction of the fuel grading has a more gradual slope than the traverse into an ungraded corner fuel assembly near the ITC. The bare traverses give the relative fission activity per atom of U-235, and it therefore appears that the reduced neutron blackness of the graded fuel zone is reflected in a less steep gradient of thermal and near-thermal neutron flux. Comparison of these traverses with similar ones made in the ungraded system indicate that the peak fluxes in the ITC and in the beryllium, per unit reactor power, are little affected by the fuel grading. This had been predicted earlier.[3]

### DETERMINATION OF A FAULTY FUEL LOADING

An experiment was performed to determine whether the mistaken insertion of an anomalously loaded fuel plate in place of one of the graded plates could be easily detected by an activation measurement. The six fuel subassemblies facing the ITC were used. Two of the six remained as reference subassemblies with unchanged graded loadings. Four subassemblies underwent fuel plate substitutions at either plate position 1

TABLE II-8-II. FAULTY FUEL FOIL EXPERIMENT

| U-Al Foil Position | Relative Activity | U-Al Relative Activity Normalized[a] | Fuel Foil Weight, g | Approximate Thickness of Anomalous Fuel Foil, mil |
|---|---|---|---|---|
| Anomalous fuel foil in plate position 1 | | | | |
| Between ITC shroud and 1st fuel foil | 1.00 | 1.00 | 11.89 | 0.9 (Reference Graded Foil) |
| 1st and 2nd fuel foils | 0.67 | 1.00 | | |
| ITC shroud and 1st fuel foil | 0.93 | 0.93 | 29.13 | 2.5 |
| 1st and 2nd fuel foils | 0.54 | 0.81 | | |
| ITC shroud and 1st fuel foil | 0.85 | 0.85 | 52.63 | 4.4 |
| 1st and 2nd fuel foils | 0.46 | 0.69 | | |
| Anomalous fuel foil in plate position 3 | | | | |
| Between 2nd and 3rd fuel foils | 0.44 | 1.00 | 20.21 | 1.6 (Reference Graded Foil) |
| 3rd and 4th fuel foils | 0.30 | 1.00 | | |
| 2nd and 3rd fuel foils | 0.41 | 0.93 | 38.80 | 3.3 |
| 3rd and 4th fuel foils | 0.28 | 0.91 | | |
| 2nd and 3rd fuel foils | 0.39 | 0.89 | 52.69 | 4.4 |
| 3rd and 4th fuel foils | 0.26 | 0.86 | | |

[a] Each foil position independently normalized to the activity of the reference foil.

or 3, counting from the aluminum ITC shroud. Uranium-aluminum foils on aluminum spears were placed on either side of the fuel foil in question. The results are shown in Table II-8-II. The activity perturbations are seen to range from 7% to 31%, for the cases studied. The activity of the foil on the core side of the anomalous fuel plate was more sensitive to the anomaly than was the activity of the foil on the ITC side.

### CHECK OF POWER DENSITY DISTRIBUTIONS

A spot check experiment was performed to confirm the assumption that the fission rate distributions as measured with wires located between the fuel plates were in fact indicative of the actual fission rate distributions in the fuel. A sample was punched from the middle of one of the 1.2 mil fuel plates in the graded region, approximately 3 cm below the midplane, and the same was done for one of the regular 4.4 mil fuel plates located deeper in the core. The actual fuel foil locations were respectively 0.14 in. and 1.34 in. from the inner edge of a graded fuel assembly adjacent to the ITC.

Radiochemical analysis of the fission rate of the thin fuel foil punching to the standard fuel foil punching yielded a ratio of 5.7. The smooth curve values (o) of Fig. II-8-4 indicate a ratio of 6.1 between the same two points. Both irradiations were obtained with all blades fully withdrawn and with criticality controlled by adjusting the water level. The agreement was considered satisfactory.

### REFERENCES

1. J. Daughtry, T. Johnson, F. Kodrick, K. Plumlee, W. Robinson and G. Stanford, *Critical Experiments for AARR Design*, Reactor Physics Division Annual Report, July 1, 1964 to June 30, 1965, *ANL-7110, pp. 61-73.*
2. W. Robinson and G. Stanford, *Argonne Advanced Research Reactor Critical Experiments—Activation and Power Distribution Measurements*, Reactor Physics Division Annual Report, July 1, 1965 to June 30, 1966, ANL-7210, pp. 59–70.
3. D. H. Shaftman and R. P. Savio, *The Argonne Advanced Research Reactor (AARR)*, Proceedings on AEC-ENEA Seminar on Intense Neutron Sources (SINS), Santa Fe, New Mexico, September 19–23, 1966, CONF-660925, pp. 215–259.

# II-9. Argonne Advanced Research Reactor Critical Experiments—Neutron Temperature in the Internal Thermal Column And Reactivity Worths of Samples and Voids

K. E. Plumlee, W. R. Robinson and T. W. Johnson

## Introduction

The measurements reported in this paper relate directly to the internal thermal column (ITC). The high flux in the ITC, approximately $4 \times 10^{15}$ neutrons/cm$^2$-sec at 100 MW, is expected to be used primarily in support of research in the field of nuclear chemistry, and especially for production of transuranic isotopes. Measurements described in this report include the neutron temperature, the worth of beryllium, the reactivity coefficient for small fractional voiding as a function of the presence of beryllium, and the reactivity worth of large partial voiding of the ITC. These data are needed for ITC design, for accident analysis, and for prediction of safe operating limits for installing and removing samples during operation of the Argonne Advanced Research Reactor (AARR).

## Neutron Temperature Measurements

The thermal neutron temperature in the internal thermal column (ITC) of the AARR Critical Experiment was measured from 50 to 60°C by cadmium ratios of various pairs of activated foils. Reasonably consistent results were obtained; however, examination of the equations used showed the existence of serious limitations on the accuracy of the method involving cadmium ratios. Errors in cross sections were also found.

A difficulty (discussed below) involving cadmium ratios may have affected the reported temperature measurement, although there is no convenient way of estimating the magnitude of such error at this time. Other errors include a ±5°C uncertainity because of computational and associated errors in Westcott's coefficients;[1] possibly ±2°C error arising from correction for the cadmium cut-off energy which appears in the equations used; and an unknown error inherent in correction of observed cadmium ratios to infinite dilution as implied in the cross section equations. Effort was limited to use of available tables and approximations.

## Discussion of the Method Requiring Cadmium Ratio Measurements

A flux-averaged cross section $\bar{\sigma}_a$ is calculated by Eq. (1), using Westcott's nomenclature.[1]

$$\bar{\sigma}_a = \sigma_{a2200} \sqrt{(\pi T_0)/4T} \, [g(T) + rS(T)]. \quad (1)$$

The foregoing terms include the 2200 m/sec neutron absorption cross section; the neutron temperature ($T_0$) associated therewith; the thermal neutron temperature ($T$) of the environment in which $\bar{\sigma}_a$ applies; a ratio $r$ between epithermal and thermal flux components; the ratio $g(T)$ between thermal activation of the particular isotope for which $\bar{\sigma}_a$ applies and that of a 1/v absorber having the same $\sigma_{a2200}$; and a term $S(T)$ relating non-1/v epithermal absorption to thermal absorption in a flux having temperature $T$ and epithermal flux magnitude $r$ relative to thermal flux. Note that $g(T) = 1.0$ for a pure 1/v absorber, and $S(T) = 0.0$. If resonances are present, $S(T) \neq 0.0$. Some materials have 1/v thermal cross sections and $g(T) = 1.0$ even though $S(T) \neq 0.0$.

Tables of $g(T)$ and $S(T)$ are readily available for several materials. These have been tabulated for Maxwellian thermal neutron energy distribution functions arbitrarily joined with a $1/E$ epithermal flux component. The tabulated values do not apply under conditions which distort the flux distribution. An obvious example for which they do not apply would be a plutonium fueled zone.

The equation for cadmium ratio of a material at infinite dilution is typically written as in Eq. (2). The numerator is the average cross section defined by Eq. (1) and the denominator is a flux-averaged epicadmium cross section. Application of Westcott's terminology is not accurate for isotopes having resonances in the vicinity of the cadmium cutoff energy because the $g(T)$ term is determined mostly by activation rate below a 4.95 $kT$ joining region. The activation in the range of energy between 4.95 $kT$ and 18 $kT$, the latter being roughly the cadmium cutoff energy, must be eliminated from the cross section used in the denominator of Eq. (2):

$$Cd\,R = \frac{g(T) + rS(T)}{r[S(T) + P(T)]} = \frac{1 + \dfrac{g(t)}{rS(T)}}{1 + \dfrac{P(T)}{S(T)}}, \quad (2)$$

$$r = \frac{g(T)}{Cd\,R[S(T) + P(T)] - S(T)}. \quad (3)$$

The term $P(T)$ is a function of cadmium cutoff energy which is adjusted as needed to account for nonresonance activation in the epicadmium energy range. The value for a pure 1/v material in a $1/E$ flux energy distribution is readily calculated, noting that $S(T) \equiv 0$

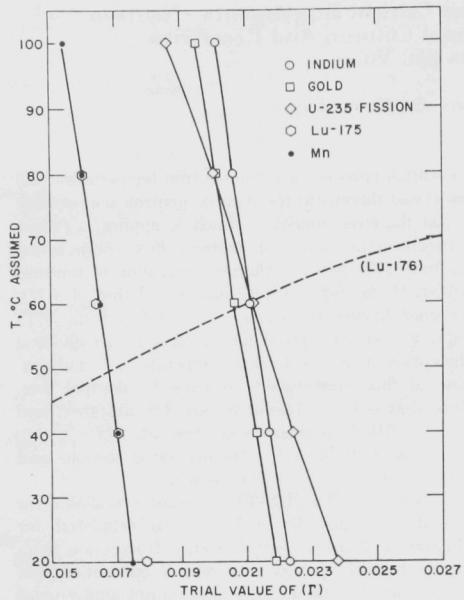


FIG. II-9-1. Plot of Trial ($r$) for Determination of Neutron Temperature in AARR Large ITC. *ANL Neg. No. 112-9099.*

and $g(T) \equiv 1$ for such a material:

$$[Cd\ R]_{1/v} = \frac{1 + r \cdot 0}{r \cdot 0 + r[P(T)]_{1/v}} = \frac{1}{r[P(T)]_{1/v}},$$

$$[P(T)]_{1/v} = \left(\frac{16kT}{\pi k T_{cd}}\right)^{\frac{1}{2}} = \frac{1}{K}\left(\frac{T}{T_0}\right)^{\frac{1}{2}} \approx \tfrac{1}{2}\left(\frac{T}{T_0}\right)^{\frac{1}{2}}.$$

The term $K$ and the approximation $K \approx 2$ are Westcott's terminology, but the approximation is limited to room temperature moderator and ~0.02 in. thick cadmium covers.

Solution of Eqs. (2) or (3), the latter being a rewritten form of Eq. (2), requires two or more measured cadmium ratios. Typically, trial values of $T$ are chosen and a consistent value of $T$ is found by plotting or iteration, such that the value of $r$ from Eq. (3) is the same for both materials. As may be seen by Fig. II-9-1, the trial values of $r$ for Lu-176 cut sharply across the other plots and give reproducible temperature determinations. If error limits were assigned to gold and indium, the two would overlap and no temperature determination could be made therefrom. On the other hand, the manganese and Lu-175 plots are too far removed from the others, except for Lu-176, to find any temperature which would reconcile the measurements.

The discrepancy between gold, indium and U-235 fission on one hand and manganese and Lu-175 on the other might indicate a distortion in the neutron energy distribution. This was found in the fuel region[2] but is not expected in the ITC. However, the use of $S(T)$ values from Westcott's tabulation for indium would place the $r$ values for indium in excellent agreement with the manganese results. The Westcott values of $S(T)$ for indium were from absorption resonance integral measurements and they apply to reactivity but not to activation measurements. Use of the activation resonance integral in determining $S(T)$ for indium placed the plot in excellent agreement with gold, which is the accepted standard. Thus the manganese and Lu-175 values appear questionable.

This results in a different outlook than was previously expressed by other workers who generally reported manganese and indium measurements, using Westcott's tabulation, and give little credence to gold and U-235 measurements. Other authors have reported the use of $S(T)$ values for manganese and indium which were different from those tabulated by Westcott but apparently they failed to find the simple explanation applicable to indium. No explanation was found for the discrepancy with manganese or Lu-175, even though several possibilities were explored.

### Discussion of a Second Procedure Using Bare and Cadmium Covered Foils (Two Isotopes)

Equations (4) and (5) are forms similar to that used by L. Schmid and W. Stinson,[3] for use of relative activities $A_x$ and $A_y$ for isotopes $x$ and $y$:

$$\frac{A_x}{A_y} = \frac{g_x(T)}{g_y(T)} \frac{n_x \sigma_{a2200}^x}{n_y \sigma_{a2200}^y} \frac{\left[1 + r\dfrac{S_x(T)}{g_x(T)}\right]}{\left[1 + r\dfrac{S_y(T)}{g_y(T)}\right]}, \tag{4}$$

$$1 + r\frac{S_x(T)}{g_x(T)} = \frac{Cd\ R_x}{Cd\ R_x - \alpha_x(T)}. \tag{5}$$

Schmid and Stinson tabulated values of $\alpha(T)$ for lutetium isotopes. It is easily shown through Eqs. (2) and (5) that Westcott's terms have the following relations to $\alpha(T)$:

$$\frac{P(T)}{S(T)} = \frac{1 - \alpha(T)}{\alpha(T)}$$

or

$$\alpha(T) = \frac{1}{1 + \dfrac{P(T)}{S(T)}}. \tag{6}$$

Intercomparison of $S^{176}(T)$ and $\alpha^{176}(T)$ from the two tabulations indicates significant disagreement. Still, the use of such methods appears to have given reasonable results in several measurements. The fol-

lowing development indicates that errors in $\alpha(T)$ or $S(T)$ may have little effect if the cadmium ratio is large compared with $\alpha(T)$. Substitution of Eq. (2) and Eq. (5) into Eq. (1) results in Eq. (7a) or (7b), respectively, for the activation ratio of materials $x$ and $y$. However, the available data does not satisfy Eq. (7b):

$$\frac{g_y(T)}{g_x(T)} = \frac{A_y}{A_x}\frac{n_x\sigma^x_{a2200}}{n_y\sigma^y_{a2200}}\frac{(Cd\ R)_x}{(Cd\ R)_y} \cdot \frac{\left[1+\dfrac{P(T)}{S_x(T)}\right]\left[(Cd\ R)_y\left(1+\dfrac{P(T)}{S_y(T)}\right)-1\right]}{\left[1+\dfrac{P(T)}{S_y(T)}\right]\left[(Cd\ R)_x\left(1+\dfrac{P(T)}{S_x(T)}\right)-1\right]} \quad (7a)$$

and

$$\frac{g_y(T)}{g_x(T)} = \frac{A_y}{A_x}\frac{n_x\sigma^x_{a2200}}{n_y\sigma^y_{a2200}}\frac{(Cd\ R)_x}{(Cd\ R)_y}\left[\frac{(Cd\ R)_y-\alpha_y}{(Cd\ R)_x-\alpha_x}\right]. \quad (7b)$$

Irradiation of foils in a thermal column permits substitution of relative count rates for relative activation measurements, as shown in Eq. (8):

$$\frac{g_y(T)\ g_x(th)}{g_x(T)\ g_y(th)} = \frac{C^T_y\ C^{th}_x}{C^T_x\ C^{th}_y}\frac{(Cd\ R)_x}{(Cd\ R)_y} \cdot \frac{\left[1+\dfrac{P(T)}{S_x(T)}\right]\left[(Cd\ R)_y\left(1+\dfrac{P(T)}{S_y(T)}\right)-1\right]}{\left[1+\dfrac{P(T)}{S_y(T)}\right]\left[(Cd\ R)_x\left(1+\dfrac{P(T)}{S_x(T)}\right)-1\right]}. \quad (8)$$

## Failure of Equations for Neutron Temperature Measurement

Casual examination of Eq. (3) does not indicate a region where the mathematical solution fails since it is obvious that $r$ is a small well-behaved term greater than zero. Thus one might conclude that the denominator on the right hand side does not go to zero. The denominator goes to zero *if* the following occurs:

$$Cd\ R = \frac{S(T)}{S(T)+P(T)} = \alpha(T). \quad (9)$$

If Eq. (9) is satisfied, Westcott's definition of $Cd\ R$, Eq. (2), is violated because $g(T) > 0$ for any material having a finite cross section for thermal absorption:

$$Cd\ R = \frac{g(T)+rS(T)}{rS(T)+rP(T)} = \frac{\dfrac{g(T)}{r}+S(T)}{S(T)+P(T)} \neq \frac{0+S(T)}{S(T)+P(T)}. \quad (10)$$

TABLE II-9-1. Cadmium Ratios and Correction to Infinite Dilution

| Foil Material | Foil Size, cm | | Uncorr. $Cd\ R$ AARR ITC[a] | AHFR ITC[b] | Correction Factor[c] | Inf. Dil $C\,d\ R$ | |
|---|---|---|---|---|---|---|---|
| | Thickness | Width | | | | AARR ITC | AHFR ITC |
| 12.5% Lu-Al | 0.040 | 2.54 (sq) | | | | | |
| Lu-176 | | | 131.41 (L) | — | ~1.0 | 131.41 (L) | — |
| Lu-175 | | | 2.52 (L) | — | 0.956 | 2.40 (L) | — |
| 90% Mn-Cu | 0.0064 | 0.817 (diam) | 44 (S) | — | 1.00 | 44 (S) | — |
| | | | 50 (L) | — | | 50 (L) | — |
| 80% Mn-Cu | 0.0102 | 0.559 (diam) | — | 55 (C-1 and C-2) | 1.007 | — | 55 |
| Au | 0.0025 | 1.0 (sq) | 7.42 (S) | 10.5 (C-1) | 0.390 | 2.89 (S) | 4.10 |
| | | | 9.11 (L) | 9.4 (C-2) | 0.390 | 3.55 (L) | 3.67 |
| 17% U-Al | 0.0051 | 0.817 (diam) | 60 ± 12 (S) | — | 1.055 | 63.3 (S) | — |
| | | | 90 ± 9 (L) | — | 1.055 | 95.0 (L) | — |
| | 0.0660 | 0.599 (diam) | — | 72 ± 14 (C-1) | 1.082 | — | 77.9 |
| | | | — | 31 ± 1 (C-2) | 1.082 | — | 33.5 |
| 4% Dy-Al | 0.0203 | 0.559 (diam) | — | 312 ± 80 (C-1) | 1.006 | — | 314 |
| | | | — | 290 ± 30 (C-2) | 1.006 | — | 292 |
| In | 0.0030 | 0.818 (diam) | 8.2 (L) | — | 0.464 | 4.34 (L) | |
| | 0.0127 | 0.559 (diam) | — | 14.7 ± 0.6 (C-1) | 0.443 | — | 7.07 |
| | | | | 13.5 ± 0.2 (C-2) | 0.443 | — | 6.54 |

[a] (S) and (L) distinguish between large and small flux trap.

[b] (C-1) and (C-2) are two different core loadings (see Ref. 1).

[c] Data from DP-608 (G. M. Jacks)[4] or DP-817 (N. P. Baumann).[5] This factor includes thermal flux depression, cadmium thickness, and infinite dilution corrections. The correction for Lu-176 would reduce the measured neutron temperature by about 3°C; however, it was omitted pending a revised value which is nearer unity, per N. P. Baumann.[7]

TABLE II-9-II. USE OF ACTIVATION CADMIUM RATIOS IN DETERMINATION OF NEUTRON TEMPERATURE ($T_n$) AND EPITHERMAL INDEX ($r$)

| Isotope | Assumed Temperature, °C | $g(T)$ | $S(T)$ | $P(T)$ | Denominator of Eq. (3) | Epithermal Index |
|---|---|---|---|---|---|---|
| In-115 | 20 | 1.0192 | 13.04[a] | 0.482 | 45.645 | 0.0223 |
| | 40 | 1.0231 | 13.47[a] | 0.497 | 47.147 | 0.0217 |
| | 60 | 1.0271 | 13.90[a] | 0.512 | 48.648 | 0.0211 |
| | 80 | 1.0310 | 14.30[a] | 0.528 | 50.054 | 0.0206 |
| | 100 | 1.0350 | 14.71[a] | 0.562 | 51.570 | 0.0201 |
| Au | 20 | 1.0053 | 17.30 | 0.482 | 45.826 | 0.0219 |
| | 40 | 1.0064 | 17.88 | 0.497 | 47.358 | 0.0213 |
| | 60 | 1.0075 | 18.44 | 0.512 | 48.840 | 0.0206 |
| | 80 | 1.0086 | 18.98 | 0.528 | 50.273 | 0.0201 |
| | 100 | 1.0097 | 19.51 | 0.562 | 51.746 | 0.0195 |
| $U^{235}$ fission | 20 | 0.9759 | −0.0502 | 0.482 | 41.071 | 0.0238 |
| | 40 | 0.9711 | −0.0410 | 0.497 | 43.361 | 0.0224 |
| | 60 | 0.9665 | −0.0324 | 0.512 | 45.594 | 0.0212 |
| | 80 | 0.9662 | −0.0244 | 0.528 | 47.866 | 0.0201 |
| | 100 | 0.9581 | −0.0169 | 0.562 | 51.801 | 0.0186 |
| Lu-176 | 20 | 1.7011 | 1.669 | ~0.169[b] | 183.326 | 0.0093 |
| | 40 | 1.8373 | 1.218 | ~0.174[b] | 138.887 | 0.0132 |
| | 60 | 1.9769 | 0.757 | ~0.179[b] | 93.451 | 0.0212 |
| | 80 | 2.1175 | 0.303 | ~0.185[b] | 49.117 | 0.0431 |
| | 100 | 2.2576 | −0.130 | ~0.197[b] | 6.874 | 0.3284 |
| Lu-175 | 20 | 1.00 | ~39[c] | 0.482 | 55.757 | 0.0179 |
| | 40 | 1.00 | ~41[c] | 0.497 | 58.593 | 0.0171 |
| | 60 | 1.00 | ~42.6[c] | 0.512 | 60.869 | 0.0164 |
| | 80 | 1.00 | ~44[c] | 0.528 | 62.867 | 0.0159 |
| Mn | 20 | 1.00 | 0.666 | 0.482 | 56.734 | 0.0176 |
| | 40 | 1.00 | 0.689 | 0.497 | 58.611 | 0.0171 |
| | 60 | 1.00 | 0.710 | 0.512 | 60.390 | 0.0166 |
| | 80 | 1.00 | 0.731 | 0.528 | 62.219 | 0.0161 |
| | 100 | 1.00 | 0.752 | 0.562 | 64.948 | 0.0154 |

[a] For In-115 activation, the activation resonance integral is used as listed by Ref. 8. Westcott's listing[4] for In appears to use the absorption resonance integral which is ~35% larger. Selection depends on application to activation or reactivity measurements.

[b] At the cadmium cutoff energy the Lu-176 cross section is ~0.35 as large as that calculated from Lu-176 $\sigma_{2200}$ for (1/v) cross section. Thus 0.35 of the 1/v value of $P(T)$ was used as an approximation or upper bound of $P(T)$ for Lu-176.

[c] Only approximate values were found for Lu-175; see Fig. 15.2.7b of Ref. 9. Similar values were obtained from resonance integral and cross section data supplied by Ref. 7.

Another constraint is that $Cd\ R > 1$ so that

$$|\, g(T) + rS(T) \,| > |\, rS(T) + rP(T) \,|,$$

and

$$g(T) > |\, rP(T) \,|,$$

by necessity.

Nevertheless it seems likely, on inspection of Westcott's tabulated values,[1] that most of the materials for which negative values of $S(T)$ are listed will indeed satisfy Eq. (9) at some point on the temperature scale. These include gadolinium, Lu-176, possibly U-235 fission, Pu-239 and Pu-241. It does not appear that the tabulated $\alpha(T)$'s by Schmid and Stinson[3] would encounter such difficulty; however, these are limited to two isotopes of lutetium and failed to give reasonable results for the data taken in the AARR Critical Experiment.

Referring to Tables II-9-I and II-9-II, it may be noted that the estimates of $P(T)$ should be different for a non-1/v material such as Lu-176, than for the 1/v materials. Setting $P(T) = 0$ for Lu-176 would move the line down in Fig. II-9-1. The resulting estimate of neutron temperature would be about 5°C lower than shown. This uncertainty is a limiting factor in the accuracy of the method followed, which was limited to the use of readily available tables and approximations. Presumably it would be possible to tabulate the exact $P(T)$ terms along with $g(T)$ and $S(T)$ for materials such as Lu-176, thus making possible a substantial improvement in the accuracy of the results obtained by a user of Westcott's tables.

In addition to errors arising from estimation of $P(T)$, it is estimated that there is about ±5°C error in neutron temperature measurements because of computational errors.[1] If this is typical for a denominator of unity, then the overall errors would be inversely proportional to the denominator, or worse, of the trial values.

## Data Evaluation

A tabulation of ITC cadmium ratios for both AARR and AHFR[6] is given in Table II-9-I. The AHFR core was aluminum and the fuel density was much lower than that of the AARR experiment. Although no neutron temperature evaluation was made of AHFR data, it is evident that the ITC data for the large AARR correspond closely with the ITC data for AHFR. Table II-9-II and Fig. II-9-1 indicate neutron temperatures from 50 to 60°C.

## Worth of Beryllium and the Effect on the Void Coefficient of Reactivity due to the Radial Distribution of Beryllium in the ITC

Beryllium is being considered for inserts in static-irradiation tubes in the ITC, when these tubes are not intended for use during all or part of a given core cycle. Introduction of a full length 2.5 x 2.5 cm beryllium parallelepiped at the axis of the enlarged 7.2 cm area-equivalent radius stainless steel ITC increased reactivity by 0.26%. A 5 x 5 cm paral-

TABLE II-9-III. REACTIVITY COEFFICIENTS OF BERYLLIUM AND TEFLON IN THE STAINLESS STEEL ITC, ASSEMBLY 4b

| Case No. | Beryllium | Plan Areas ($cm^2$) $H_2O$ + Teflon | Teflon | Reactivity Change, % | Reactivity Coefficient, %/(% $H_2O$ displaced) | Reactivity Coefficient, %/(% of ITC vol.) |
|---|---|---|---|---|---|---|
| Reference | — | 152.3 | — | — | — | — |
| Be-1 | 6.4 | 145.9 | — | 0.26[d] | 0.062[d] | 0.062[d] |
| Be-2 | 25.8 | 126.5 | — | 0.94[d] | 0.056[d] | 0.056[d] |
| Teflon[a] | — | 152.3 | 10.4 | 0.36 | 0.053 ± 0.005 | 0.053 ± 0.005 |
| Teflon[b] | 6.4 | 145.9 | 6.6 | 0.24 | 0.054 ± 0.005 | 0.055 ± 0.005 |
| Teflon[c] | 25.8 | 126.5 | 6.6 | 0.24 | 0.047 ± 0.005 | 0.055 ± 0.005 |

[a] No beryllium present.
[b] 2.5 × 2.5 cm sq. column of beryllium at axis of ITC.
[c] 5 × 5 cm sq. column of beryllium at axis of ITC.
[d] The reactivity worth of beryllium was measured as the difference in critical configurations between a reference run and other runs. It is much less accurately measured than for Teflon, where samples were withdrawn by remote methods during reactor operation, with compensation by a calibrated control blade.

lelepiped was worth 0.94%. As shown by Table II-9-III, this is roughly equal to Teflon, on a volume basis.

Theoretical analysis has predicted that the reactivity coefficient of voiding water in the ITC is essentially independent of the radial distribution of beryllium, but does depend primarily upon the volume of ITC water displaced.[10] To measure this effect, part to the ITC water was replaced with Teflon during three different loadings of the ITC:

(a) 100% water,
(b) 2.5 x 2.5 cm sq. column of beryllium at the axis of the ITC,
(c) 5 x 5 cm sq. column of beryllium at the axis of the ITC.

Carbon, one of the constituents of Teflon, is a neutron moderator. Taking the carbon content into account, it has been calculated that the reactivity coefficient of air void in the water in the reactor core is approximately 1.1 times the reactivity coefficient of displacement of core water by Teflon. In the ITC, the correction factor is not as large and thus Teflon is almost, but not quite, equivalent to a gas void.[11] Figure II-9-2 shows the locations of the five cylinders and two rectangular columns of Teflon used. In Case (a) all seven pieces of Teflon were present for a total water displacement of 6.8%. For Cases (b) and (c) only the two rectangular columns and the two outermost rods of Teflon were present. Table II-9-III summarizes the compositions and the results. In similar experiments with the 5.9 cm ITC (no beryllium), only the five rods of Teflon were used. As may be seen from Table II-9-III, the reactivity changes due to the small volumes of Teflon are almost independent of the beryllium content of the ITC, within the ranges studied. The reactivity increase was proportional to the volume of the Teflon in the ITC; that is, the reactivity coefficient upon displacing water by Teflon, in units of %/$cm^2$ Teflon, was almost constant.

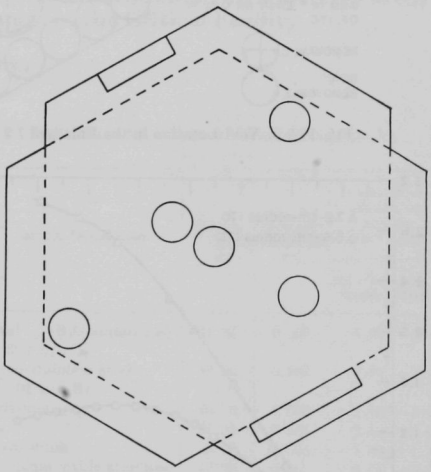

FIG. II-9-2. Location of Full-Length Columns of Teflon in the Two ITC's *ANL Neg. No. 112-9045. Legend:* Region bordered by dashed line: Small ITC (5.9-cm-radius). Region bordered by solid line: Oversized ITC (7.2-cm-radius).

## REACTIVITY WORTHS OF LARGE PARTIAL VOIDINGS OF THE ITC

An important factor in accident analysis is a risk of steam void formation because of the high flux of neutrons and gamma radiation in the ITC samples. If the coolant flow fails, high flux will cause steam void formation around the samples. Another possibility for gaining reactivity is by the displacement of a large amount of water in the ITC during sample loading. A major constraint on the detailed ITC design, and on the samples to be inserted, is the minimization of the risk inherent in water loss from the ITC. Void worth measurements for small voids (1% to 6%)

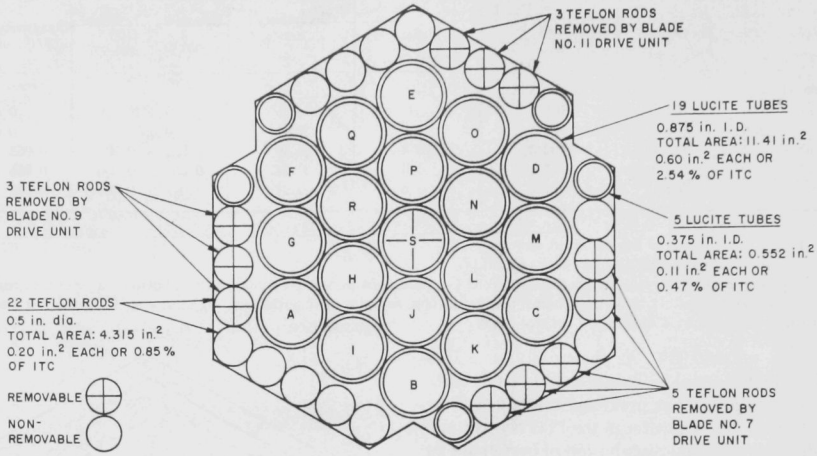


FIG. II-9-3. Void Location in the Enlarged 7.2 cm Area Equivalent Radius ITC. *ANL Neg. No. 112-9101.*

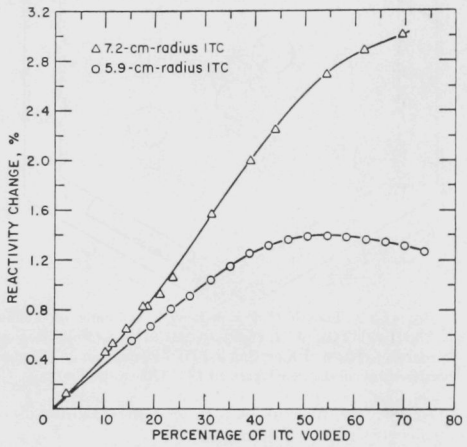


FIG. II-9-4. Reactivity Effect of Large Partial Voidings in Core 4. *ANL Neg. No. 112-8218.*

have been reported for loadings 1 to 4 in previous papers. Void worth measurements for large voids with the 5.9 cm area-equivalent radius ITC in cores 3 and 4a have been reported previously.[10] Core 4b had the large ITC of 7.2 cm area-equivalent radius which was expected to minimize the flux depression in the ITC when representative samples were introduced. To facilitate the ITC change, it was necessary to remove seven fuel plate positions from the inner edge of each of the subassemblies bordering the ITC. The remaining subassemblies were not modified although portions of fuel plates extended into the reentrant corners of the ITC.

In order to measure the reactivity gained by the displacement of a large amount of water from the ITC, a large void was simulated by voided Lucite tubes and Teflon rods as shown in Fig. II-9-3. Each tube or rod ran the full length of the 46 cm high "active" portion of the ITC. Reactivity effect was measured by removing the void incrementally and observing the change in a calibrated control blade. Results of the experiment are shown in Fig. II-9-4 (upper curve). The maximum measured reactivity gain was approximately 3% at approximately 70% void. The lower curve in Fig. II-9-4 shows the results of the large void experiment for the same core loading density but with the smaller 5.9 cm area-equivalent radius ITC.

## REFERENCES

1. C. H. Westcott, *Effective Cross Sections for Well-Moderated Thermal Reactor Spectra*, (CRRP-960) AECL-1101 (November 1, 1960).
2. G. S. Stanford and W. R. Robinson, *Argonne Advanced Research Reactor Critical Experiments—Cadmium Ratio Measurements*, Reactor Physics Division Annual Report, July 1, 1965 to June 30, 1966, ANL-7210, pp. 57–58.
3. L. C. Schmid and W. P. Stinson, *Lutetium as a Spectral Index Detector*, HW66319 (August 3, 1960).
4. G. M. Jacks, *A Study of Thermal and Resonance Neutron Flux Detectors*, DP-608 (August 1961).
5. N. P. Baumann, *Resonance Integrals and Self-Shielding Factors for Detector Foils*, DP-817 (January 1963).

6. J. W. L. deVilliers (Ed.), *Critical Experiments for the Preliminary Design of the Argonne High Flux Reactor*, ANL-6357 (1961).
7. N. P. Baumann, Savannah River Laboratory (private communication).
8. A. E. McArthy and P. J. Persiani, ANL Reactor Physics Constants Center Newsletter No. 11, *Neutron Resonance Integral and Age Data*, January 1965.
9. K. H. Beckurts and K. Wirtz, *Neutron Physics* (translated by L. Dresner) (Springer Verlag, New York, Inc., 1964).
10. D. H. Shaftman, C. N. Kelber, B. N. Kristianson and R. P. Savio, *Argonne Advanced Research Reactor Calculations—Analysis of Criticality-Facility Loadings*, Reactor Physics Division Annual Report, July 1, 1964 to June 30, 1665, ANL-7110, pp. 59–60.
11. *Reactor Development Program Progress Report*, ANL-7249 (1966), p. 68.
12. J. Daughtry, T. Johnson, F. Kodrick, K. Plumlee, W. Robinson and G. Stanford, *Critical Experiments for AARR Design*, Reactor Physics Division Annual Report, July 1, 1964 to June 30, 1965, ANL-7110, pp. 61–73.
13. W. Robinson and J. Daughtry, *Argonne Advanced Research Reactor Critical Experiments—Void Worth, Temperature Coefficient and Material Reactivity Worths*, Reactor Physics Division Annual Report, July 1, 1965 to June 30, 1966, ANL-7210, pp. 70–73.

# II-10. Argonne Advanced Research Reactor Critical Experiments—Reactivity Worths Obtained by Traversing Small Samples in the Critical Facility

J. W. Daughtry

## Introduction

The Argonne Advanced Research Reactor (AARR) Critical Facility has been described in several earlier reports.[1,2,3,4] During the course of experimentation with this facility, four uniform loadings and one graded loading were assembled. The five core loadings and various modifications to each have been described in the two previous annual reports[3,4] and in this annual report (see Paper II-6). The measurements reported herein were performed in loading 47. This was the original fourth core, referred to as the full uniform core loading, consisting of 1215 fuel foils, giving a total of 61.5 kg of U-235, and 1620 boron-stainless steel poison plates, having a total of 850 grams of natural boron. This loading had the unmodified (4.8 liter) hexagonal internal thermal column (ITC).

The reactivity worths of an assortment of small samples were measured at the midplane of the hexagonal annular fuel region in each of the first four cores.[3,5] This information has been extended by the present series of measurements to include the worths of a number of materials as a function of their axial distance from the midplane. The measurements were made for comparison with calculations, to provide additional information on burnup rates of fuel and burnable poison and to compare materials under consideration as control rod constituents. Other commonly used absorbing materials were included for comparison, since little information was available from nuclear reactor measurements involving a similar neutron spectrum.

The set of space-dependent worth measurements reported here was obtained using a sample traversing system with "on-line" computer processing of the data.[6] Starting with the reactor critical, samples were moved vertically between the midplane of the core and a position below the reactor. The samples were traversed in both directions to reduce the probability of systematic error. The resulting change of the neutron flux level in the reactor was detected by an ion chamber and transmitted to the computer by means of an electrometer and voltage-to-frequency converter system. The sample position and neutron flux data were received simutaneously by the computer which was

TABLE II-10-I. Samples used for Reactivity Traverses

| Sample Description | Sample Weight, g | Sample Thickness, cm | Midplane Worth of Sample, $10^{-4}$ $\Delta k/k$ | |
|---|---|---|---|---|
| | | | by traversal | by period[a] |
| Boral ($B_4C$-aluminum) (22.2 w/o B) | 17.86 | 0.508 | −5.99 | −5.96 |
| Boron-stainless steel (1.01 w/o B) | 53.96 | 0.508 | −2.21 | −2.21 |
| Cadmium | 62.70 | 0.508 | −2.89 | −2.80 |
| | 31.35 | 0.254 | −2.12 | −2.09 |
| Dysprosium | 3.06 | 0.025 | −1.39 | −1.38 |
| Europium oxide-stainless steel (31 w/o Eu) | 43.30 | 0.396 | −6.67 | −6.56 |
| Hafnium-zirconium (97.5 w/o Hf) | 55.13 | 0.302 | −4.59 | −4.64 |
| | 92.27 | 0.508 | −6.12 | −6.08 |
| Uranium-aluminum [17.44 w/o U (93.17 a/o U-235)] | 19.91 | 0.462 | +0.50 | +0.54 |

[a] See Reference 5.

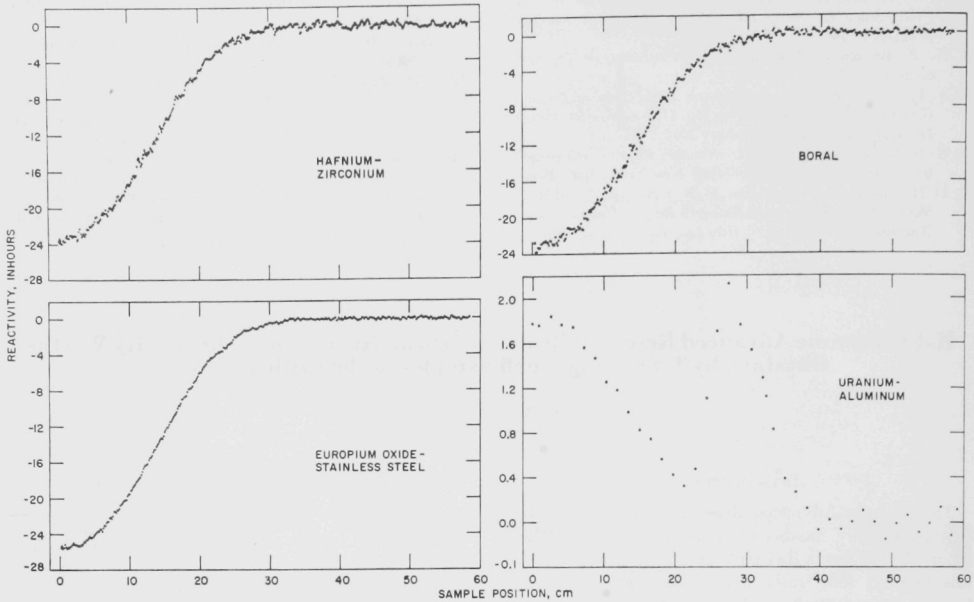


FIG. II-10-1. Vertical Reactivity Worth Traverses of Small Samples in the AARR Critical Facility. *ANL Neg. No. 112-8585.*

equipped with on-line data input scalers. The reactivity was calculated by the computer from the flux data using a set of one-energy-group spaced-independent kinetic equations.[7] The results were presented in the form of plots of reactivity versus sample position.

## EXPERIMENTAL DETAILS

Table II-10-I lists the materials for which useful worth traverses were obtained. The samples were held in dummy control blade-sample holders. The sample holders had the same dimensions as the standard interior control blades of the AARR critical facility and were made of 2S aluminum. With the sample holders fully inserted into the reactor the sample positions were approximately 58 cm below the midplane of the reactor. Three sample holes, 2.18 x 2.18 cm, were in a horizontal row across the width of each sample holder. The sample holders were inserted in one of the three radial control blade slots (7, 9 or 11). This placed the centers of the three sample positions at radii of 9.5, 15.7, and 21.9 cm from the centerline of the reactor. The data in Fig. II-10-1 and Table II-10-I were obtained with samples in all three positions. The sample weights given in Table II-10-I are for three samples, each 2.18 x 2.18 cm, with thicknesses as shown in the table. For cases in which the sample thickness was less than the thickness of the sample holder (0.508 cm), the remaining volume of the sample hole was filled with an aluminum spacer to bring the total thickness to 0.508 cm. The immediate environment of the samples consisted of the aluminum sample holders which moved in control blade slots approximately 0.635 cm thick. The region within the slots not occupied by the sample holders was filled with water during reactor operation. This provided a 0.064 cm water gap between the samples and the fuel assemblies. The samples were traversed from their positions below the core to the midplane, or in the reverse direction, using the standard control blade drive mechanism, which employs a stepping motor. The stepping pulses provided a convenient source of sample position information for use by the computer. Each pulse corresponded to a sample position increment of 0.01 cm.

A boron lined ion chamber was placed at the centerline of the reactor, just above the ITC, to detect changes in the neutron flux. The ion chamber current was transmitted to an electrometer which provided a 0–10 volt signal proportional to the input current. The voltage signals were converted to a train of pulses by

means of a voltage-to-frequency converter. The pulses were summed by a data input scaler at the computer.

With the reactor critical at a sufficiently high power level and with the computer program and delayed neutron parameters loaded, data taking was initiated and the computer began receiving flux level and sample position information. The samples were traversed at approximately 0.3 cm/sec. A time interval of 0.5 sec was selected for storing data. As the flux data were accumulated the reactivity change was computed. At the end of the run the resulting curve of reactivity versus sample position was plotted by the computer. Figure II-10-1 shows four representative traverse plots. The zero sample position is the midplane of the core. The half length of the fuel plates is 22.85 cm. The uranium-aluminum sample worth has a peak at about 4 cm from the edge of the fuel region which exceeds the midplane worth of this sample. The uncertainties in the traverse data are not well established; however, a comparison with results obtained by period measurements, as shown in Table II-10-I, indicates that the two methods provide comparable accuracy, since the errors in the period results have been estimated to be about $1 \times 10^{-5}$ $(\Delta k/k)$.


References

1. C. N. Kelber, E. F. Groh and K. E. Plumlee, *Safety Analysis Report for the Argonne Advanced Research Reactor Critical Experiment*, ANL-6929 (1965).
2. K. E. Plumlee, E. Groh and G. S. Stanford, *Preparation of Critical Experiment for Argonne Advanced Research Reactor (AARR) Design*, Reactor Physics Division Annual Report, July 1, 1963 to June 30, 1964, ANL-7010, pp. 66–67.
3. J. Daughtry, T. Johnson, F. Kodrick, K. Plumlee, W. Robinson and G. Stanford, *Critical Experiments for AARR Design*, Reactor Physics Division Annual Report, July 1, 1964 to June 30, 1965, ANL-7110, pp. 61–73.
4. K. E. Plumlee, J. W. Armstrong, J. W. Daughtry, T. W. Johnson, F. F. Kodrick, W. R. Robinson, R. A. Schultz and G. S. Standord, *Argonne Advanced Research Reactor Critical Experiments—Preface*, Reactor Physics Division Annual Report, July 1, 1965 to June 30, 1966, ANL-7210, pp. 47–48.
5. W. R. Robinson and J. W. Daughtry, *Argonne Advanced Research Reactor Critical Experiments—Void Worth, Temperature Coefficient and Material Reactivity Worths*, Reactor Physics Division Annual Report, July 1, 1965 to June 30, 1966, ANL-7210, pp. 72–73.
6. C. E. Cohn, *Initial Usage of a Computer for On-Line Data Reduction in Reactor Physics Experiments*, Trans. Am. Nucl. Soc. **8**, 585 (1965).
7. C. E. Cohn and J. J. Kaganove, *Digital Method for Control Rod Calibration*, Trans. Am. Nucl. Soc. **5**, 388 (1962).


## II-11. Argonne Advanced Research Reactor Critical Experiments—Measurements of Control and Safety Enhancement Devices

K. E. Plumlee, T. W. Johnson, F. H. Martens and W. R. Robinson

### Introduction

Several measurements were made to obtain comparisons between components which might be used for control or safety absorbers in AARR. The effective neutron absorption cross sections are quite small for in-core control blades because of the very hardened neutron energy distribution associated with the high fuel loading density of the AARR stainless steel core. Design of safety and control devices is further complicated by the compact nature of a high flux reactor core, by rapid burnup of absorber atoms, and by high heat flux. Measurements with coupons of several materials of interest in control/safety absorber studies, and comparisons of $Eu_2O_3$-stainless steel control blades with hafnium blades were reported earlier[1] and continued work is described in Paper II-10.

This paper reports the control and safety blade calibrations for Assemblies 4b and 5; the reactivity effect of thickening a full size hafnium safety blade from the 0.38 cm standard thickness for the critical experiment to 0.51 cm; the reactivity controlled by a removable Internal Thermal Column (ITC) safety liner intended for increased shutdown margin during shipment, storage, and loading of a packaged core; and the reactivity effects to be expected from attachment of a section of temporary beryllium reflector to the follower of a safety blade, for greater shutdown margin.

### Control and Safety Blade Worths in Assemblies 4a and 4b

Removal of the small ITC (Assembly 4a) and installation of the large ITC (Assembly 4b) resulted in removal of 42 fuel positions, and a compensating removal of boron-stainless steel throughout the core. One each of the four geometrically dissimilar types of blades was calibrated, specifically Nos. 5, 6, 9 and 10, before and after the change in ITC dimensions.

The blade worths are given in Table II-11-I. The

TABLE II-11-I. Control Blade Worths in Assemblies 4a and 4b

| Blade Positions | Worth in Assembly 4a, % | Worth in Assembly 4b, % |
|---|---|---|
| 1, 3, 5 | 1.12 | 1.44 |
| 2, 4, 6 | 1.20 | 1.51 |
| 7, 9, 11 | 1.01 | 1.14 |
| 8, 10, 12 | 1.07 | 1.18 |

TABLE II-11-II. Comparison of Blade Worths in Non-Graded and Graded Loadings 4b and 5

| Blade Position and Type[a] | Worth in Graded Loading 5, % | Worth in Non-Graded Loading 4b, % | Ratio of Graded-to-Non-Graded Loading |
|---|---|---|---|
| 1-3-5 | 1.15–1.23 | 1.44 | 0.80–0.85 |
| 2-4-6 | 1.19–1.21 | 1.51 | 0.79–0.80 |
| | 1.13 (banked) | 1.44 | 0.78 |
| 2 (thin) | 0.93 | 1.18[b] | 0.79 |
| 6 (thick) | 1.34 | 1.43[b] | 0.94 |
| 7 (thin) | 1.1–1.47 | 1.22 | 0.9–1.2 |
| 8-10-12 | 1.09–1.20 | 1.182 | 0.9–1.0 |

[a] Unless designated thick or thin, the blades contain 0.38 cm thickness of hafnium metal and 0.13 cm thickness stainless steel, with 0.51 cm aluminum followers. Thin blades are 0.38 cm thick hafnium with 0.38 aluminum follower. Thick blades are 0.51 cm thick hafnium with standard aluminum followers. Blades 1–6 are peripheral (19.1 x 66.7 cm hafnium dimensions). Blades 7–12 are in-core (16.5 x 66.7 cm hafnium dimensions).

[b] In slightly different configuration with more shadowing than in Assembly 5.

worths increased by a factor of approximately 1.27 in the safety (peripheral) positions Nos. 1 through 6, and approximately 1.12 in the control (in-core) positions Nos. 7 through 12. Control blade descriptions are given with Table II-11-II. It should be noted that all calibrations described in this paper are for control/safety blades with aluminum followers, whereas earlier work was generally with stainless steel followers. The aluminum followers were more representative of the cross section of zirconium followers normally used with hafnium, than were the stainless steel followers.

### Control and Safety Blade Worths at Room Temperature in Assemblies 4b and 5

The localized reduction in fuel loading which was made in changing Assembly 4b to the graded loading (or power-flattened) Assembly 5 resulted in about 20% loss in worths of the peripheral blades, which are located at the outer boundary of the fuel region. The in-core blade worths were only slightly affected even though the boron-stainless steel content was reduced throughout the core to compensate for the partial removal of fuel from the graded region. Experience with uniformly loaded cores indicated that control blade worths increased as fuel loading decreased.

Since during the early part of the core cycle the graded portions will deplete more rapidly than the remainder of the fuel region, because of the higher flux level therein, the blade worths may fall below their initial values.

Blades were calibrated by rising periods following incremental withdrawal of blades from critical configurations. A compensating blade was used to reestablish criticality after each rising period. Interdependence was noted between various blades, with individual worths ranging down to 0.7 of their highest values, when heavily shadowed by surrounding blades. To be valid intercomparisons must be made using similar configurations.

The ratios of individual blade worth measurements in Assemblies 4b and 5 are given in Table II-11-II.

### Increase in Control Blade Worths During Temperature Coefficient Test in Assembly 5

It was noted during a temperature coefficient test in Assembly 5 that control blade configurations were not in agreement with critical water height measurements. The control (in-core) blades were recalibrated at 65°C, showing their reactivity worths to be about 1.07 times as great as at 26°C. Correction for the calibration change brought the temperature coefficient result into reasonable agreement as indicated by Fig. II-11-1. A calibration from banked configuration is shown by Fig. II-11-2. Blade No. 8 was withdrawn incrementally, for rising period measurements of worth and blade No. 10 was used for compensation. Blades Nos. 7 through 12 were banked initially at the two starting points (25.83 and 25.70 cm).

More than half of the apparent temperature coefficient indicated by the plot based on the 26°C blade calibration is caused by a calibration change as a function of temperature.

### Measurement of Worth of a Thick Hafnium Safety Blade

Since hafnium control and safety blades generally are not clad, any comparison with another absorber material requiring cladding raises the following question. How significant is the added thickness of hafnium if the hafnium blade is made equal in thickness to a clad blade? It has been estimated[1] from earlier in-core measurements with small coupons of hafnium[2] that an increase of 0.13 cm in the hafnium thickness (from 0.38 to 0.51 cm) would increase the worth by less than a factor of 1.1.

Experiments with full size hafnium safety (peripheral) blades of 19.1 x 66.7 cm gave a measured improvement by a factor of 1.06, which is consistent with the preceding estimate. Measurements were done partly by rod-drop techniques, using on-line data analysis by a small computer.[3] In the first (blade No. 6) position tested the measured blade worth changed from 1.331% reactivity to 1.426%, or a factor of 1.07, when thickened. Tests in a second position (No. 2) gave worths of 1.449% and 1.509%, or a factor of 1.04 improvement.

More accurate measurements of the reactivity differences were obtained by use of a calibrated control blade which indicated a change of critical position measuring 0.090% in reactivity between the two thicknesses of hafnium when fully inserted in the first location, and 0.084% in the second location. These differences correspond with factors of 1.068 and 1.058 improvement in worth.

The added thickness of hafnium was achieved by replacing an 0.13 cm thick stainless steel backing sheet with 0.13 to 0.14 cm thick hafnium, resulting in a combined hafnium thickness of 0.51 cm for the blade being tested, with little or no change in local metal or water volumes.

### Experiments with an ITC Safety Liner Mockup

A large shutdown margin would be needed during shipment if an AARR stainless steel core were to be received and loaded into the reactor as a packaged unit, containing about 60 kg of highly enriched uranium. The use of a removable ITC safety liner for increased shutdown margin appeared feasible, and a measurement was made of the reactivity worth of such a mockup in Assembly 5. Although a thick heavily absorbing liner might otherwise have been tested, the available supply of hafnium was limited to an 0.13 cm thick liner which would replace the 0.16 cm thick stainless steel wall of the small ITC or 80% of the perimeter of the large ITC. (The ITC's are indicated in Fig. II-6-6 of Paper II-6). Since there were consistent thickness data from tests with small coupons[2] and from safety blade experiments, it seemed reasonable to measure the worth of the thin hafnium liner and to use that measurement as a basis for an estimate of the worth of a thick liner. Furthermore, the excess reactivity of the available core loading 5 equaled the anticipated worth of the thin liner; thus this experiment would not require reloading of the reactor. A thicker liner would require either reloading or resort to subcritical measurements which are not very accurate.

After a reference run, the six 6.0 cm wide, 0.16 cm thick stainless steel sides of the large ITC were replaced by 0.13 cm thick hafnium, but the reentrant

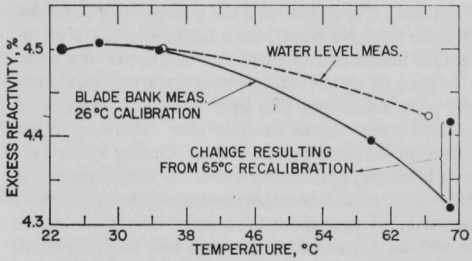


Fig. II-11-1. Reactivity Versus Temperature, Graded Core. *ANL Neg. No. 112-8938.*

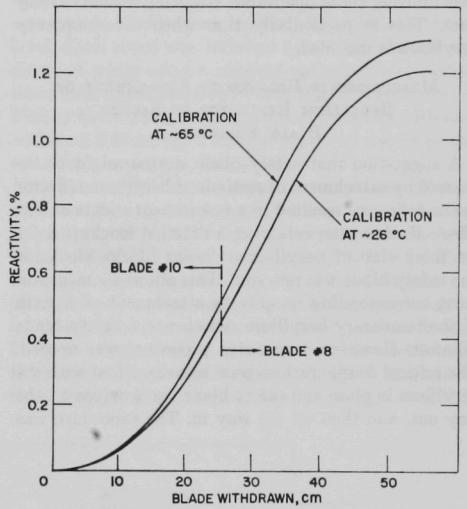


Fig. II-11-2. Blade Worths at 26°C and 65°C. *ANL Neg. No. 112-8820.*

corners were not changed. This resulted in 80% of the ITC perimeter being hafnium and 20% being stainless steel. This partial ITC liner controlled 3.16% reactivity, as measured by control blade calibration based on rising periods, in the reference condition.

Cadmium sheet 0.093 cm thick was shaped to fit the reentrant corners and was then inserted between the ITC and the adjacent fuel. This composite ITC liner controlled 3.93% reactivity which was the difference between the reference $k_{ex}$ and a remainder of 0.25%. The reactivity ratio between the cadmium portion and the hafnium portion of the ITC liner was $0.77/3.16 = 0.24$ as compared with the area ratio $0.20/0.80 = 0.25$. Since the cadmium was fitted into corners, its geometry was less favorable than that of the hafnium, and this measurement underestimates cadmium worth relative

to hafnium. Compared with the nearest control blades (0.38 cm thick hafnium), the 0.13 cm thick hafnium in the ITC liner was 1.13 times as effective per unit area.

Judging by the hafnium coupon data, one would expect a thick hafnium ITC liner to control up to twice as much reactivity as the thin liner. There are other factors to be considered, however. During an experiment involving partial removal of the beryllium radial reflector, it was shown that control blade calibrations were reduced throughout the reactor. This characteristic will be discussed in the next few paragraphs. A precise measurement would be possible only with mockups of the shipping and loading arrangements, anticipated during those operations requiring an ITC safety liner. This is particularly true when the temporary beryllium is included.

### Measurements Related to Attachment of Beryllium Reflector to Safety Blade Follower

A suggestion that safety blade worths might be increased by attachment of sections of beryllium reflector to the followers resulted in a few measurements of this effect. Rather than construct a detailed mockup, a 5.1 cm thick slab of beryllium reflector blocks alongside one safety blade was removed. This allowed a measurement corresponding roughly to attachment of a sixth of the temporary beryllium reflector to a safety blade follower. However, a two-step procedure was needed. The critical configurations were measured first with the beryllium in place and safety blade No. 3 driven all the way out, and then all the way in. The procedure was repeated with the 5.1 x 25.4 x 48.3 cm beryllium slab removed and the space filled by water.

The loss of reactivity attributed to beryllium removal was 1.8 ± 0.2%. Recalibration of safety blade No. 3 by rising periods indicated a worth of −0.54%, compared with −1.44% initially. Since the blade is only three-fourths as wide as the beryllium removed, a combination with beryllium would yield (0.54 + 0.75 × 1.8) = 1.9%, which is 1.31 times the worth of the safety blade with beryllium remaining in the reflector. During review of the data it was noted that both adjacent peripheral blades were somewhat shadowed (by about 0.1% in reactivity) after removal of beryllium. If this is mutual, the worth of a safety blade with beryllium attached to the followed would be reduced to 1.7% if the neighboring blades were similar in design. Under the foregoing assumption of mutual shadowing, the improvement in reactivity control using reflector attachment to six safety blade followers appears to be a factor of 1.7/1.44, or about 1.18.

### References

1. J. W. Daughtry, *AARR Critical Experiments—Control Blade Worths*, Reactor Physics Division Annual Report, July 1, 1965 to June 30, 1966, ANL-7210, p. 48–51.
2. J. W. Daughtry, T. Johnson, F. Kodrick, K. Plumlee, W. Robinson and G. Stanford, *Critical Experiments for AARR Design*, Reactor Physics Division Annual Report, July 1, 1964 to June 30, 1965, ANL-7110, pp. 61–73.
3. C.E.Cohn, *Use of a Small Digital Computer in Data Analysis and Control of Critical Facilities—Reactivity Measurements*, Reactor Physics Division Annual Report, July 1, 1965 to June 30, 1966, ANL-7210, pp. 330–337.

## II-12. Argonne Advanced Research Reactor Critical Experiments—Beam Tube Yield and Reactivity Worth Measurements

T. W. Johnson and K. E. Plumlee

### Beam Tube Optimization

The Argonne Advanced Research Reactor beam tubes should provide a maximum yield of thermal neutrons as well as high ratios of thermal to epithermal and fast neutron fractions. The epithermal and fast fractions of the emerging beam will result in undesirable radiation damage and in competing reactions which may interfere with some of the proposed uses. It was expected that a blanket of water between the beam tube tips and the surrounding radial beryllium reflector would increase the thermal neutron yield without increasing the yield of higher energy neutrons. Experiments were conducted to indicate what thickness of water would be optimal, and how sensitive the neutron yield might be to variations in dimensions. Dimensional variations are the result of construction tolerances, which must be specified.

The experimental arrangements are shown in Figs. II-12-1 and II-12-2. The "compound collimator" is a cadmium box filled by a blend of borax and paraffin. The axial collimator hole is lined with cadmium. A $BF_3$-filled counter tube about 5 cm long was used. The

collimated counting arrangement appeared fairly immune to uncollimated neutrons, with the count rate dropping to about 8% of the maximum level when the beryllium filler blocks in the through-tube were backed out about 61 cm from the position shown in Fig. II-12-2, inside an extended through-tube.

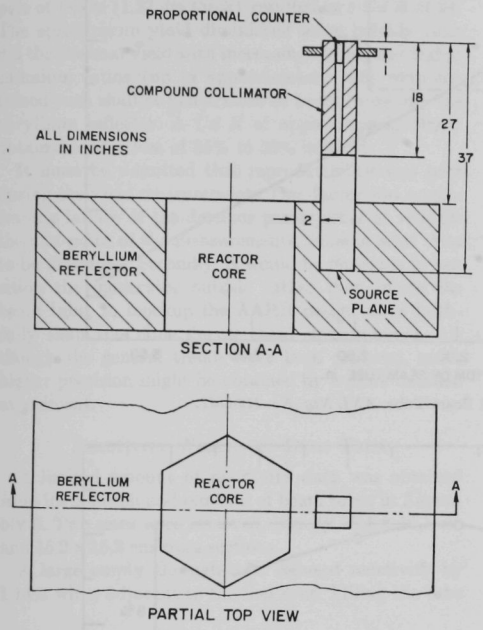


FIG. II-12-1. Configuration for Measuring Yield in a Vertical Beam Tube. *ANL Neg. No. 112-8887.*

The aluminum beam tubes used for this measurement were 10.1 x 10.1 cm outside dimensions and 0.32 cm thick walls. The vertical tube was positioned with its tip at the same radius and elevation as was the horizontal tube, resulting in apparently identical yields. A through-tube was also used as a tangential tube by partial filling with beryllium as shown in Fig. II-12-2.

A broad maximum in neutron yield was observed near 2 cm (~0.8 in.) $H_2O$ thickness in the vertical tube, as indicated in Fig. II-12-3. The $BF_3$ count rate was recorded while operating the reactor at a fixed flux level. Each count was followed by an incremental addition of water using a solenoid valve and an interval timer until approximately 9 cm of $H_2O$ had been added. Finally there was a measurement of the yield with and without a 0.95 cm thick layer of plastic at the tip of the tube, for comparison with water.

Similar results were obtained with plastic filler in the through-tube, which was used as a tangential tube by partially filling the tube with beryllium as shown in Fig. II-12-2. The plastic was pulled up into position facing the collimator, one piece at a time, without interruption of reactor operation. The resulting relative neutron yield versus plastic thickness is shown in Fig. II-12-4. Displacement of the maximum yield at a thickness of plastic slightly greater (Fig. II-12-4) than that of $H_2O$ (Fig. II-12-3) would disappear if the

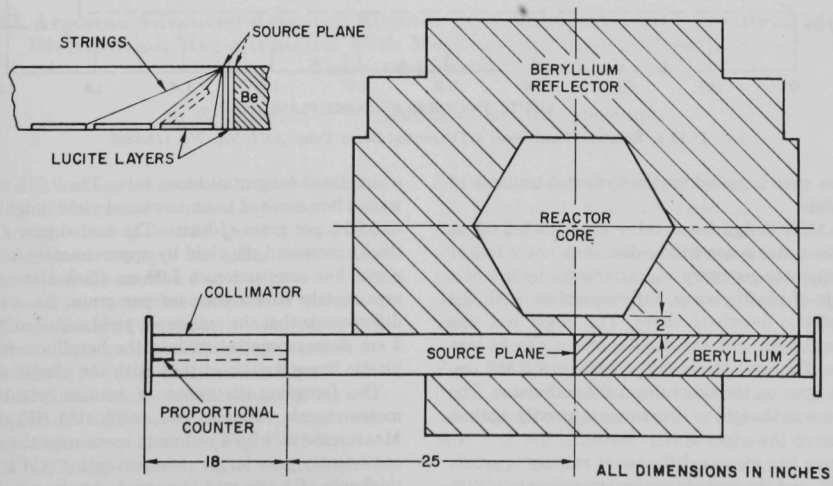


FIG. II-12-2. Configuration for Measuring Beam Tube Yield in a Tangential Beam Tube. *ANL Neg. No. 112-8817.*

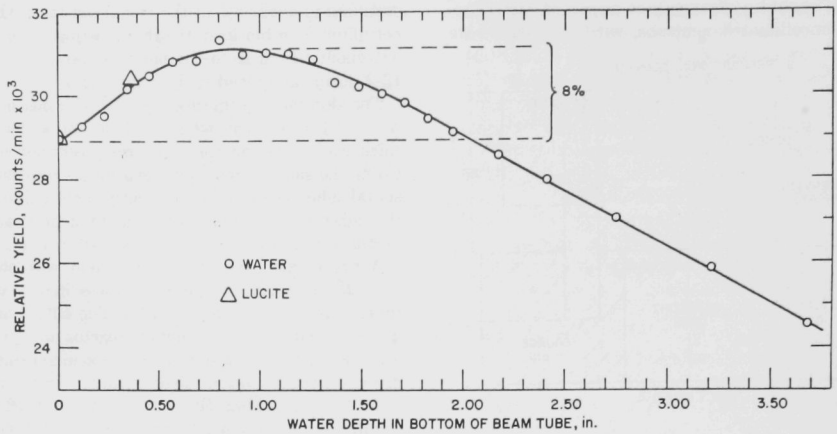


FIG. II-12-3. Relative Yield from a Vertical Beam Tube. *ANL Neg. No. 112-8821.*

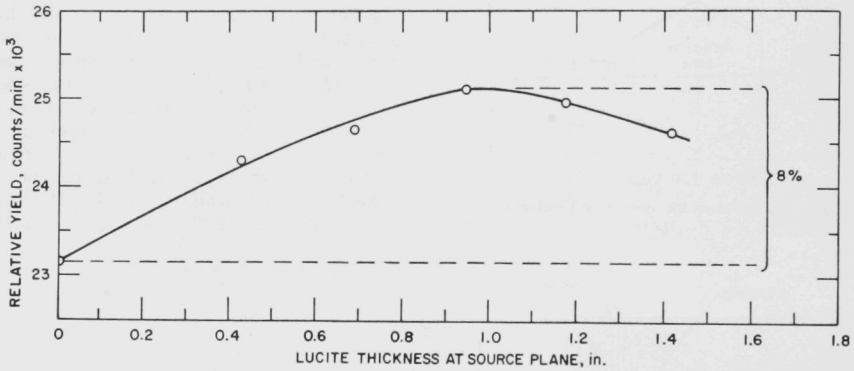


FIG. II-12-4. Relative Yield From a Tangential Beam Tube. *ANL Neg. No. 112-8890.*

thicknesses were adjusted for the hydrogen contents of the materials.

Since AARR design beam tubes are rounded off at the tips, the water space will be dished. A crude test of dished moderator geometry was attempted by use of a nested pair of plastic boxes, for comparison with the slabs of plastic described above. The larger box was 9.2 x 9.2 x 9.2 cm, and the smaller was a slip-fit into the larger. The wall thickness of each was 0.635 cm. Both were open on the side toward the collimator. The collimation was thought to discriminate heavily against neutrons from the edges of the plastic.

The larger box increased the count rate by approximately 16% and the nested pair by approximately 22% above the level found with beryllium alone at the tip of a simulated tangential beam tube. The 0.635 cm thick walled box resulted in an increased yield roughly equal to 0.06% per gram of lucite. The nested pair (1.27 cm thick) increased the yield by approximately 0.05% per gram. For comparison, a 1.09 cm thick slab gave approximately 0.04% increase per gram. An additional difference is that the maximum yield occurred at about 4 cm deeper penetration into the beryllium when the plastic boxes were used than with the plastic slabs.

The foregoing discussion of neutron yields is for measurements with the bare, collimated $BF_3$ detector. Measurements with a cadmium cover over the detector consistently gave larger cadmium ratios (*Cd R*) as the thickness of lucite was increased. At the penetrations giving the greatest count rates, the *Cd R* was 18.5 for

beryllium, but 18.7 for beryllium plus 0.64 cm lucite, and 23 for beryllium plus 0.95 cm lucite. The nested pair of boxes (1.27 cm thick) resulted in a *Cd R* of 24. The epicadmium yield diminished more quickly than did the thermal yield with increasing radius, and higher cadmium ratios (up to approximately 100) were obtained with shallow penetration of beam tubes into the beryllium reflector. A *Cd R* of approximately 100 is obtainable at a loss of 25% to 50% in yield.

It must be admitted that reproducibility was poor during the yield measurements. One factor was a misleading failure of the detector preamplifier at roughly the mid-point of the measurements, causing some data to be discarded. Secondly, it would be desirable to position the moderator outside rather than inside the beam tube, to mockup the AARR design more faithfully than was done during these measurements. Although the general trends have been explored, much higher precision might be obtained by a more detailed experiment.

### Reactivity Worths of Beam Tubes

A limited amount of reactivity data was obtained from installation and removal of beam tubes in Assembly 5. Two sizes were involved, namely 10.1 x 10.1 cm and 15.2 x 15.2 cm cross sections.

A large empty through-tube reduced reactivity by 1.14% when adjacent to the fuel zone. Filling the tube with beryllium recovered all but 0.15 to 0.22% of the reactivity. (The beryllium filler blocks did not fit perfectly in the tube). Placement at 10.1 cm distance from the fuel zone reduced the worth by roughly a factor of five. A large radial tube worth was measured at about 0.28 ± 0.05% when 10.1 cm of beryllium separated it from the fuel zone. This measurement was complicated by a preceding temperature coefficient test which affected the reference conditions.

The combined worth of a small radial and a small through-tube was 0.52%. The measured reactivity ratio between large and small tubes was therefore approximately 2.7 as compared to a volume ratio of approximately 2.3. Moving a small through-tube to a position 10.1 cm from the fuel zone recovered 0.12% or 0.16% reactivity (two measurements), indicating a significantly smaller dependence on radial location than in the case of the large tube.

Comparison with data reported earlier for Assembly 4a shows that the reactivity worths of 10.1 x 10.1 cm beam tubes are smaller by at least one third in Assembly 5.

### References

1. K. E. Plumlee, T. W. Johnson, W. R. Robinson and G. S. Stanford, *Argonne Advanced Research Reactor Critical Experiments—Beam Tube Experiments*, Reactor Physics Division Annual Report, July 1, 1965 to June 30, 1966, ANL-7210, pp. 73–75.

## II-13. Argonne Advanced Research Reactor Critical Experiments—Neutron Flux Distribution Measurements With Mocked-Up Pressure Vessel, Beam Tube, and Shroud

K. E. Plumlee, J. W. Armstrong and R. A. Schultz

Unavoidable leakage of neutrons from beam tubes results in locally increased radiation exposure of components through which these tubes pass. A number of traverses were made using a travelling $BF_3$ neutron counter to indicate the neutron distribution near a 10.2 cm square beam tube and other components perturbing the flux. The geometry of the region is indicated by Fig. II-13-1. The aluminum shroud mockup was not installed during the traverses illustrated in Figs. II-13-2 through II-13-6, but was present for those of Figs. II-13-7 through II-13-9. The armor plate was present only during the measurement shown in Fig. II-13-5.

Figure II-13-2, upper curve, shows the count rate along a *Y*-direction traverse which passed close by the two aluminum braces (1.27 x 6.35 cm) attached to the 0.64 thick aluminum retainer for the reflector blocks. The lower curve was made under identical conditions except that the braces were removed. The twin peaks of the upper curve were attributed to streaming of neutrons through the braces, which nearly doubled the count rate in comparison with the unperturbed traverse.

A perturbation near the beam tube is observable in Figs. II-13-2 and II-13-3. These traverses were made in planes above or below the beam tube, which was located at the midplane of the core ($Z = 0$). The beam tube was retracted during these traverses and filled with beryllium to the edge of the reflector. Filling was only about 80% complete because the selection of filler blocks was limited.

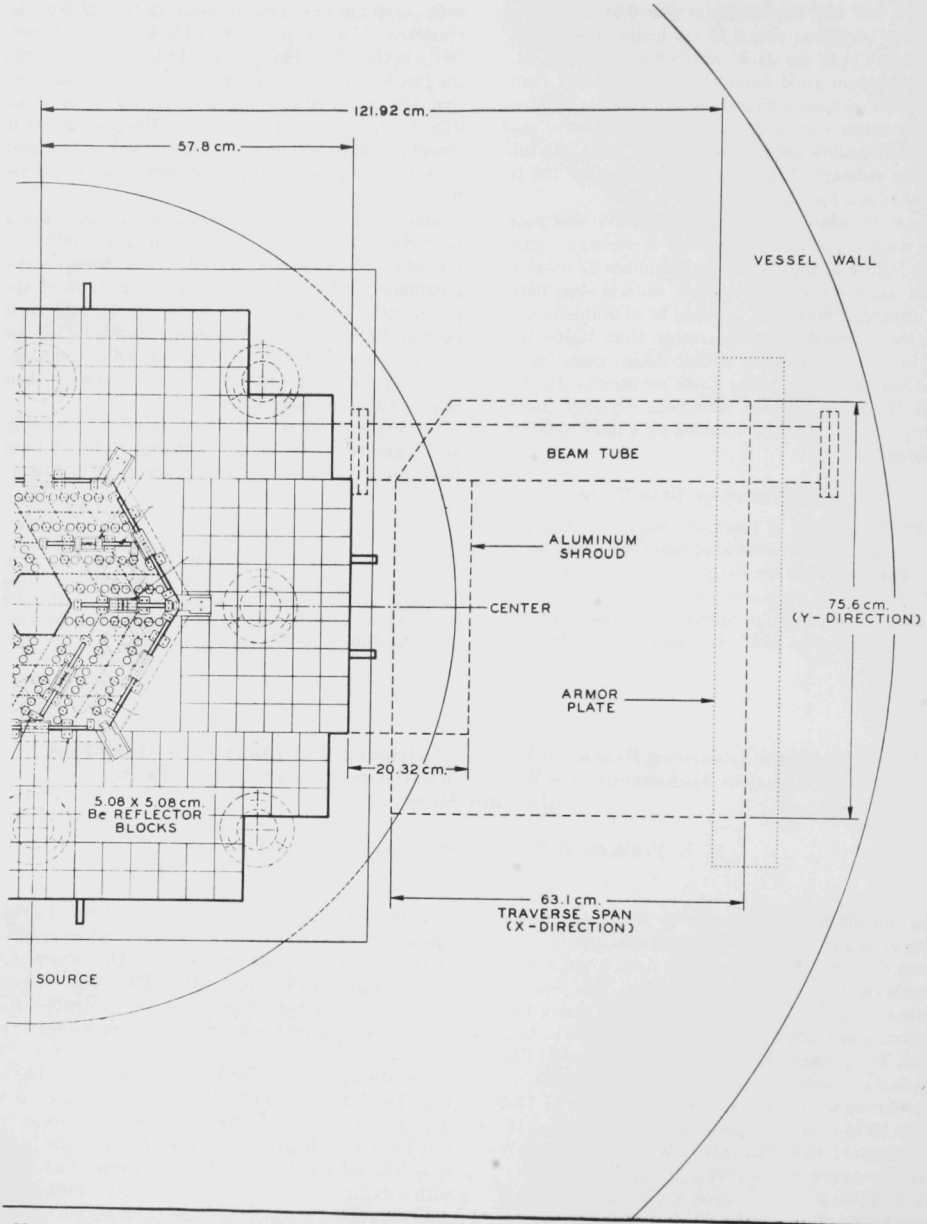


FIG. II-13-1. Top View of AARR Critical Core with Mockup of Shroud, Pressure Vessel, and Beam Tube. *ANL Neg. No. 112-9006.*

Traverses in the vertical (Z) direction are given in Figs. II-13-4 and II-13-5. The traverse at 67 cm radius corresponds with the center of Figs. II-13-2 and II-13-3. The traverse at 135 cm radius was just outside the armor plate which is 70 cm high, 91 cm wide, and 11.75 cm thick. The armor plate roughly simulated a sector of 244 cm i.d. pressure vessel for traverses shown in Fig. II-13-5. The shift downward in the peak flux indicated by Fig. II-13-5 was attributed to leakage of neutrons streaming along the 1.27 cm. thick base plate which supported core, reflector, shroud, and armor plate. Another flux distortion resulted from room-scattered neutrons, which were much more intense than in the $H_2O$ radial reflector at 135 cm radius. Thus the highest count rate observed took place with the detector raised above the water level, during that traverse. Room-scattered neutrons were thought to result mostly from leakage through the nuclear instrument thimbles, which are designated by Roman numerals in Fig. II-13-1. The water level was raised an additional 90 cm during subsequent experiments, to reduce the leakage of neutrons into the reactor room and to further shield the regions being traversed.

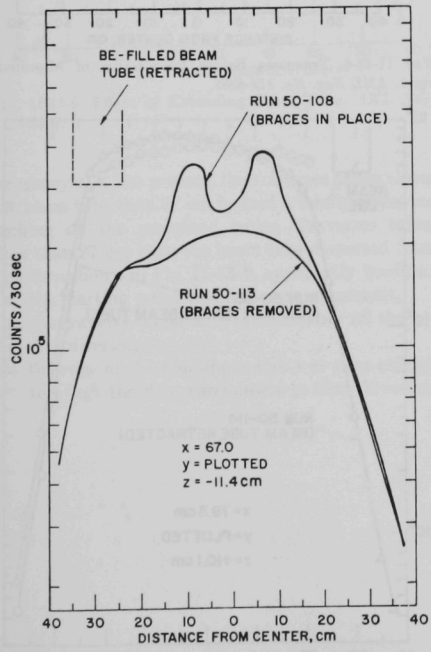


FIG. II-13-2. Effect of Aluminum Braces on Neutron Spatial Distribution. *ANL Neg. No. 112-8985.*

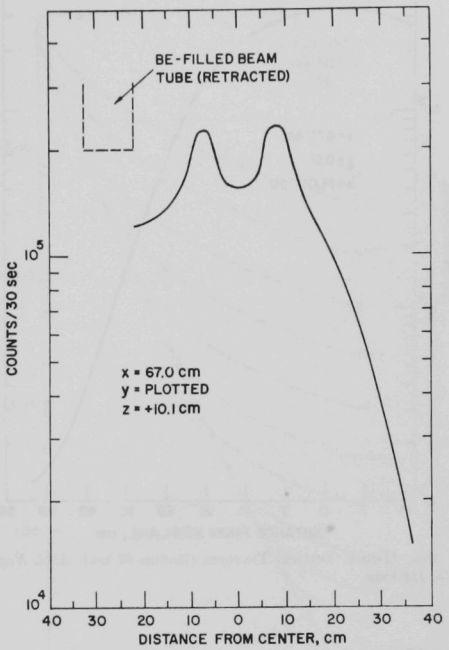


FIG. II-13-3. Traverse in Plane Above Beam Tube. *ANL Neg. No. 112-8981.*

Figures II-13-3, II-13-4 and II-13-6 show traverses taken before installation of the aluminum shroud sector, and the effect of this 45.7 x 45.7 by 20.3 cm thick aluminum slab is shown by the curves of Figs. II-13-7 and II-13-8 labeled Run 50-114.

Figures 7 and 8 also show the effect of extending and partially voiding the through-tube to provide a 10.1 x 10.1 cm square tangential beam tube. A very convenient aspect of the traverse at $x = 79.3$ cm is the flat (within a few percent) portion extending from the beam tube to about 37 cm away. This made it feasible to plot Fig. II-13-9 as a family of curves commencing at approximately the same flux level, when traversing in the $x$-direction rather than in the $y$-direction. The traverses of Fig. II-13-8 ($x = 82$ cm) indicate that the beam tube is a major source of the neutrons detected in this vicinity. In this traverse the perturbation is noticeable as far as approximately 40 cm from the beam tubes.

The traverses of Fig. II-13-9 were in the midplane ($Z = 0$) parallel to the beam tube. Five traverses were almost identical, at distances of 27 to 37 cm from the tube, and these are shown as a smoothed curve. Within

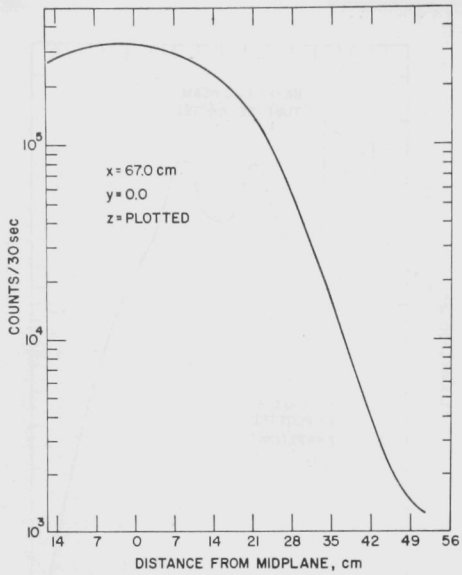


FIG. II-13-4. Vertical Traverse (Radius 67 cm). *ANL Neg. No. 112-8989.*

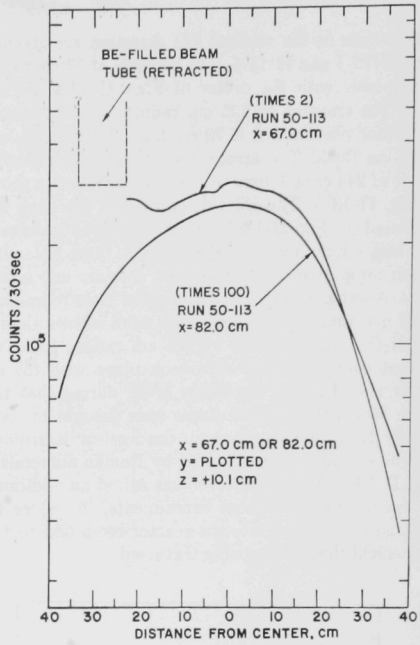


FIG. II-13-6. Traverses Before Installation of Aluminum Shroud. *ANL Neg. No. 112-8983.*

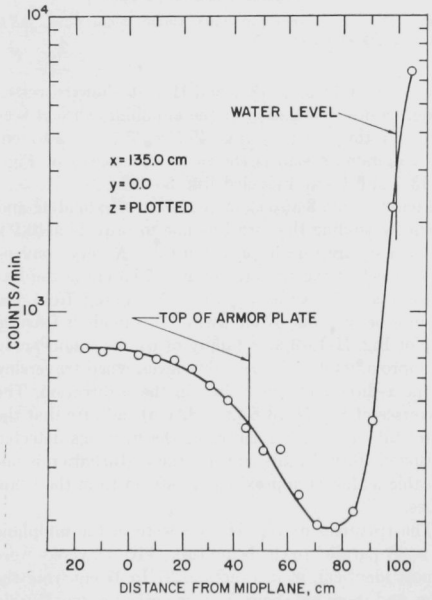


FIG. II-13-5. Vertical Traverse Behind Armor Plate (Radius 135 cm). *ANL Neg. No. 112-8987.*

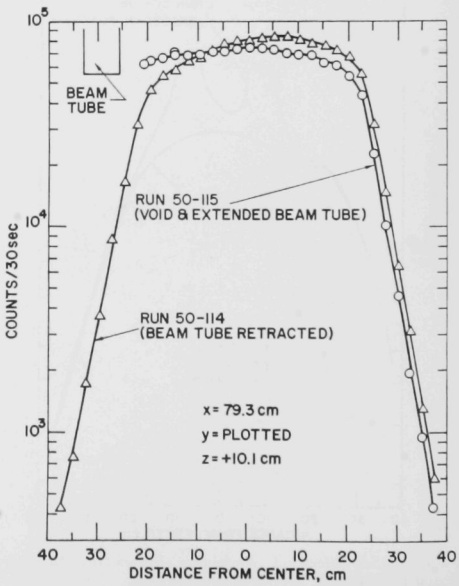


FIG. II-13-7. Effect of Extending Beam Tube (Aluminum Shroud Installed). *ANL Neg. No. 112-8986.*

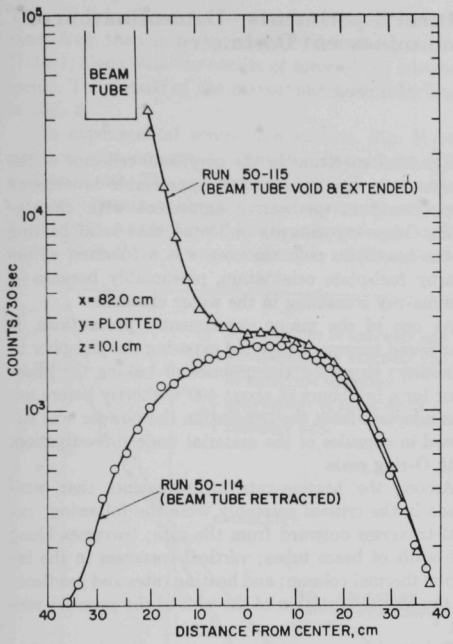


FIG. II-13-8. Effect of Extending Beam Tube. *ANL Neg. No. 112-8984.*

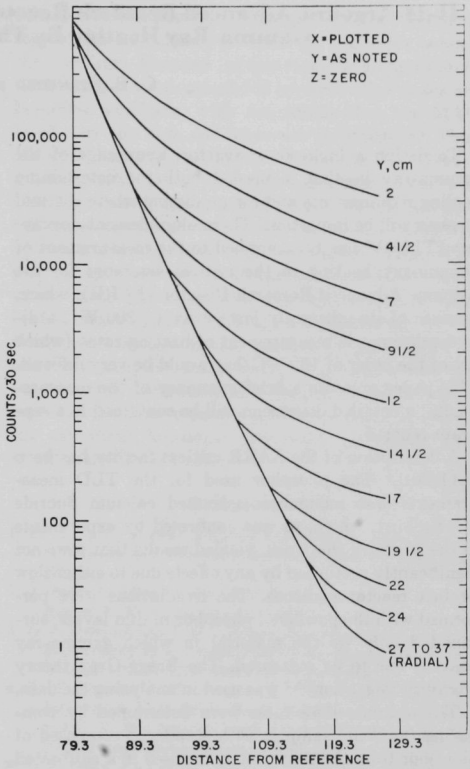


FIG. II-13-9. Traverses Parallel to Beam Tube, in Midplane. *ANL Neg. No. 112-8998.*

an accuracy of a few percent, the traverses taken closer to the beam tube than 27 cm formed a family of curves branching off the smoothed curve. Traverses taken farther than 37 cm from the beam tube dispersed from the pattern shown in Fig. II-13-9, apparently because:

(a) the starting point was no longer consistent,
(b) the traverse direction was noticeably off the radial direction,
(c) the edge of the aluminum slab was near enough to affect the flux distribution in that direction.

The data presented in this paper are sufficient for estimation of flux perturbations around beam tubes of the geometry tested. Because of the strong dependence on details of geometry, the results shown here should be used with caution in relating to other situations.

# II-14. Argonne Advanced Research Reactor Critical Experiments—Determination of Gamma-Ray Heating By Thermoluminescent Dosimetry

G. S. Stanford and T. W. Johnson

To design a high-power reactor, knowledge of the gamma-ray heating is needed both for determining cooling requirements and for predicting where thermal stresses will be important. Thermoluminescent dosimetry (TLD)[1,2] has been applied to the measurement of gamma-ray heating in the critical assembly for the Argonne Advanced Research Reactor (AARR), where, because of its inherently low power ($\lesssim$300 W), a direct calorimetric measurement of heating rates (which are of the order of $10^{-3}$ °C/hr) would be very difficult. This paper presents a brief summary of the measurements; a detailed discussion will be contained in a separate report.[3]

A description of the AARR critical facility has been published.[4] The phosphor used for the TLD measurements was manganese-activated calcium fluoride ($CaF_2$:Mn), which, as was confirmed by experiments in the course of this work, yielded results that were not significantly perturbed by any effects due to either slow or fast reactor neutrons. The irradiations were performed with the powdered phosphor in thin layers, surrounded only by the material in which gamma-ray heating was to be measured. The Bragg-Gray theory of cavity ionization[5,6,7] was used in analyzing the data.

The absolute dose rates were determined by comparing the TLD samples with standards composed of phosphor from the same batch, exposed in a calibrated gamma-ray irradiation facility.

A correction factor is needed to allow for the difference in gamma-ray spectra between the calibration facility and the critical assembly. The correction was determined empirically, for a position in the beryllium reflector 10 cm from the core, in an experiment in which the response of TLD samples was compared with that of an ion current chamber, in the Co-60 irradiation facility and in the critical assembly. For the position at which the measurement was made, the factor amounted to 1.20 ± 10%. All TLD measurements in the reactor were corrected by this factor, although it would be expected to vary somewhat with the point of measurement; the magnitude of the change is not known, but the uncertainty in this correction does not contribute greatly to the overall experimental error. The factor thus determined would also correct for any sensitivity to neutrons, but on the basis of calculations and other experiments it was concluded that any sensitivity is small.

The result of the above experiment indicated that the gamma spectrum in the beryllium reflector of the reactor near the core had an appreciable low-energy component,[8] in qualitative agreement with calculations. Other experiments indicated that local heating in the beryllium near the core was a function of the nearby fuel-plate orientation, presumably because of gamma-ray streaming in the water channels.

As one of the major experimental precautions, it was found necessary to avoid exposing the phosphor to humidity; therefore, the practice of baking the phosphor for a few hours at about 400°C shortly before use was adopted. Also, for irradiation the powder was enclosed in capsules of the material under investigation, with O-ring seals.

Among the heating-rate measurements that were made in the critical assembly were the following: radial traverses outward from the core; traverses along the walls of beam tubes; vertical traverses in the internal thermal column; and heating rates and gradients at the planned location of the wall of the pressure vessel.

Relative measurements were typically reproducible to within 5 or 10%. The absolute measurements were subject to an additional uncertainty of ±15% in the determination of the reactor power, and there was also the uncertainty in the spectrum correction factor, amounting to ±10% at the point where the factor was measured. The experimental program was discontinued before this factor was determined more accurately or at more locations. Combining the errors quadratically, the net uncertainty in the absolute measurements ranged from ~20% near the core to 35% or so at a 48-in. radius. Further improvements in the TLD technique could reduce these uncertainties somewhat, but the principal source of error—the power calibration—was unrelated to TLD.

In applying the results of these measurements to the design of the AARR, an additional uncertainty arises from the fact that an aluminum HFIR-type core with about 17-in. of beryllium for a reflector is to be used, rather than the heavily loaded stainless steel design, with 12 in. of beryllium, that had been mocked up in the critical experiments.

Some calculations of the gamma-ray heating rates to be expected in the critical facility were made by A. E. McArthy and D. H. Shaftman,[8] using simplified geometry and the computer program MAC. A homogeneous core with a flat power distribution was assumed.

The calculated heating rate as a function of radial distance from the outer edge of the fuel is plotted in Fig. II-14-1, along with the results of some of the measurements. The details of the measurements will be found in Ref. 3.

The experimental errors indicated in Fig. II-14-1 represent the estimated reproducibility of the TLD measurements. The experimental curve is also subject to a systematic calibration and spectrum-correction uncertainty, as mentioned above, amounting to ±20% or so. Thus there is some indication of disagreement between calculation and experiment in the beryllium region; the discrepancy is worse for the water outside the beryllium. However, as this report is going to press the heating rates as calculated by some other codes are becoming available, with indications that the MAC results are too high and otherwise inconsistent.[9] Thus the significance of the calculated curve in Fig. II-14-1 is questionable. Also, the entire experimental curve is based on a single power calibration. Time did not permit more experiments to confirm the results. Indicative of what might have been found are the two extra points plotted at the position of the pressure-vessel wall, which came from two different, independently calibrated measurements. Although the consistency of the three measurements at that position is not as good as one would like, the scatter is not incompatible with the experimental calibration uncertainties—and it is also true that the three measurements were made at different azimuthal locations; how much difference this would make is not known.

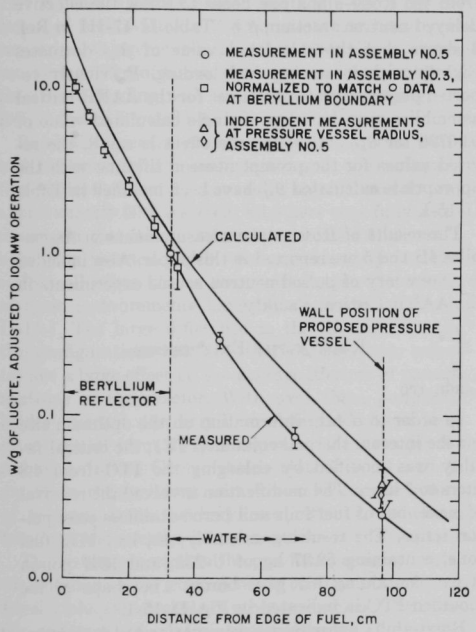


FIG. II-14-1. Measured and Calculated Gamma-ray Heating Outside the Core of the AARR Critical Assembly. *ANL Neg. No. 112-9091.*

## REFERENCES


1. F. H. Attix, *Present Status of Dosimetry by Radiophotoluminescence and Thermoluminescence Methods*, NRL-6145 (1964).
2. Z. Spurný, *Thermoluminescent Dosimetry*, Atomic Energy Review **3**, No. 2, pp. 61–115 (1965).
3. G. S. Stanford and T. W. Johnson, *Determination of Gamma-Ray Heating in a Critical Facility by Thermoluminescent Dosimetry*, ANL-7373 (1967) (to be published).
4. K. E. Plumlee, J. W. Armstrong, J. W. Daughtry, T. W. Johnson, F. F. Kodrick, W. R. Robinson, R. A. Schultz and G. S. Stanford, *Argonne Advanced Research Reactor Critical Experiments—Preface*, ANL-7210 (1966), p. 47.
5. L. H. Gray, *An Ionization Method for the Absolute Measurement of γ-Ray Energy*, Proc. Roy. Soc. (London), 1936, A-156, pp. 578-596.
6. L. H. Gray, *The Ionization Method of Measuring Neutron Energy*, Proc. Cambridge Phil. Soc. **40**(1944), pp. 72–102.
7. L. V. Spencer and F. H. Attix, *A Theory of Cavity Ionization*, Radiation Research **3**(1955), pp. 239–254.
8. A. E. McArthy and D. H. Shaftman, Argonne National Laboratory (private communication).
9. D. H. Shaftman, Argonne National Laboratory (private communication).

# II-15. Argonne Advanced Research Reactor Critical Experiments—Rossi-Alpha and Pulsed Neutron Measurements

J. W. Daughtry

## Introduction

The Rossi-alpha experiment provides a method for determining the prompt neutron lifetime of a critical system. It can also be used to measure small reactivities near critical. Experience with the Experimental Boiling Water Reactor indicates that the Rossi-alpha experiment does not give useful data with plutonium fueled, $H_2O$ systems due to the inherent neutron source from spontaneous fission. The effect of these spontaneous fission neutrons is to produce a large number of overlapping neutron chains causing the time-correlated events to be lost in the random background.

The pulsed neutron source method will yield the same information as the Rossi-alpha method, and is faster and more accurate. Furthermore, the pulsed source method can be used in situations where the high uncorrelated neutron background would make the Rossi-alpha method ineffective. The Rossi-alpha method is most useful near critical. The pulsed neutron method has been used to measure relatively large subcritical reactivities.

The prompt neutron lifetime of a nuclear reactor is important for safety considerations, since the period of the exponential increase in the reactor power is proportional to the prompt neutron lifetime when the excess multiplication is very large.

During the program of critical experiments to assist in the design of a stainless steel core for the Argonne Advanced Research Reactor (AARR), a number of reactor cores were assembled. Table II-6-I gives the designations for the various core loadings. For more detailed information on specific cores see Refs. 1, 2 and 3.

TABLE II-15-I. Summary of Prompt Neutron Lifetime Measurements in the AARR Critical Facility

| Assembly No. | Calculated $\beta_{eff}$[a] | Prompt Neutron Lifetime, $\mu$sec | Number and Type of Control Blades Inserted During Experiment |
|---|---|---|---|
| 1 | 0.00727 | 39.5 ± 1.0 | 0.3 interior |
| 2b | 0.00721 | 33.0 ± 2.0 | 2.5 peripheral |
| 3 | 0.00718 | 31.9 ± 2.0 | 2.3 peripheral |
| 4a | 0.00712[b] | 26.7 ± 1.0 | 2.0 peripheral |
| 4b | 0.00712[b] | 27.8 ± 2.0 | 2.3 peripheral |
| 5 | 0.00712[b] | 33.7 ± 2.0 | 3.6 interior |
| 5 | 0.00712[b] | 22.3 ± 2.0 | 3.3 peripheral |

[a] Ref. 3.

[b] Assumed to be equivalent to 1215/2000 loading of Ref. 3.

Prompt neutron lifetimes, deduced from Rossi-alpha experiments, were reported for Assemblies 1, 2b, 3 and 4a in Ref. 4. To obtain the prompt neutron lifetime from the Rossi-alpha one needs to know the effective delayed neutron fraction, $\beta_{eff}$. Table II-17-III in Ref. 3 shows that the calculated value of $\beta_{eff}$ decreases slightly with increasing fuel loading. Previously reported prompt neutron lifetimes for the AARR critical assemblies were based on a single calculated value of 0.00726 for $\beta_{eff}$. Although the effect is small, the revised values for the prompt neutron lifetime with the appropriate calculated $\beta_{eff}$ have been included in Table II-15-I.

The results of Rossi-alpha measurements in Assemblies 4B and 5 are reported in this paper. Also included is a summary of pulsed neutron source experiments in the AARR Critical Facility.

## Rossi-Alpha Experiments

### Large ITC

In order to obtain information on the optimum size for the internal thermal column (ITC), the critical facility was modified by enlarging the ITC from 4.8 liters to 7 liters. The modification involved the removal of a number of fuel foils and boron-stainless steel poison strips. The resulting assembly, 4b, had 1173 fuel foils, containing 59.37 kg of U-235, and 1347 poison strips, containing 707 g of boron. The shape of the modified ITC is indicated in Fig. II-15-1.

Rossi-alpha experiments were performed in this assembly using two $BF_3$ proportional counters placed horizontally on top of the core. Other details of the experimental technique are identical to those described in Ref. 4. Control blades 2 and 5 were fully inserted, blade number 6 was approximately 30% inserted, and all other blades were fully withdrawn. Control blade locations are indicated by number in Fig. II-15-1. Assuming a value of 0.00712 for $\beta_{eff}$, the prompt neutron lifetime was found to be 27.8 ± 2.0 $\mu$sec (Table II-15-I).

### Graded Loading

The Argonne Advanced Research Reactor will have a heavily absorbing core with an $H_2O$ internal thermal

column and a beryllium reflector. This design tends to produce steep gradients in the thermal neutron flux distribution at the inner and outer boundaries of the annular core, which in turn produce sharp peaks in the power density. To reduce these peaks the fuel density can be reduced in the regions of the core that would be subject to power peaking. In the critical facility this was accomplished by a graded loading in which thinner fuel foils were substituted for the standard fuel foils near the core boundaries. The fuel grading did not change the total number of fuel foils in the assembly; however, the amount of U-235 was reduced to 57.31 kg. To compensate for the loss of reactivity due to the removal of fuel, a total of 258 boron-stainless steel poison strips was removed. This left 1089 poison strips, containing 572 g of boron. Other details of Assembly 5, the graded loading with the 7 liter ITC, are given in Ref. 5 and in Paper II-6.

Rossi-alpha measurements in Assembly 5 were made with two control blade configurations. In one configuration blades 7, 9 and 11 were fully inserted and 12 was approximately 60% inserted; all others were fully withdrawn. In the other configuration blades 1, 3 and 5 were fully inserted and 6 was approximately 30% inserted; all other blades were withdrawn. The results of these measurements have been included in Table II-15-I. The large difference in the lifetimes for the two configurations indicates that the beryllium reflector has a large effect on the average lifetime of prompt neutrons in the reactor. With over three peripheral blades inserted, the beryllium reflector is to a large extent cut off from the fuel region by the strongly absorbing hafnium. Control blade slots 7, 9, 11 and 12 are all in the fuel zone and do not hinder the return of neutrons from the beryllium reflector. Beryllium lengthens the average life of neutrons in the reactor.

The results reported in the previous paragraph raise the question of the control blade configuration during Rossi-alpha experiments in other assemblies. The number and type of control blades inserted during the Rossi-alpha experiments have been included in Table II-15-I. The sensitivity of the measured prompt neutron lifetime to the control blade configuration tends to complicate the interpretation of the results. However, the configuration for Assemblies 2b, 3, 4a and 4b were sufficiently similar to permit direct intercomparison of results.

There are no plans at this time for additional Rossi-alpha experiments in stainless steel cores for the AARR. If experiments of this type are resumed at some future time, effort should initially be concentrated in two areas. First, an attempt should be made to isolate and reduce the rather large uncertainties in the experimental values for the prompt neutron lifetimes obtained from Rossi-alpha measurements. Second, the relationship between the prompt neutron lifetime and the control blade configuration should be investigated more thoroughly.

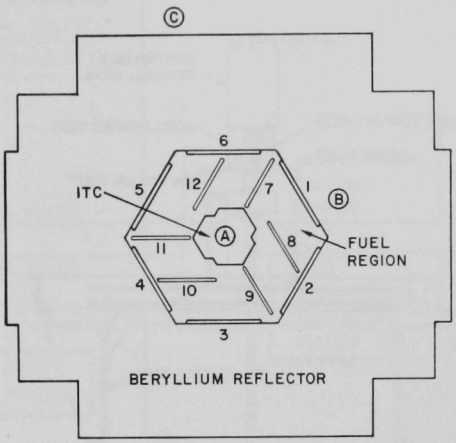


FIG. II-15-1. Top View of AARR Critical Facility. *ANL Neg. No. 122-9157.*

## PULSED NEUTRON MEASUREMENTS

A pulsed neutron generator was installed in the ZPR-5 cell for a series of experiments with the AARR Critical Facility. Figure II-15-2 shows its location on the main support platform directly above the critical facility. Measurements were made with the target just above the core, as shown in Fig II-15-2, and with the target inserted into the ITC to the midplane of the core by using a longer drift tube. With minor modifications the generator could be removed from its position above the reactor and set up for operation in a horizontal position.

The neutron generator operates at potentials up to 150 kV. It uses an rf type ion source. With a deuteron beam and a tritium target neutrons are produced with energies of approximately 14 MeV. The maximum beam current at the target with a distance of 10½ feet from the end of the accelerating tube to the target is approximately 0.5 mA. The neutron yield at 150 kV and 0.5 mA is estimated to be $5 \times 10^{10}$ neutrons per sec. The neutron generator is equipped with pre- and post-acceleration pulsing, providing a very low between-pulse neutron production rate. The width of the beam pulses is continuously variable from one microsecond to five seconds, compatible with a pulse repe-

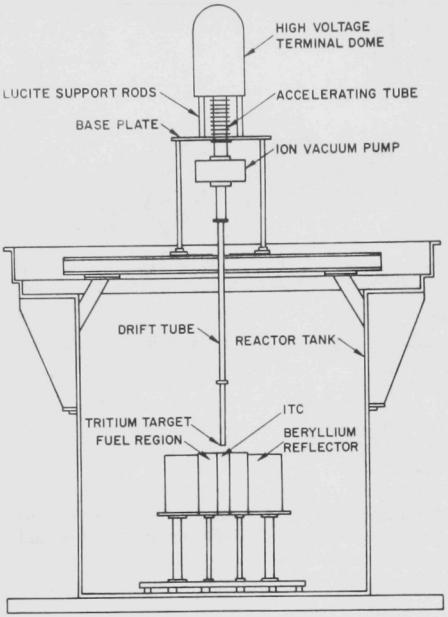


FIG. II-15-2. Sectional View of AARR Critical Facility Showing Reactor and Pulsed Neutron Generator. *ANL Neg. No. 112-9164.*

tition rate continuously variable from $5 \times 10^5$ pulses per sec. to one pulse every ten seconds and a maximum duty cycle of 90% in pulsed operation. There is also provision for external triggering of the pulsing system, thus permitting non-periodic pulsing which would be of value for pseudo-random impulse response studies, for example.

Figure II-15-3 is a block diagram of the pulsing and time analysis system. The pre- and post-acceleration pulsing systems operate simultaneously to minimize the beam current between pulses. The deuteron beam is allowed to reach the tritium target during the time interval between the initital and final pulses from the Timing Pulse Generator. The final pulse was also used as the start signal for the time analyzer. Signals from a neutron detector in the reactor were analyzed in time relative to this start signal which coincided with the trailing edge of the accelerator beam pulse. A 400-channel analyzer provided memory and readout equipment. The time interval covered by a "sweep" of the analyzer is equal to the product of the number of channels (400) and the preselected channel width. For this set of experiments, channel widths of 16, 20, 40 and 80 $\mu$sec were used.

The initial phase of operation was directed toward familiarization and de-bugging. This was followed by a series of exploratory measurements. The first of these was to determine which combinations of pulse width, repetition rate, beam current and generator voltage would be compatible with normal reactor operation. Different detector types were compared and the effect of detector location was studied. A search for fundamental modes was made with different critical configurations. The magnitude of higher order modes was determined in different locations in order to ascertain the optimum detector location for different measurements. Data analysis programs were developed concurrently.

Four types of neutron detectors were used in the pulsed measurements:

1.) $BF_3$ proportional counter, 1 in. diam, 2 in. active length, 65 cm Hg filling pressure;
2.) $BF_3$ proportional counter, 1 in. diam, 15 in. active length, 120 cm Hg filling pressure;
3.) $BF_3$ proportional counter, ½ in. diam, 6 in. active length, 140 cm Hg filling pressure;
4.) U-235 fission chamber, ½ in. diam, 1 in. active length.

Although the detection efficiency varied over a wide range, there was no indication that any of the results were dependent on detector type.

Figure II-15-4 shows the decay of the neutron population at three locations in the reactor. Curve 4a was obtained with the neutron detector at the center of the ITC, 4b was obtained with the detector at the flux peak in the beryllium reflector and 4c was obtained with the detector at the outer edge of the beryllium. These locations are shown as A, B and C in Fig. II-15-1. For these three runs control blades 1 through 6 were fully withdrawn and blades 7 through 12 were fully inserted. The tritium target was at the centerline of the reactor 14 in. above the midplane of the core.

The solid lines in Fig. II-15-4 represent least squares fits to the experimental data, assuming a single exponential decay after an appropriate waiting time. The decay constants were found to be the same within 1%. The transient response, on the other hand, is significantly different in the three locations. A detector location near "B" seems to be desirable for fundamental mode measurements because of the small contribution of transients to the decay in this region.

In most runs, after the subtraction of background (predominantly delayed neutrons), the resulting data indicated an asymptotic exponential decay. For the far subcritical case in which all control rods were inserted, the existence of a pure exponential decay was not definitely established.

As observed in the Rossi-alpha experiments, decay constants were more sensitive to peripheral control

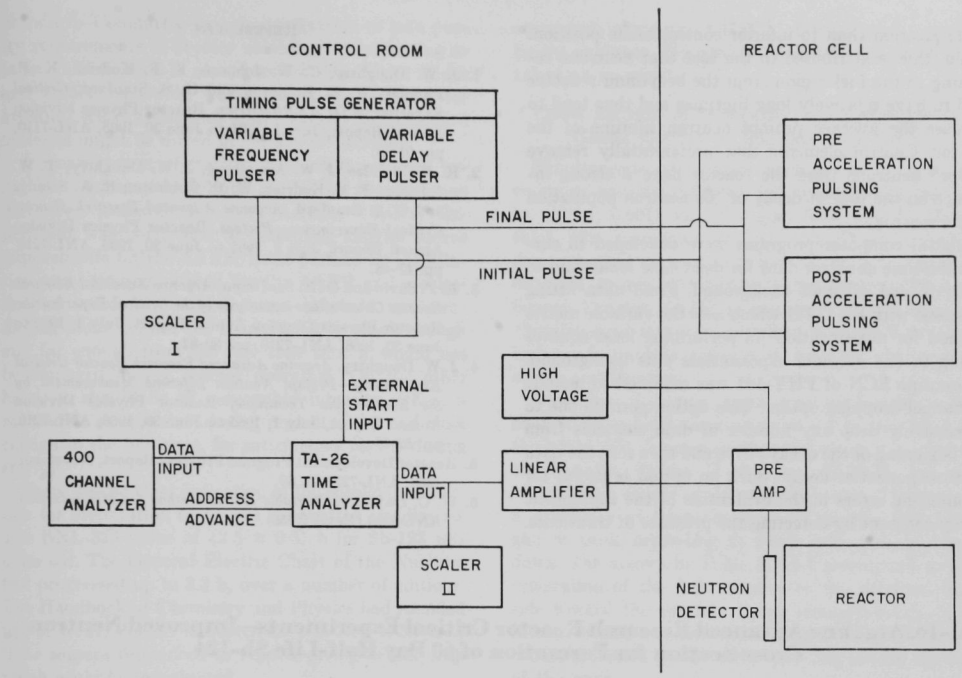


FIG. II-15-3. Schematic Diagram of Pulsing and Time Analysis System. *ANL Neg. No. 112-9156.*

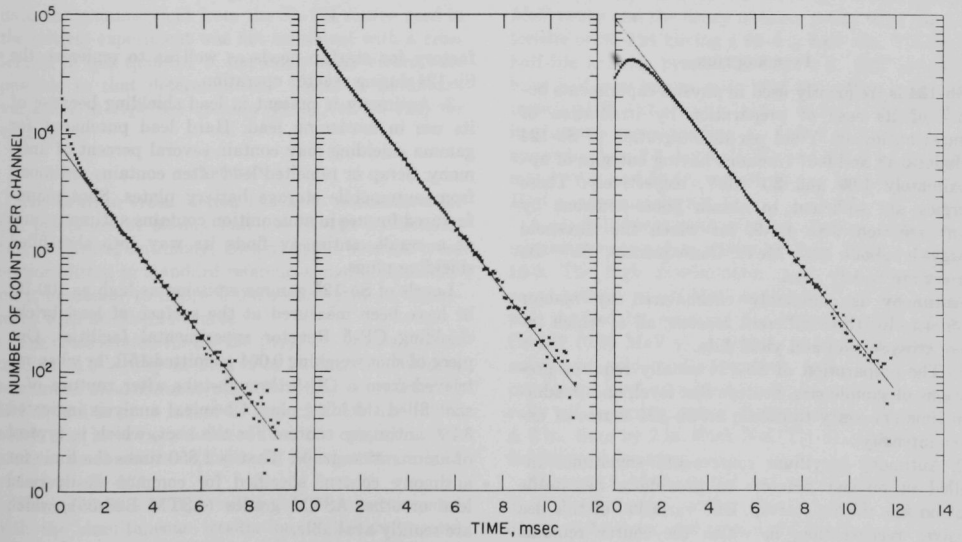


FIG. II-15-4. Response Curves a, b, and c (Left to Right) for Detector Positions. *ANL Neg. No. 112-9398.*

blade position than to interior control blade position. Again, this is attributed to the fact that neutrons returning to the fuel region from the beryllium reflector tend to have relatively long lifetimes and thus tend to increase the average prompt neutron lifetime of the reactor. Control elements that preferentially remove "older" neutrons from the reactor have a strong influence on the rate of decay of the neutron population in the reactor.

Digital computer programs were developed to correct the time analyzer data for dead time losses and to estimate and subtract background. Final data fitting was done with PHY-141 which uses the variable metric method for minimization[6] in performing least squares fitting to one or more exponentials plus background. Subroutine FCN of PHY-141 was modified to include a channel dropping option. This option permits one to successively drop any number of data channels from the beginning of the decay curve and then refit the data to an exponential decay. Such an option is useful for eliminating errors in the evaluation of the asymptotic decay constant by detecting the presence of transients.

### References


1. J. W. Daughtry, T. W. Johnson, F. F. Kodrick, K. E. Plumlee, W. R. Robinson and G. S. Stanford, *Critical Experiments for AARR Design*, Reactor Physics Division Annual Report, July 1, 1964 to June 30, 1965, ANL-7110, pp. 61-73.
2. K. E. Plumlee, J. W. Armstrong, J. W. Daughtry, T. W. Johnson, F. F. Kodrick, W. R. Robinson, R. A. Schultz and G. S. Stanford, *Argonne Advanced Research Reactor Critical Experiments—Preface*, Reactor Physics Division Annual Report, July 1, 1965 to June 30, 1966, ANL-7210, pp. 47-48.
3. R. P. Savio and D. H. Shaftman, *Argonne Advanced Research Reactor Calculations—Analysis of the Critical Experiments*, Reactor Physics Division Annual Report, July 1, 1965 to June 30, 1966, ANL-7210, pp. 80-82.
4. J. W. Daughtry, *Argonne Advanced Research Reactor Critical Experiments—Prompt Neutron Lifetime Measurement by the Rossi-Alpha Technique*, Reactor Physics Division Annual Report, July 1, 1965 to June 30, 1966, ANL-7210, pp. 52-57.
5. Reactor Development Program Progress Report, November, 1966, ANL-7279, p. 80.
6. W. C. Davidson, *Variable Metric Method for Minimization*, ANL-5990 (Rev.) (1959).


## II-16. Argonne Advanced Research Reactor Critical Experiments—Improved Neutron Cross Section for Formation of 60 Day Half-Life Sb-124

K. E. Plumlee

### Introduction

Sb-124 is frequently used in physics experiments because of its ease of preparation by irradiation of natural antimony. Yield per disintegration of Sb-124 includes 0.48 and 0.07 fractions having energies of approximately 1.69 and 2.1 MeV, respectively. These energies are sufficient to obtain photo-neutrons by $(\gamma,n)$ reaction with Be-9, for which the threshold energy is about 1.67 MeV. Consequently, $Sb^{124}$-Be sources are widely used.

Antimony is commonly encountered by reactor physicists for three different reasons, all of which involve cross section and yield data.

1. The preparation of Sb-124 usually requires predictions of sample size, neutron flux level, and irradiation time necessary to obtain an Sb-124 source of desired intensity.

2. Antimony-beryllium sources are sometimes installed in nuclear reactors to provide a detectable neutron flux during startup. One variation of this use involves regeneration, in which the source remains semi-permanently installed at a location which is satisfactory for startup needs as well as to replenish the Sb-124 during reactor operation.

3. Antimony is present in lead shielding because of its use in hardening lead. Hard lead purchased for gamma shielding may contain several percent of antimony. Scrap or remelted lead often contains antimony from automobile storage battery plates. Shot manufactured for use in ammunition contains antimony, and as a result, antimony finds its way into shot-filled shielding plugs.

Levels of Sb-124 gamma emission as high as 100 R/hr have been measured at the surface of lead bricks shielding CP-5 Reactor experimental facilities. One piece of shot weighing 0.064 g emitted 15R/hr when retrieved from a CP-5 through-tube after rupture of a shot-filled shielding plug. Chemical analysis indicated 3.7% antimony content for the shot, which is typical of ammunition grade. That is 1,850 times the limit for antimony content specified for common desilverized lead or other ASTM grades (ASTM B29-55), which are readily available.

A recommendation has been submitted to the ANS

Standards Committee for standardization of lead purity requirements in reactor shielding. Color coding or other identification is recommended for all lead bricks and similar shielding which might be salvaged for eventual reuse. Otherwise standard and non-standard material might be mixed in storage or handling.

A measurement of startup instrument response using an antimony-beryllium source in the Argonne Advanced Research Reactor (AARR) Critical Experiment was performed to determine startup source requirements for the AARR. Semi-permanent installation was being considered for the AARR and a selection of source size and location involved two conflicting factors. First the source must be small enough and far enough from the fuel zone that it would not be damaged during reactor operation. On the other hand, it should be of reasonable intensity (thus, a reasonable sample size, during regeneration) and close enough to the fuel zone, for satisfactory results during startup.

There was no clear indication of the correct cross section for preparation of Sb-124 by neutron irradiation. The BNL-325 value of (2.5 ± 0.5) b for Sb-123 was quite old. The General Electric Chart of the Nuclides had progressed up to 3.3 b, over a number of editions. The Handbook of Chemistry and Physics had rounded to 3 b. W. H. Walker indicated 3.7 b in Ref. 1. None of those sources referenced to reports giving actual data which could be reevaluated.

It was noted that a comparison between irradiation data and gamma yield from the Sb-124 source used in the critical experiment was not consistent with a cross section of less than 3.1 b, but fairly large errors were possible in that determination.[2] There is significant variation in reported gamma yields for Sb-124, for example.

## Summary

The neutron cross section has been remeasured for the formation of 60-day half-life Sb-124 by irradiation of natural antimony. Disagreement between cross sections listed in standard references made remeasurement necessary to improve the accuracy of an experiment with an Sb-124 source.

The cross section for Sb-123 $(n,\gamma)$ Sb-124 was measured at (4.0 ± 0.8) b. This is to be compared with a referenced measurement of (2.5 ± 0.5) b reported in Ref. 3, and to more recent listings of 3, 3.3, and 3.7 b, which may have been deduced from the original measurement on the basis of improved information on beta yield from Sb-124.

The measurement reported in this paper commenced with the simultaneous irradiation of antimony and gold samples. The subsequent gamma yields were compared, using an NaI(Tl) detector and a pulse height analyzer. The gold cross section and yield were taken as standards.

## Cross Section Measurement by Comparison of Gamma Counts of Antimony and Gold

Simultaneous irradiations were made of bare and cadmium-covered antimony pills (0.25 in. dia. and 0.1 in. thick), 0.0011 in. thick gold foils, and 0.0025 in. thick 90% manganese-copper foils. These materials were attached to a rotating disc for uniform exposure during a 30 min. irradiation in the Argonne Thermal Source Reactor (ATSR) graphite thermal column. (Similar irradiations are described in Paper V-2). Four inches of graphite intervened between the reactor source and the disc.

A number of gamma counts were made using a 400 channel pulse height analyzer and a 3 in. dia. by 3 in. thick NaI(Tl) detector positioned 3 cm or 10 cm below the samples. Tables II-16-I and II-16-II compare several such counts on an arbitrary basis. These show a difference of approximately 5% in the 1.69 MeV gamma peak, depending on which side of the pill was down. The arrows in Table II-16-I correspond to the orientation of the foils relative to the detector. The side toward the reactor during irradiation was also turned toward the detector during irradiation during counts indicated by the arrow pointing toward the top of the page.

As expected, the cadmium ratio for the 1.69 and 2.1 MeV peaks and the decay of those peaks were characteristic of Sb-124 having a 60-day half-life. The short half-life activity present on March 3, 1967 seems to have had a cadmium ratio (*Cd R*) which is characteristic of Sb-122 activity. About 43.5% of the activity in channels corresponding to 1.29–1.45 MeV was of approximately 2.8-day half-life and *Cd R* of approximately 6.1, and 56.5% was of 60-day half-life and *Cd R* of approximately 8.8.

A much different result was found on examination of integral counting data shown by Figs. II-16-1 and II-16-2. The high discriminator level was intended to count activity of 0.8 MeV and higher, and this setting was checked by counting Mn-54 (0.84 MeV $\gamma$) and Cs-137 (0.66 MeV $\gamma$) standards sequentially with the antimony, gold, and manganese foils. The low discriminator level permitted integral counting of practically all incoming pulses distinguishable from noise. A 2 in. diam by 2 in. thick NaI(Tl) detector was used for integral counting.

About 72% of the initial activity counted using the high discriminator setting decayed with a half-life of about 2.3 days, and gave a *Cd R* of approximately 8.4. Thus, most of this short half-life activity may have

TABLE II-16-I. MULTICHANNEL ANALYZER DATA SUMMARY
*(Note: Bare Sb wt. = 523g; Cd-covered Sb int. = 532g)*

| Channel Levels, MeV | Distance to Detector, cm | Counts on 3/15/67 (10 min) | | | | Counts on 4/6/67 | | Ratios ↑ vs ↓ | |
|---|---|---|---|---|---|---|---|---|---|
| | | 17:14 Cd Covered↓ | 17:58 Bare↓ | 18:18 Bare↓ | 18:40 Bare↑ | 16:45 Cd Covered↓ | 16:27 Bare↑ | 18:40 / 17:58 | 16:27 / 18:18 |
| 2.04–2.18 | 3 | 182 | — | 1559 | — | 142 | 1279 | — | 1.057[a] |
| | 10 | — | 272 | — | 288 | — | — | 1.058 | — |
| 1.63–1.79 | 3 | 1459 | — | 12352 | — | 1147 | 10033 | — | 1.047[a] |
| | 10 | — | 2741 | — | 2874 | — | — | 1.048 | — |
| 1.29–1.45 | 3 | 2164 | — | 14834 | — | 809 | 6513 | — | 0.565[a] |
| | 10 | — | 2322 | — | 2511 | — | — | 1.081 | — |

[a] Decay corrected for 60-day half-life only. The ratios in the 1.29–1.45 MeV channels are affected by short half-life activity.

TABLE II-16-II. MULTICHANNEL ANALYZER DATA COMPARISON

| Channel Levels, MeV | Distance, cm | Integral[a] Count Eff. | Peak/Total Ratio | Activities (cps/mg) corrected to 17:30, 3/15/67[b] | | | | | |
|---|---|---|---|---|---|---|---|---|---|
| | | | | 17:14 Cd Covered | 17:58 Bare | 18:18 Bare | 18:40 Bare | 16:45 Cd Covered | 16:27 Bare |
| 2.04–2.18 | 3 | 0.069 | 0.24+ | 0.0394 | — | 0.344 | — | 0.0397 | 0.344 |
| | 10 | 0.0145 | 0.245 | — | 0.268 | — | 0.268 | — | — |
| 1.63–1.79 | 3 | 0.073 | 0.29− | 0.245 | — | 2.11 | — | 0.248 | 2.11 |
| | 10 | 0.0155 | 0.29+ | — | 2.12 | — | 2.10 | — | — |
| 1.29–1.45 | 3 | 0.079 | 0.335 | 0.293 | — | 2.05 | — | 0.141 | 1.10 |
| | 10 | 0.0165 | 0.34+ | — | 1.44 | — | 1.37 | — | — |

[a] Mass absorption curves for counting efficiency of 3 in. diam by 3-in. thick NaI(Tl) detector.

[b] Decay corrected for 60-day half-life only. Activities have been corrected for counting efficiency and peak/total ratio. All data from Table II-16-I with symbol (↓) were multiplied by 1.05 to correct to condition where most active side (reactor side) of foil is toward detector. A 4% increase was made to adjust for self-absorption of gamma by Sb at 1.69 and 2.1 MeV, and 4½% at 1.35 MeV. A 4% increase was made in the 3 cm data because of finite pill thickness (curves were for 3 cm, pills were at 3.0 to 3.3 cm).

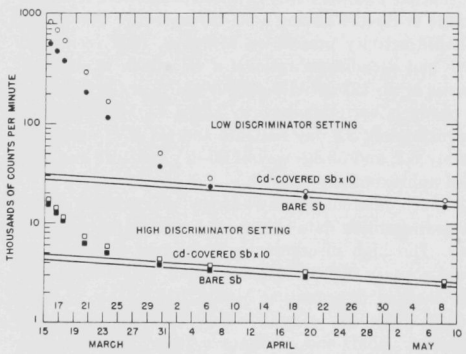


FIG. II-16-1. Integral Counting Data Using Bare and Cd-Covered Sb. *ANL Neg. No. 112-8331.*

been from an isotope other than Sb-122. The remainder of the activity counted using the high discriminator appeared to be 60-day half-life Sb-124. A review of the available multi-channel analyzer data indicated that the short half-life activity had a *Cd R* of approximately 6.1 in all channels. Thus there is nothing in the multi-channel analyzer data to confirm the high discriminator counting. If this discrepancy had been foreseen, more data would have been taken with the multi-channel counter. However, there was no interference at energies above the threshold energy of approximately 1.67 meV for beryllium $(\gamma,n)$ reaction.

The multi-channel analyzer data from April 6, 1967 were processed using ANL computer code RP-296[4] which fits a Gaussian curve to a data peak and computes the area under the curve. The foil activities (decay corrected to time of scram, and stated in cps/mg) were as follows for 1.69 MeV gamma radiation of Sb-124 and for 0.41 MeV of Au-198. Bare antimony activity was 1.882 and cadmium-covered activity was 0.2067, leaving a net subcadmium activity of 1.62. Adjustments to be applied to the foregoing results include an increase of 4% for self-absorption of $\gamma$ radiation in the antimony pill; and a 0.7% increase (which later cancels a similar adjustment for gold) to change thermal activation to C. Westcott notation.[5] A 4% adjustment to counting efficiency was made because of the 0.25 cm antimony thickness which is 8% as great as

the 3 cm separation between pill and detector during counting. This adjustment improved the agreement for 1.69 MeV (but not for 2.1 MeV) data taken at 3 cm and at 10 cm. The adjusted thermal activation was 1.77 $\gamma_{1.69}/s$ per mg of antimony.

The bare and cadmium-covered gold activations were 3,200 and 343.0 $\gamma_{0.41}/s$-mg corrected to time of scram. An adjustment of 0.2% was made for gold decay during irradiation, 0.6% for self-absorption of 0.41 MeV $\gamma$ in 0.0011-in. thick gold, and 0.7% to change to Westcott notation thermal activation. The adjusted thermal activation of gold was 2,900 $\gamma_{0.41}/s$-mg.

The number of atoms $N$ of an isotope are related to the yield $Y$, decay constant $\lambda$ and activity $A$ as follows:

$$N_{124}Y_{1.69} = \frac{1}{-\lambda_{124}} A_{1.69}$$

$$= 7.48 \times 10^6 A_{1.69} = 1.32 \times 10^7/\text{mg},$$

$$N_{198}Y_{0.41} = 3.366 \times 10^5 A_{0.41} = 9.76 \times 10^8/\text{mg}.$$

The neutron cross section $\sigma$ of Sb (nat.) for formation of Sb-124 is related to that of Au-197 as follows:

$$\sigma_{Sb} = \frac{n_{197}\,\sigma_{197}\,N_{124}}{n_{Sb}\,N_{198}} = \frac{122}{197}\,\frac{1.32 \times 10^7\,Y_{0.41}}{9.76 \times 10^8\,Y_{1.69}}\,\sigma_{197}.$$

Using a thermal flux depression correction factor of 0.963 for gold, $\sigma_{197} = 98.8 \times 0.963 = 95.1$ b. Assuming $Y_{0.41} = 0.956$ and $Y_{1.69} = 0.48$ gives $\sigma_{Sb}$(nat.) $= (1.58 \pm 0.16)$ b. This result must be corrected for thermal flux depression in the antimony pill ($\sim$0.93) and the fraction of Sb-123 in natural antimony. The measured 2200 m/s neutron cross section of Sb-123 yielding Sb-124 is then $(4.0 \pm 0.8)$ b, with half the error limit being attributed to experimental measurements and half to uncertainties in the cross section of gold, yields of $\gamma_{0.41}$ and $\gamma_{1.69}$, and in various adjustments for flux depression, etc.

## Details of Corrections Applied to Activations

### Relation of Thermal to Subcadmium Activation

Using Westcott's notation the ratio of thermal to total activation for an irradiated material is given in terms of $g(T)$, a ratio of effective cross section to ideal (1/v) cross section in a Maxwellian thermal velocity distribution of neutrons; $r$, a ratio of epithermal to thermal flux intensities; and $S(T)$, a ratio of effective resonance to thermal cross sections weighted according to a prescribed energy distribution:

$$\frac{\text{Thermal Activation}}{\text{Total Activation}} = \frac{g(T)}{g(T) + rS(T)}.$$

The $Cd\ R$ is also related to $g(T)$, $r$, and $S(T)$ but by use of a term $P_{cd}(T) \approx 0.48\sqrt{T/T_0}$ for gold or antimony cross sections:

$$\frac{Cd\ R - 1}{Cd\ R} = \frac{g(T) - rP_{cd}(T)}{g(T) + rS(T)}$$

$$= \frac{g(T)}{g(T) + rS(T)} - \frac{rP_{cd}(T)}{g(T) + rS(T)},$$

$$\frac{\text{Thermal Activation}}{\text{Total Activation}} = \frac{Cd\ R - 1}{Cd\ R} + \frac{P_{cd}(T)}{[g(T)/r] + S(T)}.$$

$(Cd\ R - 1)/Cd\ R = 0.887$ for Sb-124 and 0.890 for gold. Assuming a neutron temperature $T$ of $\sim$60°C (333°K), $P_{cd}(T) \approx 0.512$. Unfortunately $g(T)$ and $S(T)$ for Sb-123 were not accurately known; however, for either gold or antimony the corrections are quite small and nearly cancel in the final result. For gold, $g(T) = 1.008$ and $S(T) = 18.44$. For Sb-123, $g(T) \approx 1$ and $S(T) \approx 33$. Finally, $r$ was estimated from the Cd R = 54 of manganese in the same location, for which $g(T) = 1.00$ and $S(T) = 0.710$:

$$r = \frac{g_x(T)}{(Cd\ R)_x[S_x(T) + P_{cd}(T)] - S_x(T)} = 1/65.28,$$

$$\frac{P_{cd}(T)}{[g(T)/r] + S(T)} = 0.006 \text{ (for gold)};$$

$$\text{or} \sim 0.005 \text{ (for Sb-123)}.$$

The thermal activation yielding Sb-124 was thereby estimated to be $(0.887 + 0.005) \times$ total activation, which is 0.6% greater than that obtained by subtraction of epicadmium foil activation from bare foil activation, for both Sb-124 and for gold.

This correction effectively canceled out of the calculation of cross section. The underlying reasons are: (a) a choice of antimony pill thickness which gave a

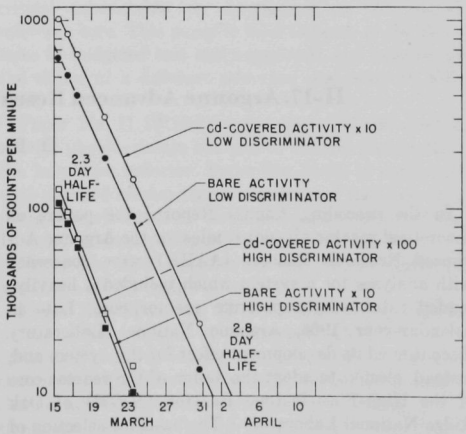


Fig. II-16-2. Integral Counting Data Less 60-day Half-life Activity. *ANL Neg. No. 112-8330.*

*Cd R* nearly as large as that found using the gold foil; and (b) a fairly small value of r in the thermal column.

EQUATIONS RELATING CROSS SECTION OF Sb-123 TO GOLD

Since antimony and gold were irradiated on a rotating disc to obtain uniform exposure, the ratio of atoms activated is

$$\frac{N_{Au}}{N_{Sb\text{-}124}} = \frac{n_{Au}\sigma_{Au}}{n_{Sb}\sigma_{Sb}},$$

$$\sigma_{Sb} = \frac{n_{Au}N_{Sb\text{-}124}}{n_{Sb}N_{Au}}\,\sigma_{Au}.$$

Both cross sections still must be corrected for thermal flux depressions or self-shielding.

DESCRIPTION OF EQUIPMENT

Counting was done with a 3 in. diam. by 3-in. thick NaI(Tl) detector inside a heavy shield of lead lined with copper. Attenuation (i.e. integral) curves were used in conjunction with peak-to-total ratio curves to estimate counting efficiencies for peaks at various energies.

The analyzer accommodated pulses corresponding to values between zero and 4 Mev in 400 channels. Deadtime was 4 to 5% for the cadmium-covered measurement and initially ~25% for the bare antimony measurement with 3 cm distance between pill and detector. The preset live time circuitry functioned quite well during these experiments as shown by the decay adjusted data of Table II-16-II.

DIRECTIONAL FLUX DURING IRRADIATION

A 5% difference in 2.1 MeV and 1.69 MeV count rates resulted from inverting the antimony pills. This is thought to be a consequence of irradiation in a directional flux in the ATSR thermal column. The 5% difference significantly exceeds the estimate based on thermal flux and is attributed mostly to resonance activation. Since there may have been complicated decay in progress at lower energies, it was not determined whether the Sb-122 activity had similar properties.

EXISTENCE OF UNCOMPLICATED 60-DAY HALF-LIFE IN 2.1 AND 1.69 MeV GAMMA PEAKS

Comparison of decay-corrected data in Table II-16-II indicates no short half-life activation in the 2.1 and 1.69 MeV peaks. The 60-day half-life accounted for about 56.5% of the activity in channels corresponding to 1.29 to 1.45 MeV. The remainder agreed in *Cd R* and in half-life with Sb-122 decay.

REFERENCES

1. W. H. Walker, *Yields and Effective Cross Sections of Fission Products and Pseudo-Fission-Products*, CRRP-913 (AECL-1054), (March 1960).
2. K. E. Plumlee, *Improved Neutron Cross Section for Formation of 60-day Half-Life Sb-124*, Trans. Am. Nucl. Soc. **10**, 226, June 1967.
3. D. J. Hughes and J. A. Harvey, *Neutron Cross Sections*, BNL-325 (July 1955).
4. W. C. Davidon, *Variable Metric Method for Minimization*, ANL-5990 (Rev.) (1959).
5. C. H. Westcott, *Effective Cross Section Values for Well-Moderated Thermal Reactor Spectra*, CRRP-960 (AECL-1101), (November 1, 1960).

## II-17. Argonne Advanced Research Reactor Calculations—Preface

D. H. SHAFTMAN

In the preceding Annual Report,[1] the papers on theoretical reactor physics studies for the Argonne Advanced Research Reactor (AARR) were concerned with analyses for a system which included a heavily-loaded intermediate-spectrum reactor core. Late in calendar-year 1966, Argonne National Laboratory discontinued its development effort for this system and, instead, elected to adopt the design of the reactor core of the High-Flux Isotope Reactor (*HFIR*) of Oak Ridge National Laboratory.[2] The basis for selection of the HFIR core design for the AARR was the necessity to effect substantial cost reductions in the research and development program for the AARR.

The HFIR core was a particularly suitable alternative because it too is designed to provide a small, thin fuel zone, from which a large fraction of the neutrons produced could leak into zones containing experimenters' facilities. Moreover, cores of this design have operated quite successfully at 100 MW, in the HFIR. The HFIR design includes a central zone for an internal flux trap (ITC) of thermalized neutrons, and the size of this zone is approximately the same as the

size of the earlier reference AARR system. The active height (20 in.) of the HFIR fuel is only a little larger than the active height (18 in.) of the earlier reference AARR fuel. The coolant for the ITC, the core, and the reflector of the HFIR is water ($H_2O$), which was the reference coolant for the AARR.

The adoption of the HFIR core design was extended also to the duplication of the HFIR control-rod system and the removable portions of the outer radial beryllium reflector. However, the so-called "permanent" beryllium zone of the AARR is quite different from that of the HFIR; it is thicker, and it contains a much larger number of experimenters' facilities. Indeed, to the extent feasible, the earlier reference designs of the zones containing the experimenters' facilities were retained as the reference system to be incorporated with the chosen duplicates of HFIR zones. The purposes of the AARR are unchanged, namely, to provide high thermal neutron fluxes in a variety of experimenters' facilities, for basic research. In particular, the Internal Thermal Column (ITC) of the AARR is intended for research-type irradiations by high-intensity fluxes of thermalized neutrons, in contradistinction to larger scale fixed production of certain transplutonium isotopes for which the HFIR was designed. Accordingly, it is intended that the ITC of the AARR will have lighter loadings of target tubes and targets than the HFIR, and a variety of rabbit tubes and static irradiation facilities will be included.

As a consequence of these changes in the AARR design, the reactor physics research and development work for the AARR has been redirected. The criticality-experiments program was terminated, and the AARR Criticality Facility has been closed down. The scheduled programs of theoretical reactor physics studies have been revised to take into account the fact of existing designs for important portions of the reactor, and to make use of the data available from the reactor physics studies and the power operation of the HFIR. To this purpose, closer contacts have been established with the HFIR staffs of reactor design and operation, Oak Ridge National Laboratory, notably with: R. D. Cheverton and H. C. Claiborne, on reactor physics design; H. C. Claiborne and H. A. McLain, on the design of the radiation shielding of the plant; A. L. Boch and T. E. Cole, on the general plant design; and R. V. McCord, on the reactor operation.

Because there are important differences in the design of the ITC and of the permanent beryllium reflector, because there are important differences in the purposes of reactor operation, and because there are significant differences in the overall plant design, a continuing reactor physics research and development effort is essential for the AARR. This effort is divided into a number of categories:

1. reactor physics studies leading to optimized designs of experimenters' facilities in the ITC and in the beryllium reflector, within the constraints of: a fixed design of the reactor core, the ITC size, the control-rod configuration, and the removable-beryllium zones; required number, sizes, and variety of experimenters' facilities; financial budget; and schedule of design and construction;

2. studies intended to provide an independent analysis of certain outstanding problems of reactor physics analysis, e.g., the prediction of the reactivity life of a new core as a function of the total irradiation history of the beryllium reflectors; and analyses to provide additional data upon which criteria of operation may be based, e.g., reactivity effects of target capsules to be introduced into experimenters' facilities;

3. collaboration with Project engineers and with the Architect-Engineer in establishing the radiation-shielding design of the plant; collaboration with Project engineers and AARR Users in resolving radiation-shielding and heating-analysis problems in the experimenters' facilities;

4. collaboration with other Project personnel in safety analyses, with the ultimate purposes of designing a safe plant and of demonstrating this in the Final Safety Analysis Report for the AARR;

5. general project-physics support for other aspects of the design work.

Each of the abovementioned activities has been given considerable reactor physics effort in FY-1967.

Paper No. II-18 reports on certain analyses of the critical experiments on simulations of the earlier reference core. This paper is brief because of the pressures of budgeted cost and manpower, and because of the choice of a different reference core early in FY-1967.

Paper No. II-19 reviews the status of the general reactor physics design analysis of the reactor core and the beryllium reflector. Paper No. II-20 is concerned with detailed reactor physics analysis of the space and energy distributions of thermal neutron fluxes in the Internal Thermal Column, for the fresh reactor.

Paper No. II-21 summarizes the present status of work of a shield-design nature.

Paper Nos. II-22 and II-23 discuss certain aspects of the safety analysis of the revised AARR. In FY-1967, as a result of changes in the reactor core and in the models of release of contaminated airborne material outside the Reactor Containment Building, additional analyses were performed, and the Preliminary Safety Analysis Report for the AARR was rewritten.

These two papers respectively summarize accident analyses and analyses of radiation doses to people off the AARR site as a consequence of a postulated maximum credible reactor accident.

In some cases, the activities involved substantial participation by personnel from other divisions of Argonne National Laboratory. The authorship of the papers is intended to reflect this participation. Of course, in project physics work others contribute also, including personnel of the Reactor Physics Division and of other divisions. Unfortunately, it has not been feasible to acknowledge all of the other contributions in the six papers that follow.

### References

1. D. H. Shaftman, A. E. McArthy and R. P. Savio, "*Argonne Advanced Research Reactor Calculations—Preface*," Reactor Physics Division Annual Report, July 1, 1965 to June 30, 1966, ANL-7210, pp. 79–109.
2. F. T. Binford and E. N. Cramer, Eds., *The High-Flux Isotope Reactor, A Functional Description*, **1**, ORNL-3572 (May 1964).

## II-18. Argonne Advanced Research Reactor Calculations—Analysis of Critical Experiments with the Intermediate-Spectrum Core

R. P. Savio* and D. H. Shaftman

### Introduction

As a result of the selection of the lightly-loaded HFIR-type reactor core for the AARR (see Paper II-17) to reduce research and development costs of the AARR, the program of critical experiments with intermediate-spectrum cores was terminated in calendar-year 1967. The final measurements included a foreshortened version of the planned loadings of graded fuel, and thermoluminescent-dosimetry measurements of heating rates in the reflector. Most of the previously unreported experiments have been summarized in Papers II-6 to II-16.

There have been extensive reportings on theoretical reactor physics analyses of the critical experiments in Refs. 1, 2 and 3. Also, there have been reports on the reactor physics design analyses for the AARR, with the earlier, intermediate-spectrum core.[4,5] The reporting in the present paper reflects the shift in the theoretical effort toward analyses of the modified AARR, with the HFIR-type reactor core. The contents of this paper are essentially limited to:

1. comparison of the calculated $k_{eff}$'s, for the various fuel loadings, with $k_{eff}$'s inferred from measurements of control rod positions for criticality and measured differential reactivity worths of the control rods;

2. multigroup two-dimensional calculations of the reactivity gain which would occur in the event of a massive partial voiding of water in the ITC; ITC's of two different sizes were studied;

3. comparisons of calculated and measured data on peak absolute thermal neutron fluxes in the ITC's per watt of fission power;

4. comparisons of calculated and measured radial distributions of fission power in the single graded-fuel loading on which critical experiments were performed.

### Methods and Parameters of Reactor Physics Analysis

Discussions of the models of reactor physics analysis are presented in Papers II-19 and II-20, and the reader is referred to them for details. As indicated in these papers, 16-group one-dimensional calculations and associated 6-group two-dimensional calculations were made in the context of diffusion theory. The 6-group cross sections for the 100%-$H_2O$ ITC were used also for the axial water reflectors.

The 16-group and 6-group sets were compared by calculating identical systems in one-dimensional geometry. Consistently, the 6-group reactivities were smaller than the 16-group reactivities. This reactivity bias, 0.3%, is considered to be an inadequacy of the group-synthesis procedure, in reducing the number of groups from 16 to 6. Therefore all reactivities inferred from 2-D calculations have been increased by 0.3% to attempt to minimize the reactivity change due to the use of only six groups rather than sixteen. The 2-D 6-group calculations, with the CANDID2D program[6] on Argonne's CDC-3600, converged very slowly, and it was not feasible to perform the 2-D analysis with the 16-group set, in view of the monetary costs of such calculations.

All calculations were performed for idealized cases where the control rods were fully withdrawn and the

* Reactor Operations Division, Argonne National Laboratory.

TABLE II-18-I. REACTIVITY DATA FOR CRITICAL ASSEMBLIES WITH STAINLESS STEEL-WATER-URANIUM CORES

| Assembly No. | U-235 Loading, kg | Boron Loading, g | Composition of the Beryllium Reflector, v/o | Measured Reactivity, % | Calculated Reactivity [16 energy groups; 1-D diffusion theory] % | Calculated[b] Reactivity [6 energy groups; 2-D diffusion theory] % |
|---|---|---|---|---|---|---|
| 1 | 16.1 | 0 | 10% Plexiglas 90% Be | 0.4 | 1.6[a] | — |
| | 16.1 | 0 | Be | — | 3.0[a] | 0.9 |
| 2a | 31.4 | 220 | 10% Plexiglas 90% Be | 3.6 | 4.5 | — |
| | 31.4 | 0 | 10% Plexiglas 90% Be | — | 15.5 | — |
| 2b | 31.4 | 220 | Be | 4.8 | 5.6 | 3.2 |
| | 31.4 | 0 | Be | — | 16.5 | — |
| 3 | 41.4 | 425 | Be | 2.7 | 3.9 | 1.2 |
| | 41.4 | 0 | Be | — | 18.9 | — |
| 4a | 61.5 | 850 | Be | 2.5[c] | 3.6 | 2.6 |
| | 61.5 | 0 | Be | — | 21.3 | — |
| 4b | 59.4 | 821 | Be | 3.8[c] | 3.6 | — |
| 5 (Graded Loading) | 57.3 | 572 | Be | 4.5[d] | 3.8 | — |

[a] This includes a correction (−3%) for the reactivity effects of the gross spatial inhomogeneities of fuel loading.

[b] These values of reactivity include a correction (+0.3%) for the reactivity effect of using the 6-group rather than the 16-group cross sections.

[c] Measurements with Assembly No. 4 were made with beryllium-filled aluminum beam tubes installed in the reflector. A differential reactivity of 0.3% has been added to correct for this.

[d] Measurements with Assembly No. 5 included a tangential beam tube located 5.1 cm from the fuel zone. A differential reactivity of 0.2% has been added to correct for this.

water level was high. This corresponds to the philosophy of the measurements from which $k_{eff}$'s were deduced. However, the computation of neutron flux and fission power distributions did not duplicate measured conditions wherein criticality was attained by insertions of control rods. For some experiments, criticality was achieved by adjusting the water level, and control rods were fully withdrawn. No attempt has been made to analyze these particular experiments.

All 16-group calculations were performed in cylindrical geometry, with a fixed bare-equivalent height of 60 cm assigned to all regions of all critical assemblies.

## Comparison of Measured and Computed Values of $k_{eff}$

Table II-18-I lists the measured and computed data of $k_{eff}$ for various loadings of fuel and boron and for two ITC sizes. It has been calculated[1] that the heterogeneities of the distributions of fuel foils in Assembly No. 1 reduces reactivity by approximately 3%. Assemblies Nos. 2a and 2b are also subject to an effect of this type but of lesser magnitude.

Referring to Table II-18-I, note that the biased 2-D calculations all yield values of $k_{eff}$ smaller than those predicted by the 16-group 1-D calculations. The 6-group $k_{eff}$'s are smaller than the measured data, when the latter are corrected for heterogeneity effects, for Assemblies Nos. 1-3. The 6-group $k_{eff}$ for Assembly No. 4a is a little larger than the measured value. On the whole, for Assemblies Nos. 1-3 the 16-group (1-D) $k_{eff}$'s are closer to the experimentally determined $k_{eff}$.

## Comparisons of Measured and Computed Values of the Reactivity Effects of Uniform Partial Voidings of ITC Water

In Fig. II-18-1, one-dimensional 16-group computations of reactivity effects of uniformly voiding some of the ITC water are compared with measurement. The curve for the measured values in Assembly No. 4b probably is somewhat distorted by non-uniformity of

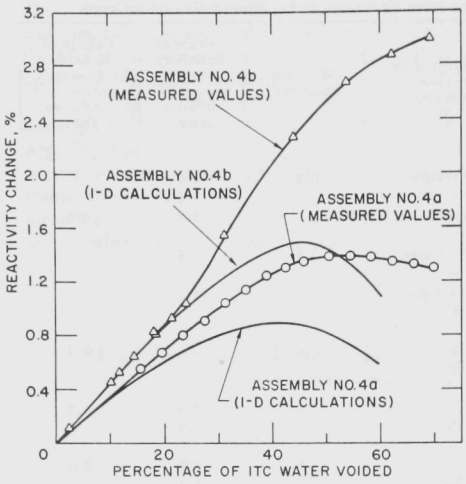


FIG. II-18-1. Comparison Between Measured and Calculated Reactivity Effects Resulting from the Partial Voidings of ITC Water in AARR Critical Assemblies. *ANL Neg. No. 112-9498.*

TABLE II-18-II. REACTIVITY EFFECT OF VOIDING 50% OF THE WATER IN THE 6-cm ITC

| Assembly No. | U-235 Loading, kg | Boron Loading, g | Reactivity Effect of Voiding, % | | |
|---|---|---|---|---|---|
| | | | Measured | Calculated | |
| | | | | 16 groups; one space dimension | 6 groups; two space dimensions |
| 1a | 16.1 | 0 | — | 1.17 | — |
| 2b | 31.4 | 220 | — | 0.98 | — |
| 3 | 41.4 | 425 | 1.5 | 0.93 | 1.43 |
| 4a | 61.5 | 850 | 1.4 | 0.84 | 1.58 |

voiding at smaller percentages of void. The 1-D calculations underestimate the void percentage at which the peak reactivity gain occurs, and they underestimate the peak reactivity gain. There is an increase in the axial reflector savings when voids are introduced into the active portion of the ITC, and this is accounted for by the 2-D analysis but not by the 1-D analysis. This results in a larger reactivity gain for a given void fraction in the ITC water.

Table II-18-II summarizes experimental data and 1-D and 2-D calculations for voidings of 50% of the ITC water in various critical assemblies. The 2-D results agree more closely with measured data for the two cases of measurement.

Another effect that has not been included in the analysis is an increased reactivity-control worth of the ITC when control rods are partially inserted at the outer radial boundary of the core. There is a correspondingly larger change in the control worth of the ITC when voids are present.

### PEAK THERMAL NEUTRON FLUX IN THE ITC

In Paper II-7, values are reported of the absolute peak thermal neutron flux in the ITC, as inferred from measurements in the ITC's of the various critical assemblies. In some of the experiments, reactivity was controlled by adjustment of reactor water level. In other cases, criticality was achieved with control-rod positioning. There are substantial uncertainties in extrapolating measured data of power distributions to estimate absolute power, and there are other uncertainties of theory and measurement in estimating the value of the peak thermal neutron flux per unit power. Nevertheless, there is some interest in the comparison of measured and computed values of the peak flux per unit power, and Table II-18-III is a mixed bag of such comparisons. The experiments wherein criticality was attained by varying reactor water level are included although admittedly this control procedure does not match the design reference control by positioning of control rods.

All $k_{eff}$ calculations were performed for the idealized reactor state wherein all control rods were withdrawn fully. Table II-18-III lists also the values of the peak thermal neutron flux in the beryllium reflector (groups Nos. 15 plus 16; 0–0.4 eV). As discussed in Paper II-20, however, listings of integrated flux alone do not permit an experimenter to determine neutron absorption rates in dilute samples, since the details of the spectra are important. Although, in general, agreement between calculation and measurement appears to be good, there is no intent here to conclude that such is indeed the case.

In these critical assemblies, the beryllium reflector did not contain water. At the time of the termination of the critical-experiment work, fabrication of a new reflector had been completed for improved simulation of the AARR design reflector, but it was not feasible to use this reflector in the final measurements. The calculated peak thermal neutron flux per unit fission power is smaller in the design reactor, apparently because a larger fraction of the total power is produced near the beryllium reflector of the design reactor. Indeed, the graded-fuel loading simulated in the final critical experiments is based upon calculations of the

TABLE II-18-III. Absolute Thermal Neutron Fluxes in Critical Assemblies with Stainless Steel-Water-Uranium Cores

| Assembly No. | U-235 Loading, kg | Boron Loading, g | Composition of the Beryllium Reflector, v/o | Peak Thermal Neutron Flux in the ITC at 100 MW, $10^{15}$ $\frac{\text{n-cm}}{\text{cm}^3\text{-sec}}$ | | Peak Thermal Neutron Flux in the Beryllium Reflector at 100 MW, $10^{15}$ $\frac{\text{n-cm}}{\text{cm}^3\text{-sec}}$ |
|---|---|---|---|---|---|---|
| | | | | Measured | Calculated[a] (0–0.4 eV) | Calculated[a] (0–0.4 eV) |
| 1 | 16.1 | 0 | 10% Plexiglas 90% Be | — | 4.50 | 1.16 |
| | 16.1 | 0 | Be | — | 4.47 | 0.92 |
| 2a | 31.4 | 220 | 10% Plexiglas 90% Be | — | 4.26 | 1.05 |
| | 31.4 | 0 | 10% Plexiglas 90% Be | — | 4.29 | 1.08 |
| 2b | 31.4 | 220 | Be | — | 4.25 | 0.94 |
| | 31.4 | 0 | Be | — | 4.40 | 0.95 |
| 3 | 41.4 | 425 | Be | 4.2 ± 0.6[e] | 4.12 | 0.90 |
| | 41.4 | 0 | Be | — | 4.18 | 0.92 |
| 4a | 61.5 | 850 | Be | 3.8 ± 0.5[e] | 3.91 | 0.81 |
| | 61.5 | 0 | Be | — | 4.01 | 0.84 |
| 4b[b] | 59.4 | 821 | Be | 4.1 ± 0.5[d,e]<br>4.4 ± 0.5[d,e] | 4.02 | 0.91 |
| 5[b] (Graded Loading) | 57.3 | 572 | Be | 4.5 ± 0.7[c,e]<br>4.8 ± 0.5[d]<br>4.4 ± 0.7[c,e] | 3.93 | 0.89 |

[a] These are the results of 16-group one-dimensional diffusion theory calculations. The equivalent bare reactor height was 60 cm.
[b] These assemblies had 7-cm-radius ITC's; the other five assemblies had 6-cm-radius ITC's.
[c] Criticality controlled by positioning of control rods.
[d] Criticality controlled by water level.
[e] For Assemblies 4b and 5, more than one run was made for fixed conditions of reactivity control. The parameters varied were total running time and power level. (See Paper II-20.)

design reactor, and the power distribution calculated for the design reactor is flatter than the power distribution measured in that loading.

### Radial Distribution of Fission Power Density in the Graded-Fuel Loading

Because of the required termination of the program of critical experiments with SS-U-$H_2O$ cores, measurement of fission power density was made in only one graded-fuel loading (see Paper II-8). It was possible to perform "clean" measurements in one fuel assembly at the outer boundary of the reactor core, and a comparison is presented between measured and calculated fission-power distributions in the graded-fuel zone at this boundary. Reference is made to Fig. II-18-2, which shows the positioning of U-Al wires in the measurement, and to Fig. II-18-3, which shows agreement between measured and computed power distributions in this zone. In Fig. II-18-3, the measured and computed distributions are normalized to coincide at the minimum in the power curve near the outer boundary.

In the calculations, the graded-fuel regions were represented as separate homogenized fuel-foil cells, grouping the fuel foil and the associated steel and water. The calculated distribution should be smoothed by fitting a curve to the midpoint values in the fuel-foil cells.

Fig. II-18-3 indicates that computation and measurement (Fig. II-18-4) diverge at the inner boundary of the fuel zone. The margin of disagreement indicates that additional measurements and more detailed calculations are in order. Possibly, partitioning of the ther-

mal neutron energy range into a larger number of groups would help to resolve the disagreement. At this time of reporting, there has been insufficient time available to investigate the discrepancy further. Measurements appear to be out of the question for the predictable future. The data therefore are presented for the sake of completeness rather than because there is a real and unresolvable disagreement between sophisticated computation and sophisticated measurement.

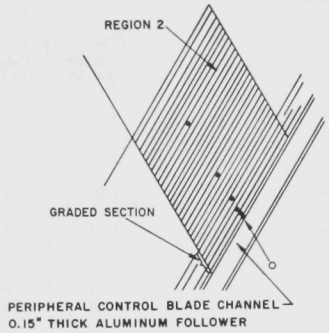


FIG. II-18-2. Locations of Uranium-Aluminum Wires for Measurement of Radial Fission-Power Distribution Near Beryllium Reflector of Graded Fuel Loading. *ANL Neg. No. 12-9004 Rev. 1.*

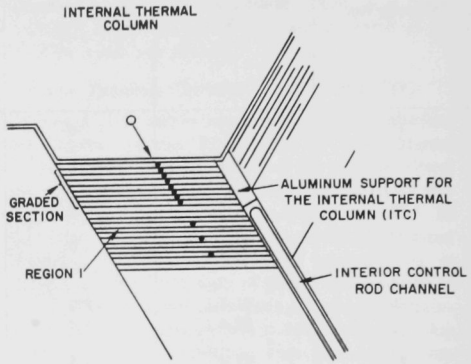


FIG. II-18-4. Locations of Uranium-Aluminum Wires for Measurement of Radial Fission-Power Distribution Near ITC of Graded Fuel Loading. *ANL Neg. No. 112-9433.*

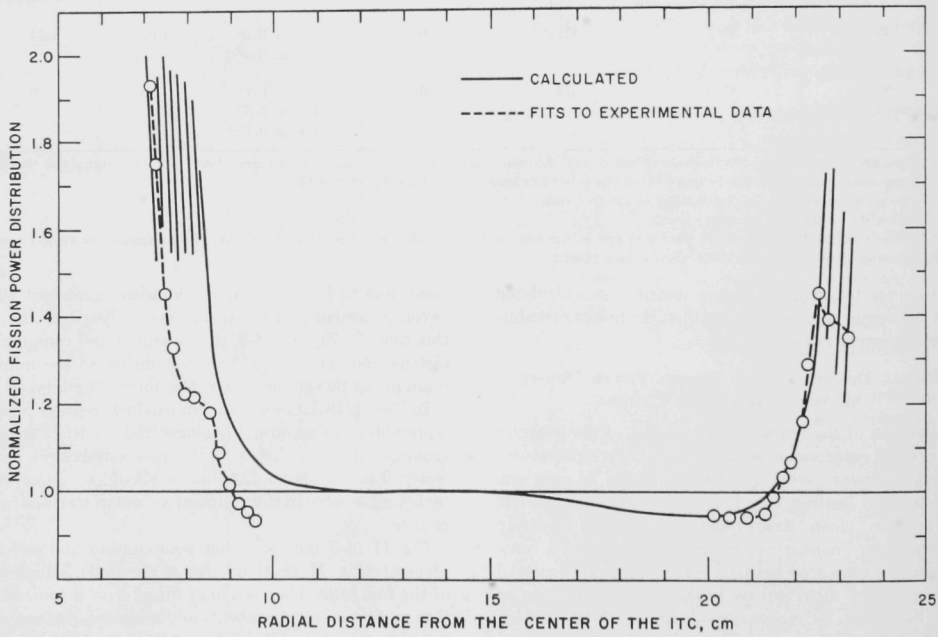


FIG. II-18-3. Comparison Between Measured and Calculated Fission Power Distribution in the Graded AARR Critical Assembly. *ANL Neg. No. 112-9421.*

REFERENCES

1. D. H. Shaftman, C. N. Kelber, B. N. Kristianson and R. P. Savio, *Argonne Advanced Research Reactor Calculations—Analysis of Criticality-Facility Loadings*, Reactor Physics Division Annual Report, July 1, 1964 to June 30, 1965, ANL-7110, pp. 51–60.
2. R. P. Savio and D. H. Shaftman, *Argonne Advanced Research Reactor Calculations—Analysis of the Critical Experiments*, Reactor Physics Division Annual Report, July 1, 1965 to June 30, 1966, ANL-7210, pp. 80–82.
3. D. H. Shaftman and R. P. Savio, *Comparisons of Theory and Measurement for AARR Critical Experiments*, Trans. Am. Nucl. Soc., **9**, June 1966, p. 183.
4. D. H. Shaftman and R. P. Savio, *Argonne Advanced Research Reactor Calculations—General Reactor Physics Design Analyses*, Reactor Physics Division Annual Report, July 1, 1965 to June 30, 1966, ANL-7210, pp. 82–92.
5. D. H. Shaftman and R. P. Savio, *The Argonne Advanced Research Reactor (AARR)*, Seminar on Intense Neutron Sources, Santa Fe, New Mexico, September 19–23, 1966, CONF-660925, pp. 215–259.
6. G. K. Leaf, A. S. Kennedy and G. J. Jensen, *ANL-CANDID, A Two-Dimensional Diffusion Theory Code Based on CANDID2D*, ANL-7305 (to be published).

## II-19. Argonne Advanced Research Reactor Calculations—General Reactor Physics Design Analysis

D. H. SHAFTMAN and R. P. SAVIO*

For budgetary reasons which are noted in the Preface to these papers on the AARR calculations, in Fiscal-Year 1967 the HFIR designs of the reactor core, control rods, and removable-beryllium reflector zones were adopted by Argonne National Laboratory in place of the corresponding zones of the earlier design AARR with an intermediate-spectrum reactor core. The HFIR cores have operated quite successfully at 100 MW in the HFIR, and there have been extensive reactor physics studies by Oak Ridge National Laboratory (ORNL) scientists on flux-trap reactors with cores of approximately this composition. (See Appendix C, Ref. 1, for bibliographies of ORNL and other reports on high-flux reactors, and of ORNL reports on the HFIR reactor). Nevertheless there are important justifications for independent detailed studies by Argonne National Laboratory on the reactor physics characteristics of the new reference AARR.

The purpose of the AARR plant has not changed, namely, to supply a versatile research reactor for many basic studies involving irradiations or bombardments of materials with high-intensity fluxes of thermal neutrons. The experimental facilities of the AARR include: a central $H_2O$-moderated flux trap or Internal Thermal Column (ITC), containing static irradiation facilities, hydraulic-rabbit tubes, and gas-cooled rabbit tubes; a total of 6 blind beam tubes which are tangential to the reactor fuel zone, and two through tubes, all in the radial beryllium reflector; and a large number of vertical irradiation facilities in the beryllium reflector. The ITC of the AARR will be more lightly loaded than the flux-trap zone of the HFIR, and the AARR permanent-beryllium reflector will be thicker and will include more experimental facilities. Therefore, the ITC and the permanent-beryllium reflector of the AARR will be quite different from the corresponding zones of the HFIR, and the operation of the reactor perforce will be different from that of the HFIR. For these reasons alone, an independent study by Argonne National Laboratory is essential.

Another motivation for these reactor physics studies of the AARR is that certain physics characteristics of the HFIR inferred from measurement have proved to be difficult to calculate. One such characteristic is the reactivity variation of the system during reactor operation. The cores have endured somewhat longer than the calculated reactivity life, and perhaps this is related to uncertainties in the calculated net buildup of neutron poisons in the beryllium reflector during reactor operation. Hopefully, the independent analyses by Argonne scientists will be helpful in resolving these computational uncertainties. In any event, the methods of reactor physics analysis and the neutron cross sections used by Argonne are sufficiently different that independent studies are essential to establish levels of confidence in the results of the reactor physics statics and dynamics analyses.

The present paper summarizes reactor-statics calculations of:

1. excess reactivity of the fresh unpoisoned reactor;
2. reactivity coefficients of partial voidings of water in the reactor fuel zone and in the ITC;
3. reactivity effects of neutron poisoning, and of partial displacement of ITC water by aluminum;

* Reactor Operations Division, Argonne National Laboratory.

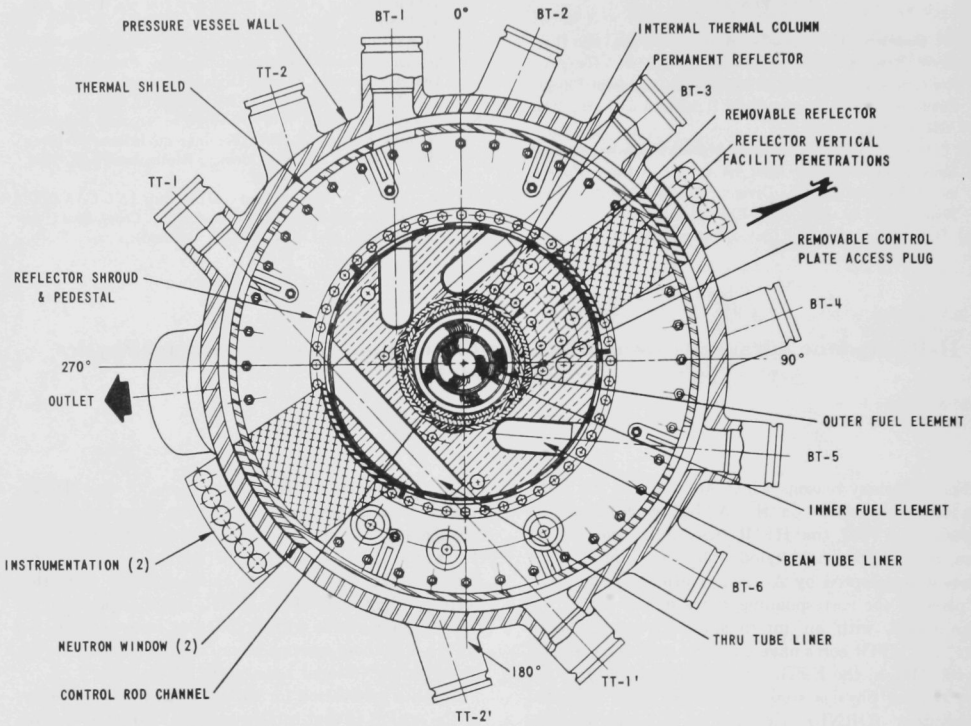


FIG. II-19-1. Reactor Vessel Horizontal Section. *ANL Neg. No. 112-9437.*

4. effects of neutron poisoning of the beryllium reflector on reactivity and on thermal neutron flux;

5. effects of control-rod insertion on neutron flux;

6. radial and axial distributions of fission power;

7. reactivity worths of soluble neutron poisons in the reactor water;

8. the effective delayed-neutron fraction, $\beta_{eff}$, and the mean prompt neutron lifetime, $l^*$.

Paper II-20 discusses in some detail the space dependence and energy dependence of the thermal neutron fluxes in the ITC. Paper II-22 includes a tabulation of calculated gross reductions in reactivity which would obtain in the event of a massive partial voiding of water in the fuel zone.

## Methods and Parameters of the Reactor Physics Analyses

Reference 1 contains detailed figures and descriptions of the two involute-plate fuel-element annuli that comprise the reactor fuel zone, and the reader is directed to this reference for additional details. For convenience, however, Fig. II-19-1 is included here to give a plan view of the AARR reactor core and its internal and external flux-trap zones. Figure II-20-1 of Paper II-20 is a plan view of the reference ITC core assembly.

The majority of the analyses reported in the present paper are based upon multigroup diffusion theory calculations of neutron statics in one and two $(r,z)$ space dimensions. The methods of analysis and the choice of group cross sections have been described in other reports[2,3] and additional detail is given in Paper II-20. One principal model of diffusion theory calculations involves a 16-group partition of the neutron energy range, namely, the Hansen-and-Roach partition.[4] For this model, the cross sections for groups Nos. 1–14 are based on the Hansen-and-Roach prescriptions, and the cross sections for thermal groups Nos. 15–16 have been obtained from THERMOS[(5)] analyses plus a calculation of net-downscatter of neutrons from group No. 15

(0.1–0.4 eV) to group No. 16 (0–0.1 eV) (see Paper II-20).

The second principal model of diffusion theory calculations utilizes a 6-group synthesis of the 16-group set, with reactor multigroup fluxes providing the weighting factors (see Table II-19-I). The two thermal groups (Nos. 15 and 16) of the 16-group set are retained in the 6-group set. The 6-group set was developed for two-dimensional $(r,z)$ calculations because even one 6-group calculation with the CANDID2D program has required hours of machine time on the CDC-3600 computer at Argonne National Laboratory. To compare 6-group and 16-group results which one might expect, one-dimensional calculations of the AARR have been performed with the two sets of cross sections. For idealized calculations wherein the aluminum control-rod followers were assumed to be fully inserted into the active-core zone, it was found that the 6-group $k_{eff}$ was slightly lower than the 16-group $k_{eff}$. The reactivity difference is 0.3%.

With a correction for the abovementioned bias noted in the one-dimensional computations, an equivalent bare height of 69.7 cm, was inferred for $k_{eff}$-equivalent one-dimensional calculations with the 16-group set.

The fresh reactor fuel elements nominally are azimuthally symmetric. However, there is a degree of azimuthal asymmetry in the reference ITC core assembly (see Fig. II-20-1 of Paper II-20), and there is considerable azimuthal asymmetry in the permanent-beryllium reflector. Also, there is vertical asymmetry in the permanent beryllium. For the one-dimensional calculations, the permanent-beryllium zone has been partitioned into three radial annuli and into four azimuthal sectors. Average volume fractions of materials in each annulus and azimuthal sector have been computed by averaging locally over elevations corresponding to the top and bottom boundaries of the 20-in.-high active-fuel zone. Similarly, the ITC and the fuel zone have been partitioned into a number of radial annuli, for detailed multiregion, multigroup analyses. The gas-cooled rabbit tubes in the ITC have been ignored in the present analyses; they occupy a small fraction of the target-tube volume in the ITC, and the emphasis in the reactor physics studies has been on fluxes in the water-cooled target tubes. Table II-19-II summarizes the spatial partitions of the reactor which were chosen for the multiregion computations, and it lists the computed region compositions.

TABLE II-19-I. Multigroup Partitions of the Neutron-Energy Range

A. Sixteen-Group Partition

| Neutron Energy Group | Neutron-Energy Range | Normalized Fission-Spectrum Partition |
|---|---|---|
| 1 | 3–∞ MeV | 0.204 |
| 2 | 1.4–3 MeV | 0.344 |
| 3 | 0.9–1.4 MeV | 0.168 |
| 4 | 0.4–0.9 MeV | 0.180 |
| 5 | 0.1–0.4 MeV | 0.090 |
| 6 | 17–100 keV | 0.014 |
| 7 | 3–17 keV | 0 |
| 8 | 0.55–3 keV | 0 |
| 9 | 100–550 eV | 0 |
| 10 | 30–100 eV | 0 |
| 11 | 10–30 eV | 0 |
| 12 | 3–10 eV | 0 |
| 13 | 1–3 eV | 0 |
| 14 | 0.4–1 eV | 0 |
| 15 | 0.1–0.4 eV | 0 |
| 16 | 0–0.1 eV | 0 |

B. Six-Group Partition

| Neutron Energy Group | Neutron-Energy Range | Normalized Fission Spectrum | Synthesized Groups of the Sixteen-Group Set |
|---|---|---|---|
| 1 | 0.9–∞ MeV | 0.716 | 1 to 3 |
| 2 | 17–900 keV | 0.284 | 4 to 6 |
| 3 | 0.03–17 keV | 0 | 7 to 10 |
| 4 | 0.4–30 eV | 0 | 11 to 14 |
| 5 | 0.1–0.4 eV | 0 | 15 |
| 6 | 0–0.1 eV | 0 | 16 |

## Calculated Values of Available Excess Reactivity

One-dimensional, 16-group-theory calculations of available excess reactivity for the fresh reactor, at operating temperatures but without xenon, indicate an available excess reactivity of: 6.7%, for the reactor with a 100%-$H_2O$ ITC; and 7.1%, for the reactor with a fully loaded reference ITC core assembly (Type-C ITC; see Paper II-20) containing additional target neutron absorption equivalent to 0.5 g boron in the ITC. These reactivities are based upon an assumed equivalent bare core height of 66.0 cm.

Two-dimensional $(r,z)$ 6-group diffusion theory calculations yielded 8.1% and 8.6%, respectively, for the two cases listed above. These values include corrections of +0.3% reactivity for the difference between 16-group one-dimensional computations and 6-group one-dimensional computations. The reactivity difference, 1.5%, between the 2-D and 1-D calculations would be compensated by an increase in the equivalent bare height of the reactor to 69.7 cm, in the 16-group 1-D analysis.

## Calculated Reactivity Effects of Partial Voidings of Reactor Water

For small percentages of uniformly dispersed voids in the water in various zones of the reactor, one-

TABLE II-19-II. EQUIVALENT CYLINDRICAL GEOMETRY FOR THE AARR CORE

| Description | Outer radius,[a] cm | Atom density,[a] $10^{24}$ atoms/cm$^3$ | | | | | | |
|---|---|---|---|---|---|---|---|---|
| | | H | O | Al | Be | $U^{235}$ | $U^{238}$ | Natural Boron |
| *ITC REGION* | | | | | | | | |
| Region 1 Central (hydraulic-rabbit) tube | 0.9525 | 0.01571 | 0.00785 | 0.04589 | — | — | — | 27.46E-6[b] |
| Region 2 Water | 2.0638 | 0.06574 | 0.03287 | — | — | — | — | — |
| Region 3 Static basket tubes, hydraulic-rabbit tubes, and gas-rabbit tubes | 5.2388 | 0.05142 | 0.02571 | 0.01313 | — | — | — | 6.44E-6 |
| Region 4 Water | 6.0744 | 0.06574 | 0.03287 | — | — | — | — | — |
| Region 5[c] ITC shroud and portion of inner fuel element side plate and associated water | 7.1450 | 0.02027 | 0.01014 | 0.04170 | — | — | — | — |
| *INNER FUEL REGIONS* | | | | | | | | |
| Region 6 | 7.3203 | 0.03287 | 0.016640 | 0.02944 | — | 1.973E-4 | 0.1485E-4 | 0.9720E-4 |
| Region 7 | 7.8019 | 0.03287 | 0.017101 | 0.02931 | — | 2.340E-4 | 0.1761E-4 | 0.8733E-4 |
| Region 8 | 8.4305 | 0.03287 | 0.017272 | 0.02910 | — | 2.937E-4 | 0.2211E-4 | 0.7123E-4 |
| Region 9 | 9.1755 | 0.03287 | 0.017468 | 0.02885 | — | 3.620E-4 | 0.2724E-4 | 0.5284E-4 |
| Region 10 | 10.0096 | 0.03287 | 0.017650 | 0.02862 | — | 4.254E-4 | 0.3202E-4 | 0.3574E-4 |
| Region 11 | 11.3861 | 0.03287 | 0.017742 | 0.02851 | — | 4.577E-4 | 0.3445E-4 | 0.2702E-4 |
| Region 12 | 12.3647 | 0.03287 | 0.017593 | 0.02869 | — | 4.057E-4 | 0.3053E-4 | 0.4106E-4 |
| Region 13 | 12.5885 | 0.03287 | 0.017446 | 0.02888 | — | 3.545E-4 | 0.2668E-4 | 0.5484E-4 |
| *WATER-ALUMINUM REGION* | | | | | | | | |
| Region 14 Portions of inner and outer fuel element side plates, and coolant gap | 15.1308 | 0.02712 | 0.01356 | 0.03543 | — | — | — | — |
| *OUTER FUEL REGIONS* | | | | | | | | |
| Region 15 | 15.4206 | 0.03287 | 0.017645 | 0.02863 | — | 4.238E-4 | 0.3190E-4 | — |
| Region 16 | 16.2763 | 0.03287 | 0.017961 | 0.02823 | — | 5.341E-4 | 0.4020E-4 | — |
| Region 17 | 18.1943 | 0.03287 | 0.018330 | 0.02777 | — | 6.627E-4 | 0.4988E-4 | — |
| Region 18 | 18.9669 | 0.03287 | 0.018119 | 0.02804 | — | 5.891E-4 | 0.4434E-4 | — |
| Region 19 | 19.7985 | 0.03287 | 0.017747 | 0.02847 | — | 4.690E-4 | 0.3530E-4 | — |
| Region 20 | 20.6786 | 0.03287 | 0.017406 | 0.02893 | — | 3.404E-4 | 0.2562E-4 | — |
| Region 21 | 20.9347 | 0.03287 | 0.017173 | 0.02922 | — | 2.593E-4 | 0.1951E-4 | — |
| *CONTROL ROD REGION* | | | | | | | | |
| Region 22 Portions of outer fuel element side plate, and control rod channels | 24.1275 | 0.02117 | 0.01058 | 0.04088 | — | — | — | — |
| *REMOVABLE BERYLLIUM REGIONS* | | | | | | | | |
| Region 23 | 25.1155 | — | — | — | 0.1229 | — | — | — |
| Region 24 | 30.1170 | 0.001538 | 0.000769 | — | 0.1200 | — | — | — |
| Region 25 | 30.3327 | 0.06574 | 0.03287 | — | — | — | — | — |
| Region 26 | 33.3375 | 0.000771 | 0.000385 | — | 0.1215 | — | — | — |

TABLE II-19-II. *Continued*

| Description | Outer radius,[a] cm | Atom density,[a] $10^{24}$ atoms/cm | | | | | | |
|---|---|---|---|---|---|---|---|---|
| | | H | O | Al | Be | $U^{235}$ | $U^{238}$ | Natural Boron |
| *PERMANENT BERYLLIUM REGIONS* | | | | | | | | |
| Region 27 Vertical- | 40.9575 | 0.005186 | 0.002593 | 0.001989 | 0.10914 | — | — | — |
| Region 28 facilities | 53.6575 | 0.003497 | 0.001749 | 0.001628 | 0.11304 | — | — | — |
| Region 29 sector | 66.0400 | 0.002150 | 0.001075 | 0.000844 | 0.11716 | — | — | — |
| Region 27 Blind-beam | 40.9575 | 0.003050 | 0.001525 | 0.003557 | 0.10201 | — | — | — |
| Region 28 tubes sec- | 53.6575 | 0.003077 | 0.001538 | 0.003956 | 0.09643 | — | — | — |
| Region 29 tor | 66.0400 | 0.003017 | 0.001509 | 0.004179 | 0.09434 | — | — | — |
| Region 27 Through- | 40.9575 | 0.000953 | 0.000476 | 0.0007296 | 0.11963 | — | — | — |
| Region 28 tubes sec- | 53.6575 | 0.005489 | 0.002744 | 0.007556 | 0.07111 | — | — | — |
| Region 29 tor | 66.0400 | 0.004372 | 0.002185 | 0.006126 | 0.08108 | — | — | — |
| *OUTER WATER REGIONS* | | | | | | | | |
| Region 30 | 68.58 | 0.03491 | 0.01745 | 0.02195 | — | — | — | — |
| Region 31 | 113.03 | 0.05953 | 0.02976 | 0.001429 | — | — | — | — |
| (Note: Region 31 also includes $N_{Fe}$ = 0.000862, $N_{Ni}$ = 0.000226, $N_{Cr}$ = 0.000143) | | | | | | | | |

[a] The numbers tabulated are the input values in the computations. There is no implication intended that these values are absolutely meaningful to this number of decimal places.

[b] The notation 27.46E-6 is used as a more convenient form for $27.46 \times 10^{-6}$. This type of notation is used throughout this table.

[c] For a case in which the ITC insert has been removed, the outer radius of Region No. 4 is 6.4351 cm and the composition of Region No. 5 is as follows:

$N_H$ = 0.01222
$N_O$ = 0.00611
$N_{Al}$ = 0.04910

dimensional calculations of reactivity change have agreed closely with two-dimensional analyses. A uniform voiding of 10% of the water in the fuel zone corresponds to a reactivity loss of 2.4%; voiding 20% of the water is calculated to reduce reactivity by 5.1%, thus demonstrating that there is a typical nonlinearity in the curve of the differential reactivity worth of partial voiding of fuel-zone water.

For small percentages of uniformly dispersed voids in all of the ITC water up to the inner fuel element, there is a net reactivity gain. This region will be spoken of as the ITC. If there were no aluminum in the ITC, the calculated differential reactivity effect would be ~0.05%/% void. For a fully-loaded ITC, the differential reactivity gain of voids in the water in the ITC is calculated to be ~0.04% per percent void in the water. The difference can be explained by noting that a 1% void in the water of the loaded ITC displaces a smaller volume of water than does a 1% void in the water in the ITC when there are no target tubes. Perhaps a better definition of the differential reactivity effect would be % per unit void volume in the ITC.

For larger percentages of voids which are limited to the water in the 20-in.-high active-portion of the ITC, two-dimensional calculations are needed to account for the increased reactivity worth of the axial reflectors above and below the active portion of the ITC. Figure II-19-2 summarizes 1-D and 2-D calculations of the reactivity effects of uniform voidings in the water inside the ITC. Two cases have been examined: a Type-A (100%-$H_2O$) ITC; and a Type-C ITC (fully loaded reference ITC core assembly), with a total additional neutron absorption area in the ITC equivalent to the absorption area of 0.5 g boron. For both ITC types, the 1-D reactivity change peaks at a fractional void of 0.5, and the 2-D reactivity change has a higher peak value, at a larger fractional void (~0.7). As noted, the 2-D curve for the Type-A ITC is not quite comparable to the other curves of Fig. II-19-2; for these 2-D calculations, it was assumed that the portions of the ITC which are axially beyond the active portion also have the same percentage void in the water. A single 2-D calculation has been made for the case where a 70% void is continued above and below a Type-C ITC containing 0.5 g boron; the calculated reactivity gain was lowered by 0.2%, as compared with the case of a 70% void in the ITC water but only in the 20-in.-high active portion of the ITC. It is estimated that if a 70%-voiding of a Type-A ITC were not continued above and below the active ITC the reactivity gain would be ~0.1% higher.

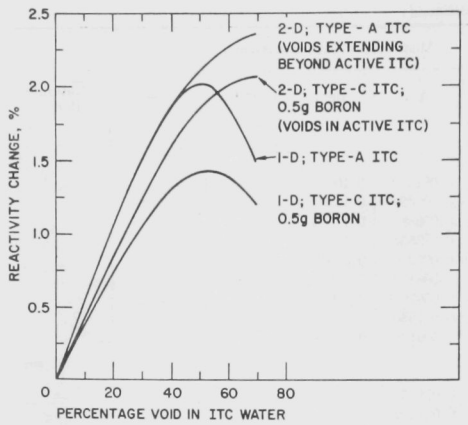


FIG. II-19-2. Calculated Reactivity Gain for Uniform Partial Voidings of Water in the ITC. *ANL Neg. No. 112-9415.*

### REACTIVITY EFFECTS OF ALUMINUM AND 1/*v*-TARGET POISONING IN THE ITC

Starting with a 100%-$H_2O$ ITC, displacement of a small fraction of the ITC water by aluminum is calculated to increase reactivity. Table II-19-III summarizes reactivity changes as the ITC composition is changed from Type-A toward Type-C. Also tabulated is the reactivity effect of additional neutron poisoning by target material, assumed to be distributed uniformly over the target-tube regions of the ITC (regions Nos. 1 and 3, Table II-19-II).

### PERTURBATIONS OF REACTIVITY AND THERMAL NEUTRON FLUX BY NEUTRON POISONS IN THE BERYLLIUM REFLECTOR

Neutron poisonings of the beryllium reflector are anticipated due to the inclusion of chemical impurities in the beryllium, within the specifications established. Part or all of the beryllium may be affected. The reference specifications for chemical impurities in the beryllium permit very small percentages (several ppm) of some rare-earth isotopes with very high capture cross sections for thermal and near-thermal neutrons. Sixteen-group calculations of the reactivity and flux perturbations of allowed levels of chemical impurities in the beryllium zones considered also low-cross-section and intermediate-cross-section neutron absorbers.

In these one-dimensional calculations, the beryllium region compositions chosen are those representative of the azimuthal sector containing the bulk of the vertical irradiation facilities in the reflector. All impurities other than gadolinium and europium are replaced by an equivalent neutron absorption by natural boron. The actual gadolinium and europium contents of the beryllium are expected to be much lower, and these high-cross section impurities will burn out rapidly during reactor operation. The results are summarized in Table II-19-IV.

Table II-19-IV does not include data of thermal neutron fluxes far out in the permanent beryllium reflector because the present model of multigroup calculations yields group-16 neutron fluxes which are considerably too high near the outer boundary of the beryllium. The cause of this error is the use of a net-downscatter cross section from group No. 15 to group No. 16, discussed earlier in this paper. In deleting a term of removal from group No. 16, corresponding to upscattering to higher-energy groups, the total removal cross section in group No. 16 is reduced, and the migration area ($L_{16}^2$) for group-16 neutrons is overestimated. Thus, there is an overestimate in the diffusion of group-16 neutrons from regions in the beryllium where the group-16 flux is high, and this results in large overestimates of the group-16 flux farther out, in the permanent-beryllium zone. To retain the feature of having more than one thermal group, it will also be necessary to retain neutron upscattering, in future calculations of the thermal neutron flux in the permanent beryllium.

### FLUX PERTURBATIONS BY CONTROL RODS

Paper II-20 includes a detailed discussion of problems of calculating idealized cases where the aluminum

TABLE II-19-III. REACTIVITY EFFECTS OF ALUMINUM AND 1/v-TARGET POISONING IN THE ITC

| ITC Description | Reactivity Change,[a] % |
|---|---|
| Type A[b] | −0.75 |
| Type B[c] | 0 |
| Type C[d] | |
| ⅛ g boron | −0.09 |
| ¼ g boron | −0.17 |
| ⅜ g boron | −0.25 |
| ½ g boron | −0.32 |
| ¾ g boron | −0.46 |
| 1 g boron | −0.59 |
| 1½ g boron | −0.82 |

[a] All reactivity changes are normalized to zero reactivity change for the Type-B ITC.

[b] This ITC is 100% water.

[c] This ITC contains the reference ITC core assembly fully loaded with dummy aluminum target capsules.

[d] The ITC contains the reference ITC core assembly fully loaded with dummy aluminum target capsules containing additional poison evenly distributed over the sample volume.

TABLE II-19-IV. PERTURBATIONS OF REACTIVITY AND THERMAL NEUTRON FLUX BY NEUTRON POISONS IN THE BERYLLIUM REFLECTOR[a]

| Case Number | Beryllium Zones Poisoned | Poisoning | Reactivity Effect, % | Thermal Neutron Fluxes in Beryllium Reflector, $10^{15}$ n-cm/cm$^3$-sec | | | | |
|---|---|---|---|---|---|---|---|---|
| | | | | Peak Flux | | | Fluxes at Inner Surface of Permanent Beryllium[b] | |
| | | | | Radial Position of Peak Flux, cm | Group-16 Flux | Group-15 Flux | Group 16 | Group 15 |
| 1 (Reference case) | None | — | 0 | 29.8 | 1.28 | 0.30 | 1.19 | 0.22 |
| 2 | Removable | 2 ppm B | −0.07 | 29.8 | 1.26 | 0.30 | 1.18 | 0.23 |
| 3 | Removable | 3 ppm Gd | −0.33 | 29.8 | 1.21 | 0.30 | 1.13 | 0.22 |
| 4 | Removable | 3 ppm Eu | −0.04 | 29.8 | 1.27 | 0.30 | 1.18 | 0.23 |
| 5 | Permanent | 12 ppm B<br>3 ppm Gd<br>3 ppm Eu | −0.30 | 28.8 | 1.19 | 0.32 | 1.05 | 0.22 |
| 6 | Removable and Permanent | 12 ppm B<br>3 ppm Gd<br>3 ppm Eu | −1.00 | 28.8 | 1.05 | 0.31 | 0.95 | 0.22 |

[a] The beryllium region compositions are representative of the azimuthal sector in the beryllium reflector which contains most of the vertical irradiation facilities (see Table II-19-II).

[b] These values are close to the fluxes at the tips of the blind beam tubes. The radial position is $r = 33.3$ cm.

followers or the "black" portions of the control rods are in the active-core zone. For these cases, Paper II-20 describes the perturbations of thermal neutron fluxes in the ITC. Similarly, there are perturbations of the thermal neutron flux in the beryllium. The idealized change from aluminum followers to black absorbers in the active-core zone results in a reduction of ~50% in the peak group-16 flux in the beryllium, and a reduction of ~50% in the peak group-15 flux.

### RADIAL AND AXIAL DISTRIBUTIONS OF FISSION-NEUTRON PRODUCTION RATE

Figures II-19-3a and II-19-3b present radial distributions of fission-neutron production rate, at core midheight, for two idealized cases of control rod positioning: all rods fully inserted into the reactor core (Fig. II-19-3a); or all rods fully withdrawn, leaving aluminum followers in the active-core zone (Fig. II-19-3b). These distributions are absolute rates, normalized to 100 MW. The corresponding distributions of fission-power density are obtained by applying the factor 0.41. There is actually a smooth variation in the fuel content of each plate as a function of radial distance from the center of the ITC. The computer program used limits the total number of regions to 35, and it was necessary to approximate to this continuous fuel grading by a rather coarse multiregion partition of the fuel zones. In each region, the material compositions were volume averaged. Thus, the distributions shown in Figs. II-19-3a and II-19-3b have unreal step-function discontinuities at interval boundaries.

Figure II-19-4 presents a typical axial distribution of power density, at the radial location of the center of the outer fuel element in the fresh reactor, as inferred from a 6-group 2-D computation. The power density is normalized to unity at core midheight.

For Figs. II-19-3 and II-19-4, the aluminum rod followers were assumed to be in the active-core zone. A Type-C ITC was assumed, with 0.5 $g$ boron.

### REACTIVITY WORTHS OF SOLUBLE NEUTRON POISONS IN THE REACTOR WATER

The control effectiveness of dissolved boron or cadmium as a soluble neutron poison in the reactor water was determined by one-dimensional 16-group diffusion theory computations. Figure II-19-5 summarizes these computations, which were made to assess the relative merits of a slow-acting secondary system of reactivity control utilizing a soluble neutron poison. Cadmium has been designated as the reference soluble poison for the HFIR and also for the AARR, in the form of a highly concentrated solution of cadmium nitrate which is pumped into the primary system.

### REACTOR KINETICS PARAMETERS: $\beta_{eff}$ AND $l^*$

Computations have been made of the effective delayed-neutron fraction, $\beta_{eff}$, and the mean prompt neutron lifetime, $l^*$, in the fresh reactor, as a function

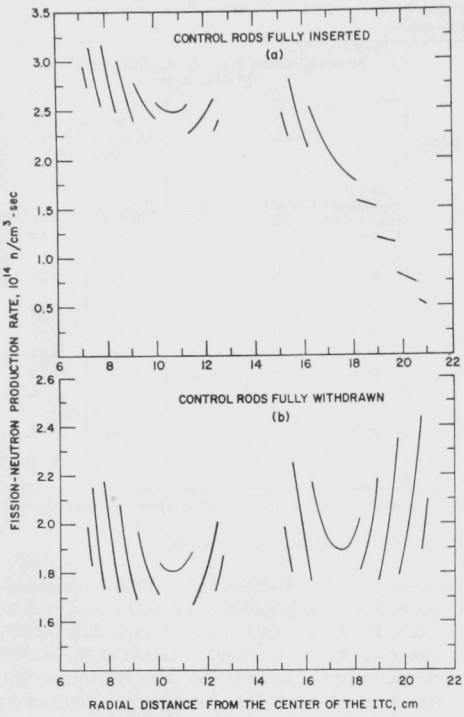


FIG. II-19-3. Radial Distributions of Fission-Neutron Production Rate in the Fresh Reactor. *ANL Neg. No. 112-9424.*

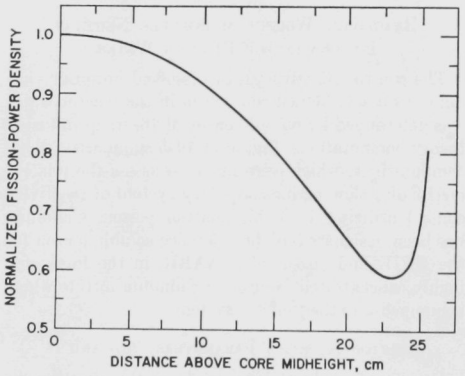


FIG. II-19-4. Normalized Axial Distribution of Fission-Power Density in the Fresh Reactor. *ANL Neg. No. 112-9435.*

of the idealized positions of the reactor control rods and for various characterizations of the ITC and of the permanent-beryllium reflector. The values of $\beta_{eff}$ are essentially independent of variations in the ITC and of variations in the permanent beryllium over the various azimuthal sectors.

For the idealized extreme wherein the control rods were withdrawn fully, $\beta_{eff} = 0.0075$; with control rods inserted fully, $\beta_{eff} = 0.0076$.

As expected, the calculated mean prompt neutron lifetime is strongly influenced by the degree of return of neutrons from the beryllium reflector. For the case where control rods are fully withdrawn, $l^* \approx 60$ $\mu sec$. The neutron lifetime drops to a calculated value of $\sim 25$ $\mu sec$ when the control rods are inserted fully. These calculations are based upon a crude diffusion theory treatment of the control-rod effectiveness, and they must be regarded as preliminary.

## Uncertainties in Neutron-Flux Distributions in Idealized Calculations of Off-Critical Reactors

The 1-D and 2-D calculations described in this paper typically are $k_{eff}$ calculations for off-critical systems, i.e., $k_{eff} \neq 1$. The space and energy distributions of neutron flux are distorted, and therefore also power distributions are idealized and distorted from reality. The distributions of the power density now are determined principally by the distributions of thermal neutron flux in the AARR, which has become a thermal reactor. It must be recognized that these sins of commission are openly stated, and the purpose of these particular computations is to determine differential effects resulting from shifts from one idealized extreme of control-rod insertion to the other. For the most part, the calculated differential effects are small enough

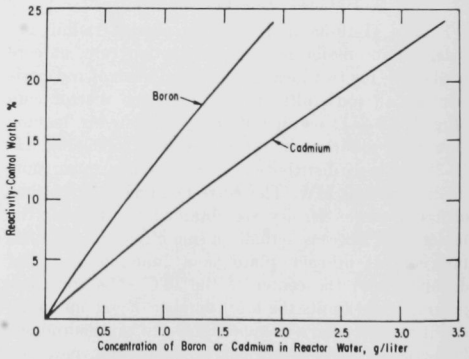


FIG. II-19-5. Reactivity-control Worths of Soluble Poisons in the AARR (Fully Loaded ITC). *ANL Neg. No. 112-9391.*

that the indicated effects may be assigned values of uncertainty.

### References


1. F. T. Binford and E. N. Cramer, Eds., *The High-Flux Isotope Reactor, A Functional Description*, **1**, ORNL-3572 (May 1964).
2. D. H. Shaftman, C. N. Kelber, B. N. Kristianson and R. P. Savio, *Argonne Advanced Research Reactor Calculations—Analysis of Criticality-Facility Loadings*, Reactor Physics Division Annual Report, July 1, 1964 to June 30, 1965, ANL-7110, pp. 51-60.
3. D. H. Shaftman and R. P. Savio, *Argonne Advanced Research Reactor Calculations—General Reactor Physics Design Analysis*, Reactor Physics Division Annual Report, July 1, 1965 to June 30, 1966, ANL-7210, pp. 82-92.
4. G. E. Hansen and W. H. Roach, *Six and Sixteen Group Cross Sections for Fast and Intermediate Critical Assemblies*, LAMS-2543 (December 1961).
5. B. J. Toppel and I. Baksys, *The Argonne-Revised THERMOS Code*, ANL-7023 (1965).


## II-20. Argonne Advanced Research Reactor Calculations—Spatial and Energy Distributions of Thermal Neutron Flux in the Internal Thermal Column

R. P. Savio,* D. H. Shaftman and L. K. Volodka

### Introduction

The Internal Thermal Column (ITC) of the AARR will be used for research-type neutron irradiations of a variety of target isotopes, especially transplutonium isotopes. For these irradiations, high-intensity fluxes of neutrons of low energy are essential. In general, it is expected that the production rate will be maximized if the thermal neutron flux in the target is maximized, but there are indications that neutron capture at low-epithermal energies will be important in some of the irradiation chains. At present, the design emphasis is to obtain high target neutron fluxes in the range from zero to approximately ½ eV. To accomplish this purpose, and yet to provide space for a number of targets, the reference ITC core assembly (Fig. II-20-1) leaves a large volume fraction of neutron moderator ($H_2O$) as bulk ITC fluid around rings of individual target tubes. It is anticipated that there might be some special irradiation cycles with special ITC core assemblies containing fewer target tubes, to provide still higher levels of thermal neutron flux. For this reason, preliminary analyses have been made of the safety of operating with larger volume fractions of water in the ITC, to the idealized extreme of 100% $H_2O$ (see Paper II-22). Ultimately, the range of admissible ITC core assemblies and the range of admissible targets will be determined first by safety considerations and then by program requirements. The present calculations are for ITC core assemblies with water contents ranging up to a 100%-$H_2O$ ITC.

* Reactor Operations Division, Argonne National Laboratory.

### Reactor Physics Models of ITC Types

The design of the present reference ITC core assembly (Fig. II-20-1) includes hydraulic-rabbit tubes, static irradiation facilities, and also gas-cooled rabbit tubes. Small capsules will be injected for short-period irradiations in the gas-cooled tubes. The other ITC irradiation facilities will have the capability of irradiating strings of target capsules, with a total string length corresponding to the height of the active fuel zone.

The target capsules will have one or more encapsulating (containment) shells; probably the encapsulating material will be aluminum. The target zone of a capsule typically will consist of aluminum diluent and uniformly dispersed target isotope(s). In the calcula-

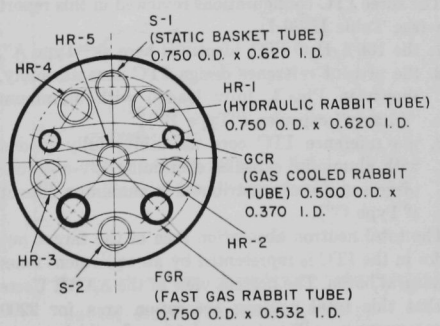


Fig. II-20-1. ITC Core Assembly. *ANL Neg. No. 112-9396.*

TABLE II-20-I. ITC Volume Fractions of Water and Aluminum for the ITC Analyses

| ITC Description | Radial Partitioning of the ITC | | | | | | | |
|---|---|---|---|---|---|---|---|---|
| | Region 1 (0–0.95 cm) | | Region 2 (0.95–2.06 cm) | | Region 3 (2.06–5.24 cm) | | Region 4 (5.24–6.07 cm) | |
| | $H_2O$ | Aluminum | $H_2O$ | Aluminum | $H_2O$ | Aluminum | $H_2O$ | Aluminum |
| Type A: 100% $H_2O$ | 1.0 | 0 | 1.0 | 0 | 1.0 | 0 | 1.0 | 0 |
| Type B: Reference ITC core assembly loaded with dummy capsules | 0.24 | 0.76 | 1.0 | 0 | 0.78 | 0.22 | 1.0 | 0 |
| Type C: Reference ITC core assembly loaded with target capsules | 0.24 | 0.76 | 1.0 | 0 | 0.78 | 0.22 | 1.0 | 0 |

[a] The volumes of the gas-cooled rabbit tubes have been ignored in these analyses.

tions discussed in the present report, it is assumed that the entire capsule will be essentially 100% aluminum, with a small volume fraction of target material. Throughout these analyses, 1/v neutron capture by the targets has been assumed to be representative; in fact, a wide spectrum of absorbers is expected. Neutron fluxes at high thermal energies and low epithermal energies will be important for certain irradiations.

Very little of the target-tube volume in the fully-loaded ITC will be gas-rabbit volume. To arrive at a more representative radial profile of the ITC, for one-dimensional and two-dimensional $(r,z)$ calculations of the neutron flux, the gas volumes were deleted when determining average compositions of regions in the reference ITC.

The three ITC configurations reviewed in this report are (see Table II-20-I):

1. the 100%-$H_2O$ ITC, identified here as "Type A",
2. the present reference design ITC core assembly, shown in Fig. 1, fully loaded with aluminum "dummy" capsules ("Type B"),
3. the reference ITC core assembly, fully loaded with aluminum capsules containing 1/v-absorber targets uniformly distributed in aluminum diluent ("Type C").

The total neutron absorption area of the target nuclides in the ITC is represented by an equivalent mass of natural boron. The present view of the AARR Users is that this total neutron absorption area for 2200 m/sec neutrons will not exceed 10 $cm^2$, which corresponds approximately to a total target poisoning of ¼ g boron. Data are given for cases of zero boron (Type-B ITC), ½ g boron, and 1½ g boron, to show the flux-depression effects of target absorption for a range of poisonings extending well beyond the present reference absorption area.

Table II-20-I summarizes the 4-region partitioning of the interior of the ITC core assembly shown in Fig. II-20-1. The regions are chosen to represent the center target tube (region No. 1), and the annular zone (region No. 3) which contains the remaining vertical irradiation facilities in the ITC.

### Models for Multigroup Diffusion Theory Analysis

Spatial distributions of neutron flux have been calculated for the fresh operating reactor, for several types of ITC configurations and for several idealized configurations of reactivity-control rods. The models of ITC types are discussed above. A description of the reactivity-control configurations and a summary of neutron flux calculations for idealized extremes of control-rod positioning and of ITC types are given in the next section. In each case, emphasis is placed on the influences of the ITC and control-rod configurations on the thermal neutron flux in the ITC.

All of these flux calculations were made with computer programs of multigroup diffusion theory. The basic, more detailed analyses are for one-dimensional (cylindrical) geometry, for a reactor of fixed bare-equivalent height. The Hansen-and-Roach 16-group partition of the neutron energy range[1] was adopted for these 1-D computations. The 16 groups then were synthesized to form a 6-group set with group parameters calculated by flux weighting, using the neutron fluxes of 1-D 16-group reactor computations. The 16-group set partitions the thermal energy range from 0 to 0.4 eV into two groups: group No. 15, 0.1 eV to 0.4 eV; and group No. 16, 0 to 0.1 eV. The 6-group set retained these two thermal neutron groups.

Two-dimensional $(r,z)$ diffusion theory calculations, with 6 groups of neutrons, yielded a value of $k_{eff}$ from which a uniform equivalent bare height was inferred for later 16-group calculations in one space dimension. The radial 2-D and 1-D thermal neutron flux spectra in the ITC are in close agreement at core midheight, in spite of the coarser spatial division used in the CANDID-2D[2] calculations, and in spite of the coarser representation of the above-thermal neutrons.

The group parameters for the thermal groups Nos. 15 and 16 were calculated with the THERMOS program,[3] using the Nelkin scattering model for the water molecule and the heavy-gas model for other nuclides. Calculations were made separately for cells characteristic of the 100%-$H_2O$ ITC, the average core composition, and the beryllium reflector, and the thermal group parameters

were chosen accordingly. The 1-D calculations typically were made with a multigroup program, MACH-1[4], which did not permit neutron upscattering from lower energy to higher energy. Therefore, cross sections for a net downscattering to group No. 16 from group No. 15 were calculated in the manner described in earlier Annual Reports.[5,6] In the ITC, the net-downscatter cross section for water was inferred from the small difference of two relatively large group-transfer rates. Therefore, it is subject to uncertainties of differences between the THERMOS model and the actual situation where the thermal spectrum in the ITC is influenced by the core and by axial leakage.

For the 100%-$H_2O$ ITC, a macroscopic cross section for net downscatter by water from group No. 15 to group No. 16 was chosen to be $\Sigma_{S_{net}}^{H_2O}(15 \rightarrow 16) = 0.095$. This is slightly smaller than the value inferred from THERMOS calculations for an infinite $H_2O$ medium with a spatially uniform source at high epithermal energy; the infinite-medium value is $\Sigma_{S_{net}}^{H_2O}(15 \rightarrow 16) = 0.109$. More recently, using an Argonne modification of THERMOS,[7] space-dependent group-transfer cross sections have been calculated for the case where the reactor has a 100%-$H_2O$ ITC. At the center of the ITC, a value $\Sigma_{S_{net}}^{H_2O}(15 \rightarrow 16) = 0.079$ was inferred.

The actual value chosen for a net-downscatter cross section in the 100%-$H_2O$ ITC is midway between the infinite-medium result and that inferred from the recent space-dependent THERMOS analysis. Clearly, there is good reason to use more than one thermal group, but it is also clear that there remain uncertainties in the absolute magnitudes of the thermal neutron fluxes and in the detailed thermal spectrum. In a later section of this report, calculated data of flux level and flux spectrum in the ITC are given for different values of $\Sigma_{S_{net}}^{H_2O}(15 \rightarrow 16)$ in the ITC, to indicate effects of the uncertainty in the value of the net cross section for neutron downscatter from group No. 15 to group No. 16. Note, therefore, that all of the data presented of spatial and energy distributions of the thermal neutron flux have been obtained from calculations wherein the cross section for net downscatter to group No. 16 might be somewhat high. Thus, perhaps the ITC spectrum is harder than the curves indicate. This is discussed in additional detail in the later section on ITC flux spectra.

It should be noted that the magnitudes of these effects of spectra hardening on the absolute rate of neutron capture by 1/v targets in the ITC are not very large (see section on thermal neutron flux spectra). On the other hand, even a change of, say, 5% is significant to the production of ultra-heavy isotopes, since these productions will require chains of neutron bombardments. What may be of greater importance in determining production rates in chains where one or more isotopes might be non-1/v absorbers is that if the ratio (group-16 flux/group-15 flux) is in the neighborhood of 4 rather than 7, the group-15 fraction of the neutron flux in the energy range 0 to 0.4 eV is ~0.2 rather than ~0.13, or a 50% increase. The effects of ITC flux spectrum on production rates of ultra-heavy isotopes in AARR are yet to be studied in detail.

## Range of Flux-Perturbation Effects of Reactivity Control and of ITC Type

Calculations of the absolute thermal neutron flux in the ITC of the operating fresh reactor have been made for two principal idealized configurations of the reactivity-control rods: (1) control rods withdrawn fully, and aluminum rod-followers in place in and beyond the active core zone; and (2) poison sections of the control rods inserted and matched. All fluxes shown are for the fresh reactor, without xenon, operating at a total fission power level of 100 MW. These configurations are idealized in the sense that this system would be supercritical with all control rods withdrawn, and subcritical with the black portions of all control rods inserted.

The reference control rods of the AARR are identical to the HFIR rods.[1] There are four arcs, essentially cir-

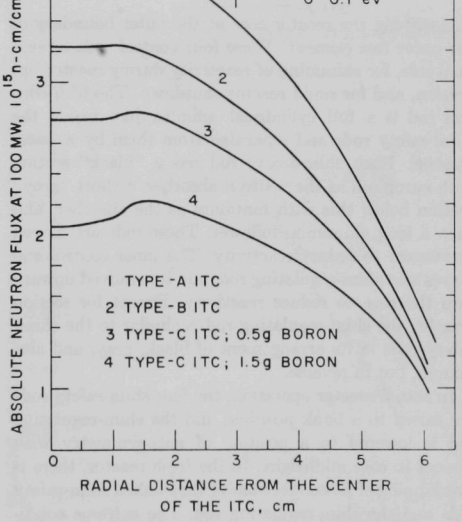


FIG. II-20-2. Radial Distributions of (Peak) Group-16 Neutron Flux at Core Midheight for Power of 100 MW in Fresh Reactor (Control Rods Withdrawn). *ANL Neg. No. 112-9428.*

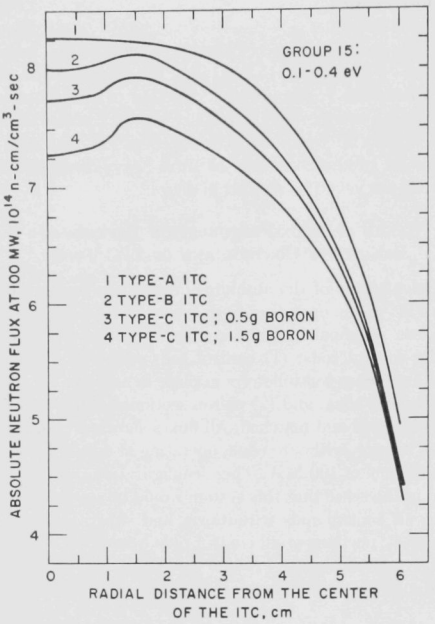


FIG. II-20-3. Radial Distributions of (Peak) Group-15 Neutron Flux at Core Midheight for Power of 100 MW in Fresh Reactor (Control Rods Withdrawn). *ANL Neg. No. 112-9427.*

cumscribing the reactor core at the outer boundary of the outer fuel element. These four control rods serve a dual role, for shimming of reactivity during reactor operation, and for rapid reactor shutdown. The fifth control rod is a full cylindrical annulus just inside the shim-safety rods and separated from them by a water channel. Each shim-safety rod has a "black" section with europium as the neutron absorber, a short "gray" section below this with tantalum as the absorber, and then a long aluminum follower. These rods are moved downward to reduce reactivity. The inner control rod serves as a shim-regulating rod, and it is moved upward into the core to reduce reactivity. Except for section lengths, the shim-regulating rod is similar to the shim-safety rods in its arrangement of black, gray, and aluminum, but in reverse.

In actual reactor operation, the four shim-safety rods are raised to a bank position, and the shim-regulating rod is lowered to a position of anti-symmetry with respect to core midheight. In the fresh reactor, there is overlapping of poison sections of the banked shim-safety rods and the shim-regulating rod. The extreme conditions of control-rod influence on thermal neutron fluxes in the ITC occur when: (1) the rod-followers are fully inserted (minimum average ITC fluxes); or (2) the black portions of the control rods are fully inserted. The general effect of control-rod insertion for criticality is to distort the radial distribution of the power density toward the ITC, with a resulting increase in the levels of the thermal neutron flux in the ITC.

Figure II-20-2 summarizes calculated 16-group radial distributions of the group-16 neutron flux (0–0.1 eV) in the ITC of the fresh reactor at core midheight, for various ITC configurations, and for the idealized case where the control rods are fully withdrawn. Figure II-20-3 presents similar data, for group 15 (0.1–0.4 eV). In these figures and in all other figures, any neutron absorption by target nuclides is assumed to be 1/v in spectrum, and this poisoning is assumed to be uniformly distributed over the capsule volume.

Figures II-20-4 and II-20-5 present curves for groups Nos. 16 and 15, respectively, for two ITC configurations and for idealized cases where the gray or black sections of the control rods are matched.

Figures II-20-2 through II-20-5 present the peak

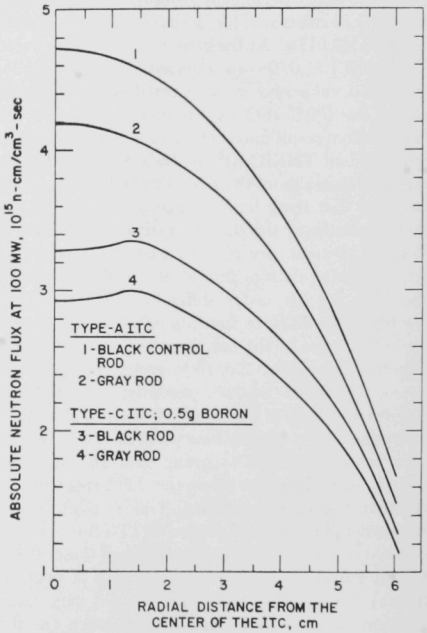


FIG. II-20-4. Radial Distributions of (Peak) Group-16 Neutron Flux at Core Midheight for Power of 100 MW in Fresh Reactor (Control-rod Poisons Inserted). *ANL Neg. No. 112-9422.*

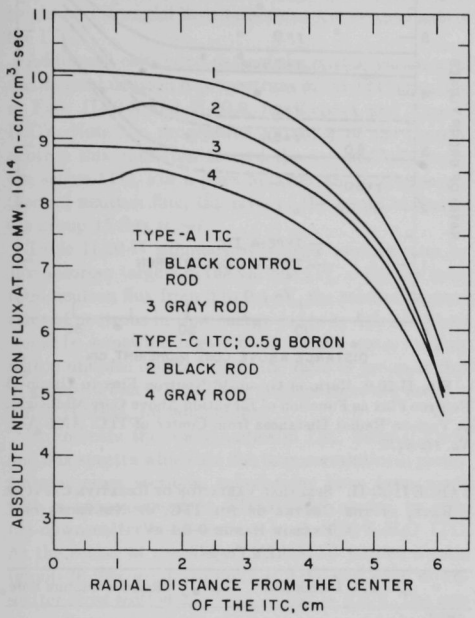


FIG. II-20-5. Radial Distributions of Peak Group-15 Neutron Flux at Core Midheight for Power of 100 MW in Fresh Reactor (Control-rod Poisons Inserted). *ANL Neg. No. 112-9426.*

fluxes, at core midheight. The data were obtained from one-dimensional calculations. In each case, a $k_{eff}$-calculation was made, with the converged neutron flux normalized to a total fission neutron production rate corresponding to the reactor operation at 100 MW in the actual active portion of the reactor core. The calculated fluxes result from slowing down and diffusion of these virgin source neutrons. It is emphasized once again that these are preliminary results, indicating the influences of the control rods on ITC fluxes. Future analyses will represent control rod positions more realistically, in two space dimensions $(r,z)$ and for various stages of fuel burnup.

Referring to Figs. II-20-2 and II-20-3, and using the Type-A ITC as a standard of comparison, note that displacement of water by aluminum tubing and capsules lowers the peak and average thermal neutron flux in the ITC. Addition of target poisons further reduces the neutron fluxes in the ITC, but the present reference maximum neutron poisoning by target nuclides is small enough that this additional neutron poisoning causes only a small additional percentage reduction.

## Thermal Neutron Flux Spectra and Neutron Capture by 1/v-Targets in the ITC

In an earlier section, on models of the multigroup calculations, uncertainties in the specification of cross sections for net downscatter from group No. 15 to group No. 16 were discussed. All of the calculations indicate that the thermal neutron flux in the ITC is distorted from a Maxwellian spectrum. Even at the center of the ITC, the calculated spectrum is harder than the Maxwellian at ITC temperature. Indeed, it is harder than the thermal spectrum in an infinite medium of water containing a spatially uniform source of epithermal-energy neutrons. The spectrum hardening in the ITC is most pronounced near the outer radius of the ITC, i.e., near the inner surface of the fuel zone. This state of affairs may prove to be useful for irradiations of some target nuclides.

In view of the spectral distortion of the thermal neutron flux in the ITC, the spatial distributions and the magnitudes of the total thermal neutron flux, say, the sum of the fluxes in groups Nos. 15 and 16 (0–0.4 eV) are of less interest and utility than are the fluxes for the component groups and the capture rates by target nuclides.

Figures II-20-2 through II-20-5, preceding, sum-

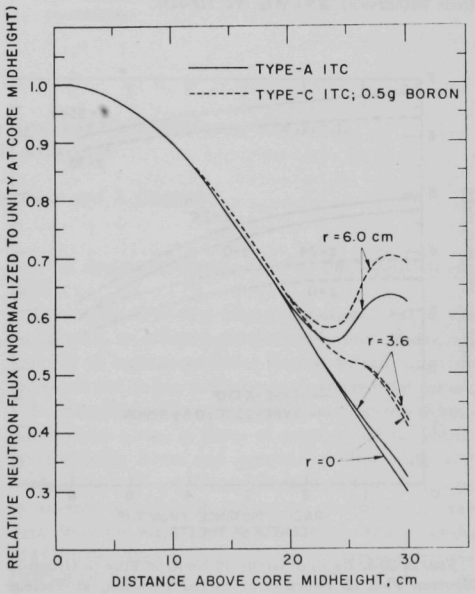


FIG. II-20-6. Relative Axial Distributions of Group-16 Neutron Flux at Various Radial Locations in the ITC (Control Rods Withdrawn). *ANL Neg. No. 112-9409.*

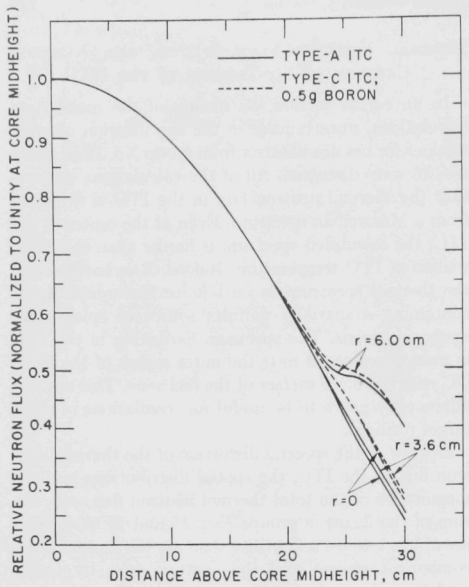


FIG. II-20-7. Relative Axial Distributions of Group-15 Neutron Flux at Various Radial Locations in the ITC (Control Rods Withdrawn). *ANL Neg. No. 112-9425.*

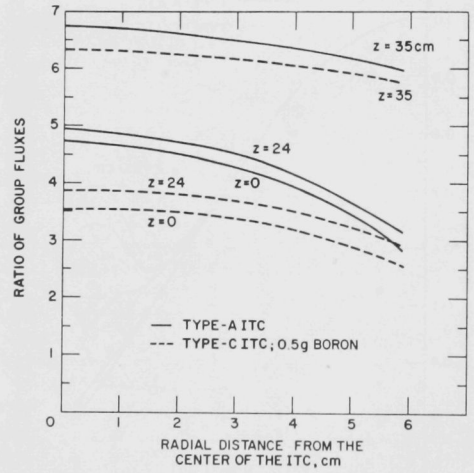


FIG. II-20-8. Ratio of Group-16 Neutron Flux to Group-15 Neutron Flux as Function of Radial Location, at Various Elevations, Z, above Core Midheight (Control Rods Withdrawn). *ANL Neg. No. 112-9429.*

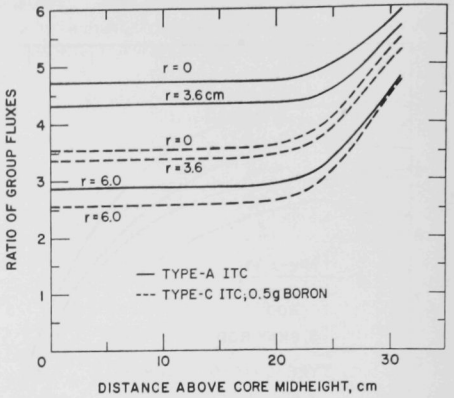


FIG. II-20-9. Ratio of Group-16 Neutron Flux to Group-15 Neutron Flux as Function of Elevation Above Core Midheight, at Various Radial Distances from Center of ITC. *ANL Neg. No. 112-9418.*

TABLE II-20-II. SPECTRAL VARIATION OF RELATIVE CAPTURE RATE, AT THE CENTER OF THE ITC, OF NEUTRONS OF ENERGY RANGE 0–0.4 eV

(1/*v* Target)

| ITC Description | Relative Capture Rate |
|---|---|
| Type-A ITC | 0.98[a] |
| Type-B ITC | 0.96[a] |
| Type-C ITC, 0.5 g boron | 0.95[a] |
| Type-C ITC, 1.5 g boron | 0.93[a] |
| Type-A ITC | 0.96[b] |

[a] These rates are normalized to unit capture rate in an infinite water medium with a spatially uniform high-energy neutron source, and also to a fixed value of the total thermal neutron flux between 0 and 0.4 eV (groups Nos. 15 plus 16). All values are based upon $\Sigma_{S_{net}}^{H_2O}(15 \rightarrow 16) = 0.095$ for the ITC water.

[b] This value is based upon $\Sigma_{S_{net}}^{H_2O}(15 \rightarrow 16) = 0.079$ for the ITC water.

marize calculated absolute distributions of component fluxes for various idealized cases. These curves are based upon 16-group calculations. Figures II-20-6 and II-20-7, for two-dimensional, 6-group calculations, display the calculated axial variation of the group-16 and group-15 neutron fluxes at various radial locations in the 100%-$H_2O$ ITC (Type A). Each curve is normalized to unity at core midheight. Note that over the interior of this ITC assembly the two-dimensional thermal neutron fluxes in the fresh reactor are almost separable into

simple products of the radial distributions at core mid-height and the axial distributions at the vertical axis of the ITC.

Additional calculated data of the spatial variation of the thermal neutron flux spectrum in the ITC are given in Figs. II-20-8 and II-20-9, for Type-A and Type-C ITC's. Note the progressive softening of the thermal neutron flux spectrum toward the top and bottom of the active ITC. For a pure Maxwellian distribution of thermal neutron flux, the ratio of the group-16 flux to the group-15 flux is ~7.

Table II-20-II summarizes relative capture rates by 1/v-absorber targets in the various ITC's. For the same total neutron flux from 0 to 0.4 eV, the relative capture rates of neutrons in that energy range by 1/v absorbers would be somewhat higher in an infinite water medium with a uniform source, where the ratio of group-16 flux to group-15 flux is 6.5. These capture rates are listed in Table II-20-II, for comparison.

To indicate the uncertainties in ITC thermal fluxes and flux spectra which are due to uncertainties in group-transfer cross sections, calculations have been made with a space-dependent THERMOS model[7] to infer net-downscatter cross sections in the 100%-$H_2O$ ITC. At the center of the ITC, THERMOS yielded a ratio (group-16 flux/group-15 flux) = 3.96, and a net down-scatter cross section $\Sigma_{s_{net}}^{H_2O}$ (15 → 16) = 0.079. The corresponding ratio obtained at the center of the ITC, when this cross section is used in a 16-group reactor calculation, is 3.92. (The ratio shown in Fig. II-20-8 is 4.7.) For this case, the calculated value of the absolute group-16 flux at the center of the 100%-$H_2O$ ITC is ~3% lower than the value inferred with $\Sigma_{s_{net}}^{H_2O}$ (15 → 16) = 0.095. The group-15 flux is higher by ~15%. The total flux in groups Nos. 15 plus 16 is unchanged.

### References


1. G. E. Hansen and W. H. Roach, *Six and Sixteen Group Cross Sections for Fast and Intermediate Critical Assemblies*, LAMS-2543 (December 1961).
2. G. K. Leaf, A. S. Kennedy and G. J. Jensen, *ANL-CANDID, A Two-Dimensional Diffusion Theory Code Based on CANDID2D*, ANL-7305, (to be published).
3. B. J. Toppel and I. Baksys, *The Argonne-Revised THERMOS Code*, ANL-7023 (1965).
4. D. A. Meneley, L. C. Kvitek and D. M. O'Shea, *MACH 1, A One-Dimensional Diffusion-Theory Package*, ANL-7223 (1966).
5. D. H. Shaftman, C. N. Kelber, B. N. Kristianson and R. P. Savio, *Argonne Advanced Research Reactor Calculations—Analysis of Criticality-Facility Loadings*, Reactor Physics Division Annual Report, July 1, 1964 to June 30, 1965, ANL-7110, pp. 51-60.
6. D. H. Shaftman and R. P. Savio, *Argonne Advanced Research Reactor Calculations—General Reactor Physics Design Analyses*, Reactor Physics Division Annual Report, July 1, 1965 to June 30, 1966, ANL-7210, pp. 82-92.
7. D. A. Sargis, Argonne National Laboratory (private communication).


## II-21. Argonne Advanced Research Reactor Calculations—General Shield-Design Analysis

A. E. McArthy, D. H. Shaftman and I. Charak*

### Introduction

The general shield-design analyses for the AARR in FY-1967 have included the following categories of activities:

1. collaboration with the Architect-Engineer in establishing the design of plant shielding against radiation sources outside the reactor pressure vessel;

2. determination of the sources of radiation in the primary-coolant water, and radiation source levels at the outer surface of the reactor pressure vessel;

3. analysis of radial and axial distributions of heating rates in: (a) the beryllium reflector sectors; (b) experimenters' facilities within the reactor vessel; (c) structures supporting the reactor core and reflectors; (d) the neutron windows; and (e) the reactor vessel itself;

4. analysis of neutron flux distributions: (a) at the vessel wall, to estimate rates of radiation damaging; and (b) in instrument tubes located within the reactor vessel and in two sectors outside the reactor vessel;

5. evaluation of the relative merits of various shielding-analysis codes, in terms of accuracy of the calculated neutron fluxes and gamma-ray dose rates and heating rates. The primary purpose of this work was to attempt to establish factors of uncertainty in the data inferred from calculations using the program MAC(1) as adapted and modified by Argonne for the CDC-3600 computer.[2] This code has been the basic working tool for analyses in categories Nos. 3 and 4 above. A secondary purpose was to provide checks for

* Reactor Engineering Division, Argonne National Laboratory.

evaluation of levels of accuracy to be expected from the composite of programs NRN[3] and QAD[4], selected by the Architect-Engineer for the evaluation of heating rates and biological dose rates in regions outside the reactor pressure vessel during reactor operation at power.

The intent of this paper is to report on the status of the various activities of shielding design and analysis at the conclusion of FY-1967, and to summarize significant conclusions of the work performed during FY-1967. These broad activities will be continued, to various degrees, in FY-1968.

In the third quarter of FY-1967 it was discovered that the computations of neutron fluxes in the instrument-tube zones beyond the reactor pressure vessel were seriously in error. Also, comparisons of heating rates, inferred from Argonne-MAC computations and from computations with other programs, were begun late in FY-1967, and this work is continuing into FY-1968. Preliminary results indicate that the operating gamma-ray heating rates in the beryllium, inferred from the Argonne version of the MAC program on the CDC-3600 computer, may be quite conservative. Therefore, it has been decided to limit the present reporting of detailed quantitative results of MAC computations to essential comparisons.

## Design of Neutron Window and Neutron-Detector Environment

In the Reactor Physics Division Annual Report for FY-1966[5], a report with this identical title was presented on analyses performed with the Argonne-MAC program. At that time, the reference reactor design included a heavily loaded reactor core with stainless steel-clad cermet fuel plates. The design of the neutron windows was complicated by the necessity of reducing radiation-damage rates of the reactor pressure vessel which at that time was a carbon steel vessel with a stainless steel cladding. It was therefore essential to alter the spectrum and intensities of the high-energy neutron flux at the vessel wall, and, at the same time, to obtain high thermal neutron fluxes in the instrument-tube zones beyond the reactor vessel for purposes of reactor operation. To accomplish these purposes, a composite neutron window was designed. The window included a thick zone of stainless steel, to attenuate the high-energy neutron flux by inelastic scattering, with a zone of aluminum beyond the steel, to permit transport of above-thermal neutrons. These computations also indicated that there would be a significant gain in the thermal neutron flux in the instrument-tube zone if the volume fraction of water in that zone was severly limited and some beryllium was introduced into the tube. The preliminary designs of neutron window and instrument-tube zone appeared to resolve the basic design problems.

The Argonne-MAC program had been applied to the calculation of thermal neutron fluxes in a simplified simulation of aluminum windows in the AARR Criticality Facility. There was reasonable agreement between measured and calculated thermal neutron fluxes, and this indicated that these computations should be adequate for the actual design of the window and instrument-tube details. Neither experiment nor analysis probed effects of water gaps needed for clearances. In fact, as discovered early in calendar year 1967, there are deficiencies in the Argonne-MAC computations of the window problem, and the window results presented in Ref. 5 are erroneous.

The pressure-vessel material, and the reactor core and reflector compositions and sizes all were changed in FY-1967. It was decided to use a solid stainless steel vessel, and this has essentially eliminated concern about radiation-damage effects to the vessel regions adjacent to the neutron windows. With this constraint removed, it appeared that the neutron window could be simplified, and Argonne-MAC computations were made for windows of aluminum with a small percentage (1%–2%) of coolant water. The window design was then examined in greater detail, to investigate perturbations of the neutron flux in the instrument-tube zone when water channels were introduced for clearances in installing the aluminum window. Clearances were required at the outside of the beryllium reflector and between the window and the inside wall of the reactor vessel. An additional water channel (¼ in. thick) is needed at the outer surface of the reactor vessel; this water gap had been included in the earlier design window analysis. Other refinements of the design included a small increase in the thickness of the lead gamma-ray shield before the instrument-tube zone, a reduction in the size of the instrument tubes, and the introduction of a 1½-in.-thick lead gamma-ray shield after the instrument tubes.

Neutron-flux computations for these configurations were made with the Argonne-MAC program in spherical geometry, varying the percentage of water in the aluminum window. At 100 MW, sphere-geometry thermal neutron fluxes of $\sim 1 \times 10^{10}$ were indicated in the centers of the instrument tubes, in the absence of perturbations by the neutron detectors that would be inserted into the tubes. This level compared with a hoped-for value of $2 \times 10^{9}$, or more, for the thermal neutron flux in the detectors at design reactor power (100 MW).

Subsequently, a more detailed investigation was made of the effects on the detector flux arising from variations in the beryllium reflector due to insertions

of materials into experimenters' facilities. For these analyses, the reflector was partitioned into a larger number of regions. To stay within the MAC limitation of 20 regions, the ¼-in.-thick water channel between the reactor vessel and the lead shield was deleted in the analysis. The result was a calculated reduction in the thermal neutron flux to one-tenth of the level indicated with that water channel included. Additional computations were made to be certain that the indicated reduction was not a spurious result solely due to not using a fine enough spatial partition of the water channel and neighboring regions. To investigate this matter further, calculations were made with the code DSN[6] in slab geometry, to examine the local effects of water channels in such an environment. The neutron source was a plane source at an inner boundary which was taken to be at a point in the aluminum window, some 6 in. away from the inner wall of the reactor vessel. The result of the DSN computations was that the effect of the thin water gap was small—a matter of ~10% change in the thermal fluxes in the instrument-tube zone.

The abovementioned Argonne-MAC computations were made in spherical geometry. Additional calculations were made in slab geometry. Except for geometry, the problems were identical to the sphere problems. In the case of slab geometry, the calculated effect of introducing the ¼-in.-thick water gap was a doubling of the thermal neutron flux in the instrument tube zone. Thus, the error is smaller in slab geometry, but it is still unacceptably large for this purpose of window analysis. It has not been determined whether there are inadequacies in the basic formulation of MAC, perhaps in the numerical analysis when steep gradients occur, as in these gap problems. There may also be undetected errors in the locally generated subroutines which are used in curved geometry calculations. In any event, the Argonne-MAC calculations of neutron flux yielded grossly incorrect neutron fluxes.

In view of the uncertainties in these calculations of thermal neutron flux in the instrument-tube zone, check calculations are being made with other computing programs. The Architect-Engineer, for example, will use the code NRN[3] to compute neutron fluxes beyond the reactor vessel, and these computations will also provide data of the distribution of thermal neutron flux in the instrument-tube zone.

At Argonne's request, H. C. Claiborne and F. R. Mynatt, of Oak Ridge National Laboratory, are applying the ORNL Code ANISN[7] to obtain neutron flux distributions. One result, obtained early in FY-1968, is that the presence of the abovementioned thin water channel at the outer surface of the reactor vessel causes a *reduction* of ~20% in the thermal neutron flux in the instrument-tube zones outside the vessel. Another result of the ANISN work is that there is little or no increase in the thermal neutron flux in the instrument-tube zone when beryllium is introduced to fill a void to the extent of 40% of the volume of that zone. Both results are opposite to results obtained with the Argonne-MAC program (see Ref. 5).

The ANISN result, corrected for geometry effects, is that the unperturbed thermal neutron flux in the instrument-tube zone is $\sim 2 \times 10^9$ at 100 MW, with the new window design, including the effects of the water gap and including 2% water in the window. This flux is approximately five times the flux inferred from comparable Argonne-MAC computations which were made with the troublesome water gap omitted. The ANISN calculations were performed with an $S_{10}$ discrete-ordinate partition and with $P_3$ Legendre expansions of the angular distributions of neutron scattering.

Concurrently, recently developed wide-range circuitry is being evaluated for possible application in the AARR. The intent would be to modify the nuclear channels associated with neutron detectors in instrument tubes inside the reactor vessel so as to provide wider-range detectors in instrument channels for detectors positioned in regions of higher thermal neutron flux. It is anticipated that an adequate margin of reactor control would be provided if a perturbed thermal neutron flux of $7 \times 10^8$ could be attained in the out-of-vessel neutron detectors. The intent is to provide an adequate coverage of the entire significant range of reactor powers even if the thermal neutron flux in the out-of-vessel detectors proved to be somewhat lower than is now indicated by ANISN. Also, it is important to minimize the net water content between the beryllium reflector and the instrument-tube zone, and this will be considered in the design.

It is intended that a "design critical" experiment will be performed in FY-1969 or FY-1970. At that time, direct measurements could be made with well simulated conditions of reactor design, to provide further confirmation of the adequacy of the neutron-window design.

## AARR Plant Shield Design

In Fiscal Year-1967, the Title-II shield design proceeded for the plant. The scope of the shield-design work by the Architect-Engineer comprises all of the AARR facilities outside the reactor pressure vessel. An exception to this scope is that, in analyzing radiation levels at the outside surface of the bulk radial biological shield, streaming in penetrations by beam tubes and through tubes are excluded. These penetrations offer special problems, and the designs of the

tubes and analysis of the radiation streaming now are in the direct purview of the work by Argonne National Laboratory.

The principal activities of the Reactor Physics Division for the shield design work in FY-1967 have been: refinement of the shielding criteria set for the Title-I work; collaboration with the Architect-Engineer in establishing priorities for their detailed shield-design effort, and in the general scoping of the significant problems of shield-design; review of the methods and computer programs proposed by the Architect-Engineer for shield-design analysis; setting of radiation source intensities in the primary-coolant water; collaboration in establishing neutron group cross sections for multigroup computations of neutron flux distributions; and continuing review of the results of the shield-design analysis, in terms of the degrees of accuracy which are to be expected from the calculations, the adequacy of the preliminary-design shield, and evaluation of design changes proposed by the Architect-Engineer to resolve indicated problems of radiation shielding. It is the responsibility of the Architect-Engineer to ensure that, in developing the detailed design of the entire plant, the criteria of radiation shielding are met. This has required also a continuing review by Argonne staff both of the Architect-Engineer work on general plant design and of the work by other Argonne engineers on certain aspects of the plant design.

TABLE II-21-I. Design Dose Rates to Personnel[a]

| Location | Design Dose Rate |
|---|---|
| Outer surface of lateral biological shield[b] | ¼ mrem/hr, at 100 MW |
| Surface of Reactor Pool, above the reactor | 5 mrem/hr, at 100 MW |
| Top surfaces of pools and canals, with "hot" material in storage | ¼ mrem/hr |
| Top surfaces of pools and canals, with "hot" material in transit | 5 mrem/hr at an elevation of 3 ft above the surface |
| Control Rod Drive Access Room | 25 mrem/hr, at 100 MW |
| General background on Experiment Floor | ¼ mrem/hr at an elevation of 3 ft above the floor slab, at 100 MW |
| Outer surface of shield wall of primary-demineralizer cell | 10 rem/hr, 24 hr after core melt |
| General background for limited-access areas of Service Floor of Reactor Containment Building | 5 mrem/hr, at 100 MW |

[a] The design dose rates include radiations from all normal sources, unless otherwise indicated. The design dose rates given in this table may be exceeded where normal personnel access is physically impossible.

[b] Radiation streaming in beam tubes and through tubes is not included. Special criteria for "hot spots", i.e., locally high radiation levels, will be developed.

### CRITERIA FOR PLANT SHIELDING OF PERSONNEL AGAINST RADIATION

The criteria of allowable design radiation dose rates to personnel have been revised from the criteria set for the Title-I design. The changes reflect implications of the results of the Title-I work and a change in the philosophy of accessibility of personnel to certain areas of the Service Floor of the Reactor Containment Building.

Equipment and piping runs on the Service Floor are being rearranged to separate the Service Floor into two principal zones. In general, equipment and piping which will contain high-intensity sources of radiation during reactor operation will be located on a "hot" (west) side of the Service Floor, which will be closed to personnel during reactor operation. Included in this category are piping runs for primary-coolant water coming from the reactor, primary-coolant pumps, and heat exchangers for the primary system. Demineralizers and filters for the primary system will be located in shielded compartments. On the "cold" (east) side of the Service Floor will be equipment which can be easily shielded against radiations during reactor operation, and to which controlled access is both desirable and feasible during normal reactor operation. An important example is the Control Rod Drive Access Room, which is below the reactor vessel and is well shielded against radiations from the core and other sources.

Table II-21-I summarizes revised allowed design dose rates based on radiations from all sources. This tabulation constitutes direction to the Architect-Engineer in establishing the detailed plant design. As the Title-II design proceeds, additional detailed criteria for shield design will be developed, and possibly there will be modifications of some of the criteria listed in Table II-21-I.

The levels of radiation sources and attenuation distances are determined as follows:

1. The reactor, with a HFIR-type core, is assumed to have operated at 100 MW continuously for 30 full-power days before shutdown.

2. It is assumed that before normal transfer of spent fuel elements to storage the fuel has cooled for six hours after a prompt reactor shutdown from normal operation at full power. It is assumed that spent fuel elements will be transferred along paths with fixed

minimum distances from the fuel element to pool walls. It is further assumed that the freshly spent fuel element will be stored in a location in the storage rack so that there will be a minimum distance from fuel to pool walls while the fuel is decaying to levels which will permit later shifting to new storage locations for the remaining time of its storage before transfer out of that pool.

3. It is assumed that non-defective fuel elements will be stored in the Spent Core Storage Pool for 8 months after reactor shutdown, prior to their transfer out of the Reactor Containment Building and shipment for reprocessing.

4. In the event of a reactor accident which released additional sources of radiation as a result of some fuel melting, but which did not result in breaching of the primary-system containment, it is assumed that no personnel will enter the Service Floor for a certain minimum time after reactor shutdown. The design dose rates for such conditions will be chosen to correspond to certain cooling times and to certain assumed concentrations of radiation sources following an accident. The design concentrations are established at: 0.5% of the total core inventory of fission products other than the noble gases, in the primary-coolant demineralizers and filters; 0.05% of the total core inventory of fission products, in the pool and canal demineralizers.

### STATUS OF THE PLANT SHIELD DESIGN

In FY-1967, basic analyses of gamma-ray radiation dose rates were performed using standard formulas[8,9] for calculations of gamma-ray flux for:

1. the water purification system, including the demineralizers and filters for the primary-coolant system;

2. pools and canals, during transfer of spent fuel from the reactor vessel to the Spent Core Storage Pool, and during storage of this fuel;

3. the Service Floor and the Experiment Floor in the Reactor Containment Building, including effects of all radiations from: (a) the piping runs, pumps, and heat exchangers for the primary-coolant water, on the Service Floor; and (b) the primary-coolant water purification system. However, detailed calculations have not yet been made for radiation dose rates due to radiation penetrating the bulk reactor biological shields.

The analyses of the shielding of the primary-coolant purification system have delineated details of the thicknesses of walls serving both as structural and shielding walls. Under normal conditions of reactor operation, the dominant radiation is the gamma-ray activity from sodium-24, produced by neutron capture in the aluminum in the reactor core and in the various experimenters' facilities. The sodium-24 is trapped by ion exchange in the primary coolant cation bed. Other activants have been considered, e.g., magnesium-27, and it has been shown that the sodium-24 determines the radiation doses from this system both because of its level of concentration and activity and because of the relatively high penetrability of the gamma rays emitted by the sodium. Radiation from materials trapped by the filters is negligible, by comparison with radiation from the demineralizers.

The analyses of gamma-ray dose rates from spent fuel, during transfer and in storage, have resulted in modifications of the design. The gate between the Reactor Pool and the Spent Core Storage Pool has been shifted so as to be essentially centered laterally in the wall separating these two pools, to increase the shielding thickness of the pool water during transfer of spent fuel. The storage racks for the spent fuel, in the Spent Core Storage Pool, have been located to provide enough attenuation by the pool water to reduce biological dose rates and to satisfy dose-rate criteria, and also to reduce the heating rates in the walls and floor of the pool, arising from capture of gamma-rays emitted by the spent fuel. It has been decided also to store freshly spent fuel only in certain storage cells, so that thermal shielding of the pool walls will not be required. An additional ½-ft thickness of water shielding will be provided by lengthening the support structure of the fuel-storage racks; this will eliminate the need for thermal shielding of the pool floor.

Other potential problems have been discovered of high radiation dose rates to personnel during transfer of spent fuel, because of certain design penetrations of pool walls. The magnitudes of these dose rates, and solutions to the problems, will be investigated in FY-1968.

The dominant radiation source in the primary-coolant piping runs, pumps, and heat exchangers is N-16, produced by $O^{16}(n,p)N^{16}$ reactions in the reactor water during power operation. N-16 has a short half life (~7 sec), and it emits high-energy gamma-rays (6–7 MeV) which are highly penetrating in shield materials. To protect personnel on the Experiment Floor in the area above the "hot" side of the Service Floor, a floor slab thickness of 6 ft of ordinary concrete is required. Actually, this floor-slab thickness is determined by structural and load-support requirements, and coincidentally it is calculated that with this thickness of concrete the relevant dose rate criteria (Table II-21-I) are met.

These preliminary Title-II dose-rate analyses have been reviewed by Argonne National Laboratory, and

milestone reports by the Architect-Engineer are being prepared.

Scoping calculations have been made to estimate the radiation dose rates at the outside surface of the reactor bulk lateral biological shield. To provide access to beam-tube facilities, the inner radius of the concrete biological shield has been increased by 1 ft, and the thickness of the shield has been reduced accordingly, from 8 ft to 7 ft. The scoping analysis has indicated that the revised shield should be conservatively adequate.

For detailed calculation of neutron flux distributions in the lateral and axial shields during reactor operation, it has been decided to use the computing program NRN.[3] These calculated neutron fluxes will be used to generate capture-gamma source distributions for detailed calculations of gamma-ray fluxes with the computing program QAD.[4] QAD is a kernel-integration code programmed by scientists of the Los Alamos Scientific Laboratory. The QAD analysis will also account for the other gamma-ray sources, including gamma rays generated during fission, by decay of fission products, and by various other reactions of neutrons with matter. In preparation for the NRN analysis, the Architect-Engineer is testing the various routines in the NRN code. The NRN library of neutron cross sections is being revised to incorporate more recent measurements, with guidance by Argonne scientists as to suitable sources of neutron cross section data.

When the NRN/QAD package is readied, calculations will be made of radiation-dose-rate distributions along various ray paths emanating from the reactor core. Paths chosen will be representative of radial, axial, and slant directions of significance to the evaluation of the design shielding of radiations from zones within the reactor pressure vessel.

Studies will be made of radiation dose rates to personnel inside the Laboratory and Office Building or in the Active Material Handling Building, following a postulated maximum credible accident. Scoping calculations were reported previously (see Ref. 5). The new calculations will be more detailed, and doses at other locations will be evaluated.

### Miscellaneous Calculations

Reactor Physics Division work has included also: analyses of the preliminary design shields within the reactor pressure vessel; and heating rates in the beryllium reflector, in neutron windows, and in the reactor pressure vessel.

For the most part, the calculations of gamma-ray dose rates and heating rates have been made with the Argonne-MAC program. The calculated gamma-ray heating rate at the inside surface of the beryllium reflector is much larger than the gamma-ray heating rate obtained by scientists of Oak Ridge National Laboratory for the HFIR.[10] Indeed, the values obtained with Argonne-MAC are approximately 60% higher, for a case where the differences between the AARR and the HFIR are considered to be insignificant. The Argonne-MAC calculations were perforce made in slab geometry, and the effect of this approximation of geometry should be to yield somewhat higher heating rates. Toward the end of FY-1967, neutron-flux calculations were begun with the ANISN program; these calculations are being made by scientists of ORNL, with the cooperation of H. C. Claiborne and F. R. Mynatt (ORNL). Preliminary results were obtained early in FY-1968 which confirm the HFIR results and imply that the Argonne-MAC data of gamma-ray heating rates in the radial beryllium reflector near the reactor core are quite conservative—approximately twice as high as the ANISN data. The ANISN computations were made in cylindrical geometry. Additional computations will be made, to investigate the effects of the slab-geometry approximation in the Argonne-MAC analyses, and to include capture-gamma production in the beryllium reflector.

In FY-1968, it is intended also that the NRN/QAD package will be applied to calculations of gamma-ray dose rates and heating rates in various regions within the reactor pressure vessel.

In view of the present uncertainties regarding heating-rate calculations based on Argonne-MAC output, no detailed heating rates will be presented here. The heating rates in the beryllium reflector drop off rapidly with increasing radial distance from the reactor core. Close to the reactor core, the heating rates in the AARR will be essentially the same as the heating rates in the HFIR beryllium, because the fuel, control rods, and the removable-beryllium sections will duplicate the HFIR system. However, there is much more neutron-capturing material in the permanent-beryllium zone of the AARR, because there are many more experimenters' facilities in the AARR reflector. Also, the AARR beryllium reflector is much thicker. Therefore, there will be differences in the gamma-ray flux and heating-rate distributions in the AARR reflector, and additional analyses are judged to be required, in spite of the fact that the HFIR has operated at full power (100 MW) without any apparent problems about cooling of the beryllium reflector during reactor operation and after reactor shutdown.

Other analyses of the AARR have estimated the streaming of gamma-rays in thermocouple tubes which penetrate the axial shield below the reactor core. These analyses indicate that there will be highly local-

ized gamma-ray streaming which would yield no more than a few mr/hr at the bottom surface of the bottom head of the reactor pressure vessel. The analyses are for streaming in long, thin, water-filled tubes penetrating highly-attenuating zones of steel. They are therefore subject to the usual uncertainties of such difficult problems. Nevertheless such streaming is not considered to be a problem, especially since there do not appear to be high gamma-ray dose rates at the bottom head of the HFIR vessel having similar penetrations.

### References


1. E. G. Peterson, *MAC-A Bulk Shielding Code*, HW-73381 (April 1962).
2. A. E. McArthy and H. Yamanouchi, *Revision of the Bulk Shielding Code MAC for the CDC-3600 Computer*, Reactor Physics Division Annual Report, July 1, 1965 to June 30, 1966, ANL-7210, pp. 396–399.
3. L. Hjärne, et al., *A User's Manual for the NRN Shield Design Method*, AE-145 (June 1964).
4. R. E. Malenfant, *QAD—A Series of Point-Kernel General-Purpose Shielding Programs*, LA-3573 (April 1967).
5. A. E. McArthy and D. H. Shaftman, *Argonne Advanced Research Reactor Calculations—Shield-Design Analyses*, Reactor Physics Division Annual Report, July 1, 1965 to June 30, 1966, ANL-7210, pp. 100–104.
6. B. Carlson, C. Lee and J. Worlton, *The DSN and TDC Neutron Transport Codes*, LAMS-2346 (October 1959).
7. W. W. Engle, Jr., *A User's Manual for ANISN—A One Dimensional Discrete Ordinates Transport Code with Anisotropic Scattering*, K-1693 (March 1967).
8. T. Rockwell III, Ed., *Reactor Shielding Design Manual*, (D. Van Nostrand Company, Inc., Princeton, N. J., 1956).
9. E. P. Blizard, Ed., *Reactor Handbook, Volume III, Part B, Shielding*, Second Edition (Interscience Publishers, 1962).
10. D. R. Vondy, unpublished Oak Ridge National Laboratory internal memorandum.


## II-22. Argonne Advanced Research Reactor Calculations—Analyses of Accidents Associated with Major Reactivity Insertions

D. H. Shaftman and J. H. Tessier*

### Introduction

The Reactor Physics Division Annual Report for July 1, 1965 to June 30, 1966[1] includes a summary of analyses of specific postulated reactivity accidents which appeared in an unpublished Preliminary Safety Analysis Report (PSAR) for the earlier AARR. For that system, the design reactor power level was 100 MW, and a heavily loaded, intermediate-spectrum reactor core was designated as the reference core. Subsequently, a budgetary decision was made to adopt the designs of the core, reactivity-control rods and control-rod drives, and removable beryllium reflectors of the High-Flux Isotope Reactor (HFIR)[2] of Oak Ridge National Laboratory (ORNL). The PSAR for the AARR has been revised to reflect these changes in the plant. In some cases, analyses of specific postulated reactivity accidents simply have been copied from the final accident analysis report and supplements and addenda for the HFIR.[3] With the cooperation of scientists of ORNL, additional safety analyses have been performed with the HFIR analog network at ORNL. Specific postulated reactivity accidents were evaluated, with parameters appropriate to AARR conditions, including a cold-water accident, and massive partial voidings of coolant ($H_2O$) in the Internal Thermal Column (ITC). The ITC of the Argonne reactor is intended for research-type neutron irradiations rather than for larger scale production of specific isotopes, which is the case for the HFIR. The designs of the ITC insert are sufficiently different from the HFIR design that separate analysis is required.

The postulated cold-water accident would result in the addition of approximately one dollar in reactivity, with the reactor operating initially at 100 MW and with conservative assumptions of gross reactivity coefficients of temperature. Massive partial voidings of water in the ITC would result in reactivity insertions ranging up to 4½ dollars (3.2%). Therefore, these postulated accidents are associated with major reactivity insertions, and they are reviewed in the present paper. The conclusions are: (1) with normal response of the safety system, the excursions would be limited without any melting of reactor fuel; and (2) even without safety-system response, the consequences of such accidents are not severe enough to rupture the primary-coolant containment.

Two simplified models of reactor response to hypothetical rapid reactivity insertions of several dollars or more are presented in the final section of this paper, and computational results are given for step-function

* Reactor Engineering Division, Argonne National Laboratory.

and short-period-ramp injections of one to seven dollars in reactivity, with the reactor operating initially at 100 MW. The intent of this preliminary analysis is to demonstrate that even without safety-system response there would not be a prompt massive metal-water reaction of the fuel plates, which is an important consideration in the evaluation of the survival potential of the containment boundary of the primary coolant.

The HFIR accident analysis report (Ref. 3) summarizes hypothetical major reactivity additions stemming from control-rod accidents where: (1) all 5 control rods are driven out at the maximum speeds of their drives; or (2) the shim-regulating control rod is driven out because of a mechanical failure of the drive mechanism. In these cases, it was shown that, whereas the potential total reactivity insertions are large, the reactivity addition rates are small enough that safety-system action would shut down the reactor without serious core damage, and, in particular, without any melting of fuel plates.

### Model of Safety-System Response

In the PSAR computations of the responses of the reactor to the postulated cold-water accident and ITC-voiding accident, the safety-system model employed was for Mode 1 operation of the HFIR. (See Ref. 3, pp. 73–74.) In this mode, designed for cases of pressurized operation, detection of either of two abnormal changes in operating conditions will signal for reactor shutdown by rapid injection of the four safety control rods. The two abnormalities are: (1) a high ratio of power level to coolant flow rate, with trip point set at 1.3 times the normal ratio; and (2) a high rate of change of power, with trip point at 20 MW/sec and with the proviso that the total change in reactor power is at least 5 MW.

When reactor shutdown is signaled, there is a time delay for delatching the safety control rods. This time delay was assumed to be 10 msec, which is the typical lag for Mode 1. Once delatched, the safety rods are accelerated downward into the active fuel zone by a combination of springs, hydraulic forces of coolant flow, and gravity. In the analog computation the safety rods were assumed to have a net initial acceleration of 4 g, and the acceleration was reduced linearly to 1 g in the first 6 in. of rod travel. Thereafter, the rods were assumed to move in at a constant acceleration of 1 g. The differential reactivity control worth depends upon the time in the core cycle. In the computations, conservative values of differential control rod worths were used. (For more details, see Ref. 3, p. 79.)

### Analysis of Hypothetical Cold-Water Accident

It is considered to be highly unlikely that a significant rapid change could occur in the temperature of coolant water entering the operating reactor core. Three separate primary-coolant heat exchangers are in operation at power, there are large mixing volumes between the heat exchangers and the core inlet, and primary-coolant temperatures will be monitored with an instrumentation system designed to protect the reactor against abnormal changes in these temperatures. Nevertheless, it is instructive to examine the consequences of a reactivity accident wherein a slug of cold water suddenly enters the reactor operating initially at 100 MW.

Accordingly, computations were made with the HFIR analog code. In these analyses it was assumed that the coolant temperature at the inlet of the operating reactor was reduced suddenly by 85°F, from 120 to 35°F, and that this temperature reduction persisted indefinitely. No credit was taken for the negative reactivity effect of a reduction in water temperature in the Internal Thermal Column. For additional conservatism, the reactivity changes corresponding to the coolant-temperature transient were calculated using the reactivity coefficients of temperature at the 100-MW values rather than at the lower transient temperatures. Neutronic, thermal, and safety-system parameters were assigned values appropriate to: (1) the fresh reactor; or (2) the end of core life. The maximum reactivity change was ~1 dollar, inserted at a constant rate over a period of 30 msec. Additional cases were studied wherein safety-system action was excluded. It was conservatively assumed that thermal insulation would occur at the fuel-plate hot spots if the peak heat flux at the outer surface of the cladding reached $3 \times 10^6$ Btu/ft$^2$-hr. This is the calculated level at which incipient boiling would occur during steady-state operation under normal conditions of coolant temperature (120°F) at the inlet to the reactor core.

Principal results of the analog computations of cold-water accidents are given in Table II-22-I. The computations imply that only moderate power excursions would occur with the safety system operating. No fuel melting would occur. It is indicated that in the event of a complete failure of the safety system there would be melting at hot spots. However, in all of the calculations no credit was taken for the added margin against incipient boiling which is provided by the increased subcooling of core coolant. If this effect were included, it is doubtful that hot-spot melting would be indicated.

TABLE II-22-I. AARR RESPONSE TO COLD-WATER ACCIDENT

| Case Number | Safety System Action | Time in Core Cycle | Peak Power, MW | Quasi-Equilibrium Power[a], MW | Integrated Power, MW-sec | Maximum Hot-Spot Metal Temp., °F | Maximum Average Metal Temp.[b], °F | Maximum Hot-Spot Heat Flux, Btu/ft²-hr | Maximum Net Positive Reactivity, $\Delta k/k$ | Time of Peak Power, msec |
|---|---|---|---|---|---|---|---|---|---|---|
| 1 | Yes | Beginning | 170 | 0 | 20 | 460 | 230 | $2.9 \times 10^6$ | 0.004 | 40 |
| 2 | No | Beginning | 240 | 200 | — | >Melting | 270 | $>3 \times 10^6$ | 0.005 | 50 |
| 3 | Yes | End | 140 | 0 | 15 | 700 | 250 | $2.6 \times 10^6$ | 0.0025 | 40 |
| 4 | No | End | 150 | 150 | — | >Melting | 250 | $>3 \times 10^6$ | 0.0035 | 60 |

[a] The reactor power level is defined here to be "in quasi-equilibrium" whenever its rate of change is small compared to the thermal response times of the reactor. For this accident, this condition is achieved immediately following the initial rapid rise in power level subsequent to the cold water insertion.

[b] This is the peak transient value of the axially and radially averaged temperature of the average fuel plate.

## Analyses of Hypothetical Reactivity Accidents Stemming from Partial Voidings of Water in the Internal Thermal Column

The Internal Thermal Column (ITC) basically is a large flux-trap zone where high-energy neutrons leaking from the reactor core are thermalized to provide a high thermal neutron flux for research-type irradiations. In the planned ITC core assembly (Fig. II-22-1), approximately two-thirds of the ITC volume is water, and it is the water that moderates the neutrons to thermal energies. Most of the remaining volume of the ITC consists of aluminum, in the form of structural material and encapsulating and diluent material for the irradiation targets. There is a small void fraction, consisting of the internal volume of the active portion of the gas-rabbit tubes.

Thus, the ITC is a large sink of neutrons. Displacement of some of the ITC water by voids would lower its reactivity control effectiveness and there would be an increase in reactivity. Also, when capsules are inserted into the hydraulic-rabbit tubes, the displacement of water is calculated to yield a small net reactivity gain. However, the largest hydraulic-rabbit tube planned for the ITC has an i.d. of 0.620 in., and the corresponding interior plan area of this tube represents only 1½% of the total cross-sectional area of the ITC. Even if the tube were initially filled with water, complete voiding of one such target tube would cause a reactivity gain of less than 0.1%. A reactivity gain of 0.1% would be managed easily by the safety system, and no damage would occur.

The hypothetical voiding accidents of greater concern are those wherein large fractions of the bulk ITC water, outside the target tubes, might be displaced by voids. The present design ITC core assembly includes a number of target tubes, but the safety analyses must also consider the implications of a possible future interest in optimizing the peak thermal

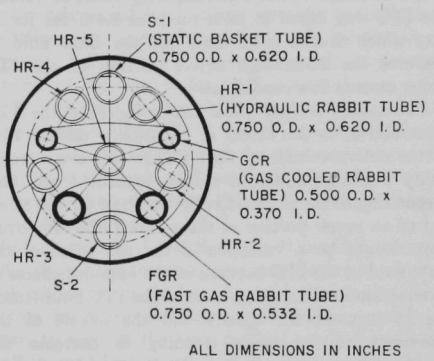


FIG II-22-1. ITC Core Assembly. *ANL Neg. No. 112-9396.*

neutron flux in the ITC for a special high-flux irradiation. For the reference ITC size, the peak thermal neutron flux would be obtained in an essentially 100%-water ITC, with a minimum volume of vertical irradiation facilities. With nothing but water initially in the ITC, the measured maximum reactivity gain resulting from uniform partial voiding of the active portion of the ITC is 3.2%. The void fraction associated with the peak reactivity gain is approximately 0.7. With the reference ITC core assembly and a full loading of irradiation capsules, the maximum change in reactivity would be reduced.

Computations have been performed at ORNL with the HFIR analog code, to study postulated reactivity accidents resulting from accidental partial voiding of water in a 100%-$H_2O$ ITC of the AARR. The AARR values of the flow rate (4 ft/sec) of bulk water in the ITC and the positive reactivity effect of such a voiding were used. Conservative values were chosen for thermal conditions, the response time of the safety system, control-rod reactivity worths, and reactivity coeffi-

TABLE II-22-II. RESULTS OF ANALOG CALCULATIONS FOR ITC VOIDING ACCIDENTS[a]

| Case Number | Time in Core Cycle | Input Reactivity, %/sec | Peak Power, MW | Integrated Power, MW-sec | Maximum Hot-Spot Metal Temp., °F | Maximum Average Metal Temp.[b], °F | Maximum Average Coolant Temp.[c], °F | Maximum Hot-Spot Heat Flux, Btu/ft²-hr | Maximum Net Positive Reactivity, $\Delta k/k$ | Time of Peak Power, msec |
|---|---|---|---|---|---|---|---|---|---|---|
| 1 | Beginning | 4.2 | 120 | — | 420 | 240 | 160 | $2.2 \times 10^6$ | — | 50 |
| 2 | Beginning | 8.4 | 125 | — | 430 | 240 | 160 | $2.3 \times 10^6$ | — | 30 |
| 3 | End | 4.2 | 130 | 15 | 685 | 260 | 165 | $2.4 \times 10^6$ | 0.002 | 60 |
| 4 | End | 8.4 | 170 | 18 | 780 | 285 | 170 | $2.8 \times 10^6$ | 0.004 | 60 |

[a] Safety-system action is assumed.
[b] This is the peak transient value of the axially and radially averaged temperature of the average fuel plate.
[c] This is the peak transient value of the axially averaged temperature of bulk coolant in the average fuel-plate channel.

cients of temperature. The reactivity effect of voiding the ITC was taken to be a ramp of 8.4%/sec for ⅜ sec, which is the total time for the bulk fluid to traverse the 20-in.-high active portion of the ITC under normal flow conditions.

One model is that voids are swept into the ITC from above, to the extent of eventually voiding 70% of the active volume of the ITC. In this event, reactivity would be added at a time-dependent rate corresponding to the net reactivity worth of partial voiding of an upper portion of the active ITC. Moreover, there would be a variation in the net speed of the bulk fluid in the ITC because of the opposite effects of a reduction in the average mass of the ITC fluid (tending to increase the speed) and the effects of the buoyancy of the voids (tending to decrease the speed). Thus, these results must be considered to be appropriate to the purpose of preliminary safety analysis. More detailed studies will be made for the Final Safety Analysis Report of the AARR.

The total reactivity added in this postulated accident was 3.2%. However, with normal response of the safety system the calculated maximum net reactivity was only 0.4%, well below prompt criticality (~0.7%). Calculated fuel-plate temperatures remained well below the melting point, and the hot-spot heat flux did not reach $3 \times 10^6$ Btu/ft²-hr, assumed to be the level at which local thermal insulation would occur.

In Table II-22-II, calculated results are given for 4 cases: (1) beginning of core life: 2 cases; and (2) end of core life: 2 cases. The other two cases studied corresponded to insertion of reactivity at one-half of the reference rate, with a total insertion of 1.6% in reactivity.

Assuming complete failure of the reactor safety systems, the calculations indicate that the average fuel-plate temperature might exceed the postulated point of incipient boiling. Bulk-boiling might occur in the coolant channels of the average fuel plate, and a major coolant-flow reduction might result. It is conceivable that under these conditions core disassembly would occur. However, it has been calculated that the consequences of such an accident would not be so severe as to cause a breach of the containment boundary of the primary-coolant system.

## ANALYSES OF HYPOTHETICAL MAJOR REACTIVITY ACCIDENTS

In the PSAR for the AARR, analyses were presented of models of the response of the operating reactor to hypothetical rapid injections of positive reactivity of as much as 7 dollars. The intent was to demonstrate that the inherent shutdown capability of the operating system would be effective in limiting the damage effects of rapidly introduced positive-reactivity far in excess of prompt-criticality levels. In particular, it was shown that even for a step reactivity addition of as much as $k_{ex}/\beta_{eff} = 7$ there should not be a prompt massive metal-water reaction of the fuel plates. This conclusion is important to the evaluation of consequences of reactivity accidents, for example, whether the primary-coolant containment provided by the reactor pressure vessel and other components would survive such an excursion. It must be emphasized that these are parameter studies only, to indicate margins of reactor safety.

Two models of reactivity feedback have been considered for the preliminary safety analysis of the AARR. In each model, it is assumed that thermal expansion of the fuel is compensated by buckling of the fuel plates and ejection of some coolant from the fuel zone. Model "A" postulates that, in response to a rapid rise in reactivity to well above prompt criticality, the extra heat would be stored in the fuel plates, and the corresponding volumetric thermal expansion of the plate would eject the same volume of water from the fuel zone without a change in the spatial dimensions of the fuel zone. Since the reactor fuel zone is already undermoderated, this further increase in the metal-to-water ratio would result in a large reactivity loss. Moreover, conduction of heat

to the water would reduce reactivity further in a short-period transient.

In Model "B", it is assumed that the lateral thermal expansions of the fuel plates buckle the plates and thereby increase the metal-to-water ratio in the fuel zone. The fuel zone is assumed to retain its original total lateral area. Longitudinal thermal expansion is assumed to occur to the extent of one-third of the total volumetric plate expansion. Other negative-reactivity effects, which have not been included in Model B, are: (1) thermal conduction from the fuel plates to the coolant water would result in rapid local heating of water, with the probable formation of steam bubbles; and (2) substantial elongations of the fuel plates would extend a fraction of the fuel beyond the vertical extent of the beryllium reflector and into regions where the "black" portions of the control rods are effective.

TABLE II-22-III. CALCULATED CHANGE IN $k_{eff}$ DUE TO FUEL-PLATE EXPANSION[a]

| Percentage Expansion | $k_{ex}/\beta_{eff}$[b] | |
|---|---|---|
| | Model A | Model B |
| 30 | −10.6 | −5.0 |
| 60 | −25.4 | −10.8 |
| 80 | −39.0 | −15.4 |

[a] Normalized to $k_{eff} = 1$ for zero fuel-plate expansion.

[b] The value of $\beta_{eff}$ is 0.0071. Note that $k_{ex} \equiv k_{eff} - 1$ is not the change in "reactivity", as it is usually defined, namely, $\rho = (k_{eff} - 1)/k_{eff}$. These values of $k_{ex}/\beta_{eff}$ do not include effects of higher fuel-plate temperature other than fuel-plate expansion.

Table II-22-III summarizes the computed feedback component of $k_{ex}$ as a function of the assumed uniform volumetric expansion of the fuel plates for Models A and B. The fractional volumetric expansion of the fuel plate, $\Delta V/Vo$, was approximated by linear functions of the incremental heat stored in the plate, $\Delta H$. In the solid phase, $[\Delta V/Vo] = 8.8 \times 10^{-5}\,\Delta H$, where $\Delta H$ is in units of Watt-sec/gram. In the transition phase, the additional thermal expansion of the metal is $[\Delta V/Vo] = 1.9 \times 10^{-4}\,\overline{\Delta H}$, where $\overline{\Delta H} \equiv \Delta H - (\Delta H)_1$ is the heat of fusion of the fuel plate. This linear relationship is a good approximation in the liquid phase, as well: $[\Delta V/Vo] = 1.9 \times 10^{-4}\,\overline{\Delta H}$, where $\overline{\Delta H}$ is the heat added to the molten fuel.

With these models of reactivity feedback, the peak reactor power and total energy released in the hypothetical excursion were obtained with a digital-computer program. Table II-22-IV summarizes the computed response of the reactor for total inputs of 4 to 7 in $k_{ex}/\beta_{eff}$, as steps or ramps.[4] The reactor is assumed to be operating at 100 MW at the time of the reactivity injection. It may be seen that for this range of excursions the total incremental energy release to the time of reactor shutdown is almost the same for the step and for the 10-msec ramp.

In both models, A and B, it was assumed that every fuel plate receives the same incremental thermal energy. Both models ignore the loss of heat due to thermal conduction from the cladding surface into the coolant water. In view of the high thermal conductivity and small thermal time constant of the fuel plates, this results in an underestimation of reactivity feedback. The

TABLE II-22-IV. SUMMARY OF REACTOR RESPONSES TO REACTIVITY TRANSIENTS, ASSUMING ONLY FUEL-PLATE-EXPANSION FEEDBACK OF REACTIVITY

| Total Change in $k_{ex}/\beta_{eff}$ | 4 | | | 5 | | | 6 | | | 7 | | |
|---|---|---|---|---|---|---|---|---|---|---|---|---|
| Total time for ramp reactivity insertion, msec | 0 | 10 | 30 | 0 | 10 | 30 | 0 | 10 | 30 | 0 | 10 | 30 |
| MODEL A (FIXED REACTOR CORE VOLUME) | | | | | | | | | | | | |
| Maximum percentage expansion of average fuel plate | 21 | 21 | 18 | 27 | 27 | — | 33 | 32 | — | 38 | 37 | 24 |
| Total incremental energy release, MW-sec | 100 | 99 | 87 | 122 | 121 | — | 143 | 142 | — | 163 | 160 | 112 |
| Ratio of peak power to initial power of 100 MW | 200 | 194 | 111 | 321 | 309 | — | 463 | 442 | — | 625 | 583 | 210 |
| MODEL B (FIXED LATERAL CORE AREA) | | | | | | | | | | | | |
| Maximum percentage expansion of average fuel plate | 40 | 40 | 35 | 51 | — | — | 62 | — | — | 72 | 71 | 49 |
| Total incremental energy release, MW-sec | 172 | 171 | 153 | 214 | — | — | 254 | — | — | 293 | 290 | 205 |
| Ratio of peak power to initial power of 100 MW | 323 | 317 | 201 | 524 | — | — | 766 | — | — | 1051 | 1009 | 377 |

reactivity coefficient for partial voiding of coolant water in the fuel zone is negative and large ($-\frac{1}{4}$ %/% void). The conduction of heat to the water also would lower the fuel temperature, and possibly the reactor would be shut down without ignition of the metal in the presence of steam.

If the reactivity excursion were large enough, it is conceivable that an effect similar to the SL-1 fuel-plate eruption might occur. In the SL-1 accident, it appeared that molten fuel was injected into the water and a steam explosion occurred which disrupted the core and shut down the reactor. The problem for the AARR is more complicated because certain motions of fuel could result in an increase of reactivity. However, it is reasonable to expect that a rapid disassembly of metal fuel plates would result also in an ejection of water, and this negative reactivity effect should be considerably larger in magnitude. The SL-1 fuel plate was more than twice as thick (120 mils) as the 50-mil-thick AARR fuel plate, with a cladding thickness more than three times as large as that of the AARR plate. The thermal time constant of the AARR fuel plate is much smaller. Note that in the case of the SL-1 reactor, the destructive excursion resulted in the melting of approximately 50% of the plate area of the core but only $\sim 1\frac{1}{2}$% of the core aluminum participated in a metal-water reaction.[5]

### References


1. D. H. Shaftman, *Argonne Advanced Research Reactor Calculations—Analyses of Hypothetical Reactor Accidents*, Reactor Physics Division Annual Report for July 1, 1965 to June 30, 1966, ANL-7210, pp. 104–109.
2. F. T. Binford and E. N. Cramer, Eds., *The High-Flux Isotope Reactor—A Functional Description*, **1**, ORNL-3572 (May 1964).
3. F. T. Binford, T. E. Cole and E. N. Cramer, Eds., *The High-Flux Isotope Reactor Accident Analysis*, ORNL-3573 (April 1967).
4. L. K. Volodka, Reactor Physics Division, Argonne National Laboratory (private communication).
5. D. R. De Boisblanc and S. Cohen, *Safety Analysis Report—Advanced Test Reactor*, **2**, IDO-17021, p. 507 (April 1965)


## II-23. Argonne Advanced Research Reactor Calculations—Analysis of Biological Doses from Maximum Credible Accident

D. H. Shaftman and H. Moses*

### Introduction

In the preceding Annual Report of the Reactor Physics Division,[1] a summary was given of calculated radiation doses to receptors outside the Reactor Containment Building (RCB) of the AARR in the event of a postulated maximum credible accident (MCA). The calculations were for a reactor with a heavily loaded, intermediate-spectrum core, operated continuously for 90 days at a reactor power level of 100 MW. As a result of the budgetary decision to use a reactor core of the type designed for the High-Flux Isotope Reactor (HFIR),[2] the analysis of MCA radiation doses has been revised. With the HFIR-type core, the fuel cycle is greatly shortened at the same power level (100 MW).

If core life were the only difference in the MCA model, the MCA radiation doses would be no larger than those calculated for the longer-lived, heavily loaded core. However, it was decided also to increase the postulated reference leakage rate of air from the RCB to the guaranteed maximum leakage rate of 1.0%/day at building design overpressure (7.5 psig), although the design air leakage rate is still 0.1%/day at that overpressure. Of course, this large increase in postulated leakage rate alone corresponds to a factor of 10 multiplication of short-period inhalation doses to the thyroid, since the important radioactive iodines essentially saturate to the same levels after ~20 days of operation as after 90 days of operation. Therefore, the MCA model was made less conservative in other respects, to account more realistically for certain reductions in the average level of iodine contamination of air inhaled by a fixed receptor, namely, the effects of meandering of the leakage plume, and the effects of dilution by air turbulence in the lee of the RCB (building-wake dilution).

An important factor of conservatism that was left unchanged in the calculation of 30-day radiation doses is the composite assumption of fixed atmospheric-stability condition (Category E), constant wind speed, and a constant wind direction toward the fixed receptor. To assess the degree of conservatism of this composite assumption, calculations have been made of inhalation dose to the thyroid of a fixed receptor, as

* Radiological Physics Division, Argonne National Laboratory.

TABLE II-23-I. RADIATION DOSES FOLLOWING AN MCA

| Dose Period | Distance, m | Whole-Body Doses, rem | | | Bone Doses, rem | | | Inhalation Dose to the Thyroid, rem |
|---|---|---|---|---|---|---|---|---|
| | | Direct Dose from RCB[a] | Total Plume Dose | Total | Direct Dose from RCB[a] | Total Plume Dose | Total | |
| 2 hours[b] | 100 | 16. | 104. | 120. | 16. | 290. | 306. | 334. |
| | 200 | 3. | 32. | 35. | 3. | 85. | 88. | 315. |
| | 500 | 0.1 | 6.8 | 6.9 | 0.1 | 16.5 | 16.6 | 220. |
| | 1000 | — | 2.1 | 2.1 | — | 4.9 | 4.9 | 105. |
| | 1500 | — | 1.0 | 1.0 | — | 2.5 | 2.5 | 63. |
| | 2000 | — | 0.6 | 0.6 | — | 1.5 | 1.5 | 43. |
| | 5000 | — | 0.15 | 0.15 | — | 0.35 | 0.35 | 12. |
| 30 days[c] | 200 | 21. | 127. | 148. | 21. | 1150. | 1171. | 6000. |
| | 500 | 0.9 | 25. | 26. | 0.9 | 225. | 226. | 2500. |
| | 1000 | — | 7.7 | 7.7 | — | 68. | 68. | 1050. |
| (Reference case: No RCB refrigeration) | 1500 | — | 4.0 | 4.0 | — | 35. | 35. | 600. |
| | 2000 | — | 2.5 | 2.5 | — | 22. | 22. | 410. |
| | 5000 | — | <1. | <1. | — | 5.8 | 5.8 | 115. |
| | 10000 | — | <1. | <1. | — | 2.3 | 2.3 | 45. |
| 30 days[c] | 200 | 21. | 56. | 77. | 21. | 330. | 351. | 3100. |
| | 500 | 0.9 | 11. | 12. | 0.9 | 64. | 65. | 1200. |
| | 1000 | — | 3.4 | 3.4 | — | 20. | 20. | 490. |
| (Refrigeration case) | 1500 | — | 1.8 | 1.8 | — | 10.2 | 10.2 | 280. |
| | 2000 | — | <1 | <1. | — | 6.5 | 6.5 | 195. |
| | 5000 | — | <1 | <1. | — | 1.7 | 1.7 | 55. |
| | 10000 | — | <1 | <1. | — | <1. | <1. | 21. |

[a] The tabulation of values for the direct dose from the RCB are based on very detailed calculations, including the large attenuation by the walls of the RCB, for the case of a reactor operation at 100 MW for 90 days. The attenuated direct dose from the RCB is a small fraction of the total dose, and this conservative approximation is admissible.

[b] All 2-hour doses are based on: a constant RCB leak rate of 0.75%/day; Category-F meteorological conditions; constant gross wind direction; and wind speed of 1 m/sec. The inhalation dose to the thyroid is the calculated maximum for all 2-hour dose periods following the initiation of the MCA. The plume doses to the body and to the bone have not been modified for: building-wake dilution; plume meander; or plume travel time.

[c] All 30-day doses are based on: appropriate time-dependent leak rate from the RCB; Category-E meteorological conditions; constant gross wind direction; and wind speed of 2 m/sec. The inhalation dose to the thyroid has been corrected for building-wake dilution and plume meander; it is the infinite-time dose, ignoring "breathing" effects of the RCB after the overpressure is nullified.

a function of: (1) the direction of the receptor relative to a fixed point source; (2) the distance of the receptor from the source; and (3) the duration of the time period of exposure. The numerical results apply to the Argonne National Laboratory site, and they are based upon detailed measurements, over periods of 4–5 years, of such meteorological data as wind direction, wind speed, and air temperature at two fixed elevations. Some of the significant conclusions are summarized in the present paper. For more details, the reader is directed to Ref. 3.

## CONCLUSIONS ABOUT SITING OF THE AARR

The Code of Federal Regulations, Title 10, Part 100[4] provides criteria for siting of nuclear power reactors. These criteria define emergency radiation doses to the off-site public for specific dose periods following a reactor accident, which, in turn, set minimum distances from the reactor, for an "exclusion area," a "low population zone," and a "population center distance." The exclusion area, low population zone, and population center distance for the AARR have been established with consideration for the physical area controlled by the Laboratory, and the population distribution and the communications and transportation facilities available for warning and evacuation of people in the surrounding area. The radii established, namely: 1500 m, for the radius of the exclusion area; 5000 m, for the outer radius of the low population zone; and 7000 m, for the population center distance, are much larger than the minimum distances, as defined in the Code of Federal Regulations and inferred from the calculated radiation doses summarized in Table II-23-I of the present paper.

These minimum distances are determined by the doses to the thyroid, principally the inhalation doses.

For this reason, the calculations of inhalation dose to the thyroid are emphasized in the present paper.

### Discussion of the MCA Model

The MCA is assumed to be an accident occurring during reactor operation at 100 MW near the end of core life, after 2000 MWd of continuous operation. The accident is assumed to result in a rapid massive rupture of the primary-coolant containment and in a rapid melt of 100% of the reactor fuel with an immediate dispersal of fission products uniformly into the RCB. Of the fission products in the fuel, it is postulated that 100% of the noble gases, 50% of the halogens, and 1% of the solids are so dispersed. Half of the escaping halogens are assumed to deposit on walls and other surfaces, and this material is not available for leakage from the RCB.

It is considered to be incredible that the containment of the RCB would be breached coincidentally with the occurrence of an MCA. There remain two avenues of escape of fission products from the RCB: (1) through the 250-ft-high stack, before closure of the containment-isolation valves; and (2) through the walls of the RCB, by leakage. In this paper, an analysis is given of the incremental radiation doses which might result from release of fission products before the containment-isolation valves are fully closed and the RCB is isolated. The calculated incremental doses are small by comparison with doses calculated to result from leakage of air from the RCB following isolation.

The RCB ventilation ducts and other RCB penetrations open to the building air are sealed automatically by isolation valves upon sensing of high radiation levels. However, as a result of injection of heat and water vapor into the air of the RCB following the initiation of the MCA, the normally negative RCB air pressure increases to a calculated maximum overpressure of 4.4 psig. The postulated sources of overpressure are: (1) ejected primary coolant water; (2) metal-water reaction and thermite reaction of all of the aluminum in the reactor core, and ignition of the evolved hydrogen; and (3) decay heat from the reactor core. At a given time after the initiation of the MCA, and after isolation of the RCB, the rate of leakage of contaminated air from the RCB is taken to be proportional to the square root of the RCB air pressure, with a reference leakage rate of 1.0% of the building air mass per day at design overpressure (7.5 psig). The leakage is assumed to be through one small area of the RCB; in the analysis of radiation doses to receptors outside the RCB, it is assumed that the leakage corresponds to a point source at ground level.

This model is conservative in a number of respects. It is assumed that all of the fuel melts, although none of the various postulated specific accidents analyzed indicates that 100% of the core would melt. Fission product dispersal might be slow enough for peak RCB overpressure to occur before the RCB air contamination peaks. The design leakage rate at design overpressure is only one-tenth of the postulated reference (guaranteed maximum) leakage rate. The RCB air overpressure was calculated with very conservative assumptions of the supply of heat and water vapor to the RCB air. The leakage rate from the RCB is conservatively assumed to be proportional to the square root of the building overpressure, and to leak at one point at ground level. Probably, the air leakage would occur at a number of points around the outer wall of the RCB, and at various elevations.

The Title-I design includes a 5000-cfm air-exhaust line, with an efficient air filtration system. This component of the RCB ventilation system could be used to rapidly reduce air-activity levels in the RCB, by recirculation of air within the isolated building. The effectiveness of this system for this purpose will be evaluated in Title-II design. In the present computations of radiation doses to receptors outside the RCB, cleanup of RCB contamination is not included.

In the design reference PSAR analysis, no credit is taken for reduction in overpressure by operation of auxiliary devices, e.g., an air refrigeration system. In Title-II design, various systems which would be effective in limiting the escape of fission products from the RCB will be evaluated. Therefore, for illustrative purposes, a comparison study is presented of the computed radiation doses for two cases: (1) the "reference" model, wherein only natural heat losses are assumed; and 2) a model wherein an air refrigeration system is operative. Indeed, it is conservatively assumed that only one half of the full refrigeration capacity is in use. This second model will be referred to as the "refrigeration case."

Short-period doses, e.g., for the first two hours, are essentially unaffected by the air cooling. The calculations of radiation dose were simplified by the conservative step-function approximations to the calculated time-dependent leak rates from the RCB. These fittings are shown in Figs. II-23-1 and II-23-2.

### Calculations with the Reactor-Siting Program AISITE-II

A digital-computer program, AISITE-II,[5] has been employed for the basic computations of radiation doses to various organs of the body, as a function of total time of exposure and as a function of distance. The program is based upon: (1) the model of J. J. Di Nunno, et al. (TID-14844),[6] in computing the isotope

inhalation dose to an organ; (2) the model of WASH-740,[7] in computing the direct dose from the escape plume; and (3) the formulation by F. Pasquill[8] of categories of transport and diffusion characteristics of the plume.

The AISITE-II program includes a correction for decay of fission products in the leakage plume from the RCB during the time of travel of the plume front to the location of the receptor. However, it does not correct for the reduction in actual exposure during a given time interval due to the plume travel time; for example, with an assumed wind speed of 1 m/sec, for the first 25 min a receptor at 1500 m would receive essentially zero plume-inhalation dose, and the dose for the first two hours following the accident thereby would be reduced.

In calculating the net plume-inhalation doses to the thyroid, additional correction factors were applied for: (1) the dilution of the plume by the turbulence generated in the lee of the RCB (the "building-wake factor"); and (2) the meandering of the plume, thereby presenting average plume concentrations to the receptor during significant time intervals (15 min or more). Conservatively, neither of these two correction terms was applied to the calculated radiation doses to the whole body or to the bone, because significant fractions of these doses are due to non-inhalation doses from the plume. A detailed discussion of these two correction terms is given later in this paper.

The AISITE-II output separately lists the direct dose from the RCB and the total dose (sum of the plume dose and the direct dose from the RCB). No provision is included for time-dependence of leakage rate. Therefore, the plume dose rate as a function of time was determined from AISITE by appropriate calculation of incremental doses, and correction factors were applied to account for the variation in leakage rate as the RCB overpressure varies with time.

AISITE-II does not calculate the very significant attenuation of the direct gamma rays from the RCB by the thick steel and concrete building wall. It is computed that the direct gamma-ray dose rate from the Reactor Containment Building is reduced by factors of from 185 to 600 with a shield-equivalent of a 24-in. thickness of ordinary concrete. The actual value of the attenuation factor within this range depends upon the length of time after the fuel melt and upon the distance to the receptor. These detailed calculations were performed earlier, for a case of operation at 100 MW for a period of 90 days.[1] Comparison calculations for cases of 20-day operation and 90-day operation, with AISITE-II, indicate that the 2-hour direct doses from the RCB are almost identical in magnitude. The total direct doses from the RCB which

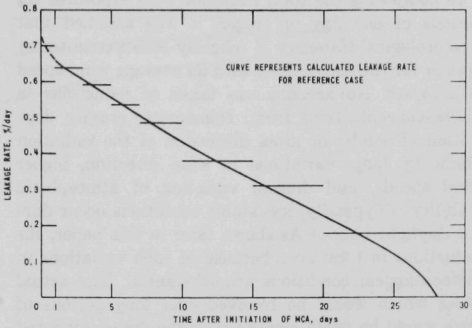


FIG. II-23-1. Step-Function Approximation to Time-Dependent Leakage Rate from Reactor Containment Building Following an MCA (Reference Case). *ANL Neg. No. 112-9432.*

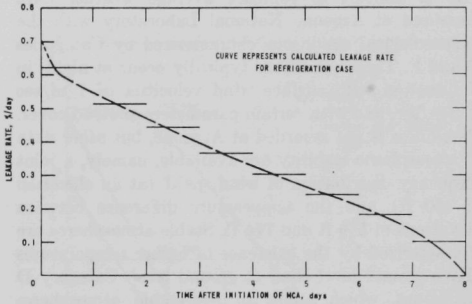


FIG. II-23-2. Step-Function Approximation to Time-Dependent Leakage Rate from Reactor Containment Building Following an MCA (Refrigeration Case). *ANL Neg. No. 112-9431.*

would result from exposure of receptors for 30 days differ by approximately 25% at distances close to the RCB, and the fractional error lessens with increasing distance. Since the attenuated direct dose is a small fraction of the total dose to the body organs, except perhaps within the first few hundred meters, the conservative values of the direct dose as determined for the 90-day case are listed. In these calculations it is assumed conservatively that the entire fission product inventory is dispersed in the above-grade portions of the RCB.

## Choice of Atmospheric-Dispersion Parameters

In computing the 2-hour radiation doses, it was assumed that the dispersion parameters of Category F (moderately-stable conditions) apply, with an average wind speed of 1 m/sec.

In computing the total radiation dose exposures for periods of one day or longer, it was assumed that meteorological Category E (slightly-stable conditions) applies for the entire time, with an average wind speed of 2 m/sec. No account was taken of reductions in plume-concentrations from: rainstorms; gravity deposition of solids; or gross dispersion of the radiation plume by large variations in wind direction, higher wind speeds, and diurnal variation of atmospheric stability. (Typically, less stable conditions occur during daylight hours.) As shown later in this paper, the reductions in total dose because of such variations in meteorological conditions are substantial. The actual doses which would be received over long periods of time would be much smaller than the doses computed for the assumed constant conditions (Category E; wind of constant direction; and average wind speed of 2 m/sec).

It is difficult to compare average weather data measured at Argonne National Laboratory with the meteorological conditions characterized by Categories E and F. These conditions typically occur at night, in conjunction with surface wind velocities of 1 m/sec to 5 m/sec, and with certain parameters of cloud cover. Cloudiness is not recorded at Argonne, but other data of atmospheric stability are available, namely, a joint frequency distribution of wind speed (at an elevation of 150 ft) and the temperature difference between elevations of 5½ ft and 144 ft. Stable atmospheres are characterized by the existence of higher temperatures above ground level than at ground level. Category-D conditions, which apply to less-stable atmospheres than those in Categories E or F, are characterized by Meade and Pasquill as "neutral". The detailed meteorological data indicate that temperature-inversion conditions occur at Argonne approximately 45% of the time.[9] Insofar as effects of ground-level leakage are concerned, it seems reasonable to assume that the radiation plume travels at a speed represented by the data available for wind speed at an elevation of 19 ft. It is estimated that atmospheric conditions which are more unfavorable than Category F plus a wind speed of 1 m/sec would occur less than 10% of the time, and that even the degree of atmospheric stability assumed for the computation of the 30-day doses (Category E, with a wind speed of 2 m/sec) would be expected appreciably less than 20% of the time.

Therefore, the atmospheric-stability models employed in the calculation of the 2-hour doses (Category F; 1 m/sec), and of the long-period doses (Category E; 2 m/sec) appear to be reasonable.

The reference report[5] for the AISITE program lists meteorological parameters for only one category—the Pasquill Category F. The code has been modified at ANL to allow for the optional use of Category-E meteorological data as well.[8]

### Building-Wake Factor and Plume Meander

When air flows around a large obstruction such as the Reactor Containment Building, a turbulent wake is produced on the lee side. Because of the rapid mixing in this region, materials leaking from the RCB are diffused quickly. According to J. J. Fuquay,[10] the material leaking in one second is diluted into a volume given numerically by the product:

$$D_B = cAu,$$

where

$A$ is the cross sectional area of the building normal to the direction of the wind, m²

$u$ is the wind speed, m/sec

$c$ is a diffusion coefficient, with values in the range ½ to 2.

In the analyses for the AARR, the conservative value $c = ½$ has been used.

In calculating the concentration of materials at points downwind from the building, the building-wake-dilution volume, $D_B = cAu$, is incorporated in the following manner:

$$\chi = \frac{Q}{\pi u \sigma_y \sigma_z + cAu} \exp\left[-\frac{y^2}{2\sigma_y^2} - \frac{z^2}{2\sigma_z^2}\right],$$

where

$\chi$ is the concentration, in $g$ or $C$ per cubic meter

$Q$ is the emission rate of the material, in $g$ or $C$ per sec

$y$, $z$ are the lateral and vertical coordinates of the receptor, respectively

and

$\sigma_y$, $\sigma_z$ are the standard deviations of concentration according to the Pasquill-Gifford diagram.[11]

The "building-wake factor", $R$, is defined by:

$$R \equiv \frac{\pi \sigma_y \sigma_z}{\pi \sigma_y \sigma_z + cA}.$$

Thus $R$ is the ratio of the material concentration, with building-wake dilution included, to the concentration which would exist if there were no building-wake effects. The variation of the building-wake factor with distance from the RCB is given in Fig. II-23-3, for meteorological Categories E and F. It is applied directly as a distance-dependent correction factor to the plume-inhalation dose to the thyroid which is inferred from the AISITE-II output.

In the AISITE-II analyses, the receptor is assumed to be positioned at the centerline of the plume. As a result of the eddy diffusion process, the concentration of material in the plume resulting from building leak-

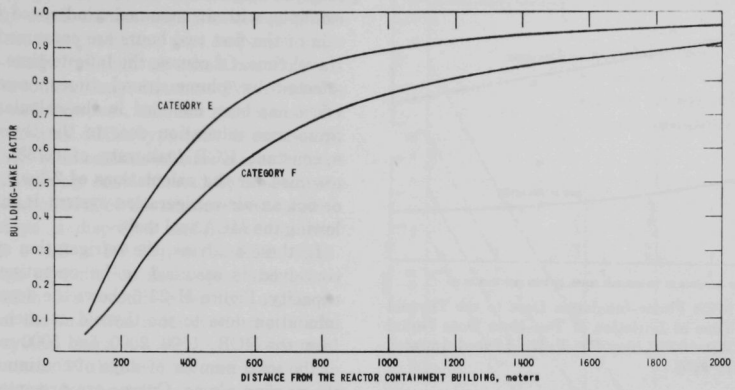


FIG. II-23-3. Building-Wake Factors for Meade-Pasquill Meteorological Categories E and F. *ANL Neg. No. 112-9368.*

age is distributed according to a Gaussian function, i.e., the concentrations in any section perpendicular to the centerline may be represented by a bivariate normal distribution. For wind speeds of 1 m/sec or greater, the atmosphere is usually turbulent and the plume nearly always exhibits a degree of meander. The concentration experienced by a receptor at a fixed point therefore is represented by an average of the concentrations. Assuming that the edges of the plume are truncated at a value of one-tenth of the maximum concentration, the average concentration is 0.57 times the maximum. Therefore, a correction factor of 0.6 has been applied directly to the plume-inhalation dose to the thyroid inferred from AISITE.

## MCA Radiation Doses to Persons Outside the Reactor Containment Building, Exclusive of Effects of Leakage from the Stack before RCB Isolation

Calculated radiation doses from direct gamma-ray radiation from the RCB and from radiation effects of the plume from ground-level leakage are summarized in Table II-23-I and in Figs. II-23-4 through II-23-8. All distances are measured from the center of the Reactor Containment Building. This is equivalent to the approximation that all direct radiation is emitted from a point source at the center of the RCB, and that the leakage plume arises from leakage at this point. This approximation does not lead to significant error at distances large in comparison with 20 m, which is approximately the value of the radius of this building in horizontal plan view. Care must be taken in extrapolating the tabulated data to points closer to the RCB.

Figure II-23-4 includes the distance dependent 2-

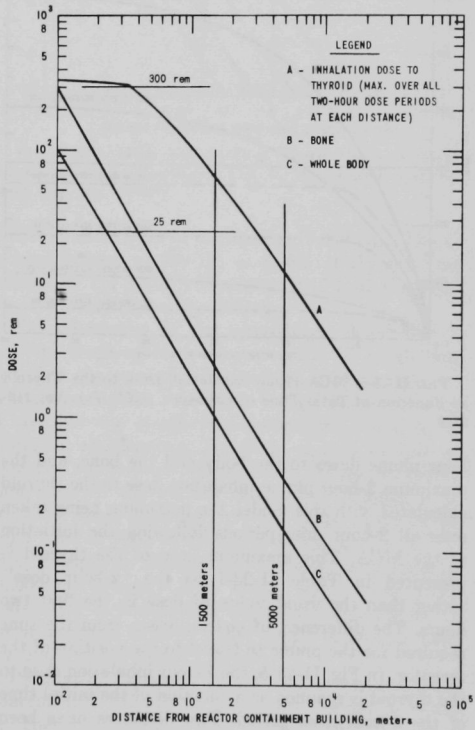


FIG. II-23-4. MCA Plume Doses to Body Organs for Two-Hour Dose Periods (Constant Leak Rate: 0.75%/day; Cat. F; Wind Speed: 1m/sec). *ANL Neg. No. 112-9372.*

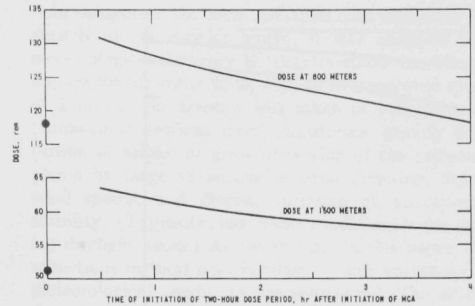


FIG. II-23-5. MCA Plume-Inhalation Dose to the Thyroid as Function of Time of Initiation of Two-Hour Dose Period (Constant Leak Rate: 0.75%/day, Cat. F; Wind Speed: 1m/sec). *ANL Neg. No. 112-9410.*

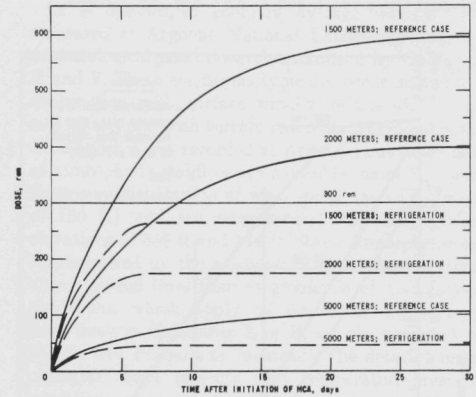


FIG. II-23-6. MCA Plume-Inhalation Dose to the Thyroid as Function of Total Time of Exposure. *ANL Neg. No. 112-9369.*

hour plume doses to the body and the bone, and the maximum 2-hour plume-inhalation dose to the thyroid calculated with this model, the maximum being taken over all 2-hour dose periods following the initiation of the MCA. This maximum dose to the thyroid is presented in Table II-23-I as the "2-hour dose", rather than the usual value of dose in the first two hours. The difference, of course, arises from the time required for the plume to travel to the position of the receptor. In Fig. II-23-5, the 2-hour inhalation dose to the thyroid is graphed as a function of the initial time of the 2-hour dose period. Two distances have been chosen: 800 m, and 1500 m, to illustrate the effect of plume-travel time. The effect of the plume lag is quite large, at large distances from the RCB. At 5000 m, for example, with an assumed wind speed of 1 m/sec, 83 min of the first two hours are consumed by the plume travel time. Of course, the infinite-time doses are little affected by plume travel times; nevertheless, this effect has been included in the calculation of the infinite-time inhalation dose to the thyroid. Note that a constant RCB leak rate of 0.75%/day has been assumed for the calculations of 2-hour doses, whether or not an air-refrigeration system is in operation following the MCA fuel melt.

In these analyses, the refrigeration system which is conceived is assumed to be operative at only half capacity. Figure II-23-6 shows the accumulated MCA inhalation dose to the thyroid at each of 3 distances from the RCB: 1500, 2000, and 5000 m, as a function of the total number of days of continuous exposure to the passing plume. Curves are presented both for the reference case (no air refrigeration) and for the case of RCB air refrigeration at one half of refrigeration capacity. For the reference case, at 5000 m, which is the designated distance to the low-population zone, the constant-conditions value of the infinite-time dose to the thyroid is approximately 115 rem. This conservatively computed dose in only slightly more than ⅓ of the value of the emergency dose (300 rem). The effect of half-capacity RCB air refrigeration would be to reduce the dose to the thyroid by another 50%. (See also Table II-23-I.)

Figures II-23-7 and II-23-8 include other graphs of various radiation doses of particular importance in the analysis of site acceptability. The doses given are for the reference case, and, for comparison, also for the refrigeration case; the curves show the rate of dropoff in dose level with increasing distance from the Reactor Containment Building.

### Maximum (MCA) Inhalation Dose Contribution to the Thyroid of Receptors Outside the Reactor Containment Building Due to Stack Release Prior to Containment Isolation of the Building

Following the fuel melt postulated in the MCA model, there will be some dispersal of fission products into the bulk air volume of the Reactor Containment Building. It is expected that the increase in air contamination would be slow enough that the radiation monitors in the building-ventilation system would detect a potentially dangerous level of activity and there would be a rapid automatic actuation of isolation valves to close off the RCB from the stack long before the activity of the air in the exhaust line

reached the level postulated for the MCA. In this realistic case, the stack release would be a negligible contribution to the total radiation dose to people outside the RCB—much less than an inhalation dose of 1 rem to the thyroid, at any distance. For conservatism, it is assumed, however, that the rate of release of activity following an MCA-type melt is extremely rapid, and that not even seconds of time elapse before the RCB air is massively contaminated. It is assumed further that a total of 25% of the reactor inventory of each iodine isotope is dispersed uniformly into the bulk air volume ($\sim 1.2 \times 10^6$ ft$^3$) of the RCB. With the present design of radiation monitoring and isolation valving, within two seconds after this contaminated air reaches the radiation monitors in the building ventilation system there is a signal to isolate the RCB from the stack. Within two seconds after this, the RCB is isolated. In the following analysis, it is assumed that the total stack release of unfiltered air

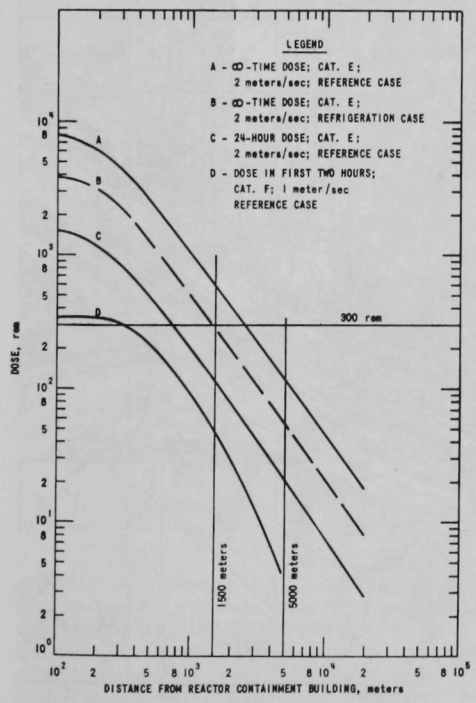


FIG. II-23-7. MCA Plume-Inhalation Dose to the Thyroid as a Function of Distance from the Reactor Containment Building. *ANL Neg. No. 112-9370.*

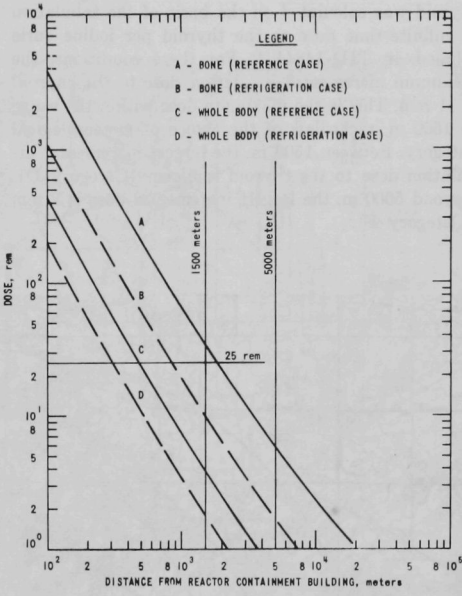


FIG. II-23-8. MCA Infinite-Time Plume Doses to Body Organs (Constant Conditions: Cat. E; Wind Speed: 2m/sec). *ANL Neg. No. 112-9371.*

corresponds to 3 sec of full flow at 15,000 cfm. This is a total volume of 750 ft$^3$, or 0.06% of the total air volume of the RCB, containing 0.015% of the total reactor inventories of the iodines.

The calculation of the atmospheric dispersion of activity resulting from release of 750 ft$^3$ of air was based on the generalized Gaussian plume formula for a continuous point source, for a total release time of 3 sec. No one standard meteorological category is worst for all distances. Therefore, at each distance a category was selected which yielded the largest radiation dose. Of the various categories, Category A is worst for short distances from the RCB. In the range from 1500 to 4000 m, Category D appears to be the most pessimistic. Beyond that distance, until roughly 10,000 m, Category E is worst; and, beyond that, Category F is worst. All of these statements are based on an assumed effective stack height of 76.4 m (250 ft), and a wind speed of 1 m/sec.

Postulating Category-A condition, the maximum air concentration (C/m$^3$) at ground level occurs at ~300 m. There, numerically, it is $\sim 3\frac{1}{2} \times 10^{-5}$ times the stack radiation-release rate (in units of C/sec). The corresponding total plume inhalation dose to the

thyroid was calculated on the basis of the tabulation of infinite-time dose to the thyroid per iodine curie inhaled, in TID-14844.[6] For these conditions, the maximum incremental inhalation dose to the thyroid is 11 rem. This is the maximum dose within the range to 1500 m, regardless of the choice of meteorological category. Between 1500 m, the largest incremental inhalation dose to the thyroid is 5 rem (Category D). Beyond 5000 m, the largest incremental dose is 2 rem (Category F).

### Distributions of Inhalation Doses, Based on Statistical Treatment of Observed Meteorological Conditions

Over a period of years, Argonne National Laboratory has amassed detailed records of wind direction, wind speed, and atmospheric stability on the Laboratory's DuPage County, Illinois, site. Because plume-inhalation doses, and especially the thyroid dose, would be the most significant radiation doses to receptors

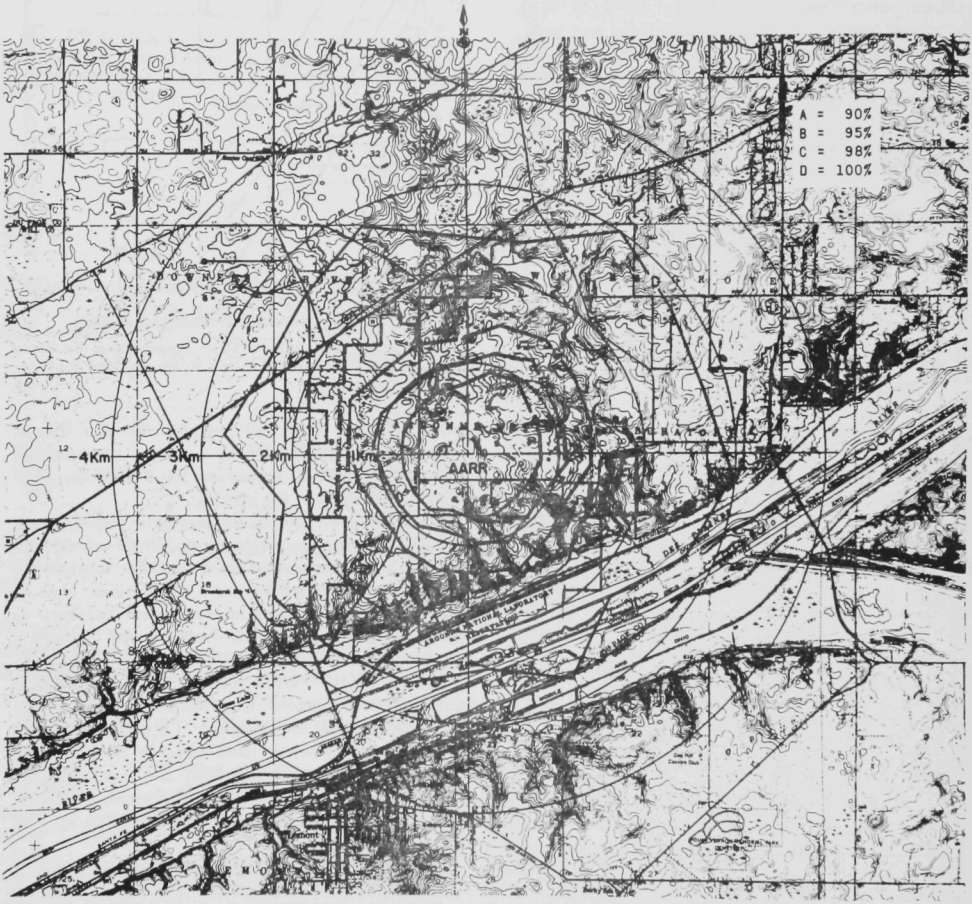


Fig. II-23-9. Isopleths Showing Minimum Distances at which the 24-hour Dose is Equal to or Less Than 75 Rem 90, 95, 98, or 100 Percent of the Time. *ANL Neg. No. 112-9365.*

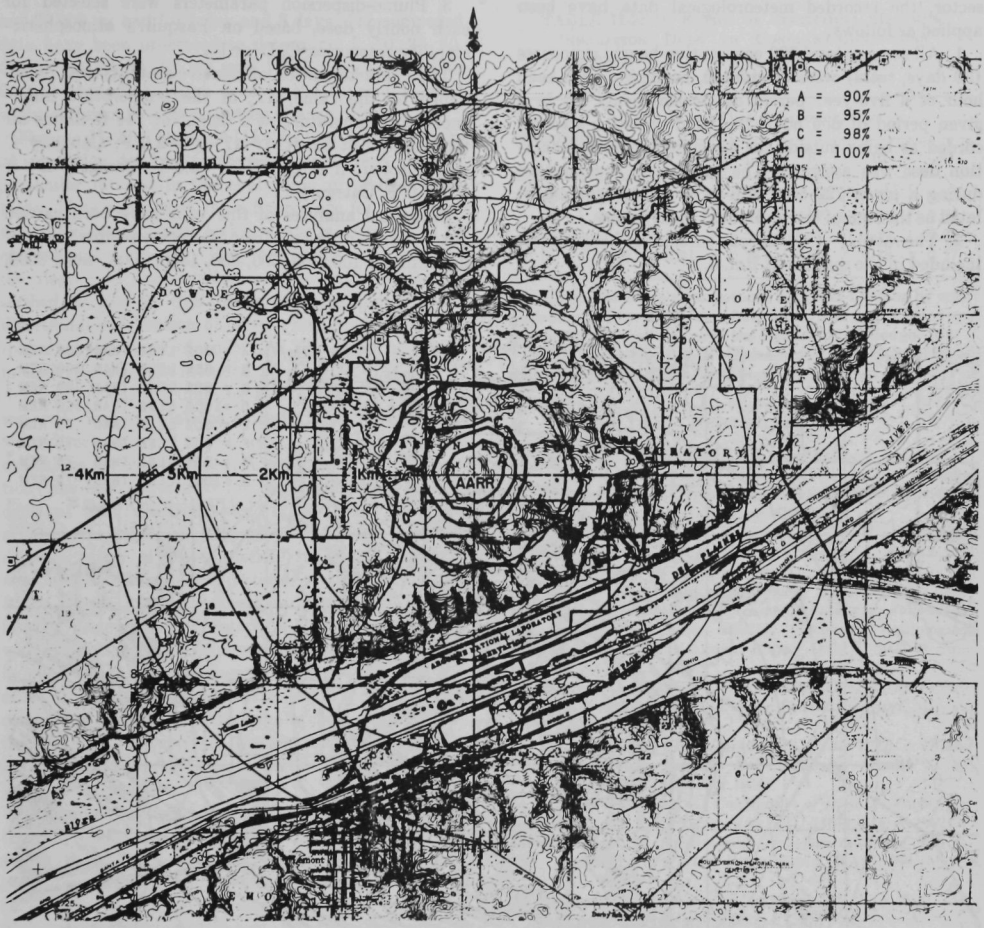


FIG. II-23-10. Isopleths Showing Minimum Distances at which the 24-hour Dose is Equal to or Less Than 300 Rem 90, 95, 98 or 100 Percent of the Time. *ANL Neg. No. 112-9366.*

outside the RCB following an MCA, a digital computer program has been written to apply the meteorological data to obtain statistical distributions of plume-inhalation doses. This program has been applied to the case of the inhalation dose to the thyroid from the fission-product iodines, for the special case of a constant leakage rate of 1.0% of the RCB air mass per day. Depletion and decay of the individual fission-product iodine isotopes are included, but no correction is made for the time required for the plume to travel to the receptor, or for the dilution effects of turbulent air conditions in the lee of the RCB (building wake). The calculations are based on the methods of TID-14844.[6]

The radiation plume is assumed to originate from a point source at a fixed location. The entire circle with center at the point source is divided into eighteen 20-degree sectors. In determining the statistical 30-day inhalation dose to the thyroid for a receptor in a given

sector, the recorded meteorological data have been applied as follows:

1. All sequences of 720 consecutive hourly exposures (30 days, total) were calculated, beginning with each hour of a five-year period of measurements. If, in a given period of one hour, the wind direction was recorded as being outside the given sector, zero inhalation dose was assigned. The total dose accumulated during a given 720-hour (30-day) period was calculated as the sum of the individual hourly doses.

2. The actual wind speed, measured hourly, was included in the manner of Ref. 6.

3. Plume-dispersion parameters were selected for each hourly dose, based on Pasquill's atmospheric-stability categories, C, D, or F.

The characterization of relative stability was determined by the value, $\Delta T$, of the temperature difference: air temperature at a height of 144 ft minus air temperature at 5.5 ft. If $\Delta T \leqq -2.0°F$, Category C was selected; if $0 \geqq \Delta T > -2.0°F$, Category D: if $\Delta T > 0°F$, Category F.

Statistical analyses of this type have been carried out for: each of the eighteen 20-degree sectors; each of 9 distances: 100, 300, 500, 800, 1500, 2000, 4800, 8000,

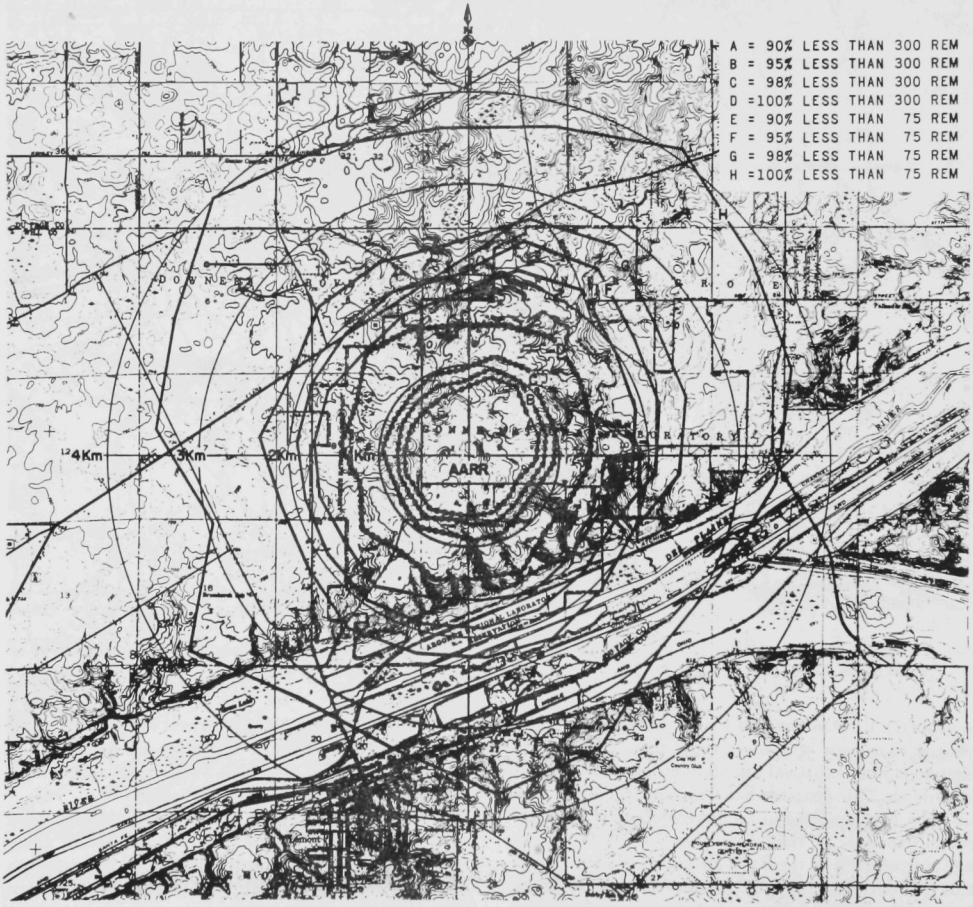


FIG. II-23-11. Isopleths Showing Minimum Distances at which the 30-day Dose is Equal to or Less Than the Indicated Value 90, 95, 98 or 100 Percent of the Time. *ANL Neg. No. 122-9367.*

and 20,000 m; and for 1 day and 3 days. The computed data have been processed to determine, 5, 10, 20, 40, 50, 70, 80, 90, 95, 98, 99, and 100*th*-percentile values for the plume-inhalation dose to the thyroid in each of the eighteen 20-degree sectors at each distance.

Figures II-23-9 through III-23-11 present isopleths of inhalation dose to the thyroid, for various cases of particular interest in the evaluation of site acceptability. Note again that these figures are for the hypothetical case where the leakage rate is assumed to be constant, at 1.0%/day. They are included to indicate the degree of conservatism of the calculations described earlier in this paper, and to indicate the directional distribution of doses which might be anticipated in the event of an MCA. The effect of plume meandering has been included.

These special calculations also provide a comparison with dose calculations wherein gross variations in wind direction, wind speed, and atmospheric-stability conditions are not included. A separate set of calculations has been performed for the hypothetical case of constant wind direction, wind speed (2 m/sec), and atmospheric stability (Category E). Table II-23-II supplies ratios of the statistical inhalation doses to the Category-E dose, at a distance of 4800 m from the RCB, for the special case where the half-life of the inhaled fission-product isotope is long by comparison with the total time of exposure of the plume. It may be observed that if 95*th*-percentile ratios are used the effect of the expected gross variations in meteorological conditions is to reduce the inhalation-dose contributions of these isotopes by 75% or more. Some of the important bone seekers (e.g., Sr-90 and Ce-144) fall into this category.

The maximum 720-hour inhalation dose to the thyroid from fission-product iodines has been determined to be 61 rem at 4800 m. This value is the absolute maximum over all radial sectors, and over a period of 5 years of recorded data. The maximum 95*th*-percentile value is 28 rem. For this same case of a constant RCB leakage rate of 1.0%/day, but constant conditions of wind direction, wind speed (2 m/sec), and atmospheric stability (Category E), the AISITE-II result for the inhalation dose to the thyroid is at least three times as large as the abovementioned absolute maximum, and it is at least six times as large as the maximum 95*th*-percentile value.

Additional details of this analysis are given in Ref. 3.

TABLE II-23-II. RATIOS OF STATISTICAL MAXIMUM INHALATION DOSE TO CONSTANT-CONDITIONS DOSE, AT A DISTANCE OF 4800 METERS FROM THE REACTOR CONTAINMENT BUILDING[a]

| Percentile | Total Time of Exposure, days | | | | | |
|---|---|---|---|---|---|---|
| | 1 | 2 | 4 | 8 | 16 | 30 |
| 100 | 1.71 | 1.37 | 0.74 | 0.58 | 0.42 | 0.33 |
| 98 | 0.66 | 0.53 | 0.44 | 0.33 | 0.27 | 0.23 |
| 95 | 0.50 | 0.40 | 0.32 | 0.26 | 0.22 | 0.20 |
| 90 | 0.35 | 0.31 | 0.26 | 0.21 | 0.18 | 0.17 |

[a] These ratios apply for isotopes with half-life long by comparison with the total time of exposure. The ratios listed are the maximum of all values in the eighteen 20-degree sectors.

By "constant-conditions" is meant: Category E; wind speed of 2 m/sec; and constant wind direction.

## REFERENCES


1. D. H. Shaftman, *Argonne Advanced Research Reactor Calculations—Analysis of Hypothetical Reactor Accidents*, Reactor Physics Division Annual Report, July 1, 1965 to June 30, 1966, ANL-7210, pp. 104–105.
2. F. T. Binford and E. N. Cramer, Eds., *The High-Flux Isotope Reactor, A Functional Description*, **1**, ORNL-3572 (May 1964).
3. Harry Moses, et al., *The Influence of Meteorological Conditions Upon Radiation Doses due to Inhalation Following a Maximum Credible Reactor Accident*, Radiological Physics Division Annual Report, July 1, 1966 to June 30, 1967, ANL-7360.
4. *Reactor Site Criteria*, Code of Federal Regulations, Title 10, Part 100, Published in the Federal Register, May 12, 1962.
5. R. A. Blaine and E. L. Bramblett, *AISITE II, A Digital Computer Program for Investigation of Reactor Siting*, NAA-SR-9982 (October 1964).
6. J. J. Di Nunno, et al., *Calculation of Distance Factors for Power and Test Reactor Sites*, TID-14844 (March 1962).
7. *Theoretical Possibilities and Consequences of Major Accidents in Large Nuclear Power Plants*, WASH-740 (March 1957).
8. F. Pasquill, *Atmospheric Diffusion*, (D. Van Nostrand, Princeton, New Jersey, 1962).
9. H. Moses and J. H. Willett, *Five Year Climatological Summary, July 1949–June 1954*, ANL-5592, unpublished updating of Table 238 to include data for additional years.
10. J. J. Fuquay, as communicated to F. A. Gifford, Jr., *Atmospheric Dispersion Calculations Using the Generalized Gaussian Plume Model*, Nucl. Safety **2**, No. 2 (December 1960).
11. F. A. Gifford, Jr., *Use of Routine Meteorological Observations for Estimating Atmospheric Dispersion*, Nucl. Safety **2**, No. 4 (June 1961).

# Section III

# Fast Reactor Physics

Section III describes analytical and experimental work related to fast power breeder reactor development. The first five papers are concerned with the Doppler effect; the next paper treats physics parameters for a uranium-carbide core; and the following two discussions are on zoned-core studies. Neutron spectrum studies follow in the next several papers, and then three papers describe work on sodium voids. Four papers are devoted to EBR-II and two papers to the Fast Fuel Test Facility. The remaining five papers treat a miscellany of topics.

# III-1. Analysis of Small-Sample Doppler-Effect Measurements

R. A. Lewis and C. E. Till

Measurements of the reactivity Doppler effect of U-238, U-235 and plutonium in fast reactor critical mockups, by the technique in which small heated samples of these materials are oscillated in and out of the core center, have been made extensively at Argonne[1] and elsewhere. A perspective view of the oscillator equipment used in the ZPR-6 and -9 measurements is shown in Fig. III-1-1. The Zero Power Reactor (ZPR) assemblies use mixtures of small plates of fertile, fissile and diluent materials to reproduce the homogenized compositions of the fast reactor cores under study. Typically, the small plates are loaded into stainless steel drawers, nominally 2 in. square by 24 in. long, which are in turn loaded into the stainless steel matrix tubes of the ZPR facility. Normally, there is a pattern of a few drawer types repeated periodically throughout the assembly. In the Doppler measurements, the central core drawer is replaced by the oscillator assembly which then runs axially through the reactor core.

There has been continuing theoretical discussion[2, 3] of the interpretation of such measurements which are complicated by the effect of interaction between the heated sample and the unheated reactor medium surrounding the sample. In general, unheated resonance material of the sample is present, in the surrounding reactor where it affects the microstructure of the neutron flux incident on the sample and is, in turn, affected by changes in the sample temperature. These effects are particularly pronounced in the case of U-238 samples because of the high concentration of this isotope in the reactor cores of interest.

The calculational results discussed in this paper were obtained as a result of a re-analysis of the measurements of the Doppler effect of U-238, in $UO_2$ and uranium-metal samples of various sizes, in the dilute, carbide, uranium-fueled Assembly 4Z[1] of ZPR-6. A preliminary analysis of the Assembly 4Z measurements based upon equivalence theory in which the samples were considered isolated and the room temperature resonances in the core ignored, was reasonably successful in predicting the magnitude of the Doppler effect in the 1 in. diam $UO_2$ standard samples. However, the technique was unsuccessful in predicting the relative magnitudes of the Doppler effect in samples of varying size and composition; i.e., samples with varying core-sample interaction.

The re-analysis of the measurements specifically included the core-sample resonance interaction effects through the application of the RABBLE[4] code to the configuration of the measurements. The RABBLE code is designed to perform a detailed resonance absorption calculation in multiregion reactor cells and to generate region-dependent group cross sections. In the calculation, the cell is divided spatially into several concentric regions and the energy range of interest is subdivided into many extremely narrow groups. The calculation obtains regional reaction rates and fluxes, as a function of energy, from the regional slowing-down sources and first-flight escape and transmission probabilities. The code allows arbitrary compositions, containing mixtures of reasonance and non-resonance materials at different temperatures, in the various regions of the cell. Probably the most serious limitation of the code is the assumption of cosine interface currents, between regions, in the calculation of transmission probabilities. Within this approximation the escape and transmission probabilities are exact and no rational approximation is used.

The configuration of the immediate sample environment in the ZPR-6 measurement is shown in cross section (normal to the core axis) in Fig. III-1-2. The sample is shown inside its double-containment canning and oscillator drawer. The core-drawer pattern shown* is repeated vertically and horizontally around the sample. In the calculations, the configuration was simplified to three concentric zones; the sample, a reduced-density stainless steel zone (to mockup the sample can, oscillator drawer and adjacent matrix material) and the homogenized core. Each of these zones was subdivided in the calculation to improve spatial resolution.

In order to illustrate the magnitude and trend of the core-sample interaction effects calculated by the RABBLE code for the configuration of the measurements, it is useful to consider individual resonances spaced throughout the Doppler range. Table III-1-I summarizes the results of such calculations for average U-238 $s$-wave resonances at 450, 2000 and 20,000 eV for the case of the 1 in. diam natural $UO_2$ sample. This sample is of the standard size and density of the Doppler samples normally used at Argonne. The ener-

* The three drawers shown are left-to-right, Types 1, 2 and 3. The numbers in the figure represent similar drawer types.

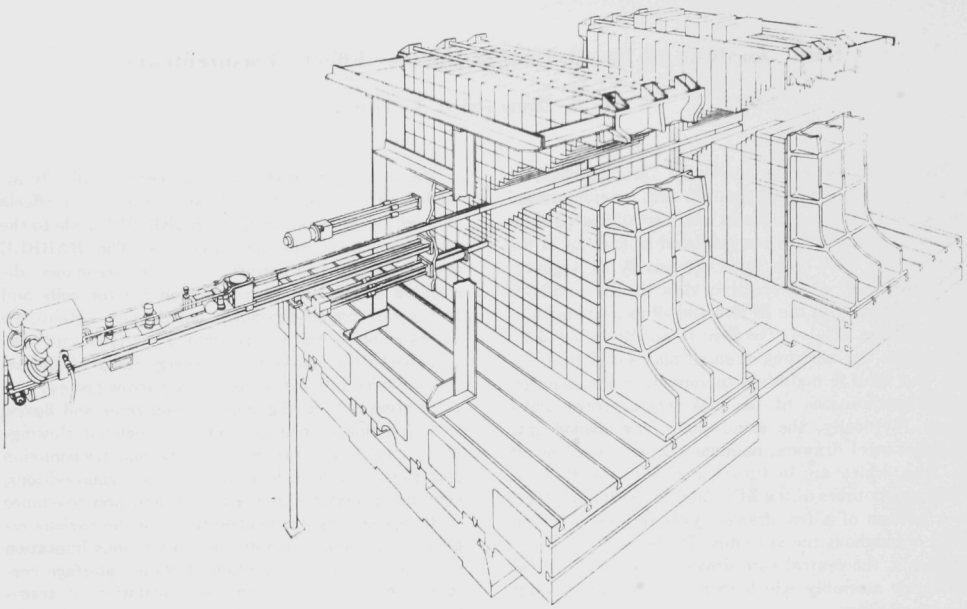

FIG. III-1-1. Doppler Equipment in ZPR-6. *ANL Neg. No. 112-5834 T-1.*

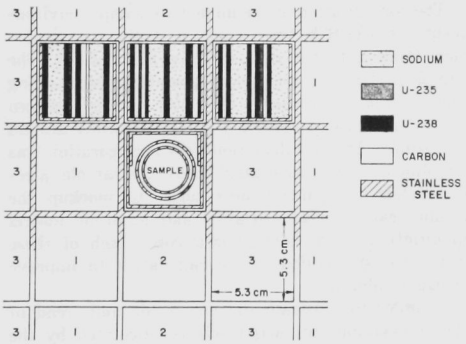


FIG. III-1-2. Doppler Sample Environment in ZPR-6 Assembly 4Z. *ANL Neg. No. 112-8354.*

gies were chosen because they are approximately the 10, 50 and 90% points of the flux and adjoint-weighted integral of the reactivity Doppler effect in this particular core. The cross sections listed are regional U-238 absorption rates, divided by the flux integrals, taken over a sufficient energy interval to include all of the resonance integrals and Doppler changes. The sample and core cross section changes are listed per U-238 atom in the sample. Subscript 1 refers to the sample region; subscript 2 to the core region. The temperatures 293°K and 1100°K refer to the room temperature cross section in the sample region and Doppler changes in the sample and core U-238 absorption cross sections to 1100°K.

Calculational results in Table III-1-I are listed for five assumed sample environments. The first column, labelled "core w/o resonances," gives the results without U-238 resonances in the core. The second column, labelled "core," is the case in which the core (with U-238 resonances) begins at the surface of the sample. Column three, labelled "SS zone, core," is the configuration of the measurements in which a zone of reduced-density stainless steel is interposed between the core (with U-238 resonances) and the sample. Columns four and five are included as a comment on the problem of determining the amount of error introduced by homogenizing the heterogeneous plate structure of the core. In these two cases, the eight drawers adjacent to the sample position have been considered as a separate zone interposed between the stainless steel zone

TABLE III-1-I. CALCULATED U-238 ABSORPTION CROSS SECTIONS, 1 IN. DIAMETER NATURAL UO SAMPLE

| Resonance Energy, eV | U-238 Absorption Cross Section[a] b | Sample Environment | | | | |
|---|---|---|---|---|---|---|
| | | Core (w/o Res.) | Core | SS Zone, Core[b] | Adjacent 8—U-238 | |
| | | | | | Outside | Inside |
| 450 | $\sigma_1(293)$ | 0.943 | 0.597 | 0.784 | 0.916 | 0.757 |
| | $\delta\sigma_1(1100)$ | 0.457 | 0.434 | 0.447 | 0.455 | 0.444 |
| | $\delta\sigma_2(1100)$ | 0.000 | −0.048 | −0.022 | −0.006 | −0.053 |
| | Sum $\delta\sigma$ | 0.457 | 0.386 | 0.425 | 0.449 | 0.391 |
| 2000 | $\sigma_1(293)$ | 0.619 | 0.429 | 0.514 | 0.603 | 0.474 |
| | $\delta\sigma_1(1100)$ | 0.213 | 0.226 | 0.220 | 0.214 | 0.220 |
| | $\delta\sigma_2(1100)$ | 0.000 | 0.005 | 0.004 | 0.000 | −0.005 |
| | Sum $\delta\sigma$ | 0.213 | 0.231 | 0.224 | 0.214 | 0.215 |
| 20,000 | $\sigma_1(293)$ | 0.06954 | 0.06197 | 0.06453 | 0.06759 | 0.06089 |
| | $\delta\sigma_1(1100)$ | 0.00402 | 0.00660 | 0.00573 | 0.00469 | 0.00697 |
| | $\delta\sigma_2(1100)$ | 0.00000 | 0.00200 | 0.00139 | 0.00058 | 0.00212 |
| | Sum $\delta\sigma$ | 0.00402 | 0.00860 | 0.00712 | 0.00527 | 0.00909 |

[a] 1, sample; 2, core.
[b] Configuration of measurement.

TABLE III-1-II. CALCULATED U-238 ABSORPTION CROSS SECTIONS, 1 IN. DIAMETER DEPLETED METAL SAMPLE

| Resonance Energy, eV | U-238 Absorption Cross Section[a] b | Sample Environment | | | | |
|---|---|---|---|---|---|---|
| | | Core (w/o Res.) | Core | SS Zone, Core[b] | Adjacent 8—U-238 | |
| | | | | | Outside | Inside |
| 450 | $\sigma_1(293)$ | 0.587 | 0.434 | 0.517 | 0.575 | 0.501 |
| | $\delta\sigma_1(1100)$ | 0.262 | 0.253 | 0.258 | 0.262 | 0.258 |
| | $\delta\sigma_2(1100)$ | 0.000 | 0.017 | −0.007 | −0.002 | −0.021 |
| | Sum $\delta\sigma$ | 0.262 | 0.236 | 0.251 | 0.260 | 0.237 |
| 2,000 | $\sigma_1(293)$ | 0.407 | 0.315 | 0.356 | 0.399 | 0.335 |
| | $\delta\sigma_1(1100)$ | 0.187 | 0.187 | 0.187 | 0.187 | 0.187 |
| | $\delta\sigma_2(1100)$ | 0.000 | 0.000 | 0.000 | 0.000 | −0.004 |
| | Sum $\delta\sigma$ | 0.187 | 0.187 | 0.187 | 0.187 | 0.183 |
| 20,000 | $\sigma_1(293)$ | 0.06205 | 0.05679 | 0.05857 | 0.06070 | 0.05602 |
| | $\delta\sigma_1(1100)$ | 0.00725 | 0.00880 | 0.00828 | 0.00765 | 0.00904 |
| | $\delta\sigma_2(1100)$ | 0.00000 | 0.00115 | 0.00081 | −0.00024 | 0.00124 |
| | Sum $\delta\sigma$ | 0.00725 | 0.00995 | 0.00909 | 0.00741 | 0.01028 |

[a] 1, sample; 2, core.
[b] Configuration of measurement.

and the homogenized core (with U-238 resonances). In column four, the U-238 in the adjacent eight drawers has been concentrated, at metal density, along the outside of an annular region having the same volume as the eight drawers; the other materials in these drawers were concentrated, in the inner portion of the annulus. Column five shows the results for the inverse case with the U-238 inside next to the stainless steel zone. These cases represent extreme variations with respect to the simple homogenization scheme. In all cases, except where the core-sample interaction is small and changing signs, the homogenized core case (column 3) falls between, and nearly at the average, of these two extreme cases. This would tend to support the homogenization assumption.

The general trend in Table III-1-I in comparing the measurement configuration (column 3) with the case without core resonances (column 1), is an enhancement of the Doppler effect at high energies (about +77% at 20,000 eV), a small enhancement at inter-

TABLE III-1-III. CALCULATED U-238 ABSORPTION CROSS SECTIONS, ½ IN. DIAMETER NATURAL $UO_2$ SAMPLE

| Resonance Energy, eV | U-238 Absorption Cross Section[a] b | Sample Environment | | | | |
|---|---|---|---|---|---|---|
| | | Core (w/o Res.) | Core | SS Zone, Core[b] | Adjacent 8—U-238 | |
| | | | | | Outside | Inside |
| 450 | $\sigma_1(293)$ | 1.342 | 0.626 | 1.018 | 1.289 | 0.970 |
| | $\delta\sigma_1(1100)$ | 0.626 | 0.572 | 0.601 | 0.620 | 0.589 |
| | $\delta\sigma_2(1100)$ | 0.000 | −0.092 | −0.046 | −0.013 | −0.098 |
| | Sum $\delta\sigma$ | 0.626 | 0.480 | 0.555 | 0.606 | 0.491 |
| 2,000 | $\sigma_1(293)$ | 0.805 | 0.461 | 0.616 | 0.776 | 0.547 |
| | $\delta\sigma_1(1100)$ | 0.191 | 0.240 | 0.218 | 0.195 | 0.221 |
| | $\delta\sigma_2(1100)$ | 0.000 | 0.013 | 0.014 | 0.002 | 0.002 |
| | Sum $\delta\sigma$ | 0.191 | 0.253 | 0.232 | 0.197 | 0.223 |
| 20,000 | $\sigma_1(293)$ | 0.07397 | 0.06285 | 0.06603 | 0.07028 | 0.06094 |
| | $\delta\sigma_1(1100)$ | 0.00235 | 0.00600 | 0.00485 | 0.00332 | 0.00668 |
| | $\delta\sigma_2(1100)$ | 0.00000 | 0.00264 | 0.00198 | 0.00089 | 0.00291 |
| | Sum $\delta\sigma$ | 0.00235 | 0.00864 | 0.00683 | 0.00421 | 0.00959 |

[a] 1, sample; 2, core.
[b] Configuration of measurement.

TABLE III-1-IV. COMPARISON WITH MEASUREMENTS OF U-238 REACTIVITY EFFECT CALCULATED BY ERIC-II AND RABBLE CODES, (293 to 1100°K)

| | Reactivity Ratios | | Doppler Effect Magnitude 1 in. Natural $UO_2$ Ih/kg U-238 |
|---|---|---|---|
| | ½ in. Natural $UO_2$ / 1 in. Depleted Metal | 1 in. Natural $UO_2$ / 1 in. Depleted Metal | |
| ERIC-II | 1.01 | 1.04 | −0.214 |
| RABBLE | 1.18 | 1.12 | −0.264 |
| Measured | 1.25 ± 0.06 | 1.12 ± 0.02 | −0.288 ± 0.008 |

mediate energies (about +5% at 2000 eV) and a reduction at low energies (−7% at 450 eV).*

Tables III-1-II and III-1-III contain the results of similar three-resonance calculations for samples specifically chosen in the measurements to emphasize any core-sample interaction effects. Table III-1-II shows the results for a 1 in. diam depleted uranium metal sample which depends relatively less on the surrounding core for resonance energy neutrons than does the standard 1 in. diam natural $UO_2$ sample. In this case the enhancements are smaller; +25% at 20,000 eV, 0% at 2000 eV and −4% at 450 eV. Table III-1-III lists similar results for a ½-in. dia. natural $UO_2$ sample which illustrates the sensitivity of small samples due to their strong dependence on the core for resonance energy neutrons. In this case, the enhancements are larger; +191% at 20,000 eV, +21% at 2000 eV; and −11% at 450 eV.

These same trends were found in the application of the RABBLE analysis to the full Doppler range for the three samples in Tables III-1-I, III-1-II and III-1-III. The results of this analysis are summarized in Table III-1-IV for the configuration of the measurements; i.e., sample, stainless steel zone, and core (with U-238 resonances). The calculations used the J. Schmidt[5] parameter compilation for resolved and unresolved U-238 resonances. Flux-weighted regional absorption cross sections and cross section changes were calculated with RABBLE for eleven coarse energy groups over the range 40,000 to 30 eV. The reactivities were calculated using a diffusion theory perturbation calculation (checked by $S_n$ calculations). The results in the tables labelled "ERIC-II[6]" are the earlier calculations in which the rational approximation was used and the core-sample interaction effects ignored.

The results of Table III-I-IV for the RABBLE analysis show a significant improvement compared with the measurements, over the ERIC-II analysis both in the magnitude of the reactivity Doppler effect and in the relative Doppler effect among the three samples. The RABBLE analysis indicates that in the spectrum of ZPR-6 Assembly 4Z the calculated reactivity Doppler effect for the standard 1 in. diam natural $UO_2$ sample has been enhanced by about 20% over that calculated by the ERIC-II analysis. The enhancement is due partly to an improved sample-

* For the five columns of Table III-1-I: 20,000, 0%, +114%, +77%, +31%, +126%; 2000, 0%, +8%, +5%, 0%, 0%; 450, 0%, −16%, −7%, −2%, −14%.

flux-depression calculation and partly due to the inclusion of core-sample interaction effects. Rough calculations indicate that about 80 to 85% of the calculated enhancement over the ERIC-II results is due to the core-sample interaction effects in the natural $UO_2$ samples; about 70 to 75% of the enhancement is core-sample interaction in the depleted metal sample. Thus, there is, approximately, a 17% interaction effect in the standard 1 in. diam natural $UO_2$ sample.

The RABBLE analysis leads to a calculated reactivity Doppler effect about 8% lower than measured. It should be pointed out, however, that an agreement in magnitude is mainly dependent on the correctness of the low-energy fission and capture cross sections used in the calculation of the gross flux in the core in the Doppler-energy range. These cross sections are uncertain for many reasons. For example, the uncertainty in the effective U-238 absorption cross sections at Doppler energies due to the heterogeneous plate structure of the core in itself introduces an uncertainty of the order of the 8% deviation.


REFERENCES

1. C. E. Till, R. A. Lewis and R. N. Hwang, *ZPR-6 Doppler Measurements and Comparisons with Theory*, Proc. International Conference on Fast Critical Experiments and their Analysis, October 10–13, 1966, ANL-7320, pp. 319–333.
2. F. Storrer, A. Khairallah and J. Ozeroff, *Theoretical Aspects of the Measurement of the Doppler Coefficient in a Critical Facility*, Proc. Conference on Breeding, Economics, and Safety in Large Fast Reactors, October 7–10, 1963, ANL-6792, pp. 823–852.
3. E. A. Fischer, *Interpretation of Doppler Coefficient Measurements in Fast Critical Assemblies*, KFK-473 (1966).
4. P. H. Kier and A. A. Robba, *RABBLE, a Program for Computation of Resonance Absorption in Multiregion Reactor Cells*, ANL-7326 (1967).
5. J. J. Schmidt, *Resonance Properties of the Main Fertile and Fissionable Nuclei*, Proc. Am. Nucl. Soc. National Topical Meeting on Reactor Physics in the Resonance and Thermal Regions, February 7–9, 1966 (The MIT Press, Massachusetts Institute of Technology, Cambridge, Massachusetts). Vol. II, pp. 223–256.
6. H. M. Sumner, *ERIC-II, a FORTRAN Program to Calculate Resonance Integrals and Fission Cross Sections*, AEEW-R323 (1964).


## III-2. Fissile Doppler Effect Measurement and the Effects of Thermal Expansion

C. E. TILL

Measurement of the Doppler effect of a fissile material by measuring the reactivity change as a function of temperature presents a variety of problems, but the most imı ortant is the separation of the reactivity effects due to resonance broadening—the true Doppler effects—from those due to thermal expansion. Most of the problems involved in reactivity Doppler effect measurements are enhanced somewhat when the material is fissile. This is due in general to the high reactivity worth of the material itself, and a correspondingly lower ratio of Doppler reactivity change to overall worth. This is reflected in a necessity for increased control over experimental conditions generally, and decreased tolerances in positioning, etc. The signals in this type of measurement are not large at any time, and in general are smaller for for fissile than fertile materials.

Techniques have been developed that allow the reactivity measurements to be made to adequate precision, and it has proven possible to design and construct equipment to sufficiently fine tolerances that positioning and dimensional uncertainties are not felt to represent a problem. (The two Laboratories in the U.S. that have substantial Doppler effect measurement programs, Atomics International and Argonne National Laboratory (ANL), have taken slightly different approaches to the reactivity measurement problem. Both approaches, however, are based on the oscillation of the Doppler sample in and out of the critical assembly, taking advantage of the capability that this allows for separation of the oscillatory reactivity change from reactor drifts. The Atomics International method involves analysis of the power trace, whereas the ANL method uses a calibrated servo-rod. In theory, the two methods are equivalent—both are ultimately limited in precision by the reactor statistics, as reflected in the total number of fissions in the measurement period. Proponents of either system can advance arguments favoring their choice, but the quoted results of both indicate that both achieve precisions approaching the theoretical limit, and the choice between the two is probably a rather subjective one.)

The problem that remains, however, and that will continue to remain with measurements of this kind, is the thermal expansion problem. The problem arises because the reactivity effect of expansion of a fissile material is typically of the same order as the Doppler

effect to be measured. Depending on the experimental arrangement, the expansion effects can be very considerably larger than the Doppler effect, or can be made less than the Doppler effect. However, if the experimenter wishes to leave some latitude in the range of variables affecting the Doppler effect, he must deal with expansion effects that are usually of the same order of magnitude as the Doppler effect he is trying to measure. The problem is a continuing one because each new reactor environment, and each new Doppler-effect sample material and configuration, causes a different split in the reactivity effects due to expansion and Doppler broadening.

The earliest experimental evidence of the degree to which expansion effects can mask the Doppler effects arose in the first Atomic International attempts to measure the U-235 Doppler effect.[1] The result on heating a sample of U-235 metal in a fast spectrum showed a small negative reactivity effect, initially tentatively identified as a negative Doppler effect. Later work at both AI and ANL showed the initial interpretation was not correct, and that in fact a large negative expansion effect was swamping the positive Doppler effect of the material in this spectrum. But the result served to stimulate an attack on the expansion problem at both Laboratories. The Atomics International approach has been to use subsidiary experiments to evaluate the effect of expansion, and then to subtract the reactivity effect so determined from the total reactivity effect measured upon sample heating. The subsidiary measurements involved measurements of the differences in reactivity between samples artificially expanded to simulate the effects of thermal expansion. The thermal expansion simulation measurements have been done using a variety of different methods of expanding the material to allow a cross check between various methods, and over a range of spectra as well. Expanded solid U-235 metal, expanding foils, and measurements of the reactivity change at the phase change in uranium metal have all been done for U-235 and the results look quite consistent.

The ANL approach to the expansion problem took a somewhat different direction. It is based on the use of reduced density samples, with advantage taken of the decreased reactivity coefficient of expansion attendant upon reduction in sample density. The residual expansion effect is evaluated through the use of differing sample types, in which the expansion is physically constrained in various ways. The method allows a rather direct experimental separation of the effects of expansion from Doppler broadening—the expansion effects are evaluated using the same samples from which the Doppler effect data are derived.

This paper discusses the major factors involved in the reactivity effects of expansion of a fissile material. Two companion papers give experimental information; the first gives a description of the techniques and equipment used at ANL for evaluation of expansion effects and a summary of the experimental data obtained on several dilute carbide fast reactor mockups, and the second gives data from a series of cores designed explicitly to investigate the systematics of the U-235 Doppler effect (see Papers III-3, III-4).

## The Reactivity Effects of Expansion of a Sample of Fissile Material

The effects are broadly of two types. The first is a macroscopic effect due to sample expansion into regions of different reactivity worth, which is related to the overall macroscopic reactor flux and adjoint profiles in which the sample finds itself. In the usual type of Doppler measurement in which a cylindrical sample of material is heated at the center of a Zero Power Reactor, this can be considered to be an axial expansion effect. It can be minimized by positioning the sample in a region where the axial profiles are reasonably flat, and in general this effect is not felt to present much of a problem. The second type of effect may be thought of as a microscopic effect, related to the changes in the sample collision probabilities as the dimensions and density change. With cylindrical samples, this is mainly a radial expansion effect. This latter effect is the one that presents the major problem to fissile Doppler effect measurements, and it is to this effect that this paper is addressed.

The effects are broadly analogous to the heterogeneity effects in a thermal reactor caused by lumping of the fuel: as the lump expands, there is a decrease in the self-multiplication at high energy and a corresponding decrease in the self-shielding at lower energies. At high energies the expansion effects therefore cause negative reactivity changes, and at low energies the reactivity changes are positive. The net effect of expansion is a balance of the two effects, and is dependent on the particular reactor flux and adjoint spectrum.

The reactivity worth of a Doppler sample, and changes in its worth caused by expansion, are usually described by some form of perturbation expression. Each of the various forms of the group-diffusion theory perturbation expressions is based on the usual expression for the worth of a sample of material relative to void:

$$\frac{\Delta k}{k} = \frac{V_s}{D} \sum_i \phi_i' \sum_j \left(\chi_j \nu_i \Sigma_{f_i} + \Sigma_{i\to j}\right) \phi_j^* - \Sigma_{t_i} \phi_i^*, \quad (1)$$

where

$V_s \equiv$ sample volume

$D = \int_{Reactor} \sum_j \chi_j \phi_j^* \sum_i \phi_i \nu_i \Sigma_{f_i} \, dV$

$\phi_i' \equiv$ average perturbed flux in group $i$ in the sample

$\phi_j \equiv$ unperturbed reactor flux in group $j$

$\phi_j^* \equiv$ unperturbed reactor adjoint flux in group $j$

$\chi_j \equiv$ fraction of fission neutrons born in group $j$

$\nu_i \equiv$ number of neutrons per fission in group $i$

$\Sigma_{f_i} \equiv$ macroscopic fission cross section in group $i$

$\Sigma_{i\to j} \equiv$ macroscopic transfer cross section from group $i$ to $j$

$\Sigma_t \equiv$ total cross section in group $i$.

As written, the expressions include in-group scattering, $\phi_i' \Sigma_{i\to i}$, but one could equally well exclude $\Sigma_{i\to i}$ from the $j$ summation and define $\Sigma_{t_i}$ excluding $\Sigma_{i\to i}$ as well. Within the group-diffusion theory context, Eq. (1) is exact. If we write Eq. (1) in terms of the cross sections per fissile atom in the sample, $\sigma_i \equiv \Sigma_i / N_f$, and note that $N_f = N_0 M_s / A V_s$, ($N_0 = 6.03 \times 10^{23}$, $M_s \equiv$ sample mass, $A \equiv$ atomic weight),

$$\frac{\Delta k}{k} = \frac{N_0 M_s}{AD} \sum_i \phi_i' \sum_j (\chi_j \nu_i \sigma_{f_i} + \sigma_{i\to j}) \, \phi_j^* - \sigma_{t_i} \phi_i^* . \quad (2)$$

The term in front of the summations is independent of volume changes, as are the cross sections written in this form, so the changes in worth due to expansion are all contained in the changes of $\phi_i'$ as the sample expands. It is in the calculation of $\phi'$ that approximations enter. Various approximations have been made.

At ANL, in the work being reported here, the perturbed flux calculation was based on an expression of neutron balance:

$$V_0 \Sigma_{t_{0_i}} \phi_{0i} = P_{00_i} V_0 \sum_k (\Sigma_{k\to i_0} + \chi_i \nu_k \Sigma_{f_{k0}}) \phi_{0_k} + P_{10_i} V_1 \sum_k (\Sigma_{k\to i_1} + \chi_i \nu_k \Sigma_{f_{k1}}) \phi_{1_k} , \quad (3)$$

where

$\phi_{0_i} = \phi_i' \equiv$ the perturbed flux in the sample

$P_{00_i} \equiv$ probability of a neutron born in the sample in the $i$th group making its first collision in the sample

$P_{10_i} \equiv$ probability of a neutron born in the reactor in the $i$th group making its first collision in the sample.

The subscripts 0 and 1 refer to the sample and reactor respectively.

The collision probabilities are taken to be flat-source probabilities so that application of reciprocity

$$(P_{10} V_1 \Sigma_{t_i} = [1 - P_{00}] V_0 \Sigma_{t_0})$$

and rearrangement of Eq. (3) gives

$$\phi_{0_i} = \frac{P_{00_i} \sum_{k\neq i} (\Sigma_{k\to i_0} + \chi_i \nu_k \Sigma_{f_{0k}}) \phi_{0_k}}{\Sigma_{t_{0_i}} - P_{00_i} (\Sigma_{i\to i_0} + \chi_i \nu_i \Sigma_{f_{0_i}})} + \frac{(1 - P_{00_i}) \Sigma_{t_{0_i}} \sum_k (\Sigma_{k\to i_1} + \chi_i \nu_k \Sigma_{f_{1k}}) \phi_{1k}}{\Sigma_{t_{1_i}} [\Sigma_{t_{0_i}} - P_{00_i} (\Sigma_{i\to i_0} + \chi_i \nu_i \Sigma_{f_{0_i}})]} . \quad (4)$$

The solution is iterative, but converges rapidly.

A reasonably accurate simplification results from equating the source in any group to the reaction rate in the group in the reactor term of Eq. (4); that is,

$$\sum_k (\Sigma_{k\to i_1} + \chi_i \nu_k \Sigma_{f_{k1}}) \phi_{1_k} \approx \Sigma_{t_{1_j}} \phi_{1_j} \quad (5)$$

and if this substitution is made in Eq. (4), the perturbed flux in the sample is given in terms of the sample cross sections only:

$$\phi_{0_i} = P_{00_i} \sum_{k\neq i} \cdot \frac{(\Sigma_{k\to i_0} + \chi_i \nu_k \Sigma_{f_{0k}}) \phi_{0_k} + (1 - P_{00_i}) \Sigma_{t_{0_i}} \phi_{1_i}}{\Sigma_{t_{0_i}} - P_{00_i} (\Sigma_{i\to i_0} + \chi_i \nu_i \Sigma_{f_{0_i}})} . \quad (6)$$

The flat-source collision probabilities for a cylindrical rod are calculated from $P_{00} = 1 - P_e$, where

$$P_e = \frac{2}{3} \Sigma_a \Big\{ 2[\Sigma_a \{K_1(\Sigma_a) I_1(\Sigma_a) + K_0(\Sigma_a) I_0(\Sigma_a)\} - 1] + \frac{K_1(\Sigma_a) I_1(\Sigma_a)}{\Sigma_a} - K_0(\Sigma_a) I_1(\Sigma_a) + K_1(\Sigma_a) I_0(\Sigma_a) \Big\} \quad (7)$$

as given by K. Case et al.[2] ($a \equiv$ sample radius.)

In order to examine the major variables upon which the expansion effects depend, let us introduce some approximations in Eqs. (2) and (6):

a.) At low energies

$\chi_i = 0$ and $\Sigma_{k\to i} \to 0$, $k \neq i$, for heavy elements. For any group $i$, Eq. (6) becomes

$$\phi' \equiv \phi_{0_i} \approx \frac{(1 - P_{00}) \Sigma_{t_0} \phi_1}{\Sigma_{t_0} - P_{00} \Sigma_{i\to i_0}} = \frac{(1 - P_{00}) \phi_1}{1 - P_{00} \dfrac{\Sigma_{i\to i_0}}{\Sigma_{t_0}}} ;$$

for small $P_{00}$,

$$\phi' \approx 1 - \left(1 - \frac{\Sigma_{i\to i_0}}{\Sigma_{t_0}}\right) P_{00} \phi_1$$

or with expansion,

$$\delta\phi' = -\left(1 - \frac{\Sigma_{i\to i_0}}{\Sigma_{t_0}}\right) \phi_1 \delta P_{00} \approx -\left(1 - \frac{\sigma_s}{\sigma_t}\right) \phi_1 \delta P_{00} .$$

Introducing the rational approximation for $P_{00} = (\Sigma_t \bar{l})/(1 + \Sigma_t \bar{l})$, $\bar{l} \equiv$ mean chord length, then again for small $P_{00}$,

$$\delta\phi' = -\left(1 - \frac{\sigma_s}{\sigma_t}\right)\sigma_t\delta(Nl)$$
$$= -(\sigma_t - \sigma_s)\delta(Nl)\phi_1 = -\sigma_a\delta(Nl)\phi_1.$$

Equation (2), under the same simplifying assumptions, for group $i$, reduces to

$$\left.\frac{\Delta k}{k}\right|_i = \frac{N_0 M_s}{AD}\,\phi_i'(\phi_f^*\nu_i\sigma_{f_i} - \sigma_{a_i}\phi_i^*),$$

where $\phi_f^* \equiv$ reactor fission neutron adjoint. Taking $\sigma_f^* \approx \sigma_i^*$, for small expansions

$$\delta k \approx \frac{N_0 M_s}{AD}(\nu\sigma_f - \sigma_a)\delta\phi' \tag{8}$$
$$= -\frac{N_0 M_s}{AD}\phi_1(\nu\sigma_f - \sigma_a)\sigma_a\delta Nl$$
$$= -\frac{N_0 M_s}{AD}\phi_1([\nu - 1]\sigma_f - \sigma_c)(\sigma_f + \sigma_c)\delta(Nl)$$
$$\approx -\frac{N_0 M_s}{AD}\phi_1([\nu - 1]\sigma_f^2)\delta(Nl). \tag{9}$$

At low energies, therefore, the expansion effects are approximately proportional to $(\nu - 1)\sigma_f^2$ for the particular isotope. Secondly, $Nl = (N_0 M_s/AV)(4V/S) = 4N_0 M_s/AS$, where $V$ is the volume of sample and $S$ is the surface area. So $\delta(Nl) = (4N_0 M_s/A)\delta(1/S)$, and as the sample expands $S$ increases, so $\delta(1/S)$ is negative. The reactivity effect of sample expansion in the energy range below the fission threshold therefore, is positive, as expected.

b.) At high energies, where significant numbers of neutrons are born in the fission process:

$$\phi_{0_i} = \frac{P_{00_i}\sum_{k\neq i}\chi_i\nu_k\Sigma_{f_{0k}}\phi_{0_k} + (1 - P_{00_i})\Sigma_{t_{0i}}\phi_{1_i}}{\Sigma_{t_{0i}}\left[1 - P_{00_i}\dfrac{(\Sigma_{i\to i_0} + \chi_i\nu_i\Sigma_{f_{0i}})}{\Sigma_{t_{0i}}}\right]};$$

for small $P_{00}$,

$$\phi_{0_i} \approx \frac{P_{00_i}\sum_{k\neq i}\chi_i\nu_k\Sigma_{f_{0k}}\phi_{0_k} + (1 - P_{00_i})\Sigma_{t_{0i}}\phi_{1_i} + P_{00_i}(\Sigma_{i\to i} + \chi_i\nu_i\Sigma_{f_{0i}})}{\Sigma_{t_{0i}}}$$
$$\approx \frac{\chi_i\overline{\nu\Sigma_f\phi}P_{00_i} + \Sigma_{t_{0i}}\phi_{1_i}}{\Sigma_{t_{0i}}};$$

for small expansions,

$$\delta\phi' = \frac{\chi_i\overline{\nu\Sigma_f\phi}}{\Sigma_{t_{0i}}}\delta P_{00} \approx \chi_i\overline{\nu\sigma_f\phi}\delta(Nl).$$

Again,

$$\delta k \approx \frac{N_0 M_s}{AD}(\nu\sigma_f - \sigma_a)\delta\phi', \tag{8}$$

so at high energies

$$\delta k_i \approx \frac{N_0 M_s}{AD}\chi_i\overline{\nu\sigma_f\phi}(\nu\sigma_{f_i} - \sigma_{a_i})\delta(Nl) \tag{9}$$

or

$$\delta k_i \approx \frac{N_0 M_s}{AD}\chi_i\phi\nu(\nu - 1)\sigma_f^2\delta(Nl). \tag{10}$$

As $\delta(Nl)$ is negative, the expansion effect is negative at high energies, and in any energy group $i$, the magnitude is proportional to the $\chi_i$ for the group. Overall, the expansion effect is approximately proportional to $\nu(\nu - 1)\sigma_f^2$ in this energy region.

As these considerations indicate, differences in $\nu$ and $\sigma_f$ among the various fissile isotopes cause considerable differences in the magnitude of their expansion effects. Further, the relative magnitudes of the expansion effects in different fissile isotopes will vary from reactor to reactor as the real flux and adjoint spectra change. For Assembly 5 of ZPR-6, for example, which has a spectrum typical of a large dilute fast reactor (see Paper III-6), the fluxes and adjoints are such that the (negative) high energy effect in U-235 is about double the (positive) low energy effect and the net expansion effect in U-235 is therefore negative.

As an illustration of the way in which variations in values of $\nu$ and $\sigma_f$ for various isotopes influence their expansion effects, Table III-2-I gives the approximate ratios at high and low energies for U-233, Pu-239 and Pu-241, each relative to U-235. To give the net effect in any given spectrum, the relative weighting of the high and low energy effects must also be specified. The ratios for the isotopes other than U-235 are quoted in the table relative to U-235 itself, and taking Assembly 5 as a reference, where the high energy effect is about twice the low energy effect, a rough normalization for the other isotopes can be effected. The net effect is shown in the last column of Table III-2-I. As shown, the net effect is negative in this spectrum for all the isotopes and considerably larger for the isotopes other than U-235 than for U-235 itself. These very rough considerations predict the relative magnitudes of the expansion effect in the various isotopes reasonably well, as a comparison to the more exact calculations given in the next section will show. The approximate relationships clearly illustrate the main reasons for the

differences in the expansion effects between various isotopes.

### Expansion Effects in Various Fissile Isotopes

Figure III-2-1 shows the results of calculations of the reactivity effect of expansion for various fissile isotopes as a function of sample density, for a nominal 1 in. diam sample at the center of ZPR-6 Assembly 5. The calculations used Eq. (6) for the perturbed flux in the sample, the collision probabilities given by Eq. (7), and the sample worth given by Eq. (2). The expansion effect was obtained from the difference between two reactivity worth calculations, one for the sample at a nominal density and the second for the sample slightly expanded, both calculations utilizing Eq. (2). (The expansion effect is sufficiently linear in sample density over limited ranges, that typically the calculation was done for a nominal 1% decrease in optical path.) The results in Fig. III-2-1 are quoted in terms of Ih/kg of heavy isotope for $10^{-3}$ in. per in. of linear expansion. That is, the sample was assumed to freely expand in three dimensions, as it would with the temperature change without constraint of any kind. (As discussed in another paper (see Paper III-3), the results differ if some form of constraint is present).

TABLE III-2-I. Approximate Relative Magnitudes of Expansion Effect in a Typical Fast Spectrum

| Fissile Isotope | High Energies | | Low Energies | Net Effect |
|---|---|---|---|---|
| | $\frac{\nu(\nu-1)}{\sigma_f^2}$ Ratio | $\times(-2)$ | $\frac{(\nu-1)}{\sigma_f^2}$ Ratio | |
| U-235 | 1 | −2 | 1 | −1 |
| U-233 | 3 | −6 | 2 | −4 |
| Pu-239 | 3 | −6 | $\frac{1}{3}$ | −6 |
| Pu-241 | 4 | −8 | 3 | −5 |

TABLE III-2-II. Reactivity Worths and Expansion Effects in ZPR-6 Assembly 5

| Isotope | Ih/kg Metal | | | | |
|---|---|---|---|---|---|
| | Measured Worth | Calculated Worth, Dilute | Calculated Worth, 1 in. diam Metal | Calculated Excess Worth Due to Lumping | Expansion Effect of $10^{-3}$ in./in. |
| U-235 | 50 | 56.6 | 61.5 | 4.9 | 0.016 |
| U-233 | 83 | 100 | 120 | 20 | 0.077 |
| Pu-239 | 70 | 76 | 106 | 30 | 0.108 |
| Pu-241 | — | 132 | 165 | 33 | 0.122 |

The fluxes and adjoints, and the corresponding perturbation normalization, were obtained from a diffusion theory calculation for the unperturbed core, using cross sections generated largely by MC², as described in Ref. 3. The absolute magnitudes of the expansion effects are therefore dependent on this normalization, but the relative magnitudes are insensitive to it. The worths of three of the fissile materials shown were measured in Assembly 5, and a comparison of the measured worths with the calculated worths indicate that the fluxes and normalization are probably fairly good, so that the ab-

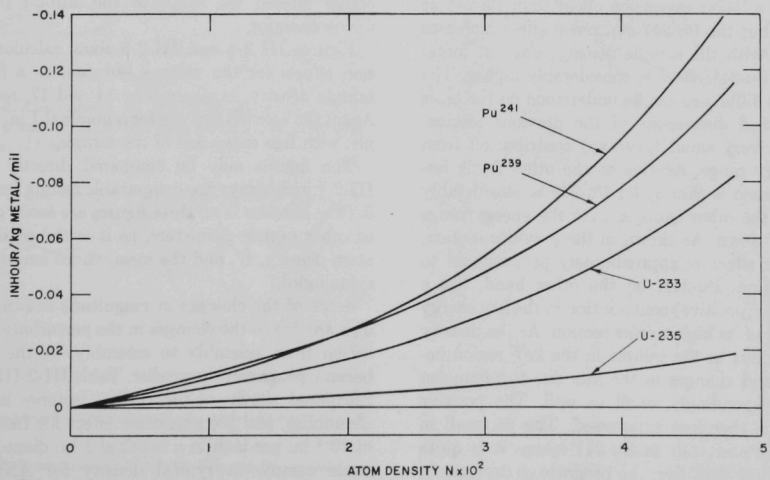


Fig. III-2-1. Expansion Effects for a 1 in. dia cylinder in Assembly 5, ZPR-6. *ANL Neg. No. 112-9416 Rev. 1*

solute magnitudes should be reasonably close as well. Columns 2 and 3 in Table III-2-II compare the worths calculated using the methods described above with the measured worths (see Paper III-6). As can be seen, the U-235 and Pu-239 worths are reasonably well predicted; the U-235 agreement is somewhat poorer, perhaps a reflection on the particular cross sections used for U-233 in this study. The calculated worths in Column 3 are for materials dilute only in the sense that no additional heterogeneity effects are taken into account over those implicit in the choice of $\sigma_p$ in the resonance region. The resonance region cross sections correspond to a $\sigma_p$ typically in the range of a 100 b; no particular effort was made to make the $\sigma_p$ for the sample correspond to the actual sample size. Disagreements of the order shown, therefore, are not unexpected.

Table III-2-II also lists the calculated worths of a 1 in. diam fully dense metal sample, and the difference in the worth per kg of the 1 in. metal sample and the dilute sample—a measure of the difference in worth due to lumping. The expansion effect for the 1 in. metal sample is given in the final column. The table illustrates that the expansion effects are approximately proportional to the total worth difference due to lumping, as might be expected, and not to the worth of the material itself.

Figure III-2-1 and Table III-2-II show the large differences in the expansion effect between various fissile isotopes, which were expected on the basis of the simplified considerations of the previous section. Figure III-2-1, however, also shows that the shape of the expansion reactivity versus sample density curve differs from isotope to isotope. In particular, Pu-239 in this spectrum has a larger expansion effect than Pu-241 at low densities but the Pu-241 expansion effect increases more rapidly with the sample density, until at metal densities the Pu-241 effect is considerably higher. The reason for the difference can be understood on the basis of the simplified discussions of the previous section. Pu-239 has a very small (positive) contribution from the low energy range, relative to the other fissile isotopes. The reason is that $\sigma_f$ for Pu-239 is considerably smaller than the other isotopes over the energy range from 100 keV down. As shown in the previous section, the expansion effect is approximately proportional to $\sigma_f^2$ in this region. Pu-241, on the other hand, has a relatively large (positive) contribution in the low energy range because of its higher cross section. As the density increases, the flux in the sample in the keV region becomes small and changes in the flux due to expansion becomes correspondingly small as well. The positive contribution is therefore suppressed. This is small in Pu-239 in any case, but in Pu-241 where it is quite significant at low densities, the progressive decrease in its importance relative to the high energy contribution causes the net expansion effect to increase more rapidly with density. The result is a crossing of the two curves at a density somewhat less than the density of $PuO_2$.

### The Effect of Flux and Adjoint Spectrum Changes on the Expansion Coefficient

The expansion coefficients of the various isotopes are sensitive in varying degrees to both the flux and adjoint spectrum. Quite realistic changes in the material compositions of the reactor can change the magnitude of the expansion coefficient very significantly, and in some cases can even cause it to change sign. To give a basis for the discussion of these effects, calculated expansion effects for the various isotopes are compared between ZPR-6 Assembly 5, and ZPR-9 Assemblies 14 and 17. The compositions and characteristics of the latter two assemblies are listed in Paper III-4. Both assemblies have considerably softer spectra than Assembly 5, and the variation in the adjoint flux with energy is considerably different between the two. Comparisons of the calculated flux and adjoint spectra at the center of the three assemblies are given in Figs. III-2-2 and III-2-3 respectively.

The changes in material compositions between the three assemblies are related in the following way. Starting with the Assembly 5 composition, Assembly 14 was constructed by removing a fraction of the U-238 and replacing it with polyethylene and graphite to substantially soften the original spectrum. For Assembly 17, the remainder of the U-238 plates was removed and replaced with graphite which further softened the flux spectrum somewhat, but more importantly, considerably altered the shape of the adjoint function at fission energies.

Figures III-2-4 and III-2-5 show calculated expansion effects for the various isotopes, as a function of sample density, in Assemblies 14 and 17, respectively. Again the calculations are for a nominal 1 in. diam sample, with free expansion of the sample.

The figures may be compared directly with Fig. III-2-1 which gave the comparable results for Assembly 5. (The abscissa in all three figures are easily generalized to other sample diameters, as it is the product of the atom density, $N$, and the mean chord length, $\bar{l}$, that is meaningful.)

Some of the changes in magnitude shown in the figures are due to the changes in the perturbation normalization from assembly to assembly, as the assemblies became progressively smaller. Table III-2-III shows the calculated worths of the various isotopes in the three assemblies, and the expansion effect for free expansion of $10^{-3}$ in. per inch in a nominal 1 in. diam 70% dense oxide sample (a typical density for ANL Doppler samples).

Where quantities were measured, they are quoted in the table in parentheses. The calculations were done only to illustrate the effects under discussion, and they tend to be rather rough, but they are felt to be sufficiently precise to reasonably represent the physical situation.

Comparison of the measured and calculated worths illustrates that the fluxes, adjoints and normalization used in the calculations are probably reasonable, and comparison of the worths of the fissile materials between the various assemblies gives a fair idea of the differences in the magnitude of the expansion effects that are due to normalization changes from assembly to assembly.

Figures III-2-1, III-2-4 and III-2-5 show the very different behavior of the expansion effects in the three assemblies. Not only does the expanison effect of several of the isotopes change sign between assemblies, but they also change sign as the sample density changes within a given assembly.

The explanation of the sign changes as a function of sample density in the two softer spectrum assemblies is

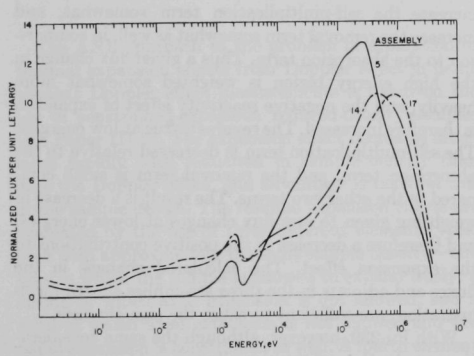


FIG. III-2-2. Comparison of the Real Flux Spectra in Assemblies 14 and 17 of ZPR-9 and Assembly 5 of ZPR-6. *ANL Neg. No. 112-9407.*

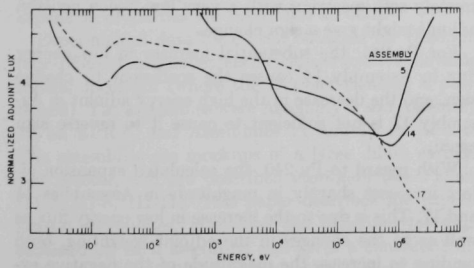


FIG. III-2-3. Comparison of Adjoint Spectra in Assemblies 14 and 17 of ZPR-9 and Assembly 5 of ZPR-6. *ANL Neg. No. 112-9415.*

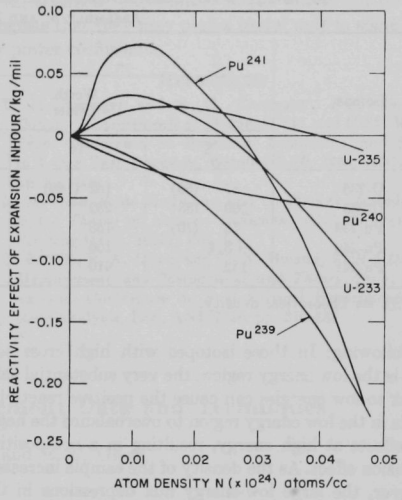


FIG. III-2-4. Reactivity Effect of Expansion of Various Heavy Isotopes in Assembly 14, ZPR-9. *ANL Neg. No. 112-9444.*

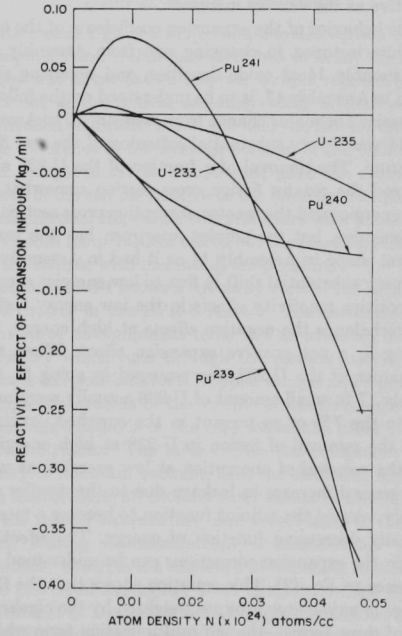


FIG. III-2-5. Reactivity Effect of Expansion of Various Heavy isotopes in Assembly 17, ZPR-9. *ANL Neg. No. 112-9443.*

TABLE III-2-III. Comparison of the Reactivity Worths and Expansion Effects in ZPR-6 Assembly 5, and ZPR-9 Assemblies 14 and 17

| Isotope | Ih/kg Metal | | | | | |
|---|---|---|---|---|---|---|
| | Worth, Dilute | | | 1 in. diam Oxide (70% T.D.)[a] Expansion Effect for $10^{-3}$ in./in. | | |
| | 5 | 14 | 17 | 5 | 14 | 17 |
| U-235 | 57 (50) | 152 (148) | 161 (145) | −0.003 | +0.023 | −0.007 |
| U-233 | 100 (83) | 262 | 304 | −0.012 | +0.023 | −0.013 |
| Pu-239 | 76 (70) | 158 | 192 (237) | −0.020 | −0.036 | −0.086 |
| Pu-240 | +3.4 | −106 | −366 | — | −0.033 | −0.072 |
| Pu-241 | 132 | 410 | 565 | −0.019 | +0.061 | +0.057 |

[a] T.D. ≡ Theoretical density.

the following: In those isotopes with high cross sections is the low energy region, the very substantial shift of flux to low energies can cause the positive reactivity effects in the low energy region to overbalance the negative effects at high energy, resulting in a net positive expansion effect. As the density of the sample increases, however, the large low-energy flux depressions in the sample cause the positive contribution to lessen in comparison to the high energy self-multiplication contributions. The result is a change in sign from positive to negative as the density increases.

The behavior of the expansion coefficients of the two uranium isotopes, in changing sign from Assembly 4Z to Assembly 14 at oxide densities, and reversing sign again in Assembly 17, is to be understood on the following basis: The major change from Assembly 5 to Assembly 14 was a very substantial softening of the real flux spectrum. The removal of a fraction of the U-238 also changed the reactor fission cross section somewhat at high energies and the reactor absorption cross section at low energies, but the adjoint spectrum has the same general shape in Assembly 14 as it had in Assembly 5. The very substantial shift in flux to low energies caused the positive reactivity effects in the low energy region to overbalance the negative effects at high energy, resulting in a net positive expansion effect. When the remainder of the U-238 was removed in going to Assembly 17 (a small amount of U-238 actually remained, due to the 7% or so present in the enriched uranium fuel) the removal of fission in U-238 at high energies, and the removal of absorption at low energies, as well as a general increase in leakage due to the smaller assembly, caused the adjoint function to become a monotonically decreasing function of energy. The effect of this on the expansion corrections can be understood by reference to Eq. (2). This equation shows that the flux change in any energy group is weighted by the algebraic sum of three terms—the self-multiplication term which is weighted by the fission neutron adjoint, the removal term which is weighted by the adjoints at energies below those of the group under consideration, and the absorption term which is weighted by the adjoint of the group itself. At the highest energies then, the effect of a monotonically decreasing adjoint flux with energy is to increase the self-multiplication term somewhat, and increase the removal term somewhat as well, in comparison to the absorption term. Thus a given flux change in the high energy region is weighted somewhat more heavily, and the negative reactivity effect of expansion is therefore increased. The reverse is true at low energies. The self-multiplication term is decreased relative to the absorption term, and the removal term is small compared to the other two terms. The result is a decrease in weighting given to any flux changes at lower energies, and therefore a decrease in the positive contributions to the expansion effect. The calculated changes in the fluxes and adjoints in the three assemblies chosen for illustration, are sufficient to cause the sign changes.

With Pu-239, however, although the same considerations apply, the positive contributions at low energy are sufficiently small in any case that the coefficient remains negative in all three assemblies. This stability in sign should be characteristic of this material—only an extremely soft spectrum with a very low fission neutron adjoint might give a sign change.

For Pu-241, the substantial increase in low energy flux in Assembly 14 causes the coefficient to change sign, and the decrease in the high energy adjoint in Assembly 17 is not sufficient to cause it to reverse sign again.

With regard to Pu-240, the calculated expansion effect increases sharply in magnitude in Assemblies 14 and 17. This is due to the increase in low energy flux as well as to the changes in the adjoint weighting, both tending to increase the magnitude of the negative expansion coefficient.

### Conclusions

The foregoing considerations illustrate the sensitivity of the expansion effect to reactor fluxes and adjoints, and illustrate the necessity for experimental verification of expansion corrections. Secondly, however, they also illustrate the possibility of utilizing the very different behavior of the expansion effect in the various isotopes with changes in fluxes and adjoints, to aid in the evaluation of the expansion effects themselves. Thirdly, the effects predicted for U-233 and the plutonium isotopes in fast spectra demonstrate the need for caution in identifying measured reactivity effects due to heating as Doppler effects until a thorough evaluation of the expansion effects has been made. Finally, the magnitude of these effects, particularly in the plutonium isotopes suggests that they may play a useful part in some reactor power coefficients.

### References

1. T. H. Springer and S. G. Carpenter, *Fast Spectrum Doppler Measurements of Th-232, U-238, and U-235 Metals*, Proc. Conference on Breeding, Economics, and Safety in Large Fast Reactors, October 7–10, 1963, ANL-6792, pp. 897–905.
2. K. M. Case, F. de Hoffmann and G. Placzek, *Introduction to the Theory of Neutron Diffusion*, (U.S. Government Printing Office, 1953), Vol. I.
3. C. E. Till, R. A. Lewis and R. N. Hwang, *ZPR-6 Doppler Measurements and Comparisons with Theory*, Proc. International Conference on Fast Critical Experiments and their Analysis, 1966, ANL-7320, pp. 319–333.

## III-3. U-235 Doppler Effect Measurement Data and Techniques

C. E. Till, R. A. Lewis and E. F. Groh

The ANL approach to the problem of separation of thermal expansion effects from Doppler effect in fissile element Doppler effect meausrements is based on the use of constrained-expansion reduced-density samples (see Paper III-2). The expansion effect decreases much more rapidly with reduction in sample density than does the Doppler effect, and advantage is taken of this in the sample design. The residual expansion effects are evaluated by the use of three different element types, each with approximately the same sample density—one type in which the sample is allowed to expand freely, a second in which axial expansion is not allowed, and a third in which axial expansion is not allowed and the radial expansion is constrained as well. A fourth element type, containing U-235 metal, has also been used to check the results. The proof of the method, therefore, must lie in the consistency of the results given by the various element types, when the known differences in expansion properties are taken into account.

Experimental data have been obtained for U-235 in four different assemblies, each designed to have the same central spectrum (where the Doppler element is positioned). The assemblies were Assembly 5 and Assembly 4Z on ZPR-6, and Assemblies 11 and 12 on ZPR-9. The assemblies are mockups of a large dilute carbide fast reactor, and are described elsewhere (see Papers III-6, III-8, III-11). This paper describes the experimental techniques, assembles the experimental data obtained on each assembly, and gives a consistent intercomparison of the data from the various element types on the different assemblies, so that some judgment can be made of the consistency and reliability of the U-235 Doppler effect data.

### Equipment and Techniques

Reference 1 gives a more complete description of the equipment and techniques used, but in brief, the technique was to oscillate a Doppler sample repetitively in and out of the critical assembly while a small servo-controlled calibrated boron rod held the reactor critical. The difference in the average position of the calibrated rod, sample-in minus sample-out, gave the reactivity worth of the sample relative to the reference sample-out configuration. Repeating this procedure with the sample at various temperatures traced out the reactivity change of the sample with increasing temperature.

Figure III-3-1 shows a cut-away view of the oscillator and drawer in the ZPR-6 reactor. The oscillator unit consists of an equipment table and an attached drawer assembly which runs through the reactor matrix. The drawer has positions for a Doppler sample and a dummy sample. Separation of the sample positions is such that when one sample is at the core center the other is outside the reactor. The table carries the equipment necessary to maintain vacuum, heat the elements, monitor the temperature, air cool the outer sheath of the element to the reactor temperature, and detect leaks in the system. During a measurement a master-timer automatically controls the sequence of oscillator movement and servo-rod averaging. Data analysis is done by the method of E. Bennett and R. Long,[2] which allows elimination of first and second order reactivity drifts. This

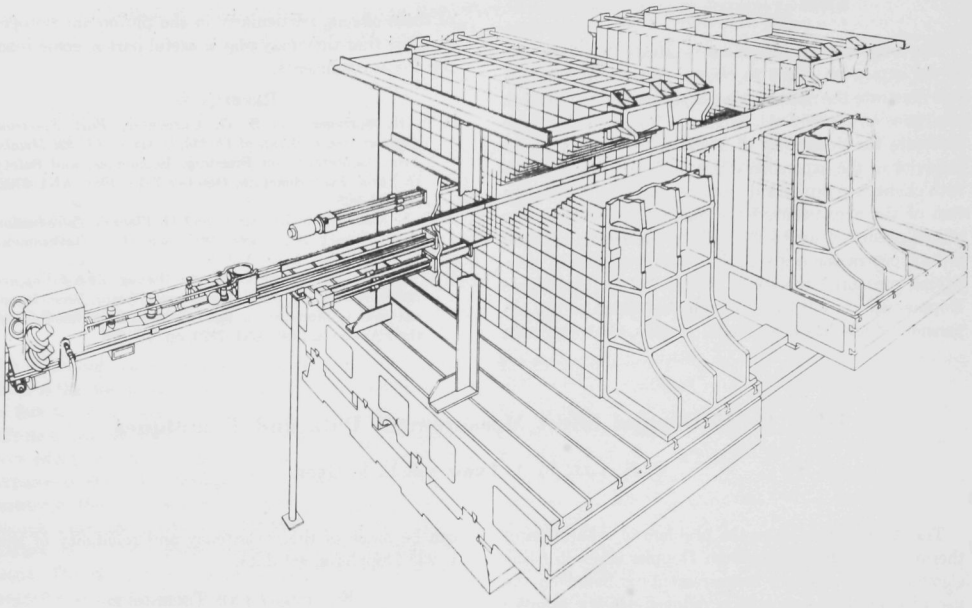

FIG. III-3-1. Dopper Equipment in ZPR-6. *ANL Neg. No. 112-5834 T-1.*

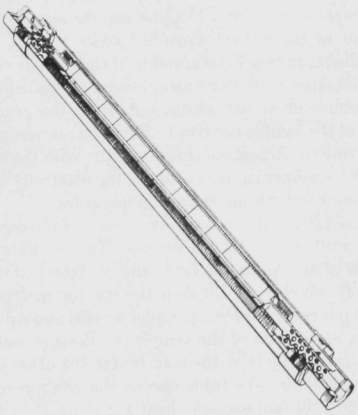

FIG. III-3-2. Type 2 Element (Expansion Constrained). *ANL Neg. No. 112-6967.*

system gives a precision of about 0.0025 Ih for 80 min of reactor operation at about 20 W.

Measurements were made with four basically different types of samples, each with different thermal expansion properties. Three of these samples types used reduced density $UO_2$ and the expansion was variously constrained axially and radially. The fourth type contained uranium metal, much more strongly shielded, which although not directly comparable to the others, would be expected to give results consistent with the others when the known differences are taken into account.

The samples in which the expansion was controlled had the following characteristics in common. They consisted of a cylindrical $UO_2$ sample, about 1 in. diam and 12 in. long, enclosed in a 50-mil thick nickel-alloy heater tube, which in turn was suspended in a 50-mil SS outer container. (Vacuum was maintained in a 95-mil annulus between the heater tube and the outer container to minimize heat loss from the element.) A typical element is shown in Fig. III-3-2. In the tables and graphs in this paper, the expansion properties of the element are denoted as FE (freely expanding), NE (no axial expansion), or NNE (no axial expansion and limited radial expansion).

In the FE elements the heater tube material was Inconel and the sample was made up of twelve 1.043 in. diam x 1.0 in. long $UO_2$ pellets of approximately 70% theoretical density. In the NE elements, the heater tube was also Inconel but instead of being sealed with welded end caps at each end, the pellet stack was held by a piston at each end. As the heater tube increased in temperature, it expanded over the piston at each end, and

the expansion was taken up by bellows that completed the seal. The dimension between the pistons, in which the pellet stack was constrained, was held constant. When this element is heated, the axial constraint causes the low density pellets to deform inelastically, allowing a fixed length to be held. The design of the NNE element was identical to the NE element except that the heater tube material was Invar. A vibratory compaction process was used to fill this element so that zero clearance could be maintained between the $UO_2$ and the Invar containing tube. Invar has an essentially zero expansion coefficient over a range from room temperature to about 200°C. Thus over this range the $UO_2$ sample was constrained both axially and radially. Above 200°C the Invar expansion coefficient almost parallels that of Inconel, and the element then acts very similarly to NE elements.

The elements containing other than the 1-in. diam $UO_2$ samples were all of the freely expanding type. The uranium metal element consisted of ten 1-in. diam, 1-in. long uranium pellets in an Inconel heater tube. One pellet from the nominal number of 12 was removed from each end and replaced by a 1-in. long quartz dummy pellet. This was done to keep the axial temperature profile along the pellet stack as flat as possible, so that when the element temperature was taken through the alpha-beta phase change in the metal all the material in the sample passed through the phase change at the same

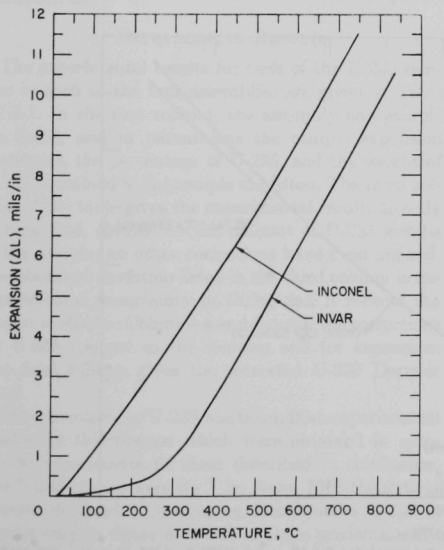


FIG. III-3-3. Thermal Expansion Heater Tubes. *ANL Neg. No. 112-6941.*

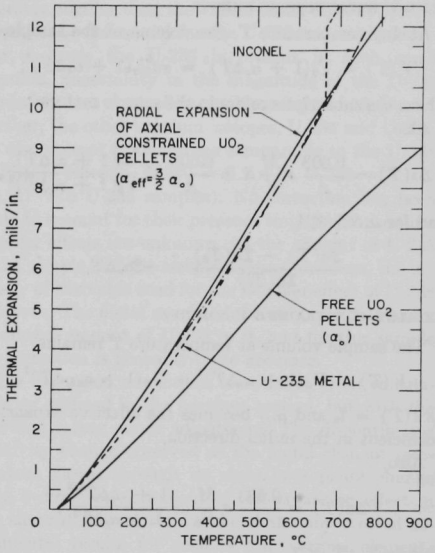


FIG. III-3-4. Radial Expansion of Axial Constrained $UO_2$ Pellets [$\alpha_{eff} = (3/2)\,\alpha_0$]. *ANL Neg. No. 112-6939.*

time. The discontinuous change in volume through the alpha-beta phase change in the metal was used to calibrate the effect of expansion on this element.

The expansion characteristics of the Doppler element materials are shown in Figs. III-3-3 and III-3-4. Figure III-3-3 compares the expansion characteristics of Inconel and Invar, illustrating the different radial expansion characteristics of the NE and NNE elements. Figure III-3-4 gives the expansion characteristics of the $UO_2$ pellets and the uranium metal, both taken from quartz dilatometer measurements of material with a metallurgical history identical to the material used in the elements, and shows the Inconel expansion characteristic for comparison.

As discussed in another paper (see Paper III-2), the reactivity effects of expansion are related through the flux changes to the quantity $\Sigma a$($\Sigma \equiv$ total macroscopic cross section, $a \equiv$ sample radius).

Defining additionally,

$l \equiv$ sample length
$\alpha \equiv$ linear coefficient of expansion
$\Delta T \equiv$ temperature change
$V \equiv$ sample volume
$\Sigma \equiv$ total macroscopic cross section
$M \equiv$ sample mass
$A \equiv$ atomic weight.

Consider the way in which expansion affects $\Sigma a$ in the different types of elements:

FREELY EXPANDING ELEMENTS

At any temperature $T$, the volume of the sample is

$$V(T) = V_0(1 + \alpha_s \Delta T)^3 = \pi a_0^2 l_0 (1 + \alpha_s \Delta T)^3,$$

where the subscript $s$ refers to the sample material.

Also,

$$\Sigma a(T) = \frac{0.603}{A} \sigma \frac{M}{V} a = \frac{0.603}{A} M \frac{a_0(1 + \alpha_s \Delta T)}{V_0(1 + \alpha_s \Delta T)^3},$$

and for $\alpha_s \Delta T \ll 1$,

$$\frac{\Sigma a(T) - \Sigma a(T_0)}{\Sigma a(T_0)} = -2\alpha_s \Delta T.$$

AXIALLY CONSTRAINED ELEMENTS

The sample volume at temperature $T$ remains

$$V(T) = V_0(1 + \alpha_s \Delta T)^3 = V_0(1 + \alpha_{eff} \Delta T)^2,$$

as $l(T) = l_0$ and $\alpha_{eff}$ becomes the effective expansion coefficient in the radial direction.

Also,

$$\Sigma a(T) = \frac{0.603}{A} \sigma \frac{M}{V_0} a_0 \frac{1 + \alpha_s \Delta T^{3/2}}{1 + \alpha_s \Delta T^3},$$

and for $\alpha_s \Delta T \ll 1$,

$$\frac{\Sigma a(T) - \Sigma a T_0}{\Sigma a T_0} = \frac{-3}{2} \alpha_s \Delta T.$$

AXIALLY AND RADIALLY CONSTRAINED ELEMENTS

The sample volume is now given by

$$V(T) = \pi a_0^2 (1 + \alpha_I \Delta T)^2 l_0,$$

where $\alpha_I$ is the expansion coefficient of the Invar heater tube.

Also,

$$\Sigma a(T) = \frac{0.603}{A} \sigma \frac{M}{V_0} a_0 \frac{1 + \alpha_I \Delta T}{1 + \alpha_I T^2},$$

and for $\alpha_I \Delta T \ll 1$,

$$\frac{\Sigma a(T) - \Sigma a T_0}{\Sigma a T_0} = -\alpha_I \Delta T.$$

EXPANSION CALCULATIONS

The reactivity effect of expansion of the various elements were calculated using the procedures described in another paper in this report (see Paper III-2). The expansion effects were calculated as a function of $N\bar{l}$ for the sample ($N$ = atoms/cc, $\bar{l}$ = mean chord length) for each of the four assemblies. The fluxes, adjoints, and perturbation normalization were taken from MACH-I calculations for each assembly using $MC^2$-derived cross sections appropriate to the test zone composition of each assembly.

A typical result is shown in Fig. III-3-5, for Assemblies 4Z and 5 of ZPR-6. (The calculated fluxes and normalizations are so close to being equal in these two assemblies that the calculated reactivity effects of expansion are also equal.) The figure shows the reactivity change in Ih/kg of U-235 for $10^{-3}$ in. per inch free expansion of the sample as a function of $N\bar{l}$. The

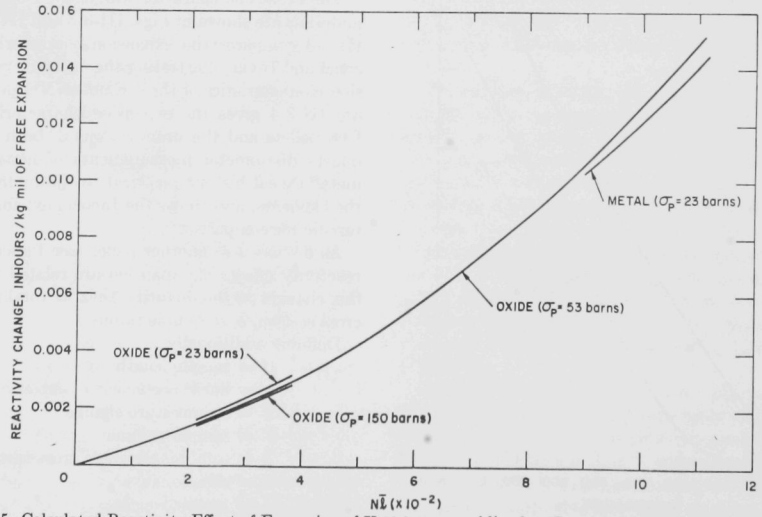


FIG. III-3-5. Calculated Reactivity Effect of Expansion of U-23 in5 Assemblies for 4Z and 5, ZPR-6. *ANL Neg. No. 112-9419.*

main relationship shown is for a typical 1 in. diam reduced density oxide sample with an equivalent potential scattering cross section in the resonance region of 53 b. Also shown on the figure is the calculated result for a uranium metal sample of 1 in. diam, which corresponds to an equivalent potential scattering cross section of 23 b. Further, as an index of the sensitivity of the results to the choice of $\sigma_{p_{eq}}$ (equivalent potential scattering cross section) in the resonance region, results are also shown for oxide samples with $\sigma_{p_{eq}}$ of 23 b and 150 b. It is seen that the results are not very sensitive to the choice of $\sigma_{p_{eq}}$.

It might be suspected that the calculational procedure would be weakest in the resonance region where, in effect, broad-group averaged cross sections are defined in the resonance region, and the flux change due to expansion is calculated based on the group averaged cross sections. It is not clear that the flux changes so calculated need necessarily correspond to the actual case where the cross sections retain the rapid fluctuation with energy characteristic of the resonance region. However, it is possible to check this method of handling the low energy region through the direct use of the RABBLE code, which describes the situation directly without recourse to group-averaged cross sections. (For a typical usage of the RABBLE code see, for example, Paper III-1.) Initial comparisons of the results given by the two methods indicate that the typical difference between the two is unlikely to be more than 10% in this spectrum.

## Experimental Results

The experimental results for each of the U-235 samples in each of the four assemblies are given in Table III-3-I. In the first column, the assembly and sample are listed, and in parentheses the sample expansion properties, the percentage of U-235, and the weight of U-235 contained in the sample are listed. The third column of the table gives the experimental result, directly as measured, divided by the amount of U-235 isotope in the sample; no other corrections have been applied. The standard deviation listed in the third column is the experimental uncertainty in Ih/kg and it reflects the reactor statistics. Columns 4 and 5 detail the corrections for U-238 content in the samples and for expansion. The final column gives the corrected U-235 Doppler effect.

The correction for U-238 was taken from experimental results for this isotope which were obtained in companion experiments to those described in this paper. The U-238 results were for 1 in. diam, 70% theoretical density, depleted $UO_2$ samples. Because the U-238 is present only in dilute amounts in these predominantly U-235 samples, the U-238 Doppler effect may be considerably smaller than the values taken directly from a proration of the results for the U-238 1-in. rods. However, because the U-238 is present in such small amounts, uncertainty in the magnitude of the U-238 correction does not lead to significant error in any case. Further, the other uranium isotopes, U-234 and U-236, are also present in quantities comparable to the U-238 (U-234 = 1.0 w/o, U-236 = 0.2 w/o, U-238 = 1.1 in the 9.7 w/o U-235 samples). No correction has been made to account for their presence simply because their Doppler effects are unknown. As the amount of U-238 in the sample and the sample density increases, the accuracy of the value used for the Doppler effect of U-238 improves. The metal sample is the only one that had a significant amount of U-238 in it, and for this sample the correction is probably quite accurate.

The expansion corrections were taken from calculations as outlined in the previous section, but with the following rather minor adjustment. The discontinuous reactivity change observed as the metal element temperature passes through its alpha-beta phase change gives a direct measurement of the expansion effect in this element. Figure III-3-6 shows the uncorrected experimental results for each of the various elements measured in Assembly 4Z. From this figure, the observed reactivity change through the phase change per kilogram of U-235 was $-(0.104 - 0.0735) = -0.0305$ Ih. Figure III-3-4 shows the dilatometer result for a sample with the same metallurigcal history, which gave a discontinuous expansion increase of 1.85 mil, resulting in a reactivity effect of $-0.0305/1.85 = -0.0165$ Ih/mil of expansion per kilogram of U-235.

The calculated expansion effect for the metal element, from Fig. III-3-5 was $-0.01425$ Ih/kg-mil expansion. There is therefore a 15% difference between the calculated and measured expansion effects in the metal element. (This is about half the discrepancy reported in Ref. 1. The difference is that the calculations of the expansion effect reported in this paper have been redone with more up-to-date cross section values.) The calculated expansion effects for the other elements were adjusted by this amount as well, on the basis that this was not a large difference, and the knowledge of the fluxes, adjoints, and normalizations, as well as the approximations in the calculational technique itself, is certainly not better than the 15% difference. As will be noted in Table III-3-I, the expansion corrections for the oxide elements vary from 15–30% of the Doppler effect, and uncertainties of the order of 15% in the correction itself would not affect the inferred Doppler effect very much. In the metal element, where the correction is large, the result is direct.

Figure III-3-7 gives the Assembly 4Z results for the U-235 Doppler effect, correct for expansion, as meas-

TABLE III-3-I EXPERIMENTAL RESULTS

| Assembly and Sample Type | Sample Temperature, °K | Measured Ih/kg of U-235 | Std. Dev. | Correction for U-238, Ih/kg of U-235 | Correction for Expansion, Ih/kg of U-235 | Doppler Effect, Ih/kg of U-235 |
|---|---|---|---|---|---|---|
| Assembly 5 ZPR-6: Sample HE-8 (FE, 97.7%, 892.3 g U-235) | 428 | 0.021 | 0.001 | +0.001 | +0.004 | 0.026 |
| | 612 | 0.040 | | +0.002 | +0.009 | 0.051 |
| | 839 | 0.049 | | +0.002 | +0.017 | 0.068 |
| | 1058 | 0.050 | 0.001 | +0.003 | +0.023 | 0.076 |
| Assembly 5 ZPR-6: Sample HE-10 (NNE, 97.7%, 788.5 g U-235) | 339 | 0.010 | 0.001 | 0 | 0 | 0.010 |
| | 370 | 0.014 | | 0 | 0 | 0.014 |
| | 395 | 0.020 | | +0.001 | 0 | 0.021 |
| | 428 | 0.025 | | +0.001 | 0 | 0.026 |
| | 469 | 0.030 | | +0.001 | 0 | 0.031 |
| | 486 | 0.034 | | +0.001 | 0 | 0.035 |
| | 578 | 0.041 | | +0.002 | +0.001 | 0.044 |
| | 774 | 0.054 | | +0.002 | +0.006 | 0.062 |
| | 958 | 0.061 | 0.001 | +0.003 | +0.010 | 0.074 |
| Assembly 4Z ZPR-6: Sample HE-1 (FE, 97.7%, 942.2 g U-235) | 480 | 0.032 | 0.003 | +0.001 | +0.006 | 0.039 |
| | 659 | 0.046 | | +0.002 | +0.012 | 0.060 |
| | 851 | 0.055 | | +0.002 | +0.019 | 0.076 |
| | 1051 | 0.061 | 0.003 | +0.003 | +0.025 | 0.089 |
| Assembly 4Z ZPR-6: Sample HE-2 (NE, 97.7%, 980.9 g U-235) | 319 | 0.006 | 0.003 | 0 | +0.001 | 0.007 |
| | 356 | 0.016 | | 0 | +0.002 | 0.018 |
| | 362 | 0.011 | | 0 | +0.002 | 0.013 |
| | 410 | 0.022 | | +0.001 | +0.003 | 0.026 |
| | 456 | 0.028 | | +0.001 | +0.004 | 0.033 |
| | 589 | 0.044 | | +0.002 | +0.007 | 0.053 |
| | 783 | 0.058 | | +0.002 | +0.013 | 0.073 |
| | 1011 | 0.065 | 0.003 | +0.003 | +0.017 | 0.085 |
| Assembly 4Z ZPR-6: Sample HE-5 (NNE, 97.7%, 695.0 g U-235) | 329 | 0.013 | 0.003 | 0 | 0 | 0.013 |
| | 364 | 0.026 | | 0 | 0 | 0.026 |
| | 417 | 0.033 | | +0.001 | 0 | 0.034 |
| | 447 | 0.037 | | +0.001 | 0 | 0.038 |
| | 479 | 0.042 | | +0.001 | 0 | 0.044 |
| | 734 | 0.062 | | +0.002 | +0.004 | 0.068 |
| | 936 | 0.069 | 0.003 | +0.003 | +0.009 | 0.081 |
| Assembly 4Z ZPR-6: Sample HE-4 (FE, 97.6%, 235.1 g U-235) | 488 | 0.016 | 0.007 | +0.001 | +0.002 | 0.019 |
| | 1048 | 0.035 | 0.007 | +0.003 | +0.008 | 0.046 |
| Assembly 4Z ZPR-6: Sample HE-3 (Metal, 93.1%, 2206.3 g U-235) | 474 | −0.001 | 0.002 | +0.005 | +0.040 | +0.044 |
| | 706 | −0.028 | | +0.010 | +0.098 | +0.080 |
| | 899 | −0.066 | | +0.013 | +0.157 | +0.104 |
| | 969 | −0.111 | | +0.014 | +0.209 | +0.112 |
| | 1020 | −0.123 | 0.002 | +0.015 | +0.226 | +0.118 |
| Assembly 11 ZPR-9: Sample HE-2 (NE, 97.7%, 980.8 g U-235) | 331 | 0.011 | 0.004 | 0 | +0.001 | 0.012 |
| | 377 | 0.018 | | +0.001 | +0.001 | 0.020 |
| | 424 | 0.040 | | +0.001 | +0.004 | 0.045 |
| | 472 | 0.048 | | +0.001 | +0.006 | 0.055 |
| | 616 | 0.075 | | +0.002 | +0.012 | 0.089 |
| | 808 | 0.092 | | +0.003 | +0.020 | 0.115 |
| | 1064 | 0.112 | 0.004 | +0.004 | +0.030 | 0.146 |
| Assembly 11 ZPR-9: Sample HE-5 (NNE, 97.7%, 695.0 g U-235) | 343 | 0.007 | 0.004 | 0 | 0 | 0.007 |
| | 378 | 0.017 | | +0.001 | 0 | 0.018 |
| | 443 | 0.036 | | +0.001 | 0 | 0.037 |
| | 494 | 0.045 | | +0.001 | +0.001 | 0.047 |
| | 628 | 0.060 | | +0.002 | +0.003 | 0.065 |
| | 820 | 0.091 | | +0.003 | +0.009 | 0.103 |
| | 1032 | 0.113 | 0.004 | +0.004 | +0.015 | 0.132 |
| Assembly 12 ZPR-9: Sample HE-5 (NNE, 97.7%, 695.0 g U-235) | 325 | +0.032 | 0.005 | 0 | 0 | 0.032 |
| | 364 | +0.039 | | +0.001 | 0 | 0.040 |
| | 425 | +0.054 | | +0.001 | 0 | 0.055 |
| | 479 | +0.062 | | +0.001 | +0.001 | 0.064 |
| | 664 | +0.079 | | +0.002 | +0.004 | 0.085 |
| | 847 | +0.079 | 0.005 | +0.003 | +0.013 | 0.095 |

ured by the five different types of elements. It can be seen that the corrections for expansion bring the 1 in. diam $UO_2$ results for the three elements with differing expansion properties into agreement. The metal result is somewhat higher, and the half-inch oxide result considerably lower, as theory predicts.

## Discussion of Results

Figures III-3-8, III-3-9, and III-3-10 show the results for the 1 in. diam $UO_2$ samples for each of the four assemblies. Each figure shows the uncorrected experi-

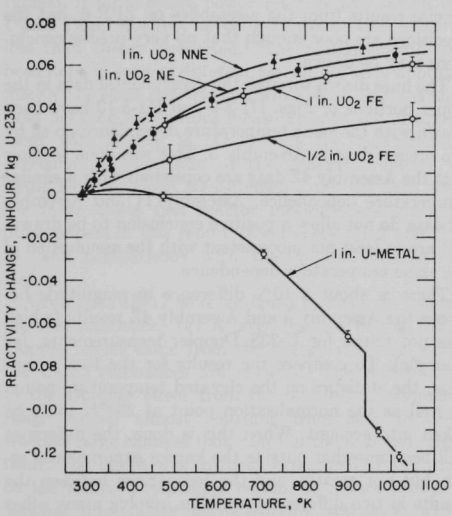


Fig. III-3-6. Assembly for 4Z, ZPR-6, U-235 Experimental Data Reactivity Change on Heating. *ANL Neg. No. 112-9440.*

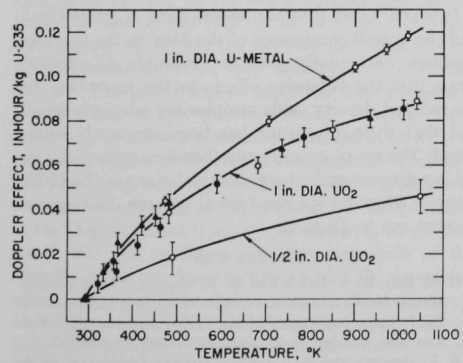


Fig. III-3-7. Assembly for 4Z, U-235 Doppler Effect (Corrected for Expansion). *ANL Neg. No. 112-9430.*

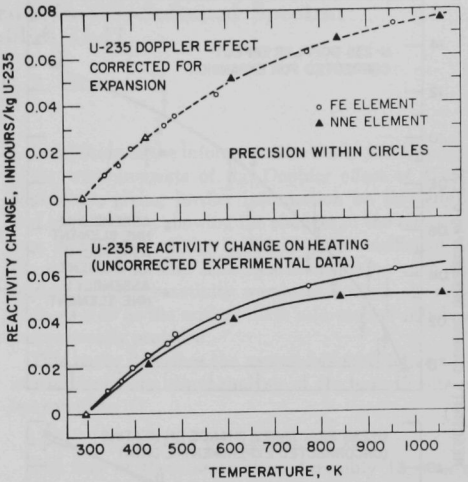


Fig. III-3-8. Assembly 5, ZPR-6, in. dia $U^{235}O_2$ samples. *ANL Neg. No. 112-9423.*

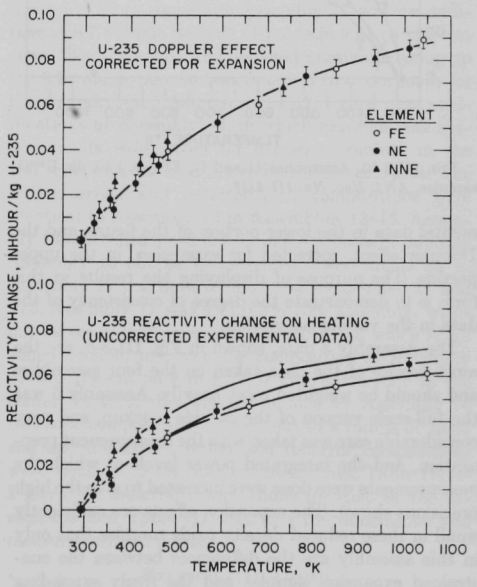


Fig. III-3-9. Assembly for 4Z, ZPR-6, 1 in. dia $U^{235}O_2$ samples. *ANL Neg. No. 112-9412.*

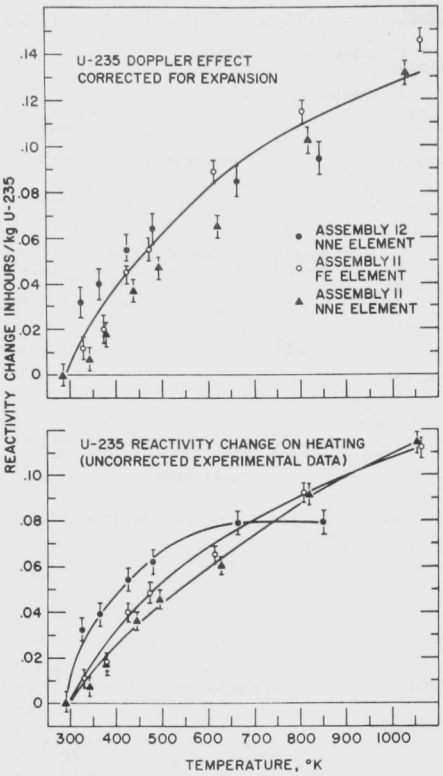


FIG. III-3-10. Assemblies 11 and 12, ZPR-9, 1 in. dia $U^{235}O_2$ samples. *ANL Neg. No. 112-9417.*

mental data in the lower portion of the figure, and the Doppler effect, corrected for expansion, in the upper portion. The purpose of displaying the results in this form is to demonstrate the degree of consistency of the data in the various assemblies.

The Assembly 5 data, shown in Fig. III-3-8, are the most precise of the data taken on the four assemblies and should be weighted most heavily. Assembly 5 was the full-scale version of the carbide mockup, and very considerable care was taken with the measurement preparation, and the integrated power levels at which the measurements were done were increased to give the high precisions shown. The expansion effects are sufficiently small in these reduced density oxide samples that only in this assembly are the differences between the constrained expansion samples and the freely expanding sample unambiguously outside statistics. The figure shows the way that the expansion corrections bring the results of the two different types of elements precisely into line.

Figure III-3-9, showing the Assembly 4Z results, also demonstrates the consistency of the results given by the various types of elements, although the precisions on these measurements were somewhat less.

The results from Assemblies 11 and 12 of ZPR-9, shown in Fig. III-3-10, show considerably more scatter. Assemblies 11 and 12 were small zone assemblies in which it is known that complete spectral equilibration was not achieved, and one may conclude from the results that they are reasonably consistent with the more precise results from the assemblies on ZPR-6, but the precisions are poor enough that no very precise conclusions may be drawn.

The lines drawn through the experimental data in the upper portions of Figs. III-3-9 and III-3-10 have been drawn with the same temperature dependence given by the precise data in Assembly 5. This was done to show that the Assembly 4Z data are consistent with a similar temperature dependence. Assembly 11 and Assembly 12 data do not allow a positive conclusion to be drawn, but are at least not inconsistent with the assumption of the same temperature dependence.

There is about a 10% difference in magnitude between the Assembly 5 and Assembly 4Z results (which was not found for U-238 Doppler measurements, for example). To compare the results for the two assemblies, the statistics on the elevated temperature points as well as the normalization point at 293°K must be taken into account. When this is done, the difference still lies somewhat outside the known experimental error, but not greatly, and the comparison between the results in two different assemblies involve many other possibilities for systematic error that are not present in comparing results given by different elements in the same assembly.

It is concluded that the precise data of Assembly 5, and the overall consistency of the data on the other assemblies, particularly that on Assembly 4Z, demonstrate that the expansion effects in the assemblies for the reduced density oxide samples are relatively small, and that their magnitude has been accurately established. The set of experiments therefore represent a reliable reference against which calculations of the U-235 Doppler effect for spectra typical of large dilute power reactors can be checked.

## REFERENCES

1. C. E. Till, R. A. Lewis and R. N. Hwang, *ZPR-6 Doppler Measurements and Comparisons with Theory*, International Conference on Fast Critical Experiments and Their Analysis, October 10–13, 1966, ANL-7320, pp. 319–333.
2. E. F. Bennett and R. L. Long, *Precision Limitations in the Measurement of Small Reactivity Changes*, Nucl. Sci. Eng. **17**, 425–432 (1963).

# III-4. Doppler Effect Measurements in $CH_2$-Softened Spectra; ZPR-9 Assemblies 13–17

R. Pond and C. E. Till

## Introduction

Assemblies 13–17 comprised a series of zoned cores with progressively softer spectra, designed primarily to investigate the systematics of the Doppler effect of U-235. Previous measurements done in spectra typical of large dilute power reactors had shown the U-235 Doppler effect to be a factor of two or three less than theory predicted.[1] The measurements had been done in several different assemblies with approximately the same spectra, and while some discrepancies exist between the various measurements, the disagreement with theory is far outside the measurement precision. A discussion of the general problems of fissile Doppler effect measurements and the data from the large dilute fast reactor mockups are given in other papers in this report (see Papers III-2 and III-3), and comparisons with theory are discussed in Ref. 1.

Assemblies 13–17 were designed to have the following characteristics: (a) A large fraction of the U-235 Doppler effect came from the energy range in which the U-235 resonances are resolved. The contribution to the Doppler effect from the unresolved resonance range stayed almost constant from core to core, whereas large changes took place in the resolved range itself. The intent was to focus experimental attention on the resolved resonance region, to reduce interpretational uncertainty accompanying statistical averaging techniques. (b) The Doppler effect was very sensitive to the relative magnitudes of the source and sink terms making up the fissile element Doppler effect. The source and sink terms in these assemblies were almost equal, and the net Doppler effect in each assembly was therefore very sensitive to the precise balance. The intent was to make the measurements a sensitive test of how well the balance is being calculated, and to allow a reasonable attempt at identification of the area in which the calculational error lies. (c) The signal was very substantially increased due to the overall softening of the spectrum, so that changes in the Doppler effect from core to core were large compared with the statistics. (d) The magnitude of the Doppler effect was large compared with the expansion effect. The systematics of the reactivity effect of sample expansion are such that increasing the Doppler energy fluxes and adjoints in these assemblies reduces the expansion effect overall, and reduces it very substantially relative to the Doppler effect itself.

In addition to the information on the U-235 Doppler effect, measurements of the Doppler effect of U-238 were done, giving further information on this effect, and in particular, showing the changes in the temperature dependence of the U-238 Doppler coefficient as the spectrum softens. The measurements on each assembly included reactivity worths of a range of materials, as well as the critical mass information which is automatically provided.

This paper describes the assemblies and the experimental data only, since analysis of the experiments is not complete.

## Description of Assemblies 13–17

The first of these assemblies, Assembly 13, was a relatively simple modification of Assembly 12. The latter assembly was the last of the zoned versions of the full-scale mockup of a large dilute carbide fast power reactor, Assembly 5 of ZPR-6. (For a description of Assembly 12 see Paper III-11 and for Assembly 5 of ZPR-6 see Paper III-6.) The modification of Assembly 12 to convert to Assembly 13 was an addition of 8.7 volume percent of polyethylene to the test zone. (Some graphite and depleted uranium making up the 8.7 volume percent was removed to make room for the polyethylene.) Assemblies 14–17 in turn were modifications of Assembly 13, in which graphite was systematically substituted for depleted uranium in the test zone, keeping all other compositions constant. The buffer, driver and reflector zone compositions were identical to Assembly 12 in Assemblies 13–16. Assembly 15 was constructed briefly in the process of building Assembly 16 but no measurements were made on it. Assembly 17 was built in two versions, denoted 17 and 17Z. Assembly 17 was a uniform core assembly, without driver or buffer regions. Assembly 17Z was a small zoned version, in which the composition of Assembly 17 was present only in a 15.57 cm radius zone at the center. In turn, this was surrounded by Assembly 16 test zone composition material out to a radius of 25.87 cm, and the driver, buffer and reflector compositions were identical to the previous assemblies. Table III-4-I gives the material compositions for each of the assemblies and Table III-4-II lists the dimensions and measured critical masses.

## Experimental Detail

The Doppler measurement methods and techniques were generally similar to those described in Ref. 1 (see

TABLE III-4-I. MATERIAL COMPOSITIONS FOR ZPR-9 ASSEMBLIES NOS. 12-17 INCLUSIVELY

| Type of Zone Material | Atom Densities, (atoms/cm³) × $10^{24}$ | | | | | | | |
|---|---|---|---|---|---|---|---|---|
| | Fe | Ni | Cr | Na | C | U-235 | U-238 | H |
| Core of Assy. 12 | 0.009086 | 0.001148 | 0.002593 | 0.009028 | 0.012986 | 0.001547 | 0.010633 | — |
| Core of Assy. 13 | | | | | 0.014920 | 0.001541 | 0.007389 | 0.006754 |
| Core of Assy. 14 | | | | | 0.016363 | 0.001539 | 0.006580 | |
| Core of Assy. 15 | | | | | 0.017806 | 0.001537 | 0.005771 | |
| Core of Assy. 16 | | | | | 0.019249 | 0.001536 | 0.004963 | |
| Core of Assy. 17 | | | | | 0.027906 | 0.001525 | 0.000110 | |
| Buffer | 0.008829 | 0.001116 | 0.002520 | 0.003917 | 0.034630 | 0.000020 | 0.009704 | — |
| Driver | 0.010643 | 0.001345 | 0.003038 | 0.007833 | 0.012986 | 0.006784 | 0.005335 | — |
| Depleted reflector | 0.004256 | 0.000538 | 0.001215 | — | — | 0.000083 | 0.040034 | — |
| Steel reflector | 0.077772 | 0.000891 | 0.002036 | — | — | — | — | — |

TABLE III-4-II. REACTOR DIMENSIONS FOR ZPR-9 ASSEMBLIES NOS. 12-17 INCLUSIVELY

| Assembly No. | Zone Radius, cm | | | | | Critical Mass, kg |
|---|---|---|---|---|---|---|
| | Core[a] | Buffer | Driver | Depleted Reflector | Steel Reflector | |
| 12 | 25.87 | 32.51 | 40.83 | 52.43 | 80.00 | 579.6 |
| 13 | 25.87 | | 37.85 | | | 402.8 |
| 14 | 25.87 | | 37.35 | | | 374.1 |
| 15 | 25.87 | | 36.97 | | | 352.9 |
| 16 | 25.87 | | 36.62 | | | 333.1 |
| 17Z | 15.57, 25.87 | — | 35.15 | | | 250.8 |
| 17 | 27.46 | — | — | | | 126.7 |

[a]Nominal 115 kg U-235 in 25.87 cm core region.

also Paper III-3). In the U-235 measurements reported here two types of samples were used, both $UO_2$, one in which the expansion was constrained and the other in which free expansion was allowed. The U-238 sample was freely expanding. The reactivity measurement technique was similar to that described in Ref. 1, involving the use of a calibrated auto rod. The rod used in this work differs somewhat from that used for the work described in Ref. 1; in this work the rod was a tapered boron-filled rod extending through both halves of the reactor, designed for linearity over its full travel.

The reactivity worth measurements on various materials were made using a sample changer and repeated period measurements similar to the work reported in Ref. 2.

## RESULTS

The results of the Doppler measurements are given in Table III-4-III and the reactivity worth measurements are given in Table III-4-IV. To illustrate the progressive change in the Doppler effect from assembly to assembly, the U-238 Doppler effect measurements are plotted for each of the assemblies in Fig. III-4-1, and the U-235 Doppler effect, as measured by the freely expanding sample, in Fig. III-4-2. The results shown in Fig. III-4-2 are not corrected for expansion effects, but as perusal of the data in Table III-4-III will show, expansion effects in these assemblies are a small fraction of the total reactivity change due to heating.

The effects of the systematic changes from assembly to assembly are to reduce the reactor absorption in the Doppler energy range, causing both the flux and adjoint to increase in this energy region. The effect of this on the Doppler coefficients is to increase the U-238 Doppler coefficient and to decrease the U-235 coefficient. The latter effect arises because the increase in the Doppler energy adjoint weights the absorption term in the fission-absorption balance more heavily, outweighing the increase in the flux itself, and leading to a decrease in the U-235 Doppler coefficient from assembly to assembly.

The increase in the U-238 Doppler effect shown in Fig. III-4-1, acts as a monitor of the increase in the Doppler energy flux because the flux changes are considerably larger than the adjoint changes. The increases shown in Fig. III-4-1 are not entirely due to flux and adjoint charges however because the perturbation normalization also changes from assembly to assembly. Change in this quantity leads to changes in the measured U-238 Doppler effect in the same direction as that due to increased Doppler energy fluxes, and this factor is also present in Fig. III-4-1.

The progressive decrease in the U-235 coefficient shown in Fig. III-4-2 demonstrates the way the increased adjoint outweighs the effect of the increased Doppler fluxes. The results shown in Fig. III-4-2 also

TABLE III-4-III. EXPERIMENTAL DOPPLER RESULTS

| Assembly[a] | Element[b] | (Type)[c] | Average Temperature, Average Reactivity Worth, Standard Deviation of the Average Reactivity Worth | | | | | | | | | | | |
|---|---|---|---|---|---|---|---|---|---|---|---|---|---|---|
| | | | °K | Ih/kgU$^x$ | ±Ih/kgU$^x$ | °K | Ih/kgU$^x$ | ±Ih/kgU$^x$ | °K | Ih/kgU$^x$ | ±Ih/kgU$^x$ | °K | Ih/kgU$^x$ | ±Ih/kgU$^x$ |
| 13 | N1 | (FE) | 293 | 0.0 | 0.010 | 393 | −0.276 | 0.009 | 498 | −0.590 | 0.010 | 715 | −1.160 | 0.009 |
| | | | 877 | −1.518 | 0.005 | 1076 | −1.916 | 0.010 | | | | | | |
| 13 | HE-8 | (FE) | 294 | 0.0 | 0.004 | 420 | +0.131 | 0.005 | 517 | +0.247 | 0.003 | 668 | +0.407 | 0.002 |
| | | | 881 | +0.601 | 0.002 | 1074 | +0.765 | 0.005 | | | | | | |
| 13 | HE-9 | (NNE) | 293 | 0.0 | 0.004 | 389 | +0.084 | 0.003 | 443 | +0.141 | 0.003 | 488 | +0.181 | 0.003 |
| | | | 590 | +0.283 | 0.003 | 692 | +0.386 | 0.004 | 893 | +0.532 | 0.004 | 1070 | +0.634 | 0.007 |
| 14 | N1 | (FE) | 288 | 0.0 | 0.005 | 390 | −0.365 | 0.005 | 499 | −0.715 | 0.004 | 681 | −1.217 | 0.004 |
| | | | 898 | −1.710 | 0.003 | 1073 | −2.082 | 0.002 | | | | | | |
| 14 | HE-8 | (FE) | 291 | 0.0 | 0.004 | 428 | +0.159 | 0.002 | 515 | +0.238 | 0.004 | 668 | +0.375 | 0.003 |
| | | | 899 | +0.552 | 0.002 | 1078 | +0.672 | 0.003 | 378 | +0.106 | 0.006 | | | |
| 14 | HE-9 | (NNE) | 292 | 0.0 | 0.005 | 397 | +0.116 | 0.004 | 456 | +0.160 | 0.004 | 507 | +0.211 | 0.004 |
| | | | 589 | +0.286 | 0.003 | 703 | +0.382 | 0.007 | 911 | +0.513 | 0.004 | 1057 | +0.601 | 0.004 |
| 16 | N1 | (FE) | 292 | 0.0 | 0.002 | 380 | −0.365 | 0.006 | 480 | −0.730 | 0.009 | 688 | −1.368 | 0.004 |
| 16 | N1 | (FE) | 291 | 0.0 | 0.003 | 458 | −0.640 | 0.003 | 593 | −1.072 | 0.002 | 882 | −1.855 | 0.005 |
| | | | 1079 | −2.314 | 0.004 | | | | | | | | | |
| 16 | HE-8 | (FE) | 291 | 0.0 | 0.004 | 409 | +0.082 | 0.002 | 501 | +0.153 | 0.004 | 588 | +0.212 | 0.002 |
| | | | 710 | +0.284 | 0.003 | 903 | +0.386 | 0.003 | 1076 | +0.474 | 0.002 | | | |
| 17Z | HE-8 | (FE) | 292 | 0.0 | 0.005 | 429 | −0.200 | 0.004 | 592 | −0.361 | 0.004 | 813 | −0.525 | 0.005 |
| | | | 1089 | −0.702 | 0.003 | | | | | | | | | |
| 17 | HE-8 | (FE) | 293 | 0.0 | 0.003 | 405 | −0.176 | 0.003 | 495 | −0.283 | 0.003 | 596 | −0.384 | 0.004 |
| | | | 709 | −0.483 | 0.005 | 898 | −0.612 | 0.003 | 1091 | −0.732 | 0.005 | | | |
| 17 | HE-10 | (NNE) | 293 | 0.0 | 0.007 | 402 | −0.200 | 0.007 | 472 | −0.310 | 0.007 | 521 | −0.379 | 0.007 |
| | | | 609 | −0.467 | 0.007 | 747 | −0.593 | 0.008 | 900 | −0.707 | 0.009 | 1048 | −0.796 | 0.010 |
| 17 | N1 | (FE) | 294 | 0.0 | 0.003 | 385 | −0.634 | 0.002 | 497 | −1.302 | 0.004 | 616 | −1.937 | 0.007 |
| | | | 755 | −2.605 | 0.005 | 902 | −3.251 | 0.008 | 1067 | −3.936 | 0.008 | | | |

[a] Assembly 13: 1% $\Delta k/k$ = 437.85 Ih.
Assembly 14: 1% $\Delta k/k$ = 435.69 Ih.
Assembly 16: 1% $\Delta k/k$ = 428.07 Ih.
Assembly 17Z: 1% $\Delta k/k$ = 415.19 Ih.
Assembly 17: 1% $\Delta k/k$ = 391.78 Ih.

[b] N1: 1.26629 kg $UO_2$; 1.11623 kg U; 1.10818 kg U-238; 0.00799 kg U-235.
HE-8: 1.03758 kg $UO_2$; 0.91328 kg U; 0.01012 kg U-238; 0.89187 kg U-235.
HE-9: 0.91219 kg $UO_2$; 0.80419 kg U; 0.00891 kg U-238; 0.78534 kg U-235.
HE-10: 0.91560 kg $UO_2$; 0.80710 kg U; 0.00894 kg U-238; 0.78818 kg U-235.
HE elements w/o U: U-234, 1.026%; U-235, 97.656%, U-236, 0.209%; U-238, 1.108%.
N1 elements w/o U: U-234, 0.0057%; U-235, 0.7158%; U-238, 99.2785%.
U$^x$—Inhours per kg of predominate uranium isotope.

[c] FE: Freely expanding $UO_2$ element 1 × 12 in. pellet cylinder.
NNE: Non expanding $UO_2$ element 1 × 12 in. powder cylinder (total axial constraint and limited radial constraint).

TABLE III-4-IV. REACTIVITY WORTH MEASUREMENTS

| Sample[a] | Weight, g | Can Weight, g | Assembly 12[b], Net Ih/kg | Assembly 13[c], Net Ih/kg | Assembly 14[d], Net Ih/kg | Assembly 16[e], Net Ih/kg | Assembly 17[f], Net Ih/kg |
|---|---|---|---|---|---|---|---|
| Mo | 598.8 | — | −8.059 ± 0.017 | −19.41 ± 0.05 | −20.28 ± 0.00 | −21.43 ± 0.01 | −24.87 ± 0.12 |
| Ni | 546.1 | — | −2.992 ± 0.018 | −11.60 ± 0.03 | −11.99 ± 0.02 | −12.79 ± 0.00 | −14.44 ± 0.01 |
| Fe | 484.3 | — | −2.110 ± 0.021 | −6.186 ± 0.03 | −6.084 ± 0.015 | −6.040 ± 0.002 | −3.494 ± 0.008 |
| Be | 114.3 | — | +12.20 ± 0.09 | +39.20 ± 0.06 | +46.13 ± 0.11 | +56.89 ± 0.03 | +128.69 ± 0.03 |
| C | 102.0 | — | +1.578 ± 0.109 | +10.52 ± 0.04 | +13.66 ± 0.08 | +17.74 ± 0.01 | +48.81 ± 0.31 |
| Al | 167.1 | — | −2.561 ± 0.060 | −1.143 ± 0.150 | −0.325 ± 0.006 | +0.993 ± 0.000 | +10.64 ± 0.04 |
| Na | 51.39 | 56.42 (SS) | −1.376 ± 0.200 | −1.323 ± 0.720 | +0.108 ± 0.049 | +1.693 ± 0.078 | +13.90 ± 0.33 |
| W | 1108. | — | −7.340 ± 0.009 | −23.07 ± 0.32 | −27.53 ± 0.32 | −30.01 ± 0.32 | −42.19 ± 0.32 |
| Ta | 924.7 | 27.54 (SS) | −17.982 ± 0.016 | −49.04 ± 0.38 | −57.58 ± 0.38 | −62.16 ± 0.38 | −89.23 ± 0.38 |
| B | 75.2 | 20.6 (SS) | — | −824. ± 6. | −975. ± 3. | −1090 ± 5 | −1660 ± 5 |
| Poly | 58.988 | — | +443.40 ± 0.25 | +436.65 ± 0.08 | +487.39 ± 5.93 | +488.2 ± 3.9 | +707.8 ± 4.2 |
| Poly | 13.70 | 72.32 (SS) | — | +469.0 ± 3.1 | +512.2 ± 3.1 | +550.1 ± 0.9 | +905.7 ± 1.3 |
| SS | 481.0 | — | −2.364 ± 0.021 | −7.958 ± 0.029 | −8.059 ± 0.004 | −8.281 ± 0.019 | −7.029 ± 0.023 |
| SS can | 72.38 | — | −2.542 ± 0.138 | −8.994 ± 0.041 | −9.600 ± 0.034 | −9.837 ± 0.111 | −8.635 ± 0.290 |
| $B_4C$ | 59.62 | 64.70 (SS) | — | −713.2 ± 5.9 | −757.0 ± 5.9 | −837.1 ± 5.9 | −1295. ± 6. |
| Depleted uranium | 1155. | — | −4.674 ± 0.009 | −8.510 ± 0.005 | −8.911 ± 0.012 | −9.191 ± 0.001 | −11.88 ± 0.04 |
| Al can | 26.36 | — | — | — | — | +1.328 ± 0.076 | +10.85 ± 0.27 |
| Enriched uranium | 18.11[g] | 72.38 (SS) | +70.12 ± 0.88[h] | — | — | — | — |
| Enriched uranium | 18.24[g] | 72.34 (SS) | — | +134.5 ± 0.5[h] | — | — | — |
| Enriched uranium | 18.17[g] | 72.34 (SS) | — | — | +137.4 ± 0.3[h] | +143.6 ± 0.0[h] | +135.0 ± 0.7[h] |
| Pu | 119.24[i] | 22.27 (SS)<br>6.85 (Al) | +93.05 ± 1.68[j] | — | — | — | — |
| Pu | 121.55[i] | 19.77 (SS)<br>7.05 (Al) | — | — | — | +199.0 ± 2.0[j] | +228.1 ± 2.2[j] |

[a] All samples are nominal 1 x 2 x 2 in. except the enriched uranium which is 1/16 x 1/2 x 2 in. and the Pu which is 1/4 x 2 x 2 in.
[b] Assembly No. 12: 1% $\Delta k/k$ = 451.2 Ih.
[c] Assembly No. 13: 1% $\Delta k/k$ = 438.86 Ih.
[d] Assembly No. 14: 1% $\Delta k/k$ = 435.69 Ih.
[e] Assembly No. 16: 1% $\Delta k/k$ = 428.07 Ih.
[f] Assembly No. 17F: 1% $\Delta k/k$ = 391.78 Ih.
[g] 93.2 w/o U-235.
[h] Uranium mixture.
[i] 0.01 w/o Pu-238; 95.05 w/o Pu-239; 4.48 w/o Pu-240; 0.45 w/o Pu-241; 0.01 w/o Pu-242.
[j] Plutonium mixture.

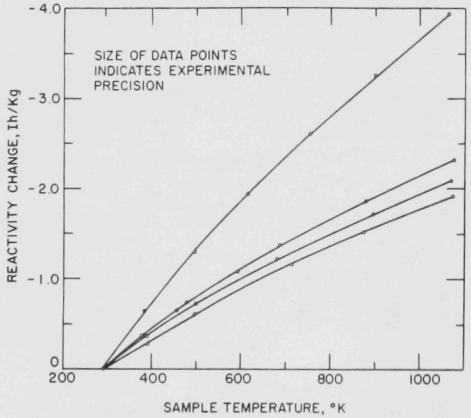


FIG. III-4-1. U-238 Doppler Effect Measurements on Assemblies 13, 14, 16, and 17, ZPR-9. *ANL Neg. No. 112-9394.*

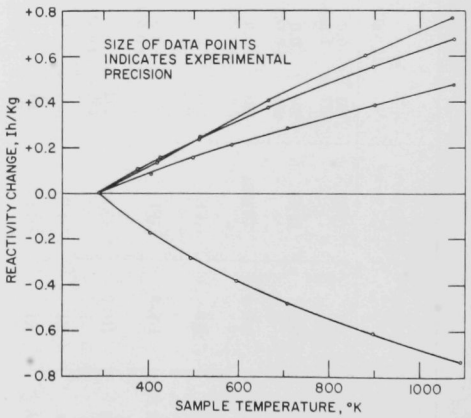


FIG. III-4-2. U-235 Doppler Effect Measurements on Assemblies 13, 14, 16 and 17 of ZPR-9. *ANL Neg. No. 112-9395.*

include the change in the perturbation normalization. The effect of this factor in this case is to decrease the apparent change in the Doppler effect from assembly to assembly where the Doppler effect remains positive, and to exaggerate the magnitude of the change somewhat in the assemblies where the U-235 Doppler coefficient turned negative. (Approximate ratios of the perturbation denominators relative to Assembly 13 are 1.028, 1.097, 1.400 for Assemblies 14, 16 and 17, respectively.

The effect of including this factor would be to shift the curves somewhat relative to one another but not to change the general characteristics of the results.

The results demonstrate very clearly the sensitivity of fissile element Doppler effects to the reactor adjoint spectrum. The increase in the Doppler energy flux, for example, from Assembly 13 to Assembly 17 was only fractional, while the U-235 Doppler coefficient reversed sign, changing from strongly positive in the first assembly to strongly negative in the final one.

### References

1. C. E. Till, R. A. Lewis and R. N. Hwang, *ZPR-6 Doppler Measurements and Comparisons with Theory*, Proc. International Conference on Fast Critical Experiments and Their Analysis, October 10–13, 1966, ANL-7320, pp. 319–333.
2. R. A. Karam, A. Ancarani, F. H. Helm, W. Y. Kato, G. Main and G. K. Rusch, *Measured Physics Parameters in a Zoned Fast Uranium Carbide Core, ZPR-6, Assembly No. 4Z*, Reactor Physics Division Annual Report, July 1, 1965 to June 30, 1966, ANL-7210, pp. 137–153.

## III-5. Comparison and Analysis of Theoretical Doppler Coefficient Results For Fast Reactors[1]

R. N. Hwang and K. Ott*

### Introduction

During the past few years there has been a great deal of theoretical work done on Doppler effect studies for large fast reactors. Refined methods of calculating the Doppler coefficient of a fast system have been developed. Simultaneously, our knowledge of resonance data has been significantly improved. Thus, good agreement among the Doppler coefficients as calculated by different laboratories for identical reactor systems has been realized. An extensive comparison proposed by D. Okrent[2] was presented in 1965. Ten different laboratories contributed their independently calculated Doppler coefficients for various systems. Comparisons of the Doppler coefficient results showed surprisingly large discrepancies. The discrepancies were the differences between the respective results and the median value defined as the average over the results obtained by all laboratories. The discrepancies ranged from about $-85\%$ to $+60\%$ of the median value. Such disagreement was certainly unsatisfactory and demanded further consideration.

These comparisons were based on the Doppler coefficients at a given temperature. Undoubtedly, still larger discrepancies will be expected at other temperatures of practical importance. For fast reactor studies, the temperature range of practical interest varies from room temperature to about 3600°K. The Doppler coefficient may vary by a factor of 30 or more within this temperature range, especially when a sharp rise in temperature is accompanied by loss of sodium. Hence, the incorrect prediction of the temperature behavior of the Doppler coefficient in the normal operating temperature range may lead to much more serious errors in the event of a power excursion. For this reason, R. Froelich, et al.[3] have carried out a more detailed comparison in which not only the magnitude but also the temperature behavior of the Doppler coefficients as obtained by two independent calculations was considered. The latter comparison, however, led only to preliminary conclusions. In recent experiments,[4,5] the temperature behavior of the Doppler reactivity has been under serious consideration. However, $1/T$ fitting for the U-238 Doppler coefficient was used exclusively. The use of $1/T$ fitting is believed to be inconclusive since the temperature behavior of the Doppler coefficient is characterized by the spectrum of a particular system under consideration. Furthermore, a different temperature distribution, $(1/T)^{1.1}$ for instance, may give just as good a fit to the measured values as $1/T$, within the limit of experimental errors and the limited temperature range considered.

The purpose of this paper is to extend the comparison of at least two independent results into greater detail. In this comparison the temperature, energy,

* On leave from Kerforschungszentrum, Karlsruhe, Germany, within the framework of the USAEC-EURATOM Scientist Exchange Program.

TABLE III-5-I. Atomic Concentrations, atoms/cc

| Case | $y$ | Pu-239 | U-238 | Na | SS | O |
|---|---|---|---|---|---|---|
| 1 | 9.0 | 0.00072 | 0.00648 | 0.0123 | 0.011 | 0.0144 |
| 2 | 7.0 | 0.00090 | 0.0063 | 0.0123 | 0.011 | 0.0144 |
| 3 | 5.0 | 0.0012 | 0.0060 | 0.0123 | 0.011 | 0.0144 |
| 4 | 2.5 | 0.00206 | 0.00514 | 0.0123 | 0.011 | 0.0144 |

and enrichment dependence of the Doppler coefficient has been carefully examined. It is believed that the results of this comparison will give some indication of possible causes responsible for the large discrepancies mentioned previously. In particular, it will be shown that two independent calculations with the best available data and methods as carried out at Argonne National Laboratory and Kernforschungszentrum, Karlsruhe, give excellent agreement.

## General Description of the Comparison

For convenience, some bare systems typical of fast reactor compositions as proposed by Okrent[2] were again used in the present work. To further simplify the problem, the simplest cases with no Pu-240 and no fission products present were chosen for the reactor composition. Table III-5-I gives the concentrations in atoms per cc for the constituents of the systems under consideration. The fertile-to-fissile ratios $y$ were taken to be 9.0, 7.0, 5.0 and 2.5, respectively.

In the present work, a much more detailed comparison of the Doppler coefficients of these four bare systems calculated independently at Argonne National Laboratory and at Karlsruhe are given. In addition, two other results calculated in the following manner are presented along with ANL and KFK results:

(1) Calculations were based directly on ABN group constants,[6] using original ABN self-shielding factors.

(2) Spectra were based on ABN group constants but the temperature derivatives of reaction cross sections $\partial\Sigma_f/\partial T$ and $\partial\Sigma_a/\partial T$ calculated with the Karlsruhe Doppler Program were used. The ABN set is used with original $1/E$ weighting in all groups. The former will be referred to as ABN results whereas the latter will be referred to as ABN-KFK results in the later discussions.

## Results and Conclusions

Tables III-5-II through III-5-IV sum up the numerical results obtained at ANL and KFK, respectively, using group constants of three different origins. Both accidental and the self-overlap effect of resonance of fissile and fertile isotopes were taken into account in all three calculations. Tables III-5-III and III-5-IV show values of $dk/dT$ at 300°K and 900°K, respectively, for four different systems. Excellent agreement between ANL and KFK values was observed for all cases considered. ABN-KFK values were generally higher than both ANL and KFK values.

Figure III-5-1 shows the variations of $x$-values as a function of the fertile-to-fissile ratio $y$, with $x$ being defined as the exponent in the temperature law; that is,

$$\frac{dk}{dT} = \frac{C}{T^x}.$$

The quantity $x$ is a measure of the temperature behavior of the Doppler coefficient. It has been shown in Ref. 2 that the $x$-values calculated at various laboratories are generally in poor agreement. A small error in either the Doppler broadened cross sections or the Doppler reactivity change may significantly affect the $x$-values. In other words, good agreement in $\delta k$ or $dk/dT$ at a given temperature may not insure that the $x$-values will agree. Poor agreement in the $x$-values implies that the calculated Doppler coefficient for extremely high temperatures will be considerably different.[3]

Agreement in $x$-values between ANL and KFK results is generally good, but certainly not as good as those in $dk/dT$. For comparison, $x$-values calculated from ABN spectra and ABN reaction cross sections

TABLE III-5-II. $\delta k$ Values Calculated at ANL

| Case | $y$ | $\delta k$, 750–300°K | $\delta k$, 1100–750°K |
|---|---|---|---|
| 1 | 9.0 | −0.01494 | −0.006052 |
| 2 | 7.0 | −0.009578 | −0.003905 |
| 3 | 5.0 | −0.005073 | −0.002022 |
| 4 | 2.5 | −0.001092 | −0.000406 |

TABLE III-5-III. $\left(\frac{dk}{dT}\right)_{900°K}$

| Case | $y$ | ANL, $10^6$ | KFK, $10^6$ | ABN-KFK, $10^6$ |
|---|---|---|---|---|
| 1 | 9.0 | −17.13 | −16.59 | −18.89 |
| 2 | 7.0 | −10.99 | −10.89 | −12.63 |
| 3 | 5.0 | −5.82 | −5.83 | −6.92 |
| 4 | 2.5 | −1.18 | −1.26 | −1.60 |

TABLE III-5-IV. $\left(\frac{dk}{dT}\right)_{300°K}$

| Case | $y$ | ANL, $10^6$ | KFK, $10^6$ | ABN-KFK, $10^6$ |
|---|---|---|---|---|
| 1 | 9.0 | −54.92 | −53.30 | −61.78 |
| 2 | 7.0 | −35.21 | −35.70 | −42.58 |
| 3 | 5.0 | −19.25 | −19.80 | −24.37 |
| 4 | 2.5 | −4.37 | −4.55 | −6.24 |

are also included in Fig. III-5-1. Significant discrepancies, not only in magnitude but also in the general variation of $x$-values, are found when ABN results are considered. If one assumes that two independent calculations give identical values of $dk/dT$ at room temperature, the discrepancy of 0.5 in the $x$-value implies a deviation of $(10)^{0.5} = 3.16$ in $dk/dT$ at 3000°K between the two calculations. It is interesting to note that $x$ is also extremely sensitive to small effects, such as $p$-wave contributions and overlap effect of U-238 resonances. These effects will not only significantly change the magnitude of $x$ but also change the slope of $x$ with respect to $y$ as indicated in Fig. III-5-1. It is believed that the differences in Pu-239 resonance parameters which determines the relative contribution

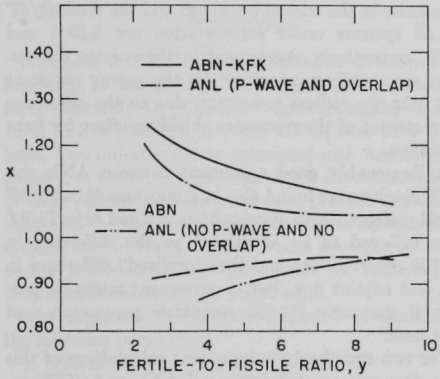


FIG. III-5-1. $x$ versus Fertile-to-Fissile Ratio. *ANL Neg. No. 112-7569 Rev. 1.*

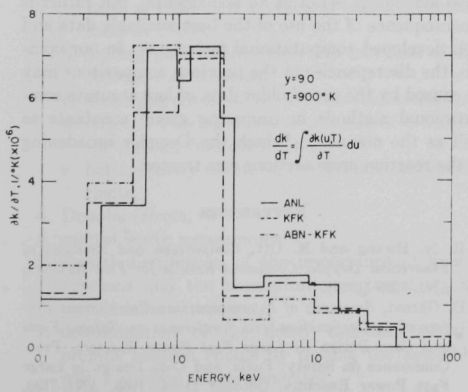


FIG. III-5-2. Group-wise Doppler Coefficient at 900°K for $y = 9.0$. *ANL Neg. No. 112-7510.*

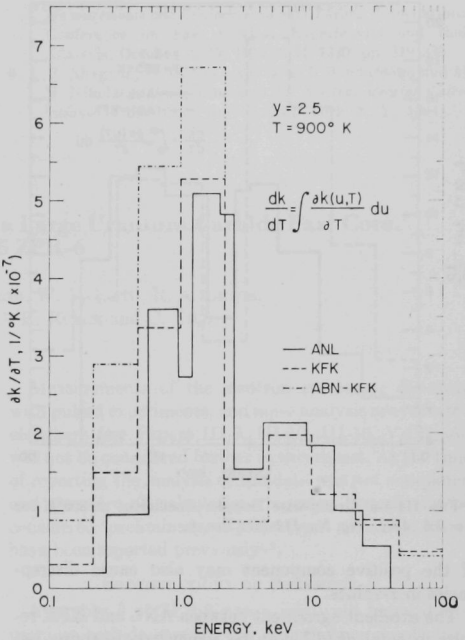


FIG. III-5-3. Group-wise Doppler Coefficient at 900°K for $y = 2.5$. *ANL Neg. No. 112-7511.*

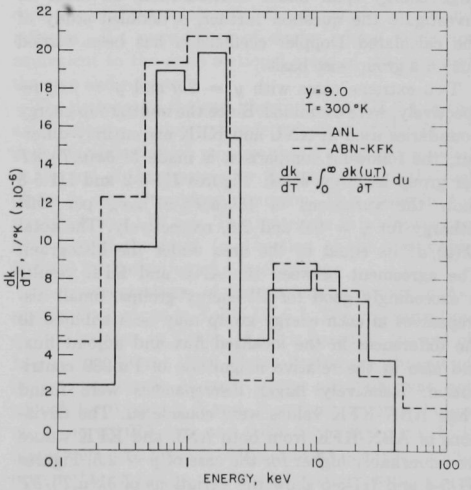


FIG. III-5-4. Group-wise Doppler Coefficient at 300°K for $y = 9.0$. *ANL Neg. No. 112-7576 Rev. 1.*

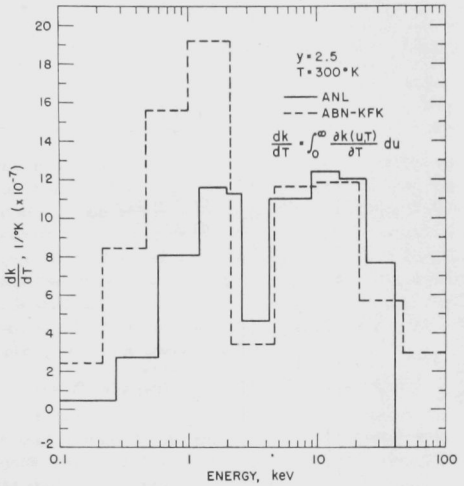


FIG. III-5-5. Group-wise Doppler Coefficient at 300°K for $y = 2.5$. *ANL Neg. No. 112-7575 Rev. 1.*

of the positive component may also cause discrepancies in $x$-values.

The excellent agreement between ANL and KFK results in total $dk/dT$ may be somewhat deceiving because larger discrepancies in the "localized" values of $\partial k(u,T)/\partial T$ might compensate one another over the large energy span under consideration. In order to investigate the question further, a detailed study of the calculated Doppler coefficients has been carried out on a group-wise basis.

Two extreme cases with $y = 2.5$ and $y = 9.0$, respectively, were examined. Since the multigroup energy boundaries used at ANL and KFK are entirely different, the following comparison is made of $\partial k(u,T)/\partial T$ per group lethargy width. Figures III-5-2 and III-5-3 show the variations of $(\partial k(u,T)/\partial T)_{900°K}$ per unit lethargy for $y = 9.0$ and 2.5, respectively. The total $dk(u)/dT$ is equal to the area under the histogram. The agreement between the ANL and KFK results is exceedingly good for all energy groups. Small discrepancies in each energy group may be attributed to the differences in the localized flux and adjoint flux, and also in the relative magnitude of Pu-239 contribution. Relatively larger discrepancies were found when ABN-KFK values were considered. The deviations of ABN-KFK from both ANL and KFK values are remarkably higher for the case of $y = 2.5$. Figures III-5-4 and III-5-5 show the variations of $\partial k(u,T)/\partial T$ at 300°K. KFK values are not available for this temperature. Again much larger discrepancies (Figs. III-5-2 through III-5-5) seem to suggest that the Pu-239 component of $\partial k(u,T)/\partial T$ in ANL values may have been higher than the KFK values below 1 keV. Better agreement would have been possible if the same set of plutonium parameters were used in both calculations.

From the results discussed in the preceding section, one is led to the following conclusions:

1. Excellent agreement between ANL and KFK results was observed in
   (a) criticality calculations
   (b) spectra
   (c) total $dk(T)/dT$
   (d) temperature dependence of $dk/dT$ (in terms of $x$ values)

for all systems under consideration. Maximum discrepancies in the critical bucklings and the total $dk/dT$ for all systems under consideration are 8.39% and 6.5%, respectively. Agreement in the spectra calculations are equally good except for the energy region at and near the sodium resonance, due to the difference in treatment of the resonance shielding effect for light scatterers.

2. Reasonably good agreement between ANL and KFK results were found also in group-wise $\partial k(u,T)/\partial T$ for all systems. Small discrepancies in $x$ and $\partial k(u,T)/\partial T$ were believed to be attributed to the difference in Pu-239 contributions and the "localized" difference in flux and adjoint flux. Better agreement might be possible if the same Pu-239 resonance parameters had been used.

For two completely independent calculations of this type, the agreement between all ANL and KFK results, in general, may be considered to be exceedingly good. The authors are inclined to believe that such good agreement is not at all coincidental, but rather is a consequence of the use of the best available data and well developed computational techniques. In our opinion, the discrepancies in the previous comparisons may be caused by the use of older data or less accurate computational methods in preparing group constants as well as the manner in which the Doppler broadening of the reaction cross sections was treated.

## REFERENCES

1. R. N. Hwang and K. Ott, *Comparison and Analysis of Theoretical Doppler-Coefficient Results for Fast Reactors*, ANL-7269 (1966).
2. D. Okrent, *Summary of Intercomparison Calculations Performed in Conjunction with Conference on Safety, Fuels and Core Design in Large Fast Power Reactors*, Proc. Conference on Safety, Fuels, and Core Design in Large Fast Power Reactors, October 11-14, 1965, ANL-7120, pp. 3-23.

3. R. Froelich, K. Ott, G. Shavin and S. Yiftah, *Results of Doppler Coefficient Calculations for Fast Reactors and Comparison of Different Methods*, ANL-7120 (1965).
4. C. E. Till, R. A. Lewis and E. F. Groh, *Recent Doppler Measurements with ZPR-6*, ANL-7120 (1965).
5. C. E. Till, R. A. Lewis and R. N. Hwang, *ZPR-6 Doppler Measurements and Comparisons with Theory*, International Conference on Fast Critical Experiments and their Analysis, October 10–13, 1966, ANL-7320, pp. 319–333.
6. I. P. Abagyan, N. O. Bazazyants, I. I. Bondarenko and M. N. Nikolaeu, *Group Constants for Nuclear Reactor Calculations*, (Consultants Bureau, New York, N. Y., 1964).

# III-6. Measured Physics Parameters in a Large Uranium Carbide Fast Core, Assembly 5 ZPR-6

R. A. Karam, L. R. Dates, E. Groh, W. Y. Kato, R. A. Lewis, G. Main, J. E. Marshall, G. K. Rusch and C. Till

## Introduction

Assembly 5 of ZPR-6 was a 2600-liter uranium carbide core. It was the reference assembly for the zoned cores [Assembly 4Z of ZPR-6[1] and Assemblies 11 and 12 of ZPR-9 (Ref. 2 and Paper III-8)] that have been built. Two objectives were associated with Assembly 5; namely, to obtain integral data which are characteristic of large carbide systems and which provide important checks on the theoretical methods used to analyze such systems and to verify the zoned core concepts by comparing predicted physics parameters for Assembly 5 from measurements in the zoned cores.

The experimental program consisted of measuring the following parameters:

1. critical mass,
2. heterogeneity effects,
3. sodium-void effects,
   a. effect of sodium removal on the absolute fission rates in U-235 and U-238 and absolute capture rates in U-238,
   b. loading pattern effects on and traverses of the sodium-void cofficient,
   c. streaming effects on the sodium-void coefficient,
   d. effect of varying the concentration of U-238 on the sodium-void coefficient,
   e. heterogeneity effects on the sodium-void coefficients,
4. Doppler effects,
5. central worth measurements,
6. spatial distribution of the importance of fission neutrons and the normalization integral of the perturbation expression,
7. determination of the decay constants of the prompt neutron chains by pulsing the assembly with a neutron source generator,
8. noise analysis with polarity correlation for determining Rossi-$\alpha$.

Measurements of the neutron spectrum, die-away with pulsed experiments, and noise analysis are reported elsewhere (see Papers III-9, III-10, III-16, V-12) and will not be considered further in this report. At the time of reporting the analysis of the data was not completed and therefore all calculations reported here should be considered preliminary. Verifications of zoned cores have been reported previously[1,2].

## Specifications of Assembly 5

Assembly 5 of ZPR-6 was a relatively large, dilute uranium carbide core. It was essentially a simple two-region system with cylindrical configuration. Figure III-6-1 is a schematic diagram of Assembly 5 with all appropriate dimensions. The radial dimension of the core, $R_c$, and the total radial dimension of the core and reflector, $R_t$, were those of circles whose areas are equivalent to the cross sectional areas of the core and the core and reflector.

The presence of the gap, shown in Fig. III-6-1 in the axial reflector, is due to a safety feature of the ZPR-6 and -9 facilities[3] which requires that a space be provided at the end of the drawers for the expansion of the fuel plates in case of a minor excursion. This space in Assembly 5 was 1.07 cm. The materials in a drawer are held toward the front (mid-section of the split table facility) by the action of a steel spring.

The concentrations of the various materials in Assembly 5 are given in Table III-6-I. The concentration of U-235 shown in Table III-6-I is based on the use of $\frac{1}{16}$-in. (0.159 cm) thick plates having enrichment of 93%. The supply of such plates available was not enough for Assembly 5 and, therefore, double columns of $\frac{1}{32}$-in. (0.079 cm) and 0.026-in. (0.066 cm) thick plates were used in some of the drawers near the periphery of the core. The use of such plates resulted in a lower concentration of U-235 by 7%. Figure III-6-2 shows a cross-sectional view of Assembly 5 as loaded.

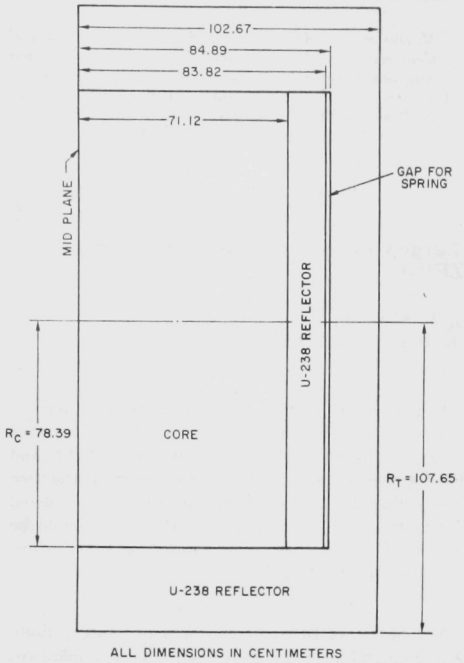


FIG. III-6-1. Schematic Diagram for Assembly 5 of *ZPR-6*. *ANL Neg. No. 112-9240.*

TABLE III-6-I. ATOMIC DENSITIES IN ASSEMBLY 5

| | Concentrations, atoms/cc × $10^{24}$ | | |
|---|---|---|---|
| | Region | | |
| Material | Core | Reflector | Gap for Spring |
| U-235 | 0.00154 | 0.000081 | 0.0000 |
| U-238 | 0.01056 | 0.03993 | 0.0000 |
| Na | 0.00920 | 0.0000 | 0.0000 |
| C | 0.01293 | 0.0000 | 0.0000 |
| Fe | 0.00904 | 0.004322 | 0.010982 |
| Ni | 0.00113 | 0.00054 | 0.0009106 |
| Cr | 0.002386 | 0.00114 | 0.001953 |

Concentration of U-235 in the central region was the same as that given in Table III-6-I and the concentration of U-235 in Region 2 was 1.442 × $10^{21}$ atoms/cc. Concentrations of the other materials are given in Table III-6-I. Regions 1 and 2 of Fig. III-6-2 had equivalent outer radii of 62.73 and 77.86 cm, respectively.

Assembly 5 was loaded with a three-drawer cell pattern which was similar to the loading pattern of Assembly 4Z.[4] Figure III-6-3 shows the pattern of the three-drawer cell of the core regions of Assembly 5. This pattern was slightly different from the pattern of Assembly 4Z, the difference being that in the latter the first and eighth columns of the second-drawer of the three-drawer cell were $\frac{1}{16}$-in. (0.159 cm) thick plates of depleted uranium. These two columns were replaced in Assembly 5 with one $\frac{1}{8}$-in. (0.318 cm) thick column of the same material. This modification in the loadings of the two assemblies was dictated by the insufficient inventory of $\frac{1}{16}$-in. (0.159 cm) thick plates. The loading pattern shown in Fig. III-6-3 will henceforth be referred to as "normal pattern".

## CRITICAL MASS

The measured critical mass of Assembly 5 for the loading shown in Fig. III-6-2, corrected for excess reactivity only, was 1583 kg of U-235. The relative reactivity of a drawer in region 2 (Fig. III-6-2) to that of a drawer in region 1 was measured as a function of position with few drawers. The results from these measurements were used to obtain the critical mass of a core that had the same U-235 concentration in regions 1 and 2. The critical mass of such a core was 1564 kg of U-235. The extrapolation of the critical mass to one region in the core is a first-order correction; however, it is suffi-

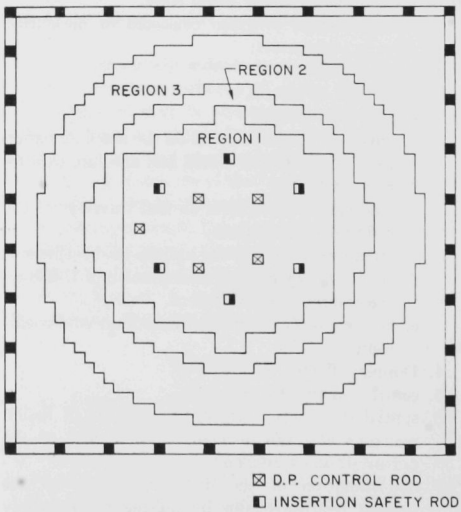


FIG. III-6-2. Cross Sectional View of Assembly 5 of ZPR-6. *ANL Neg. No. 112-9161.*

TABLE III-6-II. CALCULATED[a] VALUES OF THE CRITICAL MASS OF ASSEMBLY 5 OF ZPR-6

| Cross Section Set | No. of Core Regions | Comments | $\sigma_p$ of U-238 and U-235, *b* | | | | Critical Mass, kg U-235 |
|---|---|---|---|---|---|---|---|
| | | | Core | | Reflector[b] | | |
| | | | U-238 | U-235 | U-238 | U-235 | |
| 224[c] | 2 | Calculated as loaded (Fig. III-6-2) | 40 | 200 | 40 | 200 | 1589 |
| 801[d] | 2 | Calculated as loaded | 40 | 200 | 40 | 200 | 1477 |
| 801 | 2 | | 40 | 70 | 40 | 70 | 1604 |
| 801 | 2 | | 35 | 78 | 15 | 78 | 1550 |
| ZPR-6-5[e] | 2 | | 35 | 78 | 35 | 78 | 1545 |
| ZPR-6-5 | 2 | | 35 | 78 | 15 | 78 | 1539 |
| ZPR-6-5 | 2 | | 25 | 78 | 15 | 78 | 1454 |
| ZPR-6-5 | 2 | | 15 | 78 | 15 | 78 | 1300 |
| ZPR-6-5 | 1 | Calculated with region 2 having same U-235 atom density as region 1 of the core (Fig. III-6-2) | 35 | 78 | 35 | 78 | 1530 |

[a] Calculated with one dimensional diffusion Code 9.

[b] The reflector is depleted uranium which contained 0.2% U-235.

[c] Cross section set 224 is a "workhorse" type set[6] which was Elmoe averaged for typical large carbide cores.

[d] Cross Section set 801 is a 25-group Elmoe averaged set for Assembly 5 of ZPR-6 (central region only).

[e] ZPR-6-5 cross section set was generated by the MC[2] code[8] for Assembly 5 (central region only) by R. A. Lewis.

ciently accurate, because the magnitude of the correction is not large.

### HETEROGENEITY EFFECTS

Table III-6-II lists some calculated values of the critical mass. It is seen from Table III-6-II that the effective potential scattering cross sections of U-235 and U-238 strongly influence the critical mass value. This effect is understandable since the effective resonance absorption integral is proportional to the potential scattering cross section, $\sigma_p$. The accuracy with which $\sigma_p$ can be calculated for the complicated and heterogeneously loaded plate-type unit cells of Assembly 5 has never been ascertained and R. Lewis[9] and D. Meneghetti[10] have attempted to calculate $\sigma_p$ for U-235 and U-238 in Assembly 5 by the equivalence relation[11] for the loading pattern shown in Fig. III-6-3. Both obtained values $\sigma_p^{238} \approx 25$ b and $\sigma_p^{235} \approx 78$ b. The calculated critical mass with these $\sigma_p$ values was 1454 kg of U-235, as may be seen from Table III-6-II. This value of the critical mass is about 8% lower than the measured value. The critical mass value obtained with cross section Set 224 is in best agreement with the measured value. This agreement, however, is fortuitous because the fission cross sections in Set 224 (isotope Nos. 1 and 4) are known to be in error.[12] It is apparent, therefore, that the strong dependence of the critical mass on the potential scattering cross sections of U-235 and U-238 requires that the limitations and validity of the equivalence relation should be verified. Accurate consideration of resonance absorption is quite important, especially in the large carbide or oxide cores where the neutron spectrum is relatively soft.

The equivalence relation, at least in principle, accounts for self-shielding and resonance absorption in materials of a unit cell. Another heterogeneity effect which influences the critical mass is the fast fission factor. This factor may be defined as the gain in reactivity due to neutrons whose spectrum is harder than the asymptotic or equilibrium spectrum. The factor depends on three things: (1) the physical shape of the fissile material, i.e., thickness and length of column; (2) the enrichment of the fissile material; and (3) the physical separation between fissile and fertile materials. The thickness of the plate of fissile material contributes to the reactivity of the system through an increase in the yield of neutrons per fission due to fission neutrons that never leave the plate before causing another fission, and to neutrons that leave the plate and return to cause fissions with a spectrum that is still harder than the equilibrium spectrum. The length of the plate affects the reactivity of the system in a similar manner. Another effect which counteracts the increase in reactivity due to self-multiplication is self-shielding. This effect depletes the low-energy neutrons in the vicinity of the fissile plates and thus causes a decrease in reactivity. Presumably this effect can be accounted for by the equivalence relation. Experimentally, as will be shown later, the reactivity of the fissile material as a function of thickness is a straight line indicating that the self-shielding and self-multiplication reactivity effects cancel each other in Assembly 5 of ZPR-6. The calculated

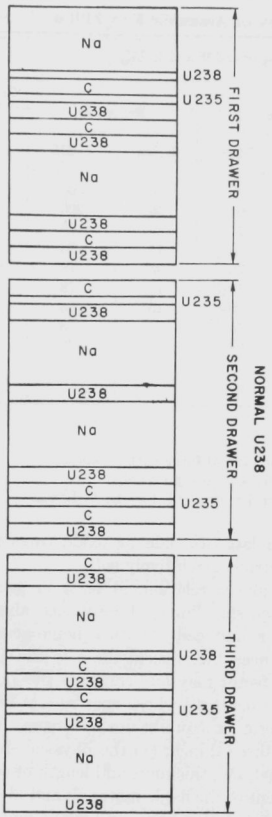


FIG. III-6-3. Normal Loading Patterns of Three-Drawer Cell in Assembly 5 of ZPR-6. *ANL Neg. No. 112-9277.*

values of the critical mass (Table III-6-II) should in principle account for the self-shielding but not the self-multiplication effects. For this reason the calculated critical mass value should be slightly higher than the measured value.

The fast fission factor is also affected by the increase or decrease in the total fissions of U-238 in the heterogeneous system over that of the homogeneous system. In Assembly 5 the fissile material was metallic U-235 with an enrichment of 93%. The fertile material was metallic U-238 (0.2% enrichment). The graphite was in plate form and all three materials simulate uranium monocarbide fuel with an enrichment of 12.7%. The number of fissions in U-238 is obviously dependent on the exposure of U-238 to fission neutrons and neutrons harder than those of the equilibrium spectrum. Therefore, the fission in U-238 is affected by the physical separation between the U-235 and U-238 plates. The enrichment of the U-235 plates also affects the total fissions in U-238 because in such plates the exposure of U-238 to fission neutrons is maximum. Thus the increase or decrease in U-238 fissions because of heterogeneity is the quantity of interest and the magnitude of this quantity depends on the loading pattern.

The problems of accounting for the various heterogeneity effects quantitatively are not trivial. Meneghetti's method[13] for treating the heterogeneity effects on the sodium-void coefficient is a considerable step forward. The dependence of this method on the validity of the equivalence relation is decreased considerably because the equivalence relation is used to obtain relative and not absolute values of $\sigma_p$. If uncertainties in the evaluation of $\sigma_p$ can be eliminated or minimized there remains the problem of obtaining the group dependent cross sections as a function $\sigma_p$. This problem however is dependent on the basic cross section and the resonance parameters. Comparison of measurements with theory would then reflect or perhaps point out the problem areas with the basic data.

Three different types of experiments designed to yield pertinent data on the heterogeneity effects were conducted on Assembly 5 of ZPR-6. The first type of experiment was designed to vary $\sigma_p^{238}$. The second type consisted of cylindrical fuel elements (pellets of UC with proper enrichment) in type 304 stainless steel tubes which were surrounded with sodium. The third type consisted of homogeneous samples in which the UC and sodium and, in some cases type 304 stainless steel powder, were mixed together and housed in a type 304 stainless steel can. The last two types of experiments feature simple geometries with which the equivalence relation can be applied with more confidence than with the heterogeneous plate-type loading pattern (Fig. III-6-3).

### VARIATION OF $\sigma_p^{238}$

The potential scattering cross sections of U-238 were varied in Assembly 5 of ZPR-6 in order to study the following four related effects:

1. effect of decreasing $\sigma_p$ on the critical mass,
2. environmental effects as a result of bunching U-238 plates,
3. effect of $\sigma_p$ on the absolute fission rates of U-235 and U-238 and absolute capture rate of U-238 as a function of position in the three-drawer cell,
4. effect of decreasing $\sigma_p$ on the sodium-void coefficient.

The effect of decreasing $\sigma_p$ on the sodium-void coefficient is discussed in the section on Sodium-Void Effects.

The variation in $\sigma_p$, achieved by bunching the U-238 plates, was performed in two steps. First, the normal three-drawer cell loading (Fig. III-6-3) was reloaded as shown in Fig. III-6-4. This step was deemed necessary so that the bunching of U-238, shown in Fig. III-6-5, would not require any shifting in position of either the U-235 plates or the sodium cans. Thus, the loading pattern shown in Fig. III-6-4 was the reference case for the loading pattern shown in Fig. III-6-5. It should be noted that the spacing between the U-235 plates in the three-drawer cell is essentially equidistant. The region in which the loading patterns was changed was a square comprising the central 9 by 9 drawers (49.72 cm) in each half of the reactor. At a radius of about 20 cm from the center of this region there were four control rods

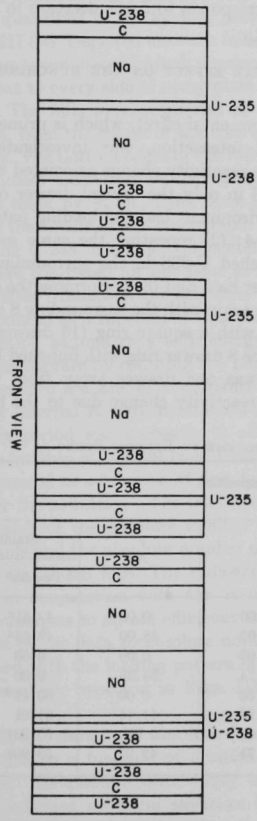


FIG. III-6-4. Reference Loading Patterns of Three-Drawer Cell for Bunching U-238 in Assembly 5 of ZPR-6. *ANL Neg. No. 112-9223.*

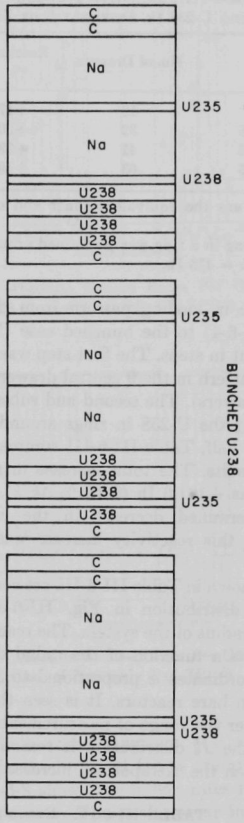


FIG. III-6-5. Bunched U-238 Loading Patterns in Three-Drawer Cell of Assembly 5 of ZPR-6. *ANL Neg. No. 112-9278.*

per half (Fig. III-6-2), equally spaced about the center. The loading pattern of these control rods (or drawers) was the same as that of the central drawer shown in Fig. III-6-3 and this pattern was maintained in all experiments. The number of drawers in which the loading patterns were changed was 77 per half.

### THE EFFECT OF VARYING $\sigma_p^{238}$ ON CRITICAL MASS

The reactivity change in the system due to the change in the loading pattern shown in Fig. III-6-3 to that shown in Fig. III-6-4 was $(-13.4 \pm 0.4)$ Ih for the 154 drawers involved in both halves. This reactivity decrease may be due to either a slight increase in $\sigma_p^{238}$ relative to the normal loading pattern of Fig. III-6-3 or an increase in the streaming through the light density channels of sodium.

TABLE III-6-III. Reactivity Change due to Bunching U-238 in Assembly 5 of ZPR-6

| $R_i - R_0$[a], cm | No. of Drawers | Reactivity Change[b], Ih |
|---|---|---|
| 0.0–9.35 | 18 | +17.5 ± 0.4 |
| 9.35–15.85 | 32 | +30.6 ± 0.4 |
| 15.85–21.95 | 41 | +33.6 ± 0.4 |
| 21.95–28.45 | 63 | +49.9 ± 0.4 |

[a] $R_i$ and $R_0$ are the equivalent inner and outer radii of cylindrical rings.

[b] The bunching in a ring was performed around a bunched region. $1\%\ \Delta k/k$ = 476 Ih.

The change in loading pattern from the reference case (Fig. III-6-4) to the bunched case (Fig. III-6-5) was carried out in steps. The first step was a change of the loading pattern in the 9 central drawers per half (a total of 18 drawers). The second and subsequent steps were bunching the U-238 in rings around the central 9 drawers per half. Table III-6-III summarizes the experimental results. The total increase in reactivity in this region was +131.6 Ih (0.275% $\Delta k/k$). The experimentally determined decrease in the critical mass equivalent to this reactivity increase was 51.6 kg of U-235.

The data shown in Table III-6-III are compared with $J_0^2(2.405r/\tilde{R})$ distribution in Fig. III-6-6. $\tilde{R}$ is the extrapolated radius of the system. The reactivity worth of a sample as a function of the radial dimension in cylindrical coordinates is proportional to $J_0^2(2.405r/\tilde{R})$ distribution in bare reactors. It is seen that the fit is reasonable over the range of measurements. If it is assumed that the $J_0^2$ distribution is reasonable for the entire core then the extrapolated increase in reactivity

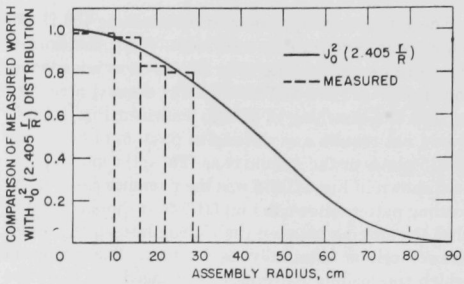


Fig. III-6-6. Extrapolation of the Worth of U-238 Bunching in Assembly 5 of ZPR-6. *ANL Neg. No. 112-9163.*

due to bunching of U-238 is 218 Ih. This increase in reactivity corresponds to 5.6% decrease in the critical mass (87.2 kg).

### Environmental Effect on the Bunching of U-238 Plates

The environmental effect, which is primarily due to the Dancroff interaction, was investigated by: (1) measuring the reactivity change associated with bunching the U-238 in only the central drawer of each half when the environment had the loading pattern shown in Fig. III-6-4; (2) repeating the same measurement with the bunched U-238 in the surrounding 8-drawer square ring per half, and (3) performing the same measurement once again with the surrounding 8 drawers unbunched but with a square ring (16 drawers per half) adjacent to the 8 drawer ring with bunched U-238. This square ring was one drawer away from the central drawer. The reactivity change due to the bunching of

TABLE III-6-IV. Description of Samples used in Heterogeneity Effects Study

| Sample No. | Physical Description | Composition g | | | | | |
|---|---|---|---|---|---|---|---|
| | | U-235 | U-238 | C | Na | Stainless Steel | |
| | | | | | | Powder[a] | Can[b] |
| 1 | Heterogeneous[e] | 82.95 | 635.78 | 25.00 | 0.00 | 49.51[d] | 23.74 |
| 2 | Heterogeneous | 82.95 | 635.78 | 25.00 | 48.00 | 49.65[d] | 23.74 |
| 3 | Homogeneous | 107.31 | 739.68 | 45.05 | 0.00 | 0.00 | 24.45 |
| 4 | Homogeneous | 108.96 | 751.01 | 45.74 | 34.36 | 0.00 | 43.37 |
| 5 | Homogeneous | 86.63 | 597.08 | 36.36 | 0.00 | 60.14 | 30.08 |
| 6 | Homogeneous | 87.86 | 605.59 | 36.88 | 44.44 | 61.01 | 29.08 |
| 7 | Pellets | 86.73 | 597.83 | 33.47 | 0.00 | 59.96[c] | 54.52 |
| 8 | Pellets | 87.38 | 602.30 | 33.71 | 42.29 | 59.90[c] | 54.56 |

[a] Some samples had SS powder (type 304) mixed with the UC and sodium.

[b] All samples were canned in SS (type 304).

[c] These samples were 1.875 x 1.875 x 1.875 in.

[d] This quantity of SS was in the form of cans (2 x 2 x ½ in.) some of which were filled with sodium.

[e] The SS tubes weigh about 60 g; it is not powder.

the two central drawers alone was (+1.56 ± 0.08) Ih. The reactivity change that resulted from bunching the two central drawers when the surrounding eight drawers per half were bunched was (+2.02 ± 0.07) Ih. The reactivity change that resulted from the last case was (+1.54 ± 0.07) Ih. These results show that the effect of bunching the U-238 in the eight drawers per half square ring adjacent to the central drawers increased the reactivity due to the bunching in the two central drawers by about 25%. Such an effect was totally absent when the bunching was in the ring that was one drawer away from the central drawers.

### THE EFFECT OF $\sigma_p^{238}$ ON FISSION AND CAPTURE RATES

The effect of varying $\sigma_p^{238}$ on the capture and fission in U-238 and fission in U-235 was investigated by measuring these quantities in the loading patterns of Figs. III-6-4 and III-6-5. Depleted uranium foils, 5 mils thick by $\frac{5}{8}$ in. diam, were placed in such a manner that there was a foil next to every side of every plate in the three-drawer cell. The foils were positioned at an axial distance of 2 in. from the center of the core in one half of the assembly. The bottom edges of the foils were touching the stainless steel drawers. Similarly, the U-235 foils, 5 mils thick by $\frac{3}{8}$ in. diam, were placed in the other half of the assembly at a comparable position with respect to the U-238 foils from the center of the core. The foils were irradiated for one hour at about 50 W. Five hours after irradiation the activities of the U-238 foils were counted as a function of time for fission fragments (counting gamma rays with energy above 0.41 MeV) and for capture by counting the 106 keV gamma rays from excited Pu-239 in coincidence with x-rays produced by internal K conversion electrons. The five-hour waiting period was necessary to allow sufficient time for the buildup of Np-239 from U-239. The U-235 foils were counted as a function of time for fission fragments. After the counting, a few foils were radiochemically analyzed for the absolute number of fissions in the U-235 foils and the absolute number of fissions and captures in the U-238 foils. The radiochemical results were used in conjunction with the results from the counting techniques to obtain efficiency factors to convert the rest of the data to absolute numbers. The results obtained with the loading pattern of Fig. III-6-5 (bunched case) are reported in Figs. III-6-7 through III-6-11.

Figure III-6-7 shows the absolute fission rates per gram of U-235 as a function of position in the three drawer cells. The relative uncertainty in each point due to the inherent counting statistics is 0.2%. The absolute uncertainty which is based on the statistics of the radiochemical analysis is about 2%. It is noted from Fig. III-6-7 that there are more fissions in the

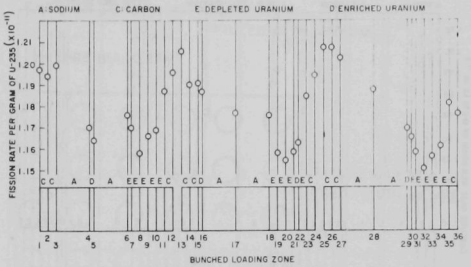


FIG. III-6-7. Absolute Fission Rates Per Gram of U-235 in Bunched U-238 Case of Assembly 5 of ZPR-6. *ANL Neg. No. 112-9238.*

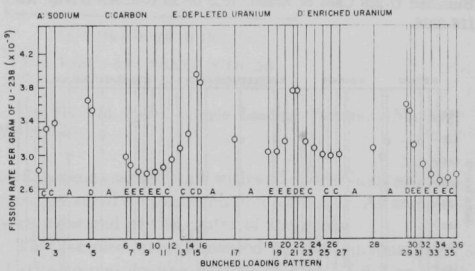


FIG. III-6-8. Absolute Fission Rates Per Gram of U-238 in Bunched U-238 Case of Assembly 5 of ZPR-6. *ANL Neg. No. 112-9235.*

graphite regions than anywhere else and that the fission rates in the bunched U-238 are at a minimum.

Figure III-6-8 shows the fission rates in U-238 as a function of position. The peaks occur in the vicinity of U-235 fuel plates.

Figure III-6-9 shows the absolute capture rates per gram of U-238. The size of the flag on the data is due to the error in the absolute measurements. The relative error is typically 0.2%. It may be noted from Fig. III-6-9 that there are considerable dips in the capture rates within the bunched U-238.

Figures III-6-10 and III-6-11 show the ratios of U-238 captures to U-235 fissions and of U-238 fissions to U-235 fissions as a function of position, respectively. It is noted that these ratios vary as much as 30% within the three-drawer cell.

The fission rates of U-235 and U-238 and capture rates of U-238 in the reference loading of the three-drawer cell (unbunched case, Fig. III-6-4) are given in Figs. III-6-12 through III-6-14. It may be seen from Fig. III-6-14 that there is a decrease in capture in foils Nos. 7 and 31. These foils were placed between

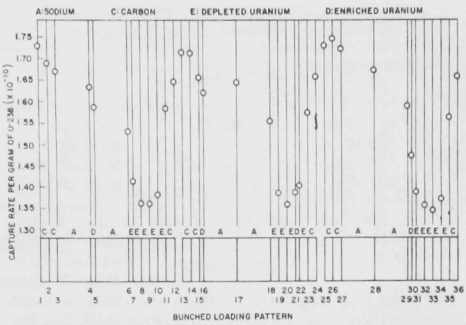


FIG. III-6-9. Absolute Capture Rates Per Gram of U-238 in Bunched U-238 Case of Assembly 5 of ZPR-6. *ANL Neg. No. 112-9232.*

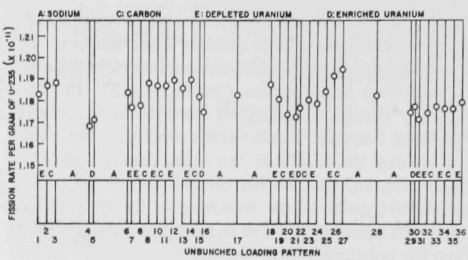


FIG. III-6-12. Absolute Fission Rates Per Gram of U-235 in Unbunched U-238 Case of Assembly 5 of ZPR-6. *ANL Neg. No. 112-9234.*

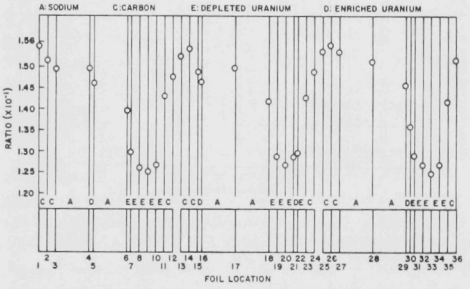


FIG. III-6-10. Absolute U-238 Captures Per U-235 Fission in Bunched U-238 Case of Assembly 5 of ZPR-6. *ANL Neg. No. 112-9233.*

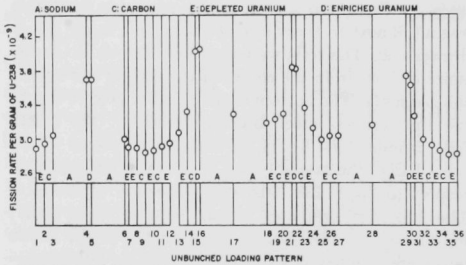


FIG. III-6-13. Absolute Fission Rates Per Gram of U-238 in Unbunched U-238 Case of Assembly 5 of ZPR-6. *ANL Neg. No. 112-9236 Rev. 1.*

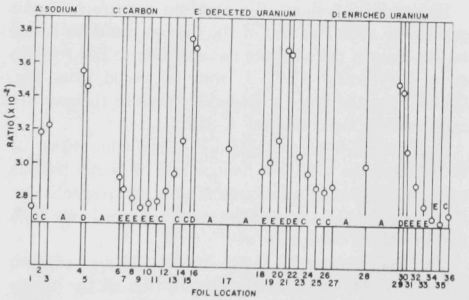


FIG. III-6-11. Absolute U-238 Fission Per U-235 Fission in Bunched U-238 Case of Assembly 5 of ZPR-6. *ANL Neg. No. 112-9242.*

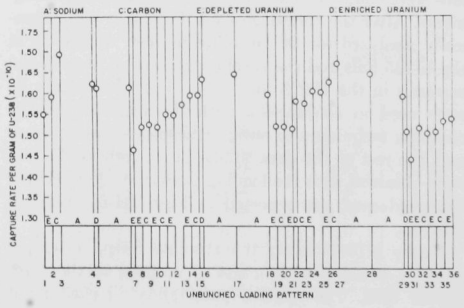


FIG. III-6-14. Absolute Capture Rates Per Gram of U-238 in Unbunched U-238 Case of Assembly 5 of ZPR-6. *ANL Neg. No. 112-9237.*

$\frac{1}{16}$ in. and $\frac{1}{8}$ in. U-238 plates. This indicates that self-shielding within these plates is significant.

### Relative Reactivities of Homogeneous and Heterogeneous Samples

The heterogeneity effects were also studied by comparing the reactivity worths of homogeneous samples with those of plate type and pellet-type heterogeneous samples. Figure III-6-15 shows the arrangement of materials in the plate-type heterogeneous sample and Fig. III-6-16 shows the pellet-type heterogeneous sample. The homogeneous samples consisted of a mixture of UC powder and sodium and in some cases UC powder, sodium and stainless steel powder. The powder and pellet forms of the UC had an enrichment of 12.7 % which was the same as that of the plate-type heterogeneous samples. The stainless steel powder was added to the mixture of UC and sodium in amounts equivalent to the stainless steel in the tubes of the pellet-type heterogeneous samples (Fig. III-6-16). Tables III-6-IV lists the composition of each sample used.

The reactivities of the samples were measured using the period and the oscillator methods. Samples whose worths were greater than an inhour were measured by the period method relative to void. This was necessary because the total worth of the linear auto-rod used with the oscillator was 1.1 Ih. The reactivity worth of sodium, stainless steel in the form of cans, and the relative worth of two samples such as one homogeneous and one heterogeneous sample having essentially the same material concentrations, or two

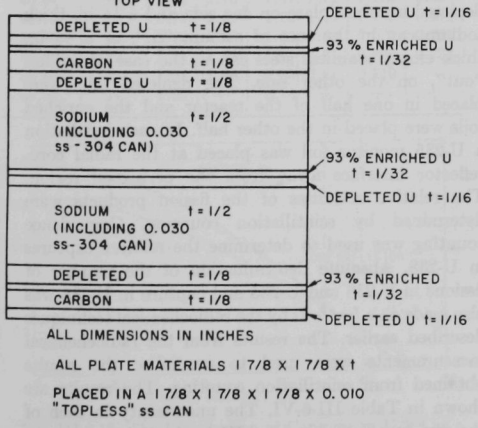


Fig. III-6-15. Heterogeneous Sample Loading Pattern. *ANL Neg. No. 112-9244.*

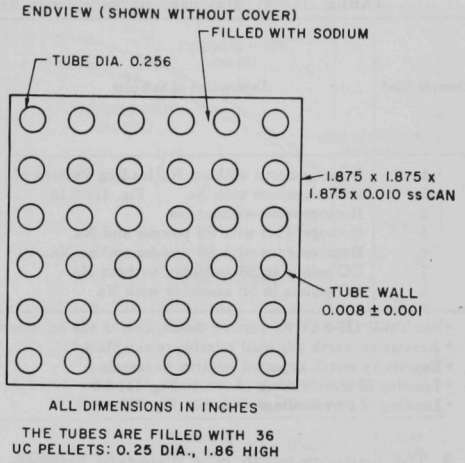


Fig. III-6-16. Pellet Sample Loading Pattern. *ANL Neg. No. 112-9276.*

homogeneous samples one with and one without sodium, were measured by the oscillation technique. All samples were measured at the center of the core.

The samples were measured in two surroundings: (1) the normal loading pattern of Fig. III-6-3 and (2) the bunched loading pattern of Fig. III-6-5. The bunched loading pattern was used in 8 drawers per half around the sample changer oscillator drawer which extended in both halves of the ZPR-6 machine. The bunched pattern was also used in 8 in. (20.32 cm) sections around the sample in the oscillator drawer. The results are given in Table III-6-V.

The values of the reactivity worths of UC/kg listed in the third and fourth columns of Table III-6-V are based on the difference between the total worth of the samples which contained no sodium and the worth of stainless steel. In most cases, minor adjustments in the worth of a sample had to be made because there were minor differences in the proportions of the various materials (Table III-6-IV). The same type of adjustment was applied to the values listed in the fifth and sixth columns.

The following conclusions may be made on the bases of the results shown in Table III-6-V:

1. The effect of changing the surrounding from the normal (Fig. III-6-3) to the bunched (Fig. III-6-5) loading is about 1–2 % of the worth of the sample.
2. The reactivity worth of UC only in a plate-type heterogeneous sample is about 13 % greater than that of an equivalent homogeneous sample.

TABLE III-6-V. MEASURED HETEROGENEITY EFFECTS AT THE CENTER OF THE ASSEMBLY 5 OF ZPR-6

| Sample No.[a] | Description of Samples | Worth of UC[b], Ih/kg | | Worth of (UC + Na + SS)[c] Mix, Ih/kg | |
|---|---|---|---|---|---|
| | | Loading of Surrounding | | Loading of Surrounding | |
| | | Normal[d] | Bunched[e] | Normal | Bunched |
| 1 | Heterogeneous without Na loading Pattern of | 3.436 ± 0.070 | 3.391 ± 0.009 | — | — |
| 2 | Heterogeneous with Na Fig. III-6-15 | — | — | 2.698 ± 0.010 | 2.644 ± 0.008 |
| 3 | Homogeneous without Na | 3.027 ± 0.007 | 2.982 ± 0.007 | — | — |
| 5 | Homogeneous with SS powder and Na | — | — | 2.234 ± 0.006 | 2.221 ± 0.008 |
| 6 | Homogeneous with SS powder and no Na | 2.991 ± 0.011 | 2.932 ± 0.012 | — | — |
| 7 | UC pellets in SS assembly without Na | 2.970 ± 0.009 | — | — | — |
| 8 | UC pellets in SS assembly with Na | — | — | 2.227 ± 0.007 | — |

[a] See Table III-6-IV for further description of the composition of the samples.
[b] Reactivity worth adjusted relative to sample 6.
[c] Reactivity worth adjusted relative to sample 5.
[d] Loading of surroundings shown in Fig. III-6-3.
[e] Loading of surroundings shown in Fig. III-6-5.

3. The reactivity worth of a plate-type heterogeneous sample composed of UC, sodium, and stainless steel is about 20% greater than an equivalent homogeneous-sample.
4. The difference in the reactivity worths of a pellet-type heterogeneous sample and that of an equivalent homogeneous sample is within 1% and may be negligible.

If it is assumed that the effect of the surrounding on the worth of the sample is negligible and the reactivity difference between the plate-type heterogeneous and the homogeneous samples is extrapolated with $J_0^2$ $(2.405r/\tilde{R})$ dependence radially and $\cos^2(\pi h/2\tilde{H})$ axially then the heterogeneity effect on the critical mass of Assembly 5 would be 75 kg of U-235 to be distributed uniformly in the system. The symbol $\tilde{H}$ is the extrapolated half-height of the system.

## SODIUM-VOID EFFECTS

An extensive series of experiments designed to study different aspects of the sodium-void effects were performed on Assembly 5 of ZPR-6. These experiments dealt with the following effects:

1. the effect of sodium removal on the absolute fission rates in U-235 and U-238 and absolute capture rates in U-238,
2. loading pattern effects on and traverses of the sodium-void coefficient,
3. streaming effects on the sodium-void coefficient,
4. the effect of varying the concentration of U-238 on the sodium-void coefficient,
5. the heterogeneity effects on the sodium-void coefficient.

### THE EFFECT OF SODIUM REMOVAL ON FISSION AND CAPTURE RATES

The effects of sodium voiding on the fission densities in U-235 and U-238 and the capture density in U-238 were investigated in Assembly 5. Enriched and depleted uranium foils (93% and 0.2%, respectively) were irradiated in the central drawer of Assembly 5. Two irradiations were performed: one with the sodium "in" and another with the sodium "out" from a central region of 25 cm in radius. The sodium was removed from the entire axial height of the core. The foils were placed at intervals of two inches along the axial length at approximately the mid-section of the central drawer. The materials adjacent to the foils were $\frac{1}{8}$ in. thick depleted uranium plate on one side and a $\frac{1}{2}$ in. thick sodium can in the case of sodium "in", or a $\frac{1}{2}$ in. thick empty stainless steel can in the case of sodium "out", on the other side. The depleted foils were placed in one half of the reactor and the enriched foils were placed in the other half. In each irradiation a U-235 monitor foil was placed at the radial core-reflector interface away from the perturbed region. The relative activities of the fission products were determined by scintillation counting. Coincidence counting was used to determine the relative captures in U-238. Absolute determination of the number of fissions in U-238 and U-235 and capture in U-238 was also made on a few foils by the radiochemical techniques described earlier. The results from the radiochemical measurements were used to normalize the results obtained from scintillation counting. The results are shown in Table III-6-VI. The uncertainty in each of the numbers in Table III-6-VI is about 2%.

The results show: (1) Fissions per gram of U-238

are not affected by the removal of sodium. (2) Captures per unit weight of U-238 decrease by about 15% when the sodium is voided. (3) Fissions in U 235 also decrease by about 12% upon removal of the sodium.

The captures in U-238 and the fissions in U-235 are plotted as a function of the axial distance for the two cases in Figs. III-6-17 and III-6-18. The results shown in Figs. III-6-17 and III-6-18 have been normalized to the values obtained at the center with the sodium "in". It is noted that the reflector saving in the axial direction increases by about 5% when the sodium is removed.

### TRAVERSES OF AND LOADING PATTERN EFFECTS ON THE SODIUM-VOID COEFFICIENT

The sodium-void coefficient was measured as a function of the axial and radial directions in Assembly 5 with the normal loading pattern of Fig. III-6-3. The measurements in the axial direction consisted of determining the reactivity worth of sodium filled cans in sections 4 in. (10.16 cm) long in each half of the reactor relative to empty cans which were the same as the sodium containers. The sodium-void effect was measured in 9 central drawers per half (equivalent outer radius of 9.37 cm). The results are given in Table III-6-VII. The physical location of each section referred to in Table III-6-VII is defined in Fig. III-6-19. The uncertainty in the values listed in Table III-6-VII is about 0.1 Ih. Radial sodium-void coefficient measurements were made by voiding the sodium from the front 8 in. (20.32 cm) of three drawers in each reactor half at five different radial positions. The centers of the drawers were located along a horizontal radius and were 0, 4, 7, 10 and 14 drawer locations from the center of the reactor. The results are given in Table III-6-VIII. Some of the values shown in Table III-6-

TABLE III-6-VI. THE EFFECTS OF SODIUM VOIDING ON THE ABSOLUTE FISSION DENSITIES IN U-238 AND U-235 AND THE CAPTURE DENSITY IN U-238

| $Z$, cm | Foil No. | Absolute Fissions/g U-238 | | Absolute Captures/g U-238 | | Absolute Fissions/g U-235 | |
|---|---|---|---|---|---|---|---|
| | | with Na, $10^9$ | w/o Na, $10^9$ | with Na, $10^{10}$ | w/o Na, $10^{10}$ | with Na, $10^{11}$ | w/o Na, $10^{11}$ |
| 0.00 | 1 | 3.66 | 3.69 | 1.92 | 1.63 | 1.489 | 1.298 |
| 5.08 | 2 | 3.64 | 3.67 | 1.92 | 1.61 | 1.474 | 1.297 |
| 10.16 | 3 | 3.64 | 3.68 | 1.88 | 1.59 | 1.477 | 1.291 |
| 15.24 | 4 | 3.57 | 3.61 | 1.84 | 1.57 | 1.448 | 1.271 |
| 20.32 | 5 | 3.46 | 3.41 | 1.80 | 1.51 | 1.389 | 1.225 |
| 25.40 | 6 | 3.37 | 3.31 | 1.74 | 1.45 | 1.337 | 1.190 |
| 30.48 | 7 | 3.09 | 3.18 | 1.66 | 1.40 | 1.280 | 1.120 |
| 35.56 | 8 | 3.08 | 2.99 | 1.61 | 1.31 | 1.208 | 1.072 |
| 40.64 | 9 | 2.72 | 2.76 | 1.47 | 1.22 | 1.122 | 0.994 |
| 45.72 | 10 | 2.79 | 2.51 | 1.32 | 1.14 | 1.045 | 0.912 |
| 50.80 | 11 | 2.22 | 2.26 | 1.21 | 1.03 | 0.931 | 0.823 |
| 55.88 | 12 | 1.92 | 1.98 | 1.07 | 0.91 | 0.909 | 0.733 |
| 60.96 | 13 | 1.65 | 1.62 | 0.93 | 0.81 | 0.710 | — |
| 66.04 | 14 | 1.29 | — | 0.76 | — | — | — |

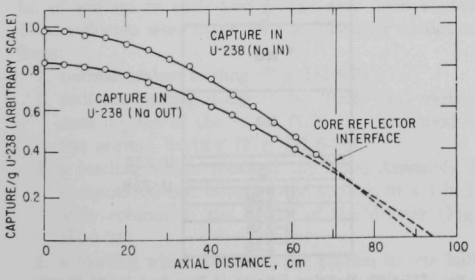


FIG. III-6-17. The Distribution of Captures in U-238 as a Function of the Axial Distance with and without Sodium. *ANL Neg. No. 112-9246.*

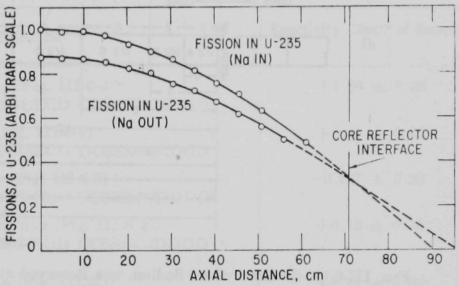


FIG. III-6-18. The Distribution of Fissions in U-235 as a Function of the Axial Distance with and without Sodium. *ANL Neg. No. 112-9247.*

TABLE III-6-VII. SODIUM-VOID COEFFICIENT AS A FUNCTION OF THE AXIAL DIRECTION

| Section Voided[a] | Measured Worth, Ih | Na Weight, kg | Specific Worth[b], Ih/kg |
|---|---|---|---|
| A | 1.02 | 0.886 | 1.15 |
| B | 1.98 | 1.772 | 1.12 |
| C | +1.90 | 1.955 | 0.97 |
| D | +0.85 | 1.955 | 0.44 |
| E | −0.40 | 1.955 | −0.20 |
| F | −2.00 | 1.955 | −1.02 |
| G | −2.64 | 1.955 | −1.35 |
| H | −3.00 | 1.955 | −1.54 |
| B + C | +4.69 | 3.727 | +1.26 |
| B + C + D + E + F + G + H | −3.95 | 13.502 | −0.293 |

[a] See Fig. III-6-19 for explanation of sections.
[b] $1\%\ \Delta k/k$ = 476 Ih.

function of the axial and radial directions in Assembly 5 with the normal loading pattern of Fig. III-6-3. The measurements in the axial direction consisted of determining the reactivity worth of sodium filled cans in sections 4 in. (10.16 cm) long in each half of the reactor relative to empty cans which were the same as the sodium containers. The sodium-void effect was measured in 9 central drawers per half (equivalent outer radius of 9.37 cm). The results are given in Table III-6-VII. The physical location of each section referred to in Table III-6-VII is defined in Fig. III-6-19. The uncertainty in the values listed in Table III-6-VII is about 0.1 Ih. Radial sodium-void coefficient measurements were made by voiding the sodium from the front 8 in. (20.32 cm) of three drawers in each reactor half at five different radial positions. The centers of the drawers were located along a horizontal radius and were 0, 4, 7, 10 and 14 drawer locations from the center of the reactor. The results are given in Table III-6-VIII. Some of the values shown in Table III-6-

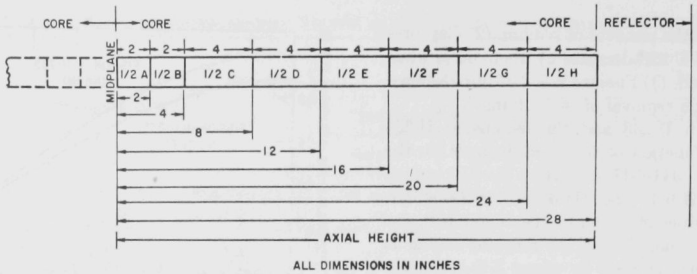


FIG. III-6-19. Sections where Sodium was Removed at Center of Assembly 5 of ZPR-6. *ANL Neg. No. 112-9224.*

TABLE III-6-VIII. SODIUM-VOID COEFFICIENT AS A FUNCTION OF THE RADIAL DIRECTION

| Section Voided (drawers from reactor center) | Na Weight, kg | Specific Worth[a], Ih/kg |
|---|---|---|
| 0 | 1.242 | +1.10 |
| 0 | 1.242 | +1.08 |
| 4 | 2.585 | +0.65 |
| 4 | 2.585 | +0.64 |
| 7 | 2.585 | −0.15 |
| 10 | 2.585 | −0.79 |
| 10 | 2.585 | −0.83 |
| 10 | 2.585 | −0.77 |
| 14 | 2.585 | −0.75 |
| 14 | 2.585 | −0.77 |

[a] 1% $\Delta k/k$ = 476 Ih.

VIII were taken on different days, which may be interpreted as an indication of reproducibility.

The sodium-void coefficient was also measured in the central 18 drawers with the loading patterns shown in Figs. III-6-3, III-6-4, III-6-5 and III-6-20. In each case the sodium was removed from the front 4 in., from the front 8 in., and from the entire axial length (28 in.) in each half of the reactor. The difference between the loading patterns in Figs. III-6-5 and III-6-20 is simply that the bunched U-238 was moved away from the sodium cans by inserting a ⅛ in. plate of graphite between these two materials. The results are given in Table III-6-IX. It may be noted that the difference in the sodium-void coefficient obtained with the loading patterns of Figs. III-6-4 and III-6-5 is mainly due to the decrease in $\sigma_p^{238}$. It is not expected that $\sigma_p$ of the loading pattern in Fig. III-6-4 would be lower than that of the normal loading. It is conceivable however that the streaming effect in the reference case is more prominent than in the normal loading because the sodium cans in all three drawers of the reference case are bunched. The study of the streaming

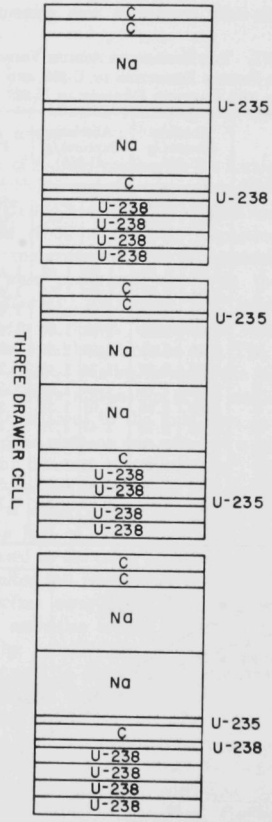


FIG. III-6-20. Position Effects of Bunched U-238 Loading Patterns on Na-Void Coefficient. *ANL Neg. No. 112-9222.*

TABLE III-6-IX. SODIUM-VOID COEFFICIENT DEPENDENCE ON LOADING PATTERN

| Section Voided, kg | Loading Pattern | Reactivity Effect[a] of Sample, Ih |
|---|---|---|
| Front 4 in. (1.772) | Normal Loading (Fig. III-6-3)[b]<br>SdCEDCDSDCD CEDSDSDCECD CDSdCDCEDSD | +1.98 ± 0.20 |
| (1.955) | Ref. Case (Fig. III-6-4)<br>DCSESdDCDCD DCESSDCDECD DCSSEdDCDCD | +1.51 ± 0.10 |
| (1.955) | Bunched Case (Fig. III-6-5)<br>CCSESdDDDDC CCESSDDDEDC CCSSEdDDDDC | −0.017 ± 0.30 |
| (1.955) | Position effect of bunching (Fig. III-6-20)<br>CCSESCdDDDD CCESSCDDEDD CCSSECdDDDD | +0.10 ± 0.30 |
| Front 8 in. (3.727) | Normal Loading (Fig. III-6-3) | +4.11 ± 0.20[c] |
| (3.91) | Ref. Case (Fig. III-6-4) | +2.70 ± 0.24 |
| (3.91) | Bunched Case (Fig. III-6-5) | +0.13 ± 0.20 |
| 28 in. (13.50) | Normal Loading (Fig. III-6-3) | −3.95 ± 0.20 |
| (13.62) | Ref. Case (Fig. III-6-4) | −10.17 ± 0.02 |
| (13.62) | Bunched Case (Fig. III-6-5) | −16.97 ± 0.03 |
| (13.62) | Position effect of bunching (Fig. III-6-20) | −17.11 ± 0.55 |

[a] 1% $\Delta k/k$ = 476 Ih.
[b] Key: $C$ = $\frac{1}{8}$ in. thick graphite.
$S$ = $\frac{1}{2}$ in. thick Na can.
$d$ = $\frac{1}{16}$ in. thick depleted uranium (0.2% enrichment).
$D$ = $\frac{1}{8}$ in. thick depleted uranium (0.2% enrichment).
$E$ = $\frac{1}{16}$ in. thick enriched uranium (93% enrichment).
[c] This number is the sum of two adjacent 4 in. sections.

effect on the sodium-void coefficient discussed below will substantiate this point.

There was no significant effect on the sodium-void coefficient when the loading pattern of Fig. III-6-5 was replaced by that shown in Fig. III-6-20.

A number of other measurements were also made to investigate heterogeneity effects and/or the influence of the relative position of the U-238 plates on sodium-void coefficients. These measurements were performed in the central 18 drawers (9 in each half). In one set of measurements the central 8 in. of sodium in each half of the core were voided, and in another the entire 28 in. of sodium in each half of the core were voided. Measurements were made for the following configurations:

1. normal drawer loading (Fig. III-6-3),
2. uniform loading using $\frac{1}{4}$ in. (0.635 cm) sodium cans instead of the $\frac{1}{2}$ in. (1.27 cm) cans used in the normal loading (Fig. III-6-21),
3. a loading which retained the basic Assembly 5 composition but bunched the sodium in a 1-inch wide column in the center of the drawer (Fig. III-6-22),
4. a loading which bunched the carbon in one half of the drawer and the depleted uranium in the other half. Sodium was then selectively voided from either the carbon region or the depleted uranium region (Fig. III-6-23).

Results of these measurements are listed in Table III-6-X.

Measurements with the configuration IV arrangement, which is the bunched-carbon, bunched-depleted-uranium arrangement, yielded several bits of information. Firstly, the sodium-void coefficient for that sodium bounded by carbon was negative when the central 16 in. (40.64 cm) were voided, as well as when the entire axial height of 56 in. (142.24 cm) was voided. Secondly, the sodium-void coefficient for that sodium bounded by depleted uranium is positive when the entire 56 in. axial height was voided, as well as when the central 16 in. was voided. Thus quite different results were obtained from the two cases. It is interesting to note that the average of the two sodium-void coefficients, i.e. that in the carbon region and that in the depleted uranium region, was $(1.60-0.28)/2$ = +0.61 Ih/kg while the measured value was +0.65 Ih/kg.

### STREAMING EFFECT ON THE SODIUM-VOID COEFFICIENT

The streaming effect on the sodium-void coefficient was investigated in the following manner:

1. The drawers in each half of the matrix, loaded

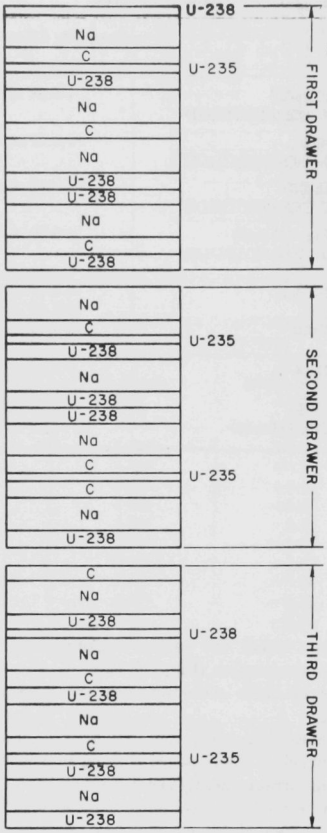


FIG. III-6-21. Uniform Loading with ¼ in. Sodium Cans in Three-drawer Cell. *ANL Neg. No. 112-9274.*

with the unbunched loading pattern of the central drawer of the three-drawer cell (middle drawer shown in Fig. III-6-4) were used. These drawers were at the center of the core and their positions in the matrix were 24-23, 23-23 and 22-23 in both halves of the reactor. Matrix position 23-23 is the center of the core.

2. The reactivity effect on the system due to the rotation of 180° of the materials in these drawers was measured. It is pointed out that the relative positions of the U-235 plates is not affected by the rotation of the materials.
3. The sodium-void coefficients of the front 8 in. section and of the entire columns (28 in.) were measured in the three drawers per half with and without the rotation of 180 deg.
4. The sodium-void coefficients of step No. 3 were measured with the second, fourth and sixth 4 in. sections of the materials in each drawer rotated 180 deg. The objective of this loading pattern shown in Fig. III-6-24, was to reduce by approximately one half the width of the sodium channels which, because of their low density, may be seen as "windows" by the neutrons. The results are shown in Table III-6-XI. It is noted that the sodium-void coefficient of the 28 in. (71.12 cm) columns in the three drawers per half is the same with or without rotation of 180 deg. With partial rotation (Fig. III-6-24), the sodium-void coeffi-

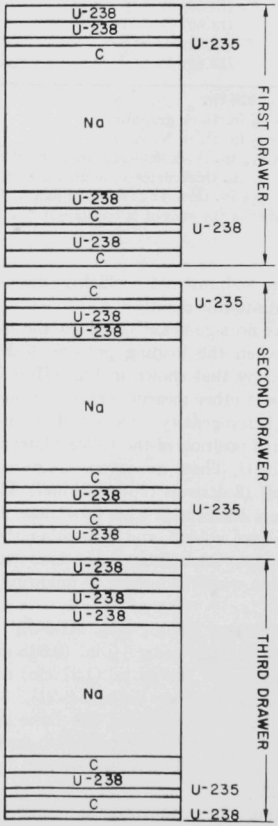


FIG. III-6-22. Bunching of Na in Three-Drawer Cell. *ANL Neg. No. 112-9275.*

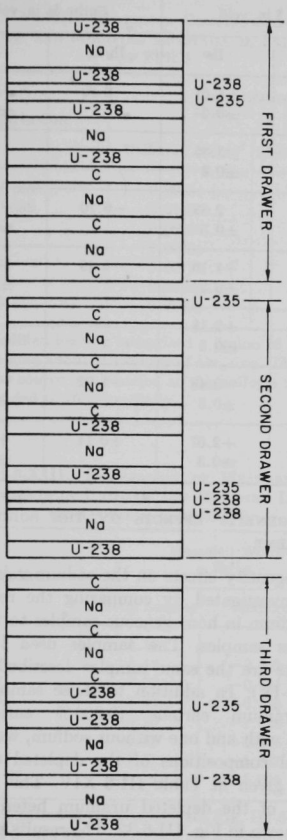


FIG. III-6-23. Loading Pattern to Study Environmental Effects on the Na-Void Coefficient. *ANL Neg. No. 112-9273.*

cient of the same amount of sodium decreased by (0.560 ± 0.116) Ih, or 13%. The coefficients of the 8 in. (120.32 cm) columns were rather small and their associated errors were relatively large, so that no conclusions based on these data can be made about the streaming effect.

The reactivity effect on the system due to the complete rotation of 180 deg of the three drawers per half was (−0.384 ± 0.555) Ih. The same effect with partial rotation was (0.129 ± 0.100) Ih.

### THE EFFECT OF VARYING THE CONCENTRATIONS OF U-238 ON THE SODIUM-VOID COEFFICIENT

The influence of the concentration of U-238 on the sodium-void coefficient in Assembly 5 of ZPR-6 was measured. The normal material concentrations in Assembly 5 were altered for this experiment in the following manner:

1. The atomic concentration of U-238 per unit volume was essentially halved in a region 30 cm in radius and throughout the axial height of the core (142 cm).
2. Cans of sodium, ¼ in. (0.635 cm) thick, were added to fill the empty space that resulted from the removal of depleted uranium plates.
3. The concentration of U-235 was decreased by 25% to counteract the increase in reactivity of the system due to the removal of U-238.

The atomic concentrations of the materials in the uniform and modified loadings of Assembly 5 are shown in Table III-6-XII. The reflector for both loadings was depleted uranium. The radial and axial thicknesses of the reflector were 27 and 30 cm, respectively.

The measurements consisted of determining the reactivity worth of the sodium-filled cans in sections 4 in. (10.16 cm) long in each half of the reactor relative to empty cans which were identical to the sodium containers. The sodium-void effect was measured in 9 central drawers per half (equivalent outer radius of 9.37 cm) as a function of the axial dimension. The results are given in Table III-6-XIII. The physical location of each section was defined in Fig. III-6-19. Uncertainties in the values of the sodium-void coefficient for the uniform loading are typically 0.15 Ih.

Fission rate traverses of U-235 and fission and capture rate traverses of U-238 were measured in both the uniform and modified loadings of Assembly 5. The purpose of these measurements was to determine the degree of power flattening in the modified loading and to make comparisons with calculations. Figure III-6-25 shows the microscopic fission rates of U-235 as a function of radius in the uniform loading. Figure III-6-26 shows the fission rate traverse of U-235 in the modified core loading. The same data shown in Figs. III-6-25 and III-6-26 were multiplied by the atomic concentrations of U-235 as a function of position and the results are shown in Figs. III-6-27 and III-6-28 respectively. These curves are indicative of the power distributions in both cores. It is noted from Fig. III-6-28 that a considerable amount of flattening in the power distribution takes place in the modified core.

Figures III-6-29 and III-6-30 show the microscopic fission rate of U-238 in both the uniform and modified loadings respectively. Figure III-6-31 shows the microscopic capture rates of U-238 in the modified core loading.

TABLE III-6-X. SODIUM-VOID COEFFICIENT IN DIFFERENT ENVIRONMENTS

| Configuration | Comments | Front 8 in. void | | Entire 56 in. void | |
|---|---|---|---|---|---|
| | | Ih/kg | Ih | Ih/kg | Ih |
| I Normal Loading (Fig. III-6-3) | Sodium contiguous to depleted uranium | +1.08 | +4.01 ±0.2 | −0.29 | −3.95 ±0.3 |
| II Uniform loading with ¼ in. Na cans (Fig. III-6-21) | Sodium contiguous to depleted uranium and to carbon | +0.97 | 3.35 ±0.3 | — | — |
| III 1 in. column of sodium loaded in center of drawer (Fig. III-6-12) | Void full 1 in. width | +0.70 | 2.33 ±0.3 | −0.70 | −9.52 ±0.03 |
| | Void two ¼ in. outside columns | +0.65 | +1.10 ±0.3 | −0.49 | −2.90 ±0.30 |
| IV Drawer loadings arranged to bunch carbon on one side of drawer and depleted uranium on the other side of the drawer | All sodium voided in region indicated | +0.65 | +2.18 ±0.3 | — | — |
| | Sodium bounded by carbon voided | −0.23 | −0.48 ±0.3 | −1.02 | −6.01 ±0.3 |
| | Sodium bounded by depleted uranium voided | +1.60 | +2.67 ±0.3 | +0.14 | +0.82 ±0.3 |

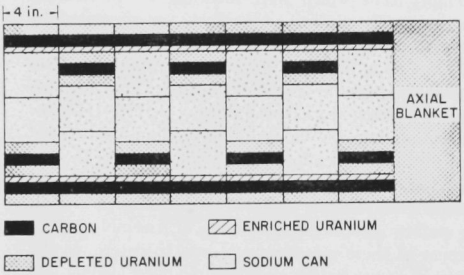


FIG. III-6-24. Rotation of Second, Fourth and Sixth 4 in. Sections of 180 deg. *ANL Neg. No. 112-9245.*

THE HETEROGENEITY EFFECTS ON THE SODIUM-VOID COEFFICIENT

The heterogeneity effects on the sodium-void coefficient were investigated by comparing the reactivity worths of sodium in homogeneous samples to those in heterogeneous samples. The samples used in these measurements are the same samples described earlier, (Table III-6-IV). In addition to those samples, two depleted uranium carbide (0.306% enrichment) samples, one with and one without sodium, were used. The material compositions of the depleted uranium samples are given in Table III-6-XIV. The material arrangement of the depleted uranium heterogeneous samples is shown in Fig. III-6-32. The results are given in Table III-6-XV.

It is seen from the results in Table III-6-XV that the effect of the environment on the sodium-void coefficient is about 70%. It is further seen that the het-

TABLE III-6-XI. STREAMING EFFECT ON SODIUM-VOID COEFFICIENTS

| Section Voided, (kg of Na) | Remarks on Loading Pattern | Reactivity Effect of Sodium Sample, Ih |
|---|---|---|
| Front 8 in., (0.326) | Not rotated | +0.507 ± 0.136 |
| " (0.326) | Rotated 180 deg throughout drawer | +0.415 ± 0.312 |
| " (0.326) | Partial rotation of 180 deg (Fig. III-6-23) | +0.511 ± 0.116 |
| Entire Column, (2.270) (28 in.) | Not rotated | −4.385 ± 0.136 |
| " (2.270) | Rotated 180 deg throughout drawer | −4.232 ± 0.100 |
| " (2.270) | Partial rotation of 180 deg (Fig. III-6-23) | −3.749 ± 0.137 |

TABLE III-6-XII. MATERIAL CONCENTRATIONS IN THE UNIFORM AND MODIFIED LOADINGS OF ASSEMBLY 5 OF ZPR-6

| Material in Core | Concentrations, atoms/cc × $10^{24}$ | |
|---|---|---|
| | Uniform Loading | Modified Loading[a] |
| U-235 | 0.00154 | 0.00115 |
| U-238 | 0.01056 | 0.00615 |
| Na | 0.00920 | 0.01120 |
| Fe | 0.00904 | 0.00992 |
| Ni | 0.00113 | 0.00125 |
| Cr | 0.002386 | 0.00264 |
| C | 0.01293 | 0.01293 |

[a] The modified loading comprised a region 30 cm in radius and 142 cm long about the center of the core. The rest of the core had the source composition as the uniform loading. This region extended to 76 cm radially.

TABLE III-6-XIII. COMPARISON OF MEASURED NA-VOID COEFFICIENTS IN UNIFORM AND MODIFIED LOADINGS OF ASSEMBLY 5 OF ZPR-6

| Section Voided[a] | Measured Worth[b], Ih/kg | |
|---|---|---|
| | Uniform Loading | Modified Loading |
| A | 1.15 | — |
| B | 1.12 | −0.221 ± 0.070 |
| C | 0.97 | −0.281 ± 0.044 |
| D | 0.44 | −0.585 ± 0.127 |
| E | −0.20 | −1.029 ± 0.127 |
| F | −1.02 | −1.254 ± 0.024 |
| H | −1.54 | −1.967 ± 0.054 |
| B → H | −0.293 | −1.195 ± 0.008 |

[a] For the position of each section see Fig. III-6-19.
[b] 1% $\Delta k/k$ = 476 Ih.

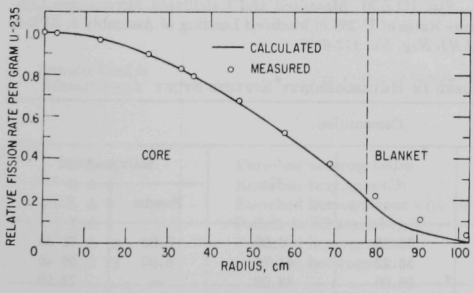


FIG. III-6-25. Measured and Calculated Microscopic Fission Rates of U-235 in Uniform Loading of Assembly 5 of ZPR-6. *ANL Neg. No. 112-9229.*

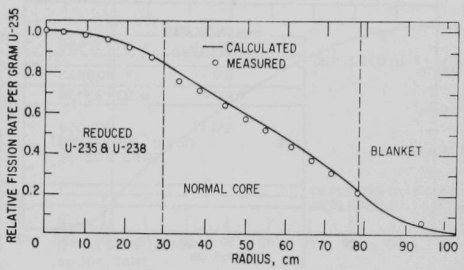


FIG. III-6-26. Measured and Calculated Microscopic Fission Rates of U-235 in Modified Loading of Assembly 5, ZPR-6. *ANL Neg. No. 112-9243.*

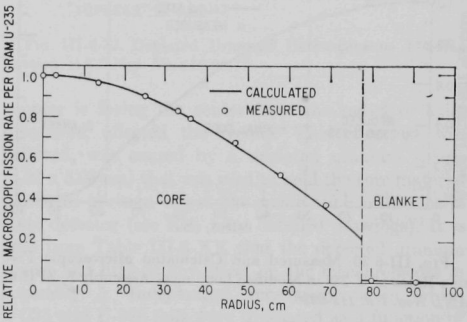


FIG. III-6-27. Measured and Calculated Macroscopic Fission Rates of U-235 in Uniform Loading of Assembly 5 of ZPR-6. *ANL Neg. No. 112-9228.*

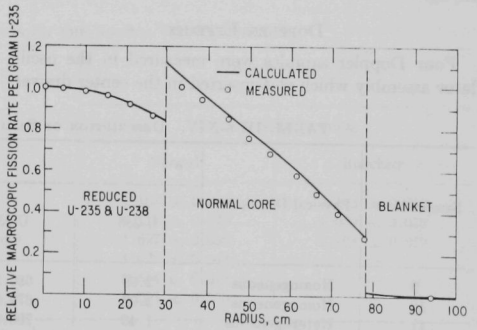


FIG. III-6-28. Measured and Calculated Macroscopic Fission Rates of U-235 in Modified Loading of Assembly 5, ZPR-6, *ANL Neg. No. 112-9227.*

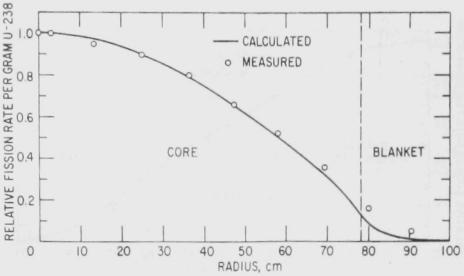


FIG. III-6-29. Measured and Calculated Microscopic Fission Rates of U-238 in Uniform Loading of Assembly 5, ZPR-6. *ANL Neg. No. 112-9225.*

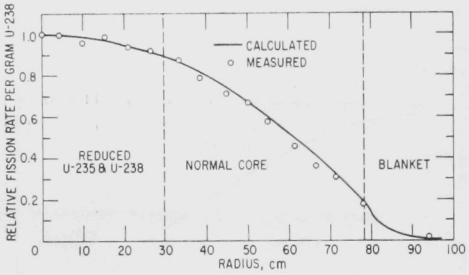


FIG. III-6-30. Measured and Calculated Microscopic Fission Rates of U-238 in Modified Loading of Assembly 5, ZPR-6. *ANL Neg. No. 112-9230.*

erogeneity effect within the sample is also about 70%.

The reactivity worth of the sodium in Sample 8 was measured without the UC pellets in the assembly. The reactivity worth of the sodium was (0.653 ± 0.0378) Ih/kg.

### Doppler Effects

Four Doppler samples were measured in the oscillator assembly which was inserted in the center drawer of Assembly 5. These were a natural $UO_2$ sample, two enriched $UO_2$ samples, and a $PuO_2$ sample. The data obtained are listed in Table III-6-XVI.

Two different sample types, distinguished by their expansion characteristics, were used in the measurements. In the freely expanding sample type (FE), the 1 in. diam x 12 in. long sample column was allowed to expand freely as the sample was heated. In the other sample type (NNE) the sample column was constrained both axially and radially to about 500°K and then was axially constrained above this temperature. In the fissile samples, where the expansion reactivity effect is significant in comparison with the Doppler effect, the two sample types gave different reactivity-temperature profiles which may be used to separate the expansion and Doppler effects.

The primary purpose of the U-238 and U-235 Doppler measurements was to provide reference measurements for comparison with similar zoned core measurements. The plutonium result was the first attempt to make this measurement with controlled thermal expansion. The plutonium results have not been confirmed by repeated measurements so that they should be regarded as tentative.

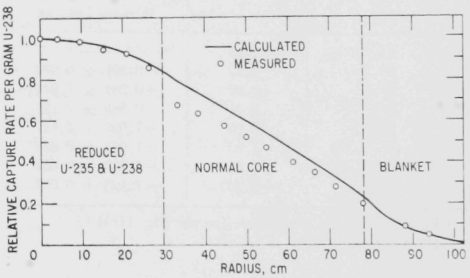


FIG. III-6-31. Measured and Calculated Microscopic Capture Rates of U-238 in Modified Loading of Assembly 5, ZPR-6. *ANL Neg. No. 112-9226.*

TABLE III-6-XIV. DESCRIPTION OF SAMPLES USED IN HETEROGENEITY EFFECTS STUDY

| Sample No.[a] | Physical Description | Composition | | | | | |
|---|---|---|---|---|---|---|---|
| | | U-235 | U-238 | C | Na | Stainless Steel | |
| | | | | | | Powder | Can |
| 9 | Homogeneous | 2.09 | 680.24 | 36.25 | 0.00 | 0.00 | 71.58 |
| 10 | Homogeneous | 2.08 | 679.69 | 36.22 | 47.74 | 0.00 | 69.40 |
| 11 | Heterogeneous | 1.40 | 700.02 | 25.00 | 48.00 | — | 73.25 |
| 12 | Heterogeneous | 1.40 | 700.02 | 25.00 | 0.000 | — | 73.25 |

[a] These samples were 1.875 x 1.875 x 1.875 in.

### Central-Worth Measurements

The reactivity worths of a large number of samples were measured at the center of Assembly 5 by the technique described in Ref. 1. The worths of these samples were measured relative to void. The results are given in Table III-6-XVII.

Some of the samples listed in Table III-6-XVIII were also measured at 16.5 cm radially from the center. The results are given in Table III-6-XVIII.

The worths of U-235, U-238, and Pu as a function of sample size is given in Table III-6-XIX. It is seen from Table III-6-XIX that the worth of U-235 as a function of thickness is essentially constant up to a thickness of $^{3}/_{32}$ in. (0.237 cm). The worth of U-235 in $^{1}/_{4}$ in. (0.635 cm) thick plate (288.03 g) is slightly higher than the others. The worth of U-238 decreased as the thickness of the sample increased. This is of course, the effect of self-shielding.

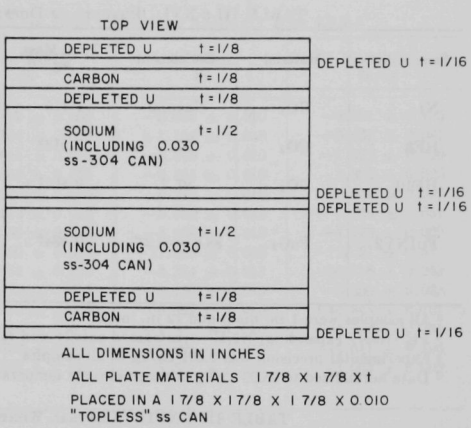


Fig. III-6-32. Depleted Uranium Heterogeneous Loading Pattern. *ANL Neg. No. 112-9241.*

### Neutron Spectrum, Fission Ratios, and Fission Rates

The neutron spectrum was measured by the proton recoil technique at the center of Assembly 5 with the sodium in the core and again when the sodium was removed from a region about 20 cm in radius. The results and conclusions are reported in Papers III-9 and III-10.

Fission ratios of U-234, U-238 and Pu-239 to U-235 were measured at the center of Assembly 5 by the technique described by Karam et al.[1] The results are shown in Table III-6-XX. Included in Table III-6-XX are fission ratios measured in Assembly 4Z of ZPR-6[(1)] and Assembly 11 of ZPR-9 (see Paper III-8). The fission ratio measurements conducted on Assembly 4Z showed that the orientation of the solid state counter with respect to the center of the core, i.e. whether the counter is facing the center from the radial or axial directions, affected the results. This effect, it was believed, was caused by a depleted uranium spacer (1.27 x 5.08 cm) that was used to hold the core material plates in position about the guide tube of the solid state detector (see Ref. 1 for detailed drawings). It is seen from Table III-6-XX that the depleted uranium spacer had little if any effect on the measurements in Assembly 5. Independent measurements in which U-235 and U-238 foils were irradiated as a function of position in the axial direction (the foils were placed between the $^{1}/_{8}$ in. U-238 plate and one of the two adjacent sodium cans shown in Fig. III-6-3) and in which the absolute number of fissions in the foils were determined by the radio-chemical technique, gave a

TABLE III-6-XV. Heterogeneity Effects on the Sodium-Void Coefficient

| Samples Used in Measurement | Description of Sample[a] | Worth of Na[b], Ih/kg | |
|---|---|---|---|
| | | Loading of Surrounding | |
| | | Normal[c] | Bunched[d] |
| 1 & 2 | Enriched heterogeneous | 1.108 ± 0.046 | 1.148 ± 0.052 |
| 3 & 4 | Enriched homogeneous | 1.717 ± 0.070 | 1.059 ± 0.079 |
| 5 & 6 | Enriched homogeneous with SS Powder | 1.697 ± 0.038 | 1.168 ± 0.059 |
| 7 & 8 | Pellets in SS assembly | 1.026 ± 0.043 | — |
| 9 & 10 | Depleted homogeneous | 2.514 ± 0.073 | — |
| 11 & 12 | Depleted heterogeneous | 1.283 ± 0.050 | — |

[a] See Tables III-6-IV and III-6-XIV for further description of samples.
[b] 1% $\Delta k/k$ = 476 Ih.
[c] Loading of surrounding is shown in Fig. III-6-3.
[d] Loading of surrounding is shown in Fig. III-6-5.

TABLE III-6-XVI. RESULTS OF DOPPLER MEASUREMENTS IN ASSEMBLY 5 OF ZPR-6

| Sample No.[a] | Material | Enrichment | Total Mass, kg | Sample Type[b] | Measured Reactivity Change versus Temperature[c,d], Ih/kg-U or Pu(°K) |
|---|---|---|---|---|---|
| N1 | $UO_2$ | Natural | 1.116 | FE | 0.000(293), −0.109(492), −0.184(687), +0.001(293), −0.241(878), −0.291(1061) |
| HE8 | $UO_2$ | 97.7 | 0.9133 | FE | 0.000(293), +0.021(428), +0.039(612), +0.048(839), +0.049(1058) |
| HE10 | $UO_2$ | 97.7 | 0.8071 | NNE | 0.000(293), +0.010(339), +0.014(370), +0.020(395), +0.025(428), +0.029(469) +0.035(486), +0.040(578), +0.053(774), +0.060(958) |
| PuINV2 | $PuO_2$ | 88.6 w/o 239 | 0.9347 | NNE | 0.000(311), −0.016(353), −0.021(398), −0.030(426), −0.028(457), −0.034(483) −0.039(522), −0.050(595), −0.066(717), −0.086(857) |

[a] All samples were 1 in. diam and 12 in. long.
[b] FE—freely expanding; NNE—constrained axially and radially.
[c] Experimental precision was 0.001 Ih/kg in all samples.
[d] Data normalized to 0.000 Ih/kg at nominal room temperature and uncorrected for expansion.

TABLE III-6-XVII. CENTRAL WORTH MEASUREMENTS IN ASSEMBLY 5 OF ZPR-6

| Sample | Sample Wt., g | Can Wt., g | Gross Worth, Ih | Net Worth, Ih | Worth, Ih/kg |
|---|---|---|---|---|---|
| Be | 114.308 | Bare | +1.143 ± 0.048 | +1.143 ± 0.048 | +9.956 ± 0.420 |
| C | 103.0 | Bare | +0.183 ± 0.022 | +0.183 ± 0.022 | +1.777 ± 0.214 |
| Ni | 546.0 | Bare | −1.134 ± 0.015 | −1.134 ± 0.015 | −2.077 ± 0.027 |
| V | 183.67 | 55.30 (SS) | −0.246 ± 0.010 | −0.136 ± 0.014 | −0.740 ± 0.076 |
| Li | 28.30 | 57.03 (SS) | −0.790 ± 0.010 | −0.677 ± 0.015 | −23.922 ± 0.530 |
| Zr | 406.0 | Bare | −0.671 ± 0.020 | −0.671 ± 0.020 | −1.652 ± 0.049 |
| Mo | 599.0 | Bare | −3.416 ± 0.015 | −3.416 ± 0.015 | −5.703 ± 0.025 |
| Al | 166.90 | Bare | −0.300 ± 0.017 | −0.300 ± 0.017 | −1.797 ± 0.102 |
| B-10 | 29.29 | 55.73 (SS) | −23.298 ± 0.030 | −23.196 ± 0.033 | −791.94 ± 1.13 |
| $B_4C$ | 59.62 | 64.70 (SS) | −6.258 ± 0.010 | −6.137 ± 0.015 | −102.94 ± 0.252 |
| POLY | 58.98 | Bare | +19.122 ± 0.010 | +19.122 ± 0.010 | +324.21 ± 0.170 |
| Nb | 481.2 | 30.10 (SS) | −3.888 ± 0.010 | −3.837 ± 0.015 | −7.974 ± 0.031 |
| W | 1108.2 | Bare | −5.792 ± 0.020 | −5.792 ± 0.020 | −5.227 ± 0.018 |
| Ta | 924.70 | 27.54 (SS) | −11.955 ± 0.010 | −11.909 ± 0.015 | −12.879 ± 0.016 |
| Na | 51.38 | 56.42 (SS) | −0.144 ± 0.008 | −0.041 ± 0.010 | −0.799 ± 0.195 |
| SS-304 | 499.6 | Bare | −0.851 ± 0.020 | −0.851 ± 0.020 | −1.703 ± 0.040 |
| Fe | 488.0 | Bare | −0.737 ± 0.005 | −0.737 ± 0.005 | −1.510 ± 0.010 |
| $Fe_2O_3$ | 296.4 | Bare | −0.356 ± 0.010 | −0.356 ± 0.010 | −1.201 ± 0.034 |
| Re | 1266.9 | Bare | −20.977 ± 0.020 | −20.977 ± 0.020 | −16.558 ± 0.016 |
| ZrH | 93.7 | 20.30 (Al) | +3.700 ± 0.010 | +3.736 ± 0.012 | +39.872 ± 0.128 |
| Cr | 220.73 | 56.30 (SS) | −0.440 ± 0.020 | −0.339 ± 0.022 | −1.536 ± 0.100 |
| Ti | 90.42 | 56.88 (SS) | −0.117 ± 0.020 | −0.016 ± 0.022 | −0.177 ± 0.243 |
| Hf | 806.0 | Bare | −9.079 ± 0.020 | −9.079 ± 0.020 | −11.264 ± 0.025 |
| Eu | 100.92 | Bare | −7.249 ± 0.200 | −7.249 ± 0.200 | −71.829 ± 1.982 |
| U-233 | 146.708<br>97.15% U-233 | 5.286 (Al)<br>19.977 (SS) | +12.188 ± 0.200 | +12.217 ± 0.200 | +83.274 ± 1.370 |
| Pu | 122.67<br>4.50% Pu-240<br>95.50% Pu-239 | 7.093 (Al)<br>20.06 (SS) | +8.539 ± 0.200 | +8.575 ± 0.200 | +69.899 ± 1.630 |

U-238 to U-235 fission ratio of 0.0246 with an uncertainty of 5%. This ratio was constant as a function of the axial distance from 50 cm to the center of the core. The results from the radio-chemical technique are in agreement with the measurements made in Assembly 5 and the radial measurements made in Assemblies 4Z and 11. The axial measurements in Assembly 4Z appear to be erroneous for unknown reasons.

Fission rate traverses with U-235 and U-238 foils were measured in both the radial and axial directions. The radial fission rate traverses are shown in Figs. III-6-33 and III-6-34. The calculated rates are also shown for comparison. The calculations were done with

TABLE III-6-XVIII. WORTH MEASUREMENTS AT 16.5 cm FROM CENTER OF ASSEMBLY 5 OF ZPR-6

| Sample | Sample Wt., g | Can Wt., g | Gross Worth, Ih | Net Worth, Ih | Worth/kg, Ih/kg |
|---|---|---|---|---|---|
| Na | 51.38 | 56.42 (SS) | −0.127 ± 0.008 | −0.035 ± 0.010 | −0.681 ± 0.195 |
| Be | 114.308 | Bare | +1.104 ± 0.010 | +1.104 ± 0.010 | +9.658 ± 0.087 |
| Fe | 488.0 | Bare | −0.645 ± 0.010 | −0.645 ± 0.010 | −1.322 ± 0.020 |
| Zr | 406.0 | Bare | −0.565 ± 0.010 | −0.565 ± 0.010 | −1.392 ± 0.025 |
| C | 103.0 | Bare | +0.212 ± 0.010 | +0.212 ± 0.010 | +2.058 ± 0.097 |
| Nb | 481.2 | 30.10 (SS) | −3.512 ± 0.012 | −3.482 ± 0.015 | −7.236 ± 0.031 |
| W | 1108.0 | Bare | −5.289 ± 0.010 | −5.289 ± 0.010 | −4.773 ± 0.009 |
| B-10 | 29.29 | 55.73 (SS) | −21.390 ± 0.010 | −21.300 ± 0.015 | −727.21 ± 0.51 |
| $B_4C$ | 59.62 | 64.70 (SS) | −5.464 ± 0.010 | −5.374 ± 0.015 | −90.138 ± 0.252 |
| Mo | 59.90 | Bare | −3.120 ± 0.015 | −3.120 ± 0.015 | −5.209 ± 0.025 |
| Enriched U 93.1% U-235 | 13.869 | 48.968 (SS) | +0.530 ± 0.005 | +0.622 ± 0.010 | +44.848 ± 0.721 |
| | 27.719 | 47.30 (SS) | +1.098 ± 0.005 | +1.200 ± 0.010 | +43.291 ± 0.361 |
| | 64.183 | 47.30 (SS) | +2.699 ± 0.005 | +2.801 ± 0.010 | +43.641 ± 0.156 |
| Depleted U 0.2% U-235 | 1153.6 | Bare | −3.533 ± 0.010 | −3.533 ± 0.010 | −3.063 ± 0.009 |

TABLE III-6-XIX. WORTH OF U-235, U-238 AND PU AS FUNCTION OF THICKNESS AT CORE CENTER

| Material | Material Size, in. | No. in Sample | Total Material, g | Sample[a], g | Gross Worth[b], Ih | Net Worth, Ih | Material Worth, Ih/kg | Isotopic[c] Worth, Ih/kg |
|---|---|---|---|---|---|---|---|---|
| U-235 (93.1% enrichment) | 2 x 2 x 0.005 | 1 | 4.511 | 20.907 | 0.2067 ± 0.0021 | 0.2067 ± 0.0021 | 45.821 ± 0.466 | 49.571 ± 0.500 |
| | 2 x 2 x 0.005 | 3 | 13.894 | 30.200 | 0.6546 ± 0.0023 | 0.6546 ± 0.0023 | 47.114 ± 0.166 | 50.877 ± 0.180 |
| | 2 x 2 x 0.005 | 9 | 41.443 | 57.852 | 1.886 ± 0.0030 | 1.924 ± 0.0037 | 46.425 ± 0.098 | 50.127 ± 0.096 |
| | 2 x 2 x 0.005 | 14 | 64.184 | 111.483 | 2.951 ± 0.010 | 3.058 ± 0.012 | 47.598 ± 0.187 | 51.393 ± 0.201 |
| | 2 x 2 x 0.005 | 23 | 105.711 | 105.711 | 4.943 ± 0.010 | 4.943 ± 0.010 | 46.760 ± 0.095 | 50.484 ± 0.102 |
| | 2 x 2 x 1/8 | 2 | 288.03 | 288.03 | 14.595 ± 0.100 | 14.595 ± 0.100 | 50.672 ± 0.347 | 54.686 ± 0.373 |
| U-238 (0.2% enrichment) | 2 x 2 x 0.005 | 1 | 5.356 | 21.810 | −0.0258 ± 0.0019 | −0.0258 ± 0.0019 | −4.817 ± 0.355 | −4.827 ± 0.0019 |
| | 2 x 2 x 0.005 | 3 | 15.949 | 32.255 | −0.0602 ± 0.0022 | −0.0602 ± 0.0022 | −3.774 ± 0.138 | −3.876 ± 0.138 |
| | 2 x 2 x 0.005 | 12 | 64.086 | 80.482 | −0.2349 ± 0.0021 | −0.2349 ± 0.0021 | −3.622 ± 0.033 | −3.774 ± 0.033 |
| | 2 x 2 x 1/8 | 1 | 140.643 | 140.643 | −0.505 ± 0.004 | −0.505 ± 0.004 | −3.501 ± 0.028 | −3.698 ± 0.028 |
| | 2 x 2 x 1 | 1 | 1153.6 | 1153.6 | −3.869 ± 0.010 | −3.869 ± 0.010 | −3.353 ± 0.009 | −3.461 ± 0.009 |
| Pu 72.2 w/o 239 | 1.83 x 1.68 x 0.05 | 1 | 36.40 | 55.486 | 2.066 ± 0.0116 | 2.102 ± 0.0117 | 57.755 ± 0.321 | |
| Pu 22.3 w/o 240 | 1.83 x 1.83 x 0.08 | 1 | 57.57 | 58.276 | 3.340 ± 0.0095 | 3.376 ± 0.0096 | 58.643 ± 0.167 | |

[a] Foils in 2 x 2 x 1/8 in. SS cans.

[b] Some measurements were made relative to a SS can; thus the net worth is measured directly.

[c] For ENR U samples, this column is Ih/kg U-235 using a U-238 worth/kg commensurate with the U-238 weight in the sample. For DEP U samples, this column is Ih/kg U-238 using a constant U-235 worth/kg of +50.0.

TABLE III-6-XX. CENTRAL FISSION RATIOS MEASURED IN ZPR-6 AND -9 ASSEMBLIES

| Fission Ratio | ZPR-6 Assembly 5 | | | ZPR-9 Assembly 11 | ZPR-6 Assembly 4Z | |
|---|---|---|---|---|---|---|
| | Radial (No Spacer)[a] | Axial | Radial (Spacer)[a] | Radial (No Spacer)[a] | Radial (Spacer)[a] | Axial |
| U-238/U-235 | 0.0238 ± 0.0008 | 0.0223 ± 0.0009 | 0.0234 ± 0.0007 | 0.0238 ± 0.0007 | 0.0238 ± 0.0007 | 0.0267 ± 0.0008 |
| U-234/U-235 | 0.166 ± 0.004 | 0.159 ± 0.005 | 0.163 ± 0.004 | 0.175 ± 0.004 | 0.172 ± 0.004 | 0.203 ± 0.005 |
| Pu-239/U-235 | 0.968 ± 0.025 | 0.949 ± 0.025 | 0.963 ± 0.024 | 0.986 ± 0.026 | 0.967 ± 0.025 | 0.949 ± 0.025 |

[a] Spacer consists of 1/2-in.-thick U-238 plate located in front drawers only when radial traverse measurements were made.

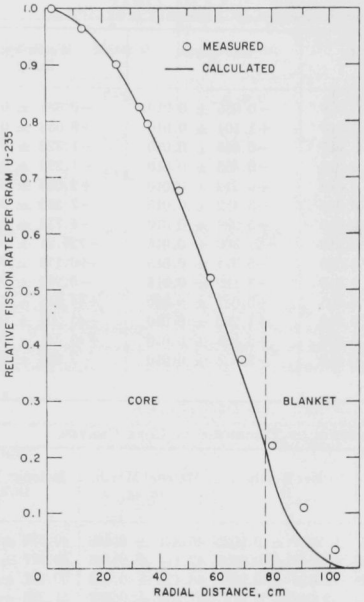


FIG. III-6-33. Fission Rates of U-235 as a Function of Radius, Assembly 5 of ZPR-6. *ANL Neg. No. 112-9231.*

Cross Section Set ZPR-6-5 which was generated for Assembly 5 by the MC² Code.[9] In these calculations the value of $\sigma_p^{238}$ used in the core and reflector were 35 and 15 b respectively. The value of $\sigma_p^{235}$ used was 78 b. The axial fission rate traverses are given in the section on sodium-void effects.

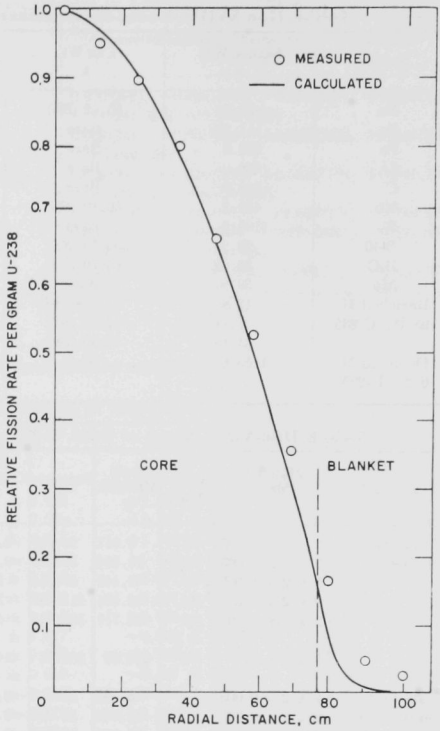


FIG. III-6-34. Fission Rates of U-235 as a Function of Radius, Assembly 5 of ZPR-6. *ANL Neg. No. 112-9239.*

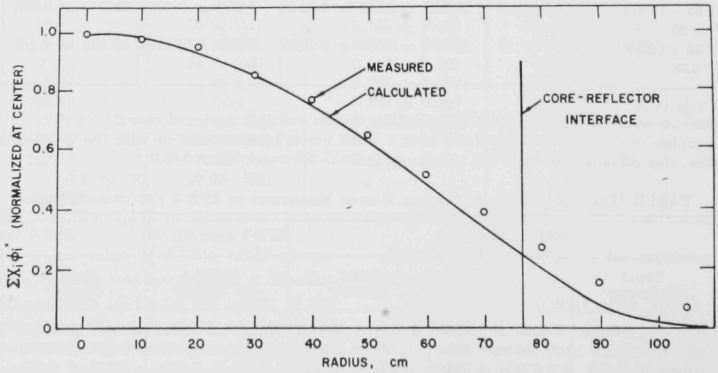


FIG. III-6-35. Importance of Fission Neutrons as a Function of Radius in Assembly 5 of ZPR-6. *ANL Neg. No. 112-9039 T-1.*

### Spatial Distribution of the Importance of Fission Neutrons and the Normalization Integral of the Perturbation Expression

The spatial distribution of the importance of fission neutrons as a function of the radial position was measured in Assembly 5 with the Cf-252 source technique described by Karam et al.[1] The results are shown in Fig. III-6-35 together with the calculated distribution which was obtained with the MACH 1 Code and ZPR-6-5 Cross Section Set (Table III-6-II).

The normalization integral of the perturbation expression was also measured in Assembly 5 by the Cf-252 source technique.[1] The measured normalization integral when the quantities $\sum_i \chi_i \phi_i^*$ and $\sum_i (\nu\Sigma_f)_i \phi_i$ are normalized to unity at the center of the reactor, was $6.645 \times 10^5$. The uncertainty in this measurement is about 5%.

#### References


1. R. A. Karam, A. Ancarani, F. Helm, W. Y. Kato, G. W. Main and G. K. Rusch, *Experimental Verification of Reactor Physics Parameters of Zoned Cores*, Proc. International Conference on Fast Critical Experiments and Their Analysis, ANL-7320 (1966).
2. R. A. Karam and L. G. LeSage, *Zoned-Core Concepts*, Trans. Am. Nucl. Soc. **10**, 270 (1967).
3. W. Y. Kato, G. J. Fischer and L. R. Dates, *Safety Analysis Report, Argonne Fast Critical Facility (ZPR-6)*, ANL-6271 (1963).
4. R. A. Karam, A. Ancarani, F. Helm, W. Y. Kato, G. W. Main and G. K. Rusch, *Measured Physics Parameters in a Zoned Fast Uranium Carbide Core, Assembly 4Z*, ANL-7281 (1966).
5. D. A. Meneley, L. C. Kvitek and D. M. O'Shea, *MACH 1, A One-Dimensional Diffusion-Theory Package*, ANL-7223 (1966).
6. D. M. O'Shea, H. H. Hummel, W. B. Lowenstein and D. Okrent, *Twenty-six Group Cross Sections*, Trans. Am. Nucl. Soc. **7**, 242 (1964).
7. A. L. Rago and H. H. Hummel, *Elmoe, An IBM-704 Program Treating Elastic Scattering Resonances in Fast Reactors*. ANL-6805 (1964).
8. B. J. Toppel, A. L. Rago and D. M. O'Shea, *MC²—A Code to Calculate Multi-group Cross Sections*. ANL-7318 (1967).
9. R. A. Lewis, Argonne National Laboratory (private communication).
10. D. Meneghetti, Argonne National Laboratory (private communication).
11. Reactor Physics Constants, ANL-5800, Second Edition, (1963) pp. 277–281.
12. D. Meneley, Argonne National Laboratory (private communication).
13. D. Meneghetti, *Calculational Studies of Sodium-Void-Reactivity Variations Due to Their Slab Heterogeneities on Fast Critical Asemblies*, Proc. International Conference on Fast Critical Experiments and Their Analysis, ANL-7320 (1966).


## III-7. Note on Worth Ratios in Zoned Versus Full Size Critical Assemblies

D. A. Meneley

Several authors (for example, Refs. 1, 2, 3) have compared the ratio of material worths in zoned and full-size critical assemblies by comparison of normalization integrals or perturbation denominators in the two assemblies. However, as is shown below, a rather different factor from the perturbation denominator must be used to maintain consistency. Define

$$W_i = \frac{PN_i}{PD_i} \tag{1}$$

as the first-order perturbation worth in assembly $i$, in $\delta k/k$ units. $PN$ denotes the usual perturbation numerator and $PD$ the denominator. The computed worth ratio in two assemblies $i$ and $j$ is given by

$$\frac{W_i}{W_j} = \frac{PN_i}{PN_j} \cdot \frac{PD_j}{PD_i}. \tag{2}$$

By appropriate flux normalization the first ratio on the right may be set equal to 1.0.

The measurements are reported in inhour units (which are almost independent of delayed parameters). The number of inhours per unit $\delta k/k$ is given by

$$\left(\frac{1}{\rho_{1h_i}}\right) = \left(\frac{\Lambda_i}{3600} + \sum_f \frac{\beta_{f,i}}{1 + 3600\,\lambda_f}\right)^{-1}, \tag{3}$$

where $\rho_{1h}$ is the reactivity corresponding to one inhour, $\Lambda$ is the prompt generation time and $\beta_f$ and $\lambda_f$ are, respectively, the effective delayed fraction and decay constant for delayed family $f$.

Recalling the definition of $\beta_{f,i}$:

$$\beta_{f,i} = \frac{\int \left[\sum_g \chi_{f,g}\phi_g^*(\mathbf{r})\right]\left\{\sum_g \left[\sum_m \beta_{f,m}\nu\Sigma_{f,m,g}(\mathbf{r})\right]\phi_g(\mathbf{r})\right\} d\mathbf{r}}{PD_i} \equiv \frac{DN_{f,i}}{PD_i}, \tag{4}$$

where the $g$ summations are taken over the neutron energy groups, $\chi_{f,g}$ is the delayed neutron emission spectrum for family $f$, $\phi_g^*(\mathbf{r})$ and $\phi_g(\mathbf{r})$ are respectively the adjoint and real fluxes in group $g$ at position $\mathbf{r}$, the $m$ summation extends over all fissionable materials at $\mathbf{r}$, and $\beta_{f,m}\nu\Sigma_{f,m,g}$ is the yield of delayed neutrons per fission in material $m$, in energy group $g$.
Also,

$$\Lambda = \frac{\int \phi_g^*(\mathbf{r}) \left(\frac{1}{v}\right)_g \phi_g(\mathbf{r})\, \mathbf{dr}}{PD_i} \equiv \frac{LN_i}{PD_i}. \tag{5}$$

We can now write

$$\left(\frac{1}{\rho_{\text{Th}}}\right)_i = PD_i \left(\frac{LN_i}{3600} + \sum_f \frac{DN_{f,i}}{1 + 3600\,\lambda_f}\right)^{-1}. \tag{6}$$

Rewriting the computed worth ratio from Eq. (2) in inhour units after normalization to eliminate the first factor, we find

$$\frac{W_i}{W_j} = \left(\frac{LN_j}{3600} + \sum_f \frac{DN_{f,j}}{1 + 3600\,\lambda_f}\right) \Bigg/ \left(\frac{LN_i}{3600} + \sum_f \frac{DN_{f,i}}{1 + 3600\,\lambda_f}\right). \tag{7}$$

The summation term is dominant in fast systems due to the high neutron velocities, so that the value of the ratio depends mainly on the $DN_f$ terms.

Due to the variation of delayed yields in the different regions of the zoned and full size cores, the integrands of the $DN_f$ terms may have quite different spatial distributions than that of the perturbation denominator. Also, any uncertainty in relative delayed neutron yields between different fissioning isotopes in the two cores is directly reflected in uncertainty of the computed worth ratio.

### References


1. G. J. Fischer and A. Travelli, *Studies of Analytical Problems in Interpretation of Zone-Loading Experiments, and Basic Considerations in Zone-Loaded Core Design*, Proc. International Conference on Fast Critical Experiments and Their Analysis, October 10–13, 1966, ANL-7320, pp. 421–428.
2. A. Travelli and G. Fischer, *Analysis of the Uncertainties in the Interpretation of Zone Loaded Experiments*, Reactor Physics Division Annual Report, July 1, 1965 to June 30, 1966, ANL-7210, pp. 154–159.
3. R. A. Karam and L. G. LeSage, *Zoned Core Concepts*, Trans. Am. Nucl. Soc. **10**, 270 (1967).


## III-8. ZPR-9 Assemblies 11 and 12—Two Small Zoned Versions of the 2600-Liter Assembly 5 ZPR-6

R. A. Lewis, L. G. LeSage and R. A. Karam

### General Description, Assemblies 11 and 12 of ZPR-9

A series of three progressively smaller zoned assemblies have been built, each of which uses the same central core composition as the reference, full-size, Assembly 5 of ZPR-6 (see Paper III-6). Assembly 5 was a large dilute uranium-carbide fast power reactor mockup. In order of decreasing size, the zoned assemblies were ZPR-6 Assembly 4Z,[1] ZPR-9 Assembly 12 and ZPR-9 Assembly 11.

The purpose of the series of zoned cores was to test the effectiveness of these assemblies in reproducing the central core spectra of the comparable full-sized assembly and therefore the environment for measurements sensitive primarily to the central spectra (see Paper III-11) discusses the results of comparisons between the zoned and full-sized assemblies of this series.

The design of zoned assemblies generally proceeds from the desire to produce a real and adjoint sp ectra match to some reference reactor over as large a region of the central zone as possible within the limitation of available materials. This has led to design concepts involving a central zone of the same composition as the reference reactor, a highly enriched driver region and a buffer region between the two to aid in spectral equilibration. This zone pattern was used in each of the three zoned assemblies. In the cases of Assemblies 11 and 12 the most important design limitation was on critical mass: 500 kg for Assembly 11 and 600 kg for Assembly 12.

Design calculations were performed using one-dimensional diffusion theory and various cross section sets. Although the calculated central spectra for the reference and zoned cores vary with the cross section set, the group-by-group matching of spectra was not particularly sensitive to the cross section set used when the reference and zone were compared on the basis of the same set. This was taken as an indication that the

TABLE III-8-I. ZPR-9 ASSEMBLIES 11 AND 12

| Assembly and Region | Outer Radius, cm | Atom Densities × $10^{-24}$ | | | | | | | |
|---|---|---|---|---|---|---|---|---|---|
| | | Fe | Ni | Cr | Na | C | U-238 | U-235 | B |
| 11 Core | 20.89 | 0.009086 | 0.001148 | 0.002593 | 0.009028 | 0.012986 | 0.010633 | 0.001547 | — |
| 12 Core | 25.88 | 0.009086 | 0.001148 | 0.002593 | 0.009028 | 0.012986 | 0.010633 | 0.001547 | — |
| 11 Buffer | 28.04 | 0.009086 | 0.001148 | 0.002593 | 0.009028 | 0.009413 | 0.012145 | 0.000025 | 0.003023 |
| 12 Buffer | 32.52 | 0.008825 | 0.001116 | 0.002520 | 0.003917 | 0.034635 | 0.009708 | 0.000020 | — |
| 11 Driver | 39.47 | 0.007014 | 0.01887 | 0.002002 | — | 0.04329 | 0.000321 | 0.004498 | — |
| 12 Driver | 40.75 | 0.010638 | 0.001345 | 0.003038 | 0.007833 | 0.012986 | 0.005381 | 0.006876 | — |
| 11 Reflector | 80.02 | 0.077772 | 0.000891 | 0.02036 | — | — | — | — | — |
| 12 Reflector | 54.52 | 0.004322 | 0.00054 | 0.00114 | — | — | 0.03990 | 0.000081 | — |
| 12 Reflector | 80.75 | 0.077772 | 0.000891 | 0.02036 | — | — | — | — | — |

matching was perhaps better than the uncertainties in the calculations.

Table III-8-I lists the regional sizes and homogenized compositions used in Assemblies 11 and 12. The loading configuration of the ZPR facilities consists of thin plates of mockup materials in nominally 2 in. x 2 in. drawers, of a length depending on the assembly, loaded into a rectangular stainless steel matrix. Drawer and assembly loading patterns for Assemblies 11 and 12 are shown in Figs. III-8-1, III-8-2 and III-8-3.

Table III-8-II shows a comparison of the calculated real and adjoint spectra of Assemblies 11 and 12 with that of the reference Assembly 5. Table III-8-III lists a few significant measured and calculated parameters.

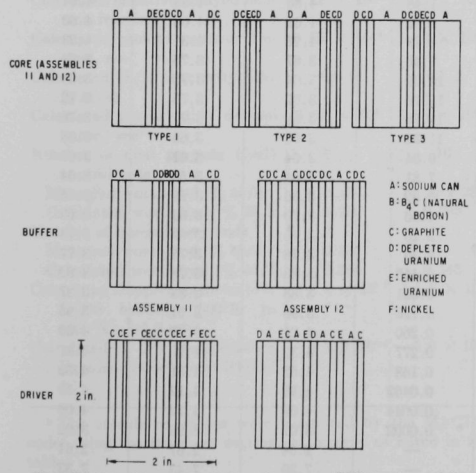


FIG. III-8-1. Drawer Loading Patterns ZPR-9 Assemblies 11 and 12. *ANL Neg. No. 112-9034.*

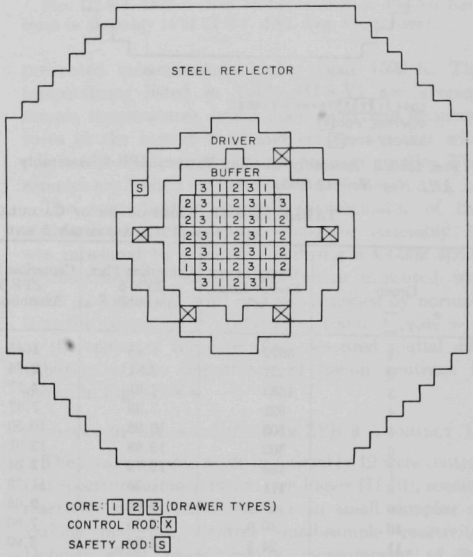


FIG. III-8-2. Assembly Loading Pattern ZPR-9, Assembly 11. *ANL Neg. No. 112-9032.*

## SUMMARY OF MEASUREMENTS IN ZPR-9 ASSEMBLY 11

The measurements made on Assembly 11 were a central real spectrum measurement (see Paper III-10), central reactivity worth measurements on small samples of various materials, central small-sample reactivity Doppler effect measurements, central fission ratio measurements (see Paper III-11), measurement of the spatial distribution of the importance of fission neutrons, measurement of the perturbation-theory normalization integral, and foil measurements of the

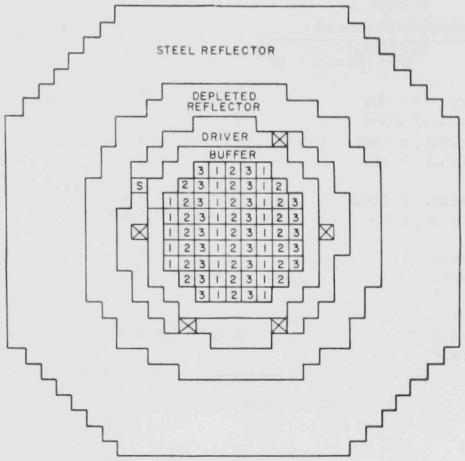


FIG. III-8-3. Assembly Loading Pattern ZPR-9, Assembly 12. *ANL Neg. No. 112-9033.*

radial and axial U-238 and U-235 fission rate distributions.[2] The spectrum measurement and the fission ratio measurement data are given in the referenced papers.

Assembly 11 central worth measurement data are summarized in Table III-8-IV. The measurement was accomplished by comparing the reactor period with and without the sample in place in a small cavity at the center of the assembly.

Table III-8-VI summarizes the results of the Doppler measurements performed on Assembly 11. The measurements were made at the core center with the assembly loading pattern of Fig. III-8-2 modified by inserting an oscillator assembly into the central core tube. Four different sample types were used. The FE, NE and NNE types are distinguished by their expansion characteristics.[3] The essential features are that the FE sample type allows free axial and radial expansion of the $UO_2$ column with temperature; the NE sample type allows no axial expansion while allowing radial expansion; and the NNE sample type allows no axial expansion and, using Invar, constrains radial expansion over the first 240 to 300°C above room temperature. The high temperature, HT, sample type is one of several sample types under development to

TABLE III-8-II. COMPARISON OF CALCULATED REAL AND ADJOINT CENTERLINE FLUXES FOR ZPR-6 ASSEMBLY 5 AND ZPR-9 ASSEMBLIES 11 AND 12[a]

| Group | Group Lower Energy Limit, keV | Centerline Flux, ZPR-6 Assembly 5 | Centerline Flux, ZPR-9 Assembly 11 | Centerline Flux, ZPR-9 Assembly 12 | Centerline Adjoint Flux, ZPR-6 Assembly 5 | Centerline Adjoint Flux, ZPR-9 Assembly 11 | Centerline Adjoint Flux, ZPR-9 Assembly 12 |
|---|---|---|---|---|---|---|---|
| 1 | 3679 | 1.48 | 1.45 | 1.48 | 4.86 | 4.88 | 4.84 |
| 2 | 2231 | 2.81 | 2.76 | 2.82 | 4.61 | 4.66 | 4.60 |
| 3 | 1353 | 4.81 | 4.77 | 4.83 | 4.23 | 4.31 | 4.23 |
| 4 | 821 | 7.39 | 7.47 | 7.46 | 3.67 | 3.75 | 3.68 |
| 5 | 500 | 10.28 | 10.50 | 10.39 | 3.64 | 3.73 | 3.66 |
| 6 | 302 | 12.68 | 12.91 | 12.76 | 3.67 | 3.75 | 3.70 |
| 7 | 183 | 12.72 | 12.84 | 12.75 | 3.68 | 3.71 | 3.70 |
| 8 | 111 | 11.36 | 11.38 | 11.34 | 3.66 | 3.65 | 3.68 |
| 9 | 67.4 | 9.67 | 9.65 | 9.64 | 3.64 | 3.61 | 3.65 |
| 10 | 40.9 | 7.85 | 7.80 | 7.81 | 3.64 | 3.58 | 3.64 |
| 11 | 24.8 | 5.96 | 5.90 | 5.92 | 3.66 | 3.58 | 3.65 |
| 12 | 15.0 | 4.71 | 4.61 | 4.66 | 3.70 | 3.62 | 3.69 |
| 13 | 9.12 | 3.30 | 3.20 | 3.26 | 3.75 | 3.67 | 3.74 |
| 14 | 4.31 | 2.40 | 2.31 | 2.36 | 3.78 | 3.73 | 3.77 |
| 15 | 2.61 | 0.441 | 0.435 | 0.446 | 3.83 | 3.78 | 3.82 |
| 16 | 2.03 | 0.539 | 0.517 | 0.531 | 3.88 | 3.83 | 3.87 |
| 17 | 1.23 | 0.825 | 0.776 | 0.798 | 3.96 | 3.91 | 3.95 |
| 18 | 0.961 | 0.258 | 0.243 | 0.250 | 4.01 | 3.97 | 4.00 |
| 19 | 0.583 | 0.287 | 0.271 | 0.277 | 4.32 | 4.29 | 4.31 |
| 20 | 0.275 | 0.172 | 0.165 | 0.168 | 4.52 | 4.51 | 4.52 |
| 21 | 0.101 | 0.0467 | 0.0454 | 0.0462 | 4.19 | 4.12 | 4.19 |
| 22 | 0.0290 | 0.0043 | 0.0042 | 0.0044 | 4.09 | 4.12 | 4.09 |
| 23 | 0.0137 | 0.0002 | 0.0002 | 0.0002 | 3.02 | 3.06 | 3.02 |
| 24 | 0.00306 | — | — | — | 2.64 | 2.67 | 2.64 |
| 25 | 0.00068 | — | — | — | 7.33 | 7.43 | 7.33 |

[a] The spectra were computed in cylindrical geometry by the MACH-1 code[5] using the 801 cross section set. The 801 set was generated by the ELMOE code.[6] The values were normalized such that $\sum_i \phi_i = 100$, $\sum_i \phi_i^* = 100$.

achieve the goal of Doppler measurements to 2000°K. The particular sample used in these measurements was constructed of an alumina inner can with a bare tantalum heater wire. Table III-8-VI includes a measurement of the reactivity signal of an empty can of this design as a function of temperature. There is a significant signal from the empty can, probably coming from the tantalum wire. Measurements in ZPR-6 Assembly 4Z[3] indicated no significant reactivity signals from empty cans of the FE, NE or NNE types. Outgassing from the structure of this HT sample

TABLE III-8-III. LIST OF MEASURED AND CALCULATED PARAMETERS FOR ASSEMBLIES 11 AND 12

| | Assembly[a] | |
|---|---|---|
| | 11 | 12 |
| Measured critical mass, kg | 480 | 579 |
| Calculated critical mass (MACH-1, 801 set), kg | 472 | 582 |
| Calculated critical mass (MACH-1, MCC set),[b] kg | 461 | 569 |
| Mass of U-235 in central core, kg | 76 | 116 |
| Total volume (excluding reflector), liter | 448 | 477 |
| Volume of central core, liter | 125 | 192 |
| Core height (excluding reflector), cm | 91.4 | 91.4 |
| Axial reflector thickness, cm | Fe-33 | U-238-12.7; Fe-20.3 |
| Reflector savings used in calculation, cm | core: 20 driver: 9.2 | 16.1 |
| Calculated effective delayed neutron fraction | $7.12 \times 10^{-3}$ | $7.20 \times 10^{-3}$ |
| Calculated prompt neutron lifetime, sec | $3.55 \times 10^{-7}$ | $1.88 \times 10^{-7}$ |
| Calculated Ih/% reactivity (Ih/% $\delta k/k$) | 428.2 | 451.2 |
| Calculated perturbation denominator,[c] $sec^{-1}$ | $3.67 \times 10^{5}$ | $4.18 \times 10^{-5}$ |
| Number of dual purpose (fuel) control rods: | 10 | 10 |
| Measured worth/rod, % $\delta k/k$ | 0.23 | 0.25–0.28 |
| Calculated worth/rod, % $\delta k/k$ | 0.250 | 0.255 |
| Number of boron safety rods | 2 | 1 |
| Measured worth/rod, % $\delta k/k$ | 0.23 | — |
| Calculated worth/rod, % $\delta k/k$ | 0.364 | 0.146 |
| Calculated Doppler coefficient for U-235 heating (300°K to 1200°K), $(\delta k/k)$/°C | $+6.0 \times 10^{-7}$ | $+4.8 \times 10^{-7}$ |
| Calculated U-235 Temperature Expansion Coefficient $(\delta k/k)$/°C | $-4.3 \times 10^{-6}$ | $-5.9 \times 10^{-6}$ |

[a] The calculated values were computed by the MACH-1 code[5] using the 801 cross section set, except as noted in the table.

[b] The MCC cross section set was generated by the MCC code.[7]

[c] The values are normalized such that $\sum_i (\nu\Sigma_f)_i\phi_i = 1$ and $\sum_i \chi_i\phi_i^* = 1$ at the center of t he core.

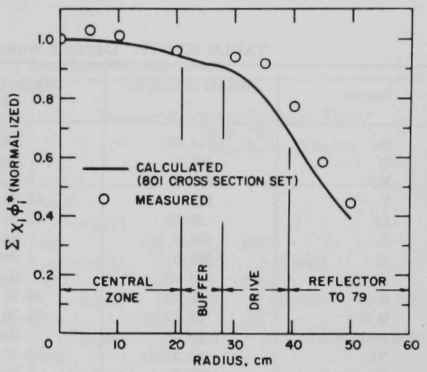


FIG. III-8-4. Distribution of Importance of Fission Neutrons in Assembly 11 of ZPR-9. *ANL Neg. No. 112-8931.*

prevented measurements higher than 1500°K. The temperatures listed in Table III-8-VI are average sample temperatures, based upon centerline temperatures at the sample ends and center, together with previously measured typical temperature profiles. The samples are heated on their outer surfaces.

The normalization integral (denominator of the standard perturbation expression) for Assembly 11 was measured by a method utilizing a Cf-252 spontaneous neutron source.[4] The value measured was $(4.22 \pm 0.2) \times 10^5$ $sec^{-1}$ and was obtained by normalizing the quantities $\sum_i (\nu\Sigma_f)_i\phi_i = 1$ and $\sum_i \chi_i\phi_i^* = 1$ at the center of the core. The measured spatial distribution of the importance of fission neutrons is shown in Fig. III-8-4.

## SUMMARY OF MEASUREMENTS IN ZPR-9 ASSEMBLY 12

The measurements made in Assembly 12 were central real spectrum measurements (see Paper III-10), central reactivity worth measurements on small samples of various materials, central small-sample reactivity Doppler effect measurements, measurement of the spatial distribution of the importance of fission neutrons, measurement of the perturbation theory normalization integral and a sodium-void reactivity measurement. ZPR-9 Assembly 18, which was installed in June of 1967, is identical to ZPR-9 Assembly 12. The experimental results from Assembly 18 are not included in this paper.

The results from the Assembly 12 central worth measurements are given in Table III-8-V. The worth samples and the measurement technique were the same as those used for Assembly 11.

The results of the Assembly 12 Doppler measurements are listed in Table III-8-VII. Sample types are the same as those used for the Assembly 11 measure-

TABLE III-8-IV. CENTRAL WORTH MEASUREMENTS IN ZPR-9 ASSEMBLY 11

| Sample | Weight of Sample, g | Weight of Can, g | Gross Worth[a], Ih | Net Worth, Ih |
|---|---|---|---|---|
| Be | 114.308 | Bare | +0.671 ± 0.057 | +0.671 ± 0.057 |
| C | 103.0 | Bare | −0.220 ± 0.057 | −0.220 ± 0.057 |
| Ni | 546.0 | Bare | −1.973 ± 0.057 | −1.973 ± 0.057 |
| V | 183.67 | 55.30 (SS) | −0.498 ± 0.057 | −0.334 ± 0.060 |
| Li | 28.30 | 57.03 (SS) | −1.378 ± 0.023 | −1.208 ± 0.029 |
| Zr | 406.0 | Bare | −1.136 ± 0.023 | −1.136 ± 0.023 |
| Mo | 599.0 | Bare | −5.293 ± 0.023 | −5.243 ± 0.023 |
| Al | 166.90 | Bare | −0.518 ± 0.023 | −0.518 ± 0.023 |
| B-10 | 29.29 | 55.73 (SS) | −35.676 ± 0.030 | −35.520 ± 0.035 |
| $B_4C$ | 59.62 | 64.70 (SS) | −9.876 ± 0.028 | −9.684 ± 0.034 |
| Polyethylene | 58.98 | Bare | +28.652 ± 0.028 | +28.652 ± 0.028 |
| Nb | 481.2 | 30.10 (SS) | −5.900 ± 0.048 | −5.811 ± 0.051 |
| W | 1108.0 | Bare | −8.928 ± 0.030 | −8.928 ± 0.030 |
| Ta | 924.70 | 27.54 (SS) | −18.30 ± 0.10 | −18.22 ± 0.10 |
| U-238 | 1153.80 | Bare | −5.908 ± 0.010 | −5.908 ± 0.010 |
| U-235 | 27.719 | 47.30 (SS) | +1.946 ± 0.025 | 1.833 ± 0.028 |
| U-235 | 64.183 | 47.30 (SS) | +4.827 ± 0.050 | +4.714 ± 0.053 |
| Na | 51.38 | 56.42 (SS) | −0.282 ± 0.015 | −0.114 ± 0.035 |
| SS-304 | 499.6 | Bare | −1.401 ± 0.040 | −1.401 ± 0.040 |
| Pu | 117.157 | 7.093 (Al)<br>20.06 (SS) | +13.714 ± 0.050 | +13.795 ± 0.055 |
| U-233 (97.15% U-233) | 146.708 | 5.286 (Al)<br>19.977 (SS) | +20.987 ± 0.200 | +21.067 ± 0.200 |

[a] 1% $\Delta k/k$ = 428.2 Ih.

TABLE III-8-V. CENTRAL WORTH MEASUREMENTS IN ZPR-9 ASSEMBLY 12

| Sample | Weight of Sample, g | Weight of Can, g | Gross Worth[a], Ih | Net Worth, Ih | Sample | Weight of Sample, g | Weight of Can, g | Gross Worht, Ih | Net Worth, Ih |
|---|---|---|---|---|---|---|---|---|---|
| Polyeth-ylene | 23.973 | Bare | +9.539 | +9.539 ± 0.010 | U-235 | 18.11 (Total) | 72.378 (SS) | +0.993 | +1.183 ± 0.015 |
| Polyeth-ylene | 58.98 | Bare | +26.155 | +26.155 ± 0.015 | | 16.87 (U-235) | | | |
| Be | 114.308 | Bare | +1.395 | +1.395 ± 0.010 | U-235 | 59.40 (Total) | 55.44 (SS) | +3.526 | +3.691 ± 0.015 |
| B-10 | 29.29 | 55.73 (SS) | −32.731 | −32.589 ± 0.015 | | 55.32 (U-235) | | | |
| C | 102.01 | Bare | +0.161 | +0.161 ± 0.011 | | | | | |
| Na | 51.38 | 54.52 (SS) | −0.210 | −0.0707 ± 0.0103 | | | | | |
| Al | 166.9 | Bare | −0.428 | −0.428 ± 0.010 | U-238 | 1153.8 | Bare | −5.398 | −5.398 ± 0.010 |
| Fe | 488.0 | Bare | −1.022 | −1.022 ± 0.010 | Pu | 148.36 (Total) | 22.27 (SS) | +11.019 | +11.094 ± 0.20 |
| SS | 480.98 | Bare | −1.137 | −1.137 ± 0.010 | | 113.34 (Pu-239) | 6.85 (Al) | | |
| SS can | 72.378 | Bare | −0.184 | −0.184 ± 0.010 | | | | | |
| Ni | 546.0 | Bare | −1.634 | −1.634 ± 0.010 | | 5.34 (Pu-240) | | | |
| Nb | 481.2 | 30.10 (SS) | −5.406 | −5.329 ± 0.015 | | | | | |
| Mo | 599.0 | Bare | −4.826 | −4.826 ± 0.010 | | 0.54 (Pu-241) | | | |
| Ta | 924.7 | 27.54 (SS) | −16.698 | −16.628 ± 0.015 | | | | | |
| W | 1108.0 | Bare | −8.133 | −8.133 ± 0.010 | | | | | |

[a] 1% $\Delta k/k$ = 451.2 Ih.

TABLE III-8-VI. RESULTS OF ASSEMBLY 11 DOPPLER MEASUREMENTS

| Date of Meas. | Sample No. | Nominal Diam. and Length, in. | Material | % Enrichment | Total U Mass, kg | Sample Type | Sample Environment | Experimental Precision $\sigma$, Ih/kg-U | Measured Reactivity Change vs. Temp.[a] Temp., °K; (Reactivity, Ih/kg-U) | | | |
|---|---|---|---|---|---|---|---|---|---|---|---|---|
| 8/1/66 | N16 | ½ x 12 | $UO_2$ | natural | 0.244 | FE | Regular Core | 0.009 | 1051 (−0.397) | | | |
| 8/2/66 | N16 | ½ x 12 | $UO_2$ | natural | 0.244 | FE | Regular Core | 0.009 | 497 (−0.154) | 773 (−0.296) | 1054 (−0.390) | |
| 8/24/66 | N1 | 1 x 12 | $UO_2$ | natural | 1.116 | FE | Regular Core | 0.003 | 495 (−0.145) | 689 (−0.251) | 878 (−0.326) | 1064 (−0.389) |
| 10/6/66 | N19 | 1 x 12 | $UO_2$ | natural | 0.716 | HT | Regular Core | 0.007 | 539 (−0.256) | 560 (−0.293) | 747 (−0.380) | 1013 (−0.482) |
| | | | | | | | | | 1207 (−0.559) | 1513 (−0.610) | | |
| 10/7/66 | empty can | 1 x 12 | — | — | — | HT | Regular Core | 0.008 | 540 (−0.045) | 722 (−0.066) | 1009 (−0.109)[b] | |
| 8/10/66 | HE6 | ½ x 12 | $UO_2$ | 97.6 | 0.240 | FE | Regular Core | 0.010 | 503 (+0.048) | 684[c] (+0.077) | 875 (+0.065) | 1068[d] (+0.072) |
| 9/6/66 | HE2 | 1 x 12 | $UO_2$ | 97.7 | 1.004 | NE | Regular Core | 0.003 | 331 (+0.011) | 377 (+0.018) | 424 (+0.039) | 472 (+0.047) |
| | | | | | | | | | 616 (+0.073) | 808 (+0.090) | 1064 (+0.109) | |
| 9/13/66 | HE5 | 1 x 12 | $UO_2$ | 97.7 | 0.712 | NNE | Regular Core | 0.003 | 343 (+0.007) | 378 (+0.017) | 443 (+0.035) | 494 (+0.044) |
| | | | | | | | | | 628 (+0.059) | 820 (+0.089) | 1032 (+0.110) | |

[a] 428 Ih = 1% $\delta k/k$. Data are normalized to 0.000 Ih/kg-U at 293°K and uncorrected for expansion.
[b] Per kg uranium in N19.
[c] $\sigma$ = 0.015 Ih/kg-U.
[d] $\sigma$ = 0.005 Ih/kg-U.

TABLE III-8-VII. RESULTS OF ASSEMBLY 12 DOPPLER MEASUREMENTS

| Date of Meas. | Sample No. | Nominal Diam. and Length, in. | Material | % Enrichment | Total U Mass, kg | Sample Type | Sample Environment | Experimental Precision $\sigma$, Ih/kg-U | Measured Reactivity Change vs. Temp.[a] Temp., °K; (Reactivity, Ih/kg-U) | | | |
|---|---|---|---|---|---|---|---|---|---|---|---|---|
| 12/16/66 | N1 | 1 x 12 | UO | natural | 1.116 | FE | Regular Core | 0.004 | 335 (−0.036) | 514 (−0.147) | 678 (−0.216) | 867 (−0.294) |
| 12/20/66 | N1 | 1 x 12 | UO | natural | 1.116 | FE | Min. Het. | 0.002 | 520 (−0.153) | 682 (−0.231) | 867[b] (−0.291) | 1062 (−0.361) |
| 1/9/67 | N1 | 1 x 12 | UO | natural | 1.116 | FE | Min. Het. | 0.003 | 854 (−0.306) | | | |
| 1/3/67 | HE5 | 1 x 12 | UO | 97.7 | 0.712 | NNE | Min. Het. | 0.005 | 325 (+0.032) | 364 (+0.038) | 425 (+0.053) | 479 (+0.060) |
| | | | | | | | | | 664 (+0.077) | 847 (+0.077) | | |

[a] 451 Ih = 1% $\delta k/k$. Data are normalized to 0.000 Ih/kg-U at 293°K and uncorrected for expansion.
[b] $\sigma$ = 0.011 Ih/kg uranium.

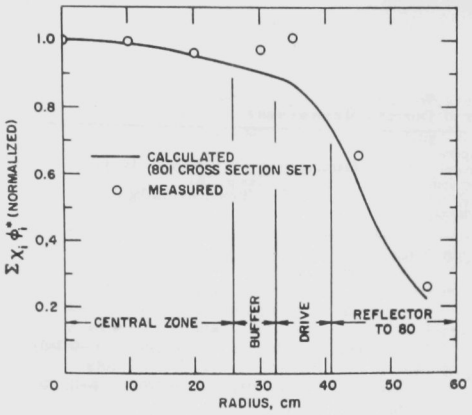


FIG. III-8-5. Distribution of Importance of Fission Neutrons in Assembly 12 of ZPR-9. *ANL Neg. No. 112-8932.*

ments. Measurements were performed in an oscillator installed in the central core drawer. The sample environment listed in Table III-8-VII as "Min. Het." was an arrangement in which the eight drawers immediately adjacent to the sample location were rearranged to minimize the plate heterogeneity around the sample. This was the arrangement used routinely in the ZPR-6 Assembly 4Z measurements.[4] This arrangement caused a small change in the local composition, as well as heterogeneity, as compared with the case where the regular core loading, with its vertical plate structure, was merely changed by removing the center drawer to allow sample access; the latter arrangement is the "Regular Core" of Table III-8-VII. It is significant that there is no measureable difference between the two environment configurations as shown by the December 16 and December 20, 1966 measurements of Table III-8-VII.

The spatial distribution of the importance of fission neutrons is shown in Fig. III-8-5. The normalization integral for Assembly 12 was measured to be $(4.47 \pm 0.2) \times 10^5$ sec$^{-1}$. The technique was the same as that described previously for the Assembly 11 measurement.

The reactivity effect of voiding the sodium in the front two inches of the nine center drawers in each half was measured. The amount of sodium removed was 0.886 kg. The worth values were obtained from period measurements made both with the normal sodium loading and with the sodium cans in this region replaced by empty cans. The result was $+1.85 \pm 0.07$ Ih/kg of sodium voided.

R. C. Doerner was the physicist responsible for the supervision of ZPR-9 during the periods that Assemblies 11 and 12 were installed and operating.

## REFERENCES

1. R. A. Karam, A. Ancarani, F. H. Helm, W. Y. Kato, G. W. Main and G. K. Rusch, *Measured Physics Parameters in a Zoned Fast Uranium Carbide Core, Assembly 4Z*, ANL-7281 (1966).
2. A. Ancarani, *Fission Rates in Zoned-Core Fast Critical Assembly*, Trans. Am. Nucl. Soc. **10**, 275 (1967).
3. C. E. Till, R. A. Lewis and R. N. Hwang, *ZPR-6 Doppler Measurements and Comparisons with Theory*, Proc. International Conference on Fast Critical Experiments and Their Analysis, October 10–13, 1966, ANL-7320, pp. 319–333.
4. R. A. Karam, *Measurement of the Spatial Distribution of the Importance of Fission Neutrons in a Fast Reactor*, Trans. Am. Nucl. Soc. **9**, 490 (1966).
5. D. A. Meneley, L. C. Kvitek and D. M. O'Shea, *MACH-1, A One-Dimensional Diffusion Theory Package*, ANL-7223 (1966).
6. A. L. Rago and H. H. Hummel, *ELMOE: An IBM 704 Program Treating Elastic Scattering Resonances in Fast Reactors*, ANL-6805 (1966).
7. D. M. O'Shea, B. J. Toppel and A. L. Rago, *MCC—A Code to Calculate Multigroup Cross Sections*, ANL-7318 (1967).

## III-9. The Effect of Sodium Voiding on the Spectrum of ZPR-6 Assembly 5

E. F. BENNETT

During the series of measurements described in (Paper III-10), the spectrum at the center of Assembly 5 was measured with a cylindrical volume of the reactor voided of sodium; the radius of the voided volume was 20 cm. Sodium is one of the principal constituents of ZPR-6 and ZPR-9 cores and its expulsion can contribute substantially to multiplication changes pertinent to the safety analysis of these cores.

The normal atom densities of all core materials are listed in Table III-9-I. The voiding process consisted of removing all of the sodium cans from a 20-cm radius central region and then adding a sufficient

amount of steel to restore material concentrations to values listed in the table.

Details of the measurement were identical with those in Paper III-10. The absence of sodium produced a 25-Ih reduction in reactivity. Measurements in the "normal" core were made with the reactor subcritical by 170 Ih; therefore the void caused reactivity to decrease to −195 Ih with respect to the "normal" core.

In order to compare the effect upon the spectrum of the sodium void, both spectra were averaged over the energy group structure of the ANL-801 cross section set (after normalizing to equal integrated flux) and group by group differences taken in the same manner in which the zoned core comparison was made. In Fig. III-9-1 a plot of these differences (normal spectrum minus voided spectrum) is shown as a function of energy. The differences are normalized to the integral flux (identical for both spectra by choice of normalization). Figure III-9-I also contains a calculated group histogram of the deviations. The calculation was made using the MACH-1 code and the ANL-801 cross section set. General trends of the calculated and measured results agree, in particular the large deviations predicted at 3 keV and near 800 keV are observed. The predicted deviations are not, however, generally within experimental errors and no explanation can be provided at present.

Improvements in experimental technique, including a method for treating wall-and-end effect distortion at the higher energies, are being developed; these may alter somewhat the results near 1 MeV. Effects of homogeneity of the environment near the detector are not easily resolved. Past measurements and calculations designed to test these effects indicate that they should have relatively little influence on an intercomparison of the kind described here.

TABLE III-9-I. Atom Densities of Assembly 5

| Material | Atom Density, $\times 10^{-24}$ cm$^3$ |
|---|---|
| Fe | 0.009086 |
| Ni | 0.001148 |
| Cr | 0.002593 |
| Na | 0.009028 |
| C | 0.012986 |
| U-238 | 0.010633 |
| U-235 | 0.001547 |

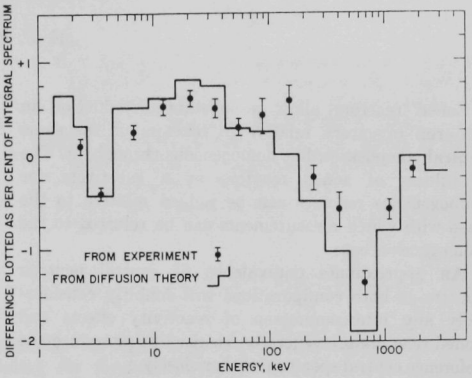


Fig. III-9-1. Group Comparison of Voided and Normal Central Spectra in Assembly 5. *ANL Neg. No. 112-8444.*

One obvious defect in the intercomparison is the arbitrary normalization of the two spectra (to equal integrated flux from about 1 keV to about 3 MeV). Since the extent of subcriticality of each measurement is known, an improved calculation taking this into account could eliminate this arbitrariness.

In summary, sodium voiding of the central region of Assembly 5 produces easily observed changes in the spectrum which are in qualitative agreement with calculation over the energy region above about 2 keV. The measured (and calculated) changes over this region are not large, however. Below 3 keV, and as energy decreases, sodium voiding produces a large increase in neutron flux (three or four times according to calculation). This increase is partially obscured by a sodium resonance near 3 keV, which is close to the lower extremity of proton-recoil measurements. The substantial softening at low energies will influence certain experiments inordinately, especially Doppler and 1/v weighted results such as neutron lifetime where the sub-keV flux may account for a large fraction of the effect. The effect of voiding will not, however, be very impressive over the energy region accessible to proton-recoil experiments.

# III-10. Experimental Neutron Spectrum Comparison of a Zoned and a Homogeneous Fast Critical Assembly

E. F. Bennett

Zoned reactors allow a substantial reduction in material inventory relative to reactors of the same central composition but homogeneous throughout. The usefulness of zoned reactors as a substitute for homogeneous reactors can be judged relative to the ease with which measurements can be referred to the homogeneous case.

An approximate equivalence of central neutron spectra in both configurations will simplify considerably any intercomparison of reactivity effects and zoned reactors are generally designed to reproduce the reference central spectrum rather closely.

Experimental spectrum measurements using proton-recoil techniques[1,2] have been made on both Assembly 5 (homogeneous) and Assembly 12 (zoned) as constructed at the ZPR-6 and ZPR-9 facilities at Argonne. The composition of the homogeneous reactor simulates that of a large dilute uranium carbide power reactor. Details of these cores can be found in Ref. 3. The zoned reactor has a central region (radius = 26 cm) with the composition of the homogeneous reactor and a concentric annulus with a high concentration of fissionable material.

Figure III-10-1 depicts the spectrum as measured in the reference core (Assembly 5). Resolution is approximately 10% (F.W.H.M.) except at the lower energies where it worsens because of statistics in proton ionization. The spectrum contains recognizable features. The large sodium resonance at 3 keV depletes the flux severely as do resonances in the lighter elements in the core at various energies across the spectrum. The result in Fig. III-10-1 is similar to an older measurement[2] except that in this measurement an improved energy calibration was available, a correction for a non-Gaussian component in the detector response function (due to finite detector size) was made, and the resolution was improved.

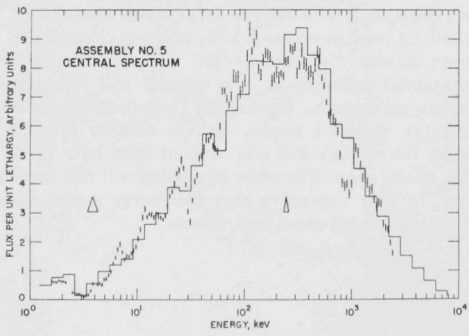


Fig. III-10-1. Central Spectrum of Assembly 5 Compared with an Energy Group Calculation. *ANL Neg. No. 112-7857.*

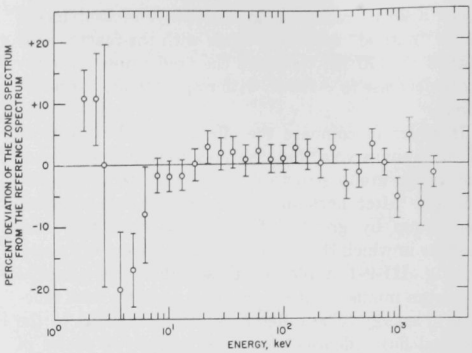


Fig. III-10-2. The Percent Deviation of the Zoned Spectrum from the Reference Spectrum Versus Energy. *ANL Neg. No. 112-7856.*

A group histogram from the MCC code[4] is also shown in Fig. III-10-1; normalization is arbitrary. There is general agreement as to shape. Data below 5 keV are probably subject to systematic errors in excess of statistics and some of the reasons for this are discussed in Refs. 1 and 2.

The spectra above 1 MeV are subject to a sizeable correction for wall and end effects. These corrections have not been made but they should not greatly influence a comparison of spectra from the two assemblies.

Figure III-10-2 is a plot of the percentage deviation of the zoned assembly from the homogeneous assembly versus energy. The measured spectrum for both cases was averaged over lethargy intervals of the same width (0.25) as the histogram in Fig. III-10-1. The spectrum for the zoned assembly was normalized (by area) to the reference spectrum. Except at low energies (below 5 keV) the deviations observed were, for the most part, within estimated statistical errors.

Below 5 keV, differences in the spectra were generally in excess of statistics. These deviations are probably not real, however. Reproducibility of spectra at low energies has generally not been within sta-

tistics; the explanation appears to be instrumental in character and improved counting apparatus can be expected to reduce these sources of systematic error substantially.

In summary, the reference core and the zoned core spectra agree within about 2½% for energies from about 5 keV to about 2 MeV. From 1.5 to 5 keV the spectra agree within about 20%; this number includes systematic errors, however, and the real discrepancy is probably less.

### References


1. E. F. Bennett, *Fast Neutron Spectroscopy by Proton Recoil Proportional Counting*, Nucl. Sci. Eng. **27**, 16 (1967).
2. E. F. Bennett, *Neutron Spectrum Measurement in a Fast Critical Assembly*, Nucl. Sci. Eng. **27**, 28 (1967).
3. R. A. Karam, F. H. Helm, W. Y. Kato and G. W. Rusch, *Measured Physics Parameters in a Zoned Fast Carbide Core, Assembly 4Z*, ANL-7281 (1966).
4. R. A. Lewis, Argonne National Laboratory (private communication).


## III-11. A Review of Data Pertaining to Spectral Equilibration and Spectral Matching in Zoned Cores

L. G. LeSage, R. A. Karam, R. A. Lewis, E. F. Bennett and G. W. Main

### Introduction

There is a considerable advantage in using a zoned critical assembly rather than a full-sized assembly for certain types of fast reactor physics measurements. The zoned assembly has the following advantages. The fuel requirement is greatly reduced, it can be constructed more easily and rapidly, the personnel radiation exposure is generally reduced and, for reactivity measurements, the signal is usually larger. In order that measurements made in a zoned assembly are interpretable in terms of a full-size reference system, it is necessary that both the real and the adjoint spectra in the zone be well matched to the reference spectra. The actual degree of matching required depends to some extent, however, on the measurements planned for the zone. For example, Doppler effect measurements generally do not require as accurate a match as worth measurements that involve scattering materials. The matching of the zone spectrum to the reference spectrum is one of the primary objectives in the zoned assembly design calculations. A number of different measurements have been performed on the zoned Assemblies 11, 12 and 4Z and on the reference core, Assembly 5, which tend to experimentally confirm the adequacy of the spectra in these zoned cores. These include the direct spectrum measurements using the proton recoil counter, central material worth measurements, fission ratios and Doppler effect measurements. Part of these experimental results have been reported elsewhere.[1-5] It is the purpose of this paper to present and discuss all the experimental data relating to the spectra in the series of zoned assemblies matched to ZPR-6, Assembly 5.

### Proton Recoil Counter Results

A comparison of the real fluxes in Assemblies 5 and 12 has been made in Ref. 1, and it was concluded that there was agreement to within about ±2.5% for energies from 5 keV to 2 MeV. Figure III-11-1, which is from Ref. 1, is a plot of the percentage deviation of the spectrum from the reference spectrum. The proton recoil counter results thus confirm approximate real spectrum matching and rule out the possibility of gross spectral mismatch between the zone and the reference. These measurements are valuable in that they are the only measurements which directly compare the energy-dependent real spectra. All the other measurements, which will be discussed in the following sections, are integral index type measurements.

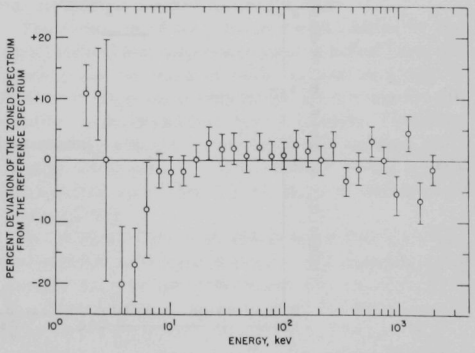


FIG. III-11-1. The Percent Deviation of the Zoned Spectrum from the Reference Spectrum Versus Energy. *ANL Neg. No. 112-7856.*

The proton recoil measurements do not go low enough in energy to provide information on the spectral matching in most of the Doppler region, which extends from about 25 keV down into the eV range.

### Central Worth Measurements

The central reactivity worths of approximately twenty materials were measured in each of the zoned cores and the full-size reference core. These measurements yield essentially no absolute spectral information, but they do contain considerable information regarding the matching between assemblies of both the real and the adjoint fluxes. The worth and the Doppler measurements are the only measurements that provide information on the adjoint fluxes. Consider the following equation which is a perturbation expression for the ratio of the central worth of a material in one assembly, designated $x$, to the worth of the same material in another assembly, designated $y$.

$$\frac{\Delta\rho(\mathrm{Ih})_x}{\Delta\rho(\mathrm{Ih})_y} = \frac{C_x}{C_y}\cdot\frac{D_y}{D_x}\cdot\frac{\int\left[\sum_{j=1}^{J}\left(\phi_j\bar{\phi}_f^*\nu\Sigma_{f_j} - \phi_j\phi_j^*\Sigma_{c+f_j} + \phi_j\sum_{k=j+1}^{J}\Sigma_{jk}(\phi_k^* - \phi_j^*)\right)\right]dV_x}{\int\left[\sum_{j=1}^{J}\left(\phi_j\bar{\phi}_f^*\nu\Sigma_{f_j} - \phi_j\phi_j^*\Sigma_{c+f_j} + \phi_j\sum_{k=j+1}^{J}\Sigma_{jk}(\phi_k^* - \phi_j^*)\right)\right]dV_y}, \tag{1}$$

where

$\Sigma_{c+f} \equiv$ capture plus fission cross section
$\Sigma_f \equiv$ fission cross section
$\Sigma_{jk} \equiv$ cross section for scattering from group $j$ to group $k$
$\nu \equiv$ number of neutrons per fission
$\Delta\rho(\mathrm{Ih}) \equiv$ reactivity change in inhours
$\phi \equiv$ real flux
$\phi^* \equiv$ adjoint flux
$\bar{\phi}_f^* = \sum_{j=1}^{J}\chi_j\phi_j^*$
$J \equiv$ number of groups
$j,k \equiv$ group numbers
$\chi_j \equiv$ fraction of fission neutrons emitted in group $j$
$C \equiv (\mathrm{Ih}/\%)/(\delta k/k)$
$D \equiv$ perturbation denominator

The integration is over the volume of the worth sample. If the real and the adjoint fluxes are perfectly matched in the two assemblies, the ratio of the central worth of a material in Assembly $x$ to its worth in Assembly $y$ is $C_xD_y/C_yD_x$ and this ratio has the same value for each material. For convenience, we will call this term the inverse denominator ratio remembering, of course, that the calculated $(\mathrm{Ih}/\%)/(\delta k/k)$ terms are also included. If the fluxes are not matched, the central worth ratios are not the same for each material. In the dilute U-235 carbide cores, such as ZPR-6, Assemblies 4Z and 5, and ZPR-9, Asesmblies 11 and 12, the adjoint flux is nearly constant with energy over the energy range from 40 keV to 1.4 MeV, which covers the peak of the real flux spectrum (see Fig. III-11-2). The values of $\phi_{i+1}^* - \phi_i^*$ in Eq. 1 are small compared with $\phi_i^*$ or $\phi_{i+1}^*$, so that small errors in $\phi_i^*$ or $\phi_{i+1}^*$ can result in large percentage errors in their difference. Materials with

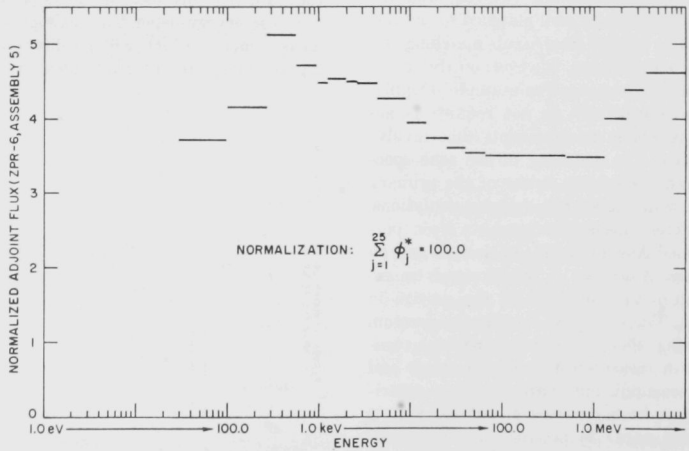


Fig. III-11-2. Normalized Adjoint Flux for Assembly 5 of ZPR-6 Calculated by the MACH-1 Code Using an MCC Generated Cross Section Set.[8] *ANL Neg. No. 112-9090.*

TABLE III-11-I. Measured and Calculated Ratios of the Central Worths in Assemblies 4Z, 11 and 12 to Those in Assembly 5

| Sample Weight, g | Ih in 4Z / Ih in 5 | | | Ih in 12 / Ih in 5 | | | Ih in 11 / Ih in 5 | | |
|---|---|---|---|---|---|---|---|---|---|
| | Measurement | Calculated[a] | | Measurement | Calculated[a] | | Measurement | Calculated[a] | |
| | | 801 Set | MCC | | 801 Set | MCC | | 801 Set | MCC |
| Polyethylene (59.98) | 1.031 ± 0.001 | — | — | 1.368 ± 0.001 | — | — | 1.498 ± 0.001 | — | — |
| Be (114.31) | 0.979 ± 0.042 | — | — | 1.235 ± 0.055 | — | — | 0.594 ± 0.056 | — | — |
| $B^{10}$ (29.29) | 0.997 ± 0.009 | 1.002 | 0.975 | 1.393 ± 0.004 | 1.444 | 1.384 | 1.538 ± 0.006 | 1.711 | 1.457 |
| C (102.0) | 1.032 ± 0.138 | 0.963 | 0.984 | 0.888 ± 0.129 | 1.842 | 1.121 | 1.202 ± 0.347 | 4.383 | 0.183 |
| Na (51.38) | 1.190 ± 0.315[b] | 1.001 | 1.009 | 1.713 ± 0.487 | 1.470 | 1.946 | 2.781 ± 0.932 | 2.365 | 5.599 |
| Al (166.90) | 0.990 ± 0.070 | 1.004 | 0.982 | 1.427 ± 0.087 | 1.451 | 1.422 | 1.727 ± 0.123 | 1.952 | 1.840 |
| SS (480.98) | 0.998 ± 0.026 | 1.009 | 0.978 | 1.389 ± 0.035 | 1.434 | 1.381 | 1.646 ± 0.057 | 1.710 | 1.541 |
| Ni (546.0) | 1.012 ± 0.016 | 1.001 | 0.971 | 1.441 ± 0.021 | 1.452 | 1.437 | 1.740 ± 0.055 | 1.750 | 1.666 |
| Nb (481.2) | 0.988 ± 0.005 | — | — | 1.389 ± 0.008 | — | — | 1.514 ± 0.017 | — | — |
| Mo (599.0) | 1.000 ± 0.006 | 1.003 | — | 1.413 ± 0.008 | 1.436 | 1.372 | 1.535 ± 0.010 | 1.719 | — |
| Ta (924.7) | 0.992 ± 0.017 | — | — | 1.386 ± 0.003 | — | — | 1.518 ± 0.009 | — | — |
| W (1108.0) | 0.990 ± 0.004 | — | — | 1.404 ± 0.005 | — | — | 1.541 ± 0.008 | — | — |
| U-235 (13.87)[c] | 0.943 ± 0.035 | 1.001 | 0.974 | 1.399 ± 0.028 | 1.412 | 1.386 | 1.415 ± 0.032 | 1.781 | 1.542 |
| U-238 (1153.8)[c] | 0.997 ± 0.004 | 1.003 | 0.976 | 1.398 ± 0.005 | 1.434 | 1.364 | 1.527 ± 0.005 | 1.720 | — |
| Pu (117.16)[c] | 0.985 ± 0.033 | — | — | 1.336 ± 0.007 | — | — | 1.609 ± 0.040 | — | — |
| Average[d] | 0.990 ± 0.018 | 1.003 | 0.975 | 1.395 ± 0.030 | 1.432 | 1.387 | 1.558 ± 0.090 | 1.728 | 1.552 |

[a] Calculations were done with the one-dimensional diffusion code MACH-1[6] using two different cross section sets. The 801 set was generated by the ELMOE code[7] and the set marked MCC was generated by the MCC code.[8]

[b] Subsequent measurements with larger samples gave a value of 1.00 for this ratio.

[c] U-235 sample was 93% enriched, U-238 sample contained 0.2% U-235 and plutonium sample was 95% Pu-239 and 5% Pu-240.

[d] The scattering materials, Be, C, Na, Al and Polyethylene, were excluded from the averaging.

significant values of $\Sigma_{ij}$, such as sodium or carbon, are quite sensitive to small errors in the adjoint flux. Therefore, the scatterers provide a good test of the adjoint flux matching in these particular assemblies.

Table III-11-I, which is from Ref. 2, lists the worth ratios between the zoned assemblies and the full-size core. The ratio between Assemblies 4Z and 5 is nearly the same for each material indicating that very good spectral matching was achieved in Assembly 4Z. The worth ratios between Assemblies 11 and 5 and between Assemblies 12 and 5 are nearly constant except for the primarily scattering materials such as carbon, beryllium and sodium. The matching in Assembly 12 appears to be somewhat better than in the smaller zone, Assembly 11. The worth ratios predicted by the DEL routine of the MACH-1 one-dimensional diffusion code[6] are also shown in Table III-11-I. Values were calculated both with the 801 cross section set and with a set generated using the MCC code.[8] The calculations predict fairly well which of the worth ratios are well matched and which are not, although the prediction of the value of the ratio is not so good for the materials that are not well matched. The calculations do, however, indicate the approximate degree of spectral mismatch necessary to produce the measured worth ratios. The calculated real and adjoint spectra in Assemblies 11 and 12 are matched to the reference within ±(1 to 2) percent, or better, in each group of the 25-group 801 cross-section set, except for the very low energy groups. The matching was slightly better for Assembly 12. The calculations indicate that the fluxes in Assembly 4Z are matched to Assembly 5 to within a few tenths of one percent. Most of the calculations were repeated using the MCC generated cross section set (see Table III-11-I). The worth ratios were predicted somewhat better, but the general conclusions are the same.

The constancy of the measured worth ratios for the absorbing and fissioning materials is an indication of the approximate matching of both the real and adjoint fluxes over the entire energy range. These ratios are not sensitive to small spectrum errors, however. Therefore, provided the real flux is reasonably well matched, their average worth ratio is a good measure of the inverse denominator ratio. The values are also indicated in Table III-11-I.

In summary, then, it should be noted that for a general material containing absorption and scattering (and possibly even fission), the expression for the worth [Eq. (1)] is rather complicated. One has little hope of reconstructing the real and adjoint flux shapes from a number of worth measurements. The usefulness of these measurements lies in comparing the worths measured in

different assemblies, since different materials are sensitive to the spectra in different ways.

### Doppler Effect Measurements

A comparison of the Doppler measurements in the assemblies provides a check of the low energy real and adjoint spectral matching. Nearly all of the Doppler effect in these cores is between 100 eV and 25 keV. The Doppler ratio between two assemblies, $x$ and $y$, for the same sample, is given by

$$\frac{\Delta\rho(\mathrm{Ih})_x}{\Delta\rho(\mathrm{Ih})_y} = \frac{C_x}{C_y}\frac{D_y}{D_x} \cdot \frac{\int \sum_j \left[\phi_j\bar{\phi}_f^*\delta(\nu\Sigma_f)_j - \phi_j\phi_j^*\delta\Sigma_{c+f_j}\right] dV_x}{\int \sum_j \left[\phi_j\bar{\phi}_f^*\delta(\nu\Sigma_f)_j - \phi_j\phi_j^*\delta\Sigma_{c+f_j}\right] dV_y}. \quad (2)$$

The summation is only over the groups in the Doppler energy range, and the integration is over the volume of the sample. For the heavy nuclides, the Doppler effect due to resonance scattering is negligible.

As was the case for the central worths, the Doppler effect ratios between assemblies will be equal to the inverse denominator ratio if the spectra are well matched. Because there is no appreciable scattering term, the Doppler ratios are not sensitive to very small spectral mismatches in the Doppler region. Agreement between the measured Doppler effect ratios and the inverse denominator ratio indicates that the ratio of the gross low energy fluxes to the total fluxes is approximately the same for the two assemblies. The measured Doppler ratios are compared in Table III-11-II with the inverse denominator ratios determined from the central worth measurements, from direct measurement[2,3] and from calculation. The most accurately measured Doppler effect ratios are those for the natural $UO_2$ samples. The values are in fairly good agreement with the measured inverse denominator ratios, although the measured Doppler ratios for 11/5, 12/5 and 11/4Z are slightly low. If one uses the calculated centerline fluxes for Assemblies 5, 11 and 12 (see Paper III-8) to make a spectral correction of the type indicated by Eq. (2), then the Doppler ratio and the inverse denominator ratio for 11/5 and 11/4Z are brought into agreement. The Doppler measurements seem to confirm that the Doppler energy range flux in Assembly 11 is a few percent low as indicated by the spectrum calculations. When the spectral correction is applied to the 12/5 ratio the value reduces from 1.36 ± 0.03 to 1.33 ± 0.03 which is still not quite in agreement with the natural $UO_2$ element ratio of 1.24 ± 0.02. A recent measurement of the natural $UO_2$ Doppler element in Assembly 12 indicated a value somewhat higher, which would tend to bring the 12/5 ratio into agreement with the inverse denominator ratio. The cause of the disagreement in the Assembly 12 measurements has not been isolated, however.

The measured Doppler ratios for the enriched elements are also in agreement with the inverse denominator ratios except in the case of the NNE ratio for 4Z/5, where the NNE elements used were not identical. When the differences between the two NNE elements are taken into account, the discrepancy between the NNE and FE ratios disappear, but the ratio

TABLE III-11-II. Comparison of Measured Doppler Effect Ratios to Measured and Calculated Perturbation Denominator Ratios for Assemblies 11, 12, 4Z and 5

| Ratio Assembly $x$ / Assembly $y$ | Measured Doppler Ratios, Ih/Ih | | | | $C_xD_y/C_yD_x$[a] | | | |
|---|---|---|---|---|---|---|---|---|
| | 1 in. Nat. $UO_2$ FE[a] | 1 in. Enriched $UO_2$ | | | From Central Worth Meas. | From D Meas. | From Multi Group Calc.[c] | |
| | | FE[b] | NE[b] | NNE[b] | | | 801 | MCC |
| 11/5 | 1.36 ± 0.02 | 1.43 ± 0.35 | | | 1.52 ± 0.09 | | 1.68 | 1.48 |
| 12/5 | 1.24 ± 0.02[d] | | | 1.48 ± 0.16 | 1.36 ± 0.03 | | 1.39 | 1.36 |
| 4Z/5 | 0.95 ± 0.02 | 1.12 ± 0.15 | | 1.24 ± 0.07 | 0.98 ± 0.02 | | 1.00 | 0.97 |
| 11/12 | 1.09 ± 0.02 | | | | 1.12 ± 0.06 | 1.03 ± 0.07 | 1.20 | 1.08 |
| 11/4Z | 1.42 ± 0.03 | | 1.48 ± 0.19 | | 1.54 ± 0.09 | | 1.68 | 1.52 |

[a] In order to make the ratios in this section of the table comparable to the measured Doppler ratios, a correction has been applied to the values to account for the fact that the axial flux shapes in the assemblies are different due to different assembly heights. Since the Doppler samples are 12 in. long, they are sensitive to the axial flux shape.

[b] The symbols FE, NE and NNE designate Doppler elements which are freely expanding, constrained to axial expansion and constrained to both axial and radial expansion, respectively.

[c] Refer to note (a) of Table III-11-I.

[d] Recent rerun of the Assembly 12 Nat. $UO_2$ Doppler indicates a preliminary value 5–8% higher.

of the U-235 Doppler effect in Assemblies 4Z and 5 is somewhat outside the known experimental error (see Paper III-3).

### Fission and $BF_3$ Counter Results

The measured and calculated fission ratios for the four assemblies are given in Table III-11-III. The ratios are generally in good agreement among the assemblies, and they tend to confirm the real flux spectral matching indicated by the other measurements. Comparison with multigroup calculations indicates, however, that the fission ratios are not very sensitive to small spectrum changes. Large spectral

TABLE III-11-III. Central Fission Ratios

| Assembly | Measured | | | Calc.[a] |
|---|---|---|---|---|
| | U-238/U-235 | Pu-239/U-235 | U-234/U-235 | U-238/U-235 |
| 5 | 0.0238 ± .0008 | 0.968 ± .026 | 0.166 ± 0.005 | 0.0261 |
| 4Z | 0.0238 ± .0007 | 0.967 ± .025 | 0.172 ± 0.004 | 0.0260 |
| 11 | 0.0238 ± .0008 | 0.986 ± .026 | 0.176 ± 0.004 | 0.0259 |
| 12 | 0.0232 ± .0008[b] | — | — | 0.0263 |

[a] Calculations were done with the one-dimensional diffusion code MACH-1[6] using a cross section set generated by the MCC code.[8]

[b] This measurement was actually made in ZPR-9, Assembly 18, which is an assembly identical to ZPR-9, Assembly 12.

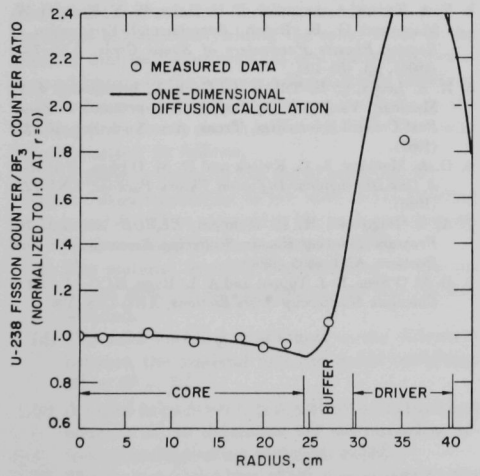


Fig. III-11-3. Measured and Calculated Ratios of U-238 Fission Counter to $BF_3$ Counter Versus Radial Position for ZPR-9, Assembly 12 (Normalized to 1.0 at $r = 0$). *ANL Neg. No. 112-9001.*

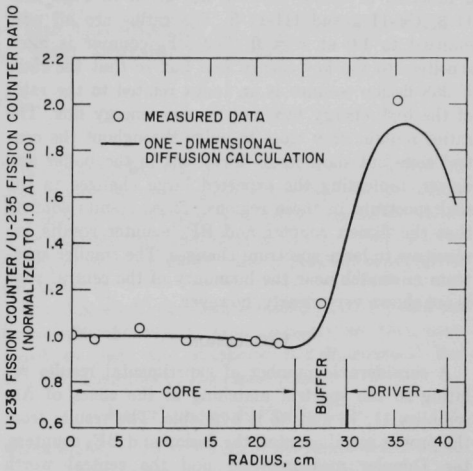


Fig. III-11-4. Measured and Calculated Ratios of U-238 Fission Counter to U-235 Fission Counters Versus Radial Position for ZPR-9, Assembly 12 (Normalized to 1.0 at $r = 0$). *ANL Neg. No. 112-8997.*

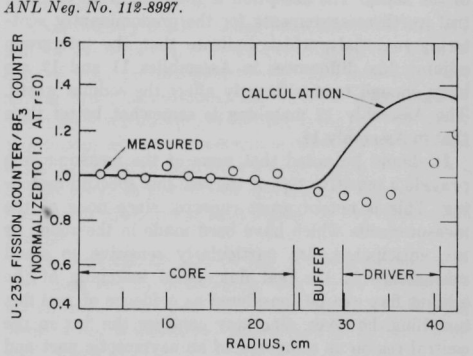


Fig. III-11-5. Measured and Calculated Ratios of U-235 Fission Counter to $BF_3$ Counter Versus Radial Position for ZPR-9, Assembly 12 (Normalized to 1.0 at $r = 0$). *ANL Neg. No. 112-9093.*

mismatches at the higher energy end of the spectrum will be indicated by the ratio of the U-238 fission detector to either the U-235 or Pu-239 fission detectors, since the U-238 detector reacts only to neutrons above its fission threshold of approximately 1.1 MeV. The fission detectors yield little information on the Doppler energy flux.

U-235 fission, U-238 fission and $BF_3$ counter measurements were also made on Assembly 12 along the radius through the central zone, buffer and driver. The ratios of the results for these three counters as

a function of radial position are given in Figs. III-11-3, III-11-4 and III-11-5. The ratios are all normalized to 1.0 at $r = 0$. The $BF_3$ counter is more sensitive to the low energy real flux so that the ratio U-238 fission counter is an index related to the ratio of the high energy flux and the low energy flux. The ratios remain very close to unity throughout the central zone but show large deviations in the buffer and driver, indicating the expected large changes in the real spectrum in these regions. These results confirm that the fission counter and $BF_3$ counter results are sensitive to large spectrum changes. The smaller spectrum mismatch near the boundary of the central zone is not shown very clearly, however.

## Conclusion

A considerable number of experimental results relating to the spectral matching in the zones of Assemblies 11, 12 and 4Z is available. The results from the proton recoil counter, the fission and $BF_3$ counters, the Doppler measurements and the central worth measurements, for most of the materials, all tend to confirm reasonable spectral matching at the centers of the zones. The exception is the data from the central worth measurements for the predominantly scattering materials, which indicate that the intergroup adjoint flux differences in Assemblies 11 and 12 are large enough to significantly affect the sodium worth. The Assembly 12 matching is somewhat better than that in Assembly 11.

It should be noted that none of the measurements provide a sensitive test of the real flux spectral matching. This is not of great concern, since none of the measurements which have been made in the zones, or are anticipated, are particularly sensitive to small mismatches in the real flux. Good matching of the adjoint flux can be considered as evidence of real flux matching, however. One may consider the flux in the central region as composed of an asymptotic part and spatial transient components which originate at the boundary of the zone and decay toward the center. The decay constants for the transients are the same for both the real and the adjoint flux, and, if the mismatch at the boundary is about the same for both the real and the adjoint fluxes, then one would expect about the same degree of matching at the center. Therefore one would, for example, expect the real flux to be very well matched in Assembly 4Z.

Good adjoint flux matching is necessary if the zones are to be used for sodium void measurements. The central worth data from Assemblies 11 and 12 indicate that the adjoint spectrum is probably not good enough to do accurate sodium void measurements in the small zones. Small zones are, however, not too suitable for off-center sodium void measurements, because the spatial flux shape (and consequently the leakage) is generally changed considerably by the high enrichment driver.

On the other hand, the data indicate that the spectral matching is adequate for Doppler measurements in any of the assemblies, and it seems that it will be possible to do Doppler measurements in even smaller zones.

## References

1. E. F. Bennett, *Experimental Neutron-Spectrum Comparison for a Zoned and a Homogeneous Fast Critical Assembly*, Trans. Am. Nucl. Soc. **10**, 271 (1967).
2. R. A. Karam and L. G. LeSage, *Zoned-Core Concepts*, Trans. Am. Nucl. Soc. **10**, 270 (1967).
3. R. A. Karam, A. Ancarani, F. H. Helm, W. Y. Kato, G. W. Main and G. K. Rusch, *Measured Physics Parameters in a Zoned Fast Uranium Carbide Core, Assembly 4Z*, ANL-7281 (1967), pp. 17 and 39.
4. R. A. Karam, A. Ancarani, F. H. Helm, W. Y. Kato, G. W. Main and G. K. Rusch, *Experimental Verification of Reactor Physics Parameters of Zoned Cores*, ANL-7320 (1966), pp. 403–420.
5. R. A. Lewis, C. E. Till, E. G. Groh, L. LeSage and J. E. Marshall, *Verification of Doppler Measurements in Zoned Fast Critical Assemblies*, Trans. Am. Nucl. Soc. **10**, 270 (1967).
6. D. A. Meneley, L. C. Kvitek and D. M. O'Shea, *MACH-1, A One-Dimensional Diffusion Theory Package*, ANL-7223 (1966).
7. A. L. Rago and H. H. Hummel, *ELMOE: An IBM 704 Program Treating Elastic Scattering Resonances in Fast Reactors*, ANL-6805 (1966).
8. D. M. O'Shea, B. J. Toppel and A. L. Rago, *MCC—A code to Calculate Multigroup Cross Sections*, ANL-7318 (1967).

# III-12. A Simple Flux-Synthesis Method for the Calculation of the Sodium-Void Effect in Reflected Single-Zone Fast Breeder Reactors[1]

A. Travelli

## Introduction

Multidimensional computations of the sodium-void effect will often be necessary for complicated geometries in the development of the large sodium-cooled fast breeder reactor. However, the high cost of these computations makes the more economical approximate techniques based on flux synthesis very attractive for simple geometries.

This paper deals with a test of a synthesis prescription which appears to be adequate for large single-zone reflected reactors. The procedure is applied to the analysis of the sodium-void effect in Assemblies No. 2[2] and 3[3] of ZPR-6. The results are compared with multidimensional computations.

## Procedure

For cylindrical reactors, the adopted synthesis technique assumes that both the real and the adjoint fluxes be separable, in a certain sense, in the radial and axial directions over the whole reactor.

One-dimensional calculations in $r$- and $z$-geometry are run through a fast-converging iteration scheme by modifying the transverse bucklings to obtain a pair of consistent calculations yielding the same value of the effective multiplication constant and transverse bucklings adding up to the corresponding material buckling. A bloc diagram indicating the steps involved in the iterating procedure is shown in Fig. III-12-1. They may be summarized as follows:

(a) A guess is made for the radial buckling, $B_R^2$ .

(b) An axial calculation is run with radial buckling equal to $B_R^2$ to determine the corresponding effective multiplication constant, $k_z(B_R^2)$.

(c) The material buckling corresponding to the obtained effective multiplication constant, $B^2(k_z)$, is found.

(d) The axial buckling is obtained as the difference between the material and the radial bucklings, $B_z^2 = B^2 - B_R^2$ .

(e) A radial calculation is run with an axial buckling equal to $B_z^2$ to determine the corresponding effective multiplication constant, $k_R(B_z^2)$.

(f) The material buckling which corresponds to the obtained value of the effective multiplication constant, $B^2(k_R)$, is found.

(g) The radial buckling for the next iteration is obtained as the difference between the material and the axial bucklings, $B_R^2 = B^2 - B_z^2$ .

When all steps from (a) to (g) have been completed, the calculation may resume from step (b). The procedure can be repeated indefinitely, until two successive values of the effective multiplication constant are found to be closer, in absolute value, than a prefixed convergence parameter $\delta$.

The flux $\phi(r,E)$ obtained in radial geometry and the flux $\psi(z,E)$ obtained in axial geometry are then combined to yield the synthetic two-dimensional flux $\Phi(r,z,E)$, according to the prescription

$$\Phi(r,z,E) = \phi(r,E)\psi(z,E)\phi_{fm}^{-1}(E), \qquad (1)$$

where $\phi_{fm}(E)$ is the spectrum of the fundamental mode. An analogous expression is used for the adjoint flux and the corresponding space-dependent sodium-void effect is obtained by means of a two-dimensional first-order perturbation calculation.

A satisfactory mathematical justification for Eq. (1) and for the definition of consistent calculations may be derived from perturbation theory. The method offers, among other advantages, the obvious advantage of insuring the separability of the flux in the various spatial coordinates when the spectrum is constant, a condition which is known to hold over a wide region of the core. It also provides the correct spectrum at the center of the reactor whenever at least one of the two dimensions is large.

The convergence rate of the iteration procedure is very fast, and by introducing some simple simplifying assumptions it can be shown that at every iteration the error in $k_{eff}$ is multiplied approximately by the factor $\epsilon_z\epsilon_R$ , where

$$\epsilon_z = \left(\frac{dk_z}{dB_R^2}\right) \Big/ \left(\frac{dk}{dB^2}\right),$$

$$\epsilon_R = \left(\frac{dk_R}{dB_z^2}\right) \Big/ \left(\frac{dk}{dB^2}\right).$$

The derivatives are calculated at the point to which the iteration converges. On the basis of perturbation theory it can be shown that $\epsilon_z$ and $\epsilon_R$ are much smaller than unity whenever the perturbation introduced by the axial or radial reflector, respectively, is small. Two iterations were found to be ample in all the tests run in connection with this work. The computing time needed to perform a full iteration is greatly reduced by the fact that the only search needed in the iteration concerns the determination of the material buckling, which is obtained in a space-independent calculation.

TABLE III-12-I. Compositions of ZPR-6 Assemblies No. 2 and 3 (atoms/cm³) × $10^{24}$

| Isotope | Core | Blanket |
|---|---|---|
| U-235 | 0.002285 | 0.000081 |
| U-238 | 0.009853 | 0.039930 |
| C | 0.012900 | — |
| Na | 0.007910 | — |
| Fe | 0.010380 | 0.004223 |
| Cr | 0.002983 | 0.001214 |
| Ni | 0.001390 | 0.000566 |

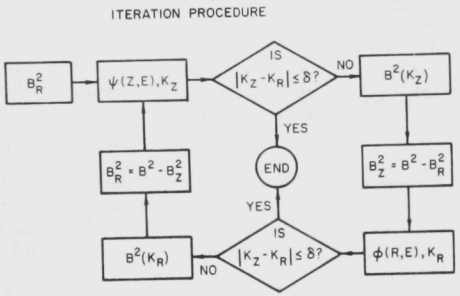


Fig. III-12-1. Iteration Procedure for Consistent Calculations. *ANL Neg. No. 112-9030.*

TABLE III-12-II. Comparison of Synthesis with Two-Dimensional Calculations

| | Assembly No. 2 | | Assembly No. 3 | |
|---|---|---|---|---|
| | Synthesis | 2-D | Synthesis | 2-D |
| $k_{eff}$ | 0.9990 | 0.9980 | 0.9976 | 0.9965 |
| $\epsilon_R$ | ~0.0033 | — | ~0.050 | — |
| $\epsilon_z$ | ~0.0017 | — | ~0.0015 | — |
| Total Na-void effect ($10^{-2}$ $\delta k/k$) | −1.998 | −2.032 | −1.682 | −1.714 |
| Central Na-void effect ($10^{-5}$ $\delta k/k$/kg) | −5.573 | −5.684 | −3.374 | −3.459 |
| Perturbation normalization integral, $H$(cm²) | 357.4 | 355.5 | 532.2 | 527.1 |

No iteration is needed for the calculation of the adjoint fluxes, because the same values of the transverse bucklings and of the effective multiplication constant that satisfy the requirements for a consistent pair of real calculations satisfy also the requirements for a consistent pair of adjoint calculations.

## Application

The synthesis method described in this paper was applied to the calculation of the sodium-void effect in Assemblies No. 2 and 3 of ZPR-6. Calculations of the sodium-void effect in the two assemblies have been previously reported.[4]

Both cores are cylindrical in shape, have the same composition fueled by U-235, and are reflected axially and radially by the same type of depleted-uranium blanket. The homogenized core and blanket compositions are given in Table III-12-I. The reactors have very different length-to-diameter ratios, approximately equal to unity in Assembly No. 2 ($L \approx D \approx 92$ cm) and to 1/3 in Assembly No. 3 ($L = 50.8$ cm, $D = 155$ cm). The shape affects considerably both the sodium worth at any point in a reactor and its critical size. The experimental critical volume is close to 610 liters for Assembly No. 2 and to 955 liters for Assembly No. 3. The blanket thickness is 30 cm in both reactors and in both directions.

Two-dimensional calculations of the sodium-void effect in both assemblies were made in $r,z$ geometry by using the two-dimensional diffusion theory code CANDID[5] combined with the two-dimensional diffusion perturbation code PERC.[6]

The unperturbed cross sections were derived from the Argonne Set 224[7], taking into account the data reported by P. White[8] for U-235 and by J. Garg et al.[9] for U-238. The elastic downscattering and transport cross sections of the light materials (carbon, sodium, iron, chromium and nickel) were calculated by the ELMOE[10] code and averaged over the spectrum of the fundamental mode. The perturbed cross sections were obtained with an analogous procedure, for a core composition from which sodium had been entirely removed. Non-linear effects of sodium voiding on the perturbed cross sections were found to be negligible. The use of these cross sections has in the past given very good agreement between calculated and measured values of the sodium void coefficient in Assemblies No. 2 and 3.[4]

The iterations leading to a consistent pair of real calculations were made for both assemblies according to the iteration procedure described in Fig. III-12-1. In order to minimize any spurious effect that might distort the comparison between the results of these calculations and the corresponding results of the two-dimensional calculations, the same CANDID code, and the same reactor sizes, cross sections, mesh distributions, and tight convergence criteria were used as in the two-dimensional calculations. In both assemblies any iteration was found to reduce the error in $k$ by at least four orders of magnitude, and two iterations were found to be amply sufficient to meet the most stringent convergence criteria.

The two-dimensional real and adjoint fluxes were then synthesized according to Eq. 1 and the result was used to calculate the space-dependent sodium void effect in first-order diffusion perturbation theory by means of the PERC code.

The main results of the calculations are given in Table III-12-II, where $H$ represents the normalization

integral of the perturbation expression, defined by:

$$H = \frac{\int_v dv \int_E dE \int_{E'} dE'\, \phi^*(E,r,z)\chi(E)\nu\Sigma_f(E')\phi(E',r,z)}{\int_v dv \int_E dE \int_{E'} dE'\, \phi^*(E,r,z)\phi(E',r,z)}.$$

The values of $\epsilon_R$ and $\epsilon_z$, which determine the convergence rate of the iteration procedure, are very small in both reactors. Accordingly, the convergence rate found in the actual calculations was found to be very fast and in good agreement with the predicted convergence rate.

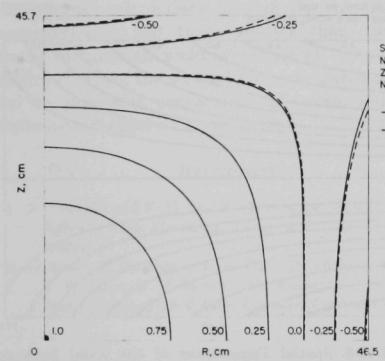


FIG. III-12-2. Spatial Dependence of the Spectral Component of the Sodium-void Effect in ZPR-6 Assembly No. 2. (Full Lines Correspond to Synthesis Calculations, Dotted Lines to Two-dimensional Calculations.) *ANL Neg. No. 112-8957.*

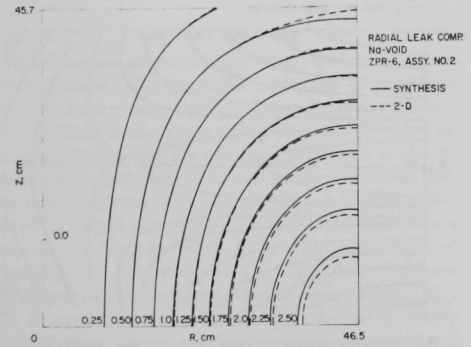


FIG. III-12-3. Spatial Dependence of Radial Leakage Component of the Sodium-void Effect in ZPR-6 Assembly No. 2. (Full Lines Correspond to Synthesis Calculations, Dotted Lines to Two-dimensional Calculations.) *ANL Neg. No. 112-8953.*

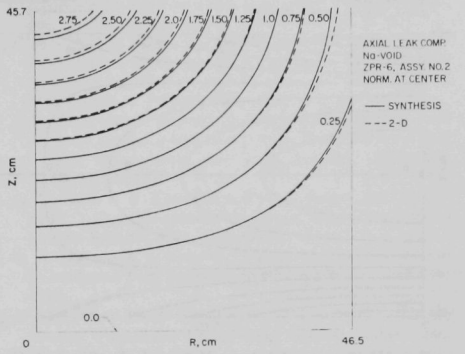


FIG. III-12-4. Spatial Dependence of the Axial Leakage Component of the Sodium-void Effect in ZPR-6 Assembly No. 2. (Full Lines Correspond to Synthesis Calculations, Dotted Lines to Two-dimensional Calculations.) *ANL Neg. No. 112-8952.*

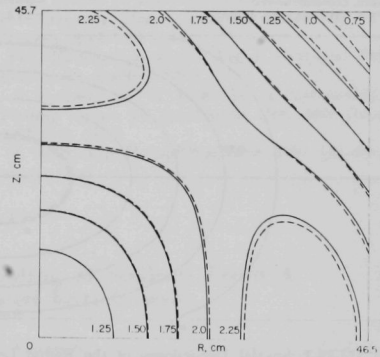


FIG. III-12-5. Spatial Dependence of the Total Sodium-void Effect in ZPR-6 Assembly No. 2. (Full Lines Correspond to Synthesis Calculations, Dotted Lines to Two-dimensional Calculations.) *ANL Neg. No. 112-8004.*

The effective multiplication constant appears to be consistently underestimated by only 0.1% by the synthesis calculations.

The reactivity effect due to total removal of sodium from the core is also consistently underestimated by approximately 2%, and an error of approximately the same magnitude and in the same direction is found for the central value of the sodium worth. Approximately half of the error found in the calculation of these sodium-void effects is due to the fact that $H$ is overestimated by approximately 1%. The value of $H$ is probably affected by the calculation of the flux in the blanket, which cannot be predicted very accurately by the synthesis in the region which is close to the corners of the core.

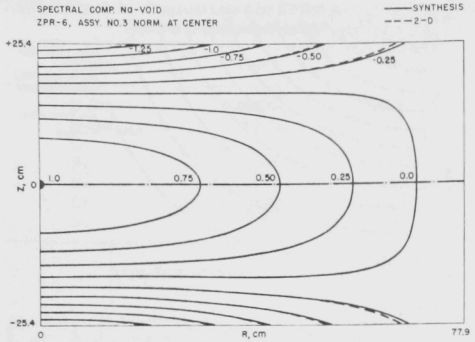


FIG. III-12-6. Spatial Dependence of the Spectral Component of the Sodium-void Effect in ZPR-6 Assembly No. 3. (Full Lines Correspond to Synthesis Calculations, Dotted Lines to Two-dimensional Calculations.) *ANL Neg. No. 112-8956.*

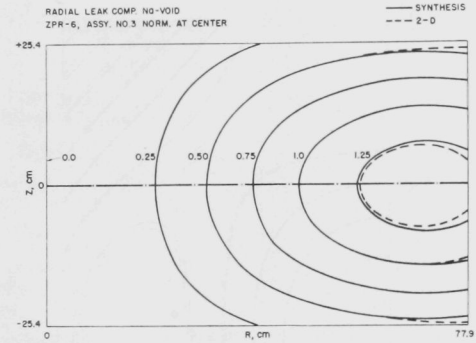


FIG. III-12-7. Spatial Dependence of the Radial Leakage Component of the Sodium-void Effect in ZPR-6 Assembly No. 3. (Full Lines Correspond to Synthesis Calculations, Dotted Lines to Two-dimensional Calculations.) *ANL Neg. No. 112-8954.*

A comparison more significant in pointing out the agreement or disagreement between synthesis and two-dimensional calculations with little danger of compensating errors concerns the spatial dependence of the sodium-void effect. The results obtained by the PERC code in every mesh interval with both methods, for both reactors, and for every component of the sodium-void effect, were normalized to the central value of the sodium-void effect and interpolated parabolically in two dimensions.[11] The corresponding isocurves were then plotted automatically by means of a computer code using the PLOT[12] routine. The results are shown in Figs. III-12-2 through III-12-9, where continuous curves represent the result of synthesis calculations and dotted curves represent the result of two-dimensional calculations.

The agreement between the two sets of curves is strikingly good in all cases. Of particular interest is the match of the spectral components, whose spatial dependence is caused exclusively by the presence of the reflector. The various leakage components are also accurately calculated at all points which are not extremely close to the reflector and, as a result, an excellent agreement between synthesis and two-dimensional calculations is found even in the comparison of the somewhat bizarre shapes that represent the isocurves for the total sodium-void effect.

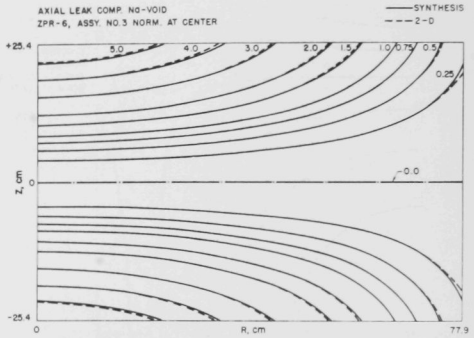


FIG. III-12-8. Spatial Dependence of the Axial Leakage Component of the Sodium-void Effect in ZPR-6 Assembly No. 3. (Full Lines Correspond to Synthesis Calculations, Dotted Lines to Two-dimensional Calculations.) *ANL Neg. No. 112-8958.*

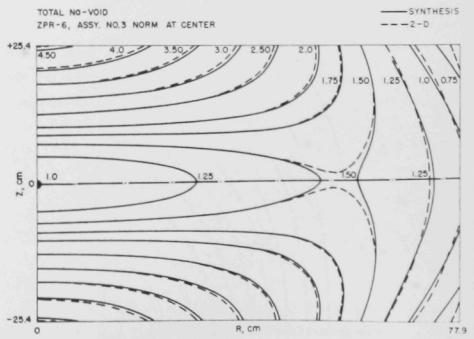


FIG. III-12-9. Spatial Dependence of the Total Sodium-void Effect in ZPR-6 Assembly No. 3. (Full Lines Correspond to Synthesis Calculations, Dotted Lines to Two-dimensional Calculations.) *ANL Neg. No. 112-8955.*

The fact that the agreement is approximately as good for Assembly No. 3 as for Assembly No. 2 confirms the fact that the method requires only one of the two reactor dimensions to be large in order to give satisfactory results.

## Conclusion

The synthesis method which has been outlined in this work appears to be adequate for the calculation of the sodium-void effect in large single-zone reflected fast breeder reactors with an accuracy of 2–3%. The computing time needed for the synthesis calculations of Assemblies No. 2 and 3 was approximately 400 times shorter than the time required by the two-dimensional calculations used in the comparison and approximately 100 times shorter than two-dimensional calculations yielding results of comparable accuracy.[13] Thus, the method could be particularly useful in programs concerning the evaluation of the sodium-void effect on a survey basis.

## References


1. A. Travelli and F. H. Helm, *Calculation of the Sodium-Void Effect by Flux Synthesis*, Trans. Am. Nucl. Soc., **10**, 275 (1967).
2. G. Rusch, E. R. Böhme, L. R. Dates, S. Grifoni, W. Y. Kato, G. W. Main, H. H. Meister, M. Nozawa and R. L. Stover, *Investigation of a 600-Liter Uranium Carbide Core (ZPR-6 Assembly 2)*, Reactor Physics Division Annual Report, July 1, 1963 to June 30, 1964, ANL-7010, pp. 91–112.
3. F. H. Helm, W. Y. Kato, G. Main and G. K. Rusch, *Physics Parameters and Sodium-Void Coefficients in a 950-Liter Pancake Core*, Reactor Physics Division Annual Report, July 1, 1964 to June 30, 1965, ANL-7110, pp. 101–113.
4. F. H. Helm and A. Travelli, *Calculation of the Sodium-Void Effect in Large Carbide Cores*, Proc. Conference on Fast Critical Experiments and Their Analysis, ANL-7320, (1966) pp. 369–374.
5. G. K. Leaf, A. S. Kennedy and G. J. Jensen, *ANL-CANDID, A Two-Dimensional Diffusion Theory Code Based on CANDID-2D*, ANL-7305 (1967).
6. G. K. Leaf and A. S. Kennedy, *PERC—A Two-Dimensional Perturbation Code Based on Diffusion Theory*, ANL-7304 (1966).
7. D. M. O'Shea, H. H. Hummel, W. B. Loewenstein and D. Okrent, *Twenty-Six Group Cross Sections*, Trans. Am. Nucl. Soc., **7**, 242 (1964).
8. P. White, *Measurements of the U-235 Neutron Fission Cross Section in the Energy Range From 0.04–14 MeV*, J. Nucl. Energy, Parts A and B, **19**, 325 (1965).
9. J. Garg, et al., *Neutron Resonance Spectroscopy III, Th-232 and U-238*, Phys. Rev. **134B**, 985 (1964).
10. A. Rago and H. H. Hummel, *ELMOE: An IBM-704 Program Treating Elastic Scattering Resonances in Fast Reactors*, ANL-6805 (1964).
11. L. Fox, *Mathematical Tables*, Vol. I, (National Physical Laboratory, London, 1956).
12. G. A. Robinson and R. F. Krupp, *A Cathode-Ray Tube Plotting System for the Control Data 3600 Computer*, ANL-7121 (1965).
13. F. H. Helm, Argonne National Laboratory (private communication).


# III-13. Two-Dimensional Study of Voiding of Sodium From A Fast Reactor Core With Zoned Enrichment

V. Z. Jankus and H. H. Hummel

Evidence is accumulating that many important characteristics of large fast reactors can be calculated well by rather simple prescriptions for the neutronics calculations. Some years ago it was noted[1] that, for large uniform cores the spectral component of the sodium void effect, which is essentially dependent only on core spectrum, could be rather accurately calculated by use of a fundamental mode flux. The same is true of the Doppler effect for a uniform core, which also depends essentially on core spectrum (compare, for example, the bare and reflected core cases in Ref. 2). It would naturally be expected that as a reactor core becomes larger, the fundamental mode spectrum would be increasingly valid for calculation of spectrum-dependent quantities, particularly those which are most important at the center of the core. It is also to be expected that as core sizes increase, separability of solutions for various dimensions will become more valid, since reflector effects become decreasingly important. The extent to which this seems to be true as shown in recent studies[3] is surprising, however. What seems most surprising is how well the leakage component of the sodium void effect, which depends on the gradient of the flux, is given by a product of one-dimensional solutions. Good results seem to be obtained even for a "chopped" bare core solution in a reflected core.

The study in Ref. 3 was for a uniform core. It seemed to be of interest to see how well the use of separable solutions worked in calculating the sodium void effect in a core with zoned enrichment. The reactor selected for this study was the Combustion En-

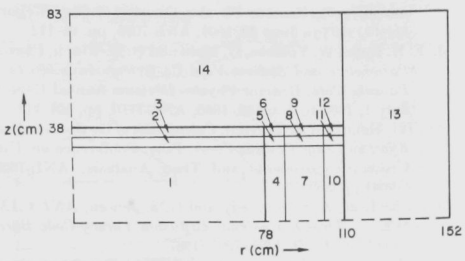


FIG. III-13-1. Regions for Sodium Void Calculation in C.E. 1000 MWe Carbide Reactor. *ANL Neg. No. 112-8939.*

TABLE III-13-I. MATERIAL DENSITY IN THE FOUR ZONES OF THE REACTOR, $10^{24}$ a/cc

| Material | Inner Core | Outer Core | Radial Blanket | Axial Blanket |
|---|---|---|---|---|
| U[a] | 0.006421 | 0.006108 | 0.015683 | 0.007784 |
| Pu(2)[b] | 0.001364 | — | — | — |
| Pu(3)[c] | — | 0.001770 | — | — |
| SS[d] | 0.006655 | 0.006655 | 0.010109 | 0.006655 |
| Na | 0.014630 | 0.14630 | 0.009460 | 0.014630 |
| C | 0.008443 | 0.008443 | 0.014841 | 0.008443 |
| FP | 0.000480 | 0.000480 | — | — |
| Fertile atom / Fissile atom | 6.61 | 5.07 | — | — |

[a] 99.7 a/o U-238, 0.3 a/o U-235.

[b] 69.3 a/o PU-239, 25.6 a/o PU-240, 4.1 a/o PU-241, 1.0 a/o PU-242.

[c] 68.1 a/o PU-239, 26.6 a/o PU-240, 4.2 a/o PU-241, 1.1 a/o PU-242.

[d] 69.44 a/o Fe, 8.62 a/o Ni, 20.53 a/o Cr, 1.03 a/o Mo, 0.38 a/o W.

gineering (C.E.) carbide-fueled 1000 MWe design.[4,5] This case was of special interest because it represented a design in which no compromise was made to make the sodium void effect less positive. The core is somewhat pancaked, so that it might be expected that axial leakage effects would be large enough to cause difficulties in a one-dimensional cylindrical calculation designed to take account of the radial enrichment zoning. Difficulties were in fact encountered in this type of calculation when group-dependent axial bucklings obtained from an independent calculation with different cross sections for the same geometry were used.[5] In the present calculations a group-independent axial buckling, adjusted to make the system critical, was used in the one-dimensional cylindrical calculation.

A two-dimensional diffusion theory calculation in 22 groups was first performed with the CANDID code,[6] using the geometrical layout in Fig. III-13-1. The dimensions are those of the C.E. design. The core (Regions 1–12 in Fig. III-13-1) has a height of 76 cm and a diameter of 220 cm. The thickness of the axial blanket (Region 14) is 45 cm and that of the radial blanket (Region 13) is 42 cm. The core has two enrichment zones of approximately equal volume, the radius of the inner zone being 78 cm.

Using as a guide the data given in Refs. 4 and 5 for masses and compositions of various materials at equilibrium concentration, atom densities were determined for the various regions. The reactor was simulated with four homogenized compositions (plutonium was neglected in the blankets), and a criticality search was performed using CANDID by varying the plutonium fraction in the fuel. Final concentrations of materials are given in Table III-13-I. Presumably because of differences in cross section sets and to a lesser extent because of the omission of plutonium in the blanket, the total fertile-to-fissile atom ratio obtained in the inner core was 6.61 and in the outer core was 5.07, as compared to ratios of 8.61 for the inner core and 6.56 for the outer core obtained by C.E. A difference in calculation method may have also had some influence since C.E. used an iteration between one-dimensional radial and axial calculations, using group-dependent bucklings.

For the calculation of the sodium void effect the reactor core was subdivided into 12 regions, with the finest divisions at the edges of the core. The size and designation of the regions is displayed in the scale drawing, Fig. III-13-1. Sodium void calculations were performed using the two-dimensional perturbation code PERC.[7] The void coefficient was separated into two components: capture plus scattering (elastic plus inelastic) and leakage. The results are given in Table III-13-II.

Using the compositions obtained in the two-dimensional calculations, a one-dimensional radial calculation and a one-dimensional axial calculation for the inner core enrichment zone were carried out. In each case an energy independent transverse buckling was used which was varied to obtain criticality. This buckling was $7.489 \times 10^{-4}$ cm$^{-2}$ for the radial case and $1.865 \times 10^{-4}$ cm$^{-2}$ for the axial case. For the radial case the axial flux was assumed to be a "chopped" cosine, while in the axial case a "chopped" $J_0$ function was used. Perturbation calculations of the sodium void effect were done using the MACH 1 Program.[8] Results of the radial calculations are compared with the two-dimensional calculations in Tables III-13-II and III-13-III. Disagreement between the two sets of results for the removal plus scattering component is significant only near the core-reflector interface and in the corners, as would be expected. For the leakage component, agreement is surprisingly good throughout the

core. Agreement for voiding the whole core is quite close for both components. The consistent disagreement in the case of the axial calculation is probably due to an inaccurate evaluation of the denominator of the perturbation expression. This denominator was based on a $J_0$ flux for a radially bare reactor.

A significant result from the above comparison is that even in the case of zoned enrichment quite good results are obtained with the use of separable flux solutions. Also, the use of group-dependent bucklings or of adjoint weighting of transverse leakage does not appear to be necessary for accurate calculation of the sodium void effect in the core.

A. Travelli and F. Helm[3] have obtained excellent agreement between two-dimensional calculations for sodium void coefficient in a uniform core and calculations based on a simple flux synthesis. It is assumed in the latter case that the flux (and adjoint) in the core is adequately represented by a product of fluxes obtained in separate radial and axial calculations divided (somewhat arbitrarily) by the spectrum of the fundamental mode:

$$\phi(r,z,E) = R(r,E)\cdot Z(z,E)/\Phi(E).$$

Use of this synthetic flux leads to a better overall agreement with results of two-dimensional calculations than use of each of the component fluxes taken separately multiplied by a "chopped" bare core solution. For the sake of expediency we could try this idea also for our zoned core using axial functions and fundamental mode spectra appropriate for each zone. The results of the calculations may require application of a slightly different normalization factor in each zone. To be really useful this synthesis method, however, still needs a prescription for determination of the criticality of a zoned core.

The need of a supplementary prescription for the synthetic flux is obviated if one determines criticality by a procedure based upon the synthesis of the two-dimensional flux (and adjoint) from functions obtained in one-dimensional calculations. One such simple method is based upon an assumption that the flux in each energy group, $i$, is adequately represented by a product of a radial function, $R_i(r)$, and an axial function $Z_i(z)$. Invocation of the variational principle shows that each of these one-dimensional fluxes should be determined from a one-dimensional diffusion calculation[9] (with incident energy dependent fission spectrum). Every cross section used in the calculation is an average of the cross sections in the transverse direction bilinearly weighted with the fluxes obtained in the transverse calculation. The solution of such coupled diffusion theory calculations should require less than twice the machine time presently needed for

TABLE III-13-II. Components of Sodium Void Reactivity ($100\cdot\Delta k/k$) from Two-Dimensional and Radial Calculations

| Region | Two-Dimensional | | Radial Calculation | | |
|---|---|---|---|---|---|
| | Removal and scat. | Leakage | Removal and scat. | Leakage | Radial leakage |
| 1 | 3.432 | −0.960 | 3.433 | −1.007 | −0.137 |
| 2 | 0.269 | −0.334 | 0.234 | −0.358 | −0.009 |
| 3 | 0.225 | −0.415 | 0.174 | −0.418 | −0.007 |
| 4 | 0.420 | −0.219 | 0.425 | −0.215 | −0.093 |
| 5 | 0.033 | −0.053 | 0.029 | −0.054 | −0.006 |
| 6 | 0.027 | −0.066 | 0.022 | −0.064 | −0.005 |
| 7 | 0.633 | −0.693 | 0.639 | −0.696 | −0.517 |
| 8 | 0.049 | −0.105 | 0.044 | −0.107 | −0.035 |
| 9 | 0.041 | −0.116 | 0.032 | −0.111 | −0.026 |
| 10 | 0.209 | −0.470 | 0.213 | −0.469 | −0.421 |
| 11 | 0.016 | −0.046 | 0.015 | −0.048 | −0.029 |
| 12 | 0.013 | −0.043 | 0.011 | −0.044 | −0.021 |
| Total | 5.366 | −3.518 | 5.271 | −3.588 | −1.306 |

TABLE III-13-III. Correctional Factors for Sodium Void Reactivity Components Obtained in Simple One-Dimensional Calculations

| Region | Radial Calculation | | Axial Calculation | |
|---|---|---|---|---|
| | Removal and scat. | Leakage | Removal and scat. | Leakage |
| 1 | 1.00 | 0.95 | 1.21 | 1.19 |
| 2 | 1.15 | 0.93 | 1.20 | 1.18 |
| 3 | 1.30 | 0.99 | 1.20 | 1.28 |
| 4 | 0.99 | 1.02 | | |
| 5 | 1.14 | 0.98 | | |
| 6 | 1.23 | 1.08 | | |
| 7 | 0.99 | 1.00 | — | — |
| 8 | 1.11 | 0.98 | — | — |
| 9 | 1.28 | 1.04 | — | — |
| 10 | 0.98 | 1.00 | — | — |
| 11 | 1.07 | 0.96 | — | — |
| 12 | 1.18 | 0.98 | — | — |

determination of criticality based upon the equality of the sum of transverse bucklings to the material buckling. It would provide a synthetic flux in Travelli's form without the need of a supplementary prescription, and would be directly applicable also to the zoned cores, albeit with diminished accuracy.

The total reactivity effect for complete voiding of sodium from the core obtained in the present calculations, assuming linearity with sodium content, is $+1.9\%$ $k$, which is lower than the value estimated in COO-285.[10] This difference is probably due more to the round-about method used in Ref. 10 than to a difference in cross sections. Uncertainty in the Pu-239 fission cross section is probably the most important

TABLE III-13-IV. Pu-239 Fission Cross Sections, barns

| Group | $E_L$ | Used In Present Work | Proposed For ENDF/B |
|---|---|---|---|
| 1 | 3.68 MeV | 1.90 | 1.95 |
| 2 | 2.27 | 1.95 | 2.01 |
| 3 | 1.351 | 1.97 | 1.92 |
| 4 | 0.820 | 1.82 | 1.76 |
| 5 | 0.498 | 1.64 | 1.62 |
| 6 | 0.302 | 1.54 | 1.49 |
| 7 | 0.183 | 1.54 | 1.48 |
| 8 | 0.110 | 1.52 | 1.52 |
| 9 | 0.0674 | 1.48 | 1.51 |
| 10 | 0.0409 | 1.46 | 1.48 |
| 11 | 0.0248 | 1.51 | 1.62 |
| 12 | 15.0 keV | 1.78 | 1.83 |
| 13 | 9.12 | 1.88 | 2.10 |
| 14 | 4.31 | 2.35 | 2.51 |
| 15 | 2.61 | 2.98 | 3.01 |
| 16 | 2.03 | 3.64 | 3.75 |
| 17 | 1.23 | 4.33 | 4.53 |
| 18 | 0.961 | 5.10 | 5.80 |
| 19 | 0.583 | 5.90 | 7.72 |
| 20 | 0.275 | 7.55 | 11.8 |
| 21 | 0.101 | 10.4 | 17.3 |
| 22 | 0.029 | 9.60 | —[a] |

[a] Not available.

single cause of uncertainty in sodium void effect calculations. Values of this cross-section used in the present calculation are compared with values based on parameters proposed for the ENDF/B compilation[11] in Table III-13-IV. The differences are relatively small except in the energy region below about 1 keV, in which the proposed ENDF/B values are higher. It is estimated that this variation in cross sections would correspond to a lowering of the positive sodium void effect for complete voiding of the core by about 0.5%$k$.

### References


1. H. H. Hummel, K. Phillips and A. Rago, *Calculations of Sodium Void Reactivity Effect for Large Fast Oxide Reactors in Spherical and Slab Geometry*, Proc. Conference on Breeding, Economics and Safety in Large Fast Power Reactors, October 7–10, 1963, ANL-6792, (1963) p. 65.
2. D. Okrent, *Summary of Intercomparison Calculations*, Proc. Conference on Safety, Fuels, and Core Design in Large Fast Power Reactors, October 11–14, 1965, ANL-7120, (1965) p. 3.
3. A. Travelli and F. Helm, *Calculation of the Sodium-Void Effect by Flux Synthesis*, Trans. Am. Nucl. Soc. **10**, 275 (1967).
4. *Liquid Metal Fast Breeder Reactor Design Study*, CEND-200 (1964).
5. *An Evaluation of Four Design Studies of a 1000 MWe Ceramic Fueled Fast Breeder Reactor*, COO-279; TID-4500 (1964).
6. Report R-152, ANL-AMD Program Library, Argonne National Laboratory.
7. G. K. Leaf and A. S. Kennedy, *PERC—A Two Dimensional Perturbation Code Based on Diffusion Theory*, ANL- (to be published).
8. D. A. Meneley, L. C. Kvitek and D. M. O'Shea, *MACH-1, A One-Dimensional Diffusion-Theory Package*, ANL-7223 (1966).
9. V. Z. Jankus, *An Appproximate Calculation of Space Dependent Flux Using A Variational Principle*, Reactor Physics Division Annual Report, July 1965-June 1966, ANL-7210 (1966) pp. 411–412.
10. *An Evaluation of the Atomics International 1000 MWe Fast Breeder Reactor*, USAEC Report COO-285 (July 1966).
11. P. Greebler, P. Aline, and B. Hutchins, *Evaluation and Compilation of $Pu^{239}$ Cross Section Data for the ENDF/B Files*, GEAP-5272 (December 1966).


## III-14. Calculational Studies of Sodium-Void Reactivity Variations Due to Heterogeneities in Fast Critical Assemblies

D. Meneghetti

### Introduction

Fast critical systems studied on the Argonne Zero Power Reactors ZPR-3, 6 and 9 are constructed of drawers containing plates of various basic materials: for example, enriched uranium, depleted uranium, steel, aluminum, sodium contained in steel cans, and graphite. The plates simulating the composition of interest are placed in some sequence relative to each other within drawers as shown in Fig. III-14-1, a schematic top view of a drawer. These heterogeneities cause variations in such parameters as critical masses and sodium-void reactivity values. Previously reported calculations of critical mass corrections relative to homogeneous values have shown that in terms of excess reactivity such heterogeneities represent effects of the order of tenths of a percent to a few percent in $k$.[1] Bare core scoping studies[2,3] with simple heterogeneous cell configurations indicated that the effects of such heterogeneities upon the nonleakage reactivity component of sodium-voiding may be increments of

the order of tenths of percent in k. These increments, moreover, may represent large fractional changes in the sodium-void value for the homogeneous case.

G. Rusch and F. Helm[4] have reported a series of measurements of sodium-void reactivity effects for various intra-drawer loading patterns for Assembly 3 of ZPR-6. The reference heterogeneous plate arrangement is that shown in Fig. III-14-2. (The depleted uranium on the right is the axial reflector portion of the drawer.) Some effects of heterogeneities upon the spectral component of the sodium-void effect for equivalent bare cores for this series have been previously reported.[5] The calculations to be described were made in an attempt to analyze the series of reported experimental plate-loading arrangements in order to gain a better understanding of the component effects responsible for the variations in the sodium-void effect and to test the efficacy of the methods employed here to calculate these effects. The present analyses[6] included considerations of the different resonance self-shielding effects of the fertile (and fissile) isotopes in the different configurations, the different advantage and disadvantage factors due to flux spatial-fine-structures, and two-dimensional geometry effects.

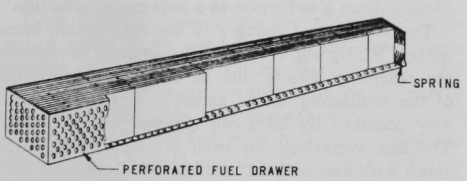


FIG. III-14-1. Cut-away View of a Core Drawer Showing Positioning of Plates in Drawer. *ANL Neg. No. 112-71.*

## CALCULATIONAL ORIENTATION

The heterogeneous $k$-values $k_{in}^{hetc}$, for sodium-in, and $k_{out}^{hetc}$, for sodium-out, situations are shown in Eq. (1) and Eq. (2) respectively. They are given by

$$k_{in}^{hetc} = k_{in}^{hom} + \Delta k_{in}^{hetf} + \Delta k_{in}^{hetr} \qquad (1)$$

$$k_{out}^{hetc} = k_{out}^{hom} + \Delta k_{out}^{hetf} + \Delta k_{out}^{hetr}, \qquad (2)$$

where $k_{in}^{hom}$ and $k_{out}^{hom}$ are corresponding homogeneous $k$-values and the other terms are correction increments. The first increment $\Delta k^{hetf}$ is the correction due to the flux variations over the cell. The flux variation gives a spatial increase of the high energy fluxes and a decrease of the lower energy fluxes in the fuel regions. The second correction increment $\Delta k^{hetr}$ accounts for the differences in resonance self-shielding for the heavy isotopes for homogeneous and heterogeneous situations. The change in $k$ due to sodium removal is shown in Eq. (3) as equal to the sum of a homogeneous value, a flux variation correction term, and a resonance self-shielding correction:

$$k_{out}^{hetc} - k_{in}^{hetc} = (\Delta k_{out}^{hom} - \Delta k_{in}^{hom}) + (\Delta k_{out}^{hetf} - \Delta k_{in}^{hetf}) + (\Delta k_{out}^{hetr} - \Delta k_{in}^{hetr}). \qquad (3)$$

It was convenient in Eqs. (1) and (2) to use the same resonance cross section for $k_{in}^{hom}$ and $k_{out}^{hom}$, and $\Delta k_{in}^{hetr}$ and $\Delta k_{out}^{hetr}$ are defined on this basis. Therefore, in order to obtain the true homogeneous sodium-void effect, $k_{in}^{homc} - k_{out}^{homc}$, a correction term giving the contribution to the sodium-void effect due to changes in resonance self-

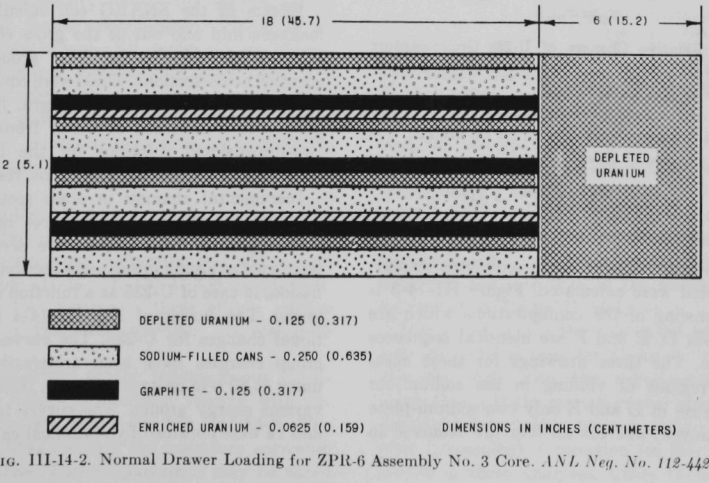


FIG. III-14-2. Normal Drawer Loading for ZPR-6 Assembly No. 3 Core. *ANL Neg. No. 112-4427.*

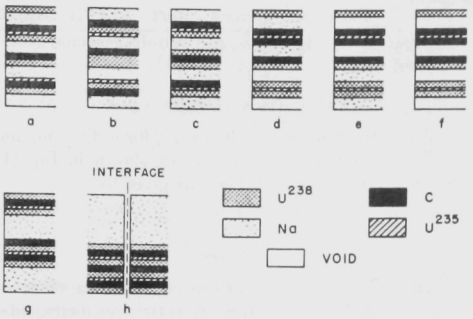


FIG. III-14-3. Inter-Drawer Configurations. *ANL Neg. No. 112-8717.*

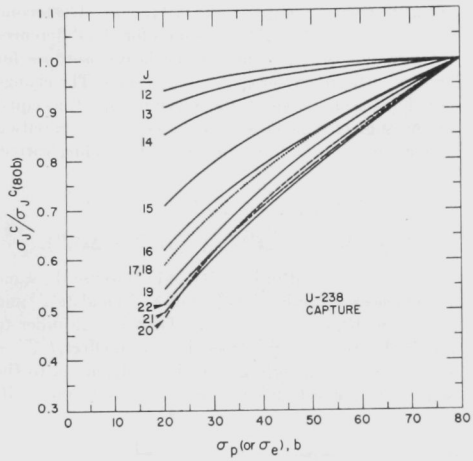


FIG. III-14-4. Relative Changes of U-238 Group-capture Cross Sections as Functions of Potential Scattering. *ANL Neg. No. 112-6950.*

shielding in the homogeneous core must be added:

$$k_{out}^{homc} - k_{in}^{homc} = (k_{out}^{hom} - k_{in}^{hom}) + (\Delta k_{out}^{homr} - \Delta k_{in}^{homr}). \quad (4)$$

## HETEROGENEOUS CONFIGURATIONS

Some of the core-drawer plate-sequences experimentally reported were calculated. Figure III-14-3 is a schematic drawing of the configurations which are calculated. Cases D, E and F are identical sequences with sodium in. The three drawings for these cases show specific regions of voiding in the sodium-out situations, because in D and E only two sodium-plate regions are removed, whereas all four are removed in F. Furthermore, all of the top sequences have four ¼ in. thick sodium-regions. The two bottom sequences have two ½ in. and one 1 in. sodium regions per drawer, respectively.

Assembly No. 3[7, 8] of ZPR-6 had a reflected pancake-shaped cylindrical core of axial dimension 50.8 cm and 155 cm diam. The gross region of core-voiding consisted of a centrally-located cylindrical region having 30.5 cm axial length and 28 cm diam.

## METHOD OF CALCULATION

Perturbation analyses employing 22-group real and adjoint fluxes from two-dimensional *R-Z* diffusion theory solutions were used to determine the various $\Delta k$ values in the previously defined correction terms. Direct two-dimensional diffusion theory calculations using the CANDID[9] program were used to obtain both the reference homogeneous sodium-in and sodium-out values of $k$. Perturbations to obtain $\Delta k_{in}$ quantities used the flux and adjoint of the homogeneous sodium-in solution; and the $\Delta k_{out}$ quantities used the flux and adjoint of the homogeneous sodium-out solution. This procedure circumvents the errors otherwise introduced if perturbation analysis is used in going from a sodium-in to a sodium-out situation.

The incremental changes to the composition-homogenized multigroup cross sections required to represent the reactivity effects due to fine-spatial variations of the multigroup fluxes across a heterogeneous cell were obtained by intra-cell regional flux weightings. The flux variations for each intracell configuration (both with and without sodium) were obtained using the Argonne discrete Sn code-SNARG.[10] For these thin-region cells a 14-angle quadrature of a modified-single-Gaussian type[11] was used.

Effects in the SNARG cell calculations of group leakages into and out of the gross core region which was voided were simulated by group-dependent absorption cross-sections. These were equal to the ratios of group net leakage to group integral flux. The integral quantities were those obtained from the multigroup two-dimensional solutions for the homogeneous sodium-in and sodium-out situations, respectively.

Incremental changes in cross sections required to evaluate the effects of differences in resonance self-shielding upon sodium-void were derived from calculated curves giving group cross sections for capture and fission, in case of U-235 as a function of potential scattering. The curves of Fig. III-14-4 show these fractional changes for U-238. The curves for the various group energies have been arbitrarily normalized to unity at 80 b in order to compare the curvatures in the various energy groups. The curves for Groups 12, 13 and 14 were obtained by statistical calculation,[12] while

those for Groups 15 to 22 were obtained by using the known resonance parameters.[13]

Values of potential scattering cross section per U-238 atom for homogeneous sodium-in and sodium-out situations are listed in Table III-14-I for a few groups. Smaller values are obtained for the sodium-out case, especially in Group 15 which contains the strong sodium scattering resonance, where the change is most noted.

The equivalence relation for lattices[14] was applied for heterogeneous cell configurations. Under the heterogeneous Case B listed in Table I three values are given for sodium-in and three values for sodium-out. These three cases correspond to estimated differences in Dancoff shielding due to differences of U-238 plate thickness and differences in intervening adjacent materials. The sodium-out has smaller values than the sodium-in for the corresponding U-238 plate regions. Especially noticeable is the fact that the sodium-in to sodium-out for Group 15 is much more pronounced in the homogeneous case.

TABLE III-14-I. Effective Potential Scattering Cross Sections in Barns per U-238 Atom

| Group j | Homogeneous | | Heterogeneous (Case B) | | | | | |
|---|---|---|---|---|---|---|---|---|
| | Na-in | Na-out | Na-in | | | Na-out | | |
| | | | 1/8 in. | 1/4 in. | 1/8 in. | 1/8 in. | 1/4 in. | 1/8 in. |
| 12 | 29.2 | 25.6 | 28.5 | 15.5 | 26.0 | 26.4 | 15.0 | 23.7 |
| 14 | 41.8 | 34.6 | 33.7 | 18.2 | 31.6 | 30.9 | 16.4 | 28.4 |
| 15 (res.) | 192.0 | 31.3 | 46.7 | 28.0 | 46.6 | 29.5 | 15.9 | 26.9 |
| 20 | 36.0 | 33.5 | 31.5 | 16.9 | 29.1 | 30.4 | 16.2 | 27.9 |

TABLE III-14-II. Sodium-Void Heterogeneity Corrections and Heterogeneous Reactivities for Various Cell Configurations of ZPR-6 Assembly 3

| Case | $\Delta k_{out}^{hetf} - \Delta k_{in}^{hetf}$, Ih | $\Delta k_{out}^{hetr} - \Delta k_{in}^{hetr}$ Ih | | Sum of corrections, Ih |
|---|---|---|---|---|
| | | $U^{238}$ | $U^{235}$ | |
| A | −0.52 | +1.00 | +0.07 | +0.55 |
| B | −0.97 | +0.32 | +0.07 | −0.58 |
| C | −0.40 | +0.55 | +0.08 | +0.23 |
| D | −0.2 | +0.6 | 0.0 | +0.4 |
| E | −0.4 | −0.1 | 0.0 | −0.5 |
| F | −0.60 | +0.51 | +0.08 | −0.01 |
| G | −0.34 | +0.53 | +0.08 | +0.27 |
| H | −0.89 | −0.11 | +0.08 | −0.92 |

TABLE III-14-III. Resonance Self-Shielding Corrections for the Homogeneous Sodium-Void Reactivity

| Case | $\Delta k_{out}^{homr} - \Delta k_{in}^{homr}$, Ih | | Sum of corrections, Ih |
|---|---|---|---|
| | $U^{238}$ | $U^{235}$ | |
| Total sodium removal | +2.85 | −0.02 | +2.83 |
| One-half sodium removal | +1.1 | 0.0 | +1.1 |

## Results and Discussion

Table III-14-II summarizes the values of the correction terms to be applied to the reference homogeneous sodium-void $\Delta k$ values. The corrections are very small. Furthermore, for this series the corrections affect essentially only the nonleakage component of sodium-voiding. The first column lists the configuration case. In Cases D and E only half the sodium is removed. The negative corrections in the second column correspond to differences in spatial fine-flux weightings. The corrections are negative in these cases because the heterogeneity effects for sodium-in are larger than those for corresponding sodium-out situations. The next two columns list separately the corrections due to resonance self-shielding differences. For these cases the U-238 is the more important. The last column gives the sum of these corrections; they are to be added to the reference homogeneous sodium removal values to obtain corrected heterogeneous sodium removal values.

Corrections to the homogeneous sodium-void values to account for the differences in resonance self-shielding between homogeneous sodium-in and sodium-out are given in Table III-14-III. The U-238 contribution again predominates; moreover, these effects require larger corrections than the previous heterogeneous cases.

Graphical comparison of the heterogeneous calculated reactivity values for sodium voiding with experimental values are shown in Fig. III-14-5. The solid horizontal lines indicate the resonance corrected homogeneous values. For comparison it may be noted that the corresponding homogeneous value, assuming invariance of resonance self-shielding upon removal of sodium, would be closer in value to the heterogeneous values, that is, negative 7.8 Ih and negative 3.8 Ih. This is because changes in effective potential scattering cross sections per absorber atom are smaller in the heterogeneous case than in the homogeneous case, as was noted in Table III-14-I.

The variations of the calculated heterogeneous reactivities shown here for Cases A, B, C, D and F correlate well with the experimental values. For Cases G and H the more negative experimental values suggest a perceptible heterogeneous leakage component (streaming). Correction for this effect is not included in these analyses. Cases G and H contained

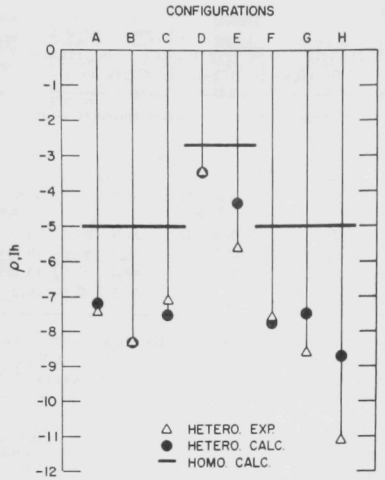


FIG. III-14-5. Comparisons of Reported Experimental Na-void Reactivity Values for Various Intracell Plate Configurations in ZPR-6, Assembly 3. *ANL Neg. No. 112-6949, Rev. 1.*

two separated ½ in. sodium regions and one 1 in. sodium region, respectively, in a drawer, whereas all of the other configurations contained four separated ¼ in. sodium regions.

The reason for the comparatively less satisfactory correlation in Case E is not clear. Experimentally the sum of the values of the sodium-void reactivity for Cases D and E differ from F by 1.4 Ih, whereas by calculation the sum is much closer to the calculated value of F.

It should be noted that the calculated correction increments in this series are very small. They do, however, represent sizeable fractional corrections to the sodium-void effect values because this effect is quite small in the cases studied.

## REFERENCES

1. D. Meneghetti, *Recent Advances and Problems in Theoretical Analysis of ZPR-III Fast Critical Assemblies*, Proc. IAEA Conference on Physics of Fast and Intermediate Reactors, Vienna, August 3–August 11, 1961, **2**, p. 457.
2. D. Meneghetti, *Calculational Studies of Effects of Thin-Slab Heterogeneities Upon Spectral Reactivity Component of Na-Voiding*, Trans. Am. Nucl. Soc. **8**, 493 (1965).
3. D. Meneghetti, *Theoretical Studies of Thin-Slab Heterogeneity Effects Upon the Spectral Reactivity Component of Sodium Voiding*, Reactor Physics Division Annual Report, July 1, 1964 to June 30, 1965, ANL-7110, pp. 148–150.
4. G. K. Rusch and F. H. Helm, *The Influence of Heterogeneity on the Measured Sodium-Void Coefficient in a 950-liter Pancake Fast Core*, Trans. Am. Nucl. Soc. **8**, 246 (1965).
5. D. Meneghetti, *Calculations of Effects of Thin-Slab Heterogeneities on the Non-Leakage Reactivity Component of Sodium Voiding*, Reactor Physics Division Annual Report, July 1, 1965 to June 30, 1966, ANL-7210, pp. 122–126.
6. D. Meneghetti, *Calculational Studies of Sodium-Void Reactivity Variations Due to Thin-Slab Heterogeneities in Fast Critical Assemblies*, Proc. International Conference on Fast Critical Experiments and Their Analysis, ANL-7320 (1966), p. 377.
7. W. Y. Kato, G. K. Rusch and F. H. Helm, *Sodium-Void Coefficients*, Proc. Conference on Safety, Fuels, and Core Design in Large Fast Power Reactors, ANL-7120 (1965), p. 598.
8. F. H. Helm, W. Y. Kato, G. Main and G. K. Rusch, *Physics Parameters and Sodium Void Coefficients in a 950-liter Pancake Core*, Reactor Physics Division Annual Report, July 1, 1964 to June 30, 1965, ANL-7110 (1966).
9. *CANDID-2D, A Two-Dimensional Neutron Diffusion Program*, Control Data Corporation (1965).
10. G. J. Duffy, H. Greenspan, S. D. Sparck, J. V. Zapatka and M. K. Butler, *SNARG-1D, A One-Dimensional Discrete Ordinate Transport Theory Program for the CDC-3600*, ANL-7221 (1966).
11. D. Meneghetti, *Discrete Ordinate Quadratures for Thin Slab Cells*, Nucl. Sci. Eng. **14**, 295 (1962).
12. R. B. Nicholson, *The Doppler Effect in Fast Neutron Reactors*, APDA-139 (1962).
13. J. B. Garg, J. Rainwater, J. S. Peterson and W. W. Havens, Jr., *Neutron Resonance Spectroscopy. III. $Th^{232}$ and $U^{238}$*, Phys. Rev. **134B**, 985 (1964).
14. Reactor Physics Constants, ANL-5800, 2nd Edition (1963) p. 277.

## III-15. Heterogeneity Effects on the Reactivity of ZPR-6 Assembly No. 3

D. MENEGHETTI

Effects of thin-slab heterogeneities upon the critical masses of Zero Power critical assemblies have often been estimated by employing infinite, periodic slab-cell calculations using group absorptions (derived from normal-mode analysis) to simulate overall leakages out of the system.[1,2,3] The calculations therefore considered only the effects of the fine spatial variations of the flux across the cell and the computed reactivities applied to the case of an equivalent bare core; that is, a simulated heterogeneous bare core multiplication is compared with a homogeneous bare core multiplication. Furthermore, the fine spatial variations of flux were assumed not to

affect significantly the average transport cross sections; that is, the homogeneous leakage absorptions were retained also in the heterogeneous cell calculations.

For the case of ZPR-6 Assembly No. 3[4,5,6] the calculated bare core reactivity estimate has been compared with a calculated reflected-core value. Since the spectrum of this assembly, which simulates a carbide-fueled reactor, contains non-negligible flux in some of the energy groups in which resonance self-shielding effects (especially in U-238) may be significant, estimates of these effects have also been calculated.

In the reflected case the analysis employed the same regional cross-section perturbations described in the summary concerning sodium-void heterogeneity effects for the computation $\Delta k_{in}^{hetf}$, $\Delta k_{in}^{hetr}$ (U-238), and $\Delta k_{in}^{hetr}$ (U-235) (see Paper III-14). Possible variations of these spectral heterogeneity effects in core regions close to the reflector are not included. This more detailed consideration may be important for analyses of the sodium-void heterogeneity effects in peripheral regions. The reference sodium-in two-dimensional real and adjoint fluxes were used in the perturbation calculations.

TABLE III-15-I. Heterogeneity Reactivity Corrections for ZPR-VI Assembly No. 3 Critical Masses

| Case | Normal Mode $\Delta k_{in}^{hetf}$, %k | Reflected | | | Total Correction (Reflected), %k |
|---|---|---|---|---|---|
| | | $\Delta k_{in}^{hetf}$, %k | $\Delta k_{in}^{hetr}$, %k | | |
| | | | $U^{238}$ | $U^{235}$ | |
| A | +0.48 | +0.42 | +0.17 | −0.01 | +0.58 |
| B | +0.55 | +0.49 | +0.22 | −0.01 | +0.70 |
| C | +0.49 | +0.45 | +0.20 | −0.01 | +0.64 |
| F | +0.58 | +0.53 | +0.20 | −0.01 | +0.72 |
| G | +0.66 | +0.62 | +0.18 | −0.01 | +0.79 |
| H | +0.91 | +0.89 | +0.22 | −0.01 | +1.10 |

Results are given in Table III-15-I for the heterogeneous reference loading Case A and for assumed entire core loadings represented by configurations B, C, F, G, and H, respectively (see Paper III-14).

Values for the normal-mode (bare core) analysis method differ by approximately 10% from the corresponding reflected values for $\Delta k_{in}^{hetf}$, except for Cases G and H which had the thicker sodium regions. These differ from the other cases because the fine spatial averagings of the group transport cross sections differ more from the homogeneous values than those used in configurations A, B, C, and F. For Case H, about +0.07 %k of the +0.89 %k value of $\Delta k_{in}^{hetf}$ represents this transport perturbation. Consideration of the resonance self-shielding increases the heterogeneity corrections by about +0.2 %k.

### References


1. J. K. Long, W. B. Loewenstein, C. E. Branyan, G. S. Brunson, F. S. Kirn, D. Okrent, R. E. Rice and F. W. Thalgott, *Fast Neutron Power Reactor Studies with ZPR-III*, Proc. 1958 Geneva Conference **12**, Paper No. 598, pp. 119–141.
2. D. Meneghetti and M. F. Loomis, *Calculation of Heterogeneity Effects in ZPR-III Fast Assemblies Using the DSN Program*, ANL-6218 (1960).
3. D. Meneghetti, *Recent Advances and Problems in Theoretical Analysis of ZPR-III Fast Critical Assemblies*, Proc. IAEA Conference on Physics of Fast and Intermediate Reactors, Vienna, August 3–August 11, 1961, **2**, p. 457.
4. G. K. Rusch and F. H. Helm, *The Influence of Heterogeneity of the Measured Sodium-Void Coefficient in a 950-liter Pancake Fast Core*, Trans. Am. Nucl. Soc. **8**, 246 (1965).
5. W. Y. Kato, G. K. Rusch and F. H. Helm, *Sodium-Void Coefficients*, Proc. Conference on Safety, Fuels, and Core Design in Large Fast Power Reactors, ANL-7120, 598 (1965).
6. F. H. Helm, W. Y. Kato, G. Main and G. K. Rusch, *Physics Parameters and Sodium Void Coefficients in a 950-liter Pancake Core*, Reactor Physics Division Annual Report, July 1, 1964 to June 30, 1965, ANL-7110, pp. 101–113.


## III-16. Pulsed Neutron Measurements on ZPR-6, Assembly No. 5

F. H. Helm

### Introduction

In recent years considerable interest has developed in neutron die-away analyses and measurements in fast multiplying media. This paper describes results of such measurements made on a very large dilute fast breeder assembly. Analyses of the measurements indicate that the kinetics of the system are essentially those of a bare fundamental mode reactor.

### Description of the Apparatus

Pulsed neutron die-away experiments were carried out on ZPR-6, Assembly No. 5, which with the Kaman Nuclear neutron generator. This machine is a 200 keV deuteron accelerator having a drift tube which can be made as long as 8 feet. A refrigerated tritium target is used to produce essentially isotropic 14 MeV neutrons from the $T(D,n)He^4$ reaction. Pulsing is ac-

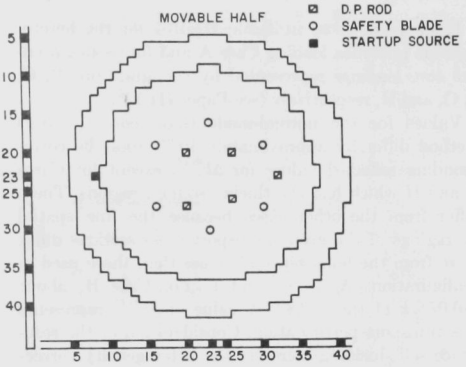


FIG. III-16-1. Outline of Assembly 5 Showing Various Source Locations. *ANL Neg. No. 112-8990.*

complished by an electrostatic deflection system located between the source and a strong focusing lens. The drift tube was inserted axially into the reactor through the central matrix tube of the stationary half so that the target was located at the center of the core.

Standard tenth-microsecond circuitry was used throughout the measurements. A General Radio pulser triggered the high voltage pulser in the deflection system of the accelerator as well as the sweep cycle of a 1024 channel time-of-flight analyzer. Pulse height discrimination was used on the detected pulses before time analysis to eliminate counter noise and rf pickup from the accelerator.

U-235 and U-238 fission chambers containing 1.7 grams of enriched uranium and 1.68 grams of depleted uranium, respectively, were used as detectors. These chambers are 2 in. diam and about 10 in. long and were located at various radial positions near the core midplane. Measurements were made at the radial locations shown in Fig. III-16-1. A survey of the most important data is given in Table III-16-I; Runs number 1 through 10 and 14 through 35 were made to compare the prompt neutron decay at different reactivities as a function of detector location in the reactor. The response of different detector materials and their varying spectral sensitivity were studied in Runs 18 thorugh 33. Runs 37 through 43 were made with much shorter pulses (150 nsec) in order to observe the decay immediately after the pulse with a higher degree of accuracy than was possible with the ½ $\mu$sec wide pulse. Finally, a preliminary attempt was made in Runs 11 through 13 to measure the time dependence of the spectrum using a protron recoil spectrometer. Run 36 was a measurement designed to determine the source intensity when a beam hole was created in the matrix by removing four core drawers, rather than the usual single drawer.

### Alpha versus Reactivity

In all cases shown in Table III-16-I, it was possible to fit at least one exponential to the observed data. The decay rate for this exponential is listed as alpha in Table III-16-I. The various levels of subcritically listed in Table III-16-I were determined from previously calibrated rod worths and fuel worths. A plot of the fundamental decay constant versus reactivity is shown in Fig. III-16-2. It can be seen that this relationship is essentially linear and extrapolates to +\$1.00 for prompt critical. This is in good agreement with point reactor theory but is a different behavior from that observed by G. Brunson and R. Huber,[1] who found a non-linear relationship for a number of fast reflected assemblies. In this case, however, the linear relationship is probably due to the very large size of the core in which the reflector is in a region of relatively low importance and the system has kinetics similar to those of a bare reactor.

An extrapolation of the measured prompt decay constants to delayed critical yields an intercept at $\alpha_c = \beta/l_p$ which is equal to $1.92 \times 10^4$ sec$^{-1}$. Calculated values for $\beta/l_p$ with various cross section sets lie between $2.2 \times 10^4$ and $2.5 \times 10^4$ sec$^{-1}$. $\beta$ is the delayed neutron fraction and $l_p$ is prompt neutron lifetime.

### Reactivity Measurements

One of the most important applications of pulsed neutron measuring techniques is the determination of large negative reactivities. There are basically two different approaches used to measure the reactivity of far sub-critical assemblies. One, which was first described by B. Simmons and J. King,[2] compares the prompt fundamental decay constant, $\alpha$, at a given condition of the reactor to the prompt decay at critical, $\alpha_c$. Following point reactor theory, a linear relationship between $\alpha$ and reactivity, $\rho$, is assumed which immediately leads to the relationship

$$\rho(\$) = \frac{\alpha - \alpha_c}{\alpha_c}. \qquad (1)$$

This is equivalent to finding the abscissa for all points in Fig. III-16-2 by demanding that they lie on a straight line which intercepts the horizontal axis at $\rho = +\$1.00$. For general work this method has two disadvantages. The first is that the system must be made critical to determine $\alpha_c$; and the second is that in smaller reflected assemblies it does not account for the higher space modes.

A second approach to reactivity measurements by

TABLE III-16-I. PULSED NEUTRON MEASUREMENTS ON ASSEMBLY 5 OF ZPR-6

| Run No. | Detector | | Table Separation cm | DP Rods Fully In[a] | Subcriticality[b] $ | Pulse Frequency kc | Pulse Width μsec | Channel Width μsec | No. of Channels | Channel 4 Indication[c] | Count Time min | Measured $\alpha$[d] $sec^{-1}$ | Remarks |
|---|---|---|---|---|---|---|---|---|---|---|---|---|---|
| | Location | Type | | | | | | | | | | | |
| 1 | 2923 | $U^{235}$ | 150 | none | | 3 | 1.5 | 0.125 | 1024 | | 10 | | |
| 2 | 2923 | $U^{235}$ | 7.65 | 3, 8 | 4.1 | 3 | 1.5 | 0.25 | 1024 | $0.16 \times 10^{-9}$ | 5 | $1.062 \times 10^{5}$ | |
| 3 | 2923 | $U^{235}$ | 2.0 | 3, 8 | 1.73 | 3 | 1.5 | 0.25 | 1024 | $0.32 \times 10^{-9}$ | 5 | $5.295 \times 10^{4}$ | |
| 4 | 2923 | $U^{235}$ | 2.0 | 3, 8 | 1.73 | 3 | 1.5 | 0.25 | 1024 | $0.85 \times 10^{-10}$ | 5 | $5.5 \times 10^{4}$ [e] | |
| 5 | 2923 | $U^{235}$ | 0 | 3, 8 | 0.982 | 3 | 1.5 | 0.25 | 1024 | $0.15 \times 10^{-9}$ | 5 | $3.81 \times 10^{4}$ [e] | |
| 6 | 2923 | $U^{235}$ | 0 | 2, 3, 4, 6, 8, 10 | 0.552 | 3 | 1.5 | 0.25 | 1024 | $0.3 \times 10^{-9}$ | 5 | $2.97 \times 10^{4}$ | |
| 7 | 2923 | $U^{235}$ | 0 | 2, 3, 4, 6, 8, 10 | 0.552 | 1 | 1.5 | 0.5 | 1024 | $0.68 \times 10^{-10}$ | 10 | $2.87 \times 10^{4}$ [e] | |
| 8 | 2923 | $U^{235}$ | 0 | all except 1 | 0.224 | 1 | 1.5 | 0.5 | 1024 | $0.142 \times 10^{-9}$ | 10 | $2.364 \times 10^{4}$ | |
| 9 | 2923 | $U^{235}$ | 0 | all except 1 | 0.224 | 1 | 1.5 | 1.0 | 512 | $0.43 \times 10^{-10}$ | 10 | $2.42 \times 10^{4}$ [e] | |
| 10 | 2923 | $U^{235}$ | 0 | all | 0.115 | 1 | 1.5 | 1.0 | 512 | $0.63 \times 10^{-10}$ | 10 | $2.12 \times 10^{4}$ | |
| 11 | | | | | | | | | | | | | |
| 12 | Runs 11–13 are time-dependent spectra measurements | | | | | | | | | | | | |
| 13 | | | | | | | | | | | | | |
| 14 | 3723 | $U^{235}$ | 0 | all except 6 | 0.224 | 1 | 1.5 | 1.0 | 512 | $0.12 \times 10^{-9}$ | 10 | $2.33 \times 10^{4}$ | Rod 6 on 15.1 |
| 15 | 3723 | $U^{235}$ | 0 | 2, 3, 4, 8, 10 | 0.661 | 1 | 1.5 | 1.0 | 512 | $0.425 \times 10^{-10}$ | 15 | $3.16 \times 10^{4}$ [e] | same |
| 16 | 3723 | $U^{235}$ | 0 | 2, 3, 4, 8, 10 | 0.661 | 3 | 1.5 | 0.25 | 1024 | $0.235 \times 10^{-9}$ | 10 | $3.20 \times 10^{4}$ [e] | same |
| 17 | 3723 | $U^{235}$ | 0 | 3, 8 | 1.06 | 3 | 1.5 | 0.25 | 1024 | $0.15 \times 10^{-9}$ | 10 | $3.91 \times 10^{4}$ | Drawer 1923 out |
| 18 | 3723 | $U^{235}$ | 0 | 3, 8 | 3.18 | 3 | 1.5 | 0.25 | 1024 | $0.75 \times 10^{-10}$ | 10 | $5.87 \times 10^{4}$ [e] | B-10 rods No. 1, 2, 5, 9, 10, 12 in |
| 19 | 4023 | $U^{235}$ | 0 | all except 6 | 0.224 | 1 | 1.5 | 1.0 | 512 | $0.544 \times 10^{-9}$ | 15 | $2.39 \times 10^{4}$ | Rod 6 on 20.0 |
| 20 | 4023 | $U^{235}$ | 0 | 2, 3, 4, 8, 10 | 0.661 | 1 | 1.5 | 1.0 | 512 | $0.175 \times 10^{-9}$ | 15 | $3.23 \times 10^{4}$ [e] | same |
| 21 | 4023 | $U^{235}$ | 0 | 3, 8 | 1.05 | 3 | 1.5 | 0.25 | 1024 | $0.68 \times 10^{-9}$ | 5 | $3.684 \times 10^{4}$ | |
| 22 | 4023 | $U^{235}$ | 2.0 | 3, 8 | 1.79 | 3 | 1.5 | 0.25 | 1024 | $0.378 \times 10^{-9}$ | 10 | $5.12 \times 10^{4}$ [e] | |
| 23 | 4023 | $U^{235}$ | 7.5 | 3, 8 | 4.16 | 3 | 1.5 | 0.25 | 1024 | $0.188 \times 10^{-9}$ | 10 | $1.024 \times 10^{5}$ | |
| 24 | 2523 | $U^{235}$ | 0 | all except 6 | 0.224 | 1 | 1.5 | 1.0 | 512 | $0.71 \times 10^{-10}$ | 10 | $2.40 \times 10^{4}$ | Rod 6 on 40.8 |
| 25 | 2523 | $U^{235}$ | 7.6 | 3, 8 | 4.12 | 3 | 1.5 | 0.25 | 1024 | $0.31 \times 10^{-10}$ | 10 | $1.05 \times 10^{5}$ [e] | |
| 26 | 2523 | $U^{235}$ | 2.0 | 3, 8 | 1.75 | 3 | 1.5 | 0.25 | 1024 | $0.595 \times 10^{-9}$ | 5 | $5.32 \times 10^{4}$ [e] | |
| 27 | 2523 | $U^{235}$ | 0 | 3, 8 | 1.01 | 3 | 1.5 | 0.25 | 1024 | $0.302 \times 10^{-9}$ | 5 | $3.76 \times 10^{4}$ | |
| 28 | 2523 | $U^{238}$ | 0 | all except 6 | 0.224 | 1 | 1.5 | 0.5 | 1024 | $0.145 \times 10^{-8}$ | 20 | | Rod 6 on 40.8 |
| 29 | 2523 | $U^{238}$ | 0 | all except 6 | 0.224 | 1 | 1.5 | 0.125 | 1024 | $0.145 \times 10^{-8}$ | 10 | | same |
| 30 | 2523 | $U^{238}$ | 0 | 2, 3, 4, 8, 10 | 0.661 | 1 | 1.5 | 0.5 | 1024 | $0.498 \times 10^{-9}$ | 20 | | same |
| 31 | 2523 | $U^{238}$ | 0 | 3, 8 | 0.982 | 3 | 1.5 | 0.25 | 1024 | $0.98 \times 10^{-9}$ | 10 | $3.80 \times 10^{4}$ | same |
| 32 | 2523 | $U^{238}$ | 2.0 | 3, 8 | 1.73 | 3 | 1.5 | 0.25 | 1024 | $0.555 \times 10^{-9}$ | 10 | | same |
| 33 | 2523 | $U^{238}$ | 7.5 | 3, 8 | 4.1 | 3 | 1.5 | 0.25 | 1024 | $0.266 \times 10^{-9}$ | 20 | | same |
| 34 | 4023 | $U^{238}$ | 0 | 3, 8 | 0.982 | 10 | 1.5 | 0.5 | 256 | $0.383 \times 10^{-8}$ | 30 | | Rod 6 on 19 |
| 35 | 4023 | $U^{238}$ | 0 | all except 6 | 0.224 | 3 | 1.5 | 1.0 | 256 | $0.490 \times 10^{-8}$ | 20 | | same } Drawer 1923 out |
| 36 | Runs under No. 36 were intensity measurements with a beamhole in the assembly. | | | | | | | | | | | | |
| 37 | 2523 | $U^{235}$ | 150 | none | | 3 | 0.15 | 0.125 | 1024 | $0.51 \times 10^{-11}$ | 50 | | |
| 38 | 2523 | $U^{235}$ | 7.5 | 3, 8 | 4.1 | 3 | 0.15 | 0.125 | 1024 | $0.115 \times 10^{-10}$ | 15 | $1.16 \times 10^{5}$ | Rod 6 on 40.8 |
| 39 | 2523 | $U^{235}$ | 0 | 3, 8 | 0.982 | 3 | 0.15 | 0.125 | 1024 | $0.31 \times 10^{-10}$ | 15 | $3.92 \times 10^{4}$ | same |
| 40 | 2523 | $U^{235}$ | 0 | all except 6 | 0.224 | 3 | 0.15 | 0.125 | 1024 | $0.115 \times 10^{-9}$ | 15 | $2.37 \times 10^{4}$ | same |
| 41 | 3723 | $U^{235}$ | 7.5 | 3, 8 | 4.1 | 3 | 0.15 | 0.125 | 1024 | $0.106 \times 10^{-10}$ | 30 | $1.15 \times 10^{5}$ | Rod 6 on 15 |
| 42 | 3723 | $U^{235}$ | 0 | 3, 8 | 0.982 | 3 | 0.15 | 0.125 | 1024 | $0.32 \times 10^{-10}$ | 60 | | same } Drawer 1923 out |
| 43 | 3723 | $U^{235}$ | | all except 6 | 0.224 | 3 | 0.15 | 0.125 | 1024 | $0.13 \times 10^{-9}$ | 45 | $2.32 \times 10^{4}$ | same |

[a] All other dual purpose rods are fully out except as shown under Remarks. The adjustments indicated in the Remarks column were generally made in order to maintain comparable reactivities for different counter locations.

[b] Subcriticality values were calculated from rod and fuel drawer worths, referencing to a critical loading, for all cases with the halves together. For the cases with the halves separated the values were estimated—very roughly—from the observed source multiplication.

[c] These data are given as an indication of the relative average neutron flux during the measurement.

[d] This column gives the observed fundamental decay constant.

[e] These values were found by graphical extrapolation. All other $\alpha$ values given were found by a least squares fit.

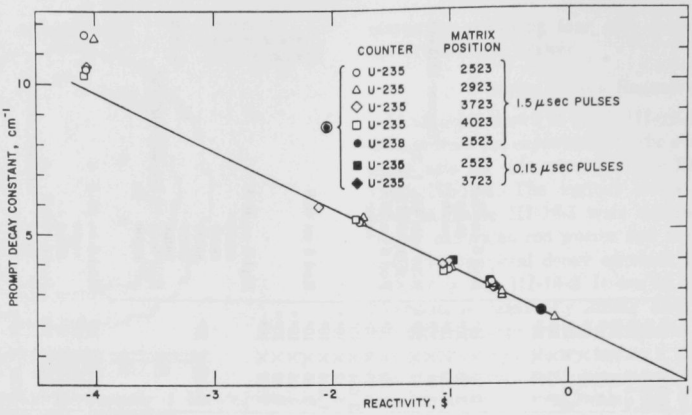


FIG. III-16-2. Prompt Decay Constant for Different Reactivity Conditions at Different Core Locations. *ANL Neg. No. 112-8999.*

pulse neutrons was originally developed by N. Sjostrand.[3] It consists essentially of comparing the prompt multiplication with the total multiplication, including the delayed neutrons. It has the advantage over the Simmons and King method in that it does not require a measurement at delayed critical. If the time-dependent neutron flux is described as a series of pulses superimposed on an essentially constant background, the time decay behavior of the pulses is determined by the kinetic response of the system to fast neutrons while the amplitude of the background is a measure of the average delayed neutron intensity.

If $A_p$ is the area under the pulse and $A_d$ is the area of the background, the relationship between neutron intensity and multiplication, k, and multiplication by prompt neutrons alone, $k_p$, is

$$\frac{A_p}{A_p + A_d} = \frac{1 - k}{1 - k_p}, \tag{2}$$

which can be written as

$$\frac{A_p}{A_d} = \frac{1 - k}{\beta} = \rho(\$), \tag{3}$$

where $\beta$ is the delayed neutron fraction. This method presupposes that only the fundamental mode contributes to the integrals since for higher modes the ratio between prompt and delayed multiplication would be different. It is also assumed that the detector is located at a place where the slight difference in the spatial distribution of the prompt and delayed flux does not affect the result of the measurement. This so-called area method was used with square pulses and a duty cycle of about 0.5.

T. Gozani[4] adopted this technique for shorter pulses and eliminated the higher harmonics from the prompt contribution by disregarding the initial part of the decay curve. Instead, the decay curve measured after a certain waiting time ($t_w$) when the higher modes have decayed, is extrapolated back to the time of the source pulse. For the reactivity in this case one obtains the relationship

$$\rho(\$) = \frac{B_{ext}F}{\alpha B_d}, \tag{4}$$

where $B_{ext}$ is the extrapolated amplitude of the fundamental decay exponential to zero time; $F$ is the pulsing frequency, $\alpha$ the fundamental decay constant and $B_d$ the amplitude of the delayed background.

E. Garelis and J. Russell[5] have found a method that combines the two approaches described above. Their technique also eliminates the necessity of making a measurement at critical. It also eliminates the effects of prompt and delayed higher modes. The time dependence of the sub-critical prompt and delayed fluxes is used to determine $k\beta/l = \alpha_c$ by the relationship

$$\int_0^\infty N_p e^{k\beta/l}\, dt - \int_0^\infty N_p\, dt = \frac{N_d}{F}. \tag{5}$$

which can be solved by iteration techniques. $l$ is the neutron lifetime, $N_p$ is the time dependent prompt flux and $N_d$ is the (constant) delayed flux determined near the end of the measurement interval, $1/F$ sec. In analyzing the data to be presented in this paper by the Garelis-Russell method, the prompt flux was divided into two parts. The first was the area under the measured curve at short times following the pulse, where the exponential decay was clearly established, and the second was an assumed decay of the prompt

flux with the fundamental exponential when the flux approached the background level. After $\alpha_c$ is found the reactivity is calculated using Eq. (1).

Table III-16-II shows the values of reactivity determined by the three different methods for a number of experimental runs, and the corresponding measurement made with calibrated control rods and fuel worths. The agreement is best at the intermediate subcriticalities (about 1 dollar) while at higher and lower reactivities, there are larger deviations. The Garelis-Russell and the Gozani methods appear to systematically depart from the measured data in going from the core center to the blanket, which is probably due to the difference in distribution of the prompt and delayed flux modes. They also tend toward negative deviations at small subcriticalities and positive deviations at large subcriticalities. The Simmons and King analysis showed no such systematic behavior.

It should be noted that the data in Table III-16-II cannot be used to judge the achievable accuracy by the various techniques because of the very large size of Assembly 5. There is a parasitic background which is not related to the delayed flux but which was included as a part of the delayed neutron density in the analysis. Then too, there is some question of the proper weighting techniques to be used in the least squares fitting process for those points in which the background is very low.

An attempt to analyze the data in runs 38 through 43 (very short pulses) by the Gozani method consistently yielded $k_{eff}$ values which were about 50% too small. A satisfactory solution to this problem has not yet been found but may reside in the parasitic background which is more important at the very low counting rates.

TABLE III-16-II. Comparison of Reactivity Measurements (Pulse Width = 1.5 μsec)

| Run No. | Counter Position | $m\rho$ (non-pulsed techniques), $ | $\rho$ Simmons & King, $ | $\rho$ Gozani, $ | $\rho$ Garelis & Russel, $ |
|---|---|---|---|---|---|
| 10 | 2923 | 0.115 | 0.104 | 0.0739 | 0.0749 |
| 24 | 2523 | 0.224 | 0.250 | 0.177 | 0.182 |
| 8 | 2923 | 0.224 | 0.231 | 0.189 | 0.195 |
| 14 | 3723 | 0.224 | 0.214 | 0.197 | 0.203 |
| 19 | 4023 | 0.224 | 0.245 | 0.203 | 0.198 |
| 6 | 2923 | 0.552 | 0.547 | 0.525 | 0.555 |
| 27 | 2523 | 1.01 | 0.958 | 0.901 | 1.08 |
| 31 | 2523 | 0.982 | 0.979 | 1.00 | 1.15 |
| 17 | 3723 | 1.06 | 1.04 | 1.05 | 1.17 |
| 21 | 4023 | 1.06 | 0.918 | 1.13 | 1.29 |
| 26 | 2523 | (1.75)[a] | | | |
| 3 | 2923 | (1.73) | 1.75 | 1.68 | 1.24 |
| 2 | 2923 | (4.09) | 4.53 | 4.67 | 6.79 |
| 23 | 4023 | (4.16) | 4.33 | 5.02 | 7.12 |

[a] Numbers in parentheses are very approximate estimates only.

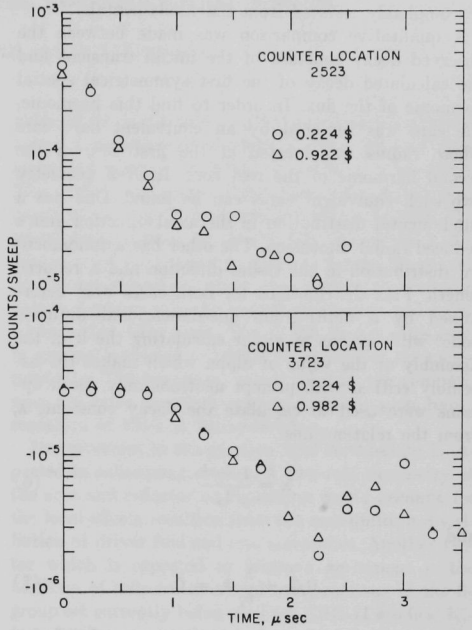


Fig. III-16-3. The Time Dependence of Higher Harmonics at Two Core Locations. *ANL Neg. No. 112-8995.*

## Higher Harmonics

The last measurements made in this series were with very short pulses (150 nsec) in order to observe any fast transient decay immediately following the pulse. Results at two different positions (one in the core and one in the reflector) and for two different levels of subcriticality are shown in Fig. III-16-3. Here, the constant background and the fundamental decay component have been removed. It should be noted that near the core center the amplitude of the transient is positive while near the core blanket boundary it is negative.

An attempt was made to approximate the decay of the transients by a series of exponentials using least squares fitting techniques. Resulting decay constants were on the order of $10^6$ $sec^{-1}$. However the exact values depended strongly on the time after the pulse which was chosen as the starting point for the fit as well as on the counter position. It was not possible

to determine a single higher decay mode which could be completely isolated from the fundamental.

A qualitative comparison was made between the observed decay constant of the initial transient and the calculated decay of the first symmetrical spatial harmonic of the flux. In order to find this harmonic, the core was replaced by an equivalent bare core whose radius was located at the first zero of the second harmonic of the real core. In *R-Z* geometry two such equivalent cores can be found. One has a fundamental distribution in the axial direction and a reduced radial dimension. The other has a fundamental distribution in the radial direction and a reduced length. Flux distributions for both cases were determined by a multi-group one-dimensional diffusion code[6] with options of either calculating the k of the assembly or the value of alpha which makes the assembly critical with prompt neutrons only. Both options were used to calculate the decay constant, $\lambda$, from the relationships

$$\lambda = \frac{1 - k}{l_p} \tag{6}$$

and

$$\Omega_j \Phi_j + \frac{\lambda}{v_j} \Phi_j = 0, \tag{7}$$

where $j$ is a group index, and $\Omega$ is the usual diffusion operator containing diffusion, fission, absorption and scattering terms, $v_j$ is the group averaged velocity and $l_p$ is the prompt neutron lifetime. A value for $\lambda$ obtained from the data of Fig. III-16-3 by the first method [Eq. (6)] was $1.7 \times 10^{-6}$ sec$^{-1}$ and is in approximate agreement with the experiments. $\lambda$ values determined from Eq. (7) however gave results which were very sensitive to the lowest energy group included in the calculation. For these calculations the ANL cross section set No. 224, in which the lowest group cuts off at 29 eV, was used. Although the flux distributions in the higher groups were very similar for both calculations there was a tendency in the latter for pile-up in the lowest group. The decay constant in this case ($2 \times 10^5$ sec$^{-1}$) is almost entirely determined by the parameters of this group. Since there are so few neutrons at these low energies in the initial transient the calculation was repeated for neutrons only to the keV region. The result gave a value of $2 \times 10^6$ sec$^{-1}$, but still showed sensitivity to the lowest group. Both the calculation and the experiment showed that although some qualitative evidence exists for the first spatial harmonic in the initial transient, a clear identification of this harmonic is not possible.

## Time Dependence of the Neutron Spectrum

Recent developments in proton recoil spectrometers by E. Bennett[7] make it possible to determine the time dependence of the spectrum from several MeV to the low keV region with about a one micro-second time resolution. In these measurements, each pulse must be analyzed with respect to amplitude and its time of arrival at the detector, as well as pulse shape, in order to suppress gamma background. The preliminary experiments performed here used only the time and height analysis. Counter voltages were relatively high (3100 volts) so that the energy resolution did not include the gamma-sensitive lower keV region. A multi-channel analyzer was used for pulse height analysis. Time analysis was performed by delayed gating of the input to the analyzer allowing it to receive pulses only after a fixed time interval following the neutron burst. Two series of measurements were made. In the first the pulse height analyzer was gated on for 10 $\mu$sec during each sweep starting 10, 30, 60, 90 and 136 $\mu$sec after the pulse. In the second series, the gating-on time was 3 $\mu$sec starting 0, 2.5, 7.5 and 12.5 $\mu$sec after the pulse. Results of these experiments did not show any significant difference in the pulse-height spectra in any of the measurements. Only a slight shift toward the higher pulses (a harder spectrum) was noted for the measurements when the analyzer was gated on during the source pulse itself. More significant results might be obtained if the time resolution could be reduced by about one order of magnitude. Then too, a small jitter exists between the triggering signal from the General Radio pulser and the actual neutron burst at the target. It is this jitter that precludes a measurement of the propagation time of the pulse to the different radial positions in the assembly.

## References

1. G. S. Brunson and R. J. Huber, *Pulsed-Neutron Die-Away Measurements in Three Fast Critical Assemblies*, Trans. Am. Nucl. Soc. **9**, 168 (1966).
2. B. E. Simmons and J. S. King, *A Pulsed-Neutron Technique for Reactivity Determination*, Nucl. Sci. Eng. **3**, 595 (1958).
3. N. J. Sjostrand, *Measurements on a Sub-Critical Reactor Using a Pulsed Neutron Source*, Arkiv Fysik **11**, 233 (1956).
4. T. Gozani, *A Modified Procedure for Evaluation of Pulse Source Experiments in Sub-Critical Reactors*, Nukleonik **4**, 348 (1962).
5. E. Garelis and J. L. Russell, *Theory of Pulse Neutron Source Measurements*, Nucl. Sci. Eng. **16**, 263 (1963).
6. D. A. Meneley, L. C. Kvitek and D. M. O'Shea, *MACH 1, A One-Dimensional Diffusion-Package*, ANL-7223 (1966).
7. E. F. Bennett, *Fast Neutron Spectroscopy by Proton-Recoil Proportional Counting*, Nucl. Sci. Eng. **27**, 16 (1967).

## III-17. Nuclear Analysis Methods Development for EBR-II

D. Kucera, J. T. Madell and P. J. Persiani

This physics analysis program is in support of EBR-II design, operation, and plant improvement, particularly with respect to improving the test-fuel irradiation capability. The general objective of the effort is to obtain a detailed understanding of the actual system neutronics under a variety of anticipated operating conditions and configurations.

The preliminary computations for checking and debugging of the burn-up cycle code, PYRO, have been successfuly completed. PYRO is a CDC-3600 code which calculates the isotopic burnup in a two-dimensional $x$, $y$ configuration as a function of time. It is structured to be used in conjunction with the transport SNARG 2D code. A series of test- and driver-fuel irradiation and replacement steps are being planned in support of the current EBR-II test-fuel irradiation program as well as in support of the EBR-II Improved Driver Fuel program.

An option included in the PYRO code is the printout of the geometrically fine regional reaction rate distribution. This allows reaction rate studies to be compared with experimental distributions determined from wire foil irradiation. A comparison has been made of the U-235 and U-238 fission rate distributions between measurements made in Run 25 and those computed using a 2D SNARG S-4 in $x$, $y$ geometry. The preliminary computations assumed a 4-fold symmetry of the Run 25 loading and utilized the EBR-II 6 group cross section set 23606. The computed U-235 fission rates were found to agree to within 20 percent of the experimental values near and in the reflector region. Agreement in the central core region was found to be within 10 percent. The U-238 fission rates were in general predicted to within 10 percent of the measurements. The computed values used in the comparisons are rates averaged over a quarter-region representation of EBR-II subassemblies.

Improvement in the reaction rate distribution is expected in subsequent studies. A two-fold symmetry of the core and reflector configuration would account for the local effects resulting from the non-uniform distribution of driver fuel and test assemblies. Another factor which is expected to improve agreement is the addition of reflector-averaged cross sections to the 6-group set currently being used for EBR-II studies. Efforts in these areas of study have been initiated.

## III-18. Multigroup Cross Section Sets for Neutronic Calculations of EBR-II

J. T. Madell

Three multigroup cross section sets have been developed to carry out a general reactor analysis program for EBR-II.

A 22 group set was developed first and served as the basis for six and five group sets. The 22 group set, designated Set 236, was produced by the MC² Code.[1] Two MC² calculations, one using the core and the other the blanket composition of EBR-II, were performed assuming zero buckling but taking account of the heterogeneities in the core and blanket design. The cross sections for nine additional nuclides were obtained from Set 224, a 22 group set weighted by a neutron spectrum softer than that used in generating Set 236. The Set 224 cross sections are considered sufficiently accurate for the present. As more accurate data become available, primarily from the Evaluated Nuclear Data File/B (ENDF/B), new cross sections will be added to Set 236. A description of Set 236 is given in Tables III-18-Ia and III-18-Ib.

Using the 22 group structure of Set 236, five and six group sets were generated by the group collapsing routine of the MACH 1 code.[2] The group structure of the collapsed sets was determined by comparing calculations performed with various five and six group structures to those using Set 236 and then selecting the group structure producing the best comparison.

The real and adjoint flux spectra at the reactor center and the reactivity worths of selected nuclides in the EBR-II core were the quantities compared in the study. The reactivity worths were obtained in three regions of the spherical core: in Ring №1 (center), in Rings №2 through №4, and in Ring №5 (outer).

TABLE III-18-Ia. Description of Cross Section Set 236

| Energy Group | Lower Energy Limit, eV | Upper Lethargy Limit |
|---|---|---|
| 1 | $3.68 \times 10^6$ | 1.0 |
| 2 | $2.23 \times 10^6$ | 1.5 |
| 3 | $1.35 \times 10^6$ | 2.0 |
| 4 | $8.21 \times 10^5$ | 2.5 |
| 5 | $4.98 \times 10^5$ | 3.0 |
| 6 | $3.02 \times 10^5$ | 3.5 |
| 7 | $1.83 \times 10^5$ | 4.0 |
| 8 | $1.11 \times 10^5$ | 4.5 |
| 9 | $6.74 \times 10^4$ | 5.0 |
| 10 | $4.09 \times 10^4$ | 5.5 |
| 11 | $2.48 \times 10^4$ | 6.0 |
| 12 | $1.50 \times 10^4$ | 6.5 |
| 13 | $9.12 \times 10^3$ | 7.0 |
| 14 | $4.31 \times 10^3$ | 7.75 |
| 15 | $2.62 \times 10^3$ | 8.25 |
| 16 | $2.03 \times 10^3$ | 8.50 |
| 17 | $1.23 \times 10^3$ | 9.0 |
| 18 | $9.61 \times 10^2$ | 9.25 |
| 19 | $5.83 \times 10^2$ | 9.75 |
| 20 | $2.75 \times 10^2$ | 10.5 |
| 21 | $1.01 \times 10^2$ | 11.5 |
| 22 | $2.90 \times 10^1$ | 12.75 |

TABLE III-18-Ib. Description of Cross Section Set 236

| Nuclide Number | Nuclide | Remarks |
|---|---|---|
| 1 | U-235 | EBR-II Core Spectrum Weighted |
| 2 | Pu-239 | " |
| 3 | U-238 | " |
| 4 | Fe | " |
| 5 | Ni | " |
| 6 | Cr | " |
| 7 | Na | " |
| 8 | Fiss. Prod. Pairs | " |
| 9 | U-235 | EBR-II Blanket Spectrum Weighted |
| 10 | Pu-239 | " |
| 11 | U-238 | " |
| 12 | Fe | " |
| 13 | Ni | " |
| 14 | Cr | " |
| 15 | Na | " |
| 16 | Mo | Set 224, Large Carbide/Oxide Spectrum |
| 17 | Nb | " |
| 18 | Zr | " |
| 19 | B(NAT) | " |
| 20 | C | Set 224, W. B. Loewenstein Data |
| 21 | O | Set 224, Large Carbide Spectrum |
| 22 | W | Set 224, Large Carbide/Oxide Spectrum |
| 23 | Ta | Set 224, Large Carbide/Oxide Spectrum |
| 24 | B-10 | Set 224, S. A. Cox et. al., Data |

The worths were calculated by the perturbation method and were based on a 1% decrease in the atom density of the nuclides. The group structure of the five and six group sets selected from the study are given in Tables III-18-IIb and III-18-IIa and the flux spectra and reactivity worths obtained from these sets are given in Figs. III-18-1 and III-18-2 and Table III-18-III, respectively. The five group set is designated as Set 23605 and the six group set as Set 23606.

TABLE III-18-IIa. Description of Cross Section Set 23606

| Energy Group | Corresponding Set 236 Groups | Lower Energy Limit, eV | Upper Lethargy Limit |
|---|---|---|---|
| 1 | 1, 2 | $2.23 \times 10^6$ | 1.5 |
| 2 | 3, 4 | $8.21 \times 10^5$ | 2.5 |
| 3 | 5, 6 | $3.02 \times 10^5$ | 3.5 |
| 4 | 7, 8 | $1.11 \times 10^5$ | 4.5 |
| 5 | 9, 10 | $4.09 \times 10^4$ | 5.5 |
| 6 | 11 through 22 | $2.90 \times 10^1$ | 12.75 |

| Nuclide Number | Nuclide | Weighting Spectrum |
|---|---|---|
| 1 | U-235 | EBR-II Core |
| 2 | Pu-239 | " |
| 3 | U-238 | " |
| 4 | Fe | " |
| 5 | Ni | " |
| 6 | Cr | " |
| 7 | Na | " |
| 8 | Fiss. Prod. Pairs | " |
| 9 | U-235 | EBR-II Blanket |
| 10 | Pu-239 | " |
| 11 | U-238 | " |
| 12 | Fe | " |
| 13 | Ni | " |
| 14 | Cr | " |
| 15 | Na | " |
| 16 | Mo | EBR-II Core |
| 17 | Nb | " |
| 18 | Zr | " |
| 19 | B(NAT) | " |
| 20 | C | " |
| 21 | O | " |
| 22 | W | " |
| 23 | Ta | " |
| 24 | B-10 | " |
| 25 | EBR-II Core | — |
| 26 | EBR-II Blanket | — |

TABLE III-18-IIb. Description of Cross Section Set 23605[a]

| Energy Group | Corresponding Set 236 Groups | Lower Energy Limit, eV | Upper Lethargy Limit |
|---|---|---|---|
| 1 | 1, 2, 3 | $1.35 \times 10^6$ | 2.0 |
| 2 | 4, 5 | $4.98 \times 10^5$ | 3.0 |
| 3 | 6, 7 | $1.83 \times 10^5$ | 4.0 |
| 4 | 8, 9 | $6.74 \times 10^4$ | 5.0 |
| 5 | 10 through 22 | $2.90 \times 10^1$ | 12.75 |

[a] Nuclide number, name, and corresponding weighting spectrum for Set 23605 are the same as those for Set 23606.

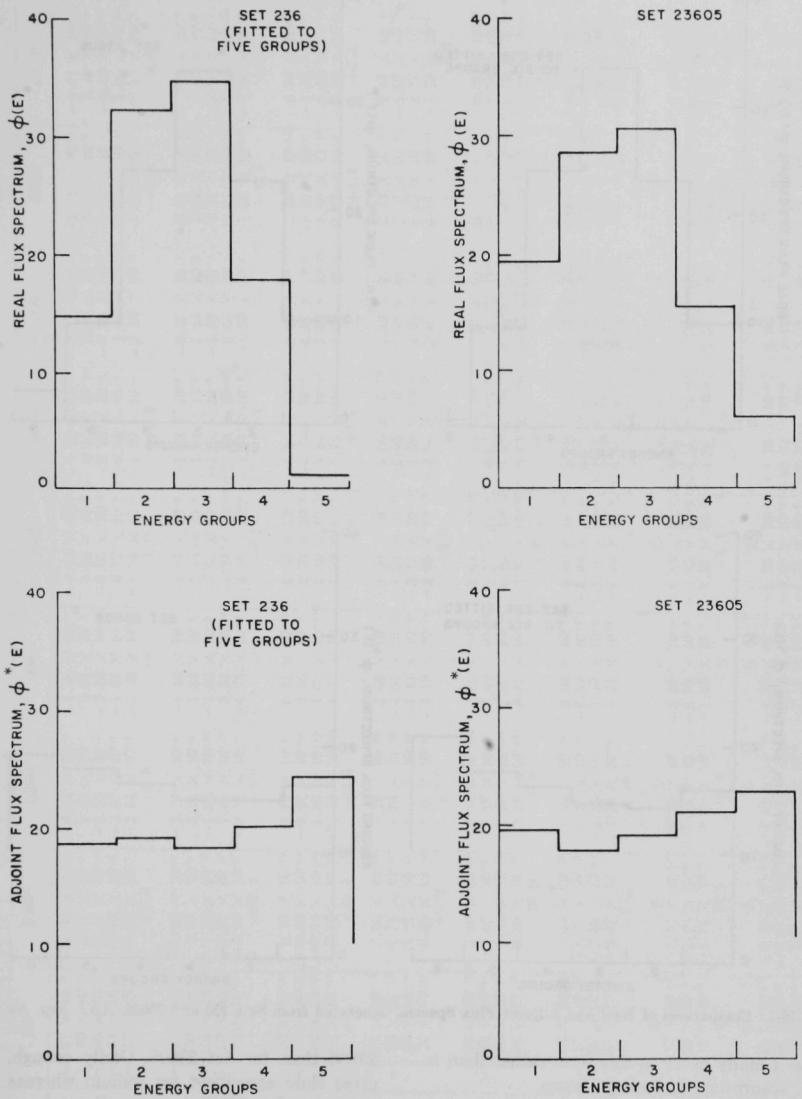


FIG. III-18-1. Comparison of the Real and Adjoint Flux Spectra Generated from Sets 236 and 23605. *ANL Neg. No. 112-8815.*

The real and adjoint flux spectra generated from Sets 23605 and 23606 agree well with those from Set 236. The overall values of reactivity of EBR-II are in close agreement for all sets: $k = 1.000$ for Set 236, $k = 1.0014$ for Set 23606 and $k = 1.0045$ for Set 23605. With only one exception, the reactivity worths ($\Delta k/k/\Delta V$) calculated for the 8 nuclides using Set 23606 agree within 10% with those calculated using Set 236. The one exception is the worth of sodium in Region #1 (Ring #1). The discrepancy arises from the elastic plus inelastic scattering term in the perturbation analysis. In fact, the greatest discrepancies for all

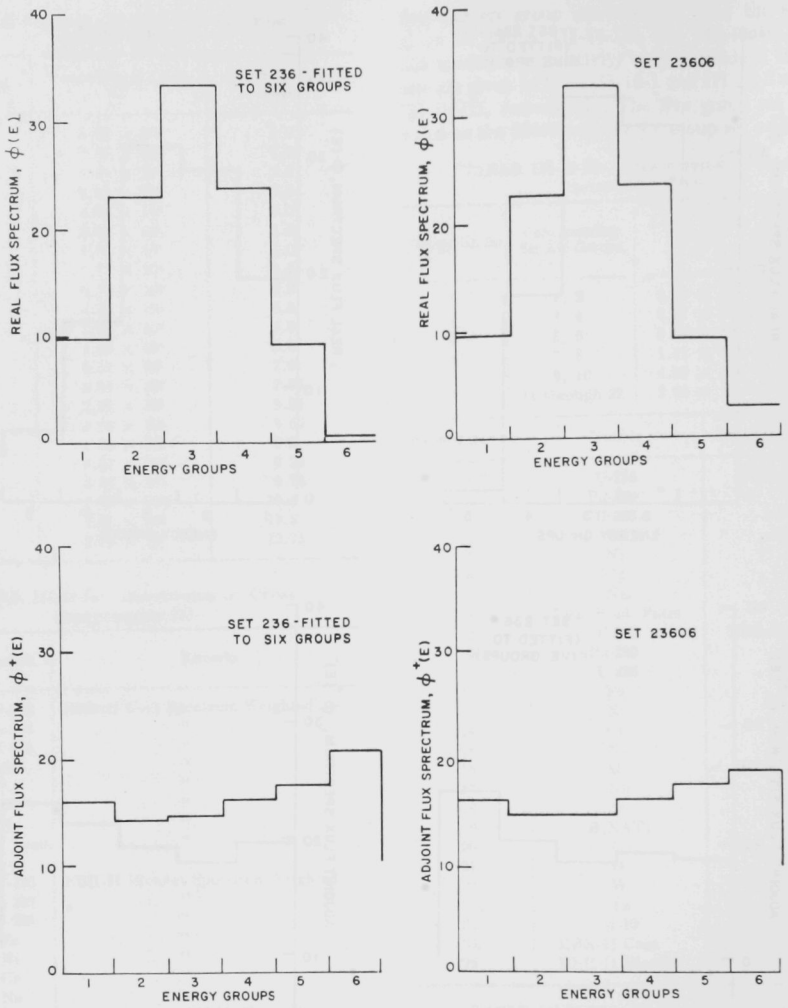


FIG. III-18-2. Comparison of Real and Adjoint Flux Spectra Generated from Sets 236 and 23606. *ANL Neg. No. 112-8816.*

the nuclides usually occur in this term rather than in the source, absorption, or leakage terms.

The results of the reactivity worth calculations using Set 23605 are also given in Table III-18-III. Again the major difficulty arises in trying to predict the worth due to elastic and inelastic scattering. Comparison with the scattering term and total worth calculated from Set 236 are generally better for Set 23606 than for Set 23605. Oddly enough, Set 23605 gives close agreement for sodium whereas the agreement for Set 23606 is poor. Rearrangement of the group structure for the five group set improved the comparison for particular nuclides but resulted in a poorer overall comparison. It was concluded that Set 23605 resulted in the best comparison for a cross section set limited to only five groups.

TABLE III-18-III. Reactivity Worths of Eight Nuclides in the Three Core Regions Calculated by the Three Cross Section Sets

| Nuclide | $\Delta k/k/\Delta V$ Terms | Region 1 | | | Region 2 | | | Region 3 | | |
|---|---|---|---|---|---|---|---|---|---|---|
| | | 236 | 23605 | 23606 | 236 | 23605 | 23606 | 236 | 23605 | 23606 |
| U-235 | Source | $-2.91 \times 10^{-7}$ | $-2.93 \times 10^{-7}$ | $-2.93 \times 10^{-7}$ | $-1.98 \times 10^{-7}$ | $-1.99 \times 10^{-7}$ | $-1.99 \times 10^{-7}$ | $-1.11 \times 10^{-7}$ | $-1.11 \times 10^{-7}$ | $-1.11 \times 10^{-7}$ |
| | $C + F$[a] | $1.40 \times 10^{-7}$ | $1.41 \times 10^{-7}$ | $1.41 \times 10^{-7}$ | $9.51 \times 10^{-8}$ | $9.56 \times 10^{-8}$ | $9.57 \times 10^{-8}$ | $5.18 \times 10^{-8}$ | $5.17 \times 10^{-8}$ | $5.18 \times 10^{-8}$ |
| | Leakage | $-1.33 \times 10^{-10}$ | $-1.33 \times 10^{-10}$ | $-1.34 \times 10^{-10}$ | $-3.86 \times 10^{-9}$ | $-3.86 \times 10^{-9}$ | $-3.90 \times 10^{-9}$ | $-6.34 \times 10^{-9}$ | $-6.34 \times 10^{-9}$ | $-6.42 \times 10^{-9}$ |
| | Scattering | $-2.34 \times 10^{-9}$ | $-1.89 \times 10^{-9}$ | $-2.17 \times 10^{-9}$ | $-1.03 \times 10^{-9}$ | $0.77 \times 10^{-9}$ | $-0.95 \times 10^{-9}$ | $1.90 \times 10^{-10}$ | $2.65 \times 10^{-10}$ | $1.96 \times 10^{-10}$ |
| | Total | $-1.53 \times 10^{-7}$ | $-1.54 \times 10^{-7}$ | $-1.54 \times 10^{-7}$ | $-1.08 \times 10^{-7}$ | $-1.08 \times 10^{-7}$ | $-1.09 \times 10^{-7}$ | $-6.53 \times 10^{-8}$ | $-6.51 \times 10^{-8}$ | $-6.53 \times 10^{-8}$ |
| | %[b] | — | +0.6 | +0.6 | — | 0.0 | +0.9 | — | −0.5 | 0.0 |
| U-238 | Source | $-2.22 \times 10^{-8}$ | $-2.22 \times 10^{-8}$ | $-2.21 \times 10^{-8}$ | $-1.43 \times 10^{-8}$ | $-1.43 \times 10^{-8}$ | $-1.43 \times 10^{-8}$ | $-6.57 \times 10^{-9}$ | $-6.54 \times 10^{-9}$ | $-6.61 \times 10^{-9}$ |
| | $C + F$[a] | $2.00 \times 10^{-8}$ | $2.02 \times 10^{-8}$ | $2.01 \times 10^{-8}$ | $1.35 \times 10^{-8}$ | $1.35 \times 10^{-8}$ | $1.34 \times 10^{-8}$ | $7.05 \times 10^{-9}$ | $7.04 \times 10^{-9}$ | $7.04 \times 10^{-9}$ |
| | Leakage | $-1.24 \times 10^{-10}$ | $-1.25 \times 10^{-10}$ | $-1.26 \times 10^{-10}$ | $-3.60 \times 10^{-9}$ | $-3.61 \times 10^{-9}$ | $-3.64 \times 10^{-9}$ | $-5.89 \times 10^{-9}$ | $-5.91 \times 10^{-9}$ | $-5.96 \times 10^{-9}$ |
| | Scattering | $-4.74 \times 10^{-10}$ | $-0.97 \times 10^{-10}$ | $-7.34 \times 10^{-10}$ | $2.19 \times 10^{-10}$ | $4.35 \times 10^{-10}$ | $-0.03 \times 10^{-10}$ | $8.05 \times 10^{-10}$ | $8.63 \times 10^{-10}$ | $6.36 \times 10^{-10}$ |
| | Total | $-2.74 \times 10^{-9}$ | $-2.26 \times 10^{-9}$ | $-2.92 \times 10^{-9}$ | $-4.23 \times 10^{-9}$ | $-3.96 \times 10^{-9}$ | $-4.46 \times 10^{-9}$ | $-4.60 \times 10^{-9}$ | $-4.55 \times 10^{-9}$ | $-4.89 \times 10^{-9}$ |
| | %[b] | — | −17.4 | +6.6 | — | −6.7 | +5.4 | — | −1.3 | +6.3 |
| Fe | $C + F$[a] | $9.10 \times 10^{-10}$ | $9.16 \times 10^{-10}$ | $9.17 \times 10^{-10}$ | $6.31 \times 10^{-10}$ | $6.32 \times 10^{-10}$ | $6.34 \times 10^{-10}$ | $3.60 \times 10^{-10}$ | $3.58 \times 10^{-10}$ | $3.60 \times 10^{-10}$ |
| | Leakage | $-9.44 \times 10^{-11}$ | $-9.48 \times 10^{-11}$ | $-9.49 \times 10^{-11}$ | $-2.76 \times 10^{-9}$ | $-2.76 \times 10^{-9}$ | $-2.77 \times 10^{-9}$ | $-4.57 \times 10^{-9}$ | $-4.59 \times 10^{-9}$ | $-4.58 \times 10^{-9}$ |
| | Scattering | $1.62 \times 10^{-10}$ | $-0.98 \times 10^{-10}$ | $1.83 \times 10^{-10}$ | $4.02 \times 10^{-10}$ | $2.13 \times 10^{-10}$ | $3.84 \times 10^{-10}$ | $5.88 \times 10^{-10}$ | $4.66 \times 10^{-10}$ | $5.43 \times 10^{-10}$ |
| | Total | $9.77 \times 10^{-10}$ | $7.23 \times 10^{-10}$ | $10.05 \times 10^{-10}$ | $-1.72 \times 10^{-9}$ | $-1.92 \times 10^{-9}$ | $-1.75 \times 10^{-9}$ | $-3.62 \times 10^{-9}$ | $-3.77 \times 10^{-9}$ | $-3.68 \times 10^{-9}$ |
| | %[b] | — | −26.1 | +2.8 | — | +11.3 | +1.7 | — | +4.1 | +1.6 |
| Ni | $C + F$[a] | $7.71 \times 10^{-10}$ | $7.63 \times 10^{-10}$ | $7.72 \times 10^{-10}$ | $5.08 \times 10^{-10}$ | $4.99 \times 10^{-10}$ | $5.08 \times 10^{-10}$ | $2.49 \times 10^{-10}$ | $2.42 \times 10^{-10}$ | $2.47 \times 10^{-10}$ |
| | Leakage | $-1.73 \times 10^{-10}$ | $-1.74 \times 10^{-10}$ | $-1.75 \times 10^{-10}$ | $-4.96 \times 10^{-10}$ | $-4.98 \times 10^{-10}$ | $-5.03 \times 10^{-10}$ | $-7.93 \times 10^{-10}$ | $-8.00 \times 10^{-10}$ | $-8.07 \times 10^{-10}$ |
| | Scattering | $-1.22 \times 10^{-10}$ | $-1.07 \times 10^{-10}$ | $-1.09 \times 10^{-10}$ | $-4.44 \times 10^{-11}$ | $-3.13 \times 10^{-11}$ | $-3.39 \times 10^{-11}$ | $3.81 \times 10^{-11}$ | $4.43 \times 10^{-11}$ | $3.77 \times 10^{-11}$ |
| | Total | $6.32 \times 10^{-10}$ | $6.38 \times 10^{-10}$ | $6.46 \times 10^{-10}$ | $-3.18 \times 10^{-11}$ | $-2.99 \times 10^{-11}$ | $-2.94 \times 10^{-11}$ | $-5.06 \times 10^{-10}$ | $-5.14 \times 10^{-10}$ | $-5.23 \times 10^{-10}$ |
| | %[b] | — | +0.8 | +2.2 | — | −6.0 | −8.2 | — | +1.8 | 3.4 |
| Cr | $C + F$[a] | $2.38 \times 10^{-10}$ | $2.40 \times 10^{-10}$ | $2.40 \times 10^{-10}$ | $1.63 \times 10^{-10}$ | $1.64 \times 10^{-10}$ | $1.65 \times 10^{-10}$ | $9.22 \times 10^{-11}$ | $9.17 \times 10^{-11}$ | $9.20 \times 10^{-11}$ |
| | Leakage | $-2.90 \times 10^{-11}$ | $-2.86 \times 10^{-11}$ | $-2.95 \times 10^{-11}$ | $-8.46 \times 10^{-10}$ | $-8.35 \times 10^{-10}$ | $-8.63 \times 10^{-10}$ | $-1.41 \times 10^{-9}$ | $-1.39 \times 10^{-9}$ | $-1.44 \times 10^{-9}$ |
| | Scattering | $1.35 \times 10^{-10}$ | $0.09 \times 10^{-10}$ | $1.10 \times 10^{-10}$ | $1.71 \times 10^{-10}$ | $0.85 \times 10^{-10}$ | $1.45 \times 10^{-10}$ | $1.93 \times 10^{-10}$ | $1.47 \times 10^{-10}$ | $1.70 \times 10^{-10}$ |
| | Total | $3.44 \times 10^{-10}$ | $2.20 \times 10^{-10}$ | $3.21 \times 10^{-10}$ | $-5.12 \times 10^{-10}$ | $-5.86 \times 10^{-10}$ | $-5.53 \times 10^{-10}$ | $-1.12 \times 10^{-9}$ | $-1.15 \times 10^{-9}$ | $-1.17 \times 10^{-9}$ |
| | %[b] | — | −36.0 | −6.7 | — | +14.2 | +8.0 | — | +2.4 | +4.5 |
| Na | $C + F$[a] | $1.40 \times 10^{-10}$ | $1.39 \times 10^{-10}$ | $1.41 \times 10^{-10}$ | $9.58 \times 10^{-11}$ | $9.49 \times 10^{-11}$ | $9.60 \times 10^{-11}$ | $5.31 \times 10^{-11}$ | $5.17 \times 10^{-11}$ | $5.22 \times 10^{-11}$ |
| | Leakage | $-1.15 \times 10^{-10}$ | $-1.17 \times 10^{-10}$ | $-1.16 \times 10^{-10}$ | $-3.34 \times 10^{-9}$ | $-3.40 \times 10^{-9}$ | $-3.37 \times 10^{-9}$ | $-5.48 \times 10^{-9}$ | $-5.59 \times 10^{-9}$ | $-5.54 \times 10^{-9}$ |
| | Scattering | $-2.69 \times 10^{-9}$ | $-2.49 \times 10^{-9}$ | $-2.26 \times 10^{-9}$ | $-1.47 \times 10^{-9}$ | $-1.34 \times 10^{-9}$ | $-1.15 \times 10^{-9}$ | $-2.57 \times 10^{-10}$ | $-2.22 \times 10^{-10}$ | $-0.49 \times 10^{-10}$ |
| | Total | $-2.67 \times 10^{-9}$ | $-2.47 \times 10^{-9}$ | $-2.24 \times 10^{-9}$ | $-4.71 \times 10^{-9}$ | $-4.65 \times 10^{-9}$ | $-4.41 \times 10^{-9}$ | $-5.69 \times 10^{-9}$ | $-5.76 \times 10^{-9}$ | $-5.53 \times 10^{-9}$ |
| | %[b] | — | −7.3 | −16.1 | — | −1.7 | −6.4 | — | +1.6 | −2.8 |
| Carbon | $C + F$[a] | 0 | 0 | 0 | 0 | 0 | 0 | 0 | 0 | 0 |
| | Leakage | $-2.36 \times 10^{-10}$ | $-2.37 \times 10^{-10}$ | $-2.39 \times 10^{-10}$ | $-6.81 \times 10^{-9}$ | $-6.85 \times 10^{-9}$ | $-6.93 \times 10^{-9}$ | $-1.11 \times 10^{-8}$ | $-1.12 \times 10^{-8}$ | $-1.13 \times 10^{-8}$ |
| | Scattering | $-1.12 \times 10^{-8}$ | $-1.00 \times 10^{-8}$ | $-1.05 \times 10^{-8}$ | $-6.68 \times 10^{-9}$ | $-5.80 \times 10^{-9}$ | $-6.10 \times 10^{-9}$ | $-1.93 \times 10^{-9}$ | $-1.52 \times 10^{-9}$ | $-1.52 \times 10^{-9}$ |
| | Total | $-1.14 \times 10^{-8}$ | $-1.02 \times 10^{-8}$ | $-1.08 \times 10^{-8}$ | $-1.35 \times 10^{-8}$ | $-1.27 \times 10^{-8}$ | $-1.30 \times 10^{-8}$ | $-1.31 \times 10^{-8}$ | $-1.27 \times 10^{-8}$ | $-1.29 \times 10^{-8}$ |
| | %[b] | — | −10.1 | −5.3 | — | −6.3 | −3.7 | — | −2.5 | −1.5 |
| Oxygen | $C + F$ | 0 | 0 | 0 | 0 | 0 | 0 | 0 | 0 | 0 |
| | Leakage | $-4.34 \times 10^{-10}$ | $-4.15 \times 10^{-10}$ | $-4.46 \times 10^{-10}$ | $-1.26 \times 10^{-8}$ | $-1.20 \times 10^{-8}$ | $-1.30 \times 10^{-8}$ | $-2.06 \times 10^{-8}$ | $-1.96 \times 10^{-8}$ | $-2.16 \times 10^{-8}$ |
| | Scattering | $-1.57 \times 10^{-8}$ | $-0.97 \times 10^{-8}$ | $-1.73 \times 10^{-8}$ | $-9.20 \times 10^{-9}$ | $-5.49 \times 10^{-9}$ | $-10.00 \times 10^{-9}$ | $-2.62 \times 10^{-9}$ | $-1.21 \times 10^{-9}$ | $-2.76 \times 10^{-9}$ |
| | Total | $-1.61 \times 10^{-8}$ | $-1.01 \times 10^{-8}$ | $-1.77 \times 10^{-8}$ | $-2.17 \times 10^{-8}$ | $-1.75 \times 10^{-8}$ | $-2.30 \times 10^{-8}$ | $-2.32 \times 10^{-8}$ | $-2.08 \times 10^{-8}$ | $-2.43 \times 10^{-8}$ |
| | %[b] | — | — | +9.9 | — | −19.3 | +6.0 | — | −10.3 | +4.7 |

[a] $C \equiv$ capture; $F \equiv$ fission.
[b] % deviation of Total $\Delta k/k/\Delta V$ with respect to Total $\Delta k/k/\Delta V$ values obtained using Set 236.

It is also of interest to note that the group structure of a collapsed set is sensitive to the real and adjoint flux spectra of the particular system. The use of the five and six energy group structures employed in the analysis of FARET gave results having rather large discrepancies with respect to the Set 236 results. The harder spectrum of the real flux and the more uniform spectrum of the adjoint flux in EBR-II compared with those in FARET require that a different approach to group collapsing of the cross section be taken. It is, therefore, realized that the use of Sets 23605 and 23606 is limited to reactors whose spectra are similar to that of EBR-II, Run 20.

### References

1. D. M. O'Shea, B. J. Toppel and A. L. Rago, *MC²*, *A Code to Calculate Multigroup Cross Sections*, ANL-7318 (1967).
2. D. A. Meneley, L. C. Kvitek and D. M. O'Shea, *MACH 1*, *One-Dimensional Diffusion-Theory Package*, ANL-7223 (1966).

## III-19. Investigation of the Temperature Coefficient of EBR-II, Run 25

J. T. Madell

The components of the temperature coefficient, exclusive of bowing and Doppler broadening effects, were calculated for the Run 25 configuration of EBR-II. In Run 25, the core contained 88 subassemblies surrounded by two rings of stainless steel pins. Depleted uranium subassemblies comprised the remainder of the reactor. This configuration differed from previous configurations in that the core included all but three subassembly positions in the first 6 rings, and stainless steel had replaced the depleted uranium pins in the 7th and 8th rings. The value of the power coefficient measured at the beginning of Run 25 was noticeably different from previously measured values. Since the temperature coefficients were last calculated for a 67 subassembly core of MARK-I design surrounded by a depleted uranium blanket,[1] calculations for the present configuration of EBR-II were desired.

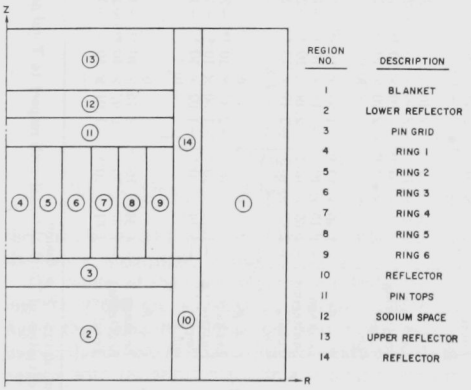


Fig. III-19-1. Representation of EBR-II for Two-Dimensional Calculations, with Region Number and Identification. *ANL Neg. No. 112-8942.*

The calculations were carried out using the two dimensional SNARG[5] code with a six group cross section set, #23606. The desired results were the reactivities for a standard configuration of EBR-II and for configurations representing changes in dimension and density due to temperature changes. The representation of EBR-II, Run 25 for these two dimensional calculations is shown in Fig. III-19-1.

### Standard Configuration

The standard configuration used as a basis for comparison in these calculations is the reactor loading for Run 25 of EBR-II at a uniform temperature of 700°F. The dimensions of the reactor, and the volume fractions, atom densities and temperatures of the reactor materials for the standard configuration and subsequent configurations were determined from design reports and drawings of EBR-II and recent status reports from Argonne's Idaho Division.[2,3,4]

Using these compositions and dimensions, the reactivity of the basic configuration of EBR-II was calculated with the two-dimensional SNARG code. The resulting value of $k_{eff}$ obtained was 1.060. This value is substantially higher than the expected value of 1.00, and the discrepancy cannot be entirely attributed to the uncertainty in the dimensions and the composition. Investigations are being conducted to determine the cause of this discrepancy. However, since for this study only the comparative values of $k_{eff}$ were of interest, it was felt that it would be better to continue with the calculations of the temperature coefficient concurrent with the investigations of the discrepancy in the absolute value of $k_{eff}$.

### Calculation of the Temperature Coefficients

The components of the temperature coefficients investigated in this study were associated only with the changes in dimension and density due to changes in the temperature. No consideration was given to the reactivity effects due to bowing or the Doppler broadening. The changes in dimension and density are strongly dependent, of course, on the values used for the linear expansion coefficients, $\alpha$, of the reactor materials. The values used in this study are

$$\text{steel: } \alpha = 10.0 \times 10^{-6}/°\text{F}$$

$$\text{fuel: } \alpha = 9.2 \times 10^{-6}/°\text{F}.$$

The change of sodium density with temperature was obtained from the Liquid Metals Handbook.[4]

The temperature coefficients are given in terms of either $\Delta k/k$ per MW or $\Delta k/k$ per °C. In obtaining these values, it was decided to use the value of the temperature increase corresponding to an increase in reactor power from zero to 45 MW. Besides calculating an overall change of reactivity from zero to 45 MW due to dimensional and density changes, calculations were made of the three components of the temperature effect. These three components produced the change in reactivity due to change in the density of the sodium to the expansion and change in density of the steel, and due to the axial expansion and change in density of the fuel. These three components of the temperature effect will be discussed separately in the following paragraphs.

### Sodium Effect

The reactivity change due to a change of sodium density with temperature was calculated in three parts. In the first part, the density of the sodium was changed in the core only; in the second part the density was changed in the core and upper reflector; the sodium density in the third part was changed throughout the reactor to correspond to 45 MW operation.

### Axial Expansion of Fuel

The increase in the height of the fuel was assumed to be uniform over the entire core and the density change is proportional to the change in the height of the core. This is true because the change in the radial dimension of the fuel with temperature does not change its density in the homogenized region. The temperature effect of the fuel material in the blanket was considered only in the calculation of the overall temperature effect. The radial expansion of the fuel expels sodium from the gap between the fuel and the jacket wall, resulting in an increase in the sodium height above the fuel pin. This displacement of sodium was ignored in the calculations because it has been shown to be a small effect.[1]

### Temperature Effects in the Stainless Steel

The temperature of the stainless steel was assumed to be that of the jacket (a small amount of the stainless steel is that of the subassembly wall which is approximately at the temperature of the sodium). It was assumed that the reactor expands as a rigid stainless steel structure in which no thermal stresses are present. Any effect of radial clearances between subassemblies in reducing radial expansion feedback was thus not taken into account, nor are any bowing effects included. In order to simplify the calculations, it was assumed that the dimensions change according to the temperature profile along the axial centerline and radial midplane of the reactor. This is not completely accurate, of course, since there are varying temperature profiles in the axial direction and also in the radial direction. Since the centerline temperatures are in the area of greatest importance, no significant errors were thought to be introduced with this assumption.

### Overall Coefficient at 45 MW Operation

By adding the sodium, stainless steel, and fuel effects, most of the effect of the dimensional and density changes should be taken into account. The last calculation performed was to make the appropriate dimensional and density changes for 45 MW; that is, to take into account all three components in one calculation.

### Isothermal Temperature Coefficient

In addition to calculating the change of reactivity between zero and 45 MW, it was also decided to calculate the isothermal temperature coefficient. The value of the reactivity of the EBR-II, Run 25 was calculated for a uniform reactor temperature of 900°F. The value of 900°F was selected to obtain a large enough value of $\Delta k$ for adequate numerical accuracy.

### Discussion of the Results

The values of the reactivity change and the power coefficients, where applicable, for the various reactor configurations considered in this study are presented in Table III-19-I. The results are examined in three areas; for internal consistency, for comparison with measured values, and for comparison with previously calculated values.

### Internal Consistency

The sum of the reactivity changes for Problems #2, #3 and #6 represents the total temperature effect of the three EBR-II components (fuel, sodium and steel)

with one exception. The exception is that the fuel temperature coefficient for the blanket is not included in Problem №2, but the fuel blanket coefficient is small. The sum of the reactivity changes in Problems №2, №3 and №6 is less negative than the total change calculated in Problem №7. The inclusion of a small, negative coefficient for the fuel in the blanket will bring the numbers into better agreement, which indicates the internal consistency of the problems. The results also suggest that the three components of temperature coefficient are somewhat interdependent.

TABLE III-19-I. Calculated Values of Reactivity Change for Various Conditions of EBR-II, Run 25

| Problem No. | Problem Description | $-\Delta k/k$ | $\Delta k/k$/MW $\times 10^{+5}$ | Comment |
|---|---|---|---|---|
| 1 | Uniform 700°F | — | — | Basic configuration |
| 2 | Fuel—960°F | 0.000457 | 1.016 | Fuel expansion coef. |
| 3 | Steel at temperature | 0.001253 | 2.785 | Structural expan. coef. |
| 4 | Na—core | 0.000480 | 1.067 | — |
| 5 | —overall | 0.000895 | 1.989 | Sodium density coef. |
| 6 | 45 MW operation | 0.002939 | 6.531 | Overall temp. coef. |
| — | Total №2, 3, 6 | 0.002605 | — | — |
| 7 | Uniform 900°F | ~0.005356 | — | Isothermal coef. |

TABLE III-19-II. Some Temperature Coefficients for the Initial and Present Arrangement of EBR-II

| Component | Initial arrangement (Ref. 1) | Present arrangement (This Paper) |
|---|---|---|
| | $-\Delta k/k$/°C $\times 10^5$ | $-\Delta k/k$/ C $\times 10^5$ |
| Sodium in core | 0.87 | 0.86 |
| Fuel in core | 0.39 | 0.32 |
| Structure in core | 1.01 | ~1.30 |

### Comparison with Measured Values

The total power coefficient, including bowing and Doppler effects, has been measured. It is difficult, however, to measure separate components of the coefficient. One measurement has been made of the fuel coefficient, and the results agreed well with the calculated value. The calculated value of the isothermal coefficient (−1.15 Ih/°F) agrees fairly well with the value of −1.04 Ih/°F which was measured for Run 25. Comparison of the total power coefficient will be made with the calculated values upon the completion of analysis of the bowing effects and may provide information on the accuracy of the calculations presented here.

### Comparison with Previously Calculated Values

The various components of the temperature coefficient were calculated for a 67 subassembly core of MARK-I design surrounded by depleted uranium axial and radial blankets.[1] This arrangement of EBR-II corresponds to that existing at the initial reactor start-up and differs considerably from the present arrangement. Even so, the calculated values of the temperature coefficients for some components compare closely (see Table III-19-II). It should be pointed out that the method of calculating the coefficients (as well as the physical arrangement) differs considerably for the two cases. Because of the differences in the basis for the two sets of coefficients no conclusion is drawn from their comparison.

### References

1. L. J. Koch, W. B. Lowenstein and H. O. Monson, *Addendum to Hazard Summary Report, Experimental Breeder Reactor-II (EBR-II)*, ANL-5719 (Addendum) (1962).
2. Reactor Handbook, Vol. 3—Section 1, USAEC, AECD-3647 (March 1955).
3. R. R. Smith, Argonne National Laboratory (private communication).
4. Liquid Metals Handbook, USAEC Report TID-5277, USAEC and Bureau of Ships (July 1, 1955).
5. G. Duffy, Argonne National Laboratory (private communication).

## III-20. Some Effects of Iron, Molybdenum, and Nickel Reflectors Placed Between the Core and Blanket of EBR-II

J. T. Madell

Results of recent changes in the loading of the EBR-II core led to this study. As the number of irradiation subassemblies in the core has increased, the core has expanded from the 5th ring into the 6th ring. The present loading of the EBR-II core (Run 25) contains 88 subassemblies almost filling the 6th and last ring of the core.

Substituting an irradiation subassembly for a fuel

TABLE III-20-I. Description and Results of Comparative Study of Eight Arrangements of EBR-II

| | Run | | | | | | | |
|---|---|---|---|---|---|---|---|---|
| | 20 | 25 | 25A | 25B | 25C | 25D | 25E | 25F |
| Composition | | | | | | | | |
| Rings 1-5 | fuel | fuel | fuel | fuel | fuel | fuel | fuel | fuel |
| 6 | fuel & blanket | fuel | fuel | fuel | fuel | fuel | fuel | fuel |
| 7 | blanket | blanket | steel | steel | molyb-denum | molyb-denum | nickel | nickel |
| 8 | blanket | blanket | blanket | steel | blanket | molyb-denum | blanket | nickel |
| 9-15 | blanket | blanket | blanket | blanket | blanket | blanket | blanket | blanket |
| $k_{eff}$ | 1.00 | 1.00 | 1.0032 | 1.0105 | 1.0005 | 1.0055 | 1.0149 | 1.0330 |
| "Fission" Power, MW | 41.1 | 42.2 | 42.2 | 42.2 | 42.2 | 42.2 | 42.2 | 42.2 |
| Fission Density, fissions/ $cm^3$-sec $\times 10^{12}$ | | | | | | | | |
| Center | 21.5 | 19.5 | 20.0 | 20.1 | 20.3 | 20.5 | 19.6 | 19.2 |
| Ring 6—peak | 9.63 | 13.3 | 13.8 | 14.1 | 13.9 | 14.2 | 14.0 | 14.3 |
| ave | 8.41 | 12.1 | 12.7 | 13.1 | 12.7 | 13.0 | 13.2 | 14.1 |
| Ring 7—peak | 1.73 | 2.17 | 0 | 0 | 0 | 0 | 0 | 0 |
| ave | 1.10 | 1.38 | 0 | 0 | 0 | 0 | 0 | 0 |
| Ring 8—peak | 0.678 | 0.837 | 1.00 | 0 | 0.815 | 0 | 0.798 | 0 |
| ave | 0.449 | 0.549 | 0.652 | 0 | 0.534 | 0 | 0.523 | 0 |
| Ring 9—peak | 0.288 | 0.348 | 0.410 | 0.483 | 0.339 | 0.320 | 0.331 | 0.355 |
| Ring 10—peak | 0.162 | 0.193 | 0.225 | 0.264 | 0.188 | 0.179 | 0.183 | 0.196 |

subassembly decreases the reactivity of EBR-II. Since most of the core positions were filled in Run 25, a means of compensating for this reactivity decrease by some manner other than adding more fuel subassemblies must be used. A previous study showed in a general fashion that the reactivity of systems similar to EBR-II increases upon the addition of a reflector between the core and the blanket.[1]

The purpose of this work was to predict the effects of substituting stainless steel, nickel and molybdenum pins for depleted uranium pins in the 7th ring only, and in both the 7th and 8th ring subassemblies. The effects of interest were restricted to the relative changes in reactivity, power density distribution from the center of the 10th ring and the flux level at the reactor vessel. It is desirable to minimize this last quantity from the standpoint of radiation damage.

The study consisted of a series of MACH 1[(2)] calculations using the latest available data on EBR-II's composition and the 22 energy group cross section Set 236 (see Paper III-18). The material composition for the eight calculations are described in Table III-20-I along with values of $k_{eff}$, power, and power density. The values of flux per megawatt at the reactor vessel appear in Table III-20-II by energy group for the last seven cases. In the calculations EBR-II was represented as a cylinder with region dependent extrapolated heights. The extrapolated heights for the reflector and blanket regions were equated to the physical height of the region. The extrapolated height of the EBR-II core was varied to achieve criticality in Runs 20 and 25. The extrapolated height of the core for Run 25 was used in the remaining calculations.

## Discussion of Results

Since these calculations are not sophisticated, the results are to be interpreted as trends rather than as absolute results.

All three reflector materials increase the reactivity, with nickel yielding three times the increase obtained for the next best material, stainless steel. The use of two rows of reflector material at least doubles the reactivity increase resulting from one row. The relatively high scattering cross sections in the upper energy groups of nickel account for its good performance as a reflector material.

Assuming that the total reactor power is constant* for all cases, the use of a reflector increases the center power density and decreases the ratio of maximum-to-average power density. The power density in the *7th*, *8th* and outer rings increased from Run 20 to Run 25. The addition of various reflectors in Run 25 has the following effects on the power densities:

* The total reactor power in all cases is 45 MW. In the seven cases of Run 25 the difference in total power and "fission" power is the power due to beta and gamma ray absorption. The difference between the "fission" power in Run 20 and Run 25 reflects the 1.1 MW generated in the axial blanket in Run 20.

TABLE III-20-II. FLUX PER MW AT THE REACTOR VESSEL FOR SEVEN ARRANGEMENTS OF EBR-II

| Energy Group Number | $E_{lower}$, eV | Lethargy (upper) | Run | | | | | | |
|---|---|---|---|---|---|---|---|---|---|
| | | | 25 | 25A | 25B | 25C | 25D | 25E | 25F |
| 1 | $3.68 \times 10^6$ | 1.0 | $2.72 \times 10^6$ | $3.074 \times 10^6$ | $3.479 \times 10^6$ | $2.629 \times 10^6$ | $2.515 \times 10^6$ | $2.488 \times 10^6$ | $2.366 \times 10^6$ |
| 2 | $2.23 \times 10^6$ | 1.5 | $4.54 \times 10^6$ | $5.131 \times 10^6$ | $5.812 \times 10^6$ | $4.385 \times 10^6$ | $4.196 \times 10^6$ | $4.155 \times 10^6$ | $3.958 \times 10^6$ |
| 3 | $1.38 \times 10^6$ | 2.0 | $1.53 \times 10^7$ | $1.728 \times 10^7$ | $1.962 \times 10^7$ | $1.475 \times 10^7$ | $1.411 \times 10^7$ | $1.399 \times 10^7$ | $1.336 \times 10^7$ |
| 4 | $8.21 \times 10^5$ | 2.5 | $3.44 \times 10^7$ | $3.923 \times 10^7$ | $4.483 \times 10^7$ | $3.294 \times 10^7$ | $3.110 \times 10^7$ | $3.192 \times 10^7$ | $3.101 \times 10^7$ |
| 5 | $4.98 \times 10^5$ | 3.0 | $6.37 \times 10^7$ | $7.278 \times 10^7$ | $8.321 \times 10^7$ | $6.054 \times 10^7$ | $5.663 \times 10^7$ | $5.596 \times 10^7$ | $5.829 \times 10^7$ |
| 6 | $3.02 \times 10^5$ | 3.5 | $1.19 \times 10^8$ | $1.363 \times 10^8$ | $1.559 \times 10^8$ | $1.129 \times 10^8$ | $1.051 \times 10^8$ | $1.118 \times 10^8$ | $1.094 \times 10^8$ |
| 7 | $1.83 \times 10^5$ | 4.0 | $1.81 \times 10^8$ | $2.074 \times 10^8$ | $2.372 \times 10^8$ | $1.715 \times 10^8$ | $1.595 \times 10^8$ | $1.702 \times 10^8$ | $1.660 \times 10^8$ |
| 8 | $1.11 \times 10^5$ | 4.5 | $2.61 \times 10^8$ | $2.983 \times 10^8$ | $3.411 \times 10^8$ | $2.468 \times 10^8$ | $2.296 \times 10^8$ | $2.448 \times 10^8$ | $2.380 \times 10^8$ |
| 9 | $6.74 \times 10^4$ | 5.0 | $3.93 \times 10^8$ | $4.492 \times 10^8$ | $5.135 \times 10^8$ | $3.721 \times 10^8$ | $3.468 \times 10^8$ | $3.684 \times 10^8$ | $3.570 \times 10^8$ |
| 10 | $4.09 \times 10^4$ | 5.5 | $4.98 \times 10^8$ | $5.686 \times 10^8$ | $6.496 \times 10^8$ | $4.717 \times 10^8$ | $4.405 \times 10^8$ | $4.661 \times 10^8$ | $4.504 \times 10^8$ |
| 11 | $2.48 \times 10^4$ | 6.0 | $6.15 \times 10^8$ | $7.015 \times 10^8$ | $8.013 \times 10^8$ | $5.830 \times 10^8$ | $5.454 \times 10^8$ | $5.751 \times 10^8$ | $5.544 \times 10^8$ |
| 12 | $1.50 \times 10^4$ | 6.7 | $8.48 \times 10^8$ | $9.655 \times 10^8$ | $1.102 \times 10^9$ | $8.040 \times 10^8$ | $7.542 \times 10^8$ | $7.914 \times 10^8$ | $7.611 \times 10^8$ |
| 13 | $9.12 \times 10^3$ | 7.0 | $1.06 \times 10^9$ | $1.203 \times 10^9$ | $1.373 \times 10^9$ | $1.004 \times 10^9$ | $9.437 \times 10^8$ | $9.859 \times 10^8$ | $9.463 \times 10^8$ |
| 14 | $4.31 \times 10^3$ | 7.75 | $2.72 \times 10^9$ | $3.090 \times 10^9$ | $3.526 \times 10^9$ | $2.587 \times 10^9$ | $2.442 \times 10^9$ | $2.532 \times 10^9$ | $2.242 \times 10^9$ |
| 15 | $2.62 \times 10^3$ | 8.25 | $9.13 \times 10^8$ | $1.038 \times 10^9$ | $1.185 \times 10^9$ | $8.698 \times 10^8$ | $8.217 \times 10^8$ | $8.511 \times 10^8$ | $8.144 \times 10^8$ |
| 16 | $2.03 \times 10^3$ | 8.50 | $8.71 \times 10^8$ | $9.893 \times 10^8$ | $1.129 \times 10^9$ | $8.295 \times 10^8$ | $7.844 \times 10^8$ | $8.110 \times 10^8$ | $7.754 \times 10^8$ |
| 17 | $1.23 \times 10^3$ | 9.0 | $1.25 \times 10^9$ | $1.416 \times 10^9$ | $1.615 \times 10^9$ | $1.188 \times 10^9$ | $1.125 \times 10^9$ | $1.161 \times 10^9$ | $1.109 \times 10^9$ |
| 18 | $9.61 \times 10^2$ | 9.25 | $8.75 \times 10^8$ | $9.934 \times 10^8$ | $1.133 \times 10^9$ | $8.342 \times 10^8$ | $7.905 \times 10^8$ | $8.144 \times 10^8$ | $7.778 \times 10^8$ |
| 19 | $5.83 \times 10^2$ | 9.75 | $2.87 \times 10^9$ | $3.257 \times 10^9$ | $3.714 \times 10^9$ | $2.740 \times 10^9$ | $2.601 \times 10^9$ | $2.670 \times 10^9$ | $2.547 \times 10^9$ |
| 20 | $2.75 \times 10^2$ | 10.50 | $3.44 \times 10^9$ | $3.904 \times 10^9$ | $4.452 \times 10^9$ | $3.289 \times 10^9$ | $3.128 \times 10^9$ | $3.202 \times 10^9$ | $3.052 \times 10^9$ |
| 21 | $1.01 \times 10^2$ | 11.50 | $1.44 \times 10^{10}$ | $1.630 \times 10^{10}$ | $1.859 \times 10^{10}$ | $1.377 \times 10^{10}$ | $1.315 \times 10^{10}$ | $1.337 \times 10^{10}$ | $1.274 \times 10^{10}$ |
| 22 | $2.90 \times 10^1$ | 12.75 | $2.64 \times 10^{10}$ | $2.993 \times 10^{10}$ | $3.415 \times 10^{10}$ | $2.534 \times 10^{10}$ | $2.425 \times 10^{10}$ | $2.458 \times 10^{10}$ | $2.344 \times 10^{10}$ |

(1) For a steel reflector, the power density increases in the blanket elements for both the one and two ring thick reflectors.

(2) For a molybdenum reflector, the power density decreases in the blanket elements for both the one and two ring thick reflectors.

(3) For a nickel reflector, the power density in the blanket decreases upon the addition of one ring of nickel but increases upon the addition of two rings of nickel.

The calculated results in Table III-20-II show that the value of the flux per megawatt at the reactor vessel increases with the addition of a steel reflector and decreases with the addition of either a molybdenum or nickel reflector. A greater change is produced by increasing the thickness of the reflector.

The calculated values of reactivity change upon the addition of one and two rings of stainless steel reflector agrees with the values measured on EBR-II. A reactivity change was measured to be 0.51% for one ring and 1.04% for two rings. Discrepancies exist, however, between the measured and calculated values of U-235 and U-238 reaction rates in the region of the reflector and they are being investigated.

### REFERENCES

1. V. Z. Jankus, Argonne National Laboratory (private communication).
2. D. A. Meneley, L. C. Kvitek, and D. M. O'Shea, *MACH 1, One-Dimensional Diffusion-Theory Package*, ANL-7223 (1966).

## III-21. Development of the Critical Experiment Program for the Fast Fuels Test Facility

P. J. PERSIANI, J. K. LONG, A. J. ULRICH and D. A. KUCERA

### INTRODUCTION

Reflector control in a fast fuel test reactor is preferable to control rods in the core because there is less neutronic interference with test fuel and less physical interference between control mechanisms and test equipment. Calculations of the effectiveness of control rods in the reflector of the 70 liter core of Assembly 46 have been adequately verified experimentally. The

application of this method of calculation to the reflector control rods of the 800 liter core of FFTF was believed to be uncertain without further experimental verification.

The ZPR-3 Assembly 48 was sufficiently similar in composition to the FFTF reference first core to serve as a good measure of computational techniques. The carbon in Assembly 48 had an effect which is comparable to the oxygen in FFTF. Assembly 46 experiments for FARET showed that a replacement of carbon by oxygen in the ratio of 0.87 to 1.0 leaves the leakage and scattering unchanged.

Therefore, the objective of phase A critical experiments, carried out between December 1, 1966 and early February 1967 was primarily to provide experimental measurements of reflector control rod effectiveness for the 400 liter core of a modified form of Assembly 48. A secondary objective was to measure material worth and reaction rates in configurations which are relatively clean and symmetrical. These measurements were to test calculational methods at the 400 liter core size and thus provide a basis for the projection of their use for the 800 liter core size of the FFTF.

## Reflector Properties

In a fast test reactor an inconel-sodium reflector is an improvement over a U-238-sodium blanket because of increased reflector savings and because the softer spectrum in the reflector gives greater worth to control rods. At the same time the spectrum is not too soft to be comparable to that of a large fast power reactor.

In Assembly 48A full reflector properties and worth of control rods in a full reflector could be observed and measured for an inconel-sodium mixture without replacing the whole blanket by reflector.

In Fig. III-21-1 the reflector savings for a core of Assembly 48 composition is plotted against the thickness of an inconel-sodium reflector in spherical geometry. The reflector savings approaches its maximum value when the thickness is 30 cm. The circled point marks the reflector savings obtained when a 20 cm thick reflector is backed by 10 cm of blanket. It is found that in this case the savings are greater than for 30 cm thick inconel-sodium reflector because of the U-238 source of fast neutrons. However, it is not as great as the maximum reflector savings obtainable with an infinitely thick inconel-sodium reflector. As a result reflector savings near the maximum amount can be obtained without replacing all of the blanket thickness by reflector.

## Reflector Control Rods

Control rods in a reflector consisting of two opposing 100 deg sectors embedded in blanket material have a worth which is within a few percent of that for the same reflector-blanket combination extending 360 deg around the core. This statement is detailed in the next few paragraphs. Sectors of 100 deg are used to provide reflector regions of large enough angular

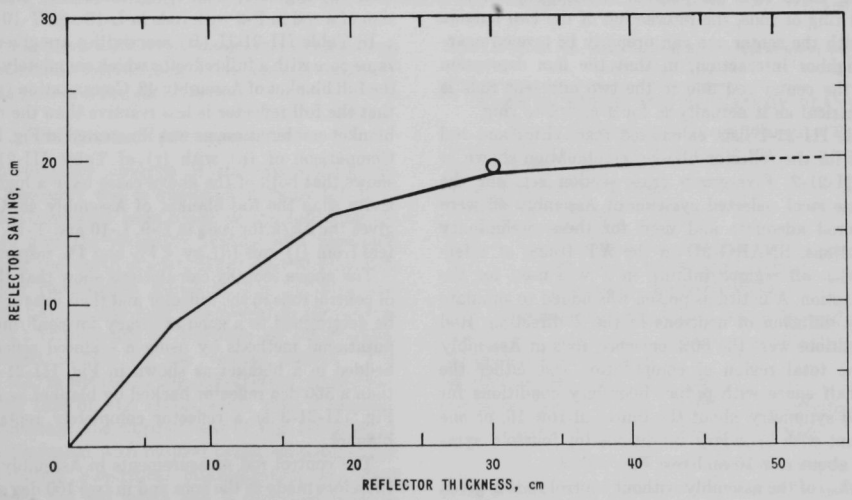


Fig. III-21-1. Reflector Saving versus Reflector Thickness for ZPR-3 Assembly 48 Core Composition with Inconel-Sodium Reflector (Spherical Geometry). *ANL Neg. No. 112-9249.*

TABLE III-21-I. CORE WITH AN OPPOSING PAIR OF REFLECTOR SECTORS EMBEDDED IN BLANKET
(see Fig. III-21-2)

| | |
|---|---|
| **Twofold Symmetry About Center of Row 16** | |
| (a) Reactivity without rods | 0.9958 |
| (b) $\Delta k/k$ for rod in L-10 (also rod in L-22 by symmetry) | −0.0116 |
| (c) $\Delta k/k$ for rod in L-10 alone (assume no interaction across line of symmetry) | −0.0058 |
| (d) $\Delta k/k$ for rods in L-10 and T-10 (also rods in L-22 and T-22) | −0.0234 |
| (e) $\Delta k/k$ for rods in L-10 and T-10 (assume no interaction across line of symmetry) | −0.0117 |
| **Fourfold Symmetry About Row 16 And Row P** | |
| (f) Reactivity without rods | 0.9958 |
| (g) $\Delta k/k$ for rod in L-10 (also T-10, L-22, T-22 by symmetry) | −0.0261 |
| (h) $\Delta k/k$ for rods in L-10, T-10 | −0.0131 |
| (i) $\Delta k/k$ for rod in P-9 alone | −0.0074 |
| (j) $\Delta k/k$ for rods in P-9, L-10 and T-10 | −0.0161 |

width to allow measurement of the worth of three control rods in the region at the same time without unduly large edge effects. Two 100 deg opposing sectors were chosen in order to maintain flux symmetry about the core axis in the plane which bisects the sectors.

It is desirable to measure the worth of three rods at a time to accurately evaluate the amount of reduction in single rod worth caused by rod interference. Considering three rods as part of a complete equally spaced ring of rods, the interaction of the two outside rods with the center one can properly be termed nearest neighbor interaction, in that the flux depression about the center rod due to the two adjacent rods is symmetrical as it actually is for a complete ring.

Table III-21-I lists calculated reactivities and rod worths for the reflector-blanket combination shown in Fig. III-21-2. Five-group cross section sets for the stainless steel reflected systems of Assembly 46 were considered adequate and used for these preliminary calculations. SNARG-2D in the $XY$ frame of reference with all regions infinite in $Z$ was used for the computation. A fictitious poison was added to simulate loss by diffusion of neutrons in the $Z$ direction. Rod compositions were the 60% enriched rods of Assembly 46. The total region of computation was either the right half space with proper boundary conditions for twofold symmetry about the center of row 16, or one quadrant with boundary conditions for fourfold symmetry about row 16 and row P.

The $k_{eff}$ of the assembly without control rods is given by computation (a) to be 0.9958, and the reactivity changes in (b) to (e) for twofold symmetry are referred to this (Table III-21-I). By comparing (e) with (c) it may be concluded that the interaction between rods in L-10 and T-10 is less than about 1%, which is less than the accuracy of the computation itself. Since L-22 is more remote from L-10 than is T-10, the assumption of no interaction between L-10 and L-22 is essentially correct. This means that interaction of rods in P-9 and P-23 can also be neglected.

Computations (f) through (j) use fourfold symmetry and the reactivity changes obtained are with respect to the $k_{eff}$ of 0.9958 in (f) for the assembly without rods. Changes in grid structure and boundary conditions alone are responsible for the differences between (a) and (f) and between (e) and (h). Computation (j) of the $\Delta k/k$ for the cluster of rods in P-9, L-10, and T-10 should be compared with the sum of (h) and (i) for the same rods without interaction. The interaction effect is found to be 0.0044 $\Delta k/k$.

Table III-21-II lists reactivities for the same core with a cylindrically symmetric reflector as shown in Fig. III-21-3. A comparison of Table III-21-II (A) and (B) with Table III-21-I shows how closely the worth of rods and their interactions in a 360 deg reflector can be duplicated in the sectored reflector. The advantages of an inconel reflector can be seen from the $k_{eff}$ value, without rods, of 1.005419 in computation (k). The $\Delta k/k$ for a rod in position P-9 in computation (l) indicates an increase in the value for the sectored case [computation (i)] by about 5%. Computation (m) is within 1% agreement with case (h) for rods in L-10 and T-10. Case (n) is greater than (j) by about 5%. The interaction of a rod in P-9 with rods in L-10 and T-10 is 0.003.

In Table III-21-II (B) reactivities are given for the same core with a full reflector which completely replaces the full blanket of Assembly 48. Computation (p) shows that the full reflector is less reactive than the reflector-blanket combination, as was illustrated in Fig. III-21-1. Comparison of (p) with (r) of Table III-21-II (C) shows that both of the above cases have a higher reactivity than the full blanket of Assembly 48. Case (q) gives the $\Delta k/k$ for rods in P-9, L-10 and T-10, and differs from (j) and (n) by <7% and 1% respectively.

The above scoping calculations show that the worth of control rods in the reflector and their interactions can be determined to a good accuracy for confirming computational methods by using a sectored reflector embedded in a blanket as shown in Fig. III-21-2 rather than a 360 deg reflector backed by blanket as shown in Fig. III-21-3 or a reflector completely replacing the blanket.

The control rod measurements in Assembly 48 were therefore made in the core and in two 100 deg sectors of inconel-sodium reflector embedded in the U-238

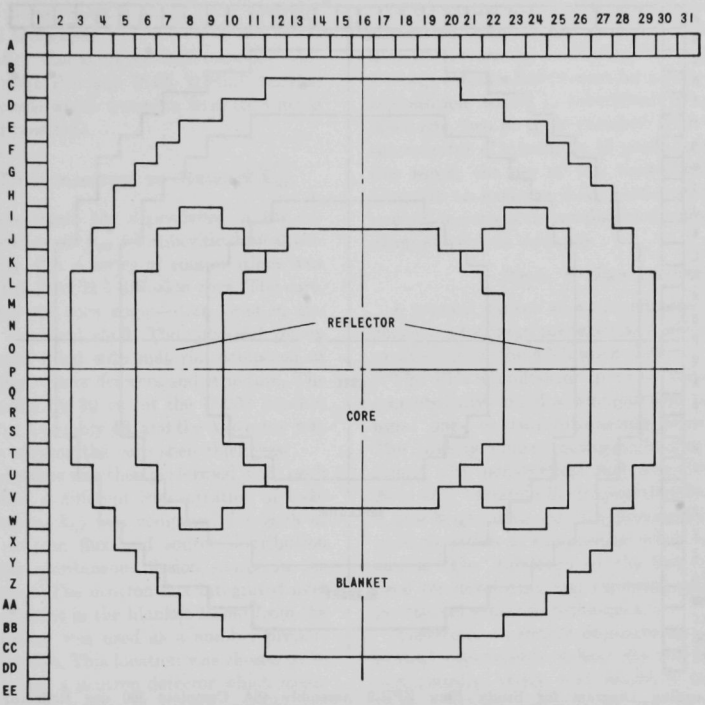


FIG. III-21-2. Loading Diagram for Study Plan ZPR-3 Assembly 48A Diagram for Sectored Reflector. *ANL Neg. No.112-9250.*

blanket. The sectors are large enough and thick enough to give a neutron environment in the control rods very similar to that of a full reflector.

### SEQUENCE OF MEASUREMENTS

The preliminary analysis of the experimental results on Assembly 48A is discussed in Paper III-22.

The measurements were made in the following sequence to give the necessary results with minimum work. First, the worth of each of the control rods with the drawer composition shown in Fig. III-21-4 was measured. Each of the rods was placed in the central column in a critical core of Assembly 48 composition, with canned sodium in the central column. The bunched $B_4C$ in the rod of Fig. III-21-4(c), when compared with that of Fig. III-21-4(b), gave a measure of self-shielding. The worth of rod of Fig. III-21-4(a) was also evaluated with natural boron substituted for enriched boron. Subcritical multiplication was used to determine the rod worth and is discussed later in this article.

TABLE III-21-II. REFLECTOR WITH CYLINDRICAL SYMMETRY (see Fig. III-21-3)

| | |
|---|---|
| **(A) 360 deg REFLECTOR BACKED BY BLANKET** | |
| Fourfold symmetry about row 16 and row P | |
| (k) Reactivity without rods | 1.0054 |
| (l) $\Delta k/k$ for rod in P-9 alone | −0.0077 |
| (m) $\Delta k/k$ for rods in L-10, T-10 | −0.0130 |
| (n) $\Delta k/k$ for rods in P-9, L-10, T-10 | −0.0169 |
| **(B) 360 deg FULL REFLECTOR (Completely Replacing Blanket)** | |
| Fourfold symmetry about row 16 and row P | |
| (p) Reactivity without rods | 1.0045 |
| (q) $\Delta k/k$ for rods in P-9, L-10, T-10 | −0.0171 |
| **(C) CORE WITH FULL BLANKET** | |
| Fourfold symmetry about row 16 and row P | |
| (r) Reactivity without rods | 0.9894 |

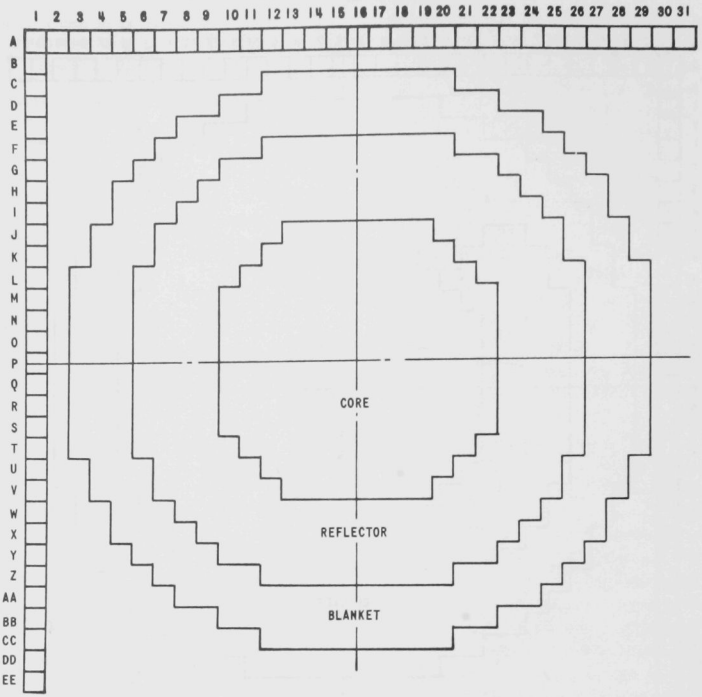


FIG. III-21-3. Loading Diagram for Study Plan ZPR-3 Assembly 48A Complete 360 deg Reflector Partial Blanket Thickness. *ANL Neg. No. 112-9251.*

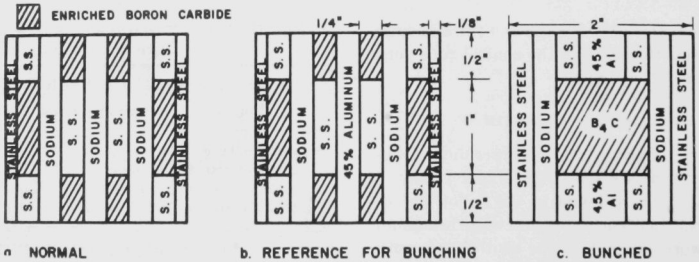


FIG. III-21-4. Cross-sectional View of Drawer Loading Showing $B_4C$ Arrangement in Poison Rod Mockups Assembly 48A. *ANL Neg. No. ID-103-2593.*

Fuel was again placed in the central column and two 100 deg sectors of inconel sodium reflector 20 cm thick were substituted for U-238 blanket and the core size was decreased until criticality was reached (Fig. III-21-2). Radial and axial reaction rates and small sample worth distributions were then measured for materials of interest, such as Pu-239, U-238, B-10, and tantalum. The worth of potential control rod materials such as europium and rhenium were also compared with $B_4C$ at the core-reflector interface at position P-9 (Fig. III-21-2).

The worth of control rods, singly and in pairs and triplets in the reflector, was determined. The interaction effects, the symmetry effects, and the B-10 enrichment effects were evaluated. The greatest change in $k_{eff}$ was determined to be less than 2% below critical

as expected. The measurements again relied strongly on the subcritical technique.

Finally, criticality was achieved with enriched control rods in positions P-9 and P-23. Radial reaction rate and small sample worth traverses were then made through these rod positions.

### Subcritical Multiplication to Measure $k_{eff}$

In order to investigate the dependence of the inverse of multiplication on $k_{eff}$ for subcritical measurements in Assembly 48A a series of computations was performed using the MACH 1 diffusion code. The core, made of Assembly 48 core composition, was in the form of a thick spherical shell. The spherical region inside the shell was filled with material composed of homogenized empty matrix drawers and structure. The core was surrounded by 30 cm of the U-238 blanket material as used in Assembly 48, and the Assembly was made critical by varying the core shell thickness.

A set of computations was then performed, with each computation having a different concentration of B-10 in the central region. $k_{eff}$ was computed for each of these, and the neutron flux and source distribution resulting from the spontaneous fission source in the core was determined. The neutron flux integrated over all 22 groups at a point in the blanket 10 cm from the core-blanket interface was used as a number proportional to multiplication. This location was chosen to be outside the core, since a neutron detector which measures multiplication is normally placed outside the core. Yet it is not close enough to the edge of the blanket to be disturbed by the vanishing neutron flux at that surface, which was introduced as a boundary condition.

In Fig. III-21-5, $10^3$ divided by total flux, $\phi$, is plotted as circled points against $k_{eff}$. This curve is to be compared with the straight dashed line drawn through the first computed point. From the small deviation of the curve from the linear assumption it can be seen that $10^3/\phi$, or the inverse of multiplication, is proportional to $1 - k_{eff}$ within 4% at 4% subcritical.

On the same graph another set of points is plotted as solid circles. These show the relation of $10^3/\phi$ to $k_{eff}$ at the same point in the blanket 10 cm from the core when B-10 is added uniformly in the first 5 cm of the blanket next to the core instead of in the central region. The obvious non-linearity is due to the depression of the flux in the blanket by the B-10 as $k_{eff}$ is also reduced. Of course this corresponds to the experimental case where the neutron flux detector is viewing the core through a control rod which moves during the sequence of subcritical measurements, or where some other effect disturbs the relationship between total flux at a given point and multiplication of the core.

Of course the above analysis is not intended to be an exhaustive study of this subject, but it does indicate that the inverse of multiplication is proportional to $1 - k_{eff}$ within a few percent for a core of Assembly 48 composition which is subcritical by a few percent. Since one, two or three enriched B-10 control rods in the reflector of Assembly 48 produce subcriticality in this range, the use of this multiplication method is adequate to measure their worth, providing the control rod insertions do not distort the flux as seen by the external neutron counters.

### Phase B. Experiments

A general outline of a second series of critical experiments has been prepared as Addendum I, Phase B experiments to the ANL work plan.

The FFTR split-core inverted conical design is a geometrically complex configuration for applying the usual one- or two-dimensional neutronics analysis. The slightly oblong hexagonally-shaped core is designed with non-vertical fuel assemblies such that a 30 to 35% variation in cross-sectional area occurs over a core height distance of approximately 100 cm. This axial variation in composition when coupled with the sizable "gap" produced by the test region imposes a need for developing and exploring analytical and experimental synthesis techniques.

Therefore, a primary objective of the next series of critical experiments (phase B) for FFTR is to experimentally verify and establish the adequacy of these synthesis methods for use in the design and physics analysis of the reactor. In order to be able to apply the computational methods determined from the critical experiment program directly to the design of the FFTR, the experiments and analysis are planned to closely reflect the geometry and composition of the reactor. An important and integral phase of this critical experiment program is the extensive theoretical effort required to define those experiments which critically test these analytical methods. The details of the experimental program must therefore be guided by preplanned analysis.

A second objective is to plan those experiments which provide preliminary estimates of nuclear parameters necessary for a Preliminary Safeguards Report and for Title II design. The geometry and the axial variation in composition of the core have introduced some interesting features to the usual reactivity feedbacks one considers in the preliminary assessment of safety problems. The two more important reactivity coefficients, besides the axial expansion of fuel and mechanical movement of fuel subassemblies, are the prompt Doppler effect and the delayed sodium density and void effect. In order to better understand the analytical techniques derived for use on the com-

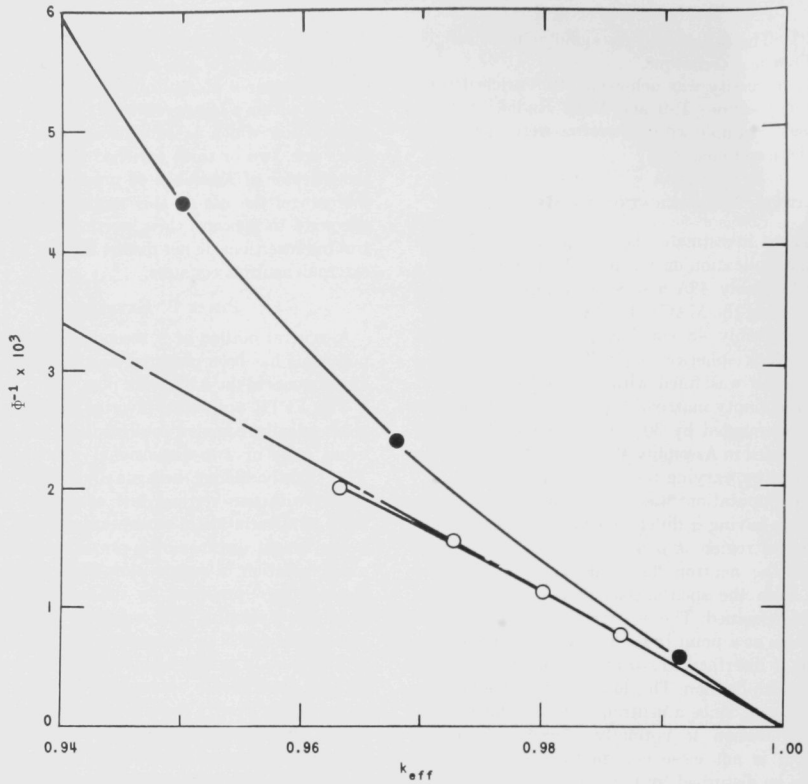


FIG. III-21-5. Relation of Reciprocal Flux (or Counts) to Reactivity for Subcritical Reactor. *ANL Neg. No. 112-9248.*

plex FFTR concept, it has been proposed that four FFTR critical assemblies be studied. The first two critical experiments will be aimed at investigating the neutronic effects of introducing a "slotted" test region into a hexagonal-cylindrical core of uniform composition. The purpose of the third experiment is to study the split-core assembly having an axial variation in composition. The fourth core is included for the combined effects of the conical geometry, and the non-uniform composition.

## III-22. Theoretical Study of the ZPR-3 Critical Experiments in Support of the Fast Fuels Test Reactor Concept

A. J. ULRICH, P. J. PERSIANI and J. C. BEITEL

### PREPARATION OF A CROSS SECTION SET

Cross section sets in 22 groups have been prepared using the MC² fundamental mode spectrum program[1] with a heterogeneous subdivision of Assembly 48 core material which simulates the actual fuel plate arrangement as closely as possible with a two region cell. Additional 22 group sets were prepared by MC² with homogenized composition and zero buckling for U-238

blanket material and nickel reflector material of Assembly 48A. The cross section sets were produced for U-235, U-238, Pu-240, iron, nickel, chromium, sodium, carbon and oxygen. These are the only isotopes currently available on the MC² library tape. Cross sections for B-10, aluminum, tantalum and molybdenum were taken from the existing ANL-224 set.

Using these cross-sections and the MACH 1 diffusion code, the critical radius was found for a spherical reactor of ZPR-3 Assembly 48 composition[2] in both core and 30 cm blanket with a small sample-holding region in the center. The change in $k_{eff}$ was then computed for samples of the same mass and density as the actual samples used in the experiment. A solid cylindrical or cubical experiment sample was replaced in the computation by a solid sphere, and a cylindrical annular sample was replaced by a spherical shell of the same thickness.

The central core worths are compared to the Assembly 48 experimental values in Table III-22-I. The first column gives measured worth in inhours per kg of material (see Ref 3). The second column gives material worth computed with the 22-group set. The experimental worth and computed worth of materials agree to within about 30% except for Pu-240, chromium, oxygen, carbon and sodium.

Based on the 22-group set several six group sets of cross sections were prepared using the MACH 1 code with energy structures given in Table III-22-II. In constructing the six group sets the perturbed worths were computed with the 22-group set in three regions of the spherical core. The purpose of this was to define a coarse structure which best simulated the overall capture, fission, scattering and leakage perturbation components of reactivity when compared with the 22-group components. The group structures of the collapsed sets were also based on the following conditions: (1) The set should reproduce the worth of materials computed by the $\Delta k_{eff}$ method within some acceptable margin of error; (2) The general energy dependence of the fine group real flux and adjoint function should be reasonably reproduced by the coarser energy group structure.

TABLE III-22-I. Experimental and Computed Central Worth in Assembly 48

| | Exp. | Set 22001 22 Group | Set 22611 6-Group | Set 22612 6-Group | Set 22614 6-Group |
|---|---|---|---|---|---|
| U-235 | +339. ± 4 | +330. | +370.4 | +362.9 | +337.4 |
| U-238 | −24.8 ± 0.5 | −22.2 | −23.0 | −23.1 | −23.1 |
| Pu-239 | +445. ± 4 | +424.2 | +457.3 | +455.8 | +467.5 |
| Pu-240 | 81. ± 20 | +46 | +28.5 | +36.1 | +23.8 |
| B-10 | −8926. ± 80 | −7694. | −9227. | −8802. | −9940. |
| SS(304) | −14.1 ± 0.2 | −15.5 | −15.4 | −15.6 | −15.3 |
| Fe | −12.3 ± 0.4 | −15. | −14.5 | −14.8 | −14.1 |
| Cr | −9.4 ± 0.4 | −16 | −15.1 | −15.3 | −16.4 |
| Ni | −18.2 ± 0.2 | −20 | −4.5 | −22.3 | −22.4 |
| Al | −15.7 ± 0.8 | −20.1 | −18.8 | −19.2 | −18.3 |
| Na | −6.3 ± 0.3 | −11.33 | −8.96 | −8.96 | −10.63 |
| C | −4.6 ± 1.2 | −8. | −9.7 | −9.7 | +0.7 |
| O | −6.8 ± 0.9 | −12.0 | −13.6 | −13.5 | −8.6 |
| Ta | −164. ± 5 | −135. | −147. | −144. | −157. |
| Mo | −43.4 ± 0.4 | −55. | −59.1 | −58.3 | −60.3 |

TABLE II-22-II. Description of 6-Group Set Structures

| Set | Distribution of 22-Groups Among 6-Groups | Lower Energy Limit, eV |
|---|---|---|
| 22611 | 1–3 | $1.35 \times 10^6$ |
| | 4–7 | $1.83 \times 10^5$ |
| | 8–10 | $4.09 \times 10^4$ |
| | 11–14 | $4.31 \times 10^3$ |
| | 15–20 | $2.75 \times 10^2$ |
| | 21–22 | $2.90 \times 10^1$ |
| 22612 | 1–3 | $1.35 \times 10^6$ |
| | 4–7 | $1.83 \times 10^5$ |
| | 8–11 | $2.48 \times 10^4$ |
| | 12–14 | $4.31 \times 10^3$ |
| | 15–20 | $2.75 \times 10^2$ |
| | 21–22 | $2.90 \times 10^1$ |
| 22614 | 1–3 | $1.35 \times 10^6$ |
| | 4–7 | $1.83 \times 10^5$ |
| | 8–11 | $2.48 \times 10^4$ |
| | 12–14 | $4.31 \times 10^3$ |
| | 15–18 | $9.61 \times 10^2$ |
| | 19–22 | $2.90 \times 10^1$ |

Worths computed with 6 groups are also recorded in Table III-22-I. Comparison of the worth of materials computed with set 22614 and 22001 show agreement to within 20% except for Pu-240, B-10, carbon and oxygen. Set 22611 compares to within 20% except for Pu-240, nickel and sodium. Finally, set 22612 gives material worths all of which agree with those of set 22001 to within 20%.

### Control Rod Worth Computations

The 6-group cross-section set 22612 was used in computational modeling of Assembly 48A control rod worth experiments.

The worths of boron control rods in the center of the core were computed to be higher than the measured values by 13 to 32%. The MACH 1 diffusion code with 22 groups, MACH 1 with 6 groups, and SNARG-2D transport in the S2 approximation with 6 groups gave worths which differed by only a few percent. This indicates that the method of collapse of the 22-group set into the 6-group set appears to be adequate. Six group $(x,y)$ and $(r,z)$ geometry in S-2 and S-4 transport calculations give results which agree to within a few percent. This indicates that with the 6-group cross-section set 22612, the transport effect is small. The transport effect with the 22-group set 22001

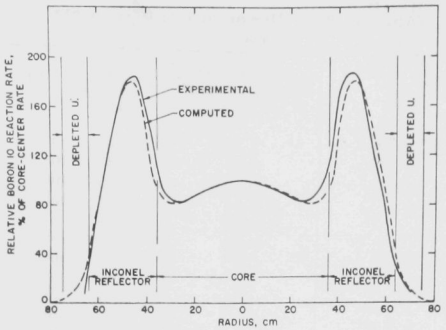


FIG. III-22-1. Radial Profiles of B-10 Reaction Rate Through Assembly 48A without Mockup $B_4C$ Rods. *ANL Neg. No. 112-9007.*

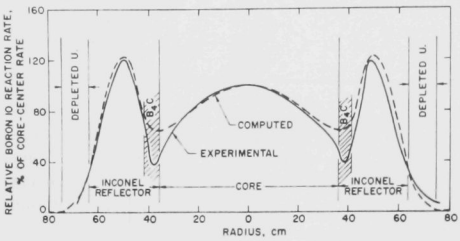


FIG. III-22-2. Radial Profiles of B-10 Reaction Rate Through Assembly 48A with Mockup $B_4C$ Rods. *ANL Neg. No. 112-9008.*

is presently being checked in a one-dimensional SNARG calculation. Further, results obtained with the Argonne 224 set have been found to agree with results obtained with the 22001 set in a diffusion calculation.

A series of computations designed to study the effect of variations in axial buckling on rod worths showed that this is not a large enough effect to explain the discrepancy between calculation and experiment. A similar conclusion may be stated of errors in cross-section or concentration of rod and sodium channel materials other than natural boron and B-10. The B-10 reaction rate at this rod surface is maximum in the 17*th* group, so that the addition of lower energy groups would not change rod worths significantly. Self-shielding effects studies again do not seem to account for the large discrepancies. Further work to resolve this disagreement is planned to recheck and reevaluate critical atomic concentrations and dimensions.

Computation of the worths of the control rods in the reflector section of Assembly 48A have not yet been possible because of an unresolved SNARG-2D code difficulty. The difficulty appears to be associated with the meshing requirement for this type of problem.

### Radial Reaction Rate Traverse Study

Radial traverses of the B-10 and plutonium reaction rates were measured in the P row of Assembly 48A under two different conditions. One pair of traverses was done in Assembly 48A critical without control rods, and the other with Assembly 48A critical with control rods in the P9 and P23 positions. The latter pair of traverses passed through the control rod positions. Computations of B-10 capture and plutonium fission reaction rates as a function of radial position in the Assembly 48A core, reflector and blanket has now been done for these two cases with 22 groups of neutron energy. One-dimensional cylindrical geometry was used in the MACH 1 code.

The measured traverses are compared with the computed ones in Figs. III-22-1 and III-22-2 for B-10 and Figs. III-22-3 and III-22-4 for plutonium. In the figures the solid curve is experimental and the dashed curve is computed. Figures III-22-1 and III-22-3 compare reaction rates without $B_4C$ rods in the reflector, while Figs. III-22-2 and III-22-4 compare reaction rates with $B_4C$ rods in the reflector.

In Figs. III-22-3 and III-22-4, three computed curves appear. All three reaction rate curves were calculated with the 22 group fluxes which were the solution of the cylindrical MACH 1 problem. In the highest curve, Pu-239 fission cross sections group-averaged in a zero buckling spectrum corresponding to the reflector composition with a very dilute Pu-239 concen-

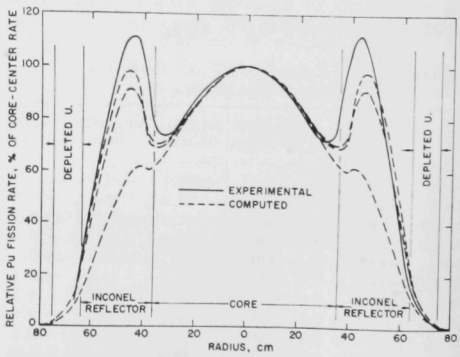


FIG. III-22-3. Radial Profiles of Plutonium Fission Rate Through Assembly 48A without Mockup $B_4C$ Rods. *ANL Neg. No. 112-9009.*

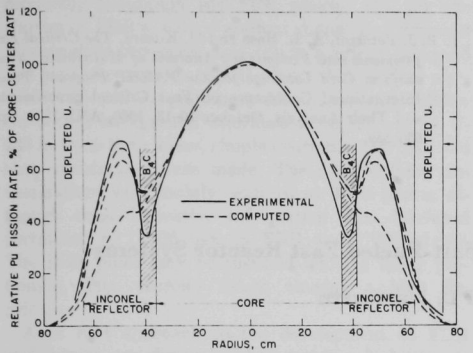


FIG. III-22-4. Radial Profiles of Plutonium Fission Rate Through Assembly 48A with Mockup $B_4C$ Rods. *ANL Neg. No. 112-9010.*

tration were used. The cross sections therefore showed very little self-shielding. The middle curve is based on blanket averaged cross-sections and is more affected by self-shielding. The lowest curve is derived from core-averaged cross-sections and is greatly depressed by self-shielding. Strictly speaking, each curve should be plotted only in the region for which its cross-section input applies, but this would imply a neutron flux discontinuity at the boundaries between core and reflector and between reflector and blanket. Because of neutron spectrum mixing at the boundaries, many more than three sets of cross-sections are actually needed to give a quasi-continuous reaction rate curve. Because these refinements have not been attempted here, each of the three curves is extended to all of the regions. Since only one cross-section was available for B-10, only one computed curve appears in Figs. III-22-1 and III-22-2.

The cases without control rods are better simulated by a one-dimensional cylindrical computation than the case with control rods, since the rods grossly violate the cylindrical symmetry. For the computation with rods, a region was set up in the form of a symmetrical cylindrical shell with a thickness equal to the rod thickness and radii that caused it to exactly include both rods. The rod and reflector materials in this region were considered to be diluted uniformly into each other. The experimental reaction rate traverse along the radius, on the other hand, passed through the control rod where the $B_4C$ was concentrated. Because of this situation the computed reaction rate was not depressed in the control rod as much as the measured reaction rate.

### REFERENCES

1. B. J. Toppel, A. L. Rago and D. M. O'Shea, *MC²—A Code to Calculate Multigroup Cross Sections*, ANL-7318 (1967).
2. A. M. Broomfield, P. I. Amundson, W. G. Davey, J. M. Gasidlo, A. L. Hess, W. P. Keeney and J. K. Long, *ZPR-III Assembly 48: Studies of a Dilute Plutonium Fueled Assembly*, Proc. International Conference on Fast Critical Experiments and Their Analysis, October 10–13, 1966, ANL-7320, pp. 216–230.
3. Reactor Development Program Progress Report, ANL-7267, (1966) p. 19, Table XIV.

## III-23. The Critical Experiments and Preliminary Analysis of Multifueled, Nonuniform Core Loadings[1] for the FARET Program

P. J. PERSIANI, A. L. HESS* and D. KUCERA

A series of small, Pu-plus-U-235-fueled fast reactor cores with steel radial and axial reflectors were constructed in Argonne's Zero Power Reactor (ZPR)-3 as part of the design program for the FARET reactor. These studies, designated ZPR-3 Assembly 46, were essentially mockups of possible loadings of the FARET core. The primary objective of the studies was to confirm the physics analysis of multifueled, nonuniform core loadings as were envisaged for the FARET system.

A principal interest in the studies was to establish experimentally the predicted reactivity control afforded by the control-rod designs for FARET. The agreement obtained between calculations and the results of experiments for control-rod worth was sufficient to establish the range of control possible in the FARET reactor. Of equal importance was the substantiation of the neutronic behavior of a mixed core in FARET when subassemblies of different types of fuels were interchanged. Analytical calculations were done for all experiments, and the methods for analysis that were adopted are discussed in Ref. 1. The

* Idaho Division, Argonne National Laboratory.

agreement of the analyses with the experimental results is found to be generally good. A study of the mixed-core systems and the comparisons of calculations with results of fuel-exchange experiments in three cores indicate that the behavior of a mixed-core loading can be understood as well as that of a uniform core loading.


REFERENCE

1. P. J. Persiani, A. L. Hess and D. Kucera, *The Critical Experiments and Preliminary Analysis of Multifueled, Nonuniform Core Loadings for the FARET Program*, Proc. International Conference on Fast Critical Experiments and Their Analysis, October 10–13, 1966, ANL-7320, pp. 550–559.


## III-24. Physics Studies of Molten-Salt-Fueled Fast Reactor Systems

D. K. BUTLER* and D. MENEGHETTI

The physics studies of molten-salt-fueled fast reactors previously reported[1,2,3] have been completed. Detailed physics and engineering results are described in Ref. 4.

The characteristics of three types of fast reactors having fuels consisting of uranium and plutonium trichlorides dissolved in alkali chlorides and alkaline earth chlorides were studied. One of the reactors was homogeneous and the other two were internally cooled. Optimization of the core sizes for a power of 1000 MW(e) resulted in 10,000-liter core volumes.

These reactors have the favorable characteristics (even for natural chlorine) of high breeding ratio, large negative temperature coefficients of reactivity, and low fuel cycle costs. The unattractive characteristics of large plutonium inventory, large volume, complex design, and container material problems indicate that a sizable program would be required to develop chloride-fueled reactors.

* Liquid Metal Fast Breeder Reactor Program Office, Argonne National Laboratory.


REFERENCES

1. D. Bulter and D. Meneghetti, *Physics Studies of Some Molten-Salt-Fueled Fast Reactor Systems*, Reactor Physics Division Annual Report, July 1, 1963 to June 30, 1964, ANL-7010, pp. 156–159.
2. P. A. Nelson, D. K. Butler, M. G. Chasanov and D. Meneghetti, *Fuel Properties and Nuclear Performance of Fast Reactors Fueled with Molten Chlorides*, Trans Am. Nucl. Soc., **8**, 153 (1965).
3. D. K. Butler and D. Meneghetti, *Additional Physics Studies of Molten-Salt-Fueled Fast Reactor Systems*, Reactor Physics Division Annual Report, July 1, 1964 to June 30, 1965, ANL-7110 pp. 189–190.
4. P. A. Nelson, D. K. Butler, M. G. Chasanov and D. Meneghetti, *Fuel Properties and Nuclear Performance of Fast Reactors Fueled with Molten Chlorides*, Nuclear Appl. **3**, 540 (September 1967).


## III-25. Preliminary Study of the Use of U-235 in A Fast Reactor Era

K. A. HUB* and V. Z. JANKUS

### INTRODUCTION

With widening geographical acceptance of water reactors, the price of electrical energy from new stations will become reasonably uniform throughout the United States. This implies that within a few years after the fast breeder reactor (FBR) power plant is commercially accepted, there will be a large demand for such plants. To meet the anticipated demand for FBR plants, large quantities of plutonium will be needed for initial core loadings. If light-water reactor (LWR) plants, some of which operate on plutonium recycle, form the backbone of the nuclear industry when FBRs are commercially accepted, a plutonium shortage will exist. Because of that possibility an investigation has been made of the use of uranium-235, assuming it to be the significant available fissile species.

U-235 may be used in three ways: (a) for water-type plants to generate power while at the same time

* Reactor Engineering Division, Argonne National Laboratory.

producing plutonium for FBR plants; (b) for the startup of FBR's, with a gradual change to plutonium as enough is produced; and (c) in specially designed fast converter reactor (FCR) plants that produce electricity as well as plutonium for fueling new FBR's. To obtain background information on the use of U-235 in these three cases, simple neutronic, thermal, and cost calculations were made. These preliminary investigations were mainly centered on FCR plants, although some indicative information was developed pertaining to U-235 uses in FBR and LWR plants. The FCR plant may be justified while a fissile plutonium, $Pu_f$, scarcity exists, causing a high $Pu_f$ price.

As a first approach to the development of FCR systematics, one-dimensional neutronic calculations in a spherical system were made, using a spherical version of the General Electric Company's 16 in. high pancake core concept[1] as a reference. Oxide fuel, stainless-steel cladding and structural material, and tantalum poison material were used. Mid-cycle equilibrium conditions at a core burnup of 50,000 MWd/tonne of heavy atoms were estimated and formed a basis for neutronic calculations.

The thermal-design aspects of the reactors were considered in setting forth the compositions for the various neutronic calculations. Sufficient sodium volume for heat transport was specified to maintain a reasonable pressure drop across the core and axial blanket. The blanket volumetric composition for neutronic calculations was about the same as that of the core in each case because the reactor model was the pancake concept; slight changes in blanket composition were specified to account for the control material normally in the blankets.

One measure of possible worth of U-235 fast converters is the comparison of their fuel-cycle costs to plutonium-fueled systems under various conditions of $Pu_f$ price and $U_3O_8$ cost. Also, U-235 fast converter designs may be partially compared on an intra-class basis by calculating fuel-cycle costs. Unfortunately, the only practical method of making a number of survey calculations at the present time is through the use of equilibrium fuel conditions, so the important startup effects were omitted.

## Neutronic Investigations

The MACH-1 code[2] with cross-section set ANL-224 was used for investigating the neutronic aspects of U-235 fast converter reactors. Eight cases using U-235 fuel and seven cases using $Pu_f$ fuel were calculated. Summaries of some of the input and output information for the $Pu_f$ and U-235 cases, respectively, are given in Tables III-25-I and III-25-II.

There were five principal pieces of desired output information: fissile weight fraction in the fuel, core conversion ratio, total breeding (conversion) ratio, sodium void effect, and Doppler coefficient. The cases using plutonium as fuel will be discussed first. These cases were calculated mainly to provide a reference basis and are reported for general information.

TABLE III-25-I. Results of Spherical Calculations for a $Pu_f$ Fast Breeder Reactor with Oxide Fuel

| Case | A | B | C | D | (B + D) | E | F |
|---|---|---|---|---|---|---|---|
| *Input Data* | | | | | | | |
| Core volume, liters | 696 | → | → | → | → | 1770 | → |
| Core radius, cm | 55 | → | → | → | → | 75 | → |
| Blanket thickness, cm | 30 | → | → | 45 | → | 40 | → |
| *Core composition, v/o* | | | | | | | |
| Fuel | 38 | 38 | 45.2 | 45 | 38 | 41 | 41 |
| Clad and structure | 18 | → | → | → | → | 17 | 17 |
| BeO | 7.3 | 7.3 | None | None | 7.3 | None | None |
| Sodium | 36 | 36.2 | 36.2 | 36.4 | 36.2 | 41.5 | 41.5 |
| Poison (Ta) | 0.7 | 0.5 | 0.6 | 0.6 | 0.5 | 0.5 | 0.5 |
| $Pu_f$ | | | | | | | |
| Inner blanket, w/o of fuel | 2.7 | → | → | 2.5 | → | → | → |
| Outer blanket, w/o of fuel | 1.7 | → | → | 1.0 | → | → | → |
| *Output Data* | | | | | | | |
| $Pu_f$ in core, w/o of fuel | 16.25 | 15.90 | 13.77 | 13.77 | 15.83 | 11.94 | 12.52 |
| Breeding ratio | 1.004 | 1.094 | 1.182 | 1.319 | 1.213 | 1.281 | 1.224 |
| Core conversion ratio | 0.634 | 0.653 | 0.711 | 0.712 | 0.655 | 0.862 | 0.814 |
| Change in reactivity for voiding Na from core, $\%\Delta k$ | 0.031 | 0.028 | 0.33 | 0.37 | 0.11 | 1.7 | — |
| Doppler coef., $T(\Delta k/\Delta T) \times 10^3$ | — | −6.5[a] | −3.7[a] | −3.3 | −5.4 | −4.4 | −4.5 |

[a] U-238 only.

TABLE III-25-II. RESULTS OF SPHERICAL CALCULATIONS FOR A U-235 OXIDE FUELED FAST CONVERTER REACTOR

| Case | A | B | C | D | E | F | G | H |
|---|---|---|---|---|---|---|---|---|
| *Input Data* | | | | | | | | |
| Core volume, liters | 696 | | | | 1770 | 2855 | | 4400 |
| Blanket, cm | 30 | | | 45 | 40 | 42 | | |
| Core radius, cm | 55 | | | | 75 | 88 | | 102 |
| *Core composition, v/o* | | | | | | | | |
| Fuel | 38 | | 45.2 | 45 | 41 | | 38 | |
| Clad and structure | 18 | | | | 17 | | 18 | |
| BeO | 7.3 | | None | | | | | |
| Sodium | 36 | 36.2 | | 36.4 | 41.5 | 41.6 | 43.6 | |
| Poison (Ta) | 0.7 | 0.5 | 0.6 | | 0.5 | 0.4 | | |
| *$Pu_f$ w/o of fuel* | | | | | | | | |
| Core | 2.3 | 1.9 | 2.7 | 1.6 | 1.8 | 2.4 | | |
| Inner blanket | 2.3 | 2.0 | 2.8 | 1.6 | 1.8 | 2.7 | | |
| *Output Data at Mid-life* | | | | | | | | |
| U-235, w/o of fuel | 21.4 | 21.3 | 18.0 | 20.0 | 15.8 | 12.9 | 13.8 | 12.5 |
| Core PDF ratio[a] | 0.337 | 0.346 | 0.393 | 0.371 | 0.491 | 0.587 | 0.550 | 0.611 |
| Reactor PDF ratio | 0.629 | 0.696 | 0.753 | 0.842 | 0.825 | 0.882 | 0.844 | 0.854 |
| Change in reactivity for voiding Na from core, $\%\Delta k$ | −1.85 | −1.90 | −1.53 | −1.76 | −1.13 | −0.18 | −0.48 | +0.27 |
| Doppler coef., $T(\Delta k/\Delta T) \times 10^3$ | — | — | — | −2.8 | −4.0 | −4.9 | −4.8 | −5.4 |

[a] Fissile atoms produced per fissile atom destroyed on an instantaneous basis.

### $Pu_f$ FUELED CASES

Case A was chosen as a 700-liter sphere to represent GE's 16-in. high two-region homogenized pancake core. The amount of tantalum in the core and blanket was greater than would be required for control. Case B is a repeat of Case A, but with less tantalum; the results are in reasonable agreement with GE's results, recognizing that the blanket was thinner than the 18 in. used in the GE case and the plutonium isotopic composition was higher in Pu-240 and Pu-242 species than that used by GE.

Cases C and D represent the results obtained assuming that the BeO was removed from the core and blanket, having been replaced by an equal volume of fuel and fertile material; Case D differs mainly from Case C in that the blanket was 50% thicker. Thus with a noticeable penalty in sodium voiding and a large penalty in Doppler coefficient, the BeO removal greatly increased the breeding gain and decreased the required fissile fraction in the fuel by about 10%.

Case (B + D) represents the situation for BeO in the core (Case B) and no BeO in the blanket (Case D). Cases E and F are for 1770-liter cores with Case F representing the influence of a $Pu_T/Pu_f$ ratio of 1.25 versus the value 1.49 used in all the previous calculations, where $Pu_T$ is the weight percent of total Pu in the fuel. The Doppler coefficient improved noticeably with the increase in core size.

### U-235-FUELED CASES

The criticality search was made only on U-235 content; the $Pu_f$ concentration was estimated prior to the computer runs. In these calculations no U-236 was specified because of the preliminary nature of the survey and because the cross-sections were not compiled.

The neutronic performance of reactors having cores of small volume (Cases A through D) are not as good as that for larger cores. The ratio of fissile material produced to that destroyed (PDF ratio) increases with reactor size. Although an insufficient number of cases was calculated to express the relationships, Fig. III-25-1 illustrates the general trends. The PDF ratio for the reactor at midlife is increased if the fuel-and-fertile-material volume fraction is not significantly decreased with an increase in reactor size. Because the average concentration of plutonium in the core increases with size, the better breeding characteristics of plutonium compared with U-235 tend to increase the PDF ratio. Normally for a plutonium-fueled breeder having a constant fuel fraction, a small decrease in instantaneous breeding ratio is expected with increase in size.

Totally voiding the core of sodium causes negative reactivity effects in reactors up to approximately 4000 liters; for smaller sizes, partial voiding causes a positive reactivity effect. To illustrate the effect of partial voiding, the change in reactivity is plotted as a function of volume-fraction voided in Fig. III-25-2.

With $\beta_{eff}$ equal to about 0.6%, the greatest change in reactivity due to sodium voiding produces a positive reactivity change of less than a dollar for core sizes up to about 3000 liters; the $Pu_f$-fueled cores meet this condition for sizes less than 700 liters.

Another significant characteristic of the U-235 sys-

tem relates to the Doppler coefficient. Increase in U-238 and decrease in U-235 concentrations in the core as reactor size is increased causes a significant increase in the reactor Doppler coefficient. The coefficient for a 4400-liter core with U-235 fuel (Case H on Table III-25-II) is about the same as that for a 700-liter core containing BeO. Thus, somewhat similar safety characteristics may be expected from the Doppler effect for a large U-235-fueled core as for a small $Pu_f$-plus-BeO core.

Another interesting feature of large U-235-fueled cores is the fact that a reactor having an average core conversion ratio of 0.5 will have a reactivity change about equal to that of a $Pu_f$-fueled breeder reactor with an instantaneous core conversion ratio of about 0.65. Thus, a smaller reactivity change may be expected in a large U-235-fueled system than in a small $Pu_f$-fueled system.

## Thermal Design Aspects

The transport of heat from the fuel and the allowable heat generation of the fuel are entwined with the mechanical and safety aspects of design. To simplify the situation for this study, the heat transport was considered within a frictional pressure-drop limitation and the allowable heat generation was considered within a range of maximum kilowatts per foot of fuel.

### Frictional Pressure Drop

The design for frictional pressure drop depends on allowed sodium velocities and temperature rises as well as the availability of equipment to do the pumping. Sodium pumps capable of developing heads equivalent to 150 psi are reasonably expected in the future. Present designs indicate that the average temperature rise in the reactor is about 300°F plus or minus 20%. Because the volume of sodium in the core serves no inherent purpose under steady-state conditions, the sodium should flow through the reactor as rapidly as cost permits. Safety considerations may require that this statement be modified, but the modification will be reflected mainly in allowable $\Delta p$ and $\Delta t$ across the reactor. For a sodium velocity of 30 ft/sec, a series of generalized curves were developed to show the frictional pressure drop per foot of fuel tube versus total sodium fraction for various fuel-tube diameters (Fig. III-25-3). Because the type of fuel-element spacer selected significantly influences the results, the curves are only indicative.

Taking into account the core, axial blanket, fission-gas chamber, transition lengths, etc., the length of fuel tube will probably never be less than 5 ft. With allowances for pressure drops in such components as the distribution plenums, subassembly nose pieces, and external loop, the upper limit for frictional drop for the fuel tube will be approximately 20 psi/ft.

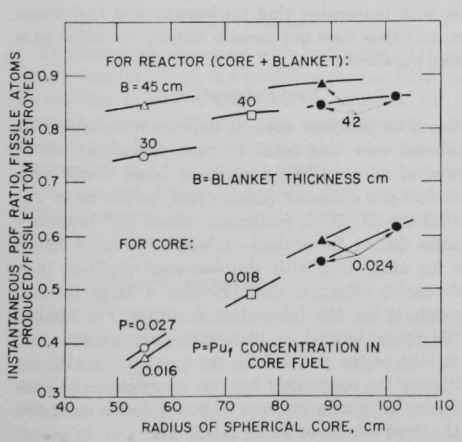


Fig. III-25-1. Trends in $Pu_f$ Ratios for Fast Converter Reactors. *ANL Neg. No. 112-8620.*

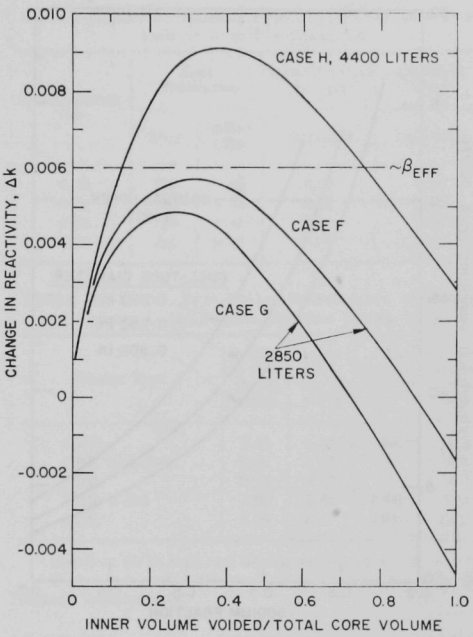


Fig. III-25-2. Effect of Partial Sodium Voiding on Reactivity of Fast Converter Reactors. *ANL Neg. No. 112-8621.*

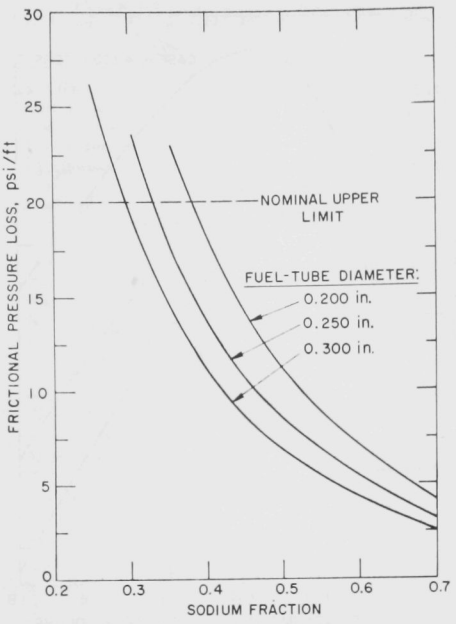


FIG. III-25-3. Variation of Frictional Pressure Loss with Core Sodium Volume Fraction Based on Maximum Sodium Flow of 30 ft/sec. *ANL Neg. No. 112-8622.*

FUEL HEAT GENERATION

For oxide fuel, the maximum allowable linear heat generation is about 20–22 kW/ft. This maximum is slightly influenced by the diameter of the fuel pin (i.e., the unclad fuel). The maximum fuel rating, which contains as a factor the core maximum-to-average ratio, is a function of design and configuration. Thus average fuel rating, in terms of specific power, is influenced strongly by the pin outer diameter; the cost implications of this will be discussed under fuel-cycle costs.

The amount of cladding, spacer, and subassembly wall material required in a design, as well as the interchannel sodium and control volume, were included in design considerations. For these calculations, it was estimated that 20% of the core volume will be filled with material other than the fuel and the coolant sodium. Because there is an incentive to maintain a high fuel fraction (0.35 to 0.45) for neutronic performance, the coolant sodium fraction will probably be in the range of 0.32 to 0.45.

## FUEL CYCLE PERFORMANCE

In order to indicate relative performance, the fuel cycle costs, $U_3O_8$ requirements, and plutonium production were estimated. It should be noted that one important way to use U-235, namely as startup fuel during a transient period, has not been investigated. When the detailed neutronic fuel cycle program portion of ARC becomes operational, this transient performance will be calculated. However, the characteristics of FCR plants are capable of illustrating a performance bound in fuel strategy studies.

ASPECTS OF FUEL-CYCLE COST

The fuel-cycle cost estimates were used in two ways: (1) to provide guidance in the selection of design parameters and (2) to indicate the relative performance of U-235 FCR's with Pu, LMFBR's, thus aiding the determination of the value of plutonium compared with the value of U-235. These two uses are not independent; some iteration is needed for proper reactor design investigations. For first estimates involving core thermal performance, it was assumed that the U-235 was worth \$12/g in FCR's and that fissile plutonium was worth \$17/g. In the more detailed fuel cycle cost estimates values were based on \$8/lb $U_3O_8$ price and \$30/kg per unit separatory work.

### *Fuel Cycle Costs for FCR's*

The principal cost components for fast converter reactor fuel cycles are due to fuel fabrication, fissile inventory, U-235 consumption, and plutonium production. This study assumes that an average core burnup of 100,000 MWd/tonne of heavy atoms will be attainable with reasonable clad thicknesses and fuel densities, and thus does not include burnup variation as a design parameter.

### *Fuel Fabrication*

Based on previous work, it appears reasonable that combined core and axial blanket fabrication costs, expressed on an average kilogram basis, might vary with fuel-pin diameter (unclad fuel) as shown in Table III-25-III. With plutonium losses and inventory charges during fabrication excluded, the costs shown are for oxide fuel with stainless-steel cladding in a fast-reactor situation that provides a large tonnage throughout for the fabrication facilities. For 100,000 MWd/tonne burnup, a blanket-to-core weight ratio of 2, 90% of the power from the core, and a 41% net efficiency for converting heat to electricity, the contribution of fabrication cost to power cost is as shown in the third column of Table III-25-III.

### *Fissile Inventory*

Core, blanket, and external inventory are included in total costs; however, a reasonable core design can be roughly estimated separately. For an example of the magnitude of core inventory costs, assume 0.13 U-235 concentration, 0.025 $Pu_f$ concentration, 11 kW/ft average linear power, 0.80 annual capacity factor, and 0.10 annual charge rate on fissile material; then the core inventory costs, using the previously mentioned U-235 and $Pu_f$ prices for the various pin sizes, are as shown in the fourth column of Table III-25-III. Thus, the core inventory costs vary appreciably with fuel-pin diameter and are of significant magnitude. Combination of the core fissile inventory charges (last column of Table III-25-III) and the fabrication costs indicates that a minimum cost would occur with a fuel-pin diameter of about 0.21 in. This of course, is only an example, but it is indicative for the region of design interest.

### *U-235 Consumption*

The consumption of U-235 over a fuel cycle is difficult to express functionally from the cases calculated; values range from 0.9 to 1.1 g/MWd. In general, as the core becomes larger, the spectrum softens, the required U-235 concentration decreases, and the $Pu_f$ concentration increases. If the fuel and fertile material volume fractions remain constant as size is increased, fewer grams of U-235 are destroyed per megawatt-day. Realistically, however, the volume of sodium increases and the fuel fraction decreases. As indicative of magnitudes, a value of 0.9 g/MWd corresponds to 1.1 mills/kWh cost for the fuel cycle.

### *$Pu_f$ Production*

$Pu_f$ production increases with increasing PDF ratio for the reactor; there is a tendency for the PDF ratio to saturate as size is increased. In addition, the $Pu_f$ burns out more readily as the core conversion ratio increases. A $Pu_f$ net production rate of 0.8 g/MWd corresponds to 1.4 mills/kWh credit for the fuel cycle. Thus, the net difference between $Pu_f$ produced and U-235 destroyed in this idealized case is a credit of 0.3 mills/kWh.

#### FUEL CYCLE COST COMPARISONS

Ideally, the cost comparisons of various concepts would include capital, fuel, and other production expenses on a year-by-year basis. In the case of the studies involving U-235 use, the only readily available way of indicating relative performance is by means of fuel-cycle costs. These are limited to equilibrium fuel performance with certain cost adjustments for initial costs.

TABLE III-25-III. PARTIAL FUEL-CYCLE COST AS A FUNCTION OF FUEL-PIN DIAMETER

| Pin Diameter, in. | Cost Fabrication | | Inventory Cost for Core | Combined Cost |
|---|---|---|---|---|
| | $/kg | mills/kWh | mills/kWh | mills/kWh |
| 0.18 | 235 | 0.65 | 0.29 | 0.94 |
| 0.20 | 200 | 0.55 | 0.36 | 0.91 |
| 0.25 | 150 | 0.41 | 0.56 | 0.97 |
| 0.30 | 120 | 0.33 | 0.81 | 1.14 |

TABLE III-25-IV. FUEL-CYCLE PERFORMANCE ESTIMATES FOR VARIOUS OXIDE-FUELED NUCLEAR POWER PLANTS[a]

| Reactor Type | Fuel-cycle Cost, $Pu_f$ at $10/g | mills/kWh, $Pu_f$ at $18/g | $U_3O_8$ Makeup, tons/20 yr | $Pu_f$ Produced, tonnes/20 yr |
|---|---|---|---|---|
| LWR | 1.48 | 1.31 | 3500 | 3.9 |
| FBR with BeO | 0.92 | 1.15 | — | 2.6 |
| FBR | 0.74 | 0.84 | — | 4.6 |
| FBR U-235 | 1.92 | 1.44 | 3900 | 9.9 |
| FCR | 1.38 | 0.87 | 3500 | 10.6 |

[a] Based on $8/lb $U_3O_8$ and $30/kg separatory work.

[b] Does not include initial or final inventories but only the makeup requirements.

To provide a broad indication of relative performance, the fuel-cycle costs for the following systems were calculated:

1. LWR, a 1088-MW(e) light-water-reactor plant of assumed characteristics,
2. FBR-BeO, a 1075-MW(e) plant with an oxide-type plutonium-fueled fast breeder reactor and with BeO added to the core (design related to that of the previously mentioned design by the General Electric Company),
3. FBR, the same general design as the FBR-BeO example, but with the BeO removed from the core and axial blankets,
4. FBR-U-235, similar to the FBR design, but with U-235 fuel in place of plutonium,
5. FCR, a 1075-MW(e) plant with a fast converter reactor specifically designed for U-235 fuel (core 60% higher than for the FBR design and fuel-pin diameter decreased slightly).

To provide a quick preliminary comparison, the characteristics of nuclear plants using each of these reactor systems were selected without emphasis on details that would be required in an expanded study. In addition, no optimization procedures were used to

adjust plant performance to changing factors of cost, such as plutonium price.

Fuel cycle calculations were made with the use of a computer code which uses an accounting procedure that might be used by the utility industry in such survey studies. The estimated cost of uranium for specified concentrations is based on optimum tailing concentrations using the input $U_3O_8$, fluorination, and separatory work costs. A program option allows for U-235 burnup costs to be estimated based on either the schedule of costs for various U-235 concentrations or on mixing of 50 w/o U-235 to reconstitute the burned up fuel. For fast converter reactors there is no effective cost penalty for using the mixing of 50 w/o U-235 option. Thus the problem of activity levels associated with the re-introduction of spent fuel into the diffusion plant is obviated; however, the fabrication cost aspects of this mixing step were not investigated. The fuel cycle costs for each year during a period of twenty years is provided by the code and a twenty year average value is calculated. The annual capacity factor used was 80% for the first five years, 75% for the next ten years and 65% for the last five years. The fuel-cycle cost estimate, $U_3O_8$ makeup, and fissile plutonium production are given in Table III-25-IV.

The unit costs for fabrication, shipping, and processing require clearer definition. A more rigorous cost model could be developed so that cost differentials between the concepts would be more meaningful. The reprocessing cost for the fast U-235 burners was increased by 25% over the FBR cost because the core and axial blanket cannot be mixed as is sometimes suggested for FBR's. Unit shipping costs should also be evaluated in terms of cask cooling requirements for axial blanket and core materials. With expected cost disadvantages applied to the FCR, there appears to be an incentive to further consider fast converters specifically designed for U-235 use. In addition, the technical and cost aspects of using U-235 as the transient fuel in starting up FBR's should be developed.

## Observations

Although this study was only preliminary, several observations can be made within the assumptions of the study:

1. Clearly, use of uranium-235 in the fast reactor era should be defined more rigorously.
2. On the basis of equilibrium fuel-cycle calculations, the FCR has a definite cost advantage over the other U-235 reactors studied.
3. The FCR and LWR require about the same tonnage of $U_3O_8$ for fuel makeup.
4. The FCR produces about twice as much fissile plutonium as LWR's.

Thus taking design advantage of the nuclear-safety characteristics of U-235 compared with $Pu_f$ significantly improves fuel-cycle performance.

## References

1. K. P. Cohen and G. L. O'Neill, *Safety and Economic Characteristics of a 1000-MWe Fast Sodium-cooled Reactor Design*, Proc. Conference on Safety, Fuels, and Core Design in Large Fast Power Reactors, October 11–14, 1965, ANL-7120, pp. 185–204.
2. D. A. Meneley, L. C. Kvitek and D. M. O'Shea, *Mach 1, a One-Dimensional Diffusion-Theory Package*, ANL-7223 (1966).

# Section IV

# Fast Reactor Safety

Analysis of the course of accidents in fast power breeder reactor cores requires a broad range of reactor physics information. It is necessary to know damage and failure thresholds of the fuel; the types of fuel and coolant motion that can result, including acceleration and rate data; reactivity changes brought about by the motions, temperature changes, changes in neutron flux distributions throughout the core, etc.; and, finally, data sufficient to analyze the accident under study to its termination. This section also presents a paper dealing with a calculation related to containment.

# IV-1. Initial (7-Pin) EBR-II Cluster Fast Reactor Safety Integral Loop Experiments in the Transient Reactor Test (TREAT) Facility

L. E. Robinson, C. E. Dickerman and F. L. Willis

The first scale-up loop experiments on meltdown of clusters of fast reactor fuel pins have been performed in TREAT, using the Mark I integral sodium loop. Two clusters of seven EBR-II Mark I pins were run. Tantalum neutron absorbers shaped the power axially to a maximum-to-minimum ratio of 1.3. Each central pin was of 9% enrichment and the six-pin rings surrounding the center consisted of 7% enriched pins, as approximate compensation for the radical neutron flux depression across the cluster. Measured ratio of the peripheral pin power to the central pin power was 0.94, in good agreement with Sn transport theory calculations. Experimental data are analyzed in Paper IV-2.

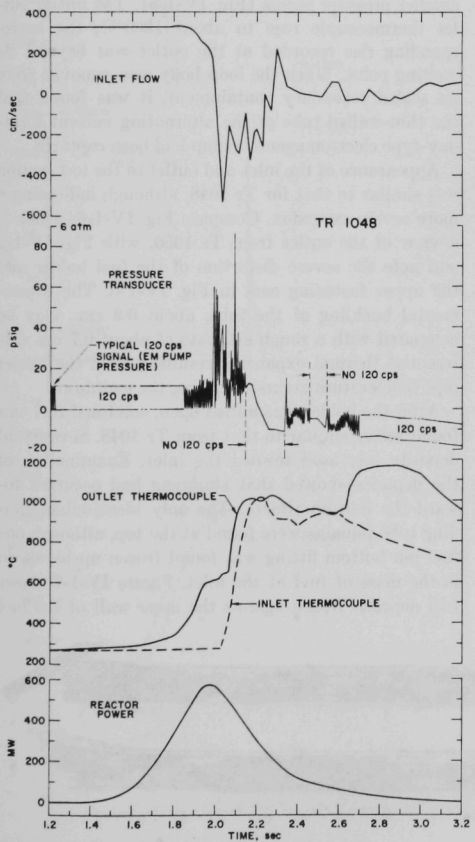


Fig. IV-1-1. Transient Data from TREAT Exposure of 7 EBR-II Mark I Pins in Flowing Sodium (Tr. 1048). *ANL Neg. No. 112-7704.*

Fig. IV-1-2. Solidified Fuel Alloy at Outlet of Test Section (Tr. 1048). *ANL Neg. No. 112-8529.*

Sodium flow was 3.3 m/sec for the first cluster (Transient 1048). Fuel energy input during the reactor power peak was 928 J/g for the internal pin and 882 J/g for each peripheral pin. Instrument data are shown in Fig. IV-1-1. Vigorous coolant accelerations, sharp-fronted pressure spikes and excessive coolant thermocouple readings of about 1000°C were generated at both inlet and outlet at the power peak. A later excursion to 1200°C was recorded on the outlet. Post-experi-

ment examination in the Argonne Hot Laboratory showed large plugs of solidified fuel at the test section inlet and outlet. Fuel was also frozen onto the inner wall of the test section, and a small amount was discovered in the remnants of the cladding tubes at the bottom of the section.

The solidified fuel at the outlet of the test section is shown in Fig. IV-1-2. Only the central part of the channel is still open. More fuel was found beyond the outlet in the hold-down fitting above the test section. This was the first TREAT loop test in which such extensive transport of fuel was found. Figure IV-1-3 is a view of the solidified fuel in the openings of the hold-down fitting. It was found necessary to split the fuel holder longitudinally in a hot laboratory milling machine and then force it apart in order to inspect the cluster remains. Figure IV-1-4 shows that only the extreme top and bottom of the fuel pins remained identifiable (cf. Fig. IV-1-3). Fuel remaining inside the test section was found solidified against the inside walls of the fuel holder pipe, although the flow channel was severely restricted by the large deposits at the inlet and outlet. Severity of deposits increased toward the outlet.

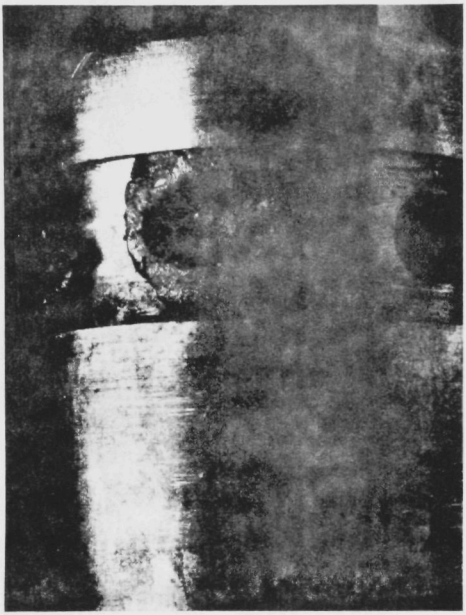

FIG. IV-1-3. Solidified Fuel Alloy in Openings of Hold-down Fitting Beyond Outlet (Tr. 1048). *ANL Neg. No. 112-8531.*

Pump power was off for the second cluster (Tr 1050). Central pin energy input during the reactor power peak was 1048 J/g; for each of the peripheral pins it was 980 J/g. Rapid expulsions were indicated by the inlet flow meter. High inlet and outlet thermocouple outputs were recorded. One large sharp pressure spike was registered near the end of the transient after smaller pressure pulses (Fig. IV-1-5). The initial outlet thermocouple rose to about 1000°C; the corresponding rise recorded at the outlet was beyond its melting point. When the loop body was removed from its sealed secondary containment, it was found that the thin-walled tube of the alternating current Faraday-type electromagnetic pump had been ruptured.

Appearance of the inlet and outlet to the test section was similar to that for Tr 1048, although indicating a more severe excursion. Compare Fig. IV-1-6, which is a view of the outlet from Tr 1050, with Fig. IV-1-2 and note the severe distortion of the fuel holder and the upper fastening ears in Fig. IV-1-6. The experimental buckling of the tube, about 0.8 cm., may be compared with a rough estimate of about 0.7 cm. differential thermal expansion resulting from the holder pipe temperature excursion during the meltdown.

After the holder was milled open, solidified fuel was found inside similar to that from Tr 1048. Severity of deposits increased toward the inlet. Examination of the deposits showed that slumping had occurred toward the bottom (inlet). The only identifiable cladding tube remains were found at the top, although one fuel pin bottom fitting was found frozen upside down in the mass of fuel at the inlet. Figure IV-1-7 shows fuel deposits frozen against the inner wall of the fuel

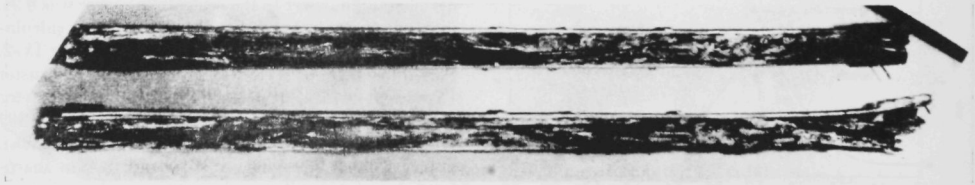

FIG. IV-1-4. Fuel Holder Pipe After Being Split Open to Expose Damaged Fuel (Tr. 1048). *ANL Neg. No. 112-8527.*

holder pipe. The wires seen in disarray in the left half are remains of 0.2 cm diameter rods which locate the fuel elements within the holder. Note the rather uniform but spattered coating of fuel in the right half.

Sodium can be seen leeching out of the heavy fuel deposit at the inlet of Tr 1050, (Fig. IV-1-8). Though this would seem to indicate a low density or spongy mass such does not, thus far, seem to be the case. Extensive deposits of frozen fuel were inside the loop proper beyond the inlet, extending through the inlet flowmeter and presure transducer instrumentation section, inside the electromagnetic pump, and beyond into the return flow tubes. Solidified fuel was packed solidly into the 5 cm. long pressure transducer stand-off tube.

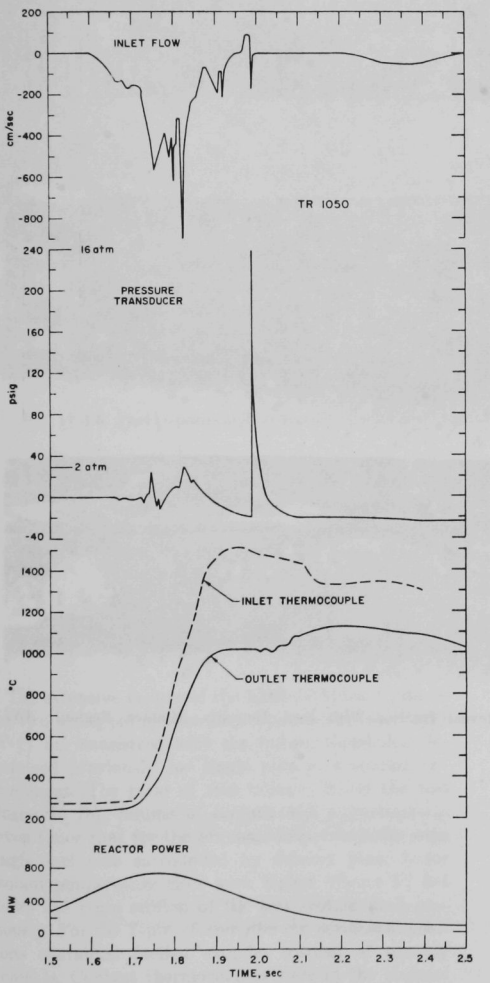


FIG. IV-1-5. Transient Data from TREAT Exposure of 7 EBR-II Mark I Pins in Initially Stagnant Sodium (Tr. 1050). *ANL Neg. No. 112-8296.*

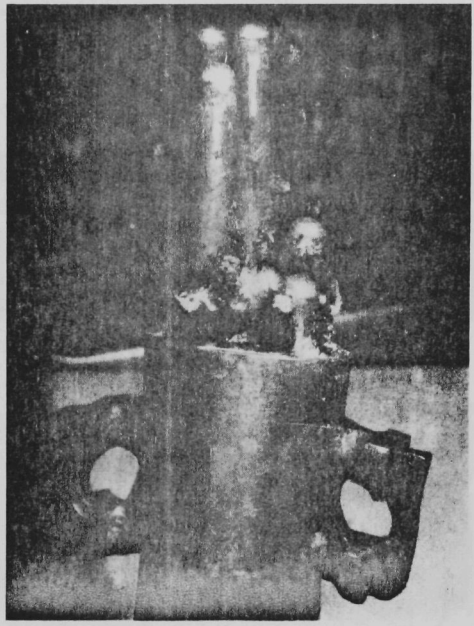

FIG. IV-1-6. Solidified Fuel and Cladding Tube Remains at Outlet of Test Section (Tr. 1050). *ANL Neg. No. 112-8528.*

Both excursions exhibited severe secondary pressure pulses. In the flowing sodium case, the secondary pulse recorded was comparable to an initial pulse which was associated with the first severe flow anomaly. In the case of Tr 1050, the two pressure pulses preceding the secondary spike were of much lower severity. Because of the extensive coolant and fuel motion, it is quite possible that enough voiding occurred to insulate the pressure transducer sufficiently that the actual pulses could have been much higher than recorded.

Coolant thermocouples were chromel-alumel sheathed in 0.010 cm. diam. stainless steel. Their output reached the limit for this type, indicating direct contact with molten fuel alloy, in good agreement with the post-experiment observations of solidified fuel. In Tr 1048 the coolant flow was upward. Distribution of fuel remains and the higher outlet temperatures showed

the influence of the initial coolant flow superimposed upon the expulsion of molten fuel away from the center of the test section. In Tr 1050, transient induced sodium flow was possible, although the pump power was off. Gravity appeared to predominate in this case, as shown by the higher inlet thermocouple temperature and the extensive distribution of solid fuel below the test section. However, the thermocouple record for Tr. 1050 (Fig. IV-1-5) indicates that the first movements were approximately symmetrical from the center, with the subsequent gravity-induced movements occurring about 0.5 seconds after the initial expulsions.

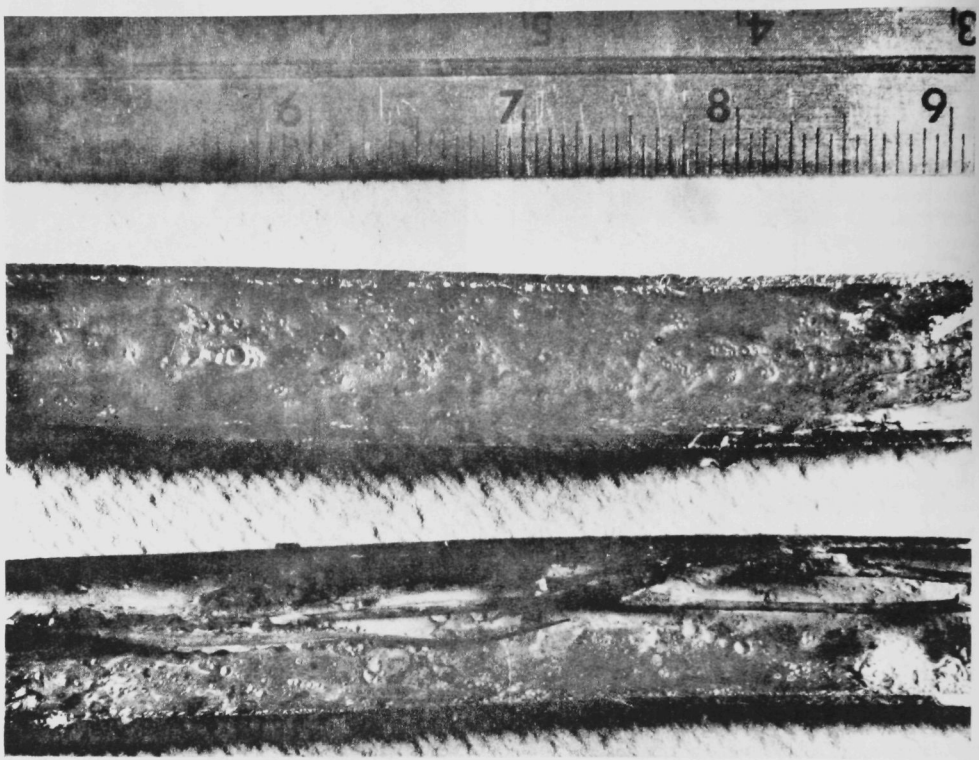


FIG. IV-1-7. Fuel Holder from Tr. 1050 Split Open to Reveal Interior With Fuel Deposits. (Center Region). *ANL Neg. No. 112-8632.*

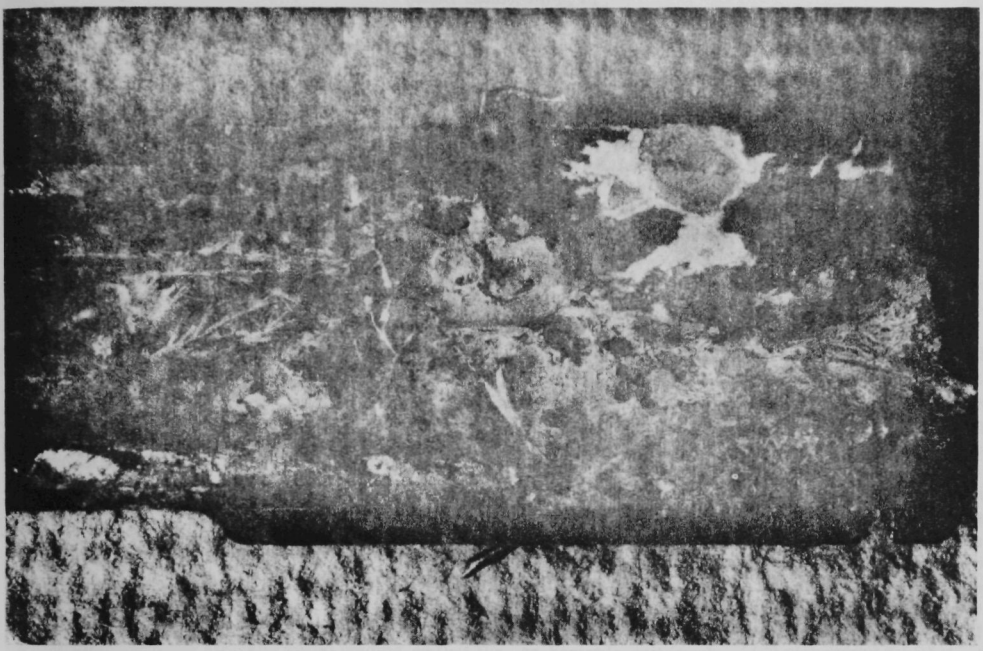

FIG. IV-1-8. Fuel Deposits at Test Section Inlet Tr. 1050. White Areas are Sodium Oxide Deposits. *ANL Neg. No. 112-8526.*

## IV-2. Analyses and Significance of Initial EBR-II Mark I Cluster Fast Reactor Safety Integral Loop Experiments in the Transient Reactor Test Facility (TREAT)

C. E. DICKERMAN, R. PURVIANCE AND A. B. COHEN

The extensive failure of the EBR-II Mark I pins in the two seven-pin cluster loop experiments (see Paper IV-1) are consistent with the failure thresholds determined previously for single pins in a sodium environment. The ratio of fuel volume inside the test cluster to the volume of coolant was approximately seven times that for the previous loop transients with single fuel pins surrounded by dummy pins; hence coolant temperature rises were higher. Figure IV-2-1 shows the cross section of the test section used previously. For the 7-pin cluster, the six peripheral positions contained fuelled samples instead of dummy elements. Coolant thermocouples were in the channel between internal and peripheral pins. In the single-pin analyses reported previously, it was found that fuel heat losses up to approximately the time peak power were determined principally by heat transfer only to the coolant between the central pin and the peripheral dummies.[1] The heat capacity of surrounding sodium and steel became significant after peak power. Thus to first approximation, the central pin of the 7-pin clusters had only half the heat loss to coolant as the single pin of the earlier experiments. Heat loss from the six peripheral pins was intermediate between the two cases. Although the boundary conditions of the 7-pin clusters still were not identical with those of an actual

fast reactor subassembly, the degree of simulation was thus increased markedly over that of the previous single-pin loop experiments.

After fuel failure occurred, the ratio of volume available for motion to fuel and heated coolant volumes was much closer to a real reactor than in the earlier loop tests. Fuel expelled from the two single-pin failures was frozen *in situ* on the test section wall, and there was no evidence of appreciable secondary fuel movements.[1,2] Post-failure fuel behavior in the 7-pin cluster would more nearly be typical of that for a real subassembly.

These two scale-up experiments thus provide the first experimental check on application to cluster geometry of the fuel pin failure modelling developed in single pin tests. In addition, the 7-pin cluster tests provide the first data on post-failure secondary fuel and coolant movement from pin arrays.

Analyses of the experiment consisted first of the correlation of data from the coolant thermocouples, test section inlet flowmeter, and inlet pressure transducer; and second, of transient heat transfer calculations using reactor power data and ratio of sample power to reactor power. Models for heat transfer calculations were essentially the same as those described in Ref. 1. Intact geometry is inherent in the calculations. Following is a summary of the information obtained on the transient behavior during the experiments:

*Tr 1048* (3.25 m/sec flow). Instrument data are presented in Fig. IV-2-2. The initial outlet coolant rise from 270°C to about 600°C is in good agreement with heat transfer calculations of outlet sodium temperatures. This rate of rise is interrupted at approximately

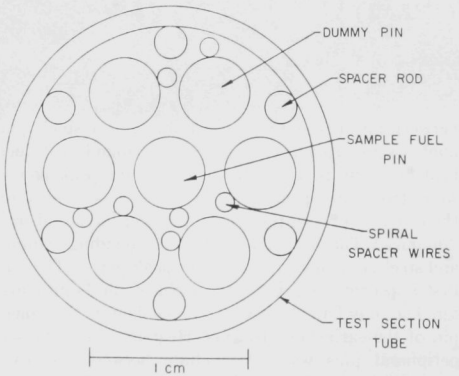


FIG. IV-2-1. Sodium Loop Test Section Cross Section. For the 7-pin Cluster Experiments, the Six Peripheral Positions Contained Fueled Samples Instead of Dummy Pins. *ANL Neg. No. 112-5637.*

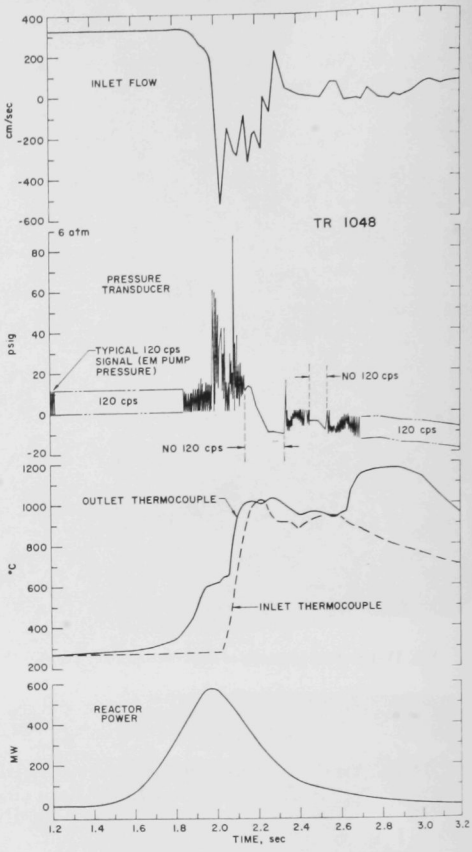


FIG. IV-2-2. Instrumentation Data from 7-pin Cluster Experiment with 3.25 m/sec Sodium Flow (Tr. 1048). *ANL Neg. No. 112-7704.*

peak power by the beginning of a rapid coolant expulsion event and by the first pressure spike of about 3.5 atm. The maximum expulsion rate measured was in excess of 5 m/sec. The break in the outlet temperature curve and onset of abrupt expulsion coincide only with a small pressure anomaly. At this time the maximum calculated cladding surface temperature is below boiling, but maximum central fuel pin temperature is 1255°C. Thus, local boiling could occur at this time due to molten high temperature fuel moving from the center of the pin through a fuel surface crack to contact the cladding. Such surface cracks have been found in pins carried to the threshold of failure. Outlet bulk coolant temperature was calculated (assuming no va-

porization) to be approximately 975°C at 2.00 sec and about 1110°C at 2.05 sec, so the first pressure spike is attributed to sodium vaporization. The rapid coolant expulsion indicated on the inlet flowmeter is also apparent on the sodium thermocouple record, showing rapid expulsion, both upward and downard, of high temperature sodium. The second pressure spike (6 atm) corresponds to the time that failure of the central, hottest, pin is calculated due to vapor pressure of the sodium bond between fuel and cladding. The time spent at temperature is not sufficient for failure by penetration due to the formation of fuel-cladding eutectic. Out-of-pile and in-pile experiments have yielded a time of approximately one second for penetration of a 0.25 mm thick steel EBR-II cladding tube by molten U-fissium alloy. Large amounts of eutectic could be formed before final solidification at the end of the experiment, however.

Voiding has grown since the inception of expulsion at about 2.00 sec, and by 2.15 sec the total expulsion recorded on the flowmeter equals the distance between the center of the fuel and the inlet pressure transducer. This is in good agreement with the disappearance of the 120 cps pump pressure signal at that time. Failure of the peripheral pins by internal sodium pressure is calculated to occur after the initial voiding, so that the pressure transducer would not necessarily detect a pressure pulse from release of bond sodium from a peripheral pin. Evidence of secondary fuel motion is seen at approximately 2.6 sec on the outlet thermocouple. The one spike of flow up into the test section (peaking at about 2 m/sec) correlates well with a small pressure spike of about 2 atm and short temporary recovery of flow past the inlet flowmeter. A second short period of no pressure modulation occurs before flow is finally reestablished at a low rate.

It should be noted that relief of bond sodium pressure by axial motion of molten fuel, such as that found for single pin loop experiments with flowing sodium,[1,2] did not appear to occur. This difference can be explained qualitatively by the flatter radial temperature gradients in these cluster experiments because of the reduced amount of heat absorber around the pins.

*Tr 1050* (no flow). Instrument data are given in Fig. IV-2-3. The initial coolant expulsion from the test section, reaching 2 m/sec, is in qualitative agreement with the movement calculated from pre-failure thermal expansion of sodium in the cluster. Cladding failure is indicated experimentally by a small (2 atm) pressure spike associated with an increased expulsion peaking at 6 m/sec. A second 2 atm spike is coincident with another expulsion peak which reaches 9 m/sec. Expulsion continues beyond this time, indicating coolant voiding extending beyond 40 cm below the test

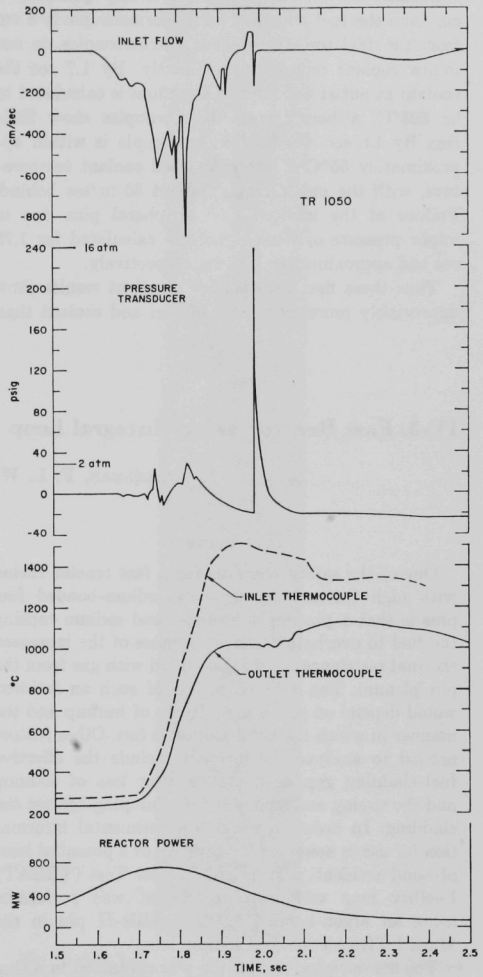


FIG. IV-2-3. Instrumentation Data from 7-pin Cluster Experiment with No Initial Sodium Flow (Tr. 1050). *ANL Neg. No. 112-8296.*

cluster inlet at the time a vigorous secondary pulse recorded as 16 atm occurred. Because of the voiding, the critical pulse may have been much higher at its point of origin. The extensive motion of molten fuel extending to ~45 cm below the test section inlet indicates that the final pressure pulse may actually have occurred in the inlet section where instrumentation and the pump are located, rather than in the test section region.

Because the inlet thermocouple is approximately 1 cm from the fuel and the outlet thermocouple is 8 cm from the fuel top, the coolant thermocouples do not follow coolant temperatures directly. By 1.7 sec the coolant at outlet and inlet fuel sections is calculated to be 605°C, although both thermocouples show little rise. By 1.8 sec, the inlet thermocouple is within approximately 55°C of the calculated coolant temperature, with the outlet lagging about 50 m/sec behind. Failure of the internal and peripheral pins due to vapor pressure of bond sodium is calculated for 1.75 sec and approximately 1.83 sec, respectively.

Thus these first loop cluster transient results show appreciably more movement of fuel and coolant than found previously for single fuel pins.[1,2] They indicate the importance of secondary fuel movements and the possibility of "trapping" sodium between plugs of high temperature fuel inside a reactor subassembly. Further scale-up loop transients and investigation of the effects of axial blanket sections will be necessary for evaluation of these post-failure effects.

### References

1. W. Stephany and C. E. Dickerman, *Analyses of Behavior of EBR-II-Type Pins Under Transient Heating in Sodium Environment*, Trans. Am. Nucl. Soc. **10**, 343 (1967).
2. L. E. Robinson, R. Purviance and F. L. Willis, *Results from High Specific Energy Input Single-Pin, Sodium Loop Meltdown Experiments in TREAT*, Trans. Am. Nucl. Soc. **10**, 343 (1967).

## IV-3. Fast Reactor Safety Integral Loop Experiment on an Argon-Bonded EBR-II Pin

C. E. Dickerman, F. L. Willis, R. Smith and A. B. Cohen

### Introduction

One of the safety concerns for a fast reactor fueled with high thermal performance sodium-bonded fuel pins is that a pin might lose its bond sodium causing the fuel to overheat and melt because of the increased thermal resistance bond region filled with gas from the pin plenum. The detailed course of such an incident would depend on pin design, degree of burnup and the manner in which the bond sodium is lost. Other factors needed to analyze the incident include the effective fuel-cladding gap conductance after loss of sodium, and the timing and modes of fuel slumping against the cladding. In order to provide experimental information for use in assessing the severity of a potential loss-of-bond accident, a Transient Reactor Test (TREAT) Facility loop meltdown experiment was performed using an argon-bonded Mark I EBR-II pin in the Mark I TREAT integral sodium loop.[1]

The 6% enriched sample pin was contained in a ring of six hollow dummy pins, on an EBR-II pitch, and the fuel holder was wrapped in stepped layers of tantalum to shape the sample power axially. Coolant flow was 4 m/sec, and the initial coolant temperature was 380°C. A target of 168 J/g of fuel was set for the average sample power, which would require a constant TREAT power level of 54 MW.

### Calculations

Calculations were performed to predict the course of the experiment. The ARGUS transient heat transfer code[2] was used. An empirical value of the fuel-cladding gap thermal conductance was obtained by analyzing the cladding surface transient temperature curves from a special series of TREAT experiments performed earlier to study cladding penetration in which both argon- and sodium-bonded EBR-II type pins were run in dry capsules with fast-response cladding surface thermocouples.[3] These pins were exposed in pairs, one of each kind, and the effective thermal conductance of 0.28 W/cm²-°C was deduced. A gap conductance of 56 W/cm²-°C was used to obtain a conservative estimate of the rate of heat transfer to cladding after the fuel was calculated to melt and contact the inner surface of the cladding.

Experimental data on fuel thermal expansion[4] and volume change upon melting[5] were used to estimate the excess volume available inside the cladding into which the molten fuel could slump. A total drop of 2.7 cm was calculated. The time for an object to fall freely this distance is 74 msec. The time actually used for the delay between melting and contact between fuel and cladding, a time during which the heat content of the fuel continues to increase due to the initial low gap conductance, was 92 msec. Fig. IV-3-1 shows the fuel surface and fuel centerline temperatures at the fuel axial midplane calculated for the reference transient. The actual power transient was somewhat more severe; Fig. IV-3-2 compares the idealized power curve used as the reference with the TREAT power curve. Although the power excursion is not a perfect "flattop," it was sufficiently severe for the purposes of the experiment. The calculations show that fuel melt-

ing should have occurred, but that the fuel-cladding interface was cooled rapidly enough after fuel slumping occurred that no significant cladding penetration would be expected. (A time of about one second is required under isothermal conditions for penetration of the 0.23 mm thick steel cladding by the molten fuel alloy.[3])

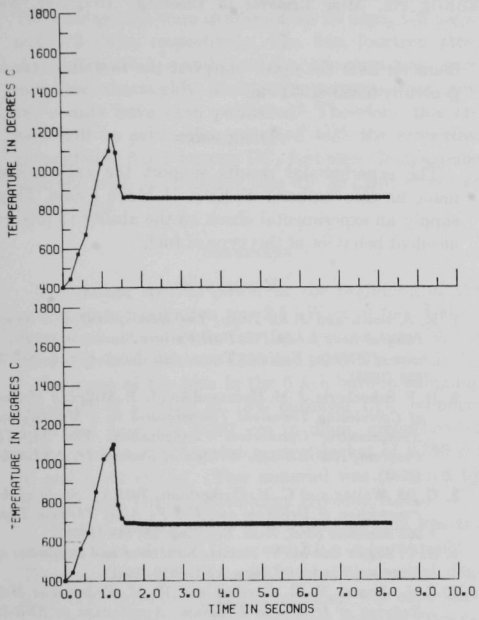


FIG. IV-3-1. Fuel Surface (Lower Curve) and Fuel Centerline (Upper Curve) Temperatures Calculated at Axial Midplane for Reference Transient on Argon-Bonded EBR-II Mark I Pin in Flowing Sodium. *ANL Neg. No. 112-9442.*

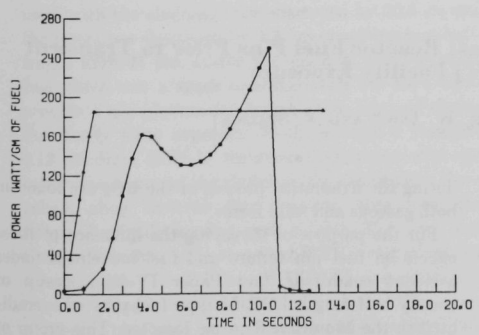


FIG. IV-3-2. Reference and Actual Power Transient Curves for Argon-Bonded EBR-II Mark I Pin Loop Experiment. *ANL Neg. No. 112-9434.*

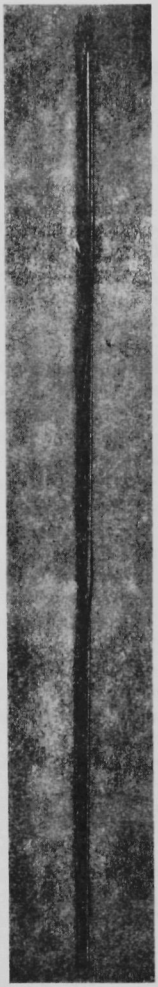

FIG. IV-3-3. Post-Experiment Condition of Argon-Bonded EBR-II Pin, Prior to Removal of Cladding. *ANL Neg. No. 112-8530.*

## RESULTS

No flow or pressure anomalies were recorded by the transient instrumentation.

Following the experiment, the loop was returned to the Illinois site for disassembly and examination of the sample in the Argonne Hot Laboratory. The clad pin, shown in Fig. IV-3-3, showed no evidence of dam-

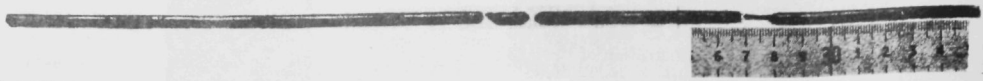

FIG. IV-3-4. Post-Experiment Condition of Argon-Bonded EBR-II Pin, After Removal of Cladding. *ANL Neg. No. 112-8307.*

age after the transient. The lack of the spiral warpage typical of TREAT exposures is in agreement with the relatively low transient cladding temperatures calculated. Measurements showed the cladding diameter to be 0.439–0.441 cm., indicating no expansion of the cladding tube.

At no point did the cladding stick to the fuel surface, and the steel was easily peeled away from the fuel alloy. Some small surface cracks, filled with eutectic, were found in the fuel. In one area a small surface scar of eutectic was found on the inner side of the cladding. An upper limit of 0.001 cm was set for cladding penetration at this location.

It is not clear from visual inspection whether the fuel had actually melted and flowed locally or whether it had merely reached the plastic state and had become deformed against the cladding. The appearance of the fuel is shown in Fig. IV-3-4. However, some of the separations and damaged areas do have the appearance of having been squeezed by gas bubbles while in a plastic condition upon reaching the melting range.

Some fuel slumping is indicated by the growth in fuel diameter from 0.366 cm. to a post-experiment maximum of 0.394 cm. The bottom tip of the fuel, at its region of contact with the lower end spade fitting, measures 0.368 cm., and there is one region of reduced diameter near the upper end; but the fuel diameter is generally 0.389–0.394 cm.

### Discussion

The experimental results support the calculations made for this "unbonded" EBR-II Mark I case. They supply an experimental check on the ability to predict accident behavior of this type of fuel.

### References

1. E. S. Sowa and J. C. Heap, *The Development of a Small Integral Loop for In-Pile Fuel Failure Studies in the Presence of Flowing Sodium*, Trans. Am. Nucl. Soc. **8**, No. 2, 559 (1965).
2. D. F. Schoeberle, J. M. Heestand and L. B. Miller, *A Method of Calculating Transient Temperatures in a Multiregion, Axisymmetric Cylindrical Configuration. The ARGUS Program, 1089/RE 248, Written in Fortran II*, ANL-6654 (1963).
3. C. M. Walter and C. E. Dickerman, *TREAT Study of the Penetration of Uranium and U-5 Fs Alloy Through Type 304 Stainless Steel*, Nucl. Sci. Eng. **18**, 518 (1964).
4. S. T. Zegler and M. V. Nevitt, *Structures and Properties of Uranium-Fissium Alloys*, ANL-6116 (1961).
5. C. L. Rosen, N. R. Chellew and H. M. Feder, *The Melt Refining of Irradiated Uranium: Application to EBR-II Fast Reactor Fuel. IV. Interaction of Uranium and its Alloys with Refractory Oxides*, Nucl. Sci. Eng. **6**, 504 (1959)

## IV-4. Properties of 6a/o Burnup Oxide Fast Reactor Fuel Pins Prior to Transient Reactor Test (TREAT) Facility Exposure

R. Stewart, C. E. Dickerman, W. Doe* and N. Stalica†

### Introduction

Steady state irradiation of gas-bonded uranium dioxide fast reactor type fuel pins produces fission products that are retained within the $UO_2$ structure and also cause changes in the fuel structure, geometry, and composition. The fission products that are generated during the irradiation process of the $UO_2$ are found in both gaseous and solid forms.

For the purpose of surveying the influence of these effects on fuel pin failure and fuel movement under accident conditions (see Paper IV-5) a group of twenty half-length EBR-II type fuel pins was irradiated in the Materials Testing Reactor. This group of twenty $UO_2$ pins was divided into three subgroups according to the respective nominal burnup of each pin. These subgroups were: the 0.7 a/o target burnup sub-

* Remote Control Division, Argonne National Laboratory.
† Chemical Engineering Division, Argonne National Laboratory.

group, consisting of six pins, pin 1 through pin 6; the 3.0 a/o target burnup subgroup, consisting of eight pins, pin 7 through pin 14; and the 6 a/o target burnup subgroup, consisting of six pins, pin 15 through pin 20. These subgroups were irradiated for 30 days, 123 days, and 273 days, respectively. The first fourteen pins, that is, the 0.7 a/o and the 3.0 a/o burnup pins, were examined thoroughly during the previous year, and the results have been published.[1] Therefore, this article will be primarily concerned with the properties of irradiated 6 a/o burnup $UO_2$ fuel pins. Comparisons with the lower burnup fuel pins will be made wherever appropriate.

## Specimens

The design specific power at the beginning of the steady state irradiation was 2.5 kW/cc of fuel. Calculated surface and centerline fuel temperatures at the start of irradiation were 1350 and 2400°C respectively.

Each one of the pins in the 6 a/o burnup subgroup consisted of a stack of 13% enriched $UO_2$ cylinders 13.97 cm long and 0.381 cm in diam, argon-bonded and sealed in a 304 stainless steel jacket of 0.396 cm id and 0.442 cm od. (This material was prepared by the Ceramics Group, Metallurgy Division, ANL).

The fuel history of the 6 a/o burnup pins was the same as that of the 0.7 a/o and 3.0 a/o burnup pins.[1] The average density was 91.96% of theoretical density.* The ratio of oxygen to uranium was calculated to be 2.019 using data from chemical analyses. The results of a spectrochemical analysis of the fuel impurities is given in Table IV-4-I.[3]

Standard EBR-II cladding and end fittings were used, with the cladding tube shortened by 20.6 cm and the restrainer shortened by 1.3 cm, resulting in a half-length EBR-II pin. Inside the cladding and above the fuel, there was a space approximately 5.7 cm long to provide a gas plenum for fission gases released during the steady state exposure. Each pin had a standard 0.12 cm diam EBR-II stainless steel spacer wire spirally wound around the cladding. An aluminum 0.1 w/o cobalt alloy neutron flux monitor wire was also wrapped spirally around each sample. The pins were then sodium bonded in standard MTR irradiation capsules designed for full-length EBR-II-size pins[4] with two half-length oxide pins per capsule. The even-numbered pins were on top and the odd-numbered pins were on the bottom inside each MTR capsule (i.e., pin 2 above pin 1, *et seq.*).

* Theoretical density of 10.96 gm/cc (obtained by x-ray measurements) from Ref. 2.

TABLE IV-4-I. Spectrochemical Analysis of Fuel Composition

| Element | Concentration, ppm |
|---|---|
| Ag | <1 |
| Al | 70 |
| As | <20 |
| B | 0.2 |
| Be | <0.5 |
| Bi | <1 |
| Ca | <50 |
| Co | <5 |
| Cr | 40 |
| Cu | 2 |
| Fe | 90 |
| K | <50 |
| Li | <5 |
| Mg | 8 |
| Mn | <1 |
| Mo | 20 |
| Na | 5 |
| Ni | 50 |
| P | <100 |
| Pb | 1(?) |
| Sb | <10 |
| Si | 50 |
| Sn | 5 |
| Ti | 100 |
| Zn | <50 |

## Post-Steady-State Irradiation Condition

### Macroscopic condition

After 273 days of irradiation in MTR, the capsules containing pins 15 through 20 were returned to the ANL Hot Laboratories in Illinois. The ensuing operations were: disassembly from their irradiation capsules; macroscopic and microscopic examination of the pins; destructive examination of a control specimen; and subsequent re-encapsulation for transient irradiation experiments in the TREAT reactor (see Paper IV-5).

Inspection procedures included checks on dimensional changes, axial gamma scanning, photography of the macroscopic condition of the pins, neutron radiographs[5] which were made using a thermal neutron beam from the Juggernaut reactor, x-ray radiographs, burnup determination by radiochemical analysis of the monitor wires and also by mass spectrochemical and radiochemical analysis of the fuel, and an analysis of the relative amounts of fission products by the laser beam vaporization technique. One pin, pin 15, was set aside for destructive examination which involved collection of released fission gases, burnup measurement by mass spectrometric determination of

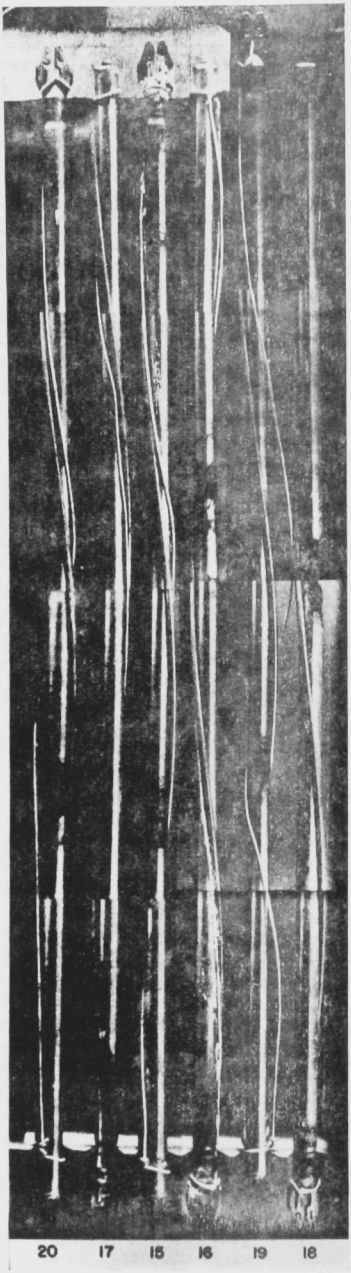


uranium isotopic ratios and ceramographic examinations.

Figure IV-4-1 displays the overall surface condition of pins 15 through 20 after removal from their sodium bonded state inside the MTR capsules. The identifying number of each pin is indicated at the bottom of the figure. The wire that is spirally wound around the pin proper and welded to it is the stainless steel spacer wire. The smaller wire which is more loosely wound and tied to the pin at each end is the aluminum 0.1 w/o cobalt monitor wire. Although surface discoloration is apparent on each pin, this is only external and is not indicative of any diametral changes. In fact, the average pin diameter was 0.1740 in. (0.442 cm) as measured twice at one-half-inch intervals, one measurement being 90 deg to the other, over the entire length of the pin. The dark discoloration which appears on each pin approximately two-thirds the way up from the spade end is believed to be the result of a "plating out" of sodium impurities in a region of temperature transition to the cooler cladding at the pin plenum. (Spectrographic analyses of the material showed iron, chromium, nickel, tin, and aluminum to be major constituents.)

No metallographic evidence was found for cladding defects in this region. The 6 a/o burnup pin run in TREAT failed in this region (see Paper IV-5). Such a failure could have occurred with "good" cladding, as a result of excessive transient thermal stresses, of mechanical stresses resulting from the bending associated with the sagging observed, or from localized overheating where the end of the fuel was thrust against the cladding as the cladding bent during the transient.

The pins were gamma scanned after a five-month "cooling" period. The results of these axial scans appear in Fig. IV-4-2. Although the gamma scanning indicated axial gradients in activity, there was no evidence of gross axial motion of fuel or fission products. But segregation of fission products was found on a microscopic scale. (The previous report,[1] stating that no segregation occurred for the lower burnup pins in this series, referred only to gross effects as detectable by the gamma scanning technique.)

A radiochemical analysis was made on samples taken from the monitor wires at the top, middle, and bottom of each pin. In addition, several oxide samples from the top, center, and bottom of pin 15 were analyzed for burnup by means of a mass spectrochemical and radiochemical analysis. This analysis supplied specific values for axial gradients of burnup within the oxide matrix of the pin. These values were lowest for

FIG. IV-4-1. Post-Irradiation Condition of Pins 15–20, Before Remote Removal of Flux Monitor Wires. *ANL Neg. No. 112-8623.*

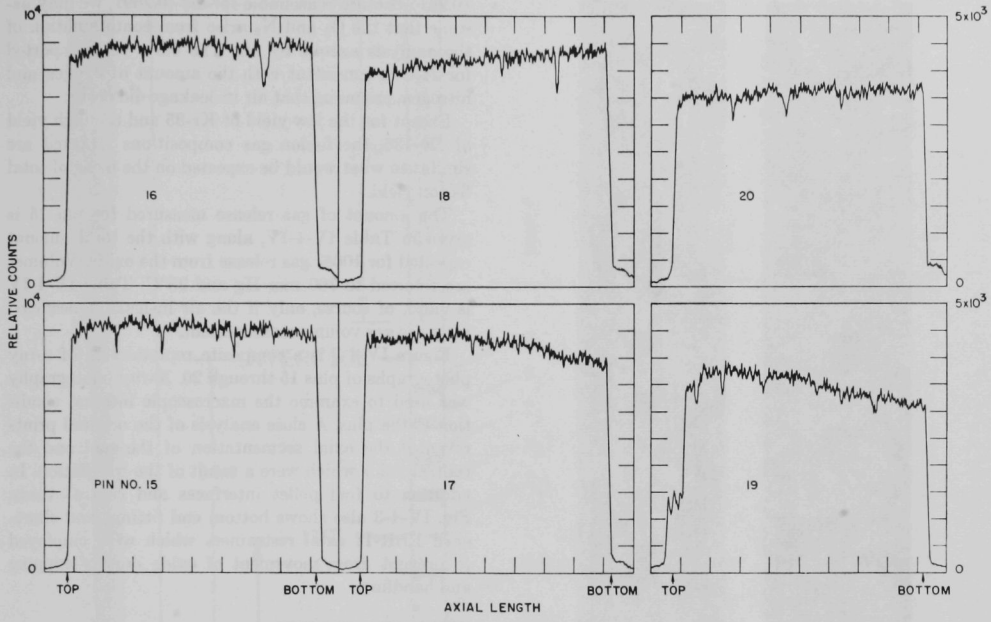


FIG. IV-4-2. Axial Gamma Ray Scan Data. *ANL Neg. No. 112-8494.*

the bottom sample, with gradually increasing values to the highest value reported for the top-most sample. Integrated neutron flux values from the monitor wires were multiplied by 0.91 to correct for flux depressions within the pins. Burnup data are shown in Table IV-4-II.

Prior to the destructive examination of pin 15, the gas contained within was collected and the volume measured. Subsequently the sample was analyzed by mass spectrometer, the results of which appear in Table IV-4-III.

The significance of the value reported for $H_2$,

TABLE IV-4-II. BURNUP DATA

| Pin No. | Nominal Burnup, a/o | Burnup from Monitor Wires, a/o | Burnup from Mass Spectrometer, a/o |
|---|---|---|---|
| 15 (bottom) | 6.0 | 6.64 | 5.4 |
| 15 (center) | 6.0 | 6.64 | 5.6 |
| 15 (top) | 6.0 | 6.64 | 6.0 |
| 16 | 6.0 | 6.23 | — |
| 17 | 6.0 | 7.41 | — |
| 18 | 6.0 | 7.63 | — |
| 19 | 6.0 | 5.64 | — |
| 20 | 6.0 | 5.66 | — |

TABLE IV-4-III. MASS SPECTROMETER ANALYSIS, %

| Gas | Pin 15, % Conc. |
|---|---|
| $H_2$ | 0.2 |
| He | <0.02 |
| $CH_4$ | <0.02 |
| $H_2O$ | 0.6 |
| $N_2$ | 68.1 |
| $O_2$ | 17.8 |
| Ar | 1.0 |
| Xe-131 | 0.93 |
| Xe-132 | 1.80 |
| Xe-134 | 2.62 |
| Xe-136 | 5.04 |
| Kr-83 | 0.41 |
| Kr-84 | 0.57 |
| Kr-85 | 0.07 |
| Kr-86 | 0.84 |

TABLE IV-4-IV. GAS YIELD

| Pin No. | Nominal Burnup, a/o | Measured Gas Volume, cc | Gas Volume for 100%, cc | Release, % |
|---|---|---|---|---|
| 15 | 6.0 | 5.3 | 22.8 | 23 |

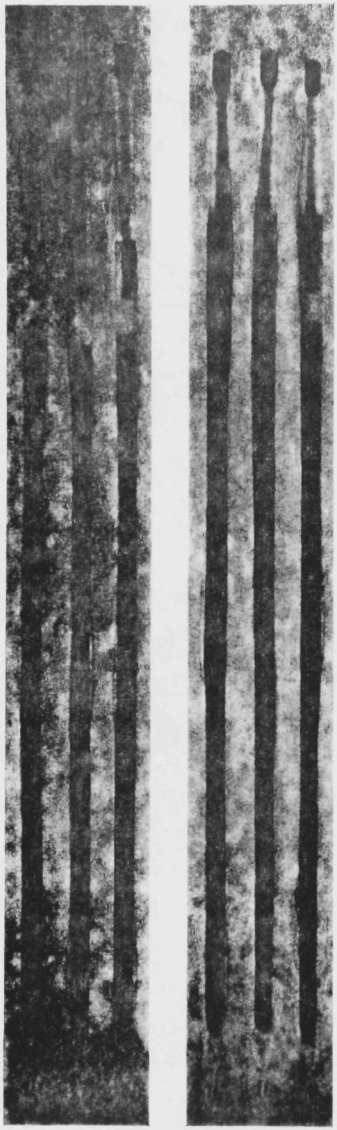

FIG. IV-4-3. Post-Irradiation X-ray Photograph of Pins 15-20. *ANL Neg. No. 112-8497.*

namely 0.2%, is not entirely clear. It is a factor of 2 greater than it should be if it is due to air in-leakage.

From the fact that the ratio of oxygen to nitrogen (0.261) is quite reasonable for air (0.269), we may assume that the $O_2$ and $N_2$ arise from contamination of the analysis sample by air. The 0.6% value reported for $H_2O$ is consistent with the amount of oxygen and nitrogen, assuming that air in-leakage did occur.

Except for the low yield of Kr-85 and the high yield of Xe-136, the fission gas compositions reported are similar to what would be expected on the basis of total fission yield.

The amount of gas release measured for pin 15 is given in Table IV-4-IV, along with the total amount expected for 100% gas release from the oxide. Volumes are referred to 760 mm Hg and 25°C. Table IV-4-IV is valid, of course, only if the air in-leakage occurred after the gas volume measurement.

Figure IV-4-3 is a composite reproduction of x-ray photographs of pins 15 through 20. X-ray photography was used to examine the macroscopic internal condition of the pins. A close analysis of the original prints revealed the axial segmentation of the fuel and the central voids which were a result of the irradiation. In addition to fuel pellet interfaces and central voids, Fig. IV-4-3 also shows bottom end fittings and shortened EBR-II axial restrainers which were employed to prevent gross movement of oxide during shipping and handling.

MICROSCOPIC CONDITION

Figure IV-4-4 is a diagrammatic reproduction of pin 15 showing the pin with its end fittings and, within, the five stacked oxide pellets. The figure indicates specific locations of the oxide interfaces with reference to the base line at the bottom of the fuel column. To the left of the diagram is shown an x-ray photograph of pin 15 which corresponds to the diagram. The labeled segments of the diagram (i.e., A, B, C, D) identify samples from three regions of pin 15 (top, central, and bottom), listing the specific analysis which was performed on each sample.

The diameter of the fuel was obtained by subtracting the known cladding thickness plus the thickness of the annulus between the fuel and cladding as measured on the photomicrograph from the outside diameter of the pin after irradiation, as measured using a micrometer.

Figure IV-4-5 is a beta-gamma autoradiograph of a control sample exposed to fine grain positive film for a period of 72 hours, developed in a high contrast developing solution and enlarged to a 23× magnification. The non-homogeneity of the initial starting fuel is clearly seen in this photomicrograph.

*A Samples*

The samples $A_1$, $A_2$, $A_3$ from the bottom, center, and top, respectively, of pin 15 were chosen exclusively for

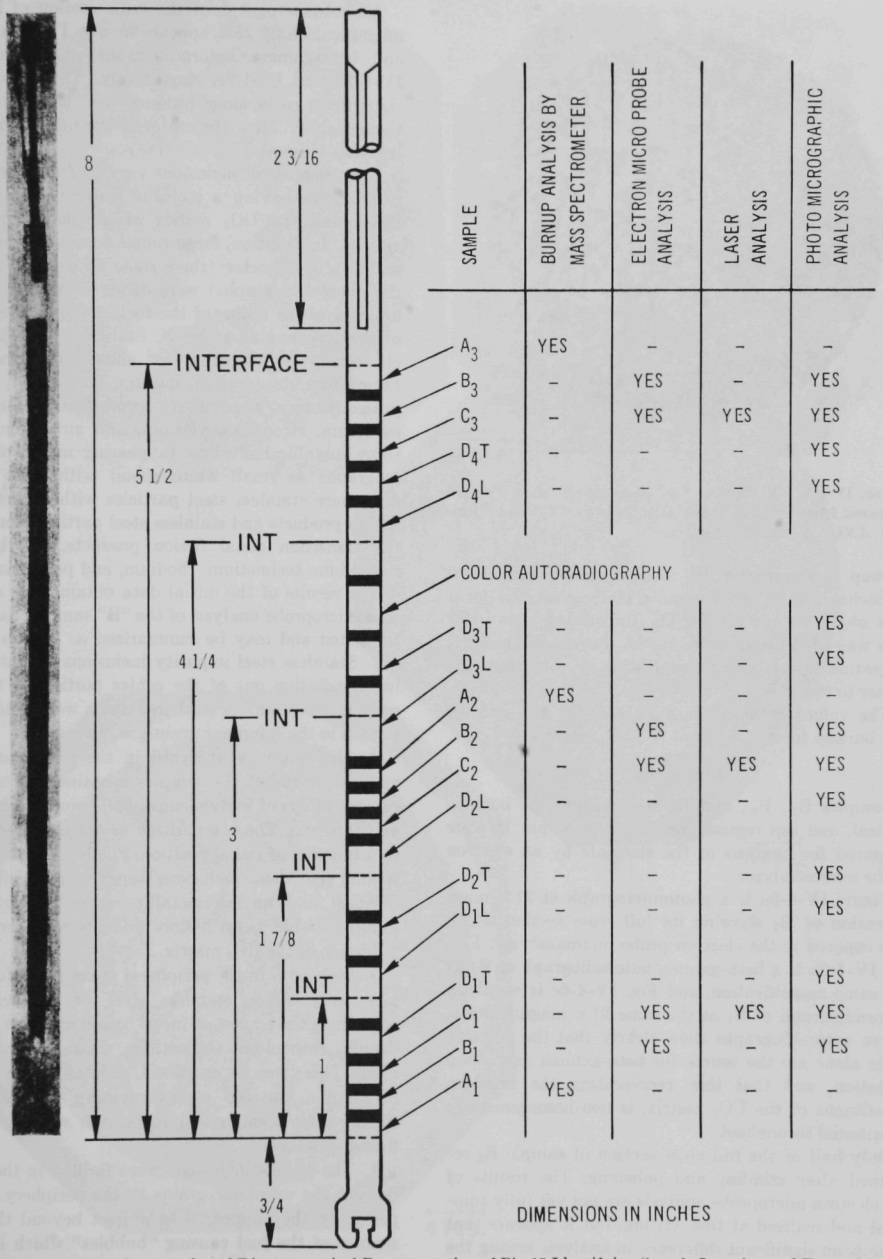


FIG. IV-4-4. X-ray Photograph and Diagrammatical Representation of Pin 15 Identifying Sample Location and Type of Analysis Performed on Respective Sample. *ANL Neg. No. 112-8892.*

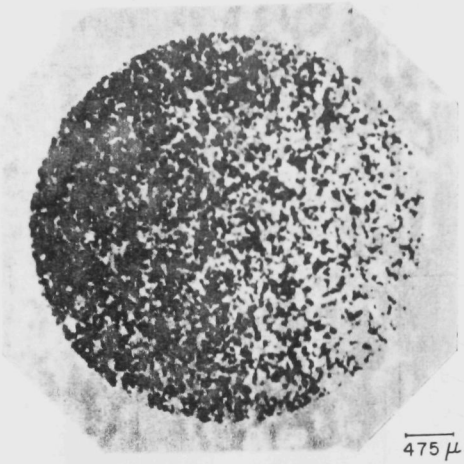


FIG. IV-4-5. Beta-Gamma Autoradiograph of a Sample Prepared from Original Material and Used as Control Specimen. *ANL Neg. No. 112-8893.*

burnup determination by mass spectrochemical and radiochemical analysis because of their specific location along the pin's axis. The underlying reason for this was to determine the extent that fission product migration occurs along the axis of the pin from the center to the ends.

The values obtained were 5.4 a/o, 5.6 a/o, and 6.0 a/o burnup for $A_1$, $A_2$, and $A_3$, respectively.

### *B Samples*

Samples $B_1$, $B_2$, and $B_3$ representing the bottom, central, and top regions, respectively, of pin 15 were prepared for analysis of the elements by an electron probe microanalyzer.

Figure IV-4-6a is a photomicrograph at 21× magnification of $B_1$ showing its full cross section which was exposed to the electron probe microanalyzer. Figure IV-4-6b is a beta-gamma autoradiograph of $B_1$ at the same magnification, and Fig. IV-4-6c is an alpha autoradiograph of $B_1$ at the same 21× magnification. These autoradiographs show clearly that the porosity spots alone are the source for beta-gamma and alpha radiation, and that this, representing the uranium constituent of the $UO_2$ matrix, is non-homogeneously distributed throughout.

Only half of the full cross section of sample $B_2$ remained after grinding and polishing. The results of the electron microprobe analysis are not yet fully compiled and realized at this writing, but it appears that there is no significant difference in analysis among the B samples.

A photomicrograph of the cross section of $B_3$ at a magnification of 21× appears in Fig. IV-4-7a. Alpha and beta-gamma autoradiographs appear as Figs. IV-4-7b and IV-4-7c, respectively. These show that the porous areas alone produce the "hot spots" near the periphery. Near the center of the fuel, the activity becomes diffused.

Numerous small inclusions varying from 1 μ to 15 μ in diameter having a metallic luster were dispersed throughout the $UO_2$ matrix of all the samples examined. In addition, large round porous inclusions up to 100 μ in diameter (these show up as dark spots in the photomicrographs) were dispersed throughout the outer ¼ of the radius of the fuel. A thorough analysis of these porous areas by N. Stalica et al.,[6] using an electron probe microanalyzer, showed that they contained uranium, cesium, barium, lanthanum, cerium, praseodymium, neodymium, promethium, samarium, europium, strontium, yttrium, and zirconium. Small shiny metallic inclusions (appearing in the photomicrographs as small white spots) within the porous area were stainless steel particles with no detectable fission products and stainless steel particles containing the transition metal fission products, molybdenum, ruthenium, technetium, rhodium, and palladium.

The results of the initial data obtained by an electron microprobe analysis of the "B" samples have been tabulated and may be summarized as follows:

1. Stainless steel impurity inclusions migrated during irradiation out of the center portion of the fuel matrix. No stainless steel inclusions were detected to remain in the columnar grain-growth region.

2. All inclusions analyzed in the columnar grain-growth regions of the samples contained metallic-appearing alloys of molybdenum, ruthenium, technetium, and rhodium. The composition of the inclusion varied as a function of radial position. Further, it was demonstrated that these inclusions were free of uranium, indicating that no intermetallics or solid solutions of uranium-noble metal fission products were formed by reduction of the $UO_2$ matrix.

3. Inclusions in the peripheral areas of the fuel samples were either stainless steel or stainless steel containing the transition metal fission products, molybdenum, ruthenium, technetium, rhodium, and palladium. There was no consistent ratio of fission product distribution in the steel-containing inclusions, although molybdenum and ruthenium were the major fission products.

4. The porous inclusions were formed in the region beyond the columnar grains to the periphery. At the periphery they appeared to project beyond the outer surface of the fuel causing "bubbles" which in many cases appeared to have burst. These porous inclusions

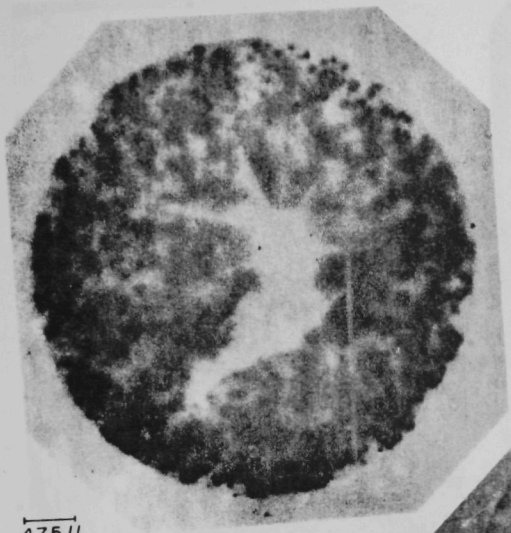


(b)

(c)

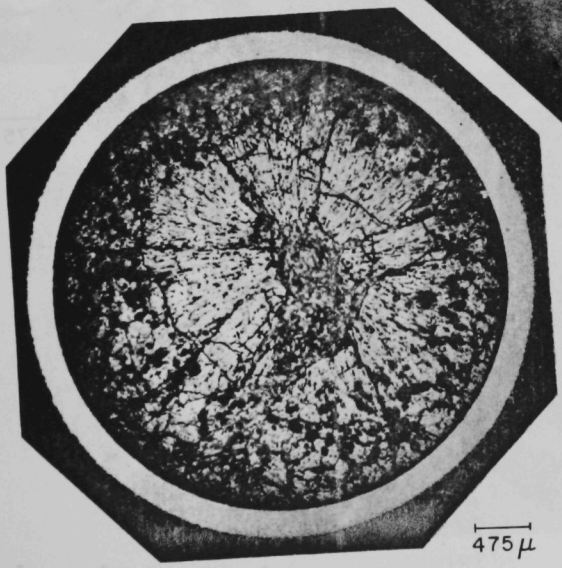


(a)

FIG. IV-4-6. Microscopic Cross Section of Pin 15, Sample $B_1$: (a) Radial Cross Section of $B_1$; (b) Beta-Gamma Autoradiograph of $B_1$; (c) Alpha Autoradiograph of $B_1$. *ANL Neg. No. 112-8897.*

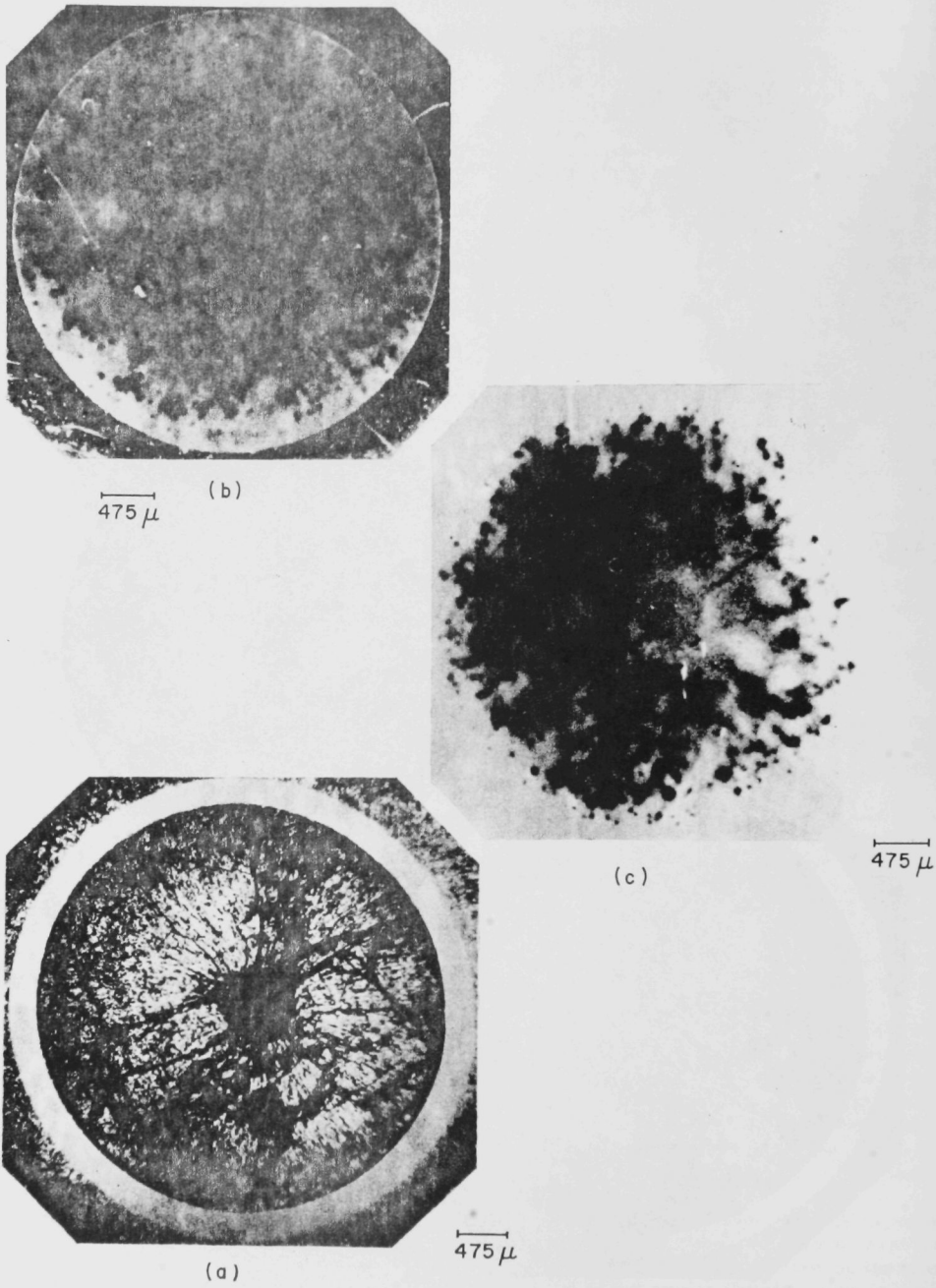


FIG. IV-4-7. Microscopic Cross Section of Pin 15, Sample $B_3$: (a) Radial Cross Section of $B_3$; (b) Alpha Autoradiograph of $B_3$; (c) Beta-Gamma Autoradiograph of $B_3$. *ANL Neg. No. 112-8898.*

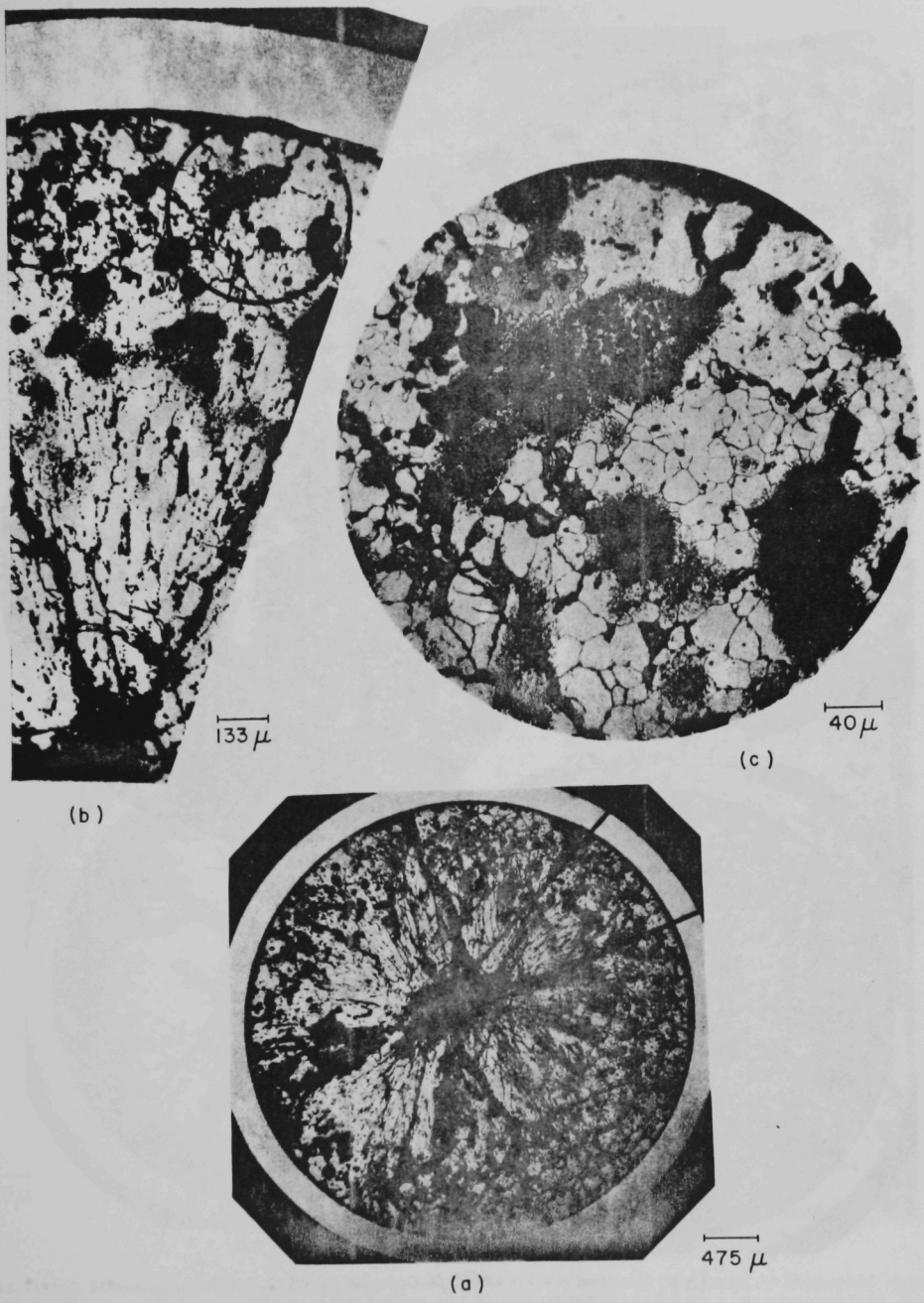


FIG. IV-4-8. Microscopic Condition of Pin 15, Sample $D_{1T}$: (a) Radial Cross Section of the Sample; (b) Enlargement of Area Indicated on Section; (c) Further Enlargement of Area Indicated on (b). *ANL Neg. No. 112-8895.*

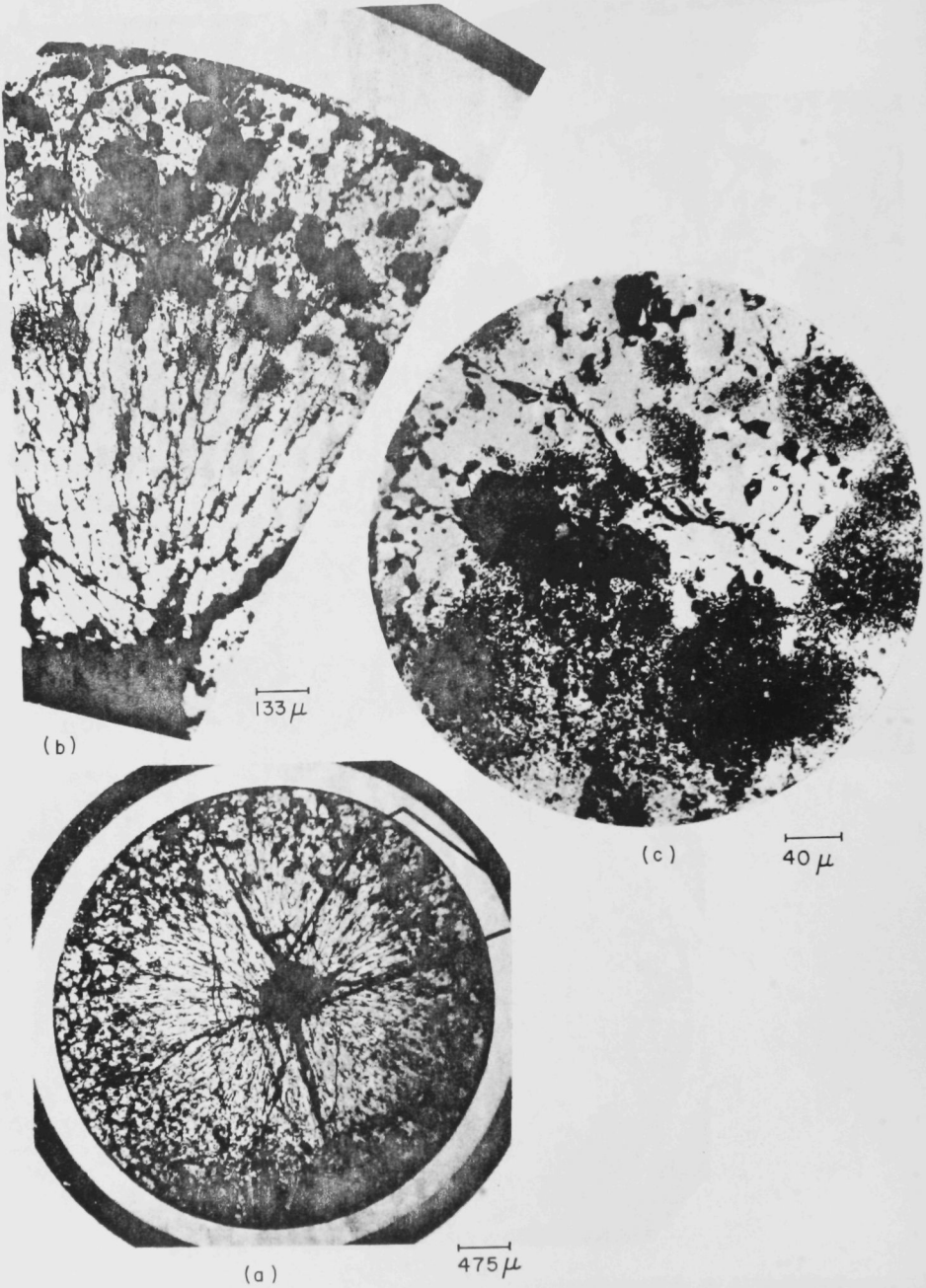


FIG. IV-4-9. Microscopic Condition of Pin 15, Sample $D_{2T}$: (a) Radial Cross Section of the Sample; (b) Enlargement of Area Indicated on Section; (c) Further Enlargement of Area Indicated on (b). *ANL Neg. No. 112-8896.*

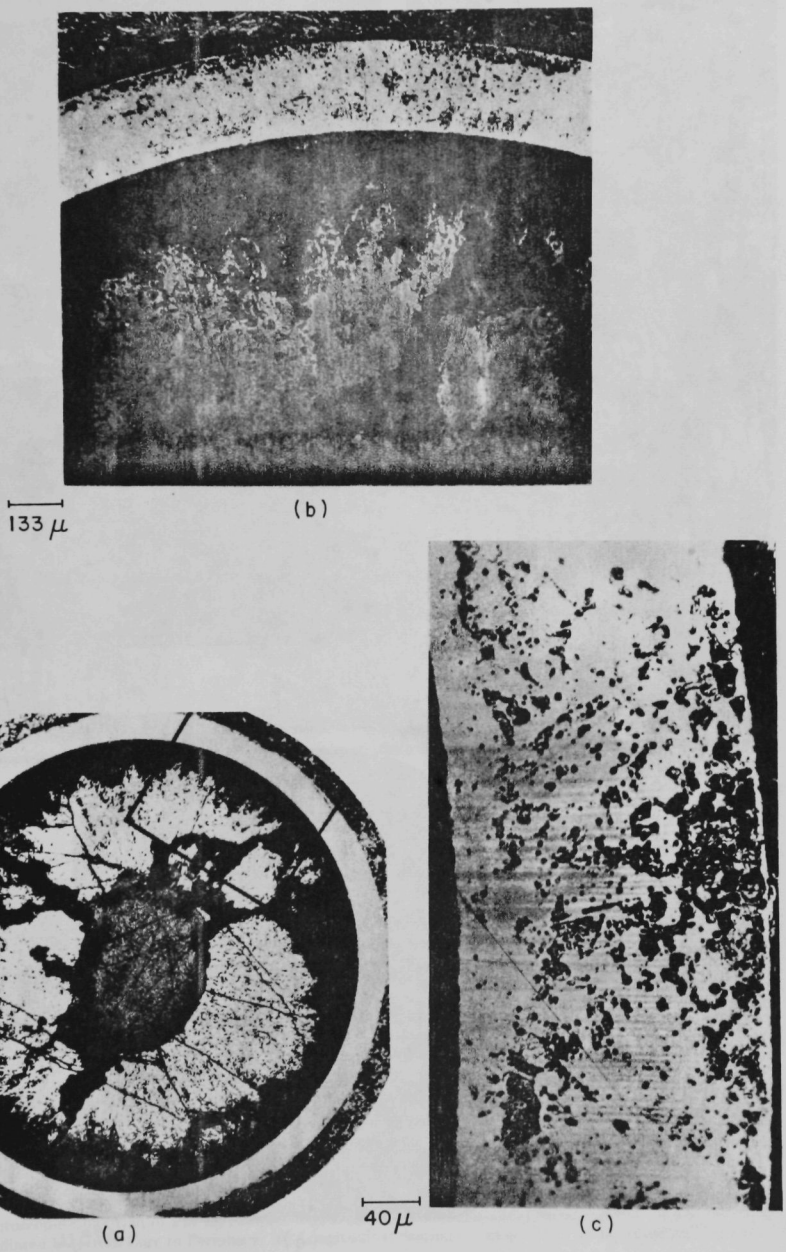


FIG. IV-4-10. Microscopic Condition of Pin 15, Sample $D_{3T}$: (a) Radial Cross Section of the Sample; (b) Enlargement of Area Indicated on Section; (c) Further Enlargement of the Cladding. *ANL Neg. No. 112-8899.*

FIG. IV-4-11. Microscopic Condition of Pin 15, Sample $D_{4T}$: (a) Radial Cross Section of the Sample; (b) Enlargement of Area Indicated on Section; (c) Enlargement of Section Showing Small Grains Near Periphery, Tiny White Inclusions Within Large Porous Inclusions, and the Typical Bubbling Effect at the Periphery Produced by the Large Porous Inclusions. *ANL Neg. No. 112-8894.*

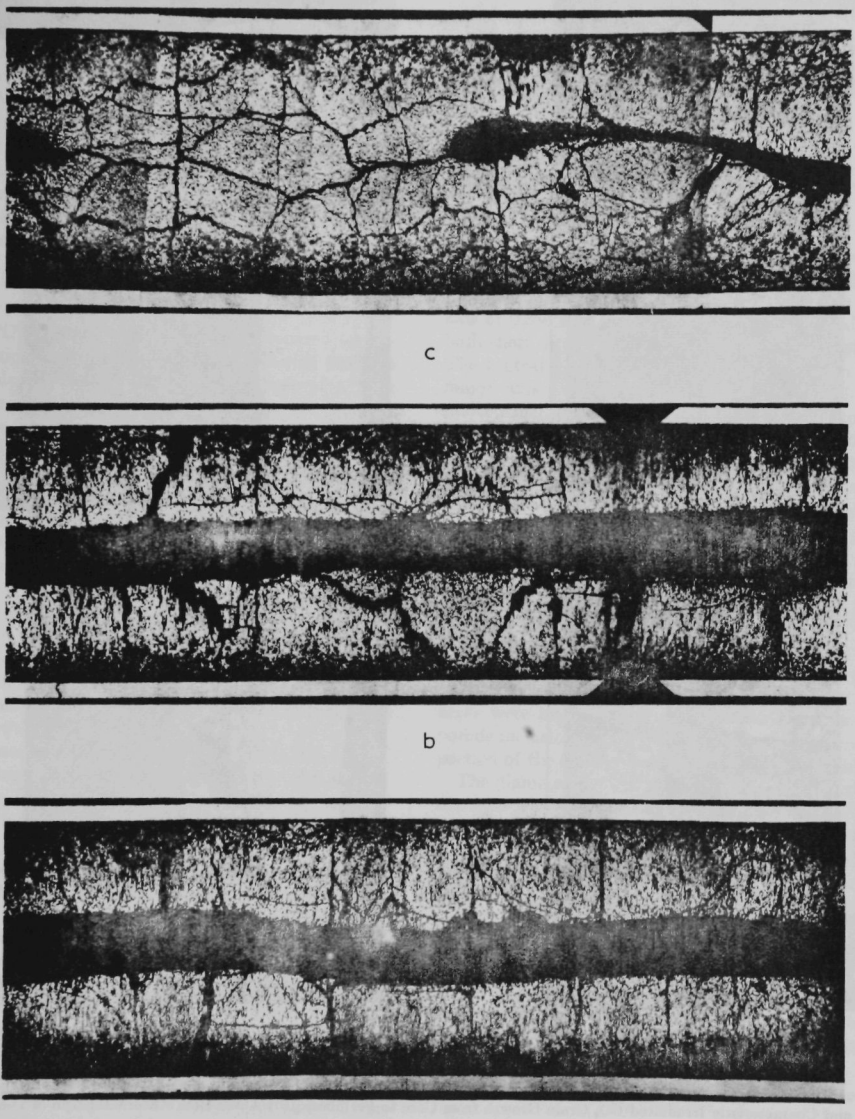


FIG. IV-4-12. Microscopic Condition of Pin 15, Samples $D_{1L}$, $D_{3L}$, $D_{4L}$: (a) Longitudinal Section of Sample $D_{1L}$ Showing Typical Features of the Irradiated $UO_2$ from Core to Periphery; (b) Longitudinal Section of Sample $D_{3L}$; (c) Longitudinal Section of Sample $D_{4L}$. *ANL Neg. No. 112-8901.*

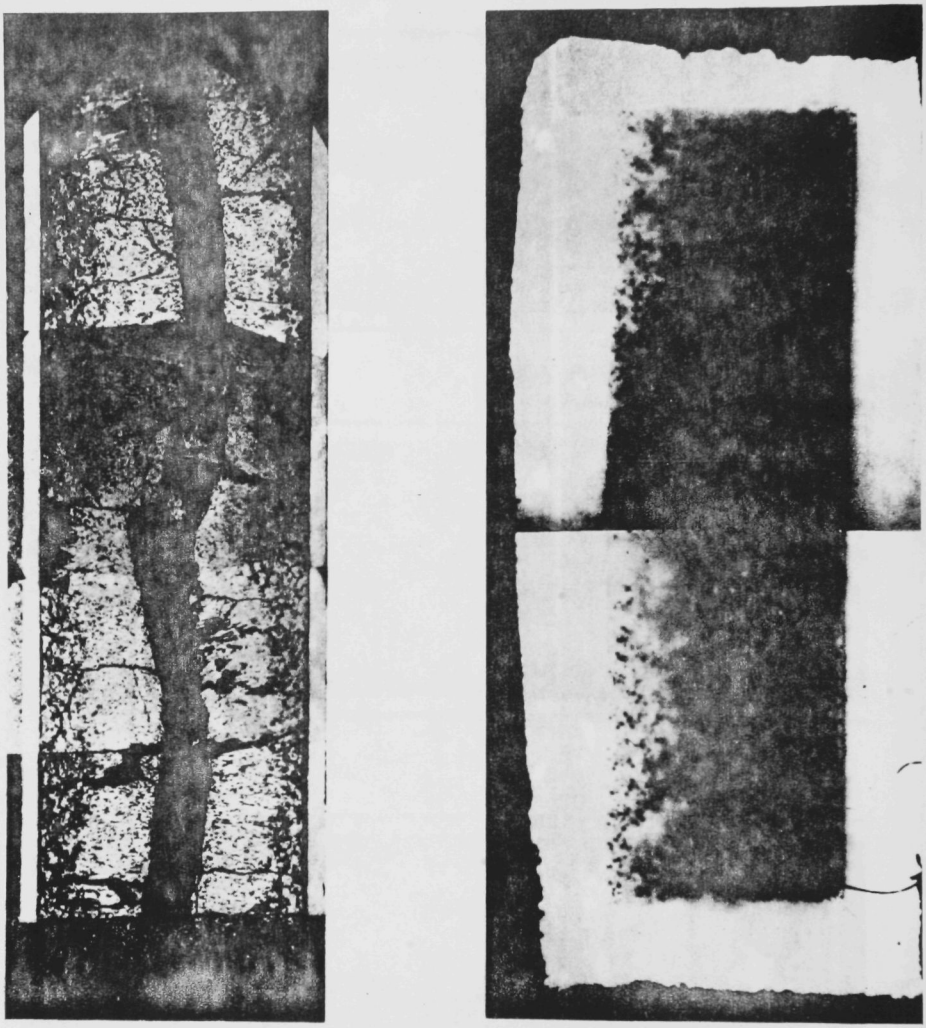


FIG. IV-4-13. Microscopic Condition of Pin 15, Sample $D_{2L}$: (a) Longitudinal Section of Sample $D_{2L}$ Showing Typical Meandering Core and Characteristic Irradiated $UO_2$ Grain Growth from Core to Periphery; (b) Alpha-Beta Autoradiograph of $D_{2L}$. *ANL Neg. No. 112-8813.*

were high-burnup regions and are associated with the fully enriched $UO_2$ particles of the original fuel material. During the irradiation, the temperature in this region remained below that required to effect the isotopic exchange of the fully enriched $UO_2$ and natural $UO_2$ particles. All the rare earth oxides, zirconium oxide, etc., also remained in the areas of the fully enriched and high-burnup $UO_2$ particles and were essen-

tially undissolved by the surrounding natural uranium oxide matrix. However, in the columnar grain-growth region the formation of solid solution oxides and uranium isotopic exchange were both virtually complete. An examination of the uranium oxide in the central region showed that zirconium and neodymium were uniformly distributed throughout the oxide matrix. Sometimes slight peaks in the concentration of these elements occurred at the outer edge of the columnar grains. These were in areas of higher porosity than the matrix and are attributed to areas rich in U-235.

### *C Samples*

The "C" samples were specifically prepared for determination of the relative amounts of fission products by the laser vaporization technique (use of a laser beam to vaporize the elements). Data are not yet available from these samples.

### *$D_T$ Samples*

The "D" samples, of which there were eight, were divided into two categories, transverse and longitudinal, denoted by the subscript T and L, respectively. The transverse "D" samples, that is, $D_{1T}$, $D_{2T}$, $D_{3T}$, $D_{4T}$, represent areas of interest directly adjacent to longitudinal samples from the bottom, center, and top of the pin and will here be compared against one another insofar as their overall appearance, diametric change, diametric growth, center core dimensions, annulus spacing, area ratio (void-to-expanded fuel), and grain growth are concerned.

The cross section of $D_{1T}$ is shown in Fig. IV-4-8a at a 21× magnification. The fuel, originally of 0.381 cm diam, has become oval with a major axis of 0.394 cm and a minor axis of 0.388 cm which represents an average diametric growth of 1.66%. The central void is oval, having a major axis of 0.042 cm and a minor axis of 0.085 cm. The minimum annulus spacing is 0.001 cm, and the maximum is 0.008 cm. The central void cross sectional area is 1.84% that of the post-irradiation area of the fuel. A close-up of the fuel, from the core to the periphery, showing the typical distribution of pores and inclusions which appeared after irradiation, is given in Fig. IV-4-8b. A higher magnification showing the enlarged fuel structure and inclusions is given in Fig. IV-4-8c.

Figure IV-4-9a shows the full cross section of $D_{2T}$ which was changed from the pre-irradiation circle of 0.381 cm diam to an oval of 0.381 cm minor axis, and 0.392 cm major axis, yielding an average radial growth of 1.4%. The major axis of the oval void is 0.060 cm, and the minor axis is 0.042 cm. The void cross section is 1.8% of the area occupied by the fuel. Annulus spacings were, for the minimum, 0.001 cm; for the maximum, 0.007 cm. Figure IV-4-9b (30 sec. etch) is an enlargement of a segment of cross section from the core to the periphery showing the fine diffuse porous areas within the columnar grain region which become more concentrated and develop into spheres toward the periphery. A further enlargement of an area in Fig. IV-4-9b giving a close-up of a typical gray inclusion among porous spots appears in Fig. IV-4-9c.

The cross section of $D_{3T}$ is shown in Fig. IV-4-10a. This cross section was not typical of others that were examined since it has a negative diametric growth, −3.33%. The post-irradiated fuel is oval with a major axis of 0.356 and a minor axis of 0.307 cm, which are both short of the pre-irradiated diameter of 0.381 cm. The central void has a major axis of 0.162 cm and a minor axis of 0.116 cm. This yields a void-to-expanded-fuel ratio of 17.36%, which is highly unusual. The annulus spacings are, for a minimum, 0.008 cm, and, for a maximum, 0.046 cm. Figures IV-4-10b and IV-4-10c show inclusions in the stainless cladding which are very similar to the microstructural appearance of $UO_2$ fuel dispersion in stainless steel reported by J. Cunningham, R. Beaver and R. Waugh.[7]

Figure IV-4-11a is the cross section of $D_{4T}$ (etched) which very clearly shows darkened porous areas (which were unseen before etching) that are within the columnar grain region. These are areas of partial isotopic exchange between the enriched and depleted $UO_2$ particles. The rare earth concentrations in these areas were intermediate to the values found in large porous inclusions in the outer periphery and the major portion of the oxide matrix in the columnar grains.

The diametric growth was 1.46% since its maximum diameter was 0.392 cm and its minimum diameter was 0.381 cm. The central core had a minimum axis of 0.046 cm and a major axis of 0.076 cm. The void-to-expanded-fuel ratio is 2.0%. Annulus measurements yielded values of 0.001 cm for the minor axis and 0.005 cm for the major axis. Shown in Fig. IV-4-11b is a typical core-to-periphery view showing the characteristic grain structure of the various regions. Figure IV-4-11c is a further enlargement of a cross section through a bubble at the surface (periphery) of the fuel. These bubbles were a characteristic of all samples examined, varying only in degree of size.

### *$D_L$ Samples*

$D_{1L}$, $D_{2L}$, $D_{3L}$, and $D_{4L}$ were longitudinal samples at pellet interfaces which show the distribution of porous spots along the axis, the peculiar meandering characteristic of the central core, and gross fissures that occur throughout the fuel but are predominately associated with the central core. Figure IV-4-12a, b, c shows $D_{1L}$, $D_{3L}$, and $D_{4L}$, respectively, and $D_{2L}$ is shown

in Fig. IV-4-13a. A beta-gamma autoradiograph of $D_{2L}$ appears in Fig. IV-4-13b.

### References


1. C. E. Dickerman, L. E. Robinson, W. Doe and R. Stewart, *Properties of Irradiated $UO_2$ Pins Prior to Transient Reactor Test (TREAT) Facility Transients*, Reactor Physics Division Annual Report, July 1, 1965 to June 30, 1966, ANL-7210, pp. 227–240.
2. Reactor Handbook, *Materials*, Vol. I (Interscience Publishers, New York, 1964) p. 293.
3. D. Huff, Argonne National Laboratory (private communication).
4. J. H. Monaweck and E. S. Sowa, *Summary Report on Irradiation of Prototype EBR-II Fuel Elements*, ANL-6010 (1960).
5. H. Berger and W. J. McGonnagle, *Progress Report on Neutron Radiography*, ANL-6279 (1962).
6. N. Stalica et al., *Electron Microprobe Analysis of $UO_2$*, (to be published).
7. J. E. Cunningham, R. J. Beaver and R. C. Waugh, *Fuel Dispersion in Stainless Steel Components for Power Reactors*, Fuel Elements Conference, Paris, TID-7546 (March 1958) pp. 243–268.


## IV-5. Results from Transient Reactor Test (TREAT) Facility Fast Reactor Oxide Fuel Pin

C. E. Dickerman and R. Stewart

### Introduction

One of the key problems in developing the capability for analyzing the behavior of fast reactor oxide fuel pins during accidents is that of obtaining a detailed description of the material behavior. Hence, the first part of the ANL program of systematic investigation of fast reactor oxide accident phenomena consists of a program of experiments on such pins performed in TREAT, using inert gas capsules. This type of environment makes possible direct observation by means of high-speed color photography, fast-response thermocouple instrumentation of cladding (which also permits direct checks on the magnitude and consistency of fuel-cladding heat transfer), and avoids possible changes in the fuel remains that might be caused by presence of a liquid coolant. Gas-bonded EBR-II size uranium oxide pins have been under study. The first experiments were conducted on unirradiated specimens.[1] Next, transients were run on half-length, nominal 0.7 a/o and 3 a/o burnup specimens.[2] To complete this survey of irradiated dry $UO_2$ accident behavior a single pin of nominal 6 a/o burnup has been tested under conditions approximating the most severe transient ever given to the lower burnup samples. Condition of the nominal 6 a/o burnup pins is described in a companion paper (see Paper IV-4).

TABLE IV-5-I. Treat Exposure Conditions for Pin 16

| Transient | Burnup, a/o | TREAT Integrated Power, MW-sec | Total Sample Energy, J/g | Max. Temperature Recorded | |
|---|---|---|---|---|---|
| | | | | Lower Thermocouple, °C | Upper Thermocouple, °C |
| 1071 | 6.2 | 74.3 | 419 | 889 | 850 |
| 1072 | 6.2 | 207 | 1151 | 1310[a] | 1300[a] |

[a] Melted.

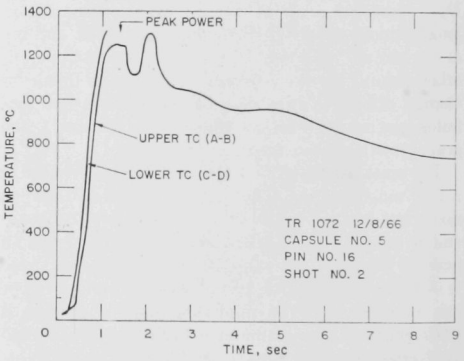


Fig. IV-5-1. Thermocouple Data from Tr 1072 Exposure of 6 a/o Burnup Oxide Pin. *ANL Neg. No. 112-8518.*

TABLE IV-5-II. Transient Temperature Calculations for Tr 1072

| Maximum Fuel Temperature, °C | Max. Fuel Surface Temperature at Time of Max. Fuel Temperature, °C | Max. Radius of Fuel Reaching Melting Point of 2750°C, cm | Total Duration Fuel is at Melting Point, sec |
|---|---|---|---|
| 2750 | 2060–2175 | 0.14 | 0.5 |

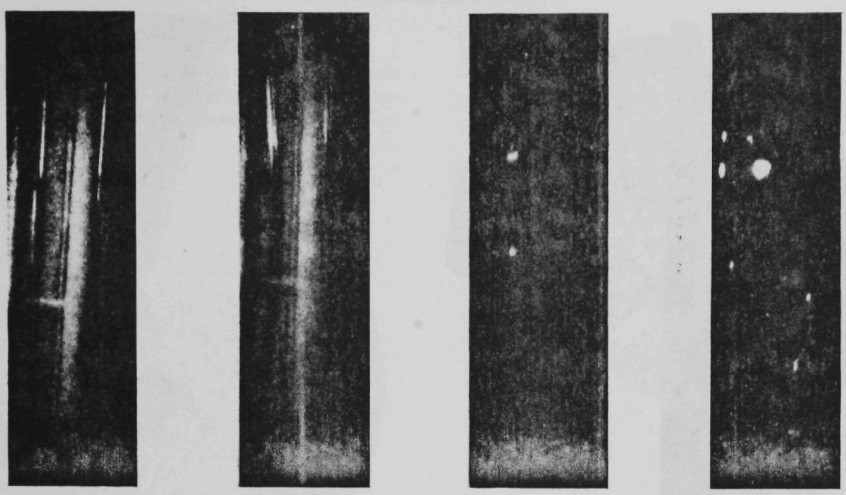


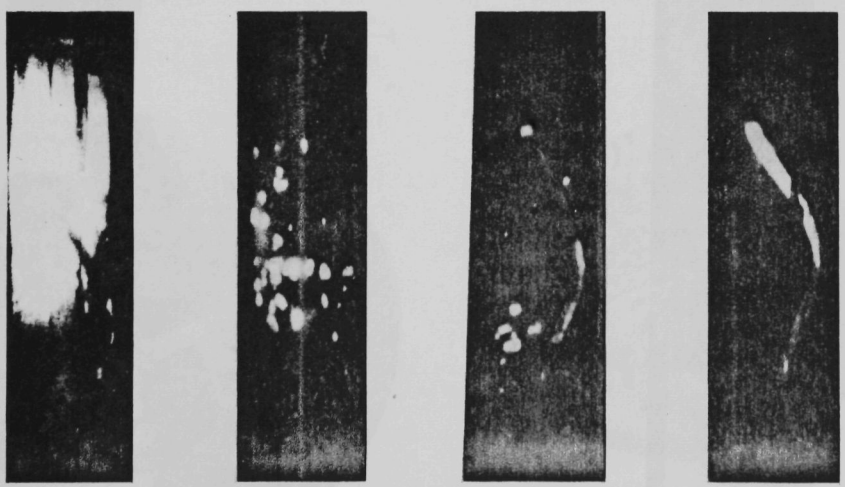


FIG. IV-5-2. Still Frames from 2000 frame/sec Record of Tr 1072. *ANL Neg. No. 112-8519.*

FIG. IV-5-3. (a) Macroscopic View of 6 a/o Burnup Oxide Sample After Tr 1072. (b) Closeup of Oxide Fuel After Tr 1072. *ANL Neg. No. 112-8521.*

### Experimental Conditions

Pin No. 16 was run in a standard transparent capsule for irradiated specimens.[3] Two chromel-alumel thermocouples were formed by spot welding the bare wires to the cladding at 2.5 cm above and below the fuel center. TREAT exposure conditions are given in Table IV-5-I. The meltdown transient 1072 was run as a

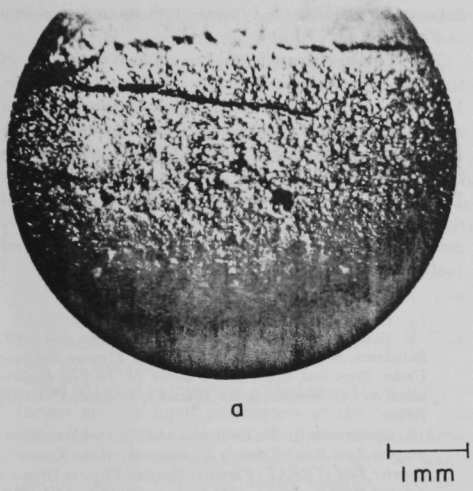


Fig. IV-5-4. Two Views of 6 a/o Burnup Oxide Fuel After Exposure to Maximum Temperature ~2750°C in Tr 1072. *ANL Neg. No. 112-8522.*

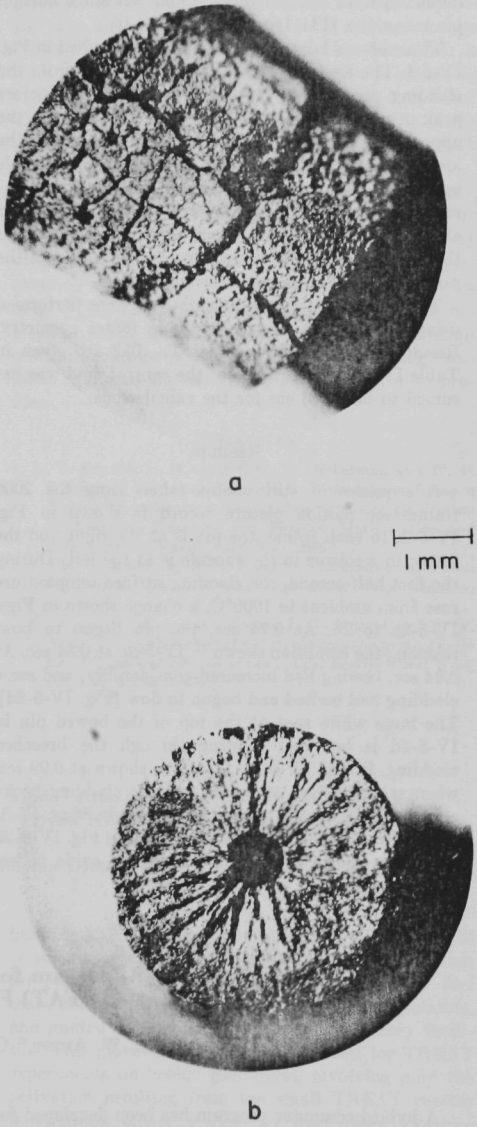


Fig. IV-5-5. (a) Closeup of Oxide Fuel From Tr 1072, Showing Fusion of Two Pellets. (b) Cross Section of 6 a/o Burnup Oxide Pin After Tr 1072. *ANL Neg. No. 112-8523.*

duplicate of Tr 1020, in which a nominal 3 a/o burnup pin was given 1141 J/g of fuel.[2]

Thermocouple data from Tr 1072 are graphed in Fig. IV-5-1. The lower thermocouple broke away from the cladding at 1.05 sec, approximately 0.35 sec before peak power was reached. At the time of the break, the upper thermocouple read about 100°C less than the lower thermocouple. Although the upper thermocouple appears to continue as a temperature-measuring instrument, peaking at about 1300°C, sample bowing and cladding failures caused interference with the upper thermocouple thermal contact to the fuel at about the same time the upper thermocouple broke.

Transient temperature calculations were performed using the ARGUS Code,[4] assuming intact geometry. Results of the calculations for Tr 1072 are given in Table IV-5-II. The radius of the central void was assumed to be 0.046 cm for the calculations.

## Results

A sequence of still photos taken from the 2000 frames/sec motion picture record is shown in Fig. IV-5-2. In each frame, the pin is at the right and the image in a mirror in the capsule is at the left. During the first half-second, the cladding surface temperature rose from ambient to 1000°C, a change shown in Figs. IV-5-2a to 2b. At 0.74 sec, the pin began to bow, reaching the condition shown in IV-5-2c at 0.84 sec. At 0.94 sec, bowing had increased considerably, and some cladding had melted and begun to flow [Fig. IV-5-2d]. The large white spot at the top of the bowed pin in IV-5-2d is hot fuel showing through the breeched cladding. In Fig. IV-5-2e, the pin is shown at 0.99 sec, when a bright flash appeared and the cladding broke completely at the top of the fuelled section. Figs. IV-5-2f and IV-5-2g show fragments falling. In Fig. IV-5-2h the pin is shown after peak power; the oxide pellets had fused together and formed a curved rod, while molten cladding continued to flow downward.

Figs. IV-5-3a and IV-5-3b are macroscopic views of the sample after TREAT exposure. The cylindrical geometry of the fuel was maintained approximately. Note the central fuel void. Extensive coverage of the surface by droplets was observed, as shown in the higher enlargement views of Figs. IV-5-4a and IV-5-4b. Fig. IV-5-5a is a close-up of the area of fusion between two pellets. A typical cross section is shown in Fig. IV-5-5b.

This transient produced no explosive release of trapped fission gasses or fragmentation of the oxide. From an examination of the post-transient sample condition, it appears that a model capable of adequate description of steady state oxide fuel performance can be used up to the melting temperature of the oxide. Despite concerns arising from possible fracturing and deformation, there was no observed evidence of movement of the fuel down the central void in advance of fuel melting.

## References

1. C. E. Dickerman, L. E. Robinson, E. S. Sowa and S. B. Skladzien, *Studies of Fast Reactor Fuel Element Behavior Under Transient Heating to Failure II. In-Pile Experiments on $UO_2$ Samples in the Absence of Coolant*, ANL-6845 (1965).
2. C. E. Dickerman, L. E. Robinson and R. Stewart, *Photographic Fast Reactor Safety Experiments at the Transient Reactor Test (TREAT) Facility*, Reactor Physics Division Annual Report, July 1, 1965 to June 30, 1966, ANL-7210, pp. 241–244.
3. L. E. Robinson and C. August, *Transparent Facility for TREAT Meltdown Experiments on Pre-Irradiated Samples*, ANL (to be published).
4. D. F. Schoeberle, L. B. Miller and J. Heestand, *A Method of Calculating Transient Temperatures in a Multiregion Axisymmetric, Cylindrical Configuration, the ARGUS Program, 1089/RE 248, Written in Fortran II*, ANL-6654 (1963).

# IV-6. Hybrid Computer Program for Transient Temperature Calculations of Transient Reactor Test (TREAT) Facility Fast Reactor Safety Experiments[1]

L. T. Bryant,* L. W. Amiot,* C. E. Dickerman and W. P. Stephany†

A hybrid computer program has been developed for calculating temperatures in a multiregion, axisymmetric, cylindrical configuration consisting of solid materials bounded by flowing coolant. One special feature of the program is the use of the digital component to set automatically the analog component.

The number of concentric regions allowed by the program is limited by the amount of analog computer equipment available. Each region may contain either

* Applied Mathematics Division, Argonne National Laboratory.
† Student, University of Michigan, Ann Arbor, Michigan.

stationary or turbulently flowing material with temperature-dependent properties. The temperatures are calculated at node points equally spaced within a region. The system described herein uses nine radial node points and ten axial increments.

The variation of conductivity and temperature along the radius is assumed linear between adjacent node points over a region. Thermal conductivity is assumed to be a continuous finite function of temperature, rather than the "standard" simplification of constant conductivity,[2] which is not valid in general for oxide fuel. Phase change in the fuel is considered, with heats of transformation added to the material at the transformation temperatures.

The hybrid computer employed consists of a stored program digital computer, having an 8K core memory, connected through a link to an analog computer. The analog computer solves the ordinary differential equations arising from a finite difference approximation of the heat transfer equations.

The duties of the digital computer can be summarized as follows: (1) parameter input; (2) arithmetic computation of the coefficients of the system; (3) analog potentiometer setting; (4) system check; (5) control; (6) storage and memory.

The physical parameters, initial conditions, and scale factors are the input parameters to the digital computer. The digital computer calculates the potentiometer settings of the analog computer, sets all analog potentiometers, resets the analog computer, performs a system check, and makes a decision to "go" or "not go." The analog functions *reset, hold,* and *operate* are "slaved" to those of the link, so that the analog is under the control of the digital computer. The analog components are multiplexed to save analog hardware.[3] The digital computer sets the initial conditions of the problem and gives the *operate* order to the link which initiates the first iteration.

The exit coolant temperature of an increment $(\Delta l)_i$ where $l$ is the length of the fuel pin, is computed by the analog, sampled in time and stored in the memory of the digital computer. This becomes the inlet temperature of the next axial increment $(\Delta l)_{i+1}$ and so on, until $\sum_{i=1}^{n} (\Delta l)_i = l$ (axial conduction of heat is neglected). Thus, by multiplexing, only one set of temperature equations is programmed on the analog computer to obtain the radial and axial temperature profiles.

### References

1. L. T. Bryant, L. W. Amiot, C. E. Dickerman and W. P. Stephany, *Transient Temperature Calculations Using a Hybrid Computer*, International Conference on Utilization of Research Reactors and Reactor Mathematics and Computation, Mexico City, May, 1967.
2. G. M. Dusinberre, *Heat Transfer Calculation by Finite Differences*, (International Text Book Co., Scranton, 1961).
3. C. K. Sanathanan, J. C. Carter, L. T. Bryant and L. W. Amiot, *The Application of a Hybrid Computer to the Analysis of Transient Phenomena in a Fast Reactor Core*, Nucl. Sci. Eng. **28**, 82 (1967).

## IV-7. Design of the Glovebox Facility for The Transient Reactor Test (TREAT) Facility Loop and Capsule Operations with Plutonium-Bearing Samples

C. E. Dickerman, L. E. Robinson and R. Ivins*

Specifications have been established for a nitrogen glovebox facility to be used in operations on TREAT loops and capsules with plutonium-bearing samples. The facility design is based on servicing Mark II integral TREAT sodium loops,[1] autoclaves for the Chemical Engineering Division TREAT programs,[2] and advanced transparent capsules for use with longer fast reactor fuel pins than previously tested in photographic experiments. Sufficient dimensional margins exist to permit work on significantly larger loop test sections and larger capsules, if required. A controlled access area is to be set up in the ANL Hot Laboratory, building D-301, for the glovebox facility. The area will be shared with a high temperature furnace installation for physical property measurements on reactor fuel materials, a hot repair "shop" for cave manipulators, and limited supporting hot chemical laboratory facilities. This glovebox complex will be used for TREAT experiments on "cold" plutonium, involving only the activation resulting from the small TREAT reactor irradiations. Hence, a glovebox with minor auxiliary in-box shielding will be adequate.

The box is to be used as a two-level glovebox, with the lower level intended for the Reactor Physics Division experiments and the upper for the Chemical Engineering Division work. Normally, reactor physics

* Liquid Metal Fast Breeder Reactor Program Office, Argonne National Laboratory.

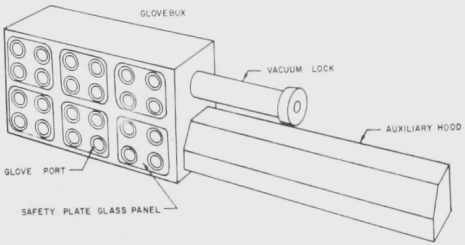


FIG. IV-7-1. Isometric View of Glovebox Facility Design. *ANL Neg. No. 112-8587 Corr.*

operations will be done from one side and chemical engineering work from the other side.

There are four basic units in the installation: glovebox, auxiliary loading hood, vacuum lock, and gas purification system and recirculating apparatus. A heat sealing unit (for sealing the plastic bags used to move items into and out of the box) and auxiliary tools for in-box operations of assembly, disassembly, and fuel inspection, complete the facility.

The glovebox is of the ANL CENHAM type, consisting of two three-module tiers. Each module is a cube approximately 105 cm on a side. Approximate overall dimensions of the composite box are length 300 cm, height 200 cm, and depth 105 cm. The depth is sufficient to permit work to be performed from opposite sides of the glovebox. Each module has two safety plate glass panels on opposite sides, each panel with four glove ports. Glove ports in a module are arranged on a square pitch, with adjacent centers separated by 45 cm. Figure IV-7-1 is a drawing of the glovebox and the locations of the vacuum lock and auxiliary hood unit.

Basic procedure for handling the Reactor Physics Division loops and capsules consists of placing the loop or capsule into the auxiliary hood and attaching the access flange of the loop body (or capsule) to the glovebox using the split flange technique. The loop fuel holder (or capsule internals) are then withdrawn into the glovebox. Reloading is accomplished while the loop (or capsule) is attached. The access flange cover is replaced and released from the glovebox split flange attachment; any decontamination required is performed inside the auxiliary hood. The hood length is approximately 3.5 m.

Chemical Engineering Division autoclaves are to be loaded elsewhere but after exposure in TREAT it is required that the autoclaves be placed into the glovebox, using the vacuum lock, and then opening them inside the box. The current class of autoclaves are not designed for reuse. Fuel specimens, fuel holder components, and tools can be bagged inside and out of the box, using the vacuum lock. Overall length of the vacuum lock is approximately 1.5 m.

### REFERENCES

1. L. E. Robinson, *Design of the Mark II Integral Transient Reactor Test (TREAT) Facility Sodium Loop*, Reactor Physics Annual Report, July 1, 1965 to June 30, 1966, ANL-7210, 245 (1967).
2. Chemical Engineering Division Special Report, May 1, 1967, Argonne National Laboratory, p. 77.

## IV-8. Remotely Operated Sodium Extruder Facility for Inert Atmosphere Glove Box

C. AUGUST and L. E. ROBINSON

Most of the fuel elements designed for use in existing and proposed liquid-metal cooled fast reactors employ metallic sodium in the molten state to provide an intimate thermal bond between the fuel and its cladding. The systematic study of fast reactor fuels in the Fast Reactor Safety Meltdown Program requires the careful preparation of large numbers of prototypes of such sodium bonded elements for experiments in the Transient Reactor Test (TREAT) facility.

As an aid in the fabrication of experimental fuels, a hydraulically actuated, remote-controlled sodium extruder has been designed and is being constructed. When attached to a multi-purpose glove box,[1] the device will permit convenient extrusion of the solid sodium in the form of cylinders for use in assembly of fuel elements and capsules. The extrusion will be performed under the protection of an inert atmosphere and within a readily cleaned enclosure.

While conceptually similar to the vertically mounted, direct extrusion unit previously used, the new design possesses several operational and functional refinements. Design criteria were based on past experience, the quantities of sodium needed, desirable operating requirements, and the projected use of the glove box. The unit, as shown in Fig. IV-8-1, will be mounted in the vertical position below the floor of the glove

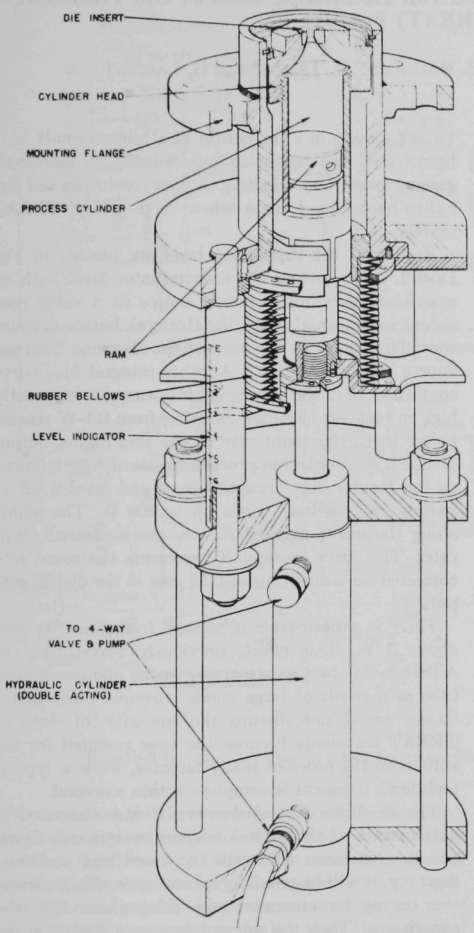


FIG. IV-8-1. Sodium Extruder. *ANL Neg. No. 112-8908.*

box, with a helium-tight attachment to the flanged extension of a 6-inch bottom port. The mounting flange has a static seal with an elastomer O-ring, and a flexible bellows encloses the extruder ram. When the glove box is in other use, the device is separated from the box interior by an O-ring-sealed port cover plate.

The cylinder head will accommodate a range of die insert sizes to allow extrusions up to 1.27 cm (0.5 inch) in diameter and limited in length only by the equivalent volume of the process cylinder. The cylinder can be refilled readily from within the glove box, using the cylindrical billet from a standard one-pound can of commercial reagent-grade sodium. The quantity of sodium remaining in the cylinder is indicated on a vertical scale showing the axial position of the extended ram, which allows more convenient planning of the extruder use schedule.

The production of extrusions with a smooth, continuous surface was assured by the design of the cylinder head and die inserts. Considering the nonlubricative metallic sodium as a highly viscous liquid, the cylinder head was designed with a convex internal contour, which, in combination with a short entrance cone of the die inserts, approximates a hyperbolic nozzle and presents a continuous streamline surface to the extruding sodium.

Foot-controlled valves and an electrically operated hydraulic pump permit the operator to extrude the sodium as required, while engaged in the assembly of fuel pins within the glove box. A three-way electrical valve, in series with a four-way manual valve, allows remote control of a double-acting hydraulic cylinder, with automatic unloading of the actuation pressure for stopping the extrusion flow. The four-way valve is used to select the actuation desired (advance to extrude or retract to withdraw the ram for refilling), while the electrical valve supplies the On-Off control. An adjustable pressure relief valve on the "advance" side of the hydraulic cylinder regulates the rate of extrusion. Commercially available components were used in the extruder controls and throughout the 10,000 psi capacity hydraulic system.

## REFERENCE

1. L. E. Robinson and C. August, *Extensible, Multi-purpose Vacuum Glove Box*, Reactor Physics Division Annual Report, July 1, 1965 to June 30, 1966, ANL-7210, pp. 258-259.

# IV-9. Extended Capability for the Fast Neutron Hodoscope Used at the Transient Reactor Test (TREAT) Facility

A. De Volpi, R. Pecina,* C. H. Freese,* E. Rolnicki,* D. Travis* and G. Larsen†

The observation of fuel pin meltdown during high flux irradiation is one of the objectives of the fast reactor safety program. Towards this end, a device known as a fast neutron hodoscope[1] has been built for the TREAT reactor in Idaho. The hodoscope collimates, detects, processes, and records fast neutron events characteristic of enriched fuel pins undergoing transient reactor power excursions. During such excursions, which may last a few hundred milliseconds, the pin is intentionally forced to destruction. The hodoscope is designed to simultaneously record up to 334 channels of data, with accompanying spatial resolution of 0.15 in. and time resolution in the order of a millisecond. The instrument, in effect, depicts the movement of fuel in the process of bending and ultimate disintegration.

## Count Rate Capability of Detection System

For reactor power levels specified in the original concept, a count rate capability of $10^5$/sec was adequate, and an associated inexpensive analog photographic display was useful as an interim readout device. For this analog readout, there were 334 phosphor-coated triode vacuum lamps, each related to a single detection channel; the number of flashes per millisecond corresponded to the count rate of the neutron detector. A fast framing camera, operating at 1000 pictures per second, recorded the complete transient.[1]

To accommodate higher reactor power levels for meltdown of sodium-cooled breeding-reactor fuel pins, the signal processing circuitry has since been extended to handle $10^6$ counts/sec. This improvement by a factor of eight over previous results was accomplished primarily by redesign of the electronic circuitry to minimize deadtime and saturation effects (Fig. IV-9-1).

These changes were sufficient to allow a higher count rate without the necessity of replacing the phosphor of the Hornyak button fast neutron detector. It was realized during early tests that the slow (microsecond) decay of ZnS:Ag incorporated in the standard Hornyak buttons was responsible for some reduction in sensitivity of the discriminator, and an effort was made to develop a new scintillator component for the Hornyak button. Several new buttons containing P16 phosphor (which decays in a few tenths of a microsecond) have been tested, but results to date indicate an inordinate gamma sensitivity resulting in poor resolution and signal-to-background ratio when used in the TREAT reactor.

Results of the supporting tests are plotted in Fig. IV-9-2. After setting the discriminator level with an americium-beryllium neutron source at a value consistent with normal usage, the Hornyak button detector was placed next to the core of the Argonne Thermal Source Reactor (ATSR). Another integral bias curve confirmed that the discriminator was set sufficiently high to bias out neutrons. Starting from 0.1-W reactor power level, the count rate of the fast digital output of the X206 electronic processing board was followed as the reactor was brought up to and leveled off at various intermediate levels up to 200 W. The points along the curve marked $R_0$ are the measured count rates. The curve marked $R$ represents the count rate corrected for a deadtime of 0.55 $\mu$sec in the digital output.

There is a noticeable departure from linearity just above 3 W. This effect, previously investigated at ATSR, is due to a gain increase in the photomultiplier tube as a result of large anode currents. Such an increase would not disturb the linearity of data in TREAT transients because the time required for the shift is in the order of many minutes, while a typical meltdown transient is complete within a second.

The deadtime corrected curve $R$ was computed in anticipation of the digital readout system now being designed. Because data will be stored and processed digitally, it will be possible to enter a deadtime correction during the computer processing phase after the experiment. Thus the upper count rate limit for the digital system is actually two million neutron counts per second of recoverable data.

It has been emphasized that the count rates involved are for neutrons; these events lead to long-tailed pulses which dominate the upper limit of the duty cycle. Small pulses generated by gamma rays may be counted at rates 50% or 100% higher.

One should note in Fig. IV-9-2 that there is a turnover point where the apparent count rate declines (at 200 W). The slope is likely to become much steeper at higher count rates. Since this double-value could be misinterpreted as a lower power level, care must be

* Electronics Division, Argonne National Laboratory.
† Idaho Division, Argonne National Laboratory.

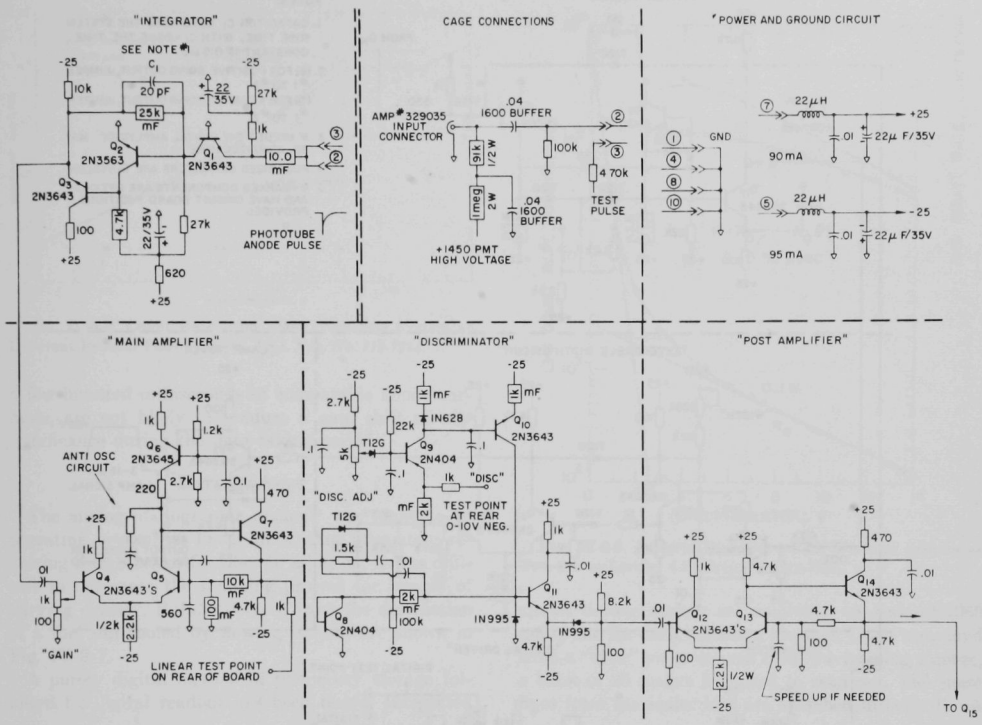


FIG. IV-9-1a. Amplifier Discriminator Board for Use with TREAT Hodoscope. *ANL Neg. No. 112-8822.*

exercised that this is not confused with fuel displacement. At extremely high count rates, the discriminator becomes much less sensitive, and at some critical value it essentially stops working so that the count rate output decreases quickly. Since the onset of this rate loss is at least a factor of four higher than the corrected saturation level of 2 MHz, it is not likely that such an excessive rate will be reached.

A comparison of integral bias curves at 0.1 W and 45 W was also made (Fig. IV-9-3). The data suggest that there is little likelihood of a sensitivity shift which would favor gamma rays; instead these data are evidence that gamma-ray pulses continue to be effectively biased out.

Since the electronics can now process a million counts a second, it is reasonable to expect that the detection system of the Fast Neutron Hodoscope will allow as many as 1200 fuel pin counts and 600 background counts from Mark-I integral sodium loop pins to be recorded every millisecond at the peak of a 5000-MW transient.

An earlier examination made at ATSR of the response of the neutron detection channel using the X155 electronic processing board[1] revealed a count rate limitation in the order of 130,000/sec, as shown in Fig. IV-9-4. In that figure, Detectors 3 and 4 were positioned in high flux locations and Detector 5 in a low flux location. Detector 1, also in a high flux location, was modified so that the dc phototube current could be directly monitored from the anode.

Another purpose of these investigations was to determine the extent and origin of gain shifts observed at high count rates. Various combinations of phototube voltage divider current, bypassing, and circuit deadtime were evaluated. It was found that capacitative bypassing of the dynode voltages was undesirable: although the bypassing increases the anode signal by reducing phase cancellation, the recharging time of the

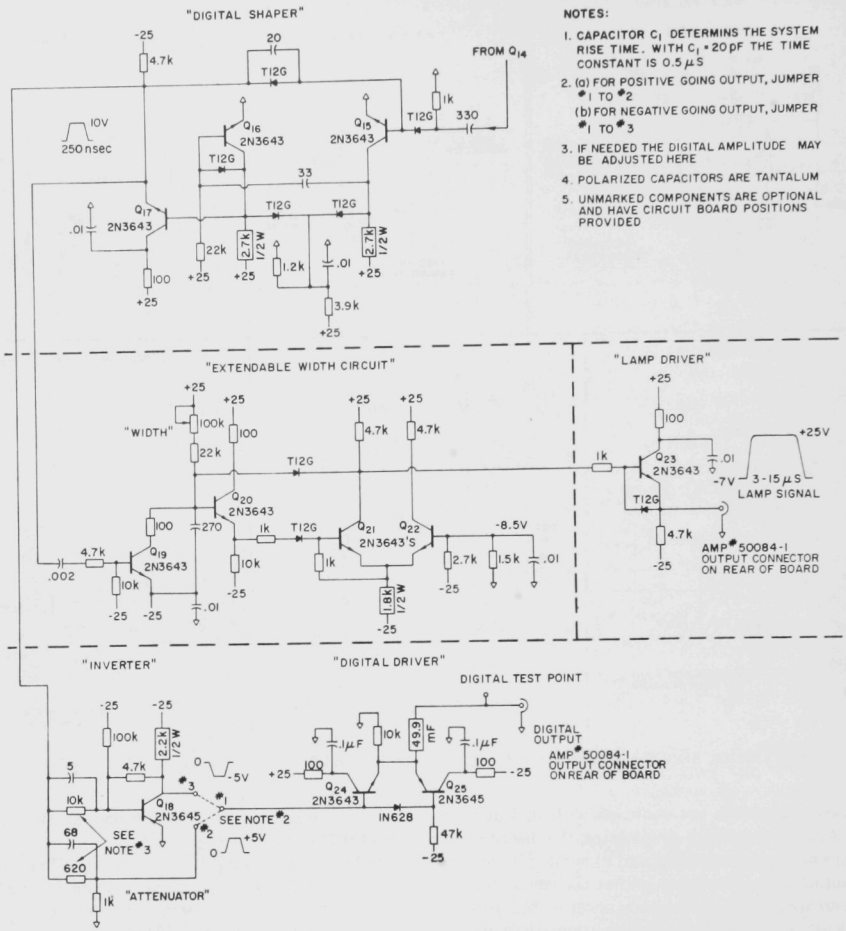


FIG. IV-9-1b. Amplifier Discriminator Board for Use with TREAT Hodoscope. *ANL Neg. No. 112-8823.*

capacitors reduces the transient response of the phototube circuit. The magnitude of current passed through the divider string had little influence on the transient reaction of the circuit.

It may be seen from Figs. IV-9-5 and IV-9-6 that the main cause of gain shift is a change in multiplication inherent to the phototubes operated at relatively high internal currents (beyond a few microamps). This is in agreement with several reports in the literature. In Fig. IV-9-5, the count rate of several detectors is obtained at different power levels of ATSR. Note the upward trend of rate as a function of irradiation time and the hysteresis effect during power reduction. On the other hand, for Fig. IV-9-6, the voltage divider string was reverse biased while the reactor was brought up to power, and readings were made in very short periods of time while forward biased. At 1534 the phototube was left in a forward biased condition, thus promoting a steady gain increase leading to larger anode current. Observe that the effects of gain shift require many minutes for significant changes; this means that TREAT transients, which usually involve

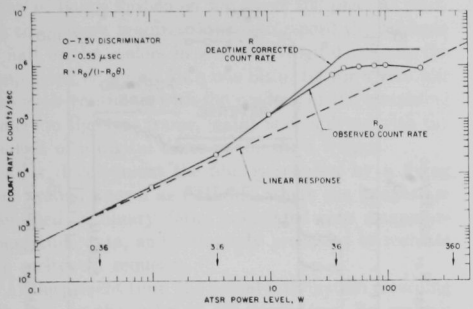


FIG. IV-9-2. Count Rate from X206 Processing System at Different Reactor Power Levels. *ANL Neg. No. 112-7814.*

a few hundred milliseconds of comparable anode currents, are not likely to produce a gain shift of any significance during the data-taking period.

## DATA READOUT

The analog photographic readout[1] was found to be operating beyond its linear limit, thus ultimately requiring image intensification. In addition, it was difficult to automate the scanning process for images of varying density. Results derived from the destruction of a fuel pin cooled by flowing sodium are shown in Fig. IV-9-7.

A purely digital method of temporary storage followed by digital readout has been tested. Integrated

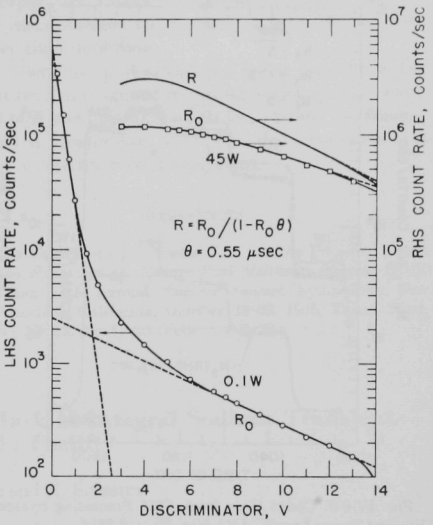


FIG. IV-9-3. Integral Bias Curves for Neutron System at Two Power Levels. *ANL Neg. No. 112-7815.*

circuit decade scalers are combined in scale-of-1000 units, one for each detection channel. Upon command from a "sync" pulse derived from the framing camera, a bank of 25 scalers is pulsed to read out. The sense lines from the scaler bits are switched directly to an

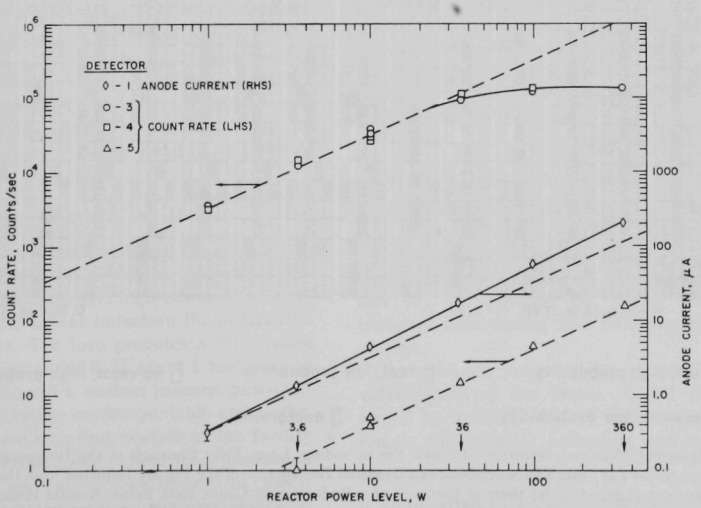


FIG. IV-9-4. Count Rate from X155 Processing System as a Function of Reactor Power Level. *ANL Neg. No. 112-7813.*

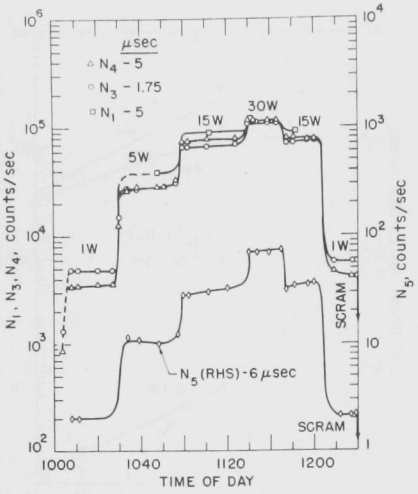


FIG. IV-9-5. Count Rate from X155 Processing System at Different Power Levels. *ANL Neg. No. 112-7312.*

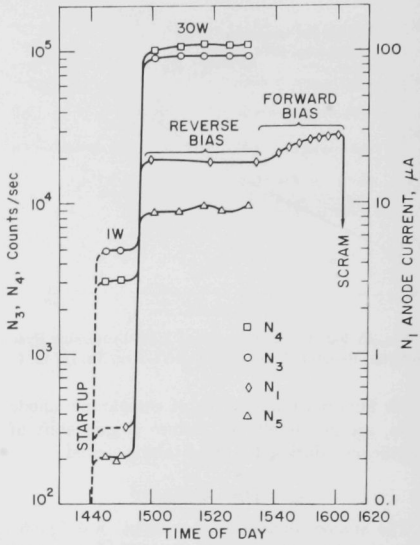


FIG. IV-9-6. Count Rate from X155 Processing System at Different Power Levels, Showing Effects of Reverse Biasing to Restrict Gain Shift. *ANL Neg. No. 112-7311.*

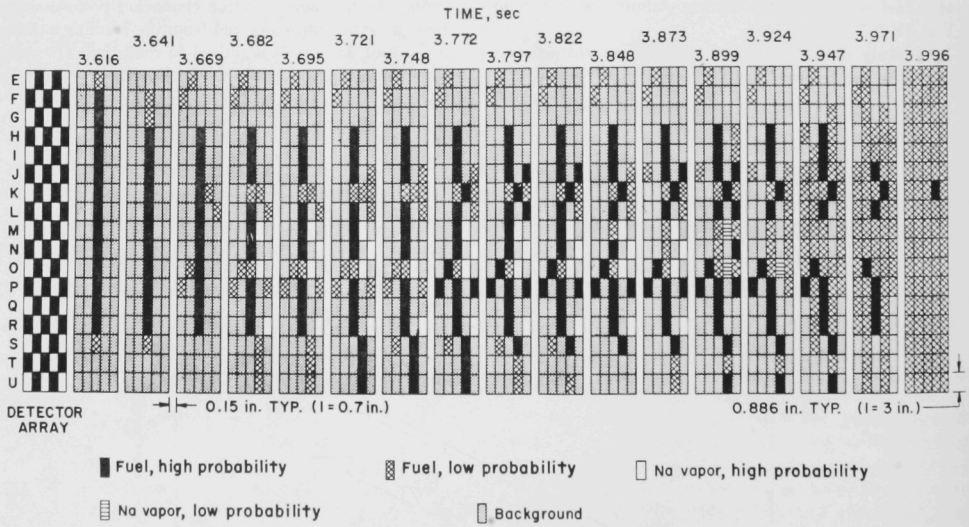


FIG. IV-9-7. Transient Meltdown Sequence of Single Pin in Sodium Loop. Fifty Channels of the Hodoscope were Scanning the Black Areas Shown on the Far Left. The Movement and Eventual Destruction of the Pin are Depicted from the Data. At the Early Stages of the Transient (3.382 seconds) there is Evidence of a Reduction in Count Rate Below Normal Background Level, which Corresponds to the Voiding or Vaporization of the Liquid Sodium in the Vicinity of the Center of the Pin. *ANL Neg. No. 112-6769.*

array of lamps flashed on for about 200 μsec. At present the camera requires 2 msec to record the contents of half of the scalers in a strictly digital format, the lamp being either on for a one bit or off for a zero bit. The cycle continues with the readout of the remaining scalers in the next frame, and it is completed with the readout of a digital timer in the third frame.

After development the film is scanned by a flying spot system known as CHLOE, where the images are identified in binary form, translated into computer-compatible data, and ultimately processed to recreate the meltdown sequence.

At the present time, the actual information recording rates are in the order of $10^7$ counts/sec. By making certain improvements in light intensity equivalent, one can expect the expanded readout system to transfer peak instantaneous count rates of over $10^9$/sec with 1-msec time resolution.

Another line of development being pursued is the application of magnetic recording media, such as wide-band tape and disc storage. So far, various limitations, as well as greater cost, have precluded acquisition of a purely electronic recording system.

### References

1. A. De Volpi and C. H. Freese, *Fast Neutron Transient Detection Hodoscope for Reactor Fuel Meltdown Studies*, IEEE Trans. 12th Annual Nuclear Science Symposium, San Francisco, California, October 18–20, 1965, Trans. Nucl. Sci. **NS-13**, No. 1, 623 (February 1966).

## IV-10. Instrumentation and Control of the Mark II Integral Sodium Transient Reactor Test (TREAT) Facility

L. E. Robinson, R. Purviance and K. Schmidt

### Introduction

The Mark II Integral TREAT Sodium Loop,[1] is a second-generation in-pile meltdown loop facility. It was designed for an order-of-magnitude higher pressure containment capability, in a simplified direct-flow configuration which permitted more nearly complete fuel meltdown data acquisition and greater ease of remote handling than the Mark I loops. Specialized instrumentation is required for precise control of loop operation and for the accurate indication and recording of steady-state and transient data. The instrumentation and control system has been designed with a minimum of complexity, consistent with space limitations, the loop design, and the need for automatic safety measures.

### Description of the Mark II Loop

The Mark II Integral Sodium Loop[1] is a direct-flow, recirculating self-contained facility, in which the coolant is driven by a miniaturized, high-power-input electromagnetic Annular Linear Induction Pump (ALIP). (See Paper IV-11). The loop provides a test section having a capacity of 19 EBR-II Mark I fuel pins, to 31 inches in length, and a sodium pressure-flow-temperature instrumentation section at inlet and outlet. The primary, or re-circulating, portion of the facility is designed to meet code specifications for a pressure of 340 atms (5000 psi) at a temperature of 538°C (1000°F); it is separated from an auxiliary system of equal containment capability by a calibrated burst disc and blowout line, mechanical valves, and back-up freeze valves. The auxiliary system provides a multi-purpose high-strength volume, which acts as a supply source of sodium, as a dump tank, and as a safety expansion volume.

The in-pile loop facility occupies a sealed secondary enclosure having outer dimensions equivalent to two TREAT fuel elements, and a wall thickness 0.127 cm (0.050 in.). An instrument indication and control console, a power supply module, and a component coolant refrigeration/circulation supply are located outside the TREAT reactor.

### General

#### Description of loop instrumentation

Instrumentation and control of the Mark II integral loop has two modes: (1) the attainment and maintenance of a pre-determined steady-state system condition prior to a programmed TREAT power transient, and (2) the accurate and precise measurement of transient data during and following the reactor excursion.

Temperature, pressure, flow, electrical power, and valve condition are measured. All parameters are sensed by detector units of conventional design, with remote measurement, indication, and control.

#### Specific instrumentation

Spiral-armored, asbestos-insulated, Chromel/Alumel

thermocouples are used for the measurement of temperatures of the loop system and of its sodium content. The temperatures of contained sodium, loop system components, and heat-sensitive detectors are continuously monitored. The thermo-electric signals from a loop monitor point drives high-impedance electronic controllers which provide fixed point control of loop temperature. Heat inputs, and hence temperatures, are controlled by ON/OFF switching of electrical heater power, supplied through adjustable autotransformers.

Most of the thermocouple outputs are monitored by remote indication only, with manual adjustment of ancillary mechanisms as sufficient control, when adverse temperatures are read. Monitor thermocouples are located on the laminated yokes and coils, within the cooling housing of the sodium pump, in an internal well within the sodium storage-dump tank, in small wells just ahead of the pressure transducer diaphragms, and on each of the flowmeter dc magnet armatures. Thermocouples are located on each of the freeze-plug valves placed in the overflow and fill lines between the loop proper and the storage tank. These sensors monitor the temperature of the silicone-cooled freeze-plugs, with the thermocouple signal interlocked to the reactor controls; transient initiation is prohibited if the freeze plug temperature is above a preset value. An additional interlock is actuated by a monitor thermocouple located on the safety burst disc blowout line, to prevent a reactor transient unless the line temperature is well above the melting point of sodium.

The steady-state temperature of the loop sodium is sensed by a thermocouple in a single well located in the test section inlet instrumentation section. Output is continuously recorded by a remote indicator-controller, which maintains a fixed sodium temperature by ON-OFF control of adjusted power to the electrical loop heaters.

The loop sodium flow is measured by dc-magnet electromagnetic flowmeters at the inlet and outlet of the loop test section. The desired flowrate is established by adjustment of power to the Annular Linear Induction Pump. The millivolt output of the electromagnetic flowmeters is pre-amplified by low-grain, wide-band dc amplifiers, and is continuously monitored on remote indicator-recorders.

Steady-state and transient pressures of the loop sodium at temperature are measured by pressure transducers at the test section inlet and outlet. These are high-temperature variable-impedance transducers, specially adapted for assembly into bellows-isolated, NaK-filled stand-off units. The sensors are encapsulated within gas-cooled housing which provide an isothermal environment for the transducers.

Auxiliary instrumentation is provided for the indication and control of pre-transient system parameters and component condition. Input electrical power to the poly-phase sodium pump and to the heater circuits is indicated by meter. Pump control is provided by autotransformer power supply adjustment at the remote control console to obtain the desired flow, pressure and temperature of the loop sodium.

The desired operating temperatures of the ALIP and the overflow and fill line freeze valves are obtained by independent adjustment of throttle valves placed in the inlet lines of recirculation loops supplying a low-viscosity, refrigerated silicone fluid. A flow-switch in the silicone coolant supply is provided as additional protection against pre-transient system fault. The switch is interlocked with the reactor transient controls and is in series with the safety interlocks from the freeze valve and blow-out line temperatures.

The condition of the mechanical valves in overflow and fill lines is indicated by the output of valve stem-mounted variable reluctance displacement detectors with remote readout. The detectors are excited by a 5-kc, 2-channel carrier amplifier.

The pressure transducers are cooled to isothermal condition by air or inert gas under forced convection, with the flowrate indicated by a remote flowmeter. An inert gas blanket is maintained within the sealed stainless steel can containing the integral loop, with the gas inlet metered for valve adjustment to a continuous low-flowrate purge through the secondary containment, and exhausting by slight over-pressure into the exhaust line of the pressure transducer coolant system.

## Reference

1. L. E. Robinson, *Design of the Mark II Integral Transient Reactor Test (TREAT) Facility Sodium Loop*, Reactor Physics Division Annual Report, July 1, 1965 to June 30, 1966, ANL-7210, p. 245.

# IV-11. Development of a Family of Annular Linear Induction Pumps for Use in Fast Reactor Safety Integral Loop Experiments

R. Carlson* and L. Robinson

## Introduction

Fast reactor safety studies concerned with reactor fuel meltdowns in flowing sodium are being performed in small integral loops which are irradiated in the Transient Reactor Test Facility (TREAT). In these studies various types of reactor fuel are subjected to an intense neutron pulse. The transient heating of these specimens causes the fuel to melt and in some cases to disintegrate vigorously. This type of fuel failure and the subsequent vaporization of sodium can cause large pressure pulses to occur within the integral sodium loop. Initial fuel meltdown experiments in flowing sodium were conducted in loops using a thin walled Faraday type pump. It was soon found that the strength of the tube wall was inadequate for the higher energy release experiments. The development of a pump having a greater static pressure rating was therefore initiated. Some of the fuels under study will contain plutonium, and this additional hazard requires an assurance of containment.

This report describes the development and testing of an Annular Linear Induction Pump (ALIP) to be used in the high-pressure high-temperature Mark II integral sodium loop. The pump has a static pressure rating of 340 atm and can move 25 gpm of sodium at 500°C through a differential pressure of 20 psi, with an efficiency of approximately 5 percent.

## Design

The factors placing the most stringent requirements on the sodium pump were: (1) the overall design pressure capability of 340 atms (5000 psi), (2) a steady-state design temperature of 538°C (1000°F), and (3) the size limitation which requires the finished loop assembly to fit into a rectangular cross section of 10 x 20.3 cm (4 x 8 in.). Other capabilities involving operational parameters were considered desirable (within limits) but not absolutely necessary for the experimental usability of the integral loop. These factors included a high flow capability (9 m/sec optimum), a programmable variability of flow, reversibility of flow direction, ease of replacement in the event of failure, reasonable efficiency, and versatility of pumping performance to meet a wide range of experimental requirements.

* Reactor Engineering Division, Argonne National Laboratory.

The combination of pressure, containment, and temperature criteria eliminated the Faraday conduction type of electromagnetic pumps, which characteristically require very thin walls for operation at measurable efficiencies, and most of the mechanically rotatable field pumps which rely on closest coupling of a permanent magnetic field with the conductive liquid metal being pumped. The size limitation effectively eliminated the poly-phase helical and the mechanical axicentrifugal type pumps. Size and the difficulty of obtaining adequate stator cooling removed the flat linear induction pump from consideration.

The only electromagnetic pump type offering a geometry and functional design conducive to miniaturization of the order required in a configuration capable of containing the internal design pressure of the Mark II loop was the Annual Linear Induction Pump. The particular geometry used as a basis for the design of the Mark II ALIP was that originated by L. Blake;[1] it was constructed and tested in a high sodium flow (~400–700 gpm) at temperatures up to 600°C. This was a direct flow, simple-annular poly-phase annular pump, although a more sophisticated modification of the annular induction pump was designed and constructed for specialized use.[2] The 8-pole, 35.5 cm diam x 127.0 cm long British ALIP was compacted into a 4-pole pump, 8.9 cm diam x 48.3 cm long for the Mark II facility. An isometric view of the Mark II ALIP is shown in Fig. IV-11-1.

The pump tube and flanges are composed of fully age-hardened Inconel X-750, rather than a stainless steel, because of the necessity for obtaining the thinnest possible wall, in a readily available, easily fabricable material. The wall thickness of the tube as designed is 0.254 cm (0.100 in.) thick. By contrast, a minimum thickness of 0.218 cm (0.086 in.) is sufficient to meet code prescriptions for the steady state loop design pressure of 340 atms at 538°C (1000°F). The ALIP is approximately 65 cm (25¾ in.) long overall, and is installed in the Mark II integral loop by mating flanges at each end which employ solid stainless steel double-oval O-ring seals, and autoclave C-type flange clamps.

The stator of the pump is composed of twelve yokes of laminated 1%-silicon transformer iron, spaced at 30° intervals about the periphery of the thermally-insulated cylindrical pump tube. Each yoke is made of 27 sheets of 29-gauge (0.014 in.) silicon iron, riveted

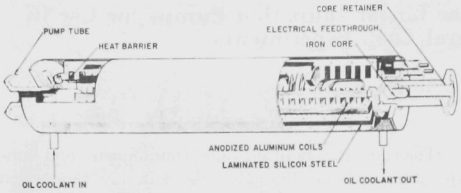


FIG. IV-11-1. Annular Linear Induction Pump for the Mark II Integral Sodium TREAT Loop. *ANL Neg. No. 112-8624.*

into rigid bundles, and containing 6 field coil slots per pole, with 2 coils per phase. With yokes of approximately the same length, the 4-pole version of the pump utilized 24 coils, while a 5-pole version used 30 field coils. The field coils were designed to consist of flat ribbon-wound pancake coils of fully anodized EC aluminum, which provide a maximum in-air operating temperature of about 275°C. Each coil contains 70 turns, and is wound without interleaving.

A return magnetic path is provided by the installation of a ½ to ⅞ in. diam central core within the pump tube and along the pump axis, thus forming a thin annular flow space for the sodium. The central core may vary in size and composition, from solid Armco ingot iron, to silicon transformer iron, dependent upon the conditions for a given experiment and the pump performance desired.

As protection for stator yokes and coils against heat conducted from the hot sodium within the loop and to facilitate pump cooling, the stator assembly is separated from the pump tube by an evacuated heat barrier consisting of a laminate of electropolished stainless steel sheet and fine-wire, large mesh screen. This laminate "dewar" barrier comprises the inner wall of a

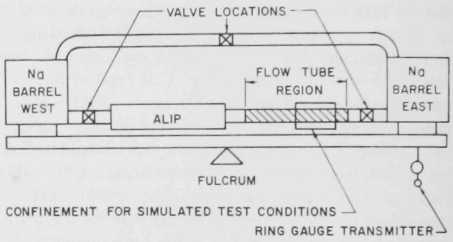


FIG. IV-11-3. Geometry of the ALIP in the Component Test Sodium Loop. *ANL Neg. No. 112-8941.*

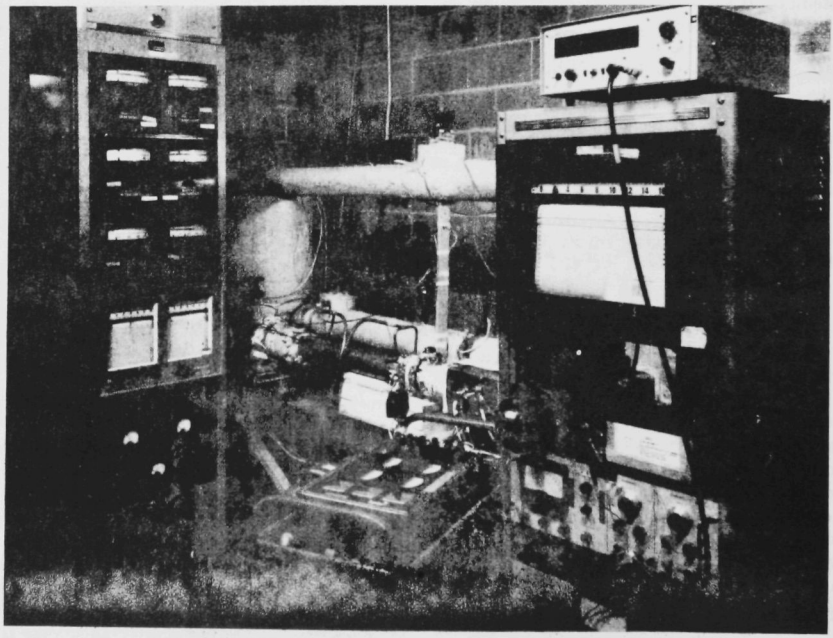

FIG. IV-11-2. ALIP in the Component Test Sodium Loop. *ANL Neg. No. 112-8687.*

sealed annular housing enclosing the entire stator assembly, through which a low-viscosity silicone liquid coolant is passed.

The ALIP unit operates on 230-volt, 3-phase, 60-cycle electrical power, with its field coils connected in a delta arrangement to ensure a constant 120 deg electrical separation between phases. Power is supplied to the pump by high-current feed-through connections inserted in the end-plates of the pump cooling housing. The poly-phase pump consumes about 7.5 kW of power at maximum capacity.

## Prototype Experiments

Two models of the ALIP pump were fabricated for testing. The prototypes used the same pump housing and pump tube, but the laminated stator and coils were of different dimensions to allow for the difference in pole pitch. The four pole pump had twenty-four $\frac{5}{16}$-in. coil slots, and the five pole pump had thirty ¼-in. coil slots. The prototype coils were wound from 16-gauge anodized aluminum wire and were potted in an epoxy resin. Mica washers were placed on each side of the coils as additional insulation between the coil and the steel laminations. The design calls for fully anodized aluminum strip coils; however, anodized aluminum wire was used for the prototype because of easy procurement.

The pumps were first assembled using ungraded coils. Grading is defined here as decreasing the number of turns on the end coils of the pump to gradually increase and decrease the strength of the magnetic field. There are several methods of grading; that is, a very gradual grading method may be used where every coil contains a different number of turns, or the grading may be rather abrupt. The more gradual grading method has the highest theoretical efficiency, but is more difficult to achieve in construction. After the test with ungraded coils, the pumps were reassembled using a grading method where the number of turns were reduced only on the four end coils.

A solid Armco Ingot Iron central core was used first on the prototype. The solid core was used because it was most easily fabricated and also the dimension of the core diameter could readily be changed. Later a core of laminated soft iron wire was tested. Various sizes of central core were tested.

The intended steady-state operating temperature of the pump installed in the Mark II loop will be 482°C (900°F), and hence, tests at temperatures of the order of 500°C were planned. For testing, a pump was placed in the test loop shown in Fig. IV-11-2. This loop consisted of two barrels located on a beam balance, as indicated in Fig. IV-11-3. The barrels were connected with piping in which the pump, flowmeters, and pres-

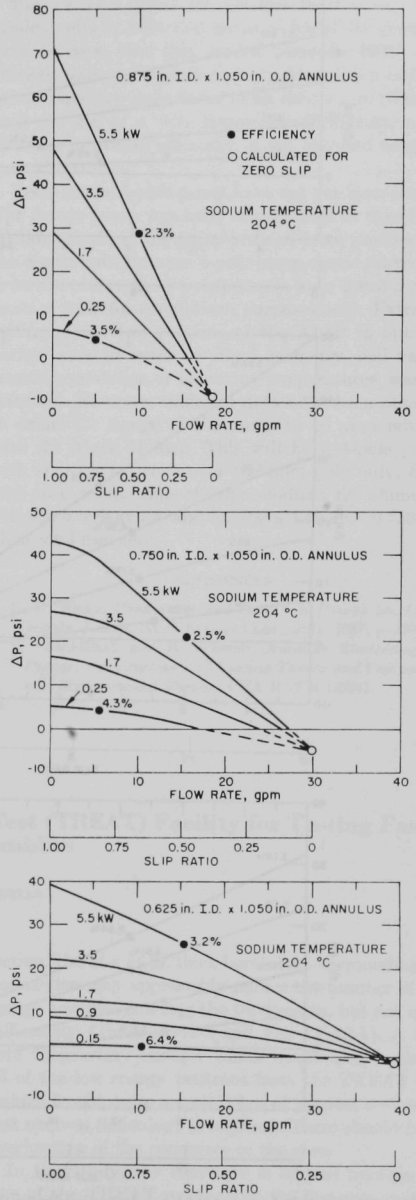


FIG. IV-11-4. 4-Pole Annular Linear Induction Pump (Solid Irod Core) Performance Curves. *ANL Neg. No. 112-8541-T-2 Rev. 1.*

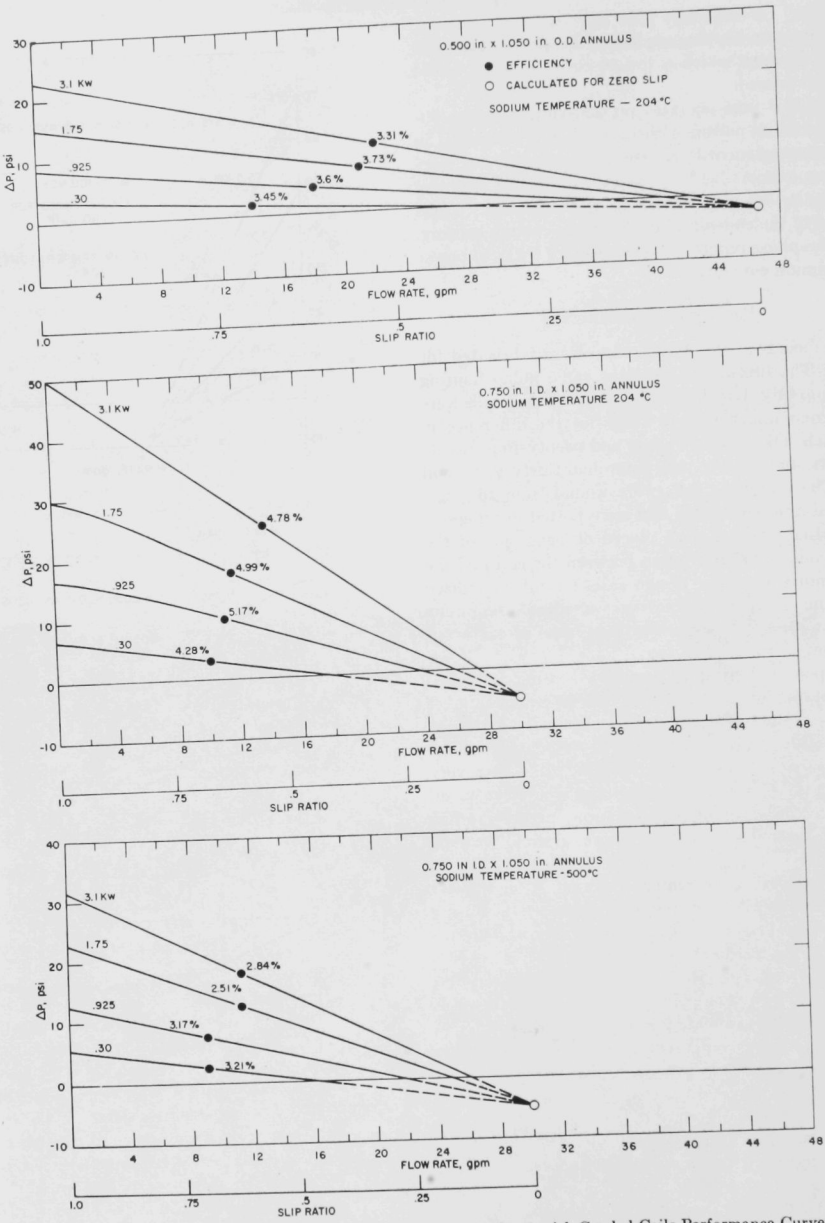


FIG. IV-11-5. 4-Pole Annular Linear Induction Pump (Wire Laminated Core) with Graded Coils Performance Curves. *ANL Neg. No. 112-8937-T-1.*

sure transducers were located. The barrels were continuously weighed by a force transducer, and as sodium was pumped from one barrel to the other the weight change was measured as a function of time. This measurement was used to compute the flowrate and calibrate the flowmeters. The pressure transducers measured the pressure differential across the pump section. The data from the instruments were recorded on strip acquisition system. The punched paper tape from the data system was used by a computer to process the data directly.

### Results

The results of tests on the 4-pole pump fitted with a solid central core and operated at relatively low temperatures are given in Fig. IV-11-4. The zero slip flowrate was the flowrate computed when the fluid moved at the same velocity as the magnetic field; for the four pole pump this velocity was 22.7 ft/sec. The calculated point for zero slip was obtained by computing the frictional pressure loss for the fluid moving at the same velocity as the magnetic field through the pump annulus. This pressure was plotted as negative on the pump performance curves because the pump could not supply this energy when the slip was zero. This calculation supplied a point through which all pump performance curves must pass. It may be seen from the figures that a core size can be selected to give the required pump performance, that is, high pressure and low flowrate, or high flowrate and low pressure.

Fig. IV-11-5 shows the increase in efficiency using graded coils in inlet and outlet poles of the pump. It may be seen that this graded pump is 100% more efficient than the ungraded pump. Also shown in Fig. 5 are preliminary indications of an increase in efficiency with the use of a wire-laminate central core, and a decrease in overall efficiency at the elevated temperature of 500°C.

Tests on the 5-pole pump have not yet been started. The 5-pole pump was built as a backup in case unacceptable ripple in the pump pressure were produced by the 4-pole unit. Because 4-pole pump ripple proved not to be a problem, the 5-pole pump is to be given a minimum of tests for comparison purposes only. Extensive testing of the two versions of the ALIP to optimize performance in terms of pump geometry, coil values, central core design or operating temperatures, was not intended. However, sufficient data have been obtained to define the design of the pump to be used initially with the Mark II loop. This will be a 4-pole pump, with step-graded coils over the inlet pole only, fitted with strip-wound coils of fully anodized EC aluminum without interleaving, and having a 1.90 cm (0.750 in.) diam solid iron core.

### References

1. L. R. Blake, *Conduction and Induction Pumps for Liquid Metals*, J. Brit. Nucl. Energy Conf., July, 1957, p. 306.
2. E. Cambillard and B. Schwab, *Annulus Electromagnetic Pumps; Construction and Testing Theory and Comparison with Experimental Results*, CEA-R-2523 (1964).

## IV-12. Conversion of the Transient Reactor Test (TREAT) Facility for Testing Fast Fuel Subassemblies

H. P. Iskenderian

Results of a study to modify the TREAT reactor[1] for carrying out satisfactory meltdown tests of fast reactor fuel subassemblies are discussed in the following.

Neutrons having the spectrum of a thermal reactor were supplied by the core of the TREAT reactor to its test section. The present arrangement of TREAT is not able to produce radially uniform heating in a highly enriched fast fuel subassembly located in the test section. To avoid excessive surface heating, which would result from testing fast subassemblies in the present TREAT reactor, the reactor must be modified to minimize the number of low energy neutrons which reach the test section. Use of a ¼ in. thick boral sheet surrounding the test section may appreciably reduce the number of low energy neutrons entering the test section, but not quite sufficiently (Table IV-12-I and Fig. IV-12-1). A suitable "converter" element which would absorb almost all of the low energy neutrons from the TREAT core (which would cause a melt-down of the test section by fast neutron fissioning) is required. There should be no overheating of the converter or the core.

In this study, the converter is located between the core of the TREAT reactor and the test section (Fig. IV-12-2), these having greatly different concentrations

TABLE IV-12-I. Characteristics of Treat with Different Converter Designs; Ratios of Fission Neutron Densities

| Design | Core Temperature | Inner Converter (max) / Center Line of Test Section | | Outer Converter (max) / Center Line of Test Section | | Center Line of Test Section / Core (max) | Ring / Center Line | $k_{eff}$ |
|---|---|---|---|---|---|---|---|---|
| | | Inner Converter (1) | Inner Converter (2) | Outer Converter (1) | Outer Converter (2) | | | |
| 1/4 in. Boral[a] | Room | — | — | — | — | 23.5 | 1.106 to 1.316 | 1.1858 |
| No. 1 | Room | 0.494 | 0.397 | 0.185 | 0.276 | 29.8 | 0.999 to 1.000 | 1.3053 |
| | 200°C | 0.490 | 0.420 | 0.188 | 0.254 | 35.4 | 0.998 to 0.999 | 1.2873 |
| | 300°C | 0.490 | 0.430 | 0.189 | 0.247 | 37.6 | 0.998 to 0.999 | 1.2835 |
| No. 2 | Room | 0.298 | 0.331 | 0.203 | 0.305 | 26.1 | 1.001 to 1.008 | 1.2468 |
| | 200°C | 0.296 | 0.351 | 0.206 | 0.280 | 31.0 | 1.000 to 1.007 | 1.2218 |
| | 300°C | 0.296 | 0.360 | 0.207 | 0.272 | 32.9 | 1.000 to 1.007 | 1.2161 |
| No. 3 | Room | 0.160 | 0.266 | 0.268 | 0.408 | 18.5 | 1.002 to 1.020 | 1.1767 |
| | 200°C | 0.160 | 0.282 | 0.270 | 0.370 | 22.2 | 1.001 to 1.016 | 1.1434 |
| | 300°C | 0.161 | 0.288 | 0.271 | 0.358 | 23.7 | 1.001 to 1.016 | 1.1354 |

[a] See Fig. IV-12-2 for location of boral sheet.

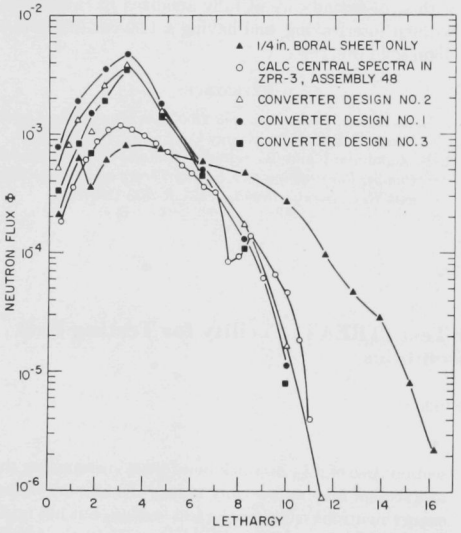


Fig. IV-12-1. Lethargy Distribution of Neutron Flux in Designs of TREAT With and Without Converter. *ANL Neg. No. 112-9104 Rev. 1.*

of fissionable isotopes. The converter consists of two sections, each having two subsections. The section facing the test section does not contain any carbon moderator. Practically all of the thermal neutrons coming from the TREAT core or from outer converter sections are absorbed in this inner converter section. Transmission of neutrons in the low resonance energy range of U-238 through the section is also reduced considerably. The section of converter facing the TREAT core, i.e., the outer converter subsection, contains reduced enrichments in two steps as the TREAT core is approached, in order to reduce the magnitude of hot spots in the converter. The radial depth (or size) of the converter sections and the concentration of U-235 in these sections are selected to allow sufficient leakage of fast neutrons into the test section for a meltdown, without overheating the converter sections.

Nuclear constants of three converters which are ex-

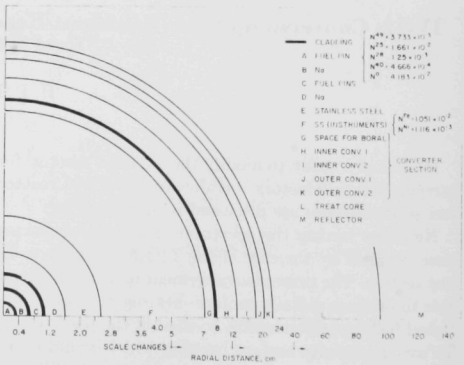


Fig. IV-12-2. Geometrical Configuration of TREAT Core, Converter and Test Section in a Radial Direction. *ANL Neg. No. 112-9102 Rev. 1.*

TABLE IV-12-II. CONSTANTS OF CONVERTER DESIGNS

*Radii of Converters*[a]

Inner Converter (1): 7.95 to 12.95
Inner Converter (2): 12.95 to 17.95
$N^{C(b)}$ (Inner Converter) = 0

Outer Converter (1): 18.0 to 20.5
Outer Converter (2): 20.5 to 23.0
$N^{C(b)}$ (Outer Converter) = 0.0722

| Design No. | $N^{25(c)}$ in converters | | | | $N^{28(d)}$ in converters | | | |
|---|---|---|---|---|---|---|---|---|
| | Inner | | Outer | | Inner | | Outer | |
| | Converter (1) | Converter (2) | Converter (1) | Converter (2) | Converter (1) | Converter (2) | Converter (1) | Converter (2) |
| 1 | 0.00793[5] | 0.00265 | $4 \times 10^{-4}$ | $2.5 \times 10^{-4}$ | 0.0185 | $7 \times 10^{-3}$ | $2.8 \times 10^{-6}$ | $1.75 \times 10^{-6}$ |
| 2 | 0.0040 | 0.0020 | $4 \times 10^{-4}$ | $2.5 \times 10^{-4}$ | 0.0224 | $6 \times 10^{-3}$ | $2.8 \times 10^{-6}$ | $1.75 \times 10^{-6}$ |
| 3 | 0.0020 | 0.0010 | $4 \times 10^{-4}$ | $2.5 \times 10^{-4}$ | 0.02445 | $2.54 \times 10^{-2}$ | $2.8 \times 10^{-6}$ | $1.75 \times 10^{-6}$ |

[a] See Fig. IV-12-2.
[b] $N^C$ = atom/cc graphite $\times 10^{-24}$.
[c] $N^{25}$ = atom/cc U-235 $\times 10^{-24}$.
[d] $N^{28}$ = atom/cc U-238 $\times 10^{-24}$.

pected to lead to a final design are listed in Table IV-12-II. The fission neutron density characteristics in the radial direction of these designs are plotted in Fig. IV-12-3. The characteristics refer to a core temperature of 200°C; they are nearly the same at room temperature. The neutron flux-versus-energy distribution characteristics are also shown in Fig. IV-12-1, comparing the converter designs with one which has a $\frac{1}{4}$ in. boral shield surrounding the test section (Fig. IV-12-2).

Important parameters in the evaluation of the performance characteristics of the converter are the temperature ratios $(T_{converter}/T_{center\ line})$, $(T_{center\ line}/T_{core})$, $(T_{ring}/T_{center\ line})$, where the temperature rise $T$ is proportional to fission density,

$$FD_l = \sum_k (\nu\sigma_f)_{k,l}\phi_{l,k} ,$$

where $l$ designates region and $k$ designates energy. Thermally, we are principally interested in the initial rise of temperature in an adiabatic process.

From thermal considerations, the limiting parameter is $(T_{converter}/T_{center\ line})$. This ratio should be as small as feasible for a high value of $T_{center\ line}$ and the allowable

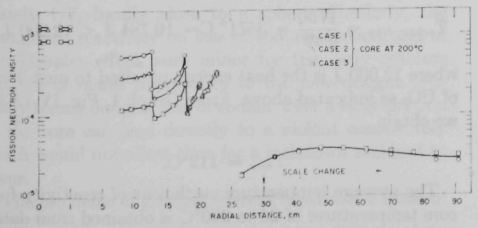


FIG. IV-12-3. Radial Distribution of Fission Neutron Density. *ANL Neg. No. 112-9037.*

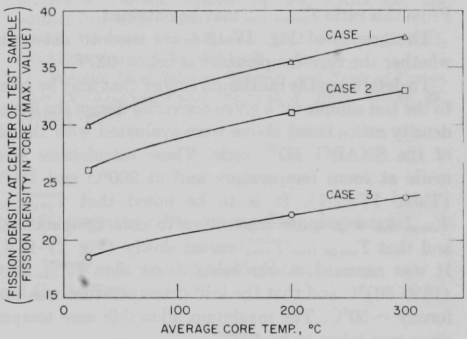


FIG. IV-12-4. Ratio of Fission Density at Center of Test Sample and In Core (Max. Value) Versus Core Temperature. *ANL Neg. No. 112-9036.*

$T_{converter}$ of (1800 − 50)°C, where 50°C denotes the initial temperature of the converters. The maximum allowable core temperature of 400°C was not the limiting factor but rather the maximum $T_{converter}$ of 1750°C was the limiting factor. All of these calculations were made with the SNARG 1D[2] one-dimensional code, using the 16 group cross section set 201[3], making appropriate corrections with the aid of C. Westcott[4] data for the 16th thermal group. The temperature rise attained by an element containing fissionable isotopes is taken to be proportional to the fission density developed in the element. Temperature data refer to single step adiabatic processes.

To determine the maximum energy that may be permitted for the test section for a maximum allowable converter temperature of 1800°C, we evaluated the

TABLE IV-12-III.

*Maximum Available Energy to Test Section*

| Design number | 1 | 2 | 3 |
|---|---|---|---|
| Max. energy available input to test section, cal/cc | 2700 | 3420 | 3820 |
| Max. core temperature, °C | 210 | 310 | 350 |
| $10^4 \times (\Delta k/\Delta T)$, per °C | 1.0 | 1.1 | 1.35 |

*Values of Thermal Constants Used in Obtaining the Above Data*

Average specific heat of $UO_2$ $\bar{C}_p\Big|_{50°C}^{1800°C}$ = 0.769 cal/cc-°C

Average specific heat of $UO_2$ $\bar{C}_p\Big|_{50°C}^{2800°C}$ = 0.895 cal/cc-°C

} density of $UO_2$ used = 10.2 g/cc

Heat required to melt 1 cc of $UO_2$—3216 cal

*Average Specific Heat of TREAT Core, cal/cc*

| Temperature, °C | 100 | 200 | 300 | 400 |
|---|---|---|---|---|
| $\bar{C}_p$, cal/cc | 0.311 | 0.345 | 0.394 | 0.437 |

fission density ratio ($FD_{converter}/FD_{center\ line}$) for the design under consideration (Table IV-12-1). It is to be noted that this ratio is insensitive to core temperatures. From this ratio $T_{center\ line}$ may be obtained.

The graphs of Fig. IV-12-4 are used to determine whether the core temperature is below 400°C.

To determine the maximum energy that may be given to the test sample for a given converter design the fission density ratios listed above were evaluated with the aid of the SNARG 1D[2] code. These calculations were made at room temperature and at 200°C and 300°C (Table IV-12-I). It is to be noted that $T^{max}_{converter}/T_{center\ line}$ was quite insensitive to core temperatures, and that $T_{center\ line}/T^{max}_{core}$ varied slowly (Fig. IV-12-4). It was assumed in our calculations that $T^{max}_{converter} \approx$ (1850–50)°C and that the initial temperature was uniformly ~50°C. The maximum allowable core temperature was taken to be 400°C.

Calculation of three converter designs listed in Table IV-12-III, yield the following information on maximum available energy input to the test section and the maximum temperature in the TREAT core.

From the data of Table IV-12-III the fission heat energy available in the test section of designs #2 and #3 is more than that required for melting $UO_2$ without overheating the converter or the TREAT core.

*Numerical Calculations*

The specific heat of $UO_2$ is given by[5]

$$C_p = 0.071 + 6 \times 10^{-6}\, T_K - 1466\, T_K^{-2},$$

where $T_K$ designates Kelvin temperature. The average specific heats from 50°C to 1800°C and 50°C to 2800°C obtained from the above expression are

$$\bar{C}_p(50°C \text{ to } 1800°C) = 0.0709 \text{ cal/g-°C} = 3.02 \text{ J/cc}$$

and

$$\bar{C}_p(50°C \text{ to } 2800°C) = 0.07408 \text{ cal/g-°C} = 3.16 \text{ J/cc},$$

respectively.

The heat of fusion of $UO_2$ is estimated to be[6]

$$21{,}200 \text{ cal/mole} = 800.9 \text{ cal/cc} = 3348 \text{ J/cc}.$$

The total heat energy required to melt 1 cc of $UO_2$ will then be

$$3.16 \times (2800 - 50) + 3348 \approx 12{,}000 \text{ J}.$$

We now evaluate the maximum heat energy that can be applied to the test section fuel pins, without melting any section of the converter or overheating the core.

Referring to the converter designs designated by Tables IV-12-I and IV-12-II, and assuming that the fission density is proportional to temperature rise, and $T^{max}_{converter} \approx (1800 - 50)°C$, we obtain the energy required to bring the converter from 50°C to 1800°C to be

$$3.02 \times 1750 = 5285 \text{ J/cc}.$$

*Case No. 1*

$$\frac{T^{max}_{converter}}{T_{center\ line}} = 0.49;$$

$$T_{center\ line} = \frac{1750}{0.49} = 3571° \text{ C} = 10{,}784 \text{ J} < 12{,}000 \text{ J},$$

where 12,000 J is the heat energy required to melt 1 cc of $UO_2$ as indicated above. From Graph 1, Fig. IV-12-3, we obtain

$$T_{core} = 112°C.$$

The average temperature coefficient of reactivity for core temperatures of 23 to 200°C is obtained from data of Table IV-12-I:

$$\frac{\overline{\Delta k}}{\Delta T} = 1.02 \times 10^{-4}/°C.$$

*Case No. 2*

$$\frac{T_{converter}}{T_{center\ line}} = 0.35;$$

hence

$$T_{center\ line} = \frac{1750}{0.35} = 5000°C = 15{,}100\ J > 12{,}000\ J.$$

From Graph 2 of Fig. IV-12-3, we obtain

$$T_{core} = 165°C.$$

The average temperature coefficient of reactivity for core temperatures of 23 to 200°C may be evaluated from data of Table IV-12-I:

$$\frac{\overline{\Delta k}}{\Delta T} = 1.41 \times 10^{-4}/°C.$$

*Case No. 3*

Greater heat energy may be applied to the test section fuel pins by further reduction of some of the hot spots at the interfaces of the converter section.

In these calculations the uniform temperature of the core was assumed to prevail over the entire reactor. This assumption should affect only the thermal fission in the subsections of the outer converter, in making them a little larger; i.e., actually the calculated peaks at the interfaces should be smaller than shown in Table IV-12-I.

The uniform temperature assumption should have negligible effect on reactivity calculations of the overall core.

### References


1. D. Okrent, C. E. Dickerman, J. Gasidlo, D. M. O'Shea and D. F. Schoeberle, *The Reactor Kinetics of the Transient Test Facility (TREAT)*, ANL-6174 (1960).
2. G. J. Duffy, H. Greenspan, S. D. Sparck, J. V. Zapatka and M. K. Butler, *SNARG-1D, A One-Dimensional, Discrete-Ordinate, Transport-Theory Program for the CDC-3600*, ANL-7221 (1966).
3. Reactor Physics Constants, ANL-5800, second edition, pp. 568–576.
4. C. H. Westcott, *Effective Cross Section Values for Well Moderated Thermal Reactor Spectra*, CRRP-960, 3rd edition (November, 1960).
5. Uranium Ceramics Data Manual, DEG Report 120 (R), UKAE Authority Compiled by B. J. Seddon.
6. L. F. Epstein, *Ideal Solution Behavior and Heats of Fusion from the $UO_2$-$PuO_2$ Phase Diagram*, J. Nucl. Mater. **22**, 340–349 (1967).


## IV-13. Fast Reactor Accident Analysis Through Computer Program Development

J. C. Carter, G. J. Fischer, T. Heames, D. R. MacFarlane, N. A. McNeal, C. K. Sanathanan, W. T. Sha and C. K. Youngdahl*

The problems of accident analysis for the current conceptual designs of large fast power breeder reactors are very different from those considered for the Fermi, EBR-II, and Douneray reactors. The spherical approximations were reasonably satisfactory for representing these early reactors since the core height-to-diameter ratio was always close to unity. For some current conceptual pancake designs this ratio can be approximately 1/7, hardly close to a sphere. Similarly, the changes of reactivity on loss of sodium coolant and of the Doppler effect were minor for the early reactors but are of acute importance to the new designs. For many recent designs, loss of sodium over a large portion of the core can lead directly to a violent disassembly which would not allow time for a meltdown accident to occur.

The problems of greatest present concern are those of accurately calculating the history of the sodium void accident, of events leading up to and including the consequences of fuel injection into the coolant, of accurately treating the Doppler effect, of accounting for spatially dependent aspects of neutron kinetics calculations, of accounting for what might be called post-burst phenomena, and for analyzing minor accidents of possibly small personnel hazard potential but whose economic implication may be very important.

Successful analysis of these problems often requires effective linking of a number of computational modules, each of which treats a major technical area important to the history of the reactor accident. These modules could compute neutron kinetics, heat transfer, fuel motions, dynamics of two-phase sodium coolant flow, and so forth. There are some distinct advantages to adoption of the modular form of program development, a procedure used in the Safety Analysis Section in its present code development work. This procedure allows

* Reactor Engineering Division, Argonne National Laboratory.

for early calculations based on use of relatively simple, rapidly programmed routines which can readily be replaced as more sophisticated modules are produced. It also allows for early scoping studies which help to indicate which aspects of the safety problem are most critical and will give maximum advancement in future programming effort. Finally, the same modules can be used in various arrangements to create a number of "standard paths", representing computations of quite different accident histories.

The programming developments of the Safety Analysis Section have concentrated to the present upon accidents related to loss of liquid metal coolant. The computational modules which have been produced to the present and linked together include the following areas:

A heat transfer module with such capabilities as variable gas bond gap conductivity associated with fuel swelling, calculation of changes of phase of the fuel, variable mesh spacing, and exceptional computational stability.

A fuel expansion dynamics module which accurately computes swelling strains and distortion of clad to the point of rupture.

A sodium dynamics module unusual in that it includes capability for calculation of two-phase flow.

Reactivity effects associated with the Doppler effect and sodium voiding and density changes are computed with attention to space dependence and using effective table look-up procedures.

An automatic linkage to a severe accident treatment module of the weak explosion type, to provide continued calculations of those histories of fast reactor accidents which do not terminate with minor energy release, is under advanced development.

A limitation of the present development is that point kinetics is employed as one other module. This can be a disadvantage for some types of reactors undergoing certain accidents. The planned near-future merger with the ANL space-dependent kinetics code QX1 (see Paper VI-12) will greatly improve this condition. The modules which have been produced under this effort are compatible with those of the ARC (Argonne Reactor Computational) system (see Paper VI-1). They have also been linked together as a free-standing code, independent of ARC, for use by laboratories which prefer not to adopt the ARC system. Computation time requirements for this linked system, and over the full history of two-phase expulsion, are very modest. Approximately 10 to 15 minutes may be needed on a CDC-3600. This would be reduced by about a factor of three to five for the CDC-6600 or IBM 360/75.

The degree of success of this effort can be seen in part by examination of results presented in another paper (see Paper IV-15) on this effort which is included in this document. The work is in the FORTRAN IV language and will be made available in a form directly compatible with IBM 360 system and CDC system computers under the code name ARC/SAS1A.

## IV-14. Transient Vaporization of Sodium in Reactor Coolant Channels

D. R. MacFarlane

### Introduction

The work presented in this paper is a continuation of previously reported studies[1,2] on the transient boiling of sodium in fast reactor coolant channels. As stated in the earlier reports, the objective of this effort is to help obtain a better understanding of coolant voiding effects in large fast power breeder reactors.

The earlier calculations were limited to cases where coolant boiling started at the exit end of the channel. However, in a typical fast reactor coolant channel there are upper and lower axial blanket segments with greatly reduced power generation rates. It was found that the coolant temperature profile peaks at or near the core upper-axial blanket interface during both flow coastdown and power transients of the type studied here. This means that coolant boiling typically starts at the core blanket interface rather than at the channel exit. The calculational complications introduced by this situation (as compared to cases where boiling starts at the end of the channel) are primarily in the nature of more difficult boundary conditions, since there are now two interfaces between single-phase or non-boiling liquid and the two-phase boiling mixture, rather than one.

In addition, the earlier restriction that the calculations could not be extended beyond the point of flow reversal at the channel inlet has been removed in the work reported here. The new calculational method devised is presented in this paper. Also, results of calculations of boiling transients with both oxide and

carbide fuels are given. These results demonstrate an important step toward realism in the description of a fast reactor coolant boiling accident.

## Formulation of the Problem

The approach used, as in the earlier work, is to seek numerical solutions on the computer for the coupled non-linear partial differential equations of fluid dynamics and heat conduction written for a single reactor coolant channel and fuel rod. The same two basic types of transients were studied: (1) mild over-power transients in which the driving function is a linearly increasing heat generation rate in the fuel; (2) flow coastdown transients resulting from an exponentially decreasing available pressure head at the coolant channel inlet. The other assumptions made in the problem formulation and listed in Ref. 2 are also valid here.

### Hydrodynamics Equations for Two-Phase Flow

The conservation equations used for the two-phase mixture are:

continuity (Eq. (11), Ref. 2):

$$(\rho_g - \rho_l)\frac{\partial \alpha}{\partial t} + \frac{\partial G}{\partial z} = 0; \tag{1}$$

momentum (Eq. (15), Ref. 2):

$$\int_0^L \frac{\partial G}{\partial t}\,dz + \frac{G^2}{\rho_l} v' \Big|_0^L + g\int_0^L \rho_l(\alpha/\beta - \alpha + 1)\,dz + \int_0^L \frac{f_{sp} G^2 (1-x)^{2-a}}{2\rho_l D_h}\,\phi_l^2\,dz + p\Big|_{p_0}^{p_N} = 0; \tag{2}$$

energy (Eq. (13), Ref. 2):

$$(\rho_g + \rho_l x)\frac{\partial \alpha}{\partial t} + G\frac{\partial x}{\partial z} = \frac{\gamma \phi(z,t)}{\lambda}, \tag{3}$$

where

$\alpha \equiv$ volume fraction of vapor,
$x \equiv$ vapor quality,
$\rho_g \equiv$ vapor density,
$\rho_l \equiv$ liquid density,
$G = \alpha G_g + (1-\alpha)G_l \equiv$ total mass flow rate,
$L \equiv$ channel length,
$H_g \equiv$ vapor enthalpy,
$H_l \equiv$ liquid enthalpy,
$\gamma \equiv$ ratio of channel perimeter to cross sectional area,
$\lambda \equiv$ enthalpy of vaporization $= H_g - H_l$,
$p \equiv$ pressure,
$\phi(z,t) \equiv$ heat flux at channel wall,
$g \equiv$ acceleration of gravity,

$$v' = \frac{\beta x^2}{\alpha} + \frac{(1-x)^2}{1-\alpha},$$

$$\beta = \rho_l/\rho_g,$$

$f_{sp} \equiv$ single phase friction factor,
$a = 0.2$,
$\phi_l^2 \equiv$ two-phase friction multiplier (see Ref. 2),
$D_h \equiv$ channel equivalent diameter,

The change made consists of breaking the momentum integral [Eq. (2)] into two parts as follows:

lower non-boiling leg and boiling portions:

$$\int_0^{z_{ub}} \frac{\partial G}{\partial t}\,dz + \frac{G^2}{\rho_l} v' \Big|_0^{z_{ub}} + g\int_0^{z_{ub}} \rho_l(\alpha/\beta - \alpha + 1)\,dz + \int_0^{z_{ub}} \frac{f_{sp} G^2 (1-x)^{2-a}}{2\rho_l D_h}\,\phi_l^2\,dz + p\Big|_{p_0}^{p_{z_{ub}}} = 0; \tag{4}$$

upper non-boiling leg:

$$\int_{z_{ub}}^{L} \frac{\partial G}{\partial t}\,dz + \frac{G^2}{\rho_l}\Big|_{z_{ub}}^{L} + g\int_{z_{ub}}^{L} \rho_l\,dz + \int_{z_{ub}}^{L} \frac{f_{sp} G^2}{2\rho_l D_h}\,dz + p\Big|_{p_{z_{ub}}}^{p_N}. \tag{5}$$

Since the mass flow rate and liquid properties are approximately constant with position in the upper non-boiling leg, integration of Eq. (5) gives

$$p_{z_{ub}} = \frac{\partial G}{\partial t}(L - z_{ub}) + g\rho_l(L - z_{ub}) + \frac{f_{sp} G^2}{2\rho_l D_h}(L - z_{ub}) + p_N. \tag{6}$$

The term $\partial G/\partial t$ in the equation is represented by the finite difference form

$$\frac{\partial G}{\partial t} = \frac{G_{ub}^{i+1} - G_{ub}^{i}}{2\Delta t^i};$$

thus, in difference form, Eq. (6) becomes

$$p_{z_{ub}}^{i+1} = \frac{G_{ub}^{i+1} - G_{ub}^{i}}{2\Delta t^i}(L - z_{ub}^{i+1}) + g\rho_l^{i+1}(L - z_{ub}^{i+1}) + \frac{f_{sp}\,|G^{i+1}|^2}{2\rho_l^{i+1} D_h}(L - z_{ub}^{i+1}) + p_N^{i+1}, \tag{7}$$

where

$z_{ub}^i \equiv$ distance from channel inlet to upper boiling interface, at $i$th time node.
$G_{ub}^i \equiv$ mass flow rate at upper boiling interface at $i$th time node.

In this manner the upstream single-phase liquid leg and the two-phase boiling portion of the channel are treated using one momentum integral [Eq. (4)] whereas the downstream liquid leg being expelled from the channel exit is treated by a second integral [Eq. (5)]. The downstream pressure boundary condition, $p_{z_{ub}}$, for the first integral is time varying as determined by Eq. (7). This is in contrast to the previous work where

TABLE IV-14-I. Input Parameters for Transient Problems

| | Oxide | Carbide |
|---|---|---|
| Core length, $L$, cm | 100 | — |
| Blanket thickness, $R$, cm | 30 | — |
| Axial extrapolation distance for cosine power distribution, cm | 20 | — |
| Fuel rod diameter, $D$, cm | 0.635 | — |
| Coolant volume fraction | 0.50 | 0.63 |
| Heat generation factor in blanket | 0.10 | — |
| Coolant inlet temperature, $T_c(0)$, °C | 500 | 400 |
| Coolant outlet temperature at $t = 0$, °C | 632 | 633 |
| Coolant mass velocity at $t = 0$, G(0), g/cm²-sec | 700 | — |
| Coolant velocity at $t = 0$, m/sec | 8.42 | — |
| Peak fuel heat generation at $t = 0$, cal/cm³-sec | 300 | 900 |
| (kW/kg) | (126) | (314) |
| Channel exit plenum pressure, $p_{ex}$, atm | 3.0 | — |
| Fuel properties: | | |
| Thermal conductivity, $k_f$, cal/sec-cm-°C | 0.0065 | 0.0325 |
| Density, $\rho_f$, g/cm³ | 10.0 | 12.0 |
| Specific heat, $C_f$, cal/cm-°C | 0.090 | 0.055 |
| Equivalent resistance of gap and cladding, $R_c$, sec-cm²-°C/cal | 2.0 | 0.8 |
| Number of radial nodes in fuel rod | 5 | — |
| Number of axial nodes in channel | 160 | — |
| Constants in convection film coefficient correlation (Eq. (16), Ref. 2) | | |
| $K_1$ | 0.025 | — |
| $K_2$ | 0.8 | — |
| $K_3$ | 5.0 | — |

there was no upstream liquid leg and, therefore, the pressure boundary condition for the first integral was the constant channel exit pressure.

*Equations for Single-Phase Flow*

The conservation equations for the single-phase fluid in the sub-cooled portion of the channel are the same as those given in Ref. 2 and will not be repeated here. A refinement was made in the treatment of the momentum equation in that terms were added at the channel inlet and outlet to account for the contraction and expansion losses from the coolant plenums to the channel. The inlet term is

$$p_I - p_0 = \frac{G_0 \mid G_0 \mid}{2\rho_0}, \tag{8}$$

where

$p_I \equiv$ inlet plenum pressure,

$p_0 \equiv$ channel pressure just inside the inlet,

which is the pressure loss for the single phase fluid at the channel inlet for an area ratio of 0.5 (corresponds to a core coolant fraction of 0.5) according to data given by P. Lottes.[3] In computing the exit loss it is assumed that none of the potential pressure increase[3] is recovered and that there is a further loss of one velocity head due to the fuel bundle end fittings, etc. Thus the exit loss term is

$$p_N - p_{ex} = \frac{G_N \mid G_N \mid}{2\rho_N}, \tag{9}$$

where

$p_{ex} \equiv$ exit plenum pressure,

$p_N \equiv$ channel pressure just inside the exit,

for either single-phase or two-phase fluid at the channel exit. Thus the values of $p_0$ and $p_N$ for use as boundary conditions in Eqs. (4) and (5) are obtained from the inlet and exit plenum pressures $p_I$ and $p_{ex}$ using Eqs. (8) and (9).

*Fuel Heat Transfer Equations*

The equations used for calculating the transient fuel temperatures are the same as those reported in Ref. 2 and are not repeated here.

*Boundary Conditions*

An additional boundary condition required in the present calculations is the velocity of the interface between boiling two-phase coolant and the downstream liquid slug being expelled from the upper axial blanket. In the present calculations it was assumed that the mass flow rate is continuous across this interface and that the interface is transported toward the channel exit with a velocity equal to that of the local coolant velocity. Thus, the position of the upper interface in the channel at any time, $t$, is given by

$$\begin{aligned} z_{interface} &= z_b + \int_{t_b}^{t} v_{interface}\, dt' \\ &= z_b + \int_{t_b}^{t} \frac{G}{\bar{\rho}_{interface}}\, dt', \end{aligned} \tag{10}$$

where

$t_b \equiv$ time when boiling starts,

$z_b \equiv$ point in channel where boiling starts.

After the upper liquid slug has been completely expelled from the channel, only one momentum integral equation [Eq. (4)] is needed and the calculation of the pressure profile is similar to that in the previous work.

## Difference Equations for Numerical Solution

The basic differencing scheme for representing the differential equations remains the same. However, some modifications are necessary to properly represent the correct physical situation when boiling starts at an intermediate point in the channel. Treatment of the momentum equation by means of two momentum integrals does not involve any change in the basic

equations, but requires some modification of computer programming details. Including the effect of entrance and exit losses in the channel also requires some rather minor changes in programming details.

The principal modification arises because a major difficulty was encountered with the iterative computational scheme used previously. It was found that the temperature gradient in the single-phase liquid in the region just before the start of boiling was much steeper than for the previous cases where boiling started at the end of the channel. Since this gradient has a direct bearing on the rate at which the single-phase, two-phase interface moves toward the channel inlet for a given coolant saturation temperature profile, the time step required to move the interface one space node was larger than previously. In general, the stability criteria for the two-phase difference equations, namely

$$\Delta t < \Delta z(\bar{\rho}_j^i/G_j^i)_{max}$$

where

$\bar{\rho}_j^i \equiv$ average coolant density at $i$th time $j$th space node,

$G_j^i \equiv$ coolant mass flow rate at $i$th time $j$th space node,

was exceeded after a few time steps into coolant boiling with the result that the iterations failed to converge. In the original scheme the time step in the boiling region was, in effect, fixed by the size of the space mesh due to the requirement that the single-phase, two-phase interface move one space node per time step. Therefore it was necessary to modify the computational scheme to allow the interface to move a specified fractional portion of a space node per time step. This was accomplished by setting up an overlay fine space mesh structure which traverses with the single-phase, two-phase interface through the coarse space mesh structure. By this means the fixed relationship in the old algorithm between the space step size, $\Delta z$, and the time step size, $\Delta t$, was removed and thus an arbitrarily small time step could be specified for a given space mesh by specifying the fine space mesh overlay. These modifications to the computing algorithm, do not involve basic changes in the method of representing the differential equations which describe the flow, but rather are changes in the computer programming required to eliminate the restrictions encountered in the present series of calculations.

Some additional modifications were necessary to extend the calculations beyond the time of flow reversal at the channel inlet. The primary change is in the single-phase coolant energy equation which was derived in a modified form for use when the coolant mass flow in the inlet liquid leg is negative. The boundary condition for this equation was also changed so that the coolant inlet temperature is no longer specified after flow reversal, but was permitted to increase in time. A new boundary condition of zero temperature gradient in the coolant at the single-phase, two-phase interface was substituted after flow reversal.

The above changes were incorporated into the original ALGOL program[2] which was then used to perform a series of calculations. No changes were made in the fuel rod heat transfer model and the original ARGUS difference equations were retained.

## Numerical Results

In performing the calculations an attempt was made to obtain a comparison between the behavior of an oxide and a carbide-fueled fast reactor. Accordingly, both power and flow coastdown transients (no scram) have been calculated for typical reactor configurations using these two fuels. The parameters are presented in Table IV-14-I. The carbide fuel, assumed to be representative of a high thermal performance fuel with a low fuel-to-clad bond resistance, has a maximum power density three times higher than the oxide fuel case. To accommodate this higher power capability of the carbide fuel while holding the coolant exit temperature constant the core coolant fraction was increased and the coolant inlet temperature was decreased from the oxide case, as shown by the data in Table IV-14-I. The transients for both fuel cases were started from the steady state conditions given in the Table. In an attempt to select realistic power and flow driving functions for the transients, the work of D. Sherer and W. Meinhardt[4] was used as a guide.

### POWER TRANSIENTS

A linear driving function, namely

$$Q(z,t) = Q(z,0)(1 + K_4 t) \tag{11}$$

was used for both the oxide and carbide power transients. Based on the results reported in Ref. 4 a value of $K_4 = 15$ sec$^{-1}$ was chosen. This corresponds to a \$2/sec ramp with $A$(Doppler) $= T\, dk/dT = -0.004$ for the oxide core and a \$2/sec ramp with $A$(Doppler) $= -0.0015$ for the carbide core. The purpose here was not to compare results with those reported in Ref. 4 but, rather, to choose a realistic driving function for the transients up until boiling, since the present calculations do not include the feedback effects which influence the shape of the power rise function.

The results of the calculations for the oxide fuel power transient are summarized in Figs. IV-14-1 through IV-14-4. As shown in Fig. IV-14-1, the coolant temperature profile maximum value occurs 2 cm downstream from the core exit at $t_b = 0.8640$ sec, the time when boiling starts. During this time the fuel power

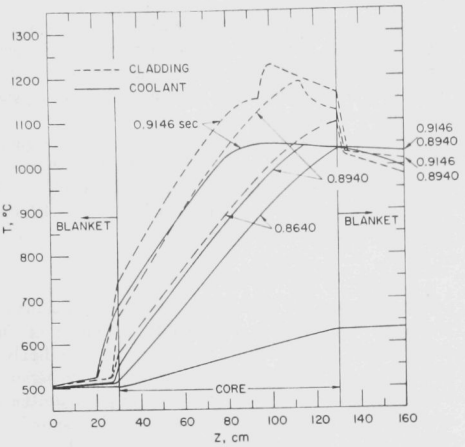


FIG. IV-14-1. Coolant Temperature Profiles at Various Times for Oxide Power Transient. *ANL Neg. No. 112-8324.*

TABLE IV-14-II. HEAT FLUXES DURING TRANSIENTS

| Transient | Heat Flux at End of Core, cal/cm²-sec | |
|---|---|---|
| | Initial Steady State | At Start of Boiling |
| Power | | |
| Oxide | 34 | 125 |
| Carbide | 101 | 273 |
| Flow Coastdown | | |
| Oxide | 34 | 17 |
| Carbide | 101 | 76 |

has increased by a factor of 14 and the heat flux by a factor of 3.7. A summary of the heat fluxes for the various cases is given in Table IV-14-II. There is a reversal in the sign of the heat flux in the blanket when boiling starts, as evidenced by the fact that the coolant temperature is higher than the cladding temperature in this region. This means that heat is actually being transported from the hotter core regions to the cooler blanket by the coolant prior to the time boiling starts. This condition has a significant effect on the coolant behavior once boiling starts since it means that there is some condensation and partial collapse of voids which have been produced in the hot core upon reaching the blanket. This is illustrated by the vapor void fraction profiles in Fig. IV-14-2. The other discontinuities in the coolant and cladding temperature profiles are produced by the rapidly changing heat transfer coefficients due to abrupt increases in flow at the point where boiling starts in the channel. This effect can be seen in the cladding temperature profiles for times of 0.8940 and 0.9146 sec in Fig. IV-14-1. Also shown in the Figure are curves for a time after flow reversal has occurred (0.9146 sec) which show increases in the coolant temperature at the channel inlet occurring as a result of flow reversal in the channel.

As shown in Fig. IV-14-2, the void increase is abrupt in the vicinity of the point where boiling starts as in previously reported calculations. The void profiles

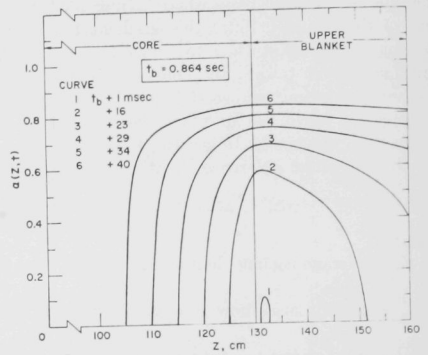


FIG. IV-14-2. Vapor Void Fraction Profiles at Various Times for Oxide Power Transient. *ANL Neg. No. 112-8312.*

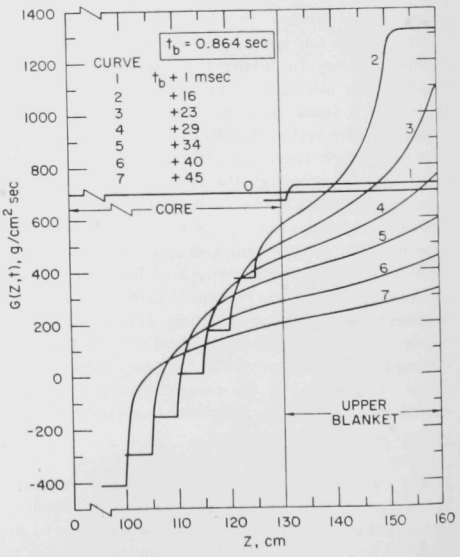


FIG. IV-14-3. Mass Flow Rate Profiles at Various Times for Oxide Power Transient. *ANL Neg. No. 112-8325.*

bend back to zero until the liquid slug in the upper blanket has been completely expelled from the channel. After this time the void fraction in the blanket builds up rapidly but still retains a negative slope due to partial condensation of vapor in the cooler blanket region. Since it is impossible to predict from available data the condition of flow, heat flux, pressure, etc. which results in channel burnout (i.e., clad melting) it was assumed in all these calculations that channel burnout occurs when the vapor void fraction exceeds 80%. Since the calculational model no longer applies if the physical integrity of the channel is destroyed, no attempt was made to interpret the calculations beyond this point.

The mass flow rate profiles for various times after the start of boiling during the transient are given in Fig. IV-14-3. The zero curve represents the initial steady state coolant mass flow rate and the short horizontal segments at the beginning of the other curves represents the single-phase mass flow rate in the inlet non-boiling portion of the channel. As shown, the increases in mass flow rate at the point where boiling starts are abrupt, in accordance with the void profile results shown in Fig. IV-14-2. The flat topped appearance of the first two curves after the start of boiling, due to the single-phase liquid slug in the blanket, is maintained until this slug has been completely expelled from the channel. As shown by the results, this problem has been carried a significant distance beyond flow reversal at the channel inlet, and in fact, curve number 7 shows the coolant expelling with a greater mass velocity from the inlet than from the exit of the channel.

Pressure profiles during the oxide power transient are given in Fig. IV-14-4. The peak channel pressure rises rather rapidly to a value between 7 and 8 atm

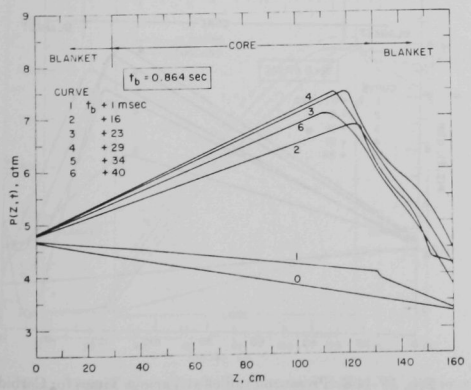


FIG. IV-14-4. Pressure Profiles at Various Times for Oxide Power Transient. *ANL Neg. No. 112-8313.*

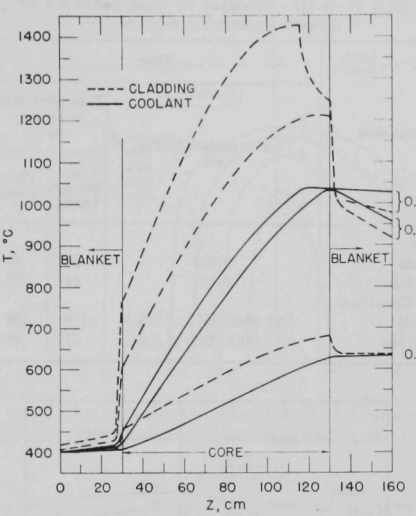


FIG. IV-14-5. Coolant Temperature Profiles at Various Times for Carbide Power Transient. *ANL Neg. No. 112-8327.*

and thereafter remains relatively constant in time. The difference between these pressure profiles and those reported previously for the problems wherein boiling started at the channel exit[2] is due primarily to the inertial pressure loading imposed on the two-phase fluid by the liquid slug as it is being expelled from the channel.

During the transient the maximum fuel centerline temperature increased from the steady state value of 1846 to 3706°C at the time boiling started and thereafter to 3837°C at the time the calculation was terminated.

Results of the power transient calculations for carbide fuel are summarized in Figs. IV-14-5 through IV-14-8. The major difference between this and the oxide case is the higher fuel thermal rating (see Table IV-14-I). As already mentioned, this case was chosen as being representative of an advanced high thermal performance fuel with a low fuel-to-cladding bond thermal resistance. As expected, the time for initiation of boiling is shorter due to the more rapid transfer of heat from the fuel (see Table IV-14-III). Consequently, the fuel heat generation rate has increased by a factor of only 7 and the heat flux by a factor of 2.7 when coolant boiling starts.

The coolant and cladding temperatures during the carbide-fuel power transient are presented in Fig. IV-14-5. The behavior of the temperatures is similar to that shown in Fig. IV-14-1 for the oxide case in that the peak coolant temperature at the start of boiling occurs

TABLE IV-14-III. Summary of Time Sequence of Events during Transients

| Transient | Time | | |
|---|---|---|---|
| | Time to coolant boiling, sec | Time after start of boiling, msec | |
| | | Upper blanket voided | Flow reversal |
| Power | | | |
| Oxide | 0.864 | 20 | 30 |
| Carbide | 0.411 | 14 | 19 |
| Flow Coastdown | | | |
| Oxide | 4.88 (flow 15% of S.S.) | >129 | 129 |
| Carbide | 3.41 (flow 29% of S.S.) | 57 | 96 |

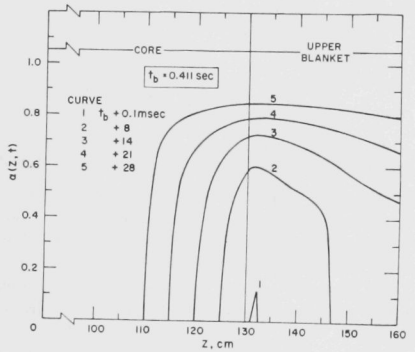


Fig. IV-14-6. Vapor Void Fraction Profiles at Various Times for Carbide Power Transient. *ANL Neg. No. 112-8321.*

about 2 cm downstream of the core exit. The higher heat fluxes for the carbide cases are reflected in the significantly higher cladding temperature obtained. Also the coolant profile at the start of boiling is somewhat more sharply peaked than for the oxide transient. A conclusion that can be drawn from the temperature profiles for the oxide and carbide cases is that the most likely point of initial clad failure by melting is in the vicinity of the point where boiling starts since the highest cladding temperatures are obtained here. This is a result of the decreasing heat transfer coefficient with reduced single-phase coolant velocities as a result of deceleration of the inlet flow.

The void profiles for the carbide transients are presented in Fig. IV-14-6. These curves are similar to those obtained for the oxide transient except that the time scale is shorter (see Table IV-14-III). The vapor qualities corresponding to the maximum void fractions obtained in these calculations are typically less than 3%.

Mass flow rate profiles for the carbide transient are shown in Fig. IV-14-7. These curves differ from those for the oxide transient in that there is an apparent wave or pulse in the mass flow profile which moves toward the channel exit in time, as shown in curves number 2, 3, and 4. Coincident with this pulse is a dip or trough in pressure profiles which also moves toward the exit in time. This is shown by curves 2, 3 and 4 in Fig. IV-14-8. It appears that this effect is directly related to the higher heat fluxes present in the carbide case. Furthermore, there is a greater tendency for condensation in the blanket for the carbide case as shown by the curves in

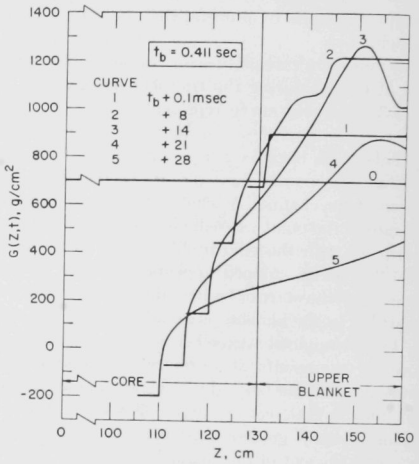


Fig. IV-14-7. Mass Flow Rate Profiles at Various Times for Carbide Power Transient. *ANL Neg. No. 112-8323.*

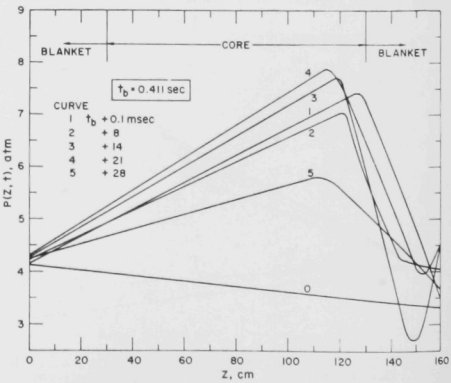


Fig. IV-14-8. Pressure Profiles at Various Times for Carbide Power Transient. *ANL Neg. No. 112-8315.*

Fig. IV-14-5 where the larger heat flow from coolant to cladding is indicated by the greater separation between cladding and coolant temperature profiles in the blanket. The combined results of these two effects produces a greater local growth of voids relative to the motion of the upper single-phase, two-phase interface and this produces a steeper gradient in the void profile at the upper interface initially (Fig. IV-14-6). The minimums in the pressure profiles (Fig. IV-14-8) result because of the recovery of momentum pressure head near the end of the channel due to condensation. As shown, the wave or pulse in mass flow coincides with the pressure trough moving toward the channel exit in time. Both disturbances are lost when they reach the end of the channel and the profiles then resemble those obtained for the oxide transient.

As shown by the pressure profiles given in Fig. IV-14-8 for the carbide transient the peak channel pressure rises quickly to a value between 7 and 8 atm and remains there during most of the calculation. The pressure rise is more abrupt than that for the oxide transient. Also, the peak pressures obtained for the carbide transient are reduced somewhat due to the pressure troughs in the profiles near the channel exit.

During the transient, the maximum fuel temperature increased from the steady state value of 1415 to 3049°C at the time boiling started and thereafter to 3196°C when the calculation was terminated.

### FLOW COASTDOWN TRANSIENTS

In the pump coastdown transients the available pressure drop across the channel (the pressure difference between the inlet and outlet coolant plenums) is assumed to decrease exponentially,

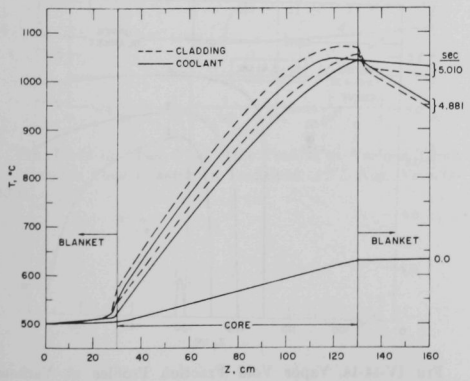


Fig. IV-14-9. Coolant Temperature Profiles at Various Times for Oxide Flow Coastdown Transient. *ANL Neg. No. 112-8322.*

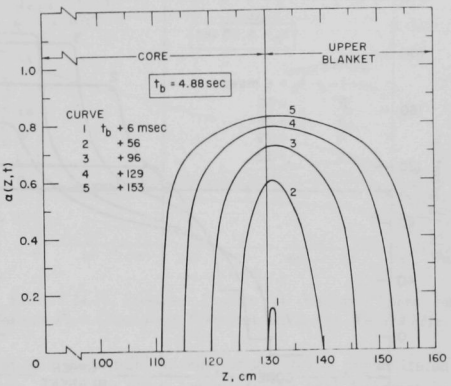


Fig. IV-14-10. Vapor Void Fraction Profiles at Various Times for Oxide Flow Coastdown Transient. *ANL Neg. No. 112-8319.*

$$\Delta p(t) = \Delta p(0) \exp(-\lambda_p t). \qquad (12)$$

A value of $\lambda_p = 0.50$ sec$^{-1}$ was chosen for the flow coastdown transient since this gave approximately 50% of full power flow in about 2 sec. This is the approximate performance of the FERMI power plant chosen as a reference case for the calculations reported by D. Sherer and W. Meinhardt.[4] The power generation in the fuel is held constant in the present calculations. This leads to slightly earlier boiling than would be expected in a real reactor since the negative feedback effects occurring before coolant boiling tends to reduce the reactor power.

The results of the oxide flow coastdown transient are summarized in Figs. IV-14-9 through IV-14-12. The coolant flow rate has decreased to 15% of the full-flow value by the time boiling starts 4.9 sec after the start of the transient (see Table IV-14-III). Coolant and cladding temperature profiles at various times are presented in Fig. IV-14-9. As in the case of the power transients, the maximum temperature in the coolant profile occurs at the core exit, the major difference being a much lower heat flux, as evidenced by the lower clad temperatures.

The void profiles for the oxide transient are presented in Fig. IV-14-10. These profiles reflect the differences due to the much lower coolant expulsion velocities generated in the flow decay transients than in the power transients. This is indicated by the symmetric distribution of the void profiles about the point where boiling started.

The mass flow rate profiles are given in Fig. IV-14-11. These profiles compare qualitatively with those obtained for the oxide power transient, the major difference again being the lower expulsion velocities. In addition, the flat-top portion of the mass flow rate profiles

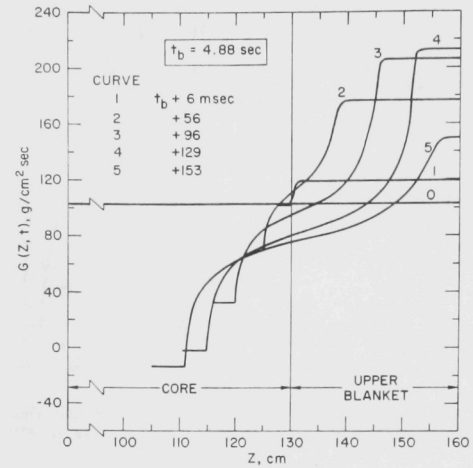


FIG. IV-14-11. Mass Flow Rate Profiles at Various Times for Oxide Flow Coastdown Transient. *ANL Neg. No. 112-8314.*

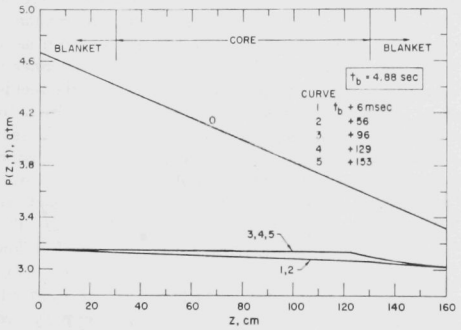


FIG. IV-14-12. Pressure Profiles at Various Times for Oxide Flow Coastdown Transient. *ANL Neg. No. 112-8317.*

is never completely eliminated since the upper liquid slug was not completely expelled from the channel by the time the calculation was terminated. This is consistent with the void profiles in Fig. IV-14-10 which show that there is still some single-phase liquid in the upper portion of the channel. This slower expulsion is a result of the much lower heat flux at the time boiling starts (see Table IV-14-II) and also the lower coolant velocities at this time.

The pressure profiles for the oxide flow coastdown transients are given in Fig. IV-14-12. The zero curve is the steady-state single-phase pressure profile and is the same as the zero curve in Fig. IV-14-4. As shown, the pressure buildup during the flow coastdown transient is very small.

The maximum fuel centerline temperature has increased from a steady state value of 1841 to 1909°C at the time boiling starts. The time from the start of coolant boiling until flow reversal at the channel inlet is 129 msec.

The results of the carbide flow coastdown transient are summarized in Figs. IV-14-13 through IV-14-16. The coolant flow rate has decreased to a value of 29% of the steady state value at the time boiling starts, 3.4 sec after the start of the transient. As in the case of the

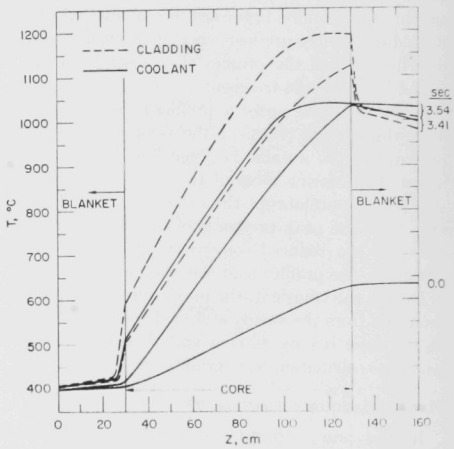


FIG. IV-14-13. Coolant Temperature Profiles at Various Times for Carbide Flow Coastdown Transient. *ANL Neg. No. 112-8326.*

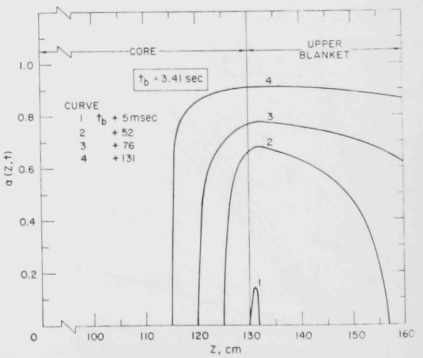


FIG. IV-14-14. Vapor Void Fraction Profiles at Various Times for Carbide Flow Coastdown Transient. *ANL Neg. No. 112-8320.*

power transients, the boiling occurs sooner with the higher thermal rating carbide fuel. The coolant and clad temperature profiles shown in Fig. IV-14-13 are similar to those for the oxide case in Fig. IV-14-9. The major difference is the higher clad temperatures resulting from the higher heat fluxes in the carbide core.

The coolant void profiles are given in Fig. IV-14-14. These profiles are both steeper at the point where boiling starts and displaced more rapidly to the channel exit than those for the oxide case, a result of the higher heat fluxes and accompanying higher coolant velocities for the carbide.

The coolant mass flow rates for the carbide transient are presented in Fig. IV-14-15. The horizontal line at 205 g/cm²-sec is the single-phase coolant flow rate at the time boiling starts, which is about a factor of 2 higher than that for the oxide transient at the start of boiling. As shown by the curves, the upper liquid slug is expelled completely from the channel well before time of coolant flow reversal at the channel inlet.

The pressure profiles are given in Fig. IV-14-16. The zero curve is the steady state single-phase profile at the start of the transient. As shown by these curves the pressure buildup in the channel during the transient is somewhat higher for the carbide than the oxide case,

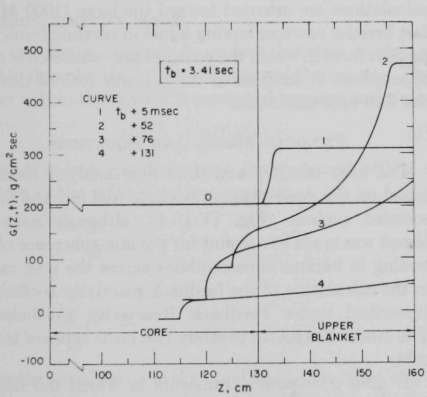


FIG. IV-14-15. Mass Flow Rate Profiles at Various Times for Carbide Flow Coastdown Transient. *ANL Neg. No. 112-8316.*

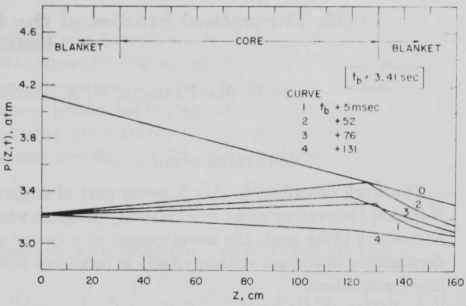


FIG. IV-14-16. Pressure Profiles at Various Times for Carbide Flow Coastdown Transient. *ANL Neg. No. 112-8318.*

but still quite mild in comparison to the power transients. As in the other transients the peak pressure increases to a maximum value and then decreases during the course of the transient.

The maximum fuel centerline temperature increases from the steady state value of 1415 to 1668°C at the time boiling starts. The time for flow reversal at channel inlet is 96 msec after the start of coolant boiling.

The work reported here completes the separate development of the sodium-voiding model. Further reporting of improvements and changes in the method of calculating the rate of formation of voids will be reported under the work on the development of a complete dynamic reactor model which includes reactor kinetics with the appropriate feedback reactivities. The first work on the development of this reactor model is presented elsewhere in this report (see Paper IV-15).

## REFERENCES

1. D. R. MacFarlane, *An Analytic Study of the Transient Boiling of Sodium in Reactor Coolant Channels*, ANL-7222, (1966).
2. D. R. MacFarlane, *Transient Vaporization of Sodium in Reactor Coolant Channels*, Reactor Physics Division Annual Report, July 1, 1965 to June 30, 1966, ANL-7210, pp. 269–279.
3. P. A. Lottes, *Nuclear Reactor Heat Transfer*, ANL-6479, (1961).
4. D. G. Sherer and W. G. Meinhardt, *An Analysis of Fast Reactor Transient Response and Safety in Selected Accidents*, GEAP-4787 (June 1966).

# IV-15. Theoretical Studies of the Response of Fast Reactors During Sodium Boiling Accidents

D. R. MacFarlane, N. A. McNeal, D. A. Meneley and C. K. Sanathanan

## Introduction

The work described in this paper is part of Argonne National Laboratory's fast reactor safety program which has as one of its goals the development of a better understanding of coolant voiding effects in large fast power breeder reactors.

A better understanding of the interplay between sodium boiling and core reactivity could lead to design modifications which would improve the safety characteristics of large fast breeder reactors. Various theoretical studies of fast reactor transients to date[1,2] have not included the reactivity effects due to voids resulting from sodium coolant boiling. In addition, there are essentially no experimental data available on the transient boiling of a liquid metal confined in a channel. The objective of the work reported here was to develop an integrated computer model to be used for calculating the behavior of a fast reactor core during transients which are slow enough so that coolant boiling occurs before the fuel surface or cladding melts. Basically, the approach taken is to seek numerical solutions for the coupled equations of coolant hydrodynamics, fuel heat conduction, and neutron kinetics. As a result then this work may serve two purposes:

1. It would provide a method of calculating the response of various fast reactor core configurations during sodium coolant boiling accidents for parametric studies of safety characteristics.

2. The sodium voiding module in the calculation would aid in the design and analysis of transient sodium boiling experiments designed to supply data and phenomenology now lacking.

While the problem formulation is quite general, the calculations are oriented toward the large (1000 MWe) fast breeder reactors having a fuel in ceramic form. The present form in which the routines are connected is most appropriate to analyses of the pancake reactor through the slab approximation.

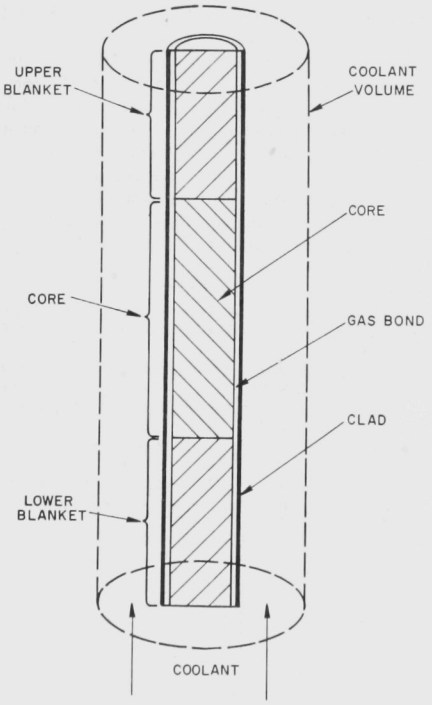


Fig. IV-15-1. Model of Reactor Channel. *ANL Neg. No. 112-8644.*

## Physical Model and Equations

The heat transfer and fluid flow analysis model is based on the description of a single fuel rod and its associated coolant (Fig. IV-15-1), although some attempt was made to account for the non-coherence of the boiling in various subassemblies across the core radius in the calculation of the feedback reactivity coefficients (described under Feedback Reactivity Coefficients). The model was set up to study two basic types of transients:

1. mild over-power transients in which the driving function is a ramp reactivity input,

2. coolant flow coastdown transients resulting from an exponentially decreasing available pressure head at the coolant channel inlet. These two cases correspond to the inadvertent addition of reactivity and coolant pump failure situations, without scram, respectively.

### Sodium Void Model

A slip flow model was used in the treatment of the two-phase fluid. In addition, the following assumptions were made in the formulation of the voiding model:

1. No sub-cooled boiling or liquid superheat occurs·

vapor is formed only when the local bulk coolant temperature exceeds the local saturation temperature.

2. There is thermodynamic equilibrium between phases, and liquid and vapor temperature equals the local saturation temperature after boiling starts.

3. The heat transfer in the boiling region is treated in a simple manner wherein the heat transfer coefficient is calculated by assuming that the liquid film stays in contact with the channel wall up to a void fraction of 80% and that burnout occurs at this void fraction.

*Hydrodynamics Equations for Two-Phase Flow*

See Paper IV-14 for a description of these equations.

HEAT TRANSFER MODEL

A one-dimensional (space) heat flow model is employed since the axial and angular conduction of heat are relatively unimportant. The heat flow equations are therefore written in one-dimensional space (namely radius, $r$). The channel is divided into several axial segments and the heat transfer and temperature calculations are made for each of the sections in succession, following the direction of the coolant flow (see Paper IV-16).

NEUTRON KINETICS MODEL

A one-group, space-independent kinetics model is used to describe the neutron kinetics of the reactor. The power within the reactor is separated in space and time:

$$Q(\mathbf{r},t) = n(t)S(\mathbf{r}), \tag{1}$$

where $S(\mathbf{r})$ is a specified shape function and $n(t)$ is a solution of the point kinetics equations,

$$\frac{dn}{dt} = \frac{\rho - \beta}{l} n + \sum_{i=1}^{6} \gamma_i C_i, \tag{2}$$

and

$$\frac{dC_i}{dt} = \frac{\beta_i}{l} n - \lambda_i C_i; \qquad i = 1,6, \tag{3}$$

where the variables have the usual meanings. Most step-by-step integration procedures for solving Eq. (2) involve the use of previously calculated values of $n$ to obtain the next value. Thus, to compute $n^{k+1}$, knowledge of $n^k, n^{k-1}, n^{k-2}, \cdots$, is required, where $k$ denotes time nodes. These methods have the disadvantage that several initial values of $n$, needed to start the calculations, must be obtained by an auxiliary process. This disadvantage can be eliminated by using one of the Runge-Kutta methods. Even then, the fact that $l$ in Eq. (2) is very small ($\sim 10^{-7}$ sec) in fast reactors, limits the time steps, $\Delta t^k$, to about $10^3 l$[3] for stable integration.

The method used here for the solution of Eqs. (2) and (3) was formulated by J. Kaganove.[4] It has the advantages of being self-starting and of being stable for large integration intervals. Kaganove's method is described briefly below; for further details, see Ref. 4. Equation (3) is solved for $\lambda_i C_i$ and the results are substituted into Eq. (2). This gives equation

$$\frac{dn}{dt} = \frac{\rho}{l} n - \sum_{i=1}^{6} \frac{dC_i}{dt}. \tag{4}$$

Equation (4) is integrated across a time interval $\tau$,

$$n(\tau) - n^k = \int_{t^k}^{t^k+\tau} \frac{\rho n}{l} dt - \sum_{i=1}^{6} (C_i(\tau) - C_i^k), \tag{5}$$

where $\tau$ is the time interval for numerical integration and $n^k$ and $C_i^k$ are $n(t^k)$ and $C_i(t^k)$ respectively. Making the transformation $t' = t - t^k$, Eq. (5) becomes

$$n(\tau) - n^k = \int_0^\tau \frac{\rho n}{l} dt' - \sum_{i=1}^{6} (C_i(\tau) - C_i^k), \tag{6}$$

where

$$\begin{aligned} n(0) &= n^k, \\ C_i(0) &= C_i^k. \end{aligned} \tag{7}$$

Equation (3) can be solved in functional form:

$$C_i(\tau) - C_i^k = -C_i^k(1 - e^{-\lambda_i \tau}) + \frac{\beta_i}{l} \int_0^\tau e^{-\lambda_i(\tau - \tau')} n d\tau'. \tag{8}$$

Substituting Eq. (8) into Eq. (6) yields

$$n(\tau) - n^k = \int_0^\tau \frac{\rho n}{l} dt' - \sum_{i=1}^{6} \frac{\beta_i}{l} \cdot \int_0^\tau e^{-\lambda_i(\tau - \tau')} n dt' + \sum_{i=1}^{6} C_i^k(1 - e^{-\lambda_i \tau}). \tag{9}$$

For the time interval under consideration, let $\rho$ and $n$ be represented by 2nd order polynomials:

$$\rho = \rho^k + \rho_1 t' + \rho_2 (t')^2, \tag{10}$$

and

$$n = n^k + n_1 t' + n_2 (t')^2. \tag{11}$$

Substitution of Eqs. (10) and (11) into Eq. (9) with the condition that Eq. (9) be satisfied both at $\tau = \Delta t^{k+1}$ and at $\tau = (\Delta t^{k+1}/2)$, yields two linear equations in the two unknowns $n_1$ and $n_2$. Substitution of the values of $n_1$ and $n_2$ into Eq. (11) gives $n(t)$ for this time interval.

The reactivity, $\rho$, in Eq. (10) is the sum of three contributions,

$$\rho = \rho_p + \rho_d + \rho_c, \tag{12}$$

where

$\rho_p$ = programmed reactivity input,

TABLE IV-15-I. REFERENCE CORE COMPOSITION

| Volume Fractions | | Isotopic Distribution | |
|---|---|---|---|
| Na | 0.50 | $Pu^{239}$ | 0.70 |
| Fuel | 0.34 | $Pu^{240}$ | 0.25 |
| Stainless Steel | 0.16 | $Pu^{241}$ | 0.05 |

TABLE IV-15-II. SODIUM REACTIVITY COEFFICIENTS FROM MACH 1 CALCULATIONS[a]

| Channel Segment, cm | | $\delta k_{Na}(z)$, $10^{-3}$ |
|---|---|---|
| Core: | $z = 0$ (midplane) to 10 | +3.49 |
| | 10–20 | +2.99 |
| | 20–30 | +2.07 |
| | 30–40 | +0.922 |
| | 40–50 | −0.221 |
| Blanket: | 50–60 | −0.555 |
| | 60–70 | −0.302 |
| | 70–80 | −0.175 |

[a] Reactivity for complete voiding of channels = \$5.14. $\beta_{eff} = 3.2 \times 10^{-3}$; $l = 3.9 \times 10^{-7}$ sec.

$\rho_d$ = Doppler feedback reactivity,

$\rho_c$ = sodium void feedback reactivity.

The reactivities $\rho_d$ and $\rho_c$ are functions of $n(t)$. From Eqs. (9) and (12) $n(t)$ is a function of $\rho_d$ and $\rho_c$ as well as $\rho_p$. These two functions must be compatible. Due to the complexity of the functions, an iterative scheme is used to achieve compatibility. The sequence of events in the calculation of $n$, $\rho_d$, and $\rho_c$ across any time interval $\Delta t^{k+1}$ is described in a following section which gives a brief description of the operation of the complete computer program.

## FEEDBACK REACTIVITY COEFFICIENTS

### *Sodium Void Reactivity*

The reference core for the calculations is a 4900 liter $UO_2$-$PuO_2$ fueled system having a fertile-to-fissile ratio of 7.2. The core height and diameter are 100 cm and 250 cm, respectively, and the upper and lower axial blankets are 30 cm thick. Core composition and heavy atom isotopic distributions are given in Table IV-15-I.

A perturbation calculation using the MACH 1[5] code was used to obtain the sodium voiding reactivity coefficients (Table IV-15-II) for the reactivity feedback calculation. The reactivity values listed in Table II are for complete voiding of the given axial segment across the core radius. In an attempt to represent the non-coherence of boiling initiation it is assumed that four different groups of fuel subassemblies (distributed uniformly across the core) start boiling at different times. Thus the sodium void feedback reactivity is a function of the form

$$\rho_{Na} = \rho(t) + \rho(t - \sigma_1) + \rho(t - \sigma_2) + \rho(t - \sigma_3),$$

where

$$\rho(t) = \frac{1}{4L} \int_{channel} \alpha(z,t)\delta k_{Na}(z)\, dz$$

and $L$ is the total channel length. The contribution from each term is zero when the argument is negative. The values $\sigma_1$, $\sigma_2$, and $\sigma_3$ are input parameters for which values are obtained from the different power densities in the four subassembly groups. In this manner the feedback reactivity based on the single channel fluid flow and heat transfer analysis is modified to be more representative of that in a multichannel reactor having radial power gradients and fuel subassemblies with different burnup histories.

### *Doppler Reactivity*

The Doppler feedback reactivity is based on the volume averaged fuel temperature over the fuel pin, $\bar{T}_f$. Reactivity is then calculated by integrating the expression

$$A(\text{Doppler}) = \bar{T}_f \frac{dk}{d\bar{T}_f},$$

where $A(\text{Doppler}) = -0.0035$ for the present calculations.

### *Fuel Expansion Reactivity*

No attempt has been made in the present model to include reactivity effects which may result from radial and axial fuel expansion. However, in cases where this feedback is important it can be readily included since detailed temperature profiles in the fuel are available.

## OPERATION OF THE INTEGRATED COMPUTER PROGRAM

A flow diagram showing the major steps in the program is presented in Figs. IV-15-2a and IV-15-2b. The version currently in use was written in Fortran for the CDC-3600 Computer at Argonne. It may be noted that there are four main subroutines, namely the steady state module, coolant dynamics module, transient heat transfer module, and neutron kinetics module. These subroutines are called as needed by a main (or control program) using a scheme involving overlay tapes to avoid exceeding the fast access memory capacity of the computer. Typical running times for calculating a reactor transient are on the order of 15 min.

The temperature dependent thermal properties of sodium are calculated as required from equations built into the sodium voiding module. Likewise the fuel thermal properties are calculated in the heat transfer module using polynomials which have been fitted to experi-

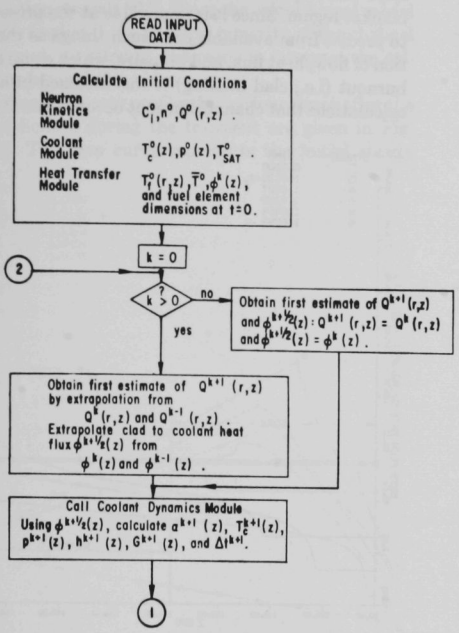


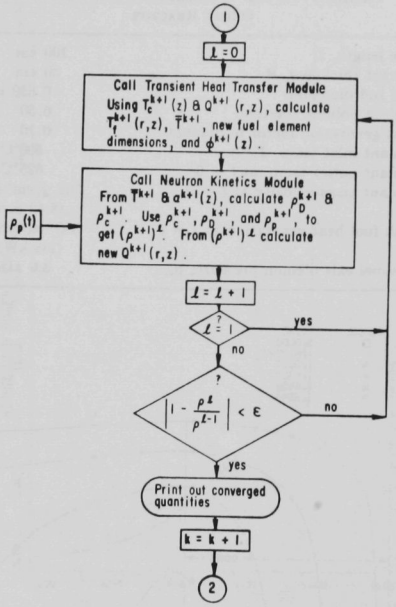


FIG. IV-15-2a. Flow Diagram of Computer Program. *ANL Neg. No. 112-9255.*
FIG. IV-15-2b. Flow Diagram of Computer Program. *ANL Neg. No. 112-9256.*

mental data over the temperature range of interest. The cladding properties are evaluated at a constant temperature which is representative of an average clad temperature during the transient.

## NUMERICAL RESULTS

As mentioned previously, the code is designed to compute transients which are slow enough so that there is time for heat transfer to the coolant before the threshold for fuel subassembly damage is reached. In the case of reactivity transients for oxide fueled cores, ramp reactivity insertions up to $2/sec have been used so far in performing calculations.

The results of a $1/sec reactivity transient for the oxide core for which the feedback reactivity parameters are given in Table IV-15-II are summarized in Figs. IV-15-3 through IV-15-10. The other parameters for the reactor are given in Table IV-15-III. The coolant temperature maximum value occurs 2 cm downstream from the core-blanket boundary at $t_b = 1.61$ sec, the time when boiling starts. As shown in Fig. IV-15-3, there is a reversal in the sign of the heat flux in the blanket when boiling starts, as evidenced by the fact that the coolant temperature is higher than the cladding temperature in

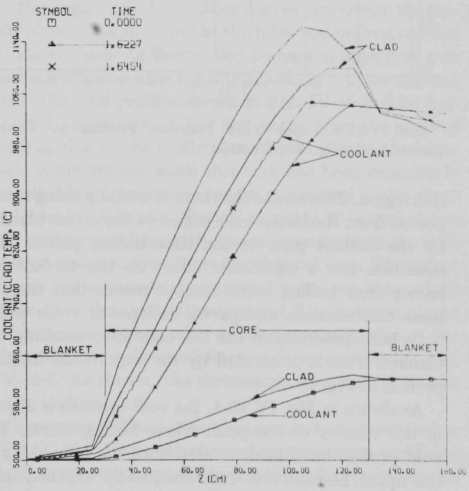


FIG. IV-15-3. Coolant Temperature Profiles at Various Times. *ANL Neg. No. 112-8553.*

TABLE IV-15-III. Parameters for Reference Oxide Reactor

| | |
|---|---|
| Core length, $L$ | 100 cm |
| Blanket thickness, $R$ | 30 cm |
| Fuel rod diameter | 0.650 cm |
| Coolant volume fraction | 0.50 |
| Heat generation factor in blanket | 0.10 |
| Coolant inlet temp. $T_c(0)$ | 500°C |
| Coolant outlet temp. at $t = 0$ | 625°C |
| Coolant mass-velocity at $t = 0$ | 700 g/cm²-sec (8.42 m/sec) |
| Peak fuel heat generation at $t = 0$ | 380 cal/cm³-sec (148 kW/kg) |
| Channel exit plenum pressure, $p_{ex}$ | 3.0 atm |

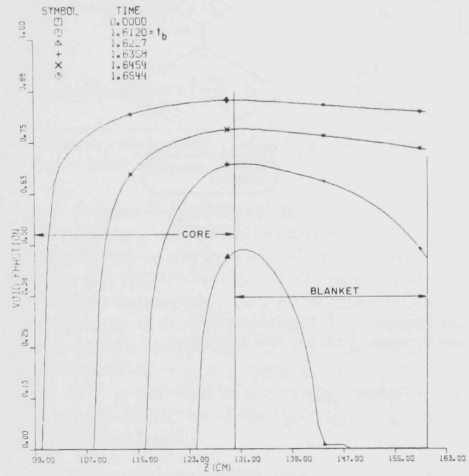


FIG. IV-15-4. Vapor Void Fraction Profiles at Various Times. *ANL Neg. No. 112-8549.*

this region. This means that heat is actually being transported from the hotter core region to the cooler blanket by the coolant prior to the time boiling starts. This condition has a significant effect on the coolant behavior once boiling starts since it means that there is some condensation and partial collapse of voids which have been produced in the hot core upon reaching the blanket. This is illustrated by the vapor void fraction profiles in Fig. IV-15-4.

As shown in Fig. IV-15-4, the void increase is abrupt in the vicinity of the point where boiling starts. The void profiles bend back to zero until the liquid slug in the upper blanket has been completely expelled from the channel. After this time the void fraction in the blanket builds up rapidly but still retains a negative slope due to partial condensation of vapor in the cooler blanket region. Since it is impossible at the present time to predict from available data such things as the condition of flow, heat flux, and pressure, which cause channel burnout (i.e., clad melting) it was assumed in all these calculations that channel burnout occurs when the vapor

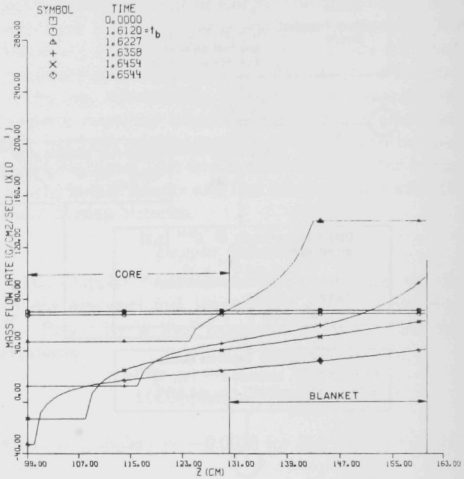


FIG. IV-15-5. Mass Flow Rate Profiles at Various Times. *ANL Neg. No. 112-8547.*

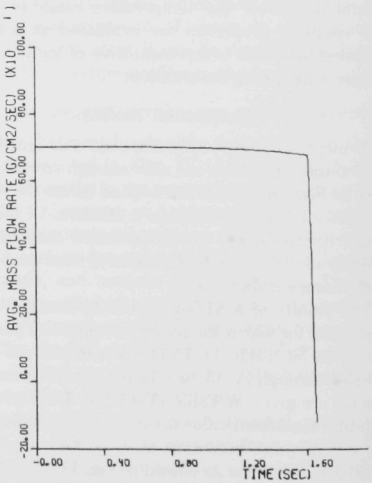


FIG. IV-15-6. Average Mass Flow Rate versus Time. *ANL Neg. No. 112-8555.*

void fraction exceeds 80 %. Since the calculational model no longer applies if the physical integrity of the channel is destroyed, no attempt was made to interpret the calculations beyond this point.

The mass flow rate profiles for various times after the start of boiling during the transient are given in Fig. IV-15-5. The zero curve represents the initial steady

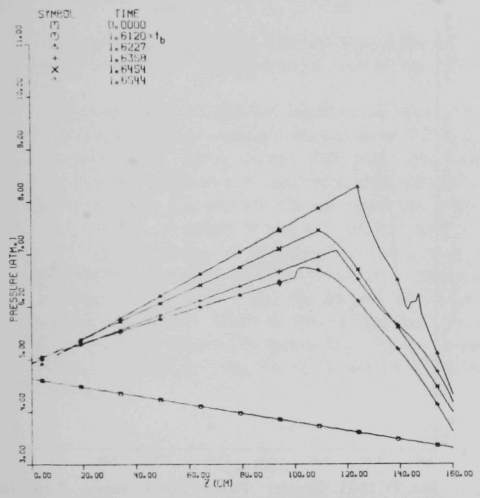


FIG. IV-15-7. Pressure Profiles at Various Times. *ANL Neg. No. 112-8554.*

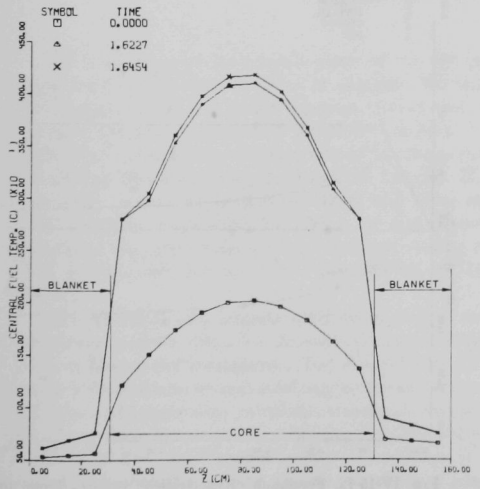


FIG. IV-15-8. Fuel Centerline Temperatures at Various Times. *ANL Neg. No. 112-8552.*

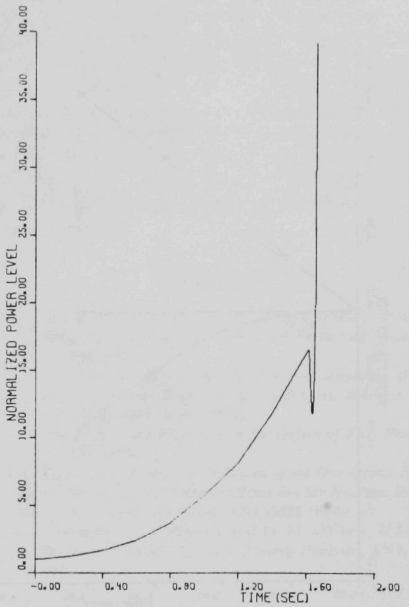


FIG. IV-15-9. Reactor Power Level versus Time. *ANL Neg. No. 112-8551.*

state coolant mass flow rate and the horizontal segments at the beginning of the other curves represents the single-phase mass flow rate in the inlet non-boiling portion of the channel. As shown, the increase in mass flow rate at the point where boiling starts is abrupt, in accordance with the void profiles shown in Fig. IV-15-5. The flat-topped appearance of the first curve after the start of boiling, due to the single-phase liquid slug in the blanket, is maintained until this slug has been completely expelled from the time beyond flow reversal at the channel inlet, and, in fact, the last curve (1.6544 sec) shows the coolant expelling with a mass velocity from the inlet almost equal to that from the channel exit. The upper liquid leg is completely expelled from the channel 19 msec after the start of boiling and flow reversal at the inlet occurs 29 msec after boiling starts. A plot of the channel-averaged mass flow rate, $\bar{G}$, is presented in Fig. IV-15-6. As shown, the decrease in flow rate is abrupt when boiling starts

Pressure profiles during the transient are presented in Fig. IV-15-7. The peak channel pressure rises rapidly to a value between 8 and 9 atm and thereafter remains relatively constant in time. The rapid pressure rise is due primarily to the inertial pressure loading imposed by the liquid slug in the upper blanket as it is being expelled

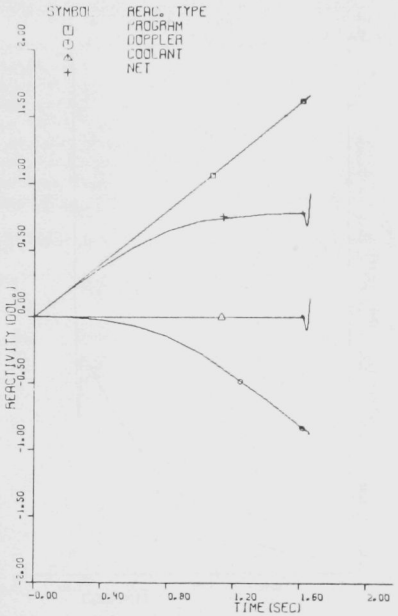


FIG. IV-15-10. Feedback Reactivities versus Time. *ANL Neg. No. 112-8546.*

from the channel. The point of peak pressure in the profiles in the figure is at the lower boundary between boiling and single-phase fluid.

As shown in Fig. IV-15-8 the maximum fuel centerline temperature increased from the steady state value of about 2000 to over 4000°C at the time boiling started. At this latter time the fuel centerline temperature exceeds the melting point of 2800°C over the entire length of the core portion. The changes in slope of the profiles near the ends of the core region occurs because the phase change from solid to liquid is still in progress close to the ends of the fuel section, whereas the central portion is completely molten at the fuel centerline.

A plot of the normalized reactor power level versus time is presented in Fig. IV-15-9. As shown, the power has increased to about 17 times the steady state value when boiling starts ($t_b$ = 1.61 sec). A sharp decrease in power level is produced by the initially negative feedback reactivity due to voiding sodium (Fig. IV-15-10). The decrease is followed by a rapid increase in power when the sodium voiding begins to add positive reactivity at a fairly rapid rate (~$20/sec). The time from the start of boiling to the termination of the calculation due to the excessively high power level is about 50 msec.

The programmed ($1/sec) ramp reactivity insertion and the feedback reactivities versus time are shown in Fig. IV-15-10. At the time boiling starts the net reactivity is slightly over 75¢ and the rate of increase has leveled off due to the buildup of the negative Doppler feedback. The curve representing the coolant (sodium void) reactivity is the sum of the reactivity contribution of the four sections of the core in which boiling is

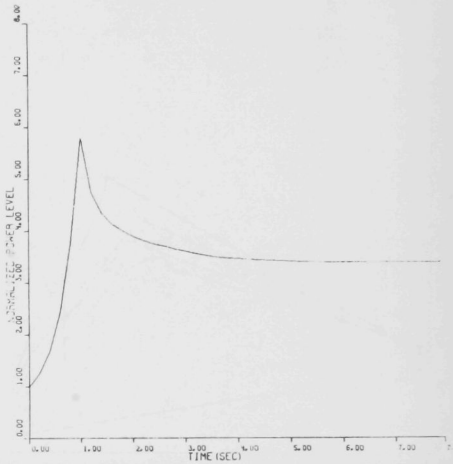


FIG. IV-15-11. Reactor Power Level versus Time for Truncated Ramp. *ANL Neg. No. 112-8550.*

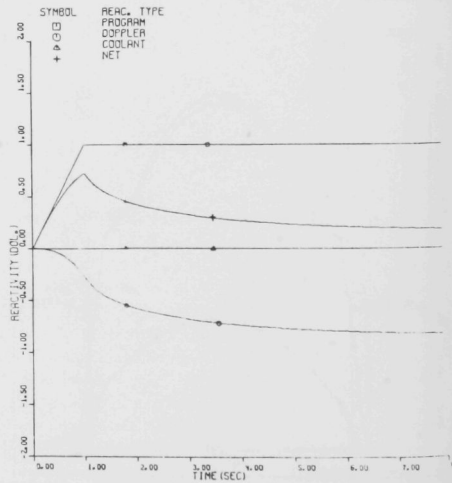


FIG. IV-15-12. Feedback Reactivities versus Time for Truncated Ramp. *ANL Neg. No. 112-8548.*

initiated at different times (see Sodium Void Reactivity). The time delays for the start of boiling are as follows:

| Region | Time Delay, msec |
|---|---|
| 1 | 0 |
| 2 | 3 |
| 3 | 35 |
| 4 | 49 |

At the time the calculation was terminated the net reactivity was about \$1 (point not shown in Fig. IV-15-10).

For purposes of comparison, another calculation was run using exactly the same parameters as in the transient summarized above, except that input reactivity ramp was cut off after 1 sec and held at \$1 thereafter. In this problem the coolant did not reach the boiling point and the transient eventually leveled out at a power about 3.3 times the initial steady state power. At this new steady state the maximum fuel centerline temperature was 4800°C and the coolant outlet temperature was 891°C. Plots of the normalized reactor power level and reactivities versus time for the transient are presented in Figs. IV-15-11 and IV-15-12, respectively.

The success in performing the calculations presented here show that the heat transfer and sodium voiding computational models which have been developed separately can be successfully incorporated into a complete dynamic model involving reactor kinetics and the various reactivity feedbacks. While the computer code thus synthesized has obvious limitations it does, nevertheless, represent a first attempt at performing such a completely integrated analysis of fast reactor coolant boiling transients.

### References

1. A. H. Kazi and B. A. Cherry, *Survey of Current Methods for Analysis of Fast Reactor Transients Including Meltdown*, UNC-5092 (1964).
2. D. G. Sherer and W. G. Meinhardt, *An Analysis of Fast Reactor Transient Response and Safety in Selected Accidents*, GEAP-4787 (June 1966).
3. R. O. Brittan, *Some Problems in the Safety of Fast Reactors*, ANL-5577 (1956), p. 7.
4. J. J. Kaganove, *Numerical Solution of the One-Group Space-Independent Reactor Kinetics Equation for Neutron Density Given the Excess Reactivity*, ANL-6132 (1960).
5. D. A. Meneley, L. C. Kvitek and D. M. O'Shea, *MACH-1, A One-Dimensional Diffusion Theory Package*, ANL-7223, (1966).

## IV-16. Heat Transfer Computation for Ceramic Fuels Undergoing Reactor Transients

C. K. Sanathanan and N. A. McNeal

The work reported here is one phase of the fast reactor safety evaluation program at Argonne National Laboratory. It pertains to the transient flow of heat in ceramic fuel pins. A numerical procedure has been developed to compute the temperature profiles, the extent of melting, and thermal expansion of the fuel pin. The computer routine, or module, is linked with other related modules to describe the history of fast reactor accidents, especially those leading to sodium voiding or fuel ejection into coolant (see Papers IV-13, IV-15, IV-19).

Since the axial and angular conduction of heat are relatively unimportant, a one-dimensional space (radial, $r$) heat flow model is employed. The channel (Fig. IV-16-1) is divided into several axial segments and the heat transfer and temperature calculations are made for each of the sections in succession, following the direction of the coolant flow. Since successive sections are thermally coupled through the coolant, the Storrer effect of heat transfer from downstream coolant to fuel is automatically included. Calculations made thus far show that the neglect of axial conduction is quite reasonable. The advantage gained thereby, namely, of not being obliged to solve the heat flow equations in two-dimensional space, represents a large saving in computing time.

This model is similar to those employed in Refs. 1 and 2. However, the numerical methods used in Refs. 1 and 2 have the following limitations:

1. Time increments must be kept small to assure numerical stability. This is so because the differencing schemes are explicit; consequently, computing time becomes excessively large.

2. Thermal expansion is neglected in computing the temperatures. In materials such as $UO_2$, whose volume increases approximately 20% between 500 and 3500°K, serious errors may be introduced in neglecting thermal expansion.

The method of analysis developed here represents an effort to eliminate these disadvantages. The transient heat conduction equations are discretized in space, $r$, and time, $t$, by means of the extrapolated Crank-Nicolson scheme as formulated in Ref. 3. This scheme is

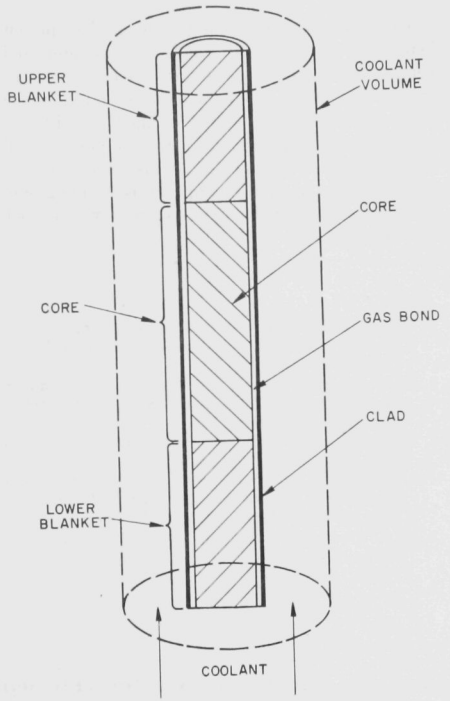


FIG. IV-16-1. Model of Reactor Channel. *ANL Neg. No. 112-8544.*

chosen because it is numerically stable for reasonably large increments of time, and also because it is efficient in handling the non-linearities of the equations resulting from the wide variation of thermal conductivity with temperature. These aspects of the numerical scheme are explained in the following section. In addition to the use of the new differencing scheme, the method of analysis also takes the following into account:

1. The dimensional changes due to thermal expansion and phase change (melting).
2. Latent heat absorption due to phase change.
3. Widely varying time increments for use in different portions of transients. The large time increments allowed by the implicit form of the equations enable more sensitive modules to control choice of time step increments.
4. Variable bond gap size and the associated variable thermal resistance.

Figure IV-16-1 illustrates the cross section of a typical fuel element under consideration. The bond may be filled either with a gas such as helium or a liquid metal such as sodium. In the former case the temperature drop in the bond is usually large. The transient heat flow equations in the fuel, bond and clad are discretized in such a manner as to enable these equations to be coupled with the transient coolant flow equations. This coupling is explained later.

Figure IV-16-2 shows the manner in which the radius of the fuel element is discretized. Temperature, $T_i$, is used to obtain the thermal expansion and melting of the radial segment $i$, which lies between radii $r_{i+1}$ and $r_i$. The first and the last radial segments are approximately half the size of the rest of the radial segments.

### TRANSIENT NUMERICAL SOLUTION

The diffusion equation in cylindrical geometry is

$$C\rho(T)\,\frac{\partial T}{\partial t} = \frac{1}{r}\,\frac{\partial}{\partial r}\left[K(T)r\,\frac{\partial T}{\partial r}\right] + q, \tag{1}$$

where

$T \equiv$ temperature,
$C \equiv$ specific heat,
$\rho \equiv$ density,
$K \equiv$ thermal conductivity,
$q \equiv$ volumetric heat generation rate in the fuel.

The discretized form of Eq. (1) when one uses the extrapolated Crank-Nicolson differencing scheme is

$$C\rho(T^{k+\frac{1}{2}})\,\frac{T_i^{k+1} - T_i^k}{\Delta t^{k+1}} = \frac{1}{r_i^k}\,D_+ \cdot\left[K(T)_{i-\frac{1}{2}}^{k+\frac{1}{2}} r_i^k D_-\left(\frac{T_i^k + T_i^{k+1}}{2}\right)\right] + q_i^{k+\frac{1}{2}}, \tag{2}$$

where the superscript $k$ pertains to time and the subscript $i$ pertains to space nodes. The space differencing operators, $D_+$ and $D_-$ are defined as follows:

$$D_+(\eta_i) \equiv \frac{2(\eta_{i+1} - \eta_i)}{(\Delta r_{i+1} + \Delta r_i)}, \tag{3}$$

where $\eta_i$ is any variable being operated on and

$$D_-(\eta_i) \equiv \frac{2(\eta_i - \eta_{i-1})}{(\Delta r_i + \Delta r_{i-1})}. \tag{4}$$

The superscript $k+\frac{1}{2}$ indicates that the variable is evaluated at the middle of the $(k+1)$th time interval and the superscript $i\pm\frac{1}{2}$ indicates that the variable is evaluated as an average between its values at the radial nodes $i$ and $i\pm1$, respectively.

If there are a number $N$ of radial nodes, Eq. (2) represents a number $N$ of coupled algebraic equations. These must be solved simultaneously to obtain $T_i^{k+1}$ for all $i$. Therefore, the differencing scheme is implicit. Since $K$ and $C\rho$ are functions of temperature, Eq. (2) is nonlinear. Consequently, an exact solution is not easily

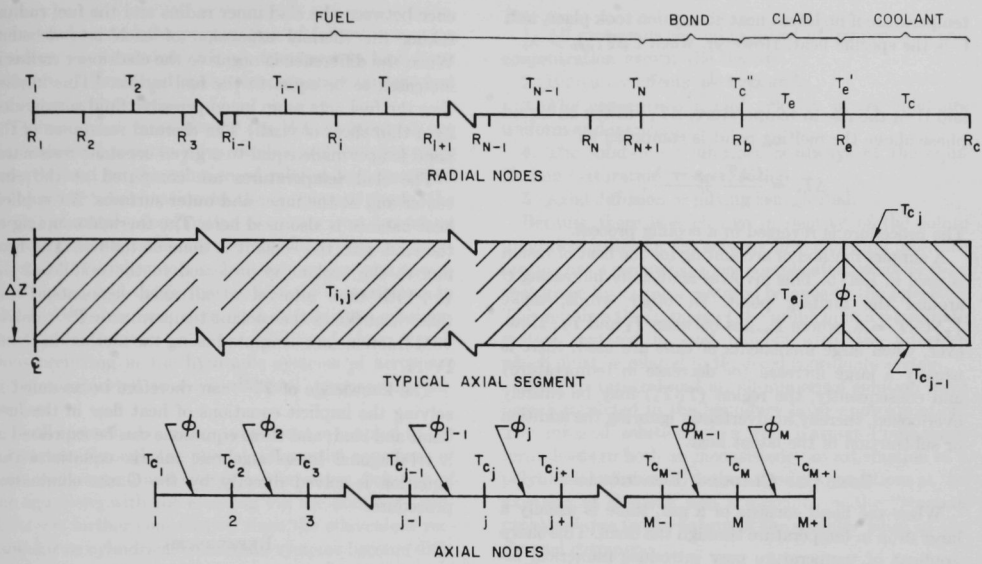


FIG. IV-16-2. Radial and Axial Nodes in Reactor Channel. *ANL Neg. No. 112-8545.*

possible. The following method suggested in Ref. 3 is found to be very effective in treating the non-linearity. Temperatures at the middle of the $(k+1)$th time interval used to evaluate $K$ and $C\rho$ are obtained by a linear extrapolation of the temperature $T_i^k$ and $T_i^{k-1}$; that is

$$T_i^{k+\frac{1}{2}} = T_i^k \frac{T_i^k - T_i^{k-1}}{2\Delta t^k} \Delta t^{k+1} \tag{5}$$

where, in general, $\Delta t^{k+1} \neq \Delta t^k$.

Using the known values for $T_i^{k+\frac{1}{2}}$ for all $i$, the values of $C\rho(T_{i\pm\frac{1}{2}}^{k+\frac{1}{2}})$ are computed and substituted into Eq. (2). This reduces Eq. (2) to a set of linear algebraic equations in $T_i^{k+1}$, which can be solved directly by the Gauss elimination procedure.[4] The effectiveness of this approach results from the "smooth" variations of the thermal properties with temperature and the smooth variation of temperature with respect to time. Mathematical proof of the numerical stability of the differencing scheme is given in detail in Ref. 3.

### Variable Space Mesh Due to Fuel Expansion

In Eqs. (3) and (4), $\Delta r_{i\pm1}$ and $\Delta r_i$ are obtained from knowledge of the temperatures $T_{i\pm1}^k$ and $T_i^k$, respectively. In other words, the spatial dimensions at the end of the $k$th time increment are used for the computations in the $k+1$ increment. A projection of the spatial increment lengths themselves to the middle of the time increment $k+1$ (as was done with temperatures) is found to be unnecessary in practice. $\Delta r_i$ is computed as follows:

if $T_i$ is less than the melting point, $T_{melt}$,

$$\Delta r_i = \Delta r_i^{(0)}[1 + \alpha_s(T_i^k - T^{(0)})];$$

if $T_i$ is at the melting point,

$$\Delta r_i = \Delta r_i^{(0)}[1 + \alpha_s(T_{melt} - T^{(0)})][1 + \chi_i\alpha_{melt}];$$

if $T_i$ is above the melting point,

$$\Delta r_i = \Delta r_i^{(0)}[1 + \alpha_s(T_{melt} - T^{(0)})] \cdot [1 + \alpha_{meld}][1 + \alpha_l(T_i^k - T_{melt})],$$

where

$\alpha_s \equiv$ linear coefficient of expansion of the solid,
$\alpha_{melt} \equiv$ expansion due to melting,
$\alpha_l \equiv$ linear coefficient of expansion of the liquid,
$\chi_i \equiv$ fraction melted at the $i$th radial node.

The computation of $\chi_i$ is done as follows. First, the temperatures are computed neglecting any melting during the time increment under consideration and the temperature rise $\Delta T_{i\,app}$ of $T_i$ above the melting point is noted. The fraction melted is then given by

$$\chi_i = \frac{C\Delta T_{i\,app}}{\lambda},$$

where $\chi_i$ is the heat of fusion, $\Delta T_{i\,app}$ is the increase in

temperature if no latent heat absorption took place, and $C$ is the specific heat. However, when $C\Delta T_{i\,app} > \lambda$,

$$\chi_i = 1,$$

and then the rise in temperature, $\Delta T_i$, of the all-liquid phase above the melting point is computed as

$$\Delta T_i = \frac{C\Delta T_{i\,app} - \lambda}{C}.$$

The procedure is reversed in a cooling process.

A simpler method of accounting for the heat of fusion is used in Ref. 5. This involves artificially increasing $C$ around the melting point. In other words, make $\int_{T_1}^{T_2} C\,dT = \lambda$, where $T_{melt}$ is between $T_1$ and $T_2$. However, when large increments of time are used, there is usually a large increase (or decrease in temperature) and consequently, the region ($T_1$-$T_2$) may be entirely overlooked, thereby inadvertantly ignoring the addition or subtraction of the latent heat.

### Bond-Gap Cladding Equations

When the bond consists of a gas, there is usually a large drop in temperature through the bond. This sharp gradient of temperature may introduce numerical instabilities. It is found that the method suggested by L. Back[6] is quite adequate for the present situation. The heat transfer through the bond is assumed to consist of conductive and radiative components. The conductive component, $\phi_1$, is considerably stronger, and it is expressed implicitly as (see Fig. IV-16-2).

$$\phi_{1(\mathrm{W/cm^2})} = \frac{h_b}{\tau^k}\left[\frac{T_N^{k+1} + T_N^k}{2} - \frac{T_c''^{k+1} + T_c''^k}{2}\right], \quad (6)$$

where $h_b$ is a constant and $\tau^k$ is the (variable) gap width at the end of time increment $k$. Since the radiative component, $\phi_2$, is small, it is computed explicitly:

$$\phi_2 = \epsilon\sigma(T_N^{k4} - T_c''^{k4}), \quad (7)$$

where $\epsilon$ is the emissivity and $\sigma$ the Steffan-Boltzmann constant. The gap width, $\tau$, is computed as the difference between the clad inner radius and the fuel radius, taking the thermal expansion of each into account. When the difference is negative the clad inner radius is increased to be equal to the fuel radius. (This implies that the fuel acts as an incompressible fluid surrounded by a thin sheet of clad.) The thermal resistance of the bond is now made equal to a given constant resistance.

The clad temperatures are computed at the clad center and at the inner and outer surfaces. An implicit heat balance is also used here. The thermal coupling of the clad with the coolant is done as follows. The heat flux to the coolant is projected to the middle of the $(k+1)$th time interval at all axial segments. Using these heat fluxes the coolant temperatures $T_c^{k+1}$ and/or void fractions are computed using the method in Paper IV-14.

The knowledge of $T_c^{k+1}$ can therefore be assumed in solving the implicit equations of heat flow in the fuel, bond and clad; and these equations can be expressed as a tri-diagonal linear algebraic matrix equation. This equation is solved directly by the Gauss elimination procedure.

### References


1. P. Greebler, et. al., *FORE, A Computational Program for the Analysis of Fast Reactor Excursions*, GEAP-4090 (October 1962)—Addenda No. EA-2 February (1965).
2. D. F. Schoeberle, et. al., *A Method of Calculating Transient Temperatures in a Multiregion, Axisymmetric, Cylindrical Configuration. The ARGUS Program, 9029/RE248, Written in Fortran II*, ANL-6654 (1963).
3. M. Lees, *An Extrapolated Crank-Nicholson Difference Scheme for Quasilinear Parabolic Equations*, Proc. Symposium on Non-Linear Partial Differential Equations, Ed. W. F. Ames, (Academic Press, to be printed).
4. D. D. McCracken and W. S. Dorn, *Numerical Methods and Fortran Programming*, (J. Wiley and Sons, New York (1964), pp. 231-246.
5. S. S. Clark and M. Troost, *RAT-3D, A General Three-Dimensional Heat Transfer Code*, GAMD-7346 (October 1966).
6. L. H. Back, *Technical Brief, Numerical Approximation of the Convective Boundary Condition*, Trans. ASME Ser. C: J. Heat Transfer (February 1962), p. 89.


## IV-17. Convective Heat or Mass Transfer with Phase Changes

J. Kaellis,* D. Miller and D. T. Wasan†

A variety of problems arising from reactor design and analysis require prediction of heat or mass transfer rates in forced convection flow where the geometry is changing with time due to the movement of boundaries. Of particular interest are problems where the transfer rates are determined by the prior history of the process due to the transfer-dependent rates of motion of the boundaries.

Problems of this type appear in such diverse areas as

* Reactor Engineering Division, Argonne National Laboratory.

† Illinois Institute of Technology, Chicago, Illinois.

in fuel failure and the propagation of failure in reactor accidents; in corrosion or mass transport in high temperature systems; and in the dissolution of nuclear fuel during reprocessing.

Technological interest and the development of the mathematical tools to solve similar problems has very recently lead to the solution of related but simplified problems.[1,2,3] Application to the freezing of foods, the casting of metals, desalination of water, frost formation on refrigeration coils, ice formation in water mains, freezing of liquid metals in heat exchangers and associated piping, and the formation of fatty constrictions in blood vessels has been suggested. In addition, consideration must be given to the possibility of phase transitions occurring in the hydraulic systems of aerospace vehicles subjected to environmental temperature extremes.

In all cases the boundary movement is coupled to the convection through the partial differential equations of mass, momentum and energy conservation. Solution of the equations with the coupling via the boundary conditions is further complicated since the convenient rectangular or cylindrical coordinate systems become difficult to use as the boundary moves.

A physical example chosen for solution is the dissolution of the channel between two initially parallel infinite blocks of salt by a slow flow of water. The salt will dissolve most rapidly at the entrance and the water will soon become saturated with salt and no additional dissolution will take place sufficiently far downstream of the entrance. The resultant channel will be "trumpet" shaped.

Similar but inverse problems could arise from the solidification of molten fuel as it enters a zone below the freezing point or by precipitation of solids in a channel due to mass transfer corrosion or cold-trapping of coolants. In principle, these problems are related to heat, mass, and momentum transfer problems with suction or blowing (such as transpiration cooling), except that the transport rates and geometry are not fixed but rather are coupled to the hydrodynamics through the boundary motion.

The following assumptions are made:

1. All properties are independent of temperature and concentration except the density.
2. Buoyancy effects are negligible.
3. The concentration and velocity in the inlet are uniform and invariant.
4. The solid-liquid interface is always at the equilibrium (saturation) concentration.
5. Axial diffusion or mixing is neglected.

Because there is a change in density of the solute upon dissolution in the solvent the solid-fluid interface motion has a somewhat more complicated behavior than that given by a simple material balance on the interface. This requires the framing of the problem in a coordinate system centered in, and moving with, the interface which must be related to the fixed coordinate system.

Both an integral and an all-numerical solution have been formulated in the boundary layer approximation. The integral solution, in a von Karman-Poulhausen form, leads to both an inconsistency in satisfaction of a polynomial solution with the boundary conditions at the axis and at the wall and a difficulty in the "starting problem" due to the nature of the singular point at the channel entrance.

The all numerical analysis avoids the well known approximations of the integral solution but includes additional stability and convergence problems. The latter can be tested by changing the size of the mesh and time intervals. This problem will lead to an "exact" solution in the limit of infinitesimal increments but it also suffers from the starting problem.

Solution of these problems will lead to a conservative solution since "upstream" diffusion will tend to smooth out the effects of the singular point.[4]

## References

1. R. D. Zerkle and J. E. Sunderland, *The Effect of Liquid Solidification in A Tube Upon Laminar-Flow Heat Transfer and Pressure Drop*, J. Heat Transfer, Trans. ASME Series C, **89**, (1967).
2. W. W. Bowley and C. H. Coogan, Jr., *Two Dimensional Melting in a Channel*, ASME Paper 67-HT-75.
3. K. T. Yang, Notre Dame University, Notre Dame, Indiana (private communication).
4. W. E. Burchill, B. G. Jones and R. P. Stein, *The Influence of Axial Heat Diffusion in Liquid-Metal-Cooled Ducts with Specified Heat Flux*, ASME Paper 67-WA/HT-26.

# IV-18. Heat Fraction in Coolant and Fuel During Transient Heating

R. O. Brittan and H. Greenspan*

In Ref. 1, the authors developed an exact solution for the temperature of a fuel-coolant system and the fraction of heat remaining in the fuel rod at any time during an exponential power transient with the coolant stagnant.

These solutions are complex combinations of Bessel's functions in an infinite series. However, the infinite series goes to zero after several $e$-folding times, and the shape of the temperature and heat distribution no longer varies with time. These shapes can then be determined as a function of the inverse period, $\alpha$. Nevertheless, the heat fractions are still given by a complex combination of Bessel's functions of different kinds and arguments.

To provide a useful tool for studying comparative behavior of different types or sizes of fuel rods and various ratios of fuel/coolant an approximate expression for the fraction of heat in coolant and fuel is desirable. The authors have determined such an expression yielding fractions which are indistinguishable from the true fractions. Herein this simplified expression is developed.

From Ref. 1, the exact expression for the fraction of heat generated which is still in the fuel after several $e$-folding times is

$$\mathfrak{F}H_f = 1 + \frac{2\rho\kappa_1}{r_1\sqrt{\alpha}}\left\{\frac{1}{\left[\dfrac{I_0\left(\dfrac{r_1}{\kappa_2}\right)K_1\left(\dfrac{r_2}{\kappa_2}\sqrt{\alpha}\right)+I_1\left(\dfrac{r_2}{\kappa_2}\sqrt{\alpha}\right)K_0\left(\dfrac{r_1}{\kappa_2}\sqrt{\alpha}\right)}{I_1\left(\dfrac{r_1}{\kappa_2}\sqrt{\alpha}\right)K_1\left(\dfrac{r_2}{\kappa_2}\sqrt{\alpha}\right)-I_1\left(\dfrac{r_2}{\kappa_2}\sqrt{\alpha}\right)K_1\left(\dfrac{r_1}{\kappa_2}\sqrt{\alpha}\right)}\right]-\rho\dfrac{I_0\left(\dfrac{r_1}{\kappa_1}\sqrt{\alpha}\right)}{I_1\left(\dfrac{r_1}{\kappa_1}\sqrt{\alpha}\right)}}\right\}, \tag{1}$$

where

$r_1 \equiv$ radius of fuel rod,

$r_2 \equiv$ equivalent radius of coolant associated with rod,

$\rho_1, \rho_2 \equiv$ density of fuel and coolant, respectively,

$C_1, C_2 \equiv$ heat capacity of fuel and coolant, respectively,

$\kappa_1, \kappa_2 \equiv$ thermal diffusivity of fuel and coolant, respectively,

$k_1, k_2 \equiv$ thermal conductivity of fuel and coolant, respectively,

$I, K \equiv$ usual Bessel's functions,

$$\rho \equiv \frac{k_2\kappa_1}{k_1\kappa_2} \equiv \sqrt{\frac{k_2\rho_2C_2}{k_1\rho_1C_1}}.$$

The fraction of heat in the coolant is obtained, of course, by subtracting Eq. (1) from unity. The authors introduce a second set of arguments and notations to simplify the development of the approximation, as follows:

$$\beta = (r_1/\kappa_1)\sqrt{\alpha},$$

$$\delta = (r_1/\kappa_2)\sqrt{\alpha},$$

$$\gamma = (r_2/\kappa_2)\sqrt{\alpha},$$

$$\lambda = 2(\gamma - \delta).$$

Introducing these into Eq. (1), rearranging terms, and subtracting from unity, the exact expression for the fraction of heat in the coolant becomes

$$\mathfrak{F}H_c = \frac{2\rho}{\beta} \Bigg/ \left\{\rho\frac{I_0(\beta)}{I_1(\beta)} - \left[\frac{I_0(\delta)K_1(\gamma) + I_1(\gamma)K_0(\delta)}{I_1(\delta)K_1(\gamma) - I_1(\gamma)K_1(\delta)}\right]\right\}. \tag{2}$$

This expression will first be investigated for small arguments. Let $\chi$ represent $\beta$, $\delta$, $\gamma$, or $\lambda$. Then as $\chi \to 0$, in general

$$I_0(\chi) \to 1, \quad I_1(\chi) \to \frac{\chi}{2}, \quad \text{and} \quad K_0(\chi) \to -XI_0(\chi),$$

where $X = [E + \ln(\chi/2)]$ and $E \equiv$ Euler's constant, while $K_1(\chi) \to XI_1(\chi) + (1/\chi)$. ($\chi$ represents $\Gamma$ and $\Delta$.) If these limiting values are substituted into Eq. (2)

$$\mathfrak{F}H_c \to \frac{2\rho}{\beta} \Bigg/ \left\{\frac{2\rho}{\beta} - \left[\frac{1\left(\Gamma\dfrac{\gamma}{2}+\dfrac{1}{\gamma}\right)-\dfrac{\gamma}{2}(\Delta\cdot 1)}{\dfrac{\delta}{2}\left(\Gamma\dfrac{\gamma}{2}+\dfrac{1}{\gamma}\right)-\dfrac{\gamma}{2}\left(\Delta\dfrac{\delta}{2}+\dfrac{1}{\delta}\right)}\right]\right\} \tag{3}$$

as $\alpha \to 0$.

If these are regrouped and it is noted that $\Gamma - \Delta = \ln(\gamma/\delta)$, while $(\gamma^2/2)\ln(\gamma/\delta) \to 0$,

$$\mathfrak{F}H_c \to \rho\frac{\delta}{\beta} \Bigg/ \left\{\left[1 \Big/ \left(\frac{\gamma^2}{\delta^2} - 1\right)\right] + \frac{\rho\delta}{\beta}\right\} \text{ as } \alpha \to 0. \tag{4}$$

Since $\rho\delta/\beta = \rho_2C_2/\rho_1C_1$ and $r_2^2/r_1^2 = \gamma^2/\delta^2$, Eq. (4) can

* Applied Mathematics Division, Argonne National Laboratory.

be put in terms of the original notation as:

$$\mathfrak{F}H_c \to \frac{\rho_2 C_2}{\rho_1 C_1}\left[\left(\frac{r_2}{r_1}\right)^2 - 1\right] \Big/ \left\{1 + \frac{\rho_2 C_2}{\rho_1 C_1}\left[\left(\frac{r_2}{r_1}\right)^2 - 1\right]\right\}. \tag{4a}$$

This is exactly the fraction of heat in the coolant when both fuel rod and coolant are at the same uniform temperature.

Next, the right member of Eq. (2) can be investigated for large arguments ($\alpha \to \infty$). The general forms for the asymptotic values of the Bessel functions are

$$I_0(\chi),\ I_1(\chi) \to e^{\chi}/\sqrt{2\pi\chi}$$

and

$$[I_0(\chi)/I_1(\chi) \to 1].$$

$$K_0(\chi),\ K_1(\chi) \to e^{-\chi}\sqrt{\pi/2\chi}$$

If these are substituted into Eq. (2),

$$\mathfrak{F}H_c \to \frac{2\rho}{\beta} \Big/ \left[\rho - \left(\frac{\frac{e^{\delta}}{\sqrt{2\pi\delta}}\cdot e^{-\gamma}\sqrt{\pi/2\gamma} + \frac{e^{\gamma}}{\sqrt{2\pi\gamma}}\cdot e^{-\delta}\sqrt{\pi/2\delta}}{\frac{e^{\delta}}{\sqrt{2\pi\delta}}\cdot e^{-\gamma}\sqrt{\pi/2\gamma} - \frac{e^{\gamma}}{\sqrt{2\pi\gamma}}\cdot e^{-\delta}\sqrt{\pi/2\delta}}\right)\right]. \tag{5}$$

On performing the indicated multiplications, multiplying numerator and denominator of the exponential fraction by $2\sqrt{\gamma\delta}$, and substituting $\lambda/2$ for $(\delta - \gamma)$, Eq. (5) becomes

$$\mathfrak{F}H_c \to \frac{2\rho}{\beta} \Big/ \left[\rho - \left(\frac{e^{\lambda/2} + e^{-\lambda/2}}{e^{\lambda/2} - e^{-\lambda/2}}\right)\right]. \tag{5a}$$

However,

$$\frac{e^{\lambda/2} + e^{-\lambda/2}}{e^{\lambda/2} - e^{-\lambda/2}} = \frac{\cosh(\lambda/2)}{\sinh(\lambda/2)} = \coth(\lambda/2) \to 1, \quad \text{as} \quad \alpha \to \infty.$$

Hence

$$\mathfrak{F}H_c \to \frac{2\rho}{\beta} \Big/ [\rho + \coth(\lambda/2)] \to \frac{2\rho}{\beta} \Big/ (1 + \rho) \quad \text{as} \quad \alpha \to \infty. \tag{5b}$$

This expression is asymptotic to zero for large $\alpha$, and is asymptotic to $\rho(\lambda/\beta)$ for small $\alpha$, rather than to

$$\frac{\rho\delta}{\beta} \Big/ \left\{\left[1 \Big/ \left(\frac{\gamma^2}{\delta^2} - 1\right)\right] + \frac{\rho\delta}{\beta}\right\}.$$

It is necessary to develop a transitional expression which reduces to Eq. (4) for small $\alpha$ and Eq. (5b) for large $\alpha$.

Eq. (4) is first put into the form

$$\frac{\frac{\rho\delta}{\beta}}{\left[X \Big/ \left(\frac{\gamma^2}{\delta^2} - 1\right)\right] + \frac{\rho\delta}{\beta}} = \mathfrak{F}H_c, \tag{6}$$

where $X$ is an unknown function to be determined.

Next Eq. (6) is put into the form of Eq. (5b) by multiplying numerator and denominator by $2/\delta$, then adding and subtracting $\rho$ in the denominator, to yield

$$\mathfrak{F}H_c = \frac{2\rho/\beta}{\left\{(2/\delta)\left[X \Big/ \left(\frac{\gamma^2}{\delta^2} - 1\right)\right] + 2\rho/\beta - \rho\right\} + \rho}. \tag{6a}$$

As $\alpha \to \infty$, the bracketed expression must $\to 1$. To accomplish this, $X$ must $\to (\delta/2)(1 + \rho)[(\gamma^2/\delta^2) - 1] - (\rho\delta/\beta)[(\gamma^2/\delta^2) - 1]$ as $\alpha \to \infty$, but it must still $\to 1$ as $\alpha \to 0$, The last term must $\to 0$ as $\alpha \to 0$. This is accomplished by multiplying $(\rho\delta/\beta)[(\gamma^2/\delta^2) - 1]$ by $[1 - e^{-f_1(\alpha)}]$ which is zero at $\alpha = 0$ and unity for large $\alpha$. Addition of a term $e^{-f_2(\alpha)}$ which varies from unity at $\alpha = 0$ to zero for large $\alpha$ completes the desired characteristics for small $\alpha$, and

$$X = \frac{\delta}{2}(1 + \rho)[(\gamma^2/\delta^2) - 1] - (\rho\delta/\beta)[(\gamma^2/\delta^2) - 1](1 + e^{-f_1(\alpha)}) + e^{-f_2(\alpha)}. \tag{7}$$

Equation (7) can now be substituted back into Eq. (6). After collecting terms, the fraction of heat in the coolant can be written in two forms:

$$\mathfrak{F}H_c = \frac{\rho\delta/\beta}{\frac{\delta}{2}(1 + \rho) + e^{-f_2(\alpha)}[(\gamma^2/\delta^2) - 1] + (\rho\delta/\beta)e^{-f_1(\alpha)}}$$

or

$$\mathfrak{F}H_c = \frac{(\rho\delta/\beta)[(\gamma^2/\delta^2) - 1]}{e^{-f_2(\alpha)} + \left[\frac{\delta}{2}(1 + \rho) + (\rho\delta/\beta)e^{-f_1(\alpha)}\right][(\gamma^2/\delta^2) - 1]}. \tag{8}$$

Numerical comparison with exact solutions for the cases of EBR-I pins, EBR-II pins, and a hypothetical case with much lower pin heat capacities and larger $r_2/r_1$ indicates that if $f_1(\alpha) = \lambda/2$ and $f_2(\alpha) = \delta$, the approximate expression of Eq. (8) yields values of the heat fraction in the coolant within 2% of the exact values over the entire range of $\alpha$ from zero to infinity. The final expression chosen then is

$$\mathfrak{F}H_c = \frac{\rho\delta/\beta}{e^{-\delta}[\gamma^2/\delta^2 - 1] + \frac{\delta}{2}(1 + \rho) + (\rho\delta/\beta)e^{-\lambda/2}} . \quad (9)$$

This expression may be used with ±2% accuracy to determine the division of heat in a pin-coolant system while the system is undergoing an exponential power excursion of any period, $\alpha$, up to the point where the thermal characteristics change abruptly (e.g., when the coolant begins to vaporize). For large $\alpha$, an approximation to the temperature at the fuel pin-coolant interface has been developed by similar means. After several $e$-folding times, for large $\alpha$, this temperature is given by

$$T(r_1) \rightarrow (q_1'/\alpha)e^{\alpha t}\left\{1 - \rho \Big/ \left(\coth\frac{\lambda}{2} + \rho\right)\right\}, \quad (10)$$

where $q_1$ is the initial heat source strength divided by $\rho_1 C_1$.

The exact temperature, after several $e$-folding times, is given in Ref. 1, App. E, as

$$T_1(r_1) = (q_1/\alpha)e^{\alpha t} \cdot \left\{1 + \rho\frac{I_0(\beta)}{I_1(\beta)} \Big/ \left[\frac{I_0(\delta)K_1(\gamma) + I_1(\gamma)K_0(\delta)}{I_1(\delta)K_1(\gamma) - I_1(\gamma)K_1(\delta)} - \rho\frac{I_0(\beta)}{I_1(\beta)}\right]\right\}.$$

## IV-19. Fuel Element Deformation Program for the Fast Reactor Safety Analysis System

C. K. Youngdahl

### Introduction

The function of the fuel element deformation program in the Fast Reactor Safety Analysis Activity is to interact with the heat transfer programs by receiving from the latter the fuel element temperature distribution and the amount of fuel melted and returning the thermoelastic deformation of the fuel, the elastic-plastic deformation of the cladding, and the change in the fuel-clad gap. In addition, clad rupture is predicted if excessive plastic yielding has occurred.

A quasi-static deformation analysis is used, which implies that there is no explosive loading on the fuel elements to produce shock effects. On the other hand, it is assumed that the time scale of the loading is short enough that long term effects such as radiation growth and viscoelastic creep can be neglected. An underlying policy in the mathematical modelling of the elastic deformation is to solve the field equations of elasticity with appropriate boundary conditions exactly with respect to radial variations but approximately with respect to axial variation of stress, displacement, and temperature. Since the radial temperature variations for a reactor fuel rod are much more severe than the axial, this approximate procedure gives results which differ from those which would be obtained from a numerical evaluation of the exact solution to the elasticity equations by amounts which are well within the limits of accuracy imposed by other physical and mathematical idealizations. The use of approximate solutions has the advantages that much less computing time is required than for an evaluation of the exact solution and the transition from elastic to plastic deformation calculations can be accomplished more easily.

### Basic Models and Solutions

In the fuel deformation program, as in the heat transfer programs, the cylindrical fuel rod is divided into axial segments such that segment $j$ is the region

$$z^j \leq z \leq z^{j+1}, \qquad j = 1, 2, \cdots . \quad (1)$$

Each segment is composed radially of concentric zones of clad, fuel-clad gap, solid fuel, partially melted fuel, and central cavity. The fuel is divided further into cells such that cell $ij$ is the region

$$r^i \leq r \leq r^{i+1}, \qquad i = 1, 2, \cdots \quad (2)$$

of axial segment $j$. The heat transfer programs furnish the average temperature $T^{ij}$ of each cell of fuel, the clad temperature $T_c^j$ (averaged through the thickness), and the fraction $f_L^{ij}$ of each cell of fuel that has melted. (Actually, $f_L^{ij}$ is the ratio of the latent heat of fusion absorbed in the cell to the amount of heat needed to

melt all the fuel in the cell, but it will be referred to loosely as the fraction of fuel melted.)

ELASTIC DEFORMATION MODEL FOR THE SOLID FUEL

The basic solution for the axisymmetric elastic displacements and stresses in the solid fuel of axial segment $j$ is taken to be

$$U_r^j(r) = -\frac{\nu_s F_{zs}^j r}{E_s A_s} + \tau_s^j(b_s) r - \frac{(1+\nu_s)}{2(1-\nu_s) r}(r^2 - a_s^2)[\tau_s^j(b_s) - \tau_s^j(r)] + \frac{1}{E_s(b_s^2 - a_s^2) r}[(1-\nu_s) r^2 (b_s^2 S_{bs}^j - a_s^2 S_{as}^j) + (1+\nu_s) a_s^2 b_s^2 (S_{bs}^j - S_{as}^j)], \tag{3}$$

$$U_{zs}^j \equiv U_z^j(z^{j+1}) - U_z^j(z^j) = (z^{j+1} - z^j) \cdot \left[\frac{F_{zs}^j}{E_s A_s} + \tau_s^j(b_s) + \frac{2\nu_s(a_s^2 S_{as}^j - b_s^2 S_{bs}^j)}{E_s(b_s^2 - a_s^2)}\right], \tag{4}$$

$$\sigma_{rr}^j(r) = \frac{(r^2 - a_s^2) E_s}{2(1-\nu_s) r^2}[\tau_s^j(b_s) - \tau_s^j(r)] + \frac{(r^2 - a_s^2) b_s^2 S_{bs}^j + (b_s^2 - r^2) a_s^2 S_{as}^j}{(b_s^2 - a_s^2) r^2}, \tag{5}$$

$$\sigma_{\theta\theta}^j(r) = \frac{E_s}{(1-\nu_s) r^2} \cdot \left\{\frac{1}{2}(r^2 - a_s^2)[\tau_s^j(b_s) + \tau_s^j(r)] + a_s^2 \tau_s^j(b_s) - r^2 \alpha_s T^j(r)\right\} + \frac{(r^2 + a_s^2) b_s^2 S_{bs}^j - (b_s^2 + r^2) a_s^2 S_{as}^j}{(b_s^2 - a_s^2) r^2}, \tag{6}$$

$$\sigma_{zz}^j(r) = \frac{E_s}{1-\nu_s}[\tau_s^j(b_s) - \alpha_s T^j(r)] + \frac{F_{zs}^j}{A_s}, \tag{7}$$

$$\sigma_{rz}^j = 0, \tag{8}$$

where*

$a_s \equiv$ inner radius
$b_s \equiv$ outer radius
$E_s \equiv$ Young's modulus
$\nu_s \equiv$ Poisson's ratio
$\alpha_s \equiv$ coefficient of thermal expansion
$U_r^j \equiv$ radial displacement
$U_z^j \equiv$ axial displacement
$\sigma_{rr}^j \equiv$ radial normal stress
$\sigma_{\theta\theta}^j \equiv$ circumferential normal stress
$\sigma_{zz}^j \equiv$ axial normal stress
$\sigma_{rz}^j \equiv$ radial shearing stress on planes $z =$ constant
$U_{zs}^j \equiv$ axial elongation of fuel segment
$T^j \equiv$ temperature measured above reference configuration temperature
$S_{as}^j \equiv$ applied surface stress on $r = a_s$
$S_{bs}^j \equiv$ applied surface stress on $r = b_s$
$F_{zs}^j \equiv$ total axial force on solid fuel of segment $j$

and

$$A_s \equiv \pi(b_s^2 - a_s^2), \tag{9}$$

$$\tau_s^j(r) \equiv \begin{cases} \dfrac{2}{r^2 - a_s^2}\displaystyle\int_{a_s}^{r} \alpha_s T^j(r) r dr, & a_s < r \leq b_s \\ \alpha_s T^j(a_s), & r = a_s. \end{cases} \tag{10}$$

The displacements and stresses given by Eqs. (3)–(8) satisfy the equilibrium equations and stress-displacement relations of thermoelasticity and meet the boundary conditions

$$\sigma_{rr}^j(a_s) = S_{as}^j, \tag{11}$$

$$\sigma_{rr}^j(b_s) = S_{bs}^j, \tag{12}$$

$$2\pi \int_{a_s}^{r} r \sigma_{zz}^j(r)\, dr = F_{zs}^j. \tag{13}$$

This solution is based on the assumption that the variations of $S_{as}^j$, $S_{bs}^j$ and $T^j(r)$ with $z$ within an axial segment can be neglected. However, the relative radial displacements of adjacent axial segments will produce non-zero shearing stresses $\sigma_{rz}^j$ and accompanying shearing displacements. To account for these shearing effects a fictitious surface stress $S_s^j$ is added to $S_{bs}^j$ to produce corrections to the displacement field. The fictitious stress is given by

$$S_s^j = \frac{E_s}{(1+\nu_s) b_s (z^{j+1} - z^j)} \left\{\frac{1}{(z^{j+2} - z^j)} \cdot \int_{a_s}^{b_s} [U_r^{j+1}(r) - U_r^j(r)] r dr - \frac{1}{(z^{j+1} - z^{j-1})} \cdot \int_{a_s}^{b_s} [U_r^j(r) - U_r^{j-1}(r)]\, r dr\right\}. \tag{14}$$

The integrals in Eq. (14) can be evaluated in closed form using Eq. (3).

In the computer calculation the initial values of $S_s^j$ and $F_{zs}^j$ are taken to be zero. The displacements $U_r^j$ and $U_{zs}^j$ are then calculated from Eqs. (3) and (4). The results are used in Eq. (14) and the overall axial restraint condition relating $F_{zf}$, the axial force on the fuel, to the sum over the axial segments of $U_{zs}^j$, and new values of $S_s^j$ and $F_{zs}^j$ are computed. The calculations are then redone based on the new values, and the procedure is repeated until it converges. In practice, only a few axial iteration cycles have been required for convergence.

* In the definitions which follow, the subscript $s$ refers to the solid fuel. Analogous quantities for the partially melted fuel and the clad are denoted by the subscripts $L$ and $c$, while subscript f will be used to refer to the fuel as a whole.

The solution given by Eqs. (3)–(8) requires a knowledge of the applied boundary stresses $S_{as}^j$ and $S_{bs}^j$ for each axial segment. These applied stresses are not given in all cases—for instance, if the fuel and clad are in contact the stress at the interface, $S_{bs}^j$, is unknown—but in each case where an applied stress is not known there is a compatability condition on the displacements which can be solved algebraically for the required quantity.

### DEFORMATION MODEL FOR PARTIALLY MELTED FUEL

For the purpose of calculating structural response it is assumed that if partial melting has occurred in a cell of fuel all the material in the cell behaves mechanically as a compressible liquid with density and bulk moduli proportioned between the properties of the liquid and solid states. In addition, the assumption is made that all cells where melting has occurred in axial segment $j$ are acted upon by the same fluid pressure $P^j$; the pressure can vary with $j$, however. Finally, it is assumed that fuel does not cross cell boundaries and that the axial expansion of an axial segment does not vary radially.

The melting fuel can expand into the central cavity of the axial segment (if one exists). Either enough cavity volume is available that the melting fuel exerts no pressure on the remaining solid fuel of the segment or the segment cavity is filled and a pressure is exerted. The fuel deformation program allows for both situations, but only the latter will be discussed here.

Let $b_L^j$ be the radius of the cylinder which the partially melted fuel of axial segment $j$ would occupy if there were no pressure, $P^j$, exerted on it by the remaining solid fuel; then, if cells $i = 1, 2, \cdots k$ have partially melted,

$$b_L^j = \left\{ \sum_{i=1}^{k} \frac{\rho_R^{ij}}{\bar{\rho}^{ij}} [(r^{i+1})^2 - (r^i)^2] \right\}^{1/2}, \tag{15}$$

where $\rho_R^{ij}$ is the density of cell $ij$ in the reference configuration and $\bar{\rho}^{ij}$ is its average density in the partially melted condition, given by

$$\bar{\rho}^{ij} = \left[ \frac{f_L^{ij}}{\rho_L} + \frac{1 - f_L^{ij}}{\rho_s} \right]^{-1}. \tag{16}$$

In Eq. (16), $\rho_L$ and $\rho_s$ are the densities of liquid and solid fuel at the melting point. Under pressure the cylinder of partially melted fuel deforms radially by an amount $U_r^j(b_L^j)$ and axially by an amount $U_{zL}^j$. The pressure and deformations are related through

$$P^j = -\bar{K}^j \left[ \frac{2U_r^j(b_L^j)}{b_L^j} + \frac{U_{zL}^j}{z^{j+1} - z^j} \right], \tag{17}$$

where the average bulk modulus $\bar{K}^j$ of cells $1j$ through $kj$ is given by

$$\bar{K}^j = \left[ \frac{1}{(b_L^j)^2} \sum_{i=1}^{k} \left\{ \rho_R^{ij} [(r^{i+1})^2 - (r^i)^2] \cdot \left[ \frac{f_L^{ij}}{\rho_L K_L} + \frac{1 - f_L^{ij}}{\rho_s K_s} \right] \right\} \right]^{-1}. \tag{18}$$

From the compatability of the stress and deformation fields of the solid and partially melted fuel and the assumptions of the analysis, the following boundary conditions are obtained:

$$S_{as}^j = -P^j, \tag{19}$$

$$a_s + U_r^j(a_s) = b_L^j + U_r^j(b_L^j), \tag{20}$$

$$F_{zf} = F_{zs}^j - \pi (b_L^j)^2 P^j, \tag{21}$$

$$U_{zL}^j = U_{zs}^j. \tag{22}$$

Equations (19)–(22), Eq. (17), Eq. (3) evaluated at $r = a_s$, and Eq. (4) are seven relations which can be solved algebraically for the seven unknowns $S_{as}^j$, $P^j$, $F_{zs}^j$, $U_r^j(a_s)$, $U_r^j(b_L^j)$, $U_{zs}^j$, and $U_{zL}^j$. Using Eqs. (3), (4), and (22) and an equation analogous to (17) which relates the interior deformations of the partially melted fuel to the pressure, the desired mesh changes in the fuel can be calculated. Note that the effect of the clad restraint on the fuel deformation must also be taken into account if the fuel and clad are in contact.

### ELASTIC DEFORMATION MODEL FOR THE CLAD

The elastic solution for the solid fuel given by Eqs. (3)–(14) applies also to the clad with the subscript $s$ replaced by $c$. If the fuel and clad are in contact the interface conditions are

$$S_{bs}^j = S_s^j + S_{ac}^j, \tag{23}$$

$$b_s + U_r^j(b_s) = a_c + U_r^j(a_c), \tag{24}$$

which are used with the equations for $U_r^j$ to solve for the unknown interface loads.

### ELASTIC-PLASTIC DEFORMATION MODEL FOR THE CLAD

The clad material is assumed to be elastic, perfectly plastic and to yield when the circumferential stress (taken to be constant across the clad thickness) reaches the yield stress $\sigma_{c0}$. The plastic stretching of the clad tube cross-section is limited since as the tube gets larger the radial force exerted by the thermally expanded fuel decreases until an equilibrium state is reached. The clad material is assumed to be incompressible during the plastic part of its deformation. Consequently, as the tube diameter grows larger its wall thickness decreases, resulting eventually in clad rupture. The applied failure criterion is based on a comparison of the reduction in thickness with the original thickness.

In order to determine the permanent clad deformations it is necessary to partition the displacements into elastic and plastic constituents. At the end of each computer time step the dimensions of the clad are changed by the amount of the plastic deformation, thus incorporating a history dependent effect into the model.

The equilibrium equation for a thin-walled clad undergoing large elastic-plastic deformations is

$$\sigma_{c0}[\delta_c + U_\delta^i] = [S_{bc}^i - S_{ac}^i][a_c + U_r^i(a_c)], \quad (25)$$

where

$\delta_c \equiv$ clad thickness
$U_\delta^i \equiv$ change in clad thickness
$U_r^i \equiv$ total displacement (elastic plus plastic) of inner radius
$S_{bc}^i \equiv$ applied outer surface load
$S_{ac}^i \equiv$ interface load exerted by expanding fuel.

Because of the incompressibility of the material during plastic flow the volume of the clad segment at the end of the deformation is the same as its volume was when it was just on the verge of becoming plastic. Combined with the assumption of no increase in length during plastic flow this yields the relation

$$[a_c + U_r^i][\delta_c + U_\delta^i] = [a_c + (U_r^i)^{ev}][\delta_c + (U_\delta^i)^{ev}], \quad (26)$$

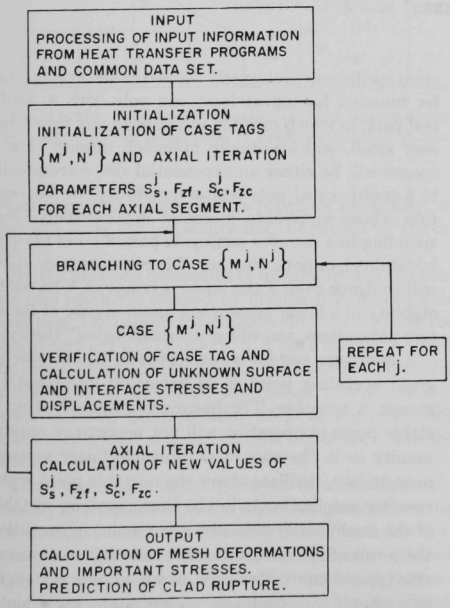


FIG. IV-19-1. Basic Flow Diagram for Fuel Deformation Program. *ANL Neg. No. 112-8692.*

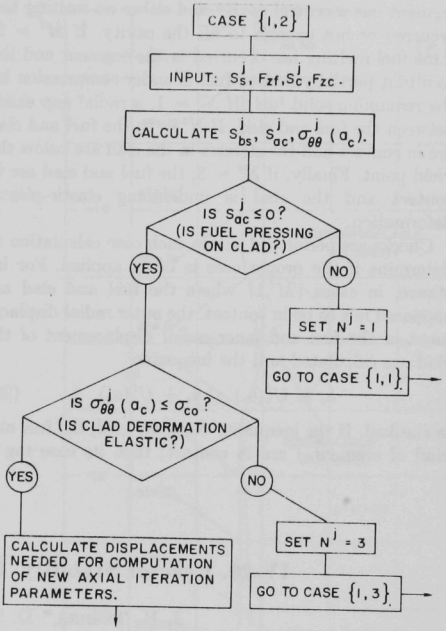


FIG. IV-19-2. Flow Diagram for Case {1, 2}. *ANL Neg. No. 112-8691.*

where superscript *ev* indicates the elastic displacements when the tube is on the verge of becoming plastic. Equations (25) and (26) when combined with the equations for the fuel deformation yield enough relations to solve for all of the unknowns.

The resulting total deformations $U_r^i$ and $U_\delta^i$ are partitioned into their elastic and plastic constituents by

$$U_r^i = (U_r^i)^e + (U_r^i)^p, \quad (27)$$

$$U_\delta^i = (U_\delta^i)^e + (U_\delta^i)^p. \quad (28)$$

The elastic components are calculated using the elastic deformation model for the clad and the final value of $S_{ac}^i$. The plastic components are then determined from Eqs. (27) and (28) and added to the original clad dimensions to determine the new clad dimensions.

## PROGRAM STRUCTURE

A rough block diagram for the fuel deformation computer program is given in Fig. IV-19-1.

Each axial segment of the fuel element is given a case tag $\{M^j, N^j\}, j = 1, 2, 3, N^j = 1, 2, 3$, which indicates the proper combination of basic deformation models to be employed. If $M^j = 1$, segment $j$ has no central

cavity and no fuel melting has occurred. If $M^j = 2$, the segment has a central cavity and either no melting has occurred or not enough to fill the cavity. If $M^j = 3$, some fuel melting has occurred in the segment and the resultant partially melted fuel is under compression by the remaining solid fuel. If $N^j = 1$, a radial gap exists between the fuel and clad. If $N^j = 2$, the fuel and clad are in contact and the stresses in the clad are below the yield point. Finally, if $N^j = 3$, the fuel and clad are in contact and the clad is undergoing elastic-plastic deformation.

Checks are performed within each case calculation to determine if the proper case is being applied. For instance, in cases $\{M^j,1\}$ where the fuel and clad are supposed not to be in contact, the outer radial displacement of the fuel and inner radial displacement of the clad are calculated and the inequality

$$b_s + U_r^j(b_s) \leq a_c + U_r^j(a_c) \qquad (29)$$

is checked. If the inequality does not hold, the fuel and clad of segment $j$ are in contact; then its case tag is changed from $\{M^j,1\}$ to $\{M^j,2\}$ and the computation is switched to the latter case. Similar inequalities are checked to verify each assumption made in the choice of $\{M^j,N^j\}$, and if an inequality is not satisfied, a switch is made to the correct case. As an illustration, the inner branching of case $\{1, 2\}$ is given in Fig. IV-19-2.

In the calculation of each case, any unknown surface or interface displacements and stresses are determined. In the axial iteration step the calculated values of $U_r^j$ in the fuel and clad in each segment are used to find new values of the equivalent shearing loads $S_s^j$ and $S_c^j$ from Eq. (14) and its analogue for the clad. The axial segment elongations of the fuel and clad, $U_{zs}^j$ and $U_{zc}^j$, are summed axially; the imposed axial restraint conditions then give new values of $F_{zf}$ and $F_{zc}$.

After the axial iteration has converged the mesh deformations needed in the heat transfer programs are computed. If any plastic flow has occurred, the clad dimensions are changed by the amount of the permanent deformations and the rupture criterion is applied.

## IV-20. Reactor Stability Considerations In Safety Analysis

J. H. Tessier,* D. W. Sparks* and J. C. Carter

### Introduction

The stability of a reactor depends to a large extent upon the nature of the reactivity feedbacks caused by a disturbance of the steady state. The characteristics of some feedbacks which can cause unsafe reactor operations are discussed in this paper.

A reactor is a closed loop nonlinear system which may have positive and negative feedbacks of widely varying amplitudes and phase angles. Usually, the effect of a large prompt negative feedback is desirable but not always obtainable in a given core design. It is frequently not obvious that the combinations of feedbacks inherent in a given reactor can cause instability. A relatively large vector component with negative sign does not always assure stability.

The time required for the power level to reach a steady state is that required for the time-derivative of the neutron flux to reach zero. The time-derivative may oscillate before reaching zero or it may never return to zero.

Instability in a linear system of equations with constant coefficients is concisely defined as the system transfer function having at least one pole with a positive real part, in which case the response to any input, however small, will eventually approach infinity. The response will be either an exponential rise corresponding to a positive real pole (static instability) or an oscillation whose amplitude increases exponentially, corresponding to a complex conjugate pair of poles (dynamic instability), or both. Further, this response once started will continue even if the input is removed. The relative stability of a linear system is a function only of the system parameters, according to "small-signal" theory.

A nonlinear system is considered to be unstable at a given operating point if its linearized incremental response is unstable. The linearized response at an unstable point of operation will not necessarily approach infinity as in the case of an unstable linear system; it may, in fact, oscillate about the unstable point with increasing amplitude. As in the linear system, instability of the nonlinear system at a given point of operation is the result of system parameters rather than of any specific type of input. However, in a nonlinear system such as a reactor with feedback, an input may cause motions

* Reactor Engineering Division, Argonne National Laboratory.

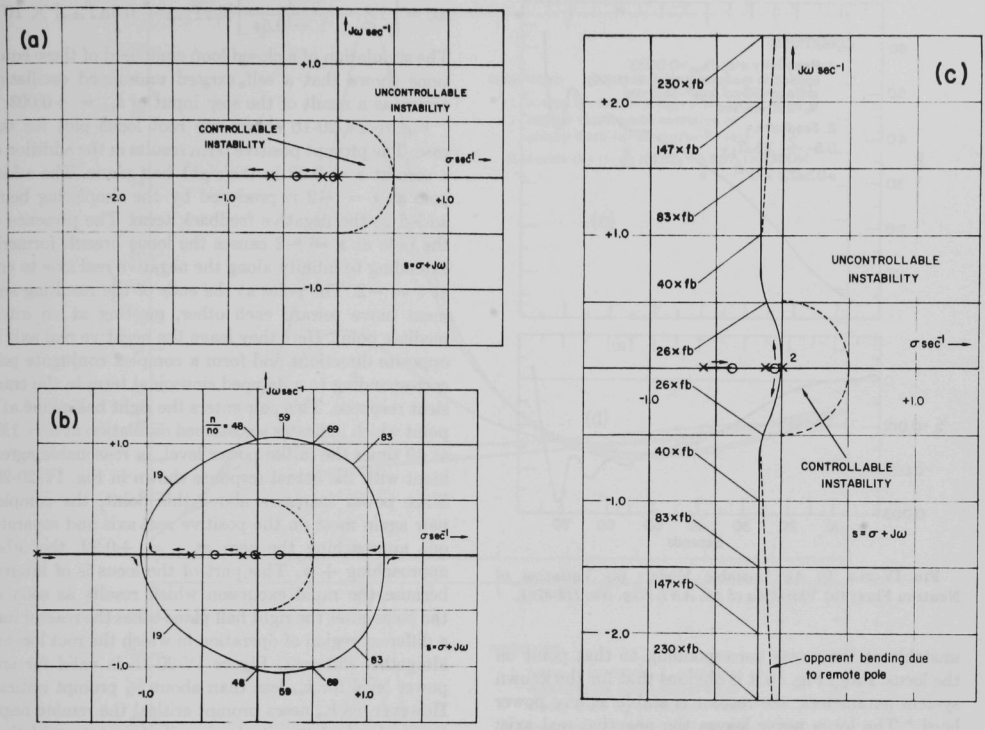


FIG. IV-20-1. Root Loci of Reactor: (a) With Known System Equations; (b) With Lagged Negative Plus Smaller Prompt Positive Feedback; (c) With Integration of Feedback. *ANL Neg. No. 112-8728.*

which carry the system into a region of instability, so that in a sense the instability may be caused by the input.

By the previous definitions of instability, normal control of a reactor is effected by placing it in an unstable condition. The control rod position effectively moves the pole at zero in Figs. IV-20-1 a, b, c, back and forth about the origin along the real axis of the $s$-plane. When it is to the right of the origin, the reactor is unstable and power is rising exponentially; when at the origin the power is constant, and when to the left of the origin the power is decreasing.

Thus, one might define a region of controllable instability as a semicircle in the right half plane about the origin within which the responses are of such low frequency or slow rate of rise that they may be controlled easily by the operator. The region outside this semicircle would then represent uncontrollable instability in which the self-excited responses are so rapid that a destructive level might be reached before the operator has time to exert control.

Figure IV-20-1a shows the root locus plot for a reactor operating with the feedback $\Delta k = c\Delta l/l$ where $c$ is a positive constant, $k$ is reactivity and $l$ is length of the fuel element. This is the model directly calculable from known system parameters. Regions of controllable and uncontrollable instability are indicated. The root locus plot is a plot on the $s$-plane of the values of $s$ corresponding to zeros and poles of the closed loop transfer function $\Delta k/k_{ex}$ of the incremental linear equivalent of the reactor, where $k_{ex}$ is excess reactivity. The locus shows the location of the poles as a function of feedback gain (or power level). The poles start at the poles of the open loop function $\Delta k/k_{eff}$ for zero power and as power increases each pole moves out along a locus in the direction indicated, ending either at one of the zeros or at infinity as power approaches infinity. If, at any point, a locus enters the right half plane, the reactor will be

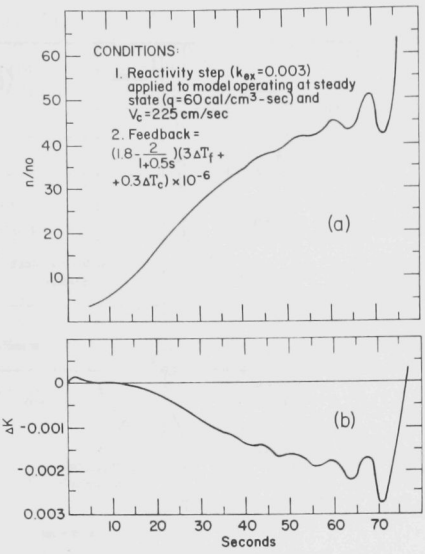


FIG. IV-20-2. In An Unstable Model: (a) Variation of Neutron Flux; (b) Variation of $\Delta k$. *ANL Neg. No. 112-8724.*

unstable at the power corresponding to that point on the locus. From Fig. 1a it is obvious that for the known system parameters, the reactor is stable at any power level.* The locus never leaves the negative real axis; hence there can be no oscillatory terms in the transient response.

### Instability Due to a Lagging Negative Feedback plus a Smaller Prompt Positive Feedback

This is a hypothetical condition. The thermodynamic conditions are those existing at some steady state operating condition. A step input of reactivity $k_{ex} = +0.003$ is an arbitrary choice. The negative component of the total feedback term has as its basis the axial expansion of the fuel rods with lag due to coulomb friction. This negative component has an arbitrary time constant of ½ sec. The positive component is due to the bowing of the fuel towards the center of the core.

The point kinetics equations are used with a plausible arbitrary feedback of

$$\Delta k = \left[1.8 - \frac{2}{1 + 0.5s}\right][3\overline{\Delta T}_{fuel} + 0.3\overline{\Delta T}_{clad}] \times 10^{-6}.$$

The simulation of a closed loop composed of these equations shows that a self excited undamped oscillation occurs as a result of the step input of $k_{ex} = +0.003$.

Figure IV-20-1b shows the root locus plot for this case. The prompt positive term results in the addition of a zero at $s = 0.22$ in the right half plane. The added pole at $s = -2$ is produced by the simple lag being added to the negative feedback term. The presence of the pole at $s = -2$ causes the locus branch formerly extending to infinity along the negative real axis to end at $s = -2$. The poles at the ends of the resulting segment move toward each other, meeting at an intermediate point. Here they leave the negative real axis in opposite directions and form a complex conjugate pair corresponding to a damped sinusoidal term in the transient response. This pair enters the right half plane at a point which indicates a sustained oscillation at $\omega = 1.05$ at 49 times the initial power level, in reasonable agreement with the actual response shown in Fig. IV-20-2b. Since power increases above this point, the complex pair again meet on the positive real axis and separate, one approaching the zero at $s = +0.22$, the other approaching $+\infty$. This part of the locus is of interest because the rapid excursion which results as soon as the poles enter the right half plane takes the reactor into a different region of operation in which the root loci are altogether different. Figure IV-20-1b is valid for any power level for $k_{ex}$ less than about ⅓ prompt critical. However, as $k_{ex}$ nears prompt critical the remote negative real pole determined primarily by neutron lifetime approaches the origin, causing the locus to bend even more rapidly toward instability. Figure IV-20-2b indicates that this is apparently what happens; it is a plot of the total feedback $\Delta k$. $k_{eff}$ is the sum of this plus the +0.003 input. Hence at time = 77 sec, $k_{eff}$ is greater than +0.033 and rising rapidly toward prompt critical (+0.00755). This, of course, is an extremely dangerous condition. Any set of conditions which result in $k_{eff}$ approaching prompt critical may be expected to produce instability since a near approach to prompt critical caused by a mild instability will always tend to intensify the condition which caused the instability.

The power level at which instability occurs in this experiment appears quite unrealistically high. However, the steady state feedback gain used is only $(\Delta k/\Delta l)_{s=0} = 0.062$.

### Instability Caused by an Increasing Positive Feedback or an Increasing Time Constant of a Negative Feedback

Increasing the positive feedback, or increasing the time constant of the negative feedback have about the

* In all root locus plots in this paper, the effect of the pole determined by the prompt neutron lifetime is neglected. It would only become important at a power level several orders of magnitude above the core melting point. Its presence, however, assures that at infinite power some of the loci will enter the right half plane, producing instability.

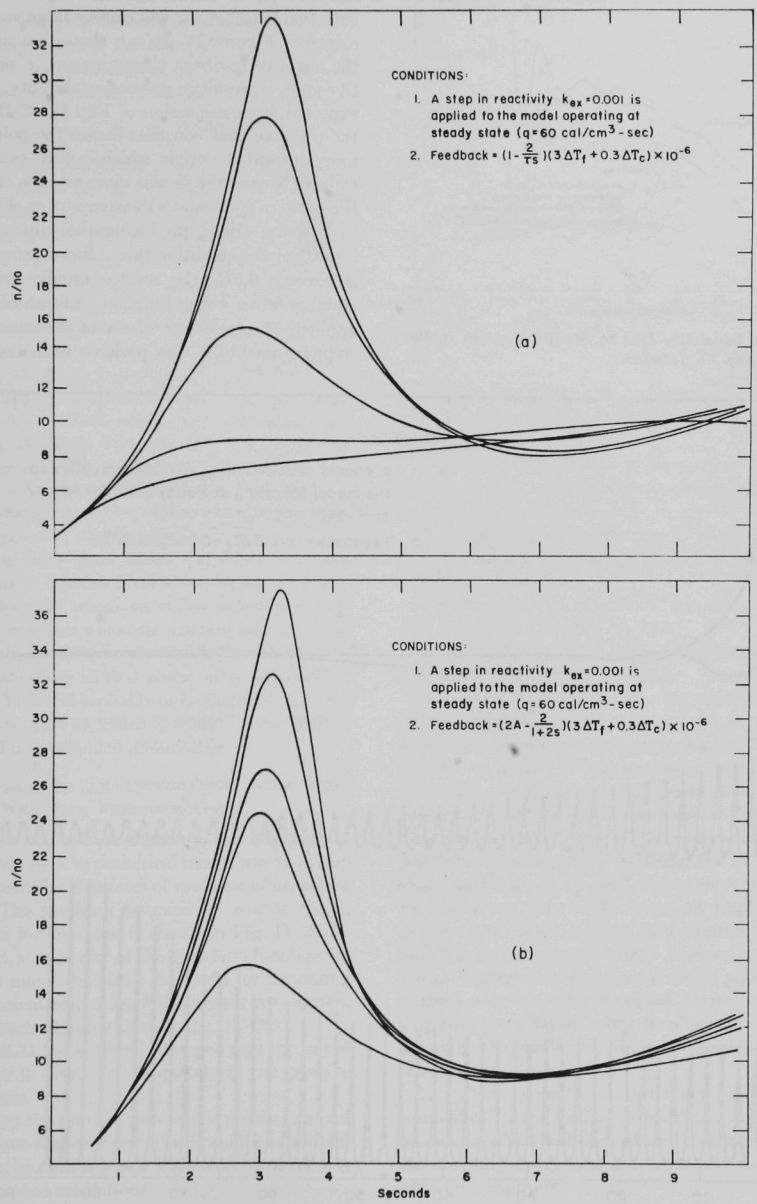


FIG. IV-20-3. (a) Effect of Varying the Time Constant of the Negative Feedback, (b) Effect of Variation in the Positive Feedback. *ANL Neg. No. 112-8729.*

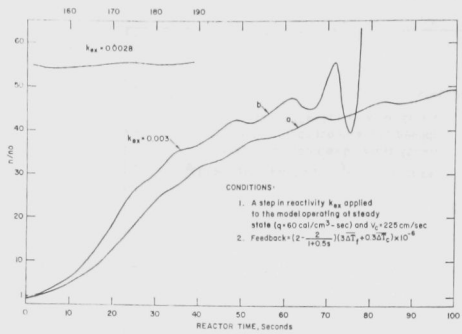


FIG. IV-20-4. Instability Due to Small Variations in Reactivity. *ANL Neg. No. 112-8726.*

same effect, as shown by Figs. IV-20-3a,b. A small variation in either one will cause a large variation in the response. Figures IV-20-3a,b show that an increase in the negative feedback time constant, $\tau$, or in the positive gain, $A$, result in decreasing stability. This may be expected from inspection of Fig. IV-20-1b. Increasing the negative time constant causes the pole $s = -2$ to move toward the origin which in turn causes the locus to bend toward the $j\omega$ axis more rapidly. An increase of the positive gain causes the zero at $s = +0.22$ to move toward the origin, producing the same effect on the locus. For the condition that either $\tau$ exceeds 1.3 sec or $A$ exceeds 0.575, the reactor rapidly approaches instability when a step function addition of reactivity is applied. The rapid rate of rise of the initial part of the response results in the positive term dominating for

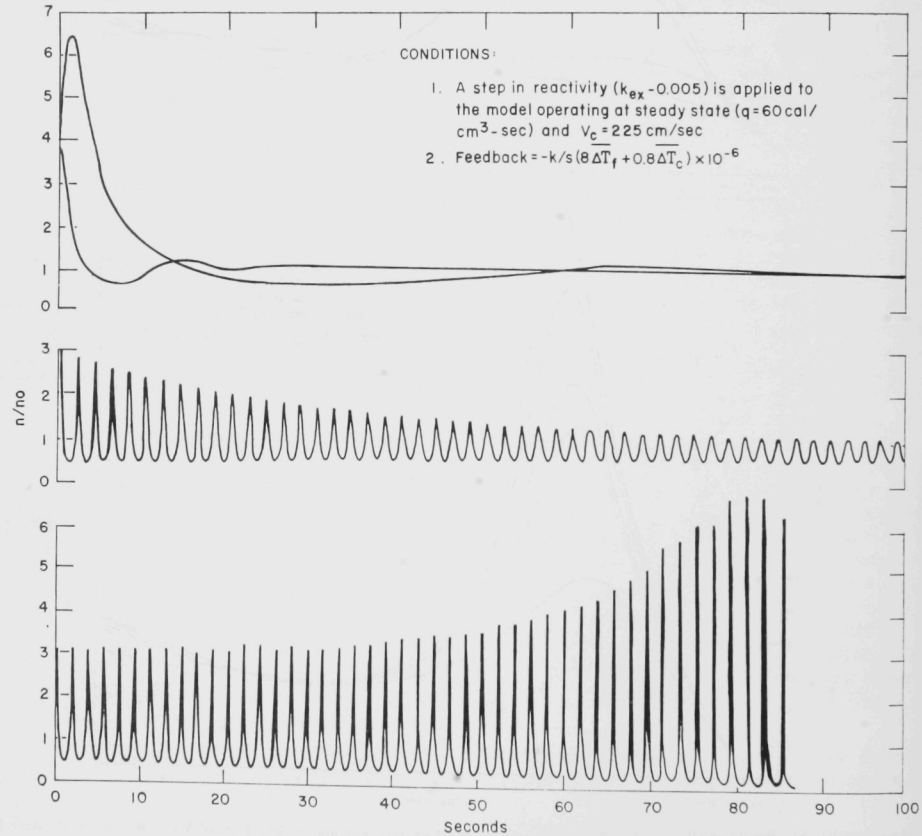


FIG. IV-20-5. Instability with Negative Feedback. *ANL Neg. No. 112-8727.*

some time due to the lag imposed on the negative term. Hence during this period the net feedback is positive and the reactor is driven rapidly to a high power and $k_{eff}$ approaches prompt critical at the power peak.

### Instability due to Small Perturbations

When increasing the power level of a reactor, it is well to know its response characteristics. A rather extreme condition is presented to show how sensitive it can be to small variations in reactivity. The feedback used is again a delayed negative feedback plus a smaller prompt positive feedback.

If the reactor is brought to full power by the introduction of a source of excess reactivity ($k_{ex} = 0.0028$) the reactor comes up to full power and it stabilizes itself (curve *a*, Fig. IV-20-4). If during the period when the reactor is coming up to power, a small step disturbance amounting to $k_{ex} = 0.005$ occurs, the reactor becomes unstable (Fig. IV-20-5). The sensitivity of the reactor is further emphasized by the fact that if the initial step in reactivity is increased to 0.003 the reactor automatically becomes unstable without any extraneous disturbance (curve b, Fig. IV-20-4).

Note that in both cases where instability occurred, the reactor was at a power level *below* the final value to which it settled and remained stable in curve a, Fig. IV-20-4. This is a case where the reactor may be stable at a given power when in steady state and then be driven into instability at that power by a rapid rate of rise of power. This will probably only happen at a power level just below that at which it would be unstable in the absence of any intended disturbance.

### Instability due to an Integration with High Negative Feedback Gain

The purpose of this exploratory investigation of variation of gain on a hypothetical model was to obtain some insight into the character of response of an actual reactor core. The feedback assumed $\Delta k = k \times (\Delta l/l)$. The root locus for this case is shown in Fig. IV-20-1c. The roots start at the poles of the open loop function for zero gain and move out along the locus for increasing gain. The transient responses of the reactor core system for a step in reactivity are shown in Fig. IV-20-5.

For $k = -0.31$ the system is damped and the initial surge in power is overcome completely in the positive part of one cycle.

For $k = -3.1$ the roots at zero form a poorly damped complex pair but the feedback is still capable of returning the system to stability at a higher power level in a few rapidly damped oscillations.

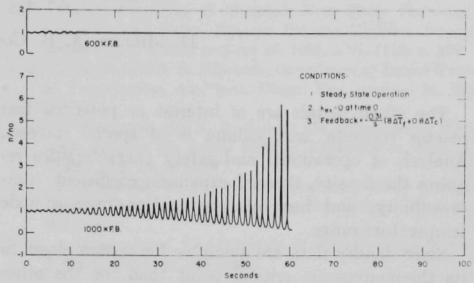


Fig. IV-20-6. Instability with Negative Feedback. *ANL Neg. No. 112-8725.*

For $k = -400$ the damping effect is greatly reduced. The system is resonant with an oscillation of slowly decreasing amplitude.

For $k = -500$ the system is resonant with an oscillation of increasing amplitude, indicating that the poles have just crossed the $j\omega$ axis.

For a gain between 400 and 500 the oscillation will just maintain itself, corresponding to the poles lying exactly on the axis.

The enormous gain necessary for a self-excited oscillation is indicated by Fig. IV-20-6.

It is apparent from this investigation that the hypothetical model is very stable.

Figure IV-20-1c indicates that the loci approach infinity parallel and to the left of the $j\omega$ axis, hence it would not become unstable at any gain. This explains the enormous gain found necessary for instability. At this extremely high gain the remote negative real root has contributed just enough phase shift to bend the locus toward the $j\omega$ axis. The second order pole at zero produces the interesting result that the locus leaves the origin tangent to the $j\omega$ axis. Hence there will always be an oscillatory term in the transient response for gain greater than zero, and as gain approaches zero the oscillations will approach zero damping. Such a very low gain integration could occur due to poisoning; hence if there were no other feedback terms, an extremely long period oscillation might be observed since without damping the mode would be continually excited by random disturbances.

$k_{ex}$, which is usually an arbitrary function of time, is modified by the feedbacks which are functions of the system variables and their derivatives. Reactor systems are in nearly every case nonlinear and must be simulated on computers.

# IV-21. Properties of Alkali Metals[1]

D. Miller, A. B. Cohen and C. E. Dickerman

The alkali metals are of interest as potential fast reactor coolants, and sodium is of special interest. Analysis of operational and safety characteristics requires the density, thermal expansion coefficient, compressibility, and heat of vaporization over a wide temperature range.

Since density data are available for cesium closer to its thermodynamic critical point than for the other alkali metals, theoretical and empirical relations were used to estimate its critical temperature, density, and pressure after testing the technique with the known characteristics of $CO_2$ and mercury. The estimated critical temperature and experimental heat of vaporization data were used to construct the relation between the entropy of vaporization and reduced temperature; i.e., the absolute temperature divided by the critical temperature. Because of the lack of sufficient high temperature data for the other alkali metals, cesium was used as the "corresponding states" model for the other metals in a method similar to the estimation technique of A. Grosse,[2] who used mercury. Since mercury has two valence electrons and the alkali metals have only one, it is believed that this procedure represents an improvement over the estimates of Grosse. Estimates of the critical constants were then used with experimental data to extrapolate properties to the critical point. These estimates are given in Table IV-21-I.

TABLE IV-21-I. Estimated Critical Constants of the Alkali Metals

| Material | Critical Temperature $T_c$, °K | Critical Density $\rho_c$, g/cc | Critical Pressure $P_c$, atm | Critical Compressibility, $Z_c$ |
|---|---|---|---|---|
| Li | 4310 ± 100 | 0.0637 | 985 | 0.3032 |
| Na | 2733 ± 40 | 0.1818 | 408.2 | 0.2302 |
| K | 2287 ± 40 | 0.1805 | 168.6 | 0.1946 |
| Rb | 2164 ± 40 | 0.3314 | 178.6 | 0.2594 |
| Cs | 2040 ± 40 | 0.4043 | 113.7 | 0.2233 |

TABLE IV-21-II. Coefficients and Exponents for Equations (1), (2), (3), and (4)

| Material | $\rho_{LR} - 1$ | | $1 - \rho_{VR}$ | | $\Delta H_v/RT_c$ | | Rectilinear Diameter Constants | |
|---|---|---|---|---|---|---|---|---|
| | $A_L$ | $B_L$ | $A_V$ | $B_V$ | $A_H$ | $B_H$ | $C$, g/cc | $D$, (g/cc-°K) × $10^{-4}$ |
| Li | 8.785 | 0.792 | 1.143 | 0.227 | 4.78 | 0.296[a] | 0.2858 | 0.532 |
| Na | 4.097 | 0.682 | 1.422 | 0.389 | 4.83 | 0.377 | 0.5082 | 1.194 |
| K | 3.702 | 0.513 | 1.329 | 0.293 | 4.55 | 0.282 | 0.4554 | 1.202 |
| Rb | 3.722 | 0.625 | 1.582 | 0.424 | 4.61 | 0.301 | 0.8168 | 2.232 |
| Cs | 3.636 | 0.559 | 1.158 | 0.187 | 4.75 | 0.327 | 1.0150 | 2.939 |

[a] Based on values from the Clapeyron equation.

The asymptotic relations that were used for behavior in the critical region were:

*Vapor Density*,[3] $\rho_V$,

$$(l - \rho_{VR}) = A_V(l - T_R)^{B_V}, \quad \text{for} \quad T_R > 0.65, \tag{1}$$

where

$$\rho_{VR} = \rho_V/\rho_c \quad \text{and} \quad T_R = T/T_c;$$

*Liquid Density*,[3] $\rho_L$,

$$(\rho_{LR} - l) = A_L(l - T_R)^{B_L}, \tag{2}$$

where

$$\rho_{LR} = \rho_L/\rho_c;$$

*Heat of Vaporization*,[4,5] $\Delta H_v$

$$\frac{\Delta H_v}{RT_c} = A_H(l - T_R)^{B_H}, \tag{3}$$

where $R$ is the gas constant.

Also the "law of the rectilinear diameter"[2] was used:

$$\frac{\rho_L + \rho_V}{2} = C - DT = \rho_c + D(T_c - T) \tag{4}$$

or

$$\frac{\rho_{LR} + \rho_{VR}}{2} = 1 + \frac{DT_c}{\rho_c}(l - T_R); \tag{5}$$

and the relation[3,6]

$$\frac{\rho_{LR} - \rho_{VR}}{2} = A(1 - T_R)^B, \tag{6}$$

The latter comes from the lattice gas model of the critical point or is an empirical generalization of the work of E. Guggenheim.[7] Constants fitted to these equations for the alkali metals are given in Table IV-21-II and these may be used to estimate the properties where no experimental data exist.

Details of the estimation technique, thermal expan-

sion, compressibility, and other results for sodium have been accepted for publication.[1]


REFERENCES

1. D. Miller, A. B. Cohen and C. E. Dickerman, *Estimation of Vapor and Liquid Density and Heat of Vaporization of the Alkali Metals to the Critical Point*, Proc. International Conference on the Safety of Fast Breeder Reactors, Aix-en Provence, France, September 19–22, 1967, (to be published).
2. A. V. Grosse, *The Temperature Range of Liquid Metals and an Estimate of their Critical Constants*, J. Inorg. Nucl. Chem. **22**, 23 (1961).
3. D. Miller, *Properties of Materials Near Their Thermodynamic Critical Point*, Reactor Physics Division Annual Report, July 1, 1964 to June 30, 1965, ANL-7110, p. 398.
4. J. J. Martin and J. B. Edwards, *Correlation of Latent Heats of Vaporization*, Am. Inst. Chem. Eng. Journal **11**, 331 (1965).
5. D. S. Viswanath and N. R. Kuloor, *On a Generalized Watson's Relation for Latent Heat of Vaporization*, Can. J. Chem. Eng. **45**, 29 (1967).
6. L. P. Kadanoff, et al., *Static Phenomena Near Critical Points—Theory and Experiments*, Rev. Mod. Phys. **39**, 395 (1967).
7. E. A. Guggenheim, *The Principle of Corresponding States*, J. Chem. Phys. **13**, 253 (1945).


## IV-22. Physical Properties of Solids and Liquids Under Extreme Conditions

D. MILLER

Evaluations of potential hazards of nuclear reactors require a knowledge of the equation of state to serve as a link between the rate of energy input from the time variation of the nuclear reactions and the changes in temperature, density, and geometry which ultimately terminate the chain reaction. Several techniques for the estimation of relations between the variables of energy, temperature, density, and pressure are under study.

The great diversity of reactor materials and the inadequate knowledge of their properties under compression and high temperatures necessitates investigation of the possibility of generalizing experimental data and obtaining unified relations describing a specific class of materials which would allow extrapolation to other materials. While such generalizations are not precise, the applied nature of the problem and the paucity of data justify the approximate nature of the approaches.

### MECHANICAL EQUATION OF STATE

One important source of information is the shock compression of materials by the use of materials in contact with explosives or the impact of materials moving at high velocity.

Since the transient stresses generated can be much greater than the shear strength of the solids, the stress system is effectively isotropic and thus equivalent to a hydrostatic pressure. Since the compressibility of solids and liquids increases with increasing pressure, a simple compressive wave builds up to a shock wave across which the dynamic and thermodynamic quantities change discontinuously.

A shock transition is described by the Rankine-Hugoniot equations relating the pressure, $P$, specific volume, $V$, or density, $\rho = 1/V$, specific internal energy, $E$, and material velocity, $v$, across the shock front to the shock velocity, $U$. If the variables ahead of the wave front are designated by the subscript 0, and if velocities are measured relative to the material velocity ahead of the wave, then conservation of mass, momentum, and energy yields,

$$\rho_0 U = \rho(U - v), \tag{1}$$

$$P - P_0 = \rho_0 U v, \tag{2}$$

$$E - E_0 = \tfrac{1}{2}(P + P_0)(V_0 - V). \tag{3}$$

Equation (3) defines a unique curve in the $P$-$V$ plane, called the Hugoniot curve, which is the locus of all possible states attainable by a single shock transition from a given initial state $P_0$, $V_0$. It can be shown[1] that the Hugoniot curve makes second order contact with the adiabat through $P_0$, $V_0$ and then diverges to regions of higher entropy. This feature enables the synthesis of the adiabats from the Hugoniot behavior. Since the temperature rise for small adiabatic compressions is negligible, this also enables the estimation of the isothermal or "cold" compression behavior.

A convenient model of material behavior is the elastic-perfectly plastic behavior shown in Fig. IV-22-1, where $Y$ is the simple tensile yield stress of this material. In the situation corresponding to this figure, the elementary theory of elastic-plastic uniaxial compression predicts that only an elastic wave will be produced on impact until the impact stress in the $x$ direction, $\sigma_x$,

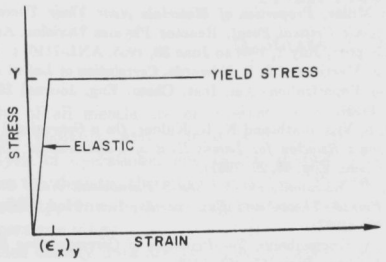


FIG. IV-22-1. Ideal Elastic-Plastic Material. *ANL Neg. No. 112-9441.*

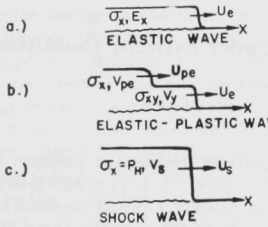


FIG. IV-22-2. Wave Patterns in Solids. *ANL Neg. No. 112-9439.*

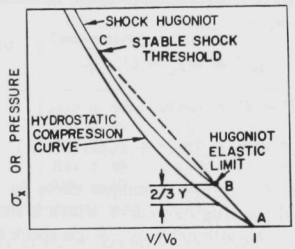


FIG. IV-22-3. Stress-Strain Curves for Compression of an Isotropic Solid. *ANL Neg. No. 112-9414.*

exceeds

$$\frac{\lambda + 2\mu}{2\mu} Y,$$

where $\lambda$ and $\mu$ are the elastic Lamé constants of the material and related to Young's modulus, $E$, and Poisson's ratio, $\nu$, by

$$\mu = \frac{E}{2(1+\nu)} \quad \text{and} \quad \lambda = \frac{E\nu}{(1+\nu)(1-2\nu)}.$$

For stresses less than this value, the conditions across the elastic wave are given by

$$\sigma_x = \rho_0 U_e v_0 \tag{4}$$

and

$$\sigma_x = (\lambda + 2\mu)\epsilon_x = -(\lambda + 2\mu)\frac{\Delta V}{V\Delta_0}, \tag{5}$$

where

$V_0 \equiv$ velocity of the disturbance
$U_e \equiv$ plane elastic wave velocity
$\epsilon_x \equiv$ strain component in the $x$ direction $(= -\Delta V/V_0)$.

This elastic segment of the stress-strain relation is represented by the segment AB in Fig. IV-22-2.

Beyond the yield point, theory predicts that the stress-strain relation becomes

$$\sigma_x = p_H + \frac{2}{3} Y, \tag{6}$$

where $P_H$ is the hydrostatic stress at the same volumetric strain $\Delta V/V_0 = -\epsilon_x$. Values of $P_H$ can be obtained by correcting hydrostatic isothermal compression data to adiabatic conditions or by extrapolating high-pressure-shock Hugoniot curves to lower pressures. In this material regime, BC in Fig. IV-22-3, an elastic-plastic wave structure (as shown in Fig. 2b) is produced.

The conditions across the elastic wave are given by Eqs. (4) and (5) as

$$\sigma_{x_y} = \rho_0 U_e v_y \tag{7}$$

and

$$\sigma_{x_y} = +(\lambda + 2\mu)\epsilon_y, \tag{8}$$

where the subscript $y$ denotes conditions at the yield point. The conditions across the plastic wave are given by applying the Rankine-Hugoniot relations, which give

$$\sigma_x - \sigma_{x_y} = \rho_y (U_{pe} - v_y)(v_0 - v_y) \tag{9}$$

and

$$U_{pe} - v_y = V_y \sqrt{\frac{\sigma_x - \sigma_{x_y}}{V_y - V_{pe}}}, \tag{10}$$

where $U_{pe}$ is the plastic wave velocity and $V_{pe}$ is the specific volume behind the plastic wave.

As the impact velocity is increased even further, a stage is reached, point C in Fig. IV-22-3, where the plastic wave overtakes the elastic wave and a stable shock is produced (as shown in Fig. IV-22-2c). This is characterized by the condition

$$\frac{\sigma_x}{V_0 - V_y} \geq \frac{\sigma_x - \sigma_{x_y}}{V_y - V_{pe}}.$$

In most cases $Y \ll P$ when the stable shock condition has been reached and Eq. (6) can then be simplified without much error to $\sigma_x \approx P_H$ and the solid may be treated as a fluid. Since the values of $Y$ determined from the plastic waves may differ by factors of two or three from the statically measured values, the point B is called the Hugoniot elastic limit to distinguish it.

As the initial shock strength is increased, the excess entropy due to the release process being along an adiabat leaves the material heated and can result in melting, vaporization, or superheating in the final state.

Over a wide range of shock compression and pressure, the experimental data within a given phase show an empirical linear relation,

$$U = U_0 + Sv, \tag{11}$$

where $U_0$ is the limiting plastic wave velocity calculated from

$$U_0 = (B/\rho_0)^{1/2}, \tag{12}$$

where $B$ is the bulk modulus, which should be taken at the pressure corresponding to the onset of the stable shock but is only slightly different from the zero pressure value. D. Pastine and D. Piacesi[2] have tried to explain the shock behavior by using the sonic velocity at zero pressure in a theory including a term in $v^2$ in Eq. (11) without considering the elastic-plastic behavior. Analysis of recent data on an aluminum alloy at 700°K and 310 kbar gives a value of 13 kbar for $Y$ versus 2.5 kbar for the uncompressed material.[3]

It can be shown that the change of the bulk modulus with pressure is given by

$$\frac{\partial B}{\partial P} = 4S - 1. \tag{13}$$

The shear modulus, $G$, is related by

$$G = \frac{3}{2}\frac{1 - 2\nu}{1 + \nu} B \tag{14}$$

and

$$E = \frac{B}{3(1 - 2\nu)}. \tag{15}$$

Examination of experimental results has shown that the assumption of constant $\nu$ is a good approximation.

Plots of the temperature dependent shear modulus versus volume at atmospheric pressure indicate that reasonably straight lines may be obtained if $G$ is raised to some power close to unity, and this modulus goes to zero at a point close to the liquid volume at the melting point as expected.[3] Coupling of the pressure dependence and temperature dependence of the shear modulus and of the yield strength (which is very dependent on the history of the sample) should produce a self-consistent model which can be used in accident calculations.

Equation (13) is the link between the mechanical and thermodynamic equations of state.

## Thermodynamic Equation of State

Calculation of the pressure and energy can be made as a function of temperature and density explicit equations of state previously given[4]:

$$P(\rho,T) = P_k(\rho) + \gamma(\rho)\rho C_v T + \tfrac{1}{4}\rho_0\beta_0(\rho/\rho_0)^{1/2}T^2, \tag{16}$$

$$E(\rho,T) = E_k(\rho) + C_v T + \tfrac{1}{2}\beta_0 T^2(\rho/\rho_0)^{1/2}, \tag{17}$$

$$P_k = \rho^2 \frac{\partial E_k}{\partial \rho}, \tag{18}$$

where $P_k$, $E_k$ are respectively the "cold" compression pressure and energy; $\gamma$ is the Grüneisen ratio; $C_v$, the heat capacity at constant volume; $T$, the temperature; and $\beta_0$ is the electronic contribution to the heat capacity. Alternately,[4] the Debye approximation to the equations of state can be used.

The cold compression pressure, $P_k$, must be known as a function of density from experiments, calculations from an assumed form of the interatomic potential, or estimated from generalized correlations. O. Anderson[5] has shown that the Murnaghan equation

$$P = \frac{B_T^0}{B_T'}\left[\left(\frac{V_0}{V}\right)^{B_T'} - 1\right], \tag{19}$$

where $B_T^0$ and $B_T'$ are constants in the pressure expansion of the isothermal bulk modulus, $B_T(P)$,

$$B_T(P) = -V\left(\frac{\partial P}{\partial V}\right)_T = B_T^0 + B_T' P + \cdots \tag{20}$$

accurately represented the data, taken in static compression and with shock waves for MgO and $Al_2O_3$ and several metals, over a very wide range of pressure. Pastine and Piacesi[2] and others have shown that these constants are very close to the adiabatic values determined by acoustic techniques:

$$B_S = -V\left(\frac{\partial P}{\partial V}\right)_S = \rho C_S^2 = B_S^0 + B_S' P, \tag{21}$$

where the subscript $S$ indicates the adiabatic condition, and that the small differences can be calculated from thermodynamic properties.

The Hugoniot relations, Eqs. (1), (2), and (3), can be combined to give the pressure, $P_H$, along the shock compression curve to yield (if the initial pressure is negligible),

$$P_H = \frac{\rho_0 C^2(1 - \rho_0/\rho)}{[1 - S(1 - \rho_0/\rho)]^2}. \tag{22}$$

TABLE IV-22-I. CONSTANTS IN EQUATION OF STATE

| Material | $\rho_0$, g/cc | $B_T^0$, kbar | $B_T'$ | $B_S$, kbar | $B_S'$ | $\theta$, °K | $\gamma$ | $S$ | $4S-1$ |
|---|---|---|---|---|---|---|---|---|---|
| U | 19.04 | 987 | 8.38 | | | 222 | 1.91 | 1.504[a] | 5.02 |
| $UO_2$ | 10.97 | 500[a] | 4.75[a] | 470 | | 154 | 1.88 | 1.438[a] | 4.75 |
| UC | 13.61 | 1700[a] | 5.22[a] | 1636 | | 320 | 2.11 | 1.555[a] | 5.22 |
| Pu | 19.79 | 457 | 8.65 | | | 178 | 2.56 | 1.780[a] | 6.12 |
| Li | 0.545 | 123 | 3.6 | | | 390 | 1.18 | 1.154 | 3.62 |
| Na | 0.971 | 74 | 3.95 | 67.5 | 3.85 | 150 | 1.17 | 1.242 | 3.97 |
| K | 0.87 | 37 | 3.85 | 30.8 | 3.77 | 93 | 1.30 | 1.188 | 3.75 |
| Fe | 7.84 | 1780 | 5.0 | 1667 | 5.04 | 467 | 1.60 | 1.58 | 5.32 |
| W | 19.35 | 3080 | 4.2 | | | 310 | 1.54 | 1.27 | 4.08 |
| Ta | 16.68 | 2005 | 5.3[a] | 1897 | | 230 | 1.68 | 1.214 | 3.86 |
| Al | 2.785 | 789 | 4.27 | 764 | 5.08 | 435 | 2.18 | 1.39 | 4.56 |
| Cu | 9.02 | 1310 | 5.20 | 1370 | 5.51 | 315 | 2.06 | 1.514 | 5.06 |
| Hg (liq.) | 13.55 | 245.4 | 8.71 | 214 | 8.82 | 92 | 1.51 | 2.068 | 7.27 |
| NaCl | 2.02 | 234.2 | 5.35 | 247 | 5.27 | 326 | 1.54 | 1.541 | 5.164 |
| $SiO_2$ (fused) | 2.20 | 371 | 6.33 | 365 | 6.15 | 490 | 0.746 | 1.56 | 5.24 |
| BeO | 3.01 | 2430 | 5.04 | 2520 | | 1280 | 1.97 | 1.36 | 4.44 |
| MgO | 3.65 | 1691 | 3.95 | 1717 | 3.915 | 946 | 1.60 | 1.223 | 3.892 |

[a] Estimated.

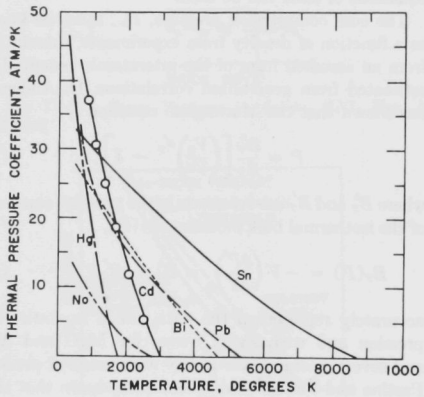


FIG. IV-22-4. Thermal Pressure Coefficient for Liquid Metals. *ANL Neg. No. 112-9420.*

Using the fact that there is a second order contact at $\rho = \rho_0$ between the Hugoniot pressure curve and the adiabatic compression curve in the Murnaghan form,

$$P_S = \frac{B_S^0}{B_S'}\left[\left(\frac{\rho}{\rho_0}\right)^{B_S'} - 1\right], \tag{23}$$

one can find that $B_T' \approx B_S' = 4S - 1$, which is given as Eq. (13). Since it has been shown[4] that

$$S = \frac{\gamma + 1}{2}, \tag{24}$$

where $\gamma$ is the Grüneisen coefficient and has the thermodynamic definitions

$$\gamma = \frac{\alpha B_S}{\rho C_p} = \frac{\alpha B_T}{\rho C_v} = \frac{(P - P_k)}{\rho(E - E_k)}; \tag{25}$$

$\alpha$ is the volumetric expansion coefficient

$$(1/V)(\partial V/\partial T)_P$$

and $C_p$ and $C_v$ are the heat capacity at constant pressure and volume. Equations (13) and (24) can be combined to give

$$B_S' = 2\gamma - 1 \cong B_T' \tag{26}$$

which relates the bulk modulus and its pressure derivative.

Values of some of the constants needed for the calculation of the cold compression or shock equation of state are given in Table IV-22-I for some materials of reactor and theoretical interest.

An additional relation for materials is the thermal pressure coefficient

$$\left(\frac{\partial P}{\partial T}\right)_v = \alpha_P B_T, \tag{27}$$

which can be used to determine the pressure change in a confined space due to a temperature rise:

$$\begin{aligned}\Delta P &= \int \left(\frac{\partial P}{\partial T}\right)_v dT + \int \left(\frac{\partial P}{\partial V}\right)_T dV \\ &= \int \alpha_P B_T \, dT - \int B_T \frac{dV}{V}.\end{aligned} \tag{28}$$

Values of the thermal pressure coefficient for several molten metals were calculated from various data[6,7] and found to smoothly extrapolate to zero at the esti-

mated critical temperatures, as expected. These are plotted in Fig. IV-22-4. For sodium and mercury the compressibility increases by 7.8 and 14.6 percent, respectively, in the melting process. While no generalization is apparent, these results will be applied to other materials to see the effect of the melting transformation, and extension will be made to reactor fuel materials.

### References


1. R. Courant and K. O. Friedrichs, *Supersonic Flow and Shock Waves* (Interscience Publishing Co., New York, 1948), p. 142.
2. D. J. Pastine and D. Piacesi, *The Existence and Implications of Curvature in the Relation between Shock and Particle Velocities for Metals*, J. Phys. Chem. Solids **27**, 1783–1792 (1966).
3. M. van Thiel and A. Kusubov, *Elastoplastic Wave Structure in Aluminum Generated by a Tangentially Accelerated Flying Plate*, UCRL-50001-66-2 (November 1966), p. 45.
4. D. Miller, *A Critical Review of the Properties of Materials at the High Temperatures and Pressures Significant for Fast Reactor Safety*, Proc. Conference on Safety, Fuels, and Core Design in Large Fast Power Reactors, October 11–14, 1965, ANL-7120, pp. 641–653.
5. O. L. Anderson, *Two Methods for Estimating Compression and Sound Velocity at Very High Pressures*, Proc. Nat. Acad. Sci. USA **54**, 667–673 (1965).
6. A. B. Coppens, R. T. Beyer, and J. Ballou, *Parameter of Non-linearity in Fluids. III. Values of Sound Velocity in Liquid Metals*, J. Acoust. Soc. Am. **41**, 1443–1448 (1967).
7. L. A. Pronin and S. I. Filippov, *State of Liquid Metals Determined on the Basis of Acoustical Data*, (in Russian) Izv. vys. Ch. Met. (5), 10–18 (1963). Available in English as ANL Trans-486.


## IV-23. Physical Properties of Uranium Monocarbide at the Melting Temperature and in the Liquid State

H. K. Richards

### Experimental Methods

A high temperature tungsten filament furnace[1] has been used to measure thermal expansion coefficients of uranium monocarbide in the solid and liquid state, including the change in volume at melting. In addition, compatibility of UC with a TaC crucible has been studied.

Figure IV-23-1 shows the furnace as it was used for these experiments. With respect to the furnace described in Ref. 1, this furnace is a modified version, providing a molybdenum ring support for the tungsten reflector. Figure IV-23-2 illustrates further details of the TaC crucible, graphite contact rod and the pedestal. The pedestal material was originally graphite but it was found that at temperatures exceeding 2600°C the graphite evaporated rapidly and attacked the tungsten heater element (probably by formation of a tungsten carbide of lower melting temperature). The tungsten filaments failed repeatedly at temperatures above 2700°C and it was observed that they had melted. Substitution of a tantalum carbide pedestal eliminated this condition.

The original technique devised to measure UC expansion consisted of measuring the distance between the cover and the bottom of the empty crucible, and then measuring the distance between the cover and the UC level, using a high frequency beat method.[2] However, above 1700°C a large dc current was observed that made this method inapplicable and it was found necessary to measure a direct contact between the upper and lower portion of the crucible and a disc on an insulated probe (Fig. IV-23 2). The disc shown in Fig. IV-23-2 permitted a contact to be made with the upper portion of the crucible and either the bottom of the crucible or the top surface of the UC. This contact was observed at the ammeter in connection with a power supply connected between the insulated probe

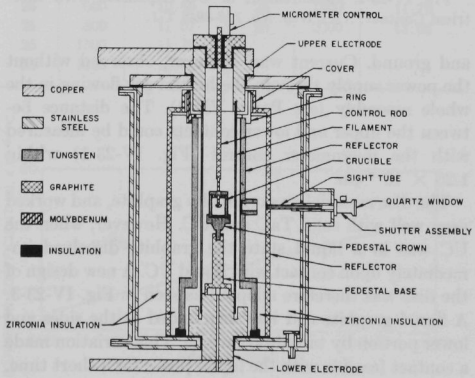


Fig. IV-23-1. Modified High Temperature Furnace with W. and Graphite Reflectors, Pedestal and Crucible. *ANL Neg. No. 112-7453 Rev. 1*

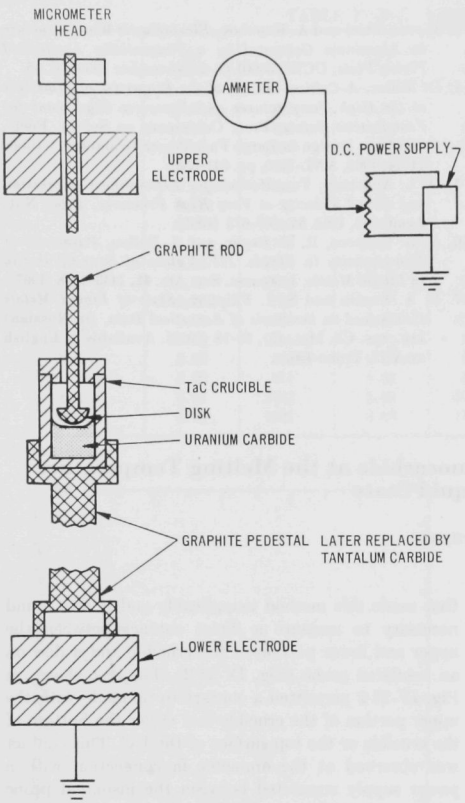


FIG. IV-23-2. Measurement of UC Expansion with Electrical Contact. *ANL Neg. No. 112-8943 T-1.*

and ground. Current was, however, observed without the power supply through the helium gas flowing in the whole assembly (see Paper VII-3). The distance between the upper and lower contacts could be measured with the micrometer control (Fig. IV-23-1) within $1.25 \times 10^{-3}$ cm.

The disc material was originally graphite, and worked very well with solid TaC and UC. However, when the UC was in a liquid state the graphite dissolved immediately upon contact with liquid UC. A new design of the disc was therefore adopted as seen in Fig. IV-23-3. A flared graphite end was surrounded at the sides and lower portion by tantalum carbide. This variation made a contact feasible with the liquid phase for a short time.

The measurements were performed by determining at a given temperature the distance between the UC surface or the crucible bottom and the upper position; that is, the contact of the disc with the crucible cover (Fig. IV-23-2). As may be seen the opening of the cover permits free movement of the graphite rod and contact between the cover inner surface and the flat portion of the disc.

A certain time is required for a heat equilibrium, before the disc contact position remains constant as read at the micrometer in Fig. IV-23-1. The next contact is established with the bottom of the crucible, or the UC level. Since an additional length, $L$, of the graphite rod enters the hot region, it again takes a certain time before equilibrium is established. From previous measurements with materials of known expansion coefficients it was found that movement of this portion produces an expansion of the whole graphite rod equivalent to the thermal expansion of the length $L$ upon being introduced into the hot section. This graphite expansion can be calculated (see Fig. IV-23-4) with the aid of Ref. 3.

The expansion coefficients of the UC can only be determined if the expansion of the TaC crucible is known in addition to that of the graphite rod. Table IV-23-I shows expansion coefficients reported for TaC.[4] Figure IV-23-5 includes the coefficients given

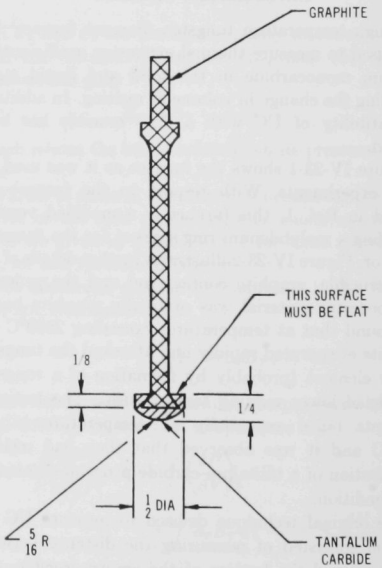


FIG. IV-23-3. Graphite Rod with Tantalum Carbide End Piece. *ANL Neg. No. 112-8812.*

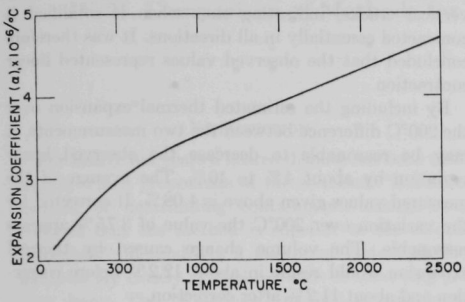


FIG. IV-23-4. Linear Expansion Coefficients of ATG Graphite in Direction of Grain. *ANL Neg. No. 112-8906.*

TABLE IV-23-I. AVERAGE TaC-EXPANSION COEFFICIENTS, 'α'

| Temp., °C | | α' (ΔL/L), °C × 10⁻⁶ | Temp., °C | | α' (ΔL/L), °C × 10⁻ |
|---|---|---|---|---|---|
| From | To | | From | To | |
| 25 | 500 | 6.32 | 25 | 800 | 8.2 |
| 25 | 1000 | 6.76 | 20 | 2380 | 8.2 |
| 25 | 1500 | 7.12 | 20 | 500 | 6.29 |
| 25 | 2000 | 7.65 | 20 | 1000 | 6.50 |
| 25 | 2500 | 8.40 | 20 | 1200 | 6.64 |
| | | | 20 | 2625 | 8.02 |

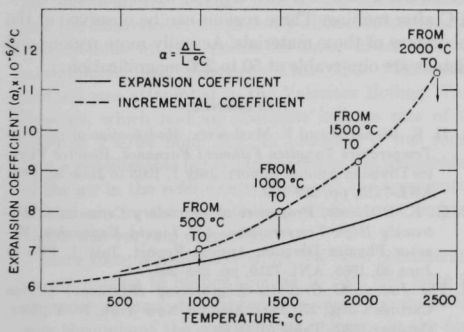


FIG. IV-23-5. Linear Expansion Coefficients of Tantalum Carbide. *ANL Neg. No. 112-8904.*

in the first column of Table IV-23-I as a solid line and the incremental values for the temperatures marked are given by the dashed line. Figure IV-23-6 gives TaC expansion coefficients obtained from measurements with a TaC crucible used for the present experiments. The graph represents the average of many runs with an estimated error of 6 × $10^{-7}$/°C.

## MEASUREMENTS OF UC EXPANSION COEFFICIENTS IN THE SOLID STATE

For comparison, Table IV-23-II presents UC expansion coefficients, α, reported previously.[5] Additional data up to 1445°C may be found in Ref. 6.

Figure IV-23-7 shows the results of measurement of sintered UC found with the method described above, where the expansion of the TaC and the graphite rod have been taken into account. The expansion coeffi-

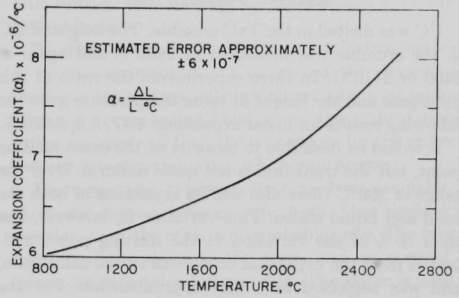


FIG. IV-23-6. Linear Expansion Coefficients of Tantalum Carbide Measured with Tantalum Carbide Crucible. *ANL Neg. No. 112-8905.*

TABLE IV-23-II. AVERAGE EXPANSION COEFFICIENTS, α', for UC

| Temp., °C | | α' (ΔL/L), °C × 10⁻⁶ | Temp., °C | | α' (ΔL/L), °C × 10⁻⁶ |
|---|---|---|---|---|---|
| From | To | | From | To | |
| 25 | 200 | 9.47 | 25 | 500 | 7.26 |
| 25 | 400 | 10.30 | 25 | 1000 | 10.67 |
| 25 | 600 | 10.68 | 25 | 1500 | 11.79 |
| 25 | 800 | 11.01 | 25 | 2000 | 13.05 |
| 25 | 1000 | 11.23 | | | |
| 25 | 1200 | 11.43 | | | |

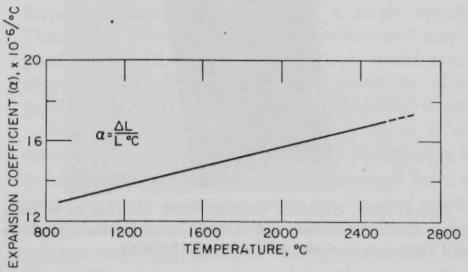


FIG. IV-23-7. Linear Expansion Coefficients of Uranium Carbide. *ANL Neg. No. 112-8907.*

cients are given here up to 2400°C. Actually UC was observed in a solid state even at 2500°C. From observations made during these experiments, it appears that the melting point of the UC sample occurred close to 2550°C. This value is close to that of 2590°C, as reported by P. C. Hiotti,[7] and different from the 2450°C usually accepted. The values in Fig. IV-23-7, somewhat higher than reported in Table IV-23-II, are the result of several careful determinations.

### Linear and Volume Changes at the Melting Point of UC

UC was melted in the TaC crucible. The height of UC in the crucible was measured at 2600°C and again at 2400 or 2410°C. In three experiments the ratio of this difference and the height at room temperature gave the following results for linear expansion: 4.47, 3.8, 3.975%.

It would be desirable to measure at the exact melting point, but the transition is not quite uniform. Over the range of 200°C there also will be expansion in both the solid and liquid states. This variation is, however, less than 10% of the variation at the melting point, estimated from the expansion coefficient in the solid state, and was neglected as a first approximation. For the foregoing numbers to be interpreted properly, however, it is necessary to determine if the measurements represent a linear or a volume change. From a later inspection of the material it was seen that the UC had many vertical cracks, indicating that when it solidified it contracted essentially in all directions. It was therefore concluded that the observed values represented linear contraction.

By including the estimated thermal expansion over the 200°C difference between the two measurements, it may be reasonable to decrease the observed linear variation by about 4% to 10%. The average of the measured values given above is 4.08%. If corrected for the variation over 200°C the value of 3.75% appears reasonable. The volume change caused by thermal expansion would result in about 12.2% before correction and about 11.2% after correction.

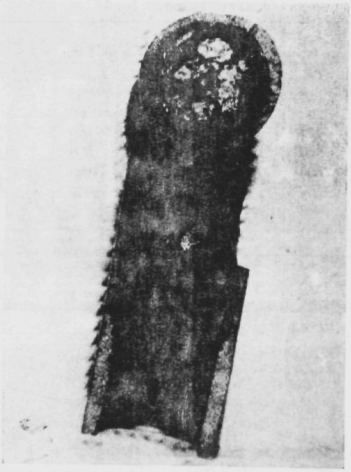

Fig. IV-23-8. Uranium Carbide After Melting in a Tantalum Carbide Crucible and Interaction of Uranium Carbide and Tantalum Carbide. *ANL Neg. No. 112-8903.*

### Volume Changes in the Liquid State

Measurements in the liquid state refer to the variation in volume; since the cross section of the crucible also expands, this contribution should be added to the observed expansion.

Only one experiment could be conducted so far. The results are rather uncertain. It appears that the volume expansion between 2650 and 2740°C is about $1.10 \times 10^{-4}$/°C, or $\alpha$(Length) $\sim 36 \times 10^{-6}$/°C. This would be above twice the value of the solid expansion coefficient at 2400°C.

### Interaction of TaC and UC

It was observed that TaC and liquid UC react. Figure IV-23-8 is a view of a TaC crucible broken open to show UC after melting. Three regions can be observed at the boundary of these materials. Actually more regions and details are observable at 50 to 200 magnification.

### References

1. H. K. Richards and E. Maslowicz, *Modification of the High Temperature Tungsten Filament Furnance*, Reactor Physics Division Annual Report, July 1, 1965 to June 30, 1966, ANL-7210, pp. 289–290.
2. H. K. Richards, *Properties of Refractory Ceramics at Extremely High Temperatures: UC Liquid Expansion*, Reactor Physics Division Annual Report, July 1, 1965 to June 30, 1966, ANL-7210, pp. 288–289.
3. *The Industrial Graphite Engineering Handbook*, (Union Carbide Corp., 270 Park Avenue, New York, N. Y., Rev. October 1960) Table 5B.02.02.
4. P. B. Shaffer, *High Temperature Materials, No. 1*, (Plenum Press, New York, N. Y., 1964) p. 116.
5. P. B. Shaffer, *ibid*, p. 129.
6. *Refractor Ceramics for Aerospace; A Materials Selectoin Handbook*, Compiled by Batelle Memorial Inst. (Published by Am. Ceramic Soc., Columbus, Ohio, 1964), p. 148/V.
7. P. C. Hiotti, *Experimental Refractory Bodies of High-Melting Nitrides, Carbides, and Uranium Dioxide*, J. Am. Ceram. Soc., **123**, (1952).

# IV-24. Comparison of Methods for Determining Containment Leakage Rates

R. O. Brittan

## Introduction

For nearly ten years a heated dispute has been underway in which proponents of the so-called "Reference" method of determining containment leakage rates contend that the method is superior to the so-called "Absolute" method. As a matter of fact, both these methods are closely related methods of observing pressure decay. The "Reference" method is considerably more complex in preparation and execution. The same measurements must be made in both methods, plus additional measurements on the reference system itself to assure adequate temperature compensation or allow correction for thermal lag, to assure leaktightness or correct for leakage, and to assure proper hygrometry or correct for condensation. In addition, the reference system must be constructed, installed and tested.

Historically, the "Reference" method was conceived to eliminate the necessity of making temperature corrections by virtue of assuming equal temperatures in the leaking containment and in the non-leaking reference volume, which are coupled by a manometer. If temperatures and hygrometry (i.e., temperatures above the dewpoint and no liquid water present initially) are identical, the leakage rate of the containment is just the difference in the pressure difference between the two systems at two points in time, divided by the containment test pressure. This first "Reference" method was attempted in the Valecitos Boiling Water Reactor, which had an allowable leakage rate of the order of 1%/24 hour day. In practice, it was found, that a considerable lag existed between the temperature of the air in the reference volume and the temperature of the air in the surrounding containment volume, which was varying diurnally.

Since then, considerable effort has been concentrated on attempting to reduce this lag to zero and have the reference volume distributed in a more representative way throughout the containment volume. At the same time, the "Reference" method (both methods, in fact) has been employed in testing containment systems for which the leak-tightness requirements have become more and more stringent, approaching allowable leakage rates of a few hundredths of a percent. For the accuracy employed in practice in reading temperatures, manometer legs and barometers, the possible error (and even the probable error) in determining leakage rates is often much greater than the leakage rate itself. The error entailed in assuming temperature compensation alone is greater than the leakage rate. For very low leakage rates, the true rate cannot usually be proved by either method, and any small advantage which one method has over the other is lost. For either method, where leakage rates are less than 0.001/24 hours, the leak testing must become a sophisticated experiment to be adequate

To allow an unbiased comparison of the two methods, it seems important to set on record the "exact" expressions for leakage rate which are obtained without assumptions regarding behavior of the state variables or the systems and then the expressions for the errors in leakage rate determination which *may* accrue.

There are two types of error analysis available to those conducting leakage rate tests. One deals with possible error, the other with probable error. The former is required in planning the tests, and as a proof of minimum detectable leakage rate. The latter is used in assessing the credence of the test after it is performed.

The "possible error" analysis sets the limitation on leakage rate determination imposed by possible errors in reading instruments or by limits of accuracy of the instrumentation. It is assumed in this analysis that every reading error or lack of built-in accuracy is in such a direction (+ or −) that the total possible error is maximum (+ or −). Comparison of this maximum with the expected or required magnitude of the quantity to be determined (leakage rate) allows determination of the precision of instrumentation needed to make the possible error a desired fraction of the leakage rate (e.g., $\frac{1}{3}$ or $\frac{1}{2}$).

It may be shown after a test that probability laws yield much lower errors with high confidence (e.g., 95%) under favorable conditions. This analysis may also take into account increased accuracy available through multiple observations of a single variable. Thus, the "probable" leakage rate calculated may be proclaimed (with low error) with high confidence. It does *not* absolutely preclude the *possibility* of the particular test having the maximum "possible" error.

Herein only the "possible" error analysis is considered. The expressions required for determining the leakage rates and such errors are developed from the basic equations governing gases for the two pressure decay methods ("Absolute" and "Reference") of leakage rate determination during pneumatic tests. "Possible" errors are compared for the two methods. An assessment of importance of changes in volume and

in weight of water vapor, and errors in determining them, is made.

Initially, only tests on containment structures under gauge test pressures of the order one atmosphere or higher are considered. In tests where the gauge test pressures are of the order of a pound per square inch, different pressure measurements are usually taken (specifically, atmospheric pressure, difference between containment pressure and atmospheric, and difference between reference vessel pressure and containment pressure). Such tests are examined later, although results are found to be the same as for the "Reference" method.

### "Possible" Error Analysis for "Absolute" Method

On considering all gases present as "perfect" gases it is assumed that the constituents of the air, including water vapor, each and as a mixture, obey the equation of state:

$$PV = NmRT \tag{1}$$

where

$P \equiv$ absolute pressure
$V \equiv$ container volume
$T \equiv$ absolute temperature
$m \equiv$ molecular weight of gas
$N \equiv$ number of molecular weights
$R \equiv$ constant for the particular gas.

The product $mR$ is assumed to be the same for all gases, and $Nm = w$ is the total weight of gas, vapor, or mixture in the container. Deviations from these asumptions require correction of the measured values only if temperature conditions initially and finally vary markedly (e.g., the ratio of the weights of air and water vapor remains constant above the dewpoint temperature, but increases below that temperature, if no water is present).

In general form, the equations relating the variables for air and water vapor in the containment vessel are

$$p_a V = w_a R_a T \tag{1a}$$

and

$$p_v V = w_v R_v T. \tag{1b}$$

(Note that partial pressures and weights are given in lower case letters, and that the subscripts used herein signify as follows:

$a \equiv$ air
$v \equiv$ water vapor
$1 \equiv$ initial point of measurement
$2 \equiv$ final point of measurement.)

Since $p_a$ is not measured, but $P$ is, and since $P = p_a + p_v$ while $w = w_a + w_v$, the equation relating the variables measured is

$$\frac{PV}{T} = w_a R_a + w_v R_v = (w - w_v) R_a + w_v R_v = w R_a + w_v \left( \frac{R_v}{R_a} - 1 \right) R_a . \tag{1c}$$

But

$$R_v / R_a = m_a / m_v ;$$

hence

$$\frac{PV}{R_a T} = w + w_v \left( \frac{m_a}{m_v} - 1 \right), \tag{1d}$$

so that

$$w = \frac{PV}{R_a T} - \left( \frac{m_a}{m_v} - 1 \right) w_v . \tag{1e}$$

Hence at two points in time $t_1$ and $t_2$, separated by $t_2 - t_1 = \Delta t$,

$$w_1 = \frac{P_1 V_1}{R_a T_1} - \left( \frac{m_a}{m_v} - 1 \right) w_{v_1} \tag{1f}$$

and

$$w_2 = \frac{P_2 V_2}{R_a T_2} - \left( \frac{m_a}{m_v} - 1 \right) w_{v_2} . \tag{1g}$$

Then the change in weight of material in the containment vessel is

$$\Delta w = w_2 - w_1 = \left( \frac{P_2 V_2}{R_a T_2} - \frac{P_1 V_1}{R_a T_1} \right) - (w_{v_2} - w_{v_1}) \left( \frac{m_a}{m_v} - 1 \right). \tag{2}$$

If now $P_2 = P_1 + \Delta P$, $V_2 = V_1 + \Delta V$, $T_2 = T_1 + \Delta T$, and $w_{v_2} = w_{v_1} + \Delta w_v$ [in general, $\chi + \Delta\chi = \chi(1 + \Delta\chi/\chi)$] are substituted into Eq. (2) and it is noted that $T_1[1 + (\Delta T/T_1)]$ is approximately equal to $T_1/(1 - \Delta T/T_1)$ since $\Delta T/T_1 \ll 1$, it is found that

$$\Delta w = \left[ \frac{P_1 V_1}{R_a T_1} \left( 1 + \frac{\Delta P}{P_1} \right) \left( 1 + \frac{\Delta V}{V_1} \right) \left( 1 - \frac{\Delta T}{T_1} \right) - \frac{P_1 V_1}{R_a T_1} \right] - \Delta w_v \left( \frac{m_a}{m_v} - 1 \right). \tag{2a}$$

However,

$$\left( 1 + \frac{\Delta P}{P_1} \right) \left( 1 + \frac{\Delta V}{V_1} \right) \left( 1 - \frac{\Delta T}{T_1} \right) = 1 + \frac{\Delta P}{P_1} + \frac{\Delta V}{V_1} - \frac{\Delta T}{T_1}$$

if products of fractional changes (such as $\Delta P \Delta V / P_1 V_1$) are neglected. With modification Eq. (2a) becomes

$$\Delta w = \frac{P_1 V_1}{R T_1}\left(\frac{R}{R_a}\right)\left[\frac{\Delta P}{P_1} + \frac{\Delta V}{V_1} - \frac{\Delta T}{T_1}\right] - \Delta w_v\left(\frac{m_a}{m_v} - 1\right). \tag{2b}$$

But

$$R/R_a = m_a/m, \qquad m = \frac{m_a\rho_a + m_v\rho_v}{\rho_a + \rho_v},$$

where $\rho \equiv$ density, and $\rho_v/\rho_a = s \equiv$ specific humidity,

whence $$R/R_a = \frac{(1+s)}{\left(1 + \frac{m_v}{m_a}s\right)}.$$

Also $w_1 = P_1 V_1/RT_1$. With these substitutions it is found that Eq. (2b) can be written

$$\frac{\Delta w}{w_1} = \frac{(1+s)}{\left(1 + \frac{m_v}{m_a}s\right)}\left[\frac{\Delta P}{P_1} + \frac{\Delta V}{V_1} - \frac{\Delta T}{T_1}\right] - \frac{\Delta w_v}{w_1}\left(\frac{m_a}{m_v}\right) - 1. \tag{2c}$$

The fraction of material leaking out in the time interval $\Delta t$ (in hours) can be obtained by subtracting the fraction of water vapor which condenses (in the containment) from both sides. Furthermore, by multiplying both sides by $24/\Delta t$ this leakage rate can be extrapolated to that for 24 hours. If these operations are performed, it is found that the 24 hour leakage rate for the "Absolute" method is

$$L_A = \frac{24}{\Delta t}\left(\frac{\Delta w - \Delta w_{v_c}}{w_1}\right) = \frac{24}{\Delta t}\left[\frac{(1+s)}{\left(1 + \frac{m_v}{m_a}s\right)}\left(\frac{\Delta P}{P_1} + \frac{\Delta V}{V_1} - \frac{\Delta T}{T_1}\right) - \frac{\Delta w_v}{w_1}\left(\frac{m_a}{m_v} - 1\right) - \frac{\Delta w_{v_c}}{w_1}\right]. \tag{3}$$

If the temperature stays above the dewpoint throughout the test, $\Delta w_{v_c} = 0$ and $\Delta w_v = \Delta w\, s/(s+1)$, and the 24 hour leakage rate becomes

$$L_A' = \frac{24}{\Delta t}\left[\frac{(1+s)^2}{\left(1 + \frac{m_v}{m_a}s\right)\left(1 + \frac{m_a}{m_v}s\right)}\right] \cdot \left(\frac{\Delta P}{P_1} + \frac{\Delta V}{V_1} - \frac{\Delta T}{T_1}\right). \tag{3a}$$

Note that the bracketed term in Eq. (3a) is always in the range 0.99 to 1.00 and hence can be taken as $\approx 1$ with less than 1% error in $L_A'$. Thus

$$L_A'' = \frac{24}{\Delta T}\left(\frac{\Delta P}{P_1} + \frac{\Delta V}{V_1} - \frac{\Delta T}{T_1}\right). \tag{3b}$$

It will be shown that $\Delta V/V$ is $<0.0001$ generally, and usually may be deleted in determining the leakage rate.

To determine the effects of errors in reading instruments or of lack of instrument precision it may be assumed that each measurement has an error $E$ of either sign associated with it. Thus the true (primed) values are

$$T_1' = T_1 \pm E_t, \qquad P_1' = P_1 \pm E_p, \qquad w_v' = w_v \pm E_{w_v}$$

etc. If these expressions for the measured variables are substituted into Eq. (3) for the differences $\Delta P$, $\Delta T$, etc:

$$(L_A)_E = \frac{24}{\Delta t}\left\{\frac{(1+s)}{\left(1 + \frac{m_v}{m_a}s\right)}\left[\frac{(P_2 \pm E_P - P_1 \pm E_P)}{P_1} + \frac{(V_2 \pm E_V - V_1 \pm E_v)}{V_1} - \frac{(T_2 \pm E_T - T_1 \pm E_T)}{T_1}\right] - \frac{(w_{v_2} \pm E_{w_v} - w_{v_1} \pm E_{w_v})}{w_1}\left(\frac{m_a}{m_v} - 1\right) - \frac{(w_{v_{c_2}} \pm E_{w_{v_c}} - w_{v_{c_1}} \pm E_{w_{v_c}})}{w_1}\right\}. \tag{3c}$$

or

$$(L_A)_E = \frac{24}{\Delta t}\left\{\frac{(1+s)}{\left(1 + \frac{m_v}{m_a}s\right)}\left[\left(\frac{\Delta P + 2E_P}{P_1}\right) + \left(\frac{\Delta V + 2E_V}{V_1}\right) - \left(\frac{\Delta T \pm 2E_T}{T_1}\right)\right] - \left(\frac{\Delta w_v \pm 2E_{w_v}}{w_1}\right)\left(\frac{m_a}{m_v} - 1\right) - \left(\frac{\Delta w_{v_c} \pm 2E_{w_{v_c}}}{w_1}\right)\right\}. \tag{3d}$$

Then the maximum "possible" error in $L_A$ is $(L_A)_E - L_A$, with all errors additive:

$$E_{L_A} = (L_A)_E - L_A = \frac{24}{\Delta T}\left[\left(\frac{2E_p}{P_1} + \frac{2E_T}{T_1} + \frac{2E_V}{V_1}\right) + \frac{2E_{w_v}}{w_1}(0.6) + \frac{2E_{w_{v_c}}}{w_1}\right]. \tag{4}$$

(Note that $\left(\frac{m_a}{m_v} - 1\right) = 0.608$ and

$$(1 + s) \Big/ \left(1 + \frac{m_v}{m_a} s\right) \approx 1).$$

It will be shown that fractional errors in determining hygrometry and volume changes are small compared to fractional errors in determining pressures and temperatures and may be ignored for values of $L_A > 0.0001$. Hence the significant error fraction can be written

$$E'_{L_A} = \frac{24}{\Delta T}\left(\frac{2E_p}{P_1} + \frac{2E_T}{T_1}\right). \tag{4a}$$

### "Possible" Error Analysis for "Reference" Method

In the "Reference" method, the same measurements should be taken as in the "Absolute" method, plus measurements of

$\delta P \equiv$ pressure difference between reference system and containment vessel $= P_R - P$

$T_R \equiv$ temperature of contents of reference system

$P_R \equiv$ pressure in reference system

$T_{R_W} \equiv$ wet bulb temperature of reference system

or

$r_R =$ relative humidity of reference system.

(From the $T_R$ and $T_{R_W}$ or $T_R$ and $r_R$, $w_{R_v}$ can be computed).

The governing equations for the containment and reference systems are:

Containment

$$\left.\begin{aligned} p_a V &= w_a R_a T \\ p_v V &= w_v R_v T \end{aligned}\right\} \qquad PV = wRT \tag{1}$$

Reference

$$\left.\begin{aligned} p_{R_a} V_R &= w_{R_a} R_a T_R \\ p_{R_v} V_R &= w_{R_v} R_v T_R \end{aligned}\right\} \qquad P_R V_R = w_R R T_R. \tag{5}$$

The fractional weight change in the containment is still as given by Eq. (2c). It is only necessary to replace $\Delta P$ with a term containing the measured values. This is done by noting that

$$P = P_R - \delta P,$$

so that

$$P_1 = P_{R_1} - \delta P_1 \quad \text{and} \quad P_2 = P_{R_2} - \delta P_2.$$

Then

$$\Delta P = P_2 - P_1 = (P_{R_2} - P_{R_1}) - (\delta P_2 - \delta P_1). \tag{6}$$

If $P_{R_2}$ is replaced by $w_{R_2} T_{R_2} R / V_{R_2}$ and $P_{R_1}$ by $w R_1 T_{R_1} R / V_{R_1}$ as given in equations 5, and if $w_{R_2} = w_{R_1}(1 + \Delta w_R / w_{R_1})$, $T_{R_2} = T_{R_1}(1 + \Delta T_R / T_{R_1})$, and $V_{R_2} = V_{R_1}(1 + \Delta V_R / V_{R_1}) \approx V_{R_1}/(1 - \Delta V_R / V_{R_1})$, then

$$\begin{aligned} P_{R_2} - P_{R_1} &= \frac{w_{R_1} T_{R_1} R}{V_{R_1}}\left(1 + \frac{\Delta w_R}{w_{R_1}}\right)\left(1 + \frac{\Delta T_R}{T_{R_1}}\right) \\ &\quad \cdot \left(1 - \frac{\Delta V_R}{V_{R_1}}\right) - \frac{w_{R_1} T_{R_1} R}{V_{R_1}} \\ &= \frac{w_{R_1} R T_{R_1}}{V_{R_1}}\left(\frac{\Delta w_R}{w_{R_1}} + \frac{\Delta T_R}{T_{R_1}} - \frac{\Delta V_R}{V_{R_1}}\right), \end{aligned} \tag{7}$$

neglecting products of fractional changes. If this is substituted into Eq. (6), then divided by $P_1$

$$\begin{aligned} \frac{\Delta P}{P_1} &= \frac{P_{R_1}}{P_1}\left(\frac{\Delta w_R}{w_{R_1}} + \frac{\Delta T_R}{T_{R_1}} - \frac{\Delta V_R}{V_{R_1}}\right) \\ &\quad - \frac{(\delta P_2 - \delta P_1)}{P_1}. \end{aligned} \tag{8}$$

Noting that

$$\frac{P_{R_1}}{P_1} = \left(\frac{P_1 + \delta P_1}{P_1}\right) = \left(1 + \frac{\delta P_1}{P_1}\right)$$

and again neglecting products of fractional changes, Eq. (8) becomes

$$\frac{\Delta P}{P_1} = \left(\frac{\Delta w_R}{w_{R_1}} + \frac{\Delta T_R}{T_{R_1}} - \frac{\Delta V_R}{V_{R_1}}\right) - \left(\frac{\delta P_2 - \delta P_1}{P_1}\right). \tag{8a}$$

If Eq. (8) is substituted into Eq. (3), the leakage rate per 24 hours is obtained directly for the "Reference" method.

$$\begin{aligned} L_R = \frac{24}{\Delta t}\Bigg\{&\left(\frac{1 + s}{1 + \frac{m_v}{m_a} s}\right)\left[\left(\frac{\Delta T_R}{T_{R_1}} - \frac{\Delta T}{T_1}\right)\right. \\ &- \left(\frac{\Delta V_R}{V_{R_1}} - \frac{\Delta V}{V_1}\right) - \left(\frac{\delta P_2 - \delta P_1}{P_1}\right) \\ &\left. + \frac{\Delta w_R}{w_{R_1}}\right] - \frac{\Delta w_v}{w_1}\left(\frac{m_a}{m_v} - 1\right) - \frac{\Delta w_{v_c}}{w_1}\Bigg\}. \end{aligned} \tag{9}$$

Again, if both $T$ and $T_R$ stay above the dewpoint and the reference system does not leak ($\Delta w_R = 0$, $\Delta w_{v_c} = 0$), and since $\Delta w_v = \Delta w[s/(1 + s)]$,

$$\begin{aligned} L'_R = \frac{24}{\Delta t}\Bigg[&\frac{(1 + s)^2}{\left(1 + \frac{m_v}{m_a} s\right)\left(1 + \frac{m_a}{m_v} s\right)}\Bigg] \\ &\cdot\Bigg[\left(\frac{\Delta T_R}{T_{R_1}} - \frac{\Delta T}{T_1}\right) - \left(\frac{\Delta V_R}{V_{R_1}} - \frac{\Delta V}{V_1}\right) \\ &- \left(\frac{\delta P_2 - \delta P_1}{P_1}\right)\Bigg]. \end{aligned} \tag{9a}$$

Then since $0.99 < [f(s)] < 1.00$ for the bracketed term in $s$,

$$L_R'' = \frac{24}{\Delta t}\left[\left(\frac{\Delta T_R}{T_{R_1}} - \frac{\Delta T}{T_1}\right) - \left(\frac{\Delta V_R}{V_{R_1}} - \frac{\Delta V}{V_1}\right) - \left(\frac{\delta P_2 - \delta P_1}{P_1}\right)\right]. \tag{9b}$$

Comments:

1) Only now can the effect of the assumption that $T_{R_1} = T_1$, $T_{R_2} = T_2$ be assessed. *If* this were true, $\Delta T_R/T_1$ would cancel $\Delta T_1/T_1$ and the *apparent* leakage would not include either term. However, $T_R$ must be measured to prove this, hence an error can be introduced. In general, such an assumption is not true because of a real thermal lag between reference and containment system.

2) If the temperatures of the reference and containment systems always stay above the dewpoint, $\Delta w_{R_v} = \Delta w_{v_c} = 0$, and the fractional change terms containing these drop out of Eqs. (3), (4), and (9).

3) The above points serve to show where other "possible" error analyses may go wrong.

To determine the maximum "possible" error in $L_R$ due to reading errors and lack of instrument precision, the same procedure is adopted as used to obtain the error in $L_A$. Expressions like $T_1 \pm E_T$ are substituted into Eq. (9) to yield $(L_R)_E$. Then $E_{L_R}$ is obtained by subtracting $L_R$ from $(L_R)_E$:

$$(L_R)_E - L_R = \frac{24}{\Delta t}\left\{\frac{(1+s)}{\left(1+\frac{m_v}{m_a}s\right)}\left[\frac{2E_{T_R}}{T_{R_1}} + \frac{2E_T}{T_1} + \frac{(E_{\delta P} + E_{\delta P})}{P_1} + \frac{2E_{V_R}}{V_{R_1}} + \frac{2E_V}{V_1} + \frac{2E_{w_R}}{w_{R_1}}\right] + \frac{2E_{w_v}}{w_1}\left(\frac{m_a}{m_v} - 1\right) + \frac{2E_{w_{v_c}}}{w_1}\right\}. \tag{10}$$

Again, letting

$$(1+s)\Big/\left(1+\frac{m_v}{m_a}s\right) = 1 \quad \text{and} \quad \left(\frac{m_a}{m_v} - 1\right) = 0.608,$$

and noting that usually $E_{T_R} = E_T$,

$$E_{L_R} = (L_R)_E - L_R = \frac{24}{\Delta t}\left[\frac{4E_T}{T} + \frac{2E_{\delta P}}{P} + \frac{2E_{V_R}}{V_R} + \frac{2E_V}{V} + \frac{2E_{w_R}}{w_R} + \frac{2E_{w_v}}{w_1}(0.6) + \frac{2E_{w_{v_c}}}{w_1}\right]. \tag{10a}$$

Since errors in determining $\Delta V$, $\Delta V_R$, $w_R$, $\Delta w_v$, and $\Delta w_{v_c}$ will be shown to be small compared to errors in determining $\Delta T$ and $\delta p$; and since a double error ($2E_H$) is made in reading manometer leg heights to obtain $\delta P$, so that $E_{\delta P} = 2(\mu E_H)$, where $\mu$ converts heights to units of $P$,

$$E'_{L_R} \simeq \frac{24}{\Delta t}\left[\frac{4\mu E_H}{P} + \frac{4E_T}{T}\right]. \tag{10b}$$

(Note, in previous analyses it was not recognized that in determining $\delta P$ a double error can be made because *each* leg of the manometer must be read. If another single reading type of pressure differential measuring device is used, the coefficient of the first error component can be reduced from 4 to 2.)

## "Possible" Error Analysis for Low Pressure "Reference" Method

If low test overpressures are employed (of the order of 1 psi) a different set of measurements are sometimes taken, as follows:

*PRESSURE*

(1) Outside atmospheric pressure
(2) Pressure difference between containment and outside
(3) Pressure difference between reference system and containment.

(2) and (3) are usually made with two-legged manometers (two readings each per measurement), and (1) is made with a mercury barometer.

*TEMPERATURE*

(1) Outside temperature
(2) Containment temperature
(3) Reference system temperature
(4) Wet bulb temperature in containment
(5) Wet bulb temperature in ref. system

} for relative humidity.

(5) should be taken but sometimes is not. It is necessary to take (4) and (5) either to show that the temperature is above the dewpoint or to determine the required correction for change in weight of water vapor. (1) must be taken at least to correct the barometer reading.

If $P_B$ is the outside air barometer reading, $H_H$ and $H_L$ are the high and low manometer leg heights respectively, and $\mu$ converts manometer heights to pressure in the same units as $P$, using the perfect gas law assumptions, the equations for this system become

$$\begin{aligned} P &= P_B + \mu(H_H - H_L) = \frac{wRT}{V}, \\ P_R &= P + \mu(H_{R_H} - H_{R_L}) \\ &= P_B + \mu(H_H - H_L) + \mu(H_{R_H} - H_{R_L}) \\ &= \frac{w_R R T_R}{V_R}. \end{aligned} \tag{17}$$

The expression for the fractional weight loss in the containment vessel is the same as for the other "Reference" method, with

$$\delta P = \mu(H_{R_H} - H_{R_L}). \tag{18}$$

The quantity $P$ does not enter into the determination of changes in pressure, and hence measurements required for $P$ do not introduce errors in $L_R$. The leakage rate per 24 hours for this Low Pressure Reference Method can therefore be written by substituting Eq. (17) and (18) into Eq. (9):

$$\begin{aligned} L_{R_L} = \frac{24}{\Delta t}\Bigg\{ & \left(\frac{1+s}{1+\frac{m_v}{m_a}s}\right)\left[\left(\frac{\Delta T_R}{T_{R_1}} - \frac{\Delta T}{T_1}\right)\right. \\ & -\left(\frac{\Delta V_R}{V_{R_1}} - \frac{\Delta V}{V_1}\right) \\ & - \frac{\mu(H_{R_{H_2}} - H_{R_{L_2}} - H_{R_{H_1}} + H_{R_{L_1}})}{[P_{B_1} + \mu(H_{H_1} - H_{L_1})]} \\ & \left.+ \frac{\Delta w_R}{w_{R_1}}\right] - \frac{\Delta w_v}{w_1}\left(\frac{m_a}{m_v} - 1\right) - \frac{\Delta w_{v_c}}{w_1}\Bigg\}. \end{aligned} \tag{19}$$

If both $T$ and $T_R$ stay above the dewpoint, and the reference system does not leak ($\Delta w_R = 0$, $\Delta w_{v_c} = 0$), Eq. (19) can be reduced to an expression analogous to Eq. (9b):

$$\begin{aligned} L''_{R_L} = \frac{24}{\Delta t}\Bigg\{ & \left(\frac{\Delta T_R}{T_{R_1}} - \frac{\Delta T}{T_1}\right) - \left(\frac{\Delta V_R}{V_{R_1}} - \frac{\Delta V}{V_1}\right) \\ & - \left[\frac{\mu(\Delta H_{R_2} - \Delta H_{R_1})}{P_{B_1} + \mu\Delta H_1}\right]\Bigg\}. \end{aligned} \tag{19a}$$

The "possible" error analysis can be made analogous to the "Reference" method if errors in determining volume change and water vapor change are neglected:

$$\begin{aligned} E_{L_{R_L}} &= \frac{24}{\Delta t}\left[\pm\frac{2E_{T_R}}{T_{R_1}} \pm \frac{2E_T}{T_1} \pm \frac{4\mu E_{H_R}}{P_{B_1} + \mu\Delta H_1}\right] \\ &= \frac{24}{\Delta t}\left[\frac{4\,|\,E_T\,|}{T_1} + \frac{\mu 4\,|\,E_{H_R}\,|}{P_{BL} + \mu\Delta H_1}\right], \\ &\qquad \text{if } |\,E_{T_R}\,| = |\,E_T\,|. \end{aligned} \tag{20}$$

The complete error fraction, if condensation occurs, can be written:

$$\begin{aligned} E'_{L_{R_L}} = \frac{24}{\Delta t}\Bigg[ & \frac{4E_T}{T_1} + \frac{\mu 4 E_H}{P_1} + \frac{E_{\Delta V}}{V_1} \\ & \frac{E_{\Delta V_R}}{V_{R_1}} + \frac{E_{\Delta w_{R_v}}}{w_{R_1}} + \frac{E_{\Delta w_v}}{w_1}\Bigg]. \end{aligned} \tag{20a}$$

*Hygrometry Corrections*

In order to examine the importance of errors in hygrometry, it is necessary to get an estimate of the quantities

$$E_{\Delta w_{R_v}}/w_R \quad \text{and} \quad w_{\Delta w_v}/w_1$$

in terms of errors in reading the wet and dry bulb temperatures. To do this, it is first noted that a relation between $P_v$ and $T_d$ exists in the normal temperature range which is (noting that this is only for the case of saturated or subcooled conditions, i.e., below the dewpoint temperature):

$$\log P_v = a + b(T_d - 459.69).$$

If $T_d$ is in degrees Rankine and lies in the range $500°\mathrm{R} < T_a < 540°\mathrm{R}$, and if $P_v$ is in inches of Hg, $a = 0.345$ and $b = 0.0347$ and

$$\frac{dp_v}{p_v} = 0.0347\, dT_d.$$

Now

$$p_{v_2} = p_{v_1} + \Delta p_v = p_{v_1}(1 + \Delta p_v/p_{v_1}) = p_{v_1}(1 + 0.0347\Delta T_d).$$

Since in general

$$p_v = \frac{w_v R_v T_d}{V},$$

$$\frac{w_{v_2} R_v T_{d_2}}{V_2} = \frac{w_{v_1} R_v T_{d_1}}{V_1}\left(1 + 0.0347\ \Delta T_d\right)$$

from which

$$\frac{w_{v_2} - w_{v_1}}{w_{v_1}} = \frac{\Delta w_v}{w_{v_1}} = \frac{T_{d_1} V_2}{T_{d_2} V_1}(1 + 0.0347\ \Delta T_d) - 1.$$

If it is assumed that $\Delta V = 0$, and since $T_{d_1}/T_{d_2} = [1 - (\Delta T_d/T_{d_1})]$, $\Delta w_v/w_{v_1} = \Delta T_d(0.0347 - 1/T_{d_1}) \approx 0.033\Delta T_d$ (for $T_{d_1}$ of the order of $500°R$); also

$$w_{v_1} = [s/(1+s)]w_1.$$

Therefore,

$$\frac{\Delta w_v}{w_1} = \left(\frac{s}{1+s}\right)(0.033\ \Delta T_d)$$

and since $s$ is always less than 0.02

$$\frac{\Delta w_v}{w_1} < 0.00066\ \Delta T_d.$$

Thus if the maximum possible error in determining $\Delta T_d$ is 1 deg, the maximum possible error in $\Delta w_v/w_1$ is 0.00066, etc. Since the maximum allowable error in determining $\Delta T_d$ is prescribed by the leakage rate which is to be measured and which must be $< 62.5 L_R$ to give at least 50% accuracy,

$$\frac{E_{\Delta w_v}}{w_1} \text{ is always } < \sim 0.04\ L_R.$$

*Volume Corrections*

To examine the importance of errors in determining $\Delta V/V$ and $\Delta V_R/V_R$, it is necessary to estimate the relations between $\Delta V/V$, $\Delta T/T$, and $\Delta P/P$; and errors in temperature and pressure measurement. The volumes of the containment vessel and reference vessel change as the material temperatures and internal pressures change. In general

$$V_2 = V_1(1 + 3\alpha\Delta T + \beta\Delta P),$$

where $\alpha$ is the linear temperature coefficient of expansion of the vessel material and $\beta$ is the pressure coefficient of expansion. For spherical vessels,

$$\beta_s = \frac{3r_s}{2Y_s h}$$

where

$r_s \equiv$ sphere radius,
$h \equiv$ wall thickness
$Y_s \equiv$ elastic modulus of sphere material.

For tubes or cylinders,

$$\beta_c = \frac{5}{2}\frac{r_c}{Y_c h}$$

where

$r_c \equiv$ cylinder or tube radius,
$Y_c \equiv$ elastic modulus of tube or cylinder material;

$$\frac{\Delta V}{V_1} = 3\alpha\Delta T + \beta\Delta P$$

and

$$\left(\frac{\Delta V}{V_1}\right)_R = 3\alpha(\Delta T + 2E_T) + \beta(\Delta P + 2E_{\Delta P}).$$

Therefore

$$\frac{E_{\Delta V}}{V_1} = 6\alpha E_T + 2\beta E_{\Delta P} = \left(\frac{\Delta V}{V_1}\right)_R - \left(\frac{\Delta V}{V_1}\right);$$

for steel $\alpha \approx 10^{-5}$/°F, $E \approx 3 \times 10^7$ psi
for copper $\alpha \approx 10^{-5}$/°F, $E \approx 1.6 \times 10^7$ psi.

If, typically, $r_s/h \approx 1000$ and $r_c/h \approx 25$ and the containment is of steel with the reference system of copper,

$$\frac{E_{\Delta V}}{V_1} \approx 6 \times 10^{-5} E_T + 10 \times 10^{-5} E_P$$

and

$$\frac{E_{\Delta V_R}}{V_R} = 6 \times 10^{-5} E_{T_R} + 0.8 \times 10^{-5} E_{P_R}.$$

$E_T$ is constrained to be less than $\sim 60L$ and $E_p < 4aL$ to insure that $E_L < L/2$. Hence $E_{\Delta V}/V_1$ will always be $<0.004\ L$ for one atmosphere overpressure ($a = 2$). Similarly $E_{T_R}$ must always be less than $30L$ and $E_{\delta P} < 2aL$. Hence $E_{\Delta V_R}/V_{R_1}$ will always be $<0.002L$ for one atmosphere overpressure ($a = 2$).

The magnitude of $\Delta V/V$ itself is small. It can be seen that for this example

$$\frac{\Delta V}{V} = 6 \times 10^{-5}\,\Delta T + 10 \times 10^{-5}\,\Delta P.$$

Hence $\Delta V/V$ will always be $<L/2$ if $\Delta T < 4000L$(°$R$) and $\Delta P < 2500L$ (in. Hg.).

Hence for $L = 0.001$, if $\Delta T < 4°R$ and $\Delta P < 2.5$ in. Hg, $\Delta V/V$ will be $<0.0005$. Thus an error in determining $\Delta V/V$ is certainly negligible.


## Summary

The leakage rates have been determined in terms of the measured variables for the cases of: I, "Absolute" method; II, "Reference" method; III, "Low Overpressure Reference" method. All of these methods are based on pressure decay, and determine the fractional loss of weight of the air and water vapor mixtures by leakage from the system. The differences lie in the methods of measuring the equation-of-state variables (pressure, temperature and volume) for assumed application of the "perfect" gas laws. The "exact" expressions for these 24-hour leakage rates are (products of fractional changes neglected):


$$\text{I.}\quad L_A = \frac{24}{\Delta t}\left[\frac{(1+s)}{\left(1+\frac{m_v}{m_a}s\right)}\left(\frac{\Delta P}{P_1}+\frac{\Delta V}{V_1}-\frac{\Delta T}{T_1}\right) - \frac{\Delta w_v}{w_1}\left(\frac{m_a}{m_v}-1\right) - \frac{\Delta w_{v_c}}{w_1}\right]. \tag{3}$$

$$\text{II.}\quad L_R = \frac{24}{\Delta t}\left\{\frac{(1+s)}{\left(1+\frac{m_v}{m_a}s\right)}\left[\left(\frac{\Delta T_R}{T_{R_1}}-\frac{\Delta T}{T_1}\right) - \left(\frac{\Delta V_R}{V_{R_1}}-\frac{\Delta V}{V_1}\right) - \left(\frac{\delta P_2-\delta P_1}{P_1}\right)+\frac{\Delta w_R}{w_{R_1}}\right] - \frac{\Delta w_v}{w_1}\left(\frac{m_a}{m_v}-1\right) - \frac{\Delta w_{v_c}}{w_1}\right\}. \tag{9}$$

$$\text{III.}\quad L_{R_L} = \frac{24}{\Delta t}\left\{\frac{(1+s)}{\left(1+\frac{m_v}{m_a}s\right)}\left[\left(\frac{\Delta T_R}{T_{R_1}}-\frac{\Delta T}{T_1}\right) - \left(\frac{\Delta V_R}{V_{R_1}}-\frac{\Delta V}{V_1}\right) - \frac{\mu(\Delta H_{R_2}-\Delta H_{R_1})}{(P_{B_1}+\mu\Delta H_1)} + \frac{\Delta w_R}{w_{R_1}}\right] - \frac{\Delta w_v}{w_1}\left(\frac{m_a}{m_v}-1\right) - \frac{\Delta w_{v_c}}{w_1}\right\}. \tag{19}$$

It has been shown that errors in determining $\Delta w_v$ and $\Delta V$ are negligible as is $\Delta V/V$ itself in determining the

leakage for fractional leakages $>0.0001$. It is noted that the expressions for $L_R$ and $L_{R_L}$ are identical, since

$$\delta P_2 - \delta P_1 = \mu(\Delta H_{R_2} - \Delta H_{R_1})$$

and

$$P_1 = P_{B_1} + \mu(\Delta H_1).$$

In fact, the pressure measurements are the same for $\delta P$ and $\Delta H_R$, although an additional set of measurements is required to obtain $P_1$ in III.

It is noted that the temperature terms in II and III cancel only if the reference system and containment system temperatures are *exactly* equal. This is not true in general because of thermal lag. Hence it is necessary to measure reference vessel air temperatures. This is usually not done and the temperature terms are dropped. If $\Delta T_R/T_{R_1}$ is different from $\Delta T/T_1$ by $(\Delta t/24)L$ a one hundred percent error is introduced immediately by assuming equal temperatures. If the readings are taken 24 hours apart and the leakage fraction is 0.001, the temperature differences must agree to within $\sim 0.5°F$ to keep the error below 100%.

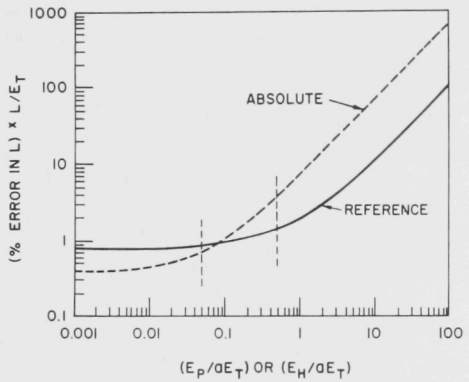


FIG. IV-24-1. The Percent Error in $L$ for Both the "Absolute" and "Reference" Methods. *ANL Neg. No. 112-9392.*

TABLE IV-24-I. MINIMUM PRECISION REQUIRED

| 24 Hour Leakage Rate Fraction, $L$ | Absolute Method | | Reference Method | |
|---|---|---|---|---|
| | $P$, in. Hg | $T$, °R | Leg H, in. $H_2O$ | $T$, °R |
| 0.01 | 0.075 | 0.67 | 0.51 | 0.33 |
| 0.005 | 0.038 | 0.33 | 0.10 | 0.17 |
| 0.001 | 0.0075 | 0.067 | 0.051 | 0.033 |
| 0.0005 | 0.0038 | 0.033 | 0.010 | 0.017 |
| 0.0001 | 0.00075 | 0.0067 | 0.0051 | 0.0033 |

If the low density liquid manometers can be read to the same linear precision as the mercury barometer, the accuracy in pressure difference measurement in the "Reference" method is $\frac{1}{2}(\rho_B/\rho_m)$ times greater than in the "Absolute" method ($\rho_B$ is the density of the barometer fluid and $\rho_m$ is the density of the manometer fluid). For a mercury barometer and a water manometer this factor would be $\sim 6.8$.

For all methods, if the temperatures are kept above the dewpoint, no correction is necessary for hygrometry in the three methods, since no condensation occurs and the value of $s = p_v/p_a$ is a constant throughout the test *if additional water is not available for evaporation.* If the temperatures fall below the dewpoint, the quantity of water vapor leaking out with the air or condensing must be accounted for continuously throughout the test, since $s$ is not constant. The same is true if liquid water is present and available for evaporation.

With these expressions for leakage rate it is shown that the maximum possible fractional errors $E_L$ in determining these leakage rates, due to reading errors or lack of instrument precision, are given by the following:

$$\text{I.}\quad E_{L_A} = \frac{24}{\Delta t}\left[\left(\frac{2E_P}{P} + \frac{2E_T}{T} + \frac{2E_V}{V}\right) + \frac{2E_{w_s}}{w}(0.6) + \frac{2E_{w_{v_c}}}{w}\right] \tag{4}$$

$$\text{II.}\quad E_{L_R} = \frac{24}{\Delta t}\left[\frac{4\mu E_H}{P} + \frac{4E_T}{T} + \frac{2E_{v_R}}{V_R} + \frac{2E_V}{V} + \frac{2E_{w_R}}{w_R} + \frac{2E_{w_v}}{w}(0.6) + \frac{2E_{w_{v_c}}}{w}\right] \tag{10a}$$

$$\text{III.}\quad E_{L_{R_L}} = E_{L_R}. \tag{20a}$$

Only the first two error terms are important in I, II, and III. By introducing $a = P_1/P_B \equiv$ pressure in container in atm, assuming $T = 520°R$, $\Delta t = 24$ hours, and $\mu E_H = (1/13.6)E_p$, these two expressions can be rewritten:

$$\%\text{ error in } L_A = \frac{100}{L_A}E_{L_A} = \left[0.39 + 6.7\frac{|E_H|}{|E_T|a}\right]\frac{|E_T|}{L_A}$$

and

$$\%\text{ error in } L_R = \frac{100}{L_R}E_{L_A} = \left[0.77 + \frac{|E_H|}{|E_T|a}\right]\frac{|E_T|}{L_R},$$

where $E_H \equiv$ inches error for each leg of the manometer or for the barometer.

The % error in $L$ for $\Delta t = 24$ hours and $E_T/L = 1$ for both methods are displayed in Fig. IV-24-1. To obtain error for other values of $\Delta t$ and $E_T/L$, values from the curve must be multiplied by $24/\Delta t$ and by $E_T/L$.

"Possible" errors can be used to predetermine the precision of measurement required to yield errors less than a desired fraction of the leakage rate. Let $\varphi L$ and $\theta L$ be the errors in leakage rate determination contributed by pressure errors and temperature errors respectively, and $\lambda L = \varphi L + \theta L$ be the desired maximum error in the leakage rate $L$. Then the precisions shown in Table IV-24-I were obtained from Eqs. (4a) and (10b) for $a = 2$, $P_0 = 30$ in. Hg, $T = 530°R$, $\mu = 1/13.6$, $\Delta t = 24$ hours, $\varphi = \theta = 0.25$, and $\lambda = 0.50$ for various $L$'s. Needed precision can be found for other values of the parameters by multiplying appropriate items by $a/2$, $P_0/30$, $T/530$, $1/13.6\ \mu$, $\Delta t/24$, $4\varphi$, and/or $4\theta$.

## IV-25. A Proposed Core Test Facility for Safety Analysis

J. C. Carter and R. H. Armstrong*

### Introduction

The safety analysis of fast reactors is proceeding along two main paths, the experimental and the theoretical. It is intended that these converge with the resultant being a substantiated set of digital computer codes through which paths may be programmed to produce simulations of both designed operations and hypothetical accidents. The objective of this study is to design and evaluate facilities which may be suitable for experimental investigations of sections of cores and small cores. The technical, and economic aspects of the test facilities are considered.

A concept of a facility for investigating experimentally the effects of the phenomena of liquid metal boiling, fuel melting, and accident propagation is presented. The problem of providing instrumentation which can obtain meaningful information, even below the threshold of an accident, is difficult, and especially so in the case of a disintegrating core. Thus reliable and replaceable instrumentation is a primary concern in all core testing facilities. The concept comprises a test core in a sealed replaceable compact test unit. The core may be a critical unit or a subcritical group of fuel elements in a driver core. It is designed to operate with the coolant in either the liquid or boiling phase, so that coolant dynamics and void worths may be studied under controlled conditions.

It is intended to incorporate maximum flexibility and instrumentation in the design, with the ability to replace core parts and instrumentation rapidly. It is anticipated that damage to the structral integrity of the core and test unit will be frequent enough to require easily replaceable parts. The test unit is self sufficient, prefabricated, and mechanically pretested and it can be placed in and quickly made integral with the external systems and controls associated with a permanent nuclear power plant of greater capacity than the test unit itself. The amount of shielding and containment will depend upon where and how the permanent facilities are constructed.

* Reactor Engineering Division, Argonne National Laboratory

### Description of the Test Unit

The core is conceived to be a small enriched core located in a highly instrumented double-walled sealed container. Its estimated thermal rating is 1.0 MW with sodium as the coolant. It is a simple version of a conventional solid-fuel fast-reactor core with reflector control. It is intended to design the core so that reactivity fluctuations due to the boiling phenomenon cannot become prompt critical and so that the reactivity feedback caused by boiling is relatively small and dominated by the strong negative feedback due to the volumetric expansion of the core.

The test unit (Fig. IV-25-1) is a double-wall shell containing the core, liquid metal, a pump, and a condenser. The liquid metal is vaporized and condensed within the test unit. It can operate with any liquid metal compatible with columbium, over a range of pressure and temperature with top limits of 10 atm and 1200°C.

The physical features of the unit are illustrated in Fig. IV-25-1, showing the longitudinal cross sections, and in Fig. IV-25-2, showing a horizontal cross section through the reactor core. The double-wall shell is similar to a large vacuum bottle with an inner shell of columbium and an outer shell of stainless steel. The space between the two shells provides a means of detecting leaks in the inner shell, of protecting the columbium from oxidation at high temperatures, and of creating a large temperature gradient between the columbium and the stainless steel shells. There are two closure plates with space between them which, in

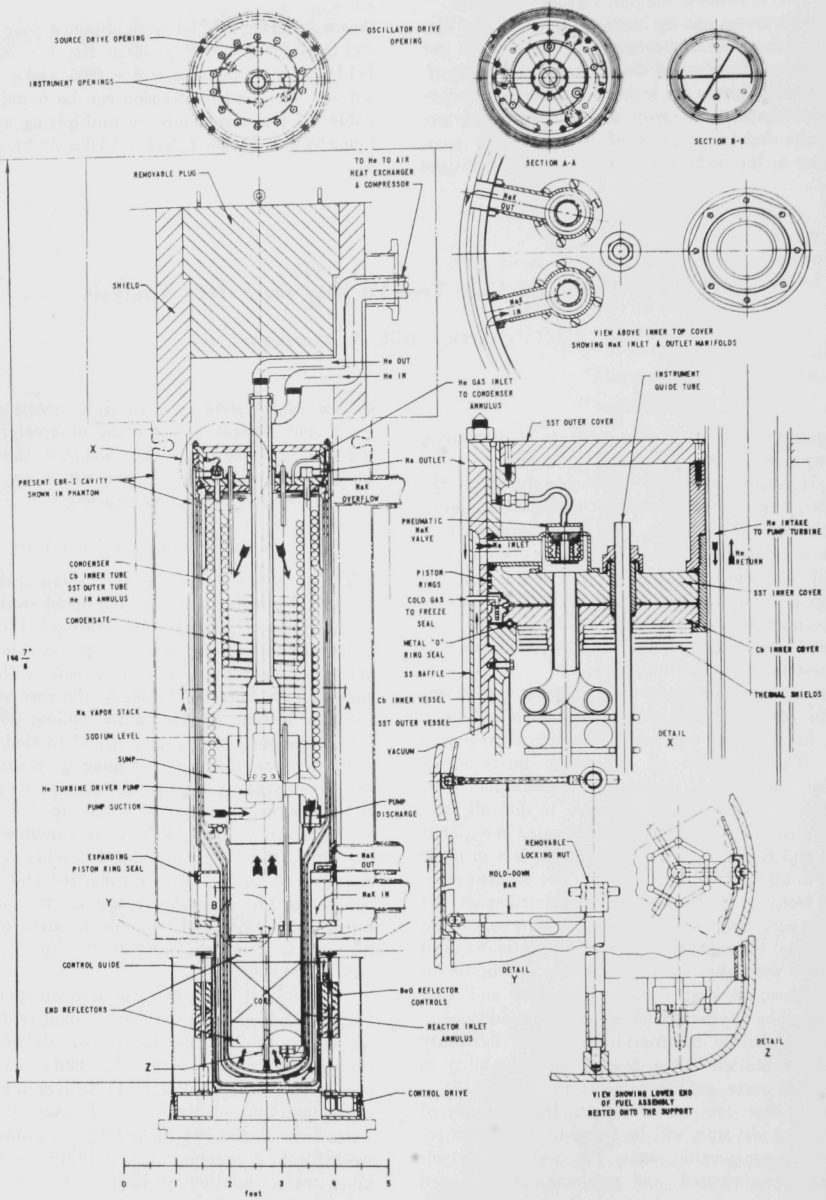


FIG. IV-25-1. Longitudinal Cross Section of Test Unit. *ANL Neg. No. 112-8337-T-1.*

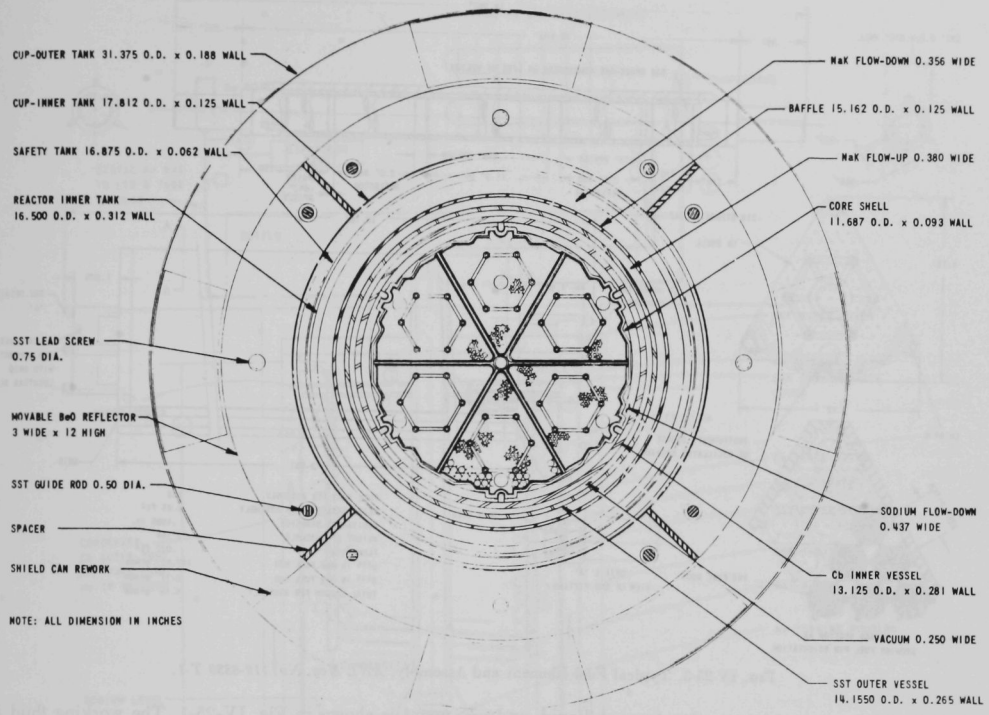


FIG. IV-25-2. Core Cross Section. *ANL Neg. No. 112-8838 T-1.*

addition to the above reasons, also eliminate temperature gradients in the closure joints.

The annular space between the stainless-steel shell of the test unit and the stainless-steel shell of the permanent installation is filled with NaK and is in series with the primary heat-transfer system. Calculations indicate that the amount of heat to be carried away at shutdown is 150 kW maximum. This heat is radiated from the inner shell to the outer shell and removed by conduction and convection to the NaK. Thus the primary heat-transfer system provides an ever-present and adequate way to remove shutdown heat, to cool the reflector control which is in the annular space, and to keep the liquid metal in the test unit above the melting point during startup.

When the test unit contains a unit core it is controlled by the movable beryllium oxide reflectors surrounding the core. The two halves of the cylindrical reflector are assembled to a framework affixed to the containment shell and are actuated independently. When the test unit contains a subcritical section of core it is controlled by the driver core into which the test unit is inserted.

The core is a bundle of niobium-clad uranium carbide rods in the form of a right cylinder. Specifically, the core shown in Fig. IV-25-2 consists of six segmental assemblies, each containing 146 fuel elements. The liquid metal is forced to flow longitudinally through the core by a multiphase pump. The two cylindrical shells of the concentric beryllium oxide reflectors move longitudinally relative to the transverse centerline of the core. The reactivity worth of the reflector shells is such that their removal from the core region will shut down the reactor.

Two longitudinal regions may exist in the core: the liquid heating region and the boiling region. The lengths in which each of the two phases of fluid may exist depend on the desired operating conditions and on which liquid metal is present in the core. The control system varies the pump speed and the reflector movement until the desired condition of the liquid metal leaving the core is obtained. This may be as a

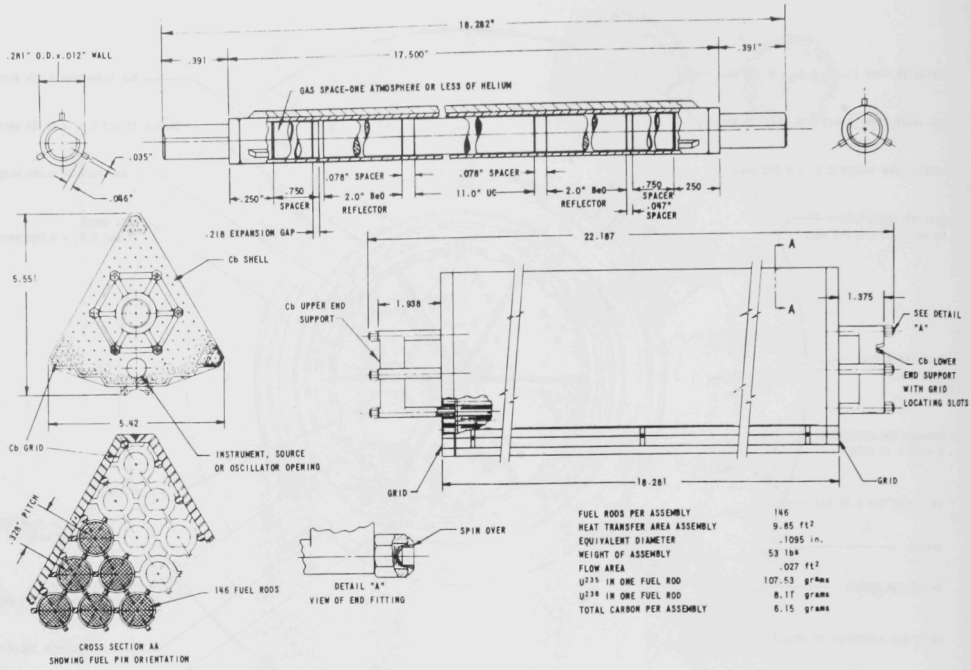


FIG. IV-25-3. Typical Fuel Element and Assembly. *ANL Neg. No. 112-8339 T-1.*

hot liquid or as a mixture of saturated liquid and vapor. The flow of boiling liquid metal is upward through the core. The metal vapor leaves the free surface above the core (see Fig. IV-25-1) and rises into the bundle of condenser tubes. The condensate falls by gravity back into the pool of liquid metal. Orificing is not currently provided in the core, but some type of orificing may be necessary to get correct flow distribution. This will be determined by experimental work before the core is built.

The test unit is arranged so that the core loading can be adjusted after the core is in place. Each of the six segments is an independent unit.

The fuel element tentatively selected is shown in Fig. IV-25-3. The fuel is uranium carbide. There is metal-to-metal contact between the uranium carbide and the columbium cladding. The three radial spacers are continuous over the length of the fuel and reflector sections of the fuel elements. The fuel element is a simple solid rod, which is considered to be satisfactory in its nuclear, thermal, and fabrication aspects.

All cladding and structural material of the core in contact with the liquid metal is columbium.

The turbine-driven pump for circulating the liquid metal is shown in Fig. IV-25-1. The working fluid in the turbine is helium. A similar pump[1] has demonstrated its capability for pumping boiling water when the available pressure head is zero. Its performance with liquid metal near the saturation point has not been investigated. The compressor in the helium circuit is an axial-flow type with a pressure ratio of 1.07. The pressure and temperature of the helium entering the compressor are 4.7 atm and 400°C, respectively.

The condenser consists of a series of helical tubes through which NaK flows and on which the metal vapor is condensed. The outer tubes of the condenser are constructed of columbium, 1% zirconium, and the inner tube is stainless steel; the annulus between them is filled with helium.

The distinctive features of this concept are:

1. The speed and ease with which damaged parts can be replaced. A section of the core, the entire core, or the complete test section can be quickly replaced.

2. The maximum possible amount of instrumentation is placed in the core in such a manner that most of it can be replaced (see Fig. IV-25-4).

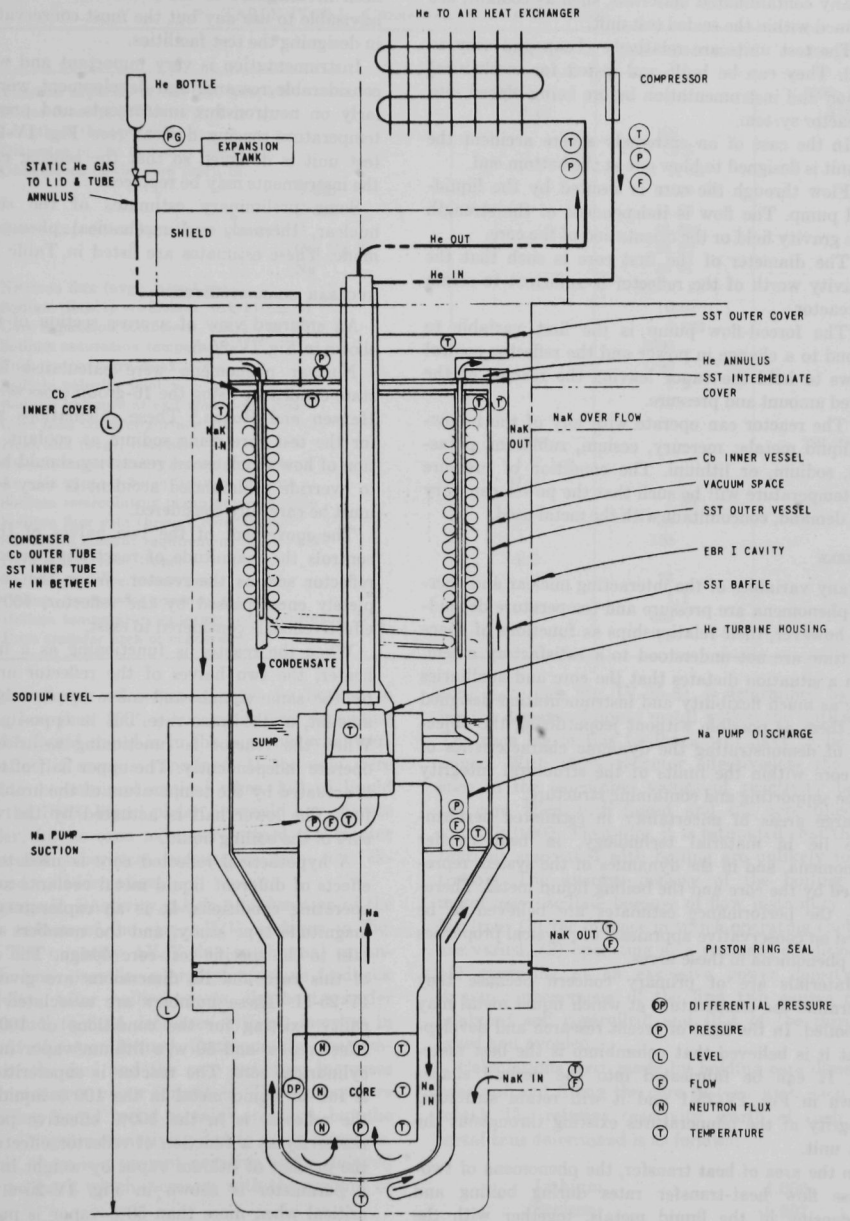


FIG. IV-25-4. Schematic of Flow Diagram Showing Instrumentation Sensing Points. *ANL Neg. No. 112-8340 T-1.*

3. Any contaminated materials, such as coolant, are contained within the sealed test unit.

4. The test units are relatively cheap and easy to install. They can be built and tested for mechanical function and instrumentation before being placed into the reactor system.

5. In the case of an extremely severe accident the test unit is designed to blow out at the bottom end.

6. Flow through the core is assured by the liquid-metal pump. The flow is independent of the strength of the gravity field or the orientation of the core.

7. The diameter of the first core is such that the reactivity worth of the reflector is sufficient to scram the reactor.

8. The forced-flow pump is the first variable to respond to a change in power and the reflector control follows to hold the vapor leaving the reactor at the desired amount and pressure.

9. The reactor can operate with any of the following liquid metals: mercury, cesium, rubidium, potassium, sodium, or lithium. The condition of pressure and temperature will be such that the power can vary with demand, concomitant with the metal used.

GENERAL

Many variables of the interacting nuclear and thermal phenomena are pressure and temperature dependent; however, their relationships as functions of space and time are not understood to a satisfactory extent. Such a situation dictates that the core and auxiliaries have as much flexibility and instrumentation designed into them as possible without jeopardizing the objective of demonstrating the dynamic characteristics of the core within the limits of the structural integrity of the supporting and containing structure.

Large areas of uncertainty in estimated performance lie in material technology, in heat-transfer phenomena, and in the dynamics of the system represented by the core and the boiling liquid metal. Therefore, the performance estimates are believed to be based on conservative appraisals of physical properties and phenomena in these areas.

Materials are of primary concern because they determine the temperature at which liquid metal may be boiled. In the light of recent research and development it is believed that columbium is the best material. It can be fabricated into the desired shapes shown in Fig. IV-25-1 and it will retain structural integrity at the temperatures existing throughout the test unit.

In the area of heat transfer, the phenomena of two-phase flow heat-transfer rates during boiling and condensing of the liquid metals, together with the burn-out fluxes at the proposed conditions, have not been investigated to the point where it is considered advisable to use any but the most conservative values in designing the test facilities.

Instrumentation is very important and will require considerable research and development work particularly on neutron-flux instruments and pressure- and temperature-sensing devices (see Fig. IV-25-4). The test unit is designed so that the sensing elements of the instruments may be replaced.

Some preliminary estimates of the steady-state nuclear, thermal, and mechanical phenomena were made. These estimates are listed in Table IV-25-I.

NUCLEAR CHARACTERISTICS

An enlarged view of a cross section of the core is shown in Fig. IV-25-5.

Nuclear phenomena were calculated for steady-state conditions using the 16-group cross section set of Hansen and Roach.[2] These calculations were made for the test core using sodium as coolant. The question of how much excess reactivity should be available to override a simulated accident is very crucial and must be carefully considered.

The movement of the two halves of the reflector controls the magnitude of reactivity; removal of the reflector scrams the reactor. When the core is completely encompassed by the reflector, 100% reflector effectiveness is considered to exist.

When the reactor is functioning as a liquid-metal heater, the two halves of the reflector are actuated by the same signals and move by exactly the same amount, at the same rate, but in opposite directions. When the reactor is functioning as a boiler, they operate independently. The upper half of the reflector is actuated by the temperature of the uranium carbide fuel. The lower half is actuated by the vapor pressure of the boiling liquid.

A hypothetical reflected core is used to study the effects of different liquid metal coolants and different operating conditions. It is an exploratory, order-of-magnitude type study, and the numbers do not pertain to the specific test-core design. The composition of this core and its dimensions are given in Table IV-25-II. These numbers are associated with criticality existing for the conditions of 100% reflector effectiveness and 50 w/o lithium vapor in an infinite cylindrical core. The reactor is supercritical when it is full of liquid metal in the 100% liquid phase and the reflector is in the 100% effective position. The reactivity as a function of reflector effectiveness with the percent of lithium vapor by weight in the core as a parameter is shown in Fig. IV-25-6. It is subcritical when more than 50% vapor is present in the core. If it is intended to operate as a liquid-metal

TABLE IV-25-I. CHARACTERISTICS OF THE CORE

| | Boiler | Boiler or Heater | Heater |
|---|---|---|---|
| Thermal capacity of the test core, kW | 1000 | | 5000 |
| Power density, MW/liter (core) | 0.06 | | 0.30 |
| Length of the test unit, in. | | 104 | |
| Diameter of the test unit (max), in. | | 22.8 | |
| Dimensions of the core (cyl), in. | | 11 × 11 | |
| Core composition by volume percent: U-235 | | 22.19 | |
| Core composition by volume percent: U-238 | | 11.09 | |
| Core composition by volume percent: C | | 18.39 | |
| Core composition by volume percent: Cb, 1% Zr | | 20.32 | |
| Core composition by volume percent: Na | | 28.01 | |
| Neutron flux (avg), n/cm²-sec | | $2.0 \times 10^{14}$ | |
| Sodium density coefficient, $(\Delta k/k)/(\Delta \rho/\rho)$ | | 0.01 | |
| Core expansion coefficient, $(\Delta k/k)/(\Delta V/V)$ | | 0.323 | |
| Sodium saturation temperature, °F | | 2000 | |
| Fuel temperature (max), °F | | 1790 | |
| Sodium velocity inlet to core, ft/sec | | 7.2 | |
| Sodium pressure at exit from core, psia | | 75 | |
| Core heat transfer surface, ft² | | 59 | |
| Heat flux (avg), Btu/hr-ft² | 57,840 | | 289,200 |
| Av exit vapor quality by weight percent | 1.6 | | |
| Av exit vapor volume fraction percent | 87.0 | | |
| Sodium recirculating pump pressure ratio | | 1.36 | |
| Sodium flow rate through core, lb/sec | | 38 | |
| Shutdown coolant requirement (max), kW | | 150 | |
| Helium flow rate, lb/sec | 1.0 | | 5.0 |
| Helium pressure (max), psia | | 77 | |
| Helium-compressor pressure ratio | | 1.1 | |
| Helium temperature entering the compressor, °F | | 600 | |
| Heat transfer area of condenser, ft² | | 78 | |

heater the reflector effectiveness must be limited to something less than 100%—how much less depending upon which liquid metal is in the core and what percentage of it, if any, is vaporized. If the core were designed to be minimal critical when full of liquid metal in the 100% liquid phase, it would not operate as a boiler, for as soon as vapor formed the reactor would become subcritical because of both core expansion and void formation.

The change in reactivity, $\Delta k/k$, as a function of the change in volume of the core, $\Delta V/V$, is shown in Fig. IV-25-7. The quantity $\Delta V/V$ due to thermal expansion of the core provides a prompt negative feedback of reactivity. After boiling starts, the heat-transfer rate from fuel to fluid decreases with an increase in the amount of vapor formed. Consequently, the temperature of the fuel and the core structure increases with an increase in vapor formation. The temperature of the boiling liquid metal remains constant, but the feedback of negative reactivity due to voids increases. As a result, there is a prompt negative and a delayed negative feedback which increases with the amount of vapor.

The change in reactivity, $\Delta k/k$, as a function of the change in density of the liquid metal within the core, $\Delta \rho/\rho$ (see Fig. IV-25-8), is determined by varying the density of liquid metal within the critical core. The time lag of this feedback will have to be determined. With 100% reflector effectiveness the difference in the calculated values of reactivity between the core filled with liquid and the core filled with vapor is 0.007. Therefore, it is estimated that the fluctuations associated with boiling are unlikely to cause trouble. The average density of the boiling liquid metal may oscillate because of flow instability resulting from (1) the manner in which operating conditions are varied, (2) operating at a resonant condition, and (3) operating at an excessive power density. The dynamic phenomena of the first two causes can be analyzed and controlled, and that of the third analyzed and avoided.

Calculations were made by holding core dimensions constant and filling the core in turn with each liquid metal. The relative reactivity worth of each liquid metal thus determined is as follows:

| | |
|---|---|
| Lithium | 1.000 |
| Sodium | 0.997 |
| Potassium | 0.991 |
| Mercury | 0.988 |

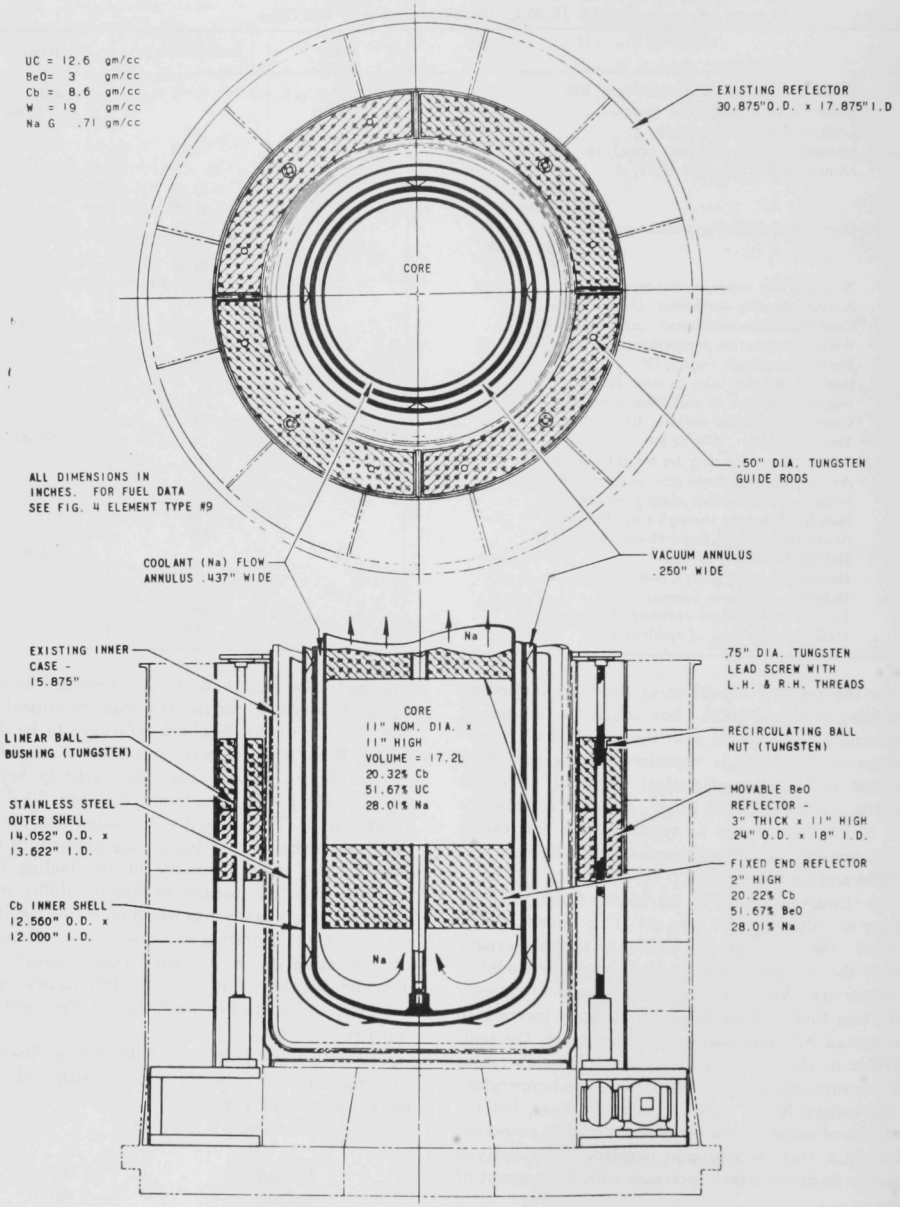


FIG. IV-25-5. Enlarged View of Core Region. *ANL Neg. No. 112-8341 T-1.*

The relative worth in reactivity of each metal pertains only to this core, and does not necessarily imply that the same relative worth will apply to cores of different dimensions and composition. The estimates are preliminary and are considered to indicate orders of magnitude and relative relationships. An additional calculation in spherical geometry, using the DSN code, was made as a check on the foregoing. The 16-group cross-section set of Hansen and Roach was used, assuming conditions of liquid sodium and 100% reflector control. Only the first 10 groups were used, including energy down to 30 eV. For sodium, the reactor was critical at the following volume fractions: fuel—0.5167; clad (Mo)—0.2036; sodium—0.2801. The sodium was then replaced with void and $k$ was found to be 0.9907. A detailed calculation of the reflector worth as a function of distance moved has not yet been attempted. Since the total worth of full-density sodium in the available void space is only about 1%, it seems unlikely that boiling fluctuations can cause the reactivity to exceed prompt critical. Changes in the density of the boiling liquid metal in the core can be caused by a change in temperature due to a change in pressure or inlet temperature, or by a fluctuation in void fraction caused by flow instability. The latter is considered to be the more significant cause.

To obtain the change in reactivity due to volumetric expansion of the core from any cause, the radius only was increased in increments of ½ up to 2%. The core mass and the thickness of all other

TABLE IV-25-II. Dimensions and Composition of a Hypothetical Core

(Core dimensions (cyl), cm: 24 × 24; core volume, liters: 11)

Core

| Material | v/o | Atoms/cc of Material, $10^{24}$ | Atoms/cc of Core, $10^{24}$ | Volume of Material, liters | Weight of Material, kg |
|---|---|---|---|---|---|
| $U^{235}$ | 26.28 | 0.0473 | 0.01243 | 2.89 | 54.35 |
| $U^{238}$ | 13.13 | 0.048 | 0.00630 | 1.44 | 27.15 |
| C | 21.79 | 0.0838 | 0.01826 | 2.40 | 6.72 |
| Nb-1% Zr | 23.81 | 0.0545 | 0.01298 | 2.62 | 22.0 |
| Liquid Metal (Li) | 15.50 | 0.463 | 0.00718 | 1.71 | 0.9 |

Reflector

| Material | Atoms of O per cc of Reflector | Atoms of Be per cc of Reflector | Volume of Materials, liters | Weight of Material, kg |
|---|---|---|---|---|
| BeO | 0.0728 | 0.0728 | 24.9 | 71 |

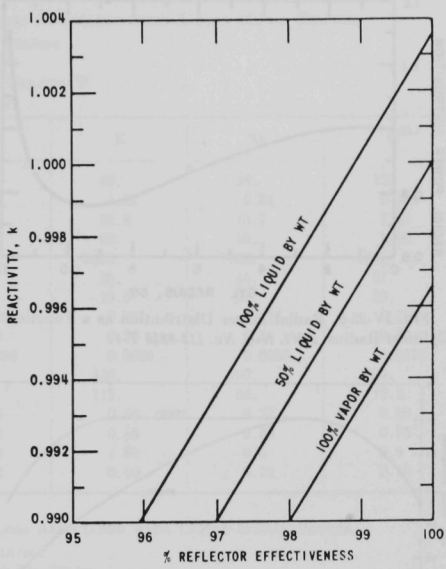


Fig. IV-25-6. Reactivity versus Reflector Effectiveness. *ANL Neg. No. 112-8342 T-1.*

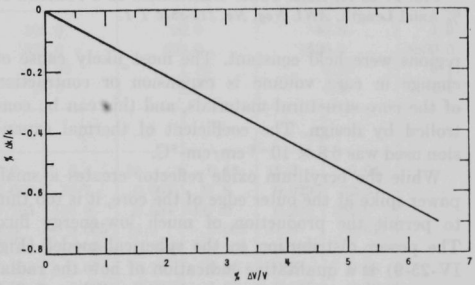


Fig. IV-25-7. Change in Reactivity as a Function of Change in Volume of Core. *ANL Neg. No. 112-8343 T-1.*

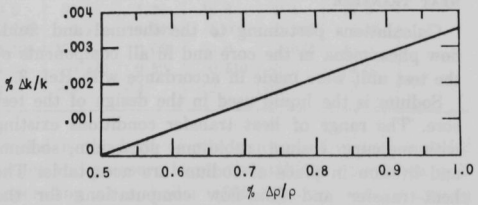


Fig. IV-25-8. Change in Reactivity as a Function of Change in Density of Liquid Metal within Core. *ANL Neg. No. 112-8344 T-1.*

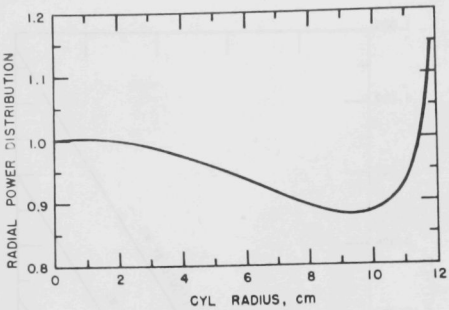


FIG. IV-25-9. Radial Power Distribution as a Function of Cylinder Radius. *ANL Neg. No. 112-8345 T-1.*

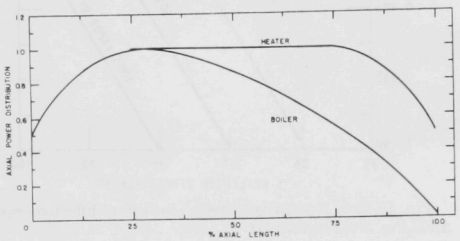


FIG. IV-25-10. Axial Power Distribution as a Function of % Axial Length. *ANL Neg. No. 112-8346 T-1.*

regions were held constant. The most likely cause of change in core volume is expansion or contraction of the core structural materials, and this can be controlled by design. The coefficient of thermal expansion used was $6.8 \times 10^{-6}$ cm/cm-°C.

While the beryllium oxide reflector creates a small power spike at the outer edge of the core, it is too thin to permit the production of much low-energy flux. The power distribution in the spherical model (Fig. IV-25-9) is a qualitative indication of how the radial power distribution in the actual core will be affected by the beryllium oxide reflector.

### HEAT TRANSFER

Calculations pertaining to the thermal and fluid-flow phenomena in the core and in all components of the test unit were made in accordance with Ref. 3.

Sodium is the liquid used in the design of the test core. The range of heat transfer conditions existing with mercury, cesium, rubidium, potassium, sodium, and lithium in place of sodium are acceptable. The heat-transfer and fluid-flow computations for the sodium cooled core were made assuming that (1) high vapor-volume fractions can exist in the core without oscillations, or (2) if oscillations do occur, they will be of such magnitude as not to affect reactivity significantly.

The vapor quality may be estimated from the presently available correlations for the flow of a two-phase mixture. However, it is believed that only the actual operation of a specific core can determine what quality is compatible with dynamic stability.

For a given system pressure, the power density of the boiling core is primarily limited by the burnout heat flux and, to a lesser degree, by the pressure drop. Therefore, for the same system pressure, the boiling core will have a lower power density than that of a core which merely heats the liquid metal. When the test core is operating as a heater, the estimated axial power distribution is as shown on the heater curve of Fig. IV-25-10; when the test core is operating as a boiler, the estimated power distribution is as shown on the boiler curve of Fig. IV-25-10. With the present arbitrary limitation of 2000°F placed on the temperature of the uranium carbide, the power density when the test core operates as a heater is estimated to be four to five times greater than when the core operates as a boiler. If it is possible to operate nearer the critical temperature of any of the liquid metals, this factor of four to five will decrease. It decreases because the ratio of forced-convection heat-transfer rates of the liquid and vapor phases of a metal for the same mass flow approaches unity as the operating pressure approaches the critical pressure. The ratio of unity cannot be approached now, because the saturation temperatures at the critical pressures are far in excess of the 2000°F limitation. For the present operating conditions, the convection heat-transfer rate decreases as the quality of the vapor increases, it is therefore necessary to reduce the power density along the uranium carbide rod by reducing the effectiveness of the neutron reflector surrounding the core.

The average heat flux and average power density which may be expected with some assurance of stability and safety when the reactor is operating as a liquid heater, are approximately 450,000 Btu/ft$^2$ and 0.45 MW per liter of core volume.[3] Until the operating characteristics are established, these values should be approached cautiously in the use of the test core. The heat transfer and pressure loss associated with the liquid metal heater are given in Table IV-25-III.

The average heat flux associated with the reactor when it is operating as a boiler, is considered to be approximately 100,000 Btu/ft$^2$-hr; this value is the result of studying several documents.[3, 4] The burnout heat flux for boiling liquid metals may vary from $0.45 \times 10^6$ to $55 \times 10^6$ Btu/ft$^2$-hr. The variation in

TABLE IV-25-III. HEAT TRANSFER AND PRESSURE LOSS ASSOCIATED WITH LIQUID-METAL HEATER

$Q$ (total heat): 4743 Btu/sec
$\Delta T$ assumed: 400°F
$Q/\Delta T$: 11.86 Btu/sec-°F
$T$ exit: 1832°F

| Liquid Metal → | Hg | Cs | Rb | K | Na | Li |
|---|---|---|---|---|---|---|
| $W$, lb/sec | 297. | 208. | 148. | 59. | 38. | 12. |
| $W/\rho$, ft³/sec | 0.423 | 2.08 | 1.90 | 1.52 | 0.84 | 0.444 |
| $v$, ft/sec | 6.94 | 34.1 | 31.0 | 24.8 | 13.7 | 7.29 |
| $P$ out, lb/in.² | 3500. | 140. | 105. | 90. | 40. | 1.00 |
| $T$ out, °F | 1832. | 1832. | 1832. | 1832. | 1832. | 1832. |
| $\rho$ av, lb/ft³ | 700. | 100. | 78. | 39. | 45. | 27. |
| $K$ av, Btu/hr-ft-°F | 10.0 | 10.7 | 8.0 | 19.5 | 31. | 29. |
| $C_p$ av, Btu/lb-°F | 0.040 | 0.057 | 0.080 | 0.201 | 0.316 | 0.989 |
| $\mu$ av, lb/ft-hr | 1.6 | 0.70 | 0.30 | 0.26 | 0.34 | 0.50 |
| $Pr$, $C_p\mu/K$ | 0.0050 | 0.0040 | 0.0030 | 0.0036 | 0.0035 | 0.0170 |
| $Pe$, $DVC_p/K$ | 590. | 550. | 720. | 410. | 190. | 204. |
| $Re \times 10^{-3}$, $VD\rho/\mu$ | 92. | 176. | 236. | 113. | 55. | 12.2 |
| $D/K \times 10^3$ | 0.84 | 0.79 | 1.05 | 0.58 | 0.27 | 0.29 |
| $f \times 10^2$ | 0.50 | 0.45 | 0.38 | 0.48 | 0.55 | 0.75 |
| $h$, Btu/ft²-sec-°F | 3.30 | 3.50 | 4.15 | 4.80 | 9.5 | 8.9 |
| $G \times 10^{-3}$, lb/ft-sec | 2.43 | 1.66 | 1.22 | 0.49 | 0.32 | 0.10 |

TABLE IV-25-IV. HEAT TRANSFER AND PRESSURE LOSS ASSOCIATED WITH LIQUID-METAL BOILER

$Q$(total heat): 950 Btu/sec
$q$(heat flux): 100,000 Btu/ft²-hr
$T$ exit: 1800°F

| Liquid Metal → | Hg | | Cs | | Rb | | K | | Na | | Li |
|---|---|---|---|---|---|---|---|---|---|---|---|
| $P$ sat, lb/in² | 3500.0 | | 140.0 | | 105.0 | | 90.0 | | 40.0 | | 1.0 |
| $h_{fg}$, Btu/lb | 120.0 | | 187.0 | | 321.0 | | 800.0 | | 1620.0 | | 8850.0 |
| $W_g$, lb/sec | 7.91 | | 5.08 | | 2.95 | | 1.19 | | 0.59 | | 0.11 |
| $G$, lb/ft²-sec | 65.0 | | 42.0 | | 24.0 | | 9.8 | | 4.8 | | 1.1 |
| Phase | $f$ | $g$ | $f$ | $g$ | $f$ | $g$ | $f$ | $g$ | $f$ | $g$ | |
| $\rho$, lb/ft³ | 700.0 | 30.0 | 100.0 | 0.7 | 78.0 | 0.4 | 39 | 0.15 | 45.0 | 0.04 | |
| $W/\rho$, ft³/sec | 0.025 | 0.510 | 0.113 | 16.2 | 0.086 | 16.7 | 0.068 | 17.8 | 0.029 | 32.3 | |
| $v$, ft/sec | 0.205 | 4.4 | 0.927 | 131.0 | 0.705 | 136.0 | 0.558 | 147.0 | 0.238 | 265.0 | |
| $K$, Btu/hr-ft-°F | 10.0 | 0.010 | 10.7 | 0.004 | 8.0 | 0.005 | 14.5 | 0.009 | 31.0 | 0.017 | |
| $C_p$, Btu/lb-°F | 0.040 | 0.030 | 0.060 | 0.060 | 0.080 | 0.100 | 0.200 | 0.210 | 0.320 | 0.620 | |
| $\mu$, lb/ft-hr | 1.60 | 0.40 | 0.70 | 0.07 | 0.30 | 0.07 | 0.26 | 0.05 | 0.34 | 0.06 | |
| $Pr$, $C_p\mu/K$ | 0.05 | 1.20 | 0.04 | 1.16 | 0.03 | 1.30 | 0.036 | 1.25 | 0.035 | 2.10 | |
| $Pe \times 10^{-2}$, $DV\rho Dp/K$ | 0.007 | 121.0 | 0.016 | 447.0 | 0.017 | 305.0 | 0.090 | 156.0 | 0.039 | 157.0 | |
| $Re \times 10^{-2}$, $DV\rho/\mu$ | 27.1 | 101.0 | 40.0 | 399.0 | 55.4 | 234.0 | 25.0 | 125.0 | 9.5 | 60.0 | |
| $f \times 10^{+2}$ friction factor | 1.40 | 0.80 | 1.00 | 0.60 | 0.90 | 0.65 | 1.30 | 0.70 | 1.50 | 0.90 | |
| $Re^{0.8} \times 10^{-2}$ | 5.60 | 16.0 | 7.6 | 48.0 | 10.0 | 32.0 | 5.24 | 18.8 | 2.4 | 10.6 | |
| $Pr^{0.4}$ | 0.300 | 1.08 | 0.276 | 1.06 | 0.246 | 1.11 | 0.249 | 1.09 | 0.262 | 1.34 | |
| $D/K \times 10^2$ | 0.084 | 84.0 | 0.079 | 227.0 | 0.105 | 156.0 | 0.058 | 93.0 | 0.027 | 49.0 | |
| $h \times 10^{-2}$, Btu/ft²-hr-°F | 46.0 | 0.470 | 61.0 | 0.520 | 54.0 | 0.530 | 0.52 | 0.510 | 53.5 | 0.57 | |
| $\Delta P$, lb/in² | <2 | <2 | <2 | <2 | <2 | <2 | <2 | <2 | <2 | <2 | |

these predictions is a result of wide disagreement among investigators as to the influence of the thermal diffusivity of the liquid phase on burnout heat flux. The liquid metal enters at a temperature close to that of saturation. The major portion of the heat transferred from the uranium carbide rods to the liquid metal is the heat of vaporization. The heat-transfer rates and pressure losses through the core when it is operating as a boiler (950 Btu/sec for vaporizing only) are given in Table IV-25-IV. The values listed[6] should be taken only as indicative of the relative merits of the liquid metals considered.

TABLE IV-25-V. PHYSICAL PROPERTIES OF LIQUID METALS

| Liquid Metal → | Hg | Cs | Rb | K | Na | Li |
|---|---|---|---|---|---|---|
| Atomic weight | 200.0 | 132.91 | 85.48 | 39.10 | 22.997 | 6.94 |
| Melting point, °F | −38.0 | 83.0 | 102.0 | 145.8 | 208.0 | 351.0 |
| Boiling point, °F | 674.0 | 1260.0 | 1270.0 | 1400.0 | 1618.0 | 2437.0 |
| Density of liquid, lb/ft | 794.0 | 104.7 | 82.15 | 41.38 | 46.4 | 31.8 |
| Density of vapor, lb/ft | 0.26 | 0.096 | 0.060 | 0.0305 | 0.0165 | |
| Thermal conductivity, Btu/hr-ft-°F | 8.1 | 10.65 | 11.8 | 18.0 | 30.1 | 27.2 |
| Specific heat (liquid), Btu/lb-°F | 0.0323 | 0.0572 | 0.0877 | 0.1868 | 0.305 | 0.98 |
| Specific heat (vapor), Btu/lb-°F | 0.0248 | 0.0372 | 0.0579 | 0.1267 | 0.214 | 0.716 |
| Latent heat of fusion, Btu/lb | 5.07 | 6.90 | 111.79 | 25.5 | 48.7 | 186.0 |
| Latent heat of vaporization, Btu/lb | 125.7 | 213.8 | 347.5 | 851.0 | 1609.0 | 9108.0 |

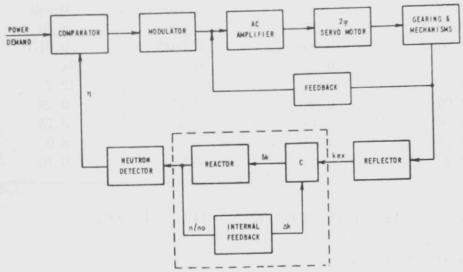


FIG. IV-25-11. Block Diagram of Control System. *ANL Neg. No. 112-8347 T-1.*

## CHOICE OF LIQUID METAL

It is proposed to investigate mercury, cesium, rubidium, potassium, sodium, and lithium.[5] The core and test equipment are designed for a wide range of operating conditions centering around the conditions with the characteristics of sodium.

The first consideration in the choice of a liquid metal for use in the reactor core depends upon the pressure of the environment. The pressure of the fluid within the core shell should be greater than the pressure of the environment but not greater than 400 lb/in.$^2$, since both the core shell and the reactor-containing shell are designed, with a safety factor of three, for 200 lb/in$^2$. A liquid metal which has a low neutron capture cross section is desirable so that fluctuations in the number of atoms of this liquid metal in the core at a given time and place do not cause significant changes in reactivity. The enthalpy, latent heat, and specific heat are important, because if these values are large, less mass flow of metal is required to provide the thermal power, which means less volume and weight of reactor, heat exchangers, and machinery, and fewer atoms to affect the reactivity.

Temperature has a far-reaching effect upon the design, since all physical properties of the liquid metal, the fuel and the structural materials are functions of temperature. At present, the maximum liquid-metal temperature of 2000°F is limited by the structural and chemical integrity of the uranium carbide rods. The next limiting factor, by a few hundred degrees, is the structural material. As the temperature limit is raised, the use of liquid metal in a nuclear reactor becomes more attractive, from a performance point of view.

At any given temperature, lithium has a lower vapor pressure than sodium, potassium, rubidium, cesium, or mercury, thus requiring less volume. The vapor pressures (psia) at 2460°F for the liquid metals considered are as follows:

| Li | Na | K | Rb | Cs | Hg |
|---|---|---|---|---|---|
| 2 | 75 | 140 | 240 | 200 | 6500 |

The highest cycle temperature compatible with material reliability over the expected lifetime of the power system under consideration is 2000°F, corresponding to a pressure of 75 psia for sodium. For convenience, some physical properties of the various liquid metals at atmospheric pressure[4] are presented in Table IV-25-V.

## DYNAMICS

This test unit is a closed-loop, non-linear system with internal and external feedbacks. In the event of an accident, the two halves of the reflector are rapidly and completely removed from the core. This combined reactivity worth is such that their removal shuts down the reactor for the postulated types of accident. During normal core operation as a heater, these two halves will be at positions equivalent to 99% effectiveness; when the core is operating as a boiler, one-half of the reflector will be at 99% and the other at less than 99% effectiveness.

The block diagram of the control system is shown in Fig. IV-25-11. The internal feedback loop is within the area bounded by the dotted lines. The

principal sources of internal feedback in this core are the volumetric expansion of the core fuel and the variations of the density of the fluid flowing through the core.

COST ESTIMATES

Since it is intended that tests be conducted which are quite likely to destroy the structural integrity of part or all of the test unit, it is desirable that it be easy and cheap to replace the damaged parts. An estimate of the cost of the complete test unit is given below:

| | | |
|---|---|---|
| A. *Cost of Fabricated Components* | | |
| Containing shell | $210,000 | |
| Core and fuel | 100,000 | |
| Reflector and mechanism | 80,000 | |
| Condenser | 60,000 | |
| Oscillator mechanism | 15,000 | |
| Recirculating pump | 155,000 | |
| Source-drive mechanism | 15,000 | |
| Heat exchanger | 5,000 | |
| Compressor | 25,000 | |
| Instruments | 75,000 | |
| Shielding change | 20,000 | |
| Fuel-handling equipment | 35,000 | |
| | $795,000 | $795,000 |
| B. *Cost of Assembling Test Unit (Labor)* | | |
| Cost of assembling test unit | $850,000 | $850,000 |
| | | $1,645,000 |

REFERENCES


1. H. E. Adams, *Pumping Boiling Fluids When the Available Static Head is Zero or Less*, ASME Paper 63, WA-220 (August 30, 1963). Presented at the November 1963 Annual Meeting.
2. G. E. Hansen and W. H. Roach, *Six and Sixteen Group Cross Sections for Fast and Intermediate Critical Assemblies*, LAMS-2543 (November 1961).
3. P. A. Lottes, *Nuclear Reactor Heat Transfer*, ANL-6469, (1961), p. 88.
4. R. P. Anderson, L. T. Bryant, J. C. Carter and J. F. Marchaterre, *Transient Analysis of Two-Phase Natural-Circulation Systems*, ANL-6653 (1962).
5. Liquid Metals Handbook, Sodium-NaK Supplement Third Edition, TID-5277, (Atomic Energy Commission and Department of the Navy, Washington, D. C., July 1955 )


## IV-26. Calculation of the Energy Yield in the Kiwi Transient Nuclear Test, Kiwi-TNT

V. Z. JANKUS

INTRODUCTION

Numerical calculation of certain classes of reactor excursions using the AX-1 code[1] have shown[2] that the results do not differ greatly from the estimates obtained using an essentially analytical Bethe-Tait[3] method. Compared with numerical calculations, the latter method uses some simplifying approximations including the neglect of the effect of wave propagation. Because of these simplifications, the calculated energy yield appears to depend on a lesser number of parameters than required by the numerical calculations. Moreover, the computational procedure of the Bethe-Tait method is quite straightforward and one can readily ascertain the influence of various parameters upon the final result. In an experimental situation the values of various parameters are not always known precisely. Therefore, it has seemed appropriate to make an analytical estimate of the energy yield in an experiment on a graphite-moderated reactor, KIWI-TNT, and compare it with the observed results.

In the process of our calculation we have generalized and (somewhat) modified the Bethe-Tait method to be able to use with it highly non-spherical geometry and a rather complicated equation of state for graphite. For the experimental reactivity insertion we find that the Bethe-Tait method is still inapplicable since a major portion of reactivity reduction occurs at initial stages, when the graphite is still solid, the velocity of wave propagation is large, and the graphite expands with negligible inertial delay following heat input. In the following section we extend Hansen's method[4] for cylindrical geometry, and we find that immediate reactivity reduction is almost of sufficient magnitude to produce the shutdown. This method takes account of wave propagation as well as inertial delay in expansion, and is based on the assumption that the power is proportional to $e^{\alpha t}$. The residual seems to depend strongly upon core geometry, boundary conditions and the details of the equation of state. In the last section we calculate the maximum energy available for destructive work for a rather peculiar graphite equation of state. We are gratified to see that simple methods used to estimate potential damage in maximum credible accident studies agree so well with the destruction observed

experimentally. We notice, however, that the numbers obtained this way may often not be accurate enough for an economic design of a reliable containment.

### Calculation of Energy Yield by the Bethe-Tait Method

The first basic assumption underlying the Bethe-Tait method is that the motions in a reactor excursion are quite small and the reactivity change due to them can be adequately calculated using first order perturbation theory. When such an assumption is applied (using diffusion theory), the reactivity change is determined to be[2]

$$k = \int \rho \mathbf{u} \cdot \mathbf{f} \, dV, \tag{1}$$

where $\rho$ is the density of homogenized material, $\mathbf{u}$ is displacement and $\mathbf{f}$ is a vector that coincides with the gradient of worth, $\nabla w$, in regions of constant composition, experiencing only finite jumps at interfaces. With this interpretation of $\mathbf{f}$, Eq. (1) may be considered self-evident as reactivity changes due to small motions are assumed to be additive. When the motion is calculated by Newton's second law and Eq. (1) is integrated by parts, one obtains

$$\ddot{k} = \int p \nabla \cdot \mathbf{f} \, dV, \tag{2}$$

where $p$ is pressure. Since $\mathbf{f}$, in general, experiences jumps at the interfaces between regions of different composition, Eq. (2) can be rewritten as

$$\ddot{k} = \sum_i \left( \int p \nabla^2 w_i \, dV - \int p \nabla w_i \cdot d\mathbf{S} \right), \tag{3}$$

where $w_i$ is material worth in region $i$ and $\ddot{k}$ is calculated by performing integrations separately over volumes and boundaries of various regions.

The second assumption of the Bethe-Tait theory is that pressure, $p$, [Eq. (2)] can be calculated considering only the heat generated at the spot. This assumption has been shown[5] justified for a constant velocity of wave propagation, $c$, and a constant Laplacian of worth, $\nabla \cdot \mathbf{f}$, but is expected, in general, to be applicable whenever the pressure wave can traverse only a fraction of the core during the initial period. Supposing that the reactor flux retains the same spatial shape $N(\mathbf{r})$ during the excursion, we calculate the pressure at various parts of the reactor using the "equation of state" at the original density,

$$p = p[Q(t)N(\mathbf{r})], \tag{4}$$

where $N$ is the power shape factor and $Q(t)$ is the heat generated at the center of the reactor (where $N = 1$) at time $t$.

After substitution of Eq. (4) into Eq. (2) and integration we obtain $\ddot{k}$ as a function of energy density at the center of the reactor:

$$\ddot{k} = -F[Q(t)]. \tag{5}$$

The energy input and reactivity change can now be calculated as a function of time only (one-point kinetics.) In large excursions of a fast reactor, the reactivity considerably exceeds prompt critical and one may neglect delayed neutrons. Thus power changes are connected with the reactivity by

$$l \frac{d}{dt} \ln \dot{Q} = k \tag{6}$$

where $l$ is prompt neutron lifetime. We can now easily solve the ordinary coupled differential Eqs. (5) and (6), using a small computer, to determine the total energy yield, $Q(t \to \infty) = Q_f$.

This, however, still involves some numerical calculations, and the results are by no means obvious if the function $F$ in Eq. (5) is somewhat complex. In the case under consideration, the equation of state to be used seems quite complex, and the effect of various approximations of it for various energy ranges are quite unclear, even upon $F$ itself. The influence of it on the final energy yield is still further removed by the solution of differential equations. Thus an approximate solution of the coupled differential equations is desirable. Such a solution has been provided in the original Bethe-Tait paper[3] where it is assumed that the energy input is exponential with time. Thereupon they calculated reactivity [from Eq. (5)] is a function of time, stopping the calculation when the reactivity reduction became equal to the reactivity inserted initially ($k_0$). This procedure of calculation can be summarized in one formula:

$$k_0^3 l^{-2} = \int_0^{Q_f} \frac{dQ'}{Q'} \int_0^{Q'} \frac{dQ}{Q} F(Q).$$

This formula gives reactivity input as an explicit function of the final energy generated. The intermediate integral over $Q'$ can be performed without knowing the form of $F$:

$$\begin{aligned} k_0^3 l^{-2} &= \int_0^{Q_f} \frac{dQ}{Q} \left( \ln \frac{Q_f}{Q} \right) F(Q) \\ &= -\int_0^1 \frac{dN'}{N'} (\ln N') F(N' Q_f). \end{aligned} \tag{7}$$

Of course, $F$ is also given in terms of an integral over volume. When $\nabla \cdot \mathbf{f}$ and the power distribution over volume is simple, the volume integration can also be performed explicitly without using the dependence of pressure upon energy input. For pressure proportional

to some power of energy input[2] a variable discrepancy of an appreciable magnitude was discovered.

Thus a modified approximation procedure is proposed here. It is based upon the observation that the total energy yield can be calculated quite simply for a "quasi-static" reactivity reduction mechanism.[6] To apply this procedure to the solution of Eqs. (5) and (6), we calculate the reactivity from Eq. (5) using an exponential dependence of heat, $Q$, upon time. We then postulate that the relationship between heat input and reactivity is maintained also for non-exponential variation of heat input. Thus we assume that the reactivity reduction is

$$k = \frac{l^2}{k_0^2} \int_0^Q \frac{dQ'}{Q'} \int_0^{Q'} \frac{dQ''}{Q''} F(Q'').$$

Then the total energy yield can be calculated quite simply. The intermediate integral can be performed analytically and a replacement for Eq. (7) can be obtained. Comparison with exact calculations for pressure proportional to some power of energy input, however, shows that the new approximation gives final pressure consistently too low by a factor approximately 2 (1.58 to 1.85). After this correction is introduced

$$k_0^3 l^{-2} = 2 \int_0^1 dN' \left( -\frac{\ln N'}{N'} + 1 - \frac{1}{N'} \right) F(N'Q_f). \quad (8)$$

Compared with Eq. (7), this expression gives less weight to the pressure values close to the end of the excursion, ($N' \to 1$).

If it is assumed that Kiwi is an axial unreflected but radially well-reflected reactor, the power shape is nearly flat radially and

$$N = \cos \frac{\pi z}{2L}.$$

If we prevent radial expansion and allow the core material to expand only axially, we would find (see next section) that

$$\nabla \cdot \mathbf{f} \propto 2 \cos^2 \frac{\pi z}{2L} - 1. \quad (9)$$

Then the approximate solution for the excursion yield would become

$$k_0^3 l^{-2} = 2 \cdot \frac{2}{\pi} (-\nabla \cdot \mathbf{f}_0 V) \int_0^1 dN \, p(NQ_f) I_k^{(2)}(N), \quad (10)$$

where

$$I_k^{(2)}(N) = \int_N^1 \frac{dN'}{N} \left( \ln \frac{N'}{N} - 1 + \frac{N}{N'} \right) \cdot \frac{2N'^2 - 1}{\sqrt{1 - N'^2}} = \frac{\pi}{4} \frac{1}{N} - \operatorname{sech}^{-1} N - \frac{1}{2N} \sin^{-1} N + \frac{1}{2} \sqrt{1 - N^2}. \quad (11)$$

As $N \to 0$,

$$I_k^{(2)}(N) = \frac{\pi}{4N} - \ln \frac{2}{N} - \frac{1}{12} N^2 - \frac{1}{160} N^4 + \cdots.$$

As $N \to 1$,

$$I_k^{(2)}(N) = \frac{1}{15N} (1 - N^2)^{5/2} \left[ 1 + \frac{11}{14} (1 - N^2) + \cdots \right].$$

On the other hand, if expansion is allowed in all directions

$$\nabla \cdot \mathbf{f} \propto 2 \cos^2 \frac{\pi z}{2L} \quad (12)$$

and correspondingly for large $N$, $I_k^{(2)}(N)$ demonstrates the same behavior as previously:

$$I_k^{(2)}(N) = \frac{\sqrt{32}}{15N} (1 - N)^{5/2}, \quad \text{as} \quad N \to 1,$$

but is much larger for small values of $N$:

$$I_k^{(2)}(N) = \frac{\pi}{4N} - \ln 2N - \frac{1}{2}, \quad \text{as} \quad N \to 0.$$

Thus, the relative importance of the equation of state at low energies is considerably enhanced if radial expansion is taken into account.

The actual evaluation of the integral in Eq. (10) for a complex dependence of pressure upon energy input would have to be done numerically. It may be noticed that $I_k^{(2)}$ is very large for small $N$ and very small for large $N$. The behavior of pressure is contrary to this, so that for large $Q_f$ the integrand in Eq. (10) has two peaks: one at $N = 0$, another at large $N$. The numerical calculation of the contribution of the large $N$ peak using the equation of state for graphite has shown unexpectedly that its contribution is very small (compared with $k_0^3 l^{-2}$) for experimentally observed $Q_f$. It increases very rapidly with increasing $Q_f$. For calculation of the contribution at low energies, a numerical integration can be avoided if the pressure is approximated by a polynomial in $Q$. If the pressure is proportional to the power, $n$, of energy input, it can be shown (quite simply) using the natural order of integrations, that

$$k_0^3 l^{-2} = 2 \frac{P(Q_f)}{n^2(n+1)} \int (-\nabla \cdot \mathbf{f}) N^n \frac{dV}{dN} \, dN.$$

When expansion in all directions is allowed in the axially bare reactor, the preceding equation becomes

$$k_0^3 l^{-2} = 2 \cdot \frac{2}{\pi} (-\nabla \cdot \mathbf{f}_0 V) \frac{\sqrt{\pi}}{2} \cdot \frac{\Gamma\left(\frac{n+3}{2}\right)}{\Gamma\left(\frac{n+4}{2}\right)} \frac{P(Q_f)}{n^2(n+1)}. \quad (13)$$

If the reactor is confined radially, [Eq. (17)],

$$k_0^3 l^{-2} = 2 \cdot \frac{2}{\pi} (-\nabla \cdot \mathbf{f}_0 V) \frac{\sqrt{\pi}}{2} \cdot \frac{\Gamma\left(\frac{n+3}{2}\right)}{\Gamma\left(\frac{n+4}{2}\right)} \left(\frac{n}{n+1}\right) \frac{P(Q_f)}{n^2(n+1)}.$$

When the pressure is proportional to the heat input ($n = 1$), we obtain for the unrestricted expansion

$$k_0^3 l^{-2} = 2 \cdot \frac{4}{3\pi} (-\nabla \cdot \mathbf{f}_0 V) P(Q_f). \quad (14)$$

When expansion is allowed only in the axial direction, the right side is only half of the right member of Eq. (14).

Having assumed the spatial dependence of $\nabla \cdot \mathbf{f}$, we can determine its magnitude experimentally from the observed isothermal expansion, as is done in Eq. (20). Substituting this value from Eq. (20) into Eq. (14) we obtain

$$k_0^3 l^{-2} = 23.96 \left[\frac{1}{L^2}\left(\frac{\partial p}{\partial \rho}\right)_s\right]\left[\left(\frac{\partial \theta}{\partial e}\right)_\rho \left(\frac{\delta k}{\delta \theta}\right)_u\right] Q_f, \quad (15)$$

where $e$ is the specific energy constant in ergs/gm and $\theta$ is temperature in degrees Kelvin. Now the experimentally measured reactivity coefficient for uniform expansion (denoted by $u$) is

$$\left(\frac{\delta k}{\delta \theta}\right)_u = 5.6 \times 10^{-6}\ ^\circ\mathrm{K}^{-1}.$$

[It is believed now that this numerical value is quoted earlier through a misinterpretation of experimental measurements and the number should be revised considerably upwards[7] to $13.2 \times 10^{-6}\ ^\circ\mathrm{K}^{-1}$.] The specific heat of graphite at room temperature is

$$C_v = \left(\frac{\partial e}{\partial \theta}\right)_\rho \approx 0.7 \times 10^7 \frac{\mathrm{erg}}{\mathrm{g}^\circ\mathrm{K}}.$$

The isothermal compressibility is nearly equal to the isentropic compressibility:

$$\left(\frac{\partial p}{\partial \rho}\right)_\theta = \left(\frac{\partial p}{\partial \rho}\right)_s - \frac{\theta}{C_v}\left[\frac{1}{\rho}\left(\frac{\partial p}{\partial \theta}\right)_v\right]^2 \approx c^2 \approx \left(2 \times 10^5 \frac{\mathrm{cm}}{\mathrm{sec}}\right)^2,$$

where $s$ is entropy and $v$ is volume.

The half height of the Kiwi core was $L = 68$ cm and the neutron prompt lifetime for the reactor was $l \approx 3 \times 10^{-5}$ sec. The maximum period observed was $(l/k_0) = 6.25 \times 10^{-4}$ sec. Thus, the left side of Eq. (15) becomes equal to $1.23 \times 10^5\ \mathrm{sec}^{-2}$, while the right side is

$$23.96 \left(\frac{1}{3.4 \times 10^{-4}\ \mathrm{sec}}\right)^2 \frac{5.6 \times 10^{-6}\ \mathrm{g}}{0.7 \times 10^7\ \mathrm{erg}} Q_f = 1.658\ 10^{-4}\ \mathrm{sec}^{-2}\left(Q_f \frac{\mathrm{g}}{\mathrm{erg}}\right).$$

Using the peak energy density inferred from the actual yield, $Q_f = 12.7 \times 10^{10}$ erg/g, we obtain that the right side of Eq. (15) is $2.11 \times 10^7\ \mathrm{sec}^{-2}$—about 170 times larger than the left side. Thus, if the pressure did not propagate from the place where it was generated, the excursion yield would have been 170 times smaller. However, this Bethe-Tait assumption is definitely unjustified, since the time needed for the pressure wave to traverse half the core ($3.4 \times 10^{-4}$ sec) is only about one half of the initial period. The disproportionate discrepancy of the estimated yield will be shown in the following section to be attributable to the large radial leakage of pressure.

### Reduction of Reactivity at the Beginning of the Excursion

For a uniform expansion the coefficient of reactivity reduction has been measured experimentally to be

$$\left(\frac{\delta k}{\delta \theta}\right)_u = 5.6 \times 10^{-6}\ ^\circ\mathrm{K}^{-1}.$$

Expressed in terms of heat input, the reactivity reduction is

$$\left(\frac{\delta k}{\delta e}\right)_u = \frac{5.6 \times 10^{-6}\ \mathrm{g}}{0.7 \times 10^7\ \mathrm{erg}} = 8 \times 10^{-13} \frac{\mathrm{g}}{\mathrm{erg}},$$

since the specific heat at the beginning of the excursion is $C_v = 0.7 \times 10^7$ erg/g. If we assume now that the same $(\delta k/\delta e)_u$ prevailed over the whole excursion and that the reactivity reduction is proportional to the heat input, we obtain a symmetrical power versus time curve, as observed experimentally. Since $k_0 = (k_0/l)l = 4.8 \times 10^{-2}$, the heat generated during this excursion should be

$$Q_f = 2k_0 \Big/ \left(\frac{\delta k}{\delta e}\right) = 11.5 \times 10^{10} \frac{\mathrm{erg}}{\mathrm{g}} \cdots. \quad (16)$$

This value is somewhat smaller than that actually obtained at the center, but definitely larger than the average value, $8.1 \times 10^{10}$ erg/g. Thus, the reactivity reduction in this model is almost sufficient by itself to account for the experimentally observed value. One may argue, however, that the actual reactivity reduction should be smaller because of non-uniform expansion, increasing

specific heat, and delay of expansion after the heat has been deposited. Thus, the actual heat generated would appear even larger than that given in Eq. (16). However, this reasoning implicitly assumes reactivity reduction to be instantaneous with heat input and neglects the accelerations and velocities produced. If, on the other hand, one computes accelerations as instantaneous functions of heat generation, as in the Bethe-Tait model discussed in the preceding section, it is seen that the reactivity reduction is too strong. Adequate calculations and results, in this case, are likely to depend strongly upon geometry and wave reflection properties. Even a minor decrease of reactivity reduction at low energies may require considerable heat generation above the triple point to shut the reactor down and yield a considerable amount of damaging pressure.

In order to examine these questions in more detail, we have calculated reactivity reduction in the inital stages of TNT, when wave propagation is of paramount importance, using the approximate method of G. Hansen.[4] His calculations were intended for spherical reactors with constant velocity of wave propagation and pressure generation rate. However, some extensions and generalizations are possible analytically. In our calculations we assume that the Kiwi core is axially bare but very strongly reflected radially. The flux is then separable into $z$ and $r$ coordinates. A one-group calculation gives

$$\phi = \cos\frac{z}{2L} J_0(\mathrm{Br}),$$

where $L$ is half-height and $B$ is radial buckling. The worth $w$, of the core material (calculated neglecting the fissions outside the core) is

$$\begin{aligned} w &= \frac{1}{\rho}\left[D(\nabla\phi)^2 + (\nu\Sigma_f - \Sigma_c)\phi^2\right] \Big/ \int \nu\Sigma_f \, dV \\ &= \frac{D}{\pi\rho L b^2 \nu\Sigma_f} \frac{1}{J_0^2(Bb) + J_1^2(Bb)} \left\{\left(\frac{\pi}{2L}\right)^2 J_0^2(Br) \right. \\ &\quad \left. + B^2 \cos^2\frac{\pi z}{2L}\left[J_0^2(Br) + J_1^2(Br)\right]\right\}. \end{aligned}$$

If the core is well reflected radially, $Br < Bb \ll 1$, and the preceding expression can be simplified to

$$w = \frac{1}{\pi\rho b^2 L}\left(\frac{DB^2}{\nu\Sigma_f}\right)\left\{\cos^2\frac{\pi z}{2L}\frac{r^2}{2}\left(\frac{\pi}{2L}\right)^2 + \left(\frac{\pi}{2Lb}\right)^2\right\}.$$

The gradient of worth is

$$\nabla w = -\frac{1}{2\rho b^2 L^2}\left(\frac{DB^2}{\nu\Sigma_f}\right)\left(\sin\frac{\pi z}{L}\hat{z} + r\frac{\pi}{2L}\hat{r}\right), \quad (17)$$

where $\hat{z}$ and $\hat{r}$ are unit vectors in axial and radial directions respectively. It is interesting to note that $\nabla w$ has a strong radial component, while the flux is practically flat in that direction. The magnitude of $|\nabla w|$, however, is proportional to the radial buckling, $B$. The Laplacian of worth is

$$\nabla^2 w = -\frac{\pi}{\rho b^2 L^2}\left(\frac{DB^2}{\nu\Sigma_f}\right)\cos^2\frac{\pi z}{2L}. \quad (18)$$

In previous calculations for the well reflected spherical reactor, $\nabla^2 w$ was usually assumed constant. In the axially bare reactor we can no longer make this assumption. For a uniform expansion

$$\rho\mathbf{u} = -\frac{\delta\rho}{3}(z\hat{z} + r\hat{r})$$

and the change in reactivity is

$$\begin{aligned} k_u &= \int \rho\mathbf{u}\cdot\nabla w \, dV \\ &= \frac{1}{3}\frac{\delta\rho}{\rho}\left(\frac{DB^2}{\nu\Sigma_f}\right)\left[\left(\frac{\pi b}{2L}\right)^2 + 1\right]. \end{aligned} \quad (19)$$

From this expression we can determine $(DB^2/\nu\Sigma_f)$ if $\delta k_u/\delta\rho$ is measured. Assuming that $\pi b/2L \approx \pi/3$ and substituting into Eq. (18) the value of $DB^2/\nu\Sigma_f$ obtained from Eq. (19), we have

$$\nabla^2 w = \frac{28.24}{VL^2}\left(\frac{\partial\theta}{\partial\rho}\right)_p\left(\frac{\delta k}{\delta\theta}\right)_u \cos^2\frac{\pi z}{2L}. \quad (20)$$

Now, if we assume that the power shape is proportional to the flux, $\cos \pi z/2L$, and that the heat input and pressure generation increase exponentially with time, for a constant velocity of wave propagation we can calculate the pressure quite simply. When the pressure wave is completely reflected from the free boundaries of the core, we obtain

$$\begin{aligned} p = \left(\frac{\partial p}{\partial e}\right)_\rho Q \frac{\alpha^2}{\alpha^2 + \left(\frac{\pi c}{2L}\right)^2}\cos\frac{\pi z}{2L} \\ \cdot\left\{1 - \frac{I_0\left(r\sqrt{\frac{\pi^2}{4L^2} + \frac{\alpha^2}{c^2}}\right)}{I_0\left(b\sqrt{\frac{\pi^2}{4L^2} + \frac{\alpha^2}{c^2}}\right)}\right\}. \end{aligned} \quad (21)$$

If the velocity of wave propagation, $c$, is very small, the pressure shape follows the heat generation

$$p_{BT} = \left(\frac{\partial p}{\partial e}\right)_\rho Q\cos\frac{\pi z}{2L}.$$

When $c$ is very large, the pressure is much lower:

$$p_{qs} = \left(\frac{\partial p}{\partial e}\right)_\rho Q\cos\frac{\pi z}{2L}\left(\frac{2L\alpha}{\pi c}\right)^2\left[1 - \frac{I_0\left(\frac{\pi r}{2L}\right)}{I_0\left(\frac{\pi b}{2L}\right)}\right]. \quad (22)$$

Averaged over the radial direction, this pressure is only

$$\left(\frac{2L\alpha}{\pi c}\right)^2\left[1-2\frac{2L}{\pi b}\frac{I_1\left(\frac{\pi b}{2L}\right)}{I_0\left(\frac{\pi b}{2L}\right)}\right]$$

$$= (0.3463)^2 \times 0.1192 = 0.0143$$

of the pressure obtained in the Bethe-Tait approximation. This practically accounts for the high reactivity reduction in the preceding section, since in the present case expansion follows heat input and no correctional factor, ($\approx 2$), should have been taken. Indeed, the expansion in this case is $\delta\rho = \nabla^2 p/\alpha^2$, independent of the assumed period.

Substitution of Eq. (22) into Eq. (2) shows that the coefficient of reactivity reduction per change of density in the core center is

$$\frac{\delta k}{\delta \rho_0} = 0.579\left(\frac{\delta k}{\delta \rho}\right)_u,$$

a little more than half of the coefficient for the uniform expansion. Thus, this model of reactivity reduction would yield $19.9 \times 10^{10}$ erg/g in the Kiwi center, 1.57 times the observed value.

It is instructive, however, to consider the change of energy yield with the initial period for this simple linear equation of state. A simple calculation shows that, when the one dimensional worth is adjusted to give the correct yield for slow excursions, it gives 8.4 times the yield of the cylindrical case for large values of $\alpha$. It is easy to understand this discrepancy qualitatively. A one dimensional calculation does not allow for radial expansion and thus the "paper" reactor acts as a cannon. It allows a much longer time for heat production before sufficient expansion takes place. Alternatively, it can be stated that: having represented correctly the worth, $w$, of the reactor material for slow excursions, we obtain a much lower worth of pressure, $\nabla^2 w$, in the "cannonical" representation. Thus the "cannonical" representation gives too high a yield. The trend would be reversed (too strongly) if $\nabla^2 w$ in one dimension would be made to match $\nabla^2 w$ of the cylindrical geometry. Thus, to interpret the results of Kiwi TNT by one dimensional calculations, the equation of state of graphite for high pressures had to be modified in addition to the necessary modification of worth.

### Analytical Estimates of the Destructive Capacity

In the preceding sections, it is noted that a major contribution to the reactivity reduction has been accomplished in the initial stage of the excursion with graphite still in the solid state. It was also made plausible that the correct cylindrical calculation may explain the observed energy yield without major alterations in the observed equation of state, worth of reactor material, or power shape. The equation of state of graphite at high energy densities has been seen to play only a minor role in the reactivity reduction mechanism for this slow ($\alpha L/c$) $< 1$ excursion. However, the highest pressures have been generated at the end of the excursion, and the destructive capacity appears almost completely divorced from the major mechanism of the reactivity reduction.

In our estimate of the destructive capacity, an experimentally observed energy yield will be assumed. It will also be assumed that the energy density distribution is flat radially and has a cosine shape in the axial direction. Since we are interested only in high temperatures where graphite has no rigidity and the velocity of wave propagation is small, we will calculate the temperatures, neglecting expansion and a relatively small amount of energy in graphite vapor. We will further assume that expansion in the solid and liquid phases is insufficient to fill the voids, and we will determine the pressures from calculated temperatures using saturated vapor curves.

Graphite is a solid that exhibits a variation of specific heat at elevated temperatures. Experimentally observed values can be approximated rather well with

$$C_v = 3R\Big/\left[1+\left(\frac{428^\circ\mathrm{K}}{\theta}\right)\right]^2, \qquad (23)$$

where $R$ is the universal gas constant. Integration of this equation from room temperature to the temperature of the triple point ($\theta_T = 3960^\circ$K) requires

$$Q_{TS} = 6.84 \times 10^{10}\ \mathrm{erg/g}$$

to reach the triple point in solid state. During the later stage of this heating the pressure rises rather rapidly to $p_T = 100$ atm. After the triple point is reached, graphite liquifies and it is necessary that

$$L_{sl} = 11\ \mathrm{kcal/mol} = 3.83 \times 10^{10}\ \mathrm{erg/g}$$

for this process. Thus, when $10.67 \times 10^{10}$ erg/g is put in, graphite becomes liquid. Its specific heat is still about

$$C_v = 3R = 2.1 \times 10^7\ \mathrm{erg/g},$$

and the pressure starts rising very rapidly:

$$p = p_T \exp\frac{L_{lv}}{R\theta_T}\left(1-\frac{\theta_T}{\theta}\right), \qquad (24)$$

where the heat of vaporization from the liquid phase is $L_{lv} = 161$ kcal/mol and

$$L_{lv}/R\theta_T = 20.47.$$

At $Q = 12.7 \times 10^{10}$ erg/g we have $\theta = 1.24\ \theta_T$ and $p_{max} = 55.2\ p_T$. The calculation shows that the pressure peak is rather narrow:

$$p(z) \approx p_{max} \exp\left[-\frac{20.47}{2}\left(\frac{\pi z}{2L}\right)^2\right]. \quad (25)$$

Starting with these initial conditions, we can compute the work available adiabatically. The work done in expansion to the triple point and the subsequent solidification of graphite will be calculated. (The work done in expansion to lower pressures is neglected since the core has already expanded to a tremendous volume.) It can be shown that the work done in an adiabatic expansion of this graphite liquid-vapor system is roughly

$$w = vp \ln (p/p_T), \quad (26)$$

where $v$ is the (small) initial volume, $p$ is the initial pressure, and $p_T$ is the final pressure. Assuming that $v = 0.8$ cm$^3$/g and averaging Eq. (26) over the core,

$$\bar{w}_1 = 0.008 \times 10^{10} \text{ erg/g} \times 17.6 = 0.14 \times 10^{10} \text{ erg/g}. \quad (27)$$

Since the average energy density is

$$\frac{2}{\pi} 12.7 \times 10^{10} \text{ erg/g} = 8.1 \times 10^{10} \text{ erg/g},$$

the efficiency is 1.73%. To this number, however, we must add the non-negligible work performed while the liquid graphite solidifies. It can be shown that the work in this adiabatic process is

$$w_T = L_{sl}\frac{R\theta_T}{L_{sv}}\left(1 - \frac{V}{V_v}\right) \approx L_{sl}\left(\frac{R\theta_T}{L_{sv}}\right) = 0.1765 \times 10^{10} \text{ erg/g}, \quad (28)$$

where $L_{sv} = L_{sl} + L_{lv}$, and $(V/V_v)$, the ratio of initial specific volume to the specific volume of vapor $[V_v = (R\theta_T/p_T) = 240 \text{ cm}^3/\text{g}]$, is negligible. The change of specific volume in this process is quite large:

$$\Delta V = V_v \frac{L_{sl}}{L_{sv}}\left(1 - \frac{V}{V_v}\right) = 15 \text{ cm}^3/\text{g}.$$

Our distribution of energy input, however, indicates that only 36% of the core was completely liquified; another 27% was partially liquified. The work at the triple point averaged over the core is

$$\bar{w}_T = w_T \times 0.5109 = 0.090 \text{ erg/g}, \quad (29)$$

about 1.11% of the average energy yield. Adding Eq. (27) and Eq. (29), we obtain an efficiency of 2.84%. From this calculation it seems that the destructive capacity of the Kiwi TNT test was equivalent to a charge of high explosive (TNT) that liberated 2.84% of its energy (since practically all the energy yield of a high explosive is capable of doing work in an isentropic expansion).

The assumption that all of the energy available adiabatically is able to do destructive work, however, is rather pessimistic. The expansions to produce all of this work are rather large. One might be inclined to argue that all of the destructive work is done during an expansion which is only a small fraction of the initial volume.

If the same argument is applied to the destructive capacity of the high explosive, we see that the equivalent energy of the high explosive is

$$e_d \lesssim \frac{1}{\gamma_d - 1}\int p\, dV \approx 3 \int p\, dV.$$

Since in our case

$$\frac{1}{M}\int p\, dV \approx 0.008 \times 10^{10} \text{ erg/g} \times 4.90 = 0.04 \times 10^{10} \text{ erg/g}$$

is only 0.48% of the average energy yield, by this method we obtain a rather low efficiency of Kiwi TNT. Only 1.45% of the total energy yield seems to be able to perform the destruction of the high explosive. The estimated equivalent high explosive yield from post-mortem examination, of course, was between 1 and 3%.[5] The large uncertainty in these numbers seems to indicate that crudeness of our calculations and the impossibility of describing a reactor excursion by means of a simple chemical explosion.

## References


1. D. Okrent, J. M. Cook, D. Satkus, R. B. Lazarus and M. B. Wells, *AX-1, A Computing Program for Coupled Neutronics-Hydrodynamics Calculations on the IBM-704*, ANL-5977 (1959).
2. V. Z. Jankus, *A Theoretical Study of Destructive Nuclear Bursts in Fast Power Reactors*, ANL-6512 (1962).
3. H. A. Bethe and J. H. Tait, *An Estimate of the Order of Magnitude of the Explosion When the Core of a Fast Reactor Collapses*, UKAEA-RHM(56)/113.
4. G. E. Hansen, *Burst Characteristics Associated with Slow Assembly of Fissionable Materials*, LA-1441 (July 1952).
5. L. J. Koch, H. D. Monson, D. Okrent, M. Levenson, W. R. Simmons, J. R. Humphreys, J. Haugsnes, V. Z. Jankus and W. B. Loewenstein, *Hazards Summary Report, Experimental Breeder Reactor II (EBR-II)*, ANL-5719, 292 (1957).
6. *Reactor Physics Constants*, ANL-5800, Second Edition, 496 (1963).
7. W. R. Stratton, Los Alamos Scientific Laboratory (private communication).

# IV-27. Qualitative Consideration of a Nuclear Excursion Initiated by a Shock Wave

V. Z. Jankus

## Introduction

Usually one assumes the maximum credible accident to be the collapse (or slumping) of a reactor core caused by gravity after the fuel elements have melted as a result of a lapse in effective cooling and the failure of shutdown controls. The velocity reached by the fuel in gravitational collapse depends upon the amount of collapse. One obtains appreciable rates of reactivity insertion at prompt critical (and an appreciable excursion yield) only if a large fraction of fuel is allowed to collapse coherently, starting from appreciable subcriticality. In contra-distinction the velocity of the fuel propelled by a shock wave reaches a high value immediately. Potentially this may be conducive to a major nuclear excursion.

The situation is less risky if the core is full of sodium. The shock front then propagates rapidly through the core and usually only a modest amount of reactivity can be inserted by this means. Often a prompt critical condition is not reached. However, when it is, the yield of the excursion is not principally determined by the rate of reactivity insertion at prompt critical as in the gravitational collapse. Rather, the nuclear burst is terminated automatically with the passage of the pressure pulse through the core, unless of course, the pressure wave is of extraordinary strength.

Strong shock waves could be generated by a nuclear burst in another core of a reactor of modular design. If primary reactivity insertion and resultant heat generation are so rapid that expansion (and reactivity reduction) are hindered by mass inertia, strong pressures are developed in the first core. The pressure wave departs from this core only after the nuclear burst is essentially terminated and leaves the core subcritical by a much larger amount than the initial reactivity input. Such a compressional wave impinging upon the second core can insert an appreciable amount of reactivity. Conceivably the second reactivity insertion may be larger than the amount of reactivity causing the primary explosion in the first core. Whether this results in a sizeable secondary explosion depends primarily upon whether the second core has been brought above prompt critical. The yield of such an excursion (when it is large) depends sensitively upon the amount or rate of reactivity inserted and less upon the initial conditions of the power in the second core at the time of the impact.

## Analytical Calculations Performed

To estimate the order of magnitude of reactivity insertion we have performed four simple analytical calculations. Acoustic theory was used in treating wave propagation. The amount of reactivity inserted has been determined using perturbation theory, considering the second core as isolated. In these calculations both the amount of reactivity inserted, $k$, and the rate of insertion, $\dot{k}$, are proportional to the magnitude of pressure, $p_0$. Two simplified calculations (cases 1 and 3, EXAMPLES) have been performed using one-dimensional plane geometry. Spherical cores were assumed in making the other two calculations. It was found that the results do not change drastically with geometry. Thus, one may expect that the conclusions reached pertain to more realistic representations of the core shape. Two calculations have treated reactivity changes due to a semi-infinite constant pressure, $p_0$, wave (cases 1 and 2, EXAMPLES). In case 3 a sawtooth shaped plane wave of peak front pressure equal to $p_0/2$ has been assumed, the pressure decreasing linearly to zero at a distance equal to the radius of the core. In case 4 the assumption has been made that a sawtooth shaped spherical wave produced by an explosion in the first core (reaching pressure $p_0$ at the edge) impinges upon a similar spherical core located at a distance $A$ between centers.

For the sake of simplicity we have considered that only the motions in the core contributed to the reactivity. Actually the motions of the adjacent blanket are also important. Thus our core radius, $b$, is somewhat larger than the radius of the physical core. Also we have assumed that the Laplacian of the reactivity worth is constant in the core. For numerical considerations we have taken $\nabla^2 W = 3/2Mb^2$, where $M$ is the mass of the core, core density $\rho = 10$ g/cm$^3$, velocity of sound $c = 3 \times 10^4$ cm/sec, and core radius $b = 30$ cm.

With these values of parameters, we have found that a semi-infinite compressional wave of $p_0 = 3000$ lb/in$^2$ $\approx 0.2$ kbar entering a plane core raises its reactivity quite rapidly. A maximum rate of $\dot{k} = 2.8\ \Delta k/k$/sec is obtained when the wave front crosses the center of the core. However, the total raise in reactivity is only $\Delta k = 0.0037$. If the core is spherical, the reactivity rise is even smaller—$\Delta k = 0.0022$. Thus, prompt-criticality is not reached and only a minor burst is obtained for $\Delta k = 0.0022$. However, since reactivity input is proportional to the magnitude of pressure, one obtains almost steplike reactivity insertion and a rapid increase in yield with a relatively small increase of incident pressure once prompt-criticality is exceeded. With continuing increase of incident pressure, the

maximum reactivity which may be inserted becomes limited by the reactivity insertion rate and the rise of yield with increasing incident pressure is slowed down. If the core is partially voided of sodium, and the velocity of sound propagation in it is considerably lower than $3 \times 10^4$ cm/sec, prompt criticality may be considerably exceeded as the result of a modest pressure wave. In a voided core the particle velocity is increased by a factor less than 2 and so also are the reactivity insertion rates. However, since the wave front takes much longer to traverse the core, the total reactivity available is much larger and the super-prompt-critical condition is more accessible.

The amount of reactivity that can be inserted by a semi-infinite pressure wave, is of limited interest. The pressure waves in a reactor are likely to be of finite extent (about the same order of magnitude as the core). Thus in the subsection EXAMPLES (case 4) we have considered the propagation of a spherical pressure wave that could be produced by an initiating excursion in a core of the same size. From Eqs. (26) and (27) the maximum reactivity inserted by such a wave is

$$k_{max} = (1.) \frac{1}{\rho c^2} p_0 \frac{b}{A} 0.02101. \qquad (1)$$

If $\rho c^2 = 9$ kbar, we see that a primary excursion developing pressure of

$$p_0 = 4.3\ A/b \text{ kbar} \qquad (2)$$

at the core edge is needed in order to insert 1% of reactivity, $\Delta k/k$, into the second core at distance $A$ between centers. The rate of reactivity insertion is largest when about one-half (0.530) of maximum reactivity has been inserted. Then it is equal to

$$\dot{k}_{max} = (1.) \frac{1}{\rho c^2} \frac{c}{b} \left( p_0 \frac{b}{A} \right) 0.02746. \qquad (3)$$

Using the numerical values for the parameters, it may be noted that

$$\dot{k}_{max} \cdot \text{sec} = 3.0 \left( \frac{p_0}{\text{kbar}} \right) \frac{b}{A} \qquad (4)$$

is still quite appreciable. However, the high reactivity insertion rate obtained does not necessarily indicate as large an excursion as would be obtained if this reactivity insertion rate were produced by a gravitational collapse of the core. The reactivity insertion rate here is not sustained for an appreciable length of time. If the core is full of sodium, the pressure wave is able to traverse it within about two milliseconds. The excursion is terminated regardless of the amount of heat produced. The situation is less favorable if the second core has lost its sodium and the velocity of wave propagation through it is considerably smaller. The particle velocity and the momentum transmitted into it are still of the same order of magnitude as in the core full of sodium. Thus achievable reactivity insertion rates are still of the same order of magnitude. Due to the velocity of wave propagation and longer time needed to traverse the core, the same incident pressure pulse that leaves the core which is full of sodium below or at prompt critical is likely to bring a voided core well above prompt critical, causing a large nuclear excursion. If the velocity of wave propagation, $c$, is allowed to vary in the second core, for some value of $c$ the maximum reactivity insertion rate given by Eq. (4) will be reached at prompt critical. An excursion of the order indicated by this reactivity insertion rate will be induced.

### Numerical Refinements Needed

The contention that reactivity insertion rates in a voided or partially voided core are the same as those in the core full of sodium are believed to be correct only to an order of magnitude. Better estimates of values could be obtained only by a numerical calculation using at least two dimensions. (Analytical calculations of the reflection of pressure of finite extent from a rarer medium become very unwieldy when no tension wave is allowed.) When we relate reactivity insertion rates uniquely with excursion yield, we assume that the initial power is very small. For the cases of moderate yield (which are most likely) this may present a serious over-estimate. Thus an improved calculation should account for the magnitude of initial power and its rise while reactivity comes up to prompt critical. In such a calculation, delayed neutrons should be included.

The initial power for the second core may be increased very sharply by the nuclear burst in the first core if coupling is not altogether negligible. Conversely, coupling restrains the power rise in the first core for a given reactivity insertion and reduces its yield. Thus the estimates obtained from uncoupled calculations may be unduly pessimistic for any plausible initiating mechanism of moderate strength. To obtain a more realistic estimate, however, a coupled kinetics code for neutronics calculation (with delayed neutrons) and at least two-dimensional hydrodynamics is needed. It is expected even then that the yield will be quite sensitive to the location and the extent of voiding in the second core (and its relationship to the "effective" velocity of wave propagation).

## EXAMPLES

### CASE 1. COMPACTION OF A PLANE CORE BY CONSTANT PRESSURE WAVE OF INFINITE EXTENT

First we will perform calculations in one dimension assuming that the reactor has cross sectional area $C$

and thickness $2b$ along the direction of a traveling wave of constant pressure $p_0$. Neglecting the influence of the motion of blanket material, the time rate of reactivity change by first order perturbation theory is

$$\dot{k} = C \int \rho \dot{u} \frac{dW}{dx} dx, \tag{5}$$

where $W$ is the reactivity worth of core material, $\rho$ is the density of core material and $\dot{u}$ is the velocity of the motion of core material induced by the incoming pressure wave. In the acoustic approximation, the particle velocity is

$$\dot{u} = p_0/\rho c \tag{6}$$

whenever the pressure wave traveling along the positive direction of the $x$-axis reaches the particle in question. For simplicity, it will be assumed that $dW/dx$ changes linearly inside the core:

$$\frac{dW}{dx} = \frac{d^2W}{dx^2} x, \qquad \text{for } -b < x < b,$$

where $(d^2W/dx^2)$ is a constant. If $x$ is the position of the front of the pressure wave,

$$\dot{k} = C \frac{p_0}{c} \frac{d^2W}{dx^2} \int_{-a}^{Min(x,b)} x \, dx;$$

that is,

$$\dot{k} = \left( - \frac{d^2W}{dx^2} 4\rho b C b^2 \right) \frac{p_0}{\rho c^2} \frac{c}{b} \cdot \frac{1}{8} \left( 1 - \frac{x^2}{b^2} \right), \qquad \text{for } -b < x < b,$$

and

$$\dot{k} = 0, \qquad \text{for } |x| > b. \tag{7}$$

Integrating the last equation with time we obtain the change of reactivity

$$k \begin{cases} = \left( - \dfrac{d^2W}{dx^2} 4\rho b C b^2 \right) \dfrac{p_0}{\rho c^2} \cdot \dfrac{1}{6} \left( \dfrac{1}{2} + \dfrac{3}{4} \dfrac{x}{b} - \dfrac{1}{4} \dfrac{x^3}{b^3} \right), \\ \qquad\qquad \text{for } -b < x < b \\ = \left( - \dfrac{d^2W}{dx^2} 4\rho b C b^2 \right) \dfrac{p_0}{\rho c^2} \cdot \dfrac{1}{6}, \qquad \text{for } |x| > b. \end{cases} \tag{8}$$

If we assume that

$$\frac{d^2W}{dx^2} 4\rho b C b^2 = 1,$$

(the actual magnitude of this quantity depends upon the composition of the core and the blanket, but probably does not deviate from the assumed value by a factor of more than 2).

$$p_0 = 2 \times 10^8 \text{ dyne/cm}^2 \approx 3{,}000 \text{ lb/in.}^2$$

$$\rho = 10 \text{ g/cm}^3$$

$$c = 3 \times 10^4 \text{ cm/sec},$$

then

$$p_0/\rho c^2 = 0.0222.$$

The maximum reactivity added by the compression of the core due to passage of the shock front is

$$k_{max} = 0.0037.$$

The reactor does not reach prompt critical for a U-235 fueled system, and barely reaches prompt critical for plutonium fuel even at a very pessimistic assumption for the velocity of sound. If it is assumed that $b = 30$ cm, it is found from Eq. (7) that the maximum reactivity insertion rate is quite large:

$$\dot{k}_{max} = 0.0222 \frac{b}{c} \cdot \frac{1}{8} \approx 2.8 \text{ [}(\Delta k/k)/\text{sec]}.$$

If the velocity of wave propagation in the blanket, $c_b$, is different from that in the core, $c$, we must substitute the transmitted pressure

$$p_t = p_0 \frac{2\rho c}{\rho c + \rho_b c_b}$$

instead of $p_0$ into our calculation; $\dot{k}$ and $k$ are larger by a factor $2\rho c/(\rho c + \rho_b c_b)$ than that given in Eqs. (7) and (8); $\rho_b$ is the density of blanket material. When $c$ decreases relative to $c_b$, $\dot{k}$ increases by a factor of 2. The total amount of reactivity inserted, however, increases without limit.

CASE 2. COMPACTION OF A SPHERICAL CORE BY A PLANE WAVE OF HALF-INFINITE EXTENT

The rate of reactivity change due to the motion in the core is determined by perturbation theory to be

$$\dot{k} = \int \rho \dot{\mathbf{u}} \cdot \nabla W \, dV,$$

where the velocity, $\dot{\mathbf{u}}$, and the gradient of the worth of a core material are vector quantities, and $V$ is the core volume. For convenience of computation, the above expression may be differentiated with respect to time, the gradient of the pressure introduced, and integration by parts performed, yielding[1, 2]

$$\ddot{k} = \int p \nabla^2 W dV - \int p \nabla W \cdot d\mathbf{S} \tag{9}$$

expressed in terms of scalar quantities. If we assume now that the worth of core material is spherically symmetric, and $\nabla^2 W$ is constant Eq. (9) becomes

$$\ddot{k} = \nabla^2 W \left[ \int p(\mathbf{r}) \, dV - \frac{1}{3} \int p(r = b) b dS \right], \tag{10}$$

where $b$ is the radius of the spherical core. If $p$ now represents an infinite plane wave propagating in the $x$ direction, we can eliminate other coordinates from Eq. (9) by geometric considerations and obtain

$$\ddot{k} = \nabla^2 W \pi \int p(x) \left(\frac{1}{3} b^2 - x^2\right) dx. \qquad (11)$$

For a semi-infinite wave of constant pressure $p_0$, traveling in the positive direction of the $x$-axis, integration of the above expression gives

$$\ddot{k} = \left(-\nabla^2 W \frac{2\rho}{3} \frac{4\pi b^3}{3} b^2\right) \frac{p_0}{\rho b^2} \cdot \frac{3}{8} \cdot \frac{x}{b} \left(\frac{x^2}{b^2} - 1\right) \qquad (12)$$

whenever the distance of the front of the pressure wave from the center of the core is $|x| < b$ ($\ddot{k}$ vanishes if $|x| > b$). The coefficient

$$-\nabla^2 W \frac{2\rho}{3} \frac{4\pi b^3}{3} b^2$$

in Eq. (12) is of order 1 (probably within a factor of 2) and for the sake of brevity will be omitted from our further qualitative discussion. Since the velocity of wave propagation $c$ is assumed constant, integration of Eq. (12) is straightforward and for $|x| < b$ one obtains the rate of reactivity change

$$\dot{k} = (1.) \frac{p_0}{\rho b^2} \frac{b}{c} \cdot \frac{3}{32} \left(\frac{x^2}{b^2} - 1\right)^2 \qquad (13)$$

and the total amount of reactivity added

$$k = (1.) \frac{p_0}{\rho c^2} \cdot \frac{1}{10} \left[\frac{1}{2} + \frac{15}{16} \frac{x}{b} - \frac{10}{16} \left(\frac{x}{b}\right)^3 + \frac{3}{16} \left(\frac{x}{b}\right)^5\right]. \qquad (14)$$

Comparing these results now with the results of the earlier plane one-dimensional computation, [Eqs. (7) and (8)] we see that the detailed variation of $\dot{k}$ with the position of the front of the plane wave is now changed. However, the maximum value of $\dot{k}$ is about the same; that is, ¾ of the previous value of $k$. The maximum reactivity inserted is ⅗ the value of $\Delta k$ in case 1.

### CASE 3. COMPACTION OF A PLANE CORE BY A SAW-TOOTH SHAPED PRESSURE PULSE

For one-dimensional calculations, Eq. (9) can be simplified into

$$\ddot{k} = \left(\frac{d^2 W}{dx^2}\right) C \left[\int p \, dx - bp(-b) - bp(b)\right], \qquad (15)$$

with the usual approximation that the second derivative of the worth of the core material is constant. We assume now that the pressure vanishes everywhere except inside of a saw-tooth wave of width $b$, where

$$p = \frac{p_0}{2b} (x - ct), \qquad \text{for} \quad 0 < x - ct < b \qquad (16)$$

so that the pressure is $p_0/2$ at the leading edge and zero at the trailing edge. Integrating Eq. (15) three different analytical expressions are obtained, depending upon whether the saw-tooth wave has only partly entered the core, completely entered the core, or partly left the core. In terms of the parameter $\tau = ct/b$,

$$\ddot{k} = \left(-\frac{d^2 W}{dx^2} \cdot 4\rho b C b^2\right) \frac{p_0}{\rho b^2} b_2(\tau), \qquad (17)$$

where

$$b_2(\tau) \begin{cases} = (\tau^2 - 2)/16, & \text{for } -2 < \tau < -1 \\ = -1/16, & \text{for } -1 < \tau < 0 \\ = (-\tau^2 + 1)/16, & \text{for } 0 < \tau < 1. \end{cases}$$

Straightforward integration of Eq. (17) with respect to time gives the first derivative of the reactivity:

$$\dot{k} = (1.) \frac{p_0}{b^2} \frac{b}{c} b_1(\tau), \qquad (18)$$

where

$$b_1(\tau) \begin{cases} = (\tau^3 - 6\tau - 4)/48, & \text{for } -2 < \tau < -1 \\ = (-3\tau - 2)/48, & \text{for } -1 < \tau < 0 \\ = (-\tau^3 + 3\tau - 2)/48, & \text{for } 0 < \tau < 1. \end{cases}$$

The maximum reactivity insertion rate $\dot{k}$ is obtained when $\tau = -1.414$, $Max(b_1) = 0.034518$. The minimum $\dot{k}$ is obtained for $\tau = 0$, which gives $Min(b_1) = -0.04167$.

Integrating Eq. (18) with time we again obtain the amount of reactivity inserted by our pressure pulse:

$$k = (1.) \frac{p_0}{\rho c^2} b_0(\tau), \qquad (19)$$

where

$$b_0(\tau) \begin{cases} = (\tau^4 - 12\tau^2 - 16\tau)/192, & \text{for } -2 < \tau < -1 \\ = (-6\tau^2 - 8\tau + 3)/192, & \text{for } -1 < \tau < 0 \\ = (-\tau^4 + 6\tau^2 - 8\tau + 3)/192, & \text{for } 0 < \tau < 1. \end{cases}$$

The maximum reactivity $k$ is inserted at $\tau = -⅔$, $Max(b_0) = 0.029514$.

CASE 4. REACTIVITY INSERTION INTO A SPHERICAL CORE BY A SPHERICAL PRESSURE PULSE ORIGINATING OUTSIDE THE CORE

We will assume that the Laplacian of the worth is constant inside the core and drops rapidly outside the core. For simplicity of calculation, we will neglect the gradient of the worth of blanket material altogether. (In an actual case the gradient of blanket material is comparable to the gradient of core material, at least in the immediate vicinity of the core.) With this simplification, the change of reactivity is taken to be due entirely to the motion of core material and is equal to

$$\begin{aligned} \ddot{k} &= \int \rho \ddot{\mathbf{u}} \cdot \nabla W \, dV \\ &= \int p \nabla^2 W \, dV - \int p \nabla W \cdot d\mathbf{S} \qquad (20) \\ &\approx \nabla^2 W \left[ \int p \, dV - \frac{b}{3} \int p \, dS \right], \end{aligned}$$

where $b$ is the radius of the core.

Now we assume that the distance between the center of the spherical wave and center of our core is $A$ $(>b)$; and that the spherical shell of radius $r_1$ and thickness $dr_1$ intersects our core. The volume of this intersection is

$$\Omega r_1^2 \, dr_1 = \frac{\pi}{A} r_1 [b^2 - (A - r_1)^2] \, dr_1$$

where $\Omega$ is a solid angle. The area of the surface of the core within the spherical shell is

$$dS = 2\pi b^2 \sin\theta \, d\theta,$$

where $\theta$ is the angle that the corresponding radius of the core makes with the direction to the center of the spherical wave. Since

$$r_1^2 = A^2 + b^2 - 2Ab \cos\theta,$$

$$dS = 2\pi \frac{b}{A} r_1 \, dr_1.$$

Substituting these expressions for volume and surface elements into Eq. (20) for reactivity change, we see that

$$\ddot{k}(t) = \nabla^2 W \frac{\pi}{A} \int p(r_1, t) \cdot \left[ \frac{1}{3} b^2 - (r_1 - A)^2 \right] r_1 dr_1 . \qquad (21)$$

If we assume that the acoustic impedances of the core and the blanket are the same, the magnitude of the pressure wave in the core depends only upon the time and its distance from the origin of the spherical wave.

If it is assumed that the spherical wave has been originated at time $t = 0$ by a violent excursion in the other core having the same radius, $b$, and nearly flat power distribution, the resultant outgoing spherical pressure wave can be described by a saw-tooth shaped pressure pulse:[3, 4]

$$p \begin{cases} = \dfrac{p_0}{2r_1} [r_1 - ct], & \text{for } 0 < r_1 - ct < b \\ = 0, & \text{otherwise.} \end{cases} \qquad (22)$$

After having substituted Eq. (22) into Eq. (21) the integration can be performed by a straightforward but somewhat tedious procedure. It is necessary to distinguish among three cases: when only part of the saw-tooth wave has entered the core $(-2b < ct - A < -b)$, when both front and back surfaces of the saw-tooth wave intersect the core $(-b < ct - A < 0)$, and when part of the pressure wave has already left

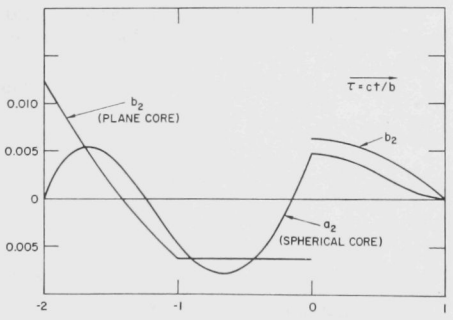


FIG. IV-27-1. Second Derivative of Reactivity Insertion by a Saw-Tooth Wave for Spherical Core: $k = (1) \cdot [(p_0 b/A)/\rho b^2] \cdot a_2$(Eq. 19A); Plane Core: $k = (1) \cdot (p_0/\rho b^2) \cdot b_2$(Eq. 13A). *ANL Neg. No. 112-8988.*

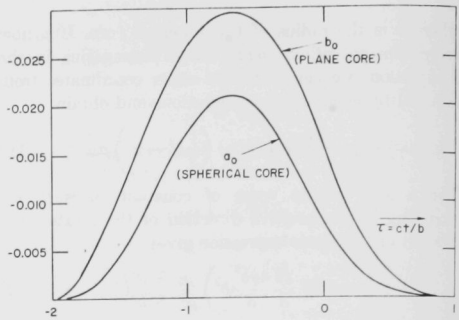


FIG. IV-27-2. Reactivity Insertion by a Saw-Tooth Wave for Spherical Core: $k = (1) \cdot p_0(b/A)(1/\rho c^2)a_0$ (Eq. 22A); Plane Core: $k = (1) \cdot p_0(1/\rho c^2)b_0$ (Eq. 15A). *ANL Neg. No. 112-8992.*

the core ($0 < ct - A < b$). In terms of the parameter $\tau = (ct - A)/b$ we obtain three polynomials describing the behavior of $\ddot{k}$, when such a saw-tooth wave impinges upon the core:

$$\ddot{k} = \left(-\nabla^2 W \frac{2\rho 4\pi b^5}{3 \times 3}\right)\left(p_0 \frac{b}{A}\right) \frac{1}{\rho b^2} a_2(\tau), \qquad (23)$$

where

$$a_2(\tau)\begin{cases} = \frac{3}{64}(-\tau^4 + 8\tau^2 + 8\tau), & \text{for } -2 < \tau < -1 \\ = \frac{3}{64}(6\tau^2 + 8\tau + 1), & \text{for } -1 < \tau < 0 \\ = \frac{3}{64}(\tau^4 - 2\tau^2 + 1), & \text{for } 0 < \tau < 1. \end{cases}$$

$a_2(\tau)$ has been plotted in Fig. IV-27-1 and compared with reactivity change, $b_2$, when a similar saw-tooth wave impinges upon a plane reactor, as obtained in case 3.

A straightforward integration of Eq. (23) with time shows that the first derivative of reactivity is given by

$$\dot{k} = (1.)\, p_0 \frac{b}{A} \frac{b}{c} \frac{1}{\rho b^2} a_1(\tau), \qquad (24)$$

where

$$a_1(\tau)\begin{cases} = (-3\tau^5 + 40\tau^3 + 60\tau^2 - 16)/320, & \text{for } -2 < \tau < -1 \\ = (30\tau^3 + 60\tau^2 + 15\tau - 8)/320, & \text{for } -1 < \tau < 0 \\ = (3\tau^5 - 10\tau^3 + 15\tau - 8)/320, & \text{for } 0 < \tau < 1. \end{cases}$$

For $\tau = -1.236068$, $a_1(\tau)$ acquires a maximum value:

$$Max(a_1) = 0.0274575 \qquad (25)$$

The minimum of $\dot{k}$ is acquired for $\tau = -0.140$, $Min(a_1) = -0.028144$.

Additional integration over time yields

$$k = (1.)\, p_0 \frac{b}{A} \frac{1}{\rho c^2} a_0(\tau), \qquad (26)$$

where

$$a_0(\tau)\begin{cases} = (-\tau^6 + 20\tau^4 + 40\tau^3 - 32\tau)/640, & \text{for } -2 < \tau < -1 \\ = (15\tau^4 + 40\tau^3 + 15\tau^2 - 16\tau + 5)/640, & \text{for } -1 < \tau < 0 \\ = (\tau^6 - 5\tau^4 + 15\tau^2 - 16\tau + 5)/640, & \text{for } 0 < \tau < 1. \end{cases}$$

The maximum value of $a_0$ is obtained for $\tau = -0.67555$, $Max(a_0) = 0.0210100$. $a_0(\tau)$ has been plotted in Fig. IV-27-2 along with reactivity change, $b_0$, produced by a plane saw-tooth wave impinging upon a plane reactor. When $k$ is maximum $a_1 = 0.02746$ and $a_0 = 0.0111456$.

## References


1. V. Z. Jankus, *A Theoretical Study of Destructive Nuclear Bursts in Fast Power Reactors*, ANL-6512 (1962), p. 8.
2. E. P. Hicks and D. C. Menzies, *Theoretical Studies on the Fast Reactor Maximum Accident*, Proc. Conference on Safety, Fuels, and Core Design in Large Fast Power Reactors, October 11–14, 1965, ANL-7120, pp. 654–670.
3. H. A. Bethe, *Theoretical Estimate of Maximum Possible Nuclear Explosion*, KAPL-294 (1950), p. 22.
4. H. G. Elrod, Jr., *The Propagation of a Spherical Sound Pulse*, NDA 14-172 (1957).

# Section V

# Experimental Techniques and Facilities

Measured integral reactor physics parameters are necessary for either direct introduction into reactor design calculations or for comparison with values obtained analytically using basic microscopic cross section data. In the latter case the objective is to verify either the cross section data or the calculational techniques. Reactor integral parameters are obtained using special measurement techniques in exponential or critical facilities. The papers presented in this section deal largely with the development of such special techniques, facilities, and radiation detection devices. Included also are papers which describe specially developed equipment useful in obtaining microscopic nuclear data. In addition, there are papers which discuss the development of special equipment used in measurements relating to power reactor fuel element failures.

# V-1. Preparation of Pu-239 and Pu-241 Isotopes for Capture-to-Fission Measurements in the Experimental Boiling Water Reactor

R. J. Armani

Capture-to-fission measurements have been performed in EBWR using Pu-239 and Pu-241 isotopes. Exposure in the EBWR core configuration imposed severe restrictions on the physical dimensions of the plutonium samples and their containers.[1] The requirements were such that a small, accurately known mass (100–300 $\mu$g) of plutonium had to be sealed into an aluminum capsule with dimensions no greater than 0.457 cm diam and 0.025 cm thick. This restricted the maximum diameter available for sample deposition to about 0.318 cm. Techniques for sealing aluminum envelopes by cold welding had been previously developed by Argonne's Central Shops. However, the problem remained to confine the sample to a diameter of 0.318 cm and to accurately determine its mass.

## Sample Deposition

A number of methods were considered for the deposition of the plutonium sample, but the following method proved successful and was adopted. The samples were deposited in liquid form on aluminum foil 1.905 cm diam by 0.0076 cm thick and then evaporated to dryness. The samples were confined to the center of the foil by pressing a small depression into the aluminum, 0.318 cm in diam and 0.0076 cm deep. A 2$\lambda$ (1$\lambda$ = $10^{-6}$ liters) volume was pipetted into the depression from a solution whose concentration was approximately 150 g/liter. This resulted in samples of approximately 300 $\mu$g. The 2$\lambda$ volume was small enough so that it did not spread beyond the confines of the depression even while being evaporated to dryness on a hot plate. An aluminum cover foil of the same thickness was placed over the sample. By means of a set of dies, the center portion of the aluminum foil with the sample was cut and the circumference cold welded to the required size of 0.457 cm diam.

## Mass Determination

Masses of samples such as these are usually determined by accurately pipetting a known volume of solution whose concentration has been established directly or indirectly by some gravimetric method. In this case 2$\lambda$ volumes are being pipetted, and it is doubtful whether the mass could be determined to within 25% by such small volume measurements. A micro balance inside of a glove hood would be necessary to determine the mass gravimetrically, but an alternative and more accurate method was used. Namely, the samples were alpha-counted.

### Pu-239

The alpha activity was calculated from the isotopic analysis and the half-lives of the isotopes. The alpha activity calculated from the material used was $4.101 \times 10^7$ $\alpha$/m for a 300-$\mu$g sample. This activity is easily counted in a low geometry chamber.[2] The thickness of the samples is about 3 mg/cm$^2$, consequently no self absorption losses occur. The solid angle can be calculated to an uncertainty of about 0.1%, so that the errors in the activity are of the order of the errors in the alpha half-lives involved.

After the samples had been pipetted and dried on the aluminum foils, they were each counted in the low geometry chamber. From the absolute activity measured and the calculated specific activity, the mass of each sample was determined.

### Pu-241

Although Pu-241 is primarily a beta emitter with an end point energy of 0.021 MeV, it also alpha decays with a branching ratio of about $4 \times 10^{-3}$%. Beta counting was not considered because of the difficulties arising in the measurement of soft betas, but alpha counting was straight forward. The beta particles are easily absorbed with a 1 mg/cm$^2$ absorber over the detector, eliminating any possible interference from pile-up.

The alpha disintegration rate per milligram of sample could not be calculated very accurately because the alpha branching ratio for Pu-241 is not very well known. But an estimate of the alpha activity was made using $4 \times 10^{-3}$% as the branching ratio. The activity from the daughter product, Am-241, was also estimated and included to give an alpha decay rate of approximately $3 \times 10^8$ $\alpha$/m for a 300 microgram sample. This activity was also easily counted in the low geometry chamber. But since the specific alpha activity could not be accurately calculated, another means was used to relate alpha decay rate to sample mass.

The plutonium for this experiment was received from the supplier in the oxide form. The oxide was

carefully weighed and put into solution with nitric acid and a small amount of hydrofluoric acid. The solution was raised to a known volume, and a large enough portion of this solution was removed to serve for accurately pipetted dilutions. These dilutions were used to prepare counting samples with accurately known masses. These samples were counted in the low geometry chamber, thus providing the necessary absolute calibration between total mass and the alpha decay rate.


REFERENCES

1. H. P. Iskenderian, Argonne National Laboratory (private communication).
2. R. J. Armani, *A Low Geometry Alpha Counting Chamber*, Reactor Physics Division Annual Report, July 1, 1965 to June 30, 1966, ANL-7210, p. 303.


## V-2. Accurate Fission Rate Measurements by Fission Track Counting

R. J. ARMANI, R. GOLD and J. H. ROBERTS*

The capabilities of the fission track counting method for precise determination of fission rates has been under investigation. In this method,[1] a solid-state track recorder (SSTR) is exposed to fission fragments. The recorder is then etched for a length of time that will suitably enlarge the fission fragment tracks. The enlarged tracks may then be observed and counted with the aid of a microscope. Mica, glass, and (synthetic) polycarbonate resin can serve as the SSTR.

Present results with mica and polycarbonate resin indicate that this technique can provide precise fission rate measurements for many neutron and fission physics experiments. A number of applications may be mentioned. For example, such data could provide the basis for more accurate thermal and fast fission cross sections. Very long spontaneous fission half-lives could be measured.[2,3] More accurate fission rate and power distributions in critical assemblies would result. The increase in precision would also enhance efforts to obtain spatial gradients of these distributions. In fact, the unmatched spatial resolution (of the order of microns) attained by this method will permit consideration of many neutron and reactor physics experiments heretofore impossible.

### SOURCE PREPARATION TECHNIQUES

The samples used in this investigation were prepared by depositing uranium on platinum discs 2.38 cm in diameter and 0.0127 cm thick. The deposits were confined to the center of the discs and to a diameter of 1.59 cm which corresponds to an area of 1.98 sq. cm. Two methods were used in the preparation of the uranium deposits. The first method was by electrodeposition and the second method by vacuum evaporation.

The electrodeposition of uranium was accomplished using a method described by F. Kirn.[4] This method was slightly modified in that no stirring was used in order to avoid swirling of the sample, and the sample was finally heated to 850°C in a furnace for one hour to convert the deposit to $U_3O_8$. This method produced samples of thicknesses ranging from 20 $\mu g/cm^2$ to approximately 3 $mg/cm^2$. The uniformity of the samples produced by this method was not satisfactory for the overall precision desired. Consequently vacuum evaporation was investigated as a method to produce samples of improved uniformity.

The vacuum evaporation of uranium was accomplished as described by G. Erickson, S. Kaufmann and L. Pahis.[5] A tungsten boat was used to melt and evaporate uranium metal. Selected samples of high quality and uniformity were produced in the thickness range of 10–400 $\mu g/cm^2$ of $U_3O_8$. As in the case of the electrodeposited samples, these samples were also heated to 850°C to convert the deposit to $U_3O_8$.

The vacuum evaporation of uranium metal proved to be quite difficult. The molten uranium tends to alloy with the tungsten boat so that in some cases a mixture of tungsten and uranium is deposited on the platinum discs. Fortunately, it is possible to detect the undesirable samples by means of a counting technique described below. In order to avoid the difficulties involved with the evaporation of uranium metal, uranium tetrafluoride was used in the preparation of a second set of vacuum evaporated samples. This compound melts and evaporates at a lower temperature than the metal, and there is no difficulty with the formation of an alloy with the tungsten boat. The samples were not heated to 850°C in this case, since the uranium tetrafluoride seems to be a very stable compound. Samples of this compound were produced in the thickness range of 10–750 $\mu g/cm^2$, and it appears

* Northwestern University, Evanston, Illinois.

possible that samples can be deposited up to several milligrams per square centimeter.

A special set of (infinitely thick) samples was made by punching uranium foil 0.0127 cm thick. They were made for the purpose of obtaining a calibration for samples similar to those which were used for measurement of spontaneous fission half-life of U-238.[3]

### Mass Determination

The mass of each uranium sample deposit was determined by absolute alpha counting in a low geometry chamber.[6] The specific alpha decay rate was calculated from knowledge of the isotopic ratios of the uranium isotopes and their half-lives. The mass was calculated from the absolute alpha decay rate and the specific alpha decay rate. In the particular uranium used in these samples, the predominant activity was that of U-234, so it was possible to determine the total mass of each uranium sample to better than 1.0% relative error.

### Source Evaluation

Each sample was evaluated for purity and uniformity. The alpha decay rate had already been obtained from the mass determination. The samples were then counted in a $2\pi$ flow counter, and the ratio of $2\pi$ counts to alpha decay rate was calculated. This ratio was plotted as a function of sample thickness. If the samples contained no impurities, the ratios would fall on a smooth curve such as that given by H. Smith and J. Balagna.[7] In addition the samples, together with detectors, were irradiated in the "rotating wheel assembly" as described in the section on Calibration. The resulting fragment track densities were plotted as a function of sample thickness, and as in the case of alpha counting, the data should result in a smooth curve. However, it was observed that some samples did not lie on this smooth curve. Similarly, the very same samples did not lie on the curve obtained by alpha particle counting. In such cases it was assumed that these samples contained impurities and consequently they were rejected.

Source uniformity was checked by making radial profiles of track densities. Agreement was generally well within statistics for vacuum evaporated sources, but difficulties have been encountered with some electroplated sources. There was usually a fall off in track density near the edges of electroplated sources. In order to avoid this problem, masks were placed over electroplated sources so that only the more uniform center portion of these sources were exposed to the SSTR. The masks consisted of aluminum discs 2.38 cm in diameter and 0.0076 cm thick with a hole 1.27 cm in diameter punched from the center.

### Etching and Track Counting Techniques

Studies undertaken thus far have been primarily with mica and polycarbonate resins (Makrofol). Mica is pre-etched in 49% HF at room temperature for at least 5 h in order to determine the fossil fission track background due primarily to the spontaneous fission of U-238 contained as an impurity in the mica. After exposure to a source of fission fragments the mica is again etched in HF of the same concentration at room temperature for about one hour and twenty minutes. The etch pits of "tracks" produced by this etching are much smaller than those due to pre-etched fossile fragments and discrimination is essentially 100% (see Fig. I-14-1, Paper I-14). Mica with a clean surface and low fossil fragment background is selected for irradiations.

The polycarbonate resin is etched with 6.2 N NaOH at room temperature for about 48 h. Similar results can be obtained at 70°C for about 40 min, but damage to the surface is more likely. Recent tests with 6 N KOH indicate faster etching so that comparable results can be obtained at room temperature in about 18 h with possibly less surface damage.

The tracks are counted with binocular microscopes in which dry objectives of 25 to 45× with 10 to 12.5× oculars are generally used. Grids divided into 36 squares that fill most of the field of view are inserted in one ocular to facilitate track counting. Microscope stages are equipped with dials that read the stage positions ($x$ and $y$) to a precision of about two microns. Two methods of track counting are used, depending on track densities. For higher track densities, tracks in a given field are counted; a track or any object crossing the top line is then moved until it crosses the bottom line, and the tracks in the next field are counted. Tracks that cross the top or left line in the eyepiece grid are not counted, but tracks that cross the bottom or right line are counted, so that on a statistical basis, the number of tracks originating in the area scanned is determined. The width of the scanning path is determined with a stage micrometer, and the length is determined by the dial readings. The area scanned is thus determined. Counting is done with a hand tally counter. If the track densities are low, the tracks are counted as they cross a line on the grid. The length of the line is calibrated with a stage micrometer, and the distance the stage is moved during counting is measured by the dial attached to the stage. Track densities from less than 100/cm$^2$ to more than 200,000/cm$^2$ have been counted using a combination of these techniques. Track counting becomes difficult because of pileup when densities are much in excess of 200,000/cm$^2$. The optimum density for rapid counting is around 50,000/cm$^2$. Observer agreement between prop-

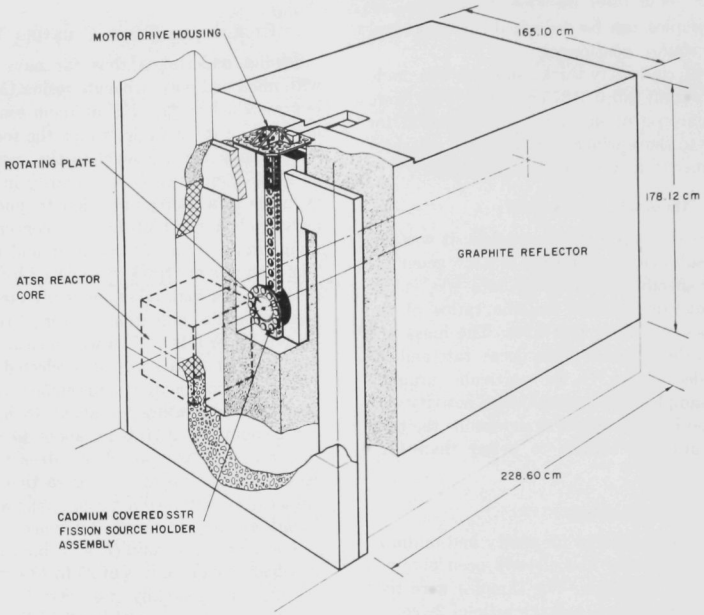


FIG. V-2-1. The Rotating Wheel Assembly in the Argonne Thermal Source Reactor. *ANL Neg. No. 112-9397.*

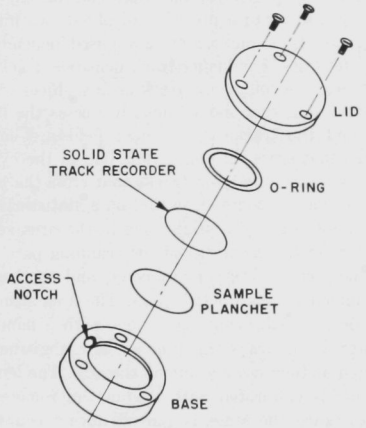


FIG. V-2-2. Geometrical Arrangement of the Sample and Solid State Track Recorder in the Sample Holder. *ANL Neg. No. 112-6468 Rev. 1 Corr.*

erly trained scanners is generally good (well within statistics). For optimum track densities, 10,000 tracks can be counted by one scanner in two or three hours.

## CALIBRATION

The relative reliability and efficiency of this method have been investigated with a "rotating-wheel assembly" in the graphite reflector of the Argonne Thermal Source Reactor (ATSR). This assembly is depicted in Fig. V-2-1. A set of fissionable sources (usually uranium) are assembled in source holders that ensure intimate contact with a given SSTR as shown in Fig. V-2-2. The source and detector assemblies are then mounted uniformly near the circumference of a wheel. The wheel is rotated in the slow neutron environment of the ATSR graphite reflector; hence, all source and detector units are exposed to the same time-integrated neutron flux. To eliminate changes in flux depression and flux perturbation, all source and detector units are cadmium covered. Consequently, the specific fission rate is constant for all sources of a given "rotating-wheel" exposure.

Under these conditions, one can perform quantitative tests on the reliability and reproducibility of the method as a whole. In particular, one can study the track scanning and counting aspects of the technique, since inconsistencies can be expected to arise between different human observers. These differences can be uncovered and resolved, thereby establishing a con-

sistent method for the optical counting of tracks. As a final goal, one could then precisely establish the relative counting efficiency as a function of source thickness for different SSTR.

Absolute calibration of the relative efficiency has been carried out with electrodeposited Cm-244 spontaneous fission sources. The spontaneous fission half-life of Cm-244 has been determined with a relative error of 0.5%.[8] This measurement has subsequently been verified by an independent experiment.[9] Different Cm-244 sources have been prepared by electrodeposition and, therefore, may serve as absolute fission rate standards with relative error less than 1.0%. Efficiencies for infinitely thin sources, when the source and SSTR are placed in good contact, are (95.0 ± 0.5)% for both mica and Makrofol.

### References


1. R. L. Fleischer, P. B. Price and R. M. Walker, *Solid-State Track Detectors: Applications to Nuclear Science and Geophysics*, Ann. Rev. Nuclear Sci. **15**, 1–29 (1965).
2. R. Gold, R. J. Armani, J. H. Roberts and A. Behkami, *Accurate Determination of Very Long Spontaneous Fission Half-Lives* ($\gtrsim 10^{14}$ *y*) *by Fission Track Counting*, Bull. Am. Phys. Soc. **11**, 825 (1966).
3. J. H. Roberts, R. Gold and R. Armani, *Decay Constant for the Spontaneous Fission of* $^{238}U$, Bull. Am. Phys. Soc. **12**, 922 (August 1967).
4. F. S. Kirn, *Neutron Detection with an Absolute Fission Counter*, Proc. 1963 IAEA Symposium on Neutron Dosimetry, Vienna, Vol. II., pp. 497–512.
5. G. F. Erickson, S. G. Kaufmann and L. E. Pahis, *Recent Neutron Detection Studies at Argonne National Laboratory*, IRE Trans. Professional Group on Nuclear Science, Vol. NS-3, No. 3 (June 1956).
6. R. J. Armani, *A Low Geometry Alpha Counting Chamber*, Reactor Physics Division Annual Report, July 1, 1965 to June 30, 1966, ANL-7210, p. 303.
7. H. L. Smith and J. P. Balagna, *A Method of Assay of U-234, U-238 and NP-237 Fission Foils*, Conference on Neutron Cross Section Technology, Washington, D. C., March 1966, Vol. I., pp. 1013–1022.
8. D. Metta, H. Diamond, R. F. Barnes, J. Milsted, J. Gray, Jr., D. J. Henderson and C. M. Stevens, *Nuclear Constants of Nine Transplutonium Nuclides*, J. Inorg. Nucl. Chem. **27**, 33 (1965).
9. R. Armani and R. Gold, *Spontaneous Fission Half-Lives of* $^{242}Cm$ *and* $^{244}Cm$. Standardization of Radionuclides, (IFEA, Vienna, 1967), p. 621.


## V-3. Experience with a New Manganese Bath System

A. De Volpi and K. Porges

For fast neutron detection involving high accuracy or difficult gamma-ray background problems, the manganese bath system has been an acknowledged success. The system consists basically of a moderator-filled tank in which dissolved manganese is activated and ultimately counted. Early techniques involved drawing a sample from the bath and counting in a facility located away from the radiation field, or, if possible, placing counters directly into the tank after the source had been withdrawn.

Newly emerging procedures[1] obtain much higher count rates, greater stability, and improved signal/background conditions by pumping the liquid in a continuous loop from the manganese bath tank to a remotely situated counter. This permits extensive shielding of the counter in a low-background location, optimum design of the detection geometry, and maximum count rate during the buildup, saturation, and decay phases of Mn-56 activation.

Such a system has been used now for a year in both reactor and non-reactor environments. Compared to the highly stable gamma-gamma coincidence system previously used,[2] the count rates now obtained are about one thousand times greater than the coincidence rate and about twenty times greater than single-channel counting of the 0.85-MeV peak. Partially offsetting this is the fact that background is a factor of 15 higher; even so a (signal)$^2$/background criterion still strongly favors the new on-line counting system.

A drawing indicating some of the chief features of the on-line system is given in Fig. V-3-1. Radioactive neutron sources may be placed at the center of the sphere to induce manganese activity proportional to the source strength. The active solution is continuously mixed by a circulating pump which returns the liquid into the sphere through a dispersal unit. Simultaneously some of the solution is pumped into the on-line counter shown in more detail in Fig. V-3-2.

A NaI(Tl) annulus, 15 x 15 cm with 2.5-cm wall, is the detection medium. The gamma rays from Mn-56 [0.85 MeV (100%); 1.8 MeV (30%); and 2.1 MeV (20%)] mostly escape from the liquid and interact in the sodium-iodide crystal with high probability. All pulses resulting in at least 50 keV transfer to light photons are accepted by the electronic level discriminator.

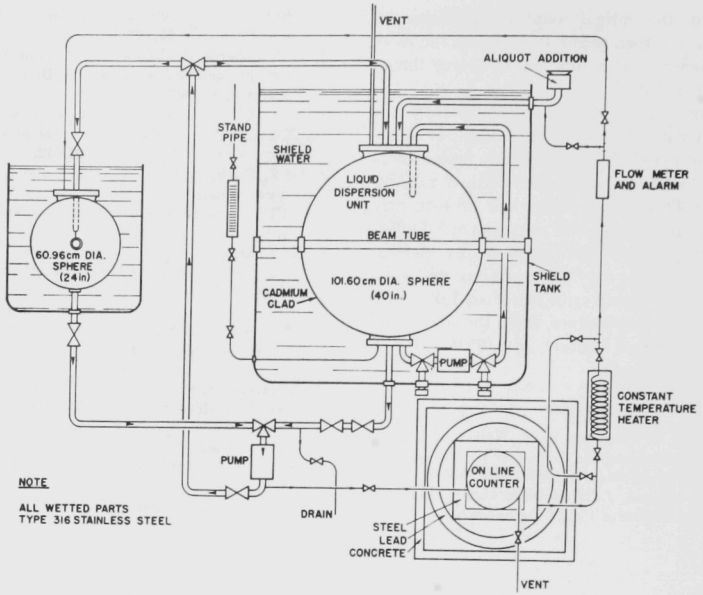


FIG. V-3-1. Manganese Bath System. *ANL Neg. No. 112-8689.*

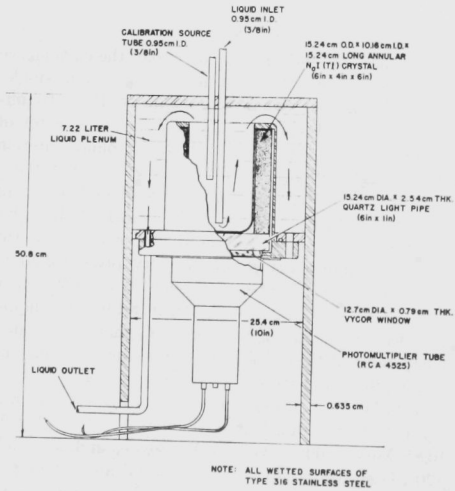


FIG. V-3-2. Details on On-line Counter. *ANL Neg. No. 112-8690.*

Provision has been made for stabilization by a light pulser, but so far this feature has not been needed. The entire bath and counting system are maintained at almost constant temperature (about 37°C). Plateau operation is obtained in high voltage amplifier gain and discriminator characteristic.

When experiments must be done at the Argonne CP-5 reactor, the counting station is placed in the equipment staging area and the manganese bath tank is located at the East thermal column. Water surrounding the cadmium-shielded sphere keeps the external background to a minimum. Neutrons from the thermal column pass along the beam tube intersecting the target at the center of the sphere, and then escape to a beam catcher placed behind the tank. The liquid is pumped through tubes which penetrate the containment shell.

Shielding for the on-line counter is depicted in Fig. V-3-3. The outer shield consists of borated concrete to reduce neutron background. The inner shield is composed of 10-cm thick plates of U.S.S. Kentucky armor plate and the cylindrical shield is made of lead. Materials in close proximity to the crystal, aside from the

manganous sulphate solution, are stainless steel, quartz, lucite, and MgO. Access is provided through the top.

Electronic processing of signals derived from the photomultiplier is rather straightforward. No active electronic elements are located within the shield: a 50-Ω cable delivers the anode signal to a low input impedance preamplifier which drives a pole-zero cancellation bipolar amplifier with gain of 1600. The output of the amplifier is loaded with 50 Ω for an adjustable paralysis discriminator (APD)[3] set at a 9.5-mA level. The combination of 1250 V applied to the phototube, the amplifier gain, preamplifier matching, and discriminator level is sufficient to count pulses in the neighborhood of 50 keV. A precise deadtime of 10 μsec is applied by the APD.

Plateaus with slopes of 0.1%/mA on the discriminator, 1%/100 V in high voltage, and comparable results in amplifier gain are obtained.

The APD feeds either or both of two scaling systems. One contains a recycling timer which initiates at pre-set intervals the readout, resetting, and count start of the scaler. The readout is printed on continuous paper tape. This readout station is mobile.

The parallel scaling system permanently located in a counting room derives a 50-Ω terminated pulse from the APD. This pulse is reshaped in one channel of a six-channel automatic readout station. The output from this system is punched on cards.

Data from either of the two readout stations may be processed by the computer program SATURATE which determines the saturated activity for each data point based on the known irradiation conditions. A weighted mean is taken for all data points. Included in the program are corrections for pumping time, mixing time, deadtime, point-by-point normalization, background, and other factors.

Performance of the system has been satisfactory. Corrections for finite pumping time for rates of 300 liters/h are in the order of ½%. The background level is now about 33 c/s integral from the lower level discriminator. Experiments indicate that by setting an upper level discriminator at about 3 MeV an additional 4 c/s, caused chiefly by cosmic rays, could be excluded in anticoincidence without loss of Mn-56 counts.

Checkouts can be made using various sources which fit a penetration in the counter. Ra-226 in equilibrium is a useful standard because its overall spectrum and endpoint is roughly equivalent to Mn-56.

The overall efficiency for counting is about 0.37% per Mn-56 disintegration in the entire bath system.

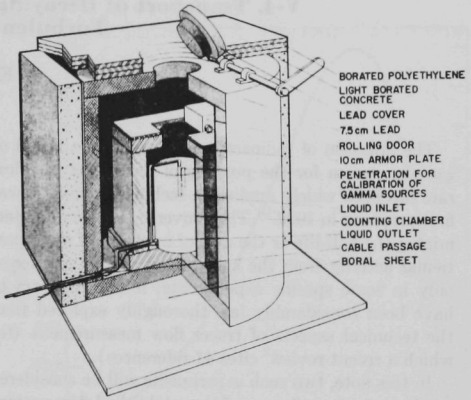


FIG. V-3-3. Shielding for On-line Counter. *ANL Neg. No. 112-8688.*

This corresponds to about 0.16% efficiency per source neutron (at a $MnSO_4$ concentration of about 400 g/liter).

Since background experience indicates a highly stable level, it is possible to consider the counting of sources with emission rates of only $10^4$/sec with precision of 0.1% in a normal cycle of two days. The two-day cycle consists of one day to activate to saturation (ten half-lives) and one day for decay to background.

A number of sources have been calibrated and compared with the U.S. standard neutron source, NBS-II, and the neutron emission rates for various fission sources have been determined for neutron yield measurements.[4] Several precision measurements of fundamental cross sections are anticipated with the aid of this improved manganese bath system.

## REFERENCES

1. P. J. Axton, P. Cross and J. C. Robertson, *Calibration of the NPL Standard Ra-Be Photoneutron Sources By An Improved Manganese Sulphate Bath Technique*, J. Nucl. Energy: Pt. A & B **19**, 409 (1965).
2. A. De Volpi, K. G. A. Porges and R. N. Larsen, *Mn-56 Coincidence Counting Facility* , ANL-6760 (1963).
3. A. De Volpi, J. J. English, A. J. Metz, K. G. Porges and S. J. Rudnick, *Versatile Gated Discriminator with Adjustable Paralysis Useful in Fast-Slow Coincidence Experiments*, Rev. Sci. Instr. **37**, 1592 (1966).
4. A. De Volpi and K. G. Porges, *Direct and Absolute Measurements of Average Fission Neutron Yield from U-235 and Cf-252*, Proc. Intern. Conference on Nuclear Data, IAEA, Paris, October 1966, *Nuclear Data for Reactors*, Vol. 1 (IAEA, Vienna, 1967), pp. 297-306.

# V-4. Transport of Decaying Activity Through Laminar and Turbulent Flow Systems

K. Porges

The injection of radioactive isotopes into a liquid or gaseous stream for the purpose of measuring the flow rate has been widely applied in technology since it was first proposed in 1922.[1] The converse problem of determining the half-life or the rate of injection of some particular activity from the known flow rate, is of interest only in some specific experiments; it thus appears to have been considerably less thoroughly explored than the technical aspects of tracer flow measurement (for which a recent review[2] cites 41 references).

In this note, two such experiments will be considered to illustrate the influence of the established flow pattern on the mean transport time through a certain duct. In either of these experiments, one wishes to infer the rate of injection or generation of a known activity from the count rate of a detector through (or past) which the activity is carried by a stream of established average flow rate. The mean transport time will be shown to depend very strongly on the type of flow, laminar or turbulent. For long ducts or short half-lives, the decay correction which must be applied to the measured count rate to obtain the injection point activity is thus poorly defined unless the duct geometry is simple enough to make the flow pattern wholly laminar or turbulent. Since this is usually not the case in practice, careful calibration experiments are mandatory for precision measurements if the parameters of the system cannot be adjusted so as to render the correction negligible. In any case, the blanket application of an exponential decay correction, frequently used in the technical literature but applicable only for an ideally turbulent flow pattern, should be discouraged.

The first of the two examples in which this decay correction is of some interest is a manganese or vanadium neutron source calibration bath with on-line flow counter.[3] In this experiment, a neutron source is inserted into a large spherical tank containing either manganese or vanadium in aqueous solution. 2.58 h $Mn^{56}$ or 3.77 m $V^{52}$, continuously generated by neutron capture, is uniformly dispersed in the bath through vigorous stirring; the solution is also pumped through a loop passing through a gamma counter, which may be located at some distance from the tank to reduce background.

The second example concerns the possibility of estimating the extent of a fuel element leak from the signal strength obtained in a calibrated delayed neutron detector situated in a loop which samples the coolant just after it has passed through the core. Such fuel failure detection systems are now installed in most sodium cooled reactors; for example, in EBR-II.[4]

To estimate the decay correction which applies for either case, we suppose that a single continuously generated activity of decay constant $\lambda$ is homogeneously dispersed in a liquid at the entrance of a circular duct of radius $a$. The specific activity $n(l)$ (decays/cc-sec) averaged over the cross section of the duct at a distance l downstream,

$$\bar{n}(l) = \int_0^a n(l,r) \cdot 2\pi r \, dr,$$

is measured; the specific activity $\bar{n}(0)$ at the point of injection is to be calculated from this measurement and the established average flow rate $F$ (cc/sec). For liquids with a viscosity comparable to that of water, one finds that the flow pattern will be purely laminar for flow velocities corresponding to a Reynolds number below about 2000, and completely turbulent for Reynolds numbers above 12,000.[5] Flow velocities within the range

$$40 \leq F/a \leq 250$$

thus do not permit a reliable calculation of the decay in transit. It is therefore expedient to calculate the decay corrections for either type of flow as limiting cases between which the actual correction must lie.

For ideal turbulent flow, continuous mixing takes place along the stream throughout the cross section of the duct; every part of the liquid moves at the same average transport velocity $F/\pi a^2$. The decay correction thus is straightforward:

$$n(0) = n(l) \exp(\lambda V/F), \tag{1}$$

where $V = \pi a^2 l$. For Poiseuille (laminar) flow, the linear flow speed $v(r)$ at radius $r$ is given by[5]

$$v(r) = (a^2 - r^2)\Delta p/4\mu l \tag{2}$$

in terms of pressure difference $\Delta p$ and viscosity coefficient $\mu$. Integration over the cross section of the pipe yields the flow rate

$$F = \pi a^4 \Delta p/8\mu l. \tag{3}$$

Combining these two equations, one can express the transit time $t(r)$ in terms of known parameters,

$$t(r) = (V/2F)(1 - r^2/a^2)^{-1}. \tag{4}$$

The average specific activity at 1 thus becomes

$$\bar{n}(1) = (\bar{n}(0)/\pi a^2) \int_0^a \exp\,[-\lambda V/2F(1 - r^2/a^2)]2\pi r\, dr$$

which can be written as an exponential integral of second degree,

$$\bar{n}(1) = b\bar{n}(0) \int_b^\infty \exp\,(-u)\,\frac{du}{u^2} = \bar{n}(0)E_2(b), \quad (5)$$

with the substitutions

$$u = b/(1 - r^2/a^2), \qquad b = \lambda V/2F. \quad (6)$$

For small values of the argument, an expansion of $E_2(b)$ is available which yields the correction

$$\begin{aligned} k_p &= [n(0) - n(1)]/n(0) \\ &= b[0.4228 - \ln b + b/2 + \cdots \\ &\quad + b^{(i-1)}/[(i-1)i! \cdots] \\ &\approx b \ln (1.526/b) + b^2/2. \end{aligned} \quad (6)$$

In contrast, this correction for the case of thorough mixing (turbulent flow) is, according to Eq. (1),

$$\begin{aligned} k_t &= [n(0) - n(1)]/n(0) \\ &= b(2 - 2b + 4b^2/3 - 2b^3/3 \cdots). \end{aligned} \quad (7)$$

The difference between the decay rate at the detector as predicted by Eqs. (1) and (5) is plotted in Fig. V-4-1, which indicates that small values of $b$, corresponding to slow decay and/or rapid flow, allow decay corrections largely independent of the flow pattern; the same is true for a narrow range of values near 0.8, when the average transit times characteristic of Poiseuille and of turbulent flow are again equal. For a system with parameters which put $b$ in the region of the peak in Fig. V-4-1, $\lambda\pi la \approx 0.3\ F/a$, it is evidently advisable to change the pumping speed, rearrange the geometry or make very careful calibration measurements.

These observations apply directly to the neutron source calibration experiment mentioned above. For a manganese bath, either correction may in principle be kept well below 1% if the solution can be pumped through the detector with a mean transport time $V/F$ of the order of 10 sec or less. This is not necessarily the case, however, when vanadium is used as a neutron capture indicator. The short lifetime of V-52, which in fact constitutes the principal advantage of this activity in activation measurements where one generally must wait for equilibrium, also makes the appearance of a correction of several per cent likely for practical flow systems; the onset of cavitation and similar flow instabilities in the detection volume imposes an upper

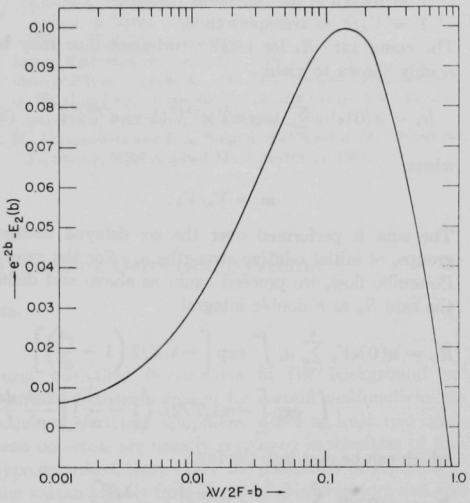


FIG. V-4-1. Decay Correction Difference, Turbulent and Laminar Flow in Cylindrical Duct. *ANL Neg. No. 112-8824.*

limit on the pumping speed. Since the viscosity of a strong salt solution is likely to be considerably higher than that of pure water, the onset of turbulence occurs at a correspondingly higher Reynold's number. At the same time, stagnant volumes and turbulent eddies make their appearance at high flow rates. All these factors militate against the possibility of system operation in the ideal turbulent regime; hence the decay correction cannot be assumed to be strictly exponential. Similar restrictions apply, in fact, to flow meters using isotopes, for which reason such equipment is usually capable of exact measurements only by comparison with a set of calibration plots.

In the second example, one requires a slight elaboration of the simple results derived above to include, on one hand, decay in transit through the detector and on the other hand a number of activities of different half-lives. The detection station for fuel element rupture monitors often consists simply of a graphite stack surrounding a certain length (3 to 4 ft.) of the loop duct; neutron detectors are embedded in the graphite, as shown schematically in Fig. V-4-2. Let

$\epsilon \equiv$ overall detection efficiency (counts per delayed neutron emitted inside the counting volume $V_c$),

$V_d \equiv$ volume of the duct between the point where fresh fission products are injected into the stream and the boundary of the detection volume (i.e. the edge of the graphite stack),

$L \equiv$ length of the detection volume,
$T = V_d/F \equiv$ transport time.

The count rate $R_t$ for ideally turbulent flow may be readily shown to yield

$$R_t = n(0)\epsilon V_c \sum_{i=1}^{6} (\alpha_i/mT)e^{-\lambda_i T}(1 - e^{-m\lambda_i T}), \qquad (8)$$

where

$$m = V_c/V_d .$$

The sum is performed over the six delayed neutron groups, of initial relative strengths $\alpha_i$. For the case of Poiseuille flow, we proceed again as above and define the rate $R_p$ as a double integral

$$R_p = n(0)\epsilon V_c \sum_{i=1}^{6} \alpha_i \int_0^a \exp\left[-\lambda_i T/2\left(1 - \frac{r^2}{a^2}\right)\right] \cdot \int_0^L \exp\left[-m\lambda_i T/2L\left(1 - \frac{r^2}{a^2}\right)\right] \frac{2r\,dr}{a^2}\,\frac{dz}{L},$$

which can be cast into the form

$$R_p = n(0)\epsilon V_c \sum_{i=1}^{6} \frac{\alpha_i}{mT}\left(e^{-\lambda_i T/2}\left\{\left[1 - \frac{\lambda_i T}{2}\right] \cdot [1 - e^{-m\lambda_i T/2}] + \frac{m\lambda_i T}{2} e^{-m\lambda_i T/2}\right\} + \left(\frac{\lambda_i T}{2}\right)^2 \cdot \left\{E_1\left(\frac{\lambda_i T}{2}\right) - (1 + m)^2 E_1\left[\frac{(1 + m)\lambda_i T}{2}\right]\right\}\right) \qquad (9)$$

after two partial integrations.

For a practical example, the choice $m = 0.05$ was made, which corresponds roughly to the EBR-II installation, and delayed neutron parameters were taken from the literature.[6] The quantities $[R_t/n(0)\epsilon V_c]$ and $[R_p/n(0)\epsilon V_c]$ were then calculated on a digital computer, for which purpose values of the exponential integrals for larger than unity arguments were approximated by a polynomial fraction[7] and for small values of the argument by the usual expansion.[8] The result is shown in Fig. V-4-3, where contributions by the first four delayed neutron emitters are plotted separately both for laminar and for turbulent flow, and the sum is also shown. It appears from this plot that the discrepancy between Eqs. (8) and (9) amounts to a factor of about two over the range of transport times of practical interest.

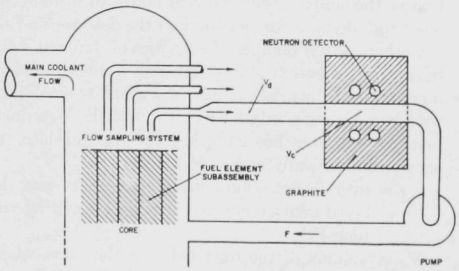


FIG. V-4-2. Schematic of Delayed-Neutron Fuel Element Rupture Detection System. *ANL Neg. No. 112-8889.*

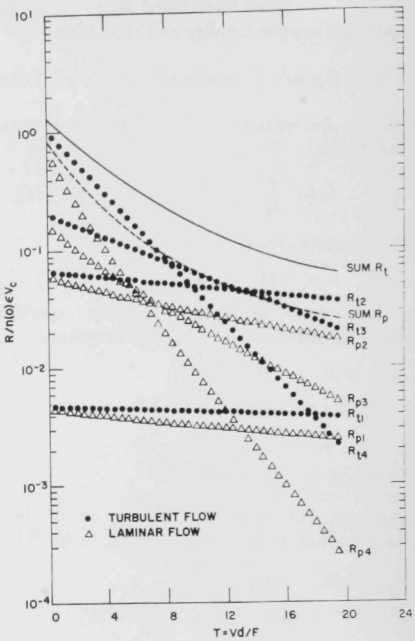


FIG. V-4-3. Plot of the Contributions by the First Four Delayed Neutron Emitters. *ANL Neg. No. 112-8818.*

Regarding the practical application of this calculation to the determination of the extent of a fuel failure, the method of sampling the coolant flow in the fuel failure monitors presently installed in fast reactors precludes any such possibility. For the next generation of such plants, however, individual sampling channels, which effectively gather the flow from a subgroup of fuel elements, may well be deemed desirable in order to expedite the difficult problem of locating a failed element. The determination of damage extent should then be considerably more accurate, and the present calculations may play a useful role in that connection.

## REFERENCES

1. J. Joly, *On a New Method of Gauging the Discharge of Rivers.* Sci. Proc. Roy. Dublin Soc. **16,** 489 (1922).

2. C. G. Clayton, *Measurement of Flow of Liquids and Gases Using Radioactive Isotopes*, Brit. Nucl. Energy Soc. **3**, 252 (1964).
3. A. De Volpi, K. Porges and R. Armani, *Absolute Calibrations of Fission Neutron Source Strength Relying on an Improved Manganese Bath Technique and Absolute Beta-Gamma Coincidence Counting*, Proc. Symposium on Standardization of Radionuclides, IAEA, Vienna 1967, p. 717.
4. K. G. Porges, *Fuel Failure Detection in Sodium-Cooled Fast Reactors*, Proc. Conference on Safety, Fuels, and Core Design in Large Fast Power Reactors, October 11-14, 1965, ANL-7120, pp. 862-867.
5. Lamb, *Hydrodynamics*, (Dover, New York, 1950).
6. *Reactor Physics Constants*, ANL-5800, Second Edition (1963).
7. C. Hastings, *Approximation for Digital Computers*, (Princeton Press, Princeton, New Jersey, 1965).
8. M. Abramowitz and I. A. Stegun, *Handbook of Mathematical Functions*, NBS Applied Math Series 55, 1964.

## V-5. Note on the Design Logic of Transient Detection Systems

K. Porges

Transient detection systems are increasingly employed in nuclear safety channels to provide timely warning and possibly automatic remedial action whenever the channel count rate exceeds a preset level and certain other conditions obtain. A typical example of such a system is the fuel element rupture detector (FERD) recently installed in EBR-2.[1] In this instrument, the outputs of four independent delayed-neutron detector channels are fed to a count rate discriminator, consisting of a count rate meter which converts the digital input into an analog signal, and of a voltage difference amplifier and trigger which compares the analog signal to some reference voltage. Ordinarily, this reference level is an adjustable dc bias; the trigger then responds to excursions superimposed on the channel background, which varies with reactor operating history (due to coolant activation as well as contamination with fissionable material). On the other hand, the slowly varying mean background level may be used as a reference level (MBR), thus making the trigger respond to excursions only. A dc reference instrument is capable of detecting slow leakage of one or several fuel pins, but evidently does not allow setting the trigger level for some specific transient amplitude above mean background. The latter type of operation is possible with an MBR excursion monitor, which in turn cannot detect slow leaks. Transients are presumably associated with sudden and violent fuel pin cladding rupture and have durations of the order of the time of passage of a piece of highly contaminated debris past the detector installation, typically a few tenths of one second. Admitting now that a fuel element rupture constitutes a clear danger to the plant, whereas the slow leakage of any number of fuel pins does not necessarily call for immediate remedial action, the advantage of using a mean background reference level becomes evident.

The operation of either type of excursion monitor is subject to a certain *false alarm frequency*, due to natural statistical fluctuations in the background or spurious transients caused by certain malfunctions in adjacent electrical equipment. Since at least two neutron detectors are usually employed in monitors of the type described, there exists the possibility of separating the output signals from the available detectors and requiring coincidence between these separate channels, which would be expected to eliminate spurious electrical noise. This further raises the question as to whether such a logical "and" system has a higher or lower rate of false alarms due to natural background fluctuation in comparison with the "or" system (in which all channels are combined ahead of the count rate discriminator), as illustrated in Figs. V-5-1a and V-5-1b.

To attempt to treat this question quantitatively, we suppose that a "typical" transient consists of a group of $M$ pulses in each of $k$ detectors, with a duration $T$ much shorter than the CRM (count rate meter) response time $T_b$, and further assume that the number $M$ is Poisson-distributed with variance $(M)^{1/2}$. This ad hoc assumption implies that a roughly constant number of delayed neutrons is emitted within reach of the detectors per transient and neglects, for the sake of simplifying the argument, the considerable range of fuel failure signal amplitudes one should actually expect.

For reasonably large values of $M$, the Poisson distribution can be approximated by a Gaussian distribution. One may then express the single channel detection efficiency $\epsilon$ for a channel trigger which fires on a group containing at least $A$ pulses above mean background:

$$\epsilon(A,M) = \tfrac{1}{2}[1 + \Phi(x)], \tag{1}$$

where

$$x = (M - A)/(2M)^{1/2} \tag{1'}$$

and $\Phi(x)$, the normalized error integral, is defined by

$$\Phi(x) = \frac{2}{\sqrt{\pi}} \int_0^x e^{-t^2}\, dt.$$

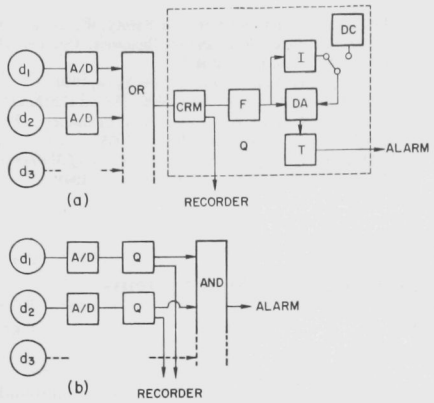


FIG. V-5-1. Logic Transient Detector System: (a) "OR", (b) "AND". *ANL Neg. No. 112-8940.*

Practical considerations demand operation of a transient detection system at efficiencies $\epsilon$ in the range $0.90 \leqslant \epsilon \leqslant 0.990$. Within that range, the efficiency function given by Eq. (1) can be closely approximated by a simple exponential function

$$\epsilon \approx 1 - \mathrm{Be}^{-px} \tag{2}$$

as shown in Fig. V-5-2, where parameters $B = 1.9$, $p = 3.17$ were used to obtain a reasonable fit. The overall efficiency of $k$ identical channels with required $k$-fold coincidence is equal to the $k$th power of the single channel efficiency,

$$E_{AND} = \epsilon^k \approx 1 - Bke^{-px}. \tag{3}$$

This must now be compared to the "or" system in which all $k$ channels are mixed ahead of a single CRM-excursion trigger unit. Supposing that the latter is set to trigger on excursions consisting of $Q$ or more pulses in a group, we find

$$E_{OR} = \tfrac{1}{2}[1 + \Phi(y)] \approx 1 - \mathrm{Be}^{-py}; \tag{4}$$

$$y = (kM - Q)/(2kM)^{1/2}. \tag{4'}$$

To provide the same detection efficiency for either type of logic, set

$$E_{AND} = E_{OR},$$

whence

$$x = y + h; \qquad h = (\ln k)/p. \tag{5}$$

We consider now the false alarm frequency, in the limit of large values of the parameter $N = nT_b$ (the number of background pulses in one CRM response period) which allows one to make use of Campbell's theorem[2]

$$\sigma_e^2 = n \int_0^\infty [F(t)]^2 \, dt, \tag{6}$$

where $F(t)$ is the voltage pulse at the discriminator input in response to a single count and $\sigma_e$ is the second moment of the trace probability distribution. The false alarm frequency $f(\alpha)$ at a trigger level $\alpha$ above mean background amounts to the combined chance of finding the trace within some distance $d\alpha$ below $\alpha$, having at the same time a positive slope $\beta$ which will make it reach or cross $\alpha$ in unit time:

$$\begin{aligned} f(\alpha) &= \int_{\beta=0}^{\infty} P_e(\alpha) \frac{d\alpha}{dt} \dot{P}_e(\beta) d\beta \\ &= P_e(\alpha) \int_{\beta=0}^{\infty} \dot{P}_e(\beta) \beta d\beta, \end{aligned} \tag{7}$$

where $P_e(\alpha)$ is the trace and $\dot{P}_e(\beta)\, d\beta$ is the slope probability distribution. The output of a CRM in response to background normally consists of a series of sharp

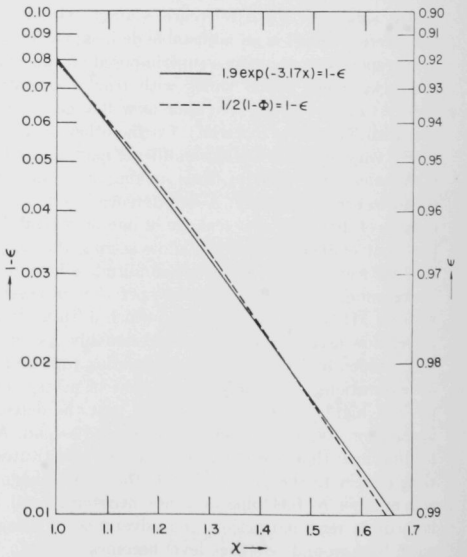


FIG. V-5-2. Detection Efficiency. *ANL Neg. No. 112-8814.*

positive steps connected by exponentially declining trace segments. The steps, say of height $\Delta V$, have a rise-time of the order of the duration of input pulses, typically 1 μsec; exponential decay follows the CRM time constant $T_b$, of the order of seconds. This type of trace clearly has a very strongly non-Gaussian slope distribution $\dot{P}_e(\beta)\, d\beta$; as a consequence, the formalism considered above would be less meaningful if applied to this "raw" CRM trace than, say, a pileup treatment along the lines suggested by R. Gold.[3] As it happens, the display equipment (servo-feedback pen recorder) usually fed by a count rate meter contains a partly electrical, partly mechanical integration (low pass filter) stage with a response time of at least 0.5 sec. Low pass filtration clearly reduces the fluctuations, hence the false alarm frequency, by a large factor. Considerations similar to those usually invoked in discussions of pulse amplifier noise[4] lead one to make the filter time constant equal to the CRM response time $T_b$. In the following, such a filter is assumed to be inserted between CRM output and trigger circuit input. At the same time, the visual recognition of debris-emitting cladding failures is evidently facilitated if a fast-responding chart writer or oscillograph is available which displays the CRM "raw" output with an integration time of perhaps one tenth of the expected transient.[5]

The filter ahead of the alarm discriminator results in a slope distribution which may be fairly represented by a Gaussian,

$$\dot{P}_e(\beta)\, d\beta = (d\beta/\sqrt{2\pi}\dot{\sigma}_e) \exp(-\beta^2/2\dot{\sigma}_e^2), \quad (8)$$

together with a similarly structured level distribution,

$$P_e(\alpha)\, d\alpha = (d\alpha/\sqrt{2\pi}\sigma_e) \exp(-\alpha^2/2\sigma_e^2). \quad (9)$$

The distribution parameters $\sigma_e$ and $\dot{\sigma}_e$ can now be calculated from Eq. (6), into which the single input response for equal time constants,

$$F(t) = \Delta V(t/T_b) \exp(-t/T_b) \quad (10)$$

and its time derivative $dF/dt$, are respectively inserted. One thus obtains

$$\sigma_e = \sqrt{nT_b}(\Delta V/2) \quad (11)$$

and

$$\dot{\sigma}_e = \sqrt{n/T_b}(\Delta V/2). \quad (12)$$

The integral indicated in Eq. (7) becomes

$$f(\alpha) = \frac{\dot{\sigma}_e}{2\pi\sigma_e} \exp(-\alpha^2/2\sigma_e^2) \quad (13)$$

for the Gaussian probability distributions given by Eqs. (8) and (9). Substitution of the second moments given by Eqs. (11) and (12) yields

$$f(\alpha) = (2\pi T_b)^{-1} \exp\{-2\alpha^2/nT_b\Delta V^2\}. \quad (13')$$

This derivation essentially follows N. Campbell and V. Francis[6] and is preferred here to the more elegant derivation outlined by S. Rice,[2] since it relates the results more directly to certain limiting assumptions. If now each channel opens a gate of length $\tau$ at the input of the coincidence circuit for the "and" logic scheme, the overall false coincidence rate amounts to the $k$-fold accidental coincidence rate

$$F_{AND} = k\tau^{k-1}f^k. \quad (14)$$

It remains to define the voltage level $\alpha$ in terms of the detection efficiency considered above. For this purpose, we require the peak filtered CRM output in response to a transient pulse group of $A$ pulses in time $T$. For the situation considered here, $T$ will come to a few tenths of one second. As regards $T_b$, Eq. (13′) shows that this time must be made large in order to reduce the false alarm frequency; an upper limit is, on the other hand, imposed by the requirement of timely warning. One thus arrives at a reasonable value $T_b \approx 10$ sec. The circuit response to the transient is then closely similar in shape to the single pulse response, given by Eq. (10), from which one readily finds a peak height $A\Delta V/e$ ($e$ = base of natural logarithms). This must be set equal to the discriminator level $\alpha$ if a group of $A$ pulses just fires the trigger. Inserting the parameter $x$ corresponding to $A$ according to Eq. (1′), and substituting the single channel false alarm frequency given by Eq. (13′) in Eq. (14), one finally arrives at the "and" logic scheme overall false alarm frequency

$$F_{AND} = k\tau^{k-1}(2\pi T_b)^{-k} \cdot \exp\left\{-\frac{2kM^2}{e^2N}\left[1 - \left(\frac{2}{M}\right)^{1/2} x\right]^2\right\}, \quad (15)$$

where $N = nT_b$. An analogous development yields the "or" logic scheme false alarm frequency

$$F_{OR} = (2\pi T_b)^{-1} \exp\left\{-\frac{2kM^2}{e^2N}\left[1 - \left(\frac{2}{kM}\right)^{1/2} y\right]^2\right\}, \quad (16)$$

whence one obtains the ratio

$$\frac{F_{AND}}{F_{OR}} = k\left(\frac{\tau}{2\pi T_b}\right)^{k-1} \cdot \exp\left\{\frac{4M}{e^2N}(\sqrt{k}\, x - y)[\sqrt{2kM} - (\sqrt{k}\, x - y)]\right\}. \quad (17)$$

Inserting now the condition of equal detection efficiency, Eq. (5), this becomes

$$\frac{F_{AND}}{F_{OR}} = k\left(\frac{\tau}{2\pi T_b}\right)^{k-1} \exp\frac{4M}{e^2N} \cdot\left\{\left(\frac{k}{k-1}\right)\left[h + \sqrt{\frac{M}{2}}\,(\sqrt{k}-1)\right]^2 - (k-1)\left[y - \frac{(\sqrt{k}-1)\sqrt{Mk/2} - hk}{k-1}\right]^2\right\}; \quad (18)$$

$$y = -p^{-1}\ln[(1 - E_{OR})/B],$$
$$h = p^{-1}\ln k,$$
$$B = 1.90,$$
$$k = 3.17.$$

The first exponential factor outweighs the second one in all but trivial cases, such that the net exponential term is positive. Whether "and" logic results in a higher or lower false alarm frequency due to fluctuations in the background thus depends largely on the ratio of the coincidence gate $\tau$ to the CRM response time $T_b$. Now the full rise-time of excursion pulses of shape given by Eq. (10) is just equal to $T_b$. As some of the channels may receive groups rather larger than $A$, the triggering delay $t$ must be expected to vary from a short time $t \ll T_b$ to $T_b$ after the onset of the event. Consequently, the gate length $\tau$ is practically limited to the order of $T_b$ if no coincidences are to be lost due to "timing inefficiency". The false alarm ratio given by Eq. (18) thus will not differ significantly from unity over a fairly wide range of conditions, a result which is intuitively reasonable since the same total amount of input "information" has been used for either scheme and only processed differently. However, just as in a similar situation which obtains in nuclear coincidence counting work, additional information is in fact available for the "and" logic scheme: the onset of the event can be ascertained at least within the time $T$ from the "raw" CRM channel trace by means of a "fast" coincidence stage whose gates may then be of length $T$. This second coincidence unit will necessarily pass a large number of false as well as true coincidences, from among which those which also fulfill the pulse height requirement imposed by the channel trigger levels are selected by a gate across the fast coincidence output opened by the "slow" coincidence stage.

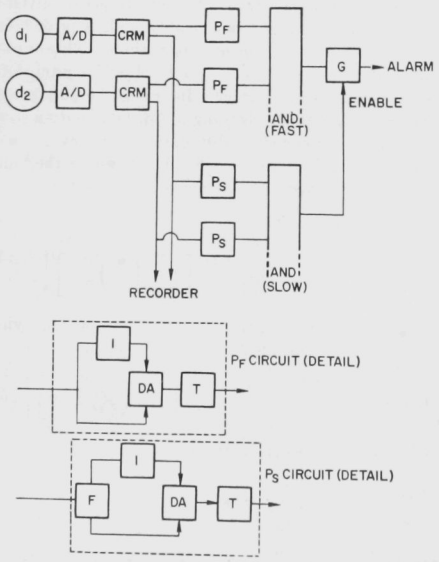


FIG. V-5-3. "Fast-Slow" and Logic Transient Detection (For Symbols see Fig. V-5-1). *ANL Neg. No. 112-8819.*

This type of system, shown as a block diagram in Fig. V-5-3, evidently can result in several orders of magnitude improvement in the false alarm frequency (or, conversely, in sensitivity of detection). Moreover, as considered above, the false alarm rate due to electrical noise pickup should also be considerably reduced. Availability of separate channel CRM's further allows the simultaneous presentation of at least two separate channels through an oscillograph equipped with two galvanometers, as a more convincing indication of the presence of some phenomenon which affects all channels.

In view of the large number of parameters ($M$, $N$, $T$, $T_b$, $E_{OR}$, $k$) involved in Eq. (18), a graphic presentation of this equation would exceed the limited scope of this note. A single numerical example must suffice here: let $M = 25$, $N = 100$, $T_b = 10$ sec, $T = 0.2$ sec, require $E_{OR} = 0.95$ hence $y = 1.16$ [cf. Fig. 2 or Eq. (4)] and consider fourfold coincidences. Eq. (16) then predicts a frequency $F_{OR} = 1.6 \times 10^{-4}$ sec$^{-1}$, whereas Eq. (15) with gates $\tau = 0.2$ sec yields $F_{AND} = 3 \times 10^{-11}$ sec$^{-1}$.

The treatment given here may be further developed to consider "voter" coincidence (where, say, any three out of four channels are accepted) as well as digital count rate meters, for which Poisson statistics would be more appropriate. As concerns a practical implementation, the FERD system was originally designed to allow "and" logic operation with some additional circuitry, but is presently using "or" logic. Before any changes are seriously contemplated in that system, the predictions made here must still be verified by experiment. Tests of this kind (for which rates and times are increased and decreased, respectively, by at least a factor of 20 in order to obtain statistically meaningful results in a reasonable running time) are in preparation.

REFERENCES

1. K. G. Porges, *Fuel Failure Detection in Sodium-Cooled Fast Reactors*, Proc. Conference on Safety, Fuels, and Core Design in Large Fast Power Reactors, October 1965, ANL-7120, p. 862.
2. S. O. Rice, *Mathematical Analysis of Random Noise*, reprinted from Bell System Technical Journal in "Selected Papers on Noise and Stochastic Processes," Nelson Wax, Ed., (Dover Publications, New York, 1954).
3. R. Gold, *Theoretical Estimates of Pile-up Distortion*, ANL-6949 (1965).
4. A. B. Gillespie, *Signal, Noise and Resolution in Nuclear Counter Amplifiers*, (Pergamon Press, London, 1953).
5. K. G. Porges and G. McGinnis, *Design of the Information Processing Unit of the FERD system of EBR-2*, IEEE Trans. Nucl. Sci. **NS 113**, No. 1, 454 (1966).
6. N. R. Campbell and V. J. Francis, *Random Fluctuations in a Cathode Ray Oscillograph*, Phil. Mag. **37**, 289 (1946).


## V-6. Time Resolution in NaI Scintillator-Junction Detector Fast Coincidence Systems

K. PORGES and R. GOLD

In a Compton-recoil-gamma spectrometer now being instrumented,[1] a large silicon junction detector is placed in a collimated gamma beam while two or more NaI scintillation detectors are arranged so as to intercept the scattered gamma radiation within a certain well-defined solid angle. A similar instrument[2] was designed primarily for a specific task not requiring capability of working with input gamma spectra covering a wide energy range; a relatively large background arising from false or accidental coincidences was thus not unacceptable.[3] In contrast, the present design aims at the precise measurement of complex gamma spectra from about 100 keV through 10 MeV and thus requires fairly elaborate means to reject false information. In particular, a coincidence requirement between fast side-channels is imposed, which is expected to eliminate background roughly to the extent to which coincidence gates can be made small. To illustrate this point, count rates in either channel, as well as the accidental-to-true coincidence ratio, are given in Table V-6-I for different input energies. Calculations were made on the basis of a 2-mC source strength; much weaker sources evidently would require excessive time for the accumulation of the upper energy region with good statistics, while much stronger sources would overtax the junction detector channel. The accidental count in the gamma channel is largely due to direct transmission of source radiation through the shielding and scattering in media other than the junction detector. The approximate numbers given in Table V-6-I were calculated by making use of the extensive literature on the subject of shielding,[4-6] and scaled to a series of tests. In addition to the fast coincidence requirement, a pulse-height discrimination scheme, described previously,[1] will be used and it is expected to reject a large fraction of the false counts passed by the fast coincidence step. It may thus be estimated that an accidental-to-true ratio of 0.1 to 0.2 will still keep the background contamination of the measured spectrum to less than 1%. For a 2-mC source, Table V-6-I indicates that this design goal requires coincidence gates $\tau$ of the order of 10 nsec.

To allow a coincidence counting efficiency of 95%, the cumulative timing dispersion of the fast channels must be kept less than about one-third of $2\tau$ (7 nsec for $\tau$ = 10 nsec). As concerns the electron channel, suitable circuitry can in principle keep the timing jitter within 5 nsec.[7] For the gamma channel, timing uncertainty arises in the first instance from the statistics of photoelectron emission, and in the second instance from dispersion in the transit time of the electron avalanche through the photomultiplier. While these effects have

TABLE V-6-I. ACCIDENTAL COINCIDENCES AND OTHER CORRECT RATES FOR GAMMA RECOIL SPECTROMETER[a]

| $E_0$, MeV | $r^b$ | | | $R_{\tau\gamma}{}^d$, cps | $R_e{}^e$, cps × $10^3$ |
|---|---|---|---|---|---|
| | $\tau^c$ = 10 | $\tau^c$ = 50 | $\tau^c$ = 100 | | |
| 0.1 | 0.001 | 0.006 | 0.010 | 28 | 2.38 |
| 0.2 | 0.004 | 0.021 | 0.043 | 20.8 | 1.96 |
| 0.5 | 0.010 | 0.050 | 0.108 | 12.2 | 1.48 |
| 1.0 | 0.017 | 0.085 | 0.174 | 7.0 | 1.16 |
| 2.0 | 0.030 | 0.148 | 0.296 | 4.4 | 0.88 |
| 5.0 | 0.074 | 0.370 | 0.740 | 1.9 | 0.64 |
| 10.0 | 0.092 | 0.460 | 0.920 | 0.84 | 0.48 |

[a] For 2 mC point source of energy $E_0$ at 40 cm from 1 cm² × 2.54 cm silicon recoil detector.
[b] (accidental/true) ratio.
[c] Coincidence gate length in nsec.
[d] Total coincidence count rate.
[e] Total recoil detector count rate.

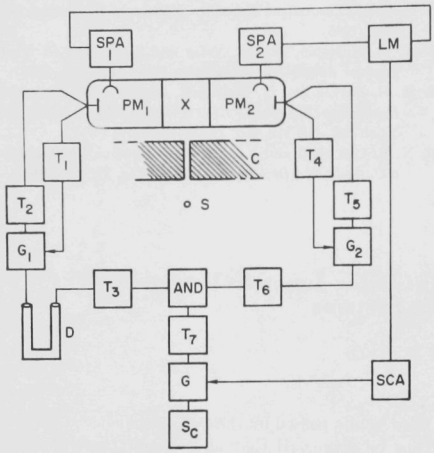


| | |
|---|---|
| S | Source of monoenergetic gamma radiation |
| $PM_{1,2}$ | Photomultipliers RCA-8575 |
| C | Collimator |
| X | NaI-Tl crystal with windows at either flat face, 2x2 in. |
| $SPA_{1,2}$ | Slow preamplifier (Gain 5) driver by Dynodes # 8 |
| $T_1 - T_7$ | Trigger (Discriminator) circuits |
| $G_1 - G_3$ | Gate circuits (enable mode) |
| SCA | Single channel analyzer |
| AND | Fast adder (coincidence) circuit |
| $S_c$ | Scaler |
| D | Delay trombone, 0-3 nsec ± 0.01 nsec |

$T_1$ $T_2$ $G_1$ and $T_4$ $T_5$ $G_2$ are each connected as antiwalk discriminators, driven by anode pulses. $T_1$ $T_4$ are set to the desired level and $T_2$, $T_5$ at a very low threshold. $T_3$, $T_6$ are pulse shaping stages providing 1 μsec paralysis and 15 nsec pulse length. $T_7$, $G_3$ are connected as a delay generator - scaler driver.

FIG. V-6-1. Coincidence System for Time Dispersion Measurements. *ANL Neg. No. 112-9436 T-1.*

been widely investigated in recent years, no data were available for the specific gamma energy range, photomultiplier and electronic circuitry considered. An investigation of the timing dispersion as a function of adjustable parameters and input energy was thus indicated.

These experiments, which will be reported more fully elsewhere, consisted of two stages. In the first step, the exact gain as a function of applied voltage as well as the dark current were measured for a number of photomultipliers of Type RCA-8575. The fast channel trigger threshold at which a given fraction of the dark current (consisting of single electron pulses) was suppressed was then determined for the two best tubes. For these measurements, the photomultipliers were cooled with dry ice in order to avoid overloading the multichannel analyzer. For the second phase of the measurements, the two selected photomultipliers were coupled optically to a double-window NaI crystal of about 2 x 2-in. size, and connected to the coincidence system shown in Fig. V-6-1. Different monoenergetic sources were collimated onto the center plane of the crystal so as to make the light delivered to either side as equal as possible. The slow channel outputs, after addition in a linear mixer capable of handling a wide range of pulse height,[8] were applied to a single-channel analyzer whose output gated on the fast coincidence output. By this means, the number, $R$, of photoelectrons released from each photocathode could be selected within a fairly narrow range. This number $R$, in conjunction with the scintillator decay period $T = 250$ nsec, plays an important part in determining the statitics of photoelectron emission mentioned above. The variance attached to the release time of the $q$th out of a total of $R$ electrons is given by the well-known formula of R. Post and L. Schiff:[9]

$$\sigma_q^2 = (qT^2/R^2)[1 + 2(q + 1)/R \cdots]. \qquad (1)$$

To show the relative magnitude of this effect, Eq. (1) is plotted in Fig. V-6-2 for an average requirement of 600-eV gamma energy per photoelectron, and gamma energy near the limit of the spectrometer (100 keV).

When anode current pulses are directly transmitted to the trigger circuits through 50-Ω cable, individual photoelectron pulses pile up near the front edge of the group, where the pulse width resulting from transit time dispersion in the multiplier is larger than the reciprocal pulse rate, but are resolved in the tail of the

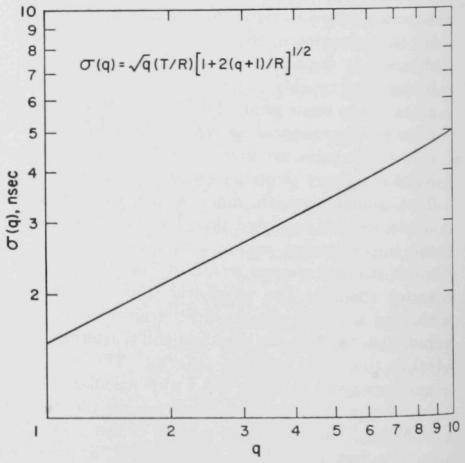


FIG. V-6-2. Time Dispersion for Photoelectron Release for $T = 250$ nsec and $R = 167$ (100 keV @ 600 eV/Photoelectron) *ANL Neg. No. 112-9411.*

group. One scintillation thus may yield a large number of pulses, which evidently must be prevented from appearing at the coincidence input in order to keep accidental coincidences from proliferating. Moreover, single electron dark current pulses, which may amount to $10^4$/sec or more, must also be blocked for the same reason. These considerations call for raising the trigger threshold to a height corresponding to pileup of the second or third photoelectron and imposition of a paralysis of several decay periods. This results in an increase of the timing dispersion which may be judged from Fig. V-6-2 as still quite acceptable for the worst case (low energy and relatively low conversion efficiency).

Delay versus count rate plots were obtained with the system shown in Fig. V-6-1 adjusted as outlined above, inserting a delay trombone in either channel alternatively and inserting additional cable delay such that the trailing edge of one channel overlapped, on the average, the leading edge of the other channel at the fast adder input. The trombone used provided about 10 ps precision; system jitter as checked with a relay pulser proved to be negligibly small. If the assumption of Gaussian shape for the overall time dispersion is reasonably valid, it may be shown that the count rate $C(t_d)$ at delay time $t_d$, is given by the expression

$$C(t_d) = \frac{C(0)}{2}\left[\Phi\left(\frac{\tau - t_d}{\sqrt{2}\,\Sigma}\right) + \Phi\left(\frac{\tau + t_d}{\sqrt{2}\,\Sigma}\right)\right], \quad (2)$$

where $C(0)$ is the zero delay count rate overlapping gates and $\Sigma = (\sigma_1^2 + \sigma_2^2)^{1/2}$. Thus, $\Sigma$ is the combined variance due to both channels, while $\sigma_i$ is the variance of each channel, $i = 1,2$. The function $\Phi$ is the error function.

Expanding Eq. (2) near the point $\tau = t_d$, one further obtains

$$C(t_d) = \frac{1}{2}C(0) \cdot \left\{1 - \left(\frac{2}{\pi}\right)^{1/2}\left(\frac{t_d - \tau}{\Sigma}\right)\left[1 - \frac{1}{3}\left(\frac{t_d - \tau}{\Sigma}\right)^2 \cdots\right]\right\}. \quad (3)$$

The quadratic term of this expansion vanishes while the third-order term is small as long as $(t_d - \tau) \ll \Sigma$. This circumstance may be exploited by least-square fitting a straight line through the measured points and computing the slope at the point $\tau = t_d$. An example of such a plot is shown in Fig. V-6-3. Referring to Eq. (3), the channel time variance $\sigma$ for the case of equal channels is given in terms of the measured slope $(dC/dt_d)_\tau$ and the count rate $C(0)$ at 100% coincidence efficiency, by the simple relation:

$$\sigma = C(0)/2\sqrt{\pi}\left(\frac{dC}{dt_d}\right)_\tau. \quad (4)$$

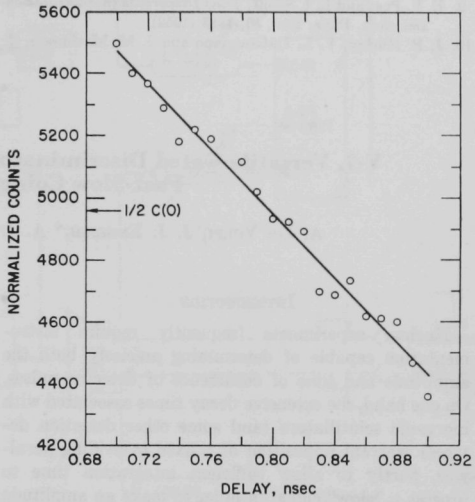


FIG. V-6-3. Least Square Fit of Delay Coincidence Data, $Co^{60}$ Source. *ANL Neg. No. 112-9438.*

Preliminary results with Co-60 and Cs-137 sources agree with a recent measurement[10] based on time-to-amplitude conversion rather than the slope fitting method outlined above, when allowance is made for the higher trigger levels used in the present tests.

## REFERENCES

1. R. Gold and K. G. Porges, *Solid-State Compton Spectrometer for Measurement of Reactor Gamma Spectra*, Reactor Physics Division Annual Report, July 1, 1965 to June 30, 1966, ANL-7210, pp. 306–308.
2. H. Hick, K. Rumpold and P. Weinzierl, *A High Resolution Compton-Spectrometer Using a Semi-Conductor Detector*, Nucl. Instr. Methods **24**, 327–328 (1963).
3. L. Buba, H. Hick and K. Rumpold, *Experimentelle Erfahrungen Mit Einem Halbleiter-Compton-Spektrometer Bei Abbrandmessungen An Brennstroffelementen*, (Osterreichische Studiengesellschaft fur Atomenergie, GES, M.B.H., Reaktorzentrum Seibersdorf, 1965), paper SGAE-PH-33/1965.
4. H. Goldstein, *Fundamental Aspects of Reactor Shielding*, (Addison-Wesley Publishing Co., Inc., Reading, Mass., 1959).
5. E. P. Blizard, Ed., *Reactor Handbook*, 2nd Ed., Vol. III, Part B, *Shielding*, (Interscience Publishers, New York, 1962).
6. G. W. Grodstein, *X-Ray Attenuation Coefficients from 10 keV to 100 MeV*. NBS Circular 583 (April 1957).
7. K. G. Porges, *Timing Circuit for Junction Detector*, (to be published).
8. K. G. Porges, J. Lockwood and C. Nelson, *High-Level Linear Adder Circuit for NaI Scintillation Pulses*, (submitted for publication in Rev. Sci. Instr.).

9. R. F. Post and L. I. Schiff, *Time Dispersion in Scintillation Detectors*, Phys. Rev. **80**, 1113 (1952).
10. J. P. Hurley, V. L. DaGragnano and J. M. Mathiesen, *A Search for a Fast Decay Component in NaI-Tl/An Evaluation of the RCA 8575 Photomultiplier Tube*, USNROL-TR-1099 (November 2, 1966).

# V-7. Versatile Gated Discriminator with Adjustable Paralysis Useful in Fast-Slow Coincidence Experiments

A. De Volpi, J. J. English,* A. J. Metz,* A. Porges and S. J. Rudnick*

## Introduction

Nuclear experiments frequently require instrumentation capable of determining precisely both the amplitude and time of occurrence of detector pulses. On one hand, the extensive decay times associated with inorganic scintillators (and some other detection devices) warrant imposition of a fixed overriding paralysis, partly to allow sufficient integration time to process a "slow" signal in order to make an amplitude decision (such as in a single-channel analyzer), partly to prevent retriggering of a discriminator during the pulse duration, and partly to permit accurate calculation of the deadtime correction factor. On the other hand, timing information must be preserved for fast coincidence analysis. Superimposed on these requirements is the fact that the analysis of accidental and instrumental coincidences is greatly simplified if the paralysis accompanying the slow energy-selected pulse is also applied to the fast timing pulse.

Features which are desirable in a versatile discriminator to be used in such applications include a fanout with independent pulse shaping provisions for fast and slow output signals, a separate high-level scaler driver output, a gating feature which allows the scaler output to be enjoined in the *absence* of a coincidence gating signal or the *presence* of a blocking signal, and a highly stable paralysis which applies to all outputs and is adjustable over a wide range.

## Characteristics

The Adjustable Paralysis Discriminator is a negative pulse discriminator with an adjustable and well-defined nonextendable paralysis. Ambiguity in output pulse width and paralysis is minimized by use of 100-MHz logic for the internal circuitry. Input impedance is 50 Ω. The discriminator threshold is continuously adjustable from 1 to 11 mA, with integral nonlinearity of ±0.5% for pulses with risetime greater than 10 nsec. The input is sensitive to negative pulses as narrow as 5 nsec. The circuits are packaged in double-width AEC-NIM standard modules. Each module contains two circulits.

The paralysis time, $\theta$, of the APD is continuously adjustable over the range 0.1 μsec to 10 μsec by means of an internal potentiometer. The range can be shifted even up to the millisecond region by insertion of an appropriate timing capacitor. The ratio, $w$, of the output pulse width to the paralysis time is also continuously adjustable from 0.3 to 0.7 by means of another internal potentiometer. Adjustment of $\theta$ and $w\theta$ is facilitated by observation of the waveform at the monitor output (Fig. V-7-1). Variation in the paralysis time and pulse width at a fixed temperature is less than ±1%, even for pulse pair separations approaching $\theta$, and variation over the temperature range of 0°C to 50°C is less than 10%. This stability for reasonable temperature fluctuations approaches the ideal conditions usually assumed in analysis of coincidence data for precision counting.

Each discriminator provides two pairs of "logic" outputs and a "scaler" output. The dual output pulse amplitude is −700 mV when both outputs of the pair are terminated in 50 Ω and −1.4 V when only one output is terminated. Since the outputs are current sources, delay-line clipping may be used with each pair independently clipped. Total circuit delay for input pulses well above threshold is 10 nsec, and the logic pulse risetime is less than 2 nsec. The scaler output pulse amplitude is −18 V into a high impedance or −4 V into 50 Ω, with risetimes less than 20 nsec and 10 nsec respectively; a silicon diode may be strapped across the scaler output to limit peak amplitude to −1 V, resulting in a risetime as fast as 3 nsec.

The gate input may be set for "blocking" or "coincidence" (by means of a toggle switch); if "blocking", a scaler pulse is issued concurrently with the logic output unless −700 mV is provided at the gate input; if "coincidence", the scaler pulse appears only as long as −700 mV is provided at the gate input.

* Electronics Division, Argonne National Laboratory.

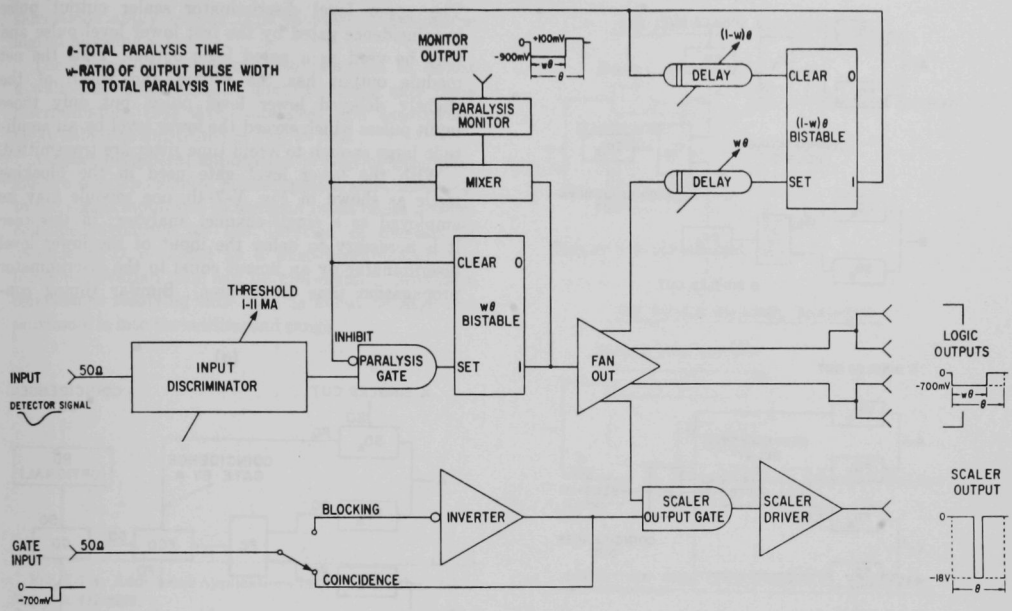


FIG. V-7-1. Internal Logic Diagram for APD. *ANL Neg. No. 143-2168.*

Both the fast logic output and the scaler output originate at the same time, but only the scaler output is affected by the gate requirement. If the limiter is utilized at the scaler output, then this output may be used as a gated "logic" pulse.

## APPLICATIONS OF THE APD

Aside from the straighforward applications of the APD in two-channel fast coincidence experiments, making use of its adjustable—but stable—paralysis, its scaler driving capability, and its pulse-shaping flexibility, there are certain useful features of the gating provision which justify a more elaborate discussion. For convenience this topic may be divided into two categories: (1) coincidence with two side channels; and (2) anti-walk coincidence and single-channel analysis.

In fast-slow or slow-fast coincidence counting there is a significant time difference and jitter between the slow output and the prompt fast pulse generated from either the leading edge or the crossover. Some past techniques have centered on introducing suitable delay to obtain time-adjusted signals when amplitude requirements are met by the input pulse. By observing that *the primary function of the coincidence logic is to block issuance of pulses to a scaler* (or multi-channel analyzer) *when preselected conditions are not met*, it is possible to circumvent the delay line requirement by making use of pulse generating and gating features incorporated in the APD circuit. Past techniques centering about passive delay lines or active delay generators suffer from various limitations, none of which are crucial; nevertheless, there is a certain convenience associated with the exclusion of long external delays which may result in risetime degradation in the purely passive case or extra cost in the other case.

One further use of the APD should be mentioned: by lowering the discriminator bias until the tunnel diode goes into regenerative oscillation, the unit can be used as a multiple output pulse generator with period equal to the paralysis $\theta$ and with pulse widths adjustable from 0.7 $\theta$ down to cable clipping capabilities; in other words widths from 4 nsec to several milliseconds and repetition rates from 10 MHz to 10 Hz.

### COINCIDENCE WITH TWO SIDE CHANNELS

Extension of the gating principle to a coincidence measurement in which side channels are required for both detectors is illustrated with the aid of Figs. V-7-2 and V-7-3. In the latter figure the fast coincidence

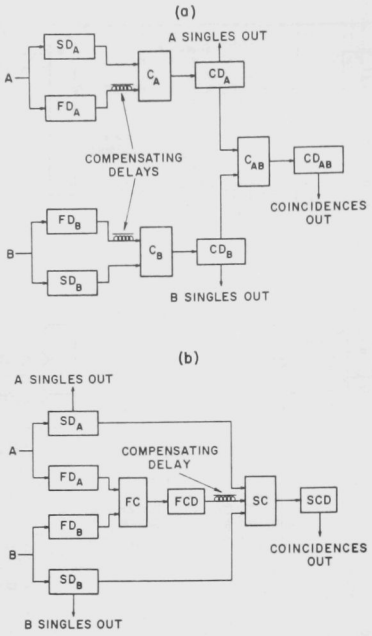


FIG. V-7-2. Simplified Block Diagrams of Conventional Four-Channel (a) Slow-Fast and (b) Fast-Slow Processing. *ANL Neg. No. 112-6564.*

output is reshaped by FCD. A gated output from FCD can only be obtained during the presence of a signal from the slow analyzer $SD_A$; subsequently the gating discriminator (GD) yields an output only when $SD_B$ carries out its gating function. Thus there is a coincidence output from GD only when there has been a fast timing coincidence and when the energy selection in both side channels is consistent with preset conditions.

### ANTI-WALK COINCIDENCE AND SINGLE-CHANNEL ANALYSIS

One module of two APD discriminators may be operated as an anti-walk pair without coincidence circuit, as shown in Fig. V-7-4a. For this application, one discriminator should usually be set about 20% above the level of the other discriminator, which may have 10 to 20-nsec walk near the tunnel diode threshold. The upper discriminator provides a relatively wide pulse equal to or greater than the total walk plus the width of the lower level pulse. The lower level signal must be delayed at least to the extent of the expected upper level jitter (probably no more than 20 nsec). The upper level discriminator scaler output pulse is coincidence gated by the fast lower level pulse and may be used as a gated logic output. Thus the net module output has the timing and width of the slightly delayed lower level pulse, but only those input pulses which exceed the lower level by an amplitude large enough to avoid time jitter are transmitted.

With the lower level gate used in the blocking mode as shown in Fig. V-7-4b, one module may be employed as a single-channel analyzer; in this case it is necessary to delay the input of the lower level discriminator by an amout equal to the discriminator propagation time (~10 nsec). Similar timing con-

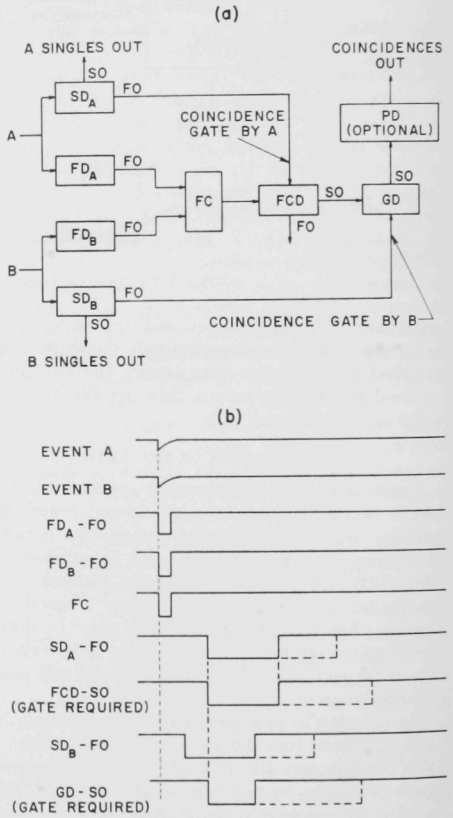


FIG. V-7-3. Application of APD Modules to the Gating Method of Fast-Slow Coincidence. *ANL Neg. No. 112-6566.*

siderations apply to any type of anti-coincidence or logical blocking action.

The above operations may be cascaded to obtain a walk-free single-channel analyzer using only three discriminators (1½ APD modules) and appropriate delay cables as illustrated in Fig. V-7-4c.

Another peripheral application is that of true coincidence overlap: square pulses applied simultaneously to the signal input and to the gate input cause a time-coincidence output for the duration of overlap. If another APD is added as a post-discriminator, the minimum overlap time can be well-defined. Minimum coincidence resolving time ($2\tau$) is about 50 nsec and maximum is into the millisecond range.

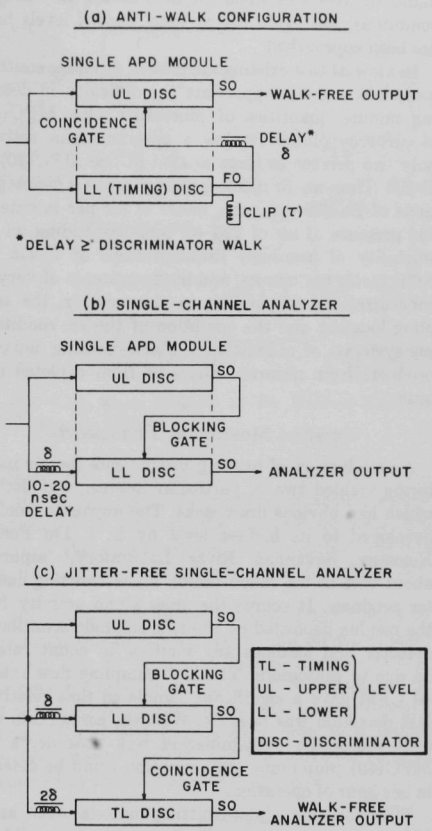


FIG. V-7-4. Additional Applications of APD Modules. *ANL Neg. No. 112-6562.*

## V-8. A Monitor For Airborne Plutonium Contamination

W. G. KNAPP

In preparation for operation of ZPR-6 and -9 with plutonium as one of the fuel components, the need for an air monitor which would specifically detect airborne plutonium in the presence of uranium and radon-thoron-daughter-products was recognized. While the plutonium fuel will be hermetically sealed in stainless steel cans, the highly enriched and depleted uranium in current use is coated only with a non-hydrogenous "paint," which provides a minimum protection against distribution of airborne dust. Air contamination from uranium has not been a problem to date, since there has been a maximum of about 0.5 of the maximum-permissible-concentration of U-235 based on a 40 hour exposure week (0.5 MPC 40). Where large quantities of depleted uranium are used or stored, emanation of radon has produced high levels of alpha air activity in the absence of fresh air circulation (such as in the reactor cells during

nights or weekends when the cells are in the "closed" condition), but again the personal hazard levels have not been approached.

In view of this existing air burden of alpha emitting materials, one can appreciate the difficulty in detecting minute quantities of plutonium. One MPC(40) of airborne plutonium has a specific alpha activity only two percent as large as that of one MPC(40) of U-235. Thus, an air monitor must detect 4.4 disintegrations of Pu-239 per cubic meter of air per minute, in the presence of up of 220 (or more depending on the solubility of uranium) disintegrations of U-235 per cubic meter per minute, and in the presence of varying concentrations (depending on the weather, the sampling location and the operation of the air conditioning systems) of radon-thoron alpha-emitting daughter products from natural sources or from depleted uranium.

## Existing Monitoring Instruments

An evaluation of existing instruments for air monitoring yielded two of particular interest, but both of which had obvious drawbacks. The impactor monitor, developed to its highest level by E. I. Du Pon de Nemours, Savannah River Laboratory,[1] separates about 95% of the radon-thoron alpha-emitting daughter products. It counts the gross alpha activity from the residue deposited on the zinc sulphide scintillation detector and assumes any increase in count rate to be due to plutonium. The high sampling flow rate of 40 CFM gave a significant sample so that relatively fast detection was possible. With the assumption that only plutonium contamination was possible, a one MPC(40) plutonium contamination could be detected in one hour of operation.

When another alpha-emitting material such as U-235 is also present, no discrimination is possible so

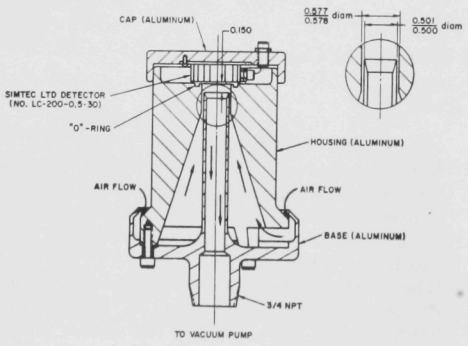


Fig. V-8-1. Airborne Plutonium Monitor. *ANL Neg. No. 112-9005.*

that a one hour sampling of air containing 0.02 MPC(40) U-235 would of necessity be interpreted as 1.0 MPC(40) of Pu-239. The uncertainty in the origin of the alpha activity would be unacceptable in the operation of ZPR-6 and -9 since concentrations of U-235 have been known to reach 0.5 MPC(40).

The second monitor, developed by the Lawrence Radiation Laboratory,[2] also has both desirable and undesirable features for application to ZPR-6 and -9 operations. In this monitor the air sample is collected on a filter which is counted with a solid-state detector. Pulse height analysis is used to discriminate Pu-239. The flow filtration rate (1 to 2 CFM) and the pulse height degradation of collected radon-thoron alpha-emitting daughter products (5.99, 6.05, 7.7, and 8.8 MeV) due to air space between detector and sample, and to dust buildup on the sample, limits detection of Pu-239 in normal situations to 8 MPC(40) hour.

## New Monitor Design

A monitor which used the best features of the two units described above was developed and tested. The impactor was fitted with a solid state detector so that heavier dust particles would collect directly on the surface of a solid state detector as shown in Fig. V-8-1. Initial studies to prove the concept used a gold-plated silicon detector. While the combination of high sampling rate, physical separation of radon-thoron alpha-emitting daughter products (about 95%), and pulse height discrimination was demonstrated, the useful life of the detector was understandably short. A lithium-drifted, $2\pi$, touchable solid state detector has subsequently been used. The monitor, shown in Fig. V-8-1, was designed for a 10 CFM sample rate in order to accomodate a 200 $mm^2$ detector size.

The detector output was initially fed to a voltage sensitive preamplifier, but difficulties were encountered because the detector leakage current increased as a result of radiation damage (a normal occurrence). Use of a charge-sensitive preamplifier overcame this problem. Preamplifier output has been fed both to a multichannel analyzer and to a linear amplifier-discriminator (lower level). The linear amplifier output was fed to a single channel analyzer.

The multichannel analyzer with an automatic printout option was useful in evaluating the performance of the monitor, and in calibrating the amplifier discriminator and single channel analyzer window settings using a plutonium source. The detector cap shown in Fig. V-8-1 lifts off to permit cleaning the detector, or it can be mated with the calibration source and the volume enclosed by the cap can be evacuated for calibrating the detector. The amplifier discriminator is normally set to pass pulses due to radon-thoron alpha-

emitting daughters, i.e., those greater than about 5.7 MeV. The single channel window is set to pass pulses due to the 5.15 MeV Pu-239 alpha events, or about 4.9 MeV to 5.4 MeV. Another single channel analyzer could be used with window settings for U-235 below 4.9 MeV.

The normal background in the Pu-239 "channel" has ranged from less than 0.2 c/m to 12 c/m depending on the radon-thoron levels (the latter occurred in the reactor cell containing large quantities of depleted uranium). With 1 MPC(40) plutonium concentration in sampled air, and a 10 CFM sampling rate, the count rate would increase in the plutonium channel at 0.5 c/m (assuming about 40% collection-detection efficiency) so that reliable indication of airborne plutonium would be given in ten to twenty minutes.

The low count so encountered is below the range of count-rate meters unless an unsatisfactorily long time constant is used. A simple counter would be suitable for most applications. Provision for resetting at given time intervals and alarming if a preset number of counts is exceeded during any designated time period should suffice for most applications.

A bidirectional scaler (Fig. V-8-2) may be used in applications involving high contributions from radon daughter products. The pulses from the randon source would be appropriately scaled down and would then drive the scaler negative. Plutonium channel pulses (including background) would then drive the scaler in the positive direction. In the absence of plutonium, the number of events in the positive direction would approximately equal those in the negative direction thus causing no alarm to be given. In the presence of plutonium, the alarm level at a selected positive count level could be approached and exceeded.

A few words need be said about the care and maintenance of the detector. The design of the monitor allows cleaning of the detector in less than one minute using tissue and a solvent such as chloroform. This should be done after about 4 to 8 hours of operation to prevent pulse height degradation due to build up of deposit. Locating the monitor outside the area to be monitored and using a pipe connection to the interior of that area may be desirable in some cases. For the detector used, it is the recommendation of the manufacturer that the detector be disconnected from the electrical power periodically. While this practice has not been followed to date, the loss of resolution magnitude was sufficiently small that monitor operation was not affected during seven weeks of constant use. It is, however, felt advisable either to operate the monitor only during periods of interest or to provide two detectors each of which could be operated 24 hours at a time. Alternately, a detector

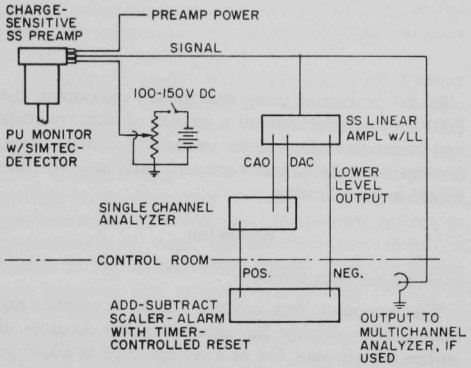


FIG. V-8-2. Block Diagram of Pu Monitor Electronics. *ANL Neg. No. 112-8982.*

without this limitation may be used. With regard to the limited operation proposal, it should suffice to automatically turn on the monitor an hour before start of the work day, and to discontinue operation, at least in many locations, when the work day is ended.

No deterioration of the detector other than loss of resolution due to continuous use and increased leakage current due to normal radiation damage has been encountered in seven weeks of use. No visible evidence of deterioration of the surface has been observed, although U-235 and Pu-239 have both been impacted on the detector surface, and the particles have been removed by cleaning as described above.

## CONCLUSION

A Pu-239 air monitor which incorporates the best features of the impactor monitor of SRL and the filter monitor of LRL has been designed and tested. It has been proven by actual application to be sensitive to Pu-239 and, with lower analyzer settings, to U-235. The use of a solid state detector as the surface of impaction has not caused noticeable deterioration of the detector. The monitor should be applicable to the monitoring of air for Pu-239 concentrations in the presence of large concentrations of U-235 and radon daughter products.

## REFERENCES

1. J. E. Hoy and J. J. Croley, *Annular Kinetic Impacter*, Am. Ind. Hyg. Assoc. Q. **18**, No. 4, 312 (December 1957).
2. C. L. Lindeken and K. F. Petrock, *Solid State Pulse Spectroscopy of Airborne Alpha Radioactivity Samples*, Health Phys. **12**, 683 (1966); also C. L. Lindeken and R. W. Lakin, *Improvements in the Solid State Plutonium Alpha Air Monitor*, UCRL-50228 (1967).

# V-9. Further Development of the DDP-24 Computer System

C. E. Cohn

In the process of using and further developing the DDP-24 computer system[1] a number of improvements and innovations have been introduced. These items, encompassing both hardware and software, are discussed in the following.

## Hardware

### Cathode-ray tube display[2]

The computer was equipped with a cathode-ray tube (CRT) display for monitoring the progress of on-line experiments. Use of a storage-type oscilloscope relieves the central processor from the task of display regeneration. A point in a pattern need be generated only once, and will then remain on the screen until the entire pattern is erased. (Non-storage operation may still be used where the display is constantly changing, as in the live display for a pulse-height analyzer.)

The oscilloscope uses two plug-in amplifiers, one for each of the two axes. It was modified to allow spot brightening under external control. The circuit that was added controls the blanking deflection plates in the CRT.

The interface circuitry for the unit translates the digital data from the computer into analog voltages for spot positioning and performs various timing and control functions. The display receives data from the computer through the 24-bit unbuffered output channel. Transfer of a single data word through this channel generates a single point on the CRT.

The $x$- and $y$-coordinates of a point are each represented by a ten-bit number. In the data word, bits 5–14 represent the $x$-coordinate and bits 15–24 represent the $y$-coordinate. Each coordinate is entered into a ten-stage flip-flop register. The analog deflection voltage is formed by a ladder attenuator connected to the flip-flop outputs. This attenuator feeds an emitter follower that transmits the voltage to the oscilloscope amplifier input.

Figure V-9-1 shows the control and timing circuits. If the output channel is ready, execution of an output instruction, with that channel enabled, will place a positive transition on the channel busy line after the output data have been loaded into the coordinate registers. That transition triggers univibrator DM1, which initiates a 20-$\mu$sec time interval, allowing time for the deflection voltages to settle to their correct values. At the close of the interval, univibrator DM2 is triggered, generating a 45-$\mu$sec pulse. This pulse activates the CRT unblanking circuit, writing a point on the screen. The termination of that pulse blanks the CRT beam and triggers univibrator DM3. The latter produces a 9-$\mu$sec pulse which is transmitted through a power amplifier to clear the coordinate registers. The pulse also is transmitted through a NAND gate to the output channel as a "device load pulse", which makes the channel ready for subsequent display operations. (The device-load-pulse line is normally at ground, and goes negative during a pulse from any of the univibrators connected to the three-input NAND gate. The channel is made ready when the line returns to ground at the termination of the pulse.)

When bit 2 is a zero, a pulse on its line triggers univibrator DM5. The resulting 0.3-sec pulse initiates erasure of the upper half of the screen and makes the output channel again ready only after the 0.25-sec erasure operation is complete. Bit 3 operates similarly to erase the lower half of the screen. If bits 2 and 3 are both pulsed, the entire screen will be erased. Either or both halves may be erased manually with push-buttons.

The display unit can intermittently monitor the status of a continuing experiment such as a fast-reactor noise analysis (see Paper V-12). Here, the experimenter decides when a display should be generated. The display remains as long as necessary for leisurely study while the collection of further data proceeds uninterrupted.

A "lockout" facility allows this type of operation. The display is generated in the normal way, except that the data for the last point includes a pulse on the line carrying bit 1. This triggers univibrator DM4 which clamps the device-load-pulse line to ground, inhibiting transmission of the pulse from DM3. Therefore, the output channel remains not ready. The program for the experiment tests the readiness of the output channel with a sense instruction at the time for generating a display. If the channel is not ready, the program bypasses the display operations and directly proceeds to collect more data. When the experimenter has finished looking at the display and wants to see a new one, he presses one of the erase buttons. When the program next tests the channel status, it finds that the channel has been left ready

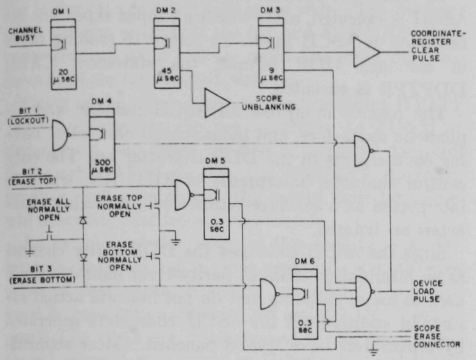


FIG. V-9-1. Control Circuits for CRT Display. *ANL Neg. No. 112-7741.*

by the erase operation, so it generates an updated display before continuing with data collection.

The display is also used for monitoring rod calibrations. Here, the operator must enter estimates of the final reactivity and rod position for scaling the display. The rod calibration curve is then traced out on the scope as the measurement proceeds, so that malfunctions can be detected immediately.

### PAPER-TAPE PUNCH CIRCUIT MODIFICATIONS[3]

Occasional unsatisfactory behavior of the computer's paper tape punch was found not to be the fault of the punch proper, but rather to result from the characteristics of the transistor drive circuits that operate the punch magnets. These transistors are protected against the inductive transients occurring on turnoff by diode or diode-resistor damping networks, allowing current to persist in the punch magnets for a time after the transistors are turned off. The magnets thus remain energized too long, and improper operation results. That difficulty was remedied by modifying the drive circuits.

A drive circuit, as modified, is shown in Fig. V-9-2. These circuits are rated for supply voltages up to 48 V, but only 24 V are actually used. This implies that the transistors could tolerate the transients that would occur with the diode-resistor damping networks returned to 48 V. This would significantly reduce the damping effect, since a network would be effective only when the amplitude of the transient exceeded 24 V across the coil.

The extra voltage is developed across a 24-V Zener diode connected in series with the network. (One 10-W diode is sufficient for all nine drive circuits.) In addition, the RC damping circuit recommended by the punch manufacturer is connected across each of the coils. This reduces the total amplitude of the transient without unduly prolonging it.

An analogous modification was made to the Nuclear Data ND-160 two-parameter pulse-height analysis system used for fast-neutron spectrometry. In this equipment, the drive transistors have no reserve in their voltage ratings. Here, it was simple to insert another driver stage using one of the new silicon NPN power transistors which have breakdown ratings in the hundreds of volts. The modified drive circuit is shown in Fig. V-9-3. The original driver transistor now furnishes base current to a 2N4063 ($BV_{CEO}$ = 350 V) which in turn switches the magnet. Because of the high breakdown rating, the RC network furnishes the only damping needed. The resistor $R_1$ must allow enough base current to saturate the transistor on its connected load. (Some nonstandard timing arrangements were also reworked to conform to the recommendations of the punch manufacturer.)

The modifications completely eliminated the punch-

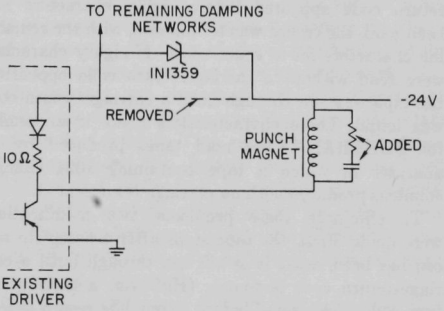


FIG. V-9-2. Modified Punch Driver from DDP-24 Computer. *ANL Neg. No. 112-8311 Rev. 1.*

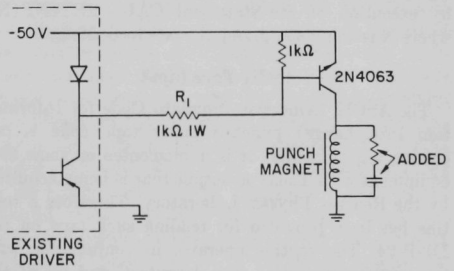


FIG. V-9-3. Modified Punch Driver from ND-160 Analyzer. *ANL Neg. No. 112-8310.*

ing errors that previously had plagued these machines.

## Software

### Use and Improvement of the FORTRAN-IV System

Early in the reporting period, the computer manufacturer issued a FORTRAN-IV software package. The new system has a number of advantages over the older FORTRAN-II system that had been in use, so it has superseded the older system. The following paragraphs describe a number of ways in which the new software package has been expanded and improved to make it more useful to us.

In particular, some improved input-output subroutines have been written for use with the system. Most of these have smaller memory space requirements than the original routines written by the computer manufacturer.

#### *Paper-Tape Input*

The original input routines were programmed for a fixed record-length of eighty characters. If a carriage-return code appeared before eighty characters had been read, the record was terminated, with the remaining characters set to space codes. If eighty characters were read without a carriage-return code appearing, the tape was run through until a carriage-return code was found. These characteristics made it impossible for FORTRAN-IV to read tapes produced by an analyzer in which a tape containing 1024 channel counts is produced with no carriage returns at all.

To eliminate these problems, two modifications were made. First, the tape stops after a complete record has been read; it is *not* run through until a carriage-return code is found. (However, a carriage-return code encountered before a complete record is read still terminates the record.) Secondly, provisions are made for changing the record length. It is still set to eighty characters upon loading, but may be changed by execution of the statement CALL SETINP(N) where N is an integer giving the new record length.

#### *ASCII Tape Input*

The ASCII (American Standard Code for Information Interchange) punched paper tape code is becoming quite popular. It is implemented on some new equipment with Teletype output that is being acquired by the Reactor Physics Laboratory. Therefore a routine has been provided for reading such tape on the DDP-24. The routine operates in conjunction with the tape-input routine just described, and all of the latter's features apply here unless otherwise noted.

To enter the ASCII mode, the statement CALL ASCII is executed, after which all input tapes are interpreted as ASCII tapes. To return to reading tapes in standard DDP format, the statement CALL DDPTPE is executed.

The routine interprets all ASCII numeric and alphabetic characters, and those special characters having counterparts in the DDP character set. The only control character interpreted is RETURN, which is interpreted as a carriage-return code. All other characters are ignored.

Since the ASCII code uses the DDP parity channel as an information channel, parity-error indications are used to assist decoding and do not indicate actual errors. In addition, all the ASCII characters generated by teleprinters have level 8 punched. (More sophisticated equipment uses level 8 as a parity level.) However, the DDP-24 is wired to inhibit parity checking in any frame having level 8 punched. This is done so that a parity error will not be indicated on a stop code, which has no data bits and no parity bit. Therefore, for proper ASCII decoding on this machine it is necessary to disable level 8. This is done by a switch that grounds the corresponding data line from the tape reader.

#### *"ENCODE/DECODE" Facility*

The FORTRAN-IV formatted READ and WRITE statements cause transfer of alpha-numeric data to or from the external input or output device selected by the unit number. However, for some applications it is convenient if such data can be transferred, instead, to or from an area in memory, so that further operations can be performed on it.[4] These latter functions are performed by the ENCODE and DECODE statements in Control Data FORTRAN and they were added to the FORTRAN-IV system by adding a suitable subroutine to the library, appropriating a unit number that was not otherwise used. The subroutine is written to transfer the data to or from an array.

The array is designated by the statement CALL BUFDEF(M,N) where M is the name of the array and N indicates the number of data words transferred at four characters per word. These assignments apply to all subsequent operations until altered by another CALL BUFDEF statement.

The unit number 8 was here selected for this use. The statement READ(8,n) list takes N words (4N characters) of alpha-numeric data from the array M, and converts them according to FORMAT statement n to fulfill the list. In the process, the input-output buffer area is loaded with N words of data from M. If N is less than the buffer length, the remainder of

the buffer area is filled with space codes. The contents of M are not altered. If the list and FORMAT statement are such as to call for multi-line input, the contents of M are transmitted repeatedly.

Going in the other direction, the statement WRITE (8,n) list converts the list according to FORMAT statement n, and stores the first N words of the result in the array M. If the list and FORMAT statement produce multi-line output, the output from later lines will overwrite that from earlier lines.

An example of the usage of this facility is as follows: Suppose an input deck contains eight different types of data cards, randomly intermixed. Each type must be read with a different list and FORMAT statement. The types are distinguished by an index digit, from 1 through 8, punched in Column 1. A card with 9 in Column 1 indicates the end of the deck.

The deck may be read by the following coding, which assumes four characters per word, and 3 as the card-reader unit number:

```
    DIMENSIØN MBUF(20),...
    ...
    CALL BUFDEF(MBUF,20)
    ...
10  READ(3,20)(MBUF(I),I=1,20)
20  FØRMAT(20A4)
30  READ(8,31)INDEX
31  FØRMAT(I1)
    GØ TØ(11,12,13,14,15,16,17,18,19),INDEX
11  READ(8,21)list 1
21  FØRMAT(1X,...)
    ...
    GØ TØ 10
12  READ(8,22)list 2
22  FØRMAT(1X,...)
    ...
    GØ TØ 10
    ...
    ...
19  ...
```

Here, statement 10 reads the information on a card into the array MBUF in alpha-numeric form. Statement 30 then decodes the first column to obtain the index digit. A computed GØ TØ branches to the appropriate READ statement (11 through 18) for the particular card. The information in MBUF is then decoded according to the appropriate format (with the first column now ignored in each case) and loaded into the appropriate list. After the information is processed, return is made to statement 10 to read another card. When a card is read having an index digit of 9, control passes to the remainder of the program, starting with statement 19.

VARIABLE METRIC MINIMIZATION

The Variable Metric Minimization (VMM) algorithm of W. Davidon[5] is a powerful method for minimizing an arbitrary differentiable function with respect to a number of parameters. It is the method of choice for performing least-squares fits to a function that is nonlinear in its parameters, such as a sum of exponentials. The algorithm had been programmed for the Applied Mathematics Division (AMD) central computers. A new version has been written in FORTRAN-IV with some improved features that facilitate its application to on-line data processing tasks on a smaller machine.

To begin with, VMM was made a subroutine instead of being a main program as in the AMD versions. This facilitates its incorporation into on-line programs, and also allows it to be placed in a library file. Furthermore, it allows various arrays used by VMM to be variable-dimensioned. This aids efficient allocation of storage for problems using various numbers of parameters. In particular, it removes the necessity of reserving the large blocks of storage needed for many parameters when only a few are being used.

This version was written as two subprograms in place of the many subprograms into which the AMD versions are divided. This saves many instructions otherwise needed for linkage and branching, and facilitates the application of variable dimensioning. In the AMD versions, all but one of the subprograms are called from only one place in the VMM main program. Therefore, there was no advantage in retaining the subdivided structure.

Inclusion of the name of FCN (the subroutine that evaluates the particular function being minimized and its derivatives) in the argument list, to be declared EXTERNAL by the calling program, makes possible the placement of VMM in a library file. If FCN were not handled in this way, its name would appear in the transfer vector of VMM. Therefore, the loader could not load FCN until after VMM had been loaded. This would prohibit the placement of VMM in a library file, since library programs are normally loaded after all of the user's programs have been loaded. However, with FCN declared EXTERNAL in the calling program, its name will appear in the transfer vector for that program. Then, FCN can be loaded after the calling program, but before VMM, so that the transfer vector of VMM will contain references only to other library programs.

[This problem has been handled (see Paper VI-19)

in another minimization subroutine by providing for a return to the calling program to perform the functions of FCN. However, that approach would be awkward for VMM, since FCN is called from a number of different places in the program, with different parameter assignments.]

The "RICOCHET" feature originally provided by Davidon[6] has been eliminated from this version. It has been stated[7] that the feature does not modify the error matrix correctly. In addition, it occupies a considerable amount of memory space without contributing greatly to the speed of convergence.

The AMD versions of VMM require a parameter to be input which specifies the size of the random steps. However, a step size that is appropriate for displacements from the correct minimum might not be adequate to remove the solution from an undesired local minimum where the function value would be much higher.[8] Therefore, the new version calculates this parameter and provides that a random step would double the value of the function if the error matrix were correct.

PAPER-TAPE DATA HANDLING FOR COSMIC-RAY EXPERIMENTS

The computer has been used for the data reduction of cosmic-ray experiments recently done here (see Papers VII-4 and VII-5). Large quantities of data were to be handled but the data rate was very low. This allowed the use of an existing paper-tape punch for data recording at minimum expense. The techniques used are useful in similar situations where the cost of magnetic storage is prohibitive.

The experiments involved the recording of data from a large number of separate events arriving at a rate of 1–30 per minute. The data from each event consisted of two six-bit binary numbers. Each computer run required the processing of around 350,000 events, recorded on about 6000 ft of tape, accumulated on a 2-ft diameter reel during one week of unattended operation of the experimental setup. Obviously, to avoid wasting large amounts of computer time, it was necessary to make elaborate provisions for detection of and recovery from tape reading errors.

The DDP-24 eight-level paper-tape code uses levels 1–4 and 6–7 as data channels, with the low-order bit in level 1. Level 5 carries the (odd) parity bit. A punch in level 8 is a "stop code", which stops the tape reader and sets a toggle that the program can test and reset.

The two six-bit numbers from each event were punched in the data levels in two successive frames. The first of these frames was overpunched with a stop code. This was done to prevent the reading from getting out of phase. The photoelectric reader on the computer strobes the data channels with the signal from the sprocket channel. Therefore, if a piece of chad is lodged in a sprocket hole, that frame will be skipped. The rest of the tape would then be read in such a way that the second number from one event and the first number from the next event would appear to the computer as a pair of numbers from one event. Clearly, the processing would be completely erroneous, unknown to the operator. As described later, the overpunched stop codes allow this type of error to be caught and corrected immediately.

To reduce the cost of the recording equipment, it was decided to omit parity generation. (Since the analysis of the events is statistical, it was felt that an occasional wrong event could be tolerated.) If the parity level were never punched, and if the second number for an event were zero, a frame would be produced having no punches except for the sprocket hole. The computer is wired to treat such frames as leader frames and skip over them. Thus, such an event would not be read properly, and the reading would get out of phase as described before. Therefore, the parity level was always punched. The program, of course, was set up to ignore parity errors.

The computer was also wired to treat frames with all levels punched as leader frames. However, such a frame is now a valid data frame, occurring if the first number for an event is $77_8$. Therefore, the circuits treating such frames as leader frames were disconnected.

The program loop which read the tape began by reading one frame. That frame was then checked for a stop code. If none was found, the reading of an event had started with the second number. The program halted so that the operator could correct the error and/or reposition the tape properly. On restart, this step was repeated.

If a stop code was found, the number was stored and the next frame was read and checked for the absence of a stop code. If one was found, the first number of an event had been read as the second number. The event then was rejected and the computer halted. Here the operator had the option of either correcting the tape and restarting with the previous step, or terminating the run and printing the results. This latter option allowed the end of the tape to be marked by manually punching extra stop codes.

If no stop code was found, the event was accepted and processed, and the program returned to the first step. The run could also be terminated after a preset number of events had been processed, to allow rejection of data accumulated at a time when the operation of the experimental setup was suspect.

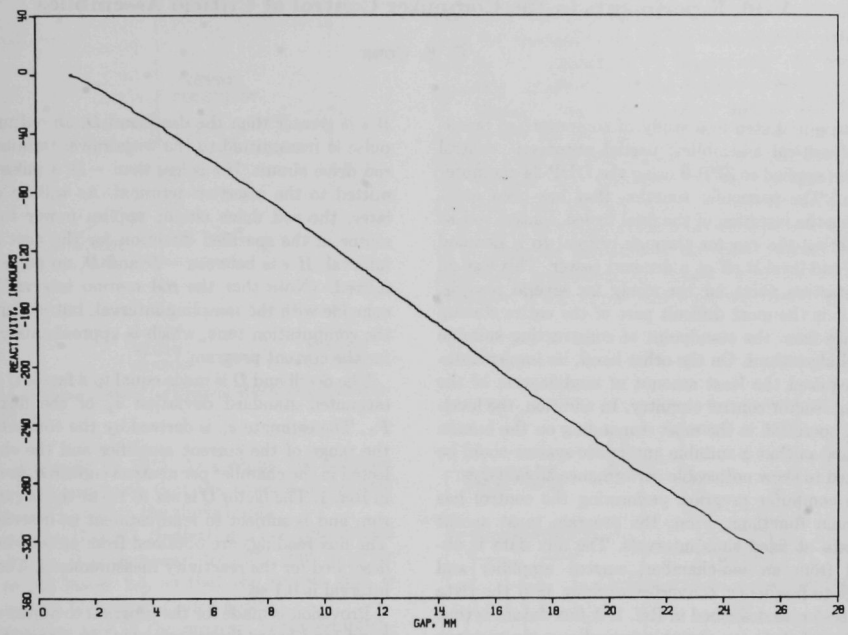


FIG. V-9-4. Gap-Worth Measurement on ZPR-6 Assembly 5. *ANL Neg. No. 112-8275.*

## APPLICATIONS

### GAP-WORTH MEASUREMENTS

The reactivity-measurement technique has been adapted for gap-worth measurements on the ZPR-6 and ZPR-9 fast criticals. The neutron flux signal is obtained and treated by the usual methods, while the gap signal is taken from the corner-separation indicator. Here, the voltage from the linear potentiometer that is fed to the digital voltmeter is also fed to an additional voltage-to-freqency converter. Pulses from the latter go to the unbuffered-channel scaler, while the flux pulses are counted in the buffered-channel scaler. A measurement is started with the reactor critical and the tables together. The tables are then separated at the 1.3 cm/min speed while the computer records the increasing separation and declining flux. The measurable range of gaps is limited to a maximum of 25 mm by the characteristics of the corner-separation indicator. Figure V-9-4 shows the result, as plotted by the computer, of a typical measurement (on ZPR-6 Assembly 5) with the scalers read at 0.5-sec intervals.

### OTHER APPLICATIONS

Other on-line applications are discussed elsewhere in Papers V-10 and V-12.

## REFERENCES

1. C. E. Cohn, *Use of a Small Digital Computer in Data Analysis and Control of Critical Facilities*, Reactor Physics Division Annual Report, July 1, 1965 to June 30, 1966, ANL-7210, pp. 330-337.
2. C. E. Cohn, *Simple Storage-Oscilloscope Displays for Small Laboratory Computers*, Rev. Sci. Instr. **38**, 984 (1967).
3. C. E. Cohn, *Solid-State Drive-Circuit Considerations for Paper-Tape Punches*, Rev. Sci. Instr. (to be published).
4. I. C. Pyle, *Character Manipulation in FORTRAN*, Commun. ACM **5**, 432 (1962).
5. W. C. Davidon, *Variable Metric Method for Minimization*, ANL-5900 (Rev.) (1959).
6. Ibid., p. 11.
7. R. Fletcher and M. J. D. Powell, *A Rapidly Convergent Descent Method for Minimization*, Computer J. **7**, 163 (1964).
8. W. W. Graham, III, D. S. Harmer and C. E. Cohn, *Accurate Delayed Neutron Parameter Measurements in a Heavy-Water Reactor*, submitted to Nucl. Sci. Eng.

# V-10. Experiments in the Computer Control of Critical Assemblies

C. E. Cohn

As an initial step in a study of computerized operation of critical assemblies, partial automatic control has been applied to ZPR-9 using the DDP-24 computer system.[1] The particular function that has been automated is the insertion of the final fueled control rod so as to bring the reactor through critical to a demand period and level it off at a demand power. This was an ideal starting point for the study for several reasons. First, it is the most difficult part of the entire startup sequence from the standpoint of constructing suitable control algorithms. On the other hand, its implementation required the least amount of modification of the existing reactor control circuitry. In addition, the leveling-off operation is the most demanding on the human operator, so that a suitable automatic system could be expected to show noticeable performance advantages.

The computer program performing the control has two main functions. First, the program must accept flux data at fixed time intervals. The flux data is obtained from an ion-chamber, current amplifier and voltage-to-frequency converter working into the data input scaler, as described in Ref. 1. A flux datum is thus the integral of the ion-chamber output over the previous sampling interval (see Paper V-13). It must decide, on the basis of that information, whether the controlled rod is to be moved during the next interval and if so, in what direction. (No provision is made for varying rod speed.) Secondly, the program must establish a demand trajectory for the flux that is attainable with the control means at hand and that results in acceptable operation.

If was found that the first of the above functions could be performed in an acceptable manner by a simple logarithmic derivative control algorithm. The program calculates the logarithmic slope between the most recent flux reading, $P_0$, and the previous reading, $P_1$ (see Fig. V-10-1). It then extrapolates this slope to the time of the reading to be taken next, and determines whether the extrapolation overshoots or undershoots the flux $P_f$ which the demand trajectory specifies for the time of the next reading. If the overshoot or undershoot is beyond a deadband, the rod is withdrawn or inserted, respectively, during the next interval. If the extrapolation is within the deadband, no rod motion is caused.

In practice, the program calculates the amount $\epsilon$ by which the extrapolation overshoots $P_f$ using the formula

$$\epsilon = \frac{P_0^2}{P_1} - P_f.$$

If $\epsilon$ is greater than the deadband $D$, an output control pulse is transmitted to the withdrawal terminal on the rod drive circuit. If $\epsilon$ is less than $-D$, a pulse is transmitted to the insertion terminal. As will be described later, the rod drive circuit applies power to the rod motor in the specified direction for the next sampling interval. If $\epsilon$ is between $-D$ and $D$, no pulse is transmitted. (Note that the rod motion interval does not coincide with the sampling interval, but is displaced by the computation time, which is approximately 30 msec for the current program.)

The deadband $D$ is made equal to a factor $Q$ times the estimated standard deviation $\sigma_p$ of the flux reading $P_0$. The estimate $\sigma_p$ is derived by the computer, given the range of the current amplifier and the charge collected in the chamber per neutron captured, as discussed in Ref. 1. The factor $Q$ is set to 1.5 at the beginning of a run, and is subject to readjustment as described later. The flux readings are obtained from an ion chamber as described for the reactivity measurements. The readout interval is 0.1 sec.

Provision is made for the program to adjust the deadband (and hence the system gain) to obtain the desired amount of rod jitter as equilibrium is approached. To do this, the operating time is broken into 50-interval segments (5 sec for the 0.1-sec interval that was actually used). The quantity $R_i$ is made equal to $+1$, 0, or $-1$ according as the rod was inserted, not moved, or withdrawn during the $i$th interval of a segment. At the end of the segment, the quantities

$$\bar{R} = \frac{1}{50} \sum_{i=1}^{50} R_i$$

and

$$\sigma_R = \sqrt{\frac{1}{50} \sum_{i=1}^{50} R_i^2 - \bar{R}^2}$$

are calculated. $\bar{R}$ is a measure of the net rod motion during the interval, while $\sigma_R$ is a measure of the jitter in the rod motion. If the magnitude of $\bar{R}$ is less than 0.1 (indicating a net rod motion of five steps or less out of fifty, and hence a system close to equilibrium) the value of $\sigma_R$ is examined. If $\sigma_R$ is greater than 0.2 (indicating that the rod was moving randomly more than one-fifth of the time) the factor $Q$ is increased by 10%, giving a corresponding increase in the deadband. On the other hand, if $\sigma_R$ is less than 0.05 (indicating that the rod was moving randomly less than one-twentieth of the time)

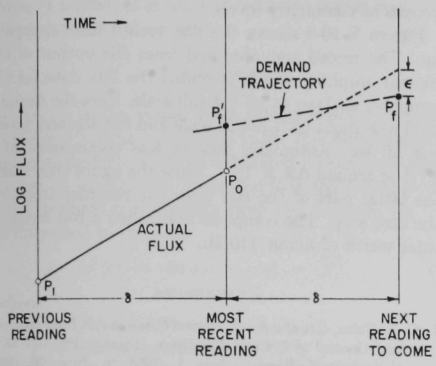


FIG. V-10-1. Nomenclature for Control Algorithm. *ANL Neg. No. 112-6597.*

then $Q$ is decreased by 10%. As a result, the program seeks a system gain such that the amount of random rod motion will be within the above limits.

If $\bar{R}$ is not less than 0.1 (indicating a non-equilibrium situation) then $Q$ is decreased by 10%, but is never allowed to fall below 1.5, so that the system gain is maintained at a high level in such a case.

The remaining task of the program is the establishment of the demand trajectory and the derivation of $P_f$ values. The simplest demand trajectory is just an exponential rise on the demand period followed by a levelling-off at the demand power. However, such a trajectory would have problems at the time of levelling off. Severe limitations on rod speed make it impossible to remove reactivity fast enough to level off from a reasonable period without overshoot. Therefore, it is desirable to lengthen the demand period as the demand power is approached in order to limit the rates of reactivity removal needed. To do this, the demand period $\tau$ at any time during the rise is obtained from

$$\frac{1}{\tau} = \left(\frac{1}{\tau_0}\right) \min\left[1, 0.1 + 2\,\frac{P_u - P_0}{P_u}\right],$$

where $\tau_0$ is the basic demand period and $P_u$ is the demand power. This formula holds $\tau$ equal to $\tau_0$ up to half demand power, and then smoothly lengthens $\tau$ to ten times $\tau_0$ at demand power.

The statistical errors in the flux readings are comparable to the rise per sampling interval of the demand period. Therefore, it was found that care must be taken in the specification of $P_f$ in order that a steady rod insertion be obtained. A workable prescription was found to be

$$P_f = \min[P_0 + (3 + Q)\,\sigma_p,\ P_f'\exp(\delta/\tau),\ P_u],$$

where $\delta$ is the sampling interval and $P_f'$ is the demand from the previous cycle. Multiplication of the exponential by $P_f'$ instead of $P_0$ insures that $P_f$ will rise smoothly, unaffected by the statistical fluctuations in $P_0$. However, the first argument insures that $P_f$ will not diverge too far from $P_0$ in the initial stages of the startup when the flux is rising much more slowly than the demand, and thus prevents an excessively rapid rise later when the flux would attempt to catch up.

It might be thought that a better approach would be to improve the statistics of the flux readings through numerical smoothing or longer sampling intervals. However, it was found that these expedients introduce

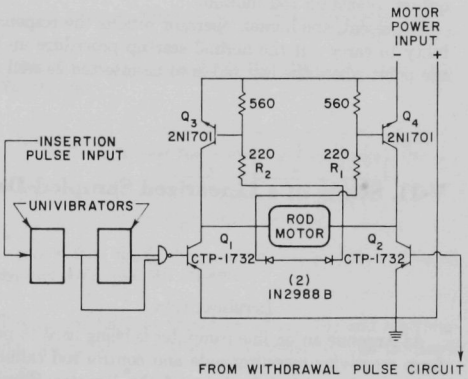


FIG. V-10-2. Control-Rod Motor Drive Circuit. *ANL Neg. No. 112-6513.*

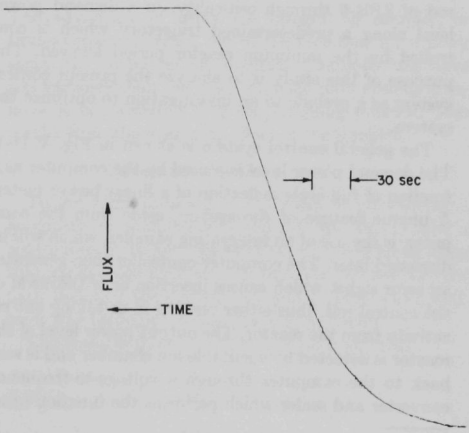


FIG. V-10-3. Flux Trace from a Typical Run Under Automatic Control. *ANL Neg. No. 112-6362.*

phase lags that decrease the smoothness and stability margin of the system without yielding any particular advantages over the method employed.

A solid-state drive circuit shown in Fig. V-10-2 allows the computer to control the power to the existing rod motors. Since these motors have permanent-magnet fields, they are reversed by changing armature polarity. Therefore, the driver uses a complementary-symmetry bridge to allow power to be applied to the armature in either direction. When triggered by an output control pulse from the computer, the circuit turns on the motor power in the desired direction for a period just smaller than the sampling interval. This gives a degree of fail-safety, in that positive action by the computer is required to sustain rod motion.

At present, the human operator retains the responsibility to carry out the normal startup procedure up to the point where the last rod is to be inserted as well as to switch ranges on the linear trips and withdraw the sources at customary levels.

Figure V-10-3 shows the flux record from a typical run. The record was obtained from the output of the current amplifier which provided the flux data for the computer and ran at $10^{-6}$ $A$ full scale. Here the demand level was about 90% of full scale and the demand period was 40 sec. Automatic control was commenced at a level of around $0.3 \times 10^{-8}$, while the figure shows only the latter part of the run after the recorder trace left the zero stop. The computer controlled a rod having a total worth of about 110 Ih.

### References

1. C. E. Cohn, *Use of a Small Digital Computer in Data Analysis and Control of Critical Facilities*, Reactor Physics Division Annual Report, July 1, 1965 to June 30, 1966, ANL-7210, pp. 330–337.

## V-11. Study of a Linearized Sampled-Data Control Algorithm for Zero-Power Reactors

T. J. Marciniak*

### Introduction

At Argonne an on-line computer is being used to perform reactivity measurements and control rod calibrations on the critical facilities of the Reactor Physics Laboratory (see Paper V-10). The computer also has the capability of controlling the insertion of the last control rod of ZPR-9 through criticality, to a demand power level along a predetermined trajectory which is controlled by the minimum reactor period allowed. The purpose of this study is to analyze the present control system as a prelude to an investigation to optimize the system.

The general control system is shown in Fig. V-11-1. The demand power level is sensed by the computer as a fraction of full-scale deflection of a linear power meter. A unique feature of the system, aside from the computer, is the use of an integrating sampler, which will be discussed later. The computer-controller then generates an error signal which causes insertion or withdrawal of the control rod, thus either putting in or taking out reactivity from the reactor. The output power level of the reactor is detected by a suitable ion chamber and is sent back to the computer through a voltage-to-frequency converter and scaler which performs the function of an integrater. The number of counts on the scaler is sampled every $T$ seconds. The scaler is immediately reset for the next integrating interval.

The computer-controller section is shown in more detail in Fig. V-11-2. Here the demand power is specified and the flux, or power level, is sampled. The pulse to the scaler is the output of an ion-chamber voltage-to-frequency converter system which emits $10^5$ pulses/sec for full-scale deflection of the linear power meter. The error calculation is performed by the computer and, depending upon the deadband of the nonlinear element, a signal is sent to the control rod. The system gain was approximated by dividing the actual ZPR-9 reactivity by one-half the deadband of the nonlinearity. The deadband is proportional to the expected variance of the flux readings—approximately $10^{-4}$.

### Linearization of the System

The block diagram of the system as it was analyzed is shown in Fig. V-11-3. Here $\bar{G}(s)$ represents the transfer function of the computer algorithm, control rod, and reactor system while $F(s)$ represents the transfer function of the integrating sampler. A brief description of each of the transfer functions used is given in the following: these represent a linearization of the system.

The transfer function of the computer is given in the

* Student, University of Notre Dame, Notre Dame, Indiana.

form of a hold. It is derived from the actual computer error algorithm given as

$$\epsilon = \frac{P_0^2}{P_1} - P_f, \tag{1}$$

where $P_0$ is the power level at the present sampling interval, $P_1$ is the power level at the preceding sampling interval, and $P_f$ is the extrapolated power level based on period constraints. Assuming that the actual power level deviated only slightly from the demand, Eq. (1) is linearized to the form

$$\epsilon'(t) = 2\epsilon(t) - \epsilon(t - T), \tag{2}$$

where

$\epsilon(t) = P(t) - P_f$

$T \equiv$ sampling interval.

The Laplace transform of Eq. (2) yields the transfer function of the hold:

$$H(s) = \frac{E'(s)}{E(s)} = \frac{2 - 3e^{-Ts} + e^{-2Ts}}{2}. \tag{3}$$

The form of this hold is similar to that of a fractional order hold[1] with one term missing.

The transfer function of the control rod is given as

$$\frac{K(s)}{E'(s)} = \frac{R}{s}, \tag{4}$$

where $R$ is the reactivity input rate per second per unit error. The time constant due to inertia is neglected. It should be noted that this representation of the linearized control rod implies that if one has a linear control rod worth curve, there is no velocity limitation on the drive system or on the maximum amount of reactivity allowed.

The reactor kinetics analysis was based on the one delayed group linear model with the transfer function

$$\frac{\delta N(s)}{n_0 \delta K(s)} = \frac{s + \lambda}{l(s + \lambda + \beta/l)}, \tag{5}$$

where

$n_0 \equiv$ steady-state reactor neutron density

$\lambda \equiv$ average one delayed group decay constant

$\beta \equiv$ fraction of delayed neutrons

$l \equiv$ prompt neutron lifetime

$\delta N(s) \equiv$ Laplace transform of deviation of neutron density

$\delta K(s) \equiv$ Laplace transform of reactivity.

Since feedback occurs through an integrating sampler (see Paper V-13), the transfer function is derived directly. The integrating sampler integrates the neutron density over a time $\tau$ and this can be represented as

$$\bar{n}(t) = (1/\tau)\int_{t-\tau}^{t} n(t)\, dt. \tag{6}$$

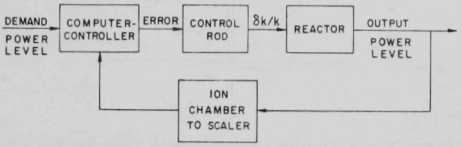


FIG. V-11-1. General Control System. *ANL Neg. No. 112-8263.*

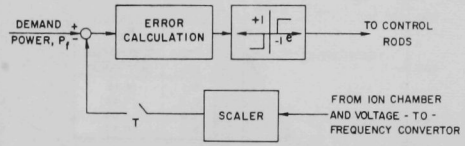


FIG. V-11-2. Computer-Controller Diagram. *ANL Neg. No. 112-8268.*

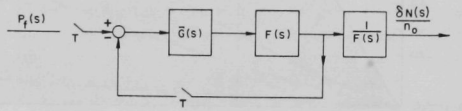


FIG. V-11-3. Block Diagram of Sampled-Data Control System. *ANL Neg. No. 112-8262.*

Taking the Laplace transform of Eq. (6) and rearranging, we obtain the transfer function of the feedback path:

$$F(s) = \frac{1 - e^{-\tau s}}{\tau s}. \tag{7}$$

The advantage of using the integrating sampler, or time-averaging circuit, lies in the fact that for a noisy signal the output of an integrating sampler will have less variance than the usual sampled-data system if the noise is uncorrelated over the sampling interval. This results from the averaging effect of the sampler.

## Continuous System Analysis

To get some estimate of the effect of introducing a computer, or sampled-data control, into the system, a continuous representation of the system was made using running average feedback. In this case the feedforward path included the control rod and reactor while feedback was through the time-averaging circuit.

The transfer function of the system is given as

$$\frac{\delta N(s)}{n_0 P_f(s)} = \frac{K'\tau s(s + \lambda)}{\tau s^3(s + \lambda + \beta/l) + K'(s + \lambda)(1 - e^{-\tau s})}, \tag{8}$$

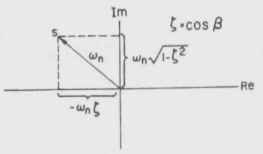


FIG. V-11-4. Continuous System with Time Average Feedback Transfer Function. *ANL Neg. No. 112-8619.*

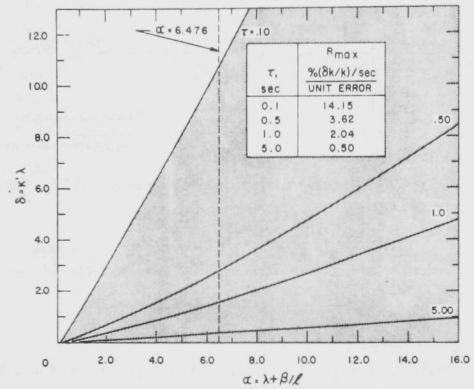


FIG. V-11-5. Stability Regions for Continuous System with Time Lag. *ANL Neg. No. 112-8266.*

where the gain, $K'$, is defined as being the reactivity per unit time per unit error divided by the prompt-neutron lifetime. It may be noted that the characteristic equation is of a transcendental form, making it difficult to determine the stability limits of the system. A method has been developed by L. Eisenberg[2] which allows one to determine the stability of such a system. It involves mapping the left-hand side of the complex $s$-plane into a parameter plane $\alpha$-$\delta$. Using the notation shown in Fig. V-11-4 where the terms are defined, one can write the characteristic equation as

$$\tau s^3\left(s+\lambda+\frac{\beta}{l}\right)+K'(s+\lambda)(1-e^{-\tau s}) = \sum_{k=0}^{n} a_k s^k = 0, \tag{9}$$

where

$$a_k(S) = \alpha b_k + \alpha c_k e^{\tau s} + \delta d_k + \delta e_k e^{\tau s} + f_k + g_k e^{\tau s} \tag{10}$$

and

$$s_k = \omega_n^k\,[T_k(-\zeta) + j(1-\zeta^2)^{1/2} U_k(-\zeta)]. \tag{11}$$

In Eq. (11), $T_k(-\zeta)$ is the Chebyshev function of the first kind and $U_k(-\zeta)$ is the Chebyshev function of the second kind. In terms of the reactor parameters the quantities $\alpha$ and $\delta$ are defined as

$$\begin{aligned} \alpha &= \lambda + \beta/l \\ \delta &= K'\lambda. \end{aligned} \tag{12}$$

Stability limits are determined by plotting the $\alpha$-$\delta$ curves as shown in Fig. V-11-5 where $\zeta = 0$, since using this value insures that all zeros of the characteristic equation will lie in the left half of the $s$-plane. From these curves it is found that the maximum stable reactivities per second per unit error are as given in Fig. V-11-5 where the averaging times vary from 0.1 to 5.0 sec. This is for a thermal system in which $l = 10^{-3}$ sec corresponds to $\alpha = 6.476$. The stable region is the shaded area under the curve. For systems with the same fuel, thus having essentially the same $\lambda$ and $\beta$ but differing prompt-neutron lifetimes, the gain can easily be found by moving along the abscissa since this involves the parameter $\alpha$. The gain may then be calculated directly from the graph. As expected, increasing the averaging time, hence the delay, causes the system to become more unstable or to have a lower maximum stable gain.

## Sampled-Data Systems

The sampled-data system was analyzed using $z$-transforms, since a linear system was being studied. The transfer function of the system using the linearized hold developed earlier is

$$\frac{\delta N(z)}{n_0 P_f(z)} = \frac{3\lambda' TK' z(2z-1)(az^2+bz+c)}{6\lambda'^4 Tlz^2(z-1)^2(z-\gamma)+K'(2z-1)(a'z^3+b'z^2+c'z+d')}, \tag{13}$$

where

$$\begin{aligned} \lambda' &= \lambda + \beta/l \\ \gamma &= e^{-\lambda' T} \end{aligned}$$

and the coefficients of the polynomials are complicated functions of the reactor parameters and the sampling interval, $T$.

Figure V-11-6 shows the root locus plot of the characteristic equation for a thermal system where the prompt-neutron lifetime is $10^{-3}$ sec. The maximum stable gain corresponds to the gain where the roots of the characteristic equation cross the unit circle in the complex $z$-plane. This is analogous to $s$-plane stability

criteria where stability is ensured if there are no roots of the characteristic equation in the right half of the $s$-plane. Since the left half of the $s$-plane is mapped into the interior of a unit circle in the $z$-plane this represents the boundary of the stability region. Analytical methods

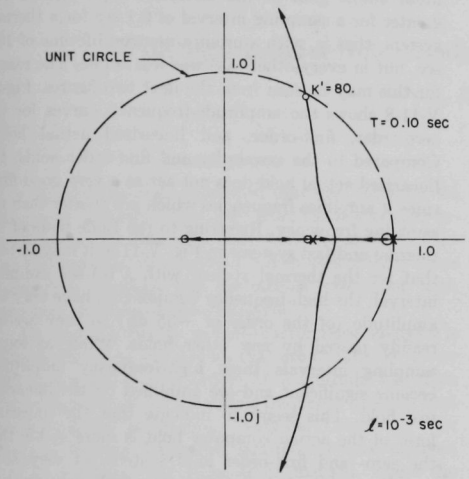


FIG. V-11-6. Root Locus Sampled System Linearized Actual Hold. *ANL Neg. No. 112-8264 Rev. 1.*

TABLE V-11-I. MAXIMUM STABLE $\%(\delta k/k)$/sec/unit error, $R_{max}$

| $T$, sec | Linearized | | Zero Order | | First Order | |
|---|---|---|---|---|---|---|
| | Thermal | Fast | Thermal | Fast | Thermal | Fast |
| 0.1 | 8.4 | 7.61 | 7.4 | 13.35 | 8.3 | 8.65 |
| 0.5 | 1.2 | 1.52 | 1.83 | 2.12 | 1.45 | 1.71 |
| 1.0 | 0.62 | 0.744 | 0.99 | 0.91 | 0.73 | 0.839 |
| 5.0 | 0.123 | 0.131 | 0.173 | 0.197 | 0.14 | 0.145 |

$l_{therm} = 10^{-3}$ sec.
$l_{fast} = 1.445 \times 10^{-6}$ sec (ZPR-9, calculated).

such as the Routh-Hurwitz criteria may be used by applying the bilinear transformation to the characteristic equation. Figure V-11-7 shows the root locus plot for the system with a prompt-neutron lifetime of $1.445 \times 10^{-6}$ sec which corresponds to that of the ZPR-9. Although it shows a greater gain, the maximum reactivity input rate per unit error is less than that for the thermal system using the same fuel (in this case, U-235) as is experienced in the actual case.

Stability limits were also determined for systems which used either the zero-order or first-order holds. These are shown in Table V-11-I where all the stability limits are given as the maximum reactivity input rate per unit error.

It is of interest to determine how stable the actual

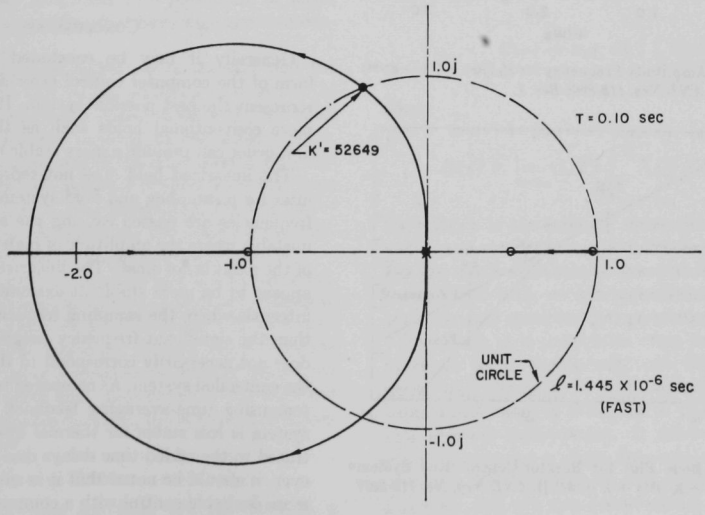


FIG. V-11-7. Sampled System with Linearized Actual Hold. *ANL Neg. No. 112-8269 Rev. 1.*

system is in this linearized form. The maximum system gain, $K'$, of the fast system with the 0.1-sec sampling interval was found to be 52650. The best estimate of the overall gain of the actual ZPR-9 control system was found to be 145,300, thus differing by a factor of almost 3. This indicates that the actual system should be unstable, or at least tend in that direction. In operation the actual system does work but there is some degree of control rod "hunting." This demonstrates that the actual system need not be unstable but it does indicate that the system could be improved. Maximum stable gains for the zero-order hold were greater by almost a factor of two than those of the linearized hold while the first-order hold represented a slight improvement for the case of the fast reactor with a neutron lifetime of the order of $10^{-6}$ sec. These results were verified by digital computer simulation of the system.

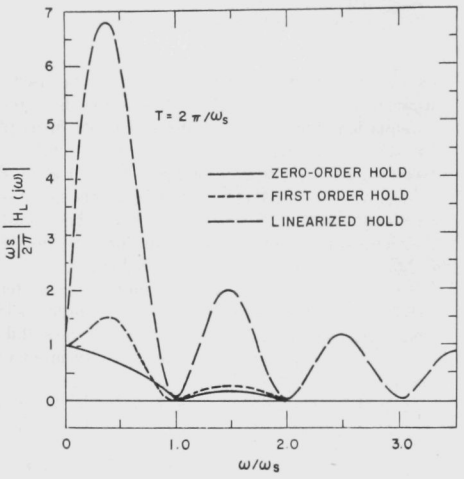


FIG. V-11-8. Amplitude-Frequency for $H_L(jw) = [(1 - e^{-jwt})/jw](2 - e^{-jwT})$. *ANL Neg. 112-8265 Rev. 1.*

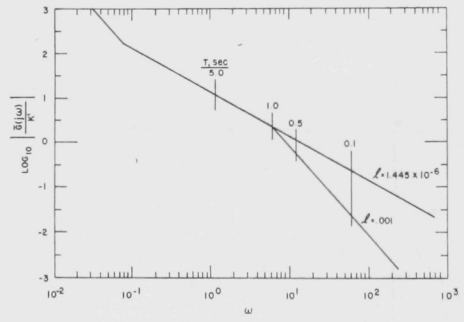


FIG. V-11-9. Bode Plot for Reactor-Control Rod System $\bar{G}(jw)/K' = [s + \lambda/[s^2(s + \lambda + \beta/l)]]$. *ANL Neg. No. 112-8267 Rev. 1.*

One curious fact which occurred was that the maximum stable gain of the linearized hold system was greater for a sampling interval of 0.1 sec for a thermal system, that is, with a prompt-neutron lifetime of $10^{-3}$ sec, but in every other case was less stable. The reason for this may be seen from the next two figures. Figure V-11-8 shows the amplitude-frequency curves for the zero-order, first-order, and linearized actual holds. Compared to the zero-order and first-order holds, the linearized actual hold does not act as a very good filter since it amplifies frequencies which are greater than the sampling frequency. Referring to the Bode plots of the thermal and fast systems in Fig. V-11-9, it may be seen that for the thermal system with a 0.1-sec sampling interval, the high-frequency components have very low amplitude (of the order of $-35$ db) so they are not readily passed by any other holds. While at longer sampling intervals these high-frequency amplitudes become significant and are amplified by the linearized real hold. This seems to indicate that the linearized form of the actual computer hold is more stable than the zero- and first-order hold systems at very short sampling intervals but at longer sampling intervals it becomes less stable because it functions less like an ideal filter.

## Conclusions

Generally it may be concluded that the present form of the computer control error algorithm does not represent the best possible system. It does appear that more conventional holds such as the zero-order and first-order can provide a more stable control system.

The linearized hold does not represent an adequate filter for a sampling and hold system. As a result, high frequencies are passed causing the system to be more unstable where the amplitude of high frequency sections of the plant is not small. The linearized actual hold does appear to be more stable at extremely small sampling intervals where the sampling frequency is much higher than the significant frequency range of the plant. This does not necessarily correspond to the "bandwidth" of the controlled system. As compared to a continuous system using time-averaging feedback the sampled-data system is less stable for thermal systems. This can be traced to the added time delays due to sampling. However, it should be noted that it is easier to synthesize a more desirable control with a computer than is possible

without it. At present the study is being extended to the problem of optimizing the system.


REFERENCES

1. B. C. Kuo, *Analysis and Synthesis of Sampled-Data Control Systems*, (Prentice-Hall, Inc., Englewood Cliffs, N. J., 1963), pp. 49–51.
2. L. Eisenberg, *Stability of Linear Systems with Transport Lag*, IEEE Trans. Auto. Control, *AC-11*, No. 2, 247–254 (April 1966).


## V-12. Fast-Reactor Noise Analysis by Polarity Cross Correlation

C. E. COHN

### INTRODUCTION

A method has been developed that uses the DDP-24 computer[1] to analyze the noise from the fast critical assemblies and to determine therefrom the prompt-chain decay constants. This method, which uses polarity cross correlation, escapes the limitations associated with previous methods of noise analysis.

The major difficulty in fast-reactor noise analysis is the low detection efficiencies that are attainable. These efficiencies are several orders of magnitude less than would be required for the simple frequency analysis that was developed at Argonne National Laboratory[2] for thermal reactors. Therefore, fast-reactor noise analysis has to date used the Rossi-alpha method, where the efficiency requirements are relaxed at very low power levels. However, power levels that are low enough are not possible close to critical with plutonium or large, dilute uranium assemblies that have high spontaneous-fission rates.

The present method makes use of the fact that the background noise due to the statistics of detection in one detector is completely uncorrelated with such noise from another detector exposed to the same reactor. Therefore, the component of the cross-correlation function between the two detector outputs resulting from detection noise has a zero expectation for any lag.[3,4] However, the two detectors see the same reactor fluctuations, so that these yield non-zero expectations.

Although the cross-correlation function of the detection noise components has a zero expectation, estimates of this function based on a finite sample will have non-zero values, which introduce random errors into the estimates of the cross-correlation function of the reactor fluctuations. In order that these errors be not excessive for a run of reasonable duration, the detection efficiency cannot be too low.

### THEORY

When random time functions are processed in a digital system, consideration must be given to the degree of quantization used, i.e. the number of bits used to represent the value of the function at the instant of a given sampling. For functions with Gaussian distributions, it has been shown[5,6] that one needs to record only one bit, i.e. whether the signal is above or below its mean at the instant of sampling.

Suppose $x(t)$ and $y(t)$ are two random functions of time, each having a Gaussian amplitude distribution and a zero mean. We wish to estimate the cross-correlation function

$$C(\tau) = \lim_{T\to\infty} (1/T) \int_0^T x(t)\, y(t+\tau)\, dt.$$

We can define the auxiliary functions $X(t)$ and $Y(t)$ as $X(t) = +1$ when $x(t) \geq 0$, and $X(t) = -1$ when $x(t) < 0$ [similarly for $Y(t)$]. It is easily shown that

$$C(\tau) = \sigma_x \sigma_y \sin\left[\frac{\pi}{2} R(\tau)\right],$$

where

$$R(\tau) = \lim_{T\to\infty} (1/T) \int_0^T X(t)\, Y(t+\tau)\, dt.$$

Here $R(\tau)$ is the polarity cross-correlation function, and $\sigma_x$ and $\sigma_y$ are the rms amplitudes of $x(t)$ and $y(t)$. For the small correlations observed in these measurements ($R < 0.1$), we can approximate the sine by its argument and consider $C(\tau)$ proportional to $R(\tau)$.

Therefore, it is possible to cross correlate two-time functions while taking only one bit of information about each function at each sampling. It has been shown[5] that there is little loss in precision caused by this extreme quantization. It allows the maximum sampling rate for a given data-rate capability of the computer. The DDP-24 can read one 24-bit word every 6 $\mu$sec, so that two time functions can each be sampled every 0.5 $\mu$sec.

## Hardware

### Detectors and Associated Circuits

Figure V-12-1 is a block diagram of the circuits associated with each of the two detectors. The detector proper is a cylindrical piece of Pilot-B plastic scintillator, 1½ in. in diameter and 12 in. long. (Detectors with smaller sensitive masses, e.g. ionization chambers of 2-in. diameter and 8-in. length, filled with 100 psia methane, had far too little detection efficiency to give usable results in a reasonable running time.) The scintillator is viewed with a photomultiplier operated at 500 V.

The photomultiplier signal is dc-coupled to an emitter follower that drives a 50-Ω cable into the reactor control room. There the noise is separated from the dc component by capacitor coupling and is amplified to about 2.5 V peak-to-peak by a vacuum-tube amplifier comprising two pentode stages and a cathode follower.

The amplified noise is quantized to a polarity signal by a Schmitt trigger. This trigger is adjusted to switch states at zero volts input and to have a minimum hysteresis (<0.04 V). The trigger output is transmitted to the computer room by a cable driver and a 50-Ω cable.

At the computer, the polarity signal controls the setting of a flip-flop. If the signal into the Schmitt trigger is negative, the set input gate of the flip-flop is enabled. A clock pulse then sets the flip-flop. Another clock pulse, one-half clock period later, resets the flip-flop. The transition occurring on reset is the data pulse.

If the signal into the Schmitt trigger is positive, the set input gate is inhibited and the flip-flop remains reset. Therefore, the reset pulse causes no change of state and no data pulse is generated.

To adjust the Schmitt trigger, its output is observed on an oscilloscope through ac coupling. The bias level is adjusted so that the trigger spends an equal amount of time in each state, as indicated by its output waveform having equal amplitude each side of zero. Even with a correct adjustment, some imbalance was indicated by the computer in actual runs. This is attributed in part to thermal drift in the Schmitt trigger. The characteristics of the flip-flop might also introduce some bias, since the capacitor-coupled set input gate must be at zero volts to charge the capacitor for at least 0.12 μsec before the clock pulse transition.

### Word-Forming Buffer

The polarity data bits being generated every 0.5 μsec are collected into words by a word-forming buffer before being read into the computer. This buffer consists of two banks of flip-flops. Each bank comprises two registers, one for each detector, and each register contains twelve flip-flops. One flip-flop from each register is under the control of each stage of a 12-stage ring counter which is driven by a 2 MHz clock.

Figure V-12-2 shows the circuitry for the flip-flops associated with one ring-counter stage. When the latter is in the set state, and the bank 1 enable signal is true (2 being false) the set inputs to the bank 1 flip-flops are enabled. The outputs of the bank 2 flip-flops are connected to the data lines of the computer's unbuffered parallel input channel. Thus, information is being loaded into bank 1 while the information that had been previously loaded into bank 2 is being read into the computer. A particular ring-counter stage is set during one 0.5-μsec interval between two clock pulses, so that the bank-1 flip-flops associated with that stage can respond

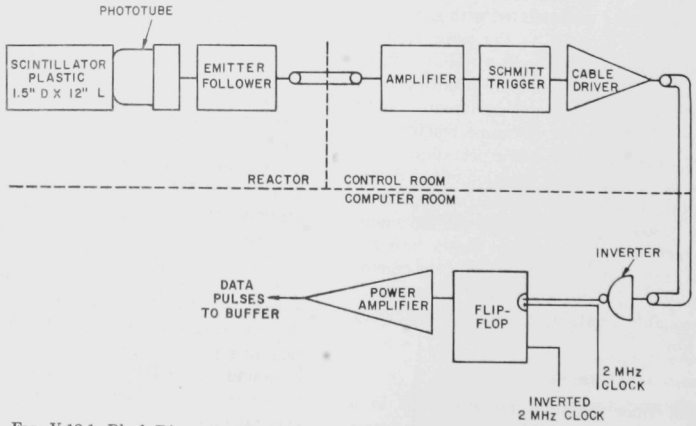


Fig. V-12-1. Block Diagram of Detector and Associated Circuits. *ANL Neg. No. 112-8507.*

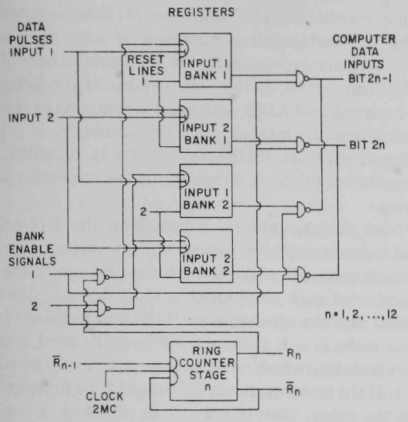


FIG. V-12-2. Block Diagram of One Stage of Word-Forming Buffer. *ANL Neg. No. 112-8483.*

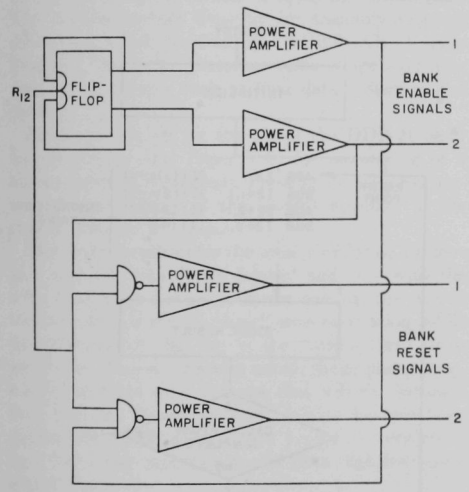


FIG. V-12-3. Auxiliary Circuits for Word-Forming Buffer. *ANL Neg. No. 112-8508.*

to data pulses only during that interval. (The data pulse actually occurs in the middle of the interval.) After the ring counter has cycled through all stages, the bank enable signals change state. The inputs of bank 1 are disabled and the outputs are connected to the computer input lines in lieu of bank 2. The bank-2 flip-flops have at this time been read and reset, and their inputs are now enabled. Thus, on this cycle bank 2 receives data while bank 1 is being read. After the ring counter again cycles through all stages, the bank enable signals change state again and the banks revert to their previous roles. In this way, the collection of the information and its transmission to the computer proceed continuously.

Figure V-12-3 shows the circuits that generate the bank enable and reset signals. The former are controlled by a flip-flop that changes state every time the ring counter recycles from stage 12 to stage 1. The reset signal is produced while stage 12 is on, the read-in being complete at this time. The signal is switched to the correct bank by the gates shown. Circuits not shown transmit an "input ready" signal to the computer while stage 1 is on.

Figure V-12-4 shows the clock circuits. The master clock is a 4-MHz crystal oscillator, whose output is divided by two to form the clock pulses that drive the ring counter. Another division by two produces a 1-MHz clock signal which replaces the computer's own clock. Since the computer is accepting input at maximum speed, it is necessary to drive both the computer and the buffer from the same clock to insure that the two will remain in step. Note that the buffer runs continuously, even when the computer is not reading the data.

### Programming

As soon as a selected number of data words (here, 70) has been collected by the computer, the words are unpacked to one bit per memory location. (For reasons that will become clear later, the bits are stored as $+1$ or $-1$ instead of 1 or 0.) The cross-correlation function is taken, and averaged with estimates gotten from previous cycles. Then the data-taking is resumed, and the process continues until manually terminated.

The calculation of the cross-correlation function is the most time-consuming part of the entire cycle. Therefore, any improvements in the speed of that calculation are of major importance in enhancing the efficiency of the process. Such improvements over conventional methods were made by means of a particularization and extension of the ideas of S. Simpson.[7]

Conventionally, correlation functions are calculated through use of a loop, as shown in the flow chart of Fig.

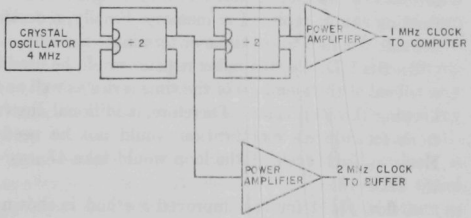


FIG. V-12-4. Clock Circuits for Word-Forming Buffer. *ANL Neg. No. 112-8509.*

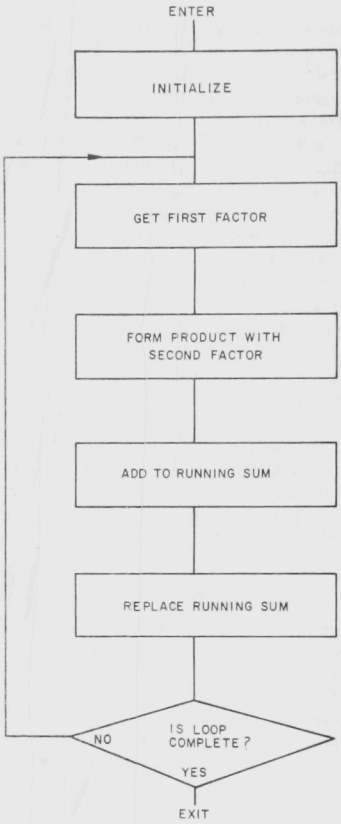


Fig. V-12-5. Flow Chart for Conventional Correlation Loop. *ANL Neg. No. 112-8505.*

V-12-5. Here, after initialization, the first instruction in the loop fetches a member of one of the time series being correlated. The next instruction forms the "product" of this with a suitably chosen member of the other time series. The product is added to a running sum and the running sum is replaced in memory. Finally, a decision is made whether to continue or terminate the loop.

On the DDP-24, the index register would be used for retrieval of the members of the time series as well as for keeping the loop count. Therefore, additional instructions for address modification would not be needed. Even so, each cycle of the loop would take 47 $\mu$sec on the DDP-24.

A flow chart for the improved method is shown in Fig. V-12-6. Here, space is allotted in memory for a string of instructions equal in length to the time series being correlated. The addresses of these instructions refer to corresponding members of one time series. The commands are compiled by examination of the other time series. If the first member of the latter is a $+1$, an indexed ADD command is compiled as the first instruction. If, instead, the first member is a $-1$, an indexed subtract (SUB) instruction is compiled. The compilation proceeds similarly for the remainder of the string.

After the compilation is complete, the accumulator and index register are cleared and the string of instructions is executed, starting with the first one. If the first member of each time series is $+1$, then a $+1$ will be added into the accumulator. If the first member of each time series is $-1$, then $-1$ will be subtracted from the accumulator, which is of course equivalent to adding $+1$. If the first member is $+1$ for one time series and $-1$ for the other, then either $-1$ is added or $+1$ is subtracted, both of which are of course equivalent. Thus the correct product of the polarity functions is obtained in any case.

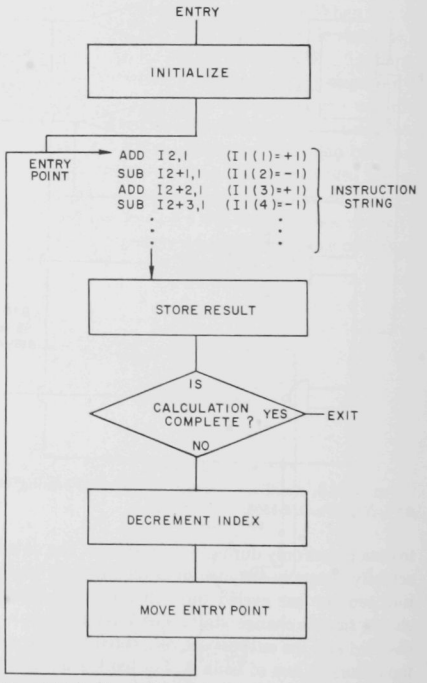


Fig. V-12-6. Flow Chart for Fast Polarity Correlation Algorithm. *ANL Neg. No. 112-8506.*

The remainder of the instructions in the string are executed similarly. The final result gives the cross correlation between the two time series at zero lag. Now, the index register is decremented by one (in two's-complement arithmetic), the entry point to the instruction string is moved down one step, and the accumulator is cleared. Execution of the string now begins with the second instruction. This instruction now acts as described on the first member of the second time series, and similarly for the remaining instructions. Now, the result is the cross correlation at a lag of one sampling interval.

In a similar fashion, the cross correlation is calculated for all lags of interest. To save time, the calculation is not done for all possible lags, i.e. in steps of one sampling interval. Rather, it is done only for a subset of these, such that the interval between lags is increased by one sampling interval each time. Thus, the lags used are 0, 1, 3, 6, 10, 15, etc. sampling intervals up to a maximum of 190, with a time-series length of 840 sampling intervals. This scheme is easy to implement and is appropriate for a cross-correlation function that is expected to be represented by a sum of decaying exponentials. The calculations are done by an assembly-language subroutine, which is called by a FORTRAN-IV main program. The latter performs tasks where execution time is not critical, such as final data reduction and plotting.

Provision is made for the use of the DDP-24 oscilloscope display (see Paper V-9) for monitoring of a measurement as it proceeds. Pressing the ERASE button initiates display of the current estimate of the cross-correlation function.

The program calculates the cross correlation twice—once with one time series delayed and once with the other time series delayed. For any one lag, the sum of the two results is the "in-phase" cross correlation, while the difference of the two is the "quadrature" cross correlation. Unless otherwise noted, the in-phase cross-correlation function is the one that will be discussed from here on. The quadrature function has not been significantly different from zero except at very short lags. The latter probably results from high-frequency spatial effects.

The system works with the cross-correlation function exclusively and dispenses with the calculation of the cross-power spectrum. There are two reasons for this omission. First, it eliminates concern regarding "aliasing", i.e. the presence of noise components higher in frequency than the Nyquist frequency (1 MHz for this system) since aliasing manifests itself only in the power spectrum and not in the correlation function. Secondly, it allows calculation of the cross-correlation function only at selected lag values instead of every lag value. With the cross-correlation function having a definite physical meaning, as previously mentioned, there is no need for the cross-power spectrum.

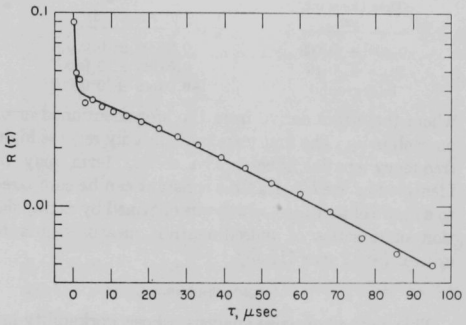


FIG. V-12-7. Results of Run on ZPR-6 Assembly 5. *ANL Neg. No. 112-8496.*

The program keeps the sum of the $+1$'s and $-1$'s from each time series. If these are not zero, a zero-order constant correction to the cross-correlation function is made by subtracting the product of the sum over the total number of points for each time series. First-order corrections[8] are either constant or proportional to the correlation, and so do not perturb the results. Since the correlations are small, higher-order corrections are negligible.

It is assumed that the error on the cross-correlation is due solely to the uncorrelated detection-noise component. Therefore, the error is calculated according to binomial statistics as $\sqrt{0.25/N}$ where $N$ is the total number of samples from each detector, i.e. 840 times the number of replications of the process.

## RESULTS

A typical result is that obtained on ZPR-6 Assembly 5. One detector was placed at the center of the movable half, while the other was placed two drawers away in the same half. Loading adjustments were made to compensate for the reactivity contribution of the detectors, which was approximately 100 Ih each.

A two-hour run at about 5 W yielded results which were fitted by variable metric minimization to two exponentials plus a background. (The latter was included to account for trigger unbalance (here giving about 65% $+1$'s and 35% $-1$'s) as well as for any components with very long time constants resulting from delayed neutrons. The error on each point, estimated as previously described, is 0.0002, which is smaller than the points shown. The data and the fitted curve are shown in Fig. V-12-7. Results of the fit are as follows:

| Time Constant, μsec | Amplitude |
|---|---|
| 0.309 ± 0.003 | 0.04996 ± 0.00014 |
| 50.38 ± 0.19 | 0.04135 ± 0.00007 |
| background | −0.00146 ± 0.00002 |

where the errors derive from the aforementioned error on each point. The first term undoubtedly reflects high-frequency spatial effects. The second term may be identified as the $l/\beta$. Its time constant can be compared to a figure of 52.1 μsec, which was obtained by extrapolation of a series of pulsed-neutron measurements to critical (see Paper III-16).

## Conclusions

This method of noise analysis, whose workability has not been established, allows measurement of $l/\beta$ with no intrinsic limitation on power level. Thus it is well suited for use with the plutonium assemblies which are to be implemented on ZPR-6 and ZPR-9 in the near future.

The major limitation of the method as now constituted is the low efficiency of data collection. That is, it takes the computer over one hundred times as long to process a string of data as it does to collect the string. Thus, the computer is accepting less than 1% of the data coming from the reactor during a run.

This inefficiency could be eliminated by construction of a wired-program cross correlator, which would accept data continuously, while simultaneously calculating the cross-correlation function. Such a device, however, would be costly and quite inflexible.

## References


1. C. E. Cohn, *Use of a Small Digital Computer in Data Analysis and Control of Critical Facilities*, Reactor Physics Division Annual Report, July 1, 1965 to June 30, 1966, ANL-7210, pp. 330–337.
2. C. E. Cohn, *Determination of Reactor Kinetic Parameters by Pile Noise Analysis*, Nucl. Sci. Eng. **5**, 331 (1959).
3. T. Nomura, *Improvement in S/N Ratio of Reactor Noise Spectral Density*, J. Nucl. Sci. Technol. (Tokyo) **2**, 76 (1965).
4. M. Edelmann, et al., *Pulsed Source and Noise Measurements on the STARK Reactor at Karlsruhe, Pulsed Neutron Research* (IAEA, Vienna, 1965), Vol. II, p. 799.
5. J. B. Dragt, *Analysis of Reactor Noise Measured in a Zero-Power Reactor and Calculations on Its Accuracy*, Proc. Symposium on Neutron Noise, Waves and Pulse Propagation, University of Florida, Gainesville, Florida, USAEC Report CONF-660206, pp. 591–617.
6. B. P. Th. Veltman and H. Kwakernaak, *Theorie und Technik der Polaritätskorrelation für die Dynamische Analyse Niederfrequenter Signale und Systeme*, Regelungstechnik **9**, No. 9, 357 (1961).
7. S. M. Simpson, *Time-Series Computations in FORTRAN and FAP*, (Addison-Wesley, Reading, Mass., 1966), Vol. I. *A Program Library*, Program PROCOR.
8. W. Heins, A. van den Bos, and B. P. Th. Veltman, *On the Polarity Correlation of Non-Zero Mean Gaussian Variables*, Cooperation Centre for Measurement and Control, Dept. Applied Physics, Technological University, Delft, Netherlands, Report No. 65-2 (July 1965).


# V-13. The Integrating Sampler

C. E. Cohn

## Introduction

Conventional sampling theory assumes that the output of the sampler yields the magnitude of the sampled signal at the instant of sampling. Analog-to-digital converters of the "sample-and-hold" type operate on this principle.

An alternative type of sampling is readily implemented and has advantages in certain applications. Here, the output of the sampler equals the integral of the signal over the sampling interval just ended. For a digital system, one could use a counter which accumulates pulses during a sampling interval and is then read out and reset. Here the sampled signal is the pulse rate, which might arise, for example, from a radiation detector. Application of this technique to analog signals is also straightforward with the availability of accurate voltage-to-frequency converters. This is the type of sampling employed for most on-line applications of the DDP-24 computer system.

Such an "integrating sampler" offers a major advantage over the conventional type. For a noisy signal, the outputs of an integrating sampler will have less dispersion than those of a conventional sampler if the noise is uncorrelated over the sampling interval. This results from the averaging effect of the integrating sampler.

## Response of the Integrating Sampler

Suppose we have a signal of the form

$$v(t) = V_0 \cos(\omega t + \theta).$$

The output of a conventional sampler from a sampling at time $t_0$ is then

$$S = V_0 \cos(\omega t_0 + \theta).$$

The maximum output of this sampler equals the peak amplitude of the signal, and is obtained when the sampling occurs at an antinode of the signal. Furthermore, the envelope of the sampler output is in phase with the signal at all frequencies.

Now, consider an integrating sampler whose output for a sampling at time $t_0$ is given by

$$S = \frac{1}{\Delta}\int_{t_0-\Delta}^{t_0} v(t)\,dt,$$

where $\Delta$ is the interval of time just preceding $t_0$ over which the integral is taken. (The scale factor $1/\Delta$ is included to facilitate comparison with the conventional sampler.) For $v(t)$ as given above, the output will be

$$S = V_0 \frac{\sqrt{2(1-\cos\omega\Delta)}}{\omega\Delta}\cos\left(\omega t_0 + \theta - \frac{\omega\Delta}{2}\right).$$

This result has two noteworthy features. First, the envelope of sampler outputs will lag the signal by the phase angle $\omega\Delta/2$. This angle varies linearly with frequency from zero at zero frequency to 90 deg at the Nyquist frequency ($\frac{1}{2}\Delta$) Hz and so corresponds to a constant time delay or transport lag of $\Delta/2$ sec. Therefore, a reading from an integrating sampler is a measure of the value of the signal at a time halfway through the interval of integration. Secondly, the maximum amplitude of the sampler output no longer equals the peak amplitude of the signal, but is multiplied by the factor

$$\frac{\sqrt{2(1-\cos\omega\Delta}}{\omega\Delta} = \left[\frac{\sin(\omega\Delta/2)}{\omega\Delta/2}\right].$$

The function decreases with frequency, having zeros at integral values of $\omega\Delta/2\pi$. The decrease is moderate up to the Nyquist frequency, and more rapid beyond it. The attenuated response to the higher-frequency signals reduces to some extent the spurious components generated by "aliasing" of such signals.

The action of an integrating sampler on a signal $v(t)$ may also be represented as the action of a conventional sampler on the signal $G(t)$ defined by

$$G(t) = \frac{1}{\Delta}\int_{t-\Delta}^{t} v(t')\,dt'$$

$$= \frac{1}{\Delta}\left[\int_0^t v(t')\,dt' - \int_0^{t-\Delta} v(t')\,dt'\right].$$

Therefore, an integrating sampler may be represented in a system block diagram as a conventional sampler preceded by the ideal running-average operator $[(1-e^{-s\Delta})/S\Delta]$.

(The designation of the Nyquist frequency as $\frac{1}{2}\Delta$ Hertz in the preceding discussion assumes that the sampler is read every $\Delta$ sec. This assumes that a new period of integration begins as soon as the previous one ends, and so neglects the time required to read out and reset the sampler. If the readout time is significant, then the samplings will occur less frequently than every $\Delta$ sec, and the Nyquist frequency will be reduced. However, the response of the sampler will still be a function only of $\Delta$ and not of the sampling rate.)

### Noise Reduction Properties

Consider a Gaussian noise with zero mean and rms amplitude $R$, whose spectrum is characterized by a single integrating time constant $\tau$. Its spectral density is

$$\phi(\omega) = \frac{2R^2\tau}{\pi}\left(\frac{1}{1+\omega^2\tau^2}\right) \text{ volts}^2/\text{rad-sec}.$$

Samples of this noise taken with the conventional sampler would have an rms dispersion equal to $R$. For the integrating sampler, the rms dispersion $\sigma$ is given by

$$\sigma^2 = \frac{2}{\Delta^2}\int_0^\infty \frac{1-\cos\omega\Delta}{\omega^2}\,\phi(\omega)\,d\omega;$$

this can be written as

$$\sigma^2 = \frac{2R^2}{\pi\Delta^2\tau^2}\,\mathrm{Re}\int_{-\infty}^{\infty}\frac{1-e^{i\Delta z}\,dz}{z^2(z+i/\Delta)(z-i/\Delta)}.$$

The integral may be evaluated by contour methods to give

$$\sigma^2 = 2R^2(\tau/\Delta)\{1-(\tau/\Delta)[1-\exp(-\Delta/\tau)]\},$$

so that

$$\sigma/R = \sqrt{2\tau/\Delta} \quad \text{for} \quad \Delta \gg \tau.$$

It is apparent that significant reductions in sample dispersion can be obtained.

### Noise Analysis with an Integrating Sampler

In analyzing random noise with any type of sampler, "aliasing" from frequency components higher than the Nyquist frequency is always a problem. Although the integrating sampler degrades the higher-frequency components, it does not eliminate them completely. Analog filters are never perfect, nor are digital filters. In addition, digital filtering requires a sampling rate greater than that corresponding to the Nyquist frequency. This poses difficulties in those cases where obtaining the minimum required sampling rate is marginally feasible.

We may attempt to bypass the "aliasing" problem by looking more closely at just where the problem enters. The autocorrelation function $C_0(\tau)$ of a stationary random function of time $x(t)$ may be written as the expectation value

$$C_0(\tau) = \langle v(t)\,v(t+\tau)\rangle.$$

To estimate this expectation value, one takes a pair of values of $x$ separated in time by $\tau$ sec and multiplies them together. To get an improved estimate, one averages this product with the products of other pairs of values. Whether these pairs of values are taken at discrete intervals or continuously, as in an analog correlator, does not affect the expectation value of the process. Furthermore, the expectation for $C_0$ at any one lag is clearly independent of estimates made at other lags. We may conclude that the correlation function estimates are unaffected by "aliasing".

Where, then, does "aliasing" enter? It enters when the correlation function is Fourier-analyzed to yield the spectrum. A well-known property of Fourier series states that a function defined at $n + 1$ points is perfectly described by a series extending through the $(n/2)$th harmonic, which is the Nyquist frequency. If such a function has contributions from frequencies higher than the Nyquist frequency, those contributions will manifest themselves as additions to the lower harmonics.

Therefore, one can bypass the "aliasing" problem if one foregoes the use of the spectrum and works only with the correlation functions. This approach is especially attractive if the theory of the underlying process indicates the form of the correlation function, and the measurement is to determine the parameters.

Results of noise analysis with the integrating sampler require small corrections for the response characteristics of the sampler. The following will discuss the response for simple exponential and exponential-cosine correlation functions.

The function to be treated here is the expectation value

$$C(\tau) = \left[\frac{1}{\Delta}\int_t^{t+\Delta} v(t')\,dt'\right]\left[\frac{1}{\Delta}\int_{t+\tau}^{t+\tau+\Delta} v(t')\,dt'\right],$$

which may be shown to be

$$C(\tau) = 4\int_0^\infty \frac{(1-\cos\omega\Delta)}{\omega^2\Delta^2}\cos\omega\tau\,\phi(\omega)\,d\omega,$$

where $\phi(\omega)$ is the spectral density conjugate to $C_0(\tau)$. (This equation reduces to Wiener's theorem as $\Delta \to 0$.)

To begin with, consider the exponential autocorrelation function

$$C_0(\tau) = e^{-\alpha\tau}, \qquad \tau > 0,$$

with conjugate spectral density

$$\phi(\omega) = \frac{\alpha}{\pi}\cdot\frac{1}{\alpha^2+\omega^2}.$$

For $\tau \geq \Delta$, we may write

$$C(\tau) = \frac{\alpha}{\pi\Delta^2}\,\mathrm{Re}\int_{-\infty}^{+\infty}\frac{2e^{iz\tau} - e^{i(\tau+\Delta)z} - e^{i(\tau-\Delta)z}}{z^2(z+i\alpha)(z-i\alpha)}\,dz,$$

which integrates over a contour in the upper half-plane to give

$$C(\tau) = \frac{2[\cosh(\alpha\Delta)-1]}{(\alpha\Delta)^2}e^{-\alpha\tau} = \left[1+\frac{(\alpha\Delta)^2}{12}+\frac{(\alpha\Delta)^4}{360}+\cdots\right]e^{-\alpha\tau}.$$

Therefore, in this domain the correlation function remains exponential with the same time constant, but the amplitude increases. The increase is less than 9% for $\alpha\Delta \leq 1$.

For $\tau \leq \Delta$, we have

$$C(\tau) = \frac{\alpha}{\pi\Delta^2}\,\mathrm{Re}\int_{-\infty}^{+\infty}\frac{2e^{i\Delta z} - e^{i(\Delta+\tau)z} - e^{-(\Delta-\tau)z}}{z^2(z+i\alpha)(z-i\alpha)}\,dz,$$

which again integrates over a contour in the upper half-plane to give

$$C(\tau) = \frac{2}{\alpha^2\Delta^2}[\alpha(\Delta-\tau) - e^{-\alpha\tau} + e^{-\alpha\Delta}\cosh\alpha\tau].$$

Thus, the function is no longer exponential in this domain. For $\tau = 0$, it reduces to

$$C(0) = \frac{2}{\alpha\Delta}\left[1 - \frac{1-\exp(-\alpha\Delta)}{\alpha\Delta}\right],$$

which is a classical result in the theory of nuclear-reactor noise.[1,2]

Now, let us consider a simple exponential-cosine autocorrelation function

$$C_0(\tau) = e^{-\alpha\tau}\cos\beta\tau, \qquad \tau > 0,$$

with conjugate spectral density

$$\phi(\omega) = \frac{2\alpha}{\pi}\cdot\frac{\omega^2+(\alpha^2+\beta^2)}{\omega^4+2(\alpha^2-\beta^2)\omega^2+(\alpha^2+\beta^2)^2}.$$

For $\tau \geq \Delta$, we may write

$$C(\tau) = \frac{2\alpha}{\pi\Delta^2}\,\mathrm{Re}\int_{-\infty}^{+\infty}\frac{(z^2+\alpha^2+\beta^2)[2e^{iz\tau} - e^{i(\tau+\Delta)z} - e^{i(\tau-\Delta)z}]}{z^2[z+(\beta+i\alpha)][z-(\beta+i\alpha)][z+(\beta-i\alpha)][z-(\beta-i\alpha)]}\,dz.$$

This integrates over a contour in the upper half-plane to yield

$$C(\tau) = A\,e^{-\alpha\tau}\cos(\beta\tau+\theta),$$

where the amplitude factor, $A$, is

$$A = \frac{2(\cosh\alpha\Delta - \cos\beta\Delta)}{(\alpha^2+\beta^2)\Delta^2} = 1 - \frac{1-g^2}{12}(\beta\Delta)^2 + \frac{1-g^2(1-g^2)}{360}(\beta\Delta)^4 + \cdots$$

There is a phase shift, $\theta$, given by

$$\theta = \tan^{-1}\left[\frac{2\alpha\beta(1 - \cosh\alpha\Delta\cos\beta\Delta) - (\beta^2 - \alpha^2)\sinh\alpha\Delta\sin\beta\Delta}{(\beta^2 - \alpha^2)(1 - \cosh\alpha\Delta\cos\beta\Delta) + 2\alpha\beta\sinh\alpha\Delta\sin\beta\Delta}\right] = \frac{g(\beta\Delta)^2}{6} + \cdots.$$

Here $g = \alpha/\beta = 1/2Q$, where $Q$ is the figure-of-merit of the tuned circuit yielding this response. So in this domain the correlation function remains an exponential-cosine, but the amplitude is again altered and the cosine is phase-shifted.

For $\tau \leq \Delta$, we have

$$C(\tau) = \frac{2\alpha}{\pi\Delta^2}\,\mathrm{Re}\int_{-\infty}^{+\infty} \frac{(z^2 + \alpha^2 + \beta^2)[2e^{i\tau z} - e^{i(\Delta+\tau)z} - e^{i(\Delta-\tau)z}]}{z^2[z + (\beta + i\alpha)][z - (\beta + i\alpha)][z + (\beta - i\alpha)][z - (\beta - i\alpha)]}\,dz,$$

which integrates to give

$$C(\tau) = \frac{1}{\Delta^2(\alpha^2 + \beta^2)}\,[2\beta(\Delta - \tau) + 2F(\tau) - F(\Delta + \tau) - F(\Delta - \tau)],$$

where

$$F(x) = e^{-\alpha x}[(\beta^2 - \alpha^2)\cos\beta x + 2\alpha\beta\sin\beta x].$$

Again, the original dependence on $\tau$ does not hold in this domain. We also have

$$C(0) = \frac{2}{\Delta^2(\alpha^2 + \beta^2)}\,[\alpha\Delta(\alpha^2 + \beta^2) - (\alpha^2 - \beta^2) - F(\Delta)].$$


References

1. E. F. Bennett, *The Rice Formulation of Pile Noise*, Nucl. Sci. Eng. **8**, 53–61 (July 1960).
2. J. A. Thie, *Reactor Noise*, (Rowman and Littlefield, Inc., New York, 1963) pp. 102–105.


## V-14. Progress in On-Line Computer Utilization

J. F. Whalen

Additional computer controlled instrumentation, in various stages of delivery, has required the design and fabrication of special interfacing circuits since none of the new devices is matched to the existing computers.

Among these new instruments are two 4096 channel analog-to-digital converters with feed-back stabilization circuits. They are to be used in $\gamma$-ray pulse height analysis using solid state detectors and they will be under computer control. The interfacing circuits are being fabricated by the manufacturer according to ANL specification. The interface will permit the computer to control and read in information from either (or both) analog-to-digital converter while operating in coincidence. Operational status is expected by September 1967.

The recent purchase of an additional 14 bit digital-to-analog converter for magnet control also required interfacing to the computer, but in order to simplify the digital-to-analog section of the system a completely new interface is being built to control both digital-to-analog as well as providing 6 additional external control signals. This new circuit is completed and is now under test.

An interfacing system was designed and built for the sample changer in the time-of-flight system. This circuit permits the computer to select one of eight samples and precisely place the selected sample in the neutron beam.

# V-15. A Multiplexing System for an On-Line Computer

J. F. Whalen and J. W. Meadows

A multiplexing system designed for data rates of less than a few hundred events per second has been constructed for the on-line computer system of the Reactor Physics Division Applied Nuclear Physics Laboratory. The operation of the system relies principally on the computer program and, as a result, little in the way of additional specialized electronic circuits were required.

Figure V-15-1 shows the logical diagram of the system as set up for a 3-parameter fission experiment. The parameters consist of the two fission fragment pulse-heights and an angle. Input 1 comes from a common detector located close to the fission source so that nearly all fissions are detected. Inputs 2–6 come from detectors located further away and determine the fission angle. The logical elements located to the right of the dashed line in Fig. V-15-1 are contained in the computer interface and basic 2-parameter input and have been previously described.[1,2] The added equipment is to the left of the dashed line and consists largely of standard amplifiers and single channel analyzers.

A signal from one or more inputs goes to S.C.A. (single channel analyzer) A and/or B. The output of these S.C.A. clears the scalers and opens the gates of S.C.A. 1–6 permitting the delayed signal to set the appropriate identifying toggels. The signal (or signals) also goes through the linear gates to the ADC (analog-to-digital converter) where it is digitalized. As soon as this occurs the linear gates are blocked. The $\overline{\text{BUB}}$

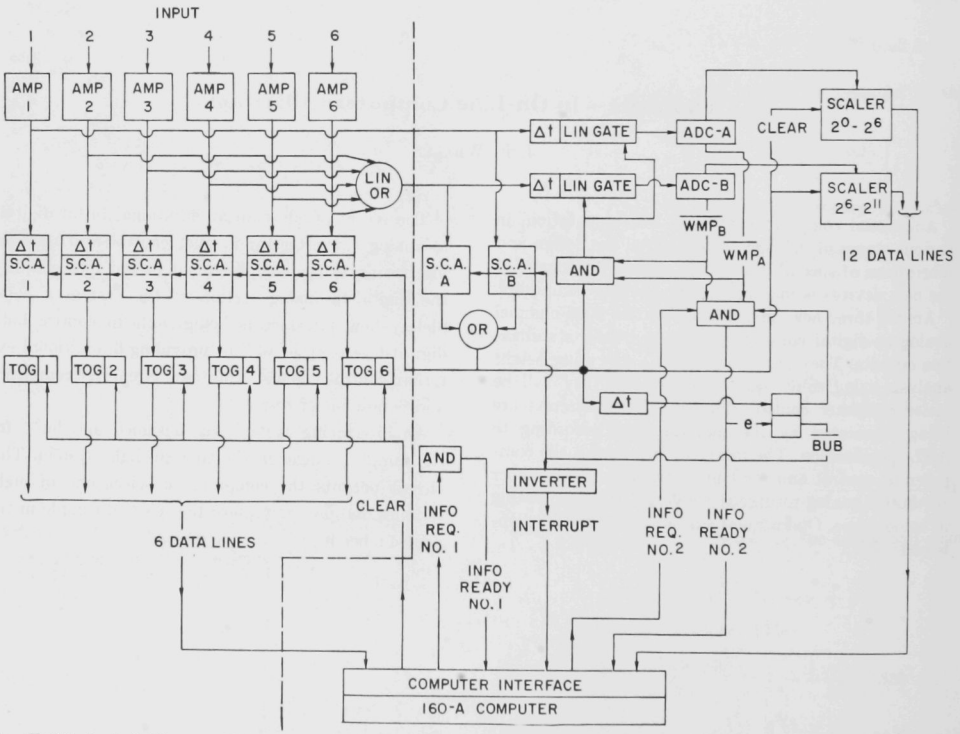


Fig. V-15-1. Logical Diagram of Multi-plexing System as Set Up for a 3-Parameter Fission Experiment. *ANL Neg. No. 112-9094.*

(see Fig. V-15-1) signal is removed, blocking S.C.A.'s A and B and in effect 1–6. The removal of $\overline{\text{BUB}}$ also sends an interrupt signal to the computer. The computer transfers to the input program and reads the 6 data lines from the toggles. When decoded, this information determines which inputs were activated, tells if the coincidence and anticoincidence requirements were met, and determines the storage area. The 6 toggles are cleared and the 12 data lines from the ADC scalers are read. If the coincidence requirements were not met, the information is discarded. When acceptable, 1 is added to the appropriate address in the previously determined storage area. The system is then ready to accept another event.

This system has proven satisfactory in the illustrated and other configurations. It can be easily expanded, the principal limitation being the increase in noise level as more inputs are added to the linear "or" input.

### References

1. J. F. Whalen, J. W. Meadows and R. N. Larsen, *On-Line Operation of a Digital Computer in Nuclear Physics Experiments*, Rev. Sci. Instr., **35**, 682 (1964).
2. J. F. Whalen, R. Roge, J. W. Meadows and A. B. Smith, *Accelerator Digital System*, Reactor Physics Division Annual Report, July 1964 to June 30, 1965, ANL-7110, pp. 307–310.

## V-16. Remote Station for On-Line Computer Control

J. F. Whalen and J. J. Eichholz*

A remote terminal facility has been designed, constructed, and tested for the purpose of performing experiments at some distant site while utilizing the Reactor Physics Division computer system for processing the data. The data and control information in digital form is transmitted serially by means of two coaxial cables up to 3000 ft long. This maximum length was chosen since it would adequately span the distance between the computer facility and the Physics Division tandem Van de Graaff where a number of experiments are performed by the Reactor Physics Division Applied Nuclear Physics Laboratory.

The basic components of the remote station consist of two 5 Mc analog-to-digital converters, (ADC), a storage oscilloscope display system and a transmit-receive console, Fig. V-16-1. The analog-to-digital converters were made identical to the models used in the existing on-line computer system. This not only gave rise to an economy of design time, but also provided "plug in" back-up instruments for the regular ADC. The display system is also a simplified version of the existing on-line model. The transmit-receive console routes all data and control information to and from the computer, decodes instructions, and synchronizes the computer operations with the remote peripheral equipment. At the computer station, a second transmit-receive circuit performs similar duties with special interface circuits to the computer. These occupy one input-output channel of the 160-A. There are also three additional circuit junctions brought out of the 160-A for clearing and starting the computer.

Nuclear events, after being digitalized in the ADC's at the remote station, are transferred to a thirty bit shift register. Each ADC is alloted 12 bits and the remaining six bits are reserved for coded instructions to the computer station regarding the routing and disposition of the 24 data bits. For simplicity of design and operation identical thirty bit shift registers were used at both remote and computer stations and each transmission was in thirty bit formats in either direction. The information in the shift register is transferred to one of the cables one bit at a time (at 2 Mc) while gating pulses are synchronously transferred to the second cable. The presence of a pulse on the first cable during the gate pulse indicates a logical "one" and the absence of a pulse on the first cable during gate time on the second cable indicates a logical zero. This mode insures fidelity of transmission independent of cable length or pulse train frequency. The same cables are used for the transmission in either direction and the full thirty bit pulse train requires 21 $\mu$sec for the 2400 ft. trip including shift register run-up time.

There are several modes of operation available to the remote experimenter. The most important of these permits the direct storage of data from both remote ADC's in the computer at a rate better than $10^4$ nuclear events (24 bits) per second. The remote experimenter may stop the data accumulation at any time and instruct the computer to display any portion of

* Electronics Division, Argonne National Laboratory.

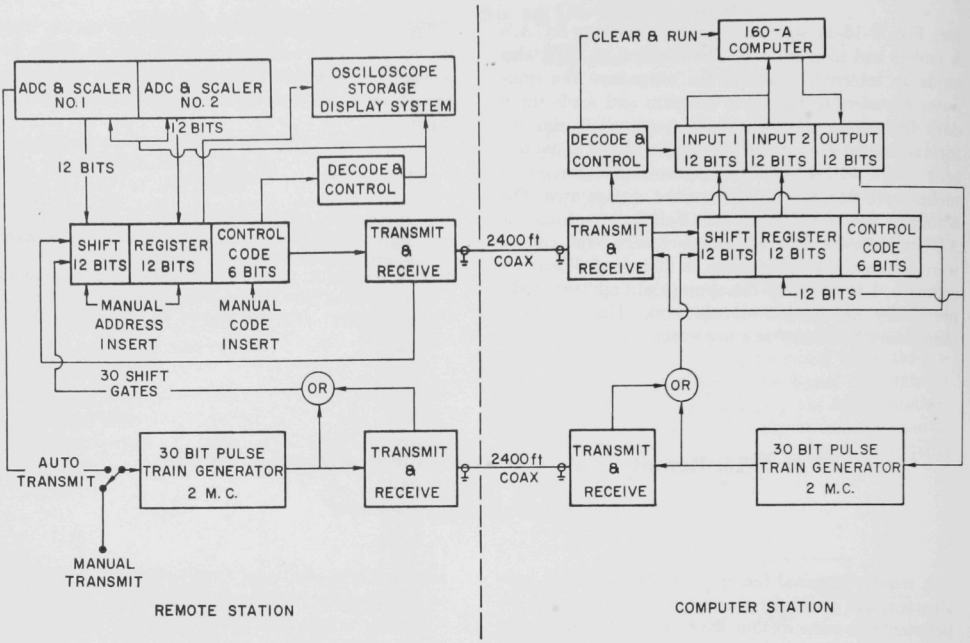


FIG. V-16-1. Remote Data Acquisition System. *ANL Neg. No. 112-9160.*

the accumulated data in the core memory on the remote storage scope. He can also modify any parameter in the resident program, change the program itself, or interrogate any particular address in the computer. In effect he has a remote console in addition to the remote high speed input channel.

The major portion of the control circuitry was assembled from commercial integrated circuit boards with special cable driving circuits designed by the Electronics Division, ANL. There is a minor software requirement in that a boot strap program must be resident in the computer before operation is possible.

## V-17. Design of the Fast Neutron Generator Facility Building

J. W. MEADOWS

The design of a building to house the new Fast Neutron Generator has been completed. The purpose of the facility is to extend neutron cross section measurements into the 3–10 MeV energy range by both time-of-flight and continuous beam methods and to provide an intense pulsed neutron source for use with critical facilities. This, along with the additional requirement that the arrangement of the experimental areas be readily adaptable to changing experimental demands and possible accelerator modifications, determined the building configuration.

The facility is located 45 ft west of Building 315 so that an ion beam can be switched into one of the critical cells. The main building is a large, high ceiling structure about 130 x 66 ft, containing the accelerator vault, target area, experimental assembly area, and

the control center. Laboratory and office space are available in a 38 x 64 ft annex. A service floor under the annex provides space for an electrical substation and the mechanical equipment. In order to maintain flexibility, the main building has no interior supports and fixed shield walls have been kept to a minimum. The only fixed wall runs the full length of the east side of the main building and is incorporated into the building srtucture. It forms one wall of the accelerator vault and provides a shadow wall to separate the target area from Building 315. All other shielding, including the remainder of the accelerator vault and a second shadow wall separating the target area and the control and assembly area, are constructed of concrete block and pre-stressed concrete beams. All these items are small enough to be handled by a 5-ton crane which has full access to the main building.

As presently conceived the target area provides space for 5 target stations. Since it is expected that time-of-flight techniques will be one of the principal methods used at this facility, one target station will be completely devoted to it. There is room inside the building for flight paths of 5 m, but longer flight paths will require detectors to be stationed outside the building. To facilitate this, a low mass window extends completely across the south and west sides of the target area at the beam height. A paved apron outside the building permits the convenient location of detectors at distances up to 20 m or more.

## V-18. A High Intensity Gas Target

J. W. Meadows

A general purpose gas target has been developed to provide an intense source of neutrons from the $H^2(d,n)$ $He^3$ reaction. The principal features of the target assembly are illustrated in Fig. V-18-1. The gas cell is separated from the flight tube vacuum by a thin nickel foil supported by a gold grid. The grid has a transmission of ~75% and is formed by electrical discharge machining. The foil is cemented to the grid with a thermosettting bonding agent. In order to cool the foil, deuterium gas is circulated through the cell at a rate of ~40 $ft^3$/h with the gas stream adjusted to blow directly across the nickel foil. The end of the gas cell is cooled with an external air jet.

A major problem when accelerating deuterons to energies in the MeV range is the production of neutrons by *d,n* reactions with the materials of the flight tube and target. In order to reduce this effect, all surfaces exposed directly to the deuterium beam are made of gold or other high Z material. As a result, the extraneous neutron yield for 3 MeV deuterons is <3% of the yield of a 3 cm-atm target. This figure increases with use due to the build-up of deuterium in the end of the gas cell.

The target has performed well with foil thicknesses of 1 $\mu$ but greater reliability has been obtained with 2 $\mu$ foils. Targets using the thicker foils have been operated for periods of over 100 h with cell pressures up to 2 atm and deuteron beam currents of 15–20 $\mu$A.

Good reliability can be obtained with higher beam currents, providing the beam spot is diffuse. In principle, this can be accomplished with the focus controls but this is difficult in practice. A more successful method involves maintaining a well focussed beam spot and applying small, high frequency, vertical and horizontal deflections. The defining slits are opened to expose 80–90% of the grid and the deflection amplitudes are adjusted to uniformly cover this area. In tests with this method beam currents of 40–50 $\mu$A have been maintained on 2 $\mu$ foils for periods of 1 h with no sign of failure.

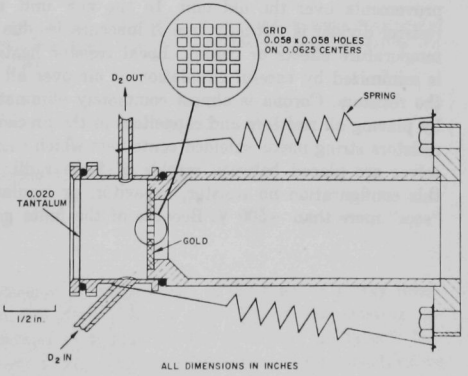


Fig. V-18-1. Assembly of High Intensity Gas Target. *ANL Neg. No. 112-8713.*

# V-19. Electrostatic Analyzer for Accelerator Energy Control

S. A. Cox

An electrostatic analyzer has been in use for over ten years for the precise control and measurement of the voltage of the Argonne 3 MeV Van de Graaff accelerator. The voltage control is affected by passing the finely collimated molecular beam through a 1 in. gap between the curved analyzer plates. The beam emerges after 25 deg deflection and strikes a pair of control slits. An error signal from the control slits is fed back to the Van de Graaff high voltage terminal via a corona stablizer unit which adjusts the terminal voltage so that the molecular beam remains centered on the control slits. It is clear that for highly stable operation of the accelerator the power supply associated with the electrostatic analyzer must be capable of supplying a precise and accurate voltage to the current deflection plates. The original power supply unit had become unstable and unreliable and has been completely replaced. The new unit was designed by R. N. Lewis[1] and built by the Electronics Division, Argonne National Laboratory. There are three main components of the unit: a high voltage generator, a precision resistor divider, and a highly fed back control unit. In operation, the high voltage generator applies a voltage to the resistor divider. The voltage developed across a small "tap" resistor at the grounded end of the divider is sent to the control unit where it is compared with the reference voltage from a precision potentiometer. The control unit then adjusts the voltage from the high voltage generator until the "tap" resistor voltage and reference voltage are equal. Several aspects of the new unit represent significant improvements over the old unit. In the new unit the resistor divider is virtually free of inaccuracies due to temperature effects or corona. Local resistor heating is minimized by careful circulation of air over all of the resistors. Corona is almost completely eliminated by placing all resistors and capacitors in the precision resistors string inside shielded containers which themselves are placed between toroids of large radii. In this configuration no resistor, capacitor, or insulator "sees" more than ~500 V. Because of the finite gain of the control unit, the "null" point is not exactly zero. In practice the voltage correction can be in error by some tens of parts per million. However, even this small error can be biased out at any given operating voltage by manual adjustments on the control unit. Thus the only error remaining in the voltage supplied to the analyzer plates must be due to uncertainty in the reference voltage (0.01%) whatever corona is present (presumably negligible), or a change in the divider ratio due to resistor heating. A unique feature of the new unit is that the divider ratio can be measured under actual working conditions, i.e. while the operating voltage is applied to the analyzer plates. This virtually eliminates the uncertainty due to changes in the divider ratio when measurements are made far from the precision calibration points. In its present form the accuracy of the voltage applied to the analyzer plates is limited almost entirely by the accuracy of the precision reference potentiometer or ~0.01%. The accuracy to which the proton beam energy can be measured is not as good because the energy calibration depends on the exact mechanical geometry of the system, which is subject to change; and the "null" position of the beam on the control slits depends slightly on the exact focal conditions of the proton beam. In actual practice the supply voltage corresponding to the $Li^7(p,n)Be^7$ reaction threshold (proton energy = 1.8803 MeV) reproduces to ±0.02% over a 2–3 week period. Since only the molecular beam is used for energy measurement and control, the monatomic (or mass one) beams remain unobstructed and thus the full beam current delivered by the accelerator can be used in experiments. This feature is vital to the success of many neutron experiments where low yield is often a problem.

## Reference

1. R. N. Lewis, *Method for the Rapid Calibration of Precision Potential Dividers While Being Operated Under Normal Conditions of Voltage, Current, and Environment*, Rev. Sci. Instr. **36**, 532 (1965).

## V-20. Neutron Precession Solenoid

S. A. Cox

A previous section of this report, dealing with neutron polarization, referred briefly to a neutron precession solenoid (see Paper I-3). This solenoid is used to precess the spin of neutrons emitted from the $Li^7(p,n)$ reaction through 180 deg so that polarization measurements may be made without moving the neutron detectors.

The solenoid is constructed of copper foil and mylar imbedded in epoxy insulation with an overall 15 in. o.d., 1.5 in. i.d., and 20 in. length. In operation, the solenoid is water cooled with an input of ~6 gal. per min at 20 kW. The power supply contains a servomechanism such that the power dissipated by the supply itself is always quite low. The solenoid current can be controlled by a manual dial on the supply or by a signal from a computer controlled digital-to-analog converter. The solenoid is completely enclosed in a ⅛-in. soft iron shell except for the 1½-in. diam central hole. The soft iron serves two purposes: the external magnetic field in the vicinity of the neutron detector is reduced, thus affording better magnetic field protection for detectors, and the edge of the solenoid field is more sharply defined, reducing the depolarizing effect of the fringe field. Because of the narrow collimation of the neutron beam (~0.5 deg) the depolarizing effect is expected to be very small. Further, the soft iron shell gives a small bonus: the field is more confined, the central field is enhanced, and thus the neutron energy range over which the solenoid is effective is increased.

The solenoid was calibrated by observing the neutron scattering from beryllium, magnesium, and silicon at energies where the scattering was known to produce polarization. One example is shown in Fig. V-20-1. Here the 90 deg yield of 950 keV neutrons scattered at 90 deg from silicon is plotted against the solenoid current. The minimum indicated by the arrow corresponds to 180 deg precession. The open circles were taken with increasing current and the closed circles with decreasing current. The solenoid calibration was based on a number of such measurements. As a result it was determined that at the full 20 kW capability the solenoid would precess the spin of 2.1 MeV neutrons through 180 deg or 8.4 MeV neutrons through 90 deg.

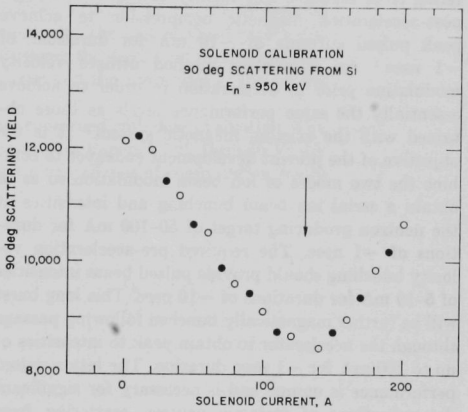


FIG. V-20-1. The Yield of Neutrons Elastically Scattered at 90 deg from Si as a Function of Solenoid Current. *ANL Neg. No. 112-8409.*

## V-21. Rotary Time-of-Flight Collimators

A. B. SMITH

Throughout several thousand hours of operation the multi-angle time-of-flight system has proven very successful and has been the source of a large amount of inelastic scattering information.[1,2] The collimator design and the experimental use was based upon incident neutron energies of 1.5 MeV and below. The success of the system within this range has encouraged extension of the program to the neutron energy interval 4–6 MeV. This is available to the existing accelerator using high current deuterium gas targets (see Paper V-18). However, the large (10 ton) multi-angle collimator system must be precisely rotated for studies above 4 MeV. A mechanical collimator rotation system has been designed, fabricated, and tested. The motion,

based upon an air flotation principle, is precise and easily positions the collimator for inelastic scattering studies at incident neutron energies of up to 6.5 MeV. Initial studies of inelastic scattering from iron indicate that the shielding of the detectors is excellent and that the positioning of the collimator is entirely suitable for studies at these higher energies.


REFERENCES

1. A. B. Smith, P. T. Guenther, R. Hayes and J. F. Whalen, *Fast Neutron Scattering from Ta, Re, and Pt*, ANL-7363 (1967).
2. A. B. Smith, P. T. Guenther, R. Larsen, C. Nelson, P. Walker and J. F. Whalen, *Multi-Angle Fast Neutron Time-of-Flight Methods*, Nucl. Instr. Methods **50**, 277 (1967).


## V-22. Pulsed and Bunched Ion Source

A. B. SMITH

Intense nanosecond bursts are the key to successful time-of-flight determinations of inelastic neutron scattering cross sections. The facility now in use employs post-acceleration magnetic compression to achieve peak pulsed currents of ~10 mA for durations of ~1 nsec.[1] An alternative method utilizes velocity modulation prior to acceleration in order to achieve essentially the same performance levels as those obtained with the existing magnetic system.[2] It is the objective of the present development endeavor to combine the two modes of ion beam modulation so as to obtain a serial ion beam bunching and intensities at the neutron producing target of 50–100 mA for durations of ~1 nsec. The required pre-acceleration velocity bunching should provide pulsed beam intensities of 5–10 mA for durations of ~10 nsec. This long burst will be further magnetically bunched following passage through the accelerator to obtain peak to intensities of up to 100 mA for ~1 nsec duration. The latter pulsed performance is unique and is necessary for significant determinations of inelastic neutron scattering from complex fissile nuclei such as Pu-239.

The pre-acceleration velocity bunching system is based upon a rf ion source providing an estimated ion beam energy homogeneity of better than 300 eV. This source is followed by suitable optical and bunching components. The entire unit has been constructed and undergone preliminary tests. During these tests, bunching factors of ~5 were observed. Modification indicated by the preliminary tests are now approaching completion and should result in bunching factors of 8 or more. The next critical step in the application of the source and velocity bunching system is the matching of the source optics to those of the existing Van de Graaff accelerator. For this purpose a test bench duplicating the optical component of the accelerator has been constructed and the source-buncher unit mounted on it. Tests are about to start using this combined test system. The necessary electronic units for use of the source within the accelerator are now under construction. It seems conservative to expect the combined source-velocity bunching-magnetic compression system to deliver the minimum expected peak pulse of 50 mA for an ~1 nsec duration. Hopefully, this minimum will be appreciably exceeded.


REFERENCES

1. A. Smith, P. Guenther, R. Larsen, C. Nelson, P. Walker and J. F. Whalen, *Multi-Angle Fast Neutron Time-of-Flight Methods*, Nucl. Instr. Methods **50**, 277 (1967).
2. C. Moak, W. M. Good, R. F. King, J. W. Johnson, H. E. Banta, J. Judish and W. H. du Preez, *Nanosecond Pulsing for Van de Graaff Accelerator*, Rev. Sci. Instr. **35**, 672 (1964).

# Section VI

# Reactor Computation Methods and Theory

The title of this section reflects the major role played in reactor physics by machine computations. Papers VI-1 through VI-6, VI-9, VI-11 and VI-16 describe efforts in the development of computation methods. The first of these papers discusses the Argonne Reactor Computation System; the next four papers are concerned with neutron cross section computations; and the remainder of the papers deal with a miscellany of topics.

Papers VI-7, VI-10 and VI-17 consider areas concerned with data evaluation. The calculation of various kinetics problems is covered in Papers VI-12 through VI-15. Finally, Papers VI-8, VI-18 and VI-19 present a miscellanea of computation methods and theory.

# VI-1. The Argonne Reactor Computation (ARC) System

B. J. Toppel

The Argonne Reactor Computation System[1] is being implemented on the Laboratory's IBM System/360 Model 50-75 computer complex. The ARC system enjoys two major advantages compared with conventional computer codes, namely:

(1) The ability to automate the linkage of computational modules in an arbitrarily complex manner, without human intervention for data handling, in order to attack sophisticated reactor problems.

(2) The ability to simply store away, and, at a later time, retrieve data generated by an ARC run to facilitate the rerunning of previous problems with data changes, or the extension of previous problems into further computational areas.

The ARC system consists of:

(1) *The Datapool*—The collection of data and computational algorithms that can be used by ARC.
(2) *Computational Modules*—Conventional program subroutines.
(3) *Standard Paths*—Control programs similar to the driver or executive portions of large conventional codes containing numerous subroutines or overlays.
(4) *Operating System*—Collection of codes which is the interface between ARC and the computer hardware.

Figure VI-1-1 is a schematic representation of the ARC system. The configuration represented corresponds to the situation in which the operating system has transferred control to a standard path which has in turn called a particular computational module into the fast core from the datapool.

From the user's point of view, ARC facilitates reactor physics calculations that involve many independent computations. These computations may be processed serially and may incorporate logical decisions.

A standard path may be used to link ARC program modules in such a manner as to effectively generate the equivalent of a present-day self-standing code. On the other hand, owing to the flexibility of the system, one may easily use standard paths to perform comparative calculations either with regard to variations in input data, or in regard to computational algorithmic methods. Indeed, since logical decisions can be made during execution of a path, the particular algorithms to be invoked need not be predetermined. Such paths involving branches based upon logical decisions involve use of the full capability of the ARC system.

## Computational Scope of the System

Table VI-1-I reflects current thinking in regard to modules for the ARC system. The module names are intended to be descriptive of the function of the modules. The box marked ARC MODULE in Fig. VI-1-1 may correspond to any of the Table VI-1-I modules. The module FORTRAN names are also given in Table I.

The listing has been grouped into five main categories. Within each category, the modules are further organized into Input, Computational, and Output Edit modules. In all categories, a blank entry has been included to imply the open ended nature of the ARC module library.

The input modules have BCD card image upper interface data sets while the computational modules generally deal with binary data sets. The edit modules have both BCD and binary upper interface data sets. Eventually, selective edits will be possible depending upon user choice. For the initial implementation, most edit modules will be similar to the output routines of classical codes in that little or no selectivity is provided in the output complexity.

Further descriptions of the various modules, together

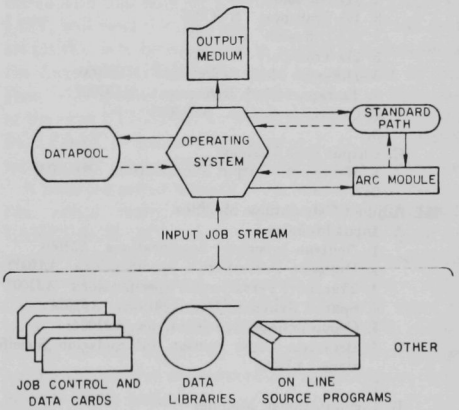


Fig. VI-1-1. Schematic Representation of the ARC System. *ANL Neg. No. 112-8616.*

TABLE VI-1-I. ARC System Modules

I. Cross Section Preparation Modules
- A. Input Modules
  1. Epi-Thermal Cross Section Specifications CSI001
  2. Thermal Cross Section Specifications CSI002
  3.
- B. Computational Modules
  1. Resonance Cross Sections CSC001
  2. Non-Resonant Cross Sections and Fundamental Mode Spectrum CSC002
  3. Thermal Cross Sections CSC003
  4. Broad Group Cross Sections CSC004
  5. Broad Group Fundamental Mode Spectrum CSC005
  6.
- C. Output Edit Modules
  1. Resonance Cross Section Edit CSE001
  2. Non-Resonant Cross Section and Spectrum Edit CSE002
  3. Thermal Cross Section Edit CSE003
  4. Broad Group Edit CSE004
  5. Broad Group Fundamental Mode Edit CSE005
  6.

II. Neutronics Calculations Modules
- A. Input Modules
  1. Neutronics Specifications NUI001
  2. Geometry Preparation NUI002
  3. Cross Section Homogenization Specifications NUI003
  4. 1D-Diffusion Specifications NUI004
  5. 1D-Transport Specifications NUI005
  6. 2D-Diffusion Specifications NUI006
  7. 2D-Transport Specifications NUI007
  8. Diffusion Mesh Refinement Specifications NUI008
  9. Transport Mesh Refinement Specifications NUI009
  10. Neutronics Output Manipulation Specifications NUI010
  11.
- B. Computational Modules
  1. Cross Section Homogenization NUC001
  2. 1D-Diffusion NUC002
  3. 1D-Transport NUC003
  4. 2D-Diffusion NUC004
  5. 2D-Transport NUC005
  6. Diffusion Mesh Refinement NUC006
  7. Transport Mesh Refinement NUC007
  8. Criticality Search NUC008
  9.
- C. Output Edit Modules
  1. Neutronics Output Manipulation NUE001
  2.

III. Adjunct Calculations Modules
- A. Input Modules
  1. Neutron Inventory Specifications AJI001
  2. Diffusion Perturbation Specifications AJI002
  3. Transport Perturbation Specifications AJI003
  4. Spatial Synthesis Specifications AJI004
  5. Group Collapse Specifications AJI005
  6. Bivariate Cross Section Interpolation Specifications AJI006
  7.
- B. Computational Modules
  1. Neutron Inventory AJC001

TABLE VI-1-I—*Continued*

III. Adjunct Calculations Modules—*Continued*
  2. Diffusion Perturbation AJC002
  3. Transport Perturbation AJC003
  4. Spatial Synthesis AJC004
  5. Group Collapse AJC005
  6. Bivariate Cross Section Interpolation AJC006
  7.
- C. Output Edit Modules
  1. Neutron Inventory Edit AJE001
  2. Diffusion Perturbation Edit AJE002
  3. Transport Perturbation Edit AJE003
  4. Spatial Synthesis Edit AJE004
  5. Group Collapse Edit AJE005
  6. Bivariate Cross Section Interpolation Edit AJE006
  7.

IV. Fuel Cycle and Depletion Calculation Modules
- A. Input Modules
  1. Fuel Cycle Specifications FCI001
  2. Economics Specifications FCI002
  3.
- B. Computational Modules
  1. Fuel Cycle FCC001
  2. Economics FCC002
  3.
- C. Output Edit Modules
  1. Fuel Cycle Edit FCE001
  2. Economics Edit FCE002
  3.

V. Safety and Accident Calculations Modules
- A. Input Modules
  1. Point Kinetics Specifications SAI001
  2. Spatial Kinetics Specifications SAI002
  3. Heat Transfer Specifications SAI003
  4. Two-Phase Coolant Flow Specifications SAI004
  5. Core Compaction Specifications SAI005
  6. Compressible Fluid Hydrodynamics Specifications SAI006
  7. Fuel Element Deformations Specifications SAI007
  8. Initiating Mechanisms Specifications SAI008
  9. Fuel-Coolant Interaction Specifications SAI009
  10.
- B. Computational Modules
  1. Point Kinetics SAC001
  2. Spatial Kinetics SAC002
  3. Heat Transfer SAC003
  4. Two-Phase Coolant Flow SAC004
  5. Core Compaction SAC005
  6. Compressible Fluid Hydrodynamics SAC006
  7. Fuel Element Deformations SAC007
  8. Initiating Mechanisms SAC008
  9. Fuel Coolant Interaction SAC009
  10.
- C. Output Edit Modules
  1. Point Kinetics Edit SAE001
  2. Spatial Kinetics Edit SAE002
  3. Heat Transfer Edit SAE003
  4. Two-Phase Coolant Flow Edit SAE004
  5. Core Compaction Edit SAE005
  6. Compressible Fluid Hydrodynamics Edit SAE006
  7. Fuel Element Deformations Edit SAE007
  8. Initiating Mechanisms Edit SAE008
  9. Fuel-Coolant Interaction Edit SAE009
  10.

with their pertinent interface quantities, are given in Ref. 2.

### System Structure

Operation of the ARC system is made possible through the use of the IBM System/360 operating system and the ARC utility programs. Some of the utility programs occupy fast core for the entire ARC run and others are called in as needed.

The first type of utility provides the following services:

(1) Communication with the user
(2) Dynamic storage allocation
(3) Location of data sets.

The second type of utility:

(1) Produces BCD data sets from card input
(2) Establishes reference numbers for data sets.

The programs in ARC are stored in two libraries:

(1) ARCLIB—contains utility programs, standard paths, and computational modules in the form produced by the compiler. These are called object modules and are not executable. They are stored in this library under the module name. Table VI-1-II lists the contents of ARCLIB.

(2) RUNLIB—contains executable members built from the members of ARCLIB. The members of RUNLIB are each an overlay structure involving computational modules and ARC utility programs.

Figure VI-1-2 shows an example of an individual member of RUNLIB. The particular modules involved MØDi, MØDj, MØDk, . . . , depend upon the requirements of the path SPi. It may be noted that each of the modules may themselves involve an overlay structure. When path i is to be executed, SPi, SNIFF and POINTR would be loaded into the core and control

TABLE VI-1-II. Contents of ARCLIB

| Program | Function |
|---|---|
| SNIFF[a] | Data set location |
| PØINTER[a] | Dynamic core storage allocation |
| BCDDS[a] | Card input processor |
| CØMSET[a] | Data set—logical unit correspondence |
| SP1 | Standard path 1 |
| SP2 | Standard path 2 |
| . | . |
| . | . |
| SPi | Standard path i |
| MØD1 | ARC module 1 |
| MØD2 | ARC module 2 |
| . | . |
| . | . |
| . | . |
| MØDi | ARC module i |

[a] System utility programs.

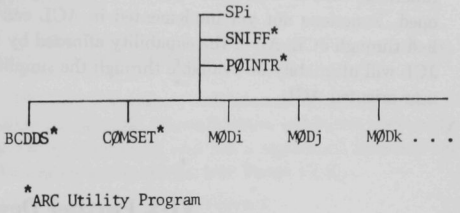


Fig. VI-1-2. A Member of RUNLIB. *ANL Neg. No. 112-8617.*

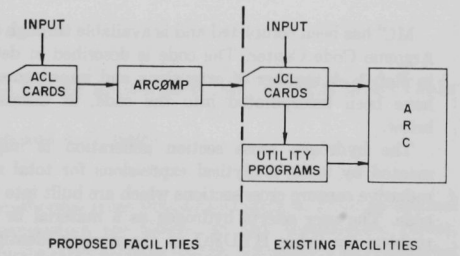


Fig. VI-1-3. Relationship Between ARC Control Language and Job Control Language. *ANL Neg. No. 112-8618.*

transferred to SPi. Program SPi would then determine options and execute the modules as required.

A path utilizes a number of data sets, the basic components of the data pool. Each data set that can be referenced by a path has a number assigned to it; this is done by COMSET. When a module calls SNIFF, with the data set name as a parameter, the number (N) associated with that data set is returned so that READ (N) LIST, will read the data set. For example, if the data set GEØM is to be referenced in a module, a data set of the form ARC.GEØM.RII must be available at run time. The operating system requires that an identifier of the type FTNNF001 be assigned to this data set if a FØRTRAN program is to reference it as NN. SNIFF returns NN when called with GEØM as a parameter.

A path is a rather difficult thing to execute as the system exists today. Many IBM JØB CØNTRØL LANGUAGE (JCL) cards must be used to interface properly with the operating system. Plans are underway to provide a simplified user-oriented language, ARC CØNTRØL LANGUAGE (ACL), that will serve as input to a program that will produce the JCL needed to run the job. Figure VI-1-3 shows the relationships among the various elements of the ARC System as related to input control.

Note that the user can interact with the system in two ways: he can write in ACL or JCL and provide identical

functions. This is important while ACL is being developed. Functions not yet implemented in ACL can be had through JCL. All of the capability afforded by the JCL will ultimately be available through the simplified user-oriented ACL.


REFERENCES

1. B. J. Toppel, *The Argonne Reactor Computation (ARC) System*, Reactor Physics Division Annual Report, July 1, 1965 to June 30, 1966, ANL-7210 pp. 349–351.
2. B. J. Toppel, *The Argonne Reactor Computation System*, ANL-7332 (to be published).


## VI-2. Further Development of the MC² Code

B. J. TOPPEL, H. H. HUMMEL, R. N. HWANG and A. L. RAGO*

MC² has been completed and is available through the Argonne Code Center. The code is described in detail in Ref. 1. A number of extensions and improvements have been incorporated into the code, as discussed below.

The hydrogen cross section generation is implemented by using analytical expressions for total and radiative capture cross sections which are built into the code. The user selects hydrogen as a material in the problem by using HYDRO as the nuclide identifier. This designator is reserved for hydrogen and may not be used for any of the library materials.

The code now requires that the reduced neutron widths, to be used in the calculation of unresolved resonance cross section, be energy dependent. Previously, only the fission widths were required to vary with energy.

Code dimensions have been enlarged so that 5500 data points can be utilized in the linear segment data portion of the library, and the code can now accept up to 800 resolved resonances in a problem. These changes improve compatibility of MC² with the ENDF/B (Evaluated Nuclear Data File) data being prepared under the supervision of Brookhaven National Laboratory.

In the course of testing the code for the calculation of the reactivity Doppler effect, it became obvious that the original treatment used for generating collapsed broad group resolved resonance cross sections was inadequate. In particular, because of the computational strategy employed for the Legendre coefficient data for elastic scattering, resonance scattering effects in the heavy elements are not properly accounted for in the calculation of the ultra fine group fundamental mode spectrum. Therefore, use of this spectrum to collapse the resolved resonance cross sections is inappropriate.

The code now obtains the broad group $(bg)J$ resolved resonance capture cross section for material $m$ using

$$\left(\overline{\sigma_c^{m}}^{bg}\right)_{resolved} = \frac{\sum_{j \text{ in } J} \left(\langle \sigma_c^{m} \rangle_j^{ufg}\right)_{resolved} \int_{E_j}^{E_{j+1}} \frac{dE}{\Sigma_t(E)} S_j^{ufg}}{\sum_{j \text{ in } J} \int_{E_j}^{E_{j+1}} \frac{dE}{\Sigma_t(E)} S_j^{ufg}}, \quad (1)$$

where

$$\langle \sigma_c^{m} \rangle_j^{ufg} = \frac{\sum_i \int_{E_j}^{E_{j+1}} \frac{\sigma_c^{m}(E)_i}{\Sigma_t(E)} dE}{\int_{E_j}^{E_{j+1}} \frac{dE}{\Sigma_t(E)}}. \quad (2)$$

$E_j$ and $E_{j+1}$ are respectively the lower and upper energy boundaries of the ultra fine group $(ufg)j$ contained within the broad group $J$. The summation in Eq. (2) is over all resonances $i$ belonging to material $m$ which contribute to the group $j$ cross section. The $\Sigma_t(E)$ includes the total resonant plus smooth background scattering for all materials in the mixture. The $S_j^{ufg}$ is the total source into the ultra fine group $j$ as calculated from the fundamental mode calculation and is a correction factor to account for the variation in the collision density across the broad group $J$.

A significant improvement has been made in the MC² code in that the total inelastic and $n,2n$ cross sections are now evaluated at the ultra fine group level. In the previous version of the code, these cross sections were evaluated at the fine-group level.

The inelastic and $n,2n$ transfer matrices are still obtained at the fine-group level, but these matrices are now normalized to the ultra fine group total inelastic and $n,2n$ absorptions for the corresponding fine group. For example, let the ultra fine group $j$ be contained in the fine group $(fg)J$. Then in the calculation of the fundamental-mode spectrum, the source into ultra fine group $j$ due to inelastic scattering, $S_{inel_j}^{ufg}$, is now evalu-

* Applied Mathematics Division, Argonne National Laboratory.

ated as

$$S^{ufg}_{inel_j} = \sum_{K \neq J} \sum_{k \text{ in } K} \Sigma^{ufg}_{inel_k} \phi^{ufg}_k \frac{\Sigma^{fg}_{inel_{K \to J}}}{\Sigma^{fg}_{inel_K}} \frac{\Delta e_j}{\Delta e_J} . \quad (3)$$

In Eq. (3), $\Sigma^{ufg}_{inel_k}$ is the total macroscopic inelastic cross section for *ufg* $k$, $\phi^{ufg}_k$ is the flux for *ufg* $k$, $\Sigma^{fg}_{inel_{K \to J}}$ is the macroscopic inelastic scattering cross section from *fg* $K$ to *fg* $J$, and $\Sigma^{fg}_{inel_K}$ is the total macroscopic inelastic cross section for *fg* $K$. The $\Delta e_j$ and $\Delta e_J$ are, respectively the energy widths of the *ufg* $j$ and the *fg* $J$.

The corresponding loss term in the denominator of the fundamental-mode flux equation is therefore given by

$$\Sigma^{ufg}_{inel_j} \left\{ 1 - \frac{\Sigma^{fg}_{inel_{J \to J}}}{\Sigma^{fg}_{inel_J}} \right\} . \quad (4)$$

The *ufg*-treatment of inelastic scattering largely eliminates the spectral discontinuities exhibited previously at the *fg* boundaries and has a significant influence on the calculated reactivity (see Paper VI-9).


REFERENCE

1. B. J. Toppel. A. L. Rago and D. M. O'Shea, *MC²—A Code to Calculate Multigroup Cross Sections*, ANL-7318 (to be published).


## VI-3. Generation of Multigroup Cross Sections Using a Coupled MC²-THERMØS Code


D. A. SARGIS, B. J. TOPPEL and A. L. RAGO


### INTRODUCTION

In the calculation of multigroup cross sections for thermal reactors an epithermal spectrum varying as $1/E$ is often assumed. The integral transport theory thermalization program THERMØS[1,2] employs this approximation in calculating slowing down source terms into the thermal group. Likewise epithermal cross section generating codes, such as MC²[3], make various assumptions about the thermal fission source terms and other thermal group cross sections.

By coupling of fast and thermal cross section modules within the framework of the Argonne Reactor Computation System, ARC[4], some of these approximations may be eliminated. In this paper we describe some preliminary results obtained by coupling the space dependent thermalization algorithms of THERMØS and the space independent epithermal MC² program.

In the second section, the general theory is described wherein slowing down sources from an MC² computation serve as epithermal sources for the thermal calculations in THERMØS. Thermal group cross sections are then found in THERMØS by solving the integral transport equation with isotropic scattering and various thermalization scattering kernels. A consistent $P_1$ or $B_1$ module is also available for energy averaging of the spatially homogenized thermal cross sections. The $P_1$ or $B_1$ calculations require input of a buckling $B^2$ from MC² and introduce first order effects of scattering anisotropy into the thermal cross section calculations. The microscopic thermal group cross sections from THERMØS may then be used in a second MC² calculation to evaluate the effects of thermal cross section changes on epithermal cross sections and spectra. If the epithermal parameters are altered to any considerable extent, further thermal cross section calculations may be carried out using the revised slowing down terms from MC².

In the third section a discussion of results is given for three different systems. The first system is similar to the thermal Experimental Boiling Water Reactor (EBWR) lattice. A plutonium dioxide and uranium dioxide fuel region with light water moderator is assumed. The second case studied is a very undermoderated high conversion lattice (Hi-C)[5]. An extremely tight uranium dioxide lattice with light water moderator is used. The spectrum in this system is considerably harder than that in the EBWR case. The third reactor considered is a steam-cooled fast reactor with plutonium dioxide and uranium dioxide in the fuel region. This fast reactor has a somewhat softer spectrum than most sodium-cooled fast reactors, for example, and thermal fissions are not completely negligible.

Finally, some general conclusions are given regarding the results obtained by coupling of the fast and thermal cross section modules.

### GENERAL THEORY

The epithermal cross section code MC² may be used to supply space independent slowing down sources to the thermalization program THERMØS. MC² requires input of various thermal cross sections, which in the first iterate may be set equal to zero or calculated by using a $1/E$ asymptotic flux in THERMØS.

The isotropic or $P_0$ component of the microscopic slowing down source, summed over MC² groups I, to a

THERMØS group $K$ for a particular isotope $m$ is given by

$$S_K^m = \sum_I \sigma_{I\to K}^m \phi_I \tag{1}$$

where the transfer cross sections, $\sigma_{I\to K}^m$ and fluxes, $\phi_I$, are calculated in MC$^2$ for a given composition and buckling.

MC$^2$ also generates a $P_1$ or linearly anisotropic source

$$S_{K_1}^m = \sum_I \sigma_{(I\to K)_1}^m \mathbf{J}_I \tag{2}$$

where $\mathbf{J}_I$ is the neutron current for the $I$th MC$^2$ group.

Since the thermal cross section module requires source terms which are space dependent, we multiply the sources of Eqs. (1) and (2) by spatial shape factors $R_0^m(\mathbf{r})$ and $R_1^m(\mathbf{r})$, respectively, where

$$R_n^m(\mathbf{r}) \equiv \rho^m(\mathbf{r}) F_n(\mathbf{r}), \qquad n = 1, 2. \tag{3}$$

Here $\rho^m(\mathbf{r})$ is the atom density at $\mathbf{r}$, for isotope $m$ in the heterogeneous lattice. $F_0(\mathbf{r})$ and $F_1(\mathbf{r})$ are shape factors proportional to the $P_0$ and $P_1$ components of the angular flux. $F_0(\mathbf{r})$ may, for example, be approximated by bare reactor spatial distributions, by spatial results from multigroup diffusion codes, or by simply assuming flat spatial fluxes in cell calculations. In the $P_1$ approximation, $F_1(\mathbf{r})$ would be proportional to the gradient of $F_0(\mathbf{r})$.

The difficulties associated with obtaining accurate space dependent sources can be eliminated in the future by using a space dependent version of MC$^2$ or other space dependent epithermal codes such as RABBLE.[6]

Using Eq. (3) in Eqs. (1) and (2) we find the $P_0$ and $P_1$ components of the slowing down source at $\mathbf{r}$ for group $K$

$$\begin{aligned} S_{K_0}(\mathbf{r}) &= \sum_m \sum_I \rho^m(\mathbf{r}) F_0(\mathbf{r}) \sigma_{I\to K}^m \phi_I \\ S_{K_1}(\mathbf{r}) &= \sum_m \sum_I \rho^m(\mathbf{r}) F_1(\mathbf{r}) \sigma_{(I\to K)_1}^m \mathbf{J}_I, \end{aligned} \tag{4}$$

where the sum is over all isotopes $m$ at space point $\mathbf{r}$.

To obtain the total source into THERMØS from MC$^2$, we sum the $S_{K_0}(\mathbf{r})$ components over the $K$ THERMØS groups and integrate over regions into which neutrons are slowing down, giving

$$\bar{S} = \int_{Region} d\mathbf{r} \sum_K \sum_m \sum_I \rho^m(\mathbf{r}) F_0(\mathbf{r}) \sigma_{I\to K}^m \phi_I . \tag{5}$$

We require that neutron conservation be maintained. If we let $L$ be an isotropic loss operator, which includes both leakage and absorption processes over the region defined by Eq. (5), then we insist that

$$L\phi = \bar{S} \tag{6}$$

where $\phi$ is the neutron flux and $\bar{S}$ is given by Eq. (5). This condition differs from the original THERMØS version[1] which is normalized to one neutron/sec slowing down into the cell.

In solving the transport equation in THERMØS, a power iteration method is used which employs the conservation restriction of Eq. (6). In operator notation the transport equation is written

$$\phi = T(S + P\phi) \tag{7}$$

where $\phi$ is the space and energy dependent flux, $T$ is the transport kernel for isotropic scattering, $P$ is the scattering kernel, and $S$ is the space dependent slowing down source term [see Eq. (4)]. An iterative solution to Eq. (7) may be found by inserting a trial solution $\phi^i$ into the right hand side of Eq. (7) to obtain an improved result $\phi^{i+1}$ on the left hand side,

$$\phi^{i+1} = T(S + P\phi^i). \tag{8}$$

To accelerate convergence of Eq. (8), we employ a renormalization or scaling technique which utilizes Eq. (6). We require that all iterates of the flux $\phi^i$ satisfy

$$L\phi^i = \bar{S}. \tag{9}$$

Equation (8) is now written as

$$\phi^{i+1} = \alpha T(S + P\phi^i), \tag{10}$$

where $\alpha$ is a renormalization factor given by

$$\alpha = \frac{\bar{S}}{LT(S + P\phi^i)} \tag{11}$$

so that Eq. (9) is satisfied for all $i$. Convergence is then further accelerated by employing an over relaxation technique.[1]

Using the converged values of the space and speed dependent flux $\phi(\mathbf{r},v)$, various cross sections of interest are found:

$$\langle \Sigma_x \rangle = \frac{\displaystyle\int_{Reg.} d\mathbf{r} \int_{v_1}^{v_2} \Sigma_x(\mathbf{r},v)\phi(\mathbf{r},v)\, dv}{\displaystyle\int_{Reg.} d\mathbf{r} \int_{v_1}^{v_2} \phi(\mathbf{r},v)\, dv}, \tag{12}$$

where the spatial integration is usually over the entire cell, and $v_1$ and $v_2$ are the speeds corresponding to the lower and upper boundaries of a particular broad energy group.

Microscopic cross sections obtained from Eq. (12) may then be used as thermal group parameters for a second MC$^2$ calculation.

In addition to the cross sections of Eq. (12), spatially averaged cross sections, $\langle \Sigma_x(v) \rangle$, and sources, $\bar{S}_K$, may be calculated in THERMØS for use in a consistent $P_1$ or $B_1$ calculation. These are defined by

$$\langle \Sigma_x(v) \rangle = \frac{\int_{cell} \Sigma_x(\mathbf{r},v)\phi(\mathbf{r},v)\, d\mathbf{r}}{\int_{cell} \phi(\mathbf{r},v)\, d\mathbf{r}} \tag{13}$$

and

$$\begin{aligned} \bar{S}_{K_0} &= \int_{cell} d\mathbf{r} \sum_m \sum_I \rho^m(\mathbf{r}) F_0(\mathbf{r}) \sigma^m_{I\to K} \phi_I, \\ \bar{S}_{K_1} &= \int_{cell} d\mathbf{r} \sum_m \sum_I \rho^m(\mathbf{r}) F_1(\mathbf{r}) \sigma^m_{(I\to K)_1} \mathbf{J}_I . \end{aligned} \tag{14}$$

The $P1$-$B1$ module uses the space independent sources and cross sections from Eqs. (13) and (14), along with a buckling $B^2$ from MC$^2$ to compute neutron fluxes, $\phi_0(v)$, and currents, $\phi_1(v)$, in either the consistent $P_1$ or $B_1$ approximation. Both the isotropic and first Legendre components of the scattering kernels are read from the THERMØS library file, so that a first order approximation to the scattering anisotropy is utilized.

Once the fluxes and currents are obtained, thermal group averaging is easily accomplished so that

$$\begin{aligned} \Sigma_x &= \frac{\int_0^{v^*} \langle \Sigma_x(v) \rangle \phi_0(v)\, dv}{\phi} \\ &= \frac{\int_0^{v^*} \left\{ \int_{cell} \Sigma_x(\mathbf{r},v)\phi(\mathbf{r},v) d\mathbf{r} \Big/ \int_{cell} \phi(\mathbf{r},v) d\mathbf{r} \right\} \phi_0(v) dv}{\phi} \end{aligned} \tag{15}$$

$$D = \frac{-\int_0^{v^*} \phi_1(v)\, dv}{\phi} \tag{16}$$

$$\phi = \int_0^{v^*} \phi_0(v)\, dv, \tag{17}$$

where $v^*$ is the cutoff speed for the thermal group.

The user may now choose to use $P_1$ or $B_1$ microscopic cross sections from Eq. (15) as thermal group constants for input to MC$^2$ rather than the isotropic THERMØS results of Eq. (12).

The MC$^2$ module interates on $B^2$ until

$$k_{eff} = [\sum_J \nu_J \Sigma_{fJ} \phi_J]_{\text{MC}^2} + [\nu\Sigma_f\phi]_{\text{TH}}$$

converges to 1.0. Hence, if the thermal source term $[\nu\Sigma_f\phi]_{\text{TH}}$ is non-negligible and is severely altered with respect to the cross sections in the previous MC$^2$ computation, changes in $B^2$ and in the epithermal cross sections may result.

## Discussion of Results

The THERMØS cell configurations for the three systems considered are given in Table VI-3-I. In each case a cylindrical cell thermal calculation was performed with a heavy outer scattering region and reflecting boundary conditions. In Table VI-3-II the THERMØS regional compositions for the three cases are given.

TABLE VI-3-I. THERMØS Cell Configurations

| System | Fuel Rod Radius, cm | Clad Outer Radius, cm | Moderator-Coolant Outer Radius, cm |
|---|---|---|---|
| EBWR | 0.4725 | — | 0.7025 |
| Hi-C | 0.46736 | 0.5285 | 0.56127 |
| Fast | 0.3175 | 0.3556 | 0.62081 |

In Table VI-3-III calculations for the EBWR cell are given. In the first column, various mixture and individual cell material cross sections are given for an isotropic THERMØS calculation using Eq. (12) and a $1/E$ asymptotic flux above the thermal cutoff. Thirty energy groups were used up to a cutoff energy of 0.532 eV. These thermal group cross sections were then used in an MC$^2$ calculation to compute slowing down sources and fluxes. A second THERMØS calculation using only the isotropic MC$^2$ slowing down sources is given in the second column of Table VI-3-III.

From column two we see that the coupled THERMØS-MC$^2$ results differ only slightly from the ordinary $1/E$ THERMØS calculations. Of particular interest is the fact that the total number of thermal fission neutrons produced per neutron absorbed, $\eta f$, changes by only 0.03 %. $\eta f$ is the quantity which has a direct effect on the perturbation in epithermal spectra and cross sections. This is easy to see since MC$^2$ iterates on $B^2$ until $k_{eff} = \sum_J \nu_J \Sigma_{fJ} \phi_J$ converges to 1.0, where $J$ is summed over all thermal and epithermal groups. For the EBWR case considered, approximately 82 % of $k_{eff}$ comes from the thermal group below 0.532 eV. Hence, if the thermal contribution to $k_{eff}$ remains relatively constant per neutron absorbed, the epithermal cross sections should be only slightly affected.

In the third column of Table VI-3-III thermal cross sections from a 48 group THERMØS calculation extending to 1.33331 eV are tabulated. A $1/E$ asymptotic flux is again assumed above the cutoff energy, and the cross sections are edited over the first 30 groups up to 0.532 eV to compare with the previous results. Again the mixture cross sections of interest are only slightly altered.

TABLE VI-3-II. THERMØS CELL COMPOSITIONS[a]

| System | Region | U-238 | U-235 | Pu-240 | Pu-239 | H-1 | O-16 | Fe-56 |
|---|---|---|---|---|---|---|---|---|
| EBWR | Fuel | 0.02156 | — | 0.000088 | 0.000352 | — | 0.0440 | — |
| | Moderator | — | — | — | — | 0.06689 | 0.033445 | — |
| Hi-C | Fuel | 0.02207 | 0.000713 | — | — | — | 0.04554 | — |
| | Clad | — | — | — | — | — | — | 0.06879 |
| | Moderator | — | — | — | — | 0.06694 | 0.03347 | — |
| Fast | Fuel | 0.0210 | — | 0.0015 | 0.0030 | — | 0.0480 | — |
| | Clad | — | — | — | — | — | — | 0.015714 |
| | Moderator | — | — | — | — | 0.0045714 | 0.0022857 | — |

[a] Atom densities in units of $10^{24}$ atoms/cc.

TABLE VI-3-III. EBWR CELL CALCULATIONS[a]

| Cross Section | $1/E$ THERMØS (30 groups) | MC²-THERMØS[a] | | $1/E$ THERMØS[a] (48 groups) | |
|---|---|---|---|---|---|
| $\langle\Sigma_a\rangle_{mix}$ | 0.18637 | 0.18463 | (−0.93) | 0.18553 | (−0.45) |
| $\langle\nu\Sigma_f\rangle_{mix}$ | 0.29171 | 0.28889 | (−0.97) | 0.29036 | (−0.46) |
| $\eta f$ | 1.56522 | 1.56470 | (−0.03) | 1.56503 | (−0.012) |
| $\langle\Sigma_s\rangle_{mix}$ | 1.7418 | 1.7453 | (0.20) | 1.7309 | (−0.63) |
| $\langle D\rangle_{mix}$ | 0.31584 | 0.31569 | (−0.05) | 0.31775 | (0.60) |
| $\Sigma_a$-239 | 0.15343 | 0.15174 | (−1.10) | 0.15305 | (−0.25) |
| $\Sigma_a$-240 | 0.007441 | 0.007407 | (−0.45) | 0.0073726 | (−0.91) |
| $\Sigma_a$-238 | 0.016298 | 0.016269 | (−0.18) | 0.016044 | (−1.56) |
| $\Sigma_a$H | 0.009202 | 0.0092139 | (0.13) | 0.0090639 | (−1.50) |

[a] The % changes with respect to the $1/E$ 30 group THERMØS calculations are shown in the parentheses.

TABLE VI-3-IV. HI-C LATTICE CALCULATIONS

| Cross Section | $1/E$ THERMØS (27 groups) | MC²-THERMØS[a] | | $1/E$ THERMØS[a] (48 groups) | |
|---|---|---|---|---|---|
| $\Sigma_{a\ mix}$ | 0.17425 | 0.17438 | (+0.07) | 0.17131 | (−1.69) |
| $\nu\Sigma_{f\ mix}$ | 0.28042 | 0.28059 | (+0.06) | 0.27554 | (−1.74) |
| $\eta f$ | 1.60930 | 1.60907 | (−0.014) | 1.60843 | (−0.05) |
| $\Sigma_{s\ mix}$ | 0.67518 | 0.67560 | (+0.06) | 0.67717 | (0.29) |
| $D$ | 0.51544 | 0.51479 | (−0.13) | 0.51361 | (−0.35) |
| $\Sigma_a$-235 | 0.13750 | 0.13760 | (+0.07) | 0.13521 | (−1.66) |
| $\Sigma_a$-238 | 0.018429 | 0.018434 | (+0.03) | 0.018130 | (−1.62) |
| $\Sigma_a$ Fe | 0.017022 | 0.17033 | (+0.06) | 0.016691 | (−1.94) |
| $\Sigma_a$ H | 0.0013074 | 0.0013067 | (−0.05) | 0.001278 | (−2.25) |

[a] The % changes with respect to the $1/E$ 27 group THERMØS calculations are shown in the parentheses.

The 48 group problem extends beyond the large Pu-240 resonance at 1.056 eV. Because of the Pu-240 present in this problem, the spectrum above 0.532 eV undoubtedly is not $1/E$. However, the 30 group problem which makes this assumption for the asymptotic flux still gives reasonably accurate results as compared with the MC²-THERMØS and 48 group THERMØS calculations.

In Table VI-3-IV thermal cross sections are given for a very tight Hi-C lattice. For this case $B^2 \approx -3.56 \times 10^{-3}/\text{cm}^2$ and only 27 % of $k_{eff}$ comes from the thermal group. Approximately 65 % of $k_{eff}$ comes from below 2.03 keV. Cross sections from a 27 group THERMØS with a $1/E$ asymptotic flux above the cutoff energy of 0.428 eV are listed in column one. Column two lists results from a THERMØS calculation employing isotropic slowing down sources from MC². These cross sections are very close to the usual $1/E$ THERMØS calculations. For completeness column three includes 48 group results which are edited over the first 27 groups. Again the simple 27 group THERMØS using $1/E$ asymptotic fluxes above 0.428 eV compares favorably with the more rigorous 48 group computation.

Since $\eta f$ in the MC²-THERMØS calculation differs from the 27 group THERMØS result by only 0.014 %, it is apparent that a second MC² calculation will be only very slightly affected by using the new thermal group cross sections. This is also evident since the spectrum in this lattice is harder than that in EBWR and the major portion of the fission source comes from the epithermal region.

In Table VI-3-V thermal cross sections are given for a steam-cooled fast reactor lattice. Column one again lists various thermal cross sections obtained from a $1/E$ THERMØS calculation with a cutoff energy of 0.532 eV. In column two, thermal cross sections are given utilizing isotropic slowing down sources from MC².

For the fast reactor, there are larger percent changes in the thermal cross sections than in the EBWR and Hi-C calculations. $\eta f$ in this case changes by almost 1 %. However, only about 1.82 % of $k_{eff}$ comes from the thermal group below 0.532 eV. Therefore, we would again expect subsequent MC² calculations to be only slightly altered by using the revised thermal cross sections.

A second MC² problem was run using the revised thermal cross sections from column two of Table VI-3-IV. The second MC² calculation was found to be very insensitive to the new thermal cross sections. $B^2$ changed from $5.67161 \times 10^{-4}/cm^2$ to $5.67985 \times 10^{-4}/cm^2$. The spectrum and epithermal cross sections were perturbed even less, with maximum changes in the spectrum of only a few hundredths of a percent.

In column three a $1/E$ THERMØS calculation using 48 groups is given for comparison. The 48 group calculation differs slightly from the 30 group THERMØS for the mixture cross sections. The individual cell material cross sections are altered to a greater extent. Again the introduction of Pu-240 with its large 1.056 eV resonance in the 48 group and MC² calculations, does not introduce large perturbations as compared with the 30 group results.

TABLE VI-3-V. FAST REACTOR THERMAL CROSS SECTIONS

| Cross Section | $1/E$ THERMØS (30 groups) | MC²-THERMØS[a] | | $1/E$ THERMØS[a] (48 groups) | |
|---|---|---|---|---|---|
| $\Sigma_{a\ mix}$ | 0.42166 | 0.42497 | (0.78) | 0.42421 | (0.60) |
| $\nu\Sigma_{f\ mix}$ | 0.67391 | 0.68540 | (1.70) | 0.68080 | (1.02) |
| $\eta f$ | 1.59823 | 1.61282 | (0.91) | 1.60487 | (0.41) |
| $\Sigma_{s\ mix}$ | 0.18370 | 0.18368 | (−0.01) | 0.18066 | (−1.65) |
| $D_{mix}$ | 4.0025 | 3.9567 | (−1.14) | 4.0449 | (1.06) |
| $\Sigma_a$-239 | 0.37732 | 0.38378 | (1.71) | 0.38381 | (1.72) |
| $\Sigma_a$-240 | 0.039651 | 0.36470 | (−8.02) | 0.035992 | (−9.23) |
| $\Sigma_a$-238 | 0.0031180 | 0.0030863 | (−1.02) | 0.002909 | (−6.70) |
| $\Sigma_a$ H | 0.00049383 | 0.00051315 | (3.91) | 0.0004693 | (−4.97) |

[a] The % changes with respect to the $1/E$ 30 groups THERMØS calculations are shown in the parentheses.

## CONCLUSION

By coupling of the epithermal MC² and the thermal THERMØS codes, we have been able to generate multigroup cross sections without introducing certain simplifying assumptions, such as a $1/E$ asymptotic flux. Our results indicate, however, that for the three systems considered $1/E$ THERMØS cross sections are quite accurate. Even for systems with a large Pu-240 resonance, the $1/E$ approximation gave favorable results.

One reason for the great success of the usual $1/E$ THERMØS calculation is no doubt due to the fact that hydrogen is the dominant moderator in all of these problems. For a hydrogen moderator, the slowing down source is independent of the final energy. Therefore, the spectral form of the asymptotic flux is immaterial for hydrogen scattering. The heavier moderators are affected by the shape of the asymptotic flux but play a secondary role in slowing down of epithermal neutrons.

Some further test problems were run using plutonium fuel rods and $D_2O$ moderator in place of $H_2O$. The cross sections in these cases were altered to a larger extent than the $H_2O$ problems, when the Pu-240 resonance was introduced. However, again $\eta f$ was changed by only fractions of a percent even in these more drastic cases.

In addition, THERMØS test problems using asymptotic fluxes varying as $E^N$, where $N$ is an arbitrary number, have been run. In these problems, moderators of various mass were used. Once again the thermal cross sections varied only slightly with changing asymptotic flux shapes. For hydrogen scattering there was no change in the cross sections as the epithermal flux was modified.

Our results indicate that for the problems considered, accurate multigroup cross sections may be obtained without resorting to coupled fast and thermal codes. Only for problems in which great accuracy is required would a coupled computation system be necessary. In these cases, it would also be appropriate to introduce space dependent epithermal cross section modules to accurately determine the spatial shape of the slowing down sources. In the calculations presented here, we have used only flat spatial slowing down sources in each cell region. It would also be useful to include the $P_1$ components of the slowing down sources available from the MC² calculations. Only the isotropic $P_0$ components were used in the results presented in this paper.

It should also be pointed out that the fast reactor cross sections were very insensitive to the thermal cross sections used in MC². The steam-cooled system has a non-negligible contribution to $k_{eff}$ from the thermal group and provides a good test of this sensitivity. For harder systems, such as a sodium-cooled fast reactor, the epithermal cross sections and spectra are much less sensitive to the thermal cross sections employed.

## REFERENCES


1. H. C. Honeck, *A Thermalization Transport Theory Code for Reactor Lattice Calculations*, BNL-5826 (September 1961).
2. B. J. Toppel and I. Baksys, *The Argonne-Revised THERMØS Code*, ANL-7023 (1965).
3. D. M. O'Shea, B. J. Toppel and A. L. Rago, *MC²—A Code to Calculate Multigroup Cross Sections*, ANL (to be published).
4. C. N. Kelber, G. Jensen, L. Just and B. J. Toppel, *The Argonne Reactor Computation System, ARC*, Proc. International Conference on Research Reactor Utilization and Reactor Mathematics, Mexico City (May 1967).
5. E. M. Pennington, *Analysis of High Conversion Critical Experiments*, ANL-7270 (1966).
6. P. H. Kier, *A Method of Computing Resonance Integrals in Multi-Region Reactor Cells*, Proc. International Conference on Research Reactor Utilization and Reactor Mathematics, Mexico City (May 1967).

# VI-4. Fortran Codes for Processing Neutron Cross Section Data

E. M. Pennington, J. C. Gajniak and W. Bohl

The evaluation and compilation of neutron cross section data and the processing of the data to produce library tapes suitable for input to codes such as MC²(1) requires the use of many computer codes. A code called MERMC2 has been written to merge data from two MC² library tapes to produce one new library tape. Four of the codes, which were written as part of the Evaluated Nuclear Data File/B (ENDF/B) project and distributed to members of the Cross Section Evaluation Working Group, have been made operational on the CDC-3600. Also, improvements have been made in the program to plot data from the MC² library tape and in codes used in the study of elastic scattering angular distributions.

## MERMC2

The MERMC2 code, written in CDC-3600 FORTRAN, requires as input two binary library tapes with neutron cross section data in the MC² library format.[1] A third MC² library tape is produced, which contains data from the two input tapes, with deletion of some materials if desired.

An MC² library tape may be produced originally with the aid of the LIB9 program,[1] using the appropriate card input, or by using the ETØE program, described below, which requires an ENDF/B tape as input. Thus MERMC2 makes it possible to produce a library tape containing both ENDF/B data and non-ENDF/B data for comparative calculations. Also a few new materials may be added to an existing MC² library tape by running ETØE or LIB9 problems for the new materials only and then using MERMC2. Formerly it was necessary to run ETØE or LIB9 for all materials, thereby using more computer time than is now required.

An MC² library tape consists of six files containing the $W$-table, a table of contents and resonance data, smooth cross sections, inelastic and $(n,2n)$ secondary energy distributions, fission spectra, and elastic scattering Legendre coefficients. The $W$-table contains the real and imaginary parts of the complex probability function and is used in the calculation of the $\psi$ and $\chi$ Doppler-broadening functions.[1] The MERMC2 code reads data in a given file, first from one tape and then the other, and writes it on the new library tape unless the deletion of the material was specified in the input. Since in using ETØE it is possible to produce a library tape without a $W$-table, provision is made to read the $W$-table from a third input tape if neither of the two tapes being merged contains a $W$-table. If the table of contents on either input tape does not agree with that specified in the MERMC2 card input, the processing of the data is stopped. The arrangement of the data in the Legendre coefficient file is such that a scratch tape is necessary for processing this file.

Printed output from MERMC2 consists of a list of the materials on the merged library tape, followed by a series of messages. A message is printed when each material in each file is processed. Thus, if the MERMC2 run should terminate abnormally, with a parity error, for example, the source of the difficulty can be easily located.

## ENDF/B Processing Codes

The FORTRAN codes, CHECKER, CRECT, DAMMET, and ETØE, which were written as part of the ENDF/B cross section project, have been made operational on the CDC-3600. Listings of these codes have been studied in detail in an attempt to find any errors, and various test problems have been run. Brief outlines of these codes are presented below.

## CHECKER

The CHECKER code[2] checks ENDF/B BCD tapes mainly for "bookkeeping" type errors. A small amount of physics checking is also done. Various minor revisions, suggested in ENDF/B newsletters, have been made in the original version of the code. All of the ENDF/B data received so far have been run through CHECKER.

## CRECT

The CRECT Program[2] is used to correct ENDF/B BCD tapes. The input ENDF/B tape is copied onto another tape, with the corrections being made as the copying proceeds. Corrections consist of deleting cards, inserting cards, or changing certain fields of existing cards. The CRECT code has proven to be quite useful, especially for correcting keypunch-type errors.

## DAMMET

The name of this code stands for *D*elete, *A*lter *M*ode, and *M*erge *E*NDF/B *T*apes. The code[2] accepts as input either one or two ENDF/B tapes and produces as output a third ENDF/B tape, with deletions if desired. There are three modes possible for ENDF/B tapes. These are (1) a BCD tape in the standard configuration, (2) a binary tape in the standard configuration, and (3) a binary tape in the alternate configuration. The term

"standard configuration" means that data are arranged in order of materials, with all data for the first material followed by all data for the second material, etc. "Alternate configuration" means that data are arranged in order of files, with the first file for all materials followed by the second file for all materials, etc. A file contains data of a particular type, such as resonance parameters or smooth cross sections, for example.

The preliminary version of DAMMET was run on the Argonne CDC-3600 by T. Pitterle* and D. Green.* They used DAMMET to convert from mode (1) to mode (3), since ETØE requires such a binary input tape. The corrections and improvements in the version of DAMMET distributed from Brookhaven National Laboratory have been made in the preliminary version. DAMMET has been used extensively to convert from mode (1) to mode (3) and to merge two mode (3) tapes to yield another mode (3) tape.

### ETØE

The ETØE code[3] (*ENDF/B TØ* MC² = *E*) converts data from an ENDF/B binary tape in the alternate configuration into a binary library tape in the format required by the MC² code.

Certain sections of ENDF/B data require only alteration of formats and ordering of the data for compatibility with MC². This category includes resonance parameters, smooth cross sections, and secondary energy distributions. Other ENDF/B data, however, can require considerable processing by ETØE. Since MC² requires that the scattering cross section be smooth without the resonance scattering being calculated, ETØE calculates the resonance scattering cross section and adds the calculated values to the smooth ENDF/B values to produce the smooth values as used by MC². Another area requiring considerable processing by ETØE is the angular dependence of elastic scattering. MC² requires angular expansions for specific energy points (2041 energies) involving products of the scattering cross section and the Legendre polynomial expansion coefficients in the center of mass system using the normalization of ENDF/B. ENDF/B permits both Legendre expansion coefficients at arbitrary energies or tabulations of probabilities versus the cosine of the scattering angle. When tabulations are given, ETØE fits Legendre expansions to the given distributions. The necessary normalization of the Legendre expansions, multiplication by the scattering cross section, and ordering of the angular data for MC² are carried out by ETØE.

The ETØE code was run by T. Pitterle and D. Green to produce a tape containing five materials from the first ENDF/B distribution. This tape was used to run an MC² problem to completion. Other tapes have also been produced by ETØE and used successfully with MC². However, the ETØE code is not yet completely debugged. A few errors have been found, mainly in seldom-used paths. The ETØE program is long and complex, and further study of the listing and testing of the code must be done before trouble-free operation can be assured.

* Atomic Power Development Associates, Detroit, Michigan.

## Improvements in Existing Codes

### MC² library plotting program

The program[4] for plotting data from the MC² cross section library tape using the Calcomp plotter has been revised with many improvements. Almost any arbitrary selection of data can now be plotted during one computer run. Previously it was only possible to plot the entire tape. Also the Legendre coefficient data can now be plotted. When the program was originally written the Legendre data was on a separate tape.

### Scattering angular distribution codes

Some modifications have been made in the SAD program,[5] which is used in the study of elastic scattering angular distributions. The use of a logarithmic *Y*-axis in plotting the angular cross section, $d\sigma/d\Omega$, versus the cosine of the scattering angle is now possible. This is useful in plotting angular distributions at high energy, which are strongly peaked in the forward direction. Another change allows cards to be punched with Legendre coefficients in the ENDF/B normalization, as well as in the MC² normalization available previously.

The DRIVER program, which reads Legendre coefficients punched by SAD at a number of energies and plots coefficients for each angular momentum component, $l$, as a function of energy, has been modified to accept input cards in the ENDF/B normalization as well as in the MC² normalization.

An ANL topical report[6] has been written which describes the SAD and DRIVER programs in detail.

### Flow diagrams

Figures VI-4-1 and VI-4-2 illustrate the preparation of library tapes for MC² beginning with the basic data evaluation. Figure VI-4-1 shows the case of preparation of the basic data in the ENDF/B format. The codes CHAD,[7] ABACUS,[8,9] OPTIC[10] and 2-PLUS[11] have been widely used by cross section evaluators. In Fig. VI-4-2 the compilation of data in the MC² card format is shown. Here LEDGYW is a revised version of LIB9,[1] which combines the data from the *W*-table tape, the card input data, and the Legendre coefficient data to produce the MC² library tape. The original

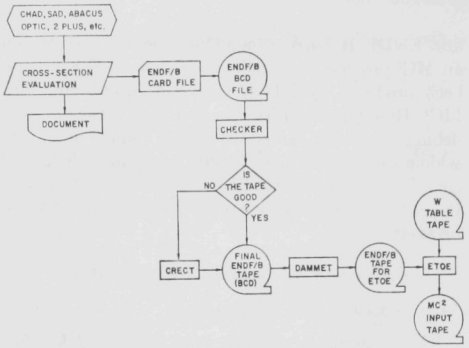


FIG. VI-4-1. Preparation of an MC² Library Tape from Basic Data in the ENDF/B Format. *ANL Neg. No. 112-8891.*

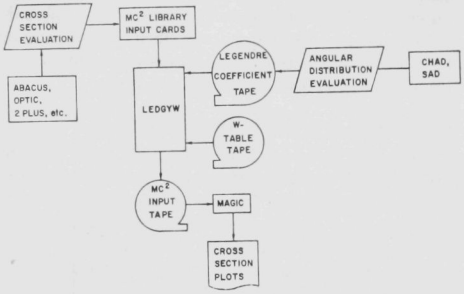


FIG. VI-4-2. Preparation of an MC² Library Tape from Basic Data in the MC² Card Format. *ANL Neg. No. 112-8888.*

LIB9 program produced a tape from the card input which was later combined off-line with the *W*-table and Legendre coefficient data to produce the final MC² library tape. The program MAGIC in Fig. VI-4-2 is the revised MC² library plotting program mentioned above.

### REFERENCES

1. B. J. Toppel, A. L. Rago and D. M. O'Shea, *MC²—A Code to Calculate Multigroup Cross Sections*, ANL-7318 (1967).
2. H. C. Honeck, U. S. Atomic Energy Commission, and J. Felberbaum, Brookhaven National Laboratory, (members of the Cross Section Evaluation Working Group), private communication.*
3. D. M. Green and T. A. Pitterle, *ETØE, A Program for ENDF/B to MC² Data Conversion*, APDA Technical Memorandum No. 44 (March 31, 1967).
4. D. M. O'Shea, J. J. Zenor and P. L. Walker, *Aids for Maintaining and Checking an Evaluated Nuclear Data File*, Reactor Physics Division Annual Report, July 1, 1964 to June 30, 1965, ANL-7110, pp. 342-343.
5. E. M. Pennington, R. A. Mewaldt and J. Gajniak, *Codes for the Analysis of Elastic Scattering Angular Distributions*, Reactor Physics Division Annual Report, July 1, 1965 to June 30, 1966, ANL-7210, pp. 399-401.
6. E. M. Pennington, J. C. Gajniak and R. A. Mewaldt, *Programs for Analysis of Scattering Angular Distributions*, ANL-7306 (1967).
7. R. F. Berland, *CHAD, Code to Handle Angular Data*, NAA-SR-11231 (December 1965).
8. E. H. Auerbach et al., *Abacus-1: A Program for the Calculation of Nuclear Cross Sections Using the Cloudy Crystal Ball Model*, KAPL-3020 (June 1, 1964).
9. E. H. Auerbach, *Abacus-2 (Revised Version), Program Operation and Input Description*, BNL-6562 (November 1962).
10. D. T. Goldman, et al., *OPTIC—A Program for the Calculation of Nuclear Cross Sections and Legendre Moments Using the Optical Model*, KAPL-3085 (May 1965).
11. C. Dunford, *2-PLUS, A Nonspherical Optical Model for Fast Neutron Cross Sections*, NAA-SR-11706 (1966).

* It is planned to publish the proceedings of the Cross Section Evaluation Working Group (CSEWG).

## VI-5. ADRIFT, A Code to Compute Bilinearly-Weighted Absorption Cross Sections

P. H. KIER

The feasibility of applying the bilinear weighting technique to Doppler effect studies is under serious consideration. The preliminary objective is to calculate bilinearly-weighted absorption cross sections and to study the variation of the adjoint function across capture and fission resonances.

ADRIFT has been written to provide a means of obtaining bilinearly-weighted absorption and fission cross sections and the detailed lethargy dependent adjoint flux for infinite, homogeneous systems. Reaction rates are computed for extremely narrow, fine groups and are accumulated over broad groups to obtain effective cross sections. ADRIFT permits 20,000 fine groups, 50 broad groups and 10 nuclides, three of which may be resonant absorbers.

### THEORY

The bilinearly-weighted absorption cross section for an arbitrary lethargy interval $(u_2 - u_1)$ is defined as

$$\bar{\sigma}_n = \frac{\int_{u_1}^{u_2} du\ \sigma_a(u)\phi(u)\phi^*(u)}{\frac{1}{u_2 - u_1}\int_{u_1}^{u_2} du\ \phi(u)\int_{u_1}^{u_2} du\ \phi^*(u)} \quad (1)$$

where $\phi(u)$ is the real flux and $\phi^*(u)$ is the adjoint flux. $\phi(u)$ is obtained from the solution of the slowing down equation:

$$\Sigma(u)\phi(u) = S(u) + \sum_{i=1}^{n}\int_{u-\epsilon_i}^{u} du' e^{-(u-u')}\Sigma_{si}(u')\phi(u')/(1-\alpha_i), \quad (2)$$

where

$$S(u) = \chi(u)\sum_{i=1}^{n}\int_0^\infty \nu_i(u')\Sigma_{fi}(u')\phi(u')\,du' \quad (3)$$

$\epsilon_i \equiv$ maximum lethargy increment per collision with nuclide $i$

$\alpha_i \equiv [(A_i - 1)/(A_i + 1)]^2$, where $A_i$ is the mass of nuclide $i$

$\Sigma_{si}(u) \equiv$ macroscopic scattering cross section of nuclide $i$

$\nu_i(u) \equiv$ nuclide yield per fission of nuclide $i$

$\Sigma(u) \equiv$ total macroscopic cross section

$\chi_i(u) \equiv$ fraction of neutrons born in fission in $du$ about $u$

$\Sigma_{fi}(u) \equiv$ macroscopic fission cross section of nuclide $i$

The adjoint flux, $\phi^*(u)$ is determined from the solution of the integral equation obtained by transposing the operators in Eq. (2):

$$\Sigma(u)\phi^*(u) = \sum_{i=1}^{n}\left\{\nu_i(u)\Sigma_{fi}(u) + \Sigma_{si}(u)\cdot\int_u^{u+\epsilon_i} du' e^{-(u'-u)}\phi^*(u')/(1+\alpha_i)\right\} \quad (4)$$

where $\phi^*(u)$ is normalized such that

$$\int_0^\infty du\phi^*(u)\chi(u) = 1$$

It is assumed that the energy range of interest is far below the range within which neutrons are born. Hence, in Eq. (3), $\chi(u) = 0$ and in Eq. (2), $S(u) = 0$. The energy range of interest is divided into many narrow intervals having equal lethargy widths much less than the maximum lethargy increment per collision with the heaviest of nuclides. The integrals in Eqs. (1), (2) and (4) are then approximated by summations over the appropriate number of these intervals. When this is done double summations appear in Eqs. (2) and (4). A recurrence relation for the slowing down source is used to reduce the double summations to single summations as was done in the RIFF-RAFF Code.[1]

### Reference

1. P. H. Kier, *RIFF-RAFF, A Program for Computation of Resonance Integrals in a Two-Region Cell*, ANL-7033 (1965).

## VI-6. RABBLE and RABZPR: Two Codes to Compute Resonance Absorption in Multi-Composition Reactor Cells

P. H. Kier

### Introduction

The standard methods of computing resonance absorption in heterogeneous systems are based on several interdependent assumptions: the narrow resonance approximation in the moderator, flat slowing down sources in the fuel, widely spaced resonances, and a resonance escape probability near unity. As these assumptions are usually valid for thermal reactors, the standard methods usually yield sufficiently accurate computations of resonance absorption for this type of reactor. Even so, there are situations where these approximations introduce significant errors in the calculation of resonance absorption by fertile materials as shown by the measurements of W. Foell[1] and the calculations of S. Iijina[2] and of P. Kier.[3]

In fast reactors, the moderator, which can have significant resonances, is usually not a light material and absorption by the closely spaced resonances of fissile materials is very important. Therefore the standard methods can be expected to be inaccurate because the assumptions upon which they are based are not valid.

Partly in response to the requirement of fast-reactor analysis, several methods[3-6] of computing resonance absorption which use space and lethargy dependent slowing down sources have been developed in recent years. However, except for Monte Carlo techniques, these methods are either unwieldy or restricted to a two-re-

gion cell with resonances only in the fuel. A formulation for multi-composition cells has been developed to provide a versatile and precise method of computing resonance absorption. Since restrictions are not placed on cross sections, this formulation permits resonances in any composition and non-uniform temperature distributions. This formulation has been used to write a computer code, RABBLE, for the CDC-3600 computer.

RABBLE[7,8] is a versatile code in which five compositions can be subdivided into twenty regions and which uses the zero current condition at the boundary of the cell. This is the appropriate boundary condition for most reactor cells but not for many cells in critical assemblies as, for example, ZPR-6 and ZPR-9. These assemblies contain drawers with variable material arrangement.[9] A cell, which may be made up of several drawers, does not necessarily have midplane symmetry. Therefore, to provide a means of analyzing measurements with such non-symmetric loadings a version of RABBLE, which is restricted to slab cells, has been written for cells with periodic boundary conditions. This computer code is called RABZPR.

## Theory Used in RABBLE

The reactor cell is divided into regions and the energy range of interest is divided into many narrow, or fine, groups. As the resonance cross section, and therefore the flux distribution, are rapidly varying functions of energy, the fine groups must be extremely narrow if resonance absorption is to be described adequately. We shall specify that the fine group is narrow compared with the maximum lethargy gain per collision with the heaviest of nuclides and we can assume, therefore, that a neutron has only one collision within a fine group. This collision will cause the neutron to be removed from the group either because it is absorbed or because it is scattered out of the group. Since a neutron will have only a single collision in a fine group, it is appropriate to use an integral transport theory formulation based on first-flight escape and transmission probabilities.

Since integral transport theory is used, the basic quantity computed is the regional, fine-group collision rate, $C_{ij}$. With use of cross sections we obtain reaction rates and fluxes. The reaction rate for process $z$ (fission, absorption or scattering) for material $m$ for fine group $i$ and region $j$ is simply

$$ {}_zR_{ij}^m = C_{ij}({}_z\Sigma_{ij}^m/\Sigma_{ij}), \tag{1} $$

where ${}_z\Sigma_{ij}^m$ is the macroscopic cross section for the process and $\Sigma_{ij}$ is the total macroscopic cross section. The integrated flux is

$$ \phi_{ij} = C_{ij}/\Sigma_{ij} . \tag{2} $$

The effective cross section for a broader energy span is the ratio of the accumulated reaction rate to the accumulated integrated flux.

In this formulation, the collision rate is obtained from expressions involving the slowing down sources, the first-flight escape and transmission probabilities, and the interface currents. First, an expression for the slowing down source is developed. Then for each geometry option, expressions are developed for the collision rates, interface currents and escape and transmission probabilities.

### Slowing down source

The calculation of the regional slowing down is based on the assumption that neutrons are scattered elastically and isotropically in the laboratory system. It is also assumed that the source is uniform within a region. As the source is allowed to vary from region to region and as a composition can be divided into several regions, the space and lethargy dependence of the slowing down source can be approximated accurately by this method.

The source for a region for the $k$th fine group is

$$ S_k = \sum_{j=1}^{J} \sum_{n=1}^{L_j} P_{nj} \Sigma_{s_{k-n,j}} \phi_{k-n} \Delta u_f , \tag{3} $$

where

$P_{nj} \equiv$ probability per unit lethargy that a neutron is scattered down $n$ groups in a scattering collision with material $j$

$L_j \equiv$ maximum number of groups through which a neutron can be down-scattered in a scattering collision with material $j$

$\Sigma_{s_{k-n,j}} \phi_{k-n} \equiv$ rate at which neutrons are scattered by material $j$ in group $k - n$

$\Delta u_f \equiv$ lethargy width of a fine group.

Equation (3) would be an extremely time consuming expression to evaluate numerically because a neutron can be scattered through so many groups. Fortunately, however, the form of $P_{nj}$ permits $S_k$ to be expressed in a much more suitable form. $P(u - u')$, the probability per unit lethargy that a neutron is scattered from lethargy $u'$ to $u$ is given by

$$ P(u - u') = \begin{cases} \dfrac{1}{1 - \alpha} e^{-(u - u')}, & u \geq u' \geq u - \epsilon \\ 0, & u' < u - \epsilon \end{cases} \tag{4} $$

where $\alpha = [(A - 1)/(A + 1)]^2$, $\epsilon = 2 \ln [(A + 1)/(A - 1)]$ and $A$ is the mass of the scattering material. The probability of a neutron being scattered through $n$ groups of width $\Delta u$ is then

$$P_n\Delta u = \frac{1}{1-\alpha}\int_{u_0}^{u_0+\Delta u} du \int_{u_0-n\Delta u}^{u_0-(n-1)\Delta u} du' \cdot \exp\left[-(u-u')\right]$$

$$= \frac{1}{1-\alpha}(1-e^{-\Delta u})^2 e^{-(n-1)\Delta u} \tag{5}$$

$$\approx \frac{\Delta u}{1-\alpha}(1-e^{-\Delta u})(1-\Delta u/2)e^{-(n-1)\Delta u}$$

$$\approx \frac{\Delta u}{1-\alpha}(1-e^{-\Delta u})e^{-(n-1)\Delta u}.$$

Because $P_n = e^{-\Delta u}P_{n-1}$, Eq. (3) can be reduced to

$$S_k = \exp(-\Delta u_f)S_{k-1} + \sum_{j=1}^{J} P_{1j}\,\Sigma_{s_{k-1,j}}\,\phi_{k-1} - \exp(\Delta u_f)\sum_{j=1}^{J} P_{L_j,j}\,\Sigma_{s_{k-L_{j-1},j}}\,\phi_{k-L_j-1}. \tag{6}$$

In Eq. (6), we need evaluate only two terms for each material. Although evaluation of Eq. (6) does not require excessive time, it does require excessive memory for the storage of the fine group fluxes and scattering cross sections. We shall introduce the intermediate group which contains a specified number of fine groups and we shall specify that the width of an intermediate group is less than the maximum lethargy gain per collision with the heaviest material present. Then the fine group scattering rates of the last term on the right side of Eq. (6) will be approximated by the intermediate group scattering rate divided by the number of fine groups per intermediate group. This approximation, which is reasonable since the intermediate group is narrow itself, permits $S_k$ to be computed from the source and scattering rates for the $(k-1)$th fine group and the intermediate group scattering rates, thus greatly reducing storage requirements.

## COLLISION RATES

We shall develop expressions for the regional, fine group collision rates in terms of the slowing down sources, interface currents and first-flight escape and transmission probabilities for the four geometry options.

### *Homogeneous Cell*

Although RABBLE has been written for the computation of resonance absorption in heterogeneous reactor cells, it does have a space independent option because of the simplicity of this homogeneous case. Because the fine group is narrow, a neutron will have only one collision within a fine group. Therefore neutron conservation requires that the collision rate must equal the rate at which neutrons are slowed down into the group; that is,

$$C_i = S_i. \tag{7}$$

### *Cylindrical Cell*

For a cell described in terms of cylindrical coordinates, the outer boundary of the cell is assumed to be circular. With the assumption of cosine currents at the interfaces between regions, the collision rates are obtained in terms of the following quantities:

$J_i^+ \equiv$ cosine current impinging on the inner surface of the $(i+1)$th region
$J_i^- \equiv$ cosine current impinging on the outer surface of the $i$th region
$P_i^+ \equiv$ escape probability through outer surface of $i$th region for flat volume source
$P_i^- \equiv$ escape probability through inner surface of $i$th region for flat volume source
$T_i^{OI} \equiv$ transmission probability from inner to outer surface of $i$th region
$T_i^{IO} \equiv$ transmission probability from outer to inner surface of $i$th region
$T_i^{OO} \equiv$ transmission probability from outer to outer surface of $i$th region

If the center region is the first region and the outermost region is the $I$th region, then the collision rates are

$$C_i = \begin{cases} (1-T_i^{OO})J_i^- + (1-P_i^+)S_i, & i=1 \\ (1-T_i^{OI})J_{i-1}^+ + (1-T_i^{OO}-T_i^{IO})J_i^- & \\ \quad + (1-P_i^+-P_i^-)S_i, & i=2,1. \end{cases} \tag{8}$$

The interface currents are obtained from the statement of neutron conservation at each interface and the assumption of isotropic return at the outer boundary of the cell:

$$J_1^+ = \begin{cases} T_i^{OO}J_i^- + P_i^+S_i, & i=1 \\ T_i^{OI}J_{i-1}^+ + T_i^{OO}J_1^- + P_i^+S_i, & i=2,I \end{cases} \tag{9}$$

$$J_i^- = \begin{cases} T_{i+1}^{IO}J_{i+1}^- + P_{i+1}^-S_{i+1}, & i=1,I-1 \\ J_i^+, & i=I. \end{cases} \tag{10}$$

Equations (9) and (10) yield $2I$ equations in $2I$ unknown interface currents. These equations are readily solved by Gauss-Jordan reduction. The first flight escape and transmission probabilities that appear in these equations are expressed[7,8] in terms of integrals of Bickley functions, $Ki_n(\chi)$.

### *Slab Cell—Cosine Interface Currents*

Although the assumption of cosine interface currents introduces little error for a circular cell, it might intro-

duce appreciable error for a slab cell because of the properties of plane geometry. Therefore, RABBLE has two options for the slab cell: one based on cosine interface currents and another which allows for both cosine and (cosine)$^2$ interface currents.

For the option which is based on cosine interface currents, the collision rate is expressed in terms of the following quantities:

$J_i^+ \equiv$ cosine current impinging on the inner surface of the $(i+1)$th region

$J_i^- \equiv$ cosine current impinging on the outer surface of the $i$th region

$P_i \equiv$ escape probability from the $i$th region for a flat volume source

$T_i \equiv$ transmission probability through the $i$th region for a cosine surface current.

The collision rate in terms of these quantities is

$$C_i = \begin{cases} 2(1-T_i)J_i^- + (1-P_i)S_i, \\ \qquad\qquad i = 1 \\ (1-T_i)(J_i^- + J_{i-1}^+) + (1-P_i)S_i, \\ \qquad\qquad i = 2,I. \end{cases} \tag{11}$$

As before, the interface currents are obtained from the statement of neutron conservation at the interfaces and isotropic return at the boundary of the cell.

$$J_i^+ = \begin{cases} T_iJ_i^- + (\tfrac{1}{2})P_iS_i, & i = 1 \\ T_iJ_{i-1}^+ + (\tfrac{1}{2})P_iS_i, & i = 2,I \end{cases} \tag{12}$$

$$J_i^- = \begin{cases} T_{i+1}J_{i+1}^- + (\tfrac{1}{2})P_{i+1}S_{i+1}, & i = 1,I-1 \\ J_i^+, & i = I. \end{cases} \tag{13}$$

Equations (12) and (13) form a system of $2I$ equations in the $2I$ unknown interface currents that is readily solved by Gauss-Jordan reduction. For this case, only one escape probability, $P_i$, and one transmission probability, $T_i$, are needed. $P_i$ is the current emerging from the $i$th region for a unit uniform volume source in that region. Similarly, $T_i$ is the current emerging from the $i$th region for a unit cosine incident surface current. These quantities are given by

$$P_i = \frac{1}{\tau}\{\tfrac{1}{2} - E_3(\tau)\} \tag{14}$$

and

$$T_i = 2E_3(\tau), \tag{15}$$

where $\tau$ is the thickness of the region in mean free paths and $E_n(\tau)$ is the $n$th order exponential integral function.

*Slab Cell—Cosine and (Cosine)$^2$ Interface Currents*

For this option the collision rate is expressed in terms of the following quantities:

$J_{0,i}^+ \equiv$ cosine component of the current impinging on the inner surface of the $(i+1)$th region

$J_{1,i}^+ \equiv$ (cosine)$^2$ component of the current impinging on the inner surface of the $(i+1)$th region

$J_{0,i}^- \equiv$ cosine component of the current impinging on the outer surface of the $i$th region

$J_{1,i}^- \equiv$ (cosine)$^2$ component of the current impinging on the outer surface of the $i$th region

$P_{0,i} \equiv$ contribution to cosine component of the current leaving the $i$th region from unit volume source

$P_{1,i} \equiv$ contribution to (cosine)$^2$ component of the current leaving the $i$th region from unit volume source

$T_i^{00} \equiv$ contribution to cosine component of the current leaving the $i$th region from unit, incident cosine current

$T_i^{10} \equiv$ contribution to (cosine)$^2$ component of the current leaving the $i$th region from unit, incident cosine current

$T_i^{01} \equiv$ contribution to cosine component of the current leaving the $i$th region from unit, incident (cosine)$^2$ current

$T_i^{11} \equiv$ contribution to (cosine)$^2$ component of the current leaving the $i$th region from unit, incident (cosine)$^2$ current.

In terms of these quantities, the collision rate is given by

$$C_i = \begin{cases} 2(1-T_i^{00}-T_i^{10})J_{0,i}^- + 2(1-T_i^{01} \\ \quad -T_i^{11})J_{1,i}^- + (1-P_{0,i}-P_{1,i})S_i, \\ \qquad\qquad i = 1 \\ (1-T_i^{00}-T_i^{10})(J_{0,i}^- + J_{0,i-1}^+) \\ \quad + (1-T_i^{01}-T_i^{11})(J_{1,i-1}^+ + J_{1,i}^-) \\ \quad + (1-P_{0,i}-P_{1,i})S_i, \qquad i = 2,I. \end{cases} \tag{16}$$

The interface currents are obtained from the statement of neutron conservation at each interior interface and no net current at the outer boundary of the cell:

$$J_{0,i}^+ = \begin{cases} T_i^{00}J_{0,i}^- + T_i^{01}J_{1,i}^- + (\tfrac{1}{2})P_{0,i}S_i, & i = 1 \\ T^{00}J_{0,i-1}^+ + T_i^{01}J_{1,i-1}^+ \\ \quad + (\tfrac{1}{2})P_{0,i}S_i, & i = 2,I \end{cases} \tag{17}$$

$$J_{1,i}^+ = \begin{cases} T_i^{10}J_{0,i}^- + T_i^{11}J_{1,i}^- + (\tfrac{1}{2})P_{1,i}S_i, & i = 1 \\ T_i^{10}J_{0,i-1}^+ + T_i^{11}J_{1,i-1}^+ \\ \quad + (\tfrac{1}{2})P_{1,i}S_i, & i = 2,I. \end{cases} \tag{18}$$

$$J_{0,i}^{-} = \begin{cases} T_{i+1}^{00} J_{0,i+1}^{-} + T_{i+1}^{01} J_{1,i+1}^{-} \\ \quad + (1/2) P_{0,i+1} S_{i+1}, & i = 1,I-1 \\ J_{0,i}^{+}, & i = 1 \end{cases} \quad (19)$$

$$J_{1,i}^{-} = \begin{cases} T_{i+1}^{10} J_{0,i+1}^{-} + T_{i+1}^{11} J_{1,i+1}^{-} \\ \quad + (1/2) P_{1,i+1} S_{i+1}, & i = 1,I-1 \\ J_{1,i}^{+}, & i = I. \end{cases} \quad (20)$$

Equations (17), (18), (19) and (20) form a set of $4I$ equations in the $4I$ unknown interface currents which can be solved by Gauss-Jordon reduction.

For this case several escape and transmission probabilities are required. These are obtained from the zero*th* and first angular moments of the neutron flux that emerges from a region for the appropriate unit source (volume or surface). It is found that

$$P_{0,i} = \frac{1}{\tau_i} [(1/2) - 2E_2(\tau_i) + 3E_3(\tau_i)], \quad (21)$$

$$P_{1,i} = \frac{2}{\tau_i} [E_2(\tau_i) - 2E_3(\tau_i)], \quad (22)$$

$$T_i^{00} = 4E_2(\tau_i) - 6E_3(\tau_i), \quad (23)$$

$$T_i^{10} = 8E_3(\tau_i) - 4E_2(\tau_i), \quad (24)$$

$$T_i^{01} = 6E_3(\tau_i) - 9E_4(\tau_i), \quad (25)$$

$$T_i^{11} = 12E_4(\tau_i) - 6E_3(\tau_i), \quad (26)$$

where $\tau_i$ is the thickness in mean free paths of region $i$ and $E_n(\tau_i)$ is the $n$th order exponential integral function.

## RABZPR

The formulation used in RABZPR is identical with that used in RABBLE except that periodic rather than zero-current boundary conditions are assumed at the surface of the cell. These periodic boundary conditions are that the number and angular distribution of neutrons leaving one surface of the cell are identical with the number and angular distribution of neutrons impinging on the other surface of the cell.

For the slab cell with cosine interface currents the expressions for collision rates and interface currents are identical with Eqs. (11–13) except for these changes:

$$C_1 = (1 - T_1)(J_i^{-} + J_I^{+}) + (1 - P_1)S_1, \quad (11a)$$

$$J_1^{+} = T_1 J_I^{+} + (1/2) P_1 S_1, \quad (12a)$$

$$J_1^{-} = T_1 J_1^{-} + (1/2) P_1 S_1, \quad (13a)$$

where the subscripts 1 and $I$ now refer to the left most and the right most regions, respectively.

For the slab cell with cosine and (cosine)$^2$ interface currents, the expressions for collision rates and interface currents are identical with Eqs. (16–20) except for these changes:

$$C_1 = (1 - T_1^{00} - T_1^{10})(J_{0,1}^{-} + J_{0,I}^{+}) + (1 - T_1^{01} - T_1^{11})(J_{1,1}^{-} + J_{1,I}^{+}) + (1 - P_{0,1} - P_{1,1})S_1, \quad (16a)$$

$$J_{0,1}^{+} = T_I^{00} J_{0,I}^{+} + T_1^{01} J_{1,I}^{+} + (1/2) P_{0,1} S_1, \quad (17a)$$

$$J_{1,1}^{+} = T_1^{10} J_{0,I}^{+} + T_I^{11} J_{1,I}^{+} + (1/2) P_{1,1} S_1, \quad (18a)$$

$$J_{0,I}^{-} = T_1^{00} J_{0,1}^{-} + T_1^{01} J_{1,1}^{-} + (1/2) P_{0,1} S_1, \quad (19a)$$

$$J_{1,I}^{-} = T_1^{10} J_{0,1}^{-} + T_1^{11} J_{1,1}^{-} + (1/2) P_{1,1} S_1, \quad (20a)$$

## References


1. W. K. Foell and T. J. Connolly, *An Investigation of Resonance Absorption in Mixtures of Uranium-238 and Thorium-232*, Nucl. Sci. Eng. **26,** 399 (1966).
2. S. Iijima, *Resonance Absorption and the Resonance Disadvantage Factor*, Nucl. Sci. Eng. **17,** 22 (1963).
3. P. H. Kier, *A Method of Calculating Resonance Absorption in a Circularized Cell*, Nucl. Sci. Eng. **26,** 230 (1966).
4. F. T. Adler and E. E. Lewis, *Comparison of Exact and Approximate Treatments of Resonance Effects in Cylindrical Lattices*, Trans. Am. Nucl. Soc. **11,** No. 1, 29 (1964).
5. F. E. Driggers, *A Method of Calculating Neutron Absorptions and Flux Spectra at Epithermal Energies*, Trans. Am. Nucl. Soc. **8,** No. 1, 206 (1965).
6. P. H. Kier, *RIFF-RAFF, A Program for Computation of Resonance Integrals in a Two-Region Cell*, ANL-7033 (1965).
7. P. H. Kier, *A Method of Computing Resonance Integrals in Multi-Region Reactor Cells*, Proc. Intern. Conference Research Reactor Utilization and Reactor Mathematics, Mexico City, May 1967 (to be published).
8. P. H. Kier and A. A. Robba, *RABBLE, A Program for Computation of Resonance Absorption in Multi-Region Reactor Cells*, ANL-7326 (to be published).
9. R. A. Karam, A. Ancarani, F. H. Helm, W. Y. Kato, G. Main and G. K. Rusch, *Measured Physics Parameters in a Zoned Fast Uranium Carbide Core, ZPR-6 Assembly No. 4Z*, Reactor Physics Division Annual Report, July 1, 1965 to June 30, 1966, ANL-7210, pp. 137–153.

# VI-7. The Present Status of the Unresolved Parameters for U-235, Pu-239 and U-238

R. N. Hwang and A. Travelli

## Introduction

The purpose of this investigation is to examine the reasonableness of various choices of the unresolved resonance parameters for three isotopes: namely, Pu-239, U-235 and U-238. The latter part of this paper discusses the effect of the various choices of these unresolved parameters for fast reactor calculations. In particular, their influence on the sodium void effect and the Doppler coefficients is discussed in some detail.

## Uncertainties in the Choices of the Unresolved Parameters and Their Influence on the Infinitely Dilute Cross Sections

Since the various unresolved parameters for the three isotopes under consideration were chosen on different bases, it is more appropriate to discuss each separately.

### *Pu-239*

The unresolved resonance parameters for Pu-239 proposed by P. Greebler et al.[1] for the ENDF/B files are essentially the same as those recommended by J. Schmidt,[2] except that in Ref. 2 there is no provision for fluctuations in the *s*-wave strength functions below 1 keV. This condition was imposed because of limitations that existed at the time in the processing of ENDF/B data. Hence, Schmidt's parameters and those of Ref. 1 ($S_0$ varying) for Pu-239 will be used interchangeably in the following discussions. Schmidt's parameters, based on extensive analysis of the recent high resolution measurements at Harwell and Saclay and the theoretical predictions of the channel theory, are believed to be the best single level Pu-239 parameters to date. In fact, these parameters have already been used extensively in our Doppler effect calculations since they became available during February 1966. The main differences between Schmidt's parameters and the previous parameters are in the *s*-wave average fission widths, the strength functions, and the average spacings. The uncertainties in the choice of these quantities and their effect on the infinitely dilute cross sections are given as follows.

$$\langle \Gamma_f \rangle_J^{l=0}$$

The recent Harwell and Saclay experiments[3-7] have indicated that plutonium resonances apparently can be subdivided into two groups with large and small fission widths respectively. The arbitrary assignment of $\Gamma_f = 300$ mV as a "boundary" between the two *s*-wave sequences leads to average fission widths of 1.3 eV and 0.065 respectively. Schmidt has postulated, on the basis of the channel theory along with the experimental results of J. Northrop et al.,[8] that resonances with large and small fission widths can be identified with $J = 0^+$ and $J = 1^+$ sequences, respectively. According to the channel theory, the ratio of the average fission width to the average spacing for a given spin state and parity is given by the expression,

$$\frac{\langle \Gamma_f \rangle^{J,\pi}}{\langle D \rangle^{J,\pi}} = \frac{\sum_{i=1}^{N} P_i}{2\pi}, \tag{1}$$

where $P_i$ is the penetration probability introduced by D. Hill and J. Wheeler[9] and the summation is over all fission thresholds for the compound state $J$. For the potential energy curve of an inverted harmonic oscillator with the circular frequency $\omega_i$, $P_i$ has the form

$$P_i = \frac{1}{1 + \exp\left[2\pi(E_i - E)/\hbar\omega_i\right]}, \tag{2}$$

where $E_i$ is the $i$th fission threshold. The detailed discussions have been given in Refs. 9 through 11. From Eqs. (1) and (2), it is apparent that, for a constant $\hbar\omega_i$, $\langle\Gamma_f\rangle^{J,\pi}/\langle D\rangle^{J,\pi}$ approaches $N/2\pi$ asymptotically whenever $E$ becomes much greater than $E_i$. On the other hand, $P_i$ becomes much smaller than unity when $E_i \gg E$.

The usefulness of Eq. (1) depends upon our knowledge of $E_i^{J,\pi}$, $\hbar\omega_i$ and $\langle D\rangle^{J,\pi}$. The experiments of Northrop et al.,[8] have indicated that two fission thresholds at $-1.61$ MeV and $-0.72$ MeV below the neutron binding energy with barrier widths of 0.525 MeV and 0.682 MeV, respectively, belong to the $J = 0^+$ state. The use of these values leads to the calculated $\langle\Gamma_f\rangle_{J=0^+} = 2.8$ eV. Unfortunately, the experimental information about these quantities for the $J = 1^+$ state is still lacking. In view of the unexpected dip in the Hopkins-Diven $\alpha$ measurement around 50 keV, Schmidt[2] suggested that the $J = 1^+$ state could possess a fission threshold in the vicinity of 50 keV. For a fixed $E_i^{J=1^+}$ at 50 keV, Schmidt has estimated that a barrier width between 0.15 and 0.18 MeV would give $\langle\Gamma_f\rangle^{J=1^+}$ comparable to the value derived from the resolved parameters; this width would also give a "reasonable" fit to the measured $\alpha$ values in the subsequent calculations. The recommended $\langle\Gamma_f\rangle^{J=1^+}$ in Ref. 1 is based on $\hbar\omega^{J=1^+} = 0.15$ MeV, which gives an asymptotic value of 55 mV in the low energy region.

From the foregoing discussion, one may conclude that the uncertainties in the average fission width for the $J = 1^+$ state are more serious than those for the $J = 0^+$ state. For the $J = 0^+$ state, the averaged fission width is overwhelmingly greater than the corresponding average neutron and capture widths. Consequently, the discrepancies between the calculated and the observed values are believed to have very little effect on the magnitude of the calculated average cross sections, total $\alpha$ value, and self-shielding effect. The recommended value of $\langle \Gamma_f \rangle^{J=0^+} = 2.8$ eV is certainly acceptable provided the Breit-Wigner equation is still valid under such conditions. The possibility of taking multilevel multichannel interference effects into account and the feasibility of using $R$-matrix parameters for all cases where $\langle \Gamma \rangle / \langle D \rangle$ is not small, are now under serious consideration.

For the $J = 1^+$ state, however, the calculated values of the average fission cross section and $\alpha$-value, as well as the self-shielding effect, are rather sensitive to small variations of $\langle \Gamma_f \rangle^{J=1^+}$ since the recommended value is of the same order of magnitude as the corresponding $\Gamma_\gamma$. For this reason, calculations with at least one different choice of $\langle \Gamma_f \rangle^{J=1^+}$ were made in order to study the possible uncertainties.

*Fluctuations in s-Wave Strength Function*

According to J. Schmidt,[2] the best $S_0$ values for Pu-239 to date are those obtained by C. Uttley[5] from a best fit to his $\langle \sigma_T \rangle$ measurements between 100 eV to 100 keV. Uttley's overall $S_0$ is $1.07 \times 10^{-4}$ with an accuracy of $\pm 10\%$. Fluctuations in $S_0$ were observed when $\langle \sigma_T \rangle$ was fitted on small energy subintervals. Table VI-7-I gives a list of $S_0$ values in different intervals as taken directly from Ref. 2. These fluctuations in $S_0$ are believed to be important in fast reactor calculations not only because they may account for the observed fluctuations in the measured Pu-239 fission cross sections, but also because they may significantly influence the self-shielding effect. The effect of these fluctuations in $S_0$ will be discussed later.

TABLE VI-7-I. *s*-WAVE STRENGTH FUNCTIONS

| | Energy Interval keV | $S_0 \times 10^4$ $(\text{eV})^{-1/2}$ |
|---|---|---|
| Schmidt's $S_0$ | 0.1–0.2 | 1.15 |
| | 0.2–0.3 | 1.54 |
| | 0.3–0.4 | 1.02 |
| | 0.4–0.5 | 0.76 |
| | 0.5–0.6 | 1.71 |
| | 0.6–0.7 | 0.80 |
| | 0.7–0.8 | 0.83 |
| | 0.8–0.9 | 0.84 |
| | 0.9–1.0 | 1.29 |
| | 1.0–2.0 | 1.00 |
| | $2.0 \rightarrow \infty$ | ~1.07 |
| "Mocked-up" $S_0$ | 1.5–2.0 | 0.70 |
| For Petrel variations[a] | 2.0–2.5 | 0.70 |
| Ref. 12 | 2.5–4.0 | 0.90 |

[a] Other parameters were taken to be the same as those in Ref. 1, except for the varying $S_0$.

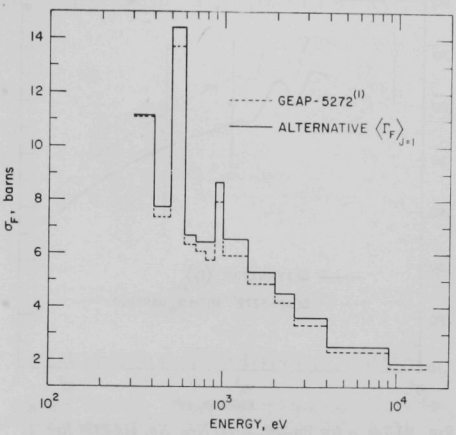


FIG. VI-7-1. Infinitely Dilute Fission Cross Section For Pu-239 (*S*-Wave Only). *ANL Neg. No. 112-8229 Rev. 1.*

Unfortunately, the more detailed fluctuations in $S_0$ are not available in Uttley's results for the energy region between 1 keV and 4 keV. This is of great concern in fast reactor calculations. Neither the recommended fission cross sections of Ref. 1 nor those of Schmidt[2] account for the significant dip in the observed values of Petrel results within this energy range. For the sake of comparison, a set of "mocked-up" values of $S_0$, given in Table VI-7-I, is introduced to take into account the dip in the observed fission cross section.

*Average Spacing*

The recommended average spacing was based on the results of the recent $\sigma_f$ measurements of Saclay.[14,15] Since $\sigma_f$ measurements eliminated the contribution from the background, $\sigma_p$, more levels were observed. The Saclay[14,15] value of $\langle D \rangle_{obs}$ is 2.3 eV as compared with Uttley's value of 2.5 and L. Bollinger's (Physics Division, ANL) value of 2.64 eV which was used extensively in the past. In view of possible missing levels, Schmidt has indicated that $\langle D \rangle_{obs} = 2.3$ eV may still be too high, with an estimated error of about $\pm 10\%$.

*Infinitely Dilute Cross Sections*

In order to show quantitatively how sensitive the magnitudes of the cross sections are to the different

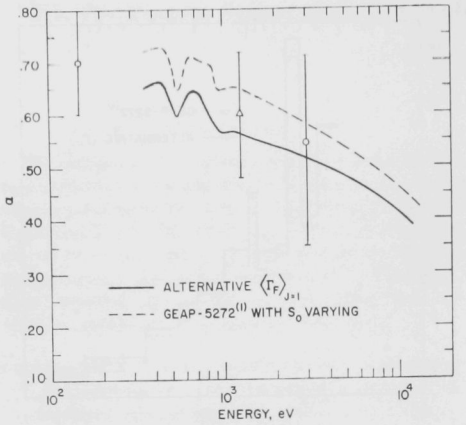


FIG. VI-7-2. $\alpha$ for Pu-239. *ANL Neg. No. 112-8226 Rev. 1.*

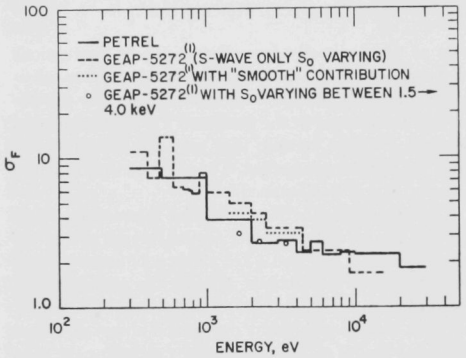


FIG. VI-7-3. Comparison of Pu-239 Fission Cross Sections to Petrel Data. *ANL Neg. No. 112-9162.*

selections of statistical parameters, calculations have been made in two illustrative examples. Figure VI-7-1 shows the calculated $s$-wave fission cross sections with $B$ parameters of Ref. 1 and an alternate choice of $\langle \Gamma_f \rangle$ for the $J = 1^+$ state only. In both cases, the fluctuations in $S_0$ were included. The latter was chosen by using Eq. (1) with $E_\lambda^{J=1^+} = 50$ keV and $\hbar\omega^{J=1^+} = 0.17$ MeV. As may be seen, the discrepancies in $\sigma_f$ between two cases is as much as 10% for such a small change in $\hbar\omega^{J=1^+}$. Figure VI-7-2 shows the corresponding variations in the $\alpha$-value. Poor information on the measured $\alpha$-value in the low keV region makes impossible any definite conclusion of the reasonableness of a particular set of the unresolved parameters, especially when the capture cross sections are considered. It is quite evident that more accurate measurements of $\alpha$-values in the low energy regions are needed for Pu-239.

Figure VI-7-3 shows the fission cross sections obtained by various parameters as compared with the recent Petrel results.[12] It is interesting to note that the Petrel results show a significant dip in $\sigma_f$ between 1.5 and 4 keV which is not accounted for in the Ref. 1 parameters. (Detailed variations in $\sigma_f$ are given in Ref. 12.) Since the dip is in the region where the 2.85 keV sodium resonance occurs, it may have some effect on the spectral component of the sodium void coefficient, which is extremely sensitive to the low energy adjoint flux. This effect will be discussed later. By using the argument that the fluctuations in the low energy fission cross section may be caused by the fluctuations in the $s$-wave strength function, a better agreement between the calculated and the measured values can be achieved by using the "mocked-up" $S_0$ given in Table VI-7-I. Parameters and smooth cross sections, in the energy region other than 1.5 to 4.0 keV are assumed to be the same as those of Ref. 1 (with $S_0$ varying).

### *U-235*

The most recent unresolved parameters for U-235 are also those recommended by Schmidt.[2] Unlike the case of Pu-239, our lack of knowledge in $E_\lambda^{J,\pi}$ and $\hbar\omega_\lambda$ makes impossible the use of Eq. (1) as the basis for predicting $\langle \Gamma_f \rangle^{J,\pi}$ Schmidt's recommended parameters were based strongly on the recent measurements and analysis of W. Shi-Di et al.[13] and also those of A. Michaudon et al.[13,14] The striking differences between the recommended parameters and those previously used are: (1) $\Gamma_\gamma$ is much larger (45% higher than the previously used value of $\Gamma_\gamma = 0.033$ eV); (2) a $\chi$-squared distribution function of 4 degrees of freedom is used according to Wang Shi-Di et al.;[13] (3) level spacings $\langle D \rangle^{J,\pi}$ are generally much smaller than those used previously, as a result of greater accuracy in the recent measurements; (4) fluctuations in the $s$-wave strength function below 2 keV are accounted for.

The average fission widths were determined by the standard technique in such a way that the resulting infinitely dilute fission cross section and $\alpha$ are in agreement with those measured values. The average fission widths determined this way are not unique in view of the great uncertainties in $\alpha$ values below 10 keV. Figure VI-7-4 shows the variation of the calculated fission cross sections of U-235 as compared with the Petrel results.[12] The dotted curve represents the calculated fission cross sections using ANL unresolved parameters (Table VI-7-II) which were used extensively in previous work. Figure VI-7-5 compares the corresponding calculated $\alpha$ values with the measured $\alpha$ values below 20 keV.[13,16]

Both Schmidt's[2] and the ANL parameters give reasonably good agreement in the fission cross section as compared to the Petrel data.[12] The "agreement" in the low energy $\alpha$ values is rather arbitrary. For fast reactor calculations, Schmidt's parameters are preferred since they were based on the most recent experimental information.

It is quite evident that more theoretical and experimental work are needed.

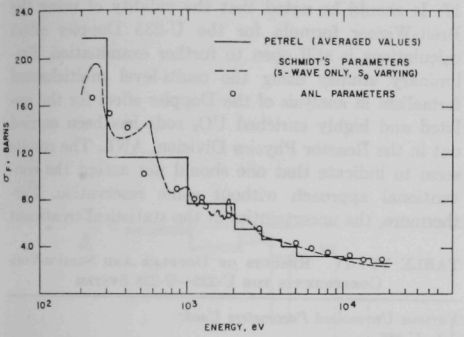


FIG. VI-7-4. Infinitely Dilute Fission Cross Sections for U-235. *ANL Neg. No. 112-8227.*

TABLE VI-7-II. AVERAGE FISSION WIDTHS FOR U-235

| $E^*$ | Schmidt Parameters[a] $\langle\Gamma_f\rangle_{J=3,4}$, | ANL Parameters[b] $\langle\Gamma_f\rangle_{J=3,4}$, |
|---|---|---|
| 0.2 | 0.090 | 0.090 |
| 0.25 | 0.100 | 0.120 |
| 0.35 | 0.150 | 0.150 |
| 0.45 | 0.220 | 0.180 |
| 0.55 | 0.230 | 0.160 |
| 0.65 | 0.200 | 0.140 |
| 0.75 | 0.150 | 0.120 |
| 0.85 | 0.130 | 0.115 |
| 0.95 | 0.115 | 0.105 |
| 1.05 | 0.110 | 0.130 |
| 1.15 | 0.130 | 0.150 |
| 1.25 | 0.145 | 0.160 |
| 1.35 | 0.155 | 0.160 |
| 1.45 | 0.165 | 0.160 |
| 1.55 | 0.175 | 0.150 |
| 1.65 | 0.180 | 0.150 |
| 1.75 | 0.190 | 0.150 |
| 1.85 | 0.195 | 0.150 |
| 1.95 | 0.200 | 0.150 |
| 2.5 | 0.175 | 0.155 |
| 3.4 | 0.140 | 0.160 |
| 6.5 | 0.220 | 0.150 |
| 12.0 | 0.175 | 0.155 |
| 15.0 | 0.180 | 0.180 |
| 20.0 | 0.200 | 0.200 |

[a] Fluctuations in $S_0$ are given in Ref. 1; $\nu_F = 4$.
[b] $S_0$ is fixed at $1.0 \times 10^{-4}$; $\nu_F = 2$; $S_1 = 2.5 \times 10^{-4}$.

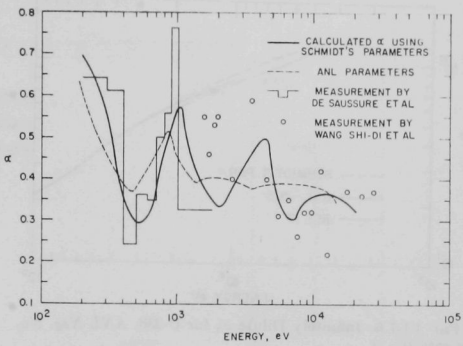


FIG. VI-7-5. $\alpha$ for U-235. *ANL Neg. No. 112-8225.*

TABLE VI-7-III. UNRESOLVED PARAMETERS FOR U-238

| | $S_0 \times 10^4$, $(eV)^{-1/2}$ | $S_1 \times 10^4$, $(eV)^{-1/2}$ | $\langle D\rangle^{l=0}_{J=1/2}$ | $\langle D\rangle^{l=1}_{J=1/2}$ | $\langle D\rangle^{l=1}_{J=3/2}$ | $\Gamma_\gamma$ |
|---|---|---|---|---|---|---|
| Ref. 17 | 0.94 | 1.58 | 18.5 | 18.5 | 9.25 | 0.0246 |
| Ref. 2 | 0.90 | 2.5 | 20.8 | 20.8 | 11.4 | 0.0248 |

### *U-238*

The unresolved parameters in the MC[2] library for U-238 are listed in Table VI-7-III. The $p$-wave strength function was taken from the preliminary report for ENDF/B file by W. A. Wittkopf et al. A more careful study of the unresolved parameters for U-238 was given by J. Schmidt.[2] Schmidt's parameters are also listed in Table VI-7-III. The latter parameters show greater average level spacing and greater $p$-wave strength function than the former. The greater average level spacings for the $s$-wave is the direct consequence of the recent high-resolution measurement by J. Garg et al.[18] and the work of G. Thomas and L. Bollinger[19] which makes possible the identification of some $p$-wave resonances in the resolved region. The $p$-wave strength function is consistent with the recent result by C. Uttley.[20] Figure VI-7-6 shows the variations of the infinitely dilute $\sigma_\gamma$ calculated by using the two sets of parameters as compared with the recommended curve in BNL-325. It is seen that $\sigma_\gamma$ as obtained by using Schmidt's parameters[2] is somewhat higher than that obtained by using the other parameters.

It is this author's opinion that Schmidt's parameters, based on more recent experimental work and more careful analysis, are to be preferred over those of Wittkopf et al.[17] for fast reactor calculations. As a matter of fact, Schmidt's parameters have been used in the reevaluation of ZPR-3 Doppler measurements.[20] The agreement between the calculated values and the measured values

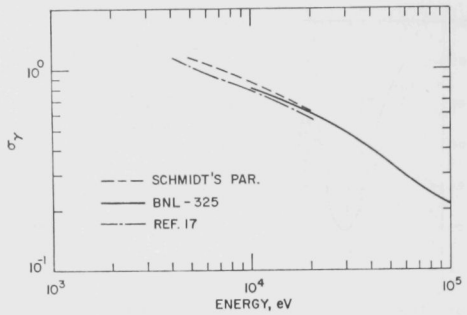


FIG. VI-7-6. Infinitely Dilute $\sigma_\gamma$ for U-238. *ANL Neg. No. 112-8228 Rev. 1.*

was better than that found by using the values of Ref. 17.

REACTOR CALCULATIONS

Calculations have been made using various choices of the unresolved parameters for various fast systems with particular attention to their influence on the sodium void and Doppler coefficients. At the time when the calculations were made, the ETOE code, which converts the ENDF/B parameters into the MC$^{2\,(21)}$ format, was not yet available. Therefore, various parameters for the unresolved capture and fission cross sections were put into MC$^2$ manually. It should be noted that no attempt was made to study the effects of cross sections other than the fission and capture cross sections in the resonance region. Other cross sections that are not within the scope of this investigation were taken to be the same as those in the existing MC$^2$ library.

The results for U-235—U-238 and Pu-239—U-238 systems are discussed separately as follows.

*U-235—U-238 Systems*

For simplicity, a bare system with the same composition as of Assembly 5 was chosen for these studies. The composition in (atoms/cc) $\times 10^{24}$ is as follows:

| U-235 | U-238 | C | Na |
|---|---|---|---|
| 0.00153 | 0.01056 | 0.01293 | 0.0092 |

| Fe | Ni | Cr |
|---|---|---|
| 0.00904 | 0.00113 | 0.002386 |

Calculations were made for the various combinations of resonance parameters given in Table VI-7-IV. In order to isolate the contributions due to different components to the total reactivity, perturbation calculations were made using the MACH-1 code[22] with the 22-group cross section sets taken from MC$^2$ calculations. The results of calculations are also tabulated in Table VI-7-IV.

For the Doppler coefficient, the effect of using various combinations of cross sections is quite straightforward as indicated by the tabulated values. The use of Schmidt's parameters[2] for U-235 gives a positive contribution, about 20% smaller than that obtained with the ANL parameters (Table VI-7-II), whereas the use of Schmidt's parameters for U-238 yields a higher negative component than that obtained from those of Ref. 17. It should be noted that the validity of using the Breit-Wigner formula for the U-235 Doppler effect calculations is still open to further examination. Preliminary studies using the multi-level multichannel formalism in analysis of the Doppler effect for the isolated and highly enriched $UO_2$ rods has been carried out in the Reactor Physics Division, ANL. The results seem to indicate that one should not accept the conventional approach without some reservation. Furthermore, the uncertainties in the statistical treatment

TABLE VI-7-IV. RESULTS OF DOPPLER AND SODIUM-VOID COEFFICIENTS FOR U-235—U-238 SYSTEM

*Various Unresolved Parameters Used:*

1. *U-235*
   - U-235 E..... ANL Parameters (Table VI-7-II)
   - U-235 D..... Schmidt's Parameters (Ref. 2)
   - U-235..... Old MC$^2$ Parameters

2. *U-234*
   - U-238 B..... Schmidt's Parameters (Ref. 2)
   - U-238 E..... Ref. 17 Parameters
   - U-238..... Old MC$^2$ Parameters

A. Doppler Coefficient in $\delta k/k^{(a)}$, % ($T_2 - T_1 = 750 - 800°K$)

| Combinations | Production | Absorption | Total |
|---|---|---|---|
| U-235 E–U-238 E | 0.139645 | −0.97848 | −0.838935 |
| U-235 E–U-238 B | 0.136010 | −1.00515 | −0.871898 |
| U-235 D–U-238 E | 0.166992 | −0.958202 | −0.78880 |

B. Sodium-Void Coefficient in $\delta k/k$, % (*25% Sodium Removal*)

| Combinations | $B^2$, $10^{-4}$ | Absorption | Scattering | Leakage | Total |
|---|---|---|---|---|---|
| U-235 :U-238 | 9.7138 | 0.09722 | 0.016639 | −0.68326 | −0.56868 |
| U-235 E :U-238 E | 8.9957 | 0.09454 | 0.079357 | −0.63335 | −0.45446 |
| U-235 E :U-238 B | 8.6887 | 0.096036 | 0.10714 | −0.611207 | −0.40307 |
| U-235 D :U-238 E | 9.09348 | 0.093167 | 0.104108 | −0.638907 | −0.440506 |

[a] Self overlap effect was not included.

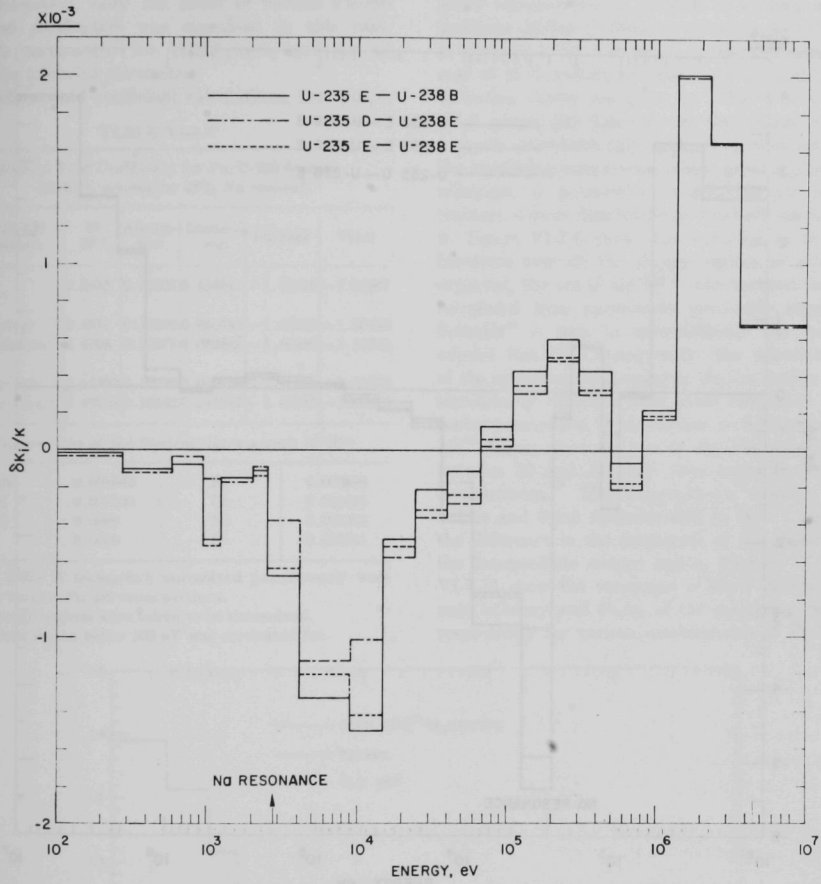


FIG. VI-7-7. Scattering Component of Sodium Void Coefficient for U-235-U-238 System. *ANL Neg. No. 112-8293.*

for U-235 in the presence of U-238 when applied to the low energy region are believed to be exceedingly large as implied by the work of C. Kelber and P. Kier.[23] The status of the theoretically predicted Doppler effect for the fissile isotopes in the low energy region is being re-examined. Details on these subjects will be reported.

For the sodium void coefficient, the tabulated values could be somewhat deceiving especially when the scattering component is considered. In the particular case chosen for this study, the leakage component is overwhelmingly larger than other contributions. Since the scattering component with positive contribution to the reactivity is of great concern for large fast reactors, a detailed study has been carried out on a group-wise basis. Figure VI-7-7 shows the scattering component $\delta k_i/k$ per unit lethargy for 25% sodium removal in various cases. From Fig. VI-7-7, it is quite clear that the scattering component is extremely sensitive to the relative magnitude of the positive contribution in the high energy region with respect to the negative contribution in the low energy region. The relative magnitude is, in turn, sensitive to the variation of the adjoint flux in the keV region. From perturbation theory, the scattering component for any group $i$ is given by

$$\frac{\delta k_i}{k} = \phi_i \sum_{j>i} (\phi_j^* - \phi_i^*)\delta\Sigma_{si\to j}. \qquad (3)$$

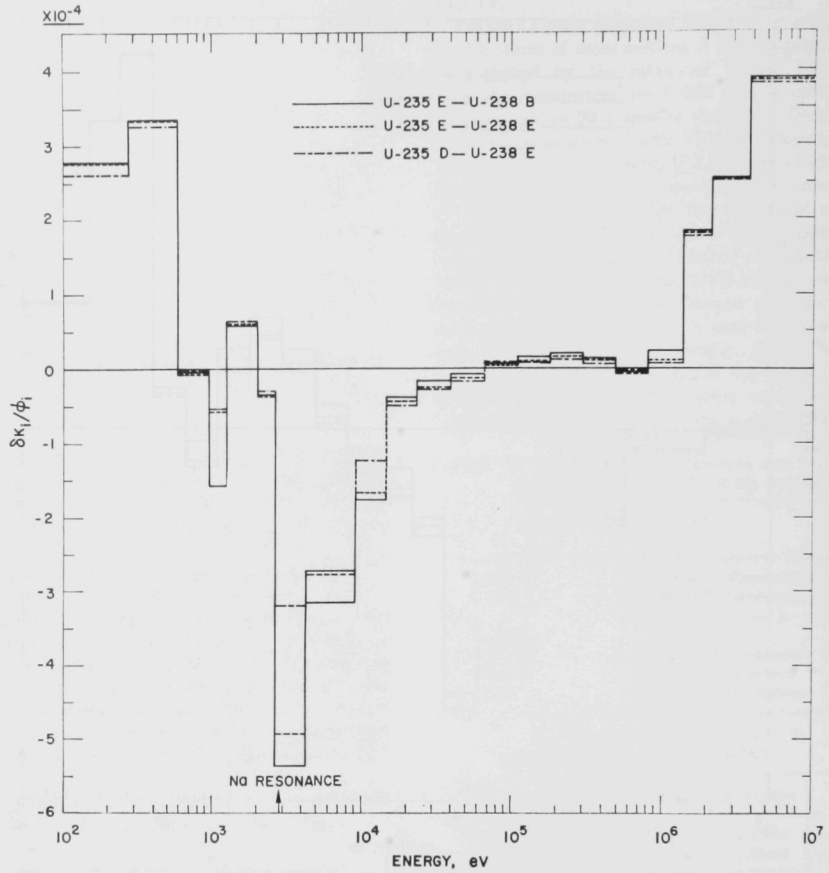


FIG. VI-7-8. Scattering Component Normalized to the Group Flux for U-235-U-238 System. *ANL Neg. No. 112-8295.*

In order to reach a more general conclusion, it is desirable to isolate the spectral effect from other effects. Figure VI-7-8 shows the variation of $\delta k_i/\phi_i$ scattering for various cases. The higher discrepancies in the low keV region imply that the discrepancies in $\delta k/k$ (scattering) may well be higher for systems with softer spectra than in the case considered here. The use of Schmidt's parameters for both U-235 and U-238 generally gives higher values of $|\delta k_i/\phi_i|$ than other combinations. From these results, one may conclude that the sodium void effect is relatively insensitive to reasonable choices of the unresolved parameters for U-235 and U-238 generated by fitting the given cross section and $\alpha$ curves. The reason is that the resonance self-shielding effect is generally small in the energy region of interest. It is important to realize, however, that the discrepancies in the measured fission cross sections used as the basis for the calculations, particularly in the energy region between 20 keV and 100 keV, may have a significant effect on the sodium void coefficient. The choice of the basic fission cross sections for fissile isotopes beyond 20 keV is not within the scope of this investigation. Further studies are needed in this area.

*Pu-239—U-238 System*

Since the effect of various selections of the U-238 unresolved parameters can be deduced from the pre-

ceding discussion, only the effect of various Pu-239 unresolved parameters was examined in this case. Schmidt's parameters[2] for U-238 were used for all cases in the following discussions.

For sodium void coefficient calculations, the system under consideration is assumed to be bare with compositions similar to those of Assembly 48 as tabulated in Table VI-7-VB. The results of the calculations for the case of 25% sodium removal based on first-order perturbation theory are given in Table VI-7-VA. For a small system like Assembly 48, the leakage component is again overwhelmingly larger than other terms. Since the scattering component, which gives a positive contribution, is potentially troublesome for large fast reactors, a more detailed study has been carried out for it. Figure VI-7-9 shows the variation of the adjoint functions over all the energy regions of interest. As expected, the use of old $MC^2$ cross sections for Pu-239, calculated from parameters previously suggested by Schmidt[24] is seen to underestimate the low energy adjoint flux.[25,26] Consequently, the negative portion of the scattering component in the low energy region is significantly different from those calculated by using newer parameters. It should also be noted that the old $MC^2$ fission cross sections in the intermediate region between 20 and 100 keV were based on P. White's measurement.[27] The discrepancies between White's values and those recommended in Ref. 1 account for the difference in the magnitude of the adjoint flux in the intermediate energy region. Figures VI-7-10 and VI-7-11 show the variations of $\delta k_i/k$ (scattering) per unit lethargy and $\delta k_i/\phi_i$ of the scattering component respectively for various combinations of Pu-239 cross

TABLE VI-7-V

A. Sodium Void Coefficient for Pu/U-238 System.
*($\delta k/k$ in percent for 25% Na removal)*

| Various Pu-239 Cross Sections | $B^2$, $10^{-3}$ | Absorption | Scattering | Leakage | Total |
|---|---|---|---|---|---|
| $MC^2$ | 2.3883 | 0.10001 | 0.15481 | −1.41410 | −1.16567 |
| Ref. 1[(b)] ($S_0$ varying) | 2.4517 | 0.10198 | 0.050786 | −1.45233 | −1.30432 |
| Petrel variation[b] | 2.4795 | 0.10273 | 0.052543 | −1.46886 | −1.31913 |
| Ref. 1 ($S_0$ varying) | 2.45502 | 0.10263 | 0.040750 | −1.45259 | −1.31398 |
| Petrel variation[c] | 2.48298 | 0.10342 | 0.041987 | −1.46913 | −1.32929 |

B. Composition of the System, (atoms/cm³) × $10^{24}$

| | | | |
|---|---|---|---|
| Pu-239 | 0.001644 | Fe | 0.009899 |
| U-238 | 0.007406 | Cr | 0.002658 |
| U-235 | 0.0069 | Ni | 0.001308 |
| Na | 0.0069 | C | 0.020761 |

[a] Only U-238 B (Schmidt's unresolved parameters)[2] were used with various Pu-239 cross sections.
[b] All energy regions were taken to be unresolved.
[c] Resolved region below 300 eV was accounted for.

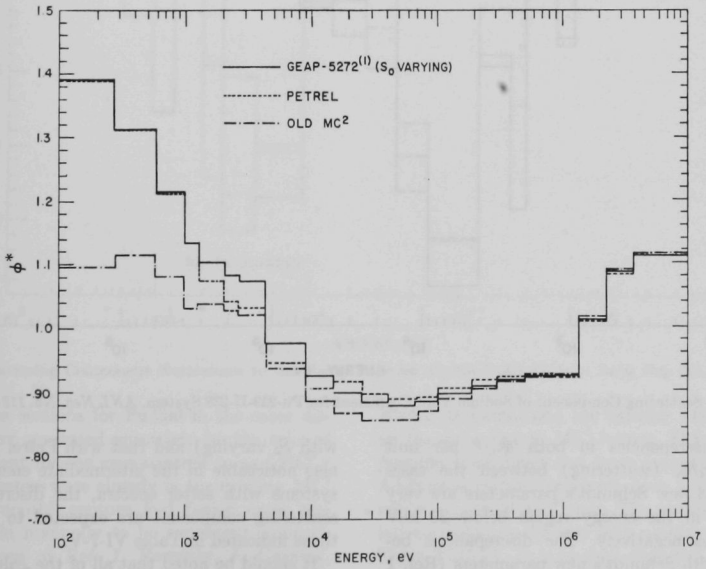


FIG. VI-7-9. Adjoint Fluxes Calculated from Various Pu-239 Parameters. *ANL Neg. No. 112-8278 Rev. 1.*

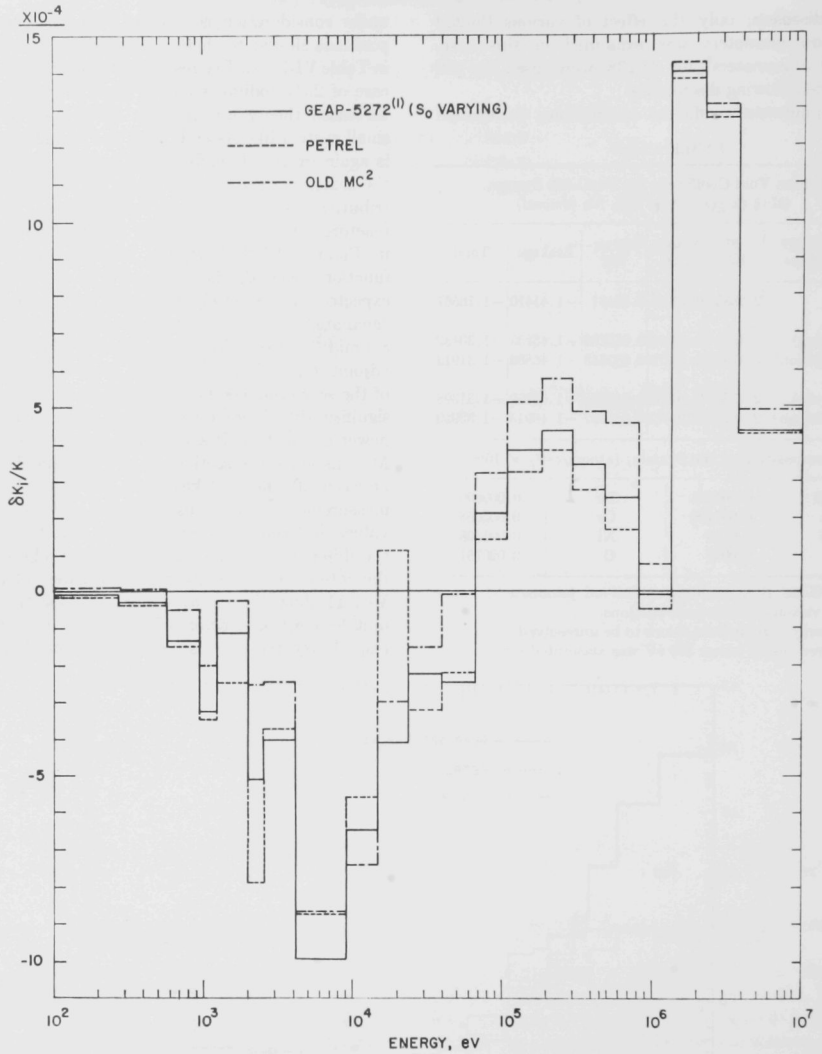


FIG. VI-7-10. Scattering Component of Sodium Void Coefficient for Pu-239-U-238 System. *ANL Neg. No. 112-8294 Rev. 1.*

sections. The discrepancies in both $\delta k_i/k$ per unit lethargy and $\delta k_i/\phi_i$ (scattering) between the cases using the old and new Schmidt's parameters are very large, especially in the energy region below 20 keV which contributes negatively. The discrepancies between the case with Schmidt's new parameters (Ref. 1 with $S_0$ varying) and that with Petrel variations[12] are also noticeable in the intermediate energy region. For systems with softer spectra, the discrepancies in the scattering component are expected to be larger than those indicated in Table VI-7-V.

It should be noted that all of the calculated capture

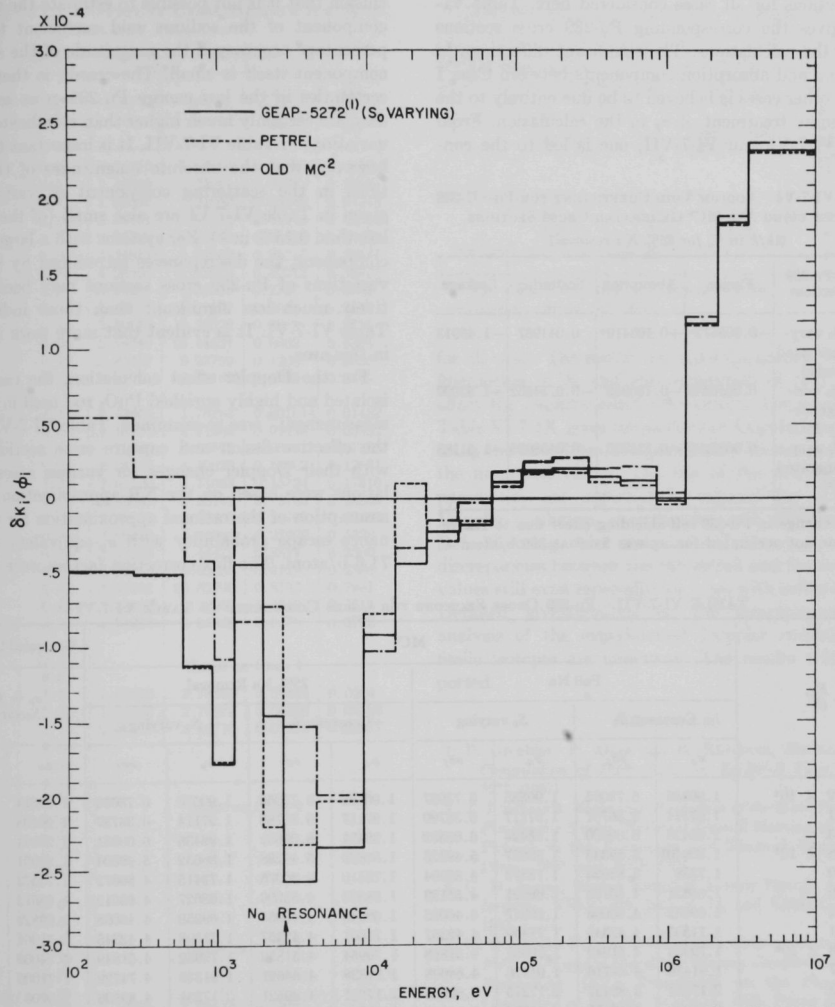


FIG. VI-7-11. Scattering Component Normalized to the Group Flux for Pu-239-U-238 System. *ANL Neg. No. 112-8277 Rev. 1.*

and fission cross sections for Pu-239 in the cases discussed so far were generated separately for the sake of saving time, except for the case referred to as "MC²" where the parameters were already in the existing MC² library. The "smooth" capture and fission cross sections were put in manually to be consistent approximately with those of Ref. 1. Recently, J. Gajniak, Reactor Physics Division, ANL, has completed a program that can combine cross sections in the ENDF/B format and the existing MC² cross sections on the same tape in MC² format. This program makes possible more direct and more consistent comparisons. Additional calculations have been made by using the newly generated MC² tape. The results of these calculations including the case with constant $S_0$ are given in Table VI-7-VI. It is evident that the scattering component of the sodium void coefficient is extremely sensitive to the low energy Pu-239 capture and fission

cross sections for all cases considered here. Table VI-7-VII gives the corresponding Pu-239 cross sections used in the calculations. The significant differences in the fission and absorption components between Case 1 and the other cases is believed to be due entirely to the approximate treatment of $\sigma_p$ in the calculation. From Tables VI-7-VI and VI-7-VII, one is led to the conclusion that it is not possible to estimate the scattering component of the sodium void coefficient to a high percentage accuracy if the magnitude of the scattering component itself is small. The reason is that the uncertainties in the low energy Pu-239 cross sections to date are certainly much higher than is indicated by the variations in Table VI-7-VII. It is important to realize, however, that the absolute magnitudes of the deviations in the scattering component of various cases given in Table VI-7-VI are also small (of the order of less than 0.15% in $k$). For systems with a large spectral component, the discrepancies introduced by the small variations of Pu-239 cross sections may become relatively much less significant than those indicated in Table VI-7-VI. It is evident that more work is needed in this area.

TABLE VI-7-VI. Sodium Void Coefficient for Pu—U-238 System using All MC² Generated Cross Sections
($\delta k/k$ *in % for 25% Na removal*)

| Various Pu-239 Cross Sections | Fission | Absorption | Scattering | Leakage |
|---|---|---|---|---|
| Ref. 1 ($S_0$ varying, generated separately) | −0.005572[a] | +0.103419[a] | 0.041987 | −1.46913 |
| Ref. 1 ($S_0$ constant, generated by MC²) | 0.0616438 | −0.136952 | −0.0734552 | −1.52000 |
| Ref. 1 ($S_0$ varying, generated by MC²) | 0.0667289 | −0.134720 | −0.0458885 | −1.51188 |

[a] The change in Pu-239 self-shielding effect due to Na removal was not accounted for. $\sigma_p$ was fixed at 300 b/atom of Pu-239.

For the Doppler effect calculation, the case of the isolated and highly enriched $PuO_2$ rod used in ZPR III measurement[25] was re-examined. Table VI-7-VIII gives the effective fission and capture cross sections along with their Doppler changes for various cases. Calculations were based on the NR-approximation and the assumption of the rational approximation for the resonance escape probability with $\sigma_p$-equivalent equal to 71.6 b/atom. The flux correction factors were included

TABLE VI-7-VII. Pu-239 Cross Sections for Cases Considered in Table VI-7-VI

| $E_L$, eV | MC² | | | | | | | | Generated by RP 270 | |
|---|---|---|---|---|---|---|---|---|---|---|
| | Full Na | | | | 25% Na Removal | | | | $\sigma_p$ = 300 b, $S_0$ varying | |
| | Constant $S_0$ | | $S_0$ varying | | Constant $S_0$ | | $S_0$ varying | | | |
| | $\sigma_a$ | $\nu\sigma_f$ | $\sigma_a$ | $\nu\sigma_f$ | $\sigma_a$ | $\nu\sigma_f$ | $\sigma_a$ | $\nu\sigma_f$ | $\sigma_a$ | $\nu\sigma_f$ |
| $3.679 \times 10^6$ | 1.90586 | 6.73095 | 1.90585 | 6.73087 | 1.90580 | 6.73056 | 1.90576 | 6.73059 | 1.89814 | 6.70294 |
| 2.231 | 1.97114 | 6.36787 | 1.97117 | 6.36790 | 1.97117 | 6.36788 | 1.97114 | 6.36787 | 1.96708 | 6.35619 |
| 1.343 | 1.98428 | 6.09600 | 1.98424 | 6.09592 | 1.98431 | 6.09631 | 1.98436 | 6.09631 | 1.98644 | 6.11576 |
| $8.208 \times 10^5$ | 1.866401 | 5.49335 | 1.86637 | 5.49325 | 1.86629 | 5.49288 | 1.86632 | 5.49304 | 1.86901 | 5.51688 |
| 4.979 | 1.7338 | 4.85923 | 1.73373 | 4.85904 | 1.73410 | 4.86076 | 1.73415 | 4.86072 | 1.73573 | 4.89365 |
| 3.019 | 1.68621 | 4.55183 | 1.68621 | 4.55183 | 1.68623 | 4.55200 | 1.68627 | 4.55212 | 1.68612 | 4.55305 |
| 1.832 | 1.69952 | 4.46066 | 1.69947 | 4.46055 | 1.69946 | 4.46055 | 1.69952 | 4.46065 | 1.69829 | 4.46068 |
| 1.111 | 1.71595 | 4.42345 | 1.71499 | 4.42357 | 1.71601 | 4.42357 | 1.71598 | 4.42345 | 1.71064 | 4.41509 |
| $6.738 \times 10^4$ | 1.79953 | 4.51849 | 1.79957 | 4.51858 | 1.79954 | 4.51852 | 1.79952 | 4.51849 | 1.74000 | 4.3764 |
| 4.087 | 1.91430 | 4.64716 | 1.91426 | 4.64698 | 1.91338 | 4.64621 | 1.91339 | 4.74729 | 1.71000 | 4.13703 |
| 2.479 | 2.17214 | 4.89497 | 2.17215 | 4.89506 | 2.17231 | 4.89521 | 2.17234 | 4.89526 | 2.0700 | 4.57011 |
| 1.503 | 2.45279 | 5.19473 | 2.45278 | 5.19466 | 2.45273 | 5.19463 | 2.34275 | 5.19473 | 2.500 | 5.22720 |
| $9.119 \times 10^3$ | 3.6237 | 7.38497 | 3.62361 | 7.38469 | 3.62378 | 7.38513 | 3.62380 | 7.30526 | 3.0433 | 6.10764 |
| 4.307 | 3.60130 | 6.97727 | 3.60129 | 6.97718 | 3.60396 | 6.98140 | 3.60390 | 6.98133 | 3.4754 | 6.70364 |
| 2.612 | 4.67320 | 8.71987 | 4.67316 | 8.71993 | 4.65128 | 8.68234 | 4.65130 | 8.68237 | 4.7067 | 8.74168 |
| 2.035 | 5.8482 | 10.67997 | 5.84825 | 10.6799 | 5.81503 | 10.6256 | 5.81500 | 10.62523 | 5.8850 | 10.56367 |
| 1.234 | 6.9706 | 12.61928 | 6.97064 | 12.6192 | 7.00079 | 12.6656 | 7.00080 | 12.66580 | 6.5495 | 11.79131 |
| $9.611 \times 10^2$ | 9.39310 | 16.94170 | 9.23342 | 16.5109 | 9.44883 | 17.0263 | 9.28110 | 16.58239 | 7.96360 | 14.24712 |
| 5.829 | 11.2357 | 21.43666 | 11.0440 | 21.1823 | 11.3325 | 21.5724 | 11.16370 | 21.36108 | 9.9700 | 17.5298 |
| 2.754 | 15.8304 | 31.88798 | 14.1249 | 26.5751 | 16.0489 | 32.2121 | 14.3663 | 26.92817 | 15.080 | 26.83253 |
| 1.013 | 23.9447 | 47.77655 | 23.9443 | 47.7762 | 24.4409 | 48.5440 | 24.4410 | 48.54399 | 24.648 | 44.3039 |
| $2.902 \times 10$ | 32.3222 | 75.53549 | 32.3227 | 75.5363 | 33.0128 | 76.9223 | 33.0130 | 76.92212 | 34.5139 | 79.22018 |

TABLE VI-7-VIII. EFFECTIVE CROSS SECTIONS FOR ½ IN. ISOLATED $PuO_2$ ROD[a]

[$(\sigma_p^{(e)} = 71.6$ *b/atom) s-wave only*]

| | $E_0$, keV | ~500°K, $\sigma_\gamma$ | ~500°K, $\sigma_f$ | ~500 → 1100°K, $\delta\sigma_\gamma$ | ~500 → 1100°K, $\delta\sigma_f$ |
|---|---|---|---|---|---|
| CASE 1[b] | 12.0 | 0.74610 | 1.69466 | 0.00788 | 0.01408 |
| | 6.5 | 1.18399 | 2.31001 | 0.02272 | 0.03184 |
| | 3.4 | 1.83090 | 3.21052 | 0.06338 | 0.07348 |
| | 2.25 | 2.34491 | 3.93396 | 0.11440 | 0.12083 |
| | 1.70 | 2.73720 | 4.48613 | 0.16550 | 0.16509 |
| | 1.20 | 3.24814 | 5.24602 | 0.25117 | 0.23541 |
| | 0.95 | 4.05808 | 6.72960 | 0.40212 | 0.36975 |
| | 0.85 | 3.24814 | 4.99699 | 0.2737 | 0.5188 |
| | 0.75 | 3.39373 | 5.21077 | 0.3014 | 0.2549 |
| | 0.65 | 3.50199 | 5.36022 | 0.3303 | 0.2726 |
| | 0.55 | 5.84049 | 10.44521 | 0.8602 | 0.6866 |
| | 0.45 | 3.85437 | 5.93799 | 0.4268 | 0.3333 |
| | 0.35 | 4.98014 | 8.23169 | 0.6985 | 0.5419 |
| CASE 2[c] | 12.0 | 0.72065 | 1.76285 | 0.007614 | 0.01482 |
| | 6.5 | 1.13795 | 2.41585 | 0.02183 | 0.03382 |
| | 3.4 | 1.75285 | 3.36673 | 0.06057 | 0.07836 |
| | 2.25 | 2.24145 | 4.12628 | 0.10902 | 0.12881 |
| | 1.70 | 2.61120 | 4.71063 | 0.15724 | 0.17610 |
| | 1.20 | 3.10536 | 5.50742 | 0.23755 | 0.25059 |
| | 0.95 | 3.87079 | 7.06407 | 0.38108 | 0.39403 |
| | 0.85 | 3.09030 | 5.24066 | 0.27022 | 0.5328 |
| | 0.75 | 3.23068 | 5.46477 | 0.2817 | 0.3500 |
| | 0.65 | 3.32958 | 5.62058 | 0.3117 | 0.2884 |
| | 0.55 | 5.57731 | 10.89790 | 0.8135 | 0.7951 |
| | 0.45 | 3.66419 | 6.22267 | 0.4019 | 0.3516 |
| | 0.35 | 4.74216 | 8.62620 | 0.6578 | 0.5725 |
| CASE 3[d] | 12.0 | Same as Case 1 | | | |
| | 6.5 | | | | |
| | 3.4 | 1.63870 | 2.78650 | 0.04984 | 0.0564 |
| | 2.25 | 1.76643 | 2.76573 | 0.06389 | 0.06196 |
| | 1.70 | 2.06117 | 3.15710 | 0.09295 | 0.00577 |
| | 1.20 | Same as Case 1 | | | |
| | 0.95 | | | | |
| | 0.85 | | | | |
| | 0.75 | | | | |
| | 0.65 | | | | |
| | 0.55 | | | | |
| | 0.45 | | | | |
| | 0.35 | | | | |
| CASE 4[e] | 12.0 | Same as Case 1 | | | |
| | 6.5 | | | | |
| | 3.4 | | | | |
| | 2.25 | | | | |
| | 1.70 | | | | |
| | 1.20 | | | | |
| | 0.95 | 3.61920 | 5.80119 | 0.3233 | 0.2914 |
| | 0.85 | 3.79270 | 6.07760 | 0.3614 | 0.3200 |
| | 0.75 | 3.98925 | 6.39517 | 0.4076 | 0.3533 |
| | 0.65 | 4.21078 | 6.77211 | 0.4637 | 0.3936 |
| | 0.55 | 4.46552 | 7.22827 | 0.5329 | 0.4416 |
| | 0.45 | 4.76500 | 7.79607 | 0.6204 | 0.4996 |
| | 0.35 | 5.12217 | 8.54490 | 0.7326 | 0.5707 |

[a] Overlap effect was not included.
[b] Case 1 = Ref. 1 with $S_0$ fluctuating (Schmidt's parameters).
[c] Case 2 = Alternate $\langle\Gamma_f\rangle^{J=1}$ (other parameters same as Case 1).
[d] Case 3 = Petrel variations (Ref. 12).
[e] Case 4 is the same as Case 1 except $S_0$ = constant.

TABLE IV-7-IX. COMPARISON BETWEEN THEORY AND EXPERIMENTS

(*ZPR-3 Measurements—½ in.* $PuO_2$, $T_2 - T_1 = 1100 - 500°K$)

| Assembly | Experiments[a], $\Delta k/k \times 10^{-6}$ | Theory[b] (using new Schmidt's parameters), $\Delta k/k \times 10^{-6}$ |
|---|---|---|
| 45 | +1.07 | +4.62 |
| 45A | +0.25 | +2.57 |
| 45A (with $BC_4$ surrounding) | +1.73 | +1.72 |

[a] The expansion effect was accounted for.
[b] Overlap effects included.

for all cases. The results are self-explanatory. Both the fluctuation in $S_0$ and the magnitude of $\langle\Gamma_f\rangle^{J=1^+}$ will affect the Doppler effect calculations. For comparison, Table VI-7-IX gives the calculated Doppler coefficients using the new Schmidt's parameters[2] as compared with the measured values. The use of the new Schmidt's parameters has significantly reduced the calculated Doppler coefficient as compared with those given in Ref. 25 using older parameters.[24] However, sizeable discrepancies between the calculated and the measured values still exist especially for cases with softer spectra. Detailed investigations on the interpretation and analysis of the experimental Doppler coefficient for fissile isotopes are underway. The results will be reported.

## REFERENCES


1. P. Greebler, P. Aline and B. Hutchins, *Evaluation and Compilation of $Pu^{239}$ Data for ENDF-B Files*, GEAP-5272 (1967).
2. J. J. Schmidt, *Resonance Properties of the Main Fertile and Fissionable Nuclei*, National Topical Meeting on Reactor Physics in the Resonance and Thermal Regions, San Diego, 1966 (also KFK-120).
3. G. D. James, United Kingdom Atomic Energy Authority Reports, NRDC-139, 1963, p. 14, and EANDC-33 "U", 1963, p. 14.
4. G. D. James, *Fission Cross Section Measurements on $Pu^{239}$, $Pu^{241}$, $U^{232}$ and a Search for Fission Components of $Pu^{238}$ Resonances*, IAEA Symposium on the Physics and Chemistry of Fission, Salzburg, 1965, Paper SM-60/15; AERE-NP/PR, 1965, pp. 5-6.
5. C. A. Uttley, *Single Level Analysis of the Resonances in the Total Cross Section of Pu-239 from 100 eV to 300 eV*, EANDC Conference on Study of Nuclear Structure with Neutrons, Antwerp, 1965, p. 535; UKAEA Reports AER-ENP/PR-8, 1965, p. 2, and EANDC(UK) 40 "L", 1964.
6. G. de Saussure, J. Blons, C. Jousseaume, A. Michaudon and Y. Pranal, *Mesure et Analyse de la Section Efficace de Fission du Pu-239*, IAEA Symposium on the Physics and Chemistry of Fission, Salzburg, 1965, Paper SM-60/13.
7. J. Blons, H. Derrien, A. Michaudon, P. Ribon and G. de Saussure, *Study of Resonance Parameters of Pu-239*,

EANDC Conference on the Study of Nuclear Structure with Neutrons, Antwerp, 1965, p. 564.
8. J. A. Northrop, R. H. Stokes and K. Boyer, *Measurement of Fission Thresholds of $Pu^{239}$, $U^{233}$, $U^{235}$, and $U^{238}$ Using the (d, p) Reaction*, Phys. Rev. **115**, 1277, (1959).
9. D. L. Hill and J. A. Wheeler, *Nuclear Constitution and Interpretation of Fission Phenomena*, Phys. Rev. **89**, 1102 (1953).
10. M. S. Moore and O. D. Simpson, *Measurement and Analysis of Cross Sections of Fissile Nuclides*, National Topical Meeting on Reactor Physics in the Resonance and Thermal Regions, San Diego, MIT Press, 1966.
11. J. E. Lynn, *Quasi-Resonances and the Channel Theory of Neutron Induced Fission*, EANDC Conference on the Study of Nuclear Structure with Neutrons, Antwerp (1965).
12. *Fission Cross Sections from Petrel*, LA-3586 (1966).
13. Shi-di Wang, Yun-Chan Wang, E. Dermendzhiev and Y. V. Ryabov, IAEA Symposium on the Physics and Chemistry of Fission, Salzburg, 1965 (Paper No. SM-60/86).
14. A. Michaudon, *Contribution to the Study of the Interaction of Slow Neutrons with $U^{235}$ Using the Time-of-Flight Method*, CEA-R 2552, Vol. I & II, 1964.
15. A. Michaudon, A. Lottin, D. Paya and J. Trochon, *Proprietes Statistiques Des Niveaux De l'$U^{236}$ Induits Dans l'$U^{235}$ par Los Neutron Lents*, Nucl. Phys. **69**, 545 (1965).
16. G. de Saussure, L. W. Weston, R. Gwin, J. E. Russell and R. W. Hockenbury, *Measurement of $\alpha$, the Ratio of the Neutron Capture Cross Section to the Fission Cross Section, for $U^{235}$ in the Energy Region from 3.25 eV to 1.8 keV*, ORNL-3738 (1965).
17. W. A. Wittkopf, et al., unpublished preliminary report for ENDF/B file.
18. J. B. Garg, J. Rainwater, J. S. Peterson and W. W. Havens, *Neutron Resonance Spectroscopy. III. $Th^{232}$ and $U^{238}$*, Phys. Rev. **134B**, 985 (1964).
19. G. E. Thomas and L. M. Bollinger, *P-Wave Resonances in $U^{238}$ at Very Low Energy*, EANDC Conference on Study of Nuclear Structure with Neutrons, Antwerp, 1965, p. 96.
20. C. A. Uttley, EANDC(UK)-35 "L", 2 (1964).
21. D. O'Shea, B. J. Toppel and A. L. Rago, *$MC^2$—A Code to Calculate Multigroup Cross Sections*, ANL-7318 (to be published).
22. D. A. Meneley, L. C. Kvitek and D. M. O'Shea, *A One-Dimensional Diffusion-Theory Package*, ANL-7223 (1967).
23. C. N. Kelber and P. H. Kier, *The Effect of Randomness on Group Cross Sections*, Nucl. Sci. Eng. **24**, 389, **26**, 67 (1966).
24. J. J. Schmidt, *Nuclear Data for Pu-239 in the Energy Regions of Resolved and Unresolved Resonances*, AEC-ENEA Seminar on the Evaluation of Neutron Cross Section Data, BNL (1965).
25. G. J. Fischer, D. A. Meneley, R. N. Hwang, E. F. Groh and C. E. Till, *Doppler Effect Measurements in Plutonium-Fueled Fast Power Breeder Reactor Spectra*, Nucl. Sci. Eng. **25** (1966), p. 37.
26. R. N. Hwang, K. Ott, J. G. Hodgkinson and J. G. Wall, *Comparison and Analysis of Theoretical Doppler-Coefficient Results for Fast Reactors*, ANL-7269 (1967).
27. P. H. White, *Measurement of Fission Cross Sections for Neutrons of Energies in the Range 40-500 keV*, IAEA Conference on Physics and Chemistry of Fission, Salzburg, Austria, EANDC(UK)-53 "S" (1965).

## VI-8. The Crystalline Effects on the Doppler-Broadened Cross Section and Resonance Integrals of Uranium in a $UO_2$ Lattice

C. R. Adkins*, P. J. Persiani and R. N. Hwang

The crystalline effects on the Doppler-broadened cross section and on the resonance integrals have been studied to investigate the extent and effect of the asymmetry and shift in the Breit-Wigner line shape. The changes in the line shape, due to crystalline binding, can affect the magnitude of the resonance parameters determined from the fitting of experimental cross-section data, as well as the size of the calculated Doppler effect in critical assemblies and reactors at low power.

The scattering and absorption cross sections were developed for the system of nuclei bound in a $UO_2$ crystalline lattice. The absorption cross section is essentially that derived by W. Lamb[2] except that the actual phonon frequency distribution replaces the Debye distribution. The Doppler-broadened cross sections are also reduced to the form of the gas model by making the short compound nucleus lifetime approximation (SCNL) which is the "weak binding" approximation discussed by Lamb.

In addition to the several phonon frequency distributions developed from the Born-von Karman description of crystal,[3] the study also included the $UO_2$ phonon spectrum determined by G. Dolling et al.[4] The latter frequencies were obtained from a theoretical fitting to the experimentally determined dispersion curves of $UO_2$.

The effect of crystalline binding on the Doppler-broadened cross sections of the U-238 resonance at 6.68 eV for a temperature of 300°K is presented in Fig. VI-8-1. In general, the study indicated that pronounced line shifts and asymmetry with respect to the SCNL and the gas model prevailed at higher than room temperatures for the low lying levels.

* Carnegie Institute of Technology, Pittsburgh, Pennsylvania.

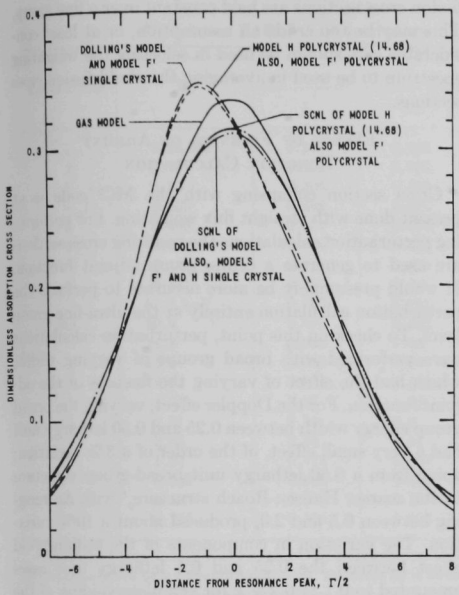


FIG. VI-8-1. Capture Line Shape—6.68-V Resonance of U-238 at 300°K. *ANL Neg. No. 112-6026.*

An estimate of the effect on resonance integrals was made in the NRIA and NR approximation for the U-238 resonances at 6.68 and 190 eV, respectively. The results, listed in Table VI-8-I show that differences of greater than 5% can be expected between the crystalline model and the "effective-temperature" gas model (SCNL). Of significance is that an improper computation of an effective temperature, such as using the Debye model, could increase the magnitude of the error.

TABLE VI-8-I. RESONANCE INTEGRALS IN THE NR AND NRIA APPROXIMATIONS FOR THE U-238 RESONANCE IN THE TEMPERATURE RANGES (*I*) 50 TO 300°K AND (*II*) 300 TO 500°K

| Model | NRIA Approx. (6.68V, $\sigma_p^{eff}$ = 17.52 b) | | NR Approx. (190V, $\sigma_p^{eff}$ = 40 b) | |
|---|---|---|---|---|
| | Change in Reaction Rate[a], % | | Change in Reaction Rate, % | |
| | $(\Delta RI)_I/RI_b$ | $(\Delta RI)_{II}/RI_b$ | $(\Delta RI)_I/RI_b$ | $(\Delta RI)_{II}/RI_b$ |
| SCNL F' Poly | 0.2264 | 0.2697 | 0.6288 | 0.8273 |
| SCNL H Poly (14.68) | 0.2240 | 0.2697 | 0.6223 | 0.8264 |
| SCNL Dolling | 0.2183 | 0.2739 | 0.6097 | 0.8152 |
| CRYS H Poly (14.68) | 0.4441 | 0.2534 | 0.5603 | 0.7791 |
| GAS | 0.3694 | 0.3092 | 0.9874 | 0.8981 |

[a] $(\Delta RI)_I = RI(300°K) - RI(50°K)$
$(\Delta RI)_{II} = RI(500°K) - RI(300°K)$
$RI_b = RI_{Gas}(300°K)$

## REFERENCES

1. C. R. Adkins, P. J. Persiani and R. N. Hwang, "The Crystalline Effects on the Doppler-Broadened Cross Section and Resonance Integrals of Uranium in a $UO_2$ Lattice," Trans. Am. Nucl. Soc. **10,** No. 1, 228 (1967).
2. W. E. Lamb, Jr., *Capture of Neutrons by Atoms in a Crystal,* Phys. Rev., **55** (1939).
3. C. R. Adkins, P. J. Persiani, R. N. Hwang and J. J. Kaganove, *The Chemical Binding Effects of the Resonance Line Shapes of Uranium-238 in a $UO_2$ Lattice,* Proc. Conference on Neutron Cross Section Technology, Washington, D. C., Conf. 660303, p. 134 (March 1966). C. R. Adkins, *Effects of Chemical Binding on the Doppler Broadened Cross Section of Uranium in a $UO_2$ Lattice,* Thesis: Carnegie Institute of Technology-Argonne National Laboratory (April 1966).
4. G. Dolling, R. A. Cowley, and A. B. D. Woods, *The Crystal Dynamics of Uranium Dioxide,* Can. J. Phys., **43,** 1397 (August 1965).

## VI-9. Comparative Physics Analysis of Fast Reactor as a Function of Refinement in Multigroup Cross Section Preparation

B. J. TOPPEL and H. H. HUMMEL

A paper bearing the above title was presented at the International Conference on Research Reactor Utilization and Reactor Mathematics, at Mexico City, May 2-4, 1967.[1] Some of the most important results of this paper are summarized in the following.

The flexibility of the MC[2] cross-section code[2] made it possible to study the effect of various approximations on the broad-group cross sections ordinarily used in space-dependent calculations. In MC[2], flux calculations are performed for a fundamental mode using "ultra-

fine" groups of lethargy width 0.00833, as in ELMOE,[3] or in "fine" groups of lethargy width approximately 0.25, but with the choice of width arbitrary within limits. A fine group must contain an integral number of ultra-fine groups. Collapsed broad-group cross sections are generated by weighting with the ultra-fine or the fine group fluxes, depending on which option in the code has been selected. Inelastic transfers are carried out only for the fine groups in either case, and fission and capture cross sections are held constant over fine groups except in the resolved resonance region in which ultra-fine group cross sections are used. The broad group widths are arbitrary within limits but must contain an integral number of fine groups. Using this flexibility, the following investigations were carried out.

### Effect on Fineness of Inelastic Scattering

In the MC² treatment of inelastic scattering, the transferred neutrons are distributed uniformly in energy over each fine group. No inscattering is allowed within the group from which removal is occurring. In the original version of the code, inelastic removal was constant over each fine group. An improvement used in the ESSELEM Code[4] and subsequently incorporated into MC² is to allow the inelastic removal cross section to vary from one ultra-fine group to the next, in effect, continuously with energy. With the older treatment, there were large distortions of the high energy flux associated with the discontinuities in inelastic removal cross section. These in turn caused errors in elastic transfer cross sections, which caused too hard a high energy flux to be calculated and resulted in too large a reactivity by over 2% $k$ in the case studied when a fine group lethargy width $\Delta u$ of 0.5 was used. This error resulted from too large a calculated threshold fission effect in U-238. A decrease to a width of 0.25 eliminated 1.4% $k$ of this error, and a further decrease to a width of 0.167 gave a further, smaller improvement of 0.3% $k$, with a remaining error of 0.5% $k$ or perhaps slightly more, the exact result not being known. When the ultra-fine group inelastic removal technique was used, the total change in $k$ for a change in $\Delta u$ from 0.5 to 0.167 was 0.8% $k$ with 0.6% of this change occurring between $\Delta u = 0.5$ and $\Delta u = 0.25$. This indicates that with the more refined method of inelastic removal cross section acceptable accuracy is probably obtained with fine group $\Delta u = 0.25$. No significant effects on reactivity coefficients were found with the varying fine group $\Delta u$. The inelastic removal effects occur at too high an energy to be significant for Doppler or sodium void effects, while the error in distribution of inelastically transferred neutrons does not appear to be significant for either reactivity effects or criticality.

A part of the reactivity change occurring with the change in fine group $\Delta u$ is due to the fact that U-238 fission cross sections are held constant over a fine group. This may be too crude an assumption, or at least considerable care should be used in selecting the weighting spectrum to be used in averaging threshold fission cross sections.

### Effect of Fineness of Adjoint Function Calculation

Cross section collapsing with the MC² code is at present done with straight flux weighting. For performing perturbation calculations the resulting cross sections are used to generate a coarse-group adjoint function. It would presumably be more accurate to perform the perturbation calculation entirely at the ultra-fine group level. To check on this point, perturbation calculations were performed with broad groups of varying width, which had the effect of varying the fineness of the adjoint function. For the Doppler effect, varying the broad group energy width between 0.25 and 0.50 lethargy unit had a very small effect, of the order of a 3% variation; going from a 0.50 lethargy unit broad-group structure to the coarser Hansen-Roach structure,[5] with $\Delta u$ ranging between 0.5 and 2.0, produced about a 10% variation. The variation in components of the sodium void effect between the 0.25 and 0.5 lethargy unit cases amounted to 0.1 to 0.2% $k$ for complete voiding of the core, with similar effects observed in going from the 0.50 lethargy width to the Hansen-Roach structure. It thus appears that not much is to be gained by going to an adjoint function based on a group structure finer than $\Delta u = 0.25$, when the choice of $\Delta u = 0.5$ is already giving reasonably good results.

### Effect of Fine-Group Versus Ultra-Fine Group Flux Calculations

The main effect of this variation is on the evaluation of the light element transport and elastic removal cross sections; the latter are more sensitive to the flux approximation used. In the ultra-fine group case the ELMOE[3] treatment is used for elastic removal cross section evaluation since the elastic scattering angular distributions are respresented using Legendre polynomials. In the fine-group case the rather crude assumption is made that neutrons are removed from a fine group if their energy does not exceed the lower energy of the group by an amount corresponding to $\xi$, the average logarithmic energy loss per collision; otherwise they are unaffected. For a $1/E$ weighting spectrum within a fine group, this corresponds to a removal cross section equal to the familiar $\xi\sigma_s/\Delta u$. A constant weighting spectrum, or a spectrum proportional to $E$ may also be selected by the user.

A comparison of the ultra-fine and fine group flux

TABLE VI-9-I. SODIUM ELASTIC REMOVAL CROSS SECTION, barns

| Broad Group | $E_L$ | Problem[a] | | | | | | |
|---|---|---|---|---|---|---|---|---|
| | | 1 | 18 | 19 | 20 | 3 | 13 | 14 |
| 1 | 3.68 MeV | 0.118 | 0.123 | 0.122 | 0.120 | 0.083 | 0.095 | 0.075 |
| 2 | 2.73 | 0.304 | 0.302 | 0.296 | 0.285 | 0.234 | 0.267 | 0.212 |
| 3 | 1.35 | 0.304 | 0.293 | 0.282 | 0.274 | 0.259 | 0.296 | 0.235 |
| 4 | 0.820 | 0.592 | 0.476 | 0.482 | 0.470 | 0.389 | 0.444 | 0.351 |
| 5 | 0.498 | 0.674 | 0.711 | 0.722 | 0.578 | 0.594 | 0.665 | 0.549 |
| 6 | 0.302 | 0.786 | 0.839 | 0.813 | 0.759 | 0.641 | 0.734 | 0.582 |
| 7 | 0.183 | 0.713 | 0.695 | 0.719 | 0.654 | 0.639 | 0.730 | 0.581 |
| 8 | 0.111 | 0.765 | 0.746 | 0.718 | 0.708 | 0.475 | 0.542 | 0.432 |
| 9 | 67.4 keV | 0.762 | 0.781 | 0.663 | 0.634 | 0.515 | 0.593 | 0.465 |
| 10 | 40.9 | 0.681 | 0.683 | 0.672 | 0.570 | 0.663 | 0.754 | 0.605 |
| 11 | 24.8 | 0.928 | 1.03 | 0.465 | 0.437 | 0.444 | 0.511 | 0.404 |
| 12 | 15.0 | 0.653 | 0.629 | 0.644 | 0.604 | 0.582 | 0.669 | 0.528 |
| 13 | 9.12 | 0.835 | 0.832 | 0.819 | 0.803 | 0.725 | 0.833 | 0.656 |
| 14 | 4.31 | 1.27 | 1.24 | 1.22 | 1.50 | 1.05 | 1.218 | 0.929 |
| 15 | 2.61 | 9.81 | 10.0 | 10.3 | 27.9 | 9.88 | 11.5 | 8.84 |
| 16 | 2.03 | 2.55 | 2.51 | 2.43 | 2.14 | 3.16 | 3.45 | 3.00 |
| 17 | 1.23 | 0.473 | 0.460 | 0.455 | 0.427 | 0.523 | 0.601 | 0.473 |
| 18 | 0.960 | 0.985 | 0.999 | 1.01 | 1.04 | 1.09 | 1.23 | 0.991 |
| 19 | 0.583 | 0.390 | 0.387 | 0.394 | 0.384 | 0.403 | 0.466 | 0.363 |
| 20 | 0.275 | 0.196 | 0.195 | 0.204 | 0.189 | 0.193 | 0.231 | 0.169 |

[a] Problem 1 treats only Na, Fe, and O as Legendre materials; Problem 18 treats only Na and Fe as Legendre materials; Problem 19 treats only Na as a Legendre material. Problem 20 is similar to Problem 19 except that Na is present in a very small concentration; Problem 3 is an all fine group problem with $\phi(E)$ = constant; Problem 13 is an all fine group with $\phi(E) = 1/E$; Problem 14 is an all fine group with $\phi(E) = E$.

treatments is presented in Table VI-9-I for the reactor composition given in Table VI-9-II. This is identical with Case 8 of the 1965 comparison calculations[6] except that stainless steel has been replaced by iron for simplicity. In Table VI-9-I a "Legendre" material is one which has been given the complete ELMOE treatment rather than the fine group treatment. The fine groups are the 0.25 lethargy unit groups used in MC²; they are combined to form broad groups as indicated.

When there is a mixture of Legendre and non-Legendre materials, a flux calculation is done in the ultrafine groups for which the cross sections for non-Legendre materials are held constant, while the elastic scattering source due to such materials is held constant in energy. In Problem 1, Legendre materials are sodium, iron, and oxygen, while in Problem 18 sodium and iron are treated in this way, and in Problem 19 only sodium is a Legendre material. In Problem 20 only sodium is a Legendre material, but it is present in too small an amount to influence the spectrum. In all these cases, a weighting spectrum $\phi(E)$ = constant over the fine groups was used to evaluate cross sections for non-Legendre materials. In Problems 3 and 13 all materials are treated in the fine group manner, with weighting spectra $\phi(E)$ = constant and $\phi(E) = 1/E$, respectively.

A comparison of the results of Problems 20 and 3 indicates the error that occurs with a flux weighting spectrum constant in energy because of failure to use the complete elastic transfer matrix for sodium. Errors from this source are significant in some cases but not extremely large. In most cases the results of Problems 1 and 13 agree fairly well, indicating that the choice of a $1/E$ weighting spectrum and the neglect of flux perturbations do not lead to extremely large errors. This is particularly true at higher energies. At energies below about 20 keV the choice $\phi(E)$ = constant seems better. This choice will vary with reactor composition, as the

TABLE VI-9-II. REFERENCE PROBLEM SPECIFICATIONS

| Material | Legendre treated? | Temperature | Atomic Density, $10^{24}$ atoms/cc | | |
|---|---|---|---|---|---|
| | | | Composition | Fuel Pin[a] | Coolant[a] |
| Fe | Yes | 1500°K | 0.011 | 0 | 0.01411 |
| Na | | | 0.0123 | 0 | 0.01833 |
| O | | | 0.0144 | 0.048 | 0 |
| $Pu^{240}$ | | | 0.00036 | 0.0012 | 0 |
| $U^{238}$ | | | 0.00648 | 0.0216 | 0 |
| $Pu^{239}$ | No | | 0.00072 | 0.0024 | 0 |
| Fission Products | | | 0.00036 | 0.0012 | 0 |

[a] Resonance calculations made in cylindrical geometry with 0.318 cm fuel pin radius and 0.505 cm coolant-clad radius.

TABLE VI-9-III. Reactivity Effect Calculations for Problems in Table VI-9-I

| Problem | Total Doppler $\%\delta k$, 1500°K → 1100°K | Spectral Plus Capture $\%\delta k$, 50% Na Voiding |
|---|---|---|
| 1 | 0.344 | 3.92 |
| 3 | 0.268 | 3.42 |
| 13 | 0.324 | 3.44 |
| 14 | 0.232 | 3.39 |

position of the maximum in the flux will shift correspondingly.

A comparison of Problems 1 and 18 indicates that resonances in 0–16 are not causing large effects, except in Group 4, where the influence of the resonance at 1.0 MeV is seen. This general conclusion is consistent with the observation that effective sodium cross sections are not greatly different in oxide, carbide, and metal systems with stainless steel structural material.[1] The influence of resonances in iron is particularly marked between 25 and 100 keV and not large otherwise, as is seen from a comparison of Problems 18 and 19. Finally, a comparison of Problems 19 and 20 indicates what error is incurred by neglecting resonance self-shielding in Na-23; this is seen to be marked in several strong resonance regions, but otherwise not large.

Results of reactivity coefficient calculations for some of these problems are presented in Table VI-9-III. It is seen that there are considerable changes in the Doppler effect in going from one flux weighting to another in the all fine group cases; the $\phi = 1/E$ case happens to agree with the Legendre treatment case fairly well.

These changes are caused by variation in the low energy flux. There are not large changes in sodium void effect among the all-fine group cases, although they all yield values smaller by $\sim 0.5\%$ $k$ for 50% sodium voiding than the Legendre treatment case does. The smallness of this variation in spite of the considerable changes in elastic removal cross sections among these cases is caused by a compensating shift in neutron energy spectrum; larger elastic removal cross sections shift the flux into a lower energy region, in which the adjoint function variation with energy is such as to make the sodium void effect less positive.

### References

1. B. J. Toppel and H. H. Hummel, *Comparative Physics Analysis of Fast Reactors as a Function of Refinement in Multigroup Cross Section Preparation*, Proc. International Conference on Research Reactors Utilization and Reactor Mathematics, Mexico City, May 2–4, 1967.
2. A. L. Rago and H. H. Hummel, *ELMOE: An IBM 704 Program Treating Elastic Scattering Resonances in Fast Reactors*, ANL-6805 (1964).
3. B. J. Toppel, A. J. Rago and D. M. O'Shea, *MC²—A Code to Calculate Multigroup Cross Sections*, ANL-7318 (June 1967).
4. K. Katsuragi, Y. Ishiguro and O. Kato, *Group Constants for a Fast Reactor and Sodium Void Effects*, JAERI-1109 (1965).
5. G. F. Hansen and W. H. Roach, *Six and Sixteen Group Cross Sections for Fast and Intermediate Critical Assemblies*, LAMS-2543 (1961).
6. D. Okrent, *Summary of Intercomparison Calculations Performed in Conjunction with the Conference on Safety, Fuels, and Core Design in Large Fast Power Reactors*, ANL-7120, 3 (1965).

## VI-10. Effects of Cross Section Errors on Neutron Spectra

C. N. Kelber

A recurrent problem in reactor physics is estimating the sensitivity of calculated parameters to cross section errors; to resolve these errors, attempts have been made to correlate integral data and estimate cross section corrections.[1] These attempts have been marked by a lack of consistency because of the many correlations and accidental cancellations which exist among the effects of differing errors in microscopic cross sections. In fast reactor physics one attempt to take into account correlated effects has been to develop a mechanical approach based on second order perturbation theory.[2] The attack proposed here is to treat cross section errors as lumped effects and develop techniques for estimating their size and distribution and also to develop techniques suitable for use in pure media so that the lumped effects can be related to specific isotopes.

A lumped-parameter model of fast reactor spectra is a suitable tool for use in estimating the size of combined error effects if the lumped-parameters are related to distinct physical processes such as fission, elastic scattering, inelastic scattering, capture, and leakage. Such a model has recently been proposed by W. Stacey,[3] and it can readily be shown that the mean relative error in the elastic scattering parameter, $\Delta S/S$, is given by

$$\frac{\Delta S}{S} = \frac{S(1 - S^2)\Delta R}{(1 - S)^2(R - F)}, \tag{1}$$

where inelastic scattering has been neglected, $R$ is the observed detector response, $\Delta R$ the difference between the calculated and observed detector response, and $F$ the detector response to the neutron source spectrum. When inelastic scattering is present the analysis is algebraically more complex, and detectors with distinctive responses are required. Knowing the mean relative error, information about its distribution can be obtained from detailed measurements of neutron spectra such as those recently reported by E. Bennett.[4]

To make the procedure more explicit, consider the simple case of hydrogen-like slowing down in an infinite medium with a constant scattering cross section. Suppose that the ratio of scattering to total cross section is given by

$$\sigma_s/\sigma_t = 1 + \epsilon R(u), \tag{2}$$

where $u$ is lethargy, $\epsilon$ is a small number [similar to $\Delta S/S$ from Eq. (1)] and $R(u)$ takes values at random on the interval from plus to minus one. Then by regarding the slowing down density and neutron spectrum as random variables, and using the notion of stochastic integration,[5] it is possible to relate the auto-correlation of the neutron spectrum to the auto-correlation of $R$. For the case where the auto-correlation of $R$ is given by

$$C[R(u,u')] = \exp(-2\lambda \mid u - u' \mid) \tag{3}$$

one finds

$$\frac{C[\phi(u,u')]}{\epsilon^2} = \{[1 + 2/(1 - 4\lambda^2)]^2 - 2/(1 - 4\lambda^2)\} \cdot \exp(-2\lambda\tau) - [7\lambda/(1 - 4\lambda^2)]\tau \exp(-\tau) + [(44\lambda^3 - 23\lambda)/(1 - 4\lambda^2)] \exp(-\tau) + O(\epsilon) \tag{4}$$

where $\tau = \mid u - u' \mid$ and $\lambda \neq \frac{1}{2}$.

Since the narrow resonance approximation has been used to solve the slowing down equation it is natural to suggest that auto-correlation techniques be employed to determine resonance parameters. This can be done when the resonance is very broad (>5 keV), isolated, and is not obscured by fluctuations in the spectrum from other sources.

### References


1. G. Rakavy, *Use of Integral Measurements as Supplementary Data for Determining Neutron Cross Sections*, Proc. Conference on Neutron Cross Section Technology, March 22–24, 1966. CONF-660303.
2. G. Ceschini, A. Gandini, I. Dal Bono and B. Faleschini, *Comparison Between Experimental and Theoretical Integral Data on Fast Critical Facilities. CALI, A Program for Generating Effective Nuclear Group Constants by a Perturbation Method*, Proc. International Conference on Fast Critical Experiments and their Analysis, Oct. 10–13, 1966, ANL-7320.
3. W. M. Stacey, Jr., *Spectrum and Importance Function in Spatially Independent Fast Reactor Assemblies*, Trans. Am. Nucl. Soc. **9**, 474–475 (1966).
   W. M. Stacey, Jr., Ph.D. Thesis, MIT, 1966.
4. E. F. Bennett, *Fast Neutron Spectroscopy by Proton-Recoil Proportional Counting*, Nucl. Sci. Eng. **27**, 16–27 (1967).
5. A. Papoulis, *Probability, Random Variables and Stochastic Processes*, (McGraw-Hill Book Co., Inc., New York, 1965) pp. 323–325.


## VI-11. Calculations of Detailed Neutron Fluxes Across Interfaces Between Resonance-Scattering Media

D. Meneghetti, A. L. Rago* and K. E. Phillips

### Introduction

Detailed neutron flux spectra in homogeneous bare-core fast systems containing resonance scattering materials may be calculated with the Argonne program ELMOE.[1] For a given composition the ELMOE code determines the bare-core neutron flux spectrum by using many hundreds of very fine energy groups. Coarse-group cross sections are evaluated by using these fine-group fluxes for weighting. The flux-averaged cross sections are then used in coarse-group calculations in the core regions of a reflected system.

The possible presence of resonance-scattering materials in regions in which the assumption of a normal mode flux may not be satisfactory, for example in reflectors, has led to studies of the problems of determining coarse-group cross sections for such regions. In this regard, a modified usage of the ELMOE program has previously been reported.[2,3] This method employed iterations between coarse-group, multiregion criticality

* Applied Mathematics Division, Argonne National Laboratory.

TABLE VI-11-I. Regional Atomic Densities, $10^{24}$ atoms per cm$^3$

| Case | Core | | Reflector | |
|---|---|---|---|---|
| 1 | Al | 0.0603 | Fe | 0.0847 |
| | U-235 | 0.004[a] | | |
| 2 | C | 0.054 | Ni | 0.0913 |
| | U-235 | 0.004[a] | | |

[a] Only the absorption property of fission and not the source property is used. Also these elements are not treated by the detailed Legendre polynomial expansion coefficients.

calculations and ELMOE calculations. The effects of gross space and energy dependent bucklings were simulated by substitutions of approximate coarse energy and space dependent positive and negative group-absorptions. These leakage-simulating absorptions, however, were based upon regional coarse-group leakages derived from coarse-group criticality calculations. Thus, the possible effects of interactions of differing fine-energy variations of the fluxes across an interface between media of different resonance scattering characteristics are not included in that method.

In the present study,[4] spatially-dependent fine-energy-detailed fluxes through such interfaces between scattering media were calculated directly. The fine-group spatially-dependent calculations were carried out by using fine-group cross sections for transport and elastic scattering obtained by using the ELMOE library of angular scattering data as fine-group cross sections. These fine-group cross sections were then used in a modification of the Argonne version[5] (2D-SNARG) of a two-dimensional discrete $S_n$ transport program.[6]

## Example Interface Cases

The two interface examples described in Table VI-11-I have identical slab-geometries. They simulate 60 cm thick core regions, with 30 cm thick abutting reflector regions. For simplicity and for reasonable machine-running time, only solutions for the case of an applied flat distributed fission source in the core region were obtained.

The first case has a resonance scatterer, aluminum, as the core diluent and another resonance scatterer, iron, as the reflector material. The second case, instead, has a non-resonance scatterer, carbon, as the core diluent, and a resonance scatterer, nickel, as the reflector material.

For these cases, $S_2$ flux solutions using linearly-anisotropic and isotropic scattering assumptions were obtained. Transport approximations were employed for the isotropic cases. These solutions thus correspond to consistent-$P1$ and to diffusion theory solutions since the applicable $S_2$ quadrature corresponded to that of a $P1$ or Gaussian quadrature. Indeed, if the only projected usage of an ELMOE and SNARG linkage were for $S_2$ solutions, a large saving in computation time could be obtained by employing a more direct (non-discrete-ordinate) mode of solution.

Since for these studies detailed interest is primarily in the energy region of the scattering resonances, only the fine-group solution in an energy range sufficiently wide to exhibit the characteristics of effects due to resonance-interface phenomena will be presented. For example, in these cases only the energy range from 0.5 MeV to 15 kV have been subdivided into 172 fine groups.

## Spatial Dependence of Fine-Flux Spectra

The fine-group flux spectra at various positions on both sides of the interface between the aluminum diluent core and the iron reflector are shown in Fig. VI-11-1 as functions of lethargy. For the cases to be described, the flux spectra from the isotropic solutions did not differ sufficiently from those of the anisotropic solutions to warrant reproducing a comparison of the flux spectra.

Furthermore, a higher order, $S_4$, flux solution for this case results in larger variations than the differences between anisotropic and isotropic $S_2$. The flux peak, due to troughs between resonances of one regional composition, is seen to penetrate quite deeply into the adjacent region and vice-versa.

Analogous spectra for the case with the carbon-diluent core having the nickel reflector are shown in Fig. VI-11-2. Because carbon is not a resonance scatterer, its characteristic fine flux affects only the spectral envelope on the nickel side of the interface. The flux peaks in the carbon are due to the characteristic fine flux peaks of the nickel reflector. The penetration of these flux peaks into the carbon core are less than those shown in Fig. VI-11-1.

## Position-Dependence of Collapsed Cross Sections

The spatial sensitivities of coarse-group cross sections, obtained using results of the fine-group solutions as weighting criteria, have also been studied. The energy intervals chosen for collapsing into coarse-groups $J$ correspond to those of energy groups 9, 10, 11 and 12 of the 16 group set[7] of S. Yiftah, D. Okrent, and P. Moldauer. These have half-lethargy widths. The fine groups used had lethargy widths approximately $\frac{1}{30}$ of these half-lethargy widths.

In this study, collapse of the transport cross sections utilized the formula:

$$\Sigma_{tr_j}(z) = \frac{\sum_{j \text{ in } J} \Sigma^d_{tr_j} \dfrac{d\phi^1_j(z)}{dz}}{\sum_{j \text{ in } J} \dfrac{d\phi^1_j(z)}{dz}} - \frac{\sum_{j \text{ in } J} \sum_{j'=1}^{j-1} \Sigma^1_{s_{j'\to j}} \dfrac{d\phi^1_{j'}(z)}{dz}}{\sum_{j \text{ in } J} \dfrac{d\phi^1_j(z)}{dz}}$$

where $[d\phi^1_j(z)/dz]$ is the current-divergence in fine-group $j$, and where $\Sigma^d_{tr_j}$ and $\Sigma^1_{s_{j'\to j}}$ are the fine-group diagonal transport and fine group $P1$ anisotropic transfer cross sections, respectively. The diagonal transport cross section for a given group is corrected for the elastic scattering anisotropy only of neutrons remaining in that group. Current coupling effects with other groups are not considered. The $\Sigma^1_{s_{j'-j}}$ coefficients couple currents in the consistent $P1$ approximation. The fine-group diagonal-transport-cross sections are weighted by the fine-group solutions. The coarse-group elastic transfer cross sections instead were obtained by

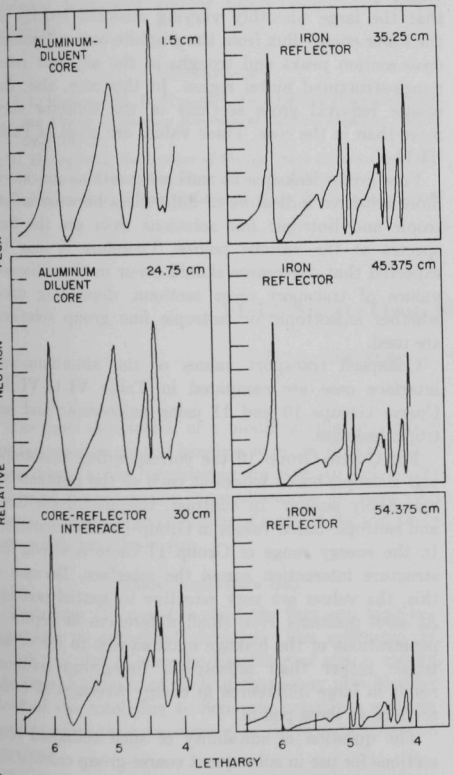


FIG. VI-11-1. Neutron Flux Spectrum at Various Spatial Positions in the Al-Diluent Core and Fe Reflector. *ANL Neg. No. 112-8142.*

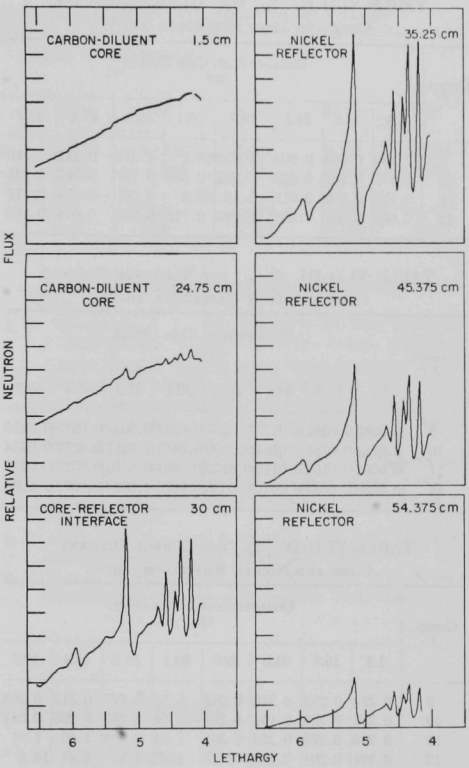


FIG. VI-11-2. Neutron Flux Spectrum at Various Spatial Positions in the C-Diluent Core and Ni Reflector. *ANL Neg. No. 112-8143.*

fine-group flux weighting. The mode of collapsing the cross sections used in this study is not to be interpreted as the only procedure or even as necessarily the best. The purpose of choosing this method of collapsing is simply to provide a basis for intercomparison of results and for discussion. (Continuation studies currently being carried out indicate that current-weighting of the transport cross section may be preferable.)

Some results of point-wise evaluation of the collapsed coarse group transport cross sections for the interface case having the aluminum core and iron reflector are listed in Table VI-11-II. These collapsed transport values are noted to vary considerably and also to take on negative values.

Small positive values, and negative values, of these collapsed coarse-group cross sections arise from the

TABLE VI-11-II. $\Sigma_{tr_J}$ FOR ALUMINUM-DILUENT CORE AND IRON REFLECTOR, $cm^{-1}$

| Group, $J$ | Distance from Core Center, cm | | | | | | | |
|---|---|---|---|---|---|---|---|---|
| | 1.5 | 16.5 | 24.8 | 29.9 | 30.1 | 35.2 | 45.4 | 49.9 |
| 9 | 0.190 | 0.166 | 0.003 | −0.076 | 15.1 | 0.043 | 0.242 | 0.110 |
| 10 | 0.171 | 0.162 | 0.093 | 0.212 | 0.538 | 0.197 | 0.317 | 0.331 |
| 11 | 0.110 | 0.109 | 0.011 | −5.10 | 52.8 | 0.581 | −0.078 | 0.117 |
| 12 | 0.085 | 0.087 | 0.088 | 0.090 | 0.715 | 0.073 | 0.094 | 0.113 |

TABLE VI-11-III. $\Sigma_{el\ re_J}$ FOR ALUMINUM-DILUENT CORE AND IRON REFLECTOR, $cm^{-1}$

| Group, $J$ | Distance from Core Center, cm | | | | | | | |
|---|---|---|---|---|---|---|---|---|
| | 1.5 | 16.5 | 24.8 | 29.9 | 30.1 | 35.2 | 45.4 | 49.9 |
| 9 | 0.0281 | 0.0281 | 0.0277 | 0.0257 | 0.0243 | 0.0227 | 0.0215 | 0.0214 |
| 10 | 0.0153 | 0.0154 | 0.0164 | 0.0200 | 0.0161 | 0.0217 | 0.0237 | 0.0234 |
| 11 | 0.0098 | 0.0102 | 0.0112 | 0.0122 | 0.0591 | 0.0403 | 0.0393 | 0.0399 |
| 12 | 0.0030 | 0.0029 | 0.0029 | 0.0028 | 0.0073 | 0.0084 | 0.0087 | 0.0084 |

TABLE VI-11-IV. $\Sigma_{tr_J}$ FOR CARBON-DILUENT CORE AND NICKEL REFLECTOR, $cm^{-1}$

| Group, $J$ | Distance from Core Center, cm | | | | | | | |
|---|---|---|---|---|---|---|---|---|
| | 1.5 | 16.5 | 24.8 | 29.9 | 30.1 | 35.2 | 45.4 | 49.9 |
| 9 | 0.274 | 0.272 | 0.218 | 0.215 | 1.13 | 0.777 | 0.512 | 0.505 |
| 10 | 0.283 | 0.293 | 0.194 | 0.291 | −3.54 | 0.183 | 0.295 | 0.364 |
| 11 | 0.295 | 0.278 | 0.259 | 0.361 | 1.94 | 0.998 | 1.00 | 1.01 |
| 12 | 0.301 | 0.291 | 0.289 | 0.278 | 4.27 | 1.87 | 2.41 | 14.6 |

TABLE VI-11-V. $\Sigma_{el\ re_J}$ FOR CARBON-DILUENT CORE AND NICKEL REFLECTOR, $cm^{-1}$

| Group, $J$ | Distance from Core Center, cm | | | | | | | |
|---|---|---|---|---|---|---|---|---|
| | 1.5 | 16.5 | 24.8 | 29.9 | 30.1 | 35.2 | 45.4 | 49.9 |
| 9 | 0.0737 | 0.0736 | 0.0728 | 0.0680 | 0.0577 | 0.0396 | 0.0386 | 0.0386 |
| 10 | 0.0731 | 0.0731 | 0.0733 | 0.0683 | 0.0418 | 0.0330 | 0.0400 | 0.0343 |
| 11 | 0.0776 | 0.0775 | 0.0770 | 0.0778 | 0.0734 | 0.0749 | 0.0721 | 0.0722 |
| 12 | 0.0751 | 0.0749 | 0.0735 | 0.0682 | 0.331 | 0.152 | 0.152 | 0.150 |

interactions of negative leakages in some fine groups with large values of fine group cross sections at scattering resonances. Similarly, large positive values arise from the interaction of large positive leakages from one region with scattering resonances of the adjacent medium. Both situations arise because of the fine-structure leakages across the interface. The corresponding collapsed values of the elastic-removal cross sections are listed in Table VI-11-III. They are also spatially sensitive; however, they do not vary as widely as in the case of the transport cross sections. Furthermore, since the elastic removal cross sections are obtained from a flux-weighted collapsing, and since the flux is always non-negative, apparent negative values of collapsed cross sections are not obtainable for this cross section.

The analogous collapsed transport cross sections for the interface case having the carbon-diluent core and the nickel reflector are listed in Table VI-11-IV. Because of the smooth non-resonant nature of the fine structure of the carbon cross sections, these collapsed transport cross-section values in the carbon region are not as widely varying as in the aluminum case. On the other hand, in the nickel region, widely varying values are again obtained. This is caused by the fact that the large smoothly varying outward leakage of the lower energy flux from the graphite core encounters cross-section peaks and troughs in the adjacent resonance-structured nickel region. In this case, also, the elastic removal cross sections in the reflector vary more than in the core. These values are given in Table VI-11-V.

Fine group leakages at various positions are much more sensitive indicators of differences between anisotropic and isotropic fine solutions than are the flux spectra at the various points. Therefore it may be expected that differences should occur in the collapsed values of transport cross sections, depending upon whether anisotropic or isotropic fine group solutions are used.

Collapsed transport values of the aluminum-iron interface case are compared in Table VI-11-VI for Coarse Groups 10 and 11 using anisotropic and isotropic leakages.

For Coarse-Group 10 the corresponding anisotropic and isotropic-based values at each of the positions are reasonably similar. In contrast, the anisotropic-based and isotropic-based values in Group 11 differ markedly. In the energy range of Group 11 there is strong fine structure interaction across the interface. Because of this, the values are very sensitive to spatial position. At such positions even small differences in depths of penetrations of the leakage maxima due to use of isotropic rather than anisotropic fine-group solutions result in large differences in energy averages of cross-sections at these points.

The question of suitability of such collapsed cross sections for use in subsequent coarse-group calculations has not, of course, been shown by these results. The cases presented are extreme situations in that the scat-

TABLE VI-11-VI. $\Sigma_{tr_J}$ FOR ALUMINUM-IRON BY ANISOTROPIC AND ISOTROPIC FINE SOLUTION WEIGHTINGS

| Group, $J$ | Fine Soln. | Distance from Core Center, cm | | | | | | | |
|---|---|---|---|---|---|---|---|---|---|
| | | 1.5 | 16.5 | 24.8 | 29.9 | 30.1 | 35.2 | 45.4 | 49.9 |
| 10 | A | 0.171 | 0.162 | 0.093 | 0.212 | 0.538 | 0.197 | 0.317 | 0.331 |
| | I | 0.171 | 0.162 | 0.093 | 0.203 | 0.567 | 0.202 | 0.316 | 0.323 |
| 11 | A | 0.110 | 0.109 | 0.011 | −5.10 | 52.8 | 0.581 | −0.078 | 0.117 |
| | I | 0.112 | 0.104 | −0.039 | −4.92 | 50.6 | 0.629 | −0.128 | 0.157 |

tering media are single isotopes. These example cases were chosen to insure that effects of interactions across interfaces would be clearly discernible. Most cases arising in fast reactor analyses will generally have more isotopes in each region, some of which are either non-resonant scatterers and/or heavy fissile and fertile materials.

### REFERENCES


1. A. L. Rago and H. H. Hummel, *An IBM-704 Program Treating Elastic Scattering Resonances in Fast Reactors*, ANL-6805 (1964).
2. D. Meneghetti, *Evaluation of Group Cross Sections for Light Reflectors*, Trans. Am. Nucl. Soc., **8**, 247 (1965).
3. D. Meneghetti, *Effects of Leakage Upon Evaluation of Fast-Reactor Multigroup Cross Sections for Reflectors*, ANL-7170 (1966).
4. D. Meneghetti, A. L. Rago and K. E. Phillips, *Use of the ELMOE-SNARG Programs to Study Details of Neutron Spectra Through Regions of Resonance-Scattering Media*, Resumenes de los Articulos Presentados en la Conferencia Internacional sobre Utilizacion de Reactores de Investigacion y Computo y Matematicas de Reactores, Mexico City (1967).
5. G. J. Duffy, H. Greenspan, S. D. Sparck, J. V. Zapatka and M. K. Butler, *SNARG-1D, A One-Dimensional Discrete-Ordinate Transport-Theory Program for the CDC-3600*, ANL-7221 (1966).
6. B. Carlson, C. Lee and J. Worlton, *The DSN and TDC Neutron Transport Codes*, LAMS-2346 (1960).
7. S. Yiftah, D. Okrent and P. A. Moldauer, *Fast Reactor Cross Sections*, (Pergamon Press, New York, 1960).


## VI-12. Space-Time Kinetics—The QX1 Code

D. A. MENELEY, K. OTT* and E. S. WIENER

The basic description of a modified adiabatic model for fast reactor spatial kinetics is given in Ref. 1 and some details of the formulation are given in Ref. 2. The following describes the approximations in somewhat greater detail and gives results of some of the test problems which have been run.

### BASIC EQUATION SET

Equations (1) and (2) show the flux and precursor equations in simplified notation. The operators $M$, $\chi_p$, $F_p$, $\chi_d$ and $F_c$ may be functions of space, energy, and time. Elements of each of these may also be functions of the total flux $\Phi$. Separate equations may determine space-time dependence of the system boundary positions.

$$v^{-1}\frac{\partial \Phi}{\partial t} = (M + \chi_p F_p)\Phi + \chi_d \lambda C, \qquad (1)$$

$$\frac{\partial C}{\partial t} = \chi_c F_c \Phi - \lambda C, \qquad (2)$$

$v \equiv$ neutron velocity vector
$\Phi \equiv$ space-energy-time dependent flux
$M \equiv$ removal and transfer operator
$\chi_p \equiv$ prompt neutron spectrum
$F_p \equiv$ prompt fission yield
$\chi_d \equiv$ delayed neutron emission spectrum
$\lambda \equiv$ decay constants
$C \equiv$ precursor concentrations
$\chi_c \equiv$ precursor spectrum—fractional yield of delayed neutron precursors in each precursor family
$F_c \equiv$ precursor fission yield.

Note that no provision for precursor concentration

* On leave from Kernforschungszentrum, Karlsruhe, Germany, within the framework of the U.S.A.E.C.—Euratom Scientist Exchange Program.

change as a function of system density is included. No great difficulty would be introduced by this addition.

The first step in the development is the separation of the flux $\Phi$ into the product of a space-energy-time-dependent shape function and a purely time-dependent amplitude function as shown in Eq. (3). (This development may be found in many publications, notably Ref. (3).):

$$\Phi(\mathbf{r},E,t) = \psi(\mathbf{r},E,t)\phi(t), \qquad \phi(o) = 1.0. \quad (3)$$

The only required conditions on the shape function $\psi$ are that it remain positive and bounded at all points in the space $(\mathbf{r},E)$ for all time.[4] We select one admissible separation within this class, namely that shown in Eq. (4):

$$\frac{\partial}{\partial t}\langle \psi^*(\mathbf{r},E), v^{-1}\psi(\mathbf{r},E,t)\rangle = 0. \quad (4)$$

This selection has some numerical advantages, as will be seen below. The brackets $\langle\rangle$ denote integration over all $\mathbf{r}$ and $E$. $\psi^*(\mathbf{r},E)$ is the solution of the system:

$$(M + \chi_p F_p + \chi_d \chi_c F^T_{c_{t=0}})\,\psi^*(\mathbf{r},E) = 0. \quad (5)$$

The operator is the transpose of the real solution operator appropriate to the critical system at time zero. The choice of $\psi^*$ as the weighting function is somewhat arbitrary. We wish, however, to allow the final equations to reduce to the point kinetics set. The choice of $\psi^*$ gives the usual perturbation theory error cancellation in this case.

Now substitute for the total flux in the original equations, multiply by the adjoint $\psi^*$, and integrate over space and energy. Due to the choice of separation, the time derivative of the weighted neutron density function drops out of the result, and we arrive at the usual point kinetics equations for the amplitude $\phi$, as shown in Eqs. (6) and (7). The subscript $f$ refers to the delayed precursor family:

$$\frac{d\phi}{dt} = \frac{(\rho - \beta)}{\Lambda}\phi + \sum_f \lambda_f \eta_f, \quad (6)$$

$$\frac{d\eta_f}{dt} = \frac{\beta_f}{\Lambda}\phi - \lambda_f \eta_f, \quad (7)$$

where

$$\frac{\rho}{\Lambda} = \frac{\left\langle \psi^*, \left[M + \frac{1}{k_0}(\chi_p F_p + \chi_d \chi_c F_c)\right]\psi\right\rangle}{\langle \psi^*, v^{-1}\psi\rangle}$$

$$\eta_f = \frac{\langle \psi^*, \chi_{d,f} C_f\rangle}{\langle \psi^*, v^{-1}\psi\rangle};$$

$$\frac{\beta_f}{\Lambda} = \frac{\langle \psi^*(\chi_{d,f}\chi_{c,f}F_c)\psi\rangle}{\langle \psi^*, v^{-1}\psi\rangle},$$

$$\frac{\beta}{\Lambda} = \sum_f \frac{\beta_f}{\Lambda}.$$

The terms $\rho$, $\beta$, and $\Lambda$ can be identified with reactivity, effective delay fraction, and generation time, after definition of an appropriate denominator term. The choice is completely arbitrary; however, to maintain consistency with definitions of perturbation reactivity we define it to be:

$$F = \langle \psi^*, (\chi_p F_p + \chi_d \chi_c F_c)\psi\rangle. \quad (8)$$

In a system which is critical at time zero, $k_0$ is always unity. The notation is preserved to cover the initially subcritical case with an applied source (see Subcritical System, below).

At this stage of the development Eqs. (4), (6), and (7), are merely the integral forms of the original set. Methods of approximation and solution of the system will now be described.

## Solution Methods

Substituting Eq. (3) into Eq. (1) and defining $\alpha = (1/\phi)/(d\phi/dt)$,

$$v^{-1}\frac{\partial \psi}{\partial t} = (M + \chi_p F_p - v^{-1}\alpha)\psi + \frac{1}{\phi}\chi_d \lambda C. \quad (9)$$

This is merely a rearrangment of Eq. (1), and as such is no easier to solve than the original system. The quasi-static approximation consists of neglecting the time derivative on the left hand side of Eq. (9). Now the solution $\psi$ at time $t$ depends entirely on the state of the reactor at $t$; the precursor term may be considered as a fixed source.

The sequence of time advance is indicated in Fig. VI-12-1. Three types of time interval are used. The one from $t^B_{i-1}$ to $t^B_i$ is that over which the shape function is assumed constant. New values of feedback parameters are used to compute $\rho$, $\beta$, and $\Lambda$ values for Eqs. (6) and (7) at the end of each $t^n$ interval. The time integration intervals, $t^k$, may be whatever is required for solution of feedback or amplitude equations. Consider a fully determined system at $t^B_{i-1}$. First assume that the shape function $\psi$ is constant from $t^B_{i-1}$ to $t^B_i$. Using an estimated time dependence of the amplitude function up to $t^n_1$, integrate the feedbacks and applied driving functions over this interval. Approximate the coefficients $\rho$, $\beta$, and $\Lambda$ in Eqs. (6) and (7) by parabolas passing through the last three computed points. Solve the set given by Eqs. (6) and (7) over the range, compare the resultant end point

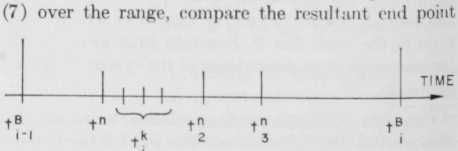


Fig. VI-12-1. Time Step Sequence. *ANL Neg. No. 112-9087.*

amplitude with the prediction, and iterate if necessary. When the time step is completed, estimate the shape function distortion since time $t^n_{i-1}$. If the distortion is small carry out another $t^n$ step.

Given a fully defined system at $t^n_{i-1}$, this portion of the solution is analogous to a point kinetics treatment. The errors present in the solution after a number of $t^n$ steps arise from several sources; first, the assumption of constant shape over the range. The value of the reactivity $\rho(t^n)$ is the most sensitive term. It may be written

$$\rho(t^n) = \frac{1}{F}\left\langle \psi^*, \Delta\left[M + \frac{1}{k_0}(\chi_p F_p + \chi_d \chi_c F_c)\right]\psi_{t^B_{i-1}}\right\rangle + \frac{1}{F}\left\langle \psi^*, \Delta\left[M + \frac{1}{k_0}(\chi_p F_p + \chi_d \chi_c F_c)\right]\delta\psi\right\rangle \tag{10}$$

The second term containing $\delta\psi$, the change in $\psi$ from $t^n_{i-1}$ to $t^n$, is neglected. This term may become large, since for perturbations local in space, $\delta\psi$ will in general be positive for a local positive change. Also, the term $\Delta(\ )$ represents the whole change in system constants from zero time.

Errors in the $\rho$ term tend to underestimate the change in $\rho$ and hence the change in amplitude over an interval. The feedback response, precursor densities, and the large influence on the magnitude of $\tilde{\psi}$, but not on its shape in space or energy. Errors in $\tilde{\phi}$ simply scale the solution. The errors in $\tilde{C}$ are ignored on the ground that the spatial distribution of delayed precursors is of secondary importance in determining the flux shape function during realistic fast reactor accidents.

The above considerations lead to the following procedure for finding the new shape function. If, during the iteration process, $\tilde{\alpha}$ is found to be so much in error that no solution for $\tilde{\phi}$ exists, a rebalance calculation is carried out and a new value of $\tilde{\alpha}$ is computed. This $\tilde{\alpha}$ is then used in subsequent iterations toward the solution $\tilde{\psi}$. When $\tilde{\psi}$ is found, it is simply renormalized using the condition of Eq. (4), and is used as the new shape function at time $t^n_i$. An alternative approach may be to find the solution of the equivalent static system at $t^B_i$. This approach would, however, completely ignore the effect of the non-equilibrium precursor shape (which is primarily determined by conditions at $t < t^B_i$) on the flux shape at $t^B_i$. It is shown in Ref. 1 that the errors introduced by this model may be very appreciable.

When the coefficients of the amplitude function are recalculated after a new $\psi$ is found, they will in general show discontinuous jumps in value as illustrated in Eq. (13) for $\rho/\Lambda$:

$$\delta\left(\frac{\rho}{\Lambda}\right) = \frac{\left\langle \psi^*, \left[M + \frac{1}{k_0}(\chi_p F_p + \chi_d \chi_c F_c)\right]\psi_{t^B_i}\right\rangle - \left\langle \psi^*, \left[M + \frac{1}{k_0}(\chi_p F_p + \chi_d \chi_c F_c)\right]\psi_{t^B_{i-1}}\right\rangle}{\langle \psi^*, v^{-1}\psi\rangle} \tag{13}$$

logarithmic derivative of the amplitude function therefore contain errors at the time $t^B_i$, when a new shape is to be calculated. Identifying these approximate terms by the symbol ($\sim$), we may rewrite Eq. (9) and the approximate solution of Eq. (2) at time $t^B_i$ as

$$0 = (M + \chi_p F_p - v^{-1}\tilde{\alpha})\tilde{\psi}_{t^B_i}\,\tilde{\phi}^{-1}_{t^B_i}\chi_d \lambda \tilde{C}_{t^B_i} \tag{11}$$

and

$$\tilde{C}_{f,t^B_i} = C_{f,0}\exp[-\lambda_f t] + \sum_{j=1}^{i-1}\int_{t^B_{i-j}}^{t^B_{i-j+1}} \chi_{c,f} F_c \psi_{t^B_{i-j}} \cdot \tilde{\phi}(t')\exp[-\lambda_f(t^B_1 - t')]\,dt', \tag{12}$$

respectively. Note that Eq. (11) is overdetermined, due to the normalization condition of Eq. (4). (If no errors were present in the coefficients, Eq. (4) would be satisfied automatically.)

Also, under some conditions the largest eigenvalue of the matrix $(M + \chi_p F_p - v^{-1}\tilde{\alpha})$ may become greater than zero, in which case Eq. (11) has no solution. This condition arises since $\tilde{\alpha}$ is almost always underestimated during positive reactivity transients, because of the use of the previous shape function in the computation of $\tilde{\alpha}$. Small errors in $\tilde{\alpha}$ thus have a very

These jumps are smoothed by assuming that they are distributed linearly forward since time $t^B_{i-1}$, as shown in Eq. (14):

$$\left(\frac{\rho}{\Lambda}\right)_{t^n_i} = \left(\widetilde{\frac{\rho}{\Lambda}}\right)_{t^n_i}[1 + \epsilon_{t^B_i}(t^n_i - t^B_{i-1})]. \tag{14}$$

The new values of $\rho$, $\beta_f$, and $\Lambda$ are then used to solve Eqs. (6) and (7) a second time over the range $t^B_{i-1}$ to $t^B_i$. This empirical "backward correction" partially accounts for the effect of the continuous variation of $\psi$ over the time range. For cases such as those described below with no feedback, this correction seems to be very effective. It may be less effective for highly nonlinear problems or those in which the major part of the accident consists of spatial redistribution of the $\psi$ function.

The whole operation of the major time step from $t^B_{i-1}$ to $t^B_i$ could be iterated; this has not yet been attempted.

## Test Cases

The first series of test problems was taken from Ref. 5. The parameters of the two cores investigated may be found in Tables I, II, and III of Ref. 5. Figure

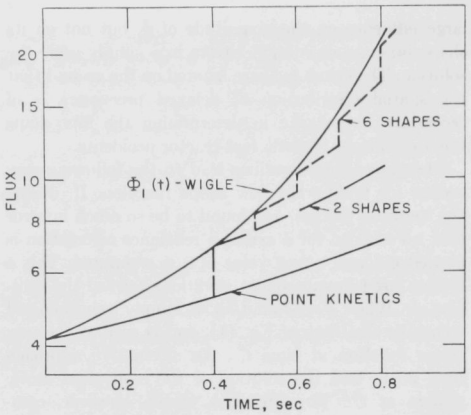


FIG. VI-12-2. Time Trajectory of Fast Flux at $x = 48$ cm in 240 cm Slab Thermal Core. Sub-prompt Transient of Ref. 5. *ANL Neg. No. 112-9089.*

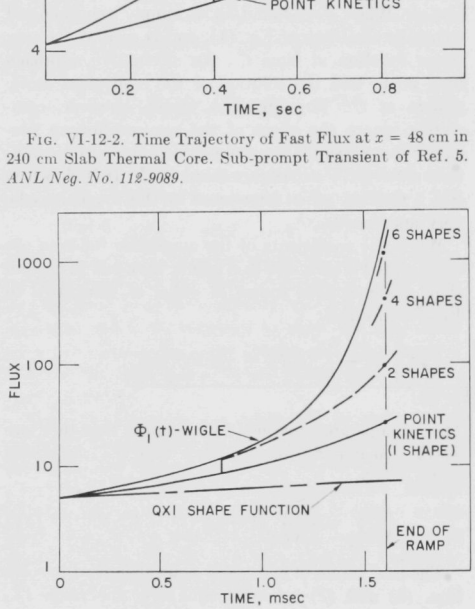


FIG. VI-12-3. Time Trajectory of Total Flux at $x = 48$ cm in 240 cm Slab Fast Core. Insertion Rate \$775 per sec up to \$1.25 at end of Ramp. *ANL Neg. No. 112-9098.*

VI-12-2 illustrates behavior typical of the approximation. This is the delayed critical transient in the 240 cm core of Ref. 5.

The upper curve is the time trajectory of the total flux at the point of maximum flux peaking, as computed by WIGLE.[6] The lowest curve was computed using the initial shape function throughout. The curve marked "2 shapes" is the result of recomputation at 0.4 seconds. Note that the large flux correction at 0.4 sec brings the QX1 solution very close to the true result. The deviation after a shape calculation is always on the low side of the solution, for this simple (linear) cross-section perturbation. The shape recalculation and backward correction are very effective in correcting the result. Any feedback effects would contain considerable errors, however, due to the initial underestimate of the time-integrated power. In this case it was possible to reproduce the WIGLE solution at 0.8 seconds to within 0.2% at every point by the use of 10 or more shape recalculations. The 60 cm core of Ref. 5 was predicted very well using two or three shape calculations.

In the artificial case of the step function super-prompt critical problems of Ref. 5, the quasistatic model behaves very much like the "adiabatic" model (see Fig. 3, Ref. 5) over the initial part of the transient. However the QX1 result is more accurate in the later part of the transient due to the improved treatment of delayed precursor distributions.

Several problems were run which were identical to the sub-prompt critical problems mentioned above except for more rapid ramp rates. In the 240 cm cores (lifetime $\sim 10^{-5}$ seconds) the quasistatic approximation introduced errors at ramp rates above \$10 per second. However, when the 240 cm core parameters were changed to those typical of a very hard spectrum, plutonium fueled reactor (lifetime $\sim 3 \times 10^{-8}$ sec) the QX1 and WIGLE solutions were essentially identical, at least up to a ramp rate of about \$750 per second. Figure VI-12-3 shows the time trajectory of the maximum point for this case. The error of the point kinetics solution is very large because the true reactivity at 1.6 milliseconds is greater than one dollar, while the point kinetics prediction is below one dollar. The maximum discrepancy between QX1 and WIGLE when conditions were recomputed at the end of the time step was around 2 percent after a flux rise of a factor of 200.

Figure VI-12-4 shows the layout of a three-enrichment-zone pancake, oxide-fueled fast reactor, with one subassembly missing on the centerline. Compositions used were typical of oxide systems. (The problem was treated in 22 energy groups, 50 mesh points.) The transient was initiated by inserting the central assembly in 1 second at a constant rate. Figures VI-12-5 and VI-12-6 show the amplitude and shape function, respectively, as computed by QX1.

The asymptotic logarithmic slope $\alpha$ of the amplitude function after the end of the ramp is smaller for the "point kinetics" solution than for the multi-shaped QX1 solution, indicating an accumulating error. A user of point kinetics calculation could easily eliminate this asymptotic error for a predefined excursion by directly computing the reactivity of the final state. However, in the case of a nonlinear feedback problem the elimination would be more difficult. The curve marked "true solution" in Fig. VI-12-6 is only an estimate, due to the

absence of any exact solution code capable of treating this case.

### Formulation for Initially Subcritical Systems

Additional terms are required when the system is subcritical at the start of the problem. These terms are not included in the QX1 algorithm at the present time.

First rewrite Eq. (1) for an initially subcritical core:

$$v^{-1}\frac{\partial \Phi}{\partial t} = (M + \chi_p F_p)\Phi + \chi_d \lambda C + \chi_e S_e, \quad (15)$$

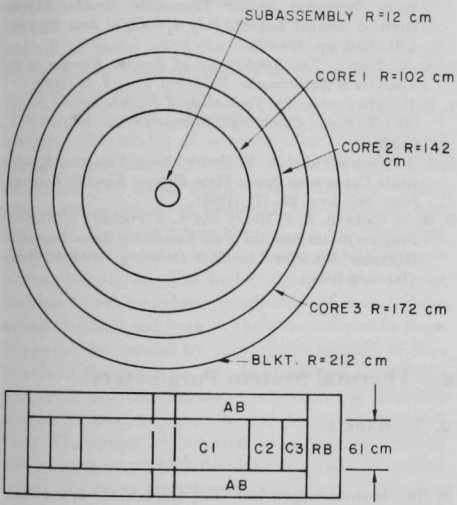


Fig. VI-12-4. Geometric Configuration of Pancake Fast Reactor For Subassembly Insertion Case. *ANL Neg. No. 112-9086.*

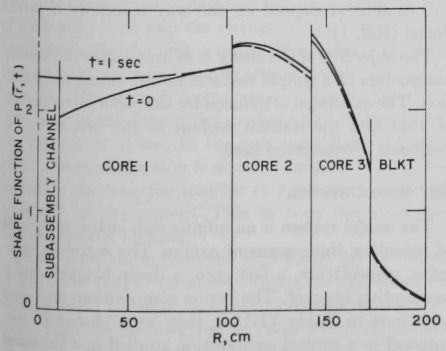


Fig. VI-12-5. Power Shape Function Along Radius of Pancake Fast Reactor Subassembly Insertion Case. *ANL Neg. No. 112-9100.*

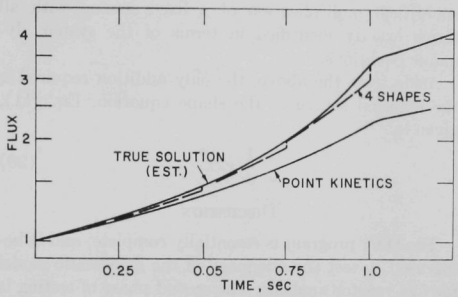


Fig. VI-12-6. Power Amplitude Function, Pancake Fast Reactor Subassembly Insertion Case. *ANL Neg. No. 112-9088.*

where $\chi_e$ and $S_e$ are, respectively, the energy spectrum and spatial distribution of the external source. Let $\psi^*$ be the solution of

$$\left[M + \frac{1}{k_0}(\chi_p F_p + \chi_d \chi_c F_c)\right]_{t=0}^{T} \psi^* = 0. \quad (16)$$

Multiply Eq. (15) by $\psi^*$ and Eq. (16) by $\Phi$, integrate over space and energy, and subtract. Then

$$\begin{aligned}\left\langle \psi^*, v^{-1}\frac{\partial}{\partial t}\Phi \right\rangle &= \left\langle \psi^*, \left[M + \frac{1}{k_0}(\chi_p F_p + \chi_d \chi_c F_c)\right]_{t=0}\Phi \right\rangle \\ &- \left\langle \Phi \left[M + \frac{1}{k_0}(\chi_p F_p + \chi_d \chi_c F_c)\right]_{t=0}^{T} \psi^* \right\rangle \\ &+ \frac{(k_0 - 1)}{k_0}\langle \psi^*, (\chi_p F_p + \chi_d \chi_c F_c)\,|_{t=t}\Phi\rangle \\ &+ \left\langle \psi^*, \left(\delta M + \frac{1}{k_0}\delta F\right)\Phi \right\rangle - \langle \psi^*, \chi_d \chi_c F_d \Phi\rangle \\ &+ \langle \psi^*, \chi_d \lambda C\rangle + \langle \psi^*, \chi_e S_e\rangle. \end{aligned} \quad (17)$$

By Green's theorem the first two terms on the right hand side cancel. Now substitute for $\Phi$ from Eq. (3) and define $\rho$, $\beta$, and $\Lambda$ as before. Then

$$\frac{d\phi}{dt} = \frac{(k_0 - 1)}{k_0 \Lambda}\phi + \frac{(\rho - \beta)}{\Lambda}\phi + \sum_f \lambda_f \eta_f + \zeta_e, \quad (18)$$

where

$$\zeta_e = \frac{\langle \psi^*, \chi_e S_e\rangle}{\langle \psi^*, v^{-1}\psi\rangle}.$$

In the static system at time zero, the amplitude is given by

$$\phi = \frac{\zeta_e \Lambda k_0}{1 - k_0}. \quad (19)$$

If $\phi$ is identified as the total number of neutrons in

the system, this becomes the familiar expression for subcritical multiplication of a fixed source, with all terms exactly identified in terms of the system dynamic equations.

Aside from the above, the only addition required is the external source in the shape equation, Eq. (11), given by

$$\frac{1}{\bar{\phi}} \chi_e S_e. \tag{20}$$

## Discussion

The QX1 program is essentially complete, and is being used to test the adequacy of the quasistatic model for fast reactor analysis. The second phase of testing is concerned with gaining experience in the importance and consequences of spatial model calculations to fast reactor excursions.

Many transient phenomena (such as coolant voiding) are not amenable to one dimensional treatment, particularly for cases in which the true overall net reactivity is around 1 dollar in the rising power phase of the accident. In such cases the computed time sequence of events may be greatly affected by quite small errors in reactivity producing large errors in the rate of energy accumulation. Therefore it is quite probable that there will be a need for two dimensional space-dependent kinetic calculation systems in the future. The QX1 method has been developed with this probability in mind, specifically with a view to minimizing the number of expensive shape recalculations. Experience in one-dimensional calculations will be very useful in guiding the design of these two-dimensional systems.

## References

1. K. Ott and J. Madell, *Quasistatic Treatment of Spatial Phenomena in Reactor Dynamics*, Nucl. Sci. Eng. **26**, 563 (1966).
2. K. Ott, D. Meneley and E. Wiener, *Quasistatic Treatment of Space Dependent Reactor Transients*, Reactor Physics Division Annual Report, July 1, 1965 to June 30, 1966, ANL-7210, pp. 370–373.
3. A. F. Henry, *The Application of Reactor Kinetics to the Analysis of Experiments*, Nucl. Sci. Eng. **3**, 52 (1958).
4. E. P. Gyftopoulos, *The Technology of Nuclear Reactor Safety*, (M.I.T. Press, Cambridge, Massachusetts, 1964), Vol. I, p. 179.
5. J. B. Yasinsky and A. F. Henry, *Some Numerical Experiments Concerning Space-Time Reactor Kinetics Behavior*, Nucl. Sci. Eng. **22**, 171 (1965).
6. W. R. Cadwell, A. F. Henry and A. J. Vigilotti, *WIGLE—A Program for the Solution of the Two-Group Space-Dependent Diffusion Equations in Slab Geometry*, WAPD-TM-416 (January 1964).

# VI-13. Space Dependent Effects on Fast-Thermal System Parameters

C. N. Kelber and J. T. Madell

## Introduction

Fast-thermal systems are space dependent with regard to kinetic effects. The vast majority of the reactivity and the power resides in the fast core. A thermal core or moderating blanket is coupled to the fast core through a heavy blanket. When the system is just critical, the chain reaction is maintained by low-energy neutrons returned from the moderating blanket or thermal core. The prompt neutron lifetime is largely determined by these very low-energy neutrons. The systems are space dependent because the buckling within the fast core is almost independent of the shape of the power within the thermal core or the return current from the moderating blanket but the thermal region is essentially driven by transmission through the blanket. Thus one region, the fast region, is almost operating in a fundamental mode, while another region, the thermal region, is operating in a mode far from the fundamental.

Under these circumstances it is expected that small changes in the fast region should produce large changes in the thermal region but that the reverse is not true. As a consequence the kinetics parameters, and especially the overall system lifetime, may change rapidly during an excursion, and the magnitude of these changes will in general depend on the way reactivity is introduced (Ref. 1).

The objective of the study is to investigate the kinetic parameters of a simple realistic model during an excursion. The excursion is induced by the rapid introduction of void into the sodium coolant in the fast core. No feedback is considered here.

### The Model System

The model system is an infinite slab lattice composed of repeating three-segment arrays. The segments comprise, respectively, a fast core, a dense blanket, and a moderating blanket. The region compositions and sizes are given in Table VI-13-I; they were chosen to correspond to a typical composition studied in a thousand megawatt electrical design study of a coupled metal

fast reactor system. Simplicity enters in regarding the lattice as a slab of infinite extent; thus the complicating details of leakage and curved geometry are avoided.

The enrichment of the fast core (Region I) was varied to achieve criticality. Using the usual static methods, the static parameters including prompt neutron lifetime and coupling coefficients were found by R. Avery's method[2] and are reported in Table VI-13-II. The parameters are given for the fundamental and first harmonic mode of the system.

Since the system has no leakage, the major reactivity effect occurs from the removal of sodium from the fast core and is positive. A static or quasistatic analysis will be useful until the reactivity introduced by sodium removal is approximately the reactivity needed to introduce a higher mode.

As M. Goldsmith[3] has pointed out, it is possible to determine the modes of a system by changing the boundary conditions according to the symmetry of the system. The model system has symmetry boundaries at the midplane of Region I, the fast core, and Region III, the moderating blanket. In the static case the boundary condition is one of zero current at each of these boundaries. The higher modes are found by inserting black boundary conditions of zero return current at either and both of these boundaries in turn. The modes determined by varying the number of neutrons born per fission, $\nu$, are distinguished from those determined by introducing everywhere a fictitious absorber of amount $\omega/v$, where $v$ is the neutron velocity. The former are referred to as $\lambda$ modes,[4] where $\lambda$ is the parameter which divides $\nu$ to make the system critical. The latter are referred to as $\omega$ modes[4] where $\omega$ is the time constant of the system. The results of this analysis are given in Table VI-13-III. The modes come in pairs with rather a wide separation between pairs and a relatively small separation between the members of each pair. Note also the change in the prompt neutron lifetime for the first $\omega$ mode. This reflects the fact that when the system is made critical by the introduction of an absorber of magnitude $\omega/v$, the major effect is to depress the flux in the moderating blanket where the absorption is low. In the fast core (Region I) the effect of such absorption is almost negligible. The effect is then to decrease the number of low-energy neutrons returning to the system. This in turn decreases the prompt neutron lifetime.

Removing sodium from the core yields $k_{ex} = 0.0683$ ($\lambda$ mode) or 0.0290 ($\omega$ mode). Based on the effective multiplication constant, $k_{eff}$, as a criterion, the expectation from the results given in Table VI-13-III is that no higher modes appear as small amounts of sodium are removed. As all of the sodium is removed, however, a higher mode would be expected to appear, inducing a change in power shape. Again referring to Table VI-13-III it is seen, however, that the prompt neutron lifetime should in fact show a change with sodium removal. Also it is reasonable to expect that there should be no substantial change in the power shape in the fast core. On this basis it is expected that a quasistatic approach[5] in which the lifetime varied with effective core composition to reflect the changing spectra within the fast core and the changing reactivity balance would be a useful technique. Because of time limitations, we chose to compare WIGLE[6] results with the results of $\omega$ mode calculations such as would be obtained in a quasistatic calculation. For the case of the large reactivity insertion studied here, the delayed neutron effects are negligible, and it is necessary only to calculate the prompt neutron distribution.

TABLE VI-13-I. Region Compositions and Sizes

| Region | Thickness, cm | Compositions | atoms/b-cm |
|---|---|---|---|
| I | 100 | U-238 | 0.015873 |
| | | Pu-239 | 0.001127 |
| | | Fe | 0.0127 |
| | | Na | 0.0127 |
| II | 10 | U-235 | 0.00012 |
| | | U-238 | 0.01688 |
| | | Fe | 0.0127 |
| | | Na | 0.0127 |
| III | 30 | Be | 0.1236 |

TABLE VI-13-II. Coupling Parameters[a]

| Mode | $K_{11}$ | $K_{12}$ | $K_{22}$ | $K_{21}$ | $\alpha_1$ | $l$, $10^{-6}$ sec | $\beta$, $10^{-4}$ |
|---|---|---|---|---|---|---|---|
| I | 0.948563 | 0.497215 | 0.502784 | 0.51436 | 0.906248 | 11.34 | 46 |
| II | 0.978083 ($\lambda$ mode) | 0.331662 | 0.175488 | 0.027370 | 0.974106 | 9.28 | 43 |

[a] As defined by R. Avery.[2]

TABLE VI-13-III. Modal Configurations

| Mode | Left Boundary[a] | Right Boundary[a] | $k,\lambda$ | $k,\omega$ | $lp$, $\mu$sec |
|---|---|---|---|---|---|
| I | 0 | 0 | 1.000000 | 1.000000 | 11.34 |
| II | 0 | B | 0.989051 | 0.973 | 9.28 ($\lambda$) |
| | | | | | 6.7 ($\omega$) |
| III | B | 0 | 0.81547 | — | — |
| IV | B | B | 0.789807 | — | — |

[a] *B* designates black boundary (zero return current); 0 designates zero flux gradient.

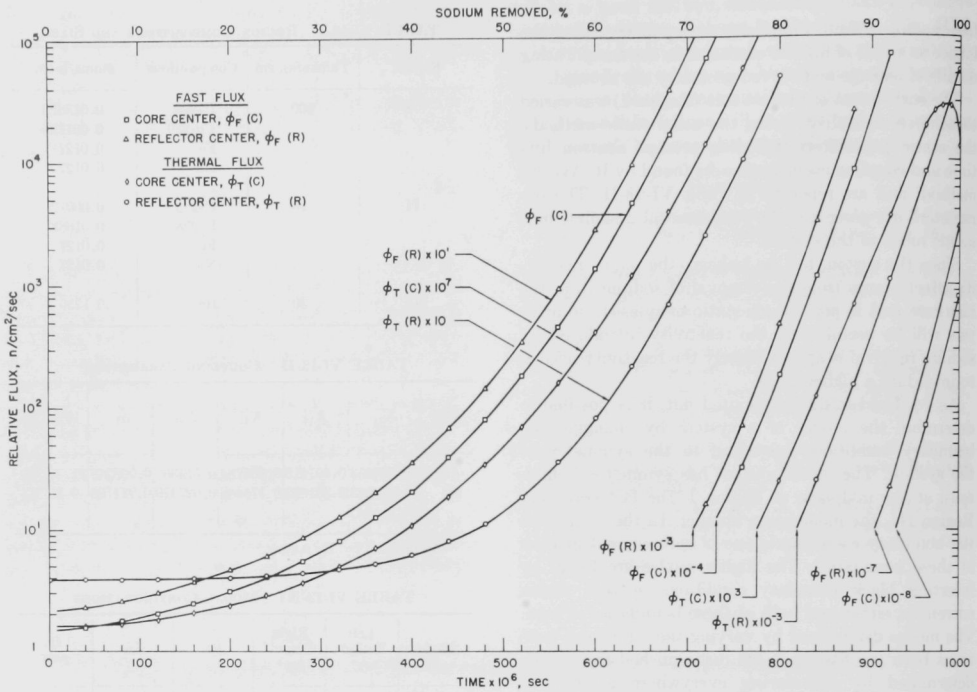


FIG. VI-13-1. WIGLE Results for Sodium Removal. *ANL Neg. No. 112-7468 Rev. 2.*

## WIGLE RESULTS

Multigroup constants and spectra were obtained at zero and 100% sodium void, and these were used to produce two group constants for use with the WIGLE code. In the collapsing process, the transport cross section was collapsed. Linear flux weighting of this sort cannot preserve the lifetime of the neutrons, but does preserve reaction rates. The effect of introducing a void in the sodium in the fast core in 1000 $\mu$sec is represented by assuming the cross sections to vary linearly in time from the zero void set to the 100% void set.

The results of the WIGLE analysis are shown in Fig. VI-13-I. It is interesting to note there that the thermal flux has a time lag of approximately 300 $\mu$sec. This represents transient and moderation time between the core and the reflector through the blanket. Since the plot is semilog, the attainment of the asymptotic state is signified by a straight line on the plot, and after about 90% void system is very nearly in the asymptotic state, except that the thermal flux is lagging. Finally, note the reduction in the magnitude of the thermal flux after 90% void is attained. This corresponds to a higher mode power shape.

## $\omega$ (ASYMPTOTIC) MODE CALCULATIONS

The Bondarenko cross section set[7] and multigroup diffusion theory were used to obtain time constants. The prompt neutron lifetime was obtained from perturbation theory using the fluxes and adjoint fluxes obtained from the system made critical by adjusting the time constant, that is, the asymptotic fluxes and their adjoints. These calculations were made at 0, 10, 30 and 100% sodium void.

The asymptotic power shapes are shown in Fig. VI-13-2 normalized to the same total power. A qualitative change in the shape occurs only at the 100% sodium void calculation. The time constants calculated in this way and the corresponding lifetimes together with the excess reactivity are given in Table VI-13-IV along with the time constants calculated from the WIGLE results using the power shape in the fast core. The prompt neutron lifetimes calculated with the param-

eters used in WIGLE are also given in Table VI-13-IV. Note the considerable discrepancy with the numbers generated by the multigroup sets reflecting the fact that in the process of group collapse the lifetime is not conserved. Table VI-13-IV also contains instantaneous values obtained from neutron inventory of the WIGLE results of the ratio of production to absorption. In a reactor on an asymptotic period the instantaneous value of this ratio is not the instantaneous value of the multiplication. The production at any moment is related, on the average, to the absorption which occurred at a mean absorption time earlier. Therefore, the instantaneous value of the ratio of production to absorption is equal to the instantaneous value of the multiplication constant, $k$, multiplied by $\exp(\alpha\delta)$, where $\alpha$ is the time constant or reciprocal period and $\delta$ is the mean time to absorption.* The mean time to absorption for the asymptotic state is computed to be 1.46 $\mu$sec which is reasonable when compared with a computed two group lifetime of 2.93 $\mu$sec. Both these numbers are much higher than the corresponding numbers as generated by the multigroup sets, but this is to be expected because of the crudeness of the spectral representation in the two group model.

### DISCUSSION OF DIFFERENCES AND CONCLUSIONS

The major differences between the detailed space-time solution obtained from WIGLE and the fluxes obtained from the asymptotic calculations are due to the crude spectrum employed in WIGLE together with the necessarily crude group collapsing method. The fact that the time constant for the asymptotic state with 100% sodium void is larger than that obtained from WIGLE is a reflection of the fact that the WIGLE results are not yet truly asymptotic and the two group lifetime is considerably different from the twenty-six group value. The observed discrepancy in time constant is thus not surprising. More important is the similar prediction of the change in lifetime and power shape as a function of the perturbation introduced.

One truly space dependent effect is the time lag for the thermal flux of approximately 300 $\mu$sec. In the study of extremely rapid transients such a time lag may be of significance, but for the admittedly extreme case studied here in which reactivity is added at the rate of several thousand dollars per second this time lag is not effective.

The spectral effects should not be expected to have much effect on the power shape in the fast core. They do, however, affect the power shape in the blanket and obviously at the core blanket interfaces as well as the reflector blanket interface.

* The mean time to absorption is flux weighted, not importance weighted, since flux weighted quantities are compared. Thus even in the model system with no leakage the mean time to absorption is not the lifetime.

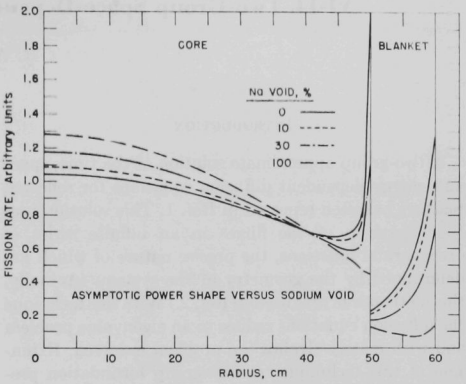


FIG. VI-13-2. Asymptotic Power Shapes as a Function of Sodium Void, $\omega$-Mode. *ANL Neg. No. 112-7327.*

TABLE VI-13-IV. COMPARISON OF $\omega$-MODE AND WIGLE CALCULATIONS

| % Na Removed | $k_{eff,\omega}$ | $l_{p,\omega}$, $\mu$sec | $l_{p,\text{WIGLE}}$, $\mu$sec | $\alpha_\omega$, sec$^{-1}$ | $\alpha^{(a)}_{\text{WIGLE}}$ | $\left(\frac{\text{PROD}}{\text{ABS}}\right)$ |
|---|---|---|---|---|---|---|
| 0 | 1.000 | 11.34 | 17.9 | 0 | 0 | 1.0 |
| 10 | 1.00388 | 6.85 | | 566 | 2000 | 1.0113 |
| 30 | 1.00827 | 1.84 | | 4491 | 7311 | 1.0374 |
| 100 | 1.0290 | 0.155 | 2.9 | 182,242 | 60,043 | 1.1239 |

[a] Computed from fluxes at the core center line.

## REFERENCES

1. See, for example, A. V. Campise, *Comparison of the Dynamic and Safety Characteristics of Fast and Fast-Coupled Reactor Systems*, Proc. Conference on Breeding, Economics and Safety in Large Fast Power Reactors, October 7–10, 1963, ANL-6792, pp. 617–641.
2. R. Avery, *Theory of Coupled Reactors*, Proc. 1958 Geneva Conference **12**, Paper No. 1858, pp. 182–191.
3. M. Goldsmith, *Symmetry Properties of Some Eigen-Functions Occurring in Reactor Analysis*, Nucl. Sci. Eng. **47**, 111–124 (1963).
4. A. F. Henry, *The Application of Inhour Modes to the Description of Nonseparable Reactor Transients*, Nucl. Sci. Eng. **20**, 338–351 (1964).
5. K. Ott and J. T. Madell, *Quasistatic Treatment of Spatial Phenomena in Reactor Dynamics*, Nucl. Sci. Eng., (to be published).
6. W. R. Cadwell, A. F. Henry and A. J. Vigolotti, *WIGLE—A Program for the Solution of the Two-Group Space-Time Diffusion Equations in Slab Geometry*, WAPD-TM-416 (1964).
7. I. I. Bondarenko (Ed.), *Group Constants for Nuclear Reactor Calculations*, (Consultants Bureau, New York, 1964).

# VI-14. Two-Group Space-Dependent Kinetics In Reflected Reactors

R. A. Karam

## Introduction

A two-group approximate solution of the time, space and energy dependent diffusion equations for reflected reactors has been reported in Ref. 1. This solution uses the expansion of the fluxes in an infinite series of orthonormal functions, the precise nature of which are determined by the geometry of the system. (Actually, this method was first used in Ref. 2.) With this technique the diffusion equations reduce to an eigenvalue problem and with matrix algebra the problem is solved. Extension of this technique to multigroup formulation presents no difficulties except for the size of the square matrix. However, there is one basic problem with this approach; namely, that the convergence of the series to the asymptotic mode can be very slow, especially in fast reactors.

A different approach to the solution of the time, space and group dependent diffusion equations in reflected reactors is used in this work. Basic to this approach is the assumption that

$$\Phi^i(r,t) = \sum_n \Phi^i_n(r,t) = \sum_n e^{-\alpha_n t} \sum_m A^i_{mn} W_{mn}(r), \quad (1)$$

where $i$ is the energy group number, $n$ is the mode number, and $m$ is the spatial function number. The exponent, $\alpha_n$, is the decay constant of mode $n$ and $A^i_{mn}$ are constants associated with group $i$, mode $n$ and function $m$. The $W_{mn}(r)$ are independent functions which are determined from the solution of the wave equation with arguments given by the group-dependent cross sections. When the expression for $\Phi^i(r,t)$ in Eq. (1) is used in the diffusion equations the solutions become similar to those of the time-independent equations except for the $\alpha_n$ dependence; such solutions have been reported in many books.[3,4,5] With this method it will be shown that the modes of a system can be analytically predicted. Furthermore, the spatial dependence of all the modes can be obtained. The decay constants of the prompt modes along with the spatial functions can be used to obtain the time dependence of the fluxes in each group as a function of space throughout the system.

This work is particularly suited to the analysis of the decay of the prompt modes encountered in the Rossi-alpha experiment. The model was tested for a specific system in which three prompt decay constants were found.

## Theory

We write the diffusion equations in one dimension for the two-group, two-region reactor:

$$D^1_c \Delta\Phi^1_c(r,t) - \Sigma^1_{Rc}\Phi^1_c(r,t) + \chi^1(\nu\Sigma_f)^1\Phi^1_c(r,t) + \chi^1(\nu\Sigma_f)^2\Phi^2_c(r,t) = \frac{1}{v^1}\frac{\partial\Phi^1_c(r,t)}{\partial t}, \qquad 0 \le r \le R_0, \quad (2)$$

$$D^2_c \Delta\Phi^2_c(r,t) - \Sigma^2_{Rc}\Phi^2_c(r,t) + \chi^2(\nu\Sigma_f)^2\Phi^2_c(r,t) + [\Sigma^{1-2}_c + \chi^2(\nu\Sigma_f)^1]\Phi^1_c(r,t) = \frac{1}{v^2}\frac{\partial\Phi^2_c(r,t)}{\partial t}, \qquad 0 \le r \le R_0, \quad (3)$$

$$D^1_R \Delta\Phi^1_R(r,t) - \Sigma^1_{RR}\Phi^1_R(r,t) = \frac{1}{v^1}\frac{\partial\Phi^1_R(r,t)}{\partial t}, \qquad R_0 \le r \le R_1, \quad (4)$$

and

$$D^2_R \Delta\Phi^2_R(r,t) - \Sigma^2_{RR}\Phi^2_R(r,t) + \Sigma^{1-2}\Phi^1_R(r,t) = \frac{1}{v^2}\frac{\partial\Phi^2_R(r,t)}{\partial t}, \qquad R_0 \le r \le R_1. \quad (5)$$

The superscripts 1 and 2 designate the energy groups, the subscripts $c$ and $R$ refer to the core and reflector and the subscripts $Rc$ and $RR$ designate the removal cross sections in the core and reflector respectively. $R_0$ is the radius at the core-reflector boundary and $R_1$ is the extrapolated boundary of the reflector. The delayed neutrons have been ignored in Eqs. (2) and (3). The removal cross sections are defined as:

$$\Sigma^1_{Rc} \equiv D^1_c(B_t)^2 + \Sigma^1_{ac} + \Sigma^{1-2}_c, \quad (6)$$

$$\Sigma^2_{Rc} \equiv D^2_c(B_t)^2 + \Sigma^2_{ac}, \quad (7)$$

$$\Sigma^1_{RR} \equiv D^1_R(B_t)^2 + \Sigma^1_{aR} + \Sigma^{1-2}_R, \quad (8)$$

and

$$\Sigma^2_{RR} \equiv D^2_R(B_t)^2 + \Sigma^2_{aR}, \quad (9)$$

where $(B_t)^2$ is the transverse buckling, $\Sigma^{1-2}$ is the down-scattering cross section and the subscripts $ac$ and $aR$ refer to the absorption cross sections in the core and reflector respectively. The other symbols used in Eqs. (1-5) are defined as follows:

$\Phi \equiv$ neutron flux per unit area and unit time,
$D \equiv$ diffusion coefficient,
$v \equiv$ velocity of the neutron, cm/sec,

$\chi \equiv$ fraction of fission neutrons released in a group,

$(\nu\Sigma_f) \equiv$ source of fission neutrons in a group.

We substitute the expression of Eq. (1) into Eq. (2) and obtain

$$\begin{aligned}\sum_n e^{-\alpha_n t} \{ & D_c^1 \Delta[A_{1n}^1 W_{1n}(r) + A_{2n}^1 W_{2n}(r)] \\ & + [\chi^1(\nu\Sigma_f)^1 - \Sigma_{Rc}^1][A_{1n}^1 W_{1n}(r) + A_{2n}^1 W_{2n}(r)] \\ & + \chi^1(\nu\Sigma_f)^2[A_{1n}^2 W_{1n}(r) + A_{2n}^2 W_{2n}(r)]\} \\ & = \frac{1}{v^1} \sum_n \left\{ \left[ A_{1n}^1 W_{1n}(r) + A_{2n}^1 W_{2n}(r) \right] \frac{de^{-\alpha_n t}}{dt} \right\}. \end{aligned} \tag{10}$$

In Eq. (10) the function index $m$ in $W_{mn}(r)$ is restricted to two values in the two-group approximations for reasons that will be apparent shortly. The number of spatial functions in three groups will be three and in $q$ groups will be $q$. We assume the functions $W_{mn}(r)$ to be independent of each other* and this implies that the terms involving $W_{1n}(r)$ on the lefthand side of Eq. (10) must be equal to the terms of $W_{1n}(r)$ on the righthand side. The same is true for the $W_{2n}(r)$ functions. Thus Eq. (10) can be separated into two equations which may be reduced to the following:

$$\begin{aligned}\frac{\Delta W_1(r)}{W_1(r)} + \frac{1}{D_c^1} \Bigg\{ & \left[ \chi^1(\nu\Sigma_f)^1 - \Sigma_{Rc}^1 \right] \\ & + \chi^1(\nu\Sigma_f)^2 \frac{A_1^2}{A_1^1} + \frac{\alpha}{v^1} \Bigg\} = 0, \end{aligned} \tag{11}$$

$$\begin{aligned}\frac{\Delta W_2(r)}{W_2(r)} + \frac{1}{D_c^1} \Bigg\{ & \left[ \chi^1(\nu\Sigma_f)^1 - \Sigma_{Rc}^1 \right] \\ & + \chi^1(\nu\Sigma_f)^2 \frac{A_2^2}{A_2^1} + \frac{\alpha}{v^1} \Bigg\} = 0, \end{aligned} \tag{12}$$

where the summation over $n$ of $\alpha_n$ has been dropped for convenience and it is to be understood that the functions $W_1(r)$ and $W_2(r)$ and the $A_m^1$ are dependent on $\alpha$. Similar treatment of Eq. (3) yields

$$\begin{aligned}\frac{\Delta W_1(r)}{W_1(r)} + \frac{1}{D_c^2} \Bigg\{ & \left[ \chi^2(\nu\Sigma_f)^2 - \Sigma_{Rc}^2 \right] \\ & + \left[ \chi^2(\nu\Sigma_f)^1 + \Sigma_c^{1-2} \right] \frac{A_1^1}{A_1^2} + \frac{\alpha}{v^2} \Bigg\} = 0, \end{aligned} \tag{13}$$

and

$$\begin{aligned}\frac{\Delta W_2(r)}{W_2(r)} + \frac{1}{D_c^2} \Bigg\{ & \left[ \chi^2(\nu\Sigma_f)^2 - \Sigma_{Rc}^2 \right] \\ & + \left[ \chi^2(\nu\Sigma_f)^1 + \Sigma_c^{1-2} \right] \frac{A_2^1}{A_2^2} + \frac{\alpha}{v^2} \Bigg\} = 0 \end{aligned} \tag{14}$$

* This assumption is the same as that usually made in the time-independent case.[4]

Equations (11–14) are in the form of the wave equation

$$\Delta W_1(r) + B_1^2 W_1(r) = 0,$$

and

$$\Delta W_2(r) + B_2^2 W_2(r) = 0. \tag{15}$$

It is noted that $B_1^2$ and $B_2^2$ are mode dependent, i.e., depend on $\alpha$. We eliminate the constants $A_m^1$ from Eqs. (11–14) in the following manner:

$$\begin{aligned}\frac{A_1^1}{A_1^2} &= \left\{ \frac{\chi^1(\nu\Sigma_f)^2}{D_c^1 B_1^2 + \Sigma_{Rc}^1 - \chi^1(\nu\Sigma_f)^1 - \dfrac{\alpha}{v^1}} \right\} \\ &= \left\{ \frac{D_c^2 B_1^2 + \Sigma_{Rc}^2 - \chi^2(\nu\Sigma_f)^2 - \dfrac{\alpha}{v^2}}{\chi^2(\nu\Sigma_f)^1 + \Sigma_c^{1-2}} \right\}, \end{aligned}$$

and

$$\begin{aligned}\frac{A_2^2}{A_2^1} &= \left\{ \frac{\chi^2(\nu\Sigma_f)^1 + \Sigma_c^{1-2}}{D_c^2 B_2^2 + \Sigma_{Rc}^2 - \chi^2(\nu\Sigma_f)^2 - \dfrac{\alpha}{v^2}} \right\} \\ &= \left\{ \frac{D_c^1 B_2^2 + \Sigma_{Rc}^1 - \chi^1(\nu\Sigma_f)^1 - \dfrac{\alpha}{v^1}}{\chi^1(\nu\Sigma_f)^2} \right\}. \end{aligned} \tag{16}$$

The righthand side of Eq. (16) gives a quadratic equation for $B^2$. The roots in the equation for $B^2$ are

$$B^2 = -\left(\frac{\eta_1 + \eta_2}{2}\right) \pm \frac{\sqrt{(\eta_1 + \eta_2)^2 - 4(\eta_1\eta_2 - \eta_3)}}{2}, \tag{17}$$

where

$$\eta_1 = \frac{1}{D_c^1} \left\{ \Sigma_{Rc}^1 - \chi^1(\nu\Sigma_f)^1 - \frac{\alpha}{v^1} \right\},$$

$$\eta_2 = \frac{1}{D_c^2} \left\{ \Sigma_{Rc}^2 - \chi^2(\nu\Sigma_f)^2 - \frac{\alpha}{v^2} \right\},$$

and

$$\eta_3 = \chi^1(\nu\Sigma_f)^2 \{\chi^2(\nu\Sigma_f)^1 + \Sigma_c^{1-2}\}/D_c^1 D_c^2. \tag{18}$$

The values $B_1^2(\alpha)$ and $B_2^2(\alpha)$ are obtained from Eq. (17). It is noted from Eq. (17) that $B_1^2(\alpha)$ and $B_2^2(\alpha)$ can take on either positive or negative values since $\alpha$ can vary between large negative values (super-critical) and large positive values (subcritical). For the asymptotic mode, when the system is near critical $B_1^2(\alpha)$ is small and positive and $B_2^2(\alpha)$ is large and negative. Equation (17) however implies that $B_1^2(\alpha)$ and $B_2^2(\alpha)$ are continuous functions of $\alpha$ and as such discrete modes do not exist. This is not so, as will be seen later;

only certain values of $B_1^2$ ($\alpha$) and $B_2^2$ ($\alpha$) exist when the system as a whole is taken into consideration.

The solutions of Eqs. (2) and (3) in cylindrical configuration can now be written as

$$\Phi_c^1(r,t=0) = \sum_n \{A_{1n}^1 J_0[B_1(\alpha_n)r] + A_{2n}^1 I_0[B_2(\alpha_n)r]\}, \quad 0 \le r \le R_0, \tag{19}$$

and

$$\Phi_c^2(r,t=0) = \left\{\sum_n a_{1n}^1 A_{1n} J_0[B_1(\alpha_n)r] + a_{2n} A_{2n}^1 I_0[B_2(\alpha_n)r]\right\}, \quad 0 \le r \le R_0, \tag{20}$$

where

$$a_{1n} = \left[\frac{\chi^2(\nu\Sigma_f)^1 + \Sigma_c^{1-2}}{D_c^2 B_1^2(\alpha) + \Sigma_{Rc}^2 - \chi^2(\nu\Sigma_f)^2 - \frac{\alpha_n}{v^2}}\right], \tag{21}$$

and

$$a_{2n} = \left[\frac{\chi^2(\nu\Sigma_f)^1 + \Sigma_c^{1-2}}{D_c^2 B_2^2(\alpha) + \Sigma_{Rc}^2 - \chi^2(\nu\Sigma_f)^2 - \frac{\alpha_n}{v^2}}\right]. \tag{22}$$

The usual conditions on $\Phi_c^1(r,t)$, that is, well behaved and finite everywhere, have been imposed on Eqs. (19) and (20).

In the reflector, we make the same assumption about the time and space dependent fluxes as in Eq. (1), namely,

$$\Phi_R^i(r,t) = \sum_n e^{-\alpha_n t}\{C_{1n}^i Z_{1n}(r) + C_{2n}^i Z_{2n}(r)\}. \tag{23}$$

We substitute Eq. (23) into Eqs. (4) and (5) and note that for $\Phi_R^1$ only $Z_{1n}(r)$ would be adequate to describe the flux in this group. Thus we get

$$\frac{\Delta Z_1(r)}{Z_1(r)} - \frac{1}{D_R^1}\left\{\Sigma_{RR}^1 - \frac{\alpha}{v^1}\right\} = 0, \quad R_0 \le r \le R_1. \tag{24}$$

Let

$$\lambda_1^2(\alpha) = \frac{1}{D_R^1}\left\{\Sigma_{RR}^1 - \frac{\alpha}{v^1}\right\}; \tag{25}$$

then in cylindrical configuration the general solution for Eq. (24) is

$$\Phi_R^1(r,t=0) = \sum_n C_{1n} Z_{1n}(r) = \sum_n C_{1n}\{b_{1n} I_0[\lambda_1(\alpha_n)r] + b_{2n} K_0[\lambda_1(\alpha_n)r]\}, \tag{26}$$

where $C_{1n}$, $b_{1n}$, and $b_{2n}$ are constants.

For the second energy group in the reflector we use Eqs. (23) and (5) and follow the same procedure used in Eqs. (10–20). We obtain the two pertinent equations

$$\frac{\Delta Z_1(r)}{Z_1(r)} - \frac{1}{D_R^2}\left\{\Sigma_{RR}^2 - \Sigma_R^{1-2}\frac{C_1^1}{C_1^2} - \frac{\alpha}{v^2}\right\} = 0, \tag{27}$$

and

$$\frac{\Delta Z_2(r)}{Z_2(r)} - \frac{1}{D_R^2}\left\{\Sigma_{RR}^2 - \frac{\alpha}{v^2}\right\} = 0, \tag{28}$$

where again the summation over $\alpha_n$ has been dropped for convenience and it is to be understood that the functions $Z_1(r)$ and $Z_2(r)$ and the constant $C_1^1$ and $C_1^2$ are dependent on $\alpha$. Equations (27) and (24) must have the same solution since they involve the same function. Thus the constant $C_1^2$ is obtained in terms of $C_1^1$ from Eqs. (27) and (24).

$$C_1^2 = \frac{D_R^1 \Sigma_R^{1-2} C_1^1}{D_R^1\left[\Sigma_{RR}^2 - \frac{\alpha}{v^2}\right] - D_R^2\left[\Sigma_{RR}^1 = \frac{\alpha}{v^1}\right]} = m_1 C_1^1. \tag{29}$$

The solution for Eq. (5) in cylindrical configuration can be written as

$$\begin{aligned}\Phi_R^2(r,t=0) &= \sum_n \{C_{1n}^2 Z_{1n}(r) + C_{2n}^2 Z_{2n}(r)\} \\ &= \sum_n \{m_{1n} C_{1n}^1 \{b_{1n} I_0[\lambda_1(\alpha_n)r] \\ &\quad + b_{2n} K_0[\lambda_1(\alpha_n)r]\} \\ &\quad + C_{2n}^2 [b_{3n} I_0[\lambda_2(\alpha_n)r] \\ &\quad + b_{4n} K_0[\lambda_2(\alpha_n)r]\}, \qquad R_0 \le r \le R_1,\end{aligned} \tag{30}$$

where $\lambda_2(\alpha_n)$ is defined as

$$\lambda_2(\alpha_n) = \left\{\frac{1}{D_R^2}\left[\Sigma_{RR}^2 - \frac{\alpha_n}{v^2}\right]\right\}^{1/2}. \tag{31}$$

Equations (19), (20), (26), and (30) contain the constants $A_1^1$, $A_2^1$, $C_1^1 b_1$, $C_1^1 b_2$, $C_2^2 b_3$ and $C_2^2 b_4$. All these constants can be evaluated relative to one constant, for example $A_1^1$, by imposition of the boundary conditions. The constant, $A_1^1$ will have to be evaluated relative to either the power level of the reactor or the initial conditions of the flux. The boundary conditions we have at our disposal are:

$$(1)\quad \Phi_c^1(R_0,t) = \Phi_R^1(R_0,t) \tag{32}$$

$$(2)\quad \Phi_c^2(R_0,t) = \Phi_R^2(R_0,t) \tag{33}$$

$$(3)\quad D_c^1(\Phi_c^1)'(R_0,t) = D_R^1(\Phi_R^1)'(R_0,t) \tag{34}$$

$$(4)\quad D_c^2(\Phi_c^2)'(R_0,t) = D_R^2(\Phi_R^2)'(R_0,t) \tag{35}$$

$$(5)\quad \Phi_R^1(R_1,t) = 0 \tag{36}$$

$$(6)\quad \Phi_R^2(R_1,t) = 0, \tag{37}$$

where the quantities $(\Phi_c^1)'$ and $(\Phi_R^1)'$ indicate the spatial derivatives of the functions. The rest of the symbols have been defined before. The application of the boundary conditions expressed in Eqs. (36) and (37)

to Eqs. (26) and (30) yields the following expressions $C_1^1 b_1$ and $C_2^2 b_3$ :

$$C_1^1 b_1 = -C_1^1 b_2 \frac{K_0[\lambda_1(\alpha)R_1]}{I_0[\lambda_1(\alpha)R_1]}, \tag{38}$$

and

$$C_2^2 b_3 = -C_2^2 b_4 \frac{K_0[\lambda_1(\alpha)R_1]}{I_0[\lambda_2(\alpha)R_1]}. \tag{39}$$

The first boundary condition, Eq. (32), and Eqs. (19) and (26) give the following expression for $C_1^1 b_2$ :

$$C_1^1 b_2 = \frac{A_1^1 J_0[B_1(\alpha)R_0] + A_2^1 I_0[B_2(\alpha)R_0]}{K_0[\lambda_1(\alpha)R_0] - \dfrac{K_0}{I_0}[\lambda_1(\alpha)R_1]I_0[\lambda_1(\alpha)R_0]}, \tag{40}$$

in which the use of Eq. (38) is implicit and $(K_0/I_0)(x)$ is defined as $K_0(x)/I_0(x)$. The expression for $C_2^2 b_4$ is obtained from boundary condition (2) and the previous results of Eqs. (38), (39) and (40). Thus the expression for $C_2^2 b_4$ is

$$C_2^2 b_4 = \frac{A_1^1(a_1 - m_1)J_0[B_1(\alpha)R_0] + A_2^1(a_2 - m_1)I_0[B_2(\alpha)R_0]}{K_0[\lambda_2(\alpha)R_0] - \dfrac{K_0}{I_0}[\lambda_2(\alpha)R_1]I_0[\lambda_2(\alpha)R_0]}. \tag{41}$$

Boundary condition (3) is used to evaluate $A_2^1$ in terms of $A_1^1$. The expression for $A_2^1$ is

$$A_2^1 = A_1^1 \gamma_3, \tag{42}$$

where

$$\gamma_3 = \frac{D_c^1 B_1(\alpha)J_1[B_1(\alpha)R_0] - D_R^1 \lambda_1(\alpha)\gamma_1 J_0[B_1(\alpha)R_0]}{D_c^1 B_2(\alpha)I_1[B_2(\alpha)R_0] + D_R^1 \lambda_1(\alpha)\gamma_1 I_0[B_2(\alpha)R_0]},$$

and (43)

$$\gamma_1 = \frac{\dfrac{K_0}{I_0}[\lambda_1(\alpha)R_1]I_1[\lambda_1(\alpha)R_0] + K_1[\lambda_1(\alpha)R_0]}{K_0[\lambda_1(\alpha)R_0] - \dfrac{K_0}{I_0}[\lambda_1(\alpha)R_1]I_0[\lambda_1(\alpha)R_0]}.$$

Finally, boundary condition (4) is used to obtain the last kinetic equation of the reactor. This equation has the following form

$$\begin{aligned} D_c^2 B_2(\alpha) a_2 \gamma_3 I_1[B_2(\alpha)R_0] - D_c^2 B_1(\alpha) a_1 J_1[B_1(\alpha)R_0] \\ = -D_R^2 J_0[B_1(\alpha)R_0]\{m_1\lambda_1\gamma_1 + \lambda_2\gamma_2(a_1 - m_1)\} \\ - D_R^2 \gamma_3 I_0[B_2(\alpha)R_0] \\ \cdot\{m_1\lambda_1\gamma_1 + \lambda_2\gamma_2(a_2 - m_1)\}, \end{aligned} \tag{44}$$

where

$$\lambda_2 = \frac{\dfrac{K_0}{I_0}[\lambda_2 R_1]I_1[\lambda_2 R_0] + K_1[\lambda_2 R_0]}{K_0[\lambda_2 R_0] - \dfrac{K_0}{I_0}[\lambda_2 R_1]I_0[\lambda_2 R_0]}, \tag{45}$$

and $A_1^1$ has been canceled out from all the terms. The lefthand side of Eq. (44) is the net current in the core at the core-reflector interface. The righthand side is the net current in the reflector at the same point. Because of the continuity condition, Eq. (35), these two sides must be equal for a particular value of $\alpha$. Thus by evaluating the righthand and lefthand sides of Eq. (44) as a function of $\alpha$, one can obtain the modes for the system at the intersections of those two quantities. Once a mode for the system has been found, i.e., an $\alpha$ for which the righthand and lefthand sides of Eq. (44) become equal, then the spatial distributions of the fluxes for groups 1 and 2 in the core and in the reflector can be determined from Eqs. (19), (20), (26) and (30) respectively. The time dependence of the spatial fluxes for any mode or for the sum of more than one mode can be readily obtained from Eq. (1). This technique of locating modes has been used by R. Sher[6] in the one group approximation.

Although the evaluation of Eq. (44) as a function of $\alpha$ is feasible by hand calculation for a few values of $\alpha$, it is not a trivial matter to handle large quantities of such calculations. Since the values $B_1^2(\alpha)$, $B_2^2(\alpha)$, $\lambda_1^2(\alpha)$ and $\lambda_2^2(\alpha)$ can be either positive or negative, this means that the arguments of the Bessel functions $J_0$, $J_1$, $I_0$, $I_1$, $K_0$ and $K_1$ can be either real or imaginary. Subroutines for calculating Bessel functions with real arguments are readily available. When the arguments of the Bessel functions were imaginary, different forms of the solutions of the wave equations were used. For example, if $B_1^2(\alpha) < 0$ and $B_2^2(\alpha) < 0$ the equation for the fluxes was taken as

$$\begin{aligned} \Phi_c^1(r, t = 0) = \sum_n \{A_{1n}^1 I_0[B_1(\alpha_n)r] \\ + A_{2n}^1 I_0[B_2(\alpha_n)r]\} \end{aligned} \tag{46}$$

instead of Eqs. (19) and (20). In Eq. (46), $B_1(\alpha)$ is defined as

$$B_1(\alpha_n) = (-B_1^2(\alpha_n))^{1/2}. \tag{47}$$

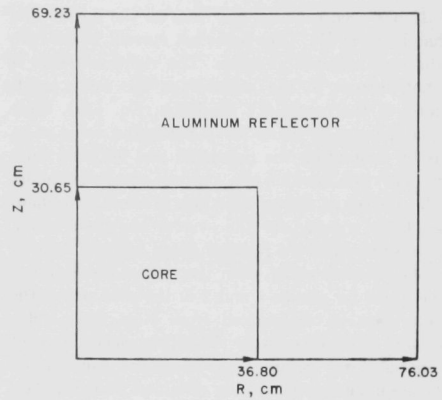


FIG. VI-14-1. Schematic of Assembly 6 of ZPR-9. *ANL Neg. No. 112-8629.*

Similar treatment was used for the cases where $B_2^2(\alpha_n) > 0$ and $\lambda_2^2(\alpha_n) < 0$.

Solutions of the time-dependent diffusion equations were also extended to two groups and three-regions in which the two outer regions were non-multiplying.[7] Extension to three or more groups and to four or more regions in which two or more regions are multiplying is straightforward. However, the algebra involved becomes increasingly tedious.

## COMPARISON OF THEORY WITH EXPERIMENTS

### EXPERIMENTS

Two systems in which the time dependence of the prompt neutron chains were measured were chosen to test the above theory. These systems were Assemblies 6 and 7 of ZPR-9[(8)]. Both assemblies had cylindrical configurations and the same material composition in the core region. Assembly 6 had an aluminum blanket in both the axial and radial directions. Assembly 7 had an aluminum oxide blanket in the radial and axial directions and had a jacket of about 11 cm of aluminum around the $Al_2O_3$ blanket in the radial direction only. Figures VI-14-1 and VI-14-2 show the pertinent experimental dimensions of these assemblies and Table VI-14-I lists the material concentrations in the various regions. The dimensions shown in Figs. VI-14-1 and VI-14-2 were obtained from cylinders with equivalent volumes of the actual loadings in both assemblies. Cross sectional views of the assemblies are shown in Figs. VI-14-3 and VI-14-4.

The experimental setup comprised two fission chambers, each containing about one gram of U-235, two preamps and two fast amplifiers, and a 1024-channel time analyzer. The time analyzer had channel widths that could be varied between 31.25 nsec and 2 $\mu$sec by factors of 2. The fission chambers were placed at the center of Assembly 7 in each half of the split table type system.[9] In Assembly 6 the fission chambers were placed in two adjacent matrix locations at the center of the core. One of the chambers (A) provided triggering pulses to start the time sweep of the analyzer cycle. The other chamber (B) provided the data pulses. If during a sweep, an event took place in chamber B the sweep would stop, a count would be added to the appropriate channel and the time analyzer would be reset. If an event did not take place in chamber B, the sweep would continue until the end of the cycle, at which time the analyzer would be automatically reset and a pulse would be given indicating that such a

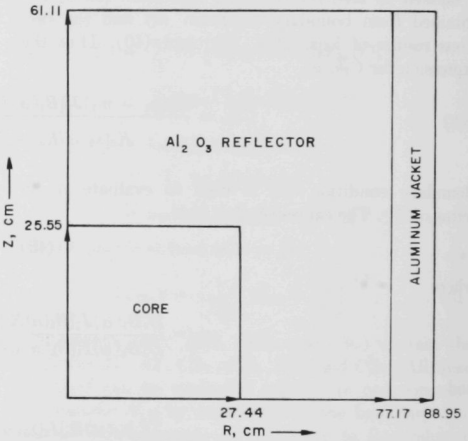


FIG. VI-14-2. Schematic of Assembly 7 of ZPR-9. *ANL Neg. No. 112-8630.*

TABLE VI-14-I. MATERIAL CONCENTRATIONS IN ASSEMBLIES 6 AND 7 OF ZPR-9

| | Atomic Concentrations, atoms/cc $\times 10^{-24}$ | | | | |
|---|---|---|---|---|---|
| | Assembly 6 | | Assembly 7 | | |
| Material | Core | Reflector | Core | Reflector 1 | Reflector 2 |
| U-235 | 0.00450 | — | 0.00450 | — | — |
| U-238 | 0.00033 | — | 0.00033 | — | — |
| Al | 0.01593 | 0.05658 | 0.01593 | 0.04364 | 0.05658 |
| O | — | — | — | 0.05508 | — |
| Fe | 0.00023 | — | 0.00023 | — | — |
| W | 0.02153 | — | 0.02153 | — | — |

sweep ended fruitlessly. The triggering pulses as well as the pulses from sweeps with no data were monitored with two separate scalers. Such monitoring provided easy checks on the desired power level which, for these experiments, must be necessarily low[10] (~ fraction of a watt). At the end of a run, which usually lasted 4-5 hours, the data were corrected according to the relation

$$P_j = \frac{C_j}{\sum_{i=j}^{n} C_i + SND}, \tag{48}$$

where

$P_j \equiv$ true count in channel $j$,
$C_j \equiv$ observed count in channel $j$,
$C_i \equiv$ observed count in channel $i$,
$SND \equiv$ number of sweeps that ended with no data stored in any channel.

This correction of the data gave the number of counts per channel opening. The corrected data were fitted to the function

$$N(t) = BG + \sum_i a_i e^{-\alpha_i t} \tag{49}$$

by the variable metric method for minimization.[11] The symbol $BG$ designates the background from uncorrelated pairs of events. The fitting of the data to the function of Eq. (49) required initial estimates of $BG$, $a_i$ and $\alpha_i$ which were obtained from the corrected data by graphical stripping. Figure VI-14-5 shows a sample of the uncorrected data that was taken in Assembly 7 with 2 μsec channel width. The corrected data from the same run is shown in Fig. VI-14-6. These data were treated in the following manner:

1) The counts from the last 100 channels were averaged in order to obtain an initial guess of the value of $BG$ in Eq. (49).
2) A line approximating the function $N(t)$ of Eq. (49) was drawn through the points as shown in Fig. VI-14-6. From this line the average background was subtracted and the results, shown in Fig. VI-14-7, were used to obtain the initial guess for the value of the decay constant of the asymptotic mode, $\alpha_1$, and the value of the intercept, $a_1$.
3) The value of $BG$ from step (1) was extrapolated to obtain the $BG$ of a run obtained with 62.5 nsec channel width. The extrapolated value of $BG$ was subtracted from a line approximating $N(t)$ for this run. The results are shown in Fig. VI-14-8 as dotted circles.
4) From the dashed line drawn through these points the quantity $a_1 e^{-\alpha_1 t}$ was subtracted, where $\alpha_1$ was determined from the 2 μsec channel width run (Fig. VI-14-7), and $a_1$ was extrapolated from Step (2) taking into consideration the difference in reactor power level and channel-width. The results of this step are shown as "crosses" in Fig. VI-14-8. It is seen from these points that there remain at least two exponentials.
5) The process of Step 5 was repeated and the initial guesses for the values of the decay constants of the second and third modes and the values of

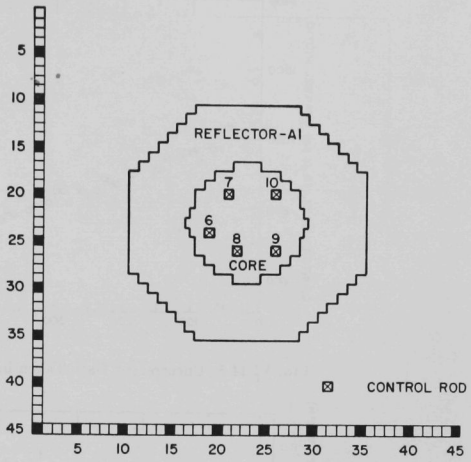


FIG. VI-14-3. Cross-Sectional View of Assembly 6. *ANL Neg. No. 112-7877 A Rev. 1.*

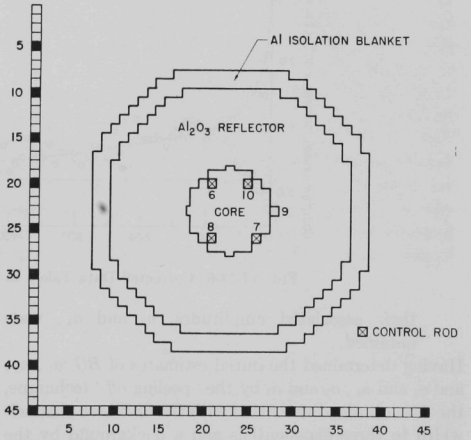


FIG. VI-14-4. Cross-Sectional View of Assembly 7. *ANL Neg. No. 112-7757 Rev. 1.*

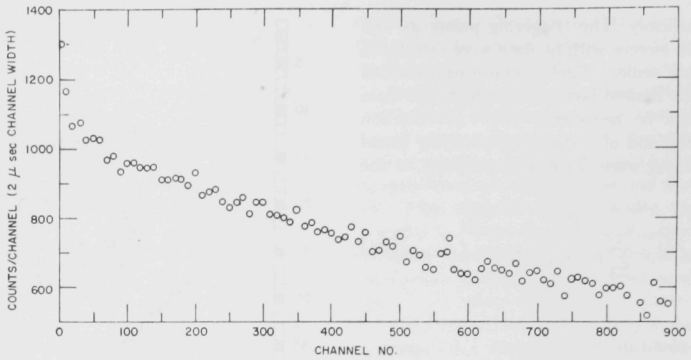


FIG. VI-14-5. Uncorrected Data Taken in Assembly 7 of ZPR-9. *ANL Neg. No. 112-8635.*

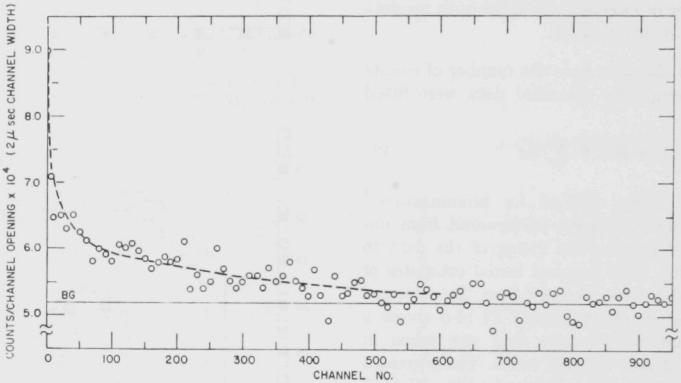


FIG. VI-14-6. Corrected Data Taken in Assembly 7 of ZPR-9. *ANL Neg. No. 112-8631.*

their associated amplitudes, $a_2$ and $a_3$, were obtained.

Having determined the initial estimates of $BG$, $a_1$, $a_2$, and $a_3$ and $\alpha_1$, $\alpha_2$ and $\alpha_3$ by the "peeling off" technique, the data obtained was fitted with the 62.5 nsec channel-width to three exponentials and a background by the variable metric code.[11,12] The results of the least squares fit and the initial estimates used are shown in Table VI-14-II.

The die-away data for the prompt chains obtained from Assembly 6 of ZPR-9 was treated in the same way as described above. Only two modes were detected in this assembly. The values of the least-square fit of the decay constants of the two modes were $(4.67 \pm 0.31) \times 10^4$ and $(2.86 \pm 1.10) \times 10^6$ per sec. The amplitudes of the asymptotic and the higher mode were $(1.60 \pm 0.02) \times 10^{-4}$ and $(1.70 \pm 0.10) \times 10^{-4}$ respectively.

COMPARISON WITH THEORY

The theory of Section II was applied to Assemblies 6 and 7 in the two-group approximation. The two-group cross sections for these two assemblies were generated from the Hansen and Roach[13] sixteen-group cross section set (known at Argonne as Set 201) by the group collapsing technique[14] in which the macroscopic cross sections are averaged over the neutron energy spectrum by flux integral weighting in each region. Table VI-14-III lists the two-group sets for both assemblies. The choice of energy grouping was somewhat arbitrary; in the two cases studied it was chosen in such a way that the fission rate of U-235 in both groups would be approximately equal. It will be shown later that the results are not independent of the group structure.

The $\Sigma_{removal}$ listed in Table VI-14-III included the axial leakage which was determined from the axial

height of the core plus the reflector saving, that is, $DB^2 = D(\pi/\tilde{H})^2$. The reflector saving was determined by the following three steps:

1) The radial critical buckling was determined by calculation along the axial direction with the sixteen-group cross section set.
2) From the radial critical buckling, an equivalent bare critical radius was obtained and used in a one region cylindrical core to calculate the axial critical buckling.
3) The critical height obtained from the axial buckling minus the core height yielded the reflector savings.

Assembly 7 was analyzed first by replacing the 11 cm jacket of aluminum by an equivalent thickness of aluminum oxide. The justification for this replacement was that the aluminum jacket was about 50 cm from the boundary of the core, and therefore it was not expected to have appreciable influence on the system.

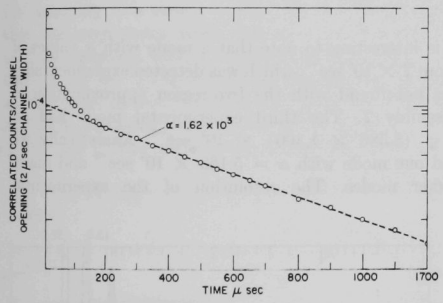


FIG. VI-14-7. Correlated Events in Assembly 7 of ZPR-9. *ANL Neg. No. 112-8636.*

TABLE VI-14-II. DECAY CONSTANTS OF THE PROMPT-NEUTRON CHAINS AND THEIR ASSOCIATED CONSTANTS IN ASSEMBLY 7 OF ZPR-9

| | Least Squares Fit | Initial Estimate |
|---|---|---|
| $BG$ | $(4.166 \pm 0.148) \times 10^{-5}$ | $4.17 \times 10^{-5}$ |
| $a_1$ | $(4.423 \pm 0.157) \times 10^{-6}$ | $4.40 \times 10^{-6}$ |
| $\alpha_1$ | $(1.507 \pm 0.135) \times 10^{3}$ sec$^{-1}$ | $1.62 \times 10^{3}$ sec$^{-1}$ |
| $a_2$ | $(5.221 \pm 0.489) \times 10^{-6}$ | $4.40 \times 10^{-6}$ |
| $\alpha_2$ | $(6.865 \pm 0.574) \times 10^{4}$ sec$^{-1}$ | $4.70 \times 10^{4}$ sec$^{-1}$ |
| $a_3$ | $(7.210 \pm 1.104) \times 10^{-6}$ | $9.40 \times 10^{-6}$ |
| $\alpha_3$ | $(8.586 \pm 1.300) \times 10^{5}$ sec$^{-1}$ | $6.57 \times 10^{5}$ sec$^{-1}$ |

Thus Assembly 7 was reduced to two regions and the lefthand and righthand sides of Eq. (44) were solved as functions of the core radius, $R_0$, and a fixed reflector thickness with $\alpha$ taken as zero. Once the two sides of Eq. (44) were identical with a particular value of $R_0$, then that value was the critical radius. It is noted that Eq. (44) gave the same value for the critical radii for Assemblies 6 and 7 as was obtained from the data listed in Table VI-14-III and the MACH 1 diffusion code.[14] The critical radius so determined is actually for a prompt critical system since delayed neutrons were neglected. After determining the critical radius, Eq. (44) was solved as a function of $\alpha$ with $\chi^1$ and $\chi^2$, the fractions of fission neutrons emitted in each group, reduced by $\beta^1_{eff}$ and $\beta^2_{eff}$. The values of $\beta^1_{eff}$ and $\beta^2_{eff}$ were determined from the sixteen-group set with the formulation given in the MACH 1 code.[14] The lefthand and righthand sides of Eq. (44) are plotted as functions of $\alpha$ in Figs. VI-14-9 and VI-14-10 for Assembly 7 in the two-region approximations. It is seen from Fig. VI-14-9 that the two sides have identical values at $\alpha = 1.580 \times 10^3$ sec$^{-1}$, which is the value of

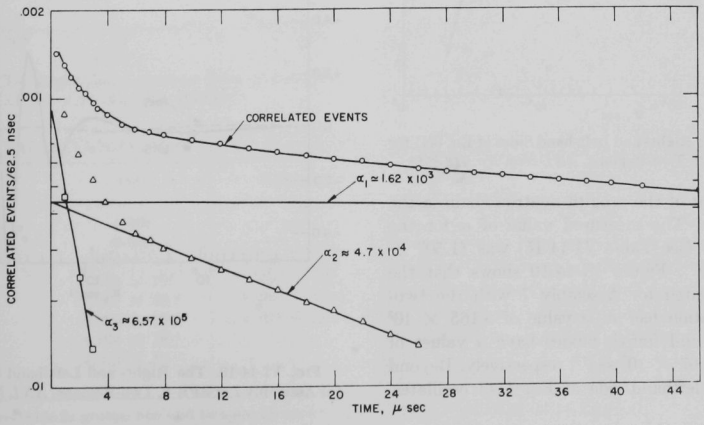


FIG. VI-14-8. Correlated Events Taken with 62.5 nsec Channel Widths in Assembly 7 of ZPR-9. *ANL Neg. No. 112-8625 Rev. 1.*

TABLE VI-14-III. TWO-GROUP[a] MACROSCOPIC CROSS SECTIONS FOR ASSEMBLIES 6 AND 7 OF ZPR-9

| Parameter[b] | Assembly 6 | | Assembly 7 | | |
|---|---|---|---|---|---|
| | Core | Al Reflector | Core | $Al_2O_3$ Reflector | Al Reflector |
| $\chi^1$ | 0.896 | — | 0.896 | — | — |
| $\chi^2$ | 0.104 | — | 0.104 | — | — |
| $v^1$ cm/sec | $1.320 \times 10^9$ | $1.320 \times 10^9$ | $1.354 \times 10^9$ | $1.354 \times 10^9$ | $1.354 \times 10^9$ |
| $v^2$ cm/sec | $3.771 \times 10^8$ | $3.771 \times 10^7$ | $1.375 \times 10^7$ | $1.375 \times 10^7$ | $1.375 \times 10^7$ |
| $\Sigma_a^1$ cm$^{-1}$ | $7.905 \times 10^{-2}$ | $6.920 \times 10^{-5}$ | $7.853 \times 10^{-3}$ | $1.890 \times 10^{-4}$ | $3.647 \times 10^{-5}$ |
| $\Sigma_a^2$ cm$^{-1}$ | $1.342 \times 10^{-2}$ | $1.706 \times 10^{-4}$ | $1.623 \times 10^{-2}$ | $2.934 \times 10^{-4}$ | $6.586 \times 10^{-4}$ |
| $(\nu\Sigma_f)^1$ cm$^{-1}$ | 1.4023 $\times 10^{-2}$ | — | 1.4036 $\times 10^{-2}$ | — | — |
| $(\nu\Sigma_f)^2$ cm$^{-1}$ | $1.943 \times 10^{-2}$ | — | $2.257 \times 10^{-2}$ | — | — |
| $\nu^1$ | 2.556 | — | 2.559 | — | — |
| $\nu^2$ | 2.456 | — | 2.455 | — | — |
| $\Sigma^{1-2}$ cm$^{-1}$ | $1.467 \times 10^{-2}$ | $1.041 \times 10^{-2}$ | $1.441 \times 10^{-2}$ | $2.205 \times 10^{-2}$ | $7.544 \times 10^{-2}$ |
| $\Sigma_{tr}^1$ cm$^{-1}$ | $1.611 \times 10^{-1}$ | $1.396 \times 10^{-1}$ | $1.586 \times 10^{-1}$ | $2.246 \times 10^{-1}$ | $1.287 \times 10^{-1}$ |
| $\Sigma_{tr}^2$ cm$^{-1}$ | $2.457 \times 10^{-1}$ | $1.258 \times 10^{-1}$ | $2.449 \times 10^{-1}$ | $2.623 \times 10^{-1}$ | $8.088 \times 10^{-2}$ |
| $\Sigma_{removal}^1$ cm$^{-1}$ | $2.534 \times 10^{-2}$ | $1.367 \times 10^{-3}$ | $2.464 \times 10^{-2}$ | $2.392 \times 10^{-3}$ | $1.051 \times 10^{-3}$ |
| $\beta_{eff}^1$ | 0.004884 | — | 0.004884 | — | — |
| $\beta_{eff}^2$ | 0.001716 | — | 0.001716 | — | — |

[a] Groups one and two energy intervals are 10 MeV–400 keV and 400 keV—0.025 eV, respectively.

[b] The superscripts 1 and 2 refer to groups one and two, respectively.

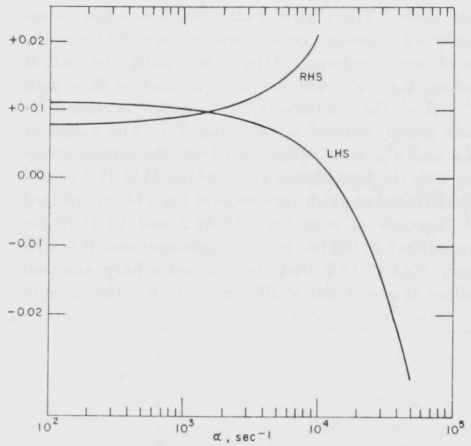


FIG. VI-14-9. The Right- and Left-hand Sides of Eq. (44) for Assembly 7 of ZPR-9, Two-Regions. *ANL Neg. No. 112-8638.*

the decay constant of the prompt-neutron chain in the asymptotic mode. The measured value of $\alpha$ for the asymptotic mode (see Table VI-14-II) was $(1.507 \pm 0.135) \times 10^3$ sec$^{-1}$. Figure VI-14-10 shows that the next mode calculated for Assembly 7 with the two-region approximation has an $\alpha$ value of $5.165 \times 10^5$ sec$^{-1}$. The third and fourth modes have $\alpha$ values of $1.48 \times 10^6$ and $2.97 \times 10^6$ sec$^{-1}$, respectively. Beyond these modes the lefthand side of Eq. (44) oscillates.

It is interesting to note that a mode with $\alpha$ values of about $7 \times 10^4$ sec$^{-1}$, which was detected experimentally, was not found with the two-region approximation of Assembly 7. The third experimental mode had an $\alpha = (8.586 \times 1.300) \times 10^5$ sec$^{-1}$. Analytically we find one mode with $\alpha = 5.165 \times 10^5$ sec$^{-1}$ and many higher modes. The resolution of the experimental

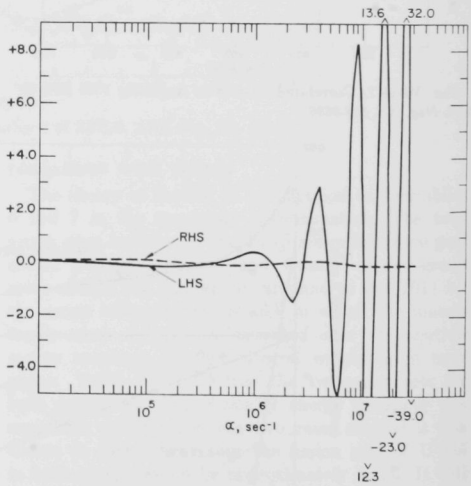


FIG. VI-14-10. The Right- and Left-hand Sides of Eq. (44) for Assembly 7 of ZPR-9, Two-Regions. *ANL Neg. No. 112-8628.*

equipment is not adequate to resolve these modes; therefore, we conclude that the third experimental mode is a composite.

Assembly 7 was reanalyzed with the aluminum jacket included. The equations for three-region analysis are given in Ref. 7. With this analysis, the three lowest eigenvalues were $1.616 \times 10^3$ sec$^{-1}$, $9.45 \times 10^4$ sec$^{-1}$ and $5.73 \times 10^5$ sec$^{-1}$. The first and third eigenvalues are in agreement with the two-region analysis. The second eigenvalue, which was not predicted by the two-region analysis, is due to the presence of the aluminum jacket. This value is slightly higher than the measured value of $(6.87 \pm 0.57) \times 10^4$ sec$^{-1}$. It is not known whether this discrepancy is caused by errors in the cross sections of aluminum or by the statistics of the data.

The analysis of Assembly 6 of ZPR-9 was carried out in the same manner as outlined above. The plot of the righthand and lefthand sides of Eq. (44) versus $\alpha$ for Assembly 6 is shown in Fig. VI-14-11. It is seen that the asymptotic mode has an $\alpha = 5.1 \times 10^4$ sec$^{-1}$ as compared with a measured value of $(4.67 \pm 0.31) \times 10^4$ sec$^{-1}$. The analytical value of the $\alpha$ of the second mode, as seen from Fig. VI-14-11, is $7.5 \times 10^5$ sec$^{-1}$. The measured value of this $\alpha$ was $(2.86 \pm 1.10) \times 10^5$ sec$^{-1}$. The measurement, however, was conducted with 0.2 $\mu$sec channel width and it is doubtful that there was adequate resolution to measure the $\alpha$ of the second mode accurately.

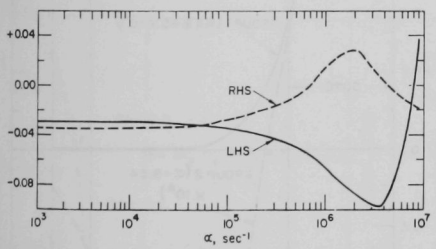


FIG. VI-14-11. The Right- and Left-hand Sides of Eq. (44) for Assembly 6 of ZPR-9. *ANL Neg. No. 112-8627.*

Assembly 6 was also analyzed with a two-group set in which the energy intervals were 10 MeV–3 keV and 3 keV to thermal. This set was produced by the same group collapsing technique described earlier from the same Hansen and Roach 16-group set.[13] The parameters used in this analysis are shown in Table VI-14-IV. The decay constant of the asymptotic mode obtained with these parameters was $5.5 \times 10^4$ sec$^{-1}$. This value compares with a value of $5.1 \times 10^4$ sec$^{-1}$, obtained with the parameters shown in Table VI-14-III. Thus, the choice of the energy interval in each group does affect the results and the magnitude of this effect on the decay constant of the asymptotic mode is about 10%.

## Dependence of Decay Constant of Asymptotic Mode on Criticality and Spatial Distribution of the Modes

The dependence of the decay constant of the asymptotic mode in Assembly 7 (two-regions approximately) on the criticality of the system was studied by varying the number of neutrons released per fission. This variation was achieved by decreasing or increasing $\chi^1$ and $\chi^2$ in the range of 1 to 10%. For example, to decrease the fission neutron production by 5%, we used 95% of the initial values of $\chi^1$ and $\chi^2$ in the analysis. Such variation in the values of $\chi^1$ and $\chi^2$ would be equivalent to introducing a $\Delta\nu$ if $\nu^1$ and $\nu^2$ were constant. This procedure is not expected to affect the neutron spectrum of the system regardless of the degree of criticality, provided of course the size of the system is kept constant. The spectral effect on the decay constant of the asymptotic mode was studied by varying $\chi^1$ with $\chi^2$ held constant and again by varying $\chi^2$ with $\chi^1$ held constant. The results of this study are shown in Fig. VI-14-12.

TABLE VI-14-IV. Two-Group[a] Macroscopic Cross Sections for Assembly 6 of ZPR-9

| Parameter | Core | Reflector | Parameter | Core | Reflector |
|---|---|---|---|---|---|
| $\chi^1$ | 1.000 | — | $\nu^1$ | 2.496 | — |
| $\chi^2$ | 0.000 | — | $\nu^2$ | 2.450 | — |
| $v^1$ cm/sec | $5.759 \times 10^8$ | $5.759 \times 10^8$ | $\Sigma^{1\to 2}$ cm$^{-1}$ | $3.223 \times 10^{-5}$ | $1.945 \times 10^{-4}$ |
| $v^2$ cm/sec | $3.766 \times 10^7$ | $3.766 \times 10^7$ | $\Sigma^1_{tr}$ cm$^{-1}$ | $2.042 \times 10^{-1}$ | $1.307 \times 10^{-1}$ |
| $\Sigma^1_a$ cm$^{-1}$ | $1.067 \times 10^{-2}$ | $1.400 \times 10^{-4}$ | $\Sigma^2_{tr}$ cm$^{-1}$ | $4.577 \times 10^{-1}$ | $7.724 \times 10^{-2}$ |
| $\Sigma^2_a$ cm$^{-1}$ | $9.629 \times 10^{-2}$ | $7.989 \times 10^{-5}$ | $\Sigma^1_{Removal}$ cm$^{-1}$ | $1.289 \times 10^{-2}$ | $3.744 \times 10^{-3}$ |
| $(\nu\Sigma_f)^1$ cm$^{-1}$ | $1.674 \times 10^{-2}$ | — | $\Sigma^2_{Removal}$ cm$^{-1}$ | $9.726 \times 10^{-2}$ | $5.849 \times 10^{-3}$ |
| $(\nu\Sigma_f)^2$ cm$^{-1}$ | 9.473 × 10 | — | $\beta^1_{eff}$ | 0.0066 | — |
| | | — | $\beta^2_{eff}$ | 0.000 | — |

[a] The energy intervals in groups one and two are 10 MeV—3 keV and 3 keV—thermal, respectively.

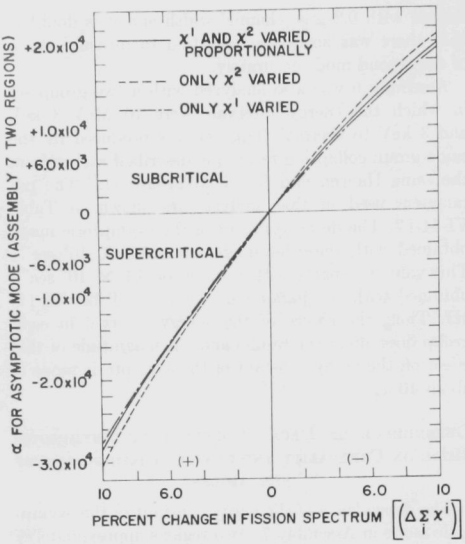


FIG. VI-14-12. The Dependence of the Decay Constant of the Asymptotic Mode on Criticality. *ANL Neg. No. 112-8626 Rev. 1.*

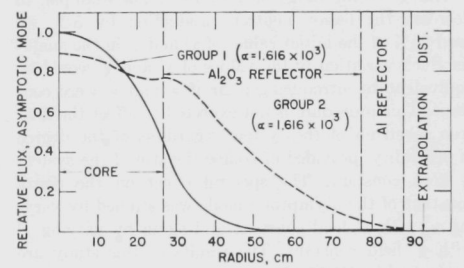


FIG. VI-14-13. Fluxes of the Asymptotic Mode ($\alpha = 1.616 \times 10^3$) in Assembly 7 of ZPR-9. *ANL Neg. No. 112-8633.*

It is seen from Fig. VI-14-12 that the lines curve toward the lower right quadrant in both the supercritical and subcritical states. The degree of curvature depends of course on the system. It is significant to note that in safety analyses where linear extrapolation of the reactivity in dollars divided by the generation time of the neutrons is used to predict the growth of the neutron population with time from point reactor kinetics, the value of the $\alpha$ of the asymptotic mode is underestimated. The magnitude of the underestimation depends of course on the degree of supercriticality. The spectral effect on the value of $\alpha$ as a function of criticality shows that by decreasing the fraction of fission neutrons released in the second group, the value of $\alpha$ increases in the subcritical state. By increasing $\chi^2$ in the supercritical state, the value of $\alpha$ becomes more negative than for the normal condition where the fission neutrons are increased uniformly. The opposite is true for increases in $\chi^1$. The eigenvalues of the higher modes were insensitive to the reactivity in the range of 5% supercritical or subcritical.

The spatial dependence of the fluxes in groups 1 and 2 of the asymptotic mode, as obtained from three-region analysis, are shown in Fig. VI-14-13. We note that the same spatial distributions were obtained with the MACH 1 diffusion code.[14] The spatial distributions

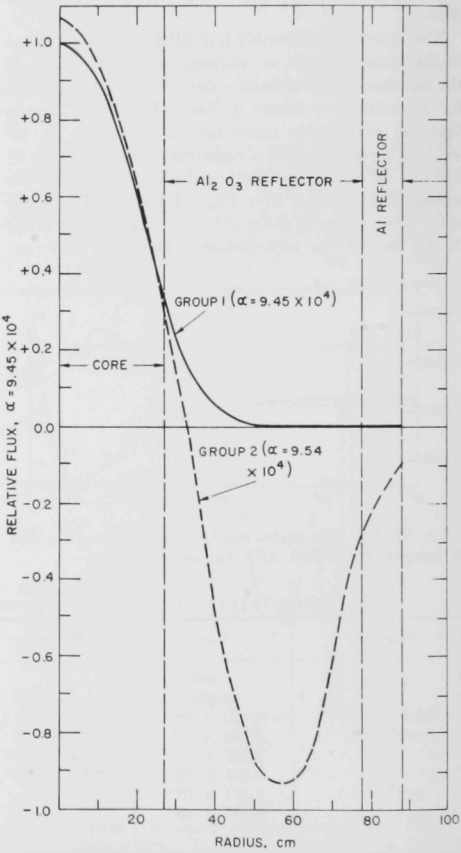


FIG. VI-14-14. Fluxes of the Second Mode ($\alpha = 9.45 \times 10^4$) in Assembly 7 of ZPR-9. *ANL Neg. No. 112-8637.*

of the second and third modes are shown in Figs. VI-14-14 and VI-14-15, respectively. The amplitude of each mode was determined by the condition that the flux in group 1 at the center of the core was unity. The relative amplitudes of the modes cannot be determined without further specifications of initial conditions and/or boundary conditions. The time dependence of the spatial distributions of the sum of the three modes for $t = 0$ and $t = 10$ $\mu$sec are shown in Fig. VI-14-16. These distributions were obtained by adding the fluxes shown in Fig. VI-14-13 to the normalized fluxes on Figs. VI-14-14 and VI-14-15. Normalization of the second and third modes was governed by the requirement that the sum of the modes be everywhere in space equal to or greater than zero at $t = 0$. With this requirement, a normalization factor of 0.122 was obtained.

It is seen from Fig. VI-14-16 that the spatial distributions of the fluxes at $t = 0$ are very different from those of the asymptotic mode shown in Fig. VI-14-13; however, at $t = 10$ $\mu$sec, the spatial distributions are essentially those of the asymptotic mode. It is noted that in 10 $\mu$sec the flux in group 2 decreases appreciably at the center of the core and increases at the core-reflector interface and at 60 cm in the reflector. The flux in group 1 decreases more in the core than in the reflector.

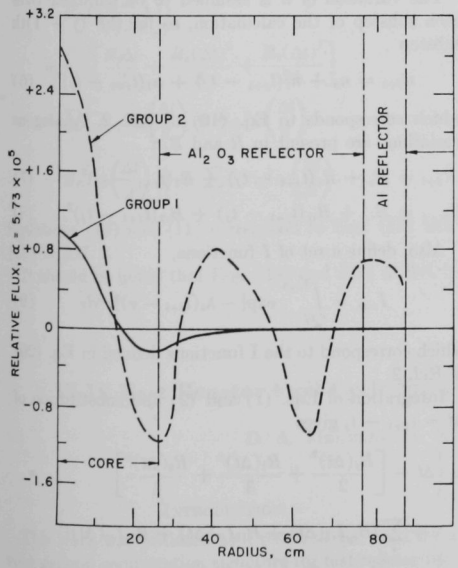


FIG. VI-14-15. Fluxes of the Third Mode ($\alpha = 5.73 = 10^3$) in Assembly 7 of ZPR-9. *ANL Neg. No. 112-8634.*

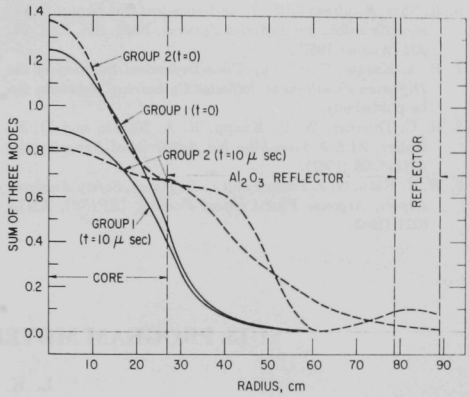


FIG. VI-14-16. Sum of the Three Modes in Assembly 7 of ZPR-9. *ANL Neg. No. 112-8632.*

## COMMENTS

The analytical method developed in this work is particularly suited for the analysis of the die-away of the prompt neutrons in delayed critical systems. In such systems, the delayed neutrons may be thought of as a source of neutrons distributed in the same way as the fluxes in the core. Because of this source the spatial distributions of the fluxes are established instantly and, at least in the core, the transport effects are minimized if not eliminated.

Extension of this work to include delayed neutrons in the formulation is the next logical step. Such an extension is not expected to present any problems. Also, the application of this treatment to pulsed neutron work should be very useful. It is not implied, however, that such application is straightforward. Extension of this work to more than three regions and two groups is straightforward but extremely laborious.

## REFERENCES

1. C. A. Preskitt and E. A. Nephew, *Transients Induced by Pulsed Neutron Sources in Multiregion Reactors*, ORNL-TM-993 (January 1965).
2. A. Foderaro and H. L. Garabedian, *New Method for the Solution of Group Diffusion Equations*, Nucl. Sci. Eng. **8**, 44 (July 1960).
3. S. Glasstone and M. C. Edlund, *The Elements of Nuclear Reactor Theory*, (D. Van Nostrand Co., Inc., New York, 1952), Chap. 8.
4. R. V. Meghreblian and D. K. Holmes, *Reactor Analysis*, (McGraw-Hill Book Co., Inc., New York, 1960), Chap. 8.
5. A. M. Weinberg and E. P. Wigner, *The Physical Theory of Neutron Chain Reactors*, (The University of Chicago Press, Chicago, 1958), Chap. 15.

6. R. Sher, *Solutions of the Time-Dependent One-Group Diffusion Equations for Reflected Systems*, Nucl. Sci. Eng. **29**, 302 (August 1967).
7. R. A. Karam, *Two-Group Time-Dependent Solution of the Diffusion Equations in Reflected Cylindrical Reactors*, (to be published).
8. R. C. Doerner, W. G. Knapp, R. A. Karam and D. K. Butler, *ZPR-9 Assemblies No. 6-9 Critical Experiments*, ANL-7208 (1967).
9. W. Y. Kato, G. J. Fischer and L. R. Dates, *Safety Analysis Report, Argonne Fast Critical Facility (ZPR-6)*, ANL-6271 (1963).
10. John D. Orndoff, *Prompt Neutron Periods of Metal Critical Assemblies*, Nucl. Sci. Eng. **2**, 450 (July 1957).
11. W. C. Davidon, *Variable Metric Method for Minimization*, ANL-5990 (Rev.) (1959).
12. B. S. Garbow, Argonne National Laboratory, (private communication).
13. G. E. Hansen and W. H. Roach, *Six and Sixteen Group Cross Sections for Fast and Intermediate Critical Assemblies*, LAMS-2543 (1961).
14. D. A. Meneley, L. C. Kvitek and D. M. O'Shea, *MACH 1, A One-Dimensional Diffusion-Theory Package*, ANL-7223 (1966).

## VI-15. PROGRAM MOVER: Point Kinetics Algorithm

L. K. Volodka

The Quasistatic Excursion Program QX1[1] requires a solution to the one group, space independent reactor kinetics equations with time-wise parabolic variation of the delayed neutron fractions and the reactivity. Since code R123[2] provides a fast and stable solution, it was decided that the method of R123 would be the most feasible approach to the solution of the reactor kinetics equations. The method of R123 does not include continuous variation of the delayed neutron fractions and has a number of options unnecessary to QX1, so a modification of R123 was necessary.

There are a few basic differences in the respective formulations of MOVER and R123. The basic equations for MOVER, corresponding to equations (1a) in Ref. 2, are

$$\dot{n} = \frac{\rho}{\Lambda} n - \sum_i \dot{c}_i \tag{1}$$

and

$$\dot{c}_i = \frac{\beta_i}{\Lambda} n - \lambda_i c_i , \tag{2}$$

where

$n \equiv$ neutron density,
$\rho \equiv$ reactivity,
$\beta_i \equiv$ delayed neutron fraction of the $i$th delayed group,
$c_i \equiv$ precursor concentration of the $i$th delayed group,
$\lambda_i \equiv$ decay constant of the $i$th delayed group,
$\Lambda \equiv$ lifetime of the reactor divided by its $k_{eff}$.

QX1 provides MOVER with the $\lambda_i$, the initial values of $n$ and $c_i$, and the coefficients of the parabola defining the variation of $\rho/\Lambda$ and $\beta_i/\Lambda$. Letting

$$R \equiv \rho/\Lambda \quad \text{and} \quad B_i \equiv \beta_i/\Lambda, \tag{3}$$

it follows from Eqs. (1) and (2) that

$$\dot{n} = Rn - \sum_i \dot{c}_i \tag{4}$$

and

$$\dot{c}_i = B_i n - \lambda_i c_i . \tag{5}$$

The variation of $n$ is assumed to be parabolic over each substep of the calculation, so for the $(j+1)$th substep

$$n_{j+1} = n_j + n_1(t_{j+1} - t_j) + n_2(t_{j+1} - t_j)^2, \tag{6}$$

which corresponds to Eq. (16) of Ref. 2. Analogous variations are present in $R$ and $B_i$:

$$R_{j+1} = R_j + R_1(t_{j+1} - t_j) + R_2(t_{j+1} - t_j)^2 \tag{7}$$

$$B_{i_{j+1}} = B_{i_j} + B_{i1}(t_{j+1} - t_j) + B_{i2}(t_{j+1} - t_j)^2. \tag{8}$$

Also, define a set of $I$ functions,

$$I_{i,m} = \int_{t_j}^{t_{j+1}} \exp[-\lambda_i(t_{j+1} - \tau)]\tau^m d\tau \tag{9}$$

which correspond to the I functions defined in Eq. (20) of Ref. 2.

Integration of Eqs. (1) and (2) and substitution of $\Delta t = t_{j+1} - t_j$ gives

$$n_1\left\{\Delta t - \left[\frac{R_j(\Delta t)^2}{2} + \frac{R_1(\Delta t)^3}{3} + \frac{R_2(\Delta t)^4}{4}\right] + \sum_i [B_{i_j} I_{i1}(\Delta t) + B_{i1} I_{i2}(\Delta t) + B_{i2} I_{i3}(\Delta t)]\right\}$$

$$+ n_2\left\{\Delta t - \left[\frac{R_j(\Delta t)^3}{3} + \frac{R_1(\Delta t)^4}{4} + \frac{R_2(\Delta t)^5}{5}\right]\right.$$

$$+\sum_i [B_{i_j} I_{i2}(\Delta t) + B_{i1} I_{i3}(\Delta t) + B_{i2} I_{i4}(\Delta t)]\Big\} \quad (10)$$

$$= n_j \left\{\left[R_j \Delta t + \frac{R_1(\Delta t)^2}{2} + \frac{R_2(\Delta t)^3}{3}\right]\right.$$

$$\left. - \sum_i [B_{i_j} I_{i0}(\Delta t) + B_{i1} I_{i1}(\Delta t) + B_{i2} I_{i2}(\Delta t)]\right\}$$

$$+ \sum_i \lambda_i c_{i_j} I_{i0}(\Delta t).$$

Substitution of $\Delta t$ and $\Delta t/2$ for $\Delta t$ in Eq. (10) gives two equations in $n_1$ and $n_2$ by which $n_1$ and $n_2$ can be determined. Substitution of $\Delta t/4$ for $\Delta t$ gives a check on the accuracy of the solution for $n_1$ and $n_2$. When $\Delta t/2$ is substituted for $\Delta t$,

$$n_1 \left\{\frac{\Delta t}{2} - \left[\frac{R_j(\Delta t)^2}{8} + \frac{R_1(\Delta t)^3}{24} + \frac{R_2(\Delta t)^4}{64}\right]\right.$$

$$+ \sum_i \left[B_{i_j} I_{i1}\left(\frac{\Delta t}{2}\right) + B_{i1} I_{i2}\left(\frac{\Delta t}{2}\right)\right.$$

$$\left. + B_{i2} I_{i3}\left(\frac{\Delta t}{2}\right)\right]\Big\}$$

$$+ n_2 \left\{\frac{\Delta t}{2} - \left[\frac{R_j(\Delta t)^3}{24} + \frac{R_1(\Delta t)^4}{64} + \frac{R_2(\Delta t)^5}{160}\right]\right.$$

$$+ \sum_i \left[B_{i_j} I_{i2}\left(\frac{\Delta t}{2}\right) + B_{i1} I_{i3}\left(\frac{\Delta t}{2}\right)\right. \quad (11)$$

$$\left. + B_{i2} I_{i3}\left(\frac{\Delta t}{2}\right)\right]\Big\}$$

$$= n_j \left\{\left[\frac{R_j \Delta t}{2} + \frac{R_1(\Delta t)^2}{8} + \frac{R_2(\Delta t)^3}{24}\right]\right.$$

$$+ \sum_i \left[B_{i_j} I_{i0}\left(\frac{\Delta t}{2}\right) + B_{i1} I_{i1}\left(\frac{\Delta t}{2}\right)\right.$$

$$\left. \left. + B_{i2} I_{i2}\left(\frac{\Delta t}{2}\right)\right]\right\} + \sum_i \lambda_i c_{i_j} I_{i0}\left(\frac{\Delta t}{2}\right).$$

Equations (10) and (11) correspond to Eqs. (17) and (18) in Ref. 2.

It should be noted that Eqs. (18) and (21) in Ref. 2 contain typographical errors; these equations should read:

$$\left\{\frac{1}{2} - \frac{\Delta t}{l}\left[\frac{k_{ex,j}}{8} - \left(\frac{1 + k_{ex,j}}{4}\right)\sum_i \beta_i I_{i1}\left(\frac{\Delta t}{2}\right)\right.\right.$$

$$+ k_1\left(\frac{1}{24} - \frac{1}{8}\sum_i \beta_i I_{i2}\left(\frac{\Delta t}{2}\right)\right)$$

$$\left.\left. + k_2\left(\frac{1}{64} - \frac{1}{16}\sum_i \beta_i I_{i3}\left(\frac{\Delta t}{2}\right)\right)\right]\right\} n_1$$

$$+ \left\{\frac{1}{4} - \frac{\Delta t}{l}\left[\frac{k_{ex,j}}{24} - \left(\frac{1 + k_{ex,j}}{8}\right)\sum_i \beta_i I_{i2}\left(\frac{\Delta t}{2}\right)\right.\right.$$

$$+ k_1\left(\frac{1}{64} - \frac{1}{16}\sum_i \beta_i I_{i2}\left(\frac{\Delta t}{2}\right)\right)$$

$$\left.\left. + k_2\left(\frac{1}{160} - \frac{1}{32}\sum_i \beta_i I_{i4}\left(\frac{\Delta t}{2}\right)\right)\right]\right\} n_2$$

$$= \frac{\Delta t}{l}\left\{n_j\left[\frac{k_{ex,j}}{2} + k_1\left(\frac{1}{8} - \frac{1}{4}\sum_i \beta_i I_{i1}\left(\frac{\Delta t}{2}\right)\right)\right]\right.$$

$$\left. + k_2\left(\frac{1}{24} - \frac{1}{8}\sum_i \beta_i (I_{i2})\right)\right]$$

$$\left. - \frac{1}{2}\sum_i l\dot{c}_{ij} I_{i0}\left(\frac{\Delta t}{2}\right)\right\} + \left(\frac{\Delta t}{2}\right) S$$

and

$$l\dot{c}_{i_{j+1}} = l\dot{c}_{i_j} e^{-\lambda_i \Delta t} + \beta_i \{[n_j k_1 + n_1(1 + k_{ex,j})] I_{i0}(\Delta t)$$

$$+ 2[n_j k_2 + n_1 k_1 + n_2(1 + k_{ex,j})] I_{i1}(\Delta t)$$

$$+ 3[n_1 k_2 + n_2 k_1] I_{i2}(\Delta t) + 4 n_2 k_2 I_{i3}(\Delta t)\}.$$

Program MOVER has been checked against R123 and has been found to give accurate results for cases in which $\Lambda$ and $\beta_i$ are constant.

### References


1. K. Ott and J. T. Madell, *Quasistatic Treatment of Spatial Phenomena in Reactor Dynamics*, Nucl. Sci. Eng. **26**, 563 (1966).
2. J. J. Kaganove, *Numerical Solution of the One Group Space Independent Reactor Kinetics Equations for Neutron Density Given the Excess Reactivity*, ANL-6132 (1960).


## VI-16. Fast Reactor Fuel Cycle Studies—Formulation and Solution Methods

D. A. Meneley, G. K. Leaf* and P. M. Walker*

### Introduction

This work was initiated as a result of the need for a very general computation structure for fast reactor fuel cycle studies. In order to be generally useful, the formulation and associated machine codes must satisfy several requirements. First, they must be sufficiently flexible to accommodate a wide range of survey problems. Second, they must be sufficiently complete and accurate

* Applied Mathematics Division, Argonne National Laboratory.

to satisfy the needs of conceptual design, economics, and core behavior studies. Further desirable features include economy of computation and ease of extension to more rigorous models.

The approach taken in an attempt to satisfy the above requirements was to specifically include all capability which could be treated within the defined limits. These are: one reactor (as opposed to an interacting power system); fuel contained in discrete lumps; fully defined external conditions; fixed fuel management definition (that is, no cycle optimization). The various models, approximations, and capabilities which are the results of the study are the subject of this paper. Two desirable features have been omitted from the initial specifications, namely concentration-dependent microscopic cross sections and economics calculations. These may be added at a later date.

The fuel cycle calculation problem may be divided into two main sections; namely, the simulation of material movements and the solution of the equation set governing fuel burnup and system behavior. The simulation of material movements requires an indexing system to describe the following phases: fuel loading, in-core shuffling, discharge, reprocessing, sale, refabrication, and storage. The equation set contains models of the space-energy-time dependent neutron flux and isotopic chains, reactivity control, time sequences, reprocessing plant fuel mixing and losses, refabrication with addition of feed material, and bred fuel disposal. The solution is subject to direct conditions imposed by the user, such as burnup time and total power, and to indirect conditions arising from the material movements as defined in space and time.

## General Capabilities

The following outline includes all features of the model currently under development. A general calculation system of this type must, of course, be built up by stages. Status of the computer algorithms is highly fluid at the present time so that a precise statement of calculation capability or solution techniques is not possible. When some reasonable stage of development is reached a production code package will be frozen and made available for use. The following represents the current best guess as to the final form of the system.

The enrichment ratio of freshly charged fuel may be adjusted to obtain a specified static criticality factor in the system without control rods at a given time during the at-power phase of the cycle. Criticality of the system may be maintained by means of space dependent control adjustment (fuel or poison) at a given number of time points. Burn time may be adjusted to satisfy burnup conditions in selected discharge batches. The search procedures necessary to achieve these conditions depend on the type of problem defined by the user.

The isotope chain matrix may contain $\beta^-$, $\beta^+$ and $\alpha$-decay terms as well as $(n,\gamma)$, $(n,p)$, $(n,\alpha)$, $(n,2n)$, and $(n,f)$ reactions. Fractional yields of fission products may be fissioning isotope dependent. Isomeric states also may be considered. Isotope decay chains may be computed throughout the external cycle, within the limitations of the real time accounting scheme. Core fluxes are normalized to a specified total power after each flux recalculation.

The fuel management scheme permits all the flexibility possible in a real reactor with solid fuel elements. All common movement patterns such as out-in shuffling and fractional batch or scatter refueling are included as special cases. The limitations are those imposed by the particular spatial model of the core in zero, one, or two space dimensions. Fractions of a discharged fuel batch may be assigned to any of the multiple reprocessing plants, each of which may have three outputs. For the purpose of simplifying refabrication specifications, one output from each plant is designated as Class 1 (normally high fissile content) and the other as Class 2 (low fissile content). The only requirement of this separation is that the system reactivity be reasonably sensitive to changes in the relative fractions of the two classes in the fresh charge. The third output represents waste and losses.

Each class of output from the several plants may be used for fabrication of one or more fuel charges, or sold, according to a user-defined priority ordering scheme. Makeup fuel may be taken from any number of predefined external feed lines, also according to the given priority ordering. The volume of Class 1 material required for a charge is defined by the enrichment fraction times the total volume; the remainder will be obtained from the Class 2 grouping. Any number of charge batches may be fabricated with different compositions and enrichments.

Two main types of problems are considered. The object of the first type is to find the equilibrium (infinite-time) operating conditions of a recycle system under fixed conditions. Current plans call for only single-step equilibrium problems, i.e., those in which the same fuel management procedures are carried out after each burn step.

The second type of problem, non-equilibrium, is a direct mockup of reactor operation, with the exception that fuel charge enrichment may be adjusted to meet burnup and reactivity requirements during the at-power phase. Comprehensive dump/restart facilities allow adjustment of parameters such as burn time and control distribution at specific points during the problem. In addition, to partially compensate for the lack of opti-

mization routines, this facility allows the user to save, for later use, information on the system condition at particular points in time.

## Reactor Core Cycle

### FUEL MANAGEMENT

The first problem is development of an indexing system which will permit location of each discrete lump of fuel in space over the whole period during which it is in the reactor. It may be loaded into the core at a particular position and irradiated for some period of time in a flux which is determined by the interaction of all the fuel lumps in the core as well as by control motions. After this initial "burn", the lump may or may not be repositioned in space; in any case if any of the fuel in the core is moved, charged, or discharged, the irradiation rate will undergo a discontinuous change at the so-called "shuffling step". After several burn-shuffle sequences the lump is discharged from the system.

The spatial movement of the fuel lump is constrained by requirements of volume preservation. Whenever it is shuffled (repositioned) in space, another lump of equal volume must be removed from its position and inserted in another location, or discharged, and a third must be moved to occupy the space vacated by the original fuel lump. This linked series of element motions is the basis of the indexing system.

The first index is given the name "material". A material consists of all the fuel lumps in the reactor at a particular time which are linked by a single shuffling sequence or "path". The individual fuel lumps, the "material-stages", are identified by the second index. This second index is 1 for a fuel lump which has just been charged into the core, 2 for a lump which has been shuffled once, and so on up to the maximum stage index, after which the fuel lump is discharged. The third index, the "region", is used to locate each material-stage in space. A region is the volume over which the average fluxes are computed in obtaining the fuel burnup; in current neutronics models the region boundaries are restricted to rather simple surfaces. A region in a cylindrical model may be an annular ring containing a number of fuel lumps of different composition and burnup history. Thus we must allow several different material-stages to be assigned to a single region, with the constraint that the sum of the volumes of all material-stages in a region equal the volume of the region.

If the compositions of the first stages (i.e. fresh charges) of all paths are held constant and the burn/refuel steps are identically repeated the compositions of the last stages (i.e. spent fuel) approach constant values as time increases, assuming that control and criticality constraints are not violated.

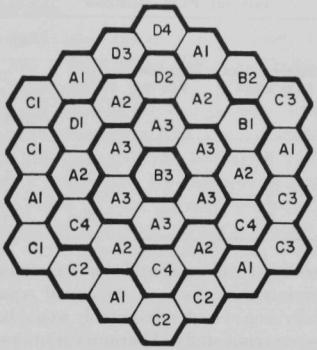


FIG. VI-16-1. Example of Loading and Fuel Shuffling Pattern. *ANL Neg. No. 112-8002.*

Two possibilities arise in the event that shuffling procedures are not the same after each burn step. The first is when a particular move sequence is to be carried out only once. Each element in the core must, in this case, be separately accounted for at the end of each burn step. The second possibility is the case in which a number of burn steps elapse without any motion within a particular path, then one discharge/charge move is made, and so on with fixed repetition factor. Clearly no equilibrium condition can be defined for the first of these. While the second case is repetitive, and hence may admit an equilibrium solution, the amount of numerical work required for each iterative sweep toward a solution is that for one burn step multiplied by the least common multiple of the repetition factors of all paths in the problem. This case has been excluded from the equilibrium search capability at the present time.

### PROBLEM OPERATION

In summary, each discrete fuel lump may be located in space at any time by the indexing triplet (material, stage, region). The fourth index, the repetition factor, fixes the number of burn steps between fuel movements in each path (material).

A particular application of the method is illustrated in Fig. VI-16-1, a plan view of a 37 subassembly core. The subassemblies marked "A" are to be charged into ring 4, shuffled to ring 3, then 2 and discharged. The "B" subassemblies are to be charged into ring 3, moved to 4, and then ring 1, at every other burn step. Similar patterns apply to materials "C" and "D". Table VI-16-I shows the input indexing system for this core, assuming that it is to be computed as a four region annular system in one-dimensional cylindrical geometry. Material-stage and region volumes are defined separately. If the system were to be computed in plan using a triangular mesh,

TABLE VI-16-I. EXAMPLE OF INDEXING SYSTEM DEFINING IN-CORE FUEL MOTIONS

| Material | Subassemblies Per Stage | Repetition Factor | Stage | | | |
|---|---|---|---|---|---|---|
| | | | 1 | 2 | 3 | 4 |
| | | | Region | | | |
| A | 6 | 1 | 4 | 3 | 2 | |
| B | 1 | 2 | 3 | 4 | 1 | |
| C | 3 | 1 | 4 | 4 | 4 | 3 |
| D | 1 | 3 | 3 | 3 | 4 | 4 |

each subassembly could be identified as a material-stage and its movements in the core accounted separately. Further subdivision of each subassembly would be possible, perhaps to permit study of burnup variations across assemblies. In such a case the spatial motions of material-stages representing parts of single subassemblies would be constrained.

It will be noted that the above indexing system is most convenient for describing repetitive, consistent fueling patterns such as the fractional batch, or scatter-refueling, schemes proposed for fast reactors. Individual fuel elements (or group of elements) can, however be accounted for separately at the end of each burn step using the conventional system by means of user-specified shuffling directions for each material-stage. In this case the volume of each stage of a material may be different, as may the type of fuel and the volume fractions of fuel, coolant, and structure. The identification of any material-stage with another becomes a mere formality. In the case of equilibrium problems, however, the linkage has a definite value. Since by definition the fueling and shuffling policy is held constant, the material-stages present in the core at any time can be considered as different phases of the burnup history of a single fuel lump. This greatly simplifies the equilibrium cycle computation for scatter-refueled cores.

A problem may be started in one of two ways. In the first, the full atom density vector of every material-stage in the reactor is specified by the user. The calculation may then proceed directly by means of a flux solution, et seq. The second method is by reference to reactor charge specifications (see REFABRICATION) for some or all of the material-stages. In this case these material-stages will be "fabricated" before the problem is started. The second option allows the enrichment of a complete core to be adjusted before the initial burn.

The computation optionally may include moveable control poisons or fuels. The volume fractions of these materials may be varied to establish criticality at each of the given number of sub-time steps into which the burn step is divided (see REACTOR BURNUP EQUATIONS).

The user specifies the destination of the discharged fuel when it leaves the reactor. (The details are discussed in the next section dealing with the EXTERNAL CYCLE). In non-equilibrium problems, partly burned fuel may be returned to the reactor from the cooling area by user-specified movements. Each material-stage is represented by an atom density-vector, a volume, and a burnup level while it is in the core. The change in isotopic atom densities as a function of irradiation is computed for each density vector, with the approximation that all vectors assigned to a given spatial region are irradiated in the average multigroup fluxes of the region. The multi-group microscopic cross-sections of the same isotope which is present in two material-stages may be different, to account for variations in fuel properties such as potential scattering and temperature. The isotopes maintain a common identification when not in the core. The fractional burnup of each material-stage is computed from the integral number of fission reactions in user-specified isotopes.

The user has the option of interrupting a non-equilibrium calculation at the end of any burn step. He may then change any parameter of the specified problem which would be adjustable in the case of a real reactor, such as fuel movements, burnup limits, burn times, and so on. He may not, however, change the consequences of previous burns, such as atom density vectors and burnup levels.

Further details of the core cycle are described below in the section on SOLUTION METHODS.

## EXTERNAL CYCLE

### FUEL DISCHARGE AND REPROCESSING

Figure VI-16-2 is a schematic of material movements in the external cycle. Consider $L$ discharged material-

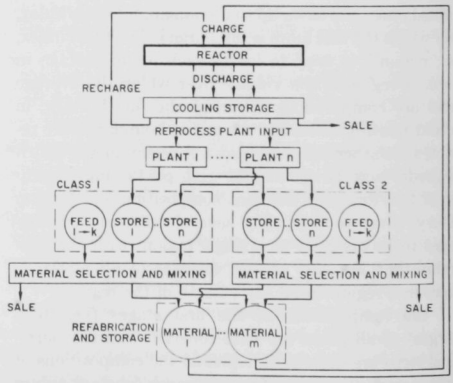


FIG. VI-16-2. Schematic Diagram of External Cycle. *ANL Neg. No. 112-7982 Rev. 1.*

stages which are to be cooled, then sold directly, sent to $J$ reprocessing plants, or held for recharging. (The last option can be applied only to non-equilibrium problems.) Define $E$, a block diagonal matrix of order $ML$, where $M$ is the number of active isotopes, (i.e., those undergoing transmutation reactions) in the problem. All elements in the $l$th $M$-dimensioned diagonal block are equal to the fraction of material $l$ which is to be sold without reprocessing. Next define the destination matrix $D$, with $MJ$ rows and $ML$ columns. Each $M$-dimensioned submatrix $D_{jl}$ is diagonal with constant elements equal to the fraction of the unsold remainder of material $l$ which is to be sent to reprocessing plant $j$. Waste and reprocessing losses are accounted for by the recovery matrix $R$, block diagonal of order $MJ$. Each $M$-dimensional block is diagonal with elements equal to the fraction of each isotope which is recovered by reprocessing plant $j$. The reprocessing plant output vector $nV_o$ is then given by:

$$nV_o = RD(I - E)V\dot{n}$$

$I \equiv$ identity matrix, order $ML$

$V \equiv$ volume matrix, block diagonal of order $ML$. Each element of a diagonal $M \times M$ block is equal to the volume of the last stage of material $l$.

$\dot{n} \equiv$ atom density vector ($ML$) for the last stage of all materials at the end of the burn step.

Now define class separation matrices $C1$ and $C2$, each block diagonal containing $J$ blocks, each of order $M$, related by $C2 = I - C1$. Each element of the $j$th $M$-dimensional block represents the fraction of that isotope which is contained in Class 1 output from reprocessing plant $j$. The system may have $F$ external feed lines, each specified by an $M$-dimensional atom density vector $n_f$, volume $V_f$, and an $M$-order class separation matrix $C1_f$.

The atom vectors of each class in storage are then defined by the product of the appropriate $Ci$ matrix and $nV$ vector. The four atom vectors $nV_o^1$, $nV_o^2$, $nV_F^1$, and $nV_F^2$ are to be used in the refabrication computations which define the charged atom density vector. Note that each $M$-dimensional subvector, representing atoms which have come from a particular discharge batch and have been cooled for a definite time and sent to a processing plant with an assigned processing time, appears in this makeup store at some discrete time. From the other end, one can define the time at which subassemblies must be at the reactor site for loading, as well as the refabrication and shipping/storage time. Thus it is possible to determine which of the atom vectors in the refabrication storage will be available for makeup of a particular charge.

REFABRICATION

The refabrication phase is particularly difficult to arrange into a fully determined, yet flexible scheme, which is reasonable in terms of input. The reasons are first, that the material enrichment ratios which define the required quantities of high and low reactivity fuel in a given batch are problem parameters which cannot be defined a priori. Also, the reprocessing plant output vectors $nV_o^1$ and $nV_o^2$ are initially unknown. The solution adopted is a priority ordering scheme which is relatively easily specified in input and is not unduly restrictive in scope. It is described below for Class 1 makeup and an example is given. The same procedure is used for Class 2.

The first part of the priority scheme is an absolute order of preference for use of each reprocessing plant output and external feed vector in makeup of each charge material. Several priority levels may be defined. At each level, if there is an excess of fuel in makeup of some charges and a deficit in others, it will be redistributed at that level before dropping to the next lower priority. The second part of the scheme is a fractional distribution system. This permits use of a single stored fuel in a number of charge batches at the same priority level. The priorities are given separately for the high fissile (Class 1) and low fissile (Class 2) fractions.

The object of the priority scheme is to arrive at two delivery matrices, designated $Q$ and $Q_F$, which represent the fraction of the atoms of each isotope in each reprocessing plant output and each external feed which are to be used in fabrication of each fuel material, respectively. The elements are computed from the given enrichment fraction, the required volume, the given full atom densities of each charge batch, and the contents of the makeup storage. The following steps are followed in computing $Q$ and $Q_F$:

1. Compute the total volume which each plant output and feed vector would occupy in the specified physical form of each material (typically oxide, carbide, metal). The Sale fraction is formally included as an additional material.

2. Determine the volume of Class 1 makeup required for fabrication of each material. (Since the volume of the Sale material is undefined, it is treated specially; see Step 7).

3. Search the priority specifications for all the highest priority materials (level 1) requiring makeup from each plant and feed line.

4. Normalize the sum of all distribution fractions at priority level 1 for a given plant or feed to 1.0 minus the fraction of that volume already used. (This fraction is naturally zero on the first distribution.)

5. For each material, sum the product of the renor-

malized distribution fractions multiplied by the volume of each plant and feed for that material (calculated in Step 1). This sum is the total volume of makeup available to the material on the first distribution

6. Compare the required volume (from Step 2) with the available volume (from Step 5) to find the actual fraction of the volume of each plant and feed used. If the required volume is less than or equal to the available volume, the requirements are satisfied for the material. If not, more makeup is required.

7. Set the distribution fractions of the Sale "materials" to zero, and also to any material whose requirements are satisfied. Accumulate the fraction of each plant or feed volume delivered to each material. Repeat from Step 4 until either no further makeup is required for any material or none remains for any plant or feed at this priority level.

8. Repeat the process from Step 3 for the next priority (level 2) and so on, until the list is exhausted.

The above process is somewhat cumbersome in concept; however, the alternative to a scheme such as this appears to be a serious reduction in flexibility of fuel makeup selection. The calculations are very simple and rapid. The following example indicates some of the capabilities of the scheme.

Consider a plutonium-uranium fueled fast breeder reactor. Assume that it has two core enrichments and a single scatter-refueled blanket. The core and radial blanket are to be processed separately in reprocessing plants A and B, respectively. The user wishes to sell ¼ of the reprocessed blanket plutonium (Class 1 fuel) and to distribute the remainder in a 2 to 1 volume ratio to the two core fuel charges. All reprocessed fertile material (Class 2) is to be used first for blanket makeup and then for core materials. Any feed required will be obtained first from a limited volume external feed vector (external feed A) and then from a second feed (external feed B). The user-defined priority table necessary to accomplish this is shown in Table VI-16-II. The values above the diagonal lines are the priority levels; those below are the distribution fractions. It is possible in this example that there may be Class 1 output from Plant B remaining after fabrication. All such makeup is conventionally designated as part of the Sale material.

TABLE VI-16-II. Example of Priority System for Selection of Fuel Charges from Reprocessing Plant Output and External Feeds

| | Class 1 | | | | Class 2 | | | |
|---|---|---|---|---|---|---|---|---|
| | Reprocessing Plant | | External Feed | | Reprocessing Plant | | External Feed | |
| | A[a] | B[b] | A[c] | B[d] | A[a] | B[b] | A[c] | B[d] |
| Core Fuel 1 | 2/1. | 1/0.5 | 3/1. | 4/1. | 2/1. | 2/1. | 3/1. | 4/1. |
| Core Fuel 2 | 2/1. | 1/0.25 | 3/1. | 4/1. | 2/1. | 2/1. | 3/1. | 4/1. |
| Blanket | — | — | — | — | 1/1. | 1/1. | 2/1. | 3/1. |
| Sale | 3/1. | 1/0.25 | — | — | — | — | — | — |

[a] Plant A reprocesses core fuel.
[b] Plant B reprocesses blanket fuel.
[c] Feed A is a limited volume feed source.
[d] Feed B is an unlimited volume feed source.

The final delivery matrices $Q$ and $Q_F$ can be constructed from the Class 1 and Class 2 delivery fractions described above.

### Fuel Charge Atom Densities

Grouping the various parts of the above computations, we can define the atom density vector $n_i$ of all materials of the fuel charge in terms of the discharge and external feed vectors. First define $S$ and $P$ as

$$\begin{aligned} S &= V^{-1}QRD(I - E)V, \\ P &= V^{-1}Q_F V_F . \end{aligned} \tag{2}$$

Then

$$n_i = S\hat{n} + Pn_F . \tag{3}$$

The vector $\hat{n}$ is related to the previous fuel charge vector $n_{i-1}$ through the burn matrix $B$, representing all transmutations within the core (see REACTOR BURNUP EQUATIONS)
Then:

$$n_i = SBn_{i-1} + Pn_F . \tag{4}$$

In an equilibrium cycle, $n_{i-1} = n_i = n$, and $n$ could in principle be found from

$$n = (I - SB)^{-1}Pn_F . \tag{5}$$

Since $S$, $B$, and $P$ are all functions of $n$, this is not a feasible scheme.

### Solution Methods

In this section, we shall concentrate on the solution of the equilibrium problem. The approach used in solving the non-equilibrium case is similar, and for the sake of brevity will not be discussed.

The object of an equilibrium calculation is to find a charge density for each material and an operating time for any burn step such that the charges produced in the external cycle are the same for every burn step. This solution is subject to the following three constraints.

1. Let $L$ denote the total number of materials under consideration and $e_l$, $1 \leq l \leq L$, the enrichment associated with the charge density for each material $l$. The solution is sought by varying the enrichment vector $(e_1, e_2, \cdots, e_L)$ along a specified straight line.

2. The burnup of the system at the end of each burn step assumes a specified value.

3. The unpoisoned $k$-effective of the reactor at a given fraction of the burn step time takes on a specified value.

REACTOR BURNUP EQUATIONS

Consider any region $r$ of the reactor and let $n$ denote an atom density vector associated with the region $r$. The dimension of $n_r$ is $M$, where $M$ is the number of isotopes being considered. The following set of equations is then taken to govern the reactor as a function of time:

$$\frac{dn_r(t)}{dt} = A_r[\phi(t)]n_r(t), \tag{6}$$

where $r$ ranges over all regions of the reactor, and $n_r$ over the atom density vectors of all material-stages in the reactor. The matrices $A_r[\phi(t)]$ have the form

$$A_r[\phi(t)] = \Lambda_r + \hat{A}_r[\phi(t)], \tag{7}$$

where $\Lambda_r$ is a constant matrix arising from radioactive decay, and the elements $a_{jk}(t)$ of $\hat{A}$ have the form

$$a_{jk}(t) = \sum_{g=1}^{G} \sigma_{jk}^{g}\phi_{gr}(t).$$

Here $\phi_{gr}$ is the average flux in group $g$ over the region $r$ and $\sigma_{jk}^{g}$ denotes the microscopic cross-section for each isotope and type of reaction. The coupling between the isotope densities and the flux is governed by a fixed power, static neutronics calculation with or without criticality being maintained, at the option of the user. The neutronics calculation will be denoted symbolically by

$$F[\phi(t); n(t); t] = 0. \tag{8}$$

An approximate solution to the coupled system of Eq. (6) and (8) over a time interval $[0, t]$ is achieved in the following manner. The interval is divided into $P$ subintervals of equal length by the points $t_p = ph$, $0 \leq p \leq P$, with $h = T/P$. Using the slowly varying character of the matrices $A_r[\phi(t)]$, the following approximation is made over each subinterval $[t_{p-1}, t_p]$:

$$A_r[\phi(u)] \approx \tfrac{1}{2}\{A_r[\phi(t_{p-1})] + A_r[\phi(t_p)]\}, \qquad t_{p-1} \leq u \leq t_p. \tag{9}$$

With this approximation the coupled system takes the form

$$\frac{dn_r}{dt} = A_{rp}n_r, \qquad t_{p-1} \leq t \leq t_p \tag{10}$$

$$F[\phi(t); n(t); t] = 0,$$

where $r$ ranges over all regions of the reactor and $p = 1, 2, \cdots, P$. Here $A_{rp}$ denotes the right hand side of Eq. (9).

This system is solved iteratively in the following manner. Assuming that $n_r(t_{p-1})$ has been found for each $r$, we define the sequence $n_r^{(q)}(t_p)$ in the following manner:

$$B_r^{(q)}[t_p\,; n^{(q)}(t_p)] = \exp[hA_{rp}^{(q)}],$$
$$n_r^{(q)}(t_p) = B_r^{(q)}[t_p\,; n^{(q)}(t_p)]n_r(t_{p-1}),$$
$$F[\phi^{(q+1)}(t_p); n_i^{(q)}(t_p); t_p] = 0, \tag{11}$$

and

$$A_{rp}^{(q+1)} = \tfrac{1}{2}\{A_r[\phi(t_{p-1})] + A_r[\phi^{(q+1)}(t_p)]\}, \qquad q = 0, 1, 2, \cdots.$$

For $p > 1$, $A_{rp}^{(o)}$ is taken to be the result of extrapolation from the preceding interval. Although the iterative procedure converges very rapidly (typically less than six iterations), the cost, in time, of each iteration is very high. For this reason, the iterates are extrapolated linearly, and no more than three iterations are performed. The evaluation of the exponential of a matrix is performed by means of a technique proposed by B. Duane in Ref. 1.

If a distribution of atom densities $n_{lk}(o)$ is given at $t = 0$ for each stage $k$ of material $l$, then the above numerical procedure yields an approximation to the atom density distribution at any later time. The resulting density $n_{lk}(t)$ can be represented in the form

$$n_{lk}(t) = B_r[t; n(o)]n_{lk}(o), \tag{12}$$

where $r = r(l, k)$ is the region in which stage $k$ of material $l$ resided. Note that through the coupling of the region-averaged flux, the matrix $B_r$ depends on the total initial density distribution in the entire reactor. This dependence is indicated by the symbol $n(o)$.

REFUELING, BURNUP, AND DISCHARGE SEQUENCES

Consider the repetitive loading, burning, and discharging of the reactor governed by the equations described in the last section. Let the operating time for each step be fixed, and let the charge density for each material-stage which is loaded in at the beginning of each burn step be fixed. Consider any material $l$, and suppose that during its $K_l$ stages it resides in regions $r_1, r_2, \cdots, r_H$ such that it is in $r_1$ for the first $k_1$ stages, $r_2$ for the next $k_2$ stages, and so on. Thus, $k_1 + k_2 + \cdots + k_H = K_l$; moreover when it reaches the $K_l$th stage in region $r_H$ it is discharged. Let $n_{l,1}$ denote the charge density for stage 1 of material $l$ which is loaded in at the beginning of every burn step. Starting at the beginning of some burn step, we follow this charge through the $K_l$ burn steps until it is discharged. Note that we are considering the case when all repetition

factors are equal to one, so that the number of stages associated with each material coincides with the number of burn steps for which the material resides in the reactor. After $k_1$ burn steps in region $r_1$, the density is given by

$$B_{r_1}^{(k_1)} \cdots B_{r_1}^{(2)} B_{r_1}^{(1)} n_{l,1}.$$

Note that since the $B$ matrices depend on the total density distribution in the reactor at the beginning of each burn step, a different $B$ matrix will be generated at each burn step. This dependence is indicated by the superscript index. Having completed $k_1$ stages in region $r_1$, the charge then moves to region $r_2$ for the next $k_2$ burn steps and then on to the next region until at the end of the $K_l$th burn step after it was introduced, it is discharged. This discharge density is given by

$$B_{r_H}^{(K_l)} \cdots B_{r_2}^{(k_1+k_2)} \cdots B_{r_2}^{(k_1+1)} B_{r_1}^{(k_1)} \cdots B_{r_1}^{(1)} n_{l,1}. \quad (13)$$

Now if we had followed the same charge density $n_{l,1}$ which was introduced one time step later than the preceding one, then its value upon discharge would be given by

$$B_{r_H}^{(K_l+1)} \cdots B_{r_2}^{(k_1+k_2+1)} \cdots B_{r_1}^{(k_1+2)} B_{r_1}^{(2)} n_{l,1}. \quad (14)$$

Thus we see that since the $B$ matrices differ from one time step to the next, the discharge densities will vary with each time step. In the limit when the conditions in the reactor are the same at the beginning of every burn step, the $B$ matrices would not depend on the time steps. Thus there would exist matrices

$$B_{r_1}, B_{r_2}, \cdots, B_{r_H}$$

such that the discharge density for material $l$ after every time step would be given by

$$B_{r_H}^{k_H} \cdots B_{r_2}^{k_2} B_{r_1}^{k_1} n_{l,1}. \quad (15)$$

This limiting state will be referred to as the cyclic mode.

The cyclic mode is achieved iteratively by repeatedly loading a fixed charge for each material and maintaining a fixed burn step time. This procedure is accelerated in two ways. First the iterative procedure is modified by ignoring the dependence of the $B$ matrices on the flux. For each material $l$, let a charge density $n_{l,1}$ be loaded, and assume that the densities of the remaining stages are arbitrary. Then it is clear that it would take $K = \max(K_l)$ time steps just to clear the reactor of the arbitrary densities. By ignoring the flux dependence we can accomplish this in one time step. Thus if

$$B_{r_1}^{(1)}, B_{r_2}^{(1)}, \cdots, B_{r_H}^{(1)}$$

are $B$ matrices for material $l$ resulting from the first loading when all but the first stage densities are arbitrary, then for the next time step we define the densities for each stage of material $l$ in the following manner:

$$n_{l,1}, B_{r_1}^{(1)} n_{l,1}, \cdots, [B_{r_1}^{(1)}]^{k_1} n_{l,1}, \quad B_{r_2}[B_{r_1}^{(1)}]^{k_1} n_{l,1}, \cdots, [B_{r_H}^{(1)}]^{k_H - 1} \cdots [B^{(1)}]^{k_1} n_{l,1}. \quad (16)$$

With this distribution for each material, we burn for one time step, thereby generating a second set of matrices

$$B_{r_1}^{(2)}, \cdots, B_{r_H}^{(2)}.$$

This second set is then used in place of the first set, and the process repeated until a converged set is obtained.

The second means by which the iterative procedure is accelerated involves linear extrapolation of the sequence of matrices $B_r^{(q)}$ and for each region $r$ in the reactor.

We shall consider next the constraints on the problem as well as the interaction between the external and internal paths. First of all, the enrichments are constrained by the relation $e_l(x) = e_l(o)(1 + x\delta_l)$ for $1 \leq l \leq L$, where $\delta_l$ is a material-dependent enrichment modification factor. Thus it is the enrichment parameter $x$ which will be adjusted to achieve a solution. Consider next a charge distribution

$$n^{(0)}(x) = [n_1^{(0)}(x), \cdots, n_L^{(0)}(x)]$$

having an enrichment parameter $x$ associated with it. Let $t^{(0)}(x)$ denote the burn step time of the reactor such that when the core is in its cyclic mode, the burnup $b[t^{(0)}(x); x; n^{(0)}(x)]$ achieves its desired value $b_0$. For each material $l$, set

$$B_l^{(0)} = [B_{r_H}^{(0)}]^{k_H} \cdots [B_{r_1}^{(0)}]^{k_1}$$

and

$$B^{(0)} = \text{diag}\,[B_1^{(0)}, \cdots, B_L^{(0)}].$$

Note that the $B$ matrices are those associated with the core in its cyclic mode and

$$B^{(0)} = B[t^{(0)}(x), x, n^{(0)}(x)].$$

Let the discharge density distribution $B^{(0)}n^{(0)}$ be passed through the external cycle, thereby generating a new charge distribution $n^{(1)}$ which is defined by

$$n^{(1)} = S[B^{(0)}n^{(0)}, x]B^{(0)}n^{(0)} + P[B^{(0)}n^{(0)}, x]n_F. \quad (17)$$

The matrices $S$ and $P$ were defined above, and as indicated depend on the discharge density and the enrichment. Let the charge distribution $n^{(1)}$ be used in place of $n^{(0)}$ thereby generating $t^{(1)}(x)$, $B^{(1)}$, and $n^{(2)}$. Repeating this process until the limiting state is reached, we would expect to obtain a charge distribution $n(x)$, a burn step time $t(x)$, and a $B$-matrix $B(x)$ such that

$$n(x) = S[B(x)n(x),x]B(x)n(x) + P[B(x)n(x),x]n_F . \quad (18)$$

When the system has achieved this state, it will be said to be in its equilibrium mode relative to a given enrichment. If the enrichment $x$ is then adjusted so that the unpoisoned $k_{eff}$ achieves its desired value $k_0$ at a specified fraction $\alpha$ of the burn step time $t(x)$ when the system is in its equilibrium mode, then we have the solution to the equilibrium problem.

APPROXIMATION TECHNIQUES

This is the basic approach used in solving the equilibrium problem. However there are non-linearities present at every level of the problem; thus to adhere too closely to the above procedure would involve a prodigious amount of calculation. For this reason the equilibrium mode is only approximated. Thus starting with a charge distribution $n^{(0)}$ and an associated enrichment $x$, the burn step time $t^{(0)}$ and the matrix $B^{(0)}$ are determined as before. The discharge density also passes through the external path generating $n^{(1)}$ as in Eq. (17). Now, however, we ignore the dependence of $t^{(0)}$ and $B^{(0)}$ on the initial charge distribution. Thus we pass $n^{(1)}$ through the core using $B^{(0)}$, thereby obtaining a discharge distribution $B^{(0)}n^{(1)}$. This is passed through the external path and the process repeated until a converged distribution $\hat{n}^{(0)}$ is obtained. Having produced $B^{(0)}$, $t^{(0)}$, and $\hat{n}^{(0)}$ we shall say that the system is in its approximate equilibrium mode.

With these concepts and procedures in mind, the solution to the equilibrium problem is achieved in the following manner. Starting with a discharge density distribution $\bar{n}^{(0)}$ and a guess $x^{(0)}$ for the proper enrichment parameter, we pass through the external path generating a charge $n^{(0)}$ with enrichment $x^{(0)}$. With this charge a burn step time $t^{(0)}$ and matrix $B^{(0)}$ are found for which the burnup constraint is satisfied when the core is in its cyclic mode. Using $B^{(0)}$ the system is then brought into an approximate equilibrium mode, thus producing a charge $\hat{n}^{(0)}$ with enrichment $x^{(0)}$. Then using $B^{(0)}$ and $\hat{n}^{(0)}$, the cyclic mode is approximated by employing the following distribution of stages for each material $l$:

$$\hat{n}_l^{(0)}, B_{r_1}^{(0)}\hat{n}_l^{(0)}, \cdots, [B_{r_H}^{(0)}]^{k_H-1} \cdots [B_{r_1}^{(0)}]^{k_1}\hat{n}_l^{(0)} . \quad (19)$$

Still holding $B^{(0)}$ and $t^{(0)}$ fixed, we calculate the unpoisoned value of $k_{eff}$ at a specified fraction $\alpha$ of the step time $t^{(0)}$. Recall that for calculational purposes, the time interval $[0, t^{(0)}]$ was divided into $P$ equal parts ($P \geq 1$). We restrict the possible specified values for $\alpha$ by insisting that $\alpha = p'/P$ for some $p'$, $1 \leq p' \leq P$. Since $B_r^{(0)} = B_r(t_p) \cdots B_r(t_1)$ for each region $r$, we can form

$$\bar{B}_r^{(0)} = B_r(t_{p'}) \cdots B_r(t_1).$$

These matrices are then used to approximate the isotope density distribution in the reactor at a time $\alpha t^{(0)}$ with the initial loading given by Eq. (19). A neutronics calculation is then performed to obtain the value of the unpoisoned $k_{eff}$. Using a second guess $x^{(1)}$ for the enrichment and the discharge density $\bar{n}^{(1)} = B^{(0)}\hat{n}^{(0)}$, the above procedure is repeated, giving rise to an unpoisoned $k_{eff}$ corresponding to $x^{(1)}$. A search is now begun on the enrichment in order that the unpoisoned $k_{eff}$ achieves its desired value.

DISCUSSION

The above described methods have been implemented as computer routines in modular form for use in a basic burnup program. Current work is concentrated on development of the system to include all the features of the model outlined above. The system will be adapted if necessary to satisfy specific needs for computation capability as they develop. It is hoped that it will provide a basic computational facility for studies of fast breeder reactor concepts at Argonne National Laboratory.

REFERENCES

1. B. Duane, *Transmutation Logic for $S_n$ Transport Analysis*, Proc. Conference on Application of Computor Methods to Reactor Problems, ANL-7050, 291 (1965).

## VI-17. Intercomparison of Various Multigroup Transport Approximations of the Dispersion Law of Neutron Waves[1]

A. TRAVELLI

INTRODUCTION

The dispersion law of neutron waves has been studied recently in several different transport approximations by various authors. In the multigroup case, the principal methods that have been developed for its calculation are based on diffusion theory,[2] on the $P$-1 and $P$-3 approximations,[3,4] and on transport theory.[5] The published results cannot be intercompared significantly,

however, because several additional simplifications have been introduced in many cases, and becuase different scattering kernels have been used.

In this paper, the complex inverse relaxation length of neutron waves at any angular frequency of the modulating source is obtained from the same canonical equation, with minor modifications, in diffusion theory, in any $P$-$L$ approximation, in any double $P$-$L$ approximation, and in transport theory. No additional simplifications are introduced into the approximations. Thus, the same method is used to determine the value of the complex inverse relaxation length in any theory and under identical conditions; this makes evident the difference in the results which is due to the transport approximation being introduced.

## The Procedure

We can represent a neutron wave in one-dimensional geometry as

$$\Phi(E,\mu,t,x) = \mathrm{Re}[\phi(E,\mu)\exp(i\omega t - \rho x)] \tag{1}$$

with

$$\rho = \alpha + i\xi, \tag{2}$$

and we shall define as the inverse complex relaxation length any value of $\rho$ for which the expression (1) satisfies the form chosen for the transport equation. The real and the imaginary components of $\rho$ ($\alpha$ and $\xi$) are, respectively, the attenuation constant and the phase constant of the wave; the way in which they depend on the angular frequency, $\omega$, defines the dispersion law.

By introducing the appropriate modifications in the Boltzmann equation, it can be shown[5,6] that $\rho$ must satisfy the canonical equation

$$\mathrm{Det}\left\{\sum_l \frac{2l+1}{\rho}\,\underline{A}\,\underline{\Sigma}_{sl}\,\underline{H}_l - \underline{I}\right\} = 0 \tag{3}$$

in all the transport approximations mentioned in the introduction. $\underline{\Sigma}_{sl}$ is the $l$th Legendre component of the scattering kernel, and $\underline{H}_l$ is defined by the recurrence relations

$$n\underline{H}_{n-1} + (n+1)\underline{H}_{n+1} - \frac{2n+1}{\rho}(\underline{\Sigma}_t^* - \underline{\Sigma}_{sn})\underline{H}_n = 0 \tag{4}$$

for $n \geq 0$. In addition,

$$H_0 = \underline{I} \tag{5}$$

$$\underline{H}_{-1} = \underline{0}. \tag{6}$$

The diagonal matrix $\underline{\Sigma}_t^*$ is given by

$$\underline{\Sigma}_t^* = \underline{\Sigma}_t + i\omega\underline{\nu}^{-1}, \tag{7}$$

where $\underline{\Sigma}_t$ is the total cross section and $\underline{\nu}$ is the neutron speed. The diagonal matrix $\underline{A}_l$ is defined by

$$\underline{A}_l = \underline{P}_l(\rho^{-1}\underline{\Sigma}_t^*)\underline{G}(\rho^{-1}\underline{\Sigma}_t^*) - \underline{W}_{l-1}(\rho^{-1}\underline{\Sigma}_t^*), \tag{8}$$

and the function $G(x)$ depends on the approximation being used. In particular,

$$G(x) = \mathrm{ctnh}^{-1}(x) \text{ in transport theory,} \tag{9}$$

$$G(x) = \frac{W_L(x)}{P_{L+1}(x)} \text{ in any } P\text{-}L \text{ approximation,} \tag{10}$$

$$G(x) = \frac{W_L^+(x)}{P_{L+1}^+(x)} + \frac{W_L^-(x)}{P_{L+1}^-(x)} \text{ in any } DP\text{-}L \text{ approximation,} \tag{11}$$

$$G(x) = \{[x-1]/[3(x - i\omega/v\rho)]\}^{-1} \text{ in diffusion theory.} \tag{12}$$

The polynomials $P_L(x)$ and $W_L(x)$, and the superscripts $(+)$ and $(-)$ are used in the standard notation of the Legendre functions and of the half-range functions extended over the entire range. In the framework of this paper, diffusion theory differs from the $P$-1 approximation because it introduces the additional assumption that the neutron current does not depend on time.

## Numerical Results

A computer code in complex arithmetic was developed to solve numerically Eq. (3) for the roots $\rho$ when the scattering is linearly anisotropic. A test run with 33 groups for the case of AGOT graphite at 20°C, in which the SUMMIT scattering kernel was used, gave the results listed in Table VI-17-I. Two types of diffusion theory were considered, depending upon whether the matrix $\Sigma_{s1}$ was diagonalized (simple diffusion) or not (full diffusion). The corresponding values of the real and imaginary components of the square of the complex inverse relaxation length are displayed graphically in Figs. VI-17-1 and VI-17-2.

The numerical results confirm the fact, noted already in monoenergetic theory,[7] that the $P$-1 approximation introduces a larger error than diffusion theory. Diffusion theory rates almost as well as the $DP$-1 and the $P$-3 approximations, especially if the so-called "transport approximation" is not introduced, and the diffusion coefficient is defined as an operator rather than as a function. Very small errors appear in the $DP$-2 and in the $P$-5 approximations at high frequencies, and no difference could be noted, within computational accuracy and the considered frequency range, among the results obtained in transport theory, in the $DP$-7 approximation, and in the $P$-15 approximation.

TABLE VI-17-I. THE COMPLEX INVERSE RELAXATION LENGTH IN GRAPHITE IN VARIOUS MULTIGROUP TRANSPORT APPROXIMATIONS

| $\omega$, rad/sec | Simple Diffusion | Full Diffusion | DP-0 | P-1 | DP-1 | P-3 | DP-2 | P-5 | Transport, DP-7, P-15 |
|---|---|---|---|---|---|---|---|---|---|
| | | | | $\alpha$, $cm^{-1}$ | | | | | |
| 0 | 0.020445 | 0.020436 | 0.023464 | 0.020436 | 0.020422 | 0.020421 | 0.020421 | 0.020421 | 0.020421 |
| 2000 | 0.071559 | 0.071569 | 0.082232 | 0.071584 | 0.071707 | 0.071763 | 0.071822 | 0.071956 | 0.071524 |
| 4000 | 0.100473 | 0.100513 | 0.114554 | 0.099717 | 0.100565 | 0.100665 | 0.100668 | 0.100669 | 0.100669 |
| 6000 | 0.122633 | 0.122701 | 0.139827 | 0.121729 | 0.122962 | 0.123138 | 0.123138 | 0.123141 | 0.123141 |
| 8000 | 0.141281 | 0.141327 | 0.161022 | 0.140308 | 0.142046 | 0.142285 | 0.142284 | 0.142288 | 0.142288 |
| 10000 | 0.156807 | 0.157108 | 0.177842 | 0.155049 | 0.157775 | 0.158198 | 0.158185 | 0.158185 | 0.158185 |
| 12000 | 0.170312 | 0.170636 | 0.192025 | 0.167374 | 0.170586 | 0.171264 | 0.171254 | 0.171256 | 0.171256 |
| 14000 | 0.182518 | 0.182838 | 0.205204 | 0.178814 | 0.182207 | 0.183094 | 0.183100 | 0.183114 | 0.183114 |
| 16000 | 0.193905 | 0.194244 | 0.217919 | 0.189868 | 0.193315 | 0.194377 | 0.194407 | 0.194440 | 0.194439 |
| 18000 | 0.204707 | 0.205095 | 0.230336 | 0.200697 | 0.204114 | 0.207319 | 0.205378 | 0.205437 | 0.205434 |
| 20000 | 0.215052 | 0.215505 | 0.242389 | 0.211270 | 0.214657 | 0.215977 | 0.216063 | 0.216150 | 0.216146 |
| | | | | $\zeta$, $cm^{-1}$ | | | | | |
| 0 | 0.000000 | 0.000000 | 0.000000 | 0.000000 | 0.000000 | 0.000000 | 0.000000 | 0.000000 | 0.000000 |
| 2000 | 0.063812 | 0.063807 | 0.073978 | 0.064496 | 0.063837 | 0.063909 | 0.063982 | 0.063983 | 0.064074 |
| 4000 | 0.088007 | 0.088003 | 0.103335 | 0.090183 | 0.088441 | 0.088338 | 0.088339 | 0.088337 | 0.088338 |
| 6000 | 0.105117 | 0.104997 | 0.124528 | 0.108797 | 0.105824 | 0.105622 | 0.105625 | 0.105628 | 0.105628 |
| 8000 | 0.117981 | 0.117945 | 0.140646 | 0.122983 | 0.118982 | 0.118714 | 0.118717 | 0.118720 | 0.118720 |
| 10000 | 0.128824 | 0.128657 | 0.154023 | 0.134613 | 0.129065 | 0.128781 | 0.128795 | 0.128805 | 0.128805 |
| 12000 | 0.138459 | 0.138188 | 0.167168 | 0.146072 | 0.138522 | 0.138085 | 0.138127 | 0.138154 | 0.138152 |
| 14000 | 0.147432 | 0.147123 | 0.180157 | 0.157454 | 0.148005 | 0.147348 | 0.147414 | 0.147460 | 0.147457 |
| 16000 | 0.155858 | 0.155553 | 0.192726 | 0.168503 | 0.157255 | 0.156351 | 0.156437 | 0.156500 | 0.156497 |
| 18000 | 0.163769 | 0.163490 | 0.204725 | 0.179068 | 0.166118 | 0.164956 | 0.165054 | 0.165130 | 0.165128 |
| 20000 | 0.171216 | 0.170974 | 0.216064 | 0.189033 | 0.174494 | 0.173083 | 0.173186 | 0.173268 | 0.173268 |

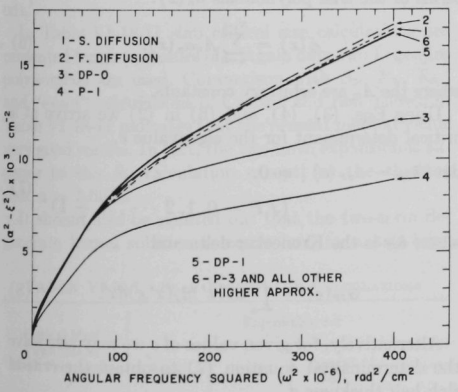


FIG. VI-17-1. The Real Part of the Squared Complex Inverse Relaxation Length in Graphite in Various Multigroup Transport Approximations. *ANL Neg. No. 112-6645.*

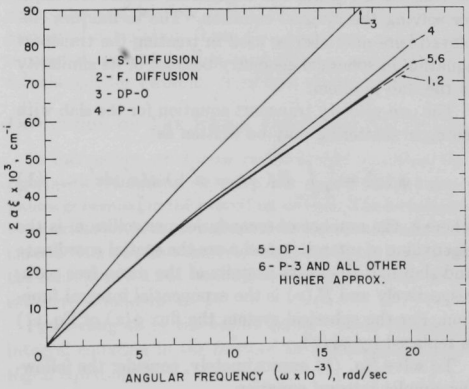


FIG. VI-17-2. The Imaginary Part of the Squared Complex Inverse Relaxation Length in Graphite in Various Multigroup Transport Approximations. *ANL Neg. No. 112-6644.*

## REFERENCES

1. A. Travelli, *Neutron-Wave Analysis in Various Multigroup Transport Approximations*, Trans. Am. Nucl. Soc. **9**, 114–115 (1966).
2. R. B. Perez and R. E. Uhrig, *Propagation of Neutron Waves in Moderating Media*, Nucl. Sci. Eng. **17**, 90–100 (1963).
3. H. H. Kunaish, R. B. Perez and R. S. Booth, *P-1 Space-Energy Dependent Theory of Neutron-Wave Propagation*, Trans. Am. Nucl. Soc. **8**, 291–292 (1965).

4. H. H. Kunaish, *Consistent P-3 Theory of Neutron Wave Propagation*, Proc. Symposium on Neutron Noise, Waves, and Pulse Propagation, Gainesville, Florida, February 14–16, 1966, pp. 87–98.
5. A. Travelli, *The Complex Relaxation Length of Neutron Waves in Multigroup Transport Theory*, Proc. Symposium on Neutron Noise, Waves, and Pulse Propagation, Gainesville, Florida, February 14–16, 1966, pp. 55–68.
6. A. Travelli, *The Dispersion Law of Neutron Waves in Multigroup Transport Theory and in Various Approximations* (To be published).
7. A. Travelli, *Neutron-Wave Parameters in Monoenergetic Transport Theory*, Trans. Am. Nucl. Soc., **8**, 293–294 (1965).

## VI-18. Orthogonal Polynomial Solutions and Error Estimates for Eigenvalues to the Integral Transport Equation

D. A. Sargis

### Polynomial Solution of The Transport Equation

Spatial Legendre polynomial expansions for the one-velocity integro-differential transport equation have been employed by G. Pomraning[1] and N. Paik,[2] et al., to obtain the critical eigenvalue c for slabs of various thicknesses. B. Carlson[3] on the other hand, has used simple non-orthogonal polynomial trial functions and the method of moments to solve the integral transport equation. In this paper we explore the possibility of using orthogonal polynomials in solving the one-velocity integral transport equation eigenvalue problem in slab geometry. The orthogonal trial functions are chosen so that a rigorous error estimating method may easily be constructed using the degenerate kernel technique for solving the integral equation.[4] The techniques employed here may also be used in treating the transport equation in spherical geometry because of its similarity to the slab problem.

The one-velocity transport equation for the slab with isotropic scattering may be written as

$$\phi(x) = \frac{c}{2}\int_{-a}^{a} E_1(|x - x'|)\,\phi(x')dx', \qquad (1)$$

where $c$, the number of secondaries per collision, is the eigenvalue of interest. $x$ and $a$ are the spatial coordinate and slab half thickness in units of the mean free path, respectively and $E_1(x)$ is the exponential integral function. For the spherical system the flux $\phi(x)$ of Eq. (1) is replaced by $x\phi(x)$.

To solve Eq. (1) approximately, consider the following simpler integral equation

$$\tilde{\phi}(x) = \int_{-a}^{a} \tilde{K}(x,x',c)\tilde{\phi}(x')dx', \qquad (2)$$

where $\tilde{\phi}(x)$ and $\tilde{K}(x,x',c)$ are the approximate flux and kernel, respectively.

Assume that the kernel $\tilde{K}(x,x',c)$ may be represented by an $N$-th order degenerate kernel

$$\tilde{K}(x,x',c) = K^{(N)}(x,x',c) = \sum_{n=0}^{N-1} \alpha_n(x)\beta_n(x',c), \qquad (3)$$

where $\alpha_n(x)$ are orthogonal trial functions and the $\beta_n(x',c)$ are determined from

$$\beta_n(x',c) = \int_{-a}^{a} \frac{c}{2} E_1(|x - x'|)\,\alpha_n^{+}(x)dx. \qquad (4)$$

The adjoint functions $\alpha_n^{+}(x)$ are defined so that

$$\int_{-a}^{a} \alpha_m(x)\alpha_n^{+}(x)dx = \delta_{mn} \qquad (5)$$

where $\delta_{mn}$ is the Kronecker delta function.

The approximate flux of Eq. (2) is also expanded in terms of the trial polynomials $\alpha_n(x)$:

$$\tilde{\phi}(x) = \sum_{n=0}^{N-1} A_n\alpha_n(x), \qquad (6)$$

where the $A_n$ are arbitrary constants.

Using Eqs. (3), (4), and (6) in (2) we arrive at a critical determinant for the eigenvalue $c$,

$$\det|\,\delta_{JP} - \alpha_{JP}(c)\,| = 0, \qquad (J,P = 0, 1, 2 \cdots, N-1) \qquad (7)$$

where $\delta_{JP}$ is the Kronecker delta and

$$\alpha_{JP}(c) = \int_{-a}^{a} \alpha_P(x')\beta_J(x',c)dx'. \qquad (8)$$

Alternatively, for given values of $c$ we may also solve the determinantal equation (7) to obtain the critical slab half thickness $a$.

For numerical calculations, the Legendre polynomials, $P_n(x/a)$,[5] are orthogonal on the interval $(-a,a)$, and form a particularly simple set of trial functions. Other polynomials which are orthogonal on this interval, such as the Jacobi, Gegenbauer, or Chebyshev polynomials,[5] could also be used. However, these polynomials involve evaluation of somewhat more complicated integrals in

the determination of the matrix elements $\alpha_{JP}$ of Eq. (8). By using Legendre polynomial trial functions, the $\alpha_{JP}$ can be found analytically with little computational effort.

Therefore, for the slab, assume

$$\tilde{\phi}(x) = \sum_{n=0}^{N-1} A_{2n} P_{2n}(x/a), \tag{9}$$

where only the even order polynomials are used so that $\tilde{\phi}(x) = \tilde{\phi}(-x)$. Similarly, for the sphere we could use

$$x\tilde{\phi}(x) = \sum_{n=0}^{N-1} A_{2n+1} P_{2n+1}(x/a) \tag{10}$$

so that the symmetry properties of the flux are maintained in both cases.

In Table VI-18-I the eigenvalue ($c$-1) has been calculated for slabs of various half thicknesses using only two Legendre polynomial trial functions ($N = 2$). The results obtained by Pomraning[1] and Paik[2] using two Legendre polynomials for the integro-differential transport equation are given in the second and third columns. "Exact" results obtained by B. Carlson and G. Bell,[6] using extrapolated end point techniques, are given in the last column.

It appears that the results obtained in this paper are approximately an order of magnitude better than the results of Pomraning[1] and Paik.[2] Furthermore, the method employed here does not appear to deteriorate for larger slab sizes as do the integro-differential methods.[1]

In Table VI-18-II slab critical size calculations are presented for given values of $c$. Again only two Legendre polynomials are used. Comparison with $S_2$, $P_5$, $S_{16}$, and "exact" calculations of Carlson and Bell[6] shown in Table VI-18-II indicates that the present method yields very good results. In fact, the two-term expansion is superior to the $S_{16}$ calculation except for the thickest slab, $a = 5.6655$.

It should also be pointed out that the two-term degenerate kernel solution is equivalent to a two-term variational calculation.[7] In fact, by proper choice of trial functions, identical results may be obtained for both methods. The degenerate kernel results should therefore also serve as upper bounds for the exact eigenvalues in these calculations.

TABLE VI-18-I. Slab Eigenvalue Calculations

| Critical Half Thickness in Mean Free Paths | Eigenvalue $c$-1 | | | |
|---|---|---|---|---|
| | Pomraning[1] | Paik[2] | Present Work | "Exact"[6] |
| 0.3108 | 1.0011 | 1.002 | 1.000755 | 1.00 |
| 0.3887 | 0.8016 | 0.802 | 0.800190 | 0.80 |
| 0.5120 | 0.6024 | 0.601 | 0.599984 | 0.60 |
| 0.7366 | 0.4035 | 0.401 | 0.400024 | 0.40 |
| 1.2893 | 0.2046 | 0.201 | 0.200026 | 0.20 |
| 2.1134 | 0.1043 | 0.101 | 0.100001 | 0.10 |
| 3.3002 | — | — | 0.050019 | 0.05 |
| 5.6655 | — | — | 0.020032 | 0.02 |

TABLE VI-18-II. Slab Critical Size Calculations

| $c$ | $S_2$ | $P_5$ | $S_{16}$ | Present Work | "Exact"[6] |
|---|---|---|---|---|---|
| 2.00 | 0.4097 | 0.3348 | 0.3116 | 0.31104 | 0.3108 |
| 1.80 | 0.4924 | 0.4101 | 0.3893 | 0.38879 | 0.3887 |
| 1.60 | 0.6197 | 0.5299 | 0.5125 | 0.51199 | 0.5120 |
| 1.40 | 0.8455 | 0.7501 | 0.7372 | 0.73664 | 0.7366 |
| 1.20 | 1.3896 | 1.2985 | 1.2902 | 1.28943 | 1.2893 |
| 1.10 | 2.1984 | 2.1210 | 2.1146 | 2.11342 | 2.1134 |
| 1.05 | 3.3718 | 3.3073 | 3.3023 | 3.30098 | 3.3002 |
| 1.02 | 5.7262 | 5.6723 | 5.6694 | 5.67059 | 5.6655 |

Since the approximate eigenvalues obtained by this method appear to be very good for the two-polynomial expansion, it would be useful to have a simple method available for obtaining a rigorous estimate of the error in the approximation scheme. The variational nature of the approximation scheme supplies us with only upper bounds for the exact eigenvalues.

In the next section we discuss a simple method for establishing error bounds for the exact eigenvalues. The error estimates obtained by this scheme are rigorous in that the bounds depend only on the difference $|c - \tilde{c}|$, where $\tilde{c}$ is the approximate eigenvalue and $c$ is the exact eigenvalue and does not depend on another approximate numerical calculation. Therefore, the error in $\tilde{c}$ can be estimated without having to perform a high order $S_n$ calculation, for example, to obtain an "exact" result.

## Derivation of The Error Estimating Technique

In this section we discuss rather briefly a method for rigorously estimating errors in the approximate eigenvalues generated in the preceding section. The technique is an extension of a very general method previously discussed.[4] Here a non-negative weighting factor $w(x)$ and the concept of a norm are employed to improve the error estimates considerably.

Proceeding as in the earlier paper,[4] write the exact integral equation in the form of an inhomogeneous integral equation

$$\phi(x) = \int_{-a}^{a} K(x,x',c)\phi(x')\,dx' + f(x), \tag{11}$$

where $f(x)$ is a source term. For isotropic scattering and slab geometry the exact integral equation kernel is

$$K(x,x',c) = \frac{c}{2} E_1(|x - x'|). \tag{12}$$

Since in general Eq. (11) can not be solved exactly, define a simpler approximate integral equation

$$\tilde{\phi}(x) = \int_{-a}^{a} \tilde{K}(x,x',c)\tilde{\phi}(x')\,dx' + f(x), \tag{13}$$

where $\tilde{\phi}(x)$ and $\tilde{K}(x,x',c)$ again represent the approximate flux and kernel, respectively.

Now define the norm of a function $g(x)$ as

$$\| g(x) \| = \max_{-a \le x \le a} \frac{|g(x)|}{w(x)}, \tag{14}$$

where $w(x)$ is a non-negative continuous function over the interval $-a \le x \le a$.

Equation (11) is now written as

$$\phi(x) = f^*(x) + \int_{-a}^{a} \tilde{K}(x,x',c)\phi(x')\,dx$$

or (15)

$$\phi(x) = f^*(x) + \int_{-a}^{a} \tilde{\Gamma}(x,x',c)f^*(x')\,dx',$$

where $\tilde{\Gamma}(x,x',c)$ is the resolvent kernel, and

$$f^*(x) = f(x) + \int_{-a}^{a} [K(x,x',c) - \tilde{K}(x,x',c)]\phi(x')\,dx'. \tag{16}$$

Using the definition of Eq. (14) in Eq. (15), find, after applying the triangle and Scwharz inequalities, that

$$\| \phi \| < \| f^* \| \times [1 + B(c)] + F_2^* B(c), \tag{17}$$

where $F_2^*$ is a non-negative constant and

$$B(c) > \max_{-a \le x \le a} \int_{-a}^{a} |\tilde{\Gamma}(x,x',c)|\,dx'. \tag{18}$$

From Eqs. (14) and (16) also find

$$\| f^* \| < \| f \| + \| \phi \| \times h(c) \tag{19}$$

where

$$h(c) > \max_{-a \le x \le a} \frac{1}{w(x)} \int_{-a}^{a} |K(x,x',c) - \tilde{K}(x,x',c)|\,w(x')\,dx'. \tag{20}$$

Combining Eqs. (17) and (19), we obtain

$$\| \phi \| < \frac{\| f \| \times [1 + B(c)] + F_2^* B(c)}{1 - h(c)[1 + B(c)]}. \tag{21}$$

For $c$ to be an eigenvalue of the exact equation (11), $\phi$ must be unbounded.[4] Therefore, since all of the numerator terms in Eq. (21) are non-negative, the eigenvalues of Eq. (11) must satisfy the inequality

$$1 - h(c)[1 + B(c)] < 0 \tag{22}$$

where $B(c)$ and $h(c)$ are given by Eqs. (18) and (20).

This result differs significantly from previous work[4] since the bound $h(c)$ of Eq. (20) has been modified to provide much sharper error estimates.

In this paper we assume that the weighting factor $w(x)$ is polynomial in form,

$$w(x) = \sum_{n=0}^{M} b_n (x/a)^n, \tag{23}$$

subject to the further restriction that $w(x) \ge 0$ for $-a \le x \le a$. The $b_n$ are adjustable coefficients which are chosen to minimize $h(c)$ and yield good error bounds.

## Numerical Results For The Error Estimating Method

In this section we present some numerical results for the error estimating technique. Our attention is restricted to the approximate eigenvalues of the slab integral transport equation using two Legendre polynomials as trial functions. For this case the approximate kernel $\tilde{K}(x,x',c)$ is given by the second order degenerate kernel.

$$K^{(2)}(x,x',c) = \sum_{n=0}^{1} \alpha_{2n}(x)\beta_{2n}(x',c), \tag{24}$$

where $\alpha_{2n}(x) = P_{2n}(x/a)$ and the $\beta_{2n}(x',c)$ are found from Eq. (4).

For the approximate kernel of Eq. (24) we limit ourselves to weighting factors of the form

$$w(x) = \sum_{n=0}^{M} b_{2n}(x/a)^{2n} \tag{25}$$

for $M = 0$, 1, and 2. Here, $b_0$ is set equal to 1.0 and the $b_2$'s and $b_4$'s are selected by a simple computer program to give good error estimates for various problems.

In Table VI-18-III error estimates are given for $|c - \tilde{c}|$ for various slabs. Here $\tilde{c}$ is the two term approximate eigenvalue found previously and $c$ is the exact eigenvalue of Eq. (1).

For a constant weighting factor $w(x) = 1.0$, the error estimates vary from 6.0% for the thinnest slab to 35.8% for the thickest slab. The results obtained using $w(x) = 1.0$ correspond to calculations presented in earlier work.[4]

By using the weighting factor $w(x) = 1.0 + b_2(x/a)^2$, the error estimates are greatly improved. For the smallest slab the error bound is 0.66%, while the largest slab has a bound of 3.84%.

Calculations using a fourth order polynomial, $w(x) =$

TABLE VI-18-III. Error Bounds for the Slab Approximate Eigenvalues

| $a$ | $\bar{c}$ | $\lvert c - \bar{c} \rvert^{(a)}$ | | |
|---|---|---|---|---|
| | | $w(x) = 1.0$ | $w(x) = 1.0 + b_2\left(\frac{x}{a}\right)^2$ | $w(x) = 1.0 + b_2\left(\frac{x}{a}\right)^2 + b_4\left(\frac{x}{a}\right)^4$ |
| 0.3108 | 2.000755 | 0.120 (6.0%) | 0.0131 (0.66%) | 0.00405 (0.20%) |
| 0.3887 | 1.800190 | 0.122 (6.8%) | 0.0138 (0.77%) | 0.00427 (0.24%) |
| 0.5120 | 1.599984 | 0.128 (8.0%) | 0.0142 (0.89%) | 0.00428 (0.27%) |
| 0.7366 | 1.400024 | 0.142 (10.2%) | 0.0156 (1.12%) | 0.00506 (0.36%) |
| 1.2893 | 1.200026 | 0.179 (15.0%) | 0.0197 (1.65%) | 0.00608 (0.51%) |
| 2.1134 | 1.100001 | 0.231 (21.0%) | 0.0268 (2.44%) | 0.00813 (0.74%) |
| 3.3002 | 1.050019 | 0.290 (27.6%) | 0.0299 (2.85%) | 0.01087 (1.04%) |
| 5.6655 | 1.020032 | 0.364 (35.8%) | 0.0392 (3.84%) | 0.01462 (1.43%) |

[a] The percent errors in $\lvert c - \bar{c} \rvert / \bar{c}$ are given in the parentheses.

$1.0 + b_2(x/a)^2 + b_4(x/a)^4$, yield still sharper error estimates. For the thinnest slab the error estimate is 0.2% while the largest slab has an error bound of 1.43%.

From the results in Table VI-18-III it is clear that higher order weighting factors are required in treating the thicker slab problems. This is due in large part to the fact that more polynomials are required in representing the approximate kernel and flux over a large spatial region than over a thin slab.

The adjustable coefficients, $b_n$, used here were chosen to give good error estimates. No attempt was made to optimize the selection procedure to give "best" error estimates. However, it is apparent that excellent results may be obtained, with little computational effort, by using the fourth order $w(x)$. The error estimates were reduced by approximately a factor of 30 in going from the constant weighting factor to a fourth order polynomial. It also appears that by going to higher order polynomials, error bounds can be obtained which are close to the exact error estimates. This would be possible, however, only at the expense of greater computational effort.

### References


1. G. C. Pomraning and M. Clark, Jr., *Spatial Expansion of the Transport Equation*, J. Nucl. Energy **18**, 191, (1964).
2. N. C. Paik, I. Kaplan and A. Travelli, *Criticality of a Bare Slab of Arbitrary Size with Anisotropic Scattering*, Trans. Am. Nucl. Soc., **8**, 504 (1965).
3. B. Carlson, *Neutron Diffusion Theory, Integral Theory Methods and Formulas*, AECD-2835 (1949).
4. D. A. Sargis and L. M. Grossman, *Analytic Error Estimates for Integral-Equation Eigenvalue Problems in Neutron Physics*, Nucl. Sci. Eng. **25**, 395 (1966).
5. M. Abramowitz and I. Stegun, Editors, *Handbook of Mathematical Functions With Formulas, Graphs, and Mathematical Tables*, National Bureau of Standards Applied Mathematics Series 55, Chap. 22 (1964).
6. B. Carlson and G. Bell, *Solutions of the Transport Equation by the $S_n$ Method*, Proc. 1958 Geneva Conference **16**, Paper No. 2386, p. 535.
7. L. Kantorovich and V. Krylov, *Approximate Methods of Higher Analysis*, (Academic Press, New York, 1959), Chap. 2.


## VI-19. A Directed-Search Subroutine for Finding Minima

G. S. Stanford

ITER 7 is a FORTRAN subroutine for finding, by a directed-search procedure, the value of $x$ corresponding to the minimum of the function $y = f(x)$, where $y$ is computed numerically. The function $f(x)$ need not be differentiable or even continuous, but there are three restrictions: (1) there must be a non-zero separation between the minimum being sought and the nearest maximum or nearest zone where $y$ is constant; (2) the region searched should not include a maximum or a zone where $y$ is constant; (3) a $\delta$-function singularity will not be discovered, but could cause trouble if it coincided with a search point.

A convergence test is provided that is independent of the slope of the function. The subroutine itself requires less than a millisecond per iteration, to which must be added the time used in computing the value of $f$. There are no dimensioned variables.

Application to the multidimensional function $f(x,y,z,$

$\cdots$) is easily accomplished, with an initially coarse search mesh that is refined as the search proceeds. In tests with simple 1-, 2-, and 3-dimensional problems, the numbers of times that $f$ had to be calculated were typically in the ratio 1:6:20, for comparable convergence criteria. In routine one-dimensional use as part of the NURF[1] foil data code, about 12 cycles provide satisfactory convergence.

### One-Dimensional Applications

The FORTRAN subroutine ITER 7 has been written for use in finding the value of $x$ that correspond to a minimum of the function $y = f(x)$, where $y$ is computed numerically. Thus $f(x)$ may be non-differentiable, but there must be a non-zero separation between extremum points. For example, $y$ might be the sum of the squares of a set of residuals, which can be minimized by appropriate selection of $x$.

ITER 7 is called repetitively to discover the minimum. An initial increment $dx$ must be specified; subsequent increments are determined by ITER 7. The calling program uses $x_0$, an initial value of $x$, to calculate an initial value of $y$, and then calls ITER 7, which returns an incremented value of $x$ to the calling program for recalculation of $y$, and so on. Let $c$ be the number selected for determining when convergence has occurred (see below), and let $n_m$ be the upper limit for the number of cycles through the loop. Then ITER 7 is used in the following manner:

```
      .
      .
      .
      X = x0
      DX = dx
      NMAX = nm
      CØNCRI = c
      NCYCL = 0
100   [calculation of y = f(X)]
140   CALL ITER 7, (NCYCL, Y, X, DX, CØN-
        CRI, NMAX, ISTØP, DDX)
150   IF (NCYCL. EQ. NMAX .ØR. ISTØP .EQ.
        1) 200, 100
200   [Continue]
      .
      .
      .
```

The parameter ISTØP is the convergence indicator: it is initially set to zero by ITER 7, and becomes 1 when the convergence criterion has been met. The only other parameters whose values are changed within the subroutine are NCYCL, X and DDX. The value of DX, the initial $x$-increment, is not changed within ITER 7, new values of the increment being stored in the location DDX. DDX is included in the parameter list because in multi-dimensional applications (see below) it is useful to have it available in the calling program; for one-dimensional problems it is not normally needed.

Because the calculation of $y$ is done in the calling program, rather than (as is done in some similar codes) by a separate subroutine called by the iterating subroutine, certain loading complications are avoided in computers such as the DDP-24, where the order of loading subroutines is important.

The FORTRAN listing (CDC-3600) for ITER 7 is given in Fig. VI-19-1. In operation, the subroutine changes X by increments DX until the minimum has been passed. (The initial direction of march is reversed if the second value of Y is greater than the first.) When a value of Y greater than (or equal to) the preceding one indicates that a minimum has been passed, the sign of DDX is reversed, and its magnitude is made half as great. Since the second such step in the reverse direction would repeat a calculation already made, that point is jumped over, the corresponding value of Y having been retained. This procedure eliminates most recalculations, but not all, since still earlier points are occasionally repeated.

The criterion used by ITER 7 in determining convergence takes advantage of the fact that each time the increment is divided by two, the new value of $x$ cannot be away from the minimum by more than three times the new increment. Thus the user inputs for CØNCRI a suitable fraction of his selected initial $dx$. (The convergence test occurs in statement 20 of the FORTRAN listing, Fig. VI-19-1.) This method for determining convergence avoids problems that can arise with a slope-sensitive criterion in the following situations:

(a) a slope which changes very gradually near the minimum. In that case the significant-figure limitation of the computer can be exceeded because successive values of $y$ become approximately equal.

(b) a slope which is discontinuous at the minimum.

(c) the case where there is some jitter in successive calculations of $y$—which can happen if, for instance, that calculation also involves an iteration procedure, as in a multidimensional application.

If, however, a different type of convergence test is desired, it can be inserted in the calling program between the statements numbered 140 and 150 in the above example. CØNCRI must be made sufficiently small, and the tests performed by statement 150 should never be bypassed, except on leaving the loop.

To test the one-dimensional performance, the parabola $y = x^2$ was used, along with the input quantities, $x_0 = 5$, $dx = 1.5462$ and $c = 1.27 \times 10^{-4}$. Thirty-two cycles were required for convergence, with the final values $x = 1.024 \times 10^{-4}$, $y = 1.048 \times 10^{-8}$.

```
      SUBROUTINE ITER 7  (NCYCL, A, B,DB, CONCRI, NMAX, ISTOP, DELB)

C       PRODUCES INCREMENTED VALUES OF  B  IN SEARCH FOR A MINIMUM VALUE OF  A.
C  INITIAL INCREMENT IS  DB,  AND CONCRI IS THE CONVERGENCE CRITERION (SEE
C  STATEMENT 20). CALLING PROGRAM MUST INITIALLY SET  NCYCL  TO ZERO, AND IT
C  MUST TEST FOR (NCYCL .GE. NMAX) AND FOR (ISTOP .EQ. 1), AND LEAVE LOOP WHEN
C  EITHER OCCURS.  ISTOP IS INITIALLY SET TO ZERO BY ITER 7, AND BECOMES 1
C  WHEN THE CONVERGENCE CRITERION HAS BEEN MET.

 9010 FORMAT (/* MESSAGE FROM ITER 7... CALLING PROGRAM HAS FAILED TO*
     2         * NOTE THAT CONVERGENCE CRITERION HAS BEEN MET. (*
     3           E10.3 *.) * / * EXECUTION TERMINATED. *)
 9020 FORMAT (/* MESSAGE FROM ITER 7... CALLING PROGRAM HAS FAILED TO*
     2         * NOTE THAT MAX. NO. OF CYCLES (* I6 *) HAS BEEN*
     3         * EXCEEDED.* / * EXECUTION TERMINATED. *)
C
      IF (NCYCL .LT. 0)  NCYCL = 0
      IF (NMAX .GT. 300)  NMAX = 300
      IF (NCYCL .GT.(NMAX+2)) GO TO 210
      NCYCL = NCYCL + 1
      IF (NCYCL .GT. 1) GO TO 10
      DELB = DB     $ ISTOP = K = 0      $ Q2=A     $ GO TO 100
   10 IF (ISTOP.EQ. 1) GO TO 200
      IF (K .EQ. 1)  GO TO 15
      Q2 = A        $ GO TO 20
   15 Q1 = A        $ Q2 = QK
   20 IF ( ABSF(DELB/DB).GT. CONCRI )  GO TO 30
   25 ISTOP = 1                 $ RETURN
   30 IF (Q2 .EQ. 0.0) GO TO 35
      IF (ABSF ((Q1 - Q2)/Q2) .LT. 1. E-10)  GO TO 50
   35 IF (Q2 .GE. Q1)  GO TO 40
C  NOTE THAT IF K=1, DELB GETS ADDED TWICE (ONCE BY STATEMENT 100).
      IF (K.EQ.0) GO TO 100  $ B = B+DELB          $ Q1=QK    $ GO TO 100
   40 IF (NCYCL .GT. 2) GO TO 50
      DELB = - DELB
      B = B + 2. * DELB                  $ RETURN
   50 IF (K .EQ. 0) GO TO 60 $ QK=Q1     $ DELB = DELB/2      $ GO TO 100
   60 DELB = -DELB/2          $ K = 1    $ QK = Q1
      B = B + DELB            $ RETURN
  100 B = B + DELB            $ IF (K.EQ.0) Q1 = Q2          $ K = 0
      RETURN

  200 PRINT 9010, CONCRI       $ STOP
  210 PRINT 9020, NMAX         $ STOP     $ END
```

FIG. VI-19-1. Fortran Listing for ITER 7. *ANL Neg. No. 112-8865.*

The CDC-3600 computer time required was checked with the same problem, with $c = 10^{-15}$. The number of cycles was 115, and the total time spent in the loop was 0.107 sec, for an average of 0.93 millisec per cycle. (The final value of $x$ was $1.4 \times 10^{-15}$.)

The approximate number of cycles, $N$, required for convergence can be estimated from

$$N \approx 2.3n + b,$$

where $n$ is given by $2^{-n} = c$, and $b$ is the number of initial increments $dx$ that must be traversed before the minimum is reached for the first time.

The memory space required by ITER 7 is minimal, since the subroutine does not use any dimensioned variables.

ITER 7 has been in routine use as part of the NURF foil data processing code.[1] In that application, satisfactory convergence is obtained in about 12 cycles.

## Multidimensional Applications

While the above discussion explicitly considers only one-dimensional problems, ITER 7 can also be used to find minima in two or more dimensions. For a two-dimensional problem, for instance, one can use two such subroutines called ITER 7 and (say) ITER 8. To find the minimum of $z = f(x,y)$, one would use ITER 7 to find the minimum of $z = f(x,y_1)$ where $y_1$ is kept fixed, followed by a single call of ITER 8 to produce an incremented $y_1$ for recalculation of $f(x,y_1)$. ITER 7 is again used to find the minimum in the $x$ direction, followed by another call of ITER 8, and so on. One possible method is as follows, where the subscripts 7 and 8 refer

respectively to the $x$ and $y$ iterations. Two separate ITER subroutines are required here, because ITER8 stores some quantities during operation of ITER7.

```
      .
      .
      .
    Y = y0
    DY = dy
    DDY = dy
    NMAX8 = nm8
    CØNCRI8 = c8
    NCYCL8 = 0
 40 F = f
    X = x0
    NMAX7 = nm7
    CØNCRI7 = c7
 50 NCYCL7 = 0
 51 DX = F*DDY
100 [Calculation of Z = f(X,Y)]
    CALL ITER7 (NCYCL7, Z, X, DX, CØN-
      CRI7, NMAX7, ISTØP7, DDX)
    IF (NCYCL7. EQ. NMAX7. ØR. ISTØP7.
      EQ.1) 200, 100
200 CALL ITER8 (NCYCL8, Z, Y, DY, CØN-
      CRI8, NMAX8, ISTØP8, DDY)
    IF (NCYCL8. EQ. NMAX8. ØR. ISTØP8.
      EQ.1) 300, 50
300 [Continue]
      .
      .
      .
```

Statements 40 and 51, in the above example, permit starting with a coarse mesh which becomes finer as the search proceeds. The $x$-convergence number $c_7$ should be made large—like 0.7. (It must be $<1$. Any $c_7$ between $\frac{1}{2}$ and 1 will cause the inner loop to be left after a single reversal of DDX.) That way ITER 7 will only be called a few times on each pass, but X will converge along with Y, since the initial increment DX for each new round is tied to DDY by statement 51. The factor F would be set equal to unity if the convergence requirements for X and Y were roughly the same. Ultimate convergence is determined by $c_8$.

As a test of this procedure, it was used to find the minimum (which occurs at the point [0,0.0]) of the pa-

```
      PROGRAM ITR3D
C                    TO CHECK 3-DIMENSIONAL PERFORMANCE OF ITER 7
C
 8010 FORMAT (4E10,3)
 9110 FORMAT (6H  DZ = F8,4, 6X9HCONCRI7 = E12,5, 6X9HCONCRI8 = E12,5,
     X        6X 9HCONCRI9 = E12,5 // )
 9120 FORMAT (* NCYCL7  NCYCL8  NCYCL9* 8X1HX, 13X1HY, 13X1HZ, 13X1HT,
     X        13X2HDX, 12X2HDY / )
 9140 FORMAT (//* ELAPSED TIME FOR ITER7,8,9 WAS **3PF8.4* SECONDS.*)
 9150 FORMAT ( 3(I5,3X), 6E14.4 )
 9160 FORMAT (//* TOTAL NUMBER OF ITER 7 CALLS WAS * I8,1H.)
 9170 FORMAT ( 1H1)
C
   20 READ 8010, CONCRI7, CONCRI8, CONCRI9, DZ    $ IF (EOF,60) 400,30
   30 X = 5                    $ Y = 5             $ Z = 5
      NMAX7 = 20               $ NMAX8 = 20        $ NMAX9 = 50
      DDZ = DZ                 $ NCYCL9 = 0
      PRINT 9110, DZ, CONCRI7, CONCRI8, CONCRI9
      PRINT 9120               $ NSUM7 = 0
C
      T0 = TIMELEFT(T0)
   50 NCYCL8 = 0               $ DY = DDZ          $ DDY = DY
  100 NCYCL7 = 0               $ DX = DDY
  150 T = X**2 + Y**2 + Z**2 + (X*Y)**2            $ NSUM7=NSUM7+1
      CALL ITEM7 (NCYCL7, T, X, DX, CONCRI7, NMAX7, ISTOP7, DDX)
      IF (NCYCL7.EQ,NMAX7 .OR. ISTOP7.EQ,1)  250,150
  250 CALL ITEM8 (NCYCL8, T, Y, DY, CONCRI8, NMAX8, ISTOP8, DDY)
      IF (NCYCL8.EQ,NMAX8 .OR. ISTOP8.EQ,1) 300,100
  300 CALL ITEM9 (NCYCL9, T, Z, DZ, CONCRI9, NMAX9, ISTOP9, DDZ)
      PRINT 9150, NCYCL7, NCYCL8, NCYCL9, X, Y, Z, T, DX, DY
      IF (NCYCL9.EQ,NMAX9 .OR. ISTOP9.EQ,1) 350,50
  350 T1 = TIMELEFT (T1)       $ TELAPSED = T0 - T1
      PRINT 9140, TELAPSED     $ PRINT 9160, NSUM7
C
      PRINT 9170               $ GO TO 20
  400 STOP          $ END
```

FIG. VI-19-2. Example of a 3-Dimensional Application of ITER 7. *ANL Neg. No. 112-8866.*

raboloid $z = x^2 + xy + y^2$, using the following input quantities:

$$x_0 = y_0 = 5$$
$$c_7 = 0.7$$
$$c_8 = 10^{-4}$$
$$dy = 1.5462$$
$$f = 1$$

Convergence was reached after ITER 8 was called 38 times. ITER 7 was called an average of 4.7 times/pass, it having been necessary to make the calculation of $z$ 180 times. (Note that $z$ does not need to be recalculated just prior to the $y$ iteration since $x$ is not changed by ITER 7 on the final call.) The total computer time spent in the iteration loop, which included 38 lines of printout, was 496 millisec. The final values were:

$$x = 2.9 \times 10^{-7}$$
$$y = 1.4 \times 10^{-4}$$
$$z = 2.0 \times 10^{-8}$$

Figure VI-19-2 contains a test program (PROGRAM ITR3D) which applies ITER 7 to the three-dimensional problem of finding the minimum of the four-space surface $t = x^2 + y^2 + z^2 + x^2y^2$. It was found that a 30 to 50% time saving occurred when CØNCRI7 and CØNCRI8 were between 0.5 and 1, as compared with the range 0.25 to 0.5. With CØNCRI7 and CØNCRI8 in the former range, and starting out at $x = y = z = 5$, six values of DZ (= DX = DY) were tried, ranging from 1.5 to 2.1. (CØNCRI9 was kept at $10^{-4}$). The number of times $t$ was calculated was variable, ranging from 483 to 1021, with an average of 710. The final magnitudes of X, Y, and Z were all below $1.6 \times 10^{-4}$, with the final values of T all below $8.4 \times 10^{-8}$.

## Discussion

ITER 7 appears to provide a reasonably efficient means for finding the minimum (or maximum, by inverting the function; or zero, by using the absolute value of the function) of a non-differentiable function of one or more variables. If the function has more than one extremum point, the subroutine can still be used, provided there is no maximum between the initial approximation and the desired minimum, and that the initial independent-variable increments are not large enough to cause one of the maxima to be passed over in the first one or two steps. A code employing ITER 7 to find successive extrema (or zeroes) could easily be written.

Some additional limitations in the use of ITER 7 should be noted for completeness: (1) The search procedure can be disrupted if between the starting point and the minimum being sought, there is a region where $y$ is constant. (2) The search process might also be disrupted if a $\delta$-function singularity happens to coincide with a search point; other such singularities will not be detected. (3) If the minimum should occur at a cusp or pole in $f(x)$, or at, or very near a discontinuity, the search procedure will still find, with the specified precision, the value of $x$ where the minimum occurs; however, the value of $y$ at that value of $x$ might differ appreciably from the actual minimum value.

As is typical of such procedures, the time required for satisfactory convergence is strongly dependent on the quality of the initial guess. In the examples given above, it is obvious that starting out closer to the origin, with correspondingly smaller initial increments, could have produced equally good convergence with many fewer iterations. As already mentioned, in routine use as part of the NURF code, about 12 iterations are needed.

## Reference

1. G. S. Stanford, *The Codes NURF, COMBØ, and TWØSØRCE for Processing Foil Counting Data*. ANL-7356 (1967).

# Section VII

# Miscellaneous

This Section is a miscellany treating a small variety of topics. The first three papers describe exploratory work which was undertaken to investigate possible objectives and areas of difficulty. Work related to thermionic conversion was terminated during the fiscal year being reported. The first paper represents work continued from the preceding two years. The last two papers were done collaboratively with and as a service for other Divisions, respectively.

# VII-1. Nuclear Pumped Carbon Dioxide Gas Laser—Model I Experiments

J. A. DeShong, Jr.

Preliminary investigations have been carried out on an electrically-pumped $CO_2$-$N_2$-He laser system.[1] The system was successfully operated in a neutron flux of $2 \times 10^{10}$ n/cm$^2$-sec (thermal), demonstrating satisfactory mirror operation at this flux level as well as successful very low level infrared detection only a few feet from the nuclear radiation.

Methods of coating quartz laser tubes internally with adherent B-10 coatings of 0.6 to 1.5 mg/cm$^2$ thickness were worked out with special vapor blasting and rotating-bakeout techniques. The coatings are adherent up to 700°F or more. The tubes were provided with electrodes to permit electrical pumping while the tube is being irradiated with a flux of reactor generated neutrons.

A series of experiments has been completed utilizing electrical pumping to study the variation in lasing threshold produced by the B-10 coatings when the above tubes are irradiated. Reactor neutron fluxes ranged up to $2 \times 10^{10}$ n/cm$^2$-sec (thermal). This was the maximum flux achieved at the laser location in the Argonne Thermal Source Reactor (ATSR) with the reactor operating at its full licensed power of 10 kilowatts.

The results of these qualitative tests showed that the electrical power required to attain the lasing threshold decreased gradually as reactor flux was increased up to a flux of about $5 \times 10^8$ n/cm$^2$-sec (thermal). Then as the flux was increased further, the electrical power needed for threshold began to rise until it exceeded the power required initially with no neutron flux. At a flux of about $5 \times 10^9$ n/cm$^2$-sec a large increase in electrical power was necessary to reach threshold. However, once the threshold power was exceeded, the laser output corresponded to that obtained for the same pumping power with no neutron flux present; i.e., the phenomenon seemed to be related only to threshold operation. The above effects were very reproducible.

An interpretation of the experiments is complicated by the fact that the electrical discharge between the electrodes in the laser tube itself could be affected by the ionizing radiation. It is possible that this is what was observed since only the tube voltage required to reach threshold could be used as a rough indication of input power. The dynamic current and power were not measured because of high voltage problems. An optical telescope and several mirrors were arranged to permit viewing the tube plasma from the reactor control room while the tube was being irradiated. It was observed that the tube plasma for a given pumping voltage became more luminous and regular when a neutron flux was applied to the tube. This would be expected in the presence of ionizing radiation and the threshold changes observed probably were caused by degraded lasing conditions rather than by reduced pumping current since a more luminous plasma would seem to indicate higher discharge current and therefore higher pumping power.

In summary, the electrical pumping experiments seem to indicate that the ionizing fragments from the B-10 coatings in the laser tube contributed useful power toward pumping of the laser at lower neutron fluxes. The degradation that occurs at higher flux is not understood as yet. Considerable time was spent in varying gas mixtures and pressures while the reactor was operated at 10 kilowatts, but no conclusive evidence of lasing was obtained using only ionization produced by the B-10 layers.

The laser also was operated in the reactor flux with cadmium shields wrapped externally over the B-10 layers. There was no detectable change in the lasing properties which were checked over the entire range of electrical pumping power while the reactor flux was varied from zero to $2 \times 10^{10}$ n/cm$^2$-sec (thermal). This demonstrated that the laser mirrors were unaffected by the reactor environment in the above flux range. Also the reactor fast neutron and gamma flux would seem to have little or no effect on lasing. Either the thermal neutron flux or the $(n,\alpha)$ reaction products therefore must be responsible for the threshold changes that were observed without cadmium shields on the tube.

The original calculations to determine the neutron flux required to pump the laser to threshold were based on crude estimates of the energy deposited in the lasing gas by the B-10 layer. A series of measurements was made recently to determine the actual energy input to the laser gas during the pumping experiments. The results are applied to recalculate the neutron flux required to pump the laser to threshold.

The maximum power actually deposited in the $CO_2$ laser gas during the ATSR nuclear pumping experi-

ments is calculated for the "standard" gas mixture which consisted of 1 torr of $CO_2$, 1.33 torr of $N_2$, and 11.67 torr of He.

$$\frac{dE}{dx}\ (\text{laser gas}) = 1133\ \text{ev/cm-torr-frag}$$

Then

$$\begin{aligned} \text{path length } (l) &= 2 \times \text{tube radius}^{(1)} \\ &= 1.9\ \text{cm} \\ \text{total pressure } (p) &= 14\ \text{torr} \\ \text{energy deposited } (E) &= (dE/dx)(p \times l) \\ &= 30138\ \text{ev/frag.} \end{aligned}$$

The power entering the gas is

$$P_{GAS} = \frac{N \times E \times A \times L}{V},$$

where

$N \equiv$ number of fragments entering the gas per $cm^2$ per sec
$E \equiv$ energy deposited per fragment
$A \equiv$ area of B-10 per cm of length
$L \equiv$ B-10 layer length
$V \equiv$ total tube volume.

Therefore,

$$P_{GAS} = \frac{N(3.01 \times 10^4)(\pi \times 1.9)(33 \times 2.54)}{\pi(0.95)^2(46 \times 2.54)}$$

$$= (4.55 \times 10^4)N.$$

Since

$$N = F\Phi,$$

where

$F \equiv$ fragments entering the gas per unit flux
$\Phi \equiv$ neutron flux averaged along length of B-10 layer,
$N = (0.0536)(1.9 \times 10^{10}) = 1.02 \times 10^9$ frags/$cm^2$-sec

whence

$$P_{GAS} = (4.55 \times 10^4)(1.02 \times 10^9)$$

$$= 4.64 \times 10^{13}\ \text{ev/cm}^3\text{-sec.}$$

The estimated power, $P_{GAS}$, that must be deposited in the $CO_2$ laser gas mixture to attain threshold was calculated in Ref. 1 to be

$$P_{GAS} = 2.43 \times 10^{12}\ \text{ev/cm}^3\text{-sec at threshold.}$$

Then, with ATSR operating at maximum power (10 kW), the calculated laser threshold condition was exceeded by a factor

$$M = \frac{4.64 \times 10^{13}}{2.43 \times 10^{12}} = 19.1.$$

However, if the usual rule-of-thumb factor of 10 increase is applied to the calculated laser threshold to take care of unknowns, the flux at which lasing was expected was exceeded by a factor of only 1.9.

A number of conclusions can be drawn from the calculations:

1. The analysis shows that a relatively modest margin of 1.9 was attained above the flux at which lasing was expected. This is insufficient to conclude that lasing is not feasible, and reactors capable of higher flux then ATSR are being considered for future experiments.

2. The energy distribution to the helium, nitrogen and carbon dioxide in the nuclear pumped system was in the ratio of 1.6:1:1, respectively. It would be helpful to know this distribution in the electrically pumped system and the role actually played by the helium. A number of investigations of this problem are being carried out at various laser development laboratories.

3. The fragment energy spectra of B-10 layers varying in thickness from 0.6 to 1.5 mg/$cm^2$ were obtained. A thickness of 0.7 mg/$cm^2$ emitted the most energy for a given neutron flux, although 0.6 mg/$cm^2$ gave very nearly the same energy. The experimental laser tubes used about 0.6 to 0.65 mg/$cm^2$, so maximum output was obtained in the experiments. It is evident from the efficiency curve of the B-10 layer that somewhat greater layer efficiency can be achieved with thinner layers at the expense of increased flux. The maximum efficiency attainable in the layer itself is 50 percent because at least half the fragments travel away from the gas space and never enter it. If overall reactor efficiency is considered, the operating point selected would depend upon whether the layer material is B-10 or U-235 and, if U-235, how much of the total U-235 is contained in laser tubes. For the present experiments, maximum output represents the correct operating point, and a B-10 layer of 0.6 mg/$cm^2$ will be used.

4. Measurements of the amount of energy absorbed by the gas correlated well with the calculated values for $CO_2$ and $N_2$. An error was located in the original helium calculation which subsequently agreed well with the measured value. Reliable calculations of heavy ion energy deposition in gases can now be made.

## Reference

1. J. A. DeShong, Jr., *A Carbon Dioxide System for Direct Conversion of Nuclear Energy to Coherent Laser Light*, Reactor Physics Division Annual Report, July 1, 1965 to June 30, 1966, ANL-7210, pp. 420–422.

# VII-2. Analysis of Plasma Ion Frequency in Low Pressure Alkali Metal Vapor Thermionic Conversion Cells

H. K. Richards

## Nomenclature

$a \equiv$ emitter-collector distance
$E \equiv$ potential gradient, V/cm
$J \equiv$ current density
$j \equiv \sqrt{-1}$
$K \equiv$ Boltzmann's constant
$m \equiv$ particle mass
$n \equiv$ variable particle density
$n_0 \equiv$ average particle density
$T \equiv$ temperature, °K
$u \equiv$ average velocity of particle
$v \equiv$ variable velocity
$V \equiv$ variable voltage
$V_0 \equiv$ dc output voltage of the cell
$T_e \equiv$ emitter temperature
$x \equiv$ direction from emitter to collector
$\lambda \equiv$ wavelength
$2\pi/\lambda = \beta \equiv$ propagation constant
$\epsilon \equiv$ electronic charge
$\omega_i^2 \equiv 4\pi\epsilon^2 n_{i0}/m_i$
$\omega_e^2 \equiv 4\pi\epsilon^2 n_{e0}/m_e$
$\Phi_e \equiv$ emitter work function
$\Phi_c \equiv$ collector work function
$\psi_0 \equiv$ sheath potential (positive)
$m.f.p. \equiv$ mean free path
$IM \equiv$ imaginary
$PM \equiv$ potential minimum
$\omega_i/\omega_e = \sqrt{\mu} \equiv m_e/m_i$
$\omega \equiv$ frequency, rad/sec
$\omega_r \equiv$ real part of $\omega$
$j\alpha \equiv IM$ part of $\omega$

subscripts:

$e$ refers to electrons
$i$ refers to ions
$a$ refers to atoms

The theory of self-excited ion plasma oscillations in a low pressure thermionic converter was treated in Ref. 1. Electrons and ions move between emitter and collector: electrons remain at the collector after reaching it, while the ions are discharged and return as neutral atoms. It was shown[1] that for this case, the electrons feed energy into the system under certain conditions, exciting oscillations. Following the assumption of L. Tonks and I. Langmuir,[2] it was assumed that the electron beam follows the potential variations instantaneously due to their negligible mass compared with that of ions. The expression for the ion plasma oscillations under these conditions was found to be

$$\omega = \beta u_i \pm j\sqrt{\mu}\,\beta u_e\left[1 - \frac{\beta^2\omega_e^2}{\omega_e^2}\right]^{-1/2} = \omega_{ri} + j\alpha_i \quad (1)$$

where $\beta u_i$ is the real part of $\omega$, while the imaginary portion $j\alpha$ represents oscillations, provided $\omega_e^2 > \beta^2 u_e^2$. For $\omega_e^2 = \beta^2 u_0^2$, this expression is no longer valid and has to be replaced by a better approximation. Equation (1) agrees quite well with most experimental results.[3,4] However, the observation that the plasma frequencies always increase with an increasing positive voltage of the collector (Fig. VII-2-1) does not follow from Eq. (1) and requires a more detailed theoretical treatment which will now be presented.

From the Boltzmann equation, the space charge equation, and the continuity equation, the following expression was derived by J. Pierce and K. Hernquist:[5,6,7]

$$1 = \frac{\omega_i^2}{(\omega - \beta u_i)^2} + \frac{\omega_e^2}{(\omega - \beta u_e)^2}; \quad (2)$$

expanded, this equation may be written as

$$\begin{aligned}\omega^4 &- 2\omega^3\beta(u_e + u_i) \\ &- \omega^2[\omega_e^2 - \beta^2 u_e^2 + \omega_i^2 - \beta^2 u_i^2 - 4\beta^2 u_e u_i] \\ &+ 2\omega\beta[u_i(\omega_e - \beta^2 u_e^2) + u_e(\omega_i^2 - \beta^2 u_i^2)] \\ &- \beta^2[u_i^2(\omega_e^2 - \beta^2 u_e^2) + \omega_i^2 u_e^2] = 0.\end{aligned} \quad (3)$$

The ratios $\omega_i^2/\omega_e^2 = m_e/m_i = \mu = 2392 \times 10^{-3}$ for sodium and are even less for cesium and potassium. Also, $(u_i/u_e)^2 \leq \mu$. Therefore $\omega_i^2 - \beta^2 u_i^2$ will be omitted in the third and fourth term and $u_i$ will be omitted in the second term. Setting $\omega_i^2 = \mu\omega_e^2$, Eq. (3) can be reduced to

$$\begin{aligned}\omega^4 &- 2\omega^3\beta v_e - \omega^2(\omega_e^2 - \beta^2 u_e^2 - 4\beta^2 u_e u_i) \\ &+ 2\omega\beta u_i(\omega_e^2 - \beta^2 u_e^2) \\ &- \beta^2[u_i^2(\omega_e^2 - \beta^2 u_e^2) + \mu\omega_e^2 u_e^2].\end{aligned} \quad (4)$$

Equation (4) has four solutions. Two of the solutions refer to large values of $\omega$, and all terms containing products with $\mu\omega_e^2$ and $u_i^2$ and $u_i$ may be neglected. These two solutions are given approximately by $\omega^2 = 2\beta u_e + \omega_e^2 - \beta^2 u_e^2$ and $\omega = \beta u_e \pm \omega_e$. These are electron

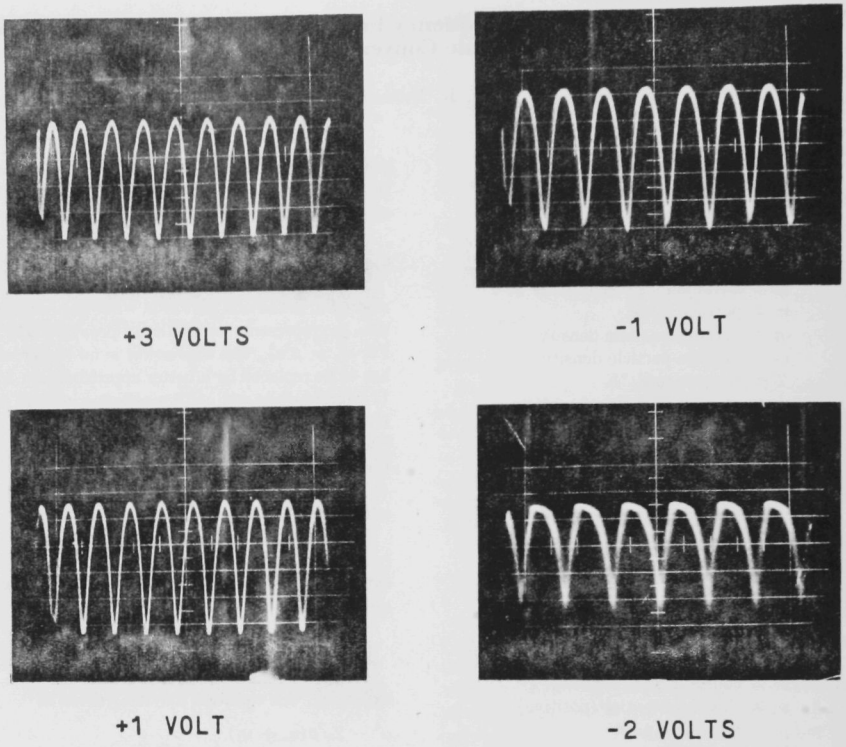


FIG. VII-2-1. Cesium Plasma Oscillations as a Function of Applied Collector Voltage. Vertical Scale, Volts/division; Horizontal Scale, μsec/division. *ANL Neg. No. 112-1635*

oscillations and will not be considered further in this report. The other solutions refer to $\omega \ll \beta u_e$ and are ion plasma oscillations. Here the term $\omega^4$ may be neglected. Hence $2\omega^3\beta u_e$ (the second term) and $4\beta^2 u_e u_i \omega^2$ of the third term will be treated as perturbations. Without these perturbation terms the result is identical with Eq. (1), viz:

$$\omega_1 = \beta u_i \pm j\sqrt{\mu}\,\beta u_e\left[1 - \frac{\beta^2 u_e^2}{\omega_e^2}\right]^{1/2} = \omega_{r1} + j\alpha,$$

where

$$\omega_1^2 = \omega_{1r}^2 - \alpha_1^2 + 2j\alpha_1\omega_{1r}\,.$$

Substituting $\omega_1 + \Delta\omega$ for $\omega$, it follows that for $\Delta\omega = \Delta\omega_r + j\Delta\alpha$,

$$\Delta\omega = -\frac{\omega_1^2\beta u_e}{\omega_e^2 - \beta^2 u_e^2}\left[1 - \frac{\beta u_i}{\omega_1 - \beta u_i}\right] = -\frac{\omega_1^2\beta u_e}{\omega_e^2 - \beta^2 u_e^2}\left[1 \pm \frac{j\beta u_i}{\alpha_1}\right]. \tag{5}$$

Introducing the values for $\omega_1$ and $\omega_1^2$, Eq. (5) becomes

$$\Delta\omega = \frac{\beta u_e}{\omega_e^2 - \beta^2 u_e^2}\left[(\alpha_1^2 + \omega_{1r}^2) \pm j(\alpha_1\omega_{1r} + \omega_{1r}^3\alpha)\right] = \Delta\omega_r + j\Delta\alpha. \tag{6}$$

Thus, from Eqs. (5) and (6)

$$\Delta\omega_r = \frac{\beta^3 u_1^2 u_e}{\omega_e^2 - \beta^2 u_e^2} + \frac{\mu\omega_e^2\beta^3 u_e^3}{(\omega_e^2 - \beta^2 u_e^2)^2} \tag{7a}$$

and

$$\omega_r = \omega_{r1} + \Delta\omega = \beta u_i\left[1 + \frac{\beta^2 u_i u_e}{\omega_e^2 - \beta^2 u_e^2}\right] + \frac{\mu\omega_e^2\beta^3 u_e^3}{(\omega_e^2 - \beta^2 u_e^2)^2} \tag{7b}$$

for $\omega_e^2 > \beta^2 u_e^2$.

Equations (7a) and (7b) show that the observed frequency, $\omega_r/2\pi$, is a function of $u_e$. As mentioned before,

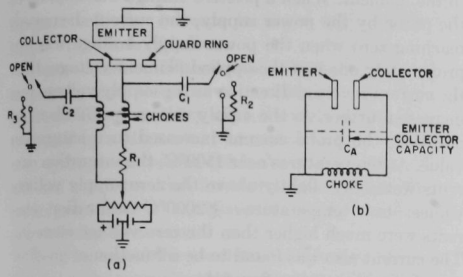


FIG. VII-2-2. (a) DC and RF Thermionic Energy Conversion Cell Schematic. (b) RF Equivalent Open Circuit. *ANL Neg. No. 112-8584 Rev. 1.*

if the collector potential becomes more positive, the rf frequency increases for all alkali metal vapor cells.

Assume now (Fig. VII-2-2a) that $\Phi_e = \Phi_c + V_0$, that is, that there is no voltage difference between the electrodes. Hence, the cell operates at the knee of the characteristic, and all electrons and ions can arrive at the collector, where the ions become neutral atoms. The rf section is open, (Fig. VII-2-2a and VII-2-2b). A positive sheath potential $\psi_0$ will exist in an ion rich plasma[8] while the plasma remains essentially neutral.

If the collector potential is increased (Fig. VII-2-2a), the electrons can still reach the collector, but more and more ions will be reflected. In order to maintain neutrality of the plasma, fewer ions can be permitted to enter from the emitter through the emitter sheath. This will be accomplished by a self-adjusted increase of the sheath potential $\psi_0$. Since the velocity of the electrons inside the plasma is given approximately by

$$u_e = \sqrt{\bar{u}_{e0}^2 + \frac{2e\psi}{m_e}},$$

where

$$\bar{u}_{e0}^2 = \sqrt{\frac{KT_e}{m_e}},$$

it is seen that $u_e$ increases with the applied collector voltage. From Eqs. (7a) and (7b) it follows immediately that this increase of the dc voltage increases the frequency of the plasma oscillations.

### REFERENCES


1. H. K. Richards, *Theory of Plasma Oscillations, Generation of Thermionic RF Energy and Interaction with DC*, Reactor Physics Division Annual Report, July 1, 1965 to June 30, 1966, ANL-7210, pp. 422-424.
2. L. Tonks and I. Langmuir, *Oscillations in Ionized Gases*, Phys. Rev. 33, 195 (1929).
3. H. K. Richards, *Thermionic Energy Conversion with a Plasma Thermocouple*, Reactor Physics Division Annual Report, July 1, 1964 to June 30, 1965, ANL-7110, pp. 372-378.
4. H. K. Richards, *DC and High Frequency Voltage and Power Output and Interaction in Cesium, Potassium and Sodium Thermionic Converters*, TID-7687, pp. 165-179, Appendix I, (February 1964).
5. J. R. Pierce, *Possible Fluctuations in Electron Streams*, J. Appl. Phys. **19**, 231 (1948).
6. J. R. Pierce, *Increasing Space Charge Waves*, J. Appl. Phys. **20**, 1060 (1949).
7. K. J. Hernquist, *Plasma Oscillations in Electron Beams*, J. Appl. Phys. **26**, 544 (1965).
8. P. Auer, *Potential Distribution in a Low Pressure Thermionic Converter*, J. Appl. Phys. **31**, 2096 (1960).


## VII-3. Experimental Investigation of Electrical Conduction Through Noble Gases at High Temperatures

H. K. RICHARDS

Electrical conduction through noble gases was observed during a series of experiments performed to measure physical properties of uranium carbide at high temperatures (see Paper VI-23). The measurements were made in a modified high temperature furnace[1] at filament temperatures between 1500 and 2400°C. The experimental setup is shown in Fig. VII-3-1. The tungsten filament is a cylinder of 7.5 cm diam. The filament was run with the upper, water-cooled, copper electrode positive and the lower, water-cooled, copper electrode at electrical ground. Surrounding the filament is a tungsten reflector. A tungsten cylindrical probe was attached to a tungsten rod passing through an insulator in the upper electrode. Temperature of the probe was measured by an optical pyrometer sighted through openings in the reflector and the filament. Helium or argon gas, slightly above atmospheric pressure, was passed through the furnace using an adjustable-flow cover gas system. The probe rod was connected, as shown in Fig. VII-3-1, to a power supply capable of variable voltage output ranging from 0 to ±30 V.

With the power supply short-circuited, the heater filament was positive relative to the probe. When the filament temperature was raised to 1500°C, a positive

current of several $\mu A$ was measured flowing from the probe to ground. Potential of the probe was measured by a voltmeter and found to be one-half of the applied (positive) filament voltage. This condition is equivalent to an electron current emitted by the probe and flowing to the filament. When a positive voltage was applied to the probe by the power supply, the current decreased, reaching zero when the power supply voltage was approximately one-half the applied filament voltage; then the current reversed direction as the supply voltage was increased further. As the supply voltage was made more negative, the probe current increased to a saturation value. At temperatures near 1500°C, the saturation currents were only slightly above the zero supply voltage values, but temperatures $\gtrsim$2000°C saturation currents were much higher than the zero voltage currents. The current also was found to be a function of gas flow rate, increasing at low flow rates.

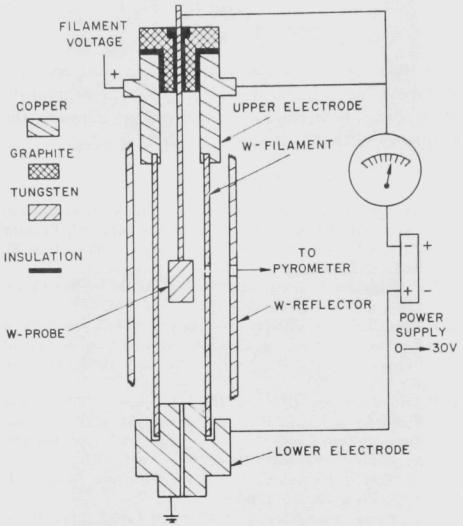


FIG. VII-3-1. Measurement of Electron Currents Through Noble Gases at 1 atm Pressure. *ANL Neg. No. 112-8586.*

Considerable differences in probe currents were observed between helium and argon. Table VII-3-I lists results for both gases, over a 900°C temperature range, obtained with supply voltages of 0 and −10 V. Measurements were taken at low gas flows. The columns marked "Supply" designate the applied supply voltages. The effective probe potentials were approximately 5–8 volts more positive, because of the effect of the filament. The $I_s$ are the saturation electron emission currents calculated for a 32.3 cm² tungsten surface in vacuum at the indicated temperatures. These values are probably different from the emission in gases, due to changes in the surface work function. Large differences are not expected. The measured currents are listed in the fourth and eighth columns. It is seen that for both helium and argon the currents increase rapidly as the temperature increases. At lower temperatures, the currents in helium are slightly higher than those in argon while at high

TABLE VII-3-I. MEASUREMENTS OF ELECTRICAL CURRENT BETWEEN PROBE AND FILAMENT THROUGH HELIUM AND ARGON[a]

| Gas: He | | | | Gas: A | | | |
|---|---|---|---|---|---|---|---|
| Supply, V | $T$, °C | $I_s$ Calculated, mA | $I$ Measured, mA | Supply, V | $T$, °C | $I_s$ Calculated, mA | $I$ Measured, mA |
| 0 | 1450 | 0.3 | 0.13 | | | | |
| 0 | 1550 | 1.94 | 0.44 | | | | |
| −10 | 1550 | 1.94 | 1.30 | | | | |
| 0 | 1575 | 3.10 | 1.40 | 0 | 1575 | 3.10 | 0.65 |
| −10 | 1575 | 3.10 | 4.00 | −10 | 1575 | 3.10 | 1.10 |
| 0 | 1790 | 69.00 | 6.20 | | | | |
| −10 | 1790 | 69.00 | 12.00 | 0 | 1810 | 97.00 | 55.00 |
| 0 | 1830 | 130.00 | 28.00 | −10 | 1810 | 97.00 | 130.00 |
| −10 | 1830 | 130.00 | 52.00 | | | | |
| 0 | 2090 | 2480.00 | 38.00 | 0 | 2110 | 3070.00 | 800.00 |
| −10 | 2090 | 2480.00 | 80.00 | −10 | 2110 | 3070.00 | 1400.00 |
| 0 | 2350 | 27,800.00 | 1300.00 | 0 | 2330 | 24,300.00 | 6000.00 |
| −10 | 2350 | 27,800.00 | 1900.00 | −10 | 2330 | 24,300.00 | 13,000.00 |

[a] Tungsten cylindrical probe area = 32.3 cm²; length = 5.4 cm; annulus between probe and filament = 2.857 cm.

temperatures the currents in argon are considerably larger than those in helium.

This conduction in a gas at 1 atm pressure was quite surprising, and therefore the nature of the effect was studied. The possibility that the conduction may be produced by a plasma may be excluded, since the ionization voltages of helium (24.5 eV) and of argon (15.68 eV) are much too high for thermal-ionization. Because noble gases have no electron attachment, negative ions are excluded as a cause.

There remained the possibility of direct electron emission from the tungsten of the cylinder and the filament. The following experiment investigated this possibility. A tungsten rod without the cylinder was inserted, but only down to the end of the upper, water-cooled electrode. The rod was again negative with respect to the filament. The temperature of the filament was about 2000°C or more. Then the rod was suddenly pushed down into the hot section. No current was observed immediately, but after some time a small current was observed and it increased slowly to saturation value. Electrons could flow only from the tungsten rod to the filament because of the applied voltage. As long as the rod was still cool, no electron emission took place; but emission did start when the rod was heated by conduction and radiation from the filament. This indicates that thermionic electron emission produces the current.

In another experiment the positive voltage was first applied to the tungsten probe. A current was now observed to flow in the opposite direction, although essentially no electron could leave the probe. When the voltage was reversed, a few seconds passed before the current reached its maximum. It appears that, unlike electron flow in a vacuum, it takes a certain time for the electrons to drift from the negative to the positive electrode through the gas.

Thus it is concluded that the thermionic electron emission from tungsten accounts for the observed conductivity. However, while in vacuum a potential minimum results; this can be eliminated only by a sufficiently high potential. The movement of the helium or argon atoms may dissipate the space charge to a large degree. While the electrons are now scattered in all directions by the atoms, there remains an average drift to the other electrode due to the applied voltage. However, the electrons drift slowly, with an observed drift time of several seconds. The electrons remain free, since noble gases have no electron attachment. It should be added that an identical effect was observed when a graphite rod was employed as the emitter electrode.

This explanation of the conduction in a gas at 1 atm pressure is only a tentative one, subject to replacement by a better theory after further investigation.

### Reference

1. H. K. Richards and E. Maslowicz, *Modification of the High Temperature Tungsten Filament Furnace*, Reactor Physics Division Annual Report, July 1, 1965 to June 30, 1966, ANL-7210, pp. 289–290.

## VII-4. Radiocarbon Production Rate Near Sea Level*

R. Gold

The natural production of radiocarbon by cosmic-ray neutrons has been experimentally observed. Proportional counters, filled with two atmospheres of nitrogen, have been employed to detect the exoergic $N^{14}(n,p)C^{14}$ reaction. A preliminary account of this work has already been given[1] and more detailed results have been submitted for publication.[2] Electronic pulse-shape discrimination is utilized to discriminate against meson- and photon-induced events. A C-14 production rate of $(1.89 \pm 0.08) \times 10^{-7}$ per sec per cm³ has been obtained for the air-land interface at the Argonne National Laboratory site. This result represents the average value for a time duration of one month, November–December 1966. The experimental results are displayed in Fig. VII-4-1. Fluctuations as large as 25 % from this average value were observed. The density of slow neutrons can also be determined from this experimental result. An average value of $(1.19 \pm 0.06) \times 10^{-8}$ neutrons per cm³ was found for the air-land interface at the Argonne National Laboratory site (53° N geomagnetic latitude).

* This work has been supported, in part, by the Radiological Physics Division, Argonne National Laboratory.

### References

1. R. Gold, *$C^{14}$ Production Rate Near Sea-Level*, Bull. Am. Phys. Soc. **12**, 591 (1967).
2. R. Gold, *Radiocarbon Production Rate Near Sea Level*, Phys. Rev. (To be published).

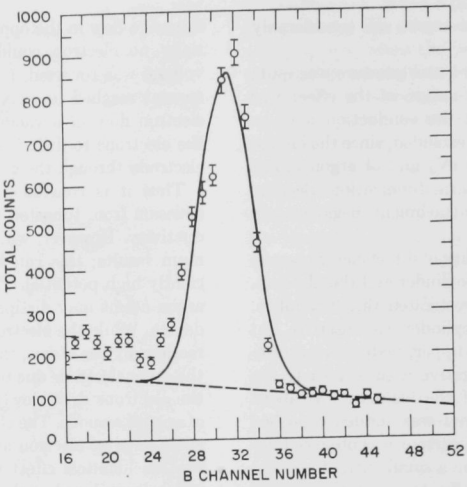


FIG. VII-4-1. The Experimental Pulse Height Distribution Due to the $N^{14}(n,p)C^{14}$ Reaction Obtained from Mid-November to Mid-December 1966 at the Argonne site. The Smooth Curve is a Gaussian Fit to the Experimental Data Above the Background Continuum (dashed curve). *ANL Neg. No. 112-7987*).

## VII-5. Energy Spectrum of Fast Cosmic Ray Neutrons Near Sea Level*

R. GOLD

Measurement of the sea level spectrum of cosmic ray neutrons in the energy region 0.05–2.0 MeV has been carried out with $4\pi$ hydrogen-recoil proportional counters. A preliminary account of this work has already been given[1] and more detailed results have been submitted for publication.[2] Electronic pulse-shape discrimination has been utilized to reject meson- and photon-induced events. Figure VII-5-1 presents the results of a series of measurements carried out from June to November 1966. In general, the flux per unit energy decreases monotonically. The experimental data reveals some structure which may be due to scattering resonances in elements that dominate the environment. An integral flux of $2.3 \times 10^{-3}$ neutrons/cm$^2$-sec in the interval 0.05–2.0 MeV has been obtained for the air-land interface at the Argonne National Laboratory site (53° N geomagnetic latitude).

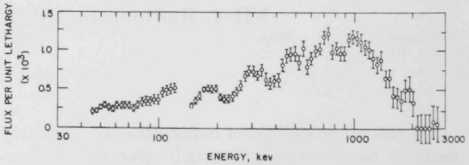


FIG. VII-5-1. Cosmic-Ray Neutron Flux per Unit Lethargy in the Energy Region 0.05–2.0 MeV. *ANL Neg. No. 112-8003.*

* This work has been supported, in part, by the Radiological Physics Division, Argonne National Laboratory.

### REFERENCES

1. R. Gold and E. F. Bennett, *Energy Spectrum of Fast Cosmic-Ray Neutrons Near Sea Level*, Reactor Physics Division Annual Report, July 1, 1965–June 30, 1966, ANL-7210, p. 419.
2. R. Gold, *Energy Spectrum for Fast Cosmic-Ray Neutrons Near Sea Level*, Phys. Rev. (To be published).

# Section VIII

# Publications

July 1, 1966 to June 30, 1967

*Open Literature*


Adkins, C. R., Persiani, P. J., Hwang, R. N. and Kaganove, J. J., *The Chemical Binding Effects on the Resonance Line Shapes of Uranium-238 in a $UO_2$ Lattice*, Conference on Neutron Cross Section Technology, Washington, D. C., March 22–24, 1966. USAEC Report CONF-660303, Book 1, pp. 134–145.

Armani, R. J., *Absolute Determination of Fission Rates in $U^{235}$ and $U^{238}$ and Capture Rates in $U^{238}$ by Radiochemical Techniques*, IAEA Symposium on Standardization of Radionuclides, Vienna, October 10–14, 1966. Intern. Atomic Energy Agency, Vienna, 1967, p. 613.

Armani, R. J., and Gold, R., *Spontaneous Fission Half-Lives of $Cm^{242}$ and $Cm^{244}$ by Absolute Alpha and Neutron Counting*, IAEA Symposium on Standardization of Radionuclides, Vienna, October 10–14, 1966. Intern. Atomic Energy Agency, Vienna, 1967, p. 621.

Bennett, E. F., *A Modified Cascode Preamplifier for Proportional Counters*, Nucl. Instr. Methods **48**(2), 170 (1967).

Bennett, E. F., *Fast Neutron Spectroscopy by Proton-Recoil Proportional Counting*, Nucl. Sci. Eng., **27**, 16–27 (1967).

Bennett, E. F., *Neutron Spectrum Measurement in a Fast Critical Assembly*, Nucl. Sci. Eng. **27**, 28–33 (1967).

Bryant, L. T., Amiot, L. W., Dickerman, C. E., and Stephany, W. P., *Transient Temperature Calculations Using a Hybrid Computer*, Resume of Articles Presented at Intern. Conference on the Utilization of Research Reactors and Reactor Mathematics and Computation, Sponsored by the Comision Nacional de Energia Nuclear de Mexico, Mexico City, May 2–4, 1967, p. 60.

Buccino, S. G., Gemmell, D. S., Lee, L. L., Schiffer, J. P., and Smith, A. B., *The (d,n) Reaction on $Mg^{24}$ and $Si^{28}$*, Nucl. Phys. **86**(2), 353–362 (October 1966).

Chien, J. P., *Fast Neutron Scattering from Be, Na, and Al*, Nucl. Sci. Eng. **26**, 500 (1966).

Cody, W. J. and Thacher, H. C., *Rational Chebyshev Approximations for Fermi-Dirac Integrals of Orders -1/2, 1/2, and 3/2*, Math. Computation **21**, 30–40 (January 1967).

Cohn, C. E., *A Diagnostic Technique for Input/Output Equipment*, Computer Design **6**, 44–46 (May 1967).

Cohn, C. E., *Two Advances in Reactor Neutron-Noise Analysis*, Power Reactor Technol. **9**(3), 142–144 (Summer 1966).

Cohn, C. E., Johnson, R. J., and MacDonald, R. N., *Calculating Space-Dependent Reactor Transfer Functions Using Static Techniques*, Nucl. Sci. Eng. **26**, 198–206 (October 1966).

Cox, S. A., *Measurement of the $Li^6$ and $B^{10}$ Neutron Absorption Cross Sections by the Shell Transmission Method*, Conference on Neutron Cross Section Technology, Washington, D. C., March 22–24, 1966. USAEC Report CONF-660303, Book 2, 701–712. (September 1966).

Cox, S. A., and Pontet, F. R., *Measurement of the $Li^6$ (n, absorption) and $B^{10}$ (n, absorption) Cross Sections by the Shell Transmission Method*, J. Nucl. Energy **21**, 271–283 (March 1967).

Devolpi, A., *High-Speed, Multichannel Data Recording for Nuclear Physics Experiments Using Fast-Framing Cameras*, Kurzzeitphotographie, Proc. 7th Intern. Congr. on High-Speed Photography, Zurich, September 12–18, 1965, ed. O. Helwich. Verlag Dr. Othmar Helwich, Darmstadt, West Germany, 1967, pp. 516–521.

Devolpi, A., Armani, R. J., and Porges, K. G., *Extension of the Range of Determination of Manganese Sulphate Content for Neutron Source Measurements*, J. Nucl. Energy **21**, 521 (June 1967) Letter.

Devolpi, A., English, J. J., Metz, A. J., Porges, K. G., and Rudnick, S. J., *Versatile Gated Discriminator with Adjustable Paralysis Useful in Fast-Slow Coincidence Experiments*, Rev. Sci. Instr. **37**, 1592–1600 (November 1966).

Devolpi, A., Porges, K. G., and Armani, R. J., *Absolute Calibrations of Fission Neutron Source Strength Relying upon an Improved Manganese Bath Technique and Absolute Beta-Gamma Coincidence Counting*, IAEA Symp. on Standardization of Radionuclides, Vienna, October 10–14, 1966. Intern. Atomic Energy Agency, Vienna, 1967, p. 717.

Dickerman, C. E., *Experiments and Analyses in Fast Reactor Safety*, Nucl. Safety **8**(3), 220–226 (Spring 1967).

Dickerman, C. E., *Fast Reactor Meltdown Program*, Nucl. Safety **7**(4), 424–434 (Summer 1966).

Dickerman, C. E., Robinson, L. E., Blumenthal, B., and Steward, R. R., *Behavior of Th-20 wt% U Fast-Reactor Fuel under Transient Heating to Failure*, Nucl. App. **3**, 9–17 (January 1967).

Dutton, J. J., Lennox, D. H., Brown, K. K., Croke, E. J., Gold, R., and Schmeh, B. A., Eds., *Power Reactor Technology*, Division of Technical Information, U. S. Atomic Energy Commission, Vol. *9(2)* (Spring 1966).

Dutton, J. J., Lennox, D. H., Brown, K. K., Croke, E. J., Gold, R., and Schmeh, B. A., Eds., *Power Reactor Technology*, Division of Technical Information, U. S. Atomic Energy Commission, Vol. **9**(3) (Summer 1966).

Dutton, J. J., Lennox, D. H., Brown, K. K., Croke, E. J., Gold, R., and Schmeh, B. A., Eds., *Power Reactor Technology*, Division of Technical Information, U. S. Atomic Energy Commission, Vol. **9**(4) (Fall 1966).

Fischer, G. J., Travelli, A., and Meneley, D. A., *Zone-Loaded Critical Experiments for Fast Breeders*, Power Reactor Technol. **9**, 162–168 (Fall 1966).

Gast, P. F., *A New Approach to Calculation of Flux Distributions in a Reactor Based Upon a Few Measured Values*, Resumé of Papers Presented at Intern. Conference on the

Utilization of Research Reactors and Reactor Mathematics and Computation, Sponsored by the Comision Nacional de Energia Nuclear de Mexico, Mexico City, May 2–4, 1967, p. 157.

Gast, P. F., and Link, L. E., *Fast Breeder Reactors*, Water Production Using Nuclear Energy, ed. R. G. Post and R. L. Seale. University of Arizona Press, Tucson, 1966, pp. 273–293.

Gold, R. and Bennett, E. F., *Electron Multiplication Process in Proportional Counters*, Phys. Rev. **147**, 201–213 (July 8, 1966).

Helm, F. H., *Activation of Gold Spheres and Foils in Nonisotropic Neutron Incidence*, Nucl. Appl. **2**, 325–334 (August 1966).

Hummel, H. H., *Sensitivity of Fast Reactor Parameters to Cross Section Uncertainties*, Conference on Neutron Cross Section Technology, Washington, D. C., March 22–24, 1966. USAEC Report CONF-660303, Book 2, pp. 809–820.

Jain, K. C., Petrick, M., Miller, D., and Bankoff, S. G., *Self-Sustained Hydrodynamic Oscillators in a Natural-Circulation Boiling Water Loop*, Nucl. Eng. Design **4**(3), 233–252 (October 1966).

Kato, W. Y., *Management of Low Power Research Reactors*, Resumé of Papers Presented at Intern. Conference on the Utilization of Research Reactors and Reactor Mathematics and Computation, Sponsored by the Comision Nacional de Energia Nuclear de Mexico, Mexico City, May, 2–4, 1967, p. 193.

Kelber, C. N., Jensen, G. C., Just, L. C., and Toppel, B. J., *The Argonne Reactor Computation System, ARC*, Resumé of Papers Presented at Intern. Conference on the Utilization of Research Reactors and Reactor Mathematics and Computation, Sponsored by the Comision Nacional de Energia Nuclear de Mexico, Mexico City, May 2–4, 1967, p. 160.

Kelber, C. N. and Kier, P. H., *The Effect of Randomness on Group Cross Sections. II.*, Nucl. Sci. Eng. **26**, 67–72 (September 1966).

Kier, P. H., *A Method of Computing Resonance Integrals in Multiregion Reactor Cells*, Resumé of Papers Presented at Intern. Conference on the Utilization of Research Reactors and Reactor Mathematics and Computation, Sponsored by the Comision Nacional de Energia Nuclear de Mexico, Mexico City, May 2–4, 1967, p. 173.

MacFarlane, D. R. and Brittan, R. O., *Transient Sodium Boiling Calculations*, Nucl. Eng. Design **4**(4), 360–374 (1966).

Marciniak, T. J., *Comments on "Stability Analysis of a Sampled-Data Controlled Nuclear Reactor System"*, Nucl. Sci. Eng. **28**, 315–316 (May 1967) Letter.

Martens, F. H., *Design Foresight Can Simplify Reactor Modifications*, Power Reactor Technol. **9**(2) (Spring 1966).

Martens, F. H., *Use of Research Reactors at Argonne National Laboratory*, Resumé of Papers Presented at Intern. Conference on the Utilization of Research Reactors and Reactor Mathematics and Computation, Sponsored by the Comision Nacional de Energia Nuclear de Mexico, Mexico City, May 2–4, 1967, p. 131.

Meadows, J. W., *$Cf^{252}$ Fission Neutron Spectrum from 0.003 to 15.0 MeV*, Phys. Rev. **157**, 1076–1082 (May 20, 1967).

Meadows, J. W. and Whalen, J. F., *Energy Dependence of $\bar{\nu}_p$ for Neutron-Induced Fission of $U^{235}$ below 1.0 MeV*, J. Nucl. Energy **21**, 157–170 (February 1967).

Meneghetti, D., Rago, A. L., and Phillips, K. E., *Use of the ELMOE-SNARG Programs to Study Details of Neutron Spectra through Regions of Resonance-Scattering Media*, Resumé of Articles Presented at Intern. Conference on the Utilization of Research Reactors and Reactor Mathematics and Computation, Sponsored by the Comision Nacional de Energia Nuclear de Mexico, Mexico City, May 2–4, 1967, p. 177.

Meneley, D. A., Leaf, G. K., Walker, P. M., and Kyong, S. H., *A Generalized Formulation for Reactor Fuel Cycle Studies*, Resumé of Papers Presented at Intern. Conference on the Utilization of Research Reactors and Reactor Mathematics and Computation, Sponsored by the Comision Nacional de Energia Nuclear de Mexico, Mexico City, May 2–4, 1967, p. 148.

Miller, D., *Atoms in Asia*, Nucl. News **10**, 21 (May 1967).

Miller, L. B., Miley, G. H., and Gast, P. F., *An Optimized Dual Perturbation Technique*, Resumé of Papers Presented at Intern. Conference on the Utilization of Research Reactors and Reactor Mathematics and Computation, Sponsored by the Comision Nacional de Energia Nuclear de Mexico, Mexico City, May 2–4, 1967, p. 126.

Moldauer, P. A., *Effects of $(n,\gamma n)$ Processes on Fast Neutron Capture and Inelastic Spectra*, Conference on Neutron Cross Section Technology, Washington, D. C., March 22–24, 1966. USAEC Report CONF-660303, Book 2, pp. 613–622.

Moldauer, P. A., *Statistical Theory of Intermediate Resonances*, Phys. Rev. Letters **18**, 249–252. (February 13, 1967).

Ott, K. and Madell, J. T., *Quasistatic Treatment of Spatial Phenomena in Reactor Dynamics*, Nucl. Sci. Eng. **26**, 563–565 (December 1966) Note.

Pennington, E. M., *Water-Reactor Lattice Calculations and Measurements*, Power Reactor Technol. **9**(3), 145–149 (Summer 1966).

Persiani, P. J., Smith, R. R., and Okrent, D., *Physics Measurements in an Operating Fast Breeder Power Reactor*, Proc. Intern. Seminar on Physics Measurements in Operating Power Reactors, Rome, May 9–13, 1966. ENEA Report (March 1967), pp. 73–107.

Porges, K. G., *Passive Adapter Circuit Drives Decade Scaler*, Electronic Design **14**(21), 92 (September 13, 1966).

Porges, K. G. and Devolpi, A., *Absolute Determination of Fission Fragment Emission Rates with a Prompt Neutron-Fission Coincidence Method*, IAEA Symposium on Standardization of Radionuclides, Vienna, October 10–14, 1966. Intern. Atomic Energy Agency, Vienna, 1967, p. 693.

Redman, W. C., *Absolute Measurement of Fission, Activation and Neutron Emission Rates*, Proc. Conference on Radiation Measurements in Nuclear Power, Berkeley Nuclear Laboratory, Gloucestershire, September 12–16, 1966. Institute of Physics, London, 1966, pp. 303–310.

Redman, W. C. and Bretscher, M. M., *Direct Determination of Uranium-235 Capture-to-Fission Ratio in a Zero-Power Reactor*, Nucl. Sci. Eng. **27**, 34–44 (1967).

Redman, W. C. and Bretscher, M. M., *Low Flux Determination of Capture-to-Fission Ratio*, Conference on Neutron Cross Section Technology, Washington, D. C., March 22–24, 1966. USAEC Report CONF-660303, Book 2, pp. 1092–1097.

Redman, W. C. and Robinson, L. E., *TREAT Experiments to Provide Data for Fast Reactor Safety Kinetics Calculations*, Neutron Dynamics and Control, Proc. Symposium on Nuclear Engineering, University of Arizona, Tucson, April 5–7, 1965. USAEC Report CONF-650413 (1966), pp. 371–385.

Reinke, C. F., Robinson, L. E., and Ivins, R. O., *High tempera-*

*ture Thermometry—Service and Related Experience*, Proc. High Temperature Thermometry Seminar, Washington, D. C., February 24–26, 1965. USAEC Report WASH-1067 (March 1966), pp. 22.1–22.2.

Sanathanan, C. K., *On the Synthesis of Space Dependent Transfer Functions*, IEEE Trans. **AC-11**(4), 724–729 (October 1966).

Sanathanan, C. K., Carter, J. C., Bryant, L. T., and Amiot, L. W., *The Application of a Hybrid Computer to the Analysis of Transient Phenomena in a Fast Reactor Core*, Nucl. Sci. Eng. **28**, 82–92 (April 1967).

Sanathanan, C. K., Carter, J. C., Bryant, L. T., and Amiot, L. W., *Hybrid Computers in the Analysis of Feed-Back Control Systems*, Proc. Fall Joint Computer Conf. **29**, 743–757 (November 1966).

Sargis, D. A. and Grossman, L. M., *Analytic Error Estimates for Integral-Equation Eigenvalue Problems in Neutron Physics*, Nucl. Sci. Eng. **25**, 395–406 (August 1966).

Sargis, D. A., Toppel, B. J., and Rago, A. L., *Generation of Multigroup Cross Sections Using a Coupled MC²-THERMØS Code*, Resumé of Papers Presented at Intern. Conference on the Utilization of Research Reactors and Reactor Mathematics and Computation, Sponsored by the Comision Nacional de Energia Nuclear de Mexico, Mexico City, May 2–4, 1967, p. 162.

Smith, A. B., *Inelastic Scattering—A Compendium*, Conference on Neutron Cross Section Technology, Washington, D. C., March 22–24, 1966. USAEC Report CONF-660303, Book 2, pp. 577–598, (September 1966).

Smith, A. B. and Hayes, R. R., *Fast Neutron Scattering from Elemental Mo, Sn, Sb, and Te*, Nucl. Phys. **A93**(3), 609–630 (1967).

Smith, A. B., Guenther, P. T., Larsen, R. N., Nelson, C. H., Walker, P. L., and Whalen, J. F., *Multi-Angle Fast Neutron Time-of-Flight System*, Nucl. Instr. Methods **50**(2), 277–291 (1967).

Spinrad, B. I., *A Larger Scope for AEC Laboratories*, Science **155**, 150 (1967) Letter.

Spinrad, B. I., *Converting AEC to a TEC, "Technological Excellence Commission"*, Nucleonics **25**(6), 52–53 (June 1967).

Spinrad, B. I., *New Departures in High-Flux Research Reactors*, Power Reactor Technol. **9**, 153–161 (Fall 1966).

Spinrad, B. I. and Croke, E. J., *Nuclear Power and Oceanic-System Energy: Concepts and Applications*, Proc. AIAA-ONR Symposium on Deep Submergence Prop. and Marine Systems, U. S. Naval Ordinance Plant, Forest Park, Ill., Feb. 28-Mar. 1, 1966. Am Inst. Aeronautics and Astronautics, Chicago, 1966, pp. 265–296.

Stanford, G. S., *Activation Methods for Undermoderated Reactors*, Proc. Conference on Radiation Measurements in Nuclear Power, Berkeley Nuclear Laboratory, Gloucestershire, September 12-16, 1966. Institute of Physics, London, 1966, pp. 440–449.

Stanford, G. S., *Techniques for Processing Large Quantities of Foil Counting Data*, Proc. Conference on Radiation Measurements in Nuclear Power, Berkeley Nuclear Laboratory, Gloucestershire, September 12–16, 1966. Institute of Physics, London, 1966, pp. 376–382.

Thacher, H. C., Jr., *Independent Variable Transformations in Approximation*, Proc. Intern. Federation of Information Processing Congress 65, New York, May 1965, ed. W. A. Kalenich. (Spartan Books, Washington, D. C., 1966, Vol. 2) pp. 576–577.

Travelli, A., *The Complex Relaxation Length of Neutron Waves in Multigroup Transport Theory*, Neutron Noise, Waves, and Pulse Propagation, Proc. Symposium, University of Florida, Gainesville, February 14–16, 1966. USAEC Symposium. Ser. 9, CONF-660206 (May 1967), pp. 55–68.

Travelli, A., *The Complex Relaxation Length of Neutron Waves in Multigroup Transport Theory*, Trans. Symposium on Neutron Noise, Waves, and Pulse Propagation, University of Florida, February 14–16, 1966. University of Florida, Gainesville, 1966, pp. 7–10.

Youngdahl, C. K., *Three-Dimensional Stress Concentration around a Cylindrical Hole in a Semi-Infinite Elastic Body*, J. Appl. Mech. **33E**(4), 855–865 (December 1966)

*Reports*

Almenas, K. K., *Study of Reflector-Based Control of Fast Nuclear Rocket Reactors*, ANL-7099 (May 1966).

Armstrong, R. H. and Carter, J. C., *An Experimental Boiling-Liquid-Metal Fast Reactor*, ANL-7212 (June 1966).

Bennett, E. F., Gold, R., and Huber, R. J., *Spectrum Measurements in a Large Dilute Plutonium-Fueled Fast Reactor*, Proc. Intern. Conference on Fast Critical Experiments and Their Analysis, Argonne National Laboratory, October 10–13, 1966. ANL-7320, pp. 477–480.

Boynton, A. R., Baird, Q. L., Plumlee, K. E., Redman, W. C., Robinson, W. R., and Stanford, G. S., *High Conversion Critical Experiments*, ANL-7203 (January 1967).

Butler D. K., Doerner, R. C., and Knapp, W. G., *Measurements and Analysis of Al-, $Al_2O_3$-, and BeO-Reflected Fast Critical Experiments*, Proc. Intern. Conference on Fast Critical Experiments and Their Analysis, Argonne National Laboratory, October 10–13, 1966. ANL-7320, pp. 186–194.

Cody, W. J., and Thacher, H. C., *Rational Chebyshev Approximations for Fermi-Dirac Integrals of Orders −1/2, 1/2, and 3/2*, ANL-7200 (May 1966).

Cohn, C. E., *Electrical Service Provisions to Minimize Stray Fields*, Proc. AMU-ANL Workshop on High-Voltage Electron Microscopy, Argonne National Laboratory, June 13–July 15, 1966. ANL-7275, p. 185.

Cohn, C. E., *Magnetic-Tape Storage System for Scanned Images*, Proc. AMU-ANL Workshop on High-Voltage Electron Microscopy, Argonne National Laboratory, June 13–July 15, 1966. ANL-7275, p. 182.

Cohn, C. E., *Notes on a Survey of Digital and Related Techniques*, Proc. AMU-ANL Workshop on High-Voltage Electron Microscopy, Argonne National Laboratory, June 13–July 15, 1966. ANL-7275, p. 177.

Cohn, C. E., *Threshold Sensitivity of Television Camera Tubes*, Proc. AMU-ANL Workshop on High-Voltage Electron Microscopy, Argonne National Laboratory, June 13–July 15, 1966. ANL-7275, pp. 178–179.

Cohn, C. E. and Roberts, J. H., *A Computer Code for Calculating the Spreading of High Energy Electrons in Detector Materials*, Proc. AMU-ANL Workshop on High-Voltage Electron Microscopy, Argonne National Laboratory, June 13–July 15, 1966. ANL-7275, pp. 180–181.

Cohn, C. E. and Roberts, J. H., *Proposed Experiments to Study Detection of High Energy Electrons*, Proc. AMU-ANL Workshop on High-Voltage Electron Microscopy, Argonne National Laboratory, June 13–July 15, 1966. ANL-7275, p. 183.

Cox, S. A., *Status of Basic Nuclear Data Required for Fast Breeder Reactor Development*, Proc. Intern. Conference on Fast Critical Experiments and Their Analysis, Argonne

National Laboratory, October 10–13, 1966. ANL-7320, pp. 3–15.

Dates, L. R., *Design, Construction Details, and Preoperational Testing of an Argonne Fast Critical Facility*, ANL-7195 (April 1966).

Doerner, R. C., Knapp, W. G., Almenas, K. K., and Karam, R. A., *Physics Measurements in Tungsten-Based, Aluminum-Reflected Fast Reactors*, ANL-7007, (March 1967).

Fischer, G. J. and Travelli, A., *Studies of Analytical Problems in Interpretation of Zone-Loading Experiments and Basic Considerations in Zone-Loaded Core Design*, Proc. Intern. Conference on Fast Critical Experiments and Their Analysis, Argonne National Laboratory, October 10–13, 1966. ANL-7320, pp. 421–428.

Geier, J. D., Ed., *Fast Reactor Test Facility (FARET). Vol. I. Description and Program*, ANL-7168 (March 1966).

Geier, J. D., Ed., *Fast Reactor Test Facility (FARET). Vol. II—Summary of Preliminary Safety Analysis*, ANL-7168, Vol. II (April 1966).

Helm, F. H. and Travelli, A., *Calculation of the Sodium-Void Effect in Large Carbide Cores*, Proc. Intern. Conference on Fast Critical Experiments and Their Analysis, Argonne National Laboratory, October 10–13, 1966. ANL-7320, pp. 369–374.

Hub, K. A., Charak, I., Lutz, D. E., Thompson, D. H., Gast, P. F., Meneley, D. A., and Keyfitz, I. M., *Feasibility Study of Nuclear Steam Supply System Using 10,000-MW Sodium-Cooled Breeder Reactor*, ANL-7183, (September 1966).

Hwang, R. N. and Ott, K., *Comparison and Analysis of Theoretical Doppler-Coefficient Results for Fast Reactors*, ANL-7269 (December 1966).

Jason, R. H., *The Role of the Adjoint Flux in Determining Reactor Stability*, ANL-7189 (March 1966).

Karam, R. A., Ancarani, A., Helm, F. H., Kato, W. Y., Main, G. W., and Rusch, G. K., *Experimental Verification of Reactor Physics Parameters of Zoned Cores*, Proc. Intern. Conference on Fast Critical Experiments and Their Analysis, Argonne National Laboratory, October 10–13, 1966. ANL-7320, pp. 403–422.

Karam, R. A., Ancarani, A., Helm, F. H., Kato, W. Y., Main, G. W., and Rusch, G. K., *Measured Physics Parameters in a Zoned Fast Uranium Carbide Core Assembly 4Z*, ANL-7281 (December 1966).

Knapp, W. G. and Doerner, R. C., *Physics Measurements with Modified Diluent Compositions in Tungsten-Based, Aluminum-Reflected Fast Reactors*, ANL-7207 (February 1967).

Link, L. E., Ayer, J. E., Butler, D. K., Hub, K. A., Loewenstein, W. B., Mecham, W. J., Meneghetti, D., Thompson, D. H., Trice, V. G., and Weills, J. T., *1000-MW(e) Metal-Fueled Fast Breeder Reactor*, ANL-7001 (June 1966).

Lister, D. B., Smith, A. B., and Dunford, C., *Fast Neutron Scattering from the 182, 184, and 186 Isotopes of Tungsten*, ANL-7288 (January 1967).

MacFarlane, D. R., *An Analytic Study of the Transient Boiling of Sodium in Reactor Coolant Channels*, ANL-7222 (June 1966).

Meneghetti, D., *Calculational Studies of Sodium-Void Reactivity Variations due to Thin Slab Heterogeneities in Fast Critical Assemblies*, Proc. Intern. Conference on Fast Critical Experiments and Their Analysis, Argonne National Laboratory, October 10–13, 1966. ANL-7320, pp. 377–385.

Meneley, D. A., Kvitek, L. C., and O'Shea, D. M., *MACH 1, a One-Dimensional Diffusion-Theory Package*, ANL-7223 (June 1966).

O'Shea, D. M., Toppel, B. J., and Rago, A. L., *The Automated Preparation of Multigroup Cross Sections for Fast Reactor Analysis Using the MC² Code*, Proc. Intern. Conference on Fast Critical Experiments and Their Analysis, Argonne National Laboratory, October 10–13, 1966. ANL-7320, pp. 27–32.

Persiani, P. J., Hess, A. L., and Kucera, D. A., *The Critical Experiments and Preliminary Analysis of Multifueled, Nonuniform Core Loadings for the FARET Program*, Proc. Intern. Conference on Fast Critical Experiments and Their Analysis, Argonne National Laboratory, October 10–13, 1966. ANL-7320, pp. 550–559.

Redman, W. C., Ed., *Proceedings of the International Conference on Fast Critical Experiments and Their Analysis, Argonne National Laboratory, October 10-13, 1966*, ANL-7320.

Rusch, G. K. and Karam, R. A., *Analysis for Large Fast Critical Assemblies (ZPR-6 and ZPR-9)*, ANL-6721 Addendum (July 1966).

Rusch, G. K., Karam, R. A., Kato, W. Y., and Main, G. W., *Physics Parameters of Large Dilute Uranium Carbide Cores*, Proc. Intern. Conference on Fast Critical Experiments and Their Analysis, Argonne National Laboratory, October 10–13, 1966. ANL-7320, pp. 231–236.

Smith, A. B. and Hayes, R. R., *Fast Neutron Scattering from Elemental Mo, Sn, Sb, and Te*, ANL-7274 (November 1966).

Till, C. E., Lewis, R. A. and Hwang R. N., *ZPR-6 Doppler Measurements and Comparisons with Theory*, Proc. Intern. Conference on Fast Critical Experiments and Their Analysis, Argonne National Laboratory, October 10–13, 1966. ANL-7320, pp. 319–333.

Toppel, B. J., Vogelberger, P. J., and Wimunc, E. A., *Safety Analysis Associated with the Plutonium Recycle Experiment in EBWR*, ANL-6841 (November 1966).

Travelli, A., *A Comment on the Comparison of Theoretical with Experimental Neutron Spectra in Fast Critical Assemblies*, Proc. Intern. Conference on Fast Critical Experiments and Their Analysis, Argonne National Laboratory, October 10–13, 1966. ANL-7320, pp. 481–485.

*Abstracts*

Adkins, C. R., Persiani, P. J., and Hwang, R. N., *The Crystalline Effects on the Doppler-Broadened Cross Section and Resonance Integrals of Uranium in a $UO_2$ Lattice*, Trans. Am. Nucl. Soc. **10**(1), 228 (June 1967).

Ancarani, A., *Fission Rates in a Zoned-Core Fast Critical Assembly*, Trans. Am. Nucl. Soc. **10**(1), 275 (June 1967).

Ancarani, A., *Uranium-238 Fission Distribution Using Strip and Foils in a Fast Assembly*, Trans. Am. Nucl. Soc. **9**(2), 492 (1966).

Bennett, E. F., *Experimental Neutron-Spectrum Comparison for a Zoned and a Homogeneous Fast Critical Assembly*, Trans. Am. Nucl. Soc. **10**(1), 271 (June 1967).

Cohn, C. E., *Fast-Reactor Noise Analysis with an On-Line Digital Computer*, Trans. Am. Nucl. Soc. **10**(1), 285 (June 1967).

Cox, S. A., *Possible Intermediate Structure in Elastic Neutron Scattering*, Bull. Am. Phys. Soc. **12**, 107 (January 1967).

Dickerman, C. E., *Use of Present TREAT Core as a Fast-Flux Loop-Meltdown Facility*, Trans. Am. Nucl. Soc. **9**(2), 551 (1966).

Dickerman, C. E., Robinson, L. E., and Stewart, R. R., *Photographic TREAT Fast-Reactor Safety Experiments on Irradiated Oxide Pins*, Trans, Am. Nucl. Soc. **9**(2), 396 (1966).

Gold, R., *$C^{14}$ Production Rate Near Sea-Level*, Bull Am. Phys. Soc. **12**, 591 (April 1967).

Gold, R., Armani, R. J., Roberts, J. H., and Behkami, A., *Accurate Determination of Very Long Spontaneous Fission Half-Lives ($\gtrsim 10^{14}$ yr) by Fission Track Counting*, Bull. Am. Phys. Soc. **11**, 825 (December 1966).

Gozani, T., Moore, R. A., Neill, J. M., and Main, G. W., *Experimental Kinetic Studies on Depleted-Uranium Sphere*, Trans. Am. Nucl. Soc. **10**(1), 280 (June 1967).

Graham, W. W., Harmer, D. S., and Cohn, C. E., *Accurate Delayed-Neutron Parameter Measurements in a Heavy-Water Reactor*, Trans. Am. Nucl. Soc. **9**(2), 465 (1966).

Iskenderian, H. P., *The Effectiveness of Control-Rod Materials*, Trans. Am. Nucl. Soc. **10**(1), 180 (June 1967).

Karam, R. A., *Measurement of the Spatial Distribution of the Importance of Fission Neutrons in a Fast Reactor*, Trans. Am. Nucl. Soc. **9**(2), 490 (1966).

Karam, R. A. and LeSage, L. G., *Zoned-Core Concepts*, Trans. Am. Nucl. Soc. **10**(1), 270 (June 1967).

Karam, R. A., Kato, W. Y., Main, G. W., and Rusch, G. K., *Measured Sodium Void Coefficient and Fission Ratios in a Large Zoned Fast Reactor*, Trans. Am. Nucl. Soc. **9**(2), 487 (1966).

Kier, P. H., Toppel. B. J., and Jones, R. F., *Initial Critical Experiments of the EBWR Plutonium Recycle Program*, Trans. Am. Nucl. Soc. **9**(2), 446 (1966).

Knapp, W. G., *Measurement of Space-Dependent Material Reactivity Worths*, Trans. Am. Nucl. Soc. **10**(1), 272 (June 1967).

Lewis, R. A. and Till, C. E., *Analysis of Small-Sample Doppler-Effect Measurements*, Trans. Am. Nucl. Soc. **10**(1), 274 (June 1967).

Lewis, R. A., Till, C. E., Groh, E. F., LeSage, L. G., and Marshall, J. E., *Verification of Doppler Measurements in Zoned Fast Critical Assemblies*, Trans. Am. Nucl. Soc. **10**(1), 273 (June 1967).

Long, J. K., Hess, A. L., McVean, R. L., Persiani, P. J., Ulrich, A. J., Baird, Q. L., Bennett, R. A., and Engstrom, S. L., *FFTF Critical Experiments—Control-Rod Studies on ZPR-3* Trans. Am. Nucl. Soc. **10**(1), 269 (June 1967).

MacFarlane, D. R., *Theoretical Studies of the Transient Boiling of Sodium in Fast-Reactor Coolant Channels*, Trans. Am. Nucl. Soc. **10**(1), 354 (June 1967).

Marciniak. T. J., *Study of a Linearized Sampled-Data Control Algorithm for Zero-Power Reactors*, Trans. Am. Nucl. Soc. **10**(1), 312 (June 1967).

Plumlee, K. E., *Improved Neutron Cross Section for Formation of 60-Day Half-Life $Sb^{124}$*, Trans. Am. Nucl. Soc. **10**(1), 226 (June 1967).

Robinson, L. E., Purviance, R. T., and Willis, F. L., *Results from High Specific Energy Input Single-Pin, Sodium Loop Meltdown Experiments in TREAT*, Trans. Am. Nucl. Soc. **10**(1), 343, (June 1967).

Robinson, W. R., Johnson, T. W., Plumlee, K. E., and Stanford, G. S., *Experiments in the Internal Thermal Column of the Argonne Advanced Research Reactor Critical Facility*, Trans. Am. Nucl. Soc. **10**(1), 182 (June 1967).

Rossin, A. D., Kirn, F. S., Armani, R. J., and Smith, D. M., *Fast-Neutron Spectra and Radiation Damage Rates in EBR-II*, Trans. Am. Nucl. Soc. **10**(1), 129 (June 1967).

Sargis, D. A., *Error Estimates for Approximate Eigenvalues to the Integral Transport Equation*, Trans. Am. Nucl. Soc. **10**(1), 170 (June 1967).

Smith, A. B., and Whalen, J. F., *Fast-Neutron Processes and Possible Intermediate Resonance Structure*, Bull. Am. Phys. Soc. **12**, 107 (January 1967).

Stanford, G. S. and Johnson, T. W., *TLD Measurement of Gamma-Ray Heating in the AARR Critical Assembly*, Trans. Am. Nucl. Soc. **10**(1), 395 (June 1967).

Stephany, W. P. and Dickerman, C. E., *Analyses of Behavior of EBR-II-Type Pins under Transient Heating in Sodium Environment*, Trans. Am. Nucl. Soc. **10**(1), 343 (June 1967).

Takeuchi, K., *Fine Structure of Doorway States*, Bull. Am. Phys. Soc. **12**, 66 (June 1967).

Till, C. E., Lewis, R. A., and Pond, R. B., *Doppler Coefficient Temperature Dependence and the Effect of Sodium-Voiding*, Trans. Am. Nucl. Soc., **10**(1), 335 (June 1967).

Travelli, A. and Helm. F. H., *Calculation of the Sodium-Void Effect by Flux Synthesis*, Trans. Am. Nucl. Soc. **10**(1), 275 (June 1967).

ARGONNE NATIONAL LAB WEST
3 4444 00011590 7